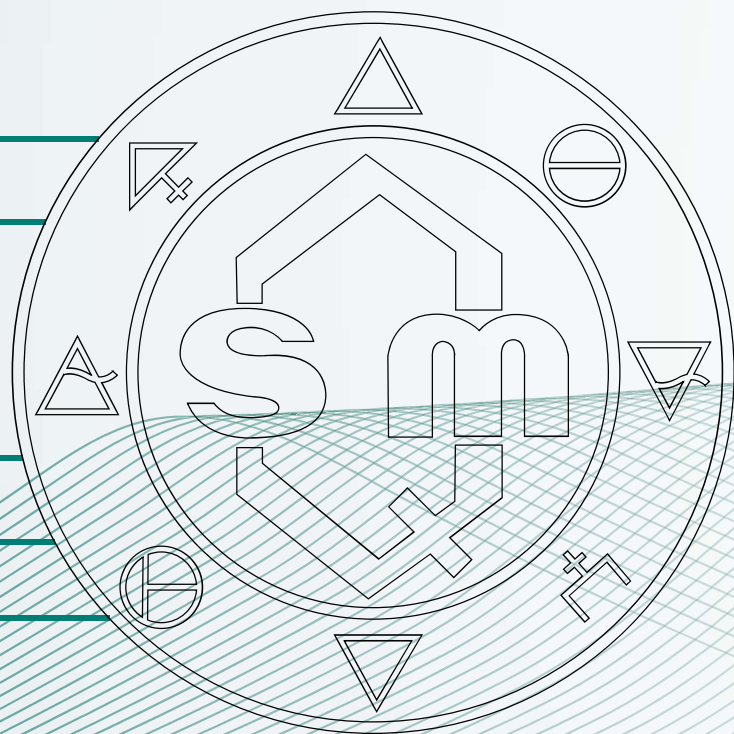


JOURNAL *of the* MEXICAN CHEMICAL SOCIETY

(J. Mex. Chem. Soc.)

Former Revista de la Sociedad Química de México (Rev. Soc. Quím. Mex.)



*Special Issue
Celebrating 50 years of Chemistry at the Universidad Autónoma Metropolitana
Part 1*

J. Mex. Chem. Soc.

Volume 68

Issue 4

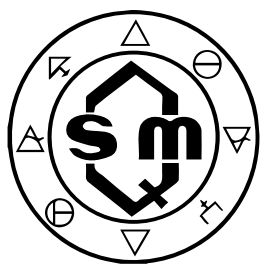
October-December

Year 2024

Quarterly publication

www.jmcs.org.mx

Mexico City



JOURNAL *of the* MEXICAN CHEMICAL SOCIETY

(J. Mex. Chem. Soc.)

Former Revista de la Sociedad Química de México (Rev. Soc. Quím. Mex.)



Special Issue

*Celebrating 50 years of Chemistry at the Universidad Autónoma Metropolitana
Part 1*

J. Mex. Chem. Soc.

Volume 68

Issue 4

October-December

Year 2024

Quarterly publication

www.jmcs.org.mx

Mexico City

The *Sociedad Química de México* was founded in 1956 as a non-profit association to promote the development of the professionals and students of chemistry in education, research, services and industry, and for the diffusion of chemical knowledge. The *Sociedad Química de México* organizes annually the *Mexican Congress of Chemistry* and the *National Congress of Chemical Education*, both congresses include activities of current interest for professionals and students of the chemical sciences. It grants annually the “*Andrés Manuel del Río*” *National Award of Chemistry* in the Academic area (field of research and field of education) and in the Technological area (field of technological development). It also grants each year the *Rafael Illescas Frisbie Best Bachelor, Master and Doctoral Thesis in Chemical Sciences Awards* and the biennial *Award of the Sociedad Química de México in honor of the Doctor Mario J. Molina, directed to the professionals in Chemistry Sciences*.

The *Journal of the Mexican Chemical Society* (*J. Mex. Chem. Soc.*) is the official journal of the *Sociedad Química de México*, it was published as *Revista de la Sociedad Química de México* (*Rev. Soc. Quím. Mex.*) from 1957 to 2003, changing its name in 2004. The *Journal of the Mexican Chemical Society* (*J. Mex. Chem. Soc.*) is a scientific, blind, peer reviewed, and open access, free of charge publication that covers all areas of chemistry and its sub-disciplines (i.e. medicinal chemistry, natural products, electrochemistry, material science, computational chemistry, organic chemistry, bioinorganic chemistry, etc). It is devoted to facilitating the worldwide advancement of our understanding of chemistry. It will primarily publish original contributions of research in all branches of the theory and practice of chemistry in its broadest context as well as critical reviews in active areas of chemical research where the author has published significant contributions. The *J. Mex. Chem. Soc.* is a quarterly publication in which language of submission and publication is English. To be suitable for publication in *J. Mex. Chem. Soc.*, manuscripts must describe novel aspects of chemistry, high quality of results and discussion an excellent bibliographic support, and contribute to the development of the field. Routine or incremental works are not suitable for publication in *J. Mex. Chem. Soc.* Authors are encouraged to send contributions in electronic form. Our online submission system guides you stepwise through the process of entering your article details and uploading your files. The *Sociedad Química de México* also publishes since 2007 articles of general interest in the *Boletín de la Sociedad Química de México*.

La *Sociedad Química de México* fue fundada en 1956 como una agrupación sin fines de lucro para promover el desarrollo de los profesionales y estudiantes de la química en las áreas educativa, investigación, servicios e industria, y para difundir el conocimiento de la química. La *Sociedad Química de México* organiza anualmente el *Congreso Mexicano de Química* y el *Congreso Nacional de Educación Química*, en los cuales se desarrollan diversas actividades de interés para los profesionales y estudiantes de las ciencias químicas. Asimismo, otorga anualmente el *Premio Nacional de Química “Andrés Manuel del Río”* en el área Académica (campos de docencia e investigación) y en el área Tecnológica (campo de Desarrollo Tecnológico). También otorga anualmente el *Premio a las Mejores Tesis de Licenciatura, Maestría y Doctorado en Ciencias Químicas, Rafael Illescas Frisbie*. De manera bienal otorga el *Premio de la Sociedad Química de México en Honor al Doctor Mario J. Molina, dirigido a los profesionistas de las Ciencias Químicas*.

El *Journal of the Mexican Chemical Society* (*J. Mex. Chem. Soc.*), es la revista oficial de la *Sociedad Química de México*. Desde 1957 y hasta 2003 fue publicada como *Revista de la Sociedad Química de México* (*Rev. Soc. Quím. Mex.*), cambiando su nombre en 2004. Es una publicación trimestral que tiene como objetivo coadyuvar al avance del entendimiento de la química; las instrucciones para los autores aparecen en cada fascículo. La *Sociedad Química de México* también publica desde 2007 artículos de interés general en el *Boletín de la Sociedad Química de México*

Journal of the Mexican Chemical Society
(*J. Mex. Chem. Soc.*)

ISSN-e: 2594-0317
ISSN 1870-249X

former

Revista de la Sociedad Química de México
(*Rev. Soc. Quím. Mex.*)

ISSN 0583-7693

Journal of the Mexican Chemical Society (*J. Mex. Chem. Soc.*)

Quarterly publication.

Editor-in-Chief: Prof. Alberto Vela Amieva

Indexed Journal

Certificate of reserved rights granted by the Instituto Nacional del Derecho de Autor (INDAUTOR): 04-2005-052710530600-102

Certificate of lawful title and content: Under procedure

Postal registration of printed matter deposited by editors or agents granted by SEPOMEX: IM09-0312

Copyright © Sociedad Química de México, A.C.

Total or partial reproduction is prohibited without written permission of the right holder.

The Figures/schemes quality and the general contents of this publication including referencing, are full responsibility of the authors.

Edited and distributed by Sociedad Química de México, A.C.

Barranca del Muerto 26, Col. Crédito Constructor,

Del. Benito Juárez, C.P. 03940, Mexico City.

Phone: +5255 56626837; +5255 56626823

Contact: soquimex@sqm.org.mx

<https://www.sqm.org.mx>

Editorial assistance: jmcs@sqm.org.mx

<https://www.jmcs.org.mx>



Table of Contents

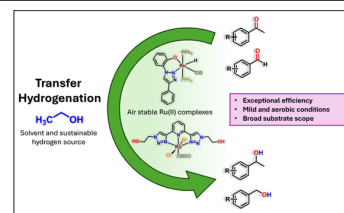
Editorial

50 years of Chemistry at the Universidad Autónoma Metropolitana

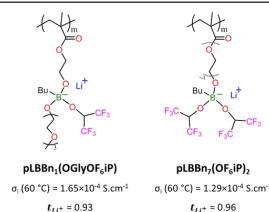
iv-v Julio César Almanza-Pérez, Jorge Garza, Ignacio González, Gregorio Guzmán-González, J. Alberto Ochoa-Tapia

Articles

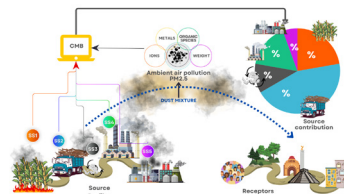
- 545-558 **Air-Stable Triazole-Based Ru(II) Complexes Catalyzed Transfer Hydrogenation of Ketones and Aldehydes Using Ethanol as a Solvent and a Hydrogen Donor**
Evelyn Vega Sánchez, Ricardo Corona Sánchez, Atilano Gutiérrez-Carrillo I, Mónica A. Rincón-Guevara I, Lucero González-Sebastián*



- 559-575 **Effect of the Linker and Substituents on the Ionic Conductivity of Borate Single-Ion Polymers for Lithium Batteries**
Soline Vauthier, Stéphane Cotte, Laurent Castro, Aurélie Guéguen, Nerea Casado, David Mecerreyes, Gregorio Guzmán-González*



- 576-592 **Fine particles composition and emission chemical profiles from sugarcane production for source reconciliation applying the Chemical Mass Balance**
Violeta Mugica-Álvarez, Fernando Millán-Vázquez, José de Jesús Figueroa-Lara, Brenda L. Valle-Hernández, Xavier Querol, Francisco Hernández-Rosas



continues...

* The asterisk indicates the name of the author to whom inquiries about the paper should be addressed.

Table of Contents

Articles

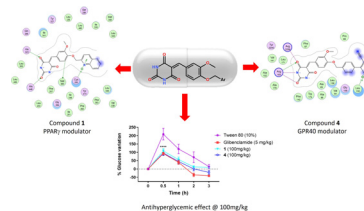
Antimicrobial and Antioxidant Activities of Four Essential Oils

593-608 Ana Laura Esquivel-Campos, Leonor Sánchez-Pérez, Marco Martín González-Chávez, Aranza Reyes-Ponce, Ernesto de Jesús Zapata-Flores, Salud Pérez-Gutiérrez*, Julia Pérez-Ramos*



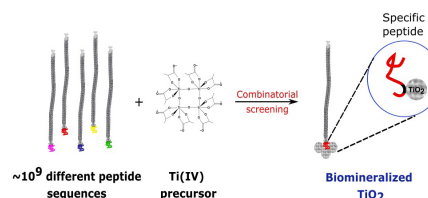
Design and Synthesis of Barbiturates and Hydantoins with Multitarget Antidiabetic Effect

609-623 Samantha Juárez-Cruz, Samuel Estrada-Soto, Blanca Colín-Lozano, Hugo Marquina-Rodríguez, Thalía Delgado-Aguilar, Carlos Martínez-Conde, Abraham Gutiérrez-Hernández, Emanuel Hernández-Núñez, Abraham Giacoman-Martínez, Julio Cesar Almanza-Pérez, Gabriel Navarrete-Vázquez*



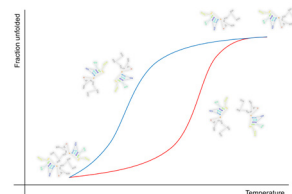
Biopanning Phage Display Libraries in Homogeneous Solution for Identification of Biomining Peptides of TiO₂

624-635 Armin Hernández-Gordillo, Andrés Hernández-Arana, L. Irais Vera-Robles*



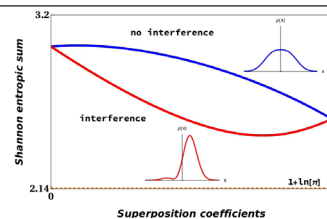
Gaining Insights into Folding/Unfolding Protein Structures and their Importance for Several Applications: Historical Research Generated in the Biophysical Chemistry Area

636-655 Arturo Rojo-Domínguez*, Leonardo D. Herrera-Zúñiga*



Entropic Uncertainty Relations and Mutual Information Correlation Sums in Two-level Superposition States of Coupled Oscillators

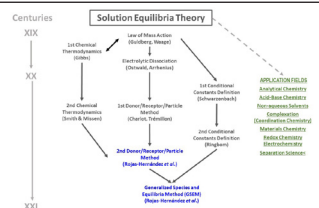
656-670 Saúl J. C. Salazar, Humberto G. Laguna, Angel García-Chung, Robin P. Sagar



Historical Reviews

Towards a Mexican School of General Analytical Chemistry

671-684 Alberto Rojas-Hernández*, María Teresa Ramírez-Silva, Annia Galano



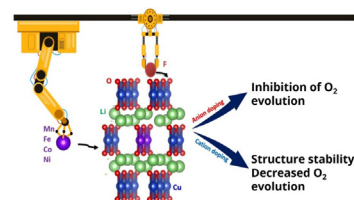
* The asterisk indicates the name of the author to whom inquiries about the paper should be addressed.

Table of Contents

Reviews

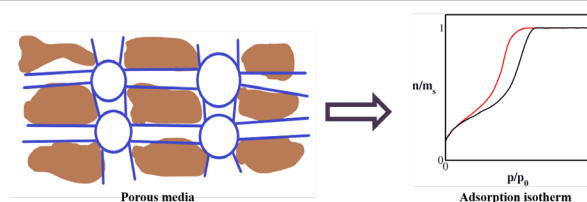
852-865 **A Review of Mexican Contributions to Li_2CuO_2 and its Chemical Modifications as Cathode Materials for Lithium-Ion Batteries**

B. A. García-Carrillo, A de J Martínez, E. L. Jiménez-Cabañas, MA Martínez Cruz, C. Juárez-Yescas*, G. Ramos-Sánchez**



866-887 **Review: Description of Porous Media and their Sorption Characteristics as Correlated Structures**

Salomón Cordero-Sánchez, Juan M. Esparza-Schulz, Ilich A. Ibarra, Víctor M. Trejos, Annabel L. Tellez-Gonzalez, Juan Villegas-Cortez, Graciela Román-Alonso, Salomón J. Alas*

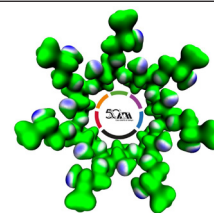


888-969 **Molecular Insights on Coffee Components as Chemical Antioxidants**

*Luis Felipe Hernández-Ayala, Eduardo Gabriel Guzmán-López, Adriana Pérez-González, Miguel Reina, Annia Galano**

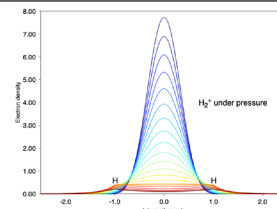
970-980 **Exploring Intermolecular and Intramolecular Interactions: A Review beyond Hydrogen Bonds**

Rubicelia Vargas, Jorge Garza, Ana Martínez*



981-995 **Contributions from UAM-Iztapalapa to the Study of Confined Atoms and Molecules**

Norberto Aquino, Salvador Cruz*, Jorge Garza*, Rubicelia Vargas**



* The asterisk indicates the name of the author to whom inquiries about the paper should be addressed.

50 years of Chemistry at the Universidad Autónoma Metropolitana

Julio César Almanza-Pérez^{1,*}, Jorge Garza^{2,*}, Ignacio González^{2,*}, Gregorio Guzmán-González^{2,*}, J. Alberto Ochoa-Tapia^{3,*}

¹Departamento de Ciencias de la Salud. División de Ciencias Biológicas y de la Salud. Universidad Autónoma Metropolitana-Iztapalapa. Av. Ferrocarril San Rafael Atlixco 186. Col. Leyes de Reforma 1ª Sección, 09310 Iztapalapa. Ciudad de México. México.

²Departamento de Química. División de Ciencias Básicas e Ingeniería. Universidad Autónoma Metropolitana-Iztapalapa. Av. Ferrocarril San Rafael Atlixco 186. Col. Leyes de Reforma 1ª Sección, 09310 Iztapalapa. Ciudad de México. México.

³Departamento de Ingeniería de Procesos e Hidráulica. División de Ciencias Básicas e Ingeniería. Universidad Autónoma Metropolitana-Iztapalapa. Av. Ferrocarril San Rafael Atlixco 186. Col. Leyes de Reforma 1ª Sección, 09310 Iztapalapa. Ciudad de México. México.

***Guest editors:** Julio César Almanza Pérez, email: jcap@xanum.uam.mx. Jorge Garza, email: jgo@xanum.uam.mx. Ignacio González, email: igm@xanum.uam.mx. Gregorio Guzmán-González, email: gguzmang@izt.uam.mx. J. Alberto Ochoa-Tapia, email: jaot@xanum.uam.mx

DOI: <http://dx.doi.org/10.29356/jmcs.v68i4.2360>

Fundamental chemistry and applied chemistry have played important roles in our country. For the past 50 years, the Universidad Autónoma Metropolitana (UAM) has contributed in both directions, initiating impactful projects and often addressing societal issues. In fundamental chemistry, new methodologies have been developed from an experimental standpoint, from the perspective of theoretical methods, or even from both viewpoints. From an applied perspective, projects have been developed that have culminated in the filing of patents or the creation of industrial prototypes.

For these reasons, this special issue of the *Journal of the Mexican Chemical Society (J.Mex. Chem.Soc.)* features contributions from various perspectives, each with a unique touch from the research groups responsible for the respective publications. *These contributions are organized in different sections: Perspectives, Historical Reviews, Full articles, Overviews, and Reviews.* It is important to note that within UAM, there is only one Department of Chemistry. However, chemistry as a discipline is developed across various departments

and different campuses of our institution. For this reason, the Guest Editors of this special issue belong to different Divisions of the Iztapalapa campus, *developing research activities in various disciplines associated with chemistry, which guarantees to have to a broad perspective on the reception of articles, especially during the peer review process that was carried out for all the articles received.*

Thus, the audience will find articles of different natures. For example, topics range from biological systems to highly theoretical subjects like fundamental quantum chemistry. *This diversity represents the varied chemistry topics developed at the UAM by highly consolidated research groups and their collaborators.* It is essential to mention that the reviewers involved in this special issue are from different institutions around the world, as is usually the case in a scientifically rigorous journal like the *J.Mex.Chem.Soc.* Therefore, the content presented in this special issue has been carefully reviewed with cutting-edge topics.

In order to publish the highest number of articles received by the deadlines proposed by the

publisher, it was necessary to divide the special issue into two parts. The first part will be the last number of **2024**, corresponding to Volume 68, issue 4, and the second will be the first number of **2025**, corresponding to Volume 69, issue 1. The selection of articles for each issue has been carried out with the idea of showing the diversity of the specialties of chemistry trying to balance the fundamental and applied contributions.

The Guest Editors of this special issue of the *Journal of the Mexican Chemical Society* extend their gratitude to all the authors, reviewers, and the editorial team of this journal for their efforts. We hope that the published articles are well received and that the lines of research involved demonstrate their impact over the next 50 years. *Long live UAM.*

Mexico City, October 2024.

Guest editors

Julio César Almanza-Pérez
Jorge Garza
Ignacio González
Gregorio Guzmán-González
J. Alberto Ochoa-Tapia

Air-Stable Triazole-Based Ru(II) Complexes Catalyzed Transfer Hydrogenation of Ketones and Aldehydes Using Ethanol as a Solvent and a Hydrogen Donor

Evelyn Vega Sánchez¹, Ricardo Corona Sánchez², Atilano Gutiérrez-Carrillo¹, Mónica A. Rincón-Guevara¹, Lucero González-Sebastián^{1,*}

¹Universidad Autónoma Metropolitana, Departamento de Química, Av. San Rafael Atlixco 186, Leyes de Reforma 1ra Secc., Ciudad de México, C.P. 09340. México.

²Universidad Autónoma Metropolitana, Departamento de Ciencias Básicas. Av. San Pablo No. 420, Azcapotzalco, Ciudad de México, C.P. 02128. México.

*Corresponding author: Lucero González-Sebastián, email: lucero.gs@xanum.uam.mx

Received May 29th, 2024; Accepted July 23rd, 2024.

DOI: <http://dx.doi.org/10.29356/jmcs.v68i4.2308>

Abstract. The synthesis and characterization of two air-stable ruthenium (II) complexes from readily available triazole-based ligands are described. Both ruthenium complexes, one bearing a bidentate ligand (**C-1**) and the other a tridentate ligand (**C-2**), were tested as catalysts in the transfer hydrogenation of ketones and aldehydes using ethanol as a sustainable hydrogen source under aerobic conditions. Notably, the **C-2** complex displayed exceptional efficiency under relatively mild conditions, demonstrating a wide substrate tolerance encompassing both alkyl and aryl ketones, as well as aryl aldehydes. Furthermore, our findings highlight the potential of Ru(II) complexes as effective catalysts for the hydrogenation of carbonyl bonds using ethanol, representing a green and sustainable approach without the necessity for an inert gas.

Keywords: Catalysis; transfer hydrogenation; ruthenium; triazole; ethanol.

Resumen. En este trabajo se describe la síntesis y caracterización de dos complejos de rutenio(II) estables al aire con ligantes basados en triazoles. En general, los triazoles pueden obtenerse fácilmente a través de reacciones simples utilizando reactivos comercialmente disponibles. Ambos complejos de rutenio, uno con un ligante bidentado (**C-1**) y el otro con un ligando tridentado (**C-2**), se probaron como catalizadores en reacciones de hidrogenación por transferencia de cetonas y aldehídos, utilizando etanol como fuente sostenible de hidrógeno en condiciones aeróbicas. En particular, el complejo **C-2** mostró una eficiencia excepcional en condiciones relativamente suaves, demostrando una amplia tolerancia tanto con cetonas alquílicas como aromáticas, además de hidrogenar eficientemente aldehídos aromáticos. Estos resultados ponen de manifiesto el potencial de los complejos de Ru(II) como catalizadores eficaces para la hidrogenación de enlaces carbonilo utilizando etanol, lo que representa un enfoque ecológico y sostenible sin necesidad de un gas inerte.

Palabras clave: Catálisis; hidrogenación por transferencia; rutenio; triazol; etanol.

Introduction

Transition metal-catalyzed transfer hydrogenation reactions are among the most effective methods for reducing unsaturated C=O, C=N, and C=C bonds. [1] This process offers significant advantages over traditional catalytic hydrogenation, as it eliminates the need for molecular hydrogen, high-pressure reactors, and harsh reaction conditions, thereby enhancing safety and convenience in both laboratory and industrial settings. In essence, transfer hydrogenation involves the transfer of a proton and a hydride from the donor molecule to the unsaturated substrate. Various hydrogen donors, such as alcohols,[2] formic acid,[3] and water,[4] have been employed in transfer hydrogenation reactions. These donors are not only inexpensive and readily available, but also much safer to handle than molecular hydrogen.

Among the non-H₂ hydrogen sources in transfer hydrogenation, alcohols have emerged as effective hydrogen donors.[2] Isopropanol, in particular, is the most commonly used hydrogen source for reducing a wide range of substrates, as its oxidized product, acetone, can be easily removed from the reaction mixture. Unlike secondary alcohols, primary alcohols have an unfavorable redox potential and are generally oxidized to aldehydes, which are much more reactive than the acetone obtained from isopropanol.[5] Consequently, the use of primary alcohols as hydrogen sources is limited compared to secondary alcohols. However, primary alcohols such as methanol and ethanol are very attractive in terms of sustainability, as they can be obtained from renewable biomass, natural gas, or carbon dioxide.[6] The use of primary alcohols in transfer hydrogenation remains challenging due to various limitations. For instance, methanol produces formaldehyde as a by-product, which under strong reaction conditions can generate carbon monoxide, potentially poisoning the catalyst. Additionally, formic acid, another by-product, can neutralize the base commonly used in these catalytic transformations.[6]

In this context, over the last few decades, a wide variety of homogeneous transition metal catalysts, including noble metals such as ruthenium,[7-9] rhodium,[10-13] and iridium,[14-16] as well as more cost-effective options like nickel,[17] cobalt,[18] iron [19] and others, have been developed for catalytic transfer hydrogenation reactions.[19-21] In general, catalytic systems employing precious metals tend to perform effectively under relatively milder conditions compared to those based on non-precious metals. Interestingly, catalysts based on ruthenium have shown remarkable catalytic activity in the activation of alcohols and their subsequent use as a hydrogen source in the hydrogenation of carbonyl bonds.[7-9]

Since Grützmacher and co-workers reported the use of ethanol as the hydrogen source in transfer hydrogenation reactions in 2008,[22] numerous studies on ruthenium-catalyzed transfer hydrogenations utilizing ethanol have been conducted (Fig. 1). For example, in 2016, Khaskin et al. employed a Ru(II)-phosphine catalyst bearing a tridentate SNS ligand (**A**) for the transfer hydrogenation of esters using ethanol at 80 °C in the presence of a strong base (KO^tBu) and toluene as the solvent.[23] Two years later, Weingart and Thiel reported on a Ru(II)-phosphine complex featuring a tridentate NNN ligand (**B**) for the reduction of aldehydes and ketones with ethanol using a strong base under a constant N₂ flow at 40°C, yielding satisfactory results.[24] However, it's worth noting that the use of strong bases in transfer hydrogenation is not ideal due to the possibility of aldehydes undergoing ketone α -alkylation, leading to non-selective reactions.[25]

Subsequently, Bagh's group reported the use of a Ru(II) complex with a triazole-based ligand (**C**) as an effective catalyst for the transfer hydrogenation of a large number of aldehydes and ketones bearing various functional groups using both methanol and ethanol under aerobic conditions and relatively mild conditions in the presence of potassium carbonate, utilizing alcohol as both the solvent and the hydrogen source, resulting in excellent yields.[5] In 2022, Gong et al. developed a bidentate Ru(II)-NC (**D**) catalyst effectively catalyzing the transfer hydrogenation from azoarenes to hydrazoarenes with excellent selectivity.[25] They used 3 mol % of catalyst with a weak base and ethanol as the hydrogen source at 120 °C for 24 hours under an inert atmosphere.

Recently, Wang et al. also used the same Ru(II)-NC (**D**) catalyst for transfer hydrogenation of ketones using ethanol under weak base conditions. In this catalytic protocol, the reactions were carried out under an argon atmosphere at 120 °C for 5 hours using 10 mol% of catalyst. The results suggest that the reaction is almost as efficient when the reaction is carried out under air.[26] According to Albrecht et al., the transfer hydrogenation of ketones using ethanol could also be catalyzed by an air-stable, coordinatively unsaturated ruthenium (II) complex (**E**), reaching 66 % and 40 % yields with ethanol and methanol, respectively, after 24 hours at 80 °C.[27] Pratihari's research group has also reported the use of a waste shrimp shell-based tetrazene-Ru (II) *p*-cymene (**F**) catalyst for the transfer hydrogenation of aldehydes with ethanol.[28]

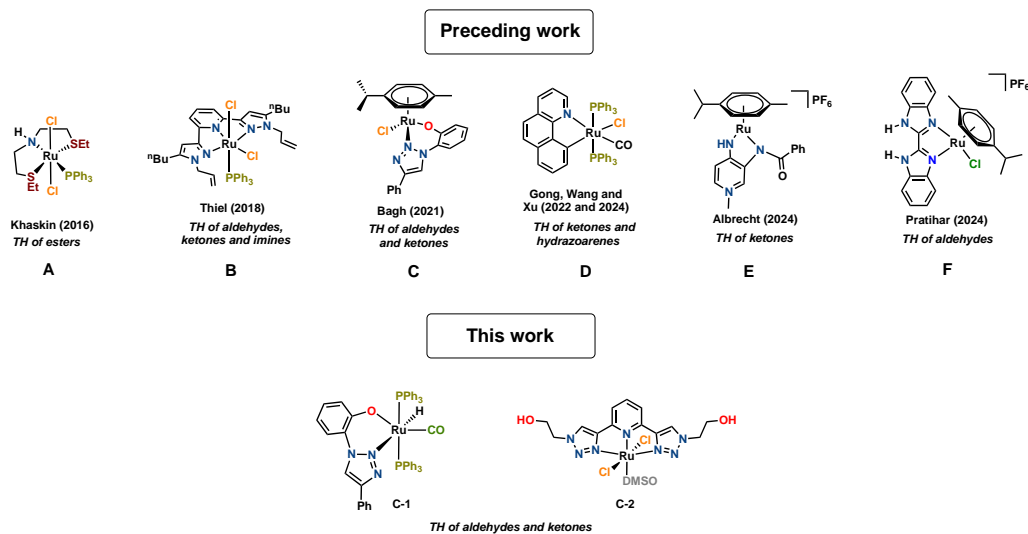


Fig. 1. Representative examples of well-defined ruthenium catalysts for the transfer hydrogenation (TH) of C=O, C=N and C=C bonds using ethanol as the hydrogen source.

As can be seen, the choice of ligands in ruthenium complexes as transfer hydrogenation catalysts plays a crucial role. In this regard, 1,2,3-triazoles, which can be easily synthesized via a copper(I)-catalyzed azide–alkyne cycloaddition reaction (CuAAC), have been extensively used as ligands in coordination chemistry. This is due to the presence of electron lone pairs on the triazole N2 and N3 atoms, which can coordinate with metal ions, forming stable metal complexes. Additionally, the predictable and modular composition of triazole-based ligands allows for fine-tuning of the steric and electronic properties of their metal derivatives by modifying the constituent substituent groups.

Motivated by the potential applications of ruthenium metal complexes and considering the importance of triazole ligands, we became interested in developing the chemistry of triazole-based ruthenium compounds. Ruthenium and triazole moieties form an effective combination for producing bioorganometallic compounds with potential biological and catalytic properties. In addition, given the growing demand for environmentally friendly methodologies and inspired by recent advancements in catalytic processes utilizing ethanol as a hydrogen source in transition metal-catalyzed transfer hydrogenations, herein, we disclose the synthesis and full characterization of two new air-stable triazole-based Ru(II) complexes and their catalytic evaluation in the homogeneous transfer hydrogenation of ketones and aldehydes under relatively mild conditions (1 mol% [Ru], 10 mol % of K₂CO₃ 90 °C, 3 and 24 h, in air), using ethanol as both the hydrogen source and solvent. This process produces secondary and primary alcohols in good to excellent yields with high selectivity.

Experimental

General considerations

Unless otherwise noted, all experiments were performed in air. All solvents were purchased from commercial suppliers and used without further purification. All other chemicals and filter aids were reagent grade and were used as received. Column chromatography was performed on silica gel (Merck, 230-700 mesh). Elemental analyses were performed in a Thermo Scientific Flash 2000 elemental analyzer. NMR experiments were recorded at 300 K on Bruker Avance DMX-500 (500 MHz) spectrometer using TMS or residual proton solvents as internal standard; and H₃PO₄ as external standard. The deuterated solvent used was CDCl₃ and DMSO-d₆; chemical shifts (δ) are quoted in ppm and coupling constants in Hz; to indicate the multiplicity of the signals of ¹H NMR spectra, the following abbreviations have been used: (s) singlet, (d) doublet, (t) triplet, (at) apparent

triplet, (m) multiplet, (dd) double doublet, (bs) broad signal. Catalysis products were quantified with a GC-MS Agilent 6890N chromatograph equipped with a 30 m DB-1MS Agilent capillary column, coupled to an Agilent Technologies 5973 Mass Spectrometer equipped with an Inert Mass Selective Detector. FTIR spectra of the samples were recorded using a Perkin–Elmer 600 spectrometer using the attenuated total reflectance (ATR) method. The absorbance peaks are reported in reciprocal centimeters (cm^{-1}). Mass Spectrometer equipped with an Inert Mass Selective Detector. Mass spectra were recorded on mass spectrometer model micrOTOF II (Bruker Daltonics Inc.) using the Compass platform (otofControl and DataAnalysis from Bruker Daltonics Inc.). Spectra were acquired in positive mode with a capillary voltage of 4500 V, nebulizer gas: 0.5 Bar, drying gas 4.0 L/min and a drying temperature of 150 °C.

Synthesis of ligands L1 and L2

Synthesis of ligand L1 (2-(4-phenyl-1H-1,2,3-triazol-1-yl)phenol)

Ligand **L1** was synthesized according to the literature procedure.[5,29] Sodium ascorbate (0.200 g, 1.0 mmol) and $\text{CuSO}_4 \cdot 5\text{H}_2\text{O}$ (0.025 g, 0.1 mmol) were added to a solution of 2-azidophenol (1.340 g, 10.0 mmol) in a 1:1 mixture of water and tert-butanol (50 mL). Thereafter, phenylacetylene (1.32 mL, 11.0 mmol) was added dropwise. The reaction mixture was stirred at 90 °C for 24 h. The resultant mixture was then added to ice-cold water (100 mL), resulting in the formation of a yellow-green precipitate. The yellow-green solid was isolated by filtration and then purified by column chromatography using silica gel and a 1:1 mixture of ethyl acetate and hexanes as eluent. The final product was isolated in 82 % yield as a light-yellow pure solid. ^1H NMR (500 MHz, CDCl_3) δ 9.89 (s, 1H), 8.30 (s, 1H), 7.93 – 7.89 (m, 2H), 7.52 – 7.45 (m, 3H), 7.44 – 7.37 (m, 1H), 7.32 (ddd, J = 8.3, 7.3, 1.5 Hz, 1H), 7.22 (dd, J = 8.3, 1.3 Hz, 1H), 7.03 (ddd, J = 8.1, 7.3, 1.4 Hz, 1H). ^{13}C NMR (126 MHz, CDCl_3) δ 149.6, 147.9, 129.9, 129.7, 129.2, 129.1, 126.2, 122.9, 120.4, 119.7, 119.5. ESI-TOF: 238.0971 $[(\text{M}+\text{H})]^+$ (100 %), calculated for $\text{C}_{14}\text{H}_{11}\text{N}_3\text{O}$: 237.0902.

Synthesis of ligand L2: (2-(4-(6-(1-(2-hydroxyethyl)-1 λ 4,2,3 λ 2-triazol-4-yl)pyridin-2-yl)-1H-1,2,3-triazol-1-yl)ethan-1-ol)

Ligand **L2** was synthesized in three steps using an adapted procedure documented previously.[30]

Synthesis of 2,6-bis((trimethylsilyl)ethynyl)pyridine: In the first step, 2,6-dibromopyridine **A** (2.13 g, 8.95 mmol), CuI (200 g, 1.05 mmol), and $\text{Pd}(\text{PPh}_3)_4$ (620 g, 0.88 mmol) were added to a 100 mL Schlenk flask. Then, 36 mL of anhydrous THF and 6 mL of Et_3N were added. The resulting yellow solution was stirred at room temperature under a nitrogen atmosphere for 15 minutes. Next, ethynyltrimethylsilane (2.19 g, 22.9 mmol) was added dropwise via syringe into the solution, and the reaction mixture was stirred under a nitrogen atmosphere for 10 hours. After the reaction time, the resulting mixture was added to a separatory funnel along with 10 mL of 1 M NH_4Cl aqueous solution and extracted with dichloromethane (3 x 20 mL). The organic phase was dried with Na_2SO_4 , filtered, and evaporated under reduced pressure, generating a brown solid. This solid was purified by flash chromatography using silica gel and a 5:95 mixture of EtOAc/Hexanes as eluent. The product, 2,6-bis((trimethylsilyl)ethynyl)pyridine, was isolated in 98.1 % yield as a light-brown solid. ^1H NMR (500 MHz, CDCl_3): δ 7.57 (dd, J = 8.1, 7.5 Hz, 1H), 7.36 (dd, J = 7.8, 0.3 Hz, 2H), 0.24 (s, 16H). ^{13}C NMR (126 MHz, CDCl_3) δ 143.5, 136.3, 126.8, 103.3, 95.5, 77.4, 77.2, 76.9, -0.2.

Synthesis of 2,6-diethynylpyridine, **B**: In the second step, 2,6-bis((trimethylsilyl)ethynyl)pyridine (1 g, 3.31 mmol) and 15 mL of dichloromethane were added to a round-bottom flask equipped with a magnetic stirrer. NaOH (530.3 mg, 13.25 mmol) dissolved in 15 mL of methanol was then added to the flask. The reaction mixture was stirred at room temperature for 30 minutes. After this time, the solvent was removed under reduced pressure, and the crude product was immediately purified by chromatography using silica gel and a 10:90 mixture of EtOAc/Hexanes as eluent. The product 2,6-diethynylpyridine, **B**, was isolated in 98 % yield as a light-yellow solid. ^1H NMR (500 MHz, CDCl_3) δ 7.62 (t, J = 7.8 Hz, 1H), 7.42 (d, J = 7.8 Hz, 2H), 3.14 (s, 2H). ^{13}C NMR (126 MHz, CDCl_3) δ 142.8, 136.6, 127.2, 82.2, 77.8.

In the final step, a 100 mL round-bottom flask was charged with 2,6-diethynylpyridine (250 mg, 1.966 mmol), $\text{CuSO}_4 \cdot 5\text{H}_2\text{O}$ (99.68 mg, 0.399 mmol), sodium ascorbate (158.18 mg, 0.7984 mmol), and 7.5 mL of $^t\text{BuOH}$. Then, 2-azidoethan-1-ol (3.937 mg, 4.52 mmol) in 7.5 mL of water was added. The reaction mixture was heated at 100 °C for 24 hours. After the reaction time, the resulting mixture was added to a separatory funnel along with 10 mL of 1 M NH_4Cl /EDTA aqueous solution and extracted with ethyl acetate (3 x 20 mL). The organic phase was

dried with Na₂SO₄, filtered, and evaporated to approximately 2/3 of the total volume under reduced pressure. A precipitate formed, which was filtered and washed with a minimum volume of cold ethyl acetate. Ligand **L2** was isolated in 86 % yield as a white crystalline solid. ¹H NMR (500 MHz, DMSO) δ 8.62 (s, 2H), 7.97 (s, 3H), 5.10 (s, 2H), 4.51 (t, *J* = 5.4 Hz, 4H), 3.86 (s, 4H), 3.33 (s, 1H). ¹³C NMR (126 MHz, DMSO) δ 150.0, 146.9, 138.1, 123.8, 118.2, 59.8, 52.5. ESI-TOF: 302.1359 [(M+H)]⁺ (100 %), calculated for C₁₃H₁₅N₇O₂: 301.1287.

Synthesis of ruthenium complexes C-1 and C-2

Synthesis of ruthenium complex C-1

A 100 mL round-bottom flask equipped with a magnetic stirring bar was charged with 200.0 mg (0.218 mmol) of [Ru(PPh₃)₃H₂CO]³¹, 39 mg (0.218 mmol) of ligand **L1** and 20 mL of THF. To this solution, 46 μL (0.744 mmol) of Et₃N was added, and the resulting reaction mixture was heated at 67 °C for 48 hours. The resulting solution was evaporated under reduced pressure, and the residue was purified by flash chromatography on silica gel using EtOAc/hexanes (20:80) as the eluent. Complex **C-1** was isolated as a white-off powder in 68 % yield. ¹H NMR (500 MHz, CDCl₃) δ 7.65 – 7.58 (m, 14H), 7.45 – 7.41 (m, 2H), 7.39 – 7.33 (m, 1H), 7.31 (s, 1H), 7.25 – 7.14 (m, 18H), 6.65 (ddd, *J* = 8.5, 6.9, 1.8 Hz, 1H), 6.50 (dd, *J* = 8.4, 1.4 Hz, 1H), 6.09 (dd, *J* = 8.0, 1.8 Hz, 1H), 6.03 (ddd, *J* = 8.1, 6.9, 1.4 Hz, 1H), -11.40 (t, *J* = 19.9 Hz, 1H). ¹³C NMR (126 MHz, CDCl₃) δ 204.7, (t, *J* = 15 Hz), 160.7, 147.3, 134.8 (at, *J* = 20.4 Hz), 134.2 (at, *J* = 6.0 Hz), 130.4, 129.1, 128.8, 128.3 (d, *J* = 5.4 Hz), 127.8 (at, *J* = 4.6 Hz), 126.2, 125.9, 125.8, 120.4, 116.9, 112.5. ³¹P{¹H} NMR (126 MHz, CDCl₃) δ 40.9. ESI-TOF: 892.1745 [(M+H)]⁺ (100 %), calculated for C₅₁H₄₁N₃O₂P₂Ru: 891.1742. Anal. Calcd. for **C-1**, C₅₁H₄₁N₃O₂P₂Ru: C, 68.76; H, 4.64; N, 4.72. Found: C, 68.75; H, 4.78; N, 4.75.

Synthesis of ruthenium complex C-2

A 100 mL round-bottom flask equipped with a magnetic stirring bar was charged with 117.4 mg (0.24 mmol) of [RuCl₂(CH₃SOCH₃)₄], 100 mg (0.24 mmol) of ligand **L2**, and 10 mL of THF. The resulting reaction mixture was heated at 67 °C for 24 hours. The solution was then evaporated under reduced pressure, and the residue was purified by flash chromatography on silica gel using CH₃OH/acetone (50:50) as the eluent. Complex **C-2** was isolated as an orange solid in 81.9 % yield. ¹H NMR (500 MHz, DMSO) δ 9.15 (s, 1H), 8.19 (d, *J* = 8.3 Hz, 1H), 8.12 (t, 1H), 4.59 (t, *J* = 5.1 Hz, 2H), 3.89 – 3.83 (m, 2H), 3.53 (s, 3H). ¹³C NMR (126 MHz, DMSO) δ 146.30, 137.20, 125.67, 118.24, 59.38, 54.07, 46.63, 23.28. Anal. Calcd. for **C-2**, C₁₅H₂₁Cl₂N₇O₃RuS: C, 32.67; H, 3.84; Cl, 12.86; N, 17.78. Found: C, 32.71.; H, 4.01; N, 17.59. The ESI-TOF mass spectra of **C-2** exhibited an [(M-Cl) + K]⁺ ion peak at *m/z* 556.05 calculated for C₁₅H₂₁ClN₇O₃RuS.

Catalytic experiments

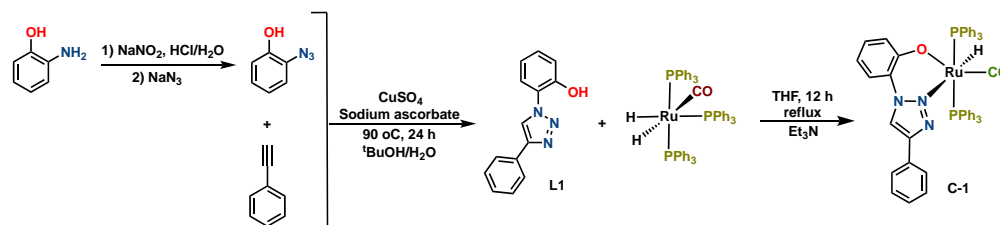
The reactions were performed in 25 mL reaction tubes equipped with an inner magnetic stirring bar using a Carousel 12 Plus reaction station. The tubes were charged with a mixture of the corresponding Ru catalyst (0.01 mmol), ketone or benzaldehyde derivatives (1 mmol), base (0.1 mmol), and 4 mL of ethanol or isopropanol. The reaction mixture was stirred and heated at 90 °C or at room temperature for different reaction times. After the prescribed reaction times, the resulting mixtures were cooled to room temperature, filtered through Celite, and analyzed by GC-MS. After taking an aliquot for GC-MS analysis, selected crude products were purified by silica gel column chromatography using ethyl acetate/hexanes as the eluent and analyzed by ¹H NMR.

Results and discussion

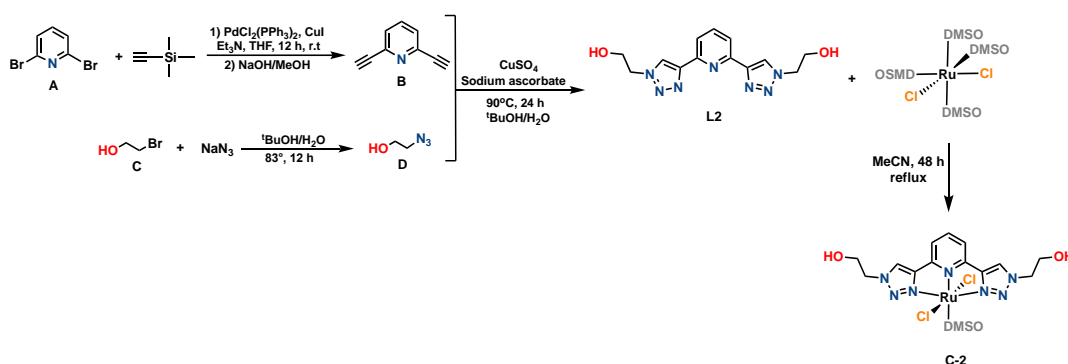
Synthesis and characterization of ruthenium complexes C-1 and C-2

Bidentate ligand **L1** was synthesized using an adapted procedure documented previously,^[5] utilizing commercially available 2-aminophenol and ethynylbenzene, as outlined in Scheme 1. **L1** was obtained in two steps through Sandmeyer/click copper-catalyzed azide–alkyne reactions and isolated as a light-yellow solid with a yield of 82 % after purification by flash chromatography. This ligand was further characterized by ¹H and ¹³C{¹H} NMR spectroscopy and structurally confirmed by direct comparison of previously reported data (full details are provided in the experimental section).

Ligand **L2** was easily obtained owing to the flexibility of copper-catalyzed azide–alkyne cycloaddition method. Consequently, the reaction between 2-azidoethanol and 2,6-diethynylpyridine yielded the desired tridentate ligand **L2** as a white solid in a good yield of 86 % after purification by chromatographic column, as illustrated in Scheme 2. Due to the C_2 -symmetry in **L2**, only a few resonances were observed in the ^1H NMR spectrum (SI, Fig. SI12). The spectrum of **L2** displayed a characteristic singlet at 8.62 ppm assigned to the proton of the triazole moiety, as well as a multiplet at 7.99 – 7.9 ppm resulting from the overlap of the pyridyl signals. The methylene bonded to the -OH group appeared as an apparent quadruplet at 3.86 ppm, and the methylene attached to the triazole ring was observed as a triplet at 4.51 ppm, while the alcohol moiety presented a triplet signal at 5.10 ppm. Additionally, $^{13}\text{C}\{^1\text{H}\}$ NMR study and mass spectrum of **L2** confirmed the formation of the tridentate **L2** (see SI, Fig. SI13).



Scheme 1. Synthesis of bidentate ligand **L1** and ruthenium complex **C-1**.



Scheme 2. Synthesis of tridentate ligand **L2** and ruthenium complex **C-2**.

The ruthenium (II) complex **C-1** was obtained through the facile coordination of **L1** with $[\text{RuH}_2(\text{PPh}_3)_3\text{CO}]$ in the presence of Et_3N , resulting in an air-stable off-white solid with a yield of 68% (Scheme 1). Similarly, the reaction of the tridentate N-donor ligand **L2** with $[\text{RuCl}_2(\text{DMSO})_4]$ in tetrahydrofuran at reflux temperature yielded air-stable complex **C-2** as an orange solid in 81.9% yield (Scheme 2).

The identities of the newly synthesized ruthenium (II) complexes **C-1** and **C-2** have been confirmed through multinuclear NMR (^1H , ^{13}C and ^{31}P for **C-1** only), ESI-TOF mass spectrometry, and satisfactory elemental analysis. As expected, the ^1H and ^{13}C NMR spectra of bidentate ruthenium (II) complex **C-1** are consistent with C_1 -symmetry. In the ^1H NMR spectrum of **C-1**, a triplet at -11.42 ppm with $^2J_{\text{H-P}} = 19.9$ Hz is observed, attributed to the Ru-H signal, consistent with its *cis*-position relative to two equivalent PPh_3 groups (Fig. 2). Furthermore, signals for aromatic protons were observed in the range of 6-7.66 ppm, integrating to 40 protons. The proposed structure of **C-1** was also further confirmed by $^{13}\text{C}\{^1\text{H}\}$ NMR, which exhibited a triplet signal for the CO ligand due to its coupling with two equivalents, mutually *cis*-phosphorus nuclei at 204.5 ppm ($^2J_{\text{C-P}} = 15$ Hz). Additionally, the phosphorus atoms of the PPh_3 groups appeared as a singlet at 40.9 ppm in the $^{31}\text{P}\{^1\text{H}\}$ NMR spectrum, confirming their equivalence due to their mutual transposition. The resulting mass spectrum is consistent with the formation of complex **C-1**, showing the molecular ion ESI-TOF: 892.1745

Catalytic activity

With both ruthenium pincer complexes in hand, their catalytic activity in the transfer hydrogenation of ketones and aldehydes using primary (EtOH) and secondary (isopropanol, IPA) alcohols as hydrogen donors was then examined and compared. We began the investigation by evaluating the activity of both ruthenium complexes (**C-1** and **C-2**) in the catalytic transfer hydrogenation reaction of 4-bromoacetophenone, using K_2CO_3 as a base in either ethanol or isopropanol (Table 1). Among the screened complexes, **C-2** was the most efficient catalyst in both alcohols, affording the 1-(4-bromophenyl)ethan-1-ol product in 89.3 % and 76.2 % yields in ethanol and isopropanol, respectively, at 90 °C for 24 h (entries 2 and 4). The distinctive reactivity observed in the **C-1** and **C-2** complexes bearing bidentate and tridentate ligands was attributed to the electronic effects and the thermal stability provided by the *mer*-tridentate pincer ligand to the catalytic compound **C-2**.

On the other hand, comparing the performance of **C-2** in both alcohols, it was better in ethanol, despite isopropanol being a better hydrogen transfer agent than ethanol (see Table 1, entries 2 and 4). This was attributed to the low solubility of complex **C-2** in the secondary alcohol. Based on this result, we decided to conduct a reaction of 4-bromoacetophenone in the presence of K_2CO_3 using a mixture of IPA:H₂O (7:3), considering that **C-2** is highly soluble in water. However, the yield remained poor (58 %) (entry 5). Reactions carried out either at room temperature or without a catalyst did not show any conversion (entries 7 and 8). Additionally, GC-MS monitoring of the reactions in ethanol revealed the formation of acetaldehyde, resulting from the dehydrogenation of ethanol, at the beginning of the reaction during the induction period (6–12 h). Subsequently, ethyl acetate was produced. We propose that the induction period is related to the generation of hydrides necessary for catalysis, and then acetaldehyde reacts with ethanol to produce ethyl acetate and release hydrogen.

Table 1. Transfer hydrogenation reaction of 4-bromoacetophenone and either ethanol or isopropanol catalyzed by ruthenium complexes **C-1** and **C-2**^a.

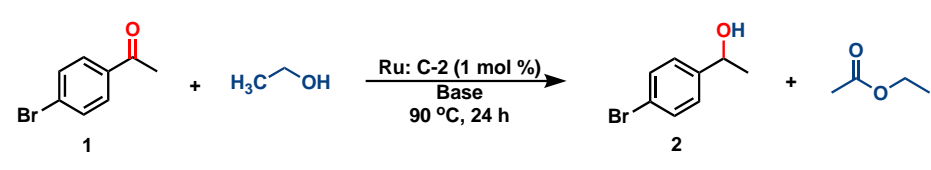
Entry	[Ru]	Hydrogen source	T (°C)	T (h)	Yield of 2 (%) ^b
1	C-1	IPA	90	24	70.5
2	C-2	IPA	90	24	76.2
3	C-1	Ethanol	90	24	33.5
4	C-2	Ethanol	90	24	89.3
5	C-2	IPA/H ₂ O, 7:3	90	24	58
6	C-2	ethanol	90	12	51.3
7	C-2	ethanol	r.t.	24	ND
8	None	ethanol	90	24	ND

^aReaction conditions: 4-bromoacetophenone (1.0 mmol), [**C-2**] (1 mol%), EtOH (4.0 mL), K_2CO_3 (0.1 mmol). ^bYields were determined by CG-MS and are the average of two independent runs. ND = Not detected. r.t. = room temperature.

As is well known, transfer hydrogenation reactions are strongly dependent on the base used. Thus, various bases were tested under the optimized reaction conditions using the best-found catalyst, **C-2** (Table 2).

The results obtained revealed that Cs_2CO_3 and K_2CO_3 afford the best yields (Table 2, entries 1 and 2). Since K_2CO_3 is cheaper than Cs_2CO_3 , the former will be used in the following experiments.

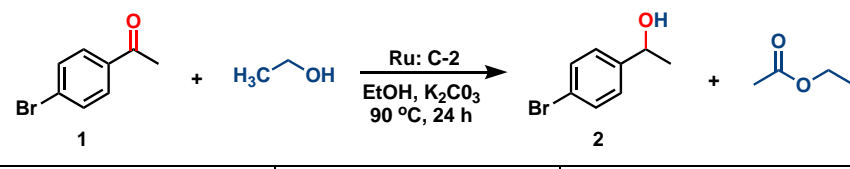
Table 2. Transfer hydrogenation reaction of 4-bromoacetophenone with EtOH catalyzed by ruthenium complex C-2 using different bases.^a

		
Entry	Base	Yield of 2 (%) ^b
1	K_2CO_3	86.3
2	Cs_2CO_3	86.6
3	Na_2CO_3	78.1
4	Li_2CO_3	85.1
5	NaOH	50.0
6	Et_3N	18.5

^aReaction conditions: 4-bromoacetophenone (1.0 mmol), [C-2] (1 mol%), EtOH (4.0 mL), base (0.1 mmol) for 24 h. ^bYields were determined by CG-MS and are the average of two independent runs.

To explore the effectiveness of complex C-2, the transfer hydrogenation reaction was also performed under the above reaction conditions with different catalyst loadings (Table 3). When 1 mol % of C-2 was used, 1-(4-bromophenyl)ethan-1-ol was obtained in 86.3 % yield after 24 hours (entry 3). Reducing the amount of catalyst to 0.1 and 0.5 mol % (entries 1 and 2) resulted in low to moderate yields of the alcohol product in 24 hours. Consequently, a catalyst loading of 1 mol % was used for further studies.

Table 3. Effect of catalyst C-2 loading.^a

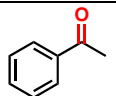
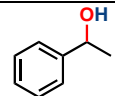
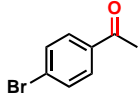
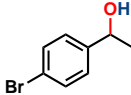
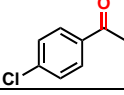
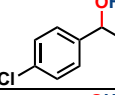
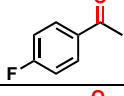
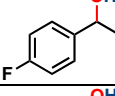
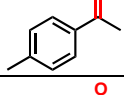
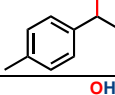
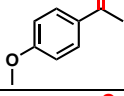
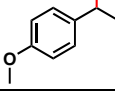
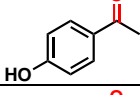
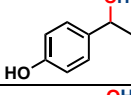
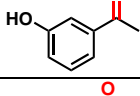
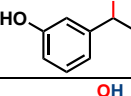
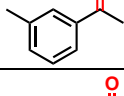
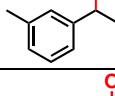
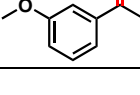
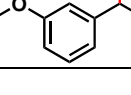
		
Entry	mol % of C-2	Yield of 2 (%) ^b
1	0.1	33.1
2	0.5	52.2
3	1	86.3

^aReaction conditions: 4-bromoacetophenone (1.0 mmol), [C-2] (0.1-1 mol%), EtOH (4.0 mL), K_2CO_3 (0.1 mmol) for 24 h. ^bYields were determined by CG-MS and are the average of two independent runs.

Hence, considering the optimized reaction conditions (1 mol % of C-2, 10 mol % K_2CO_3 , at 90 °C for 24 hours in a closed vial and encouraged by these results, we turned our attention to extend the scope of this

reaction to a series of substituted acetophenones to examine their electronic and steric effects (Table 4). Interestingly, variation of the electronic nature of the aromatic ring had little impact on the reaction efficiency and as a result, neutral (entry 1) along with electron-withdrawing and electron-donating substituents at *para*-positions provided the desired alcohol products in good yields (entries 2-7). On the other hand, *meta*-substituted acetophenones (entries 8-10) were hydrogenated slightly less effectively than the corresponding *para*-substituted derivatives (entries 5-7). Likewise, a good yield was achieved for the transfer hydrogenation of diaryl ketones. For instance, benzophenone yielded the desired reduced product, diphenylmethanol, with an 85 % yield (entry 11). Similarly, the use of aliphatic ketones, such as cyclohexanone, gave the corresponding secondary alcohol in a good yield (entry 12).

Table 4. Transfer hydrogenation reaction of ketones with EtOH catalyzed by ruthenium complex C-2.^a

$ \begin{array}{c} \text{R}_1-\text{C}(=\text{O})-\text{R}_2 \\ \mathbf{1} \end{array} + \text{H}_3\text{C}-\text{CH}_2-\text{OH} \xrightarrow[\text{K}_2\text{CO}_3, 90^\circ\text{C}, 24\text{ h}]{\text{Ru: C-2 (1 mol \%)}} \begin{array}{c} \text{R}_1-\text{CH}(\text{OH})-\text{R}_2 \\ \mathbf{2} \end{array} + \text{CH}_3\text{COOEt} $				
Entry	Ketone (1)	Alcohol (2)	Yield (%)	TOF (h ⁻¹)
1			88.5 ^b	3.68
2			89.3 ^b /84 ^c	3.72
3			89.0 ^b /83.2 ^c	3.70
4			90.1 ^b /85 ^c	3.75
5			93 ^b /89.0 ^c	3.75
6			88.7 ^b /86 ^c	3.69
7			87.9 ^b	3.66
8			78.9 ^b /76.2 ^c	3.28
9			84.8 ^b	3.53
10			85.8 ^b /81 ^c	3.57

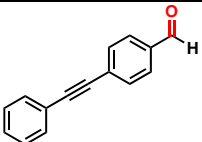
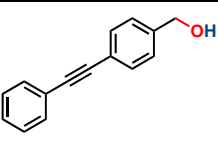
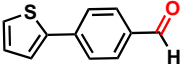
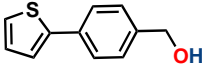
11			85 ^b	3.54
12			79.9 ^b	3.32

^aReaction conditions: Acetophenone derivative (1.0 mmol), [C-2] (1 mol%), EtOH (4.0 mL), K₂CO₃ (0.1 mmol) for 24 h. ^bYields were determined by CG-MS and are the average of two independent runs. ^cYields of isolated compounds.

Thereafter, the transfer hydrogenation of aldehydes with ethanol was investigated under the optimized reaction conditions found for ketone reductions (Table 5). First, benzaldehyde was tested, and complete conversion with a quantitative yield of benzyl alcohol was obtained. Based on this result, we decided to optimize the reaction time and performed the hydrogenation of benzaldehyde at different times: 24, 12, 6, and 3 hours. Excellent yields were achieved at 24 hours (100 %, Table 5, entry 1), 12 hours (100 %, Table 5, entry 2) and 6 hours (100 %, Table 5, entry 3), while at 3 hours the yield of the product was very poor (31 %, Table 5, entry 4). As expected, the reduction of aldehydes was easier than that of ketones, completing the reaction in only 6 hours. Then, we examined some substituted benzaldehydes using 1 mol % of C-2 and 10 mol % of K₂CO₃ at 90 °C for 6 hours, generating the primary alcohol with excellent yields.

Table 5. Transfer hydrogenation reaction of aldehydes with EtOH catalyzed by ruthenium complex C-2.^a

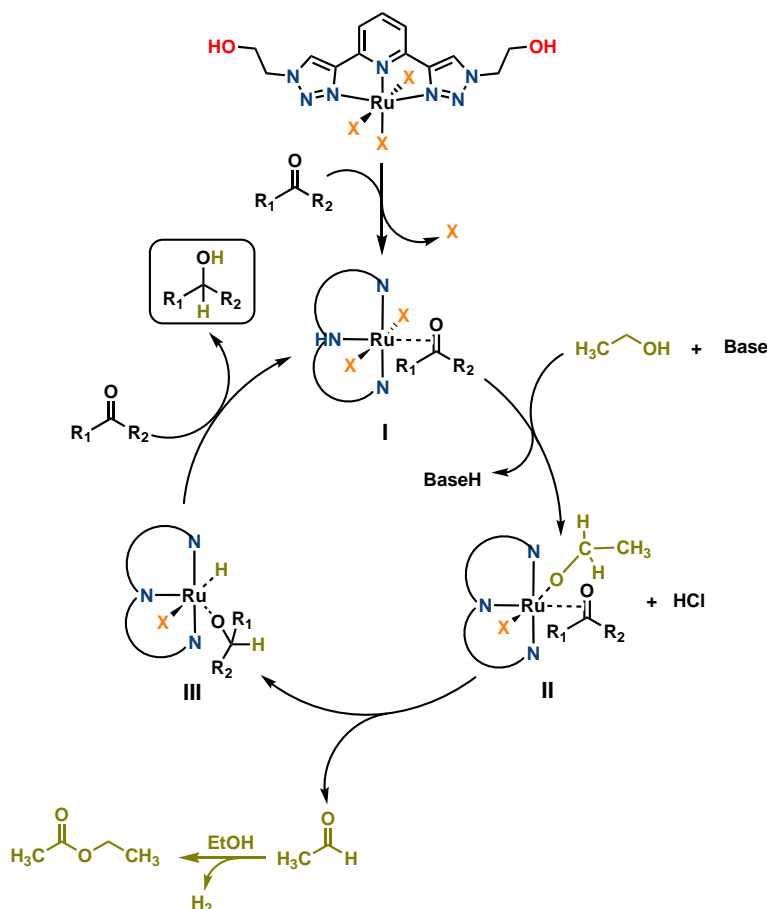
Entry	Ketone (1)	Alcohol (2)	Yield (%)	TOF (h ⁻¹)
1 ^{b*}			100 ^c	4.16
2 ^{b**}			100 ^c	8.33
3 ^{b***}			100 ^c	16.6
4 ^{b****}			31 ^c	10.3
5			100 ^c	16.6
6			95 ^c /91 ^d	15.8

7			97.5°/92 ^d	16.25
8			99 ^c	16.5

^aReaction conditions: Benzaldehyde derivative (1.0 mmol), [C-2] (0.1-1 mol%), EtOH (4.0 mL), K₂CO₃ (0.1 mmol) for 6 h.

^bReaction conditions: Benzaldehyde (1.0 mmol), [C-2] (1 mol%), EtOH (4.0 mL), K₂CO₃ (0.1 mmol) for: *24 h, ** 12h, ***6 h and ****3 h. ^cYields were determined by CG-MS and are the average of two independent runs. ^dYields of isolated compounds.

Based on literature reports,[32,33] a comprehensive mechanistic proposal for the hydrogenation of carbonyl bonds catalyzed by the ruthenium complex (C-2) is illustrated in Scheme 3. The mechanism likely involves the release of labile ligands from C-2, either through a dichlorination process or DMSO release, followed by ketone coordination to generate intermediate I. This step is presumably promoted by heating. Subsequently, intermediate I reacts with ethanol in the presence of a base to form a ruthenium-ethoxide complex II. This is followed by hydride addition to the β-position and β-hydride elimination, resulting in the release of acetaldehyde and the formation of the hydride complex III. Acetaldehyde is known to react with additional ethanol to form ethyl acetate and release hydrogen. Finally, the ruthenium complex III reacts with another ketone, releasing the secondary alcohol and regenerating the catalytically active ruthenium complex I.



Scheme 3. Mechanistic proposal for the TH of ketones with ethanol catalyzed by C-2.

Conclusions

In summary, two new ruthenium complexes with triazole-based ligands (**C-1** and **C-2**) have been synthesized in a facile manner with good yields. Both complexes were fully characterized. Complex **C-2**, bearing the *mer*-tridentate ligand, proved to be air-, water-, and thermally stable, as well as a highly active Ru catalyst for the homogeneous hydrogenation of C=O bonds, selectively producing alcohols. It operated under relatively mild conditions and addressed a broad substrate scope, covering alkyl- and aryl-ketones as well as aryl-aldehydes. The transfer hydrogenation of ketones and aldehydes using ethanol as the source of hydrogen and solvent produced secondary and primary alcohols in good to excellent yields with high selectivity. The successful use of this Ru(II) species suggests its potential for other transformations. Efforts to further explore its catalytic activity in other hydrogenation reactions are currently underway in our laboratory, as well as the exploration of the potential biological activity of this compound, given the high-water solubility of **C-2** and its biological components, such as triazole moieties. In addition, current investigations are focused on further mechanistic details. These results will be disclosed in due time.

Acknowledgments

We would like to thank M.Sc. Atilano Gutiérrez-Carrillo and Mónica A. Rincón-Guevara for technical assistance. E.V.S. would like to thank CONACYT (CVU: 1278278) for M.Sc. scholarship.

References

1. Wang, D.; Astruc, D. *Chem. Rev.* **2015**, *115*, 6621–6686. DOI: <https://doi.org/10.1021/acs.chemrev.5b00203>.
2. Taleb, B.; Jahjah, R.; Cornu, D.; Bechelany, M.; Al Ajami, M.; Kataya, G.; Hijazi, A.; El-Dakdouki, M. H. *Molecules*. 2023. DOI: <https://doi.org/10.3390/molecules28227541>.
3. Romero, A. H. *ChemistrySelect*. **2020**, *5*, 13054–13075. DOI: <https://doi.org/https://doi.org/10.1002/slct.202002838>.
4. Robertson, A.; Matsumoto, T.; Ogo, S. *Dalton Trans.* **2011**, *40*, 10304–10310. DOI: <https://doi.org/10.1039/C1DT10544B>.
5. Ghosh, R.; Jana, N. Ch.; Panda, S.; Bagh, B. *ACS Sustain. Chem. Eng.* **2021**, *9*, 4903–4914. DOI: <https://doi.org/10.1021/acssuschemeng.1c00633>.
6. Garg, N.; Sarkar, A.; Sundararaju, B. *Coord. Chem. Rev.* **2021**, *433*, 213728. DOI: <https://doi.org/https://doi.org/10.1016/j.ccr.2020.213728>.
7. Hafeez, J.; Bilal, M.; Rasool, N.; Hafeez, U.; Adnan Ali Shah, S.; Imran, S.; Amiruddin Zakaria, Z. *Arabian J. Chem.* **2022**, *15*, 104165. DOI: <https://doi.org/https://doi.org/10.1016/j.arabjc.2022.104165>.
8. Hu, Z.-Q.; Li, X.; Liu, L.-X.; Yu, C.-B.; Zhou, Y.-G. *J. Org. Chem.* **2021**, *86*, 17453–17461. DOI: <https://doi.org/10.1021/acs.joc.1c02156>.
9. Gobbo, A.; Ma, X.; Ciancaleoni, G.; Zacchini, S.; Biancalana, L.; Guelfi, M.; Pampaloni, G.; Nolan, S. P.; Marchetti, F. *Eur. J. Inorg. Chem.* **2023**, *26*, e202300078. DOI: <https://doi.org/https://doi.org/10.1002/ejic.202300078>.
10. Negrete-Vergara, C.; Vega, A.; Cantero-López, P.; Yáñez, O.; Moya, S. A.; Valdebenito, G.; Parra-Melipan, S.; Aguirre, P. *Inorg. Chim. Acta* **2024**, *568*, 122064. DOI: <https://doi.org/https://doi.org/10.1016/j.ica.2024.122064>.

11. Wang, F.; Zheng, L.-S.; Lang, Q.-W.; Yin, C.; Wu, T.; Phansavath, P.; Chen, G.-Q.; Ratovelomanana-Vidal, V.; Zhang, X. *Chem. Commun.* **2020**, *56*, 3119–3122. DOI: <https://doi.org/10.1039/C9CC09793G>.
12. Lin, X.; Wang, Y.; Hu, Y.; Zhu, W.; Dou, X. *European J. Org. Chem.* **2020**, *2020*, 1046–1049. DOI: <https://doi.org/https://doi.org/10.1002/ejoc.202000049>.
13. Wang, Y.; Chang, Z.; Hu, Y.; Lin, X.; Dou, X. *Org. Lett.* **2021**, *23*, 1910–1914. DOI: <https://doi.org/10.1021/acs.orglett.1c00341>.
14. Everaert, J.; Leus, K.; Rijckaert, H.; Debruyne, M.; Van Hecke, K.; Morent, R.; De Geyter, N.; Van Speybroeck, V.; Van Der Voort, P.; Stevens, C. V. *A Green Chem.* **2023**, *25*, 3267–3277. DOI: <https://doi.org/10.1039/D3GC00167A>.
15. Yang, Z.; Cheng, W.; Li, Z. *Catal. Commun.* **2018**, *117*, 38–42. DOI: <https://doi.org/https://doi.org/10.1016/j.catcom.2018.08.004>.
16. Jiang, X.; Cui, X.; Chen, J.; Liu, Q.; Chen, Y.; Zhou, H. *Tetrahedron Lett.* **2022**, *90*, 153627. DOI: <https://doi.org/https://doi.org/10.1016/j.tetlet.2021.153627>.
17. Xu, H.; Yang, P.; Chuanprasit, P.; Hirao, H.; Zhou, J. (Steve). *Angew. Chem. Int. Ed.* **2015**, *54*, 5112–5116. DOI: <https://doi.org/https://doi.org/10.1002/anie.201501018>.
18. Ruan, S.-H.; Fan, Z.-W.; Zhang, W.-J.; Xu, H.; An, D.-L.; Wei, Z.-B.; Yuan, R.-M.; Gao, J.-X.; Li, Y.-Y. *J. Catal.* **2023**, *418*, 100–109. DOI: <https://doi.org/https://doi.org/10.1016/j.jcat.2023.01.008>.
19. Huo, S.; Wang, Q.; Zuo, W. *Dalton Trans.* **2020**, *49*, 7959–7967. DOI: <https://doi.org/10.1039/D0DT01204A>.
20. Bolitho, E. M.; Worby, N. G.; Coverdale, J. P. C.; Wolny, J. A.; Schünemann, V.; Sadler, P. J. *Organometallics.* **2021**, *40*, 3012–3023. DOI: <https://doi.org/10.1021/acs.organomet.1c00358>.
21. Wang, W.; Yang, X. *Chem. Commun.* **2019**, *55*, 9633–9636. DOI: <https://doi.org/10.1039/C9CC04760C>.
22. Zweifel, T.; Naubron, J.-V.; Büttner, T.; Ott, T.; Grützmacher, H. *Angew. Chem. Int. Ed.* **2008**, *47*, 3245–3249. DOI: <https://doi.org/https://doi.org/10.1002/anie.200704685>.
23. Dubey, A.; Khaskin, E. *ACS Catal.* **2016**, *6*, 3998–4002. DOI: <https://doi.org/10.1021/acscatal.6b00827>.
24. Weingart, P.; Thiel, W. R. *ChemCatChem* **2018**, *10*, 4844–4848. DOI: <https://doi.org/https://doi.org/10.1002/cctc.201801334>.
25. Gong, D.; Kong, D.; Xu, N.; Hua, Y.; Liu, B.; Xu, Z. *Org. Lett.* **2022**, *24*, 7339–7343. DOI: <https://doi.org/10.1021/acs.orglett.2c02866>.
26. Li, Y.; Lian, S.; Wang, J.; Gong, D. *Asian J. Org. Chem.* **2024**, *13*, e202300496. DOI: <https://doi.org/https://doi.org/10.1002/ajoc.202300496>.
27. Beaufils, A.; Melle, P.; Lentz, N.; Albrecht, M. *Inorg. Chem.* **2024**, *63*, 2072–2081. DOI: <https://doi.org/10.1021/acs.inorgchem.3c03859>.
28. Patil, R. D.; Pratihari, S. *ACS Sustain Chem. Eng.* **2024**, *12*, 6206–6219. DOI: <https://doi.org/10.1021/acssuschemeng.3c07989>.
29. Ghosh, D.; Rhodes, S.; Hawkins, K.; Winder, D.; Atkinson, A.; Ming, W.; Padgett, C.; Orvis, J.; Aiken, K.; Landge, S. *New J. Chem.* **2015**, *39*, 295–303. DOI: <https://doi.org/10.1039/C4NJ01411A>.
30. Wu, S.-Y.; Guo, X.-Q.; Zhou, L.-P.; Sun, Q.-F. *Inorg. Chem.* **2019**, *58*, 7091–7098. DOI: <https://doi.org/10.1021/acs.inorgchem.9b00756>.
31. Samouei, H.; Grushin, V. V. *Organometallics.* **2013**, *32*, 4440–4443. DOI: <https://doi.org/10.1021/om400461w>.
32. Liu, W.-P.; Yuan, M.-L.; Yang, X.-H.; Li, K.; Xie, J.-H.; Zhou, Q.-L. *Chem. Commun.* **2015**, *51*, 6123–6125. DOI: <https://doi.org/10.1039/C5CC00479A>.
33. Tejel, C.; Ciriano, M. A.; Passarelli, V. *Chemistry – A Eur. J.* **2011**, *17*, 91–95. DOI: <https://doi.org/https://doi.org/10.1002/chem.201002921>.

Effect of the Linker and Substituents on the Ionic Conductivity of Borate Single-Ion Polymers for Lithium Batteries

Soline Vauthier^{1,2}, Stéphane Cotte², Laurent Castro², Aurélie Guéguen², Nerea Casado^{1,4}, David Mecerreyes^{1,4}, Gregorio Guzmán-Gonzalez^{*1,3}

¹POLYMAT, University of the Basque Country UPV/EHU, Joxe Mari Korta Center, Avda. Tolosa 7, 20018 Donostia-San Sebastian, Spain.

²Toyota Motor Europe Research and Development 1, Advanced Material Research Battery and Fuel Cell, Hoge Wei 33, Zaventem B-1930, Belgium.

³Departamento de Química, Universidad Autónoma Metropolitana-Iztapalapa, 09340, México City, México.

⁴IKERBASQUE, Basque Foundation for Science, 48009, Bilbao, Spain.

*Corresponding author: Gregorio Guzmán-Gonzalez, email: greg@xanum.uam.mx

Received May 7th, 2024; Accepted August 9th, 2024.

DOI: <http://dx.doi.org/10.29356/jmcs.v68i4.2273>

Abstract. Polymer electrolytes with high ionic conductivity are actively searched for their application as solid electrolytes in lithium batteries. Here, we show new borate single lithium-ion conducting polymers with high ionic conductivity and lithium transference number values. For this purpose, eight new methacrylic lithium borate polymers were synthesized and characterized with varying chemical compositions focusing on the linker between the polymer chain and the pendant borate ionic group and its substituents. The polymers with the optimum ethoxy linker and fluorinated pendant groups show a low T_g value and the highest ionic conductivity value of $1.29 \times 10^{-4} \text{ S.cm}^{-1}$ at 60 °C. This value is among the highest ionic conductivity reported for a single lithium-ion conducting homopolymer. These polymers show a high lithium transference number (between 0.88 and 0.96) and electrochemical stability close to 4.2 V vs Li⁺/Li, making them promising candidates for application as solid electrolytes in lithium batteries.

Keywords: Lithium-ion; lithium-ion batteries; polymer electrolytes; ion transport; solid electrolyte.

Resumen. Se buscan activamente electrolitos poliméricos con alta conductividad iónica para su aplicación como electrolitos sólidos en baterías de litio. Aquí, mostramos nuevos polímeros conductores de iones de litio de borato simples con valores muy altos de conductividad iónica y número de transferencia de litio. Para ello, se sintetizaron y caracterizaron ocho nuevos polímeros metacrílicos de borato de litio con composiciones químicas variables centradas en el enlazador entre la cadena polimérica y el grupo iónico borato colgante y sus sustituyentes. Los polímeros con el enlazador etoxi óptimo y los grupos colgantes fluorados muestran un valor T_g bajo y un valor superior de conductividad iónica $1,29 \times 10^{-4} \text{ Scm}^{-1}$ a 60 °C. Este valor es uno de los más altos de conductividad iónica a 60 °C. Este valor es uno de los valores más altos de conductividad iónica a 60 °C. Este valor es uno de los más altos valores de conductividad iónica registrados para un solo homopolímero conductor de iones de litio. Estos polímeros muestran un elevado número de transferencia de litio (entre 0.88 y 0.96), y una estabilidad electroquímica cercana a 4.2 V vs Li⁺/Li que los convierten en candidatos prometedores para su aplicación como electrolitos sólidos en baterías de litio.

Palabras clave: Ion-litio; baterías de ion-litio; electrolitos poliméricos; transporte de iones; electrolito sólido.

Introduction

Solid polymer electrolytes (SPEs) are of interest for developing the next generation of solid-state batteries for applications such as electric vehicles where safety is necessary. The main properties sought for SPEs are high ionic conductivity,[1] good mechanical strength, high lithium transference number, thermal and electrochemical stabilities, and good compatibility with electrodes.[2,3] Polyethers such as PEO are the most popular polymers for SPEs due to their ability to dissolve lithium salts by electrostatic interactions between ether oxygens and lithium ions.[4–6] Nowadays, poly(ethylene oxide) (PEO) is the standard polymer matrix for SPEs, part of commercial solid-state lithium batteries for the transportation sector.[4,7] The optimized PEO SPEs show high ionic conductivity values in the order of 10^{-3} S.cm⁻¹ at 70 °C.[8] However, their low lithium transference numbers ($t_{Li^+} < 0.25$) and electrochemical stability window (< 4.2 V vs Li⁺/Li) limit their applications in lithium metal batteries with high-voltage cathodes.

Single lithium-ion conducting polymer electrolytes (SLICPEs) are a family of SPEs composed of an anionic polyelectrolyte with lithium counter-ion.[9] They show a lithium transference number close to unity ($t_{Li^+} \approx 1$).[3,10,11] Its high interest is due to the limited formation of ionic concentration gradients in the solid electrolyte, which can limit dendritic growth on the lithium anode. However, in most cases, the overall ionic conductivity of SLICPEs is much lower than one of the best PEO SPEs.[12]

Nowadays, the SLIPCEs with the highest ionic conductivity are based on anionic polyelectrolytes having sulphonamides [13] or tetrahedral borates.[14,15] These single-ion conducting homopolymers show ionic conductivity values still lower than 1×10^{-6} S cm⁻¹, e.g. Poly(LiMTFSI), [16,17] and Poly(STFSI)[18,19] with 1×10^{-12} and 7.6×10^{-6} S cm⁻¹ at 25 °C, respectively or 6×10^{-6} S.cm⁻¹ at 25 °C for lithium polyvinyl alcohol oxalate borate (LiPVAOB).[20] These values of the SLIPCEs can be increased by blending with other polymers such as PEO.[21–23] For instance, Olmedo-Martínez et al. [24] measured an ionic conductivity of 2.1×10^{-4} S.cm⁻¹ at 70 °C for an optimized mixture of PEO with Poly(LiMTFSI). In another example, Meabe et al. measured an ionic conductivity of 3.2×10^{-5} Scm⁻¹ at 25°C with a blend of PEO and LiFSI.[25] Very recently, we reported a new family of single lithium-ion conducting polymer electrolytes based on highly delocalized borate groups.[1] The synthesis and the effect of the nature of the pendant substituents linked to the boron atom on the ionic conductivity were reported, highlighting the highest ionic conductivity reported for a single lithium-ion conducting polymer of 10^{-4} Scm⁻¹ at 60 °C.[26]

The main objective of this article is to investigate the effect of the ethoxy linker between the polymer chain and the borate group and its substituents to increase further the ionic conductivity of borate-based single lithium-ion conducting polymers.[27,28] After establishing the optimal ethoxy linker length and based on the previous work investigating the different substituent groups, optimized SLICPEs with varying pendant groups are presented, and their ionic conductivities are discussed. An in-depth study of the influence of the fluorine substituents on the ionic conductivity of SLICPEs is presented, and the relation between the electron density of borate groups and the number of ethoxy groups serving as ionic transport pathways in SLICPEs is discussed. Finally, the lithium transference number and electrochemical stability window for polymer electrolytes were assessed to confirm their potential for lithium battery applications.

Experimental

Materials

All chemicals, including 2-Hydroxyethyl methacrylate (HEMA, 97 %, Aldrich), Poly(ethylene glycol) methacrylate (PEGMA, molecular weight of 360 and 500 g•mol⁻¹, Aldrich), Borane tetrahydrofuran complex solution 1.0 M in THF (BH₃, Aldrich), n-Butyl lithium 2.5M solution in hexanes, (nBuLi, ACROS), 2,2'-Azobisisobutyronitrile (AIBN, initiator, 98 %, Aldrich), Trimethyl borate (TMB, ≥98 %, Aldrich), Triethyl borate (TEB, ≥95%, Aldrich), Triisopropyl borate (TiPB, ≥98 %, Aldrich), 1,1,1,3,3,3-Hexafluoro-2-propanol (HFIP, ≥99%, Aldrich), 1,1,1-Trifluoro-2-propanol (TFP, 97 %, Aldrich), were used as received. Triethylene glycol monomethyl ether (TEG, 95%, Aldrich) was distilled at the rotary evaporator at 70 °C and reduced pressure. The methanol (MeOH) and hexane solvents from Scharlab were dried with anhydrous MgSO₄ before

use. BH₃-THF complex and n-Butyl lithium are highly moisture-sensitive reagents, so they must be handled under an inert atmosphere in all steps.

Methods

NMR spectra were recorded for ¹H, ¹⁹F, and ¹¹B NMR spectroscopy analysis with the Avance III 400 MHz. Fourier transform infrared (FT-IR) spectra were obtained using the Nicolet 6700 FTIR spectrometer over the 4000-400 cm⁻¹ range. The thermal properties of the polymers were evaluated by DSC (SDTQ-600 TA instruments) with a heating rate of 10 °C/min⁻¹ from -70 to 100 °C under N₂ flow. The glass transition temperatures (T_g) were measured by the onset temperature extrapolated in the second heating scan.

Ionic conductivity values were obtained by EIS measurements using an Autolab 302N potentiostat/galvanostat (Metrohm AG) equipped with a temperature controller (Microcell HC station). The samples were placed between two stainless steel electrodes with a surface area of 0.5 cm² and a thickness of 0.1 mm. The measurements were performed every 10 °C between 95 and 25 °C with a frequency range set from 0.1 MHz to 0.1 Hz and 10 mV amplitude. The ionic conductivity values of SLICPEs were calculated following equation (1) based on literature:[29]

$$\sigma = (1/R_b) \cdot (d/S) \quad (1)$$

where σ is the ionic conductivity (S cm⁻¹), d is the thickness (cm), S is the area (cm²) of the stainless-steel electrodes, R_b (Ω) is the bulk resistance extracted from the Nyquist plot obtained by EIS. Each test was repeated at least three times, and the results showed an average with the standard deviation. The activation energy E_a of SLICPEs was calculated according to Arrhenius equation (2) based on literature:[30,31]

$$\sigma = \sigma_0 \cdot \exp(-E_a/RT) \quad (2)$$

where σ_0 is the pre-exponential factor related to the conductivity at infinite temperature, E_a is the activation energy for ion mobility, R is the universal gas constant (8.314 J mol⁻¹ K⁻¹), and T is the absolute temperature.

The lithium-ion transference numbers (t_{Li^+}) were evaluated in Li|SLICPE|Li symmetric coin cells employing the direct current (DC) polarization/alternating current (AC) impedance method. A 10 mV (ΔV) potential is applied to polarize the SLICPEs during chronoamperometry. t_{Li^+} were calculated following the equation (3) proposed by the Evans-Vincent-Bruce method:[32,33]

$$t_{Li^+} = (I_{ss}(\Delta V - I_0 R_0)) / (I_0(\Delta V - I_{ss} R_{ss})) \quad (3)$$

where I_{ss} is the steady-state current for the sample polarized, I_0 is the initial value of the current upon polarization, R_{ss} and R_0 does EIS obtain the electrode resistances after and before the polarization, respectively.

The electrochemical stability windows were evaluated with a Li|SLICPE|stainless-steel coin cell, using linear sweep voltammetry (LSV) in a range from 2 to 6 V vs Li⁺/Li at a scan rate of 0.2 mVs⁻¹ at 25 °C.

General procedure of lithium-ion monomer synthesis

A series of lithium borate methacrylic salts was synthesized. Their general chemical structure called $LBBn(OR)_2$ is represented in Fig. 1(a). They are composed of a methacrylic acid group for polymer network formation by the polymerization reaction, an ethoxy chain, where different lengths are investigated (n=1, 7, and 9); a single ion part, with a boron atom as the anionic center ionically bonded to a mobile lithium ion; a butyl function giving rise to the B-C bond; and two pendant groups (-OR), on which different functions are tested (such as moderate and high electron-withdrawing or self-solvation capabilities) for modulation of the electron density of the borate groups.

The seven monomers substituted with aliphatic groups (-R) such as methyl, ethyl, and isopropyl (LBBn₁(OMe)₂, LBBn₇(OMe)₂, LBBn₉(OMe)₂, LBBn₁(OEt)₂, LBBn₇(OEt)₂, LBBn₁(OiP)₂, and LBBn₇(OiP)₂) were synthesized following the method A as shown in Fig. 1(a-b). To synthesize the three monomers, LBBn₁(OMe)₂, LBBn₁(OEt)₂, and LBBn₁(OiP)₂, HEMA (10 mmol, 1.3 g) and dry hexane (30 ml) were charged

into a flask of 100 ml. Concerning the three monomers synthesis of $\text{LBBn}_7(\text{OMe})_2$, $\text{LBBn}_7(\text{OEt})_2$, and $\text{LBBn}_7(\text{OiP})_2$, PEGMA with a molecular weight of $360 \text{ g}\cdot\text{mol}^{-1}$ (10 mmol, 3.6 g) and dry hexane (30 ml) were charged into a flask of 100 ml. Then, for $\text{LBBn}_9(\text{OMe})_2$ synthesis, PEGMA with a molecular weight of $500 \text{ g}\cdot\text{mol}^{-1}$ (10 mmol, 5.0 g) and dry hexane (30 ml) were charged into a flask of 100 ml. Then, the solutions were stirred with argon flow and cooled in an acetone-liquid nitrogen bath, ensuring a constant magnetic stirring to avoid solidification of the system. 1 molar equivalent (1 eq.) of Tri-R borates "B(OR)₃" was added dropwise according to the desired monomer. TMB (10 mmol, 1.04 ml) for $\text{LBBn}_1(\text{OMe})_2$, $\text{LBBn}_7(\text{OMe})_2$, and $\text{LBBn}_9(\text{OMe})_2$ monomers synthesis. TEB (10 mmol, 1.7 ml) for $\text{LBBn}_1(\text{OEt})_2$ and $\text{LBBn}_7(\text{OEt})_2$ monomers synthesis. TiPB (10 mmol, 2.2 ml) for $\text{LBBn}_1(\text{OiP})_2$ and $\text{LBBn}_7(\text{OiP})_2$ monomers synthesis. The reaction mixtures were slowly heated to RT and stirred for 2 h. Subsequently, the systems were cooled again in an acetone-liquid nitrogen bath, and 1 eq. of nBuLi 2.5 M in hexane (10 mmol, 4 ml) was added dropwise. The precipitates formed were heated to RT and stirred for another 2 h more before being filtered and washed with cold diethyl ether. The white monomers obtained were placed in vials and dried on a vacuum line at 40 °C for 24h.

The method B shown in Fig. 1(a) and Fig. 1(c) was followed to synthesize the monomers $\text{LBBn}_1(\text{OF}_6\text{iP})_2$, $\text{LBBn}_7(\text{OF}_6\text{iP})_2$, $\text{LBBn}_7(\text{OF}_3\text{iP})_2$, $\text{LBBn}_1(\text{OGly})_2$, $\text{LBBn}_1(\text{OGlyOF}_6\text{iP})_2$, and $\text{LBBn}_1(\text{OGlyOF}_3\text{iP})_2$. 30 ml of dry hexane were charged into the 100 ml two-neck flask with HEMA (10 mmol, 1.3 g) except for $\text{LBBn}_7(\text{OF}_3\text{iP})_2$ and $\text{LBBn}_7(\text{OF}_6\text{iP})_2$ synthesis which used PEGMA with a molecular weight of $360 \text{ g}\cdot\text{mol}^{-1}$ (10 mmol, 3.6 g). The solutions were stirred with argon flow and subsequently cooled in an acetone-liquid nitrogen bath, avoiding solidification of the system. 1 eq. of BH_3 -THF complex solution of 1 M in THF (10 mmol, 10 ml) was carefully added "dropwise." At the same time, H_2 was expelled from the system with nitrogen flow. Then, the reaction mixtures were slowly warmed to RT and stirred for 30 min more. Before adding the subsequent reagents, the systems were cooled in an acetone-liquid nitrogen bath. Afterward, the systems were heated to RT for 1 hour to ensure that H_2 releases were complete. 2 eq. of alcohols according to the desired monomer were added dropwise such as HFIP (20 mmol, 4 ml) for $\text{LBBn}_1(\text{OF}_6\text{iP})_2$ and $\text{LBBn}_7(\text{OF}_6\text{iP})_2$; TFP (20 mmol, 4 ml) for $\text{LBBn}_7(\text{OF}_3\text{iP})_2$; and TEG (20 mmol, 4 ml) for $\text{LBBn}_1(\text{OGly})_2$. For $\text{LBBn}_1(\text{OGlyOF}_6\text{iP})_2$ and $\text{LBBn}_1(\text{OGlyOF}_3\text{iP})_2$, two different alcohols were added dropwise separately: first, 1 eq. of TEG (10 mmol, 4 ml), and secondly, 1 eq. of HFIP for $\text{LBBn}_1(\text{OGlyOF}_6\text{iP})_2$ and TFP (10 mmol, 4 ml) for $\text{LBBn}_1(\text{OGlyOF}_3\text{iP})_2$. Finally, for each synthesis, 1 eq. of nBuLi 2.5 M in hexane (10 mmol, 4 ml) was added dropwise following the same temperature control protocol. The reaction mixture was stirred at RT for another 2 hours. Finally, the product was precipitated and washed with cold diethyl ether. The monomers obtained were placed in vials and dried in a vacuum line at 40 °C for 24h.

pLBBn₁(OMe)₂. Yield: 0.9 g (97 %). ¹H NMR (400 MHz, D₂O): δ (ppm) = 3.75-3.44 (dt, 4H, CO-O-CH₂-CH₂-O-B), 3.24 (s, 6H, B-O-CH₃), 1.72 (s, 3H, CH₂-C(CH₃)-CH₂), 1.49 (q, 2H, B-CH₂-CH₂-), 1.32 (sx, 4H, B-CH₂-CH₂-CH₂-), 1.24 (br, 2H, -(CH₂-C(CH₃))-), 0.87 (t, 3H, (CH₂)₃-CH₃); ¹¹B NMR (400 MHz, D₂O): δ (ppm) = 3.8 (s, -CH₂-B-(OR)₂).

pLBBn₇(OMe)₂. Yield: 0.9 g (89 %). ¹H NMR (400 MHz, D₂O): δ (ppm) = 3.59 (dt, 28H, CO-O-(CH₂-CH₂)₇-O-B), 2.54 (sx, 6H, B-O-CH₃), 1.70 (s, 3H, CH₂-C(CH₃)-CH₂), 1.47 (q, 2H, B-CH₂-CH₂-), 1.30 (q, 2H, B-CH₂-CH₂-CH₂-), 1.20 (br, 2H, -(CH₂-C(CH₃))-), 1.01 (m, 2H, B-(CH₂)₂-CH₂-CH₃), 0.83 (q, 3H, (CH₂)₂-CH₃); ¹¹B NMR (400 MHz, D₂O): δ (ppm) = 2.5 (s, -CH₂-B-(OR)₂).

pLBBn₉(OMe)₂. Yield: 1.9 g (63%). ¹H NMR (400 MHz, D₂O): δ (ppm) = 3.70-3.60 (dt, CO-O-(CH₂-CH₂)₉-O-B), 2.54 (s, 6H, B-O-CH₃), 1.71 (s, 3H, CH₂-C(CH₃)-CH₂), 1.48 (q, 2H, B-CH₂-CH₂-), 1.30 (q, 2H, B-CH₂-CH₂-CH₂-), 1.22 (br, 2H, -(CH₂-C(CH₃))-), 1.01 (q, 2H, B-(CH₂)₂-CH₂-CH₃), 0.82 (t, 3H, (CH₂)₃-CH₃); ¹¹B NMR (400 MHz, D₂O): δ (ppm) = 2.4 (s, -CH₂-B-(OR)₂).

pLBBn₁(OEt)₂. Yield: 1.25 g (91 %). ¹H NMR (400 MHz, D₂O): δ (ppm) = 3.63-3.56 (dt, 4H, CO-O-CH₂-CH₂-O-B), 3.31 (c, 4H, B-O-CH₂), 1.71 (s, 3H, CH₂-C(CH₃)-CH₂), 1.48 (q, 2H, B-CH₂-CH₂-), 1.29 (sx, 2H, B-CH₂-CH₂-CH₂-), 1.21 (br, 2H, -(CH₂-C(CH₃))-), 1.14 (t, 6H, B-O-CH₂-CH₃), 0.86 (q, 4H, B-(CH₂)₃-CH₃); ¹¹B NMR (400 MHz, D₂O): δ (ppm) = 2.8 (s, -CH₂-B-(OR)₂).

pLBBn7(OEt)₂. Yield: 4.1 g (7 %). ¹H NMR (400 MHz, D₂O): δ (ppm) = 3.61-3.58 (dt, 28H, CO-O-(CH₂-CH₂)₇-O-B), 2.81 (q, 4H, B-O-CH₂), 1.69 (s, 3H, CH₂-C(CH₃)-CH₂), 1.47 (q, 2H, B-CH₂-CH₂-), 1.29 (q, 2H, B-CH₂-CH₂-CH₂-), 1.19 (br, 2H, -(CH₂-C(CH₃))-), 1.13 (t, 6H, B-O-CH₂-CH₃), 1.01 (m, 2H, B-(CH₂)₂-CH₂-CH₃), 0.85 (q, 6H, (CH₂)₃-CH₃); ¹¹B NMR (400 MHz, D₂O): δ (ppm) = 2.3 (s, -CH₂-B-(OR)₂).

pLBBn1(OiP)₂. Yield: 1.08 g (87 %). ¹H NMR (400 MHz, D₂O): δ (ppm) = 3.98 (m, 2H, B-O-CH(CH₃)₂), 3.67-3.56 (dt, 4H, CO-O-CH₂-CH₂-O-B), 1.71 (s, 3H, CH₂-C(CH₃)-CH₂), 1.49 (q, 2H, B-CH₂-CH₂-), 1.30 (sx, 3H, B-CH₂-CH₂-CH₂-), 1.21 (br, 2H, -(CH₂-C(CH₃))-), 1.15 (d, 12H, B-O-CH(CH₃)₂), 1.01 (d, 2H, B-(CH₂)₂-CH₂-CH₃), 0.86 (q, 4H, B-(CH₂)₃-CH₃); ¹¹B NMR (400 MHz, D₂O): δ (ppm) = 2.8 (s, -CH₂-B-(OR)₂).

pLBBn7(OiP)₂. Yield: 2.1 g (95 %). ¹H NMR (400 MHz, D₂O): δ (ppm) = 3.98 (m, 2H, B-O-CH(CH₃)₂), 3.63-3.49 (dt, 28H, CO-O-(CH₂-CH₂)₇-O-B), 1.71 (s, 3H, CH₂-C(CH₃)-CH₂), 1.49 (q, 2H, B-CH₂-CH₂-), 1.32 (q, 2H, B-CH₂-CH₂-CH₂-), 1.23 (br, 2H, -(CH₂-C(CH₃))-), 1.14-1.12 (d, 12H, B-O-CH(CH₃)₂), 1.01 (m, 2H, B-(CH₂)₂-CH₂-CH₃), 0.86 (q, 3H, (CH₂)₃-CH₃); ¹¹B NMR (400 MHz, D₂O): δ (ppm) = 3.1 (s, -CH₂-B-(OR)₂).

pLBBn1(OFaIP)₂. Yield: 1.32 g (91 %). ¹H NMR (400 MHz, D₂O): δ (ppm) = 4.63 (sp, 2H, B-O-CH(CF₃)₂), 3.63-3.56 (dt, 4H, CO-O-CH₂-CH₂-O-B), 1.71 (s, 3H, CH₂-C(CH₃)-CH₂), 1.49 (q, 2H, B-CH₂-CH₂-), 1.30 (sx, 2H, B-CH₂-CH₂-CH₂-), 1.24 (br, 2H, -(CH₂-C(CH₃))-), 1.11 (c, 2H, B-(CH₂)₂-CH₂-CH₃), 0.86 (q, 3H, B-(CH₂)₃-CH₃); ¹¹B NMR (400 MHz, D₂O): δ (ppm) = 7.8 (s, -CH₂-B-(OR)₂); ¹⁹F NMR (400 MHz, D₂O): δ (ppm) = -75.89 (s, CF₃).

pLBBn7(OFaIP)₂. Yield: 6.6 g (9 %). ¹H NMR (400 MHz, D₂O): δ (ppm) = 4.67 (m, 2H, B-O-CH(CF₃)₂), 3.70-3.55 (dt, 28H, CO-O-(CH₂-CH₂)₇-O-B), 1.71 (s, 3H, CH₂-C(CH₃)-CH₂), 1.48 (q, 2H, B-CH₂-CH₂-), 1.30 (sx, 2H, B-CH₂-CH₂-CH₂-), 1.26 (br, 2H, -(CH₂-C(CH₃))-), 1.12 (m, 2H, B-(CH₂)₂-CH₂-CH₃), 0.86 (q, 3H, (CH₂)₂-CH₃); ¹¹B NMR (400 MHz, D₂O): δ (ppm) = 8.8 (s, -CH₂-B-(OR)₂); ¹⁹F NMR (400 MHz, D₂O): δ (ppm) = -75.89 (s, CF₃).

pLBBn7(OFaIP)₂. Yield: 2.7 g (68 %). ¹H NMR (400 MHz, D₂O): δ (ppm) = 4.51-4.19 (m, 2H, B-O-CH(CF₃)(CH₃)), 3.70-3.55 (dt, 28H, CO-O-(CH₂-CH₂)₇-O-B), 1.71 (s, 3H, CH₂-C(CH₃)-CH₂), 1.49 (q, 2H, B-CH₂-CH₂-), 1.30 (sx, 2H, B-CH₂-CH₂-CH₂-), 1.26 (br, 2H, -(CH₂-C(CH₃))-), 1.12 (m, 2H, B-(CH₂)₂-CH₂-CH₃), 1.02 (d, 6H, B-O-CH(CF₃)(CH₃)), 0.86 (q, 3H, (CH₂)₃-CH₃); ¹¹B NMR (400 MHz, D₂O): δ (ppm) = 4.3 (s, -CH₂-B-(OR)₂); ¹⁹F NMR (400 MHz, D₂O): δ (ppm) = -75.98 (s, CF₃).

pLBBn1(OGly)₂. Yield: 3.54 g (68 %). ¹H NMR (400 MHz, D₂O): δ (ppm) = 3.61-3.53 (m, 28H, O-CH₂-CH₂-O), 3.07 (s, 6H, CO-CH₃), 1.65 (s, 3H, CH₂-C(CH₃)-CH₂), 1.43 (m, 6H, B-CH₂-CH₂-), 1.25 (m, 6H, B-CH₂-CH₂-CH₂-), 1.16 (br, 2H, -(CH₂-C(CH₃))-), 1.06 (m, 2H, B-(CH₂)₂-CH₂-CH₃), 0.81 (m, 9H, B-(CH₂)₃-CH₃); ¹¹B NMR (400 MHz, D₂O): δ (ppm) = 3.6 (s, -CH₂-B-(OR)₂).

pLBBn1(OGlyOFaIP). Yield: 2.16 g (91 %). ¹H NMR (400 MHz, D₂O): δ (ppm) = 4.47 (sp, 1H, B-O-CH(CF₃)₂), 3.62-3.46 (m, 16H, O-CH₂-CH₂-O), 3.40 (s, 3H, -O-CH₃), 1.62 (s, 3H, CH₂-C(CH₃)), 1.41 (m, B-CH₂-CH₂-), 1.24 (m, B-CH₂-CH₂-CH₂-), 1.07 (m, B-(CH₂)₂-CH₂-CH₃), 1.02 (br, -(CH₂-C(CH₃))-), 0.79 (m, B-(CH₂)₃-CH₃); ¹¹B NMR (400 MHz, D₂O): δ (ppm) = 5.9 (s, -CH₂-B-(OR)₂); ¹⁹F NMR (400 MHz, D₂O): δ (ppm) = -78.2 (s, CF₃).

pLBBn1(OGlyOFaIP). Yield: 2.97 g (78 %). ¹H NMR (400 MHz, D₂O): δ (ppm) = 4.51 (sp, 1H, B-O-CH(CF₃)(CH₃)), 3.54-3.63 (m, 28H, O-(CH₂-CH₂)₇-O), 3.49 (s, 3H, -O-CH₃), 1.71 (s, 3H, CH₂-C(CH₃)), 1.49 (m, B-CH₂-CH₂-), 1.30 (m, B-CH₂-CH₂-CH₂-), 1.15 (d, 12H, B-O-CH(CF₃)(CH₃)), 1.10 (m, B-(CH₂)₂-CH₂-CH₃), 1.01 (br, -(CH₂-C(CH₃))-), 0.86 (m, B-(CH₂)₃-CH₃); ¹¹B NMR (400 MHz, D₂O): δ (ppm) = 4.3 (s, -CH₂-B-(OR)₂); ¹⁹F NMR (400 MHz, D₂O): δ (ppm) = -78.2 (s, CF₃).

The general procedure of polymerization

The synthesized boron-based monomers were used to obtain a series of SLICPEs using the random radical polymerization method. The following example describes the procedure used for the synthesis of the linear polymer pLBBn₁(OMe)₂: LBBn₁(OMe)₂ monomer (0.95 g), AIBN (0.0040 g, 3 wt%), and methanol (0.40 ml) were gently mixed in a Schlenk tube at RT. To remove as much oxygen as possible, the system was bubbled for 3 min with a flow of argon and an additional 30 min after the reagents were added. The reaction flask was immersed in a hot oil bath at 60 °C and left for 6h. After the reaction, the polymers were dried on a rotary evaporator, thoroughly dried at 60 °C under vacuum for 24 h, and stored in the glove box. The monomers LBBn₁(OR)₂, LBBn₇(OR)₂, and LBBn₉(OR)₂ were used for obtaining pLBBn₁(OR)₂, pLBBn₇(OR)₂, and pLBBn₉(OR)₂ SLICPEs following the same polymerization method described above.

The obtained polymers pLBBn₁(OMe)₂, pLBBn₁(OEt)₂, pLBBn₁(OiP)₂, and pLBBn₁(OF₆iP)₂ were white solid; pLBBn₇(OMe)₂, pLBBn₇(OEt)₂, pLBBn₇(OiP)₂, pLBBn₉(OMe)₂, pLBBn₇(OF₃iP)₂, pLBBn₁(OGly)₂, pLBBn₁(OGlyOF₃iP) were gels; and pLBBn₇(OF₆iP)₂, pLBBn₁(OGlyOF₆iP) were viscous liquids.

Preparation of SLICPEs

The SLICPEs made with the white solid polymers such as pLBBn₁(OMe)₂, pLBBn₁(OEt)₂, pLBBn₁(OiP)₂, and pLBBn₁(OF₆iP)₂ were prepared by dissolution, drop-casting, and evaporation. A solution of 10 wt.% of polymer in MeOH was mixed, and 200 μL was drop-casted onto an 11 mm diameter silicone mold. First, the SLICPEs were dried at RT under nitrogen flow for 6h and then under vacuum in a BUCHI glass oven at 60 °C for 2h. The SLICPEs made with the gel polymers such as pLBBn₇(OMe)₂, pLBBn₇(OEt)₂, pLBBn₇(OiP)₂, pLBBn₉(OMe)₂, pLBBn₇(OF₃iP)₂, pLBBn₁(OGly)₂, and pLBBn₁(OGlyOF₃iP) were prepared with a hot press at 60 °C under 10 bars for 5 min. The thickness of the obtained membranes for the gel polymers was around 70 μm. The viscous liquid polymers such as pLBBn₇(OF₆iP)₂ and pLBBn₁(OGlyOF₆iP) were used as is, without any particular physical preparation for tests.

The tests with gel SLICPEs in contact with lithium metal, the polymers were used in an Ar-filled glove box. In the first step, the polymers were placed inside sealed airtight pockets inside the glove box to be pressed at 60 °C under 10 bars for 5 min, avoiding moisture environment contact. In the second step, the lithium metal was placed on the made SLICPE membrane and closed together inside a sealed airtight pocket to be pressed in the same condition that it had previously been.

Results and discussion

Synthesis of lithium borate monomers and their single lithium-ion conducting polymers

The methacrylic borate SLICPEs studied in this work were synthesized following the three steps shown in Fig. 1(a). Different ethoxy methacrylate monomers were chosen as reactants: 2-hydroxyethyl methacrylate (HEMA) to have one ethoxy repeating unit as linker (n₁), and two poly(ethylene glycol) methacrylates to have seven and nine ethoxy repeating units (n₇, and n₉ respectively). The first step of the synthesis involves the covalent bonding of the ethoxy methacrylate group to the boron atom by a -C-O-B- bond. This step is carried out using two different methods: A and B methods, which are detailed in Fig. 1(b) and Fig. 1(c). Method A allows the synthesis of BMn(OR)₂ in one step by using Tri-R borates as reagents where the R substituents of interest are already bonded to the boron. Method A is used to synthesize the seven SLICPEs with R as aliphatic substituents (methyl, ethyl, and isopropyl): pLBBn₁(OMe)₂, pLBBn₁(OEt)₂, pLBBn₁(OiP)₂, pLBBn₇(OMe)₂, pLBBn₇(OEt)₂, pLBBn₇(OiP)₂, pLBBn₉(OMe)₂. Method B splits the one-step method A into two steps; it is used for reagents where the R substituents of interest are not bonded to the boron. The steps include adding Borane to obtain the bond with the boron atom in the form -C-O-BH₂, then adding the alcohol R-OH to get the two desired -O-R substituents in BMn(OR)₂.

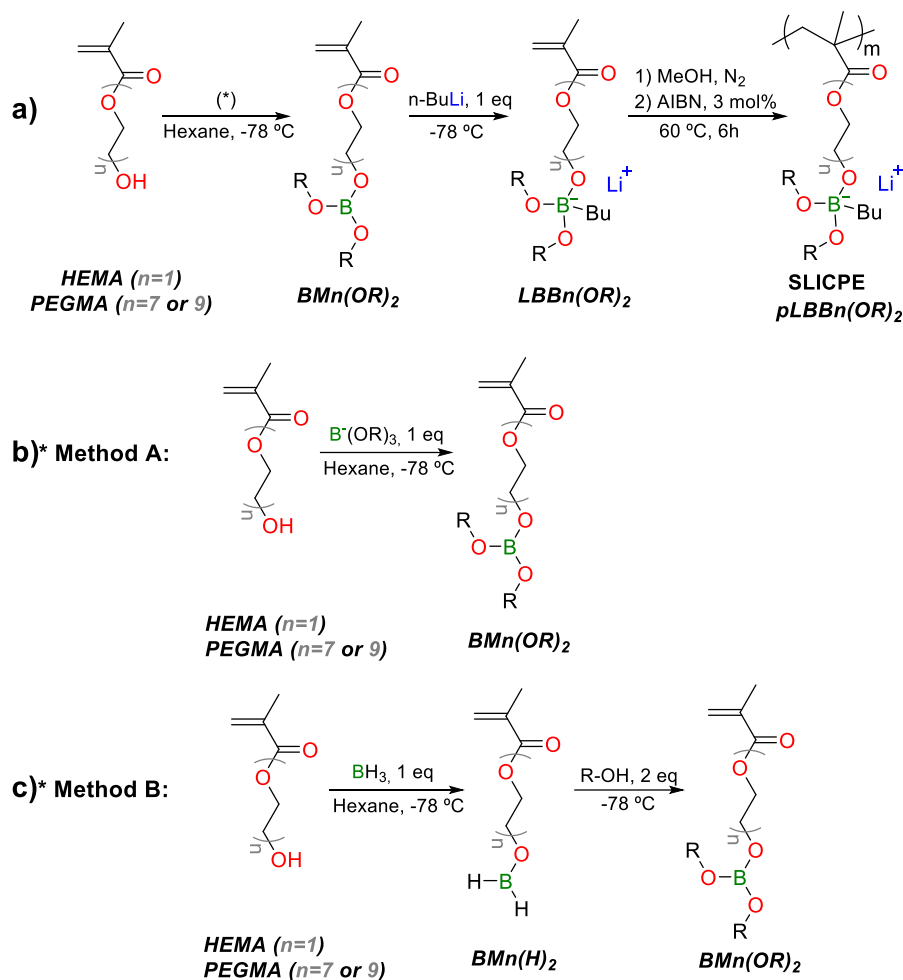


Fig. 1. (a) Synthetic routes for the general preparation of $pLBBn(OR)_2$, and the two synthetic routes to prepare monomers $BMn(OR)_2$ following the (b) method A, and (c) method B.

In the second stage (Fig. 1(a)), $nBuLi$ is added to the boron atom to give rise to the formation of the boron-lithium salts of the form $LBBn(OR)_2$, generating a covalent bond (-C-B-). Finally, the different monomers were polymerized in the last stage using a conventional free radical polymerization method, adding AIBN as an initiator. After the reaction, the polymers were purified, dried, and stored in the glove box.

All synthesized polymers are summarized in Table S1 with their corresponding name. Polymers, including three different linkers, were designed with one ethoxy unit, seven ethoxy units, or nine ethoxy units between the methacrylic polymer chain and the borate anion. They are classified into four categories of lithium borate polymers created according to the chemical characteristics of the substituents such as aliphatic, fluorinated, self-solvating, and the last group includes a fluorinated substituent and an ethylene glycol substituent, as shown in Fig. 2.[34,35]

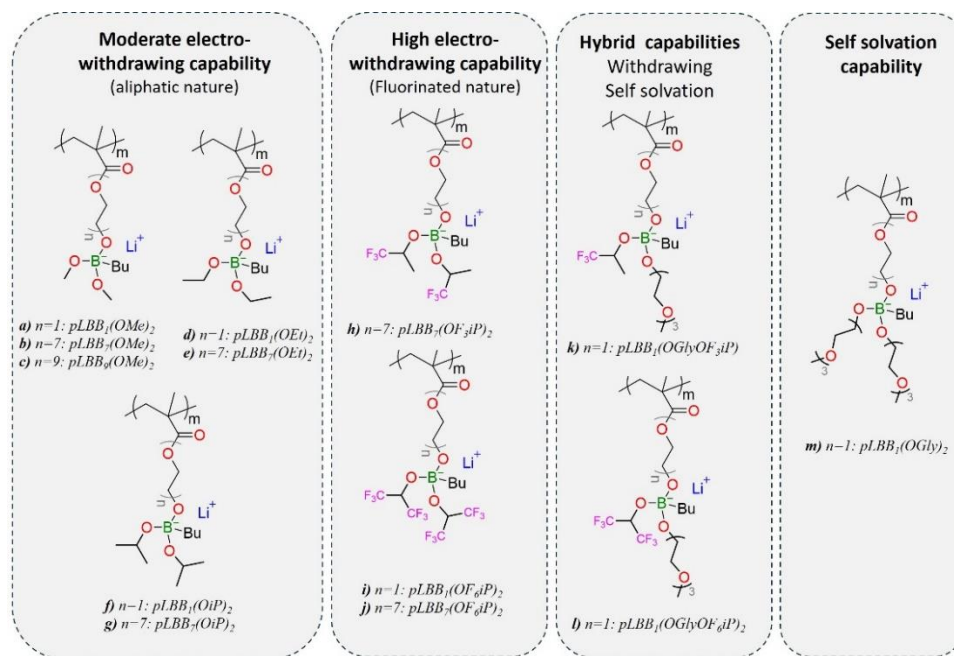


Fig. 2. The chemical structure of synthesized lithium borate SLICPEs.

Structure and thermal characterizations of lithium borate SLIPCEs

NMR and FTIR characterized each monomer and polymer to confirm their chemical structures. For example, Fig. S1 and Fig. 3(a) show the 1H NMR and FTIR spectra with peak assignment for the monomer $LBBn_7(OMe)_2$ in blue and polymer $pLBBn_7(OMe)_2$ in red. All monomers and polymers present similar signals in 1H NMR spectra (Fig. S1), such as the butyl group bonded to the boron atom in the region of 0.5 to 1.8 ppm, the methyl and polyethylene oxide of the methacrylate group around 1.7 and 3.5-3.7 ppm respectively. Depending on the substituents bound to the boron, the NMR signal is different, and in the context of our example, it is the methyl group found at 2.5 and 2.8 ppm. The typical markers of methyl methacrylate monomers are the vinylic protons between 5.2 and 6.2 ppm corresponding to the methylene group, which are absent for the polymers, confirming the total polymerization in addition to the methyl signal around 1.2 ppm. The FTIR spectra (Fig. 3(a)) show similar peaks for monomers and polymers corresponding to the alkane groups between 2800 and 3000 cm^{-1} and for carbonyl groups at 1710 cm^{-1} . Besides, the peak corresponding to the alkene groups at 1635 cm^{-1} is present for the monomers and absent for the polymers, which once again confirms the full extent of the polymerization.

Fig. 3(b) shows the 1H NMR spectra for $pLBBn_7(OiP)_2$, $pLBBn_7(OF_3iP)_2$, and $pLBBn_7(OF_6iP)_2$ polymers. In general, the assignment of peaks in the 1H NMR spectra shows a septet associated with the unprotected carbon-alpha proton of the (1,1,1,3,3,3-hexafluoropropan-2-yl)oxy with a chemical shift at 4.7 ppm for $pLBBn_7(OF_6iP)_2$. The septet signal shows a decrease in intensity and a shift to the high field (4.2 ppm) due to the effect of the substitution of three fluorine atoms by hydrogens as a substituent in the SLICPE $pLBBn_7(OF_3iP)$. This behaviour is even more pronounced for the SLICPE $pLBBn_7(OiP)_2$, in which hydrogens substitute all fluorine atoms, and the septet is shifted to 4.0 ppm.

In addition to 1H NMR analysis, ^{11}B and ^{19}F NMR spectra were studied to complement the analysis of the chemical structure of monomers and polymers and to elucidate the effect of the different electron-withdrawing groups on the electron density of the borate group. Due to the similar molecular structures of SLICPEs $pLBBn_7(OiP)_2$, $pLBBn_1(OGly)_2$, $pLBBn_1(OGlyOF_3iP)$, $pLBBn_7(OF_3iP)_2$, $pLBBn_1(OGlyOF_6iP)$, and $pLBBn_7(OF_6iP)_2$ SLICPEs these were selected for comparison and analysis of the degree of deprotection and electron density of the central boron atom, these were selected for comparison and analysis of the degree of deprotection and electron density of the central boron atom by ^{11}B NMR (Fig. S2). This is related to the chemical shifts of the signals towards the low field,

indicating less interaction with other nuclei, and is related to the increased mobility of the lithium ions through the shift of the single ^{11}B NMR signal associated with the tetra-coordinated boron atoms.[36-38]

The chemical shift of the $\text{pLBBn}_7(\text{OiP})_2$ signal is between 2.3 and 3.8 ppm for the other aliphatic polymers (Fig. S2.i). The signals are located in the high fields due to the moderate electron-withdrawing groups of aliphatic substituents, which do not influence the electron density of the boron atom. In the same way, $\text{pLBBn}_1(\text{OGly})_2$ has a signal with a chemical shift of 3.6 ppm (Fig. S2.ii). Regarding the signals of polymers $\text{pLBBn}_1(\text{OGlyOF}_3\text{iP})$, $\text{pLBBn}_7(\text{OF}_3\text{iP})_2$, $\text{pLBBn}_1(\text{OGlyOF}_6\text{iP})$, and $\text{pLBBn}_7(\text{OF}_6\text{iP})_2$, they have chemical shifts of 4.3, 4.3, 5.9, and 8.8 (Fig. S2-iii-vi). The chemical shifts move towards lower fields than the aliphatic polymers, implying a higher degree of deprotection and decreased electron density on the boron atom. This effect is related to the fluorinated groups, which increase the electro-withdrawing capability. We can notice the correlations between the evolution of chemical shifts and the increase of fluorine atoms for $\text{pLBBn}_7(\text{OiP})_2 < \text{pLBBn}_7(\text{OF}_3\text{iP})_2 < \text{pLBBn}_7(\text{OF}_6\text{iP})_2$ and for $\text{pLBBn}_1(\text{OGly})_2 < \text{pLBBn}_1(\text{OGlyOF}_3\text{iP}) < \text{pLBBn}_1(\text{OGlyOF}_6\text{iP})$.

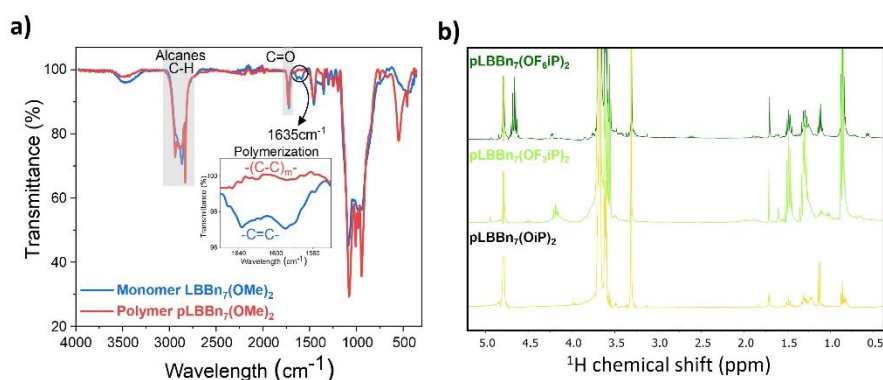


Fig. 3. (a) FTIR spectra for monomer $\text{LBBn}_7(\text{OMe})_2$ and polymer $\text{pLBBn}_7(\text{OMe})_2$; and (b) ^1H NMR spectra for $\text{pLBBn}_7(\text{OiP})_2$, $\text{pLBBn}_7(\text{OF}_3\text{iP})_2$, and $\text{pLBBn}_7(\text{OF}_6\text{iP})_2$.

Table S2 reports the T_g values determined by the DSC technique. All the polymers reported are amorphous, and their T_g values are below -40 °C. In the first instance, the T_g values obtained for the $\text{pLBBn}_1(\text{OR})_2$ type SLICPEs are compared. The lowest value of $t_g = -73$ °C is presented for the $\text{pLBBn}_1(\text{OGly})_2$ SLICPEs and is associated with the mobility of the pendant ethoxy chains to the borate group, which confers a high intrinsic ability to self-solubilize due to the easy interaction of the ions with the ethoxy groups. The decrease of free ethoxy groups in SLICPE $\text{pLBBn}_1(\text{OMe})_2$ decreases the mobility of the chains which is reflected in the increase of the value of $T_g = -65$ °C. The SLICPE $\text{pLBBn}_1(\text{OGlyOF}_6\text{iP})_2$ with a value of $T_g = -60$ °C goes out of the trend, which is associated with a strong interaction between fluorinated groups and lithium ions that decreases the mobility of the principal and pendant polymer chains of SLICPE.

Now, consider the T_g values of $\text{pLBBn}_7(\text{OR})_2$ SLICPEs type. Here, the mode of the ethoxy chain linking the main chain of the polymers with borate groups is a crucial factor. The decrease of Li^+ in SLICPEs, due to the increase of the O/Li^+ ratio, is not the primary determinant in the system. The size and electron-withdrawing ability of the substituent groups on the borate groups play a significant role in affecting the chain mobility of SLICPEs. This refers to the T_g values of -55 , -50 , and -40 °C obtained for SLICPEs $\text{pLBBn}_7(\text{OMe})_2$, $\text{pLBBn}_7(\text{OEt})_2$, and $\text{pLBBn}_7(\text{OF}_6\text{iP})_2$, respectively.

Ionic conductivity of borate SLIPCEs

The ionic conductivity of each new borate SLICPE was measured, and the results are discussed using three comparison axes. Firstly, we compare the three SLICPEs $\text{pLBBn}(\text{OMe})_2$, composed with methyl-oxo substituents in the borate pendant groups and differentiated with an increasing number of ethoxy units in the linker such as n_1 , n_7 , or n_9 . Secondly, optimized SLICPEs with ethoxy linker fixed at n_7 and some different aliphatic and fluorinated oxy substituents in the borate pendant groups are discussed. Thirdly, the influence of the fluorine number on ionic conductivity is examined by comparing SLICPE.

Effect of size of the ethoxy linker between the methacrylic polymer and borate group (n_1 , n_7 , and n_9)

First, we investigated the effect of increasing the number of ethoxy units (n_1 , n_7 , and n_9) on the linker between the methacrylic polymer backbone and the borate group on the ionic conduction properties. The compared SLICPEs must be composed of similar final substituents $-(OR)_2$, chosen by methyl-oxy substituents to have a single variable to assess the effect of ethoxy repeat unit length properly. The chemical structures and pictures of the concerning $pLBBn(OMe)_2$, which are $pLBBn_1(OMe)_2$, $pLBBn_7(OMe)_2$, and $pLBBn_9(OMe)_2$, are shown in Fig. 4(a). Their ionic conductivity results are shown in Fig. 4(b). Exclusively in this part for simplicity, $pLBBn_1(OMe)_2$, $pLBBn_7(OMe)_2$, and $pLBBn_9(OMe)_2$ will be referred to n_1 , n_7 , and n_9 . The increase in the size of the linker showed an effect on the physical appearance of the polymers. This effect was well observed for $pLBBn(OMe)_2$, as shown in Fig. 4(a), which is a powder for n_1 and viscous solids for n_7 and n_9 . [39,40]

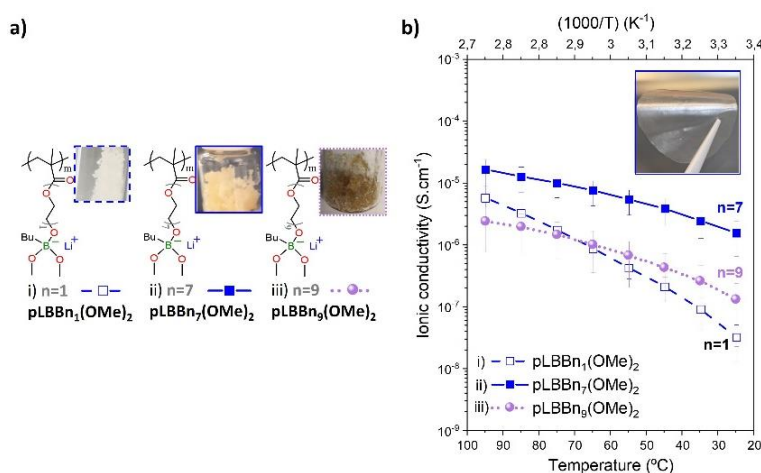


Fig. 4. Comparison of select SLICPEs $pLBBn(OMe)_2$ type: (a) Chemical structures and pictures and (b) of SLICPEs and (b) the temperature dependence of the ionic conductivity for SLICPEs. i) $pLBBn_1(OMe)_2$, ii) $pLBBn_7(OMe)_2$, and iii) $pLBBn_9(OMe)_2$.

As shown in Fig. 4(b), the highest ionic conductivity is measured for the SLICPE with intermediate ethoxy length (n_7) for all temperatures between 25 and 95 $^{\circ}C$. Indeed, the ionic conductivity values for n_7 were 1.58×10^{-6} and 7.64×10^{-6} $S\ cm^{-1}$ at 25 and 60 $^{\circ}C$ respectively, whereas the values were less than 10^{-6} $S\ cm^{-1}$ for n_1 and n_9 (3.29×10^{-8} , and 8.86×10^{-7} $S\ cm^{-1}$ for n_1 and 1.33×10^{-7} , and 1.02×10^{-6} $S\ cm^{-1}$ for n_9 at 25, and 60 $^{\circ}C$, respectively). The increase in ionic conductivity with the increase in the ethoxy repeat unit from 1 to 7 can be explained by the O/Li^+ ratio, which increases from 5 to 11. In other words, the contribution of ethoxy groups helps the self-solvating ability of borate groups, providing better ionic transport pathways for n_7 than for n_1 . However, when the number of ethoxy repeat units was increased beyond 7, for example, at n_9 , the measured ionic conductivity was lower, although the O/Li^+ ratio increased to 13. In conclusion, the self-solvation capability is improved but also limited with the Li^+ concentration. The optimized O/Li^+ ratio seems to be around 11, corresponding to a polymer with an intermediate ethoxy linker (seven units) for the aliphatic substituents.

Table 1. The activation energy for $pLBBn(OMe)_2$ SLICPEs with n_1 , n_7 , and n_9 .

Name	Ea (eV)
$pLBB_1(OMe)_2$	0.302
$pLBB_7(OMe)_2$	0.136
$pLBB_9(OMe)_2$	0.176

Moreover, the activation energies (E_a) were calculated using the Arrhenius equation (2), and the values for the three $pLBBn(OMe)_2$ SLICPEs are presented in Table 1. The E_a values provide information on the strength of the coulombic interactions and can be related to the temperature dependence of the ionic conductivity. The E_a value for n_7 and n_9 (0.136 and 0.176 eV respectively) are close, the curves have parallel behaviors to each other in the function of the temperature, whereas E_a for n_1 (0.302 eV) is much larger and shows a very temperature-dependent behavior. The ionic conductivity trend was reversed between n_1 and n_9 above 70 °C. n_1 shows a greater temperature dependence with ionic conductivity values of 3.29×10^{-8} and 5.81×10^{-6} S.cm⁻¹ at 25 °C and 90 °C respectively, whereas the ionic conductivity was more constant for n_9 with values of 1.34×10^{-7} and 2.44×10^{-6} S.cm⁻¹ at 25 and 90 °C respectively. Besides being explained by the values of E_a , this behaviour is due to the generation of spaces and conduction pathways due to the movement of substituent groups compared to the proportion of the polymer. The ionic transport is through hopping between the borate anionic centers for n_1 , whereas it is preferentially promoted by the movement of the ethoxy chains for n_7 and n_9 .

Effect of the different borate substituents with the ethoxy linker of n_7

Based on the previous study, four SLICPEs with the best ethoxy linker showing 7 units ($pLBBn_7(OR)_2$) and different aliphatic or fluorinated substituents were compared in Fig. 5. The chemical structures and pictures of the concerning $pLBBn_7(OR)_2$ are shown in Fig. 5(a), and their ionic conductivity results in Fig. 5(b). $pLBBn_7(OiP)_2$ is a viscous liquid polymer as shown the picture in Fig. 5(a-i). The three other polymers are malleable materials forming excellent transparent films (pictures in Fig. 5(a-ii-iv)).

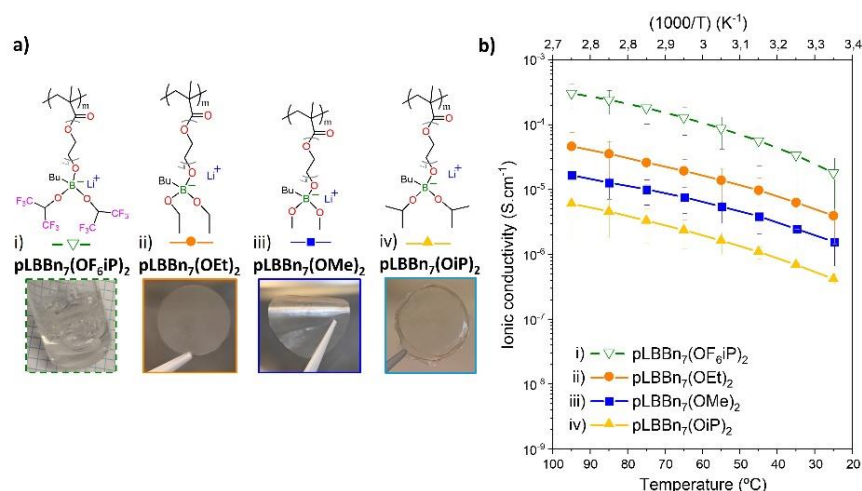


Fig. 5. (a) Chemical structures and pictures of n_7 SLICPEs i) $pLBBn_7(OiP)_2$, ii) $pLBBn_7(OEt)_2$, iii) $pLBBn_7(OMe)_2$, and iv) $pLBBn_7(OiP)_2$; and (b) temperature dependence of the ionic conductivity for n_7 SLICPEs.

As a trend, the ionic conductivity curves (Fig. 5(b)) are higher for the four SLICPEs n_7 , with values of 1.58×10^{-6} , 3.95×10^{-6} , 4.18×10^{-7} , 1.80×10^{-5} S.cm⁻¹ at 25 °C for $pLBBn_7(OMe)_2$, $pLBBn_7(OEt)_2$, $pLBBn_7(OiP)_2$, $pLBBn_7(OiP)_2$; compared to their n_1 homolog, with values of 3.29×10^{-8} , 4.42×10^{-9} , 7.78×10^{-9} , 2.35×10^{-7} S.cm⁻¹ at 25 °C for $pLBBn_1(OMe)_2$, $pLBBn_1(OEt)_2$, $pLBBn_1(OiP)_2$, $pLBBn_1(OiP)_2$ respectively (Fig. S3). Moreover, n_7 SLICPEs depend less on temperature than their n_1 counterpart, and n_7 aliphatic SLICPEs follow a similar trend between them with increasing order $pLBBn_7(OiP)_2 < pLBBn_7(OMe)_2 < pLBBn_7(OEt)_2$.

The ionic conductivity is greatly improved with the fluorinated substituents for $pLBBn_7(OiP)_2$. This can be explained by the decrease in the electron density of the boron atom, as shown in the ¹¹B NMR study previously. The boron atom is highly deprotected for $pLBBn_7(OiP)_2$ compared to the aliphatic ones due to the electronic delocalization effect with the electron-withdrawing fluorinated substituents. The interaction energy between Li⁺ and the borate group is lower for $pLBBn_7(OiP)_2$ helping the Li-ions mobility. In addition, the viscous liquid texture promotes the mobility of ions compared to materials in the form of films.

The ionic conductivity of $\text{pLBBn}_7(\text{OF}_6\text{iP})_2$ with values of 1.80×10^{-5} , 1.29×10^{-4} , and $3.05 \times 10^{-4} \text{ S cm}^{-1}$ at 25, 60, and 90 °C respectively, follows very closely the ionic conductivity of $\text{pLBBn}_1(\text{OGlyOF}_6\text{iP})$ with values of 3.26×10^{-5} , 1.65×10^{-4} , and $3.28 \times 10^{-4} \text{ S cm}^{-1}$ at 25, 60 and 90 °C respectively. $\text{pLBBn}_7(\text{OF}_6\text{iP})_2$ has an O/Li ratio of 11 mainly due to its intermediate ethoxy linker (n_7) and a F/Li ratio of 12 thanks to its two identical pendant groups isopropyl-oxy with six fluorine atoms ($-\text{O}-\text{CH}(\text{CF}_3)_2$). Its chemical structure promotes ionic conductivity with the effects of lithium solvation by oxygen atoms and of the delocalization of the anionic charge of the boron atom with the electro-withdrawing groups. $\text{pLBBn}_1(\text{OGlyOF}_6\text{iP})$ comprises a shorter ethoxy linker (n_1). Still, its O/Li ratio is 8, which is higher than for the aliphatic n_1 SLICPEs (O/Li ratio of 5), and this is due to one of its pendant groups constituted of glycol substituents. The other pendant group is an isopropyl-oxy substituent with six fluorine atoms ($-\text{O}-\text{CH}(\text{CF}_3)_2$), which gives an F/Li ratio of 6. The ^{11}B NMR study shows signals for $\text{pLBBn}_7(\text{OF}_6\text{iP})_2$ and $\text{pLBBn}_1(\text{OGlyOF}_6\text{iP})$ with chemical shifts of 8.8 and 5.9 ppm, respectively (Fig. S2-v-vi), which are in the lowest fields compared with the other studied polymers. The degree of deprotection of the borate group is higher for $\text{pLBBn}_7(\text{OF}_6\text{iP})_2$ than for $\text{pLBBn}_1(\text{OGlyOF}_6\text{iP})$, which means the interaction energy between Li and borate group is lower for $\text{pLBBn}_7(\text{OF}_6\text{iP})_2$ (Fig. S4). However, contrary to the values of the ratios, the size of the electron-withdrawing group, and the NMR study, the ionic conductivity of $\text{pLBBn}_7(\text{OF}_6\text{iP})_2$ is slightly lower than for $\text{pLBBn}_1(\text{OGlyOF}_6\text{iP})$. The difference is probably due to the geometry of the polymers. The ethoxy chain on the pendant position on the boron atom for $\text{pLBBn}_1(\text{OGlyOF}_6\text{iP})$ gives more availability for the lithium solvation, unlike the position between the boron and polymer backbone. A modeling study could help to understand and validate this hypothesis.

Influence of the fluorine content of the substituents

In this part, the evolution of ionic conductivity is discussed for two comparison cases of SLICPEs with different numbers of fluorine atoms and the same structures. In the first case, $\text{pLBBn}_1(\text{OGlyOF}_3\text{iP})$ and $\text{pLBBn}_1(\text{OGlyOF}_6\text{iP})$ are compared, their chemical structures and pictures are shown in Fig. 6(a.i-ii), and their ionic conductivity results in Fig. 6(b). For the second case, $\text{pLBBn}_7(\text{OiP})_2$, $\text{pLBBn}_7(\text{OF}_3\text{iP})_2$, and $\text{pLBBn}_7(\text{OF}_6\text{iP})_2$ are shown in Fig. 6(a.iii-v), and Fig. 6(c).

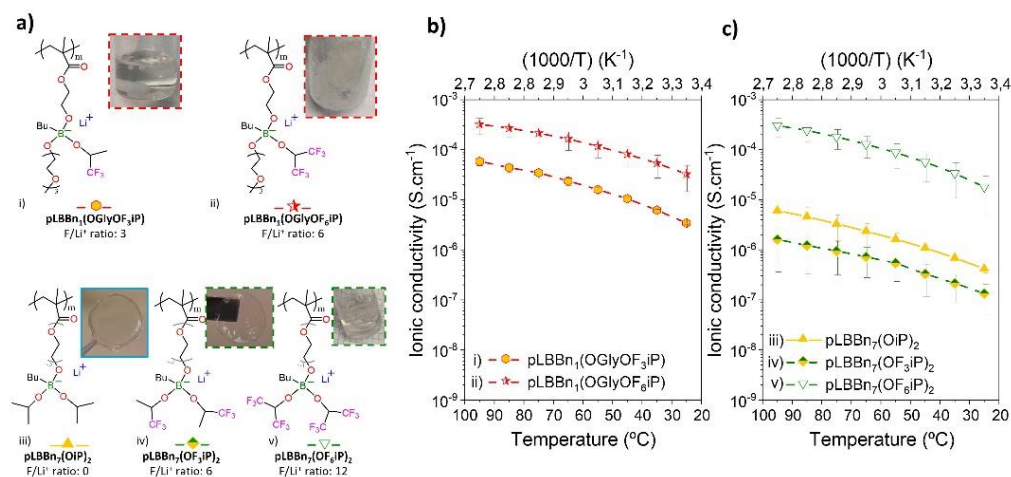


Fig. 6. (a) Chemical structures and pictures of SLICPEs i) $\text{pLBBn}_1(\text{OGlyOF}_3\text{iP})$, ii) $\text{pLBBn}_1(\text{OGlyOF}_6\text{iP})$, iii) $\text{pLBBn}_7(\text{OiP})_2$, iv) $\text{pLBBn}_7(\text{OF}_3\text{iP})_2$, and v) $\text{pLBBn}_7(\text{OF}_6\text{iP})_2$. Temperature dependence of ionic conductivity for (b) SLICPEs with 1 ethoxy linker (i-ii), and c) SLICPEs with 7 ethoxy linkers (iii-v).

In the first case (Fig. 6(a.i-ii) and Fig. 6(b)), the SLICPEs $\text{pLBBn}_1(\text{OGlyOF}_3\text{iP})$ and $\text{pLBBn}_1(\text{OGlyOF}_6\text{iP})$ are compared. Although they are composed of the ethoxy linker of n_1 , they have an O/Li⁺ ratio of 8, which is higher than for the aliphatic n_1 SLICPEs (O/Li⁺ ratio of 5) and this is due to the glycol

substituent on pendant groups. As discussed before, the increase of the O/Li⁺ ratio helps the lithium-ion solvation, and this can explain why pLBBn₁(OGlyOF₃iP) and pLBBn₁(OGlyOF₆iP) have higher ionic conductivity than the aliphatic pLBBn₁(OR)₂. In addition, pLBBn₁(OGlyOF₃iP) and pLBBn₁(OGlyOF₆iP) have a similar geometric structure with two pendant groups linked to the boron, which are: one group of triethylene glycol monomethyl ether, and the other group is an isopropyl-oxy geometry with different atoms. The isopropyl-oxy group is composed of six atoms of fluorine (-O-CH-(CF₃)₂) with a symmetric arrangement for pLBBn₁(OGlyOF₆iP) while pLBBn₁(OGlyOF₃iP) has a hybrid composition with three atoms of fluorine and three of hydrogen (-O-CH-(CF₃)(CH₃)) with an asymmetric arrangement. So, the F/Li⁺ ratio increases from 3 to 6 for pLBBn₁(OGlyOF₃iP) and pLBBn₁(OGlyOF₆iP), respectively. This increase in the F/Li⁺ ratio slightly impacts the energy density of the borate groups, as it was observed in the ¹¹B NMR study with chemical shifts of 4.3 and 5.9 ppm for pLBBn₁(OGlyOF₃iP) and pLBBn₁(OGlyOF₆iP) respectively (Fig. S2-iii and v). The ionic conductivity values also increase, from 3.43×10⁻⁶ to 3.26×10⁻⁵ S.cm⁻¹ at 25 °C for pLBBn₁(OGlyOF₃iP), and pLBBn₁(OGlyOF₆iP) respectively. The ionic conductivity higher for pLBBn₁(OGlyOF₆iP) can be explained once again by the increase in F/Li⁺ ratio, which strengthens the electron-withdrawing capability on the pendant groups and decreases the electron density on the borate groups. Thus, the Li⁺ mobility is promoted by a lower interaction energy between Li⁺ and borate for pLBBn₁(OGlyOF₆iP) than for pLBBn₁(OGlyOF₃iP), as confirmed by the ionic conductivity values.

In the second case (Fig. 6(a,iii-v) and Fig. 6(c)), the SLICPEs have a similar geometric structure composed of two identical groups of isopropyl-oxy geometry with different atoms with increasing fluorine atoms. The two isopropyl-oxy groups are aliphatic (-O-CH-(CH₃)₂) for pLBBn₇(OiP)₂, while the six hydrogens on each isopropyl group are changed for fluorine atoms (-O-CH-(CF₃)₂) for pLBBn₇(OF₆iP)₂. pLBBn₇(OF₃iP)₂ has a hybrid composition with two isopropyl-oxy groups composed each of three atoms of fluorine and three of hydrogen (-O-CH-(CF₃)(CH₃)) in an asymmetric arrangement. The F/Li⁺ ratio increased from 0, 6, and 12 for pLBBn₇(OiP)₂, pLBBn₇(OF₃iP)₂, and pLBBn₇(OF₆iP)₂ respectively; and the ionic conductivity values are 4.18×10⁻⁷, 1.34×10⁻⁷, and 1.80×10⁻⁵ S.cm⁻¹ at 25 °C respectively. It is worth mentioning that the increasing evolution of the ionic conductivity is pLBBn₇(OF₃iP)₂ < pLBBn₇(OiP)₂ < pLBBn₇(OF₆iP). The ionic conductivity behaviour of pLBBn₇(OF₃iP)₂ is the lowest and even lower than pLBBn₇(OiP)₂. Therefore, in other words, the ionic conductivity does not evolve following the F/Li⁺ ratio in this case. Although the ¹¹B NMR study had shown an evolution of chemical shifts with the increase of fluorine atoms for pLBBn₇(OiP)₂, pLBBn₇(OF₃iP)₂, and pLBBn₇(OF₆iP)₂ with chemical shifts of 3.1, 4.3, and 8.8 respectively (Fig. S2.i, iv, and vi), the ionic conductivity trend is different for pLBBn₇(OF₃iP)₂. However, we can observe that the chemical shifts do not evolve continuously, and those of pLBBn₇(OF₃iP)₂ and pLBBn₇(OF₆iP)₂ are very close compared to those of pLBBn₇(OiP)₂. The asymmetric arrangement of (-O-CH-(CF₃)(CH₃)) groups in pLBBn₇(OF₃iP)₂ probably plays a complex role in lithium mobility, and this hypothesis could be better explained with a modeling study of molecular orbitals.

Lithium transference number and electrochemical stability of optimized SLICPEs

The single lithium-ion conducting characteristics were evaluated by measuring the lithium transference number (t_{Li^+}) for the n₁ and n₇ optimized homopolymers, which are pLBBn₁(OGly)₂, pLBBn₁(OGlyOF₆iP), pLBBn₇(OEt)₂, and pLBBn₇(OF₆iP)₂. The t_{Li^+} measurements are shown in Fig. 7. The t_{Li^+} values are **0.92**, **0.93**, **0.88**, and **0.96** for pLBBn₁(OGly)₂, pLBBn₁(OGlyOF₆iP), pLBBn₇(OEt)₂, and pLBBn₇(OF₆iP)₂ respectively.

These are high values because they are close to 1, as expected for single-ion polymers. The high ionic conductivity values describe the ionic transport in SPE, which is promoted by the molecular structure of the designed polymers.[34] In highly conductive SLICPEs, ionic transport is determined by the degree of negative charge delocalization in anionic centers, which decreases the interaction energy in the ionic pair.[2,38] Furthermore, generally accepted models for Li⁺ transport in SPEs involve coupling to the segmental motion of the polymer backbone, and a more flexible backbone is naturally beneficial for conductivity.[4]

The resistance is significantly reduced with viscous liquid homopolymers. Indeed, the electrochemical impedance responses show very high resistances for the two solid SLICPEs with resistance around 75 kΩ for pLBBn₁(OGly)₂ and higher than 1000 kΩ for pLBBn₇(OEt)₂ (inset Fig. 7(a) and Fig. 7(c)). While the resistance is improved by a decrease of values less than 3 kΩ for the two viscous liquid SLICPEs pLBBn₁(OGlyOF₆iP) and pLBBn₇(OF₆iP)₂ (inset Fig. 7(b) and Fig. 7(d)).

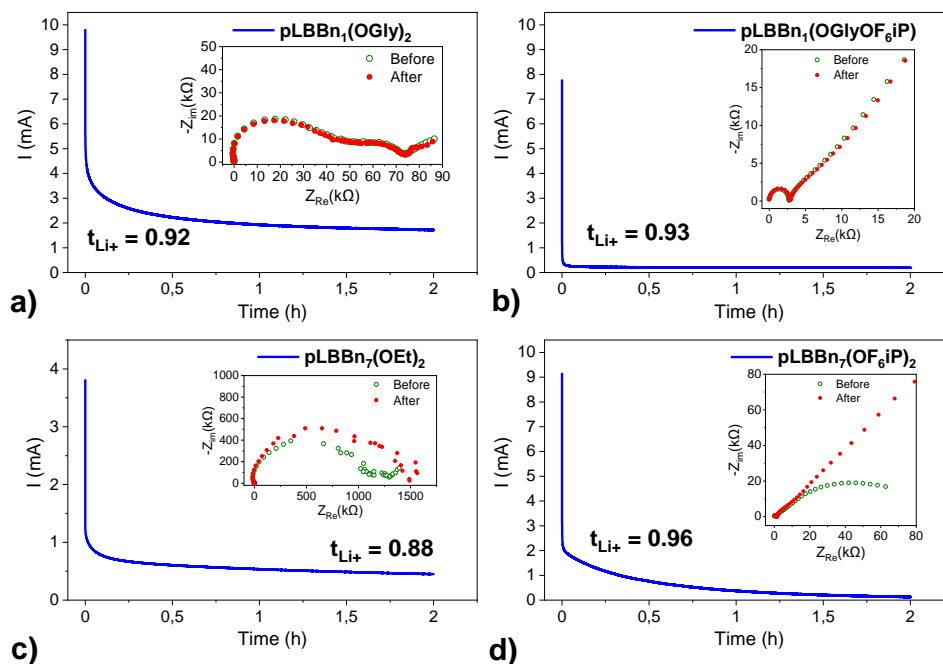


Fig. 7. Lithium transference number (t_{Li^+}) evaluation: typical current transient obtained at the polarization of 10 mV for $Li|pLBBn(OR)_2|Li$ symmetrical cells at 60 °C (inset: Nyquist plot for the same cell before and after polarization) for the SLICPEs (a) $pLBBn_1(OGly)_2$, (b) $pLBBn_1(OGlyOF_6iP)$, (c) $pLBBn_7(OEt)_2$, and (d) $pLBBn_7(OF_6iP)_2$.

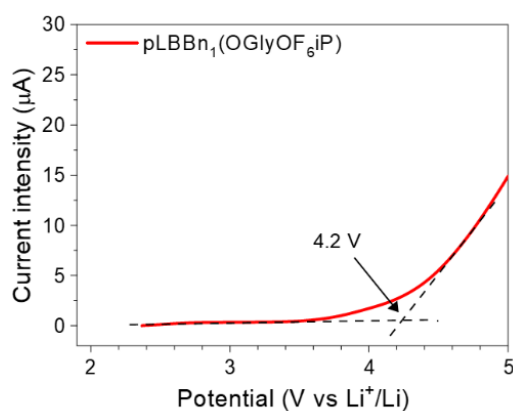


Fig. 8. Linear sweep voltammograms ($v = 2 \text{ mV}\cdot\text{s}^{-1}$) obtained in the $Li|pLBBn_1(OGlyOF_6iP)|\text{stainless steel}$ cell at 60 °C.

To evaluate the electrochemical stability of the homopolymer electrolytes, the cyclic voltammetry of $Li|pLBBn(OR)_2|\text{stainless steel}$ cell at 60 °C was studied for $pLBBn_1(OGlyOF_6iP)$. The result in Fig. 8 shows an electrochemical stability close to 4.2 V vs Li^+/Li , confirming its excellent properties as a solid electrolyte for lithium batteries.

Conclusions

New single-ion lithium conducting polymer electrolytes based on highly delocalized borate groups have been synthesized and characterized. This work shows the effects of the chemical structure on the ionic conductivity values. It highlights the importance of the polymer design in order to achieve the highest ionic conductivity values.

First, the effect study of increasing the ethoxy repeat extender (from n_1 , n_7 , to n_9) on the ionic conductivity showed the contribution of ethoxy groups helps the self-solvating capability, providing better ionic transport pathways but is also limited. The linker with the highest conductivity is the one with seven ethoxy units n_7 (O/Li⁺ ratio of 11). As an alternative, the O/Li⁺ ratio can be increased by playing with the nature of the substituent on the pendant group and not with the ethoxy repeat extender, for example, with glycol groups for pLBBn₁(OGly)₂ or pLBBn₁(OGlyOF₆iP).

Then, SLICPEs with optimized ethoxy linkers (n_7 and O/Li⁺ ratio of 11) and different aliphatic and fluorinated pendant groups showed that the SLICPE with fluorinated pendant groups (pLBBn₇(OF₆iP)₂) achieved the highest ionic conductivity values compared to the aliphatic ones. In fact, increasing the number of fluorine atoms in the substituent groups of SLICPEs improves the electron-withdrawing capacity, which is reflected in the increase of ionic conductivity.

In general conclusion, pLBBn₁(OGlyOF₆iP) and pLBBn₇(OF₆iP)₂ show, to our knowledge, the highest ionic conductivity reported for a lithium single-conduction homopolymer (1.65×10^{-4} and 1.29×10^{-4} S.cm⁻¹ respectively at 60 °C). The single ion-conducting properties were confirmed by its high t_{Li^+} , 0.93 and 0.96 for pLBBn₁(OGlyOF₆iP), and pLBBn₇(OF₆iP)₂ respectively. The chemical structures of the two optimized SLICPEs are schematized in Fig. 9 with a summary of their properties. Future work will focus on the investigation of the optimized SLIPCEs in lithium batteries.

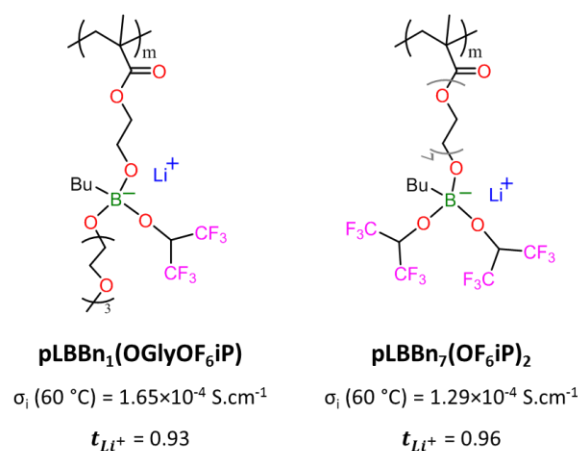


Fig. 9. Chemical structures of the two optimized SLICPEs, values of ionic conductivities, and lithium transference number for pLBBn₁(OGlyOF₆iP) and pLBBn₇(OF₆iP)₂.

Acknowledgments

This work was supported by the European Commission's funded Marie Skłodowska-Curie project POLYTE-EID (project no. 765828). G.G-G. is grateful to the National Council of Science and Technology (CONACYT), Ciencia de Frontera 2023 projects **CF-2023-I-2531** and **CF-2023-G-1266**.

References

1. Nurul, S.; Mohd, A.; Tajuddin, N. A. *International Journal of Electrochemical Science*. **2021**, *16*, 1–15. DOI: <https://doi.org/10.20964/2021.10.53>.
2. Zhang, H.; Li, C.; Piszcz, M.; Coya, E.; Rojo, T.; Rodriguez-Martinez, L. M.; Armand, M.; Zhou, Z. *Chem Soc Rev*. **2017**, *3*, 797–815. DOI: <https://doi.org/10.1039/c6cs00491a>.
3. Zhu, J.; Zhang, Z.; Zhao, S.; Westover, A. S.; Belharouak, I.; Cao, P. F. *Adv Energy Mater*. **2021**, *14*, 1–18. DOI: <https://doi.org/10.1002/aenm.202003836>.
4. Mindemark, J.; Lacey, M. J.; Bowden, T.; Brandell, D. *Prog. Polym. Sci*. **2018**, *81*, 114–143. DOI: <https://doi.org/10.1016/j.progpolymsci.2017.12.004>.
5. Xue, Z.; He, D.; Xie, X. *J. Mater. Chem. A Mater*. **2015**, *38*, 19218–19253. DOI: <https://doi.org/10.1039/c5ta03471j>.
6. Suo, L.; Zheng, F.; Hu, Y. S.; Chen, L. *Chinese Physics B*. **2015**, *1*, 0–4. DOI: <https://doi.org/10.1088/1674-1056/25/1/016101>.
7. Jiang, Y.; Yan, X.; Ma, Z.; Mei, P.; Xiao, W.; You, Q.; Zhang, Y. *Polymers*. **2018**, *4*, 1–13. DOI: <https://doi.org/10.3390/polym10111237>.
8. Croce, F.; Appetecchi, G. B.; Persi, L.; Scrosati, B. *Nature*. **1998**, *394*, 456–458. DOI: <https://doi.org/10.1038/28818>.
9. Guzmán-González, G.; Avila-Paredes, H. J.; Santos-Mendoza, I. *Journal of Solid-State Electrochemistry*. **2023**. DOI: <https://doi.org/10.1007/s10008-023-05563-1>.
10. Porcarelli, L.; Shaplov, A. S.; Bella, F.; Nair, J. R.; Mecerreyes, D.; Gerbaldi, C. *ACS Energy Lett*. **2016**, *4*, 678–682. DOI: <https://doi.org/10.1021/acsenergylett.6b00216>.
11. Shan, X.; Zhao, S.; Ma, M.; Pan, Y.; Xiao, Z.; Li, B.; Sokolov, A. P.; Tian, M.; Yang, H.; Cao, P. F. *ACS Appl. Mater Interfaces*. **2022**, *14*, 56110–56119. <https://doi.org/10.1021/acsami.2c17547>.
12. Guzman Gonzalez, G. *J. Mex. Chem. Soc.* **2023**, *4*, 602–620. DOI: <https://doi.org/10.29356/jmcs.v67i4.1959>.
13. Porcarelli, L.; Vlasov, P. S.; Ponkratov, D. O.; Lozinskaya, E. I.; Antonov, D. Y.; Nair, J. R.; Gerbaldi, C.; Mecerreyes, D.; Shaplov, A. S. *Eur. Polym. J.* **2018**, *107*, 218–228. DOI: <https://doi.org/10.1016/j.eurpolymj.2018.08.014>.
14. Zygadła-Monikowska, E.; Florjańczyk, Z.; Ostrowska, J.; Bołtomiuk, P.; Frydrych, J.; Sadurski, W.; Langwald, N. *Electrochim. Acta*. **2011**, *1*, 66–73. DOI: <https://doi.org/10.1016/j.electacta.2011.07.120>.
15. Guzmán-González, G.; Alvarez-Tirado, M.; Olmedo-Martínez, J. L.; Picchio, M. L.; Casado, N.; Forsyth, M.; Mecerreyes, D. *Adv. Energy Mater*. **2023**, *1*, 2202974. DOI: <https://doi.org/10.1002/aenm.202202974>.
16. Porcarelli, L.; Shaplov, A. S.; Salsamendi, M.; Nair, J. R.; Vygodskii, Y. S.; Mecerreyes, D.; Gerbaldi, C. *ACS Appl Mater Interfaces*. **2016**, *16*, 10350–10359. DOI: <https://doi.org/10.1021/acsami.6b01973>.
17. Shaplov, A. S.; Vlasov, P. S.; Armand, M.; Lozinskaya, E. I.; Ponkratov, D. O.; Malyshkina, I. A.; Vidal, F.; Okatova, O. V.; Pavlov, G. M.; Wandrey, C.; Godovikov, I. A.; Vygodskii, Y. S. *Polym Chem*. **2011**, *11*, 2609–2618. DOI: <https://doi.org/10.1039/c1py00282a>.
18. Meziane, R.; Bonnet, J. P.; Courty, M.; Djellab, K.; Armand, M. *Electrochim Acta*. **2011**, *1*, 14–19. DOI: <https://doi.org/10.1016/j.electacta.2011.03.074>.
19. Ma, Q.; Zhang, H.; Zhou, C.; Zheng, L.; Cheng, P.; Nie, J.; Feng, W.; Hu, Y. S.; Li, H.; Huang, X.; Chen, L.; Armand, M.; Zhou, Z. *Angewandte Chemie - International Edition*. **2016**, *7*, 2521–2525. DOI: <https://doi.org/10.1002/anie.201509299>.
20. Zhu, Y. S.; Wang, X. J.; Hou, Y. Y.; Gao, X. W.; Liu, L. L.; Wu, Y. P.; Shimizu, M. *Electrochim Acta*. **2013**, *87*, 113–118. DOI: <https://doi.org/10.1016/j.electacta.2012.08.114>.
21. Ponkratov, D. O.; Lozinskaya, E. I.; Shaplov, A. S.; Khanin, D. A.; Afanasyev, E. S.; Takazova, R. U.; Vygodskii, Y. S. *Doklady Chemistry*. **2022**, *2*, 29–36. DOI: <https://doi.org/10.1134/S0012500822020021>.
22. Rolland, J.; Brassinne, J.; Bourgeois, J. P.; Poggi, E.; Vlad, A.; Gohy, J. F. *J Mater Chem. A Mater*. **2014**, *30*, 11839–11846. DOI: <https://doi.org/10.1039/c4ta02327g>.
23. Rolland, J.; Poggi, E.; Vlad, A.; Gohy, J. F. *Polymer*. **2015**, *68*, 344–352. DOI: <https://doi.org/10.1016/j.polymer.2015.04.056>.

24. Olmedo-Martínez, J. L.; Porcarelli, L.; Alegría, Á.; Mecerreyes, D.; Müller, A. J. *Macromolecules*. **2020**, *11*, 4442–4453. DOI: <https://doi.org/10.1021/acs.macromol.0c00703>.
25. Meabe, L.; Goujon, N.; Li, C.; Armand, M.; Forsyth, M.; Mecerreyes, D. *Batter Supercaps*. **2020**, *1*, 68–75. DOI: <https://doi.org/10.1002/batt.201900119>.
26. Guzmán-González, G.; Vauthier, S.; Alvarez-Tirado, M.; Cotte, S.; Castro, L.; Guéguen, A.; Casado, N.; Mecerreyes, D. *Angewandte Chemie - International Edition*. **2021**, *7*, 1–5. DOI: <https://doi.org/10.1002/anie.202114024>.
27. Zygadlo-Monikowska, E.; Florjańczyk, Z.; Służewska, K.; Ostrowska, J.; Langwald, N.; Tomaszewska, A. *J. Power Sources*. **2010**, *18*, 6055–6061. DOI: <https://doi.org/10.1016/j.jpowsour.2009.12.097>.
28. Meabe, L.; Huynh, T. V.; Lago, N.; Sardon, H.; Li, C.; O'Dell, L. A.; Armand, M.; Forsyth, M.; Mecerreyes, D. *Electrochim Acta*. **2018**, *264*, 367–375. DOI: <https://doi.org/10.1016/j.electacta.2018.01.101>.
29. Qian, X.; Gu, N.; Cheng, Z.; Yang, X.; Wang, E.; Dong, S. *Journal of Solid-State Electrochemistry*. **2001**, *1*, 8–15. DOI: <https://doi.org/10.1007/s100080000190>.
30. Menzinger, M.; Wolfgang, R. *Angewandte Chemie International Edition in English*. **1969**, *6*, 438–444. DOI: <https://doi.org/10.1002/anie.196904381>.
31. Soydan, A. M.; Bozkurt, A. *Ionics*. **2018**, *5*, 1399–1405. DOI: <https://doi.org/10.1007/s11581-017-2286-4>.
32. Evans, J.; Vincent, C. A.; Bruce, P. G. *Polymer*. **1987**, *13*, 2324–2328. DOI: [https://doi.org/10.1016/0032-3861\(87\)90394-6](https://doi.org/10.1016/0032-3861(87)90394-6).
33. Zugmann, S.; Fleischmann, M.; Amereller, M.; Gschwind, R. M.; Wiemhöfer, H. D.; Gores, H. *J. Electrochim Acta*, **2011**, *11*, 3926–3933. DOI: <https://doi.org/10.1016/j.electacta.2011.02.025>.
34. Strauss, E.; Menkin, S.; Golodnitsky, D. *Journal of Solid State Electrochemistry*. **2017**, *7*, 1879–1905. DOI: <https://doi.org/10.1007/s10008-017-3638-8>.
35. Hamaide, T.; Le Deore, C. *Polymer*. **1993**, *5*, 1038–1046. DOI: [https://doi.org/10.1016/0032-3861\(93\)90227-2](https://doi.org/10.1016/0032-3861(93)90227-2).
36. Zygadlo-Monikowska, E.; Florjańczyk, Z.; Tomaszewska, A.; Pawlicka, M.; Langwald, N.; Kovarsky, R.; Mazor, H.; Golodnitsky, D.; Peled, E. *Electrochim Acta*. **2007**, *4*, 1481–1489. DOI: <https://doi.org/10.1016/j.electacta.2007.02.046>.
37. Guzmán-González, G.; Ávila-Paredes, H. J.; Rivera, E.; González, I. *ACS Appl Mater Interfaces*. **2018**, *36*, 30247–30256. DOI: <https://doi.org/10.1021/acsami.8b02519>.
38. Guzmán-González, G.; Ramos-Sánchez, G.; Camacho-Forero, L. E.; González, I. *Journal of Physical Chemistry C*. **2019**, *29*, 17686–17694. DOI: <https://doi.org/10.1021/acs.jpcc.9b02945>.
39. Guzmán, D. Nava, J. Vasquez-Arenas, J. Cardoso, J. A.-Ramirez. *Solid State Ionics*. **2019**, *5*, 55.
40. Nava, D. P.; Guzmán, G.; Vasquez-Arenas, J.; Cardoso, J.; Gomez, B.; Gonzalez, I. *Solid State Ionic*. **2016**, *290*, 98–107. DOI: <https://doi.org/10.1016/j.ssi.2016.03.020>.

Fine Particles Composition and Emission Chemical Profiles from Sugarcane Production for Source Reconciliation Applying the Chemical Mass Balance

Violeta Mugica-Álvarez¹, Fernando Millán-Vázquez¹, José de Jesús Figueroa-Lara¹, Brenda L. Valle-Hernández¹, Xavier Querol², Francisco Hernández-Rosas³

¹Universidad Autónoma Metropolitana Azcapotzalco. Av. San Pablo No. 420 Col. Nueva el Rosario, C.P. 02128, Azcapotzalco. Mexico City, México

²Institute of Environmental Assessment and Water Research, IDAEA-CSIC. C. Jordi Girona 18-26, 08034. Barcelona, Spain

³Postgraduate College. Campus Cordoba. Km. 348.5. 94500 Veracruz, México.

*Corresponding author: Violeta Mugica-Álvarez, email: yma@azc.uam.mx

Received May 11th, 2023; Accepted July 5th, 2024.

DOI: <http://dx.doi.org/10.29356/jmcs.v68i4.2280>

Abstract. Every year, many tons of fine particles are emitted to the atmosphere due to the sugarcane-mills operation and for inadequate agricultural practices such as sugarcane burning. In order to foster a deeper knowledge about the levels and source contributions of particles and their toxic species, the City of Cordoba was selected for two PM_{2.5} sampling campaigns to be carried out in the center and in a rural location at 9 km far, during harvesting and non-harvesting seasons; additionally, the chemical source profiles from sugarcane burning and sugar mills were determined. The PM_{2.5} levels in the City of Córdoba ranged from 29.9 to 102.1 µg m⁻³ and from 13 to 36.6 µg m⁻³ in the harvest and non-harvest periods, respectively, but toxic chemical species rose up to nine times representing an important risk health. Total carbon concentrations during harvesting were around 67 % and 64 %. With the chemical source profiles and the PM_{2.5} airborne concentrations, the Chemical Mass Balance Model was applied for source reconciliation, evincing that sugarcane processes accounted with 22 % of fine particles, vehicles with 34 to 38 %, secondary inorganic aerosols from 16 to 24 %, and suspended particles from roads from 10 to 20 %. The results show that inhabitants in this area are exposed to high levels of PM_{2.5} in harvesting, with a high risk to their health. This study provides valuable information to the authorities for the PM_{2.5} control strategies design and protect the population health, during harvesting.

Keywords: PM_{2.5}; sugarcane; biomass burning; CMB model; source profiles.

Resumen. Cada año, se emiten muchas toneladas de partículas finas a la atmósfera debido a la operación de los ingenios azucareros y a prácticas agrícolas inadecuadas como la quema de caña de azúcar. Con el fin de fomentar un conocimiento más profundo sobre los niveles y las contribuciones de origen de las partículas y sus especies tóxicas, la ciudad de Córdoba fue seleccionada para llevar a cabo dos campañas de muestreo de PM_{2.5} en el centro y en una ubicación rural a 9 km de distancia, durante las temporadas de cosecha y no cosecha; además, se determinaron los perfiles químicos de la quema de caña de azúcar e de los ingenios. Los niveles de PM_{2.5} en la ciudad de Córdoba oscilaron entre 29.9 y 102.1 µg m⁻³ y entre 13 y 36.6 µg m⁻³ en los períodos de cosecha y no cosecha, respectivamente, pero las especies químicas tóxicas se incrementaron hasta nueve veces, lo que representa un importante riesgo a la salud. Las concentraciones totales de carbono durante la cosecha fueron aproximadamente del 67 % y el 64 %. Con los perfiles químicos de origen y las concentraciones de PM_{2.5} en el aire, se aplicó el Modelo de Balance de Masas Químicas para la reconciliación de fuentes, demostrando que los procesos de caña de azúcar representaban el 22 % de las partículas finas, los vehículos el 34 al 38 %, los aerosoles secundarios del 16 al 24 %, y las partículas suspendidas de las carreteras del 10 al 20 %. Los resultados muestran

que los habitantes de esta zona están expuestos a niveles altos de $PM_{2.5}$ durante la cosecha, con un alto riesgo para su salud. Este estudio proporciona información valiosa a las autoridades para el diseño de estrategias de control de $PM_{2.5}$ y proteger la salud de la población, durante la cosecha.

Palabras clave: $PM_{2.5}$; caña de azúcar; quema de biomasa; modelo CMB; perfiles de fuentes.

Introduction

Sugarcane is cultivated in tropical countries and represents a significant economic impact for the agroindustry of the producing countries that yield sugar and ethanol [1].

More than half of the sugarcane harvest worldwide is done manually, involving the crop burning to remove foliage, snakes and venomous insects; after harvesting, mostly straw and residues are also burned for land preparing and pests control [2,3].

This agricultural practice annually generates tons of pollutant particles that have adverse effects on the health of people living in sugarcane-growing areas, causing and exacerbating cardiorespiratory diseases [4,5]. Hospital admissions for asthma crises, respiratory diseases, hypertension, and long-term kidney problems, particularly among harvesters, increase during harvesting periods [6,7]. Atmospheric fine particles are able to damage living organisms due to their so small sizes that can penetrate very deep into the lungs, but also due to their composition, since some elements, such as metals, can generate free radicals or reactive oxygen species (ROS) capable of inducing oxidative stress in the cells [8]; moreover, organic compounds like some polycyclic aromatic hydrocarbons (PAH) in particles are immunosuppressants and have mutagenic and carcinogenic properties [9]. In addition, particles resulting from incomplete biomass burning contain black carbon in soot, which is a short-lived climate pollutant (SLCP) that increases the greenhouse effect, contributing to global warming and climate change [10,11].

In Mexico, sugar production generates around 450,000 direct jobs and brings indirect benefits to more than 2.2 million people. Veracruz contributes with 40 % of national production [12]. More than 80 % of the harvest is done manually with pre-burning harvest between November and May [13]. Although Mexico has an air quality standard for respirable and fine particles (PM_{10} and $PM_{2.5}$), monitoring is only performed in cities with more than 500,000 inhabitants. Therefore, all the sugarcane-growing areas with fewer inhabitants have very little information on air pollution and lack timely notifications to protect themselves against particle concentration levels and their toxic contents, which can be very high during harvesting as was reported in the sugarcane areas of Morelos and Chiapas, where $PM_{2.5}$ concentrations were up two folds higher during harvesting and toxics, such as polycyclic aromatic hydrocarbons levels rose 2 to 6 times in that period [14,15].

During the harvesting period, the primary sources of particle emissions, which enclose a great number of inorganic and organic compounds and elemental carbon are believed to originate predominantly from sugar mills and agricultural burning, although the contribution from vehicles on freeways and trucks transporting sugarcane from fields to mills is also significant [11]. It has been reported that during harvest the visits to hospitals are increased due to the exacerbation of cardiorespiratory illness [16], moreover, some compounds included in the airborne particles from sugarcane burning and sugar-mills possess carcinogenic and mutagenic activity, representing a health risk for the population [17]. Recently, a comprehensive study reported that exposure to the ashes from sugarcane burning can lead to respiratory, cardiovascular, and renal health issues and that studies related to the ashes chemical characterization and funding are needed to understand the damage and toxicological mechanisms on people [18]. Given these multifaceted factors, it is imperative for environmental authorities to discern the relative $PM_{2.5}$ contributions of sugarcane processes and other sources to effectively safeguard public health. Mass balance receptor models have been developed to address this need, facilitating the identification and quantification of particle sources; among them, the Chemical Mass Balance model (CMB) has proven to be particularly valuable in delineating particle sources from individually collected samples, because it is possible the quantification of every source contribution in individual samples, differing of other multivariate analyses, as the Principal Component Analysis that only generates a qualitative diagnostic or the positive matrix factorization which requires a large number of analyzed samples [19,20,21]. In the context of sugarcane-growing regions specifically, Afshar-Mohajer *et al.* [22] conducted a study quantifying the contribution of several sources to the

presence of polycyclic aromatic hydrocarbons, thereby shedding light on the complex dynamics of air pollution in these areas, however, there is a lack of information related to the composition of $PM_{2.5}$, their inorganic species and the origin of them. Against this backdrop and guided by the evidences that toxic species concentrations present in particles escalate during harvesting, this study was undertaken for over a year to characterize the chemical composition of atmospheric particles with the objective to ascertain the concentrations of $PM_{2.5}$ and PM_{10} and associated toxics to which people residing in the most significant sugarcane-producing area are exposed. Additionally, $PM_{2.5}$ chemical source profiles were determined for both, sugar mills and sugarcane burning, enabling the estimation of sources contribution to the presence of $PM_{2.5}$ and its chemical species in the city center of Cordoba and a rural area located 9 km far using the CMB model.

Experimental

Sampling sites

The Cordoba municipality is a medium city of the Veracruz State with around 200,000 inhabitants of which 45.7 % are men and 54.3 % women [23]. It is located at 860 m above sea level ($18^{\circ} 53'N$; $96^{\circ} 56'W$) and is surrounded by eight sugar mills and hundreds of hectares of sugarcane crops, which are burned every year during harvesting emitting hundreds of particulate matter (PM) tons which can cause adverse effects in the exposed population, especially in agriculture workers (17 %) followed by the children up to 10 years old which constitute around 24 % and the 16 % of vulnerable population of adults over 60 years [23]. The sampling campaigns were carried out during the sugarcane harvesting and no-harvesting seasons from January 2015 to November 2016, but the sampling began four months before in the rural site, since in the downtown a special permission was required. The Municipal Palace (MP) in the Cordoba downtown was the first site for the particles monitoring, whereas a rural zone, 9 km far from the city and located in the Postgraduate College (PC), was the second sampling site. $PM_{2.5}$ Hi Vol samplers (Tisch Environment), with conditioned Whatman quartz fiber filters, were used to collect 24 h integrated samples each two weeks (Fig.1).

In the rural site PC, was installed also a PM_{10} Hi Vol sampler, in order to know the $PM_{2.5}$ fraction related to PM_{10} , since in this location there are many sugarcane crops and an intense agricultural activity. After collection, filters were wrapped with foil and stored at $4^{\circ}C$ before gravimetry and chemical analyses. The meteorological parameters were registered in the station of the Veracruz University.

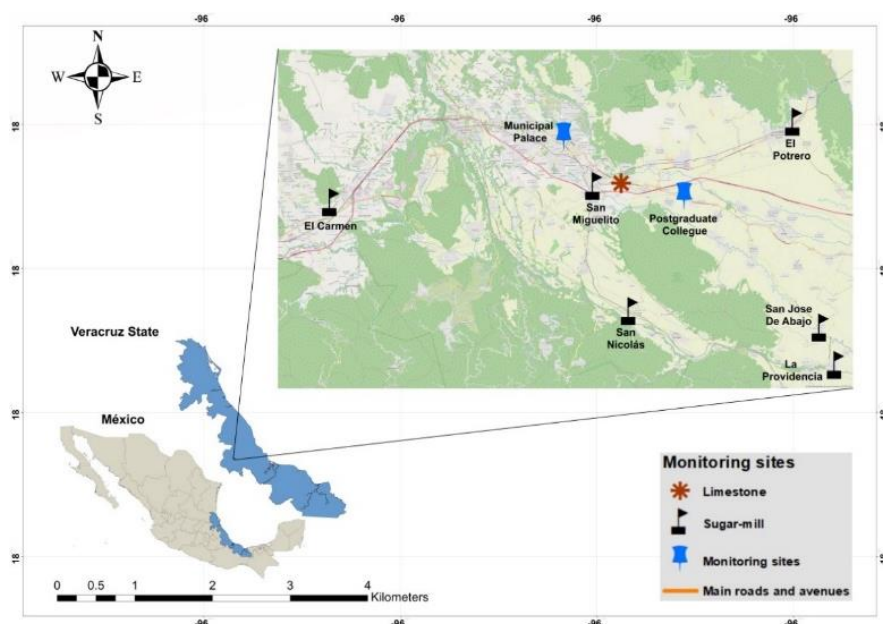


Fig. 1. Location of sampling sites Municipal Palace (MP) and Postgraduate College (PC) and sugarcane-mills.

Chemical source profiles

For the development of the PM_{2.5} chemical profile of sugarcane-mills, a sampling campaign of one week was performed at 200 m downwind from one sugar mill, when the sugarcane harvest had finished and there were no more burnings; whereas the PM_{2.5} chemical profile from crop burnings was carried out sampling at one km downwind from the sugar fields during five burning practices, at the beginning of the harvesting season when sugar mills activity was starting.

Chemical analyses

Organic and elemental carbon analyses were performed in duplicate in an Optical Carbon Aerosol Analyzer with reflectance correction (Sunset Lab, Forest Grove, OR USA), to measure the organic (OC) and elemental carbon (EC) concentrations, according with the NIOSH-5040 method described by Birch and Cary [24].

PAH were extracted ultrasonically with dichloromethane (Bransonic), during three times for 10 min periods at 10 °C and concentrated in a rotary evaporator for further quantification analysis with a chromatograph (GC model HP 6890) coupled with a mass spectrometer using a 30 m HP5-MS capillary column (0.25 mm ID, 0.25 µm film thickness).

For the ion analyses, a soluble fraction was extracted with Milli-Q deionized water in an ultrasonic bath (Branson bath, 3210) during 15 min for further evaporation at 60 °C. Samples were filtered, and the ammonia ion was quantified with an NH₄⁺ selective electrode and a Thermo ORION STAR potentiometer. Other ions were analyzed twice by HPLC chromatography (Jasco LC-NetII/ADC) with a BioLC ED50 electrochemical detector (Dionix) and a IC-Pak Anion HR, 75x4.6 mm column (Waters).

The elemental analysis was carried out by digestion of 35 cm² of the filter with nitric acid and perchloric acid in a Savillex Teflon, leading to dryness and rebuilding with a diluted acid solution. The solution was analyzed through an inductively-coupled plasma atomic emission spectrometer ICP-AES for major elements and with ICP-MS for trace elements (Thermo X series). SiO₂ and CO₃²⁻ were indirectly determined based in stoichiometric relationships.

Chemical Mass Balance Model

The Chemical Mass Balance (CMB) receptor model use multivariate analysis to estimate particles and chemical species source contributions based on the degree to which source profiles can be combined to reproduce ambient concentrations[19,25]; the CMB model requires as input data the chemical receptor concentrations, the source profile chemical composition obtained in this study and in previous researches as well as data uncertainties to estimate the source contributions for the PM_{2.5} total mass and finally the standard errors of those estimations. The CMB8.2 software was used for the estimations [19]. The fundamental equation of receptor model (equation 1) is derived from the mass conservation equation and represents the relationship between the concentration of aerosol measured at the receptor and that emitted by the sources.

$$C_i = \sum_{j=1}^J F_{ij} * S_j \quad (1)$$

where:

- C_i = Concentration of “i” pollutant measured
- F_{ij} = Fraction emitted of “i” pollutant by the source “j”
- S_j = Calculated contribution of “j” source
- J = Number of contributing sources

Environmental data obtained from sample characterization were combined with chemical profiles derived from sugarcane burning and mill emissions developed in this study. Additionally, source profiles of light-duty and diesel vehicles, were included [26]. Agricultural soils paved and unpaved roads, and limestone processes from previous studies were profiles also utilized [27]. Moreover, source profiles from industrial facilities available in the Speciate database [28] were incorporated into the analysis.

Quality assurance

Prior to sampling, quartz filters underwent calcination at 600 °C for 4 hours to eliminate any adsorbed organic matter. Flow calibration procedures were conducted before sampling during each season. Following calcination, the filters were stored in a controlled environment for 48 hours at a constant temperature of 25 ± 5 °C and relative humidity of $45 \% \pm 5$ % before being weighed using an analytical balance. To validate elemental analysis, standard urban dust reference material (SRM 1649a) was utilized adding 20 mg to a 4 cm² blank filter to determine the analysis accuracy, following the same handling and analysis procedure as the filters and blanks. The performance of the CMB model was assessed based on the recovery mass percentage and various statistical parameters R^2 and Chi^2 , blank filter to check the accuracy of the analysis.

Results

Fine particles and carbonaceous compound concentrations

The meteorological conditions prevailing in the 3 sampling periods: harvesting (January 1st to May 27th 2015), non-harvesting (May 30th to November 20th), and harvesting (February 5th to March 5th), are presented in the rose winds of Fig. 2, where it is possible to observe that the dominant winds originated from the east in the first harvest period and in the non-harvest period, while in the second harvest period there was also a significant influence of west winds, although with lower speed. This means that most of the year the emissions from the rural zone are transported to the center; however, in the latter part of the harvest period, there was a noticeable influence of westward winds, albeit at a reduced velocity.

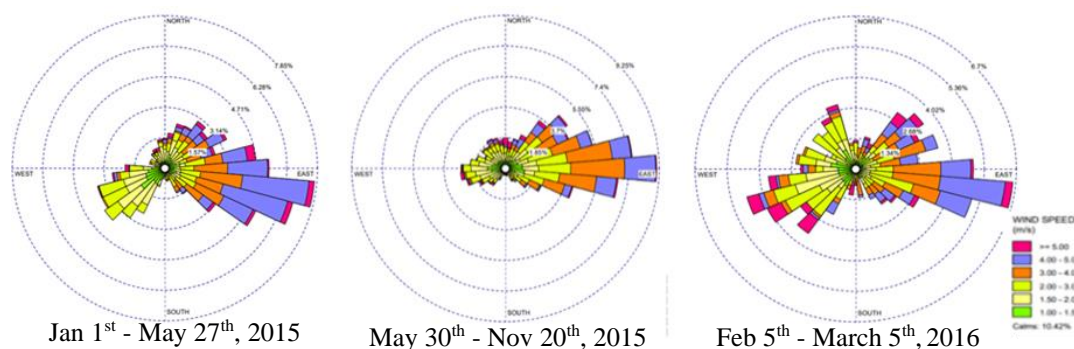


Fig. 2. Wind speed and direction during sampling campaigns.

The time series of PM_{2.5} concentrations in the downtown area (MP) and at the rural site (PC), alongside the PM₁₀ concentrations at the PC is illustrated in Fig. 3. The PM₁₀ concentrations at the PC ranged from 44 to 147 $\mu\text{g m}^{-3}$ during harvesting, with the air quality maximum permissible limit exceeded on 7 days of 35 samples. The PM_{2.5}/PM₁₀ ratio varied from 64 to 71 %, indicating a predominance of fine particles over coarse ones. During the harvesting season, PM_{2.5} concentrations at both sites were two times higher than those during non-harvesting periods, highlighting the significant impact of various sugarcane processes on air pollution. Furthermore, PM_{2.5} concentrations in the downtown area (MP) were consistently 15 % to 40 % higher than those recorded at the rural site, indicating a notable contribution from vehicular and commercial activities. PM_{2.5} mass concentrations ranged from 34 to 102 $\mu\text{g m}^{-3}$ in the city and from 27 to 90 $\mu\text{g m}^{-3}$ at the rural site during harvesting. Statistical analysis using the Mann-Whitney test revealed significant differences between sampling periods and locations (P value ≤ 0.05). Throughout the harvesting season, the PM_{2.5} Mexican air quality standard of 45 $\mu\text{g m}^{-3}$ (NOM-025-SSA1-2014) was exceeded 18 times at the MP site out of 22 samples (16 with very poor air quality and 2 with poor air quality), while at the PC site, there were 14 exceedances in 35 samples (7 with very poor air quality and 7 with poor air quality). Conversely, during the non-harvesting season, the air

quality standard was not exceeded at either site. However, the USEPA standard of $35 \mu\text{g m}^{-3}$ was surpassed on 40 % of days. These results show the necessity of major supervision in the sugarcane-mills emission, as well as the reduction of biomass burning.

Although the concentrations during the harvest period were lower than those observed in Morelos state, close to the Zacatepec sugar mill, they were higher than those reported in Chiapas [14], while the PM_{10} concentrations during harvesting were similar to those reported by de Andrade *et al.* [17], who shows the mutagenic activity of atmospheric particles emitted during the harvest season. Several authors have reported an increase in hospital admissions due to high pollution levels reached during the harvesting season, resulting in exacerbations of asthma, various respiratory diseases, and aggravation of cardiovascular problems in various cities in Brazil [16,29]. In addition, studies in Brazil and Mexico reported an increase in diseases, whereas several deaths have been associated to sugarcane burning in South Florida [30]; then, avoiding preharvest burning undertaking green cane harvest, would represent an improvement in health [31].

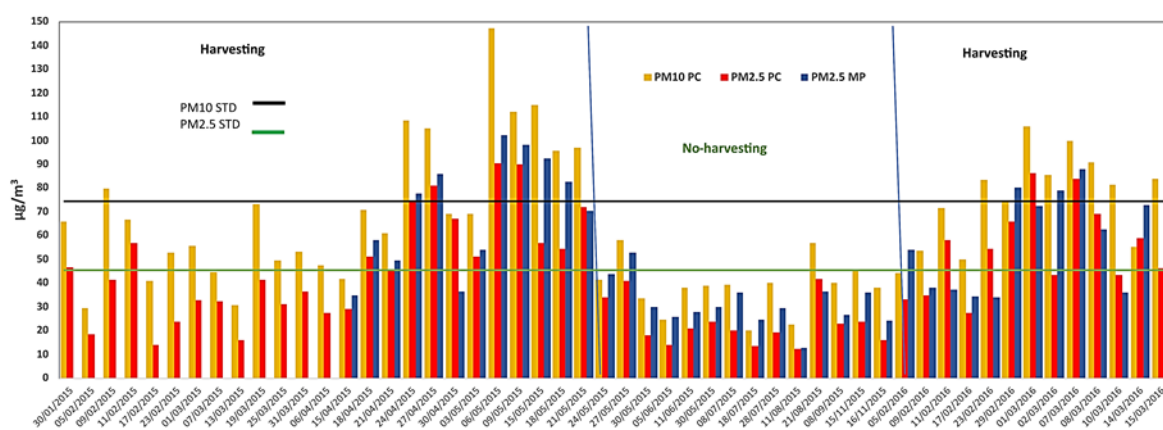


Fig. 3. Time series of $\text{PM}_{2.5}$ and PM_{10} concentrations in Cordoba, Veracruz.

Fig. 4 presents the averages of $\text{PM}_{2.5}$ and PM_{10} concentrations, alongside the average concentrations of total carbon (TC) contained within the particles, which constitutes the most abundant species formed by the sum of organic and elemental carbon (OC + EC). The TC average concentrations were around two times higher in harvesting than in non-harvesting (23 vs $10 \mu\text{g m}^{-3}$, respectively). The OC/TC ratio ranged from 0.87 to 0.92 in both particle sizes, which is higher to the studies performed in Mexico City in 1997 and 2009, with a ratio of 0.73 and 0.76 with TC concentrations average of 15.8 and $15.4 \mu\text{g m}^{-3}$, respectively [32,21]. Other characterization studies performed in rural zones in Europe reported lower $\text{PM}_{2.5}$ and TC concentrations than this study in the non-harvest season [33], in opposite, the $\text{PM}_{2.5}$ concentrations in rural zones in China are at least twice than those found in this study, with concentrations of $115 \mu\text{g m}^{-3}$ and $24 \mu\text{g m}^{-3}$ of TC, which are alike to those found in non-harvest season [34]. The greater TC concentration in $\text{PM}_{2.5}$ at MP compared to the TC concentrations in PM_{10} and $\text{PM}_{2.5}$ suggests the contribution of organic carbon from urban sources such as restaurants and intense vehicular traffic, among others. The high TC concentration in the sugarcane zone indicates a low combustion efficiency in the processes occurring in the sugarcane processing, whereas the significant contribution of sugarcane burning, and sugarcane mills is confirmed by observing that TC decreases by a third during the non-harvest season; of especial mention is the 60 % increasing of EC in harvest, since this is a climatic forcer and has been proposed that the ban of sugarcane burning could reduce the 7 % of total black carbon in Mexico [11], this measure, besides to be a mitigation action for climate change would have co-benefices in the air quality improvement.

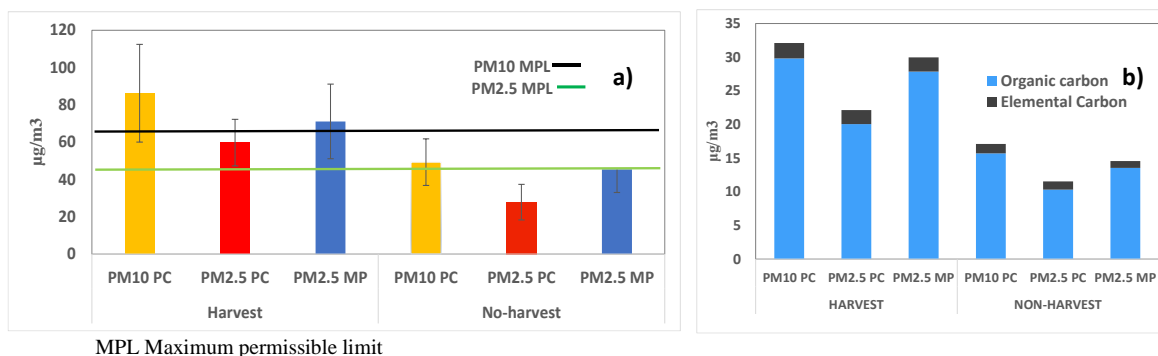


Fig. 4. (a) Average PM₁₀ and PM_{2.5} concentrations and (b) average concentration of carbon species.

Polycyclic aromatic hydrocarbons in PM_{2.5}

PAH are compounds characterized by two or more fused aromatic rings, typically formed during the pyrolysis or incomplete combustion of organic matter, leading to soot formation [14]; although these compounds, contained in the organic carbon fraction of PM_{2.5} were not used into the Chemical Mass Balance for source apportionment, due to the absence of source profiles for this compound family, 17 PAH recommended by the USEPA, were measured and characterized owing to their pronounced toxicity. The quantified PAH encompassed a range of compounds including: naphthalene (NAP), methylnaphthalene (MNAP), acenaphthylene (ACY), acenaphthene (ACE), anthracene (ANT), phenanthrene (PHE), benzo[a]pyrene (BAP), benzo[b]fluoranthene (BBF), benzo[a]anthracene (BAA), fluorene (FLU), fluoranthene (FLT), pyrene (PYR), chrysene (CRY), benzo[k]fluoranthene (BKF), 2-methylnaphthalene (MNAP), dibenzo[a,h]anthracene (DBA), indene[1,2,3-cd]pyrene (IND), and benzo[ghi]perylene (BGP). Despite PM_{2.5} and organic carbon exhibited higher concentrations in the city in comparison to the rural zone, Fig. 5 reveals that during harvesting, the highest concentrations of PAH were observed in the rural site, which is in close proximity to and surrounded by sugarcane fields that were eventually burned. Conversely, the city is situated farther away from biomass burning sites; although, during the non-harvesting period, most PAH exhibited higher concentrations in the city (MP), underscoring the significance of local sources. The sum of PAH were 5.3 and 2.9 ng m⁻³ in PC and PM, respectively in the harvest time, and individual PAH were 2 to 7 times greater than during the no-harvest period, primarily due to crop burning, emissions from sugar mills, and diesel emissions from numerous trucks queuing to unload harvested sugarcane, these results are in agreement with a study reported in Brazil [17] where concentrations were five times greater in harvest than in non-harvest. It is common during harvesting to observe soot particles suspended in the air or deposited on the ground. In non-harvest season the sum of PAH were 1.1 and 1.5 ng m⁻³ in PC and PM, showing the contribution of traffic and other combustion sources in the downtown. Of particular concern is the contribution of carcinogenic compounds to the PAH mixture, accounting for 57-58 % and 59-61 % during the harvest and non-harvest periods, respectively.

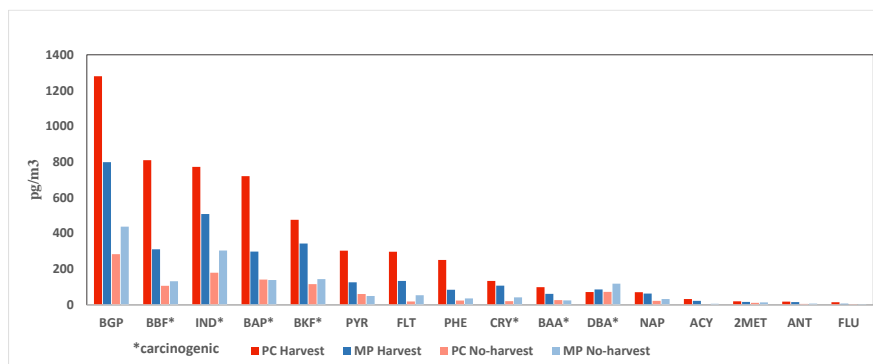


Fig. 5. Polycyclic aromatic hydrocarbons concentrations in harvesting and no-harvesting periods.

The assessment of carcinogenic potential involves the sum of the concentration of each individual PAH multiplied by its toxic equivalent factors which were proposed by Nisbet and Lagoy [35] to determine the benzo[a]pyrene equivalent concentration (BAP_{eq}). The relative individual contribution of cancer risk and the BAP_{eq} during the harvest season in the rural site of Cordoba is presented in Table 1, where is possible to observe that BAP_{eq} increased three times in MP and two times in PC and the individual PAH increase from 2 to 7 times such as BBF. Although the annual BAP_{eq} averages in PC and PM were lower with 641 and 419 $\mu\text{g m}^{-3}$ respectively, than the annual PM_{10} European Union and WHO [36] recommendation of 1000 $\mu\text{g m}^{-3}$ for health protection, they exceeded the annual PAH limit of the United Kingdom of 250 $\mu\text{g m}^{-3}$ and France of 100 $\mu\text{g m}^{-3}$ [37]; furthermore, inhabitants are exposed to high levels of PAHs during six continuous months in the harvest period, with significant health impacts associated to sugarcane processes.

Table 1. Carcinogenic potential (BAP_{eq}) of the Polycyclic Aromatic Hydrocarbon in $PM_{2.5}$.

Compound	BAP_{eq} [$\mu\text{g/m}^3$]				
	TEF Toxic Equivalency Factor	Harvesting		No-harvesting	
		MP $PM_{2.5}$ urban	PC $PM_{2.5}$ rural	MP $PM_{2.5}$ urban	PC $PM_{2.5}$ rural
Naphtalene	0.001	0.07	0.063	0.032	0.022
2-Methylnaphtalene	0.001	0.019	0.015	0.013	0.011
Acenaphtylene	0.001	0.032	0.022	0.005	0
Acenaphtene	0.001	0	0	0	0
Fluorene	0.001	0.014	0.005	0.004	0.003
Phenanthrene	0.001	0.251	0.084	0.036	0.023
Anthracene	0.01	0.18	0.15	0.07	0.05
Fluoranthene	0.001	0.297	0.133	0.053	0.018
Pyrene	0.001	0.303	0.126	0.049	0.06
Benzo [a] anthracene	0.1	9.9	6.1	2.4	2.6
Chrysene	0.01	1.33	1.07	0.41	0.2
Benzo[b]fluoranthene	0.1	81	31.1	13.2	10.6
Benzo[k+j]fluoranthene	0.1	47.6	34.3	14.4	11.6
Benzo[a]pyrene	1	720	298	139	141
Indene[1,2,3-cd]pyrene	0.1	77.3	50.9	30.4	18
Dibenzo[a,h]anthracene	1	71	86	118	72
Benzo [g,h,i] perylene	0.01	12.8	7.99	4.38	2.83
Total Benzo[a]pyrene eq		1022	516	322	259

The PAH increase in sugarcane pre-harvest burning has been documented in studies conducted in Brazil, United States, and Mexico, as well as PAH levels increase in several urban sites in the winter season; a comparison among several studies is presented in Table 2; due to the lack of data, some comparisons were made with PAH in PM₁₀. The carcinogenic potency as BAP_{eq} is a good parameter for comparison among different studies since they are directly obtained from PAH individual concentrations and the TEFs.

Table 2. Comparison of PAH levels and BAPEq (carcinogenic potency) from biomass burning with other studies.

Site	PM μg/m ³	Σ PAH ng/m ³	BAP ng/m ³	BAP eq ng/m ³	Reference
Cuernavaca, Morelos, México PM_{2.5}	-	25.4-22.5	2.6-2.2	-	Saldarriaga <i>et al.</i>, 2015[38]
Zacatepec, Morelos México harvest PM₁₀	72-203	3.9-5.8	0.46	1.014	Mugica <i>et al.</i> 2015[14]
Araraquara, Brazil harvest PM₁₀	76-182	11.6	0.5		de Andrade <i>et al.</i> , 2012[17]
Araraquara, Brazil harvest PM₁₀	29-41	14.1 ± 13	0.26		de Assunsao, <i>et al.</i> 2014[39]
Sao Paulo, sugarcane belt				0.13-3	Scaramboni <i>et al.</i> , 2024[40]
Mexico City PM ₁₀	52-164	0.7-17.8	0.04-1.4	0.41-2.18	Mugica <i>et al.</i> , 2010[41]
North, China	57.7 ± 37	15.3 ± 8.8	1.5 ± 1.2	-	Wang <i>et al.</i> , 2018[42]
Tehran, Iran	32.1 ± 17	12.2 ± 7	0.23 ± 0.17	29 ± 5.7	Taghvaei <i>et al.</i> , 2018[43]
Venice, Italy	32.2 ± 25	9.8 ± 12.5	1.2 ± 1.8	1.9 ± 2.6	Masiol <i>et al.</i> , 2012[44]
Thessaloniki Greek	36 ± 19	9.4 ± 9.3	0.7 ± 0.8	0.85 ± 0.4	Manoli <i>et al.</i> , 2016[45]
Florence, Italy	13.6-29.6	13-3.6	0.2-1	0.79-3.3	Martellini <i>et al.</i> , 2012[46]
Changzhou, China	28.9-308	235.29	24.5	41.1	Bi <i>et al.</i> , 2020[47]
PC Harvest	44.3 ± 19	5.3 ± 2.6	0.7 ± 0.4	1.02	This study
PC No Harvest	20 ± 8.4	1 ± 0.2	0.1 ± 0.08	0.25	This study
MP Harvest	62.4 ± 23	2.9 ± 0.8	0.2 ± 0.1	0.5	This study
MP No Harvest	28.1 ± 8	1.5 ± 0.4	0.1 ± 0.05	0.32	This study

Bold: studies in harvest season

The ΣPAH in this study during harvesting are similar to that reported in the sugarcane zone of Zacatepec, México, as well as the estimated BAP_{eq} that is into the range of that reported in the Sao Paulo sugarcane belt; but ΣPAH are lower than the values reported in two studies in Araraquara, Brazil during harvest, in the cities of Cuernavaca, Mexico, Theran, Venice, Florence, Changzhou and Thessaloniki, showing that PAH have usually higher total mass and carcinogenic potency in cities than in rural sites. Quite high values in the cities of Iran and China are explained for the high traffic of diesel vehicles as well as by industrial activities.

Elemental composition of PM_{2.5}

The PM_{2.5} characterization is detailed in Table 3, presenting average concentrations of chemical species identified and quantified in the 57 samples analyzed during both, harvesting and non-harvesting periods. The rise of individual concentrations in harvest is evident in almost all the species. Toxics elements concentrations such as Cu, Pb and Cd increased 9, 2 and 3 times in the Cordoba center. A Kruskal-Wallis test was conducted on all data, revealing significant differences between the two seasons at both sites (P value < 0.05). In general, higher concentrations of the major species were quantified during harvest.

Table 3. Concentrations of chemical species in PM_{2.5} samples and developed source profiles.

Period	Municipal Palace (MP)				Postgraduate College (PC)				Source profiles			
	Harvest		Non-harvest		Harvest		Non-harvest		Sugarcane-mill		Crops burning	
	Mean	SD	Mean	SD	Mean	SD	Mean	SD	Mean	SD	Mean	SD
$\mu\text{g m}^{-3}$												
PM ₁₀	-	-	-	-	86.2	26.2	49.3	12.5				
PM _{2.5}	71.1	19.98	45.39	7.29	59.77	19.32	27.88	9.54	73.6	25.6	85.49	21.8
TC	30.85	6.35	15.35	3.27	22.85	5.67	11.63	3.3	19.14	5.91	26.3	6.37
OC	27.85	5.92	13.55	3.05	20.04	5.07	10.32	2.7	16.99	4.22	19.73	4.55
EC	3	0.53	1.8	0.22	2.81	0.74	1.31	0.8	2.15	0.47	6.58	0.69
SiO ₂	1.7	0.39	0.74	0.14	2.1	1.78	0.66	0.02	7.66	0.27	1.81	0.62
Al ₂ O ₃	0.39	0.16	0.30	0.06	0.72	0.71	0.04	0.01	1.62	0.09	0.38	0.11
Cl ⁻	0.13	0.08	0.08	0.1	0.12	0.06	0.07	0.2	0.05	0.03	0.08	0.04
NO ₃ ⁻	0.47	0.24	0.99	0.10	0.91	0.59	0.23	0.14	0.72	0.21	0.11	0.08
SO ₄ ²⁻	9.01	1.94	6.87	1.36	8.86	4.49	2.78	2.94	1.98	1.54	2.85	1.72
NH ₄ ⁺	3.98	0.95	1.92	0.25	2.21	1.11	0.61	0.45	0.27	0.73	1.87	0.64
Na	0.07	0.03	0.09	0.04	0.71	0.31	0.23	0.18	6.35	0.05	0.01	0.01
K	0.98	0.143	0.58	0.31	0.68	0.35	0.23	0.21	0.7	0.32	17.23	2.76
Mg	0.06	0.02	Bdl	0.16	0.09	0.07	0.01	0.01	1.29	1.1	0.16	0.06
Al	0.19	0.10	0.23	0.11	0.38	0.38	0.2	0.09	1.62	0.97	0.38	0.18
P	0.04	0.02	0.06	0.05	0.05	0.03	0.02	0.01	0.52	0.41	0.075	0.06
Ca	0.37	0.05	1.21	1.00	0.54	0.39	0.13	0.2	3.89	1.92	0.34	0.26
Ti	0.02	0.01	0.00	0.02	0.02	0.02	0.01	0.02	0.09	0.06	Bdl	Bdl
Fe	0.24	0.07	0.29	0.14	0.24	0.23	0.05	0.02	0.41	0.13	0.07	0.04

	Municipal Palace (MP)				Postgraduate College (PC)				Source profiles			
Period	Harvest		Non-harvest		Harvest		Non-harvest		Sugarcane-mill		Crops burning	
	Mean	SD	Mean	SD	Mean	SD	Mean	SD	Mean	SD	Mean	SD
ng m⁻³												
Li	0.17	0.05	0.08	0.00	0.15	0.08	0.01	0.01	0.87	0.54	Bdl	Bdl
Be	Bdl	Bdl	Bdl	Bdl	Bdl	Bdl	Bdl	Bdl	0.03	0.02	Bdl	Bdl
Sc	0.01	0.00	0.01	0.01	0.01	Bdl	Bdl	Bdl	0.04	0.02	Bdl	Bdl
V	3.58	0.59	2.36	0.69	4.12	4.80	1.24	0.54	2.23	1.53	0.91	0.62
Cr	0.06	0.01	0.05	0.00	0.25	0.44	0.06	0.01	4.64	1.97	Bdl	Bdl
Mn	12.69	2.82	4.61	1.47	13.13	12.16	2.59	1.1	11.86	3.25	2.95	1.15
Co	0.10	0.03	0.04	0.07	0.12	0.09	0.04	0.01	0.27	0.17	0.32	0.14
Ni	2.00	0.85	0.90	0.27	2.79	2.94	0.007	Bdl	0.71	0.41	2.08	0.99
Cu	149.8	74.84	16.09	3.27	22.90	11.17	16.6	12.3	24.87	14.8	4.89	2.58
Zn	106.5	26.24	38.21	Bdl	45.94	21.77	32.8	17.5	70.14	29.8	14.47	9.36
As	0.53	0.10	0.81	Bdl	0.40	0.15	0.17	0.1	1.11	0.09	1.08	0.85
Se	0.16	0.18	0.13	0.06	0.25	0.19	0.063	0.02	0.47	0.23	Bdl	Bdl
Rb	2.00	0.31	0.99	0.08	1.79	0.79	0.80	0.21	1.91	1.1	0.81	0.53
Sr	1.50	0.31	0.71	0.08	2.91	2.68	0.03	0.01	7.89	5.32	2.2	0.98
Y	0.01	Bdl	0.01	Bdl	0.01	Bdl	0.005	Bdl	0.05	0.02	Bdl	Bdl
Zr	5.12	0.56	0.15	Bdl	3.85	2.39	3	0.92	4.04	2.26	4.99	2.33
Nb	0.08	0.04	0.03	0.02	0.07	0.05	0.04	0.01	0.05	0.03	0.05	0.03
Cd	0.35	0.07	0.09	Bdl	0.26	0.14	0.13	0.02	0.11	0.07	0.32	0.18
Sn	4.50	1.20	0.73	Bdl	3.27	2.86	1.4	0.57	0.64	0.42	1.72	1.2
Sb	1.28	0.27	1.66	0.43	1.28	0.56	0.48	0.21	1.58	0.89	0.86	0.63
Cs	0.04	0.04	Bdl	Bdl	0.05	0.05	Bdl	Bdl	0.14	0.07	0.1	0.05
Ba	13.39	5.60	24.12	0.00	12.99	8.86	3	1.1	28.31	9.43	Bdl	Bdl
Tl	0.08	0.01	0.01	0.01	0.09	0.07	0.01	0.01	0.03	0.01	0.17	0.13
Pb	15.22	6.30	7.27	3.66	14.65	7.62	5.55	3.23	2.07	1.03	3.81	2.26
Bi	0.06	0.04	0.01	0.04	0.04	0.04	0.01	Bdl	0.14	0.1	Bdl	Bdl

Th	0.01	Bdl	0.01	Bdl	0.01	Bdl	0.01	Bdl	0.08	0.04	Bdl	Bdl
U	0.01	Bdl	0.01	Bdl	0.01	Bdl	0.01	Bdl	Bdl	Bdl	Bdl	Bdl

Bdl: below detection limit

Although the concentrations of trace elements may appear similar in the examined cases, these small differences are used by the model for multivariate analysis with the source profiles, allowing the estimation of their contributions, for instance, the PM_{2.5} inorganic composition of this study is quite different from PM_{2.5} compositions in Mexico City [21,48]. Notable disparities emerged between the two profiles, establishing each as a distinct fingerprint; the profile associated with sugarcane-mills exhibits elevated levels of metals such as Ca, Mn, Cu, Cr, V, and Sr in the emissions, whereas the biomass burning profile reveals the characteristic presence of potassium. Fig. 6 illustrates the PM_{2.5} mass reconstruction in each site at the two seasons. The most abundant components were the carbonaceous species composed by elemental carbon (EC) and organic matter (OM), which was estimated with OC multiplied by the factor of 1.8 for the hydrogen and oxygen accounting of an average molecular weight of the organic compounds [49].

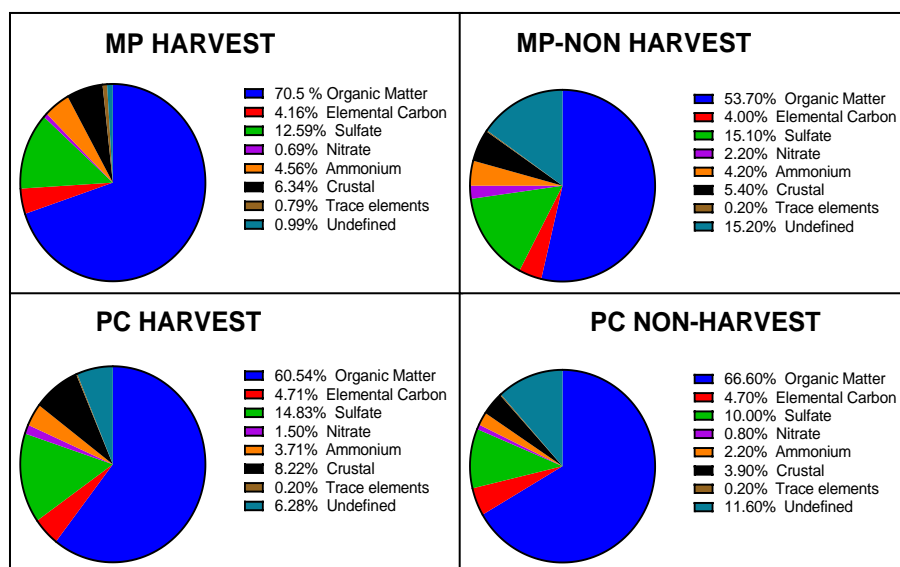


Fig. 6. Composition of PM_{2.5} in harvest and non-harvest in the urban and rural sites.

The OM contribution in the urban site during harvest was 24 % higher than in non-harvest due to the combined effect of sugarcane processes and the activities of the city; while in the rural site the OM influence was higher in non-harvest, because is an agricultural zone with additional crops than sugarcane, which are planted and harvested throughout the year, in addition to livestock and poultry farming in the area.

The second abundant component were the secondary aerosols composed by the (NH₄)₂SO₄ and NH₄NO₃, which are formed in the atmosphere when the SO₄²⁻ and NO₃⁻ ions react with the NH₃ gas emitted by the organic matter decomposition, this component is estimated by the stoichiometric relations ([SO₄²⁻]x1.375 and [NO₃]⁻x 1.29). The (NH₄)₂SO₄ was the major contributor in all cases, due to the use of diesel in vehicles and in the processes of the mills and other factories and that the presence of nitrate was low in general.

The geological or crustal component was estimated with the sum of the metal oxides, calculated for each oxide with its stoichiometric relationship (Al₂O₃ = [Al] x 1.89; Fe₂O₃ = [Fe] x 1.43; CaO = [Ca] x 1.4; K₂O = [K] x 1.2; MgO = [Mg] x 1.66; Na₂O = [Na] x 2.7; TiO₂ = [Ti] x 1.67; P₂O₆ = [P] x 2.29; and the SiO₂ = Al₂O₃ x 2.5) [50]. The crustal fraction in particles was similar in both seasons in the city, meaning that were generated

locally, but for the rural site the crustal component was twice in harvest than in non-harvest, which implies that transportation in the rural area during the harvest season caused the suspension of a large amount of soil particles. Except for particles composition from the urban site in harvest with around 1 % contribution, the trace metals accounted for 0.2 % of PM_{2.5} total mass.

Source reconciliation with the CMB model application

To the best of our knowledge, the chemical mass balance model had not previously been applied for source attribution using elemental composition profiles in sugarcane areas, although it had been applied for the case of PAH [50]. The CMB model successfully identified 9 sources during the harvest and up to 6 in non-harvest. Table 4 shows the source contribution ranges during the two periods at the urban and rural sites, whereas Fig. 7 presents the average source contributions solved by the CMB model in the 62 samples analyzed. It is possible to observe that the source chemical profiles developed in this study constitute two new chemical signatures which were recognized in the CMB model for differentiate and separate the emissions of the sugar-mills operation from the sugarcane burning emissions as well as from the other used profiles.

Table 4. Source contribution of PM_{2.5} in the urban and rural sites and CMB model performance.

	MP harvesting	PC harvesting	MP non-harvesting	PC Non-harvesting
Source				
Particles from roads	9.9-15.5	6.8-17.5	18.2-22.3	17-30.7
Agricultural soil	5.2-6.1	4.7-21.9	5.8-7.4	6-14.9
Limestone plant	0-5	1.5-11	5.4-7.5	5.4-7.5
Gasoline vehicles	11 a 36	6.8-34	25-30.7	25-30.7
Diesel vehicles	11 a 21	12.4-21.4	13.4-20.5	13.4-20.5
Secondary aerosols	14-24	15-21.7	13.9-23.3	9.7-14.9
Other factories	0	1-8	0	0
Sugar mill	3 a 29.2	3-17.8	0	0
Biomass burning	5 a 21	2-18-2	0	0
Performance				
R ²	0.96±0.03	0.95±0.03	0.93±0.02	0.98±0.01
Ch ²	3.9±1.03	3.6±1.02	3.6±0.7	3.4±1.3
Measured/Calculated	1.1±0.06	0.97±0.04	1.02±0.02	0.96±0.02

The parameters fell within acceptable ranges, indicating the robust performance of the CMB model. The coefficient of determination (R²) values averaged between 0.97 and 1, while the Chi² values were close to 4, and the ratio of measured to estimated mass averaged 1.01. The contribution to the presence of PM_{2.5} in the atmosphere from sugarcane burning combined with the operation of the sugar mill was approximately 22 %, with a greater contribution of emissions from sugarcane mills in the downtown area, as dominant winds transport emissions from surrounding mills; meanwhile, sugarcane field burning contributes similarly in both sites. The most significant contribution is attributed to vehicular activity, as a freeway passes close to the PC

site and an interstate highway is located 2 miles away from both sites. During harvesting, in addition to these roads, there are significant diesel vehicular $PM_{2.5}$ emissions from the many old trucks transporting harvested sugarcane to the sugar mills. The total vehicular contribution ranged between 34 and 38 %, with similar levels at both sites; during non-harvesting periods, gasoline vehicles accounted for more than 30 % and diesel vehicles for 27 % in the MP site, as it is also impacted by traffic from numerous streets. This suggests vehicular regulation measures, especially in the renovation of trucks. As was mentioned before, secondary aerosols are important contributors to the fine suspended particles, due to the high temperatures and combustion emissions that favors their formation.

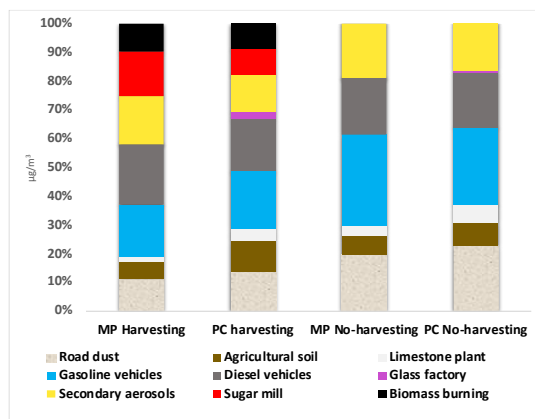


Fig. 7. Source reconciliation of $PM_{2.5}$ in the sugarcane zone in Cordoba, Veracruz.

The emissions from agricultural soils are caused by wind and soil cleaning and preparation for cultivation; therefore, the highest contribution was in the rural area (PC), where most crops are located, with 11 % and 8 % during harvesting and non-harvesting periods, respectively. Vehicle traffic on paved and unpaved roads also has a significant contribution ranging between 11 % and 23 % across different sites and seasons. A limestone facility is located between the two sites, a little closer to the PC that is in operation the whole year. Nevertheless, the contribution of this source is not only from the plant, since limestone is applied in order to neutralize the soil with pH from 4.5 to 5.5. Different blends of $CaCO_3$ and CO are applied onto the sugarcane stalks post-harvest, acting as a nutrient booster for the mother plant, facilitating better absorption of nitrogen, phosphorus, and potassium. This practice is performed for the soil preparation of other crops as well. Consequently, the impact of this source is more pronounced in the rural site during the non-harvesting season, where the majority of crops are cultivated, contributing to over 6 % of the total $PM_{2.5}$ mass. Even during the harvesting season, this source remains relevant as lime application typically commences in December, following the clearing of soil from the initial sugarcane harvesting.

Conclusions

The detailed chemical analysis of the elements and compounds that comprise fine atmospheric particles suspended in the air, known as $PM_{2.5}$, not only provides a diagnosis of the presence of toxic species for living organisms but can also be used in receptor models to determine the contribution of various emitting sources.

This study demonstrates that during the sugarcane harvest season, $PM_{2.5}$ concentrations were duplicated, exceeding the maximum permissible limits of the Mexican standard on 70 % of days, resulting in poor or very poor air quality. The 60 % increase in elemental carbon or black carbon during harvesting presents

an opportunity for achieving co-benefits in climate change mitigation and air quality improvement through decision-makers' actions.

The successful generation of chemical source profiles for the two main sugarcane processes, was achieved for the first time, because the source signatures were able to differentiate and separate emissions from mills and burnings, which had not been previously published, as well as to identify the contribution from the 2 to 5 % lime application in the field to neutralize the soil. During the harvest, mills contribute to PM_{2.5} emissions between 9 and 15 %, while biomass burning contributes around 9 %, vehicles contribute 36 % on average, and road dust and agricultural soil contribute from 18 to 22 %.

Of special concern is the increase in toxic species in particles, which can be up to 9 times higher compared to the non-harvest season. In particular, some carcinogenic polycyclic aromatic compounds were up to 7 times higher, and some inorganic toxics increased their concentration up to 9 times, mainly in urban areas where the population density is higher. This diagnosis should be used by environmental and health authorities to reinforce the need for control measures, in both, mills and in crop fields. Additionally, these results underscore the importance of conducting health risk assessments in the area.

Acknowledgements

The authors thank CONACYT for the support to Project 18123, for the FMV graduated scholarship, as well as to the IDAEA-CSIC staff, to the Postgraduate College Campus Cordoba and to the Municipal Palace authorities by the provided facilities for particle analysis and sampling.

References

1. Cardoso, T. F.; Watanabe, M. D.; Souza, A.; Chagas, M. F.; Cavalett, O.; Morais, E. R.; ... Bonomi, A. *Biofuels, Bioprod. Biorefin.* **2018**, 12, 68-82. DOI: <https://doi.org/10.1002/bbb.1828>.
2. Ma, S.; Karkee, M.; Scharf, P. A.; Zhang, Q. *Appl. Eng. Agric.* **2014**, 30, 727-739. DOI: <https://doi.org/10.13031/aea.30.10696>.
3. Sevimoglu, O.; Rogge, W. R. *Aerosol Air Qual Res.* **2015**, 15, 1720-1736. DOI: <https://doi.org/10.4209/aaqr.2015.02.0069>.
4. Mazzoli-Rocha, F.; Carvalho, G.M.C.; Lanzetti, M.; Valença, S.S.; Silva, L.F.F.; Saldiva, P.H.N.; Zin, W.A.; Faffe, D.S. *Respir. Physiol. Neurobiol.* **2014**, 191, 106e113. DOI: <https://doi.org/10.1016/j.resp.2013.11.004>.
5. Bates, J. T.; Weber, R. J.; Abrams, J.; Verma, V.; Fang, T.; Klein, M.; Russell, A. G. *Env. Sci.Tech.* **2015**, 49, 13605-13612. DOI: <https://doi.org/10.1021/acs.est.5b02967>.
6. Umbuzeiro, G.A.; Franco, A.; Magalhães, D.; Castro, F.J.V.; Kummrow, F.; Rech, C.M.; Carvalho, L.R.F.; Vasconcellos, P.C. *Environ. Mol. Mutagen.* **2008**, 49, 249-255. DOI: <https://doi.org/10.1002/em.20378>.
7. Silveira, H.; Schmidt-Carrijo, M.; Seidel, E.H.; Scapulatempo-Neto, C.; Longatto-Filho, A.; Lopes-Carvalho, A.; Vieira-Reis, R.; Saldivas, P.H. *Environ. Health.* **2013**, 12, 87.
8. Mousavi, A.; Sowlat, M. H.; Hasheminassab, S.; Polidori, A.; Shafer, M. M., Schauer, J. J.; Sioutas, C. *Sci. Total Env.* **2019**, 651, 638-47. DOI: <https://doi.org/10.1016/j.atmosenv.2019.02.009>.
9. Rajendran, P.; Jayakumar, T.; Nishigaki, I.; Ekambaram, G.; Nishigaki, Y.; Vetrivelvi, J.; Sakthisekaran, D. *IJBS.* **2013**, 9, 68.
10. Bond, T. C.; Doherty, S. J.; Fahey, D. W.; Forster, P. M.; Berntsen, T.; DeAngelo, B. J.; ... Zender, C. S. *J. Geophys. Res.* **2013**, 118, 5380-5552. DOI: <https://doi.org/10.1002/jgrd.50171>.

11. Mugica-Álvarez, V.; Hernández-Rosas, F.; Magaña-Reyes, M.; Herrera-Murillo, J.; Santiago-De La Rosa, N.; Gutiérrez-Arzaluz, M.; González-Cardoso, G. *Atmos. Environ.* **2018**, *193*, 262-272. DOI: <https://doi.org/10.1016/j.atmosenv.2018.09.013>.
12. Herrera Solano, A.; Herrera Reyes, M.; Verdejo Lara, R. A.; Real Garrido, C. J.; Castillo Morán, A. *Revista Biológico Agropecuaria Tuxpan.* **2023**, *11*, 13–20.
13. CONADESUCA (2018). Comité Nacional para el Desarrollo Sustentable de la Caña de Azúcar. Informe estadístico del sector agroindustrial de la caña de azúcar en México. Zafra 2012-2013/2021-2022. <https://www.siiiba.conadesuca.gob.mx/infocana/Consulta/ReportesP.aspx?f=1>, accessed in October 2023.
14. Mugica-Álvarez, V.; Santiago-De La Rosa, N.; Figueroa-Lara, J.J.; Flores-Rodríguez, J.; Torres-Rodríguez, M.; Magaña-Reyes, M. *Sci. Total Environ.* **2015**, 527–528.
15. Souza, K. F.; Carvalho, L. R.; Allen, A. G.; Cardoso, A. A. *Atmos. Environ.* **2014**, *83*, 193-201. DOI: <https://doi.org/10.21475/ajcs.23.17.09.p3950>.
16. Arbex, M.A.; Pereira, L.A.A.; Carvalho-Oliveira, R., Saldiva, P.H.N.; Braga, A.L.F. *J. Epidemiol. Comm. Health.* **2014**, *68*, 669-74. DOI: <https://doi.org/10.1289/ehp.8485>.
17. de Andrade, S. J.; Cristale, J.; Silva, F. S.; Zocolo, G. J.; Marchi, M. R. *Atmos. Environ.* **2010**, *44*, 2913-2919. DOI: <https://doi.org/10.1016/j.atmosenv.2010.04.026>.
18. Stem, A.D.; Gibb, M.; Roncal-Jimenez, C.; Johnson, R.J.; Brown, J.M. *Inhalation Toxicol.* **2024**. DOI: <https://doi.org/10.1080/08958378.2024.2316875>.
19. Watson, J. G.; Robinson, N. F.; Lewis, C.; Coulter, T.; Chow, J. C.; Fujita, E. M.; ... Willis, R. D. in: *Chemical mass balance receptor model version 8 (CMB8) user's manual*. Desert Research Institute, Reno, NV, **1997**.
20. Begum, B. A.; Biswas, S. K.; Hopke, P. K. *Aerosol Air Qual. Res.* **2007**, *7*, 446-468. DOI: <https://doi.org/10.1016/j.atmosenv.2004.02.042>.
21. Mugica, V.; Ortiz, E.; Molina, L.; De Vizcaya-Ruiz, A.; Nebot, A.; Quintana, R.; ... Alcántara, E. *Atmos. Environ.* **2009**, *43*, 5068-5074. DOI: <https://doi.org/10.1016/j.atmosenv.2009.06.051>.
22. Afshar-Mohajer, Nima; Wilson, Christina; Wu, Chang-Yu; Stormer James, E. *J. Air Waste Manag. Assoc.* **2016**, *66*, 377-386. DOI: <https://doi.org/10.1080/10962247.2016.1138902>.
23. INEGI. México en cifras. www.inegi.org.mx, accessed in July 2024.
24. Birch, M.E.; Cary, R.A. *Aerosol Sci. Technol.* **1996**, *25*, 221–241.
25. Hopke, P. K. *J. Air Waste Manag. Assoc.* **2016**, *66*, 237-259.
26. Mugica, V.; Mugica, F.; Torres, M.; Figueroa, J. *Sci. World J.* **2008**, *8*, 275-286.
27. Vega, E.; Mugica, V.; Reyes, E.; Sánchez, G.; Chow, J.; Watson, J. *Atmos. Environ.* **2001**, *35*, 4033-4039.
28. Speciate database 4.0. EPA. <https://www.epa.gov/air-emissions-modeling/speciate-4>, accessed in June 2022.
29. Pestana, P. R. D. S.; Braga, A. L. F.; Ramos, E. M. C.; Oliveira, A. F. D.; Osadnik, C. R.; Ferreira, A. D.; Ramos, D. *Rev. Saude Publica.* **2017**, *51*. DOI: <https://doi.org/10.1590/S1518-8787.2017051006495>.
30. Nowell, H. K.; Wirks, C.; Val Martin, M.; van Donkelaar, A.; Martin, R. V.; Uejio, C. K.; Holmes, C. D. *Env. Health Perspect.* **2022**, *130*, 087004. DOI: <https://doi.org/10.1289/EHP9957>.
31. Mnatzaganian, C. L.; Pellegrin, K. L.; Miyamura, J.; Valencia, D.; Pang, L. *Environ. Health.* **2015**, *14*, 1-8. DOI: <https://doi.org/10.1186/s12940-015-0067-y>.
32. Chow, J. C.; Watson, J. G.; Edgerton, S. A.; Vega, E. *Sci. Tot. Environ.* **2002**, 287, 177-201.
33. Błaszczak, B.; Widziewicz-Rzońca, K.; Ziola, N.; Klejnowski, K.; Juda-Rezler, K. *Appl. Sciences.* **2018**, *9*, 98. DOI: <https://doi.org/10.4209/aaqr.2012.01.0003>.
34. Zhu, C. S.; Cao, J. J.; Shen, Z. X.; Liu, S. X.; Zhang, T.; Zhao, Z. Z.; ... Zhang, E. K. *Aerosol Air Qual. Res.* **2012**, *12*, 1157-1165.
35. Nisbet, I. C.; Lagoy, P. K. *Regul. Toxicol. Pharmacol.* **1992**, *16*, 290-300.

36. WHO. *Human health effects of polycyclic aromatic hydrocarbons as ambient air pollutants: report of the Working*. WHO Regional Office for Europe, **2021**.
37. Ravindra, K.; Sokhi, R.; Van Grieken, R. *Atmos. Environ.* **2008**, *42*, 2895-2921. DOI: <https://doi.org/10.1016/j.atmosenv.2007.12.010>.
38. Saldarriaga-Noreña, H.; López-Márquez, R.; Murillo-Tovar, M.; Hernández-Mena, L.; Ospina-Noreña, E.; Sánchez-Salinas, E.; Montiel-Palma, S. *Atmosphere*. **2015**, *6*, 1259-1270. DOI: <https://doi.org/10.3390/atmos6091259>.
39. de Assuncao Joao, V.; Pesquero Célia, R.; Nardocci Adelaide, C.; Francisco, A. P., Soares Nilson, S.; Ribeiro, H. *J. Air Waste Manage. Assoc.* **2014**, *64*, 1130-1139. DOI: <https://doi.org/10.1080/10962247.2014.928242>.
40. Scaramboni, C.; Urban, R. C.; de Oliveira, D. P.; Dorta, D. J.; Campos, M. L. A. M. *Chemosphere*, **2024**, *350*, 141072. DOI: <https://doi.org/10.1016/j.chemosphere.2023.141072>.
41. Mugica, V.; Hernández, S.; Torres, M.; García, R. *J. Air Waste Manage. Assoc.* **2010**, *60*, 548-555. DOI: <https://doi.org/10.3155/1047-3289.60.5.548>.
42. Wang, X.; Zong, Z.; Tian, C.; Chen, Y.; Luo, C.; Tang, J.; ... Zhang, G. *Sci. Tot. Environ.* **2018**, *612*, 330-338. DOI: <https://doi.org/10.1016/j.scitotenv.2017.08.208>.
43. Taghvaei, S.; Sowlat, M. H.; Hassanvand, M. S.; Yunesian, M.; Naddafi, K.; Sioutas, C. *Environ. Int.* **2018**, *120*, 321-332. DOI: <https://doi.org/10.1016/j.envint.2018.08.003>.
44. Masiol, M.; Hofer, A.; Squizzato, S.; Piazza, R.; Rampazzo, G.; Pavoni, B. *Atmos. Environ.* **2012**, *60*, 375-382. DOI: <https://doi.org/10.1016/j.atmosenv.2012.06.073>.
45. Manoli, E.; Kouras, A.; Karagkiozidou, O.; Argyropoulos, G.; Voutsas, D.; Samara, C. *Environ. Sci. Pollut. Res.* **2016**, *23*, 3556-3568. DOI: <https://doi.org/10.1007/s11356-015-5573-5>.
46. Martellini, T.; Giannoni, M.; Lepri, L.; Katsoyiannis, A.; Cincinelli, A. *Environ. Pollut.* **2012**, *164*, 252-258. DOI: <https://doi.org/10.1016/j.envpol.2011.12.040>.
47. Bi, C.; Chen, Y.; Zhao, Z.; Li, Q.; Zhou, Q.; Ye, Z.; Ge, X. *Chemosphere*. **2020**, *238*, 124620. DOI: <https://doi.org/10.1016/j.chemosphere.2019.124620>.
48. Hernández-López, A. E.; Miranda Martín del Campo, J.; Mugica Álvarez, V.; Valle-Hernández, B. L.; Mejía-Ponce, L. V.; Pineda-Santamaría, J. C.; Rozanes-Valenzuela, D. *Rev. Int. Cont. Amb.* **2021**, *37*. DOI: <https://doi.org/10.20937/RICA.54066>.
49. Tao, J.; Zhang, L.; Gao, J.; Wang, H.; Chai, F.; Wang, S. *Atmos. Environ.* **2015**, *110*, 36-44. DOI: <https://doi.org/10.1016/j.atmosenv.2016.08.067>.
50. Saraga, D.; Maggos, T.; Sadoun, E.; Fthenou, E.; Hassan, H.; Tsiouri, V.; ... Kakosimos, K. *Aerosol Air Qual. Res.* **2017**, *17*, 1156-1168. DOI: <https://doi.org/10.4209/aaqr.2016.05.0198>.

Antimicrobial and Antioxidant Activities of Four Essential Oils

Ana Laura Esquivel-Campos¹, Leonor Sánchez-Pérez², Marco Martín González-Chávez³, Aranza Reyes-Ponce¹, Ernesto de Jesús Zapata-Flores³, Salud Pérez-Gutiérrez^{1,*}, Julia Pérez-Ramos^{1,*}

¹Departamento de Sistemas Biológicos, Universidad Autónoma Metropolitana.

²Departamento de Atención a la Salud, Universidad Autónoma Metropolitana.

³Facultad de Ciencia Químicas, Universidad Autónoma de San Luis Potosí.

*Corresponding author: Julia Pérez Ramos, email: jperez@correo.xoc.uam.mx; Salud Pérez Gutiérrez, email: msperez@correo.xoc.uam.mx

Received May 29th, 2024; Accepted July 25th, 2024.

DOI: <http://dx.doi.org/10.29356/jmcs.v68i4.2309>

Abstract. Various opportunistic microorganisms, such as bacteria and fungi, are responsible for multiple infectious diseases, which represent a threat to global health. Essential oils (EOs) have shown antimicrobial and antioxidant properties, making them an excellent alternative to control multi-resistant bacteria. In this work, for the first time, the antimicrobial and antioxidant activities of four EOs were evaluated, namely *Trixis angustifolia* DC (EOTA), *Dalea bicolor* Humb & Bonpl. Ex Willd (EODB), *Tagetes parryi* A.Gray (EOTP) and *Eupatorium glabratum* Kunth (EOEG). They were obtained by hydrodistillation, and their chemical composition was determined by GC-MS (Gas chromatography-mass spectroscopy) using HP5-MS column. Their antimicrobial and antioxidant activities were determined by the microdilution method and the DPPH and ABTS techniques, respectively. The main compounds of the EOs were piperitone (36.67 %) for EOTA, β -pinene (27.25) for EODB, verbenone (31.13 %) for EOTP and α -cadinol (7.78 %) and bornyl acetate (6.45 %) for EOEG. The EOs EOTA, EODB, EOTP and EOEG inhibited the development of *Candida* at a concentration of 62.5–500 $\mu\text{g/mL}$, whereas the antibacterial activities of these oils were observed at concentrations from 125–500 $\mu\text{g/mL}$. The antioxidant activity of EOTA and EODB were $\text{IC}_{50} = 0.641, 1.195 \text{ mg/mL}$, whereas those of EOTP and EOEG was lower. These results show that four EOs have antimicrobial activity.

Keywords: Essential oils; composition; antimicrobial activity; antioxidant capacity.

Resumen. Diversos microorganismos oportunistas, como bacterias y hongos, son responsables de múltiples enfermedades infecciosas, que representan una amenaza para la salud mundial. Los aceites esenciales (EOs) han demostrado propiedades antimicrobianas y antioxidantes, lo que los convierte en una excelente alternativa para el control de bacterias multirresistentes. En este trabajo, por primera vez, se evaluaron las actividades antimicrobianas y antioxidantes de cuatro EOs: *Trixis angustifolia* DC (EOTA), *Dalea bicolor* Humb & Bonpl. Ex Willd (EODB), *Tagetes parryi* A.Gray (EOTP) y *Eupatorium glabratum* Kunth (EOEG). Los aceites se obtuvieron por hidrodestilación y se determinó su composición química por GC-MS (cromatografía de gases-espectrometría de masas) utilizando una columna HP5-MS. Sus actividades antimicrobiana y antioxidante se determinaron por el método de microdilución y las técnicas DPPH y ABTS, respectivamente. Los principales compuestos de los aceites esenciales fueron piperitona (36,67 %) para EOTA, β -pineno (27,25 %) para EODB, verbenona (31,13 %) para EOTP y α -cadinol (7,78 %) y acetato de bornilo (6,45 %) para EOEG. Los aceites esenciales EOTA, EODB, EOTP y EOEG inhibieron el desarrollo de *Candida* a una concentración de 62,5–500 $\mu\text{g/mL}$, mientras que las actividades antibacterianas de estos aceites se determinaron a concentraciones de 125–500 $\mu\text{g/mL}$. La actividad antioxidante de EOTA y EODB fue de $\text{IC}_{50} = 0,641, \text{ y } 1,195 \text{ mg/mL}$.

respectivamente, mientras que las de EOTP y EOEG fueron menores. Estos resultados muestran que los cuatro EOs tienen actividad antimicrobiana.

Palabras clave: Aceites esenciales; composición; actividad antimicrobiana; capacidad antioxidante.

Introduction

Multi-resistant bacteria (ESKAPE) represent an inherent problem for the world population. In the United States, the estimated number of annual infections is higher than 2 million, whereas in developing countries, communicable diseases are the main cause of mortality, and emerging and re-emerging infectious diseases represent a major issue [1]. Antibiotic resistance jeopardises the achievements of modern medicine by impeding the treatment and prevention of infections. Some ESKAPE pathogens (*Enterococcus faecium*, *Staphylococcus aureus*, *Klebsiella pneumoniae*, *Acinetobacter baumannii*, *Pseudomonas aeruginosa*, *Escherichia coli*) can tolerate transient exposure to high doses of antibiotics without changes in their minimum inhibitory concentration (MIC). This tolerance is associated with the irreversible destruction of the active site of the antibiotic, modification of the bacterial target site, reduction of antibiotic accumulation by mutation or loss of membrane channels and persistence through cells embedded in biofilms [2,3].

The World Health Organization (WHO) and Pan American Health Organization (PAHO) have drawn special attention to multidrug-resistant bacteria, generating a critical priority list that includes dangerous multidrug-resistant bacteria that may be of nosocomial origin or acquired in the community. They are classified by their degree of lethality, treatment and hospitalization time; the ease with which they are transmitted between animals, from animals to people and between people. The list is divided into critical, high, and medium priority levels, which include *S. aureus*, *E. coli*, *E. faecalis* and *P. aeruginosa* [4].

Additionally, yeasts of the genus *Candida* are opportunistic human pathogens [5] that affect mucous membranes. More than 90 % of clinical infections are caused by species of the genus *Candida*, such as *C. glabrata*, *C. albicans*, *C. krusei* and *C. tropicalis*, highlighting their virulence factors such as membrane and cell wall barriers, dimorphism, biofilm formation, signal transduction pathways, proteins related to stress tolerance, hydrolytic enzymes and toxin production [6]. Therefore, the study of these yeasts, whose incidence has increased in the last three decades, is imperative, due to the increase in the Acquired Immune Deficiency Syndrome (AIDS) epidemic, an increasingly aging population, a greater number of immunocompromised patients and the more widespread use of medical devices permanent [4]. Resistance to antifungals has increased in many *Candida* species, contributing to treatment failure and amplifying intra-hospital issues [7].

Free radicals are chemical species present in the body that can cause oxidative stress, damaging cells and body functions, which can result in various diseases such as cancer, arthritis and respiratory diseases, among others. Antioxidants have the ability to scavenge free radicals, playing an important role in defending the body against different chronic diseases [8]. It is therefore essential to develop new compounds with antimicrobial and antioxidant activity. In this context, plants are a source of secondary metabolites, many of which have these two effects, and one of these constituents is EOs, which are complex mixtures containing between 20 and 60 components, mainly monoterpenes, sesquiterpenes, aliphatic and aromatic compounds [9].

The composition of essential oils (EOs) varies with temperature, climate, plant maturity and season, among others, and this variability could influence the properties of the EOs [10]. They play an important role in protecting plants from pathogens and predators [11] and are applied in the production of food, flavours, cosmetics and pharmaceuticals [12]. The bioactive compounds of EOs present various biological activities such as anti-inflammatory, analgesic, anti-cancer [13], antimicrobial and antioxidant activities [14,15]. Different EOs from plants of the family Asteraceae have antioxidant and antimicrobial activities [16], such as those from *Achillea millefolium* subsp. *millefolium* Afan [17] and *Pulicaria inuloides* [18]. Some EOs of plants of the Fabaceae family also possess these activities, such as those from *Myrocarpus frondosus* [19].

Recent studies found that some extracts of aerial parts of *Trixis angustifolia*, *Dalea bicolor*, *Eupatorium glabratum* and some species of *Tagetes* have antimicrobial activity against different bacteria [20-22]. However, there are no reports about antimicrobial effects of the EOs of these plants.

In this study, we determined the composition of four EOs from plants of the family Asteraceae, namely essential oil of *Trixis angustifolia* (EOTA), essential oil of *Tagetes parryi* (EOTP) and essential oil of *Eupatorium glabratum* (EOEG), and of one EO from a plant *Dalea bicolor* of the family Fabaceae, namely EODB. For the first time, the antioxidant capacities of these EOs were evaluated, as well as their antimicrobial activities toward two Gram (+) bacteria and two Gram (-) bacteria and their antifungal activities toward four *Candida* species.

Materials and methods

General

The aerial parts of *T. angustifolia*, *D. bicolor*, *T. parryi* and *E. glabratum*, were collected in San Luis Potosí State, México. The plants were identified by the taxonomist José García Pérez, and a voucher specimen of each plant was deposited in the Herbarium Isidro Palacios of the Universidad Autónoma de San Luis Potosí (Table 1).

Table 1. Data about plant species, and yield of EOs.

Plant Species	Date and place	Coordinates	Plant part	Yield (w/w)	Voucher number
<i>Trixis angustifolia</i>	February 2008, 1 km from the junction to Guadalcázar, SLP	22°38'23.7"N 100°30'49.0"W	Aerial parts	0.64	SLPM44557
<i>Dalea bicolor</i>	February 2014, at the Cañada del Lobo dam, San Luis Potosí, SLP	22°05'44.0"N 100°57'56.9"W	Aerial parts	0.45	SLPM57550
* <i>Tagetes parryi</i>	November 2013, Agua Blanca, Municipality of Villa de Zaragoza, SLP	22°03'35.7"N 100°37'11.5"W	Aerial parts	0.54	SLPM31975
<i>Eupatorium glabratum</i>	February 2008, in the Realejo, community of Guadalcázar, SLP	22°39'57.4"N 100°25'04.4"W	Aerial parts	0.19	SLPM44553

*Previously reported by González-Velasco [23].

Essential oil extraction

The EOs were obtained by hydrodistillation from the aerial parts of the fresh plants. They were extracted with diethyl ether, and this solvent was eliminated under reduced pressure at 20 °C. The EOs were then stored at 5 °C.

Composition of the EOs

The composition of EOs was determined by GC-MS using a chromatograph (Agilent Technology, model 6890N) connected to a selective mass detector model 5973 Network (MSD, Agilent Technologies, Wilmington, DE, USA). An HP-5MS capillary column (30 m length, 0.25 mm internal diameter, and 0.25 µm film width) (J&W, Folsom, CA, USA) was used for the separation. The EOs samples (10 µL) were diluted with acetone (1 mL) and the injector temperature was 240 °C, operated in the splitless mode, and the carrier gas was helium at 1mL/min. The oven temperature was programmed at 50 °C/3 min, with a heating rate of 3 °C/min up to 240 °C/2 min. The MSD was operated at 70 eV, the ion source was set a 150 °C, and the transfer line was at 240 °C and the mass range was analyzed 15-600 *m/z*. The software MSD ChemStation (Agilent B.04.02) was

used for data recording and the compounds were identified based on their mass spectra by comparison with the spectra reported in the Wiley 09 and NIST11 libraries. In addition, the Kovak index was calculated for each peak, with reference to the n-alkane standards (C6-C26) running under the same conditions.

Microorganisms

We used four yeast and four bacterial species. The yeasts, *Candida albicans* ATCC 10231, *C. glabrata* ATCC 32554, *C. krusei* ATCC 90878 and *C. tropicalis* ATCC 750, were inoculated in sterile Sabouraud dextrose broth and incubated at 37 °C/24–48 h. The bacteria, *Staphylococcus aureus* ATCC 6538, *Enterococcus faecalis* ATCC 29212, *Escherichia coli* ATCC 8739 and *Pseudomonas aeruginosa* ATCC 9027, were inoculated in sterile tryptocasein soy broth and incubated at 37 °C/24 h.

Inoculum preparation

First, 100 µL of bacterial and yeast suspensions were individually inoculated in 8 mL of sterile tryptocasein soy broth and sterile Sabouraud dextrose broth and incubated at 37 °C for 24–48 h. The microorganisms were then adjusted to a density of 10⁵ colony-forming units (CFU)/ mL (corresponding to 0.5 McFarland standards). Finally, the suspensions were diluted to 1:1,000 with saline solution [24].

Determination of the minimum inhibitory concentration (MIC)

The antimicrobial activity of the EOs was evaluated by the microdilution technique in 96-well plates to determine the MIC. First, 50 µL of sterile tryptocasein soy broth (for bacteria) [24] and sterile Sabouraud dextrose broth (for yeasts) [25] were pipetted into 96-well plates. Then, 50 µL of EOTA, EODB, EOTP and EOEG were added, and a serial dilution of each extract was subsequently carried out to obtain concentrations of 500, 250, 125, 62.5, 31.25, 15.6, 7.8, 3.9, 1.95 and 0.97 µg/mL. Finally, 50 µL of the 1:1,000 dilution of bacterial or yeast inoculate was added and incubated at 37 °C/24 h. As positive inhibition controls, we used fluconazole and itraconazole (250 to 0.12 µg/mL) for yeasts and ciprofloxacin (100 to 0.95 µg/mL) for bacteria. The MIC was determined at an absorbance of 625 nm. The activity of the EOs was compared with those of the respective controls; all tests were carried out six times.

Antioxidant activity 2,2-Diphenyl-1-picrylhydrazyl DPPH assay

The DPPH test was performed according to the method of Williams [26], with modifications. The reaction mixture contained 100 µL of 0.208 mM DPPH and 100 µL of the EOs dissolved in methanol [400–12.5 µg/mL]. The negative control consisted of 100 µL of 0.208 mM DPPH with 100 µL methanol. We used TROLOX (6-hydroxy-2,5,7,8-tetramethylchroman-2-carboxylic acid; 0–40 µg/mL) as a positive control. Absorbance was determined at a wavelength of 517 nm after 20 min in the dark. The reductive capacity of the EOs was determined using the following equation:

$$\text{RSA \%} = (A_{\text{control}} - \text{AEO} / A_{\text{control}}) \times 100$$

where A_{control} is the absorbance of the negative control, and AEO is the absorbance of the EO. The concentrations of the samples responsible for a 50 % decrease in the initial activity of the DPPH free radical (IC₅₀) were calculated by linear regression.

Antioxidant activity ABTS assay

The radical scavenging capacity of the EOs was determined with ABTS (2,2'-azinobis-3-ethylbenzothiazoline-6-sulfonic acid) as described elsewhere [27]. An ABTS+radical solution was prepared by mixing 7 mM ABTS solution and 2.45 mM potassium persulphate (K₂S₂O₈) in a 1:1 (v/v) ratio. The solution was incubated at room temperature in the dark for 12 h and subsequently diluted with water to obtain an emerald-green solution with an absorbance close to 1,000. The negative control consisted of 20 µL methanol and 180 µL ABTS+; TROLOX was used as a positive control (0–40 µg/mL). The assay was performed in a 96-well plate, where 20 µL of EO dissolved in methanol in a range of 500–100 µg/mL was mixed with 180 µL

ABTS⁺ solution, incubated for 20 min at room temperature in the dark and read at a wavelength of 734 nm. The RSA % was determined according to the following equation:

$$\text{RSA \%} = (\text{Ac}-\text{As})/\text{Ac} \times 100$$

where Ac is the control absorbance, and As is the sample absorbance. The concentrations of the samples responsible for a 50 % decrease in the initial activity of the ABTS free radical (IC₅₀) were calculated by linear regression.

Statistical analysis

The data obtained between MIC and four EOs against four species of *Candida* and MIC of four EOs against Gram (+) and Gram (-), species were analyzed, by ANOVA test. The data obtained calculating the DPPH and ABTS indexes were analysed by Tukey's test. The data was analyzed using statistical program inerSTAT20-a v. 1.3. A p-value of less than 0.05 was considered statistically significant.

Results

Chemical composition of the EOs

The chemical composition of the EOs was determined by GC-MS [28]. We found the three EOs (EOTA, EOTP, EOEG) oxygenated compounds predominate 89.58 %, 69.14 %, 40.59 %, respectively. In the case of EODB the oxygenated compounds represent only 24.8 %. The table 2 is shown for the first time the composition of EOTA. Overall, 34 compounds were identified, accounting for 86.47 % of the oil; the main compounds were piperitone (38.67 %), 1,8-cineole (14.14 %) and α -terpineol (6.38 %).

Table 2. The chemical composition of EOTA.

Compound	Rt (min)	Relative Abundance (% \pm SD)	RI _R	RI _E
Isovaleric acid	6.11	2.37 \pm 0.37	816	808
2-Methylbutyric acid	6.76	2.45 \pm 0.57	839	838
α -Phellandrene	10.38	0.53 \pm 0.01	1007	1003
<i>p</i> -Cymene	11.30	0.47 \pm 0.01	1011	1022
1,8-Cineole	11.62	14.14 \pm 0.42	1023	1029
β - <i>cis</i> -Ocimene	12.45	0.19 \pm 0.00	1024	1047
Linalool	14.83	1.07 \pm 0.03	1082	1097
(<i>E</i>)- <i>p</i> -Menth-2-en-1-ol	15.73	0.44 \pm 0.06	1123	1117
<i>cis</i> - <i>p</i> -Menth-2-en-1-ol	16.60	0.39 \pm 0.02	1118	1136
4-Terpineol	18.34	0.18 \pm 0.04	1175	1173
3,9-Epoxy-1- <i>p</i> -menthene	18.70	0.12 \pm 0.03	1178	1181
α -Terpineol	19.03	6.38 \pm 0.07	1172	1188

Compound	Rt (min)	Relative Abundance (% ± SD)	RI _R	RI _E
<i>trans</i> -2-Hydroxy-1,8-cineole	20.68	0.11 ± 0.05	1228	1224
Piperitone	22.16	38.67 ± 0.48	1243	1257
β-Bourbonene	27.55	0.12 ± 0.00	1386	1378
β-Elemene	27.92	0.78 ± 0.02	1387	1387
α-Gurjunene	28.60	0.34 ± 0.00	1412	1402
Caryophyllene	29.00	1.34 ± 0.00	1421	1412
α-Bergamotene	29.77	0.23 ± 0.02	1427	1431
Humulene	30.40	0.25 ± 0.02	1454	1447
Aromandendrene	30.70	0.41 ± 0.01	1455	1454
α-Murolene	32.39	0.13 ± 0.03	1494	1496
δ-Cadinene	33.33	4.11 ± 0.08	1514	1520
Elemol	34.36	0.86 ± 0.03	1535	1545
Palustrol	34.98	0.80 ± 0.03	1562	1561
Spathulenol	35.41	0.22 ± 0.02	1569	1571
Guaiol	36.23	1.95 ± 0.03	1588	1592
Ledol	36.37	0.43 ± 0.00	1597	1595
2-(4a,8-Diethyl-2,3,4,4a,5,6,7,8-octahydro-2-naphthalenyl)-2-propanol	36.56	1.14 ± 0.02	1598	1600
Agarospirol	37.24	0.55 ± 0.08	1631	1619
δ-Cadinol	38.06	0.28 ± 0.12	1646	1641
β-Eudesmol	38.15	0.18 ± 0.01	1644	1644
α-Cadinol	38.36	0.38 ± 0.03	1641	1650
Bisabolol	39.49	2.06 ± 0.05	1683	1681
Total identified		86.47		
Total unidentified		13.53		

Retention time (Rt), retention indexes in the literature (RI_R), and retention indexes calculated (RI_E), Standard Deviation (SD) duplicated analysis.

For EOTP, 21 constituents were determined [23], according for 87.49 % of the EO (Table 3); the main compounds were dihydrotagetone (25.77 %) and verbenone (31.13 %).

Table 3. The chemical composition of EOTP.

Compound	Rt (min)	Relative Abundance (% ± SD)	RI _R	RI _E
3-Hexenol-1-ol	5.66	0.16 ± 0.00	838	806.3
β-Phellandrene	10.03	0.37 ± 0.04	964	957.0
β-Pinene	10.13	0.32 ± 0.02	961.7	960.3
β-Myrcene	10.86	0.21 ± 0.01	979	985.6
α-Phellandrene	11.40	0.23 ± 0.00	997	1000.0
1,8-Cineole	12.63	1.46 ± 0.02	1023	1028.2
<i>trans</i> -β-Ocimene	13.06	2.10 ± 0.12	1034	1037.1
Dihydrotagetone	13.87	25.77 ± 1.57	1055	1054.1
Chrysanthenone	17.20	0.31 ± 0.10	1099	1123
Neo-allo-ocimene	17.46	0.17 ± 0.09	1131	1128.4
Tagetone	18.70	19.76 ± 1.47	1124	1153
4-Terpineol	19.75	0.11 ± 0.02	1161	1188.5
α-Terpineol	20.42	0.55 ± 0.01	1172	1188.5
2-Ethylidene-6-methyl-3,5-heptadienal	21.22	0.37 ± 0.05	1182	1205
Verbenone	22.95	31.13 ± 3.19	1228	1242.4
Thymol	23.47	0.14 ± 0.06	1266	1253.6
Isopiperitenone	24.32	2.31 ± 0.34	1249	1271.9
Eugenol	29.96	1.46 ± 0.05	1392	1393.3
Caryophyllene	31.06	0.34 ± 0.04	1424	1418
<i>p</i> -Cresol	33.12	0.11 ± 0.07	1503.9	1474.1
Elemol	36.61	0.10 ± 0.01	1535	1551.2
Total identified		87.49		
Total unidentified		12.51		

Retention time (Rt), retention indexes in the literature (RI_R), and retention indexes calculated (RI_E). Standard Deviation (SD) duplicated analysis. This composition was reported for González-Velasco [23].

In EODB, we identified 46 compounds (Table 4), accounting for 65.98 % of the total EO; the main component was β -pinene (27.25 %), followed by *tau*-cadinol (6.73 %), β -myrcene (6.23 %) and camphene (3.85 %).

Table 4. The chemical composition of EODB.

Compound	Rt (min)	Relative Abundance (% \pm SD)	RI _R	RI _E
(<i>E</i>)-2-Hexenal	7.35	0.12 \pm 0.00	822.4	810.8
Camphene	11.25	3.85 \pm 0.09	943	926.3
Benzaldehyde	11.79	0.36 \pm 0.01	927.2	942.5
β -Pinene	12.59	27.25 \pm 0.53	961	966.1
β -Myrcene	13.29	6.23 \pm 0.04	981	986.9
α -Phellandrene	13.89	0.06 \pm 0.01	997	1003.1
(3 <i>E</i>)-3-Hexenyl acetate	14.07	0.05 \pm 0.01	983	1006.8
3-methyl-3-vinylcyclohexanone	14.23	0.03 \pm 0.01	1115	1009.9
α -Terpinene	14.49	0.04 \pm 0.01	1008	1015.2
<i>p</i> -Cymene	14.89	0.05 \pm 0.00	1025	1023.2
Limonene	15.10	1.88 \pm 0.01	1018	1027.3
1,8-Cineole	15.23	0.25 \pm 0.01	1020	1030.0
β -Ocimene	16.11	1.15 \pm 0.09	1024	1047.5
γ -Terpinene	16.62	0.06 \pm 0.02	1047	1057.6
<i>trans</i> -Sabinene hydrate	17.05	0.08 \pm 0.00	1050	1066.3
Terpinoleno	18.13	0.11 \pm 0.00	1080	1087.7
Linalool	18.71	1.14 \pm 0.06	1082	1099.3
Pinocarveol	20.66	0.10 \pm 0.02	1143	1137.7
Camphor	20.97	0.14 \pm 0.01	1146	1143.7
Endo-Borneol	22.04	0.15 \pm 0.01	1148	1164.7
4-Terpinenol	22.62	0.25 \pm 0.04	1162	1176.1
α -Terpineol	23.29	0.70 \pm 0.01	1172	1189.1
Myrtenol	23.58	0.17 \pm 0.02	1212.8	1195.0
<i>cis</i> -3-Hexenyl valerate	25.34	0.05 \pm 0.01	1243	1232.0
Bornyl acetate	27.97	2.34 \pm 0.04	1270	1287.9

Compound	Rt (min)	Relative Abundance (% \pm SD)	RI _R	RI _E
Lavandulyl acetate	28.18	0.13 \pm 0.00	1292	1292.2
Myrtenyl acetate	29.84	0.21 \pm 0.08	1299	1327.6
δ -Elemene	30.43	0.62 \pm 0.03	1334	1340.1
Eugenol	31.29	0.12 \pm 0.01	1363	1358.4
Methyl cinnamate	32.46	0.54 \pm 0.01	1380	1383.3
β -Elemene	32.94	0.12 \pm 0.10	1387	1393.5
Caryophyllene	34.21	0.77 \pm 0.00	1421	1422.8
Humulene	35.73	0.33 \pm 0.05	1454	1459.0
γ -Muurolene	36.71	0.19 \pm 0.01	1471	1481.8
δ -cadinene	38.03	0.20 \pm 0.02	1514	1513.2
6-Epishyobunone	38.31	2.06 \pm 0.16	1538	1519.8
6-Epi-shyobunol	38.57	0.68 \pm 0.00	1555	1525.9
Elemol	39.76	1.09 \pm 0.14	1535	1554.2
Elemicin	39.98	0.14 \pm 0.06	1531	1559.2
Caryophyllene oxide	41.26	0.78 \pm 0.09	1575	1589.5
Viridiflorol	41.60	0.55 \pm 0.08	1594	1597.6
Guaiol	41.80	1.48 \pm 0.07	1588	1602.4
Dehydroxy-isocalamendiol	42.17	2.06 \pm 0.24	1593	1612.2
<i>tau</i> -cadinol	43.54	6.73 \pm 0.52	1628	1647.8
7R,8R-8-Hydroxy-4-isopropylidene-7-methylbicyclo[5.3.1]undec-1-ene	46.59	0.40 \pm 0.01	1754	1727.1
Isocalamendiol	47.55	0.18 \pm 0.04	1725	1752.2
Total identified		65.98		
Total unidentified		34.02		

Retention time (Rt), retention indexes in the literature (RI_R), and retention indexes calculated (RI_E). Standard Deviation (SD) duplicated analysis.

Finally, 45 compounds were determined in EOEG, corresponding to a total of 54.00% (Table 5), the major compounds were α -cadinol (7.78 %), bornyl acetate (6.45 %), and caryophyllene oxide (5.96 %).

Table 5. The chemical composition of EOEG.

Compound	Rt (min)	Relative Abundance (% \pm SD)	RI _R	RI _E
β -Pinene	9.17	0.45 \pm 0.01	961.7	949
Myrcene	9.90	0.23 \pm 0.00	981	983
α -Phellandrene	10.38	0.12 \pm 0.01	1007	1002
<i>p</i> -Cymene	11.27	1.16 \pm 0.06	1025.4	1021
Limonene	11.44	0.19 \pm 0.00	1018	1025
1,8-Cineole	11.55	0.02 \pm 0.01	1023	1027
<i>trans</i> - β -Ocimene	12.46	0.03 \pm 0.00	1034	1046
Linalool	14.83	0.25 \pm 0.02	1081	1085
Fenchol	15.31	0.21 \pm 0.03	1100	1107
Perillen	15.59	0.12 \pm 0.01	1109	1113
(<i>E</i>)- <i>p</i> -2-Menthen-1-ol	15.72	0.25 \pm 0.00	1123	1116
α -Campholenal	15.94	0.11 \pm 0.01	1120	1121
<i>cis</i> -2- <i>p</i> -Menthen-1-ol	16.60	0.19 \pm 0.02	1118	1135
(<i>Z</i>)- β -Terpineol	16.87	0.27 \pm 0.00	1125	1141
Endo-Borneol	17.73	0.41 \pm 0.03	1148	1159
Terpinen-4-ol	18.32	0.18 \pm 0.01	1175	1172
α -Terpineol	18.95	2.03 \pm 0.04	1172	1186
<i>cis</i> -Sabinol	19.47	0.74 \pm 0.08	1179	1197
(<i>E</i>)-Carveol	19.81	0.37 \pm 0.03	1206	1204
<i>cis</i> -Carveol	20.33	0.49 \pm 0.08	1207	1216
Methylthymol	21.04	0.96 \pm 0.02	1215	1232
Bornyl acetate	23.32	6.45 \pm 0.14	1285	1283
Carvacrol	24.23	0.30 \pm 0.01	1278	1303
Myrtenyl acetate	24.85	1.70 \pm 0.21	1306	1317
α -Cubebene	26.07	0.09 \pm 0.02	1350	1345
α -Copaene	27.17	0.17 \pm 0.01	1376	1369
β -Bourbonene	27.54	0.19 \pm 0.01	1386	1378

Compound	Rt (min)	Relative Abundance (% ± SD)	RI _R	RI _E
Alloaromadendrene	29.79	0.69 ± 0.03	1459	1431
Aristolene	30.02	0.22 ± 0.04	1423	1437
α-Curcumene	31.73	1.60 ± 0.03	1472	1479
Carvacryl propionate	31.91	0.43 ± 0.15		1484
β-Bisabolene	32.13	0.81 ± 0.07	1500	1489
α-Muurolene	32.39	0.96 ± 0.03	1494	1496
γ-Cadinene	32.91	1.70 ± 0.03	1505	1509
δ-Cadinene	33.34	3.93 ± 0.03	1514	1519
Nerolidol	34.99	0.90 ± 0.04	1545	1560
Spathulenol	35.42	2.18 ± 0.01	1577	1571
Caryophyllene oxide	35.61	5.96 ± 0.35	1576	1576
Ledol	35.94	1.77 ± 0.08	1597	1584
(4- <i>tert</i> -Butylphenoxy)methyl acetate	36.44	0.21 ± 0.09	1563	1597
Humulene-1,2-epoxide	36.59	0.47 ± 0.06	1601	1600
Cubenol	37.35	0.76 ± 0.09	1631	1621
tau-Muurolol	37.89	4.88 ± 0.24	1628	1636
α-Muurolol	38.05	1.08 ± 0.21	1646	1641
α-Cadinol	38.40	7.78 ± 0.33	1641	1650
Total identified		54.00		
Total unidentified		46.00		

Retention time (Rt), retention indexes in the literature (RI_R), and retention indexes calculated (RI_E). Standard Deviation (SD) duplicated analysis.

Minimum inhibitory concentration

The antimicrobial activity of the four oils was tested *in vitro* on four yeasts, two Gram (+) bacteria and two Gram (-) bacteria. As controls were used fluconazole and itraconazole for yeasts and ciprofloxacin for bacteria. The results (table 6) showed that any of the EOs inhibited the growth of *C. krusei*. However the other three yeasts were sensitive to all EOs, and the highest antimicrobial activity was found against *C. albicans*, with an inhibition concentration of 62.5 µg/mL. *C. tropicalis* was inhibited by EOTA, EOTP and EOEG and the oils had activity on *C. glabrata* at 250 µg/mL. It should be noted that the EOs inhibited the growth of three yeasts examined, with MIC values ranging from 62.5–250 µg/mL, highlighting the inhibitory activity against *C. albicans* and *C. tropicalis* (Table 6).

Table 6. Minimum inhibitory concentration of four EOs against four species of *Candida*.

Essential oils	MIC of yeast [$\mu\text{g/mL}$]			
	<i>C. krusei</i>	<i>C. glabrata</i>	<i>C. tropicalis</i>	<i>C. albicans</i>
EOTA	500	250	125	62.5
EODB	500	250	250	62.5
EOTP	500	250	125	62.5
EOEG	500	250	125	62.5
Fluconazole	0.97	1.95	0.97	0.24
Itraconazole	0.48	0.12	0.12	0.12

p value using ANOVA test $p=0.0607$

Table 7 shows the antibacterial activities of the EOs, with MIC values ranging from 125–500 $\mu\text{g/mL}$. The four oils presented mean inhibition of *S. aureus* and *P. aeruginosa* at a concentration of 125 $\mu\text{g/mL}$, except for EOTA, which inhibited *P. aeruginosa* at 500 $\mu\text{g/mL}$. However, the activity of EOTA against *E. coli* was highest at a concentration of 250 $\mu\text{g/mL}$ with respect to EODB, EOTP and EOEG. In contrast, any EOs inhibited the growth of *E. faecalis*.

Table 7. Minimum inhibitory concentration of four EOs against Gram (+) and Gram (-), species.

EOs	MIC of bacteria [$\mu\text{g/mL}$]			
	Gram (+)		Gram (-)	
	<i>S. aureus</i>	<i>E. faecalis</i>	<i>E. coli</i>	<i>P. aeruginosa</i>
EOTA	125	500	250	500
EODB	125	500	500	125
EOTP	125	500	500	125
EOEG	125	500	NA	125
Ciprofloxacin	0.19	0.19	0.095	0.19

NA (not activity). p value using ANOVA test $p=0.1104$

Antioxidant activity (DPPH and ABTS)

The antioxidant activities of the EOs were calculated in terms of the radical scavenging activity (RSA) %, which reflects the capacity of the EOs to reduce the concentrations of the radicals DPPH and ABTS. The EOs EOTA, EODB and EOTP showed antioxidant activity. With DPPH the IC_{50} values were 0.814, 1.195 and 1.050 mg/mL , respectively, and with ABTS IC_{50} values were 0.183, 0.252, 0.137. However, EOEG had a lower antioxidant activity DPPH ($\text{IC}_{50} = 3.480 \text{ mg/mL}$) and ABTS ($\text{IC}_{50} = 0.410 \text{ mg/mL}$) (Table 8).

Table 8. DPPH and ABTs radical scavenging activity of EOs.

EOs	DPPH		ABTS	
	RSA ± SE %	IC ₅₀ [mg/mL]	RSA ± SE %	IC ₅₀ [mg/mL]
EOTA	21 ± 1.61 ^a	0.814	14 ± 0.54 ^{ab}	0.183
EODB	20 ± 0.46 ^a	1.195	10 ± 0.44 ^b	0.252
EOTP	21 ± 0.32 ^a	1.050	22 ± 0.14 ^a	0.137
EOEG	6 ± 0.091 ^b	3.480	7 ± 0.05 ^b	0.410
Trolox	86 ± 0.70	0.005	90 ± 2.25	0.002

DPPH (1,1'-diphenyl-2-picrylhydrazine), ABTS (2,2'-azinobis-3-ethylbenzothiazoline-6-sulfonic acid, RSA (radical scavenging activity). p value between EOs using Tukey's test DPPH p<0.003 and ABTS p<0.009. Means not joined by the same letter show significant differences.

Discussion

Infectious diseases caused by microorganisms and their resistance to antimicrobials have increased the costs of hospital care as well as morbidity and mortality, making them some of the major public health problems [1,29]. Between 2016 and 2020, ESKAPE pathogens were the most isolated in hospitals [1], and candidiasis infections have increased in the last three decades [30]. The results of this study on ATCC microorganisms suggest need future research in clinical isolates.

In the present research, the inhibitory activity of EOTA against *Candida* strains and Gram (+) and Gram (-) bacteria was observed (Tables 6 and 7). This inhibition could be due to piperitone, whose antifungal effect has been described [31]. 1,8-cineol, a compound present in EOTA, inhibits the growth of different *Candida* species by blocking hyphal transition, the expression of genes that code for ergosterol biosynthesis (ERG11), and efflux pumps (CDR1 and CDR2) [32]. This suggests that in our study, these compounds are responsible for the inhibition of *C. glabrata*, *C. tropicalis* and *C. albicans*.

1,8-cineole also inhibits the growth of Gram (+) and Gram (-) bacteria by modifying the permeability of the bacterial membrane, an intracellular and morphological alteration of the cell, which could explain the inhibition observed for *S. aureus* and *E. coli* (125 and 250 µg/mL, respectively) [33].

Dihydrotagetone, the main bioactive component of EOTP, has antibacterial activity against Gram (+) and Gram (-) bacteria and also decreases the oxidative damage of food [34]. In our study, we observed antibacterial activity of EOTP on *S. aureus* and *P. aeruginosa* (125 µg/mL), as well as antifungal activity mainly on *C. albicans* and *C. tropicalis* (62.5 and 125 µg/mL, respectively).

Another bioactive compound is β-pinene, which is one of the main bioactive compounds identified in EODB, with antibacterial and antifungal activity. Rivas da Silva [35] documented its ability to inhibit the formation of biofilms in *C. albicans* and, consequently, the growth of this yeast. This effect is similar to the inhibition of growth observed for *C. albicans* at 62.5 µg/mL, and EODB was also able to inhibit *C. glabrata* and *C. tropicalis* (250 µg/mL). In contrast, the antibacterial activity against *S. aureus* and *P. aeruginosa* was 125 µg/mL. This may be related to the lipophilic nature of EO, which allows this oil to easily cross the cell wall, causing microbial death [36].

The main components of EOEG are α-cadinol, caryophyllene oxide and tau-Muurolol. This EO showed antifungal activity to the three yeasts studied, highlighting its activity to *C. albicans* and *C. tropicalis*; the antibacterial activity was the same as that presented by EODB to *S. aureus* and *P. aeruginosa*. Other authors also reported the antimicrobial activity of caryophyllene oxide to *S. aureus* [37].

The antimicrobial activities of the EOs tested in this study suggest that they can be used as alternatives in the treatment of nosocomial infections caused by multiresistant bacteria [38]. The EOs have antimicrobial

activity, especially against different *Candida* strains. However, some *in vivo* studies about the toxicity of these oils will be done in the close future.

Oxidative stress is generated by an excess of free radicals and has been associated with different diseases such as atherosclerosis, cancer, hypertension [39] and infections [40]. The antioxidant capacity of the four oils was determined by scavenging-methods using DPPH and ABTS. These oils diminished stable radicals, but their antioxidant activity was low (table 8). Then, these results suggest that the antimicrobial and antioxidant effect are not related. In this study was determined the antioxidant capacity by two assays, because the DPPH assay determined radical dissolved in organic solvents then this assay is suitable to hydrophobic systems, whereas ABTS assay is useful to lipophilic and hydrophilic antioxidant systems [41]

Conclusions

The rise of multidrug resistant microbes has produced high rates of morbidity and mortality, therefore, one of the main challenges of researches is to find new efficient drugs to treat infectious diseases. Many EOs possess antimicrobial activity, which could be attributed to synergism between their components. In the future might explore the activity of the main compounds and the synergistic mechanism.

The results obtained of this study show that EODB, EOEG, EOTP have a low antioxidant activity, which might relate to their oxygenated components.

This study tested the antifungal activity of these EOs against the yeasts, *C. albicans*, *C. glabrata*, *C. krusei* and *C. tropicalis*, and against the bacteria, *Staphylococcus aureus*, *Enterococcus faecalis*, *Escherichia coli* and *Pseudomonas aeruginosa*. The results show that EODB, EOEG, EOTP and EOEG inhibited the growth of bacteria Gram+ and Gram - also, they have antimicrobial activity against *C. glabrata*, *C. tropicalis* and *C. albicans*. The results of this study suggest need future research in clinical isolates.

Acknowledgments: We thank to Yessica Elisa Medina Rivera to participate in the obtaining of essential oil of *Dalea bicolor*, to Sandra Pecina Martínez and Claudia Alejandra Castillo López to obtaining and characterization of the essential oils of *Trixis angustifolia* and *Eupatorium glabratum*.

References

1. Arbune, M.; Gurau, G.; Niculet, E.; Iancu, A. V.; Lupasteanu, G.; Fotea, S.; Vasile, M. C.; Tatu, A. L. *Infect Drug Resist.* **2021**, *14*, 2369–2378. DOI: <https://doi.org/10.2147/IDR.S312231>.
2. De Oliveira, D. M. P.; Forde, B. M.; Kidd, T. J.; Harris, P. N. A.; Schembri, M. A.; Beatson, S. A.; Paterson, D. L.; Walker, M. *Clin Microbiol. Rev.* **2020**, *33*, 1-49. DOI: <https://doi.org/10.1128/cmr.00181-19>.
3. Balaban, N. Q.; Helaine, S.; Lewis, K.; Ackermann, M.; Aldridge, B.; Andersson, D. I.; Brynildsen, M. P.; Bumann, D.; Camilli, A.; Collins, J. J.; Dehio, C.; Fortune, S.; Ghigo, J. M.; Hardt, W. D.; Harms, A.; Heinemann, M.; Hung, D. T.; Jenal, U.; Levin, B. R.; Michiels, J.; Zinkernagel, A. *Nat. Rev. Microbiol.* **2019**, *17*, 441–448. DOI: <https://doi.org/10.1038/s41579-019-0196-3>.
4. Silva, S.; Negri, M.; Henriques, M.; Oliveira, R.; Williams, D. W.; Azeredo, J. *FEMS Microbiol. Rev.* **2012**, *36*, 288–305. DOI: <https://doi.org/10.1111/j.1574-6976.2011.00278.x>.
5. Soulaïmani, B.; Varoni, E.; Iriti, M.; Mezrioui, N. E.; Hassani, L.; Abbad, A. *Antibiotics.* **2021**, *10*, 1049. DOI: <https://doi.org/10.3390/antibiotics10091049>.
6. Köhler, J. R.; Hube, B.; Puccia, R.; Casadevall, A.; Perfect, J. R. *Microbiol. Spectr.* **2017**, *5*. DOI: <https://doi.org/10.1128/microbiolspec.FUNK-0014-2016>.
7. Pristov, K. E.; Ghannoum, M. A. *Clin Microbiol. Infect.* **2019**, *25*, 792–798. DOI: <https://doi.org/10.1016/j.cmi.2019.03.028>.

8. Paur, I.; Carlsen, M. H.; Halvorsen, B. L.; Blomhoff, R. in: *Herbal Medicine: Biomolecular and Clinical Aspects*. Chapter 2. Benzie, I. F., Wachtel, G. S., Ed., CRC Press/Taylor&Francis, Boca Raton, (FL), **2011**, 358.
9. Bakkali, F.; Averbeck, S.; Averbeck, D.; Idaomar, M. *FCT*. **2008**, *46*, 446-475. DOI: <https://doi.org/10.1016/j.fct.2007.09.106>.
10. Croteau, R. *J. Herbs. Spices Med. Plants*. **1986**, *1*, 81-135.
11. Gerchenzon, J.; Dudareva, N. *Nat. Chem. Biol.* **2007**, *3*, 408-414. DOI: <https://doi.org/10.1038/nchembio.2007>.
12. Bilia, A.R.; Guccione, C.; Isacchi, B.; Righeschi, C.; Firenzuoli, F.; Bergonzi, M.C. *Evid Based Complement Alternat Med*. **2014**, *2014*, 51593. DOI: <https://doi.org/10.1155/2014/651593>.
13. Najar, B.; Shortrede, J. E.; Pistelli, L.; Buhagiar, J. *Chem, Biodivers*. **2020**, *17*, e1900478. DOI: <https://doi.org/10.1002/cbdv.201900478>.
14. São Pedro, A.; Santo, I.; Silva, C.; Detoni, C.; Albuquerque, E. in: *Microbial pathogens and strategies for combating them*; Vol. 4, Méndez-Vilas, A., Ed.; Formatex Res. Center Publisher, Badajoz, **2013**, 1364-1374.
15. Fan, M.; Zhang, X.; Song, H.; Zhang, Y. *Molecules*. **2023**, *28*, 5022. DOI: <https://doi.org/10.3390/molecules28135022>.
16. Sharifi-Rad, J.; Soufi, L.; Ayatollahi, S. A.; Iriti, M.; Sharifi-Rad, M.; Varoni, E. M.; Shahri, F.; Esposito, S.; Kuhestani, K.; Sharifi-Rad, M. *Cell Mol. Biol. (Noisy-le-grand)*. **2016**, *62*, 69-74. DOI: <https://doi.org/10.14715/cmb/2016.62.9.11>.
17. Candan, F.; Unlu, M.; Tepe, B.; Daferera, D.; Polissiou, M.; Sökmen, A.; Akpulat, H.A. *J Etmopharmacol*. **2003**, *87*, 215-220. DOI: [https://doi.org/10.1016/s0378-8741\(03\)00149-1](https://doi.org/10.1016/s0378-8741(03)00149-1).
18. Al-Hajj, N.Q.; Wang, H.X.; Ma, C.; Lou, Z.; Bashari, M.; Thabit, R. *Trop. J. Pharm. Res*. **2014**, *13*, 1287-1293. DOI: <https://doi.org/10.4314/tjpr.v13i8.13>.
19. De Santi, I.I.; Gatto, D.A.; Machado, M.R.G.; Dos Santos, P.S.B.; Freitag, R.A. *Am. J. Plant Sci*. **2017**, *8*, 1560-1571. DOI: <https://doi.org/10.4236/ajps.2017.87108>.
20. Sánchez-Chávez, A. C., Salazar-Gómez, A., Zepeda-Vallejo, L. G., Hernández de Jesús, M. L., Quintos-Escalante, M.; Vargas-Díaz, M. E.; Luna-Herrera, J. *Nat. Prod. Res*. **2019**, *33*, 1477-1481. DOI: <https://doi.org/10.1080/14786419.2017.1416381>.
21. García-Sánchez, E.; Ramírez-López, C. B.; Martínez-Muñoz, R. E.; Flores-García, A.; Río, R. E. D.; Martínez-Pacheco, M. M. *Polibotánica*. **2015**, *39*, 91-101.
22. Morales-Ubaldo, YA; Rivero-Perez, N.; Morales-Ubaldo, AL; Valladares-Carranza, B.; López-Rodríguez, GM; Zaragoza-Bastida, A. *J. Vet. Res*. **2022**, *33*, 1-6.
23. González-Velasco, H. E.; Pérez-Gutiérrez, M. S.; Alonso-Castro, Á. J.; Zapata-Morales, J. R.; Niño-Moreno, P. D. C.; Campos-Xolalpa, N.; González-Chávez, M. M. *Molecules*. **2022**, *27*, 2612-2620. DOI: <https://doi.org/10.3390/molecules27092612>.
24. National Committee for Clinical Laboratory Standards. Methods for Dilution Antimicrobial Susceptibility Test for Bacteria that Grow Aerobically; Approved Standard—Tenth Edition NCCLS: Villanova, PA, USA, **2015**.
25. CLSI. Reference method for broth dilution antifungal susceptibility testing of yeast; fourth informational supplement. CLSI document 341 M27-S4. Wayne, PA: Clinical and Laboratory Standards Institute; **2012**.
26. Cascaes, M. M.; De Moraes, Â. A. B.; Cruz, J. N.; Franco, C. J. P.; E Silva, R. C.; Nascimento, L. D. D.; Ferreira, O. O.; Anjos, T. O. D.; de Oliveira, M. S.; Guilhon, G. M. S. P.; Andrade, E. H. A. *Antioxidants*. **2022**, *11*, 1709. DOI: <https://doi.org/10.3390/antiox11091709>.
27. Thaipong, B.; Unaroj, K.; Crosby, L.; Cisneros-Zevallos, L.; Hawkins D.B. *J. Food Compost. Anal*. **2006**, *19*, 669-675. DOI: <https://doi.org/10.1016/j.jfca.2006.01.003>.
28. Esmaili, A.; Moaf, L.; Rezazadeh, S. *J. Essent. Oil Bear Pl*. **2014**, *17*, 664-669.
29. Dadgostar, P. *Infec. Drug Resist*. **2019**, *12*, 3903-3910. DOI: <https://doi.org/10.2147/IDR.S234610>.

30. Ajetunmobi, O. H.; Badali, H.; Romo, J. A.; Ramage, G.; Lopez-Ribot, J. L. *Biofilm*. **2023**, *5*, 100126. DOI: <https://doi.org/10.1016/j.biofilm.2023.100126>.
31. Irajli, A.; Yazdanpanah, S.; Alizadeh, F.; Mirzamohammadi, S.; Ghasemi, Y.; Pakshir, K.; Yang, Y.; Zomorodian, K. *J. Applied Microbiol.* **2020**, *129*, 1541–1551. DOI: <https://doi.org/10.1111/jam.14740>.
32. Ivanov M.; Kannan A.; Stojković D.S.; Glamočlija J.; Calhelha R.C.; Ferreira I.C.F.R.; Sanglard D.; Soković M. *Int. J. Mol. Sci.* **2021**, *6*, 483–499. DOI: <https://doi.org/10.3390/ijms22020483>.
33. Zengin, H.; Baysal, A.H. *Molecules*. **2014**, *19*, 17773–7798. DOI: <https://doi.org/10.3390/molecules191117773>.
34. Shirazi, M.T.; Gholami, H.; Kavooosi, G.; Rowshan, V.; Tafsiy, A. *Food Sci. Nutr.* **2014**, *2*, 146–155. DOI: <https://doi.org/10.1002/fsn3.85>.
35. Rivas da Silva, A.C.; Lopes, P.M.; Barros de Azevedo, M.M.; Costa, D.C.; Alviano, C.S.; Alviano, D.S. *Molecules*. **2012**, *17*, 6305–6316. DOI: <https://doi.org/10.3390/molecules17066305>.
36. El Moussaoui, A.; Bourhia, M.; Jawhari, F.Z.; Salamatullah, A.M.; Ullah, R.; Bari, A.; Majid Mahmood, H.; Sohaib, M.; Serhii, B.; Rozhenko, A.; Aboul-Soud, M.A.M.; Ezzeldin, E.; Mostafa, G.A.E.; Bousta, D.; Bari, L. *Appl. Sci.* **2021**, *11*, 5168. DOI: <https://doi.org/10.3390/app11115168>.
37. Orchard, A.; van Vuuren, S. *Alternat. Med.* **2017**, *2017*, 4517971. DOI: <https://doi.org/10.1155/2017/4517971>.
38. Chebbac, K.; Ghneim, H.K.; El Moussaoui, A.; Bourhia, M.; El Barnossi, A.; Benziane Ouaritini, Z.; Salamatullah, A.M.; Alzahrani, A.; Aboul-Soud, M.A.; Giesy, J.P.; Guemmouh, R. *Molecules*. **2022**, *27*, 1136. DOI: <https://doi.org/10.3390/molecules27031136>.
39. Esmaeili, A.; Panahi, Z. A.; Ebrahimzadeh, M. A. *J. Essen. Oil Bear Plants*. **2014**, *17*, 806–812. DOI: <https://doi.org/10.1080/0972060X.2014.895203>.
40. Peyrusson, F.; Nguyen, T.K.; Najdovski, T.; Van Bambeke, F. *Microbiol. Spectr.* **2022**, *10*, e02313-21. DOI: <https://doi.org/10.1128/spectrum.02313-21>.
41. Kim, D.O.; Lee, K.W.; Lee, H.J.; Lee, C.Y. *J. Agric. Food Chem.* **2002**, *50*, 3713–3717. DOI: <https://doi.org/10.1021/jf020071c>.

Design and Synthesis of Barbiturates and Hydantoins with Multitarget Antidiabetic Effect[★]

Samantha Juárez-Cruz¹, Samuel Estrada-Soto¹, Blanca Colín-Lozano¹, Hugo Marquina-Rodríguez¹, Thalía Delgado-Aguilar¹, Carlos Martínez-Conde¹, Abraham Gutiérrez-Hernández¹, Emanuel Hernández-Núñez², Abraham Giacoman-Martínez³, Julio Cesar Almanza-Pérez³, Gabriel Navarrete-Vazquez^{1,*}

¹Facultad de Farmacia, Universidad Autónoma del Estado de Morelos, Cuernavaca, 62209 Morelos, México.

²Departamento de Recursos del Mar, Centro de Investigación y de Estudios Avanzados, IPN, Unidad Mérida, Yucatán 97310, México.

³Laboratorio de Farmacología, Depto. Ciencias de la Salud, Universidad Autónoma Metropolitana-Iztapalapa, 09340, México City, México.

*Corresponding author: Gabriel Navarrete-Vazquez, email: gabriel_navarrete@uaem.mx

Received May 15th, 2024; Accepted August 2nd, 2024.

DOI: <http://dx.doi.org/10.29356/jmcs.v68i4.2284>

[★]Taking in part of the Master in Pharmacy thesis of S. Juárez-Cruz

Abstract. In current work, we prepared a series of ten 4-aryloxy-5-benzylidenebarbiturates and hydantoins as 1,3-thiazolidine-2,4-dione bioisosteres. An *in silico* pharmacological consensus analysis (PHACA) was conducted to assess the pharmacokinetic, pharmacodynamics, biopharmaceutical, and toxicological properties of compounds **1-10**. The goal was to identify computationally safe *hits* using a color-coded system resembling a traffic light. The compounds identified as safe computational *hits* through PHACA were **1**, **2**, and **4** from the barbiturate series, which were then selected by *in vitro* assays targeting PPAR- γ , GPR40, and GLUT-4 gene expression. Additionally, these three compounds underwent *in vivo* evaluation through a glucose tolerance curve assay conducted on normoglycemic mice. Compounds **1** and **4** exhibited antihyperglycemic effects within the first thirty minutes post-administration. Molecular docking studies were conducted to clarify the dual effect and binding mode of compounds **1**, **2** and **4** on PPAR- γ and GPR40. Compounds **1** and **4** exhibited robust *in vitro* and *in vivo* efficacy and could be considered as multitarget modulators with antidiabetic effect.

Keywords: Diabetes; bioisosteres; multitarget effect; pharmacological consensus analysis.

Resumen. En este trabajo se preparó una serie de diez 4-ariloxi-5-bencilidenobarbituratos e hidantoínas como bioisómeros de la 1,3-tiazolidina-2,4-diona. Se realizó un análisis de consenso farmacológico *in silico* (PHACA) para evaluar las propiedades farmacocinéticas, farmacodinámicas, biofarmacéuticas y toxicológicas de los compuestos **1-10**. El objetivo era identificar *hits* computacionales seguros utilizando un sistema codificado por colores que se asemeja a un semáforo. Los compuestos identificados como *hits* computacionales seguros fueron **1**, **2** y **4** de la serie de barbituratos, que se eligieron para ensayos *in vitro* dirigidos a la expresión génica de PPAR- γ , GPR40 y GLUT-4. Además, estos tres compuestos se sometieron a una evaluación *in vivo* mediante un ensayo de curva de tolerancia a la glucosa realizado en ratones normoglucémicos. Los compuestos **1** y **4** exhibieron efectos antihiperoglucémicos dentro de los primeros treinta minutos posteriores a la administración. Se realizaron estudios de acoplamiento molecular para clarificar el efecto dual y el modo de unión de los

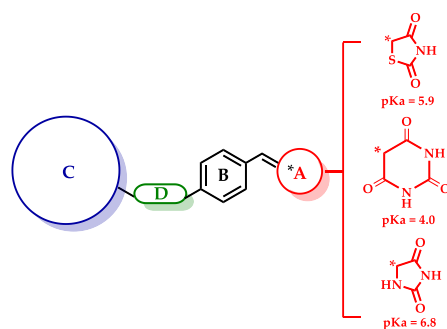
compuestos **1**, **2** y **4** en PPAR- γ y GPR40. Los compuestos **1** y **4** exhibieron una sólida eficacia *in vitro* e *in vivo*, por lo que pueden considerarse moduladores polifarmacológicos con efecto antidiabético.

Palabras clave: Diabetes; bioisómeros; efecto polifarmacológico; análisis de consenso farmacológico.

Introduction

Type 2 diabetes (T2D) is a metabolic disorder characterized by hyperglycemia exceeding 110 mg/dL, often stemming from inadequate insulin production or insufficient insulin action [1]. One approach to managing hyperglycemia involves activating peroxisome proliferator-activated receptors of the gamma subtype (PPAR- γ) just like to synthetic 1,3-thiazolidine-2,4-diones. Natural PPAR- γ agonists include both saturated and unsaturated fatty acids, such as eicosanoids and prostaglandins. Conversely, synthetic ligands function as insulin-sensitizing drugs by either fully or partially activating PPAR- γ , thereby enhancing the expression of target genes crucial for glucose-sensing in pancreatic β -cells of diabetic individuals [2]. These target genes may include the solute carrier family 2 (facilitated glucose transporter), member 4 (GLUT-4), among others [2]. Another mechanism for regulating glucose levels involves the G protein-coupled receptor 40 (GPR40), predominantly found in pancreatic β -cells and enteroendocrine cells of the gut. Activation of GPR40 by medium to long chain fatty acids stimulates insulin secretion specifically when glucose concentration is high, without affecting insulin exocytosis during low glucose levels [3]. This intriguing mechanism hints at the potential of using small molecule agonists, such as 1,3-thiazolidine-2,4-diones, for GPR40 in treating T2D offering a novel approach as insulin secretagogues with a reduced risk of hypoglycemia [4].

The aim of this study was to design, synthesize, and evaluate a series of ten 3-aryloxy-5-benzylidenebarbiturates and hydantoinas as 1,3-thiazolidine-2,4-dione bioisosteres. These compounds were screened through *in vitro*, *in vivo*, and *in silico* methods, employing combined screening strategies. The objective was to develop a single molecule capable of targeting multiple pathways for treating diabetes, specifically aimed at activating PPAR- γ , GLUT-4, and GPR40. Multitarget efficacy aligns with the concept of polypharmacology, whereby multiple drug targets are modulated to achieve a desired therapeutic outcome [5]. Compounds **1–10** were designed by leveraging the structure of benzylidene-1,3-thiazolidine-2,4-dione compounds, which adhere to the characteristic 4-point unified pharmacophore seen in synthetic GPR40 and PPAR γ agonists [2, 5, 6]. These features include: (A) an acidic group (1,3-thiazolidine-2,4-dione or surrogates); (B) a centrally substituted benzene; (C) a second lipophilic region; and (D) a flexible connector facilitating various conformations. Given these similarities, it is reasonable to infer that these barbiturates **1–5** (calculated pKa = 4.0) and hydantoinas **6–10** (calculated pKa = 6.8) may exert similar agonistic effects on these targets, owing to their shared acidic properties with 1,3-thiazolidine-2,4-dione (calculated pKa = 5.9). Scheme 1 shows the reported antidiabetic unified pharmacophore of multitarget compounds [5]. It is important to note that the pharmacophore consists of four structural features starting with an acidic head that can be replaced by carboxylic acids or their surrogates that maintain an acidic pKa, such as the azaheterocycles mentioned above. The development of multi-target compounds for GPR40, PPAR- γ and some other proteins implied in the diabetic pathogenesis may provide additional therapeutic benefits in preventing or delaying the development of diabetic complications.



Scheme 1. Unified antidiabetic pharmacophore with multitarget activity.

Experimental

Chemistry

Reagents, materials, and solvents sourced from Merck/Sigma-Aldrich were utilized without further purification. Melting points, left uncorrected, were determined using an EZ-Melt MPA120 automated melting point apparatus. Reaction progress was monitored via TLC on 0.2 mm precoated silica gel 60 F254 Merck plates. NMR spectra were acquired on a Varian Oxford instrument operating at 600 MHz for ^1H nuclei and 150 MHz for ^{13}C nuclei. Chemical shifts (δH and δC values) are reported in parts per million (ppm), while homocoupling patterns are expressed in Hertz (Hz). Mass spectrometry (EI-MS) was conducted on a JEOL JMS-700 spectrometer using the electronic impact method.

General procedure for the synthesis of barbituric derivatives 1-5

A mixture of barbituric acid (1 equivalent) and piperidine (30 % mol) were dissolved in 10 mL of toluene and stirred at 60 °C for 20 min. Besides, 1.1 equivalents of ether-aldehyde precursors **10-15** and benzoic acid (30 % mol) were added and heated to reflux (~90°C) for 2-10 h. Continuous removal of water formed was allowed with the help of the Dean-Stark apparatus. The reaction mixture was cooled, and the yellow solid was filtered off and dried.

5-(3-methoxy-4-(quinolin-2-ylmethoxy)benzylidene)pyrimidine-2,4,6 (1H,3H,5H)-trione (1). Orange crystals, yield 93 %, m.p. 187 °C (dec). ^1H NMR (600 MHz, DMSO d-6) δ : 2.79 (s, 3H), 5.02 (s, 2H), 6.72 (dd, 1H, $J_o = 7.67$ Hz), 6.79 (d, 1H, $J_o = 8.32$ Hz), 6.88 (dd, 1H, $J_o = 7.45$ Hz), 7.08 (m, 3H), 7.38 (m, 1H), 7.51 (s, 1H), 10.24 (s, 1H), 10.38 (s, 1H), ppm. ^{13}C NMR (150 MHz, DMSO d-6) δ : 56.0 (C-7), 72.2 (C-8), 112.2 (C-2), 113.8 (C-5), 119.3 (C-10), 120 (C-3'), 126.9 (C-1), 127.63 (C-6'), 128.3 (C-6), 128.9 (C-5'), 129.7 (C-8'), 130.2 (C-7'), 133.9 (C-8a'), 139.0 (C-4'), 145.5 (C-3, C-4), 147.3 (C-13), 148.8 (C-11), 151.1 (C-9), 158.2 (C-2'), 168.2 (C-12), ppm. MS: m/z (% rel. int.) 403 (M^+ , 1 %), 91 (M-312, 100 %), 148 (M-255, 45 %).

5-(3-methoxy-4-(naphthalen-1-ylmethoxy)benzylidene)pyrimidine-2,4,6 (1H,3H,5H)-trione (2). Yellow powder, yield 86 %, m.p. 202.3 – 204.2°C. ^1H NMR (600 MHz, DMSO d-6) δ : 2.93 (s, 3H), 4.84 (s, 2H), 6.56 (d, 1H, $J_o = 8.56$ Hz), 6.73 (m, 3H), 6.85 (d, 1H, $J_o = 6.96$ Hz), 7.08 (dd, 1H, $J_m = 2.04$ Hz, $J_o = 6.8$ Hz), 7.12 (d, 1H, $J_o = 8.34$ Hz), 7.16 (d, 1H, $J_o = 6.78$ Hz), 7.24 (m, 1H), 7.43 (s, 1H), 7.57 (d, 1H, $J_m = 2.1$ Hz), 10.34 (s, 1H), 10.47 (s, 1H), ppm. ^{13}C NMR (150 MHz, DMSO d-6) δ : 55.9 (C-7), 68.9 (C-8), 112.9 (C-2), 115.9 (C-5), 117.5 (C-10), 124.3 (C-3'), 125.8 (C-6'), 126.0 (C-6), 126.5 (C-7'), 127 (C-1), 127.4 (C-2'), 128.9 (C-4'), 129.4 (C-5'), 131.6 (C-8'), 131.8 (C-1'), 132.2 (C-8a'), 133.7 (C-4a'), 148.4 (C-4), 150.6 (C-3), 153.1 (C-9), 155.8 (C-13), 162.7 (C-11), 164.4 (C-12), ppm. MS: m/z (% rel. int.) 402 (M^+ , 1 %), 128 (M-274, 100 %), 141 (M-261, 25 %).

5-(4-([1,1'-biphenyl]-3-ylmethoxy)-3-methoxybenzylidene)pyrimidine-2,4,6(1H,3H,5H)-trione (3). Yellow powder, yield 83 %, m.p. 173.2 – 175.4 °C. ^1H NMR (600 MHz, DMSO d-6) δ : 3.61 (s, 3H), 5.03 (s, 2H), 6.62 (s, 2H), 6.84 (d, 1H, $J_o = 7.62$ Hz), 7.34 (t, 1H, $J_o = 7.38$ Hz), 7.39 (d, 1H, $J_o = 7.56$ Hz), 7.41 (d, 1H, $J_o = 7.32$ Hz), 7.45 (t, 3H, $J_o = 7.62$ Hz), 7.58 (d, 1H, $J_o = 7.56$ Hz), 7.63 (d, 2H, $J_o = 7.56$ Hz), 7.69 (s, 1H), 9.94 (s, 2H), ppm. ^{13}C NMR (150 MHz, DMSO d-6) δ : 55.9 (C-7), 70.7 (C-8), 112.2 (C-2), 113.8 (C-5), 119.3 (C-10), 126.5 (C-4'), 126.5 (C-2'), 127.1 (C-2", C-6"), 127.2 (C-6'), 127.9 (C-3'), 129.4 (C-3", C5"), 129.5 (C-4"), 138.7 (C-9), 140.4 (C-4), 140.6 (C-3), 145.7 (C-6), 148.8 (C-12), 151.1 (C-11, C-13), ppm. MS: m/z (% rel. int.) 428 (M^+ , 1 %), 167 (M-261, 50 %).

4'-((2-methoxy-4-((2,4,6-trioxotetrahydropyrimidin-5(2H)-ylidene)methyl)phenoxy)methyl)-[1,1'-biphenyl]-2-carbonitrile (4). Yellow powder, yield 79 %, m.p. 239.9 – 240.0 °C. ^1H NMR (600 MHz, DMSO d-6) δ : 3.33 (s, 3H), 4.83 (s, 2H), 7.08 (s, 1H), 7.12 (m, 4H), 7.29 (m, 1H), 7.40 (d, 1H, $J_o = 8.89$ Hz), 7.41 (dd, 1H, $J_o = 8.52$ Hz), 7.45 (t, 1H, $J_o = 8.02$ Hz), 7.76 (d, 1H, $J_o = 8.89$ Hz), 7.79 (s, 1H), 7.92 (d, 1H, $J_m = 1.49$ Hz), 10.68 (s, 1H), 10.8 (s, 1H), ppm. ^{13}C NMR (150 MHz, DMSO d-6) δ : 56.3 (C-7), 70.3 (C-8), 110.9 (C-6"), 113.1 (C-2), 116.1 (C-5), 117.9 (CN), 119.3 (C-10), 126.0 (C-6), 128.7 (C-1), 129 (C-3', C-5'), 129.7 (C-2', C-6'), 130.9 (C-2"), 132.1 (C-4"), 134.3 (C-3"), 134.6 (C-5"), 137.7 (C-1'), 138.4 (C-4'), 144.9 (C-1"), 148.7 (C-

4), 150.9 (C-3), 153.3 (C-9), 156.1 (C-13), 163.1 (C-11), 164.7 (C-12), ppm. MS: *m/z* (% rel. int.) 453 (M^+ , 1 %) 192 (M-261, 100 %), 165 (M-288, 10 %).

5-(3-methoxy-4-(2-morpholinoethoxy)benzylidene)pyrimidine-2,4,6(1H,3H,5H)-trione (5). Beige crystals, yield 56 %, m.p. 218.3 – 221.9 °C. ^1H NMR (600 MHz, DMSO *d*-6) δ : 3.42 (*m*, 10H), 3.72 (*s*, 3H), 4.12 (*s*, 2H), 7.49 (*dd*, 1H $J_o = 7.10$ Hz), 7.61 (*dd*, 1H, $J_o = 7.16$ Hz), 7.94 (*d*, 1H, $J_o = 7.62$ Hz), 8.44 (*s*, 1H), 11.09 (*s*, 2H), ppm. ^{13}C NMR (150 MHz, DMSO *d*-6) δ : 43.7(C-7), 52.66 (C-9), 55.5 (C-2', C-3'), 56.1 (C-1', C-4'), 64.5 (C-8), 111.7 (C-2), 119.0 (C-11), 128.6 (C-5), 129.2 (C-6), 132.9 (C1), 144.7 (C-3), 148.6 (C-4), 150.7 (C-10), 151.6 (C-12, C-14), 167.7 (C-13), ppm. MS: *m/z* (% rel. int.) 375 (M^+ , 1 %), 128 (M-247, 100 %), 85 (M-290, 20 %).

General procedure for the synthesis of hydantoin derivatives 6-10

A mixture of hydantoin (1 equivalent) and piperidine (60 % mol) were dissolved in 10 mL of toluene and stirred at 40 °C for 20 min. On the other hand, 1.1 equivalents of ether-aldehyde precursors **12-16** and benzoic acid (60 % mol) were added and heated to reflux (~90°C) for 10-15 h. Continuous removal of water formed was allowed with the help of the Dean-Stark apparatus. The reaction mixture was cooled, and the solid was filtered off and dried.

(Z)-5-(3-methoxy-4-(quinolin-2-ylmethoxy)benzylidene)imidazolidine-2,4-dione (6). Green powder, yield 62 %, m.p. 245.1 – 247.0 °C. ^1H NMR (600 MHz, DMSO-*d*₆) δ : 3.90 (*s*, 1H), 5.67 (*s*, 1H), 6.50 (*s*, 1H), 7.26 (*d*, 1H, $J_m = 1.98$ Hz), 7.33 (*t*, 2H), 7.63 (*t*, 1H, $J_o = 7.63$ Hz), 7.68 (*ddd*, 1H, $J_o = 7.44$ Hz, $J_m = 1.98$ Hz), 7.77 (*d*, 1H, $J_o = 7.02$ Hz), 8.05 (*d*, 1H, $J_o = 8.28$ Hz), 8.09 (*dd*, 1H, $J_m = 1.86$ Hz, $J_o = 6.6$ Hz), 8.21 (*d*, 1H, $J_o = 7.98$ Hz), 10.66 (*s*, 1H), 11.27 (*s*, 1H), ppm. ^{13}C NMR (150 MHz, DMSO-*d*₆) δ : 56.1 (C-7), 68.8 (C-8), 109.7 (C-9), 113.4 (C-2), 125.7 (C-6), 126.3 (C-5), 126.5 (C-3'), 126.7 (C-1), 127.1 (C-6'), 128.8 (C-10), 129.0 (C-4a'), 129.3 (C-5'), 131.6 (C-8'), 132.8 (C-7'), 133.7 (C-4'), 148.8 (C-4), 149.6 (C-3), 156.2 (C-8a'), 158.8 (C-12), 166.1 (C-2'), 174.3 (C-11), ppm; *m/z* (% rel. int) 375 (M^+ , 1 %), 264.2 (M-111, 36 %), 222 (M-153, 12 %).

(Z)-5-(3-methoxy-4-(naphthalen-1-ylmethoxy)benzylidene)imidazolidine-2,4-dione (7). Yellow powder, yield 66 %, m.p. 233.1 – 235.2 °C. ^1H NMR (600 MHz, DMSO-*d*₆) δ : 3.78 (*s*, 3H), 5.54 (*s*, 2H), 6.38 (*s*, 1H), 7.14 (*d*, 1H, $J_m = 1.98$ Hz), 7.20 (*dd*, 1H, $J_m = 1.92$ Hz, $J_o = 8.76$ Hz), 7.21 (*d*, 1H, $J_o = 8.4$ Hz), 7.50 (*t*, 1H, $J_o = 7.74$ Hz), 7.55 (*m*, 2H), 7.65 (*d*, 1H, $J_o = 7.86$ Hz), 7.92 (*d*, 1H, $J_o = 6.9$ Hz), 7.96 (*d*, 1H, $J_o = 7.68$ Hz), 8.09 (*d*, 1H, $J_o = 8.76$ Hz), 10.49 (*s*, 1H), 11.16 (*s*, 1H), ppm. ^{13}C NMR (150 MHz, DMSO-*d*₆) δ : 56.1 (C-7), 68.8 (C-8), 109.7 (C-9), 113.4, (C-2), 114.1 (C-6), 123.3 (C-5), 125.7 (C-3'), 126.3 (C-6' y C-7'), 126.5 (C-2'), 126.7 (C-4'), 128.8 (C-5'), 129.0 (C-1), 129.3 (C-10), 131.6 (C-8'), 132.8 (C-4a'), 148.8 (C-1' y C-8a'), 156.2 (C-4), 158.8 (C-3), 166.1 (C-12), 174.3 (C-11), ppm; *m/z* (% rel. int) 374 (M^+ , 1 %), 142 (M-232, 100 %), 115.0 (M-259, 30 %).

(Z)-5-(4-([1,1'-biphenyl]-3-ylmethoxy)-3-methoxybenzylidene)imidazolidine-2,4-dione (8). Yellow powder, yield 84 %, m.p. 238.9 – 241.2 °C. ^1H NMR (600 MHz, DMSO-*d*₆) δ : 3.82 (*s*, 3H), 5.19 (*s*, 2H), 6.36 (*s*, 1H), 7.07 (*d*, 1H, $J_o = 8.22$ Hz), 7.14 (*s*, 1H), 7.17 (*dd*, 1H, $J_m = 2.04$ Hz, $J_o = 7.86$ Hz), 7.32-7.37 (*m*, 1H), 7.41-7.48 (*m*, 4H), 7.62 (*d*, 2H, $J_o = 7.68$ Hz), 7.67 (*s*, 1H), 7.72 (*s*, 1H), 9.82 (*s*, 1H), 10.62 (*s*, 1H), ppm. ^{13}C NMR (150 MHz, DMSO-*d*₆) δ : 57.3 (C-7), 65.8 (C-8), 119.1 (C-9), 123.0 (C-2), 123.7 (C-5), 130.6 (C-10), 132.9 (C-6), 136.2 (C-6'), 136.3 (C-2'), 136.4 (C-1), 136.7 (C-5'), 136.9 (C-3'' y C-5''), 137.6 (C-4'), 139.0 (C-2''), 139.2 (C-4' y C-6''), 147.7 (C-1'), 150.0 (C-1''), 150.4 (C-3'), 158.3 (C-4), 159.2 (C-3), 168.4 (C-12), 183.9 (C-11), ppm; *m/z* (% rel. int) 400 (M^+ , 2 %), 121 (M-279, 45 %), 93 (M-307, 56 %).

(Z)-4'-((4-((2,5-dioxoimidazolidin-4-ylidene)methyl)-2-methoxyphenoxy)methyl)[1,1'-biphenyl]-2-carbonitrile (9). Yellow powder, yield 76 %, m.p. 226.1 – 228.0 °C. ^1H NMR (600 MHz, DMSO-*d*₆) δ : 3.84 (*s*, 3H), 5.20 (*s*, 2H), 6.37 (*s*, 1H), 7.09 (*d*, 1H, $J_o = 8.4$ Hz), 7.15 (*d*, 1H, $J_m = 2.04$ Hz), 7.18 (*d*, 1H, $J_m = 2.04$ Hz, $J_o = 8.34$ Hz), 7.59 (*m*, 6H), 7.78 (*dd*, 1H, $J_o = 7.7$ Hz, $J_m = 2.6$ Hz), 7.94 (*d*, 1H, $J_o = 7.8$ Hz), 10.48 (*s*, 1H), 11.15 (*s*, 1H), ppm. ^{13}C NMR (150 MHz, DMSO-*d*₆) δ : 56.2 (C-7), 69.8 (C-8), 109.5 (C-6''), 110.6 (C-2), 113.3 (C-9), 113.8 (C-5), 119.0 (CN) 123.3 (C-6 y C-10), 126.5 (C2''), 126.7 (C-2', C-6'), 128.5 (C-4''), 128.7 (C-1), 129.2 (C-3''), 130.6 (C-5''), 134.0 (C-5'), 134.3 (C-3'), 137.8 (C-1'), 138.0 (C-4'), 144.6 (C-1''), 148.7 (C-4), 149.6 (C-3), 156.2 (C-12), 166.1 (C-11), ppm; *m/z* (% rel. int) 425 (M^+ , 1 %), 281.0 (M-144, 40%), 192 (M-233, 100 %).

(Z)-5-(3-methoxy-4-(2-morpholinoethoxy)benzylidene)imidazolidine-2,4-dione (10). Yellow powder, yield 84 %, m.p. 237.3 – 238.9 °C. ¹H NMR (600 MHz, DMSO-d₆) δ: 2.69 (t, 2H, *J*_o = 5.64 Hz), 3.57 (t, 4H, *J*_o = 4.44 Hz), 3.82 (s, 3H), 3.84 (s, 4H), 4.10 (t, 2H, *J*_o = 5.84 Hz), 6.38 (s, 1H), 6.99 (d, 1H, *J*_o = 8.28 Hz), 7.12 (d, 1H, *J*_m = 1.92 Hz), 7.17 (dd, 1H, *J*_m = 1.93 Hz, *J*_o = 9.06 Hz), 10.48 (s, 1H), 10.61 (s, 1H), ppm. ¹³C NMR (150 MHz, DMSO-d₆) δ: 47.7 (C-9), 54.1 (C-7), 56.2 (C-1', C-4'), 57.4 (C-2', C-3'), 66.7 (C-8), 109.6 (C-10), 113.3 (C-3), 113.6 (C-2), 123.4 (C-6), 126.3 (C-1), 126.7 (C-11), 149.0 (C-4), 149.4 (C-3), 166.1 (C-13), 174.3 (C-12), ppm; *m/z* (% rel. int) 347 (M⁺, 1 %), 296 (M-51, 9 %), 264 (M-83, 32 %).

General method of synthesis for precursors 12 - 16.

A solution of 4-hydroxy-3-methoxybenzaldehyde (**11**) and potassium carbonate (2.2 equivalents) was prepared in acetonitrile and stirred at room temperature for thirty minutes. Aryl bromides **17-21** (1.1 equivalents) were added gradually, and the mixture was heated to reflux for 2-5 h. Upon completion of the reaction, the solvent was evaporated under reduced pressure, and the resulting solids were washed with cold water to remove excess K₂CO₃. The crude solid products underwent recrystallization in ethanol.

3-methoxy-4-(quinolin-2-yl-methoxy)benzaldehyde (12). Beige crystals, yield 52 %, m.p. 108.3 – 109.9 °C. ¹H NMR (600 MHz, DMSO-d₆) δ: 4.00 (s, 3H), 5.55 (s, 2H), 7.05 (d, 1H, *J*_o = 8.22 Hz), 7.37 (dd, 1H, *J*_m = 1.75 Hz, *J*_o = 7.02 Hz), 7.46 (d, 1H, *J*_m = 1.7 Hz), 7.56 (dd, 1H, *J*_m = 1.4 Hz, *J*_o = 7.8 Hz), 7.68 (d, 1H, *J*_o = 8.5 Hz), 7.75 (dd, 1H, *J*_m = 2.5 Hz, *J*_o = 7.7 Hz), 7.84 (d, 1H, *J*_o = 8.1 Hz), 8.19 (d, 1H, *J*_o = 4.98 Hz), 8.9 (d, 1H, *J*_o = 5.38 Hz), 9.83 (s, 1H), ppm; *m/z* (% rel. int) 293 (M⁺, 25 %), 142 (M-151, 100 %)

3-methoxy-4-(naphthalen-1-ylmethoxy)benzaldehyde (13). White crystals, yield 95 %, m.p. 98.5 – 99.8 °C. ¹H NMR (600 MHz, DMSO-d₆) δ: 3.80 (s, 3H), 5.66 (s, 2H), 6.60 (d, 1H, *J*_o = 5.64 Hz), 7.43 (d, 1H, *J*_m = 2.0 Hz), 7.48 (d, 1H, *J*_o = 8.28 Hz), 7.53 (dd, 1H, *J*_m = 1.32 Hz, *J*_o = 7.02 Hz), 7.56 (m, 2H), 7.69 (d, 1H, *J*_o = 6.96 Hz), 7.95 (d, 1H, *J*_o = 8.28 Hz), 7.99 (d, 1H, *J*_o = 7.38 Hz), 8.10 (d, 1H, *J*_o = 7.86), 9.87 (s, 1H), ppm; *m/z* (% rel. int) 292 (M⁺, 1 %), 264 (M-28, 100 %), 128 (M-164, 100 %)

4-([1,1'-biphenyl]-3-ylmethoxy)-3-methoxybenzaldehyde (14). White crystals, yield 64 %, m.p. 84.1 – 85.4 °C. ¹H NMR (600 MHz, DMSO-d₆) δ: 3.84 (s, 3H), 5.30 (s, 2H), 7.32 (d, 1H, *J*_o = 8.52 Hz), 7.38 (t, 1H, *J*_o = 6.78 Hz), 7.43 (s, 1H), 7.48 (m, 4H), 7.56 (d, 1H, *J*_o = 8.10 Hz), 7.66 (m, 3H), 7.77 (s, 1H), 9.85 (s, 1H), ppm; *m/z* (% rel. int) 318 (M⁺, 12.5 %), 167 (M-151, 100 %).

4'-((4-formyl-2-methoxyphenoxy)methyl)-[1,1'-biphenyl]-2-carbonitrile (15). White crystals, yield 64 %, m.p. 161.0 – 162.3 °C. ¹H NMR (600 MHz, DMSO-d₆) δ: 3.86 (s, 3H), 5.31 (s, 2H), 7.32 (d, 1H, *J*_o = 8.22 Hz), 7.44 (d, 1H, *J*_m = 1.92 Hz), 7.56 (dd, 1H, *J*_m = 1.98 Hz, *J*_o = 8.4 Hz), 7.59 (dd, 1H, *J*_m = 2.82 Hz, *J*_o = 7.86 Hz), 7.63 (m, 5H), 7.80 (dd, 1H, *J*_m = 3.36 Hz, *J*_o = 7.45 Hz), 7.97 (d, 1H, *J*_o = 7.44 Hz), 9.86 (s, 1H), ppm; *m/z* (% rel. int) 343 (M⁺, 5 %), 192 (M-151, 100 %).

3-methoxy-4-(2-morpholinoethoxy)benzaldehyde (16). White crystals, yield 84 %, m.p. 268.7 – 269.9 °C. ¹H NMR (600 MHz, DMSO-d₆) δ: 2.43 (t, 4H), 3.27 (t, 4H), 3.32 (s, 3H), 3.50 (t, 2H), 4.28 (t, 2H), 6.96 (d, 1H, *J*_o = 8.28 Hz), 7.15 (d, 1H, *J*_m = 1.92 Hz), 7.32 (dd, 1H, *J*_o = 9.06 Hz, *J*_m = 1.92 Hz), 8.88 (s, 1H), ppm; *m/z* (% rel. int) 265 (M⁺, 1%), 236 (M-29, 5 %), 98 (M-167, 100 %).

Biological Assays

Gene expression of GLUT-4 and PPAR-γ

C2C12 myocytes (ATCC/CRL-1772) were incubated and maintained in DMEM medium supplemented with 10 % fetal bovine serum (SFB), 0.5 mM sodium pyruvate, 1 mM L-glutamine, 0.05 mM non-essential amino acids, and 0.1 mg/L gentamicin, under a humidified atmosphere of 5 % CO₂ at 37 °C [3]. The cells were treated with a varying concentrations of compounds 1, 2 and 4 by 24 h to assess mRNA expression levels of GLUT-4 and PPAR-γ.

Cell culture of the RIN-m5F line

RIN-m5F pancreatic insulinoma cells (ATCC/CRL-11605) were procured and cultured in 75 cm² flasks until reaching confluence. The cells were maintained in RPMI 1640 medium supplemented with 10% fetal bovine serum (SFB), 0.5 mM sodium pyruvate, 1 mM L-glutamine, 0.05 mM non-essential amino acids, and 0.1 mg/L gentamicin, under a humidified atmosphere of 5% CO₂ at 37°C [3]. The culture medium was refreshed every 48 h.

Evaluation of the relative expression levels of PPAR- γ , GLUT4, and GPR40

C2C12 and RIN-m5F cells were plated individually in 6-well plates at a density of 8×10^4 cells per well and treated with compounds **1**, **2**, and **4** at a concentration of 1 μ M. Muscle cells were treated with 5 μ M pioglitazone as a control, while β -pancreatic cells received 400 μ M glibenclamide. Following a 24-h incubation period, total RNA was extracted from the cells using TRIZOL reagent. The RNA samples were assessed for purity by measuring absorbance at 260 and 280 nm, with an OD ratio (260/280) of 1.9 ± 0.2 , indicating minimal contamination. Reverse transcription of 2 μ g mRNA was carried out using the ImProm II reverse transcription system (Promega, Wisconsin, USA). The resulting cDNA was subjected to amplification using SYBR Green master mix (ThermoScientific, USA) and primers targeting the PPAR- γ , GLUT4, and GPR40 genes, with 36B4 and β -actin serving as reference genes. Amplification was performed using a rotor-gene system (Techne, PrimePro48, UK). Δ Ct values were computed for each sample and gene of interest by subtracting the Ct value of the reference gene from the Ct value of the target gene. Relative changes in gene expression ($\Delta\Delta$ Ct) were determined by subtracting the Δ Ct of the control group from the Δ Ct of the test group, and then reporting the result as $2^{-\Delta\Delta$ Ct} [2,3,7,8].

Insulin secretion

RIN-m5F cells were plated in 6-well plates at a density of 8×10^4 cells per well and allowed to reach 70-80% confluence. Following this, the cells were treated with glibenclamide (400 μ M) and compounds **1**, **2**, and **4** (1 μ M) for 24 h [9].

In vivo antidiabetic assay

Animals

Male C57BL/6 mice, weighing 25 ± 5 g, were accommodated in animal cages with a 12-h light-dark cycle. The mice were kept in a controlled environment at 25 °C, with free access to water and food. All experiments involving mice were conducted in accordance with protocols approved by the Mexican government NOM-065-ZOO-1999 and NOM-033-ZOO-2014 and were further authorized by the Institutional Ethics Committee of the Universidad Autónoma Metropolitana (dictum 1857), adhering to the guidelines outlined in the US National Institutes of Health Publication #85-23, revised in 1985.

Oral glucose tolerance test

Normoglycemic mice were separated in five groups (n = 6):

Group 1: Compound **1**, 100 mg/kg.

Group 2: Compound **2**, 100 mg/kg.

Group 3: Compound **4**, 100 mg/kg.

Group 4: control (isotonic saline solution, ISS).

Group 5: positive control (glibenclamide, pioglitazone or linagliptin, 5 mg/kg).

A load of 2 g/kg of glucose or sucrose solution was administered to mice 30 min after test samples. Then blood samples were obtained at time 0 (before oral administration), 0.5, 1, 1.5, 2, and 3 h after the vehicle, positive control, and compounds administrations, from the caudal vein. Glycemia was estimated by the glucose dehydrogenase method using a commercial glucometer (Accu-Chek, Performa; Roche®). The percentage change of glycemia for each group was calculated in relation to the initial (0 h) level [10].

Statistical analysis

To examine the disparities in the percentage variation of glycemia and the quantification of *in vitro* mRNA *PPAR-γ*, *GLUT-4*, and *GPR40* expression, we utilized ANOVA, supplemented with a Dunnett's multiple test. All data are presented as mean ± S.E.M. with significance set at $p < 0.05$, and the analysis was conducted using GraphPad Prism 5.0.

Molecular docking

Docking calculations were conducted using the licensed Molecular Operating Environment (MOE) version 2020.0901 [11]. The crystal structure of *PPAR-γ* complexed with rosiglitazone PDB ID: 4EMA, and 4PHU complexed with TAK-875 at a resolution of 2.54 and 2.33 Å respectively, were retrieved from the Protein Data Bank (<http://www.rcsb.org/pdb>) [12, 13]. The unnecessary molecules were removed, the hydrogen atoms and charges were adjusted using the Amber14:EHT forcefield from the MOE suite (Chemical Computing Group Inc. <http://www.chemcomp.com>). The 3D structure of compounds **1**, **2** and **4** was constructed and minimized in MOE using the MMF94xforcefield. Docking simulations were conducted, considering all residues within a 4.5 Å sphere centered on the atoms of the cocrystallized ligand. The Triangle Matcher and Alpha Triangle was selected as the placement function, the scores were calculated with the London ΔG function and the selection of the best poses was made using the GBVI/WSA ΔG (Generalized-Born Volume Integral/Weighted Surface area). This process was validated by reproducing, through docking, the same pose as the cocrystallized ligand in the *PPAR-γ* (RMSD = 1.0369 Å) with a score of -8.4423 Kcal/mol and *GPR40* crystal structure with a score of -11.3657 Kcal/mol (RMSD = 0.4234 Å). A value less than 2 Å suggests that the docking simulation parameters are effective in accurately reproducing the ligand pose within the protein. One hundred conformations were generated for each ligand, and the top-ranked conformation, determined by the docking score, was chosen for subsequent investigations in molecular docking. Following the molecular docking process, we scrutinized the optimally calculated binding poses, and graphical representations were generated using Surface Maps and Ligand Interaction tools in MOE and The PyMOL Molecular Graphics System, Version 3.0, Schrödinger, LLC. [14].

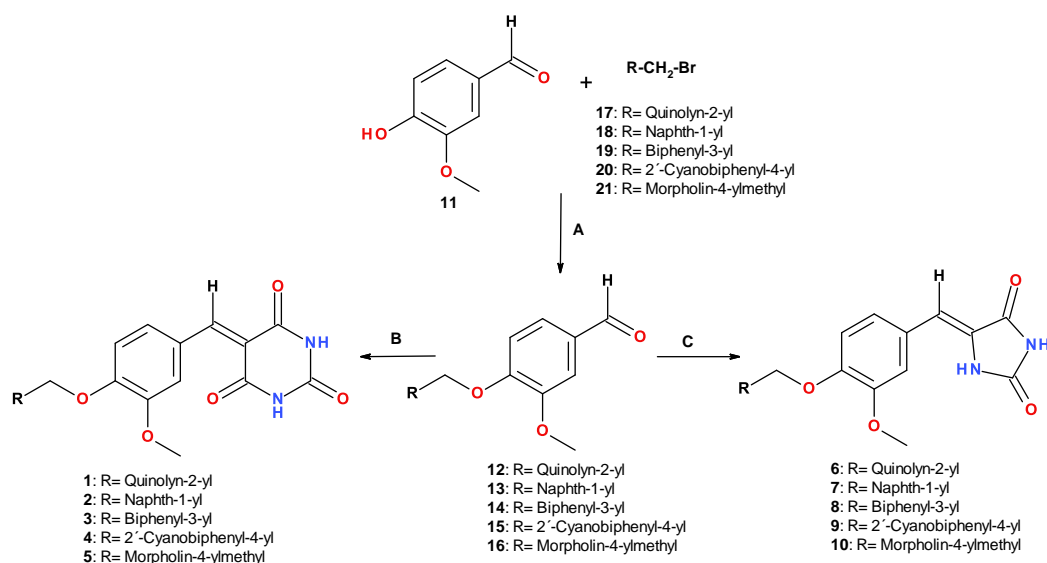
In silico prediction of biopharmaceutics, pharmacokinetics, and toxicological profile

For the estimation of the ADMET properties, to build the *in silico* pharmacological consensus analysis [15], we employed online programs like Molinspiration (<https://www.molinspiration.com>) [16], ADMETLab 3.0 (<https://admetlab3.scbdd.com/>) [17], MetaTox 2.0 (<https://www.way2drug.com/metatox>) [18]. The operation of these ADMET predictors involves three main steps: A) Input: cleaning individual molecules or batches of molecules using SMILES notation to input chemical structures; B) Operation: calculating the ADMET properties of these molecules using deep learning models; and C) Output: determining which result files to return. The modular design of this system allows for flexible combinations of functionalities. The calculation of ADMET properties includes molecular basic properties, physical chemistry, medicinal chemistry, absorption, distribution, metabolism, excretion, and toxicity, among others.

Results and discussion

Chemistry

Compounds **1–10** were prepared starting from 4-hydroxy-3-methoxybenzaldehyde (**11**), which was reacted via S_N2 with adequately substituted arylbromides **17–21**, to obtain the ether-aldehyde precursors **12–16**. These compounds were then condensed under Knoevenagel conditions with barbituric acid to afford compounds **1–5** or with 2,4-imidazolidinedione (hydantoin) to give compounds **6–10** (Scheme 2).



Scheme 2. Synthesis of compounds 1–10. Reagents and conditions: (A) K₂CO₃, acetonitrile, reflux; (B) Barbituric acid, piperidine (0.3 equiv), benzoic acid (0.3 equiv), toluene, Dean-Stark apparatus, reflux; (C) 1,3-imidazolidine-2,4-dione (hydantoin), piperidine (0.6 equiv), benzoic acid (0.6 equiv), toluene, Dean-Stark apparatus, reflux.

To synthesize the hydantoin series, it was imperative to double the quantity of the Knoevenagel additives (piperidine and benzoic acid) owing to the low yields obtained from the initial procedure. This could be attributed to the poor solubility of hydantoin. When hydantoin reacts with piperidine in an acid-base reaction, it forms a more soluble anion. This process requires twice the amount of both additives in the Knoevenagel reaction.

In silico Pharmacological Consensus Analysis

We conducted an *in silico* pharmacological consensus analysis (PHACA) and summarized the results in Table 1 using a traffic light system [15]. PHACA integrates calculations from biopharmaceutical properties, pharmacodynamics and pharmacokinetic predictions, toxicity assessments, and additional experimental data. The rationale behind pharmacological consensus analysis lies in the agreement among multiple predicted parameters indicating a compound's activity, low toxicity, and favorable pharmacokinetic profile. Accordingly, selecting a compound with a high score across various predictions enhances confidence in its suitability for synthesis. Thus, a compound receiving high scores from multiple predictions is more likely to exhibit desirable behavior in biological assays compared to one with high scores from a single prediction [15].

Table 1 presents the results of Pharmacological Consensus Analysis, which involves assessing various properties and assigning them a color-coded classification. Unsatisfactory profiles are marked in red, satisfactory profiles in yellow, and very satisfactory profiles in green. A final score is computed by summing the numeric values assigned to each profile (very satisfactory: +1; satisfactory: 0; unsatisfactory: -1). A higher score indicates superior combined pharmaceutical properties, prioritizing the molecule for synthesis and/or experimental biological evaluation. The analysis utilizes validated online programs like Molinspiration (Rule of 5) [16], ADMETLab (Human intestinal absorption Ames toxicity, carcinogenicity) [17], MetaTox 2.0 (molecular targets) [18], and ACD ToxSuite (hERG blockade, CYP inhibition) [19]. The biosimulation results suggest that compounds 1–10 demonstrate safety and favorable pharmacokinetic (PK) and pharmacodynamic (PD) properties, enhancing both permeability and intestinal absorption.

Table 1. *In silico* pharmacological consensus analysis (PHACA).

		Barbiturates					Hydantoins				
		1	2	3	4	5	6	7	8	9	10
Pharmacodynamics	Molecular Docking	Green	Green	Green	Green	Green	Green	Green	Green	Green	Green
	Molecular targets (GPR40, PPAR- γ)	Green	Green	Green	Green	Yellow	Yellow	Green	Green	Green	Yellow
Pharmacokinetics	Human intestinal absorption	Green	Green	Green	Green	Green	Green	Green	Green	Green	Green
	PGP inhibition	Green	Green	Green	Green	Yellow	Yellow	Green	Green	Green	Green
Toxicity	CYP's inhibition	Green	Green	Green	Green	Green	Green	Yellow	Yellow	Yellow	Yellow
	hERG blockage	Yellow	Yellow	Red	Yellow	Red	Red	Red	Red	Red	Red
	Ames toxicity	Green	Green	Yellow	Green	Green	Green	Green	Yellow	Yellow	Yellow
	Carcinogenic	Green	Green	Green	Green	Green	Green	Green	Yellow	Yellow	Yellow
	OECD/LD ₅₀	Green	Green	Green	Green	Green	Green	Yellow	Green	Green	Green
Biopharmaceutics Properties	Solubility	Green	Green	Green	Green	Yellow	Yellow	Green	Green	Green	Green
	Permeability	Green	Green	Green	Green	Yellow	Yellow	Green	Green	Green	Green
Final Score		10	10	8	10	5	5	7	6	6	5

Moreover, the compounds demonstrate potential *in silico* affinity for GPR40 and PPAR- γ and display favorable predictions for low cardiotoxicity, with no indications of carcinogenic or mutagenic effects. These descriptors are crucial in drug design to anticipate appropriate biopharmaceutical and pharmacokinetic profiles. Based on the analysis scores, compounds **1**, **2**, and **4** present the most promising biosimulation profiles with the highest score values (Final Score =10) (**Table 1**) and were thus selected as safe computational hits for prioritized *in vitro* and *in vivo* assays. This was the cut-off value (Final Score =10) that was taken into account to prioritize, using PHACA, the molecules that would be candidates for bioassays. On the other hand, for the hydantoin series (**6-10**), all resulted in low scores below 7, and compound **3** had a score of 8, indicating they were not prioritized for further *in vitro* or *in vivo* experiments to save financial resources and reduce the number of animals used.

***In vitro* results**

Relative expression of PPAR γ and GLUT-4

Myocytes are cells with active metabolic like to adipocytes, in both types cells it's possible develop the insulin resistance. In this paper, myocytes were used to assess the impact of selected safe computational hits **1**, **2** and **4** on PPAR- γ and GLUT-4 expression. Cells were treated with selected compounds, and pioglitazone

(5 μ M) as a positive control, for 24 h, and mRNA expression levels were evaluated. Fig. 1 illustrates that only compounds **1** and **2** significantly elevate relative expression levels of PPAR- γ (approximately three to fourfold). Activation of PPAR- γ has the potential to reduce glucose levels in diabetic individuals by mitigating insulin resistance. Furthermore, our findings suggest that compound **1** induces *GLUT-4* expression more effectively than pioglitazone. Multiple lines of evidence suggest that elevated levels of *GLUT-4* expression in skeletal muscle play a crucial role in regulating glucose homeostasis [2,3,6].

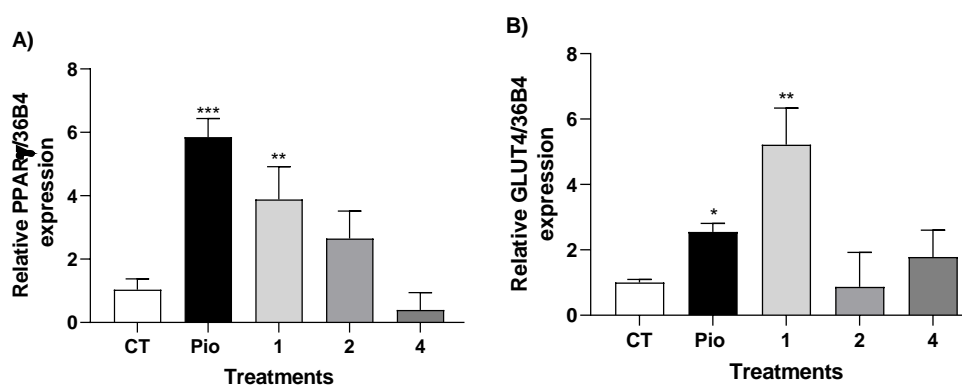


Fig. 1. Effect of compound **1**, **2**, **4** and Pioglitazone (Pio) on relative PPAR- γ expression (A) and *GLUT-4* levels (B) in C2C12 myocytes. Results are expressed as relative expression of mRNA (mean \pm S.E.M, n = 4). *p < 0.05 compared with control.

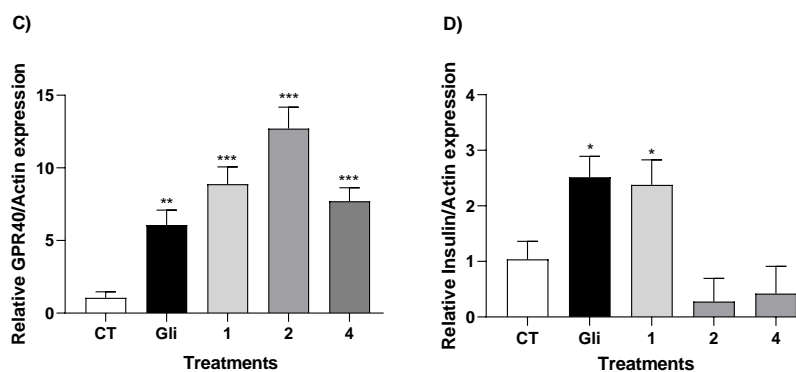


Fig. 2. Effect of compound **1**, **2**, **4** and glibenclamide (Gli) on relative GPR40 expression (C) and insulin levels (D) in RINm5F cells. *p < 0.05 compared with control.

Conversely, compounds **1**, **2**, and **4** exhibited a notable 7- to 12-fold increase in *GPR40* expression (Fig. 2). To confirm whether the substantial increase in *GPR40* expression induced insulin release, we assessed the compounds in RINm5F cells. These cells are involved in insulin secretion and intracellular calcium release [3]. We observed a reasonable insulin secretion induced by compound **1**, comparable to that induced by glibenclamide.

In vivo* antidiabetic effect of compounds **1**, **2** and **4*

Compounds **1**, **2** and **4** were the most active against three targets identified as critical elements in diabetes in this work. Consequently, they were selected to evaluate their *in vivo* activity in a glucose tolerance test. Glibenclamide, pioglitazone and linagliptin served as positive controls for antidiabetic activity. The effects

of compounds **1**, **2**, and **4** were assessed following a single oral dose of 100 mg/kg administered via the intragastric route (Fig. 3).

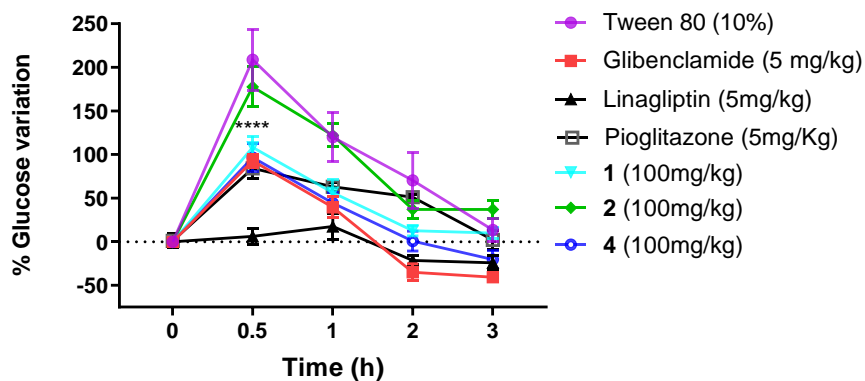


Fig. 3. *In vivo* oral Glucose Tolerance Test: Assessment of the impact of compounds **1**, **2**, and **4** on blood glucose levels following a single oral dose of 2 g/kg glucose in normoglycemic male C57BL/6 mice. Each plot displays the mean values along with the standard error of the mean (SEM) for six separate experiments. **** $p < 0.05$ indicates significance compared to the control group.

In the glucose tolerance test conducted with C57BL/6 mice (Fig. 3), the efficacy of compounds **1** and **4** is evident, as they demonstrate effectiveness within the initial 30 min of the test, mitigating the hyperglycemic peak. Furthermore, a notable decrease in glucose concentration is observed over the subsequent 60 min, with significant differences compared to vehicle. Compound **4** maintains its decreasing trend throughout the experiment, reaching levels below the basal levels along with glibenclamide, linagliptin and pioglitazone (positive controls), while compound **1** remains relatively stable.

Compound **1** demonstrated a clear increase in relative PPAR- γ expression, which was consistent with a rise in GLUT4 levels. A similar pattern was observed with the increase in GPR40 and insulin secretion. Conversely, compound **4** exhibited poor *in vitro* activity but significantly increased GPR40 expression by more than sevenfold, which may have contributed to its notable *in vivo* antihyperglycemic effect. This could be attributed to the reactive nitrile group in compound **4**, which can form reversible covalent adducts with proteins, primarily through reactive cysteine or serine side chain residues. One potential additional target implicated in this reversible covalent effect is dipeptidyl peptidase-4 (DPP-4), a serine protease that inactivates incretin hormones and is a widely exploited target for treating type 2 diabetes mellitus. It has been established that the nitrile warhead in vildagliptin and saxagliptin forms a reversible covalent bond with the Ser-630 residue [20]. This hypothesis suggests that compound **4** may have an expanded multitarget effect, which should be verified experimentally in future investigations.

Molecular docking studies

Based on *in silico* pharmacological consensus analysis (PHACA) compounds **1**, **2** and **4** were chosen to test their *in vitro* expression on PPAR- γ and GPR40 and their activation products GLUT-4 and insulin, respectively. To establish a correlation between their presumed binding patterns and their experimental activities, molecular docking was conducted on these targets. To validate our molecular docking model, the Root Mean Square Deviation (RMSD) was calculated as a measure of re-docked success of rosiglitazone over PPAR- γ with a value of RMSD = 1.0369 Å and a score of -8.4423 Kcal/mol. The molecular docking reveals that compounds (Fig. 4) **1**, **2** and **4** occupied the ligand binding pocket of PPAR- γ and form hydrogen bonds with His-323 and His-449, essential interactions for the activation of this receptor, in addition an interaction with Met-364 was observed in all compounds. However, compound **1**, exhibiting the highest activity *in vitro*,

demonstrated an additional H-arene interaction with Cys-285. This interaction has been linked to conformational changes in PPAR- γ that could potentially contribute to its activation [21].

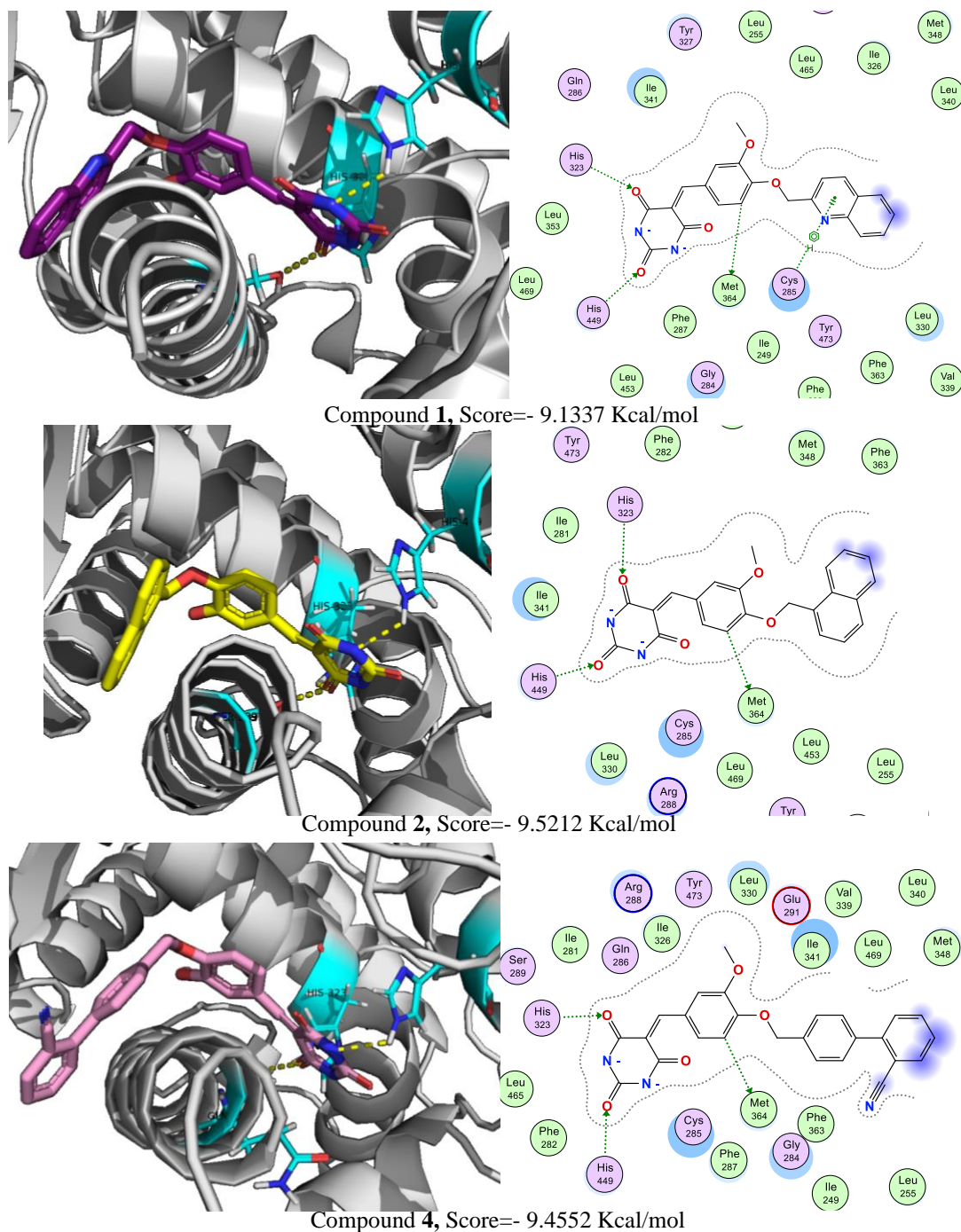


Fig. 4. 3D and 2D binding model of compounds **1**, **2** and **4** into the ligand binding pocket of PPAR- γ .

With respect of GPR40, the validation with co-crystal molecule TAK-875 has a RMSD = 0.4234 Å and a score of -11.3756 Kcal/mol.

Molecular docking on GPR40 (Fig. 5) suggests that compounds **1**, **2** and **4** established electrostatic and hydrogen bonds with Arg-183 and Arg-258 residues, which are characteristic of GPR40 allosteric agonists [22]. Additionally, compounds **1** and **4**, were the most potent in the *in vitro* and *in vivo* assays, showed an additional H-arene interaction with Phe-87, Val-84 and Leu-135. This could improve the interaction and affinity of the compounds with the GPR40 binding site and explain their experimental biological activity.

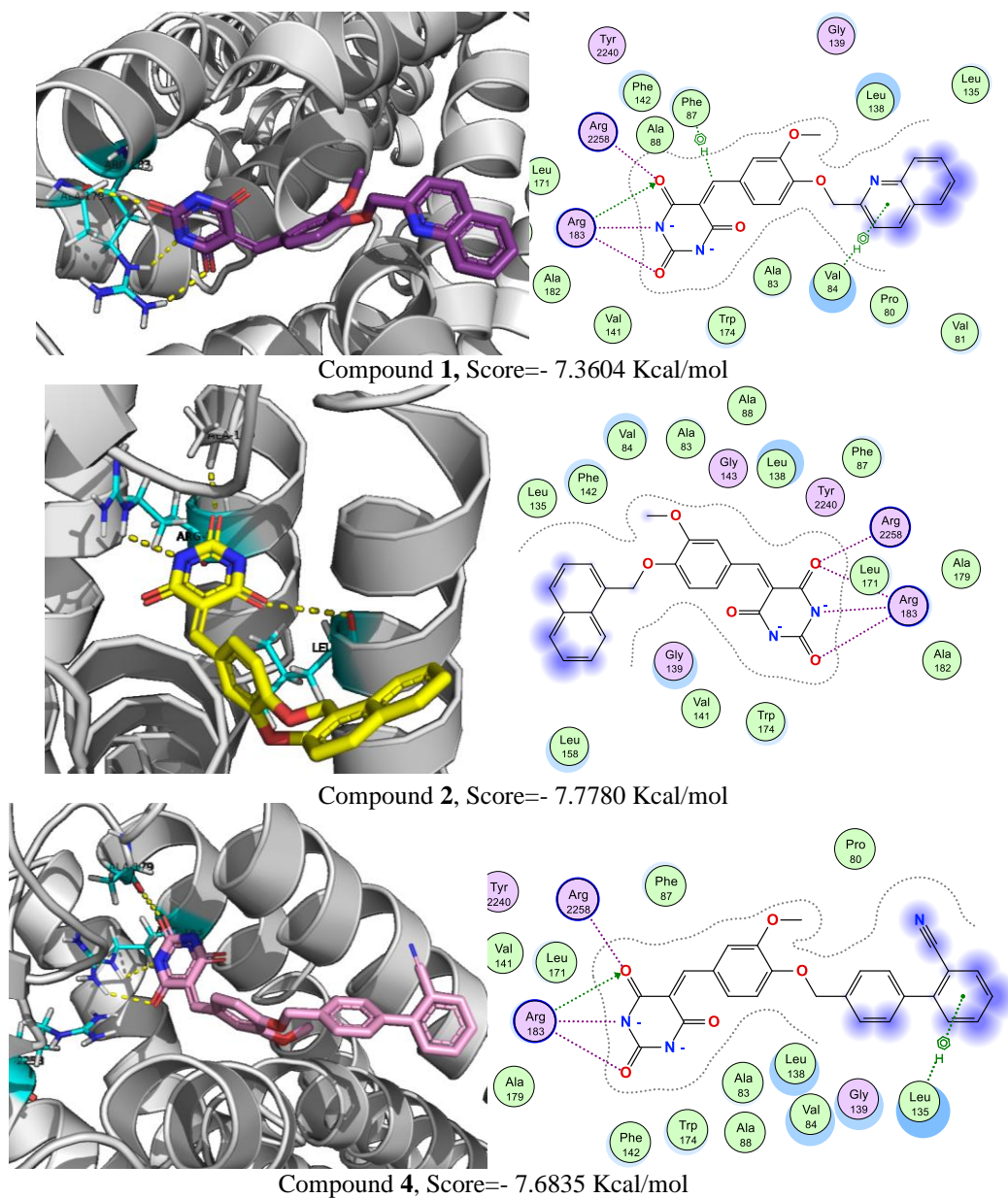


Fig. 5. 3D and 2D binding model of compounds **1**, **2** and **4** into the ligand binding pocket of GPR40.

Conclusions

In conclusion, taken together these results suggest that benzylidenebarbiturates (compounds **1-5**) showed better predicted pharmaceutical properties than the hydantoin isosteres (compounds **6-10**), behaving as safe computational hits through a pharmacological consensus analysis. Compounds **1**, **2**, and **4** have been recognized as experimental multitarget modulators of PPAR- γ , GLUT4, and GPR40 proteins, displaying *in vivo* antihyperglycemic effects alongside predicted pharmacokinetic and toxicological profiles conducive to their potential as antidiabetic candidates.

Acknowledgements

S. Juárez-Cruz received a CONAHCyT fellowship (792538) to obtain her Master in Pharmacy studies. This work received the "Maricela Plascencia García" award 2023 for the best master's theses in Pharmaceutical Sciences awarded by the Foundation for Pharmaceutical Education in Mexico, A.C., (FEFARM). We are in debt with Laboratorio Nacional de Nano y Biomateriales (LANNBIO), CINVESTAV-IPN, Unidad Mérida. This research was funded by the Consejo Nacional de Humanidades, Ciencia y Tecnología (CONAHCyT), grant No. 253814 (Ciencia Básica 2015), grant No. 252881 (PEI 2018), and also by CONACyT; FORDECYT-PRONACES (Ciencia de Frontera 377882/2020).

References

1. Mahboob, A.; Senevirathne, D.K.L.; Paul, P.; Nabi, F.; Khan, R.H.; Chaari, A. *Int. J. Biol. Macromol.* **2023**, 225, 318-350. DOI: <https://doi.org/10.1016/j.ijbiomac.2022.11.038>.
2. Madrigal-Angulo, J.L.; Ménez-Guerrero, C.; Estrada-Soto, S.; Ramírez-Espinosa, J.J.; Almanza-Pérez, J.C.; León-Rivera, I.; Hernández-Núñez, E.; Aguirre-Vidal, Y.; Flores-León, C.D.; Aguayo-Ortíz, R.; Navarrete-Vázquez G. *Bioorg. Med. Chem. Lett.* **2022**, 70, 128804. DOI: <https://doi.org/10.1016/j.bmcl.2022.128804>.
3. Hidalgo-Figueroa, S.; Rodríguez-Luévano, A.; Almanza-Pérez, J.C.; Giacomán-Martínez, A.; Ortiz-Andrade, R.; León-Rivera, I.; Navarrete-Vázquez, G. *Eur. J. Pharmacol.* **2021**, 907, 174244. DOI: <https://doi.org/10.1016/j.ejphar.2021.174244>.
4. Ren, Q.; Fan, Y.; Yang, L.; Shan, M.; Shi, W.; Qian, H. *Expert. Opin. Ther. Pat.* **2023**, 33, 565-577. DOI: <https://doi.org/10.1080/13543776.2023.2272649>.
5. Saldívar-González, F.I.; Navarrete-Vázquez, G.; Medina-Franco, J.L. *Front. Pharmacol.* **2023**, 14:1276444. DOI: <https://doi.org/10.3389/fphar.2023.1276444>.
6. Colín-Lozano, B.; Estrada-Soto, S.; Chávez-Silva, F.; Gutiérrez-Hernández, A.; Cerón-Romero, L.; Giacomán-Martínez, A.; Almanza-Pérez, J.C.; Hernández-Núñez, E.; Wang, Z.; Xie, X.; Capiello, M.; Balestri, F.; Mura, U.; Navarrete-Vázquez, G. *Molecules.* **2018**, 23, 340. DOI: <https://doi.org/10.3390/molecules23020340>.
7. Giacomán-Martínez, A.; Alarcón-Aguilar, F.J.; Zamilpa, A.; Hidalgo-Figueroa, S.; Navarrete-Vázquez, G.; García-Macedo, R.; Román-Ramos, R.; Almanza-Pérez, J.C. *Planta Med.* **2019**, 85, 412-423. DOI: <https://doi.org/10.1055/a-0824-1316>.
8. Giacomán-Martínez, A.; Alarcón-Aguilar, F.J.; Zamilpa, A.; Huang, F.; Romero-Nava, R.; Román-Ramos, R.; Almanza-Pérez, J.C. *Can. J. Physiol. Pharmacol.* **2021**, 99, 935-942. DOI: <https://doi.org/10.1139/cjpp-2021-0027>.
9. Rosiles-Alanis, W.; Zamilpa, A.; García-Macedo, R.; Zavala-Sánchez, M.A.; Hidalgo-Figueroa, S.; Mora-Ramiro, B.; Román-Ramos, R.; Estrada-Soto, S.E.; Almanza-Pérez, J.C. *J. Med. Food.* **2022**, 25, 588-596. DOI: <https://doi.org/10.1089/jmf.2021.0071>.

10. Estrada-Soto, S.; Ornelas-Mendoza, K.; Navarrete-Vázquez, G.; Chávez-Silva, F.; Almanza-Pérez, J.C.; Villalobos-Molina, R.; Ortiz-Barragán, E.; Loza-Rodríguez, H.; Rivera-Leyva, J.C.; Flores-Flores, A.; Perea-Arango, I.; Rodríguez-Carpaena, J.G.; Ávila-Villarreal, G. *Pharmaceuticals*. **2023**, *16*, 535. DOI: <https://doi.org/10.3390/ph16040535>.
11. Molecular Operating Environment (MOE). Chemical Computing group ULC; 910-1010 Sherbooke St. West, Montreal, QC, Canada, 2024; Available online: <http://www.chemcomp.com>, accessed in January 2024.
12. Srivastava, A.; Yano, J.; Hirozane, Y.; Kefala, G.; Gruswitz, F.; Snell, G.; Lane, W.; Ivetac, A.; Aertgeerts, K.; Nguyen, J.; Jennings, A.; Okada, K. *Nature*. **2014**, *513*, 124-127. DOI: <https://doi.org/10.1038/nature13494>.
13. Liberato, M.V.; Nascimento, A.S.; Ayers, S.D.; Lin, J.Z.; Cvorovic, A.; Silveira, R.L.; Martínez, L.; Souza, P.C.; Saidenberg, D.; Deng, T.; Amato, A.A.; Togashi, M.; Hsueh, W.A.; Phillips, K.; Palma, M.S.; Neves, F.A.; Skaf, M.S.; Webb, P.; Polikarpov, I. *PLoS One*. **2012**, *7*, e36297. DOI: <https://doi.org/10.1371/journal.pone.0036297>.
14. Schrödinger, L., & DeLano, W. *PyMOL*. Retrieved from <http://www.pymol.org/pymol>, accessed in 2024.
15. Domínguez-Mendoza, E.A.; Galván-Ciprés, Y.; Martínez-Miranda, J.; Miranda-González, C.; Colín-Lozano, B.; Hernández-Núñez, E.; Hernández-Bolio, G.I.; Palomino-Hernández, O.; Navarrete-Vázquez, G. *Molecules*. **2021**, *26*, 799. DOI: <https://doi.org/10.3390/molecules26040799>.
16. Molinspiration Cheminformatics free web services, Available online: <https://www.molinspiration.com>, accessed in February 2023.
17. Xiong, G., Wu, Z., Yi, J., Fu, L., Yang, Z., Hsieh, C., Yin, M., Zeng, X., Wu, C., Lu, A., Chen, X., Hou, T., Cao, D. *Nucleic Acids Res.* **2021**, *49*, W5-W14. ADMETLab 2.0 Available online: <https://admetmesh.scbdd.com>, accessed March 2022.
18. Rudik, A.V.; Dmitriev, A.V.; Lagunin, A.A.; Filimonov, D.A.; Poroikov, V.V. *ACS Omega*. **2023**, *8*, 45774-45778. DOI: 10.1021/acsomega.3c06119. MetaTox 2.0 Available online: <https://www.way2drug.com/metatox>, accessed in December 2023.
19. Diaza, R.G.; Manganelli, S.; Esposito, A.; Roncaglioni, A.; Manganaro, A.; Benfenati, E. *SAR QSAR Environ Res.* **2015**, *26*, 1-27. DOI: <https://doi.org/10.1080/1062936X.2014.977819>.
20. Bonatto, V.; Lameiro, R.F.; Rocho, F.R.; Lameira, J.; Leitão, A.; Montanari, C.A. *RSC Med. Chem.* **2022**, *14*, 201-217. DOI: <https://doi.org/10.1039/d2md00204c>.
21. Korbecki, J.; Bobiński, R.; Dutka, M. *Inflamm. Res.* **2019**, *68*, 443-458. DOI: <https://doi.org/10.1007/s00011-019-01231-1>.
22. Lückmann, M.; Trauelsen, M.; Bentsen, M.A.; Nissen, T.A.D.; Martins, J.; Fallah, Z.; Nygaard, M.M.; Papaleo, E.; Lindorff-Larsen, K.; Schwartz, T.W.; Frimurer, T.M. *Proc. Natl. Acad. Sci. U S A*. **2019**, *116*, 7123-7128. DOI: <https://doi.org/10.1073/pnas.1811066116>.

Biopanning Phage Display Libraries in Homogeneous Solution for Identification of Biomineralization Peptides of TiO₂

Armin Hernández-Gordillo^{1,2}, Andrés Hernández-Arana¹, L. Irais Vera-Robles^{1*}

¹Departamento de Química, Área de Biofísicoquímica, Universidad Autónoma Metropolitana-Iztapalapa, San Rafael Atlixco 186, Col. Vicentina, 09340, CDMX, México.

²Centro de Investigación en Nanociencias y Nanotecnología, Centro Universitario de los Valles, Carretera Guadalajara-Ameca Km. 45.5, Ameca, Jalisco, C.P. 46600, México.

*Corresponding author: L. Irais Vera-Robles, email: irrob@xanum.uam.mx

Received April 30th, 2024; Accepted August 12th, 2024.

DOI: <http://dx.doi.org/10.29356/jmcs.v68i4.2262>

Abstract. Peptides and proteins rich in positively charged residues have been the most frequently reported for TiO₂ biomineralization since their identification is based on peptide screening on its negatively charged surface. To achieve optimum interaction of the peptides with the biomimetic synthesis precursors rather than interaction with the final product, in this work, a selection of peptides with biomineralization activity was proposed by performing a biopanning directly on the precursor Titanium(IV) bis(ammonium lactate) dihydroxide (TiBALDH). Using two phage display libraries (12- and 7-mer) in different buffer systems, four possible sequences with biomineralization activity of TiO₂ were identified: TNWQALAYMQRH (TN), ENHWSLSTLMSS (EN), GLHTSATNLYLH (GL), TWYPNRPPILEL (TW). The selection of buffer and concentration of TiBALDH were vital for a reliable identification. Synthetic peptides with sequences TN and EN, were selected for *in vitro* biomineralization of TiO₂. Both peptides were able to form anatase nanoparticles at room temperature. However, the EN sequence showed lower activity than TN, specially in acetate buffer, requiring a higher concentration to initiate biomineralization. These changes in reactivity can be attributed principally to different states of protonation of the residues mainly due to the glutamic acid in EN. Although the secondary structure determined by circular dichroism results in disordered chains, a common motif could be identified between the two peptides -pol-pol-W-pol-x-x-x-M-, where the W and M residues match. The results provide new possibilities for using combinatorial techniques to find new biological templates for nanomaterial synthesis.

Keywords: Phage display; peptides; titanium oxide; biopanning; biomineralization.

Resumen. Péptidos y proteínas ricas en residuos con carga positiva han sido frecuentemente reportados para la biomineralización de TiO₂, ya que su identificación se basa en la detección de péptidos sobre su superficie con carga negativa. Para alcanzar una interacción óptima del péptido con el precursor biomimético, en lugar de la interacción con el producto final, en este trabajo, se propuso realizar un biotamizado empleando el precursor dihidroxilactatotitanato(IV) de bis-amonio (TiBALDH) para seleccionar péptidos con actividad de biomineralización. Empleamos dos librerías de fago desplegado (12 y 7 residuos) en diferentes soluciones amortiguadoras, identificando cuatro posibles secuencias con actividad biomineralizante de TiO₂: TNWQALAYMQRH (TN), ENHWSLSTLMSS (EN), GLHTSATNLYLH (GL), TWYPNRPPILEL (TW). La elección del amortiguador y la concentración de TiBALDH fueron vitales para una selección confiable. Los péptidos sintéticos TN y EN, fueron escogidos para la biomineralización de TiO₂ *in vitro*. Ambos péptidos fueron capaces de formar nanopartículas de anatasa a temperatura ambiente, sin embargo, la secuencia EN mostró menor actividad que TN, especialmente en amortiguador de acetatos, requiriendo una concentración mayor para iniciar la biomineralización. Estas diferencias de reactividad pueden ser atribuidas principalmente a los estados de

protonación de los residuos de ácido glutámico en EN. Aunque la estructura secundaria determinada por difracción circular mostró cadenas desordenadas, se identificó un motivo común entre los dos péptidos—pol-pol-W-pol-x-x-x-M-, donde los aminoácidos W y M coinciden. Los resultados abren nuevas posibilidades para usar técnicas combinatorias para hallar nuevas plantillas biológicas para la síntesis de nanomateriales.

Palabras clave: Fagos desplegados; péptidos; óxido de titanio; bioselección; biomineralización.

Introduction

In nature, biomolecules (DNA, lipids, peptides, and proteins) are responsible for using the available resources around them to guide the synthesis of inorganic materials, by a process called biomineralization. Proteins or peptide motifs that can biomineralize silica, nacre, bones, nanoparticles among others, have been found in several organisms [1-4]. Albeit some helpful inorganic structures are produced by distinct proteins; which have been identified and sequenced, other materials with relevant technological applications, such as TiO₂ are not produced naturally by biomolecules [5].

For this reason, several efforts have been made to find sequences with biomineralizing activity for non-biogenic materials. For example, microorganisms have been used to introduce titanium precursors into their metabolism to synthesize TiO₂ nanostructures, but this method does not provide information on the biomolecules involved in biomineralization [6,7].

Alternatively, the combinatorial technique known as biopanning allows the selection of peptides that bind specifically to a target [8]. In particular, the M13 phage display library consists of a collection of phages genetically engineered to express random amino acid sequences (between 7 and 12 residues) on solvent-exposed regions of protein site p3, which have been widely used to find peptides with affinity to a specific target [9]. Thus, the affinity of millions of different sequences can be tested in a single experiment. Mostly, the screening experiments are done against the material of interest; however, although some selected peptides show an affinity for specific oxides, they are necessarily not the best template to induce the formation of a particular structure from a precursor [10].

For example, making the biopanning on TiO₂ surfaces a great number of peptide sequences have been proposed for biomineralizing TiO₂ nanoparticles in their different crystalline phases and shapes [11-13]. However, some of these peptides did not exhibit biomineralizing activity and there is not a clear correlation between the role of each amino acid in biomineralization [11]. Some authors suggest that positive charges, *eg.* arginine or lysine residues, are necessary to interact electrostatically with the negative charge of the oxide and their charge seems to be closely related to the biomineralization yield of TiO₂ [11,14,15]. However, a few peptides without these positive charge residues have been reported [16,17], either as isolated motifs or as building blocks attached to other platforms, to be capable of producing controlled TiO₂ crystalline structures. Accordingly, the sequence with an affinity to the surface of the material is not the unique factor that ensures the biomineralizing [18].

Therefore, to identify of sequences with biomineralizing activity, it is necessary to perform biopanning directly on the molecular precursors instead of on a solid phase. Żelechowska *et al.* has tested this hypothesis, modifying the biopanning approach, selecting peptides that, in the presence of a precursor, can bind it and further induce the formation of a given inorganic material, *eg.* ZnO [19]. As well this approach has been helpful in finding peptides with catalytic activity for organic reactions [20]. Thus, biopanning on a molecular target can be a promising route for finding specific peptides to biomineralize TiO₂.

In this work, we proposed to use an alternative target. Instead of using TiO₂ (final material), we employed the precursor titanium(IV) bis(ammonium lactate)dihydroxide (TiBALDH), which is water soluble. It has been reported that this precursor coexists with TiO₂ nanoparticles in the equilibrium, and it shifted toward its production can be guided by experimental parameters such as solvent polarity and solution dilution, among others [21]. Accordingly, in a previous work, we investigated its stability also in different buffers, presence of ions and pH [22]. Then, TiBALDH was used to identify sequences that have biomineralization activity and affinity to the final material. Thus, if TiO₂ particles are formed, it will be indicated that there are phages with sequences that catalyze the reaction, which may also interact with the particles formed. These phages can be recovered from the aqueous solution by centrifugation, and, after DNA sequencing, the peptide sequence attached to TiO₂ can be known. With this methodology, it can be assured that the sequences obtained from biopanning have biomineralization activity with

TiBALDH, thus minimizing the requirement of a positive charge on the precursor. Once the sequences were deciphered, these two peptides were tested for TiO₂ biomineralization at room temperature to demonstrate that this methodology can be applied to find specific sequences that may work on biomineralization using other precursors.

Experimental

Biopanning in homogeneous phase

The biopanning to identify TiO₂ binding peptides was performed according to the protocol recommended by the manufacturer of the phage display libraries (New England BioLabs, Ph. D. Phage Display Libraries). Phage display libraries of 7- and 12-mer were used, modifying the section of the target material. An acidic, a neutral, and a basic buffer solution (sodium acetate pH 4.5, sodium phosphate pH 7.0, and Tris buffer pH 8.0) were chosen, and deionized water was a negative control. In brief, ~10¹¹ phages were added to 500 μL of TiBALDH (Sigma Aldrich, stored at 4 °C) 50 mM in the respective buffer. The mixed solution was placed at room temperature for 5 days to ensure the interaction of the peptides exposed on p3 proteins with the titanium precursor and consequent TiO₂ biomineralization. After incubation, the solution was centrifuged (14 000 rpm, 10 min), washed and phage eluted according to the New England Biolabs protocol. In each round of biopanning, the eluate was amplified and titrated for subsequent clone selection (20 for each experiment). DNA sequencing was performed by Eurofins MWG Operon (Louisville, KY). Three panning rounds were performed.

Biomineralization of TiO₂ using peptides

The peptide sequences were selected from biopanning results. Two peptides, TN (TNWQALAYMQRH) and EN (ENHWSLSTLMSS) (purity ≥ 96 %) were synthesized by Biomatik (USA). A stock solution of each peptide of 5.0 mg/mL was prepared in sterile deionized water. Solutions of TiBALDH 50 mM in Tris or acetate buffer (100 mM) were prepared with different peptide concentrations. After incubation for 24 h, the solution was recovered by centrifugation (14 000 rpm, 10 min), washed once with the corresponding buffer solution, and dried at room temperature. The biomineralized TiO₂ was characterized by dispersion light scattering (Zetasizer Nano, Malvern Panalytical), transmission electron microscopy (JEOL 2010 operated to 200 KeV), and Fourier Transform infrared spectroscopy (Spectrum GX, Perkin Elmer) equipped with ATR. To monitor the content of Ti in the biomineralization process, soluble Ti(IV) was quantified by colorimetry using Tiron (4,5-dihydroxy-1,3-benzenedisulfonic acid) [23]. Briefly, 10 μL of the titanium sample was added to 190 μL of Tiron 5 mM in acetate buffer. The mixture was incubated at room temperature for 2 h, and then the UV-vis absorption spectrum was acquired (NanoDrop 2000). The percentage of Ti(IV) was calculated with the absorption ratio (at 380 nm), assuming the absorption of TiBALDH in water at the same molar concentration was 100 %.

Circular dichroism

Circular dichroism (CD) spectra in the 250-190 nm region were registered with a JASCO J-715 instrument (Jasco Inc., Easton, MD) using a 1.00-mm- path length cell. Peptides were dissolved in water at concentrations ca. 0.1 mg/mL (pH ca. 6.7) and spectra were recorded at 25.0 °C. Spectral raw data were transformed to mean residue ellipticity [θ].

Results and discussion

Biopanning

Biopanning was performed using three buffered media (pH 4.5, pH 7.0, and pH 8.0) and deionized water as a negative control. Both 12- and 7-mer phage display libraries were tested to study the effect of peptide length on biopanning. In the first step, the phage display library was put in contact with the TiBALDH solution (50 mM) and incubated for a few days (Fig. 1(a)). Several days were necessary to guarantee the specific interaction, reaching of the equilibrium, and biomineralization of TiO₂ on the p3 protein (Fig. 1(b)). Phage-TiO₂ conjugates were recovered

by centrifugation since phage alone did not precipitate at 14000 rpm (Fig. 1(c)). Finally, the eluate was plated to verify that phages with probable biomineralizing activity were recovered. This procedure was repeated twice.

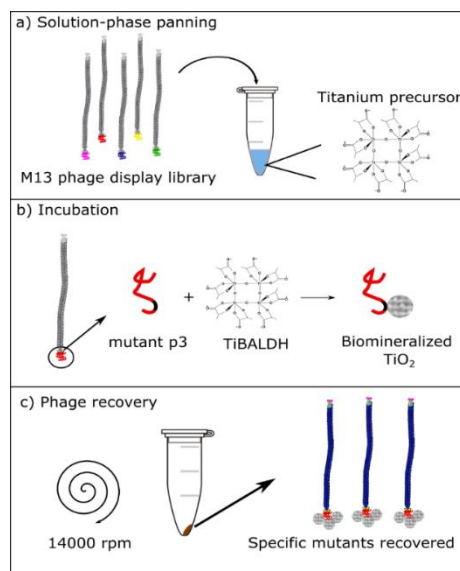


Fig. 1. Scheme biopanning procedure in homogeneous solution with TiBALDH as a target.

Interestingly, after the first biopanning cycle with TiBALDH, the results were similar with both 12- and 7-mer libraries (Table 1). For the negative control and the acetate buffer (pH 4.5), it was not possible to recover phages (no plaques were detected); this implies that the interaction of M13 mutants with the titanium precursor under those conditions was not adequate to induce TiO₂ biomineralization. A possible explanation is that the negative charge of TiBALDH is repelled by the phage, which is also negative. Also, it is known that small TiO₂ nanoparticles can be redissolved in citrate buffer, probably both factors hampering its production in detectable amounts. On the contrary, as was expected phages were recovered (plaques were clearly visible on the *E. coli* lawn) in phosphate and tris buffer. Indeed, it has been reported that phosphates promote the formation of TiO₂ nanoparticles in the presence of TiBALDH; however, they are trapped inside of their nanoparticles as a contaminant [16]. Conversely, Tris buffer does not react with TiBALDH; according to our size measurements, no shifts were detected, while phosphates increase dramatically its size from units to hundreds of nm as reported before [22]. Then, Tris buffer should allow phages with specific interaction and/or biomineralizing activity to be rescued by centrifugation, forming plaques, as shown in Table 1.

Table 1. Phages recovered after the first round of biopanning in TiBALDH (50 mM) in the selected buffers (100 mM).

Buffer	pH	Plaques after 1st biopanning cycle*
Acetate	4.5	No
Water	7.0	No
Phosphate	7.0	Yes
Tris	8.0	Yes

* The results correspond to both 12- and 7-mer phage display libraries.

Since no plaques were obtained in acetate and water systems, the second biopanning cycle was not continued in those systems. Three rounds were completed with phosphate and Tris buffer, and phages were recuperated, eluted, and plated. To identify the sequences, we selected 20 clones in each experiment of the 7-mer biopanning. For the 12-mer library, 20 and 40 plaques for PB and Tris were selected, respectively all clones found are shown in Table 2.

Table 2. Sequences found in biopanning experiments of TiBALDH.

Plaque	Sequence			
	12-mer library		7-mer library	
	PB	Tris	PB	Tris
1	TWYPNRPPILEL	ISGPWASYAIGP	WT	WT
2	FEDPRTWWVTHL	WT	TGFHLM	WT
3	TNWQALAYMQRH	WAKDPSWKVRGN	YEPYKRI	WT
4	VSNKMPDGENWR	GLHTSATNLYLH	QILVHKN	WT
5	SLNGPIHRLKKT	IPLGRDGGSYQR	FHPRTTS	WT
6	GWYAASGTSLLS	GYSFIDPPRKFH	QGYGVPT	TPTAPVR
7	WT	AIWPKTEFLIS	TTPLSHR	WT
8	ENHWSLSTLMSS	WT	GRLDTGI	WT
9	TFYLVNPGSRLG	RPDIQLLPNSWA	HNIKETH	WT
10	GLHTSATNLYLH	GLHTSATNLYLH	LRSDPVV	WT
11	TTKFPFVSVLS	VASRIHPLGIDP	DSSLFAL	GMHETHV
12	TWYPNRPPILEL	QLLPGLLKEHVQ	WT	WT
13	ENHWSLSTLMSS	TLPAILQSSGTR	WT	WT
14	SLRWPVAVHHSN	KGSLDARLLSR	YLGFDVH	WT
15	VSLSGVSSNSRV	TNWQALAYMQRH	SRPPVPA	WT
16	DWSSWVYRDPQT	WT	IKHPFGF	FASRSDT
17	SGVYKVAYDWQH	-	SPNYNII	YGAKNNL
18	TLSDWGYGNFRA	WT	GMLSDGR	QYYSFDH
19	DWSSWVYRDPQT	GVLHNLTAATSL	ASTLIVF	TPPIVWT
20	VFSSMVHVLNTH	VPVSNVWPWRPE	IHANWSP	NIPSLPF
21	-	GTGLVTLPRLTV	-	-
22	-	WT	-	-

Plaque	Sequence			
	12-mer library		7-mer library	
	PB	Tris	PB	Tris
23	-	GDLLTFQNFV M K	-	-
24	-	TN W QALAY M QRH	-	-
25	-	D W SS W VYRDPQT	-	-
26	-	SQDIRT W NGTRS	-	-
27	-	D W SS W VYRDPQT	-	-
28	-	SILDG W LVVDSS	-	-
29	-	D W SS W VYRDPQT	-	-
30	-	D W SS W VYRDPQT	-	-
31	-	VPS W FFAN W GPS	-	-
32	-	GFYSNLVGSINV	-	-
33	-	D W SS W VYRDPQT	-	-
34	-	D W SS W VYRDPQT	-	-
35	-	TDSPTSQRQPYG	-	-
36	-	D W SS W VYRDPQT	-	-
37	-	D W SS W VYRDPQT	-	-
38	-	D W SS W VYRDPQT	-	-
39	-	D W SS W VYRDPQT	-	-
40	-	D W SS W VYRDPQT	-	-

WT: wild-type phage. In red and green are indicated W and M, respectively, and the motif that is shared is underlined.

The 12-mer library gave 5 sequences that were repeated at least once. Table 3 contains the sequences most frequently found in the 12-mer library experiments. The most frequent sequence was DW (DWSSWVYRDPQT), found in both experiments (phosphate and Tris). At first sight, the DW peptide could be considered as a sequence capable of promoting TiO₂ formation from TiBALDH, but in combinatorial techniques such as biopanning, it is common to find false positives. A literature search found that this sequence has been reported with affinity to several systems, including polypropylene (the material of the tubes used in biopanning) [24,25].

Thus, the most frequent sequence DW was discarded in addition to GLHTSATNLYLH, which has also been found in some experiments but does not present similarity with the system studied here [26-28]. Therefore, the sequences considered for biomineralization experiments were TN (TNWQALAYMQRH) and EN (ENHWSLSTLMSS) because of the contrasting isoelectric points. It should be noted that despite this dissimilar charge, a sequence alignment carried out with [29] Clustal Omega showed that, although the similarity was not high, peptides EN and TN share a common motif that can be represented as follows: -pol-

pol-W-pol-x-x-x-M-, where pol and x denote polar and any amino acids, respectively. The two coincident residues, W and M, have hydrophobic characteristics that could serve as the stabilizers of the nanoparticle aggregates, while the hydrophilic motif -pol-pol- at one end would be responsible for interacting electrostatically with the titanium complex. This motif can be used as a starting point for the design of peptides with high yield in TiO₂ biomineralization. Another reason for choosing EN and TN peptides was to try not to use sequences with R or K in the central positions of the peptide [11].

It is important to note that when the alignment analysis was performed among all the 12-mer peptides found in the biopanning, it is observed that the DW peptide has a coincidence respect to the TN in residues W and Y. Thus, we do not ignore the possible biomineralizing activity of DW and further experiments are needed to establish this correlation between aromatic residues.

With respect to the 7-mer peptides found in biopanning, did not have consensus sequence. Furthermore, the alignment does not show any matching motifs with peptides EN and TN, which is the reason why 7-mer peptides were being discarded for this job. However, the align analysis shows that peptides LRSDPVV, and SRPPVPA have a motif -S-pol-P-apol-V-; where pol and apol means polar and nonpolar respectively, and peptides QILVHKN, and TTPLSHR match in residues L and H, making them good candidates for future research.

Table 3. Most frequent sequences found in biopanning experiments.

Peptide	Frequency	Sequence	Buffer	pI*
DW	13	DWSSWVYRDPQT	PB and Tris	4.47
TN	3	TNWQALAYMQRH	PB and Tris	9.06
GL	3	GLHTSATNLYLH	PB and Tris	7.38
TW	2	TWYPNRPPILEL	PB	6.25
EN	2	ENHWSLSTLMSS	PB	5.50

*Isoelectric point (pI) was calculated using the Protein Calculator [30]. Where red and green letter shows the same amino acid.

Structural characterization of EN and TN peptides

Circular dichroism spectra of the selected peptides in the far-UV region are shown in Fig. 2, where it can be seen that the most salient feature is the intense negative peak *ca.* 200 nm, with $[\theta]$ between 13,000 and 19,000 deg cm² dmol⁻¹. It is known that such intense negative CD bands appear in spectra of short lysine- and proline-rich peptides [31] and have been attributed to some content of polyproline II conformation in those peptides. However, this spectral shape is also similar to that corresponding to the unordered or coil structural type described in a CD spectral basis used for the analysis of peptide CD spectra [32].

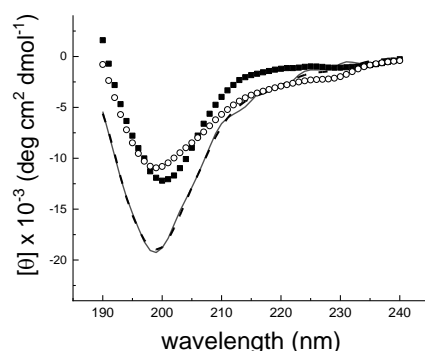


Fig. 2. CD spectra of EN (solid line) and TN (squares) peptides in water, pH *ca.* 7.0. Calculated spectra reconstructed from results of analysis by the CONTIN-LL algorithm are shown as dashed lines for EN and circles for TN.

Quantitative estimations of the secondary structures of EN and TN were carried out using two well-known algorithms used for protein secondary structure determinations: CONTIN-LL (implemented in the online server DichroWeb) [33] and BeStSel [34]. Further analysis was performed employing an unconstrained linear combination of basis spectra for typical secondary structures in peptides [32]. For both of the peptides, the three methods gave concordant results (Table 4) indicating coil (unordered) structure as the most abundant, followed by beta strands. However, the contents of turns were rather variable.

Overall, analyses of CD spectra seem to point to the presence of a few residues in beta-strand conformation in both EN and TN, and the major number of residues in unordered (irregular structure).

Table 4. Predictions of secondary structure from circular dichroism spectra.

Peptide	Method	Helix	Beta	Turns	Coil (unordered)
EN	BeStSel	3	31	19	48
EN	Contin	5	17	14	64
EN	Multiple linear regression	6	21	0	72
TN	BeStSel	0	39	21	40
TN	Contin	6	22	15	56
TN	Multiple linear regression	0	0.37	0.04	0.60

Biom mineralization of TiO₂ using the selected peptides

Thus, the two peptides, namely TN and EN, were used for biom mineralization experiments, although EN was found in phosphate buffer, it was also employed in Tris buffer for comparison purposes. Although at pH 8.0 the TN peptide is positively charged and the EN peptide is negatively charged (Fig. 3), no difference was observed in the biom mineralization product, suggesting that the reaction does not depend on the protonation state of the basic residues (R and H).

In Tris buffer, both EN and TN peptides were able to biom mineralize TIBALDH at ≥ 2.0 mg/mL concentrations. Considering that EN peptide did not emerge in Tris, a low biom mineralization activity was expected under these conditions. However, Fig. 3 shows how both TN and EN peptides at 2.0 mg/mL caused a similar increase in particle size. The particles of 3 nm present in TiBALDH solution are related to the equilibrium between titanium lactate polymers probably capping a TiO₂ core [21]. In presence of peptides the chemical equilibrium is modified due to the molecular interaction between carboxylic groups, and hydrogen bonds, probably by forming micelle-type arrangements [35]. The biom mineralization products were analyzed by TEM (Fig. 4), where nanoparticles with crystalline planes corresponding to the anatase phase are observed with both peptides. The difference between the sizes obtained by DLS and TEM can be explained by the formation of electrostatically stabilized agglomerates.

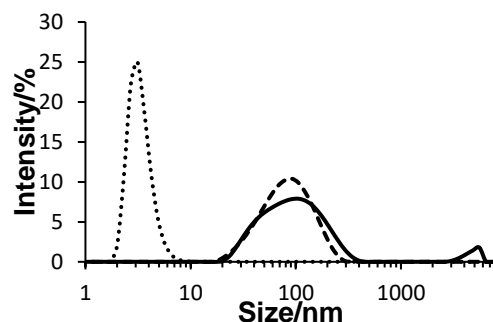


Fig. 3. Size particle distribution of TiBALDH (50 mM) alone in Tris buffer (dotted line), and after addition of TN peptide (dashed line) and EN peptide (continuous line).

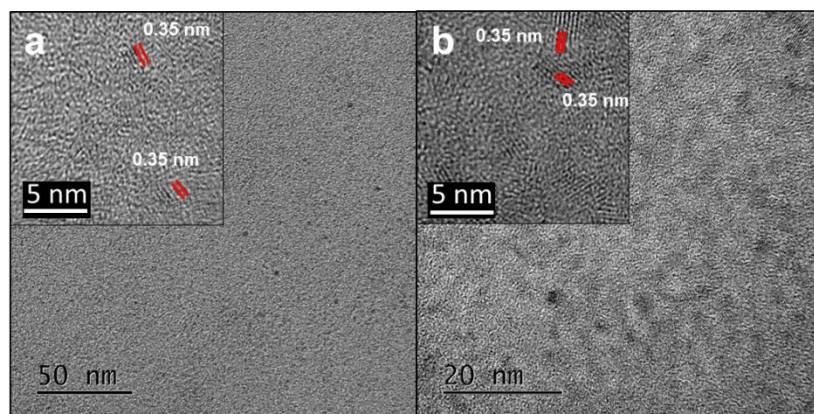


Fig. 4. TEM images of TiO₂ nanoparticles biomineralized from TiBALDH in Tris buffer and the peptides (a) TN and (b) EN.

The influence of pH and protonation states were studied using the acetate buffer. When peptides in the presence of acetates are mixed with TiBALDH, an evident increase in the biomineralization product is observed. Both peptides generate a precipitate whose size makes its characterization impossible by DLS. In acetate buffer, the TN peptide could precipitate TiO₂ even at concentrations of 0.5 mg/mL while the EN peptide caused precipitation at concentrations ≥ 2.0 mg/mL.

To determine the percentage of biomineralized TiO₂, the amount of soluble titanium (TiBALDH) was quantified (Fig. 5). In the case of the TN peptide (originally found in Tris buffer biopanning), the amount of remaining TiBALDH was 32 and 26 % in Tris and acetate buffer, respectively, these values are similar to those peptides joined to proteins [19] whose activity is larger than isolated peptides. The acetate buffer, in the absence of peptide, also decreases the soluble Ti(IV); the low pH and the presence of carboxylic groups can be responsible of this behavior [21]. On the contrary, EN peptide shows percentages of remanent TiBALDH of 82 and 40% in Tris and acetate buffer, respectively more similar to values reported by other groups for isolated peptides [11, 16]. The lower biomineralization activity of the EN peptide could be explained since this sequence was not specific to that medium. In the case of acetate medium, considering that the isoelectric point (pI) of EN peptide is 5.5, at pH 4.5 it has a lower positive charge than the TN peptide, thus its activity in acidic environments could be related to the protonation state of the more acidic residues.

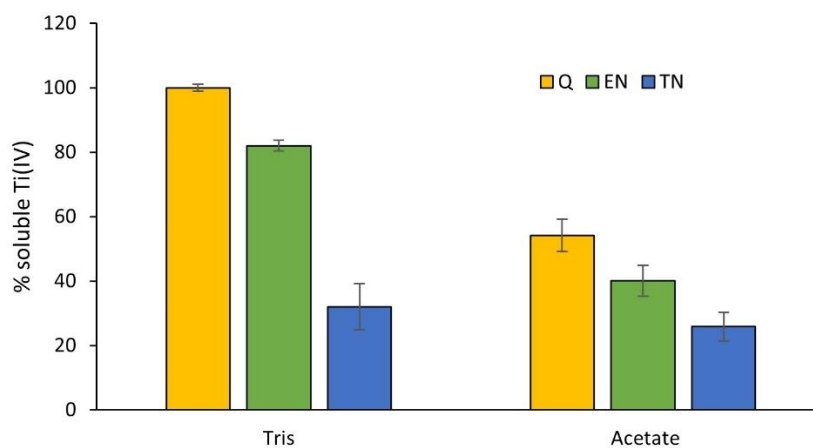


Fig. 5. Percentage of TiBALDH remaining after biomineralization for each peptide (EN in green and TN in blue) in Tris buffer and acetate buffer and negative control in absence of peptides (Q in yellow).

The peptide residues that change their protonation state from pH 8.0 (Tris) to 4.5 (acetate) are glutamate and histidine for EN and histidine for TN. Because both peptides contain histidine, therefore the protonation state of glutamate is probably what influences the difference in reactivity between peptides. At pH 4.5 the Glu residue in EN is protonated and could cause a decrease in biomineralization activity because few carboxylate groups are available to coordinate with the titanium species. A study of the molecular dynamics of peptides may also help explain their reactivity in terms of flexibility and accessibility to their functional groups.

Finally, the infrared spectra of the oxides obtained with the EN and TN peptides are shown in Fig. 7, where the characteristic band of the Ti–O bonds is below the $\tilde{\nu}$ 800 cm^{-1} . It is also observed that the samples prepared in the presence of Tris present a band in $\tilde{\nu}$ 1045 cm^{-1} that corresponds to C–O bonds in alcohols, which is possibly due to the remaining molecules from the buffer.

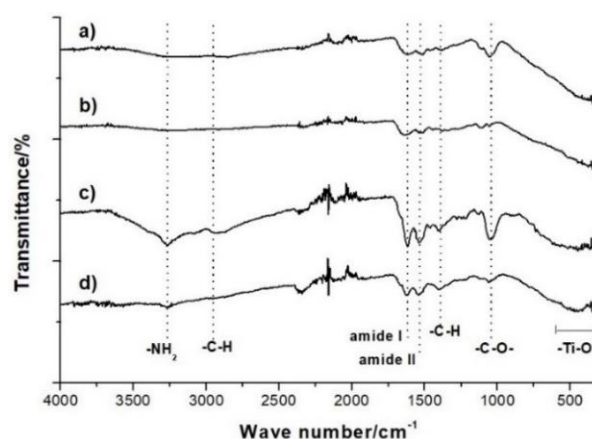


Fig. 7. FTIR spectra of TiO_2 biomineralized in the presence of TN and EN peptide in distinct buffers. TN- TiO_2 in Tris (a) and acetate (b) buffers. EN- TiO_2 in Tris (c) and acetate buffers (d). EN- TiO_2 is the material prepared with EN peptide and TN- TiO_2 corresponds to TN peptide.

In all samples, bands associated with the peptide are present; specifically, amide I bands appearing in the region of intermolecular beta structures ($\tilde{\nu}$ 1610–1625 cm^{-1}) are possibly caused by the interaction of the peptide with the surface of TiO_2 . Although the intensity of amide bands varies depending on the sample, the most intense ones were observed for EN, which would imply a better affinity of EN for TiO_2 . However, despite having a high affinity for TiO_2 , EN displays low biomineralizing activity.

Based on the above results, it can be concluded that the identification of peptides with biomineralizing activity with a particular precursor is feasible for TiO_2 . However, the results demonstrate the importance of having a specific sequence for each buffered medium since the EN peptide was not found in Tris Buffer; although biomineralization activity is observed, it shows a poor efficiency. In addition, caution must be maintained when selecting peptides because of false positives. The type of material of the vessel where biopanning takes place should not interfere with phage selection.

Conclusions

Solution-phase biopanning using a phage display library and TiBALDH as a TiO_2 precursor was proposed as an alternative method to identify sequences with biomineralizing activity. Using a 7-residue library it was not possible to identify consensus sequences, while in the 12-residue library, the sequences TNWQALAYMQRH (TN), ENHWSLSTLMSS (EN), GLHTSATNLYLH (GL), TWYPNRPPILEL (TW) were found at least twice. TN and EN peptides were tested for TiO_2 biomineralization using the precursor

TiBALDH; both peptides presented activity in 0.1 M Tris (pH 8.0) medium producing crystalline TiO₂ nanoparticles of ~ 5 nm at room temperature. At pH 4.5 in acetate buffer, the EN sequence was less active than TN, requiring a higher concentration to initiate biomineralization. These pH-dependent changes of reactivity can be attributed to the different states of protonation of the peptides, and mainly to the glutamic acid in EN. Furthermore, the effect of the peptide conformation on its biomineralizing capacity can be ruled out since both peptides seemingly display unordered conformations in solution. A biopanning methodology using precursors instead of the target material would be applied as a more convenient approach to directly find sequences with biomineralization activity.

Acknowledgments

We thank Laboratorio de Microscopía Electrónica de La Universidad Autónoma Metropolitana-Iztapalapa and Patricia Castilo for sample analysis.

References

1. Heintze, C.; Babenko, I.; Suchanova, J. Z.; Skeffington, A.; Friedrich, B. M.; Kröger, N. *Proc. Natl. Acad. Sci.* **2022**, *119*, e2211549119. DOI: <https://doi.org/10.1073/pnas.2211549119>.
2. Otter, L.M.; Eder, K.; Kilburn, M.R. *et al. Nat. Commun.* **2023**, *14*, 2254. DOI: <https://doi.org/10.1038/s41467-023-37814-0>.
3. Sharma, V.; Srinivasan, A.; Nikolajeff, F.; Kumar, S. *Acta Biomaterialia.* **2021**, *120*, 20-37. DOI: <https://doi.org/10.1016/j.actbio.2020.04.049>.
4. Liu, F.; Shah, D. S.; Gadd, G. M. *Curr. Biol.* **2021**, *31*, 358-368. DOI: <https://doi.org/10.1016/j.cub.2020.10.044>.
5. Buettner, K. M.; Valentine, A. M. *Chem. Rev.* **2011**, *112*, 1863-1881.
6. Jha, A. K.; Prasad, K.; Kulkarni, A. R. *Colloids Surf. B.* **2009**, *71*, 226-229. DOI: <https://doi.org/10.1016/j.colsurfb.2009.02.007>.
7. Lang, Y.; Monte, F. D.; Rodriguez, B. J.; Dockery, P.; Finn, D. P.; Pandit, A. *Sci. Rep.* **2013**, *3*, 3205. DOI: 10.1038/srep03205.
8. Smith G. P.; Petrenko V. A. *Chem. Rev.* **1997**, *97*, 391-410. DOI: <https://doi.org/10.1021/cr960065d>.
9. Bratkovič T. *Cell. Mol. Life Sci.* **2010**, *67*, 749-767. DOI: <https://doi.org/10.1007/s00018-009-0192-2>.
10. Rosant, C.; Avalle, B.; Larcher, D.; Dupont, L.; Fribouleta, A.; Tarascon, J.-M. *Energy Environ. Sci.* **2012**, *5*, 9936-9943. DOI: <https://doi.org/10.1039/C2EE22234E>.
11. Dickerson, M. B.; Jones, S. E.; Cai, Y.; Ahmad, G.; Naik, R. R.; Kröger, N.; Sandhage, K. H. *Chem. Mater.* **2008**, *20*, 1578-1584. DOI: <https://doi.org/10.1021/cm071515t>.
12. Sun, Y.; Tan, J.; Wu, B.; Wang, J.; Qu, S.; Weng, J.; Feng, B. *Colloids Surf. B.* **2016**, *146*, 307-317. DOI: <https://doi.org/10.1016/j.colsurfb.2016.06.032>.
13. Chen, H.; Su, X.; Neoh, K.-G.; Choe, W.-S. *Anal. Chem.* **2006**, *78*, 4872-4879. DOI: <https://doi.org/10.1021/ac0603025>.
14. Park, S.; Lee, H.; Lee, S.-Y. *Dalton Trans.* **2013**, *42*, 13817-13820. DOI: <https://doi.org/10.1039/C3DT51040A>.
15. Liu, C.; Jiang, Z.; Tong, Z.; Li, Y.; Yang, D. *RSC Adv.* **2014**, *4*, 434-441. DOI: <https://doi.org/10.1039/C3RA44630A>.
16. Puddu, V.; Slocik, J. M.; Naik, R. R.; Perry, C. C. *Langmuir.* **2013**, *29*, 9464-9472. DOI: <https://doi.org/10.1021/la401777x>.
17. Hellner, B.; Stegmann, A. E.; Pushpavanam, K.; Bailey, M. J.; Baneyx F. *Langmuir.* **2020**, *36*, 8503-8510. DOI: <https://doi.org/10.1021/acs.langmuir.0c01108>.

18. Choi, N.; Tan, L.; Jang, J.-r.; Um, Y.M.; Yoo, P.J.; Choe, W.-S. *J. Inorg. Biochem.* **2012**, *115*, 20-27. DOI: <https://doi.org/10.1016/j.jinorgbio.2012.05.011>.
19. Zelechowska, K.; Karczewska-Golec, J.; Karczewski, J.; Los, M.; Klonkowski, A. M.; Wegrzyn, G.; Golec, P. *Bioconjugate Chem.* **2016**, *27*, 1999–2006. DOI: <https://doi.org/10.1021/acs.bioconjchem.6b00196>.
20. Maeda, Y.; Javid, N.; Duncan, K.; Birchall, L.; Gibson, K. F.; Cannon, D.; Kanetsuki, Y.; Knapp, C.; Tuttle, T.; Ulijn, R. V.; Matsui, H. *J. Am. Chem. Soc.* **2014**, *136*, 15893–15896. DOI: <https://doi.org/10.1021/ja509393p>.
21. Seisenbaeva, G. A.; Daniel, G.; Nedelec, J.-M.; Kessler, V. G. *Nanoscale.* **2013**, *5*, 3330. DOI: <https://doi.org/10.1039/C3NR34068F>.
22. Hernández-Gordillo, A.; Hernández-Arana, A.; Campero-Celis, A.; Vera-Robles, L.I. *RSC Adv.* **2019**, *9*, 34559–34566. DOI: <https://doi.org/10.1039/C9RA05923G>.
23. Moharir, A.V.; Sarma, V.A.K.; Krishna Murti G.S.R. *Microchem. J.* **1972**, *17*, 167-172. DOI: [https://doi.org/10.1016/0026-265X\(72\)90169-5](https://doi.org/10.1016/0026-265X(72)90169-5).
24. Hu, Y.-F.; Gao, X.-C.; Xu, T.-Q.; Dun, Z.; Yu, X.-L. *Comb. Chem. High Throughput Screening.* **2016**, *19*, 283-289.
25. Vodnik, M.; Zager, U.; Strukelj, B.; Lunder, M. *Molecules.* **2011**, *16*, 790-817. DOI: <https://doi.org/10.3390/molecules16010790>.
26. Majerova, P.; Hanes, J.; Olesova, D.; Sinsky, J.; Pilipcinec, E.; Kovac, A. *Molecules.* **2020**, *25*, 874. DOI: <https://doi.org/10.3390/molecules25040874>.
27. Nemudraya, A. A.; Kuligina, E.V. ; Ilyichev, A. A.; Fomin, A. S.; Stepanov, G. A.; Savelyeva, A.V.; Koval, O.A.; Richter, V.A. *Oncol. Lett.* **2016**, *12*, 4547-4555. DOI: <https://doi.org/10.3892/ol.2016.5266>.
28. Zhang, H.; Guo, Z.; He, B.; Dai, W.; Zhang, H.; Wang, X.; Zhang, Q. *Adv. Healthc. Mater.* **2018**, *7*, 1800269. DOI: <https://doi.org/10.1002/adhm.201800269>.
29. Clustal Omega <https://www.uniprot.org/align/clustalo-R20220708-213026-0610-21074307-p1m>, accessed in July 2022.
30. <http://protcalc.sourceforge.net/>, accessed in January 2022
31. Rucker, A.L.; Creamer T.P. *Protein Sci.* **2002**, *11*, 980-985 doi: 10.1110/ps.4550102.
32. Reed, J.; Reed T. A. *Anal Biochem.* **1997**, *254*, 36-40 <https://doi.org/10.1006/abio.1997.2355>.
33. (a)Whitmore, L.; Wallace, B. A. *Nucleic Acids Res.* **2004**, *32*, W668–W673. DOI: <https://doi.org/10.1093/nar/gkh371>. (b)Whitmore, L.; Wallace, B.A. *Biopolymers* **2008**, *89*, 392–400. DOI: <https://doi.org/10.1002/bip.20853>. (c)<http://www.cryst.bbk.ac.uk/cdweb>, accessed in June 2022. (d)Sreerama, N.; Woody, R.W. *Anal. Biochem.* **2000**, *287*, 252–260.
34. Micsonai, A.; Wien, F.; Bulyáki, É.; Kun, J.; Moussong, É.; Lee, Y.-H.; Goto, Y.; M.; Réfrégiers, Kardos, J. *Nucleic Acids Research* **2018**, *46*, W315 W322. DOI: <https://doi.org/10.1093/nar/gky497>. <http://bestsel.elte.hu>.
35. Hernández-Gordillo, A.; Hernández-Arana, A.; Campero, A.; Vera-Robles, L.I. *Langmuir.* **2014**, *30*, 4084-4093. DOI: <https://doi.org/10.1021/la500203k>.

Gaining Insights into Folding/Unfolding Protein Structures and their Importance for Several Applications: Historical Research Generated in the Biophysical Chemistry Area

Arturo Rojo-Domínguez^{1*}, Leonardo D. Herrera-Zúñiga^{2*}

¹Departamento de Ciencias Naturales Universidad Autónoma Metropolitana - Cuajimalpa, 05348, CDMX, México.

²Área Académica de Biofísicoquímica Departamento de Química, Universidad Autónoma Metropolitana-Iztapalapa, Iztapalapa, 09340, CDMX, México.

***Corresponding author:** Arturo Rojo-Domínguez, email: arojo@correo.cua.uam.mx; Leonardo D. Herrera-Zúñiga, email: leo.hz@xanum.uam.mx

Received May 25th, 2024; Accepted August 15th, 2024.

DOI: <http://dx.doi.org/10.29356/jmcs.v68i4.2297>

Abstract. The research largely focuses on investigating the mechanisms of protein folding and unfolding in proteins, namely triosephosphate isomerase, glucosamine-6-phosphate deaminase, laccase, and bacteriophage M13. The article examines the mechanisms of protein denaturation and renaturation using kinetic equations, thermodynamic models, and molecular dynamics (MD) simulations. These results enhance our understanding of the thermodynamic and kinetic characteristics of these proteins. Furthermore, the study highlights the importance of conserved residues, as well as the influence of environmental conditions such as pH and temperature on protein stability and folding. These discoveries have potential implications in biotechnology and medicine, including the creation of protein-based products and therapies for infectious diseases, and neurodegenerative disorders. The paper acknowledges the groundbreaking contributions of Dr. Andrés Hernández Arana to the field of protein physical chemistry in México. His work has greatly influenced the progress of research in the areas of protein stability and kinetics.

Keywords: Protein stability; folding and unfolding; fluorescence and circular dichroism spectroscopy; differential scanning calorimetry; kinetics.

Resumen. La investigación se centra en los mecanismos de plegado y desplegado de proteínas; estos mecanismos incluyen la triosafosfato isomerasa, la glucosamina-6-fosfato desaminasa, lacasa y el bacteriófago M13. Se utilizan ecuaciones cinéticas, modelos termodinámicos y simulaciones de dinámica molecular (MD) para analizar los mecanismos de desnaturalización y renaturalización de proteínas. Estos hallazgos nos ayudan a comprender mejor las características cinéticas y termodinámicas de estas proteínas. Además, el estudio destaca la importancia de los residuos conservados y puentes salinos en las proteínas, así como el impacto de los factores ambientales como el pH y la temperatura en la estabilidad y el plegado de las proteínas. Estos hallazgos tienen repercusiones en los campos de la biotecnología y la medicina, como la creación de productos y terapias basados en proteínas para enfermedades infecciosas y trastornos neurodegenerativos. El artículo reconoce el trabajo pionero del Dr. Andrés Hernández Arana en México en el campo de la termodinámica de proteínas. Su trabajo ha sido fundamental para el avance de la investigación en las áreas de cinética y estabilidad de proteínas.

Palabras clave: Estabilidad de proteínas; plegamiento y desplegamiento; espectroscopía de fluorescencia y dicroísmo circular; calorimetría diferencial de barrido; cinética.

Introduction

Biophysical methods for studying proteins

Studying protein dynamics is not just an academic pursuit. It is a crucial step towards understanding the role of structural flexibility and dynamics in protein activity and catalytic efficiency, which in turn informs the design of proteins with enhanced activity. Differential scanning calorimetry (DSC), fluorescence spectroscopy, circular dichroism (CD) spectroscopy and molecular dynamics (MD) simulation are crucial methods for investigating protein characteristics, providing valuable information on their composition, durability, and performance [1-4]. This combination enables the verification and improvement of theoretical models, resulting in a more comprehensive and precise understanding of the protein folding process.

Differential Scanning Calorimetry is an effective method to study how heat affects proteins and how their structures change. It does this by precisely measuring the flow of heat energy caused by changes in structure caused by temperature. This technique provides extensive information on crucial thermodynamic characteristics, such as the melting temperature (T_m), the enthalpy change (ΔH), the heat capacity change (ΔC_p), the Gibbs free energy change (ΔG), and the entropy change (ΔS). These measurements are critical for understanding protein stability in a variety of contexts and developing more robust proteins for industrial and therapeutic applications. It is crucial to understand how past processes affect the present behavior of a protein, as in some cases, denaturation processes cannot be reversed, and the scanning rate significantly impacts studies on protein unfolding using differential scanning calorimetry [5-8]. Hysteresis, a phenomenon that illustrates the influence of a system's past trajectory on its current state, plays a crucial role in investigating unfolding and refolding processes and comprehending the branching points in folding landscapes [9,10]. Mathematically, the heat capacity (C_p) of the sample is defined as (equation 1):

$$C_p = \frac{dQ}{dT} \quad (1)$$

where dQ is the amount of heat added and dT is the change in temperature. The temperature difference (dT) between the sample and reference changes each time the sample undergoes an exothermic or endothermic transition, causing a proportional difference in heat flow rate (dQ) which is critical for accurately determining the thermodynamic parameters and understanding the thermal behavior of proteins [11]:

$$\Delta H = \int_{T_i}^{T_f} \Delta C_p dT \quad (2)$$

where ΔC_p is the difference in heat capacity between the unfolded and native states, and T_i and T_f are the initial and final temperatures of the transition. The melting temperature (T_m) is identified as the point where the heat capacity exhibits a maximum, indicating the temperature at which the protein unfolds. The Gibbs free energy change (ΔG) can be related to ΔH and ΔS using the equation 3 [11]:

$$\Delta G = \Delta H - T\Delta S \quad (3)$$

Gaining an understanding of these interconnections enables a more sophisticated analysis of differential scanning calorimetry data, which in turn leads to a more profound comprehension of protein

thermodynamics and folding processes. This knowledge also aids in the development of resilient proteins for a variety of purposes. A typical plot from a differential scanning calorimetry experiment is shown in Fig. 1. It displays a graph of heat absorbed (endothermic) and heat given off (exothermic) as a function of the sample's temperature. It is crucial to emphasize that Fig. 1 does not represent all possible transitions in a single sample. Rather, it serves as a visual representation of the most often observed forms of transition.

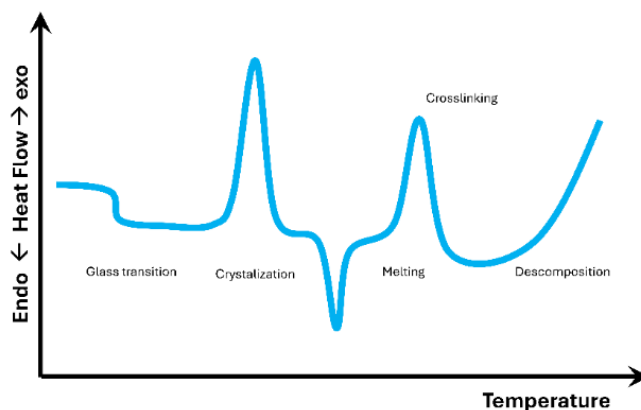


Fig. 1. Differential scanning calorimetry curve.

Circular Dichroism is a spectroscopic technique that measures the difference in absorption of left-handed and right-handed circularly polarized light by chiral molecules. This method is widely used to study protein conformation, stability, and ligand-protein interactions. By looking at the different ways that circularly polarized light is absorbed, circular dichroism gives information about the secondary and tertiary structures of biomolecules. This lets scientists figure out how changes caused by mutations, or the environment affect those structures. Ellipticity θ in circular dichroism is related to the difference in absorbance (ΔAbs) by the equation 4 [3,12]:

$$\theta = 32.98x\Delta Abs \quad (4)$$

Additionally, molar ellipticity (θ_m) calculated as (equation 5):

$$\theta_m = \frac{100 \cdot \theta}{C \cdot l} \quad (5)$$

where θ is the ellipticity in degrees, C is the molar concentration of amino acids, and l is the cell length in cm.

The far-ultraviolet spectrum, ranging from 180 to 240 nm, offers a means to assess a protein's secondary structure composition. Fig. 2 shows the characteristic circular dichroism spectra of the secondary structures α -helix, β -sheet, and random coil. In circular dichroism studies of unfolding processes, the spectra can be taken at different temperatures to monitor structural changes; another, more convenient, option is to monitor those changes as the temperature is continuously varied with a constant heating ramp, which allows for the calculation of the fraction of unfolded protein and thus the equilibrium constant for the process. The van't Hoff analysis, derived from the temperature-dependent equilibrium provides the van't Hoff enthalpy (ΔH) and entropy (ΔS), the midpoint of the unfolding transition (T_m), and the unfolding free energy (ΔG). These parameters are crucial for understanding the stability and folding behavior of proteins under varying thermal conditions [12-14]

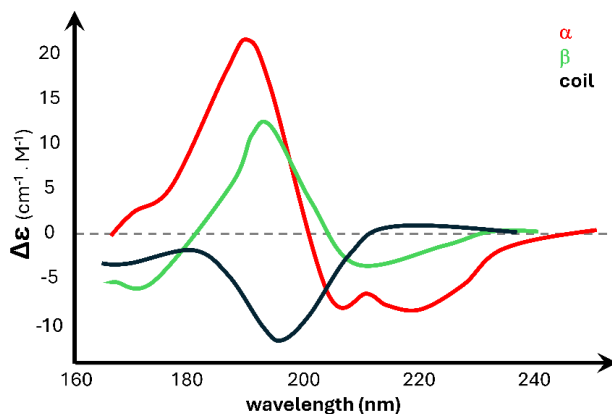


Fig. 2. Displays the circular dichroism curve representing the typical secondary structures: α -helix (red), β -sheet (green), and random coil (black).

Fluorescence spectroscopy, on the other hand, is a technique used to study the emission of light from a substance after it has absorbed light of a different wavelength. Fluorescence spectroscopy is an analytical method that is both very sensitive and selective. It is used to study the structural and thermodynamic characteristics of proteins. This approach utilizes the fluorescent properties of amino acids like tryptophan and tyrosine to detect proteins at low levels and observe real-time changes in protein structure, such as folding and unfolding. The thermodynamic parameters assessed include the free energy of the denaturation process and its cooperativity. Fluorescence intensity is related to the concentration of the fluorophore by equation 6 [15,16]:

$$I_F = k_0 \cdot \phi_F \cdot [F] \quad (6)$$

where I_F is the fluorescence intensity, k_0 is a constant depending on the detection system, ϕ_F is the fluorescence quantum yield, and $[F]$ is the fluorophore concentration expressed like $(1 - 10^{-\epsilon cl})$.

If dilute solutions are used so that less than 2 % of the excitation energy is absorbed, an approximation can be made that simplifies the fluorescence spectroscopy analysis. In this scenario, the absorbance (Abs) is sufficiently low, allowing us to assume that the relationship between fluorescence intensity (I_F) and the concentration of the fluorophore $[F]$ is linear. This linearity arises because Beer-Lambert's law, which describes light absorption, can be approximated as follows for very low absorbance values (equation 7) [17,18]:

$$I_F = k_0 \cdot \phi_F \cdot \epsilon cl \quad (7)$$

Protein fluorescence, particularly from tryptophan residues, is highly sensitive to the molecule's surrounding environment. Tryptophan residues inside the protein's interior are found in less water-soluble environments, resulting in a change in the wavelength at which they emit light. In nonpolar settings, the fluorescence maximum occurs at shorter wavelengths, whereas in polar situations, it shifts towards longer wavelengths. So, changes in the protein that affect the area around tryptophan residues, like protein-ligand interactions [19], structural changes, or unfolding, will change the fluorescence spectrum. Fluorescence's sensitivity makes it an excellent tool for examining protein dynamics, as seen in Fig. 3.

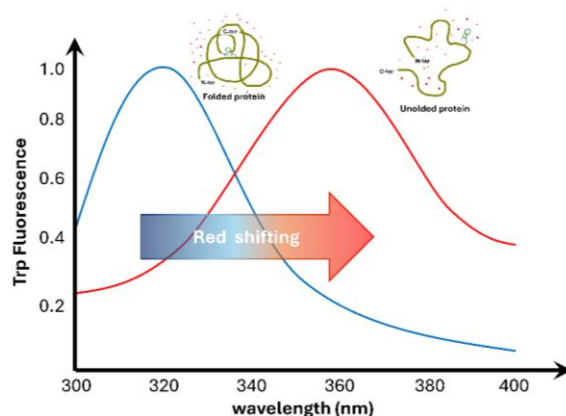


Fig. 3. Intrinsic fluorescence. Protein unfolding, followed by the movement of a tryptophan residue from the hydrophobic internal environment, to the aqueous outside (shown by the red dots). The tryptophan fluorescence spectra are shown on a graph under two conditions: native (blue) and denaturated (red). The redshift is found (arrow) when the maximum emission moves toward longer wavelengths.

Molecular Dynamics simulation enables the observation of protein's dynamic behavior at the atomic scale, providing vital atomistic information to comprehend the fundamental principles of protein stability and unfolding. These simulations have the capability to compute thermodynamic characteristics such as Gibbs free energy (ΔG), enthalpy (ΔH), entropy (ΔS), and, under some circumstances, heat capacity change (ΔC_p) [1,18,20,21].

Newton's second law is used in molecular dynamics simulations to calculate the trajectories of atoms (equation 8):

$$F = m \cdot a \quad (8)$$

where F is the force acting on an atom, m is the atom's mass, and a is the atom's acceleration.

The interaction law is determined by the potential function $U(r_1, \dots, r_N)$, which represents the potential energy of N interacting atoms based on their locations, $r_i = (x_i, y_i, z_i)$. The force acting on the i -th atom is dictated by the gradient in relation to atomic displacements. The equation $F_i = \nabla_{r_i} U(r_1, \dots, r_N)$ represents the relationship between the force F_i and the position vector $\nabla_{r_i} U$ [22].

The components of the gradient are given by (equation 9):

$$F_i = \left(\frac{\partial U}{\partial x_i}, \frac{\partial U}{\partial y_i}, \frac{\partial U}{\partial z_i} \right) \quad (9)$$

Discovering an accurate potential to replicate authentic energy surfaces is complex, yet it simplifies calculations. Atomic force field models and classical molecular dynamics rely on empirical potentials that include specific functional forms to accurately depict the system's physics and chemistry. The following is an example of a force field commonly used in biosystems simulations (equation 10):

$$U(r_1, \dots, r_N) = \sum_{bond} \frac{a_i}{2} (l_i - l_{i0})^2 + \sum_{angle} \frac{b_i}{2} (\theta_i - \theta_{i0})^2 \quad (10)$$

$$\begin{aligned}
 & + \sum_{\text{torsion}} \frac{c_i}{2} [1 + \cos(n\omega_i - \gamma_{i0})] \\
 & + \sum_{\text{atom pair}} 4\varepsilon_{ij} \left[\left(\frac{\sigma_{ij}}{r_{ij}} \right)^{12} - \left(\frac{\sigma_{ij}}{r_{ij}} \right)^6 \right] + \sum_{\text{atom pair}} k \frac{q_i q_j}{r_{ij}}
 \end{aligned}$$

In this equation

- The first term sums over all bonds, with a_i representing the bond strength and $(l_i - l_{i0})$ being the deviation from the equilibrium bond length.
- The second term sums over all angles, with b_i representing the angle force constant and $(\theta_i - \theta_{i0})$ being the deviation from the equilibrium angle.
- The third term sums over all torsions, with c_i representing the torsional force constant and $[1 + \cos(n\omega_i - \gamma_{i0})]$ accounting for the periodic torsional potential.
- The fourth term sums over all pairs of atoms not bonded chemically, with $4\varepsilon_{ij} \left[\left(\frac{\sigma_{ij}}{r_{ij}} \right)^{12} - \left(\frac{\sigma_{ij}}{r_{ij}} \right)^6 \right]$ representing the Lennard-Jones potential.
- The final term sums over all pairs of point charges q_i and q_j separated by distance r_{ij} , representing the Coulomb potential $k \frac{q_i q_j}{r_{ij}}$.

Replica exchange molecular dynamics (REMD) is an advanced approach in Molecular Dynamics simulation that greatly enhances the exploration of different conformations in a protein's structure. This technique is particularly useful for studying the intricate mechanisms involved in protein folding [23,24]

The combination of these experimental and computational methodologies allows for the examination of mutation consequences, exploration of protein-ligand interactions, and comprehension of the variables that influence protein aggregation, folding, and unfolding. Adopting this approach is crucial for enhancing our comprehension of basic biological events and has substantial implications in the fields of drug development and biotechnology. Table 1 displays the essential experimental techniques and their corresponding thermodynamic parameters used to evaluate protein stability.

Gaining a comprehensive understanding of the processes involved in protein folding and unfolding is crucial in the field of biophysical chemistry research. This knowledge allows for significant insights into the structure, dynamics, and function of proteins. Understanding this information is vital for proteins like triosephosphate isomerase (TIM), glucosamine-6-phosphate deaminase (G6PD), laccase, and bacteriophage M13, since they perform critical tasks in many biological processes [7,25-33].

The researchers in the Department of Biophysical Chemistry at the Universidad Autónoma Metropolitana (UAM), Iztapalapa campus, are dedicated to understanding the processes involved in protein folding and unfolding. These mechanisms have a profound impact on catalysis, metabolism, and biological activity. Scientists use experimental methods such as spectroscopy and calorimetry to examine the changes in protein structure and stability under various situations, such as fluctuations in temperature and variations in denaturant concentration. The study's findings provide important insights into the molecular pathways responsible for protein misfolding and aggregation, which are occurrences associated with neurodegenerative disorders. For instance, the processes of unfolding and refolding TIM proteins take place gradually within a certain temperature range where both the native and unfolded forms exist simultaneously. Researcher studies at UAMI have developed time-dependent kinetic equations to explain the unfolding and refolding mechanisms of TIM, G6PD, and laccase proteins. These equations include variables like as temperature and heating rates, which contribute to a more comprehensive comprehension of the hysteresis cycles seen in experiments. These discoveries provide valuable information on the thermodynamic and kinetic characteristics of these proteins, enhancing our understanding of protein folding and stability [7,25-30,32,33].

The main difficulties related to the irreversible thermal denaturation of proteins in aqueous solutions arise from the clumping together of unfolded polypeptide chains at elevated temperatures. Aggregation may result in irreversibility during the unfolding of proteins, making it challenging to use equilibrium

thermodynamics to investigate protein denaturation. Irreversible unfolding curves are often found in oligomeric proteins that consist of subunits of moderate to large size.

Hysteresis cycles in protein unfolding-refolding profiles during temperature scanning are characterized by distinct, non-overlapping paths for unfolding and refolding [33].

This suggests that equilibrium conditions are not achieved inside the transition area. The difference between the temperature-dependent curves during heating and cooling results in a loop-shaped pattern, which is often associated with the sluggish kinetics of the unfolding and refolding operations. This occurs within a temperature range where both the native and unfolded states coexist in equilibrium. The protein's sluggish response speeds lead to distinct behaviors throughout the processes of heating (unfolding) and cooling (refolding), which ultimately result in hysteresis. Examining these cycles yields useful observations on the dynamics of protein unfolding and refolding processes, revealing the protein transitions.

Protein transition models: two-state mechanisms and their implications

Temperature-induced transitions in small proteins can often be represented, as a simpler two-state model involving only two molecular species: the native (N) and the unfolded (U) states. This model assumes that the populations of protein molecules are nearly at equilibrium at any temperature. Therefore, equilibrium thermodynamics can be used to determine the basic thermodynamic parameters of the unfolding process, such as the enthalpy and entropy changes associated with the transition from N to U. If differential scanning calorimetry data are available, it is also possible to calculate the heat capacity change, thus allowing for a complete description of the native-protein stability given by the Gibbs free energy change as a function of temperature.

A linkage between thermodynamics and kinetics can be easily found by writing the unfolding and refolding reactions as first-order unimolecular reactions, since the equilibrium constant for the $N \leftrightarrow U$ transition is then expressed as $K = \frac{k_u}{k_r}$. This dynamical formalism, as shown below, is also very useful for analyzing systems that are reversible yet far from equilibrium.

More complex models and irreversibility

In many cases, however, some complicating factors preclude a thermodynamic, straightforward analysis. For many large proteins (i.e., those with a molecular mass of about 25 kDa or larger), irreversible reactions, such as aggregation or chemical modification of some amino acid side chains, taking place when the protein is (partially) unfolded, prevent the recovery of the native structure and its biological activity. In some instances, aggregation can be avoided by decreasing protein concentration, thus making the system reversible; in other cases, even though the N to U process can be made to behave reversibly under low protein concentrations, the unfolding-refolding curves show that the overall system is far from equilibrium.

The first case reviewed below exemplifies how irreversibility has been dealt with in many early studies of protein thermal unfolding; in summary, data analysis has been carried out by assuming that irreversibility reactions occur more slowly than unfolding-refolding processes, and thus the equilibrium formalism can be applied to those data, with the inclusion of an irreversible step at the end of unfolding: $N \leftrightarrow U \rightarrow D$, where D stands for an irreversibly denatured molecular form that can be the initiator of molecular aggregation.

Glucosamine-6-phosphate deaminase

The thermal unfolding of glucosamine-6-phosphate deaminase, an allosteric enzyme whose structure is described as a trimer of dimers ($M_r = 178.2$ kDa, Fig. 4), was studied by Hernández-Arana et al. using the scanning calorimeter at the Biophysical Chemistry Laboratory in UAMI. The unfolding/denaturation process of the enzyme was irreversible in the wide concentration range compatible with the experiments (0.6 to 7.3 mg/mL); however, analysis of scanning endotherms showed that the process is complex, involving several hexameric intermediates and, probably, two dissociated states. Evidence from this analysis suggested that some transitions are close to equilibrium, whereas at least one transition introduces irreversibility. Furthermore, applying an equilibrium formalism for data analysis seemed justified, provided scanning rates above 0.75 K/min were used.[7]

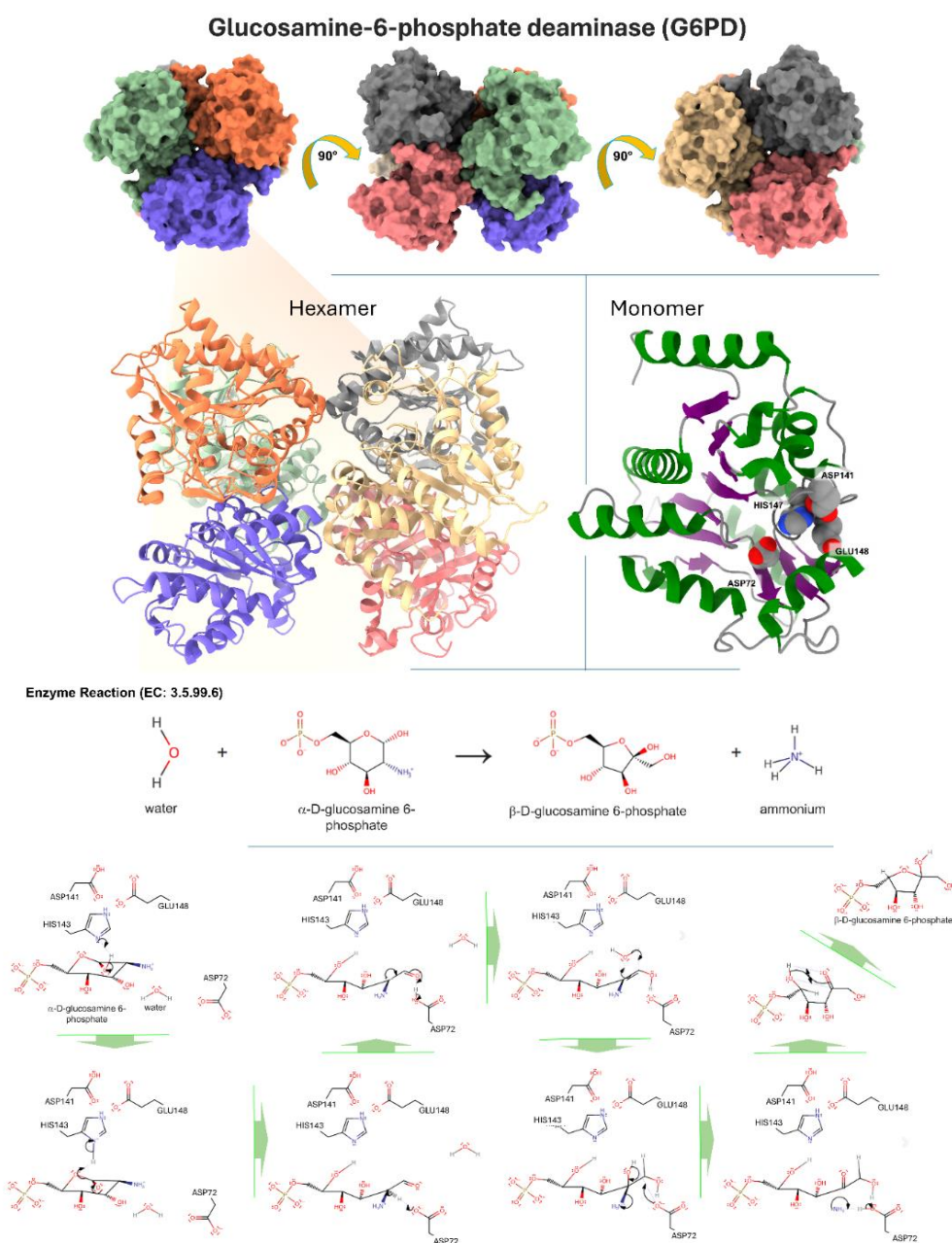


Fig. 4. Displays the three-dimensional structure of glucosamine-6-phosphate deaminase, which can be identified by its PDB code 1FS5 and UniProt code P0A759. The upper section depicts the hexameric arrangement of glucosamine-6-phosphate deaminase. The protein undergoes a 90° rotation in three different orientations, which emphasizes the presence of six monomers colored in bright green, blue, orange, red, gray, and warm yellow. The hexamer is presented as a cartoon image with the same color scheme, located in the bottom left corner. Glucosamine-6-phosphate deaminase is classified as belonging to the alpha/beta class. It has a 3-layer structure with an $\alpha/\beta/\alpha$ sandwich architecture and a Rossmann fold topology (CATH: 3.40.50.1360).

Furthermore, it has a distinctive signal of glucosamine/galactosamine-6-phosphate isomerase (Prosite). The lower middle portion exhibits a monomer that emphasizes the amino acids in the active site: ASP72, ASP141,

HIS147, and GLU148. The α -helices are shown in the color green, the β -sheets in the color purple, and the loops in the color light gray. The enzymatic reaction type and catalytic mechanism are given on the left. During the ring-opening process of α -D-glucosamine 6-phosphate, the hydroxyl group at C1 is deprotonated by HIS147. The oxyanion undergoes a collapse, resulting in the C-O link breaking. This process also leads to the deprotonation of HIS147 by the newly created oxyanion. ASP72 removes a proton from the carbon that is connected to the amino group. The carbanion that is formed initiates a rearrangement of the double bond, removing a proton from ASP72. Water undergoes electrophilic addition across the π link between carbon atoms C1 and C2. The water molecule approaches from the same side as ASP72. ASP72 works as a base by taking away a proton from the newly attached hydroxyl group. This gets rid of the ammonia in the substrate. When released, ammonia removes a proton from ASP72, forming ammonium and restoring the enzyme to its original state. The linear product spontaneously cyclizes outside the enzyme's active region, forming β -D-fructofuranose 6-phosphate and ammonium [34].

By assuming that six two-state sequential transitions are involved in the global process (two of which involve dissociation into subunits, eq. 1), the authors developed a set of equations describing the behavior of differential scanning calorimetry endotherms. Fitting to experimental data gave enthalpy changes and T_m (i.e., the temperature at the maximum of the heat capacity curve) seemingly reasonable for the unfolding and dissociation values expected of protein subunits of similar size.

Triosephosphate isomerase

Triosephosphate isomerase from *Saccharomyces cerevisiae* (γ TIM) is an enzyme that has a molecular weight of 54.52 kDa, with each subunit weighing 27 kDa (as shown in Fig. 5). Its biological function is to facilitate the reversible conversion between the triosephosphate isomers dihydroxyacetone phosphate and D-glyceraldehyde 3-phosphate. Hernández-Arana and colleagues have conducted research on this topic for more than twenty years, using circular dichroism as well as other calorimetric and spectrometric methods [25-28,32].

The triosephosphate isomerase dimer requires denaturation at around 63 °C, according to data reported by Hernández-Arana and colleagues. The unfolded state of γ TIM is maintained when a temperature heating ramp of 0.2 °C/min is applied. Still, as seen in Fig. 6, a cooling ramp of 2 °C/min restores its original characteristics, indicating that there may be related events in the folding process. Some oligomeric proteins exhibit hysteresis cycles that may indicate a complex folding mechanism. This is backed up by research conducted between 2001 and 2022, which highlights the significance of dimer formation or stability in the folding and function of γ TIM. Later on, similar findings were made in complex proteins, where functional areas impact the early folding process and impede folding. Even though these regions make folding more complicated, they may also affect other kinetic behaviors that are related to the system's stability.

The lack of hysteresis in lysozyme may be ascribed to its enduring monomeric structure and its two-state heat transition. This process exhibits a denaturation enthalpy (ΔH) and heat capacity (ΔC_p) that signify a substantial but reversible alteration in structure. Specifically, the thermodynamic parameters for lysozyme unfolding–refolding are within a range that leads to fast unfolding and refolding reactions within the transition region; therefore, the two-state system is very near to equilibrium at any temperature of the heating or cooling curves. In addition, this process reduces water-repellent surface contact and promotes effective and fast restoration of the original structure, preventing misfolding side reactions.

However, because of its dimeric structure and a more intricate denaturation process, γ TIM displays noticeable hysteresis. The enthalpy change (ΔH) required for denaturation of γ TIM is much greater, indicating the need to disrupt a larger number of intermolecular connections throughout the process. In addition, the heat capacity (ΔC_p) in γ TIM is much higher, suggesting a notable change in the exposure of polar and nonpolar surfaces after denaturation. The higher ΔC_p value means that there are a lot of hydrophobic surfaces, which helps the unfolded subunits stick together. This makes it harder for them to get back to normal, which is what causes the hysteresis that we see.

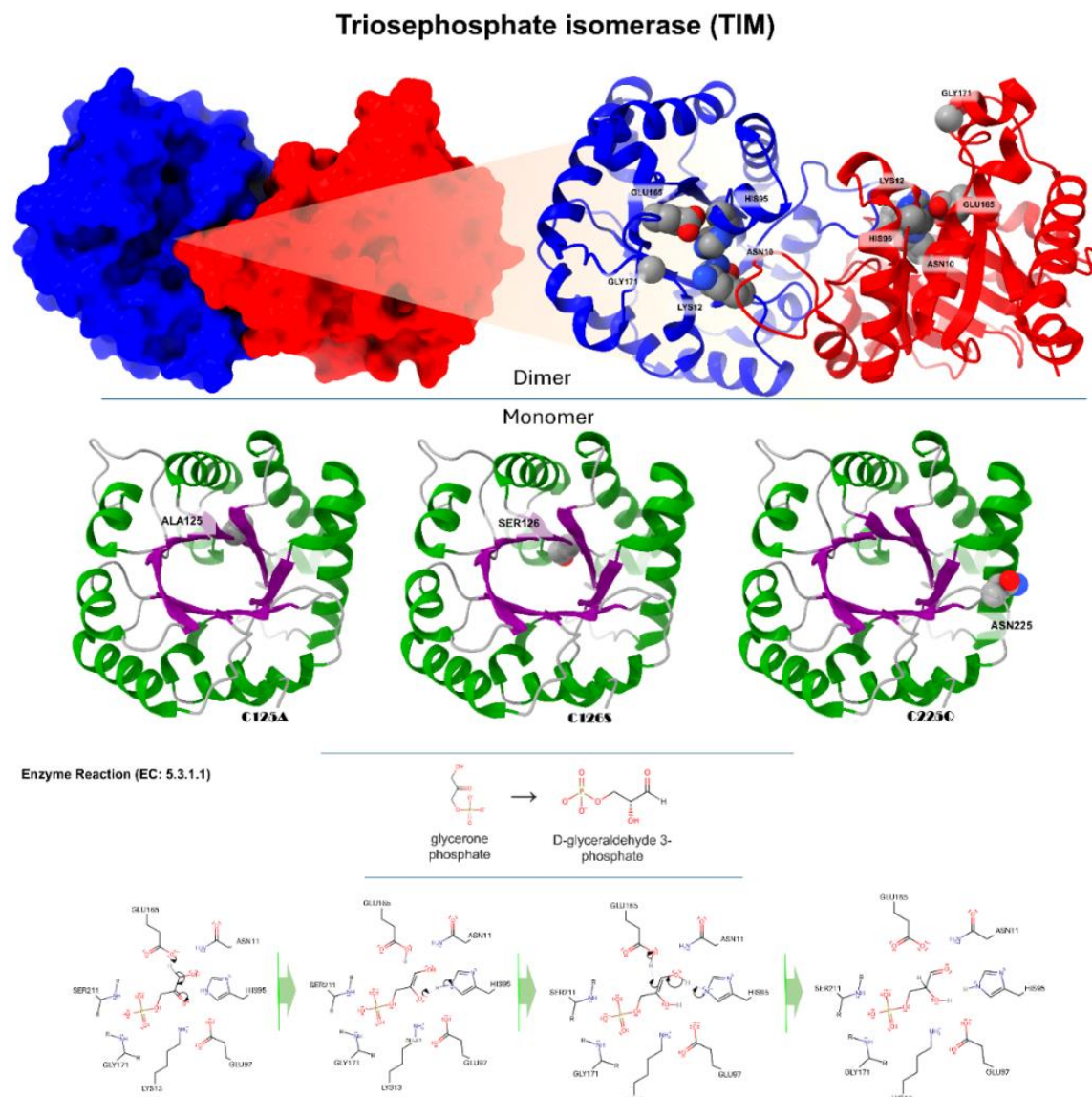


Fig. 5. Depicts the tridimensional configuration of triosephosphate isomerase (yTIM), which can be identified by its PDB code 1YPI and UniProt code P00942. The top part illustrates the dimeric configuration of yTIM. The monomers are shown in blue and red, while the dimer is illustrated in a cartoon depiction with the same color scheme. This highlights the active site amino acids: ASN10, LYS12, HIS95, GLU165, and GLY171. yTIM is categorized as an alpha/beta class protein, characterized by an Alpha/Beta Barrel structure, a TIM Barrel topology, and belonging to the Aldolase class I homology (CATH: 3.20.20.70). Moreover, it has a unique and recognizable molecular pattern and characteristics of the triosephosphate isomerase family (Prosite). The bottom portion displays a monomer with the "TIM barrel" fold. The secondary structural components are shown using α -helices in the color green, β -sheets in the color purple, and loops in the color light gray. This section focuses on three specific mutants: C125A, C126S, and C225Q. The enzymatic reaction type and catalytic mechanism are given on the left. By taking away a proton from the alpha-carbonyl carbon of glycerin phosphate, GLU165 acts as the catalytic base. HIS95 is deprotonated by the enolate. It is stronger for the hydrogen bond between the residue and the enol-transition state when HIS95 is deprotonated than when it is protonated. Now, HIS95 is the catalyst that helps the enol turn into an aldehyde while also selectively deprotonating C2. The formation of the final D-glyceraldehyde 3-phosphate is complete [34].

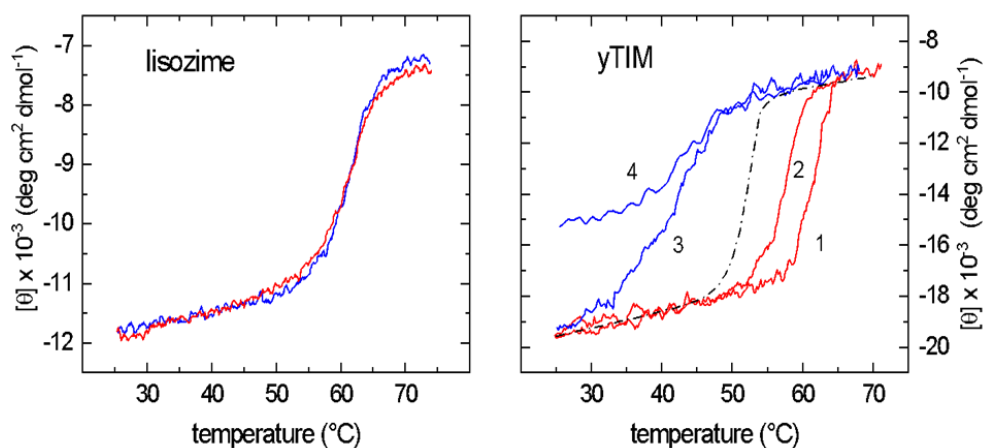


Fig. 6. Hysteresis landscape for yTIM unfolding investigations. (A) Diagram of the lysozyme's unfolding-refolding process, characterized by overlapping equilibrium curves. The graphs illustrate the fast unfolding-refolding kinetics that lead to a molecular system being very close to "equilibrium" at any temperature registered during the scanning. (B) Hysteresis graph associated with yTIM unfolding-refolding curves. In contrast to lysozyme illustrated in Figure A, the "equilibrium" unfolding and folding contours for yTIM are not equivalent. The 2.0 °C/min-heating and cooling cycle (curves 1 and 3) allows recovery of yTIM native structure and enzymatic activity. On the other hand, the heating and cooling process at 0.2 °C/min creates a misfolded state that makes it harder for yTIM to return to its original shape and structure, as shown in curves 2 and 4. For a two-state model, the apparent (hypothetical) equilibrium during the transition is denoted by the dashed line in the center. Figure redrawn from [25].

Hysteresis is a phenomenon in which systems delay their response to imposed stressors. This delay is caused by a bifurcation in the folding topography, as demonstrated by Hernández-Arana and colleagues' research on thermal unfolding and refolding in yTIM. In these experiments, a bistable system is shown, where the equilibrium state is defined by both the current and the beginning circumstances, acting as a memory for the system. Hysteresis occurs when the present and previous states of a system interact to affect its current state. Fig. 6 shows the results of the hysteresis-generating tests performed on yTIM, which include different ramps of heating and cooling. Curves 1 and 3 show quasi-perfect hysteresis behavior for yTIM, where the final state approaches the initial state but via a different pathway. On the other hand, curves 2 and 4 fall outside the hysteresis "zone," indicating non-ideal hysteresis. The dashed line shows the limit of ideal folded and refolded processes. The figure illustrates the intricate complexity of the folding domain. This finding provides further evidence that mechanisms other than folding might be influencing temperature-induced instability. When the functional dimer is formed, hysteresis takes place, as seen by the complex folding landscape of yTIM. Specifically, the stability of yTIM and the length of the catalytically active dimer half-life are determined by the temperature-dependent kinetic barrier to the unfolding mechanism. Significantly, hysteresis in TIM is reduced when heating and cooling rates are lower.

The hysteresis model of the TIM protein, as shown in Fig. 7, demonstrates a progressive temperature change at a rate of 2 °C per minute. This model exhibits unfolding at about 70 °C, followed by refolding by a different pathway. Approximately half of the protein remains in its folded configuration at a temperature of 45 °C, and its original shape is restored when the temperature is lowered to 25 °C. The enzyme activity recovers almost entirely, reaching roughly 95 % while maintaining the original structure [25].

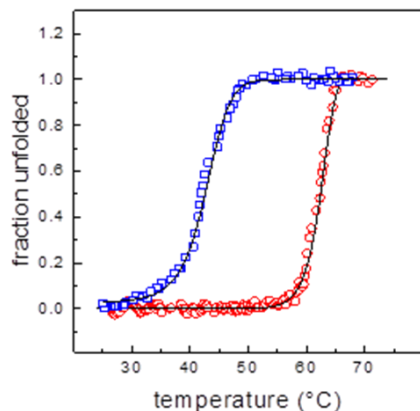


Fig. 7. Model for ideal yTIM hysteresis. Hysteresis is a characteristic that accounts for a system's delayed reaction to external forces. This phenomenon may occur when there is a split in the unfolded landscape, causing the system to have two stable conditions. This finding suggests that the system's equilibrium is influenced by both the initial and final states, demonstrating the system's ability to preserve structural information. The two graphs shown depict hysteresis curves, with red indicating unfolding and blue representing refolding, from experimental data; the separation between these two curves along the heating and cooling routes is noted, but it is important to highlight that the native state remains the same at the start and end of the cycle. Solid lines are simulations computed using a couple of differential equations (one, first-order reaction for unfolding and the other second-order for refolding), which together reproduce the characteristics of the hysteresis cycle, thus demonstrating that yTIM unfolding–refolding is a reversible far-from-equilibrium transition under kinetic control [33].

Recent studies on yTIM indicate that the hysteretic effect may be absent in some conditions. For example, mutations like ARG189-ASP225 or D225Q that disrupt the ionic interactions, or mutations like C126A and C126S1 that stop catalysis, could reduce this effect [26-28]. Hysteresis happens when folding transition states change because domain or monomer transitions affect complicated unfolding processes. Cohesive cooperation, on the other hand, makes refolding more efficient. Also, hysteresis can be seen in protein aggregation and association events, which shows how hard it is to get back to the original tertiary structure. This is particularly true for proteins like yTIM, which are very stable and have complex topologies like barrel superstructures. Hernández-Arana's current study on yTIM folding, supported by spectroscopic evidence, uses molecular dynamics simulations to clarify folding states. A first-order kinetics study showed that the structures of unfolded and refolded yTIM are different at different pH levels. This suggests that the unfolding and refolding processes are separate [32].

This is consistent with TIM's resistance to temperature and pH variations, indicating that it folds almost completely and returns to its original shape when refolded. The analysis showed a decrease in helix content and an increase in unordered structures over time, following first-order kinetics and consistent with changes in ellipticity values at fixed wavelengths. Rate constants derived from structural fractions matched those from circular dichroism data variations at specific wavelengths. Molecular dynamics simulations performed with AMBER and OPLS force fields captured essential elements of the unfolding process observed in circular dichroism experiments. The simulations demonstrated significant loss of helical regions and an increase in coil structures at high temperatures. Additionally, beta strands appeared more resilient at elevated temperatures. The unfolding process occurred faster at high pH, aligning with experimental observations. However, structural differences between low- and high-pH unfolded yTIM were relatively small in Molecular dynamics simulations, indicating the need for further refinement of Molecular dynamics simulations procedures to better match experimental data.

However, we believe that our progress in computational studies of protein unfolding can be beneficial in this field. Nonetheless, the task of estimating the fundamental process behind protein folding has not yet been tackled. In this context, we are working on a simple approach that allows us to accurately calculate the metastable states of protein unfolding in yTIM using Markov State Models (MSM) with PyEMMA [7,25-30,32,33]. This approach is based on computing the folded and unfolded states at different temperatures and pH using molecular dynamics

highlighted. The laccase enzyme is seen on the far right, with its secondary structure color-coded: α -helices are represented in green, β -sheets in purple, and loops in light gray. Laccase is considered a member of the main β -class, with a β -Sandwich architecture, an immunoglobulin-like topology, and cupredoxin-blue copper protein homology, according to the CATH database (CATH: 2.60.40.420). In addition, it includes the Multicopper oxidase signatures (Prosite).

The 2D representations in the lower left corner illustrate the catalytic site and its relationships. In the center of the 3D model, the catalytic location is displayed. This picture demonstrates the interconnection between CYS453, HIS452, and HIS454, which together constitute an electron route. Both pictures depict the OH molecule as an intermediate in the oxidation process, while the H₂O molecule is the result of the redox reaction. The enzymatic reaction type and catalytic mechanism are given on the left. The first active site, called the "blue site," is close to the surface and is where organic substrates like phenols or aromatic and aliphatic amines go through oxidation. This lets the T1 copper ion get electrons through a bonded HIS458 residue. HIS395 and CYS453 complete the coordination of the T1 copper ion, which is not exposed to the solvent. The electrons that are taken out of the substrates are sent through two internal electron transfer pathways that start with CYS453, the T1 copper ligand. The electrons are then divided between HIS452 and HIS454, which respectively attach to the T3(a) and T3(b) copper ions in the second active site. In this process, oxygen molecules undergo reduction and join together to form water molecules. This site consists of a trinuclear copper cluster, which is composed of a T2 copper ion and two T3 copper ions organized in a triangle pattern. It is located between domains I and III and is attached to eight histidine residues and two water molecules. The T2 copper is tri-coordinated, forming bonds with HIS64, HIS398, and a single water molecule. The two T3 coppers exhibit tetra-coordination. T3(a) copper is coordinated by residues HIS111, HIS400, and HIS452, whereas T3(b) copper is coordinated by residues HIS66, HIS109, and HIS454. Furthermore, a water molecule is asymmetrically bound between the two T3 copper ions [34].

In 2012, Hernández-Arana and his colleagues conducted groundbreaking research using differential scanning calorimetry to assess the heat capacity of the enzyme laccase. Using this approach, they were able to investigate the thermal changes that occurred in the enzyme in both its native and unfolded forms under a variety of pH settings. The work of Hernández-Arana and others showed that the way copper ions are coordinated inside the laccase enzyme may affect how much heat it can hold (see Fig. 9). The data provided important information about the protein's thermal properties. For instance, laccase forms heat-denatured forms related to "molten-globule-like" structures, thus resembling other proteins such as α -lactalbumin, staphylococcal nuclease, and apomyoglobin. At low pH, the compact denatured state of laccase has residual structure and a low heat capacity, in contrast to the extended denatured state formed at pH 9.0.

The presence of copper ions and their interactions with the protein matrix can affect the magnitude in the protein's heat capacity, particularly during the thermal denaturation process. Therefore, heat capacity studies may provide insights into the thermodynamic characteristics of copper-containing proteins (see Fig. 9), especially when pH is imposed as an experimental variable.

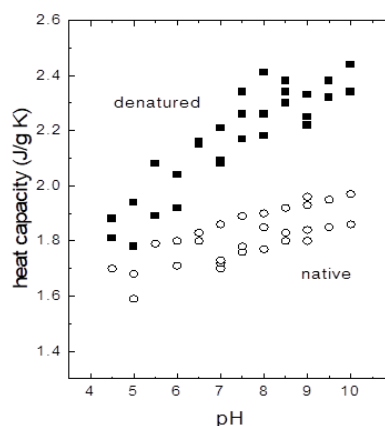


Fig. 9. The specific heat capacity (C_p) of a laccase protein in various structural states is plotted against the pH of the surroundings. Specific heat capacity is a characteristic that specifies how much thermal energy is needed to increase a substance's temperature by a certain amount. The graph shows four unique groupings of data points

that reflect various laccase states: native-compact, native-extended, denatured-compact, and denatured-extended. The "native" state refers to the laccase in its folded and fully functioning form, usually at physiological pH values. As the pH varies, the protein's conformation may alter, making it more "compact" or "extended." With subsequent pH fluctuations, the laccase eventually achieves a "denatured" condition in which it loses its functional three-dimensional structure. The graph depicts how the specific heat capacity varies with conformational state and pH, which is critical for understanding laccase's stability and function under different situations. Redrawn from Biophysical Chemistry, 2012 [29].

The work by Hernández-Arana et al. showed that changes in the specific heat capacity of denatured laccase depend on pH. These changes show that the protonation or deprotonation of certain residues, like histidine residues, is important for keeping laccase's three-dimensional structure stable. The importance of pH in influencing the laccase enzyme's stability is highlighted. Histidine residues play an essential role in laccase folding since they are required for catalysis and tertiary structure. They operate as scaffolding, anchoring coppers at the active site and enhancing laccase's functional structure. They also serve as a route for the electron transport circuit used in laccase oxidation-reduction action. By looking more closely at specific heat capacity at different pH levels, Hernández-Arana and his colleagues learned more about the thermodynamic aspects of laccase folding and unfolding processes. This explains the irreversible processes involved in laccase folding, as seen in Fig. 9. When pH approaches 7.5, denatured laccase functions similarly to a completely solvated polypeptide chain, taking on a disordered structure comparable to an unfolded polypeptide chain. Denatured laccase retains some structural integrity between pHs 4.5 and 5.5. This demonstrates the significance of histidine residue protonation for enzyme stability. In the cited research, Equation 11 was used to explain how denatured laccase converts from compact to stretched configurations as a function of pH [29].

$$d \ln \left(\frac{K_{eq}}{dpH} \right) = -2.303(V^E - V^C) \quad (11)$$

This equation shows the connection between changes in the logarithm of protonation equilibrium and the number of protons connected to the denatured laccase forms that are compact (C) and extended (E), which are shown as V^E and V^C , respectively. Its aim is to represent V^E and V^C as explicit pH functions. The constant K_{eq} represents the equilibrium transition between V^E and V^C , allowing for a quantitative understanding of how specific amino acid residues affect the transition between these conformations. Furthermore, from analysis of experimental data, it was found that two histidine residues are most likely involved in the heat capacity change shown in Fig. 9.

In a 2016 paper published in Analytical Biochemistry, Hernández-Arana and his colleagues found that the excess molar heat capacity function (C_p) for the *Myceliophthora thermophila* laccase denaturation displays a complex profile that can be analyzed by four sequential irreversible steps (Fig. 10). These authors devised an analysis method consisting in step-by-step deconvolution of experimental C_p curves that rendered kinetic constants and activation parameters for each of the four individual steps. Parameters derived from the analysis help us understand the thermal denaturation of the *Myceliophthora thermophila* laccase enzyme in more depth; moreover, these parameters can be used to extrapolate the denaturation kinetics constants to other temperatures, thus giving a way to estimate the stability of the enzyme under conditions in which it is employed in commercial processes [30].

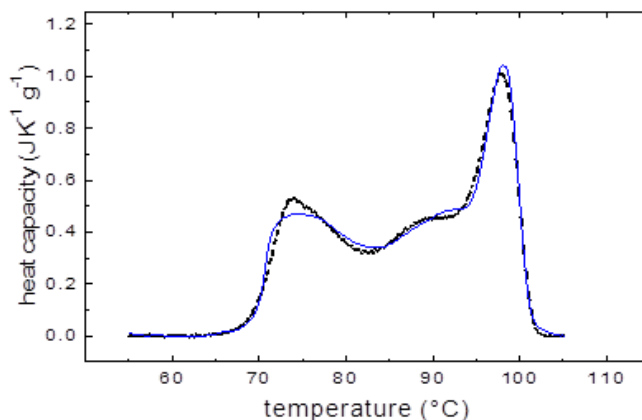


Fig. 10. Specific heat capacity (C_p) of laccase from *Myceliophthora thermophila* as a function of temperature. The graph shows a trend in which the specific heat capacity varies with temperature, with at least four peaks marking the temperature at which the laccase absorbs the greatest heat per unit rise in temperature. This suggests that four individual reaction steps take place during laccase denaturation. The graph's peaks show irreversible denaturation transitions, some of them involving structural transitions in which copper atoms participating in structural staples have probably been lost. The differential scanning calorimetry profile was recorded at a rate of $0.5\text{ }^\circ\text{C}/\text{min}$ at pH 6.0; the solid line shows the experimental curve $C_{p, \text{obs}}$ curve (dotted line). The solid line, on the other hand, shows the calculated curve ($C_{p, \text{calc}}$), which was constructed by the deconvolution method described in reference 10.

Filamentous bacteriophage M13

In 2019, Hernández-Arana and colleagues conducted research that specifically examined the thermal cooperativity in the aggregation of the filamentous bacteriophage M13, commonly referred to as M13. Their study yielded valuable insights into the stability and dynamic characteristics of the M13 coat structure under varying environmental conditions [31].

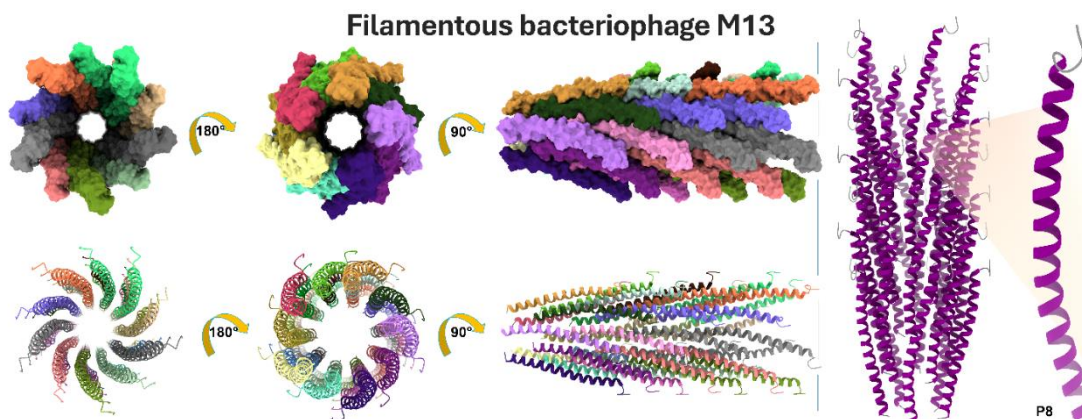


Fig. 11. Structural interpretation of the filamentous M13 phage capsid, which can be identified by its PDB code 2MJZ and UniProt code P69541. On the left, the multimeric organization of M13 is displayed, in which each individual subunit is determined by a P8 protein. The capsid undergoes a 90° and 180° rotation in three distinct orientations, revealing the existence of multimers that are colored in 35 different hues. The lower section displays the same orientations, but with ribbon representations in a cartoon-like manner. On the left, the M13 phage and the monomeric unit P8 are shown with their secondary structures color-coded. The α -helix is predominantly purple, while the N-ter and C-ter coil sections are depicted in gray. The M13 bacteriophage is classified as belonging to the Mainly Alpha

class and has an Up-down Bundle architecture and single α -helix topology (CATH: 1.20.5.80), characterized by being engaged in coiled-coils or other helix-helix interactions. Filamentous phages are elongated and semiflexible viruses composed of single-stranded DNA that have a unique affinity for infecting bacteria. The M13 phage, belonging to the *Inoviridae* family, has a length of roughly 1 micrometer and a diameter of around 7 nanometers. The P8 subunit consists of a single helix, six connections between helices, and beta turns. The structure is mostly formed of α -helical subunits that are stacked together in pentamers. These subunits exhibit a type II β -turn at the N-terminal. Each subsequent pentamer is separated by a vertical distance of 16.6–16.7 Å and an angular displacement of 36.1–36.6°. A repeated hydrophobic stacking pocket makes the subunit packing stronger. Each subunit adds a different hydrophobic residue to one of four pockets that are spread out along the subunit sequence.

The denaturation process of M13 exhibits notable changes in cooperativity in response to variations in pH and ethanol concentration. The denaturation process becomes more cooperative at elevated pH levels or greater ethanol concentrations. Specifically, the first denaturation phase gets more cooperative as the activation enthalpy for this step rises. Cooperativity is significantly enhanced by the presence of ethanol, particularly at values of 30 % and 50 %. The enhanced cooperativity is ascribed to the reinforcement of electrostatic contacts between DNA and proteins, which is caused by a reduction in the dielectric constant of the solvent [31].

P8 moieties have a vital function in modifying the arrangement of M13 bacteriophage molecules in response to surrounding conditions. Due to its versatility, the M13 coat structure has a high degree of malleability. When the virus is exposed to ethanol, it undergoes cooperative denaturation in more significant areas, demonstrating its capacity to adapt to environmental changes dynamically.

The M13 bacteriophage has remarkable heat stability compared to other viruses and nanostructures often used in research and applications. The M13 bacteriophage is characterized as a virus that can withstand high temperatures and the presence of high levels of ethanol without being affected. At higher temperatures, this virus undergoes denaturation, which occurs at a temperature higher than other filamentous and rod-like viruses, such as the rigid tobacco mosaic virus (TMV). The temperature at which denaturation is maximized (T_m) is twelve Celsius degrees higher than TMV at the same pH. Furthermore, the denaturation process of M13 exhibits a level of cooperativity equal to or greater than that of TMV under certain circumstances. The results indicate that the M13 bacteriophage has remarkable resistance to changes in temperature and shows a high degree of cooperation, making it a desirable option for a range of uses in biotechnology, materials science, and nanotechnology. The virus's ability to withstand extreme temperatures and environmental conditions creates opportunities for developing novel materials and technologies that may use its distinctive characteristics. The M13 bacteriophage has remarkable flexibility and adaptability to various pH levels and ethanol concentrations, enabling it to preserve its structural integrity and functionality even under diverse environmental circumstances. Due to its properties, it is well-suited for several applications in biotechnology and industry, including targeted medication delivery, gene therapy, and the formation of self-assembling nanostructures [31].

Conclusions

This work offers a comprehensive understanding of the dynamics and stability of important proteins by using modern biophysical methods such as differential scanning calorimetry, fluorescence, and circular dichroism. The research conducted at UAMI has provided valuable insights into the folding mechanics, stability, and possible biotechnological uses of proteins such as triosephosphate isomerase, Glucosamine-6-phosphate deaminase, laccase, and filamentous bacteriophage M13. Advancements like as deconvolution in differential scanning calorimetry analysis have facilitated a more thorough understanding of denaturation processes. The combination of multiples disciplines in this technique has significant promise for expanding the field of biotechnology and developing novel protein-based medicines.

A Tribute to Dr. Andrés Hernández Arana, a Trailblazer in the Physical Chemistry of Proteins in México

Dr. Andrés Hernández Arana is a well-regarded authority in the field of protein thermodynamics, with a remarkable career spanning five decades. He first studied biochemical engineering at IPN's National School of Biological Sciences. He then went on to get both a Master's and Doctorate in Chemistry from UAMI. Dr. Hernández Arana led the creation of the "Biofísicoquímica" (Biophysical Chemistry) research area in 1992 while serving as Head of the Chemistry Department at UAMI from 1989 to 1993. This area has evolved into a center for cutting-edge research, with a particular emphasis on investigating the stability of thermodynamic systems, studying the kinetics of proteins, and using sophisticated spectroscopic, calorimetric, and computational techniques. His scientific impact is demonstrated by the publication of more than 70 scientific papers and the guidance provided to 14 Master's and 13 Ph.D. students. The commitment of Dr. Hernández Arana has had a profound influence on Mexico's scientific community, creating an enduring heritage that continues to motivate successive generations of scholars.

Acknowledgments

We thank A. Hernández-Arana for insightful discussions and M. M. Herrera-Martínez for scientific encouragement.

References

1. Galano-Frutos, J. J.; Nerín-Fonz, F.; Sancho, J. *Journal of Chemical Information and Modeling*. **2023**, 63, 7791-7806. DOI: <https://doi.org/10.1021/acs.jcim.3c01107>.
2. Mei, G. *Encyclopedia of Life Sciences*. **2017**, 1-7. DOI: <https://doi.org/10.1002/9780470015902.A0027584>.
3. Kelly, S. M.; Price, N. C. *Encyclopedia of Life Sciences*. **2009**. DOI: <https://doi.org/10.1002/9780470015902.A0003043.PUB2>.
4. Wiczorek, G.; Niedzialek, D. *Encyclopedia of Life Sciences*. **2020**, 1-18. DOI: <https://doi.org/10.1002/9780470015902.A0003048.PUB3>.
5. Johnson, C. M. *Archives of Biochemistry and Biophysics*. **2013**, 531, 100-109. DOI: <http://dx.doi.org/10.1016/j.abb.2012.09.008>.
6. Sanchez-Ruiz, J. M. *Subcellular Biochemistry* **1995**. DOI: https://doi.org/10.1007/978-1-4899-1727-0_6.
7. Hernández-Arana, A.; Rojo-Dominguez, A.; Altamirano, M. M.; Calcagno, M. L. *Differential Scanning Calorimetry of the Irreversible Denaturation of Escherichia coli Glucosamine-6-phosphate Deaminase?*; 1993.
8. Kuril, A. K. *Journal of Pharmaceutical Research International*. **2024**, 36, 179-187. DOI: <https://doi.org/10.9734/jpri/2024/v36i77549>.
9. Nakama, T.; Rossen, A.; Ebihara, R.; Yagi-Utsumi, M.; Fujita, D.; Kato, K.; Sato, S.; Fujita, M. *Chemical Science* **2023**, 14, 2910-2914. DOI: <https://doi.org/10.1039/D2SC05879K>.
10. Barrett, J. *The International Journal of Biochemistry & Cell Biology*. **2001**, 33 2, 105-117. DOI: [https://doi.org/10.1016/S1357-2725\(00\)00083-2](https://doi.org/10.1016/S1357-2725(00)00083-2).
11. Durowoju, I. B.; Bhandal, K. S.; Jian Hu, B. C.; Kirkitadze, M. *Journal of Visualized Experiments*. **2017**, 121 (e55262). DOI: <https://doi.org/10.3791/5526>.
12. Greenfield, N. J. *Nature Protocols* **2007**, 1, 2527-2535. DOI: <https://doi.org/10.1038/nprot.2006.204>.
13. Preeti Gupta, A. I.; Ahmad, F.; Hassan, M. I. *Protein Folding Dynamics and Stability*. **2023**. DOI: https://doi.org/10.1007/978-981-99-2079-2_1.
14. Seelig, J.; Schönfeld, H.-J. Thermal protein unfolding by differential scanning calorimetry and circular dichroism spectroscopy Two-state model versus sequential unfolding. *Quarterly Reviews of*

- Biophysics* **2016**, 49, e9. From Cambridge University Press Cambridge Core. DOI: <https://doi.org/10.1017/S0033583516000044>.
15. Lakowicz, J. R. 10. Protein Fluorescence BT - *Principles of Fluorescence Spectroscopy*. **2006**, 1-47. DOI: https://doi.org/10.1007/978-0-387-46312-4_16.
 16. dos Santos Rodrigues, F. H.; Delgado, G. G.; Santana da Costa, T.; Tasic, L. *BBA Advances*. **2023**, 3. DOI: <https://doi.org/10.1016/j.bbadv.2023.100091>.
 17. Michalet, X.; Weiss, S.; Jäger, M. Single-molecule fluorescence studies of protein folding and conformational dynamics. In *Chemical Reviews*, **2006**; Vol. 106, pp 1785-1813.
 18. Basak, S.; Chattopadhyay, K. Studies of protein folding and dynamics using single molecule fluorescence spectroscopy. In *Physical Chemistry Chemical Physics*, Royal Society of Chemistry: **2014**; Vol. 16, pp 11139-11149.
 19. Gooran, N.; Kopra, K. Fluorescence-Based Protein Stability Monitoring—A Review. In *International Journal of Molecular Sciences*, **2024**; Vol. 25.
 20. Yu, M.; Si, W.; Sha, J. Molecular Dynamics Simulation for Protein Unfolding. In *15th IEEE International Conference on Nano/Micro Engineered and Molecular System, NEMS 2020, 2020/9//*, **2020**; Institute of Electrical and Electronics Engineers Inc.: pp 382-386. DOI: <https://doi.org/10.1109/NEMS50311.2020.9265552>.
 21. Caflisch, A.; Paci, E. *Protein Folding Handbook*. **2008**, 2, 1143-1169. DOI: <https://doi.org/10.1002/9783527619498.CH32>.
 22. Scheraga, H. A.; Khalili, M.; Liwo, A. Protein-folding dynamics: Overview of molecular simulation techniques. In *Annual Review of Physical Chemistry*, Annual Reviews Inc.: 2007; Vol. 58, pp 57-83.
 23. Singh, Y.; Hocky, G. M. Improved Prediction of Molecular Response to Pulling by Combining Force Tempering with Replica Exchange Methods. *The Journal of Physical Chemistry B*. **2024**, 128, 706-715. DOI: <https://doi.org/10.1021/acs.jpcc.3c07081>.
 24. Kříž, P.; Beránek, J.; Spiwok, V. *The Journal of Chemical Physics*. **2024**, 160, 184116. DOI: <https://doi.org/10.1063/5.0204992> (accessed 7/14/2024).
 25. Benítez-Cardoza, C. G.; Rojo-Domínguez, A.; Hernández-Arana, A. *Biochemistry*. **2001**, 40, 9049-9058. DOI: <https://doi.org/10.1021/bi010528w>.
 26. González-Mondragón, E.; Zubillaga, R. A.; Saavedra, E.; Cháñez-Cárdenas, M. E.; Pérez-Montfort, R.; Hernández-Arana, A. *Biochemistry*. **2004**, 43 (11), 3255-3263. DOI: <https://doi.org/10.1021/bi036077s>.
 27. Reyes-López, C. A.; González-Mondragón, E.; Benítez-Cardoza, C. G.; Cháñez-Cárdenas, M. E.; Cabrera, N.; Pérez-Montfort, R.; Hernández-Arana, A. *Proteins: Structure, Function and Genetics*. **2008**, 72, 972-979. DOI: <https://doi.org/10.1002/prot.21994>.
 28. Cruces-Angeles, M. E.; Cabrera, N.; Perez-Montfort, R.; Reyes-Lopez, C. A.; Hernandez-Arana, A. *Protein & Peptide Letters* **2011**, 18, 1290-1298. DOI: <https://doi.org/10.2174/092986611797642715>.
 29. Toledo-Núñez, C.; López-Cruz, J. I.; Hernández-Arana, A. *Biophysical Chemistry*. **2012**, 167, 36-42. DOI: <https://doi.org/10.1016/j.bpc.2012.04.004>.
 30. Toledo-Núñez, C.; Vera-Robles, L. I.; Arroyo-Maya, I. J.; Hernández-Arana, A. *Analytical Biochemistry*. **2016**, 509, 104-110. DOI: <https://doi.org/10.1016/j.ab.2016.07.006>.
 31. González-Cansino, J. L.; Vieyra-Eusebio, M. T.; Vera-Robles, L. I.; Hernández-Arana, A. *Thermochimica Acta*. **2019**, 672, 53-59. DOI: <https://doi.org/10.1016/j.tca.2018.12.010>.
 32. García-Gutiérrez, P.; Camarillo-Cadena, M.; Vera-Robles, L. I.; Zubillaga, R. A.; Hernández-Arana, A. *Spectrochimica Acta - Part A: Molecular and Biomolecular Spectroscopy* **2022**, 274. DOI: <https://doi.org/10.1016/j.saa.2022.121039>.
 33. Hernández-Arana, A. *Advances in Protein Physical Chemistry* **2008**, 139-154.
 34. Ribeiro, A. J. M.; Holliday, G. L.; Furnham, N.; Tyzack, J. D.; Ferris, K.; Thornton, J. M. *Nucleic Acids Research* **2018**, 46 (D1), D618-D623. DOI: <https://doi.org/10.1093/NAR/GKX1012>.
 35. Junghare, V.; Bhattacharya, S.; Ansari, K.; Hazra, S. Markov State Models of Molecular Simulations to Study Protein Folding and Dynamics. In *Protein Folding Dynamics and Stability: Experimental and Computational Methods*, Saudagar, P., Tripathi, T. Eds.; Springer Nature Singapore, **2023**; pp 147-164.

36. Arregui, L.; Ayala, M.; Gomez-Gil, X.; Gutierrez-Soto, G.; Hernandez-Luna, C. E.; Herrera de Los Santos, M.; Levin, L.; Rojo-Dominguez, A.; Romero-Martinez, D.; Saparrat, M. C. N.; et al. Laccases: structure, function, and potential application in water bioremediation. *Microb Cell Fact* **2019**, 18 (1), 200. From NLM Medline. DOI: <https://doi.org/10.1186/s12934-019-1248-0>.

Entropic Uncertainty Relations and Mutual Information Correlation Sums in Two-level Superposition States of Coupled Oscillators

Saúl J. C. Salazar¹, Humberto G. Laguna¹, Angel Garcia-Chung^{1,2,3}, Robin P. Sagar¹

¹Departamento de Química, Universidad Autónoma Metropolitana, Avenida Ferrocarril San Rafael Atlixco No. 186, Leyes de Reforma 1a Sección, Iztapalapa, 09310, Ciudad de México, México.

²Max Planck Institute for Mathematics in the Sciences, Leipzig, Germany.

³Tecnológico de Monterrey, Escuela de Ingeniería y Ciencias, Estado de México 52926, México.

*Corresponding author: Humberto G. Laguna, email: hlaguna@izt.uam.mx

Received May 1st, 2024; Accepted July 3th, 2024.

DOI: <http://dx.doi.org/10.29356/jmcs.v68i4.2265>

Abstract. The effects of quantum interferences and interaction strength on the entropic uncertainty relations, and on mutual information correlation sums, are examined in two-level superposition states of two coupled oscillators. The presence of quantum interferences results in a movement of the entropy sums toward the uncertainty relation bound, for both attractive and repulsive interaction potentials. On the other hand, these interferences suppress the statistical correlations in the presence of an attractive potential, while the correlations increase for a repulsive one. In general, stronger interactions between particles move the entropy sums away from bound, with the result that the systems possess larger statistical correlations. However, there are superposition and attractive interaction regimes, where the entropy sum of an interacting system can actually lie closer to the bound, in comparison to the corresponding non-interacting one. In these cases, the statistical correlations between particles is lesser for the interacting systems, as compared to the non-interacting ones. These effects are not observed when repulsive potentials are present. Here, the non-interacting systems lower-bound both the entropy sums and correlation measures. These results offer insights into the nature of superposition or quantum interference effects in interacting quantum systems, and the behavior in terms of the entropic uncertainty relations, statistical correlations and interaction strength.

Keywords: Entropic uncertainty relations; mutual information; information theory; momentum space; coupled oscillators.

Resumen. Se examinan los efectos que las interferencias cuánticas y la magnitud de la interacción tienen sobre las relaciones de incertidumbre entrópicas, así como sobre las sumas de correlaciones de información mutua, en estados de superposición de dos niveles de dos osciladores acoplados. La presencia de interferencias cuánticas da como resultado un movimiento de las sumas entrópicas hacia la cota de la relación de incertidumbre, tanto para potenciales de interacción atractivos como repulsivos. Por otra parte, en presencia de un potencial atractivo, estas interferencias suprimen las correlaciones estadísticas, mientras que las correlaciones aumentan en presencia de uno repulsivo. En general, con interacciones más fuertes entre partículas, las sumas de entrópicas se alejan de la cota, dando como resultado mayores correlaciones estadísticas en los sistemas. Sin embargo, existen regímenes de superposición e interacción atractiva, en los cuales la suma entrópica de un sistema interactuante puede estar más cerca de la cota, en comparación con el sistema no interactuante correspondiente. En estos casos, las correlaciones estadísticas entre partículas son menores para los sistemas interactuantes que para los no interactuantes. Estos efectos no se observan en los potenciales repulsivos. En este caso, los sistemas no interactuantes establecen límites inferiores tanto para las sumas entrópicas como para las medidas de correlación. Estos resultados dan información sobre la naturaleza de los efectos de superposición o interferencia cuántica en

sistemas cuánticos interactuantes, y su comportamiento en términos de relaciones de incertidumbre entrópica, correlaciones estadísticas y fuerza de interacción.

Palabras clave: Relaciones de incertidumbre entrópica; información mutua; teoría de la información; espacio de momento; osciladores acoplados.

Introduction

The Heisenberg uncertainty principle is a principal element of quantum mechanics. Much discussion has centered around its analysis and interpretation, and of the limits it provides about the behaviour of quantum systems. In recent decades, there has been a migration away from the textbook Kennard-Robertson formulation in terms of standard deviations [1], to ones in terms of Shannon information entropies, or indeed of other entropies. Developments in femtosecond spectroscopy allow one to examine chemistry at the uncertainty limit [2]. To celebrate the fiftieth anniversary of UAMI, we will first present a brief review of what has been accomplished with information theory in previous years, before moving on to discuss the particular problem.

The Shannon entropic uncertainty relation [3–6] is given as

$$S_{(N \cdot D)_x} + S_{(N \cdot D)_p} > \ln(\pi e \hbar)^{N \cdot D} \quad (1)$$

where D is the dimension of the system and N is the number of particles. The focus of this work will be to consider $D = 1$ and one and two particle systems, for which we will employ the notation of S_x and S_p , to indicate the respective entropy sums in the equation above. The Shannon entropies in position (x) and in momentum (p) space are defined in terms of the one-particle wave functions or densities as

$$S_x = S_{1_x} = - \int |\Psi(x)|^2 \ln |\Psi(x)|^2 dx, \quad (2)$$

$$S_p = S_{1_p} = - \int |\Phi(p)|^2 \ln |\Phi(p)|^2 dp.$$

The integration limits depend on the particular coordinate system that is used to represent the system. The wave function, $\Psi(x)$, in the position representation, is connected to $\Phi(p)$, the one in the momentum representation, by the Dirac-Fourier transform. All densities used in this work are normalized to unity and the integration limits are $(-\infty, +\infty)$.

One-particle Shannon entropies can also be obtained from a N -particle wave function or density, by first integrating over the $N-1$ particles to obtain one-particle reduced densities,

$$\rho(x) = \int |\Psi(x, x_2, \dots, x_N)|^2 dx_2 \dots dx_N, \quad (3)$$

$$\pi(p) = \int |\Phi(p, p_2, \dots, p_N)|^2 dp_2 \dots dp_N,$$

Shannon entropies for these reduced densities are obtained by replacing $|\Psi(x)|^2$ and $|\Phi(p)|^2$ by the reduced densities, $\rho(x)$ and $\pi(p)$, in Eq. (2). The Shannon entropies in each representation are measures of the (de)localization in the underlying distributions. Their values increase as the distributions delocalize and decrease when they localize. In fact, the Shannon entropy of a continuous distribution can be negative-valued, in contrast to a discrete one which is lower-bounded by zero. It should not be surprising that these measures have attracted attention in quantum chemistry, where questions of electron localization and delocalization are prevalent concepts. These are global measures of (de)localization in the system, in contrast to local ones which aim to locate regions within the system where electrons are localized. In a more general context, localization is

associated with phenomena resulting from wave interference, within the quantum mechanical framework. There has been keen interest in understanding the behaviour of the Shannon entropy sum in a variety of different quantum systems [6–24]. In quantum chemistry, one of the first works involved a study of the behaviour in neutral and charged atoms, as well as in the harmonic oscillator, in ground and excited states [7]. The idea put forth at this time was that the entropy sum serves as a measure of wave function quality and could be thus employed in quantum chemistry. The Shannon entropy, in the context of atomic systems, is a functional of the one-electron density, so it should also not be surprising that this work originated from a renowned density functional laboratory. Later, it was proposed that the entropy sum could be used as a correlation measure in atomic systems [10]. These ideas propelled interest into the study of molecular systems [25,26]. It was also noted that the position space Shannon entropy emerges naturally from the logarithmic mean excitation energy within the local plasma approximation, used in stopping power measurements and experiments [27].

The entropy sum is also of interest in quantum chemistry, since it combines perspectives from both the position and momentum space representations. While the position or coordinate space representation is prevalent in quantum chemistry, there has also been efforts to develop a momentum space quantum chemistry [28]. Other avenues of interest include study of the time dependent behaviour of S_r , which has been analysed in simple systems [29,30]. There has also been interest in the application of these measures to study Bose-Einstein condensates [21,22]. The relation of the entropy sum with the entropies of the marginals of the Wigner phase-space distribution has also been documented [31]. Shannon entropies of phase-space quantum distributions have been considered [31,32].

Recently, there has been considerable activity in the examination of the entropy sum in confined quantum systems, to examine the influence of physical barriers, potentials, and static and dynamic external fields [33–44]. To date, these studies have been limited to few-particle systems, however one can expect that larger systems will be addressed in the near future. Several groups in both the chemistry and physics departments of UAM-Iztapalapa are actively engaged in using Shannon measures to furthering the understanding of behaviour in confined quantum systems.

One can also consider the Shannon entropies of the pair densities in position and in momentum space, for two or more particle systems. To date, these entropies have not seen a widespread interest, as compared to the one-particle ones. Pair densities represent the probabilities of finding one particle with a particular position (momentum), and the other particle with another position (momentum). Thus, questions of particle interaction, and indeed chemical bonding in molecular systems, should be naturally encoded into these quantities. There is active research into the development of a pair density functional theory [45–47].

The Shannon pair entropy components and their sum [in Eq. (2)] have been examined in atomic systems [48–50] and in two- and three-particle coupled oscillators [51,52]. These entropies can be defined in terms of two-particle wave functions as ($S_\Gamma = S_{2_x}$, $S_\Pi = S_{2_p}$)

$$\begin{aligned} S_\Gamma &= -\int |\Psi(x_1, x_2)|^2 \ln |\Psi(x_1, x_2)|^2 dx_1 dx_2, \\ S_\Pi &= -\int |\Phi(p_1, p_2)|^2 \ln |\Phi(p_1, p_2)|^2 dp_1 dp_2. \end{aligned} \quad (4)$$

The S_T results from summation of S_Γ and S_Π . One can also calculate Shannon pair entropies from reduced densities of N -particle systems which have been reduced by integrating over $N-2$ particles,

$$\begin{aligned} \Gamma(x_1, x_2) &= \int |\Psi(x_1, x_2, \dots, x_N)|^2 dx_3 \dots dx_N, \\ \Pi(p_1, p_2) &= \int |\Phi(p_1, p_2, \dots, p_N)|^2 dp_3 \dots dp_N. \end{aligned} \quad (5)$$

For the two-particle systems in this work, there is no reduction to get the pair density since it is the squared norm of the two-particle wave function. It is hoped that the coming years will bear witness to an increasing interest in pair density information measures, especially in molecular systems.

The electron correlation problem is one that is particularly relevant in quantum chemistry, and results from the fact that there is no exact solution to the Schrödinger equation when electrons interact through repulsive Coulomb potentials. Indeed, quantum chemistry can be conceived as a field devoted to the development of methods to obtain approximate solutions of varying accuracies. Hence, there was a need for a measure to adequately capture the inclusion or exclusion of interaction effects in the wave function. The correlation energy was introduced [53] as the difference between the exact non-relativistic energy and the Hartree-Fock energy of the particular system. This quantity was thus used as a measure of evaluating the approximate wave function. It is important to emphasize here that this evaluation is not directly based on the wave function but rather on its corresponding energy. Furthermore, the Fermi correlation due to the antisymmetry of the wave function, is not included, since it is presumably subtracted out in the Hartree-Fock reference.

On the other hand, other avenues of defining correlation through statistical correlation measures have a long history [54–56]. This seems a natural evolution due to the Born interpretation of the wave function as a probability density. Hence, correlation is measured here not from the energy perspective, but rather from the wave function characteristics, in terms of the associated probability distribution. The statistical correlation coefficient from statistics was introduced as one such measure [55,56]. It captures linear relations between variables by examining differences between (linear) expectation values of the pair densities and those of the one-particle densities. One advantage is that these measures do not depend on the selection of a particular external reference such as Hartree-Fock. However, they include all correlation effects, including those from the interactions and also the symmetry of the wave function.

Pair mutual information is another statistical correlation measure, which is capable of capturing the non-linear correlations. It has been utilized in many distinct areas, both in its discrete and continuous forms [52, 57–65]. It is defined in position and in momentum space as

$$I_x = \int \Gamma(x_1, x_2) \ln \left[\frac{\Gamma(x_1, x_2)}{\rho(x_1)\rho(x_2)} \right] dx_1 dx_2 = 2S_\rho - S_\Gamma \geq 0 \quad (6)$$

$$I_p = \int \Pi(p, p_2) \ln \left[\frac{\Pi(p_1, p_2)}{\pi(p_1)\pi(p_2)} \right] dp_1 dp_2 = 2S_\pi - S_\Pi \geq 0 \quad (7)$$

In this work, the marginals of the pair densities in the denominator of the logarithmic arguments are the one-particle reduced densities defined in Eq. (3) with $N = 2$. Note that the two marginals are equal, due to particle indistinguishability of the quantum mechanical density. In the general case, these are not necessarily equal. These measures have been examined in the ground and excited states of atomic systems and coupled oscillators [51, 52, 66]. The sum of the position and momentum space mutual information will be given as

$$I_t = I_x + I_p = 2S_t - S_T \geq 0. \quad (8)$$

I_t quantifies the correlation, by taking the weighted difference between the one- and two-variable entropy sums. Statistical correlation measures provide a means to directly examine, interpret and relate behaviour, with that of the interactions that are present in a particular system. This is distinct from the previous vision of defining a correlation measure for the purpose of classifying the goodness of an approximate wave function. Quantum chemistry calculations yield approximate wave functions and densities. Thus, there is always the question if interpretation of phenomena from a particular calculation is valid, or a product of the limitations of the particular method that is used. In these instances, model systems which yield exact wave functions and densities, can offer a guide to illuminate the path forward. One such system consists of two oscillators that are coupled by a harmonic two-body potential [67] and has been used in density functional theory [68–74].

The model: Two-particle coupled oscillators

The Hamiltonian of two coupled oscillators in canonical coordinates in position space, considering atomic units ($m = \hbar = 1$) is

$$H = -\frac{1}{2} \left(\frac{\partial^2}{\partial x_1^2} + \frac{\partial^2}{\partial x_2^2} \right) + \frac{1}{2} \omega^2 (x_1^2 + x_2^2) \pm \lambda^2 (x_1 - x_2)^2, \quad (9)$$

where ω is the natural frequency of the oscillators and λ is the intensity of the interaction potential, with the positive sign for the attractive case and the negative sign for the repulsive case. The value of λ is bounded for the repulsive case by $\lambda < \omega/\sqrt{2}$ in order to obtain a bound state.

The canonical coordinates in position space (x_1, x_2) can be transformed into Jacobi coordinates (R, r), thus the eigenfunction is separable in the new coordinates, and can be written as a product of two eigenfunctions

$$\Psi(x_1, x_2) = \psi_{n_R}(R) \psi_{n_r}(r) \quad (10)$$

with

$$\psi_{n_R}(R) = \left(\frac{\alpha_1^{\frac{1}{4}}}{2^{n_R} n_R! \pi^{\frac{1}{2}}} \right)^{\frac{1}{2}} e^{-\frac{1}{2}\sqrt{\alpha_1}R^2} H_{n_R} \left(\alpha_1^{\frac{1}{4}} R \right), \quad n_R = 0, 1, \dots \quad (11)$$

$$\psi_{n_r}(r) = \left(\frac{\alpha_2^{\frac{1}{4}}}{2^{n_r} n_r! \pi^{\frac{1}{2}}} \right)^{\frac{1}{2}} e^{-\frac{1}{2}\sqrt{\alpha_2}r^2} H_{n_r} \left(\alpha_2^{\frac{1}{4}} r \right), \quad n_r = 0, 1, \dots \quad (12)$$

Here $\alpha_1 = \omega^2$, $\alpha_2 = \omega^2 \pm 2\lambda^2$, $H_n(x)$ is an n^{th} -order Hermite polynomial and n_R and n_r are the quantum numbers labelling the center of mass (R) and relative (r) coordinates. The symmetry of the wave function is controlled by the value of the n_r quantum number. Symmetric wave functions have even-valued n_r , while in antisymmetric ones they are odd-valued. For example, the $|n_R n_r\rangle = |00\rangle$ state is symmetric while the $|01\rangle$ one is antisymmetric.

The wave function in momentum space, can be obtained by applying the Fourier transform to the wave function in position space to get

$$\Phi(p_1, p_2) = \phi_{n_R}(P) \phi_{n_r}(p), \quad (13)$$

with

$$\phi_{n_R}(P) = (-i)^{n_R} \left(\frac{1}{2^{n_R} n_R! \alpha_1^{\frac{1}{4}} \pi^{\frac{1}{2}}} \right)^{\frac{1}{2}} e^{-\frac{P^2}{2\sqrt{\alpha_1}}} H_{n_R} \left(\frac{P}{\alpha_1^{\frac{1}{4}}} \right), \quad n_R = 0, 1, \dots \quad (14)$$

$$\phi_{n_r}(p) = (-i)^{n_r} \left(\frac{1}{2^{n_r} n_r! \alpha_2^{\frac{1}{4}} \pi^{\frac{1}{2}}} \right)^{\frac{1}{2}} e^{-\frac{p^2}{2\sqrt{\alpha_2}}} H_{n_r} \left(\frac{p}{\alpha_2^{\frac{1}{4}}} \right), \quad n_r = 0, 1, \dots \quad (15)$$

The pair densities in each representation are obtained as the squared norm of the respective wave function, while the reduced densities or marginals are obtained by integration over one of the original variables.

In the non-interacting limit ($\lambda = 0$), the wave function can be expressed as symmetric or antisymmetric products of orbitals, where each orbital is the harmonic oscillator solution for a particular quantum number. Taking the non-interacting state with quantum numbers (0,1) in position space as one example yields,

$$\Psi_{0,1} = \psi_0(x_1)\psi_1(x_2) - \psi_1(x_1)\psi_0(x_2), \quad (16)$$

where the orbitals here are given as

$$\psi_n(x) = \frac{1}{\sqrt{2^n n!}} \left(\frac{\omega}{\pi} \right)^{\frac{1}{4}} e^{-\frac{\omega x^2}{2}} H_n(\sqrt{\omega} x), \quad -\infty \leq x \leq \infty, \quad n = 0, 1, \dots \quad (17)$$

The momentum space wave function can be defined in an analogous manner with orbitals

$$\phi_n(p) = \frac{(-i)^n}{\sqrt{2^n n!}} \left(\frac{1}{\pi \omega} \right)^{\frac{1}{4}} e^{-\frac{p^2}{2\omega}} H_n \left(\frac{p}{\sqrt{\omega}} \right), \quad -\infty \leq p \leq \infty, \quad n = 0, 1, \dots \quad (18)$$

The motivation behind this work is an examination of the Shannon entropies and mutual information sums in two-level superposition states. As one particular example, wave functions for a two-level system comprised of ground ($|00\rangle$) and excited ($|01\rangle$) states of two interacting oscillators can be written as

$$\Psi_{0001} = c_1|00\rangle + c_2|01\rangle, \quad (19)$$

here $|c_1|^2 + |c_2|^2 = 1$. The corresponding density matrix in this basis can be written as

$$\rho' = \begin{pmatrix} c_1^* c_1 & c_1^* c_2 \\ c_2^* c_1 & c_2^* c_2 \end{pmatrix}, \quad (20)$$

where the information about quantum interferences is contained in the off-diagonal terms. The c_1 and c_2 coefficients can be imaginary numbers but for simplicity we will restrict ourselves here to only consider real numbers. Hence, we fix the phase between the two coefficients at either zero or 180 degrees.

The superposition of states is a particular feature of quantum mechanics. We wish to examine how the entropic sums change in these states, with regard to the individual states comprising the superposition, and in relation to the uncertainty bound. Stronger uncertainty relation statements are related with values lying closer to the bound [75]. The bound exists due to the incompatibility of the position and momentum representations in quantum mechanics and is the best one can hope for. The entropy sum provides a quantitative measure of this incompatibility, and one can probe this for its dependence on the system parameters. From this perspective, it is a measure of the correlation between the position and momentum variables. If the one and two-variable (particle) entropy sums are measures of the position-momentum correlations, then the differences between them, the mutual information sum, should contain information about the influence of particle interaction on these correlations. Such arguments, based on consideration of Wigner functions, have been detailed [32,76].

One can ask how do these superposition states behave with regard to the entropic uncertainty relations, and how does this depend on the values of the coefficients? Furthermore, one can expect statistical correlations

solely due to the superposition and quantum interferences that exist between the individual states. How are these additional correlations influenced by the interactions (attractive or repulsive) between the two particles? Hopefully, the ideas and results presented here will serve as a base to understand the effects of superposition which occur in other contexts, such as the behaviour of systems under the effects of external fields, or expansions in terms of multi-determinantal wave functions. In such cases, the physical description and information about these processes are mapped onto the coefficients.

Results and discussion

Harmonic oscillator

We begin the discussion by considering a two-level system of the harmonic oscillator comprised of the ground and first excited state. We wish to illustrate concepts here with one oscillator, that will aid in understanding the subsequent behaviour presented for two coupled oscillators. The wave function in position space is

$$\Psi_{01}(x) = c_1\psi_0(x) + c_2\psi_1(x), \quad (21)$$

and the integrals defining the information measures were evaluated numerically.

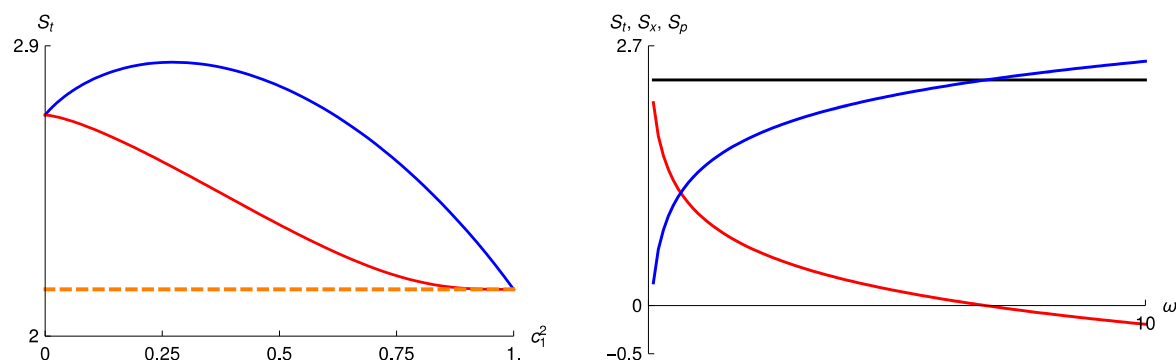


Fig. 1. Left: Plots of the entropic sum S_t of the Ψ_{01} superposition states with (red curve) and without (blue curve) quantum interferences varying c_1^2 . The value of ω is set at unity and the horizontal dashed line is the $1 + \ln \pi$ bound. Right: Plots of the entropic sum S_t (black curve) and its position (red curve) and momentum (blue curve) components vs. ω for the Ψ_{01} superposition state with $c_1 = c_2 = 1/\sqrt{2}$.

The Shannon entropy sum as a function of c_1^2 is presented in Fig. 1. When $c_1^2 = 0$, the system is in the first excited state, while when $c_1^2 = 1$, it is in the ground state. One observes that the entropy sum decreases monotonically with c_1^2 , until it saturates the uncertainty bound which is given by the dashed horizontal line. This concurs with the result that the uncertainty bound is saturated with the harmonic oscillator in its ground state [7,77]. Moreover, the entropy sum decreases from the first excited state to the ground state. This is in agreement with the result that the entropy sum increases with quantum number [7].

One can also examine the effects of the quantum interferences by eliminating them from the expression for the densities. This is achieved by suppressing the resulting c_1c_2 cross terms in the expressions for the densities. Fig. 1 illustrates that elimination of the quantum interferences moves the system further away from the uncertainty bound. On the other hand, the behaviour of the entropy sum, with and without quantum interferences, is distinct. The observed non-monotonic behaviour when no interferences are present, illustrate that there must be systems with different coefficients whose entropy sums are equal in value.

Studies of the ground and excited states of the harmonic oscillator have shown that their entropy sums are constant-valued as a function of ω , due to scaling of the wave function. This also holds for hydrogenic

atoms when the nuclear charge is increased [7]. The right-hand side of Fig. 1 presents the behaviour of the entropy sum and its components for a superposition state, when ω is varied. The position space Shannon entropy decreases (localization), while the momentum space entropy increases (delocalization). The entropy sum here is also constant valued and lies above the uncertainty bound.

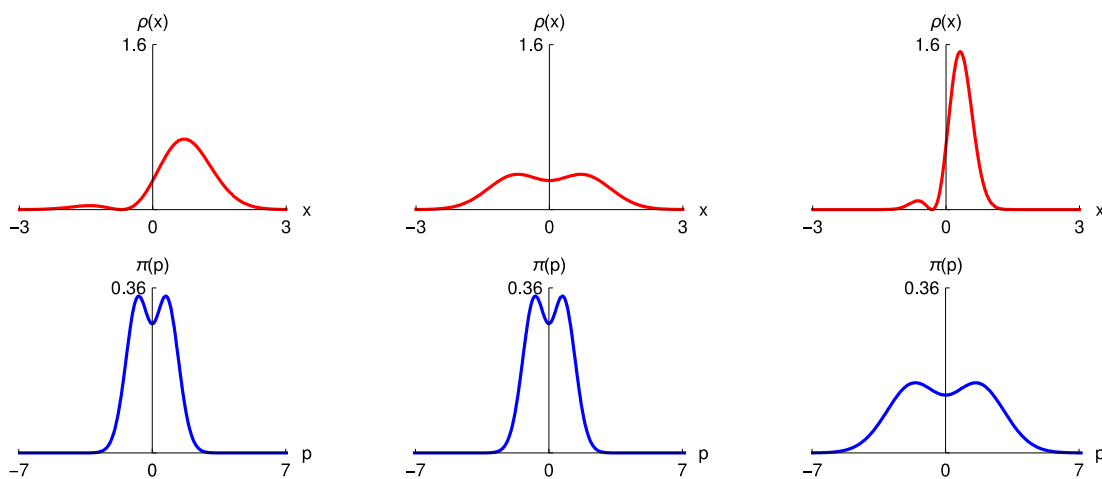


Fig. 2. Left column: Position and momentum space densities for the superposition state with $c_1 = c_2 = \frac{1}{\sqrt{2}}$ and $\omega = 1$. Middle column: Position and momentum space densities for the superposition state with $c_1 = c_2 = \frac{1}{\sqrt{2}}$ and $\omega = 1$ and no quantum interferences. Right column: Position and momentum space densities for the superposition state with $c_1 = c_2 = \frac{1}{\sqrt{2}}$ and $\omega = 5$.

The observed behaviours in Fig. 1 can be further analysed by examining the underlying position and momentum space distributions. These are presented in Fig. 2. The effects on the densities from (addition) removal of the quantum interferences can be seen by comparing the left and middle columns. These interferences induce a localization of the position space density toward the positive x regions. That the localization occurs in the positive x regions depends on the particular choice of coefficients. For example, the localization occurs in the negative x regions when c_2 is negative-valued.

On the other hand, there are no observed effects on the momentum space densities, which are equal. It is important to emphasize that this effect in momentum space, is a result of the different parities of the states used to construct the superposition, and the properties of the Fourier transform. The even parity ground state when Fourier transformed is real-valued while the odd parity first excited state is imaginary. Hence, there are no quantum interferences in momentum space, since these cancel when the density is constructed by multiplying the wave function by its complex conjugate. Thus, the differences in behaviour between entropy sums with and without quantum interferences, is due to position space. There is no cancellation if the states are of the same parity, and we shall return to this point in the last section.

Comparison of the left and right columns of Fig. 2 illustrates that larger ω localizes the position space density, while it delocalizes the density in momentum space. This is consistent with the behaviours of S_x and S_p presented in Fig. 1. The localization induced in the position space density from increasing ω , must be of an equal magnitude to the delocalization that the momentum density experiences. This is the reason why S_t is constant valued with ω .

Coupled oscillators

We now move on to analyse the behaviour when two oscillators interact either in an attractive or repulsive manner. Here, we will examine how the Shannon pair entropy sums, reduced entropy sums, and

mutual information sums behave as c_1^2 is varied, and also as the intensity of the attractive or repulsive interaction potential is increased. The two superposition states that we will consider are symmetric (Ψ_{0001}) and antisymmetric (Ψ_{0111}) with respect to particle exchange. The last section is devoted to discussion of the Ψ_{0020} symmetric state which is of even parity.

Symmetric state

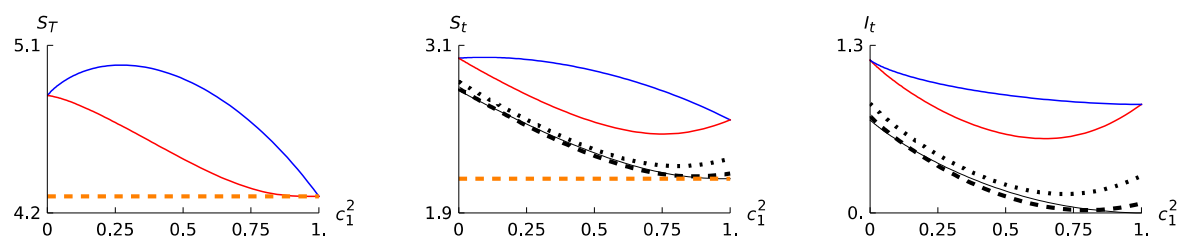


Fig. 3. Left: Plots of the Shannon pair entropic sum, S_T vs c_1^2 for the superposition function Ψ_{0010} , with attractive potential ($\lambda = 5$), with (red curve) and without (blue curve) quantum interferences. The horizontal dashed line is the $2(1 + \ln \pi)$ uncertainty bound. Center: Plots of the reduced entropic sum S_t from the superposition function ($\lambda = 5$) with (red curve) and without (blue curve) quantum interferences. The curves in black correspond to the superposition state with different values of λ (0-solid, 1-dashed, 2-dotted). The horizontal dashed line is the $1 + \ln \pi$ bound. Right: Plots of the information sum I_t vs c_1^2 for the superposition function ($\lambda = 5$) with (red curve) and without (blue curve) quantum interferences. Curves in black are as previously defined. The value of ω is set at unity in all curves.

The Shannon pair entropy sums are presented in Fig. 3. These results are similar to the ones in Fig. 1 for S_t of the single oscillator. S_T saturates the uncertainty bound for the ground state system when $c_1^2 = 1$, and increases as c_1^2 decreases, as the state moves towards the first excited one. One characteristic of these two-particle systems is that their S_T values are independent of the interaction strength (λ). Thus the curves which are presented are representative for all values of λ . The interpretation upon comparison of the curves with and without quantum interferences, is that the interferences move the S_T values closer to the bound.

This is also consistent with the curves for S_t presented in the center plot, with some important differences. First, the reduced entropy sum, S_t , does depend on λ . Different curves in black, corresponding to different λ values, are now presented. We ask the reader to consider the solid line for the non-interacting system with $\lambda = 0$. The curve when $\lambda = 2$ (dotted) is above the non-interacting one, which shows that interactions increase S_t , with movement away from the bound. This occurs for all values of c_1^2 .

On the other hand, one can observe that there is a region of c_1^2 values where the curve for relatively weaker interactions with $\lambda = 1$ (dashed line), lies below the non-interacting one. This effect is due to the superposition, since all interacting values are above those of the constituent states at $c_1^2 = 0$, and at $c_1^2 = 1$. Furthermore, the presence of minima in the S_t curves when interaction is included can be attributed to these interactions. Note that the non-interacting curve does not present a minimum. As c_1^2 approaches unity, the interacting systems move away from the bound which results in the minima. Even the curve for $\lambda = 1$, which is below the non-interacting curve at smaller c_1^2 , is now above it as c_1^2 approaches unity.

Inspection of the curves for the mutual information sums shows that the curve corresponding to no quantum interferences, lies above the one with the interferences present. In general, the correlation is larger with increasing λ . However, similar to S_t , there is a region where the $\lambda = 1$ curve dips below the non-interacting one. Thus, superposition in an interacting system can result in a correlation that is smaller than the corresponding non-interacting case, when in the presence of an attractive potential. One can also observe that the relative orderings at $c_1^2 = 0, 1$ are as expected. That is, the mutual information sums increase with increasing λ .

These tendencies can be further probed by examining how I_t changes with λ for different values of c_1^2 . The curves presented in Fig. 4 illustrate that I_t presents minima at the chosen values of c_1^2 . Thus, there are

regions where increasing the intensity of interactions yields a smaller correlation, opposite to the increasing general tendency, present in the larger λ regions. These minima are due to the S_t component as shown in the row below, since S_T is constant valued with λ .

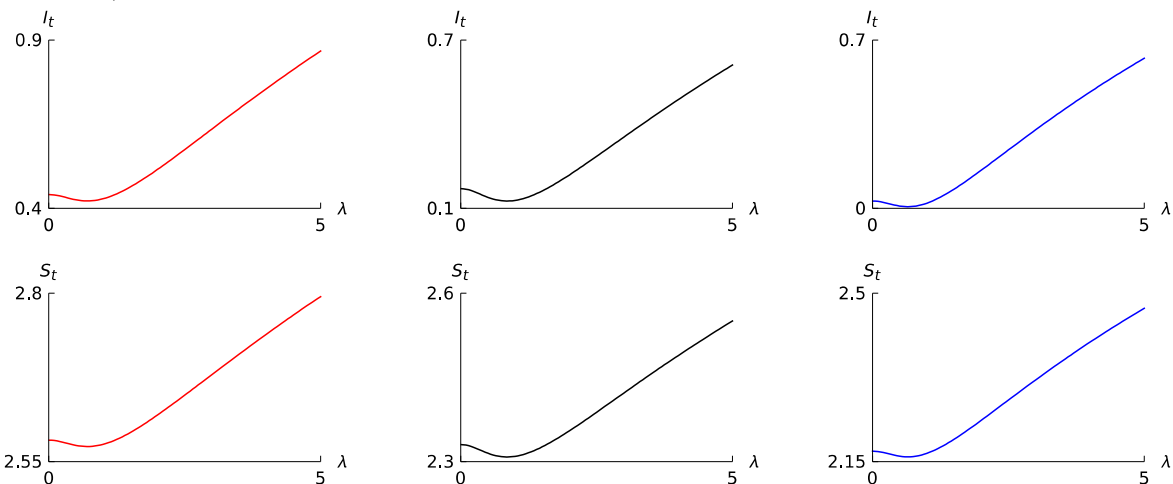


Fig. 4. First row: Plots of the mutual information sum, I_t vs. λ from the superposition function Ψ_{0010} , with attractive potential. Left: ($c_1^2 = 0.2$) Middle: ($c_1^2 = 0.5$) Right: ($c_1^2 = 0.8$). Second row: Plots of S_t for the systems in the row above. The value of ω is set at unity in all curves.

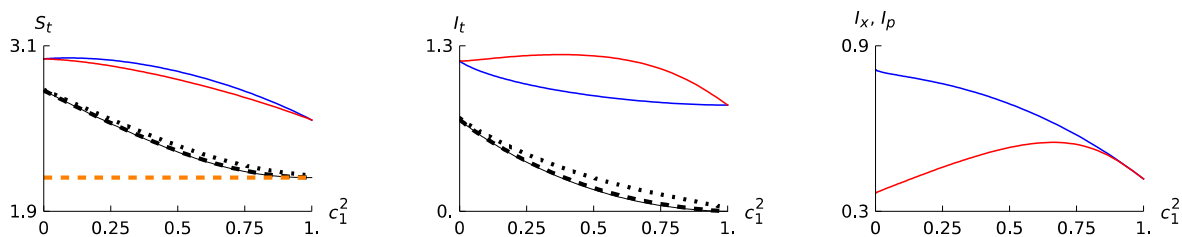


Fig. 5. Left: Plots of the reduced entropic sum, S_t , from the superposition function Ψ_{0010} , with repulsive potential ($\lambda = 0.7$), with (red curve) and without (blue curve) quantum interferences. The curves in black correspond to the superposition state with different values of λ (0-solid, 0.25-dashed, 0.5-dotted). The horizontal dashed line is the $1 + \ln \pi$ bound. Center: Plots of the information sum I_t vs. c_1^2 for the superposition function ($\lambda = 0.7$) with (red curve) and without (blue curve) quantum interferences. Curves in black are as previously defined. Right: Plots of the I_x (red curve) and I_p (blue curve) components with $\lambda = 0.7$ vs. c_1^2 . The value of ω is set at unity in all curves.

We now focus our attention on the results for the repulsive potential in Fig. 5. The corresponding curves for S_T are not presented here, since they are exactly the same as the ones for the attractive potential in Fig. 3, as the S_T values do not depend on the value or nature of the potential. The results in the relative ordering of the S_t curves with and without quantum interferences, is consistent with those from Fig. 3 for the attractive potential. That is, the quantum interferences move the values closer to the uncertainty bound. However, one can see that this effect is smaller for the repulsive case as compared to the attractive one. It is also noteworthy that all different λ -valued curves are bounded by the non-interacting one, and these are ordered with the particular λ value. Increased interaction thus induces a movement of S_t away from the uncertainty bound, for all c_1^2 values. This is distinct from the attractive case, where the $\lambda = 1$ curve was observed to be lower than the non-interacting one, in a region of c_1^2 values.

Examination of the $\lambda = 0.7$ curves for the mutual information sum show that the correlation is now larger when the quantum interferences are included. This is different from the attractive case (Fig. 3), where the opposite is observed. Furthermore, all the different λ -valued curves are lower bounded by the non-interacting curve. The I_t curves increase in value away from the non-interacting one as λ increases. Again, this is distinct from the attractive case. The I_x and I_p components are also presented. In contrast to I_p , I_x presents a minimum. While $I_p > I_x$ at smaller c_1^2 , the two components approach each other in value at larger c_1^2 , and are equal when $c_1^2 = 1$.

Antisymmetric state

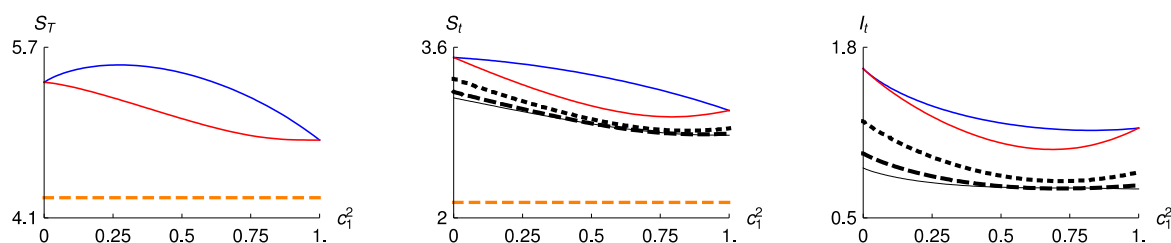


Fig. 6. Left: Plots of the Shannon pair entropic sum, S_T vs c_1^2 for the superposition function Ψ_{0111} , with attractive potential ($\lambda = 5$), with (red curve) and without (blue curve) quantum interferences. The horizontal dashed line is the $2(1 + \ln \pi)$ uncertainty bound. Center: Plots of the reduced entropic sum S_i from the superposition function ($\lambda = 5$) with (red curve) and without (blue curve) quantum interferences. The curves in black correspond to the superposition state with different values of λ (0-solid, 1-dashed, 2-dotted). The horizontal dashed line is the $1 + \ln \pi$ bound. Right: Plots of the information sum I_t vs. c_1^2 for the superposition function ($\lambda = 5$) with (red curve) and without (blue curve) quantum interferences. Curves in black are as previously defined. The value of ω is set at unity in all curves.

The plots for the antisymmetric state with attractive potential are presented in Fig. 6. The results are consistent with those presented and discussed for the symmetric state. There are, however, some notable differences in the curves for S_i and I_t . In general, the curves are ordered with respect to their λ -values. Moreover, it seems that the region where the $\lambda = 1$ curve dips below the non-interacting ($\lambda = 0$) one, is smaller for this antisymmetric state as compared to the symmetric one (Fig. 3). This effect is not as pronounced here as was seen for the symmetric state, and thus suggests that this could be due to wave function symmetry.

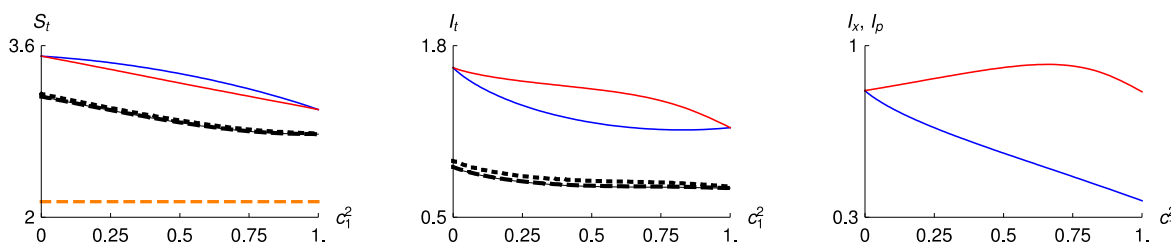


Fig. 7. Left: Plots of the reduced entropic sum, S_i , from the superposition function Ψ_{0111} , with repulsive potential ($\lambda = 0.7$), with (red curve) and without (blue curve) quantum interferences. The curves in black correspond to the superposition state with different values of λ (0-solid, 0.25-dashed, 0.5-dotted). The horizontal dashed line is the $1 + \ln \pi$ bound. Center: Plots of the information sum I_t vs. c_1^2 for the superposition function ($\lambda = 0.7$) with (red curve) and without (blue curve) quantum interferences. Curves in black are as previously defined. Right: Plots of the I_x (red curve) and I_p (blue curve) components with $\lambda = 0.7$ vs. c_1^2 . The value of ω is set at unity in all curves.

Fig. 7 presents the results for the antisymmetric state in the presence of repulsive potentials. The curves are again consistent with those for the symmetric state. However, now $I_x > I_p$, which is opposite to that observed in the symmetric state.

Same-parity superposition state

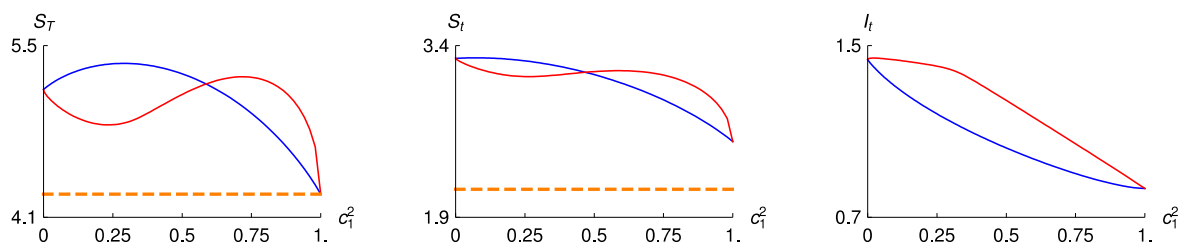


Fig. 8. Left: Plots of the Shannon pair entropic sum, S_T , vs. c_1^2 for the superposition function Ψ_{0020} , with repulsive potential ($\lambda = 0.7$), with (red curve) and without (blue curve) quantum interferences. The horizontal dashed line is the $2(1 + \ln \pi)$ uncertainty bound. Center: Plots of the reduced entropic sum S_r from the superposition function ($\lambda = 0.7$) with (red curve) and without (blue curve) quantum interferences. The horizontal dashed line is the $1 + \ln \pi$ bound. Right: Plots of the information sum I_i vs. c_1^2 for the superposition function ($\lambda = 0.7$) with (red curve) and without (blue curve) quantum interferences. The value of ω is set at unity in all curves.

Results are presented here for a symmetric superposition state Ψ_{0020} with components $|00\rangle$ and $|20\rangle$, in the presence of a repulsive potential. There are now two additional effects that are present here. The first is that the second component is a more highly excited state. The second is the even-function parity of both components, which results in quantum interferences being present in momentum space.

Fig. 8 illustrates that these effects provoke differences from the previous results. First, the result that S_T and S_r are closer to the respective bound when quantum interferences are present, is only valid for particular (smaller) values of c_1^2 . At larger values, the curves invert, and it is the curve without quantum interferences that is closest to the bound. This crossover between regimes occurs at $c_1 = c_2 = 1/\sqrt{2}$ for S_r , while it is shifted to the right in the S_T crossover.

The behaviour of the mutual information sum is consistent for the other states with repulsive potentials. That is, the correlation is larger with quantum interferences. There is another difference in the case of attractive potentials ($\lambda = 5$), which is not presented here for brevity. The curve with the quantum interferences now lies above the one without the interferences. This is similar to the result for the repulsive potential, and different from the previous ones presented for attractive potentials. Analysis of different λ values is not presented here since the resulting curves are very close together. These results highlight the importance of additional effects when higher excited states and parities are taken into consideration.

Conclusions

The effects of superposition on the entropic uncertainty relations and mutual information sums, are examined in two-level superposition states of two coupled oscillators. The changes in behaviour with the presence of an attractive or repulsive interaction potential, and the interaction strength, are explored. We find that the inclusion of quantum interferences generated by the superposition, leads to a movement of the entropy sums toward the respective uncertainty bound, when compared to the respective states with no quantum interferences. This is observed in the presence of both attractive and repulsive inter-particle potentials. However, there are notable differences when examining the correlation sums. The presence of quantum interferences augments the correlation in the presence of a repulsive potential, while it suppresses the correlation

when an attractive potential is present. We also observe that superposition in the presence of attractive potentials, is able to generate states which are lesser correlated than the corresponding non-interacting ones. On the other hand, this is not observed for the repulsive potential, where all values are lower bounded by the corresponding non-interacting ones. The regions where the interacting states with attractive potentials are lesser correlated than the non-interacting ones, are observed to be smaller when the state is antisymmetric. The role of function parity and excitation in the superposition state, and their effects on the information measures, are discussed.

References

1. Robertson, H. P. *Phys. Rev.* **1929**, *34*, 163. DOI: <https://doi.org/10.1103/PhysRev.34.163>.
2. Zewail, A. H. *J. Phys. Chem. A* **2000**, *104*, 5660. DOI: <https://doi.org/10.1021/jp001460h>.
3. Beckner, W. *Ann. Math.* **1975**, *102*, 159–182. DOI: <https://doi.org/10.2307/1970980>.
4. Bialynicki-Birula, I.; Mycielski, J. *Commun. Math. Phys.* **1975**, *44*, 129–132. DOI: <https://doi.org/10.1007/BF01608825>.
5. Hertz, A.; Cerf, N. J. *J. Phys. A: Math. Theor.* **2019**, *52*, 173001. DOI: <https://doi.org/10.1088/1751-8121/ab03f3>.
6. Yáñez, R. J.; van Assche, W.; Dehesa, J. S. *Phys. Rev. A* **1994**, *50*, 3065. DOI: <https://doi.org/10.1103/PhysRevA.50.3065>.
7. Gadre, S. R.; Sears, S. B.; Chakravorty, S. J.; Bendale, R. D. *Phys. Rev. A* **1985**, *32*, 2602. DOI: <https://doi.org/10.1103/PhysRevA.32.2602>.
8. Maasen, S. E.; Panos, C. P. *Phys. Lett. A* **1998**, *246*, 530. DOI: [https://doi.org/10.1016/S0375-9601\(98\)00524-6](https://doi.org/10.1016/S0375-9601(98)00524-6).
9. Grassi, A.; Lombardo, G. M.; March, N. H.; Pucci, R. *Int. J. Quantum Chem.* **1998**, *69*, 721–726. DOI: [https://doi.org/10.1002/\(SICI\)1097-461X\(1998\)69:6<721::AID-QUA4>3.0.CO;2-X](https://doi.org/10.1002/(SICI)1097-461X(1998)69:6<721::AID-QUA4>3.0.CO;2-X).
10. Guevara, N. L.; Sagar, R. P.; Esquivel, R. O. *Phys. Rev. A* **2003**, *67*, 012507. DOI: <https://doi.org/10.1103/PhysRevA.67.012507>.
11. Romera, E.; Dehesa, J. S. *J. Chem. Phys.* **2004**, *120*, 8906–8912. DOI: <https://doi.org/10.1063/1.1697374>.
12. Shi, Q.; Kais, S. *J. Chem. Phys.* **2004**, *121*, 5611–5617. DOI: <https://doi.org/10.1063/1.1785773>.
13. Chatzisavvas, K. C.; Moustakidis, C. C.; Panos, C. P. *J. Chem. Phys.* **2005**, *123*, 174111. DOI: <https://doi.org/10.1063/1.2121610>.
14. Sen, K.; Katriel, J. *J. Chem. Phys.* **2006**, *125*, 074117. DOI: <https://doi.org/10.1063/1.2263710>.
15. Nagy, Á. *Int. J. Quantum Chem.* **2014**, *115*, 1392–1395. DOI: <https://doi.org/10.1002/qua.24812>.
16. Lin, C. H.; Ho, Y. K. *Chem. Phys. Lett.* **2015**, *633*, 261–264. DOI: <https://doi.org/10.1016/j.cplett.2015.05.029>.
17. Pooja; Kumar, R.; Kumar, G.; Kumar, R.; Kumar, A. *Int. J. Quantum Chem.* **2016**, *116*, 1413. DOI: <https://doi.org/10.1002/qua.25197>.
18. Coles, P. J.; Berta, M.; Tomamichel, M.; Wehner, S. *Rev. Mod. Phys.* **2017**, *89*, 015002. DOI: <https://doi.org/10.1103/RevModPhys.89.015002>.
19. Sekh, G. A.; Saha, A.; Talukdar, B. *Phys. Lett. A* **2018**, *382*, 315. DOI: <https://doi.org/10.1016/j.physleta.2017.12.005>.
20. Flores-Gallegos, N. *Chem. Phys. Lett.* **2019**, *720*, 1–6. DOI: <https://doi.org/10.1016/j.cplett.2019.01.049>.
21. Kumar, R. K.; Chakrabarti, B.; Gammal, A. *J. Low Temp. Phys.* **2019**, *194*, 14. DOI: <https://doi.org/10.1007/s10909-018-2051-8>.
22. Zhao, Q.; Zhao, J. *J. Low Temp. Phys.* **2019**, *194*, 302. DOI: <https://doi.org/10.1007/s10909-018-2099-5>.
23. Panos, C. P.; Moustakidis, C. C. *Physica A: Stat. Mech. Appl.* **2019**, *518*, 384. DOI: <https://doi.org/10.1016/j.physa.2018.12.018>.
24. Nasser, I.; Zeama, M.; Abdel-Hady A. *Int. J. Quan. Chem.*, *121*:e26499, **2021**. DOI: <https://doi.org/10.1002/qua.26499>.

25. (a) Ho, M.; Smith Jr., V.; Weaver, D.; Gatti, C.; Sagar, R.; Esquivel, R. *J. Chem. Phys.* **1998**, *108*, 5469. DOI: <https://doi.org/10.1063/1.476316>. (b) Ho, M.; Weaver, D.; Smith Jr., V.; Sagar, R.; Esquivel, R.; Yamamoto, S. *J. Chem. Phys.* **1998**, *109*, 10620. DOI: <https://doi.org/10.1063/1.477761>.
26. Liu, S. *J. Chem. Phys.* **2007**, *126*, 191107. DOI: <https://doi.org/10.1063/1.2741244>.
27. Ho, M.; Weaver, D.; Smith Jr., V.; Sagar, R.; Esquivel, R. *Phys. Rev. A* **1998**, *57*, 4512. DOI: <https://doi.org/10.1103/PhysRevA.57.4512>.
28. Thakkar, A. J. John Wiley & Sons, Ltd, 2003; Chapter 5, pp 303–352. DOI: <https://doi.org/10.1002/0471484237.ch5>.
29. Dunkel, J.; Trigger, S. A. *Phys. Rev. A* **2005**, *71*, 052102. DOI: <https://doi.org/10.1103/PhysRevA.71.052102>.
30. Garbaczewski, P. *Phys. Rev. A* **2005**, *72*, 056101. DOI: <https://doi.org/10.1103/PhysRevA.72.056101>.
31. Laguna, H. G.; Sagar, R. P. *Int. J. Quant. Inf.* **2010**, *08*, 1089–1100. DOI: <https://doi.org/10.1142/S0219749910006484>.
32. Salazar, S. J. C.; Laguna, H. G.; Sagar, R. P. *Phys. Rev. A* **2023**, *107*, 042417. DOI: <https://doi.org/10.1103/PhysRevA.107.042417>.
33. Mukherjee, N.; Roy, A. K. *Int. J. Quantum Chem.* **2018**, *118*, e25596. DOI: <https://doi.org/10.1002/qua.25596>.
34. Majumdar, S.; Roy, A. *Quantum Rep.* **2020**, *2*, 189. DOI: <https://doi.org/10.3390/quantum2010012>.
35. Estañón, C. R.; Aquino, N.; Puertas-Centeno, D.; Dehesa, J. S. *Int. J. Quantum Chem.* **2020**, *120*, e26192. DOI: <https://doi.org/10.1002/qua.26192>.
36. Salazar, S. J. C.; Laguna, H.; Prasad, V.; Sagar, R. P. *Int J Quant Chem* **2020**, *120*, e26188. DOI: <https://doi.org/10.1002/qua.26188>.
37. Olendski, O. *Entropy* **2019**, *21*, 1060. DOI: <https://doi.org/10.3390/e21111060>.
38. Sen, K. D. *J. Chem. Phys.* **2005**, *123*, 074110. DOI: <https://doi.org/10.1063/1.2008212>.
39. Nascimento, W. S.; Prudente, F. V. *Chem. Phys. Lett.* **2018**, *691*, 401. DOI: <https://doi.org/10.1016/j.cplett.2017.11.048>.
40. Aquino, N.; Flores-Riveros, A.; Rivas-Silva, J. F. *Phys. Lett. A* **2013**, *377*, 2062. DOI: <https://doi.org/10.1016/j.physleta.2013.05.048>.
41. Martínez-Sánchez, M. A.; Vargas, M.; Garza, J. *Quantum Reports* **2019**, *1*, 208–218. DOI: <https://doi.org/10.3390/quantum1020018>.
42. Fotue, A. J.; Kenfack, S. C.; Tiotsup, M.; Issoufa, N.; Wirngo, A. V.; Djemmo, M. P. T.; Fotsin, H.; Fai, L. C. *Mod. Phys. Lett. B* **2015**, *29*, 1550241. DOI: <https://doi.org/10.1142/S0217984915502413>.
43. Ghosal, A.; Mukherjee, N.; Roy, A. K. *Ann. Phys. (Berlin)* **2016**, *528*, 796. DOI: <https://doi.org/10.1002/andp.201600121>.
44. Mukerjee, N.; Roy, A. K. *Ann. Phys.* **2016**, *528*, 412–433. DOI: <https://doi.org/10.1002/andp.201500301>.
45. Nagy, Á. in *Density Matrix and Density Functional Theory in Atoms, Molecules and the Solid State*. Dordrecht, **2003**; pp 79–87.
46. Higuchi, M.; Higuchi, K. *Comp. Theo. Chem.* **2013**, *1003*, 91–96. DOI: <https://doi.org/10.1016/j.comptc.2012.09.015>.
47. Sharma, P.; Bao, J. J.; Truhlar, D. G.; Gagliardi, L. *Ann. Rev. Phys. Chem.* **2021**, *72*, 541–564. DOI: <https://doi.org/10.1146/annurev-physchem-090419-043839>.
48. Guevara, N. L.; Sagar, R. P.; Esquivel, R. O. *J. Chem. Phys.* **2003**, *119*, 7030. DOI: <https://doi.org/10.1063/1.1605932>.
49. Sagar, R. P.; Laguna, H. G.; Guevara, N. L. *Int. J. Quantum Chem.* **2011**, *111*, 3497. DOI: <https://doi.org/10.1002/qua.22792>.
50. López-Rosa, S.; Martín, A. L.; Antolín, J.; Angulo, J. C. *Int. J. Quantum Chem.* **2019**, *119*, e25861. DOI: <https://doi.org/10.1002/qua.25861>.
51. Laguna, H.; Sagar, R. *Phys. Rev. A* **2011**, *84*, 012502. DOI: <https://doi.org/10.1103/PhysRevA.84.012502>.
52. Salazar, S.; Laguna, H. G.; Sagar, R. P. *Phys. Rev. A* **2020**, *101*, 042105. DOI: <https://doi.org/10.1103/PhysRevA.101.042105>, and references therein.

53. Löwdin, P.-O. *Phys. Rev.* **1955**, *97*, 1509. DOI: <https://doi.org/10.1103/PhysRev.97.1509>.
54. Wigner, E.; Seitz, F. *Phys. Rev.* **1933**, *43*, 804–810. DOI: <https://doi.org/10.1103/PhysRev.43.804>.
55. Kutzelnigg, W.; Re, G. D.; Berthier, G. *Phys. Rev.* **1968**, *172*, 49. DOI: <https://doi.org/10.1103/PhysRev.172.49>.
56. Thakkar, A. J.; Smith Jr., V. H. *Phys. Rev. A* **1981**, *23*, 473. DOI: <https://doi.org/10.1103/PhysRevA.23.473>.
57. Park, D. *Quantum Inf. Process.* **2020**, *19*, 129. DOI: <https://doi.org/10.1007/s11128-020-02626-4>.
58. Faba, J.; Martín, V.; Robledo, L. *Phys. Rev. A* **2021**, *104*, 032428. DOI: <https://doi.org/10.1103/PhysRevA.104.032428>.
59. Tam, P. M.; Claassen, M.; Kane, C. L. *Phys. Rev. X* **2022**, *12*, 031022. DOI: <https://doi.org/10.1103/PhysRevX.12.031022>.
60. Angulo, J. C.; López-Rosa, S. *Entropy* **2022**, *24*, 233. DOI: <https://doi.org/10.3390/e24020233>.
61. Schürger, P.; Engel, V. *Phys. Chem. Chem. Phys.* **2023**, *25*, 28373. DOI: <https://doi.org/10.1039/d3cp03573e>.
62. Alonso-López, D.; Cembranos, J. A. R.; Díaz-Guerra, D.; Mínguez-Sánchez, A. *Eur. Phys. J. D* **2023**, *77*, 43. DOI: https://doi.org/10.1140/ep_jd/s10053-023-00629-1.
63. Schürger, P.; Engel, V. *AIP Advances* **2023**, *13*, 125307. DOI: <https://doi.org/10.1063/5.0180004>.
64. Kumar, K.; Prasad, V. *Ann. Phys. (Berlin)* **2023**, *535*, 2300166. DOI: <https://doi.org/10.1002/andp.202300166>.
65. Peng, H. T.; Ho, Y. K. *Entropy* **2015**, *17*, 1882–1895. DOI: <https://doi.org/10.3390/e17041882>.
66. Sagar, R. P.; Guevara, N. L. *J. Chem. Phys.* **2005**, *123*, 044108. DOI: <https://doi.org/10.1063/1.1953327>.
67. Moshinsky, M. *Am. J. Phys.* **1968**, *36*, 52–53. DOI: <https://doi.org/10.1119/1.1974410>.
68. Holas, A.; Howard, I.; March, N. *Phys. Lett. A* **2003**, *310*, 451–456. DOI: [https://doi.org/10.1016/S0375-9601\(03\)00408-0](https://doi.org/10.1016/S0375-9601(03)00408-0).
69. Ragot, S. *J. Chem. Phys.* **2006**, *125*, 014106. DOI: <https://doi.org/10.1063/1.2212935>.
70. March, N. H.; Cabo, A.; Claro, F.; Angilella, G. G. N. *Phys. Rev. A* **2008**, *77*, 042504. DOI: <https://doi.org/10.1103/PhysRevA.77.042504>.
71. Dahl, J. P. *Can. J. Chem.* **2009**, *87*, 784–789. DOI: <https://doi.org/10.1139/V09-002>.
72. Niehaus, T.; March, N. *Theor. Chem. Acc.* **2010**, *125*, 427. DOI: <https://doi.org/10.1007/s00214-009-0578-0>.
73. Benavides-Riveros, C.; Várilly, J. *Eur. Phys. J. D* **2012**, *66*, 274. DOI: <https://doi.org/10.1140/epjd/e2012-30442-4>.
74. Ebrahimi-Fard, K.; Gracia-Bondía, J. J. *Math. Chem.* **2012**, *50*, 440. DOI: <https://doi.org/10.1007/s10910-011-9822-7>.
75. Floerchinger, S.; Haas, T.; Müller-Groeling, H. *Phys. Rev. A* **2021**, *103*, 062222. DOI: <https://doi.org/10.1103/PhysRevA.103.062222>.
76. Laguna, H.; Sagar, R. J. *Phys. A: Math. Theor.* **2012**, *45*, 025307. DOI: <https://doi.org/10.1088/1751-8113/45/2/025307>.
77. Majerník, V.; Opatrný, T. *J. Phys. A: Math Gen.* **1996**, *29*, 2187. DOI: <https://doi.org/10.1088/0305-4470/29/9/029>.

Towards a Mexican School of General Analytical Chemistry

Alberto Rojas-Hernández*, María Teresa Ramírez-Silva, Annia Galano

UAM-Iztapalapa. Departamento de Química. Av. Ferrocarril San Rafael Atlixco 186, Col. Leyes de Reforma 1era Sección, Iztapalapa, C.P. 09310, CDMX, México.

*Corresponding author: Alberto Rojas-Hernández, email: suemi918@xanum.uam.mx

Received May 31st, 2024; Accepted August 14th, 2024.

DOI: <http://dx.doi.org/10.29356/jmcs.v68i4.2315>

Abstract. This year the 50th anniversary of the Metropolitan Autonomous University is celebrated. It is for this reason that the JMCS decided to publish a special issue with contributions from professors from the Department of Chemistry. We thank the Editorial Committee of the issue for the invitation to write an article about the academic work that has been done in the Analytical Chemistry Area of this Department. We hope that we have managed to give a good description of the achievements we have had since the Analytical Chemistry Area was founded in the Iztapalapa Unit of the Metropolitan Autonomous University.

Keywords: General Analytical Chemistry teaching; Generalized Species and Equilibria Method (GSEM); chemical equilibrium.

Resumen. En este año se celebra el 50 aniversario de la Universidad Autónoma Metropolitana. Es con ese motivo que el JMCS decidió publicar un número especial con contribuciones de profesores del Departamento de Química. Agradecemos al Comité Editorial del número la invitación para hacer una contribución acerca del trabajo académico que se ha hecho en el Área de Química Analítica. Esperamos que hayamos logrado dar una buena descripción de los logros que hemos tenido desde que se fundó el Área de Química Analítica en la Unidad Iztapalapa de la Universidad Autónoma Metropolitana.

Palabras clave: Enseñanza de Química Analítica General; Método de Especies y Equilibrios Generalizados (MEEG); equilibrio químico.

Introduction

In mid-2000, the creation of the most recent Academic Area of the Department of Chemistry at the Metropolitan Autonomous University, Iztapalapa Unit (UAM-Iztapalapa), was authorized: the Analytical Chemistry Area.

This concluded a work of some 22 years that María Teresa Ramírez-Silva (Tere) and I had undertaken, beginning at the Faculty of Higher Studies-Cuautitlán of the National Autonomous University of Mexico (FESC-UNAM, by its acronym in Spanish), and which continued at the UAM-Iztapalapa to since 1985, within the Electrochemistry Area.

But at the same time, when the Area of Analytical Chemistry was founded at the UAM-Iztapalapa, the path towards the establishment of a Mexican School of General Analytical Chemistry began.

Our training within the Charlot's School of General Analytical Chemistry

Gaston Charlot conceived the teaching of General Analytical Chemistry, which aims to describe chemical reactions and other physicochemical processes in an analytical manner and then apply this knowledge in a systematic and controlled way. This allows not only to develop methods of chemical analysis, but also to transcend the explanation and development of other physicochemical procedures that occur in chemical synthesis and industrial chemistry (among other parts of chemistry), which are applied in solving problems in many sectors of society. [1]

As students at FESC-UNAM we learned this approach of General Analytical Chemistry thanks to Margarita Rosa Gómez-Moliné (Rosamar), Helmut Pitsch and Michel Cassir. [2,3]. But there we were also trained as teachers, and we were given the freedom to make innovations in the teaching of analytical chemistry [4].

When Tere and I were hired at the UAM-Iztapalapa (between 1985 and 1987) we were in charge of teaching Analytical Chemistry in the Undergraduate and Graduate Studies in Chemistry.

Approach to Analytical Chemistry at the UAM-Iztapalapa

This is how we were able to translate our approach to teaching the discipline in the study programs of the Analytical Chemistry subjects of the Bachelor's Degree. This approach is made up of four items: Chemical Analysis, Physicochemical Processes Analysis, Instrumental Analysis and Chemometric Analysis.

Of these four areas, the one that really characterizes Charlot's method is the Physicochemical Processes Analysis, since this is what makes this Analytical Chemistry transcend from typical problems of chemical analysis to other problems of application in the chemistry of materials or industrial chemistry. [5]

Today, teaching Analytical Chemistry in our undergraduate courses begins with the main tools of Charlot's method (such as reaction prediction scales, predominance-zone diagrams, parameters of force and stability of species, tables of variation of substance quantities, chemical separations for chemical analysis, among others) in Brønsted's acid-base chemistry. With this, it is possible to have a robust model to predict and interpret what happens in acid-base titrations and in the preparation and application of pH buffer solutions.

Charlot's tools developed for the study of Brønsted acid-base systems are so useful that they can be applied to other types of reactions, such as those that occur in the formation of coordination compounds and redox processes. However, in Charlot's approach this is done when it is assumed that the processes in these systems are two-components (or occur through the exchange of one particle) [6], which is actually a simplification. –somewhat crude– of the real behavior of these systems.

In the case of our teaching, after studying the topics from Brønsted acid-base to pH buffer systems and acid-base titrations, we proceed to learn the systems where coordination compounds and redox species are formed through the Generalized Species and Generalized Equilibria Method; or simpler: Generalized Species and Equilibria Method (GSEM) [7].

GSEM not only allows the study of the systems described above, but also many others, including separation processes such as selective precipitation, liquid-liquid extraction and ion exchange. This is why this topic is included in the mandatory Analytical Chemistry courses at the UAM-Iztapalapa

Finally, Analytical Chemistry curriculum in the Bachelor's Degree also considers aspects of Instrumental Analysis and Chemometrics in different courses.

In the following sections of the article, the different areas where it is thought that the greatest contributions have been made to teaching (with this approach) or to the knowledge of Analytical Chemistry will be considered.

Contributions to Analytical Electrochemistry and Supramolecular Chemistry

Perhaps the main contribution to electrochemical field has been the proposal to using carbon paste electrodes in multiple studies, modifying the electrode surface with substances such as conductive polymers, surfactants or cyclodextrins. [8-14]

Fig. 1. shows an example of this kind of research in neurotransmission field.

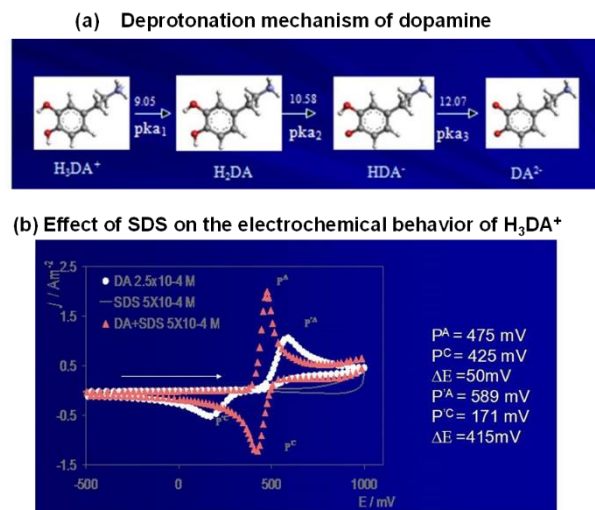


Fig 1. In 2009 Tere, with students and other professors of UAM-Azcapotzalco, received the research award of CBI Division of UAM, by the paper cited as [10], related with the effect of sodium dodecylsulfate (SDS) in the electrochemical behavior of dopamine over a carbon paste electrode.

Tere also proposed using composite graphite-epoxy electrodes to construct Flow Injection Electroanalytical systems. [15-17]

The Analytical Chemistry Area was one of the first groups in Mexico to use conductive polymers to develop highly selective ion sensors, by the collaboration of Tere with Dr. Salvador Allegret, from Barcelona. And with the aid of Dr. Manuel Palomar-Pardavé (from Materials Area of UAM-Azcapotzalco) it was possible to use theoretical current transients models (used at that time mainly to study the electrodeposition of metals) to fit the experimental data and obtain important information about the electropolymerization process, the diffusion of the ion through the polymer, and its correlation with the analytical performance. [18]

Taking about the contributions in the field of cyclodextrins and their polymers, and neurotransmitters, it is important to mention that in the comprehensive characterization of these systems, Charlot's approach was used, and all of these led to the development of important quantitative methodologies for trace determination of lead, mercury, and cadmium. [19-21]

Contributions to Brønsted's acid-base teaching and research

From an educational point of view, possibly the greatest contribution has been the development of a robust calculation algorithm to predict and interpret titration curves, as well as their first derivative, which has also led to interesting interpretations of the concept of buffer capacity. [22-25]

Nevertheless, teaching Brønsted acid-base systems with this approach requires knowledge of the acidity constants, and this led to establishing a line of research to determine these parameters. Thus, in 1990 the SQUAD program [26] was captured and compiled, as part of a master's thesis [27]. SQUAD determines acidity constants by fitting absorption spectra of systems of different chemical composition by non-linear least squares.

Acidity constants of organic substances (such as curcumin, mangiferin, and neurotransmitters, among others) have been determined, in aqueous solution and in other solvents; confirming previously reported values, but also providing unreported values in some cases (see Fig. 2). [28-33]

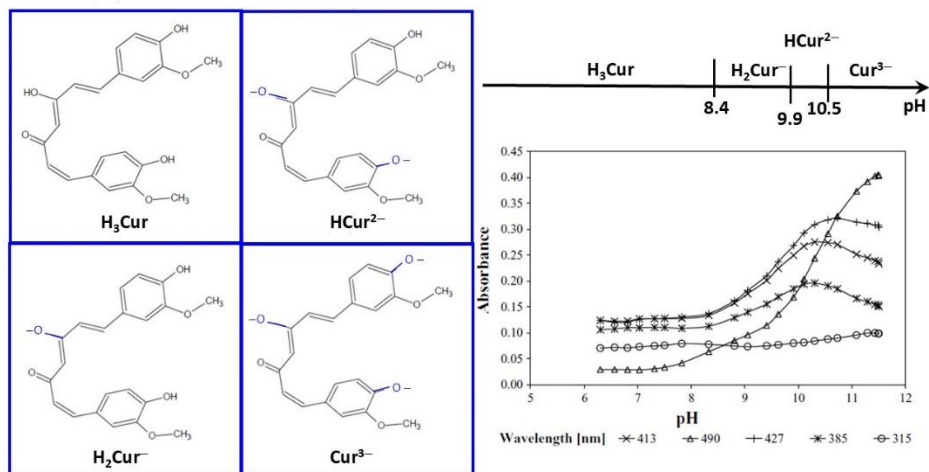


Fig. 2. This spectrophotometric study of curcumin is consistent with three pKa values, and not with two as reported until 2004. Reference [29] is one of our most cited papers. (Adapted from [29].)

As it can be seen in these works, various experimental methods (such as NMR, capillary electrophoresis, potentiometry, conductimetry, voltammetry) are frequently used to confirm the values obtained experimentally. [34,35]

Since it is sometimes not possible to do experiments to confirm the information obtained by spectrophotometry or potentiometry, in 2008 Annia Galano joined the group, with the aim of complementing the experimental studies with the help of computational chemistry and providing some relevant information, generally structural, but also kinetic (see Fig. 3). [36-42]

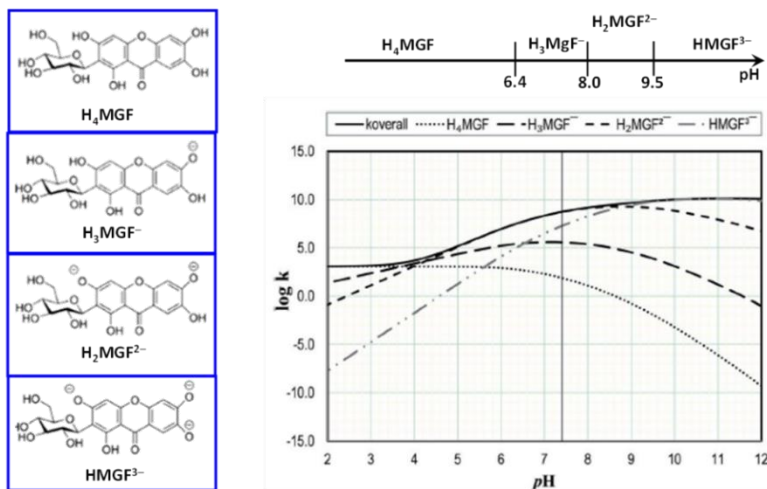


Fig. 3. Maniferin (H_4MGF) has antioxidant activity. In reference [40] the overall rate constant was calculated by computational chemistry calculations, and pKa values were confirmed by NMR studies. The species contributing the more to this rate constant is H_2MGF^{2-} if $3.5 \leq pH \leq 9.0$, even though not always is the predominant species. This demonstrates that H_2MGF^{2-} is more labile to hydrogen abstraction than H_3MGF^- and H_4MGF . (Adapted from [40].)

We were pioneers in carrying out this type of multidisciplinary theoretical-experimental studies in the same Analytical Chemistry group.

Contributions to the determination of equilibrium constants of coordination and inclusion compounds

Despite using SQUAD to refine acidity constants has been our most frequent work, formation constants of coordination and inclusion compounds have also been determined in systems with pharmacological properties and material precursors, mainly. [43-51]

Contributions to systematize Charlot's method for teaching General Analytical Chemistry

There are several innovations that we have made to Charlot's approach during these forty-five years, which we have not collected in books nor articles. But some contributions are worth mentioning regarding the use of the reaction prediction scale and to the construction of the predominance zone diagrams, giving maximum importance to the role played by the dismutation equilibria of the ampholytes in their construction (from the reaction prediction scale). [52,53]

We have also studied the validity of the approximations of representative equilibria, insisting on the advantages of Charlot's method when using only the equilibrium with the greatest physical significance in the system, and not the complete set of independent equilibria. Generally, this description can give an approximate answer, within the error margin considered acceptable [54].

It was also possible to demonstrate that Charlot's method is applicable to the study of systems in which polynuclear species are formed and, then the so-called thermodynamic mechanism of polymerization was established [55].

Finally we must highlight a work where it is demonstrated that species distribution diagrams summarize the distributions of the species of a system, as discrete variable distributions. There the variables are the stoichiometric coefficients of the components in the species, and the interpretation of an intrinsic buffer capacity is given as the variance of those distributions [56].

We think that this work may be the precursor of a statistical thermodynamics of substance quantity for particle polydonor systems and with polynuclear species.

The generalized species and equilibria method

The scheme shown in Fig. 4 describes the contributions of Brønsted's acid-base theory and Arrhenius's theory of electrolytic dissociation to the emergence of the donor/receptor/particle model proposed by Charlot in the 1940s in France.

Although in essence Charlot's method follows Brønsted's acid-base theory (when the exchanged particle is the proton), it generalizes it to the exchange of other particles [6]. This generalization can be done very well for two-components systems, but when there are more components and the simultaneous exchange of two or more particles appears, Charlot's generalization is not so good. In those cases, then, the same French professors introduce the definition of conditional constants and complexation coefficients made by Professor Anders Ringbom [57,58].

We have made some contributions to the donor/receptor/particle model to improve the understanding of Mexican students, as noted in the previous section. One of them consists of a more direct formalization within the Chemical Thermodynamics framework, closely following the approach of Professors Smith and Missen [59], especially for the definition of components and the set of independent equilibria in a system.

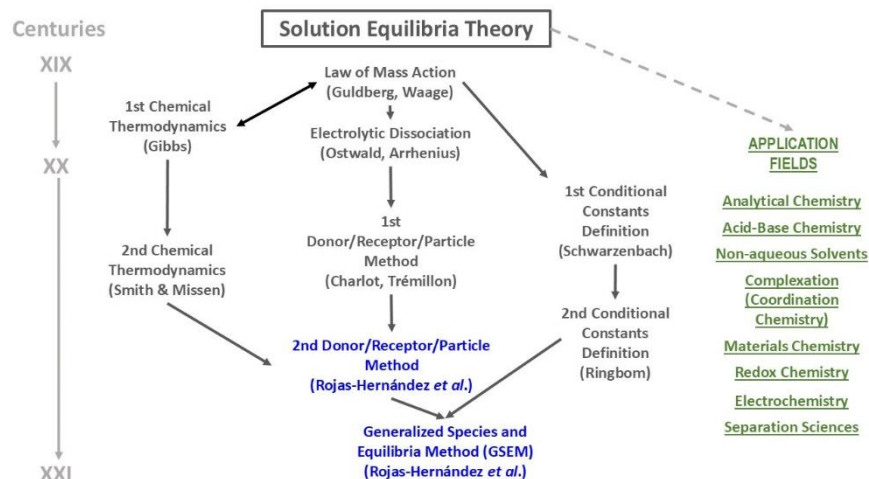
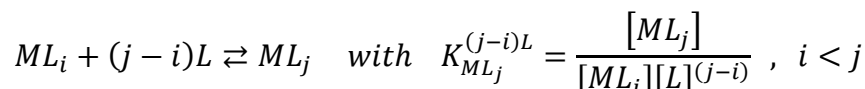


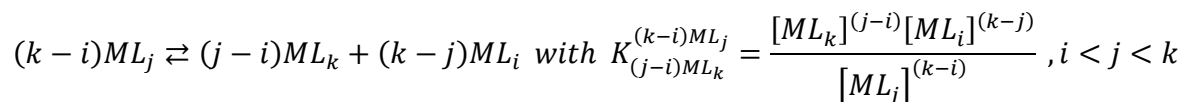
Fig. 4. Brief timeline and conceptual relationship of several methods used in Solution Chemical Equilibria Theory. This theory is applied in different Chemistry branches and is very useful in many cases.

But something that we also sought during some time was to generalize the Charlot's method to systems where there are more than two components under buffer conditions.

Charlot's method for two-components systems (M-L), which are polydonors of the L particle: $(ML_n/ML_{(n-1)}/\dots/ML_j/\dots/ML/M/L)$, has a complete set of n independent equilibria (containing all the chemical information of the system), which are selected from the collection of formation equilibria

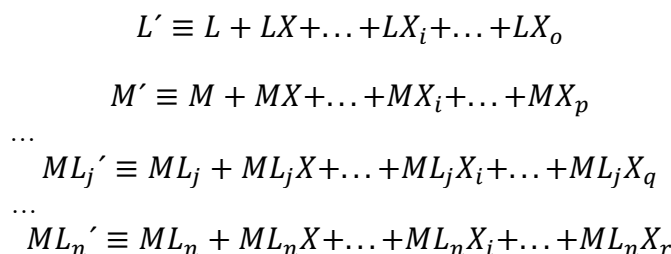


and the set of dismutation equilibria



From a set of n independent equilibria, Charlot's method selects the equilibrium with the greatest physical significance (given the initial conditions of the system) or representative equilibrium, as if it were the only one present in that system.

Thus, for three-components systems (M-L-X), where X is the buffered component ($pX = \text{constant}$), the generalization of the method leads to the proposal of a generalized species scheme that follows a model of polydonors of the L' generalized particle: $(ML_n'/ML_{(n-1)}'/\dots/ML_j'/\dots/ML'/M'/L')$, in agreement with definitions of generalized species



with molarities

$$[L'] = [L] + [LX] + \dots + [LX_i] + \dots + [LX_o] = [L]\alpha_{L(X)}$$

$$[M'] = [M] + [MX] + \dots + [MX_i] + \dots + [MX_p] = [M]\alpha_{M(X)}$$

$$\dots$$

$$[ML_j'] = [ML_j] + [ML_jX] + \dots + [ML_jX_i] + \dots + [ML_jX_q] = [ML_j]\alpha_{ML_j(X)}$$

$$\dots$$

$$[ML_n'] = [ML_n] + [ML_nX] + \dots + [ML_nX_i] + \dots + [ML_nX_r] = [ML_n]\alpha_{ML_n(X)}$$

where $\alpha_{L(X)}$, $\alpha_{M(X)}$, $\alpha_{ML_j(X)}$, ..., $\alpha_{ML_n(X)}$ are the complexation coefficients of L, M, ..., ML_j , ..., ML_n , which depend of the molarity of the buffered component, [X], through polynomials (with exponents that are natural or integer numbers and coefficients that are global formation constants of the species involved in each case).

With these generalized species definitions, generalized formation equilibria can be defined

$$ML_i' + (j - i)L' \rightleftharpoons ML_j' \quad \text{with} \quad K_{ML_j'}^{(j-i)L'} = \frac{[ML_j']}{[ML_i'][L']^{(j-i)}}$$

$$= K_{ML_j}^{(j-i)L} \frac{\alpha_{ML_j(X)}}{\alpha_{ML_i(X)}[\alpha_{L(X)}]^{(j-i)}}$$

as well as the generalized dismutation equilibria

$$(k - i)ML_j' \rightleftharpoons (j - i)ML_k' + (k - j)ML_i' \quad \text{with} \quad K_{(j-i)ML_k'}^{(k-i)ML_j'} = \frac{[ML_k']^{(j-i)}[ML_i']^{(k-j)}}{[ML_j']^{(k-i)}}$$

$$= K_{(j-i)ML_k}^{(k-i)ML_j} \frac{[\alpha_{ML_k(X)}]^{(j-i)}[\alpha_{ML_i(X)}]^{(k-j)}}{[\alpha_{ML_j(X)}]^{(k-i)}}$$

$K_{ML_j'}^{(j-i)L'}$ representing the conditional formation constant of the generalized species ML_j' from the generalized species ML_i' , while $K_{(j-i)ML_k'}^{(k-i)ML_j'}$ represents the conditional dismutation constant of the generalized species ML_j' that gives rise to the generalized species ML_k' and ML_i' . Substituting subscripts i, j, k properly, all generalized equilibria of each type in the system are obtained.

From these two sets of generalized equilibria, n independent generalized equilibria are selected.

It can be shown that if the value of pX is imposed on the system, the complexation coefficients and the conditional constants are constant [60], so under these conditions everything that was done with simple chemical equilibria in the system, with Charlot's Method, can be done with generalized equilibria, namely: diagrams of predominance zones, reaction prediction scales, tables of variation of substance quantities, reaction schemes for complexation or redox titrations, separation conditions of different chemical species, etc.

GSEM is different from the Ringbom's method, because in the latter only one equilibrium of "primed species" is handled, which in the case of particle polydonor systems will have a conditional constant that does not depend only on the buffered pX.

GSEM is generalizable to systems of four or more components with double or multiple buffering, since the multiconditional constants, of the second-order or higher-order generalized equilibria, only depend on the conditions imposed for the buffered components. [60]

Finally, GSEM can be handled approximately with representative equilibria, constructed with the predominant species for each generalized species. This can make it very intuitive. [61-63]. Fig. 5. shows the different approaches to the description of complexation titration of Cu(II) with EDTA at imposed pH = 5.0 with a buffer of acetic acid/acetate 0.25 M.

Although GSEM has been documented by us in a doctoral thesis [60] and different articles [64-72], where its potential is shown to make graphical representations in multi-component and multi-reacting systems (considering the formation of coordination compounds, polynuclear species, redox equilibria, condensed phases, liquid-liquid extraction or ionic exchange), its full potential has not been shown in books and articles, generalizing Charlot's method in calculations, which could make it more popular. We teach Analytical Chemistry using GSEM from 1985 to this date.

It is necessary to mention the contributions provided by Dr. Ignacio González (who agreed to direct my doctoral thesis [60]) and Dr. Jorge Ibáñez to the GSEM, established in some publications [64-70].

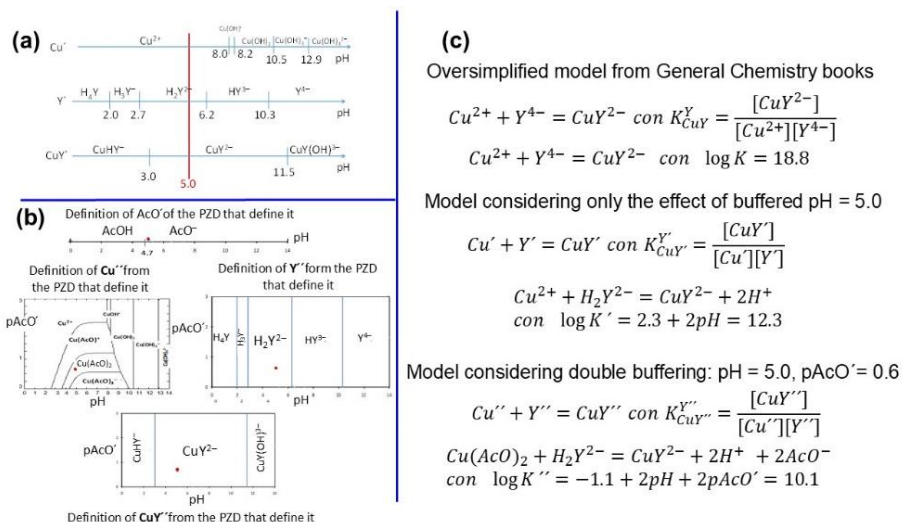


Fig. 5. Several models that could be considered to explain the complexation reaction of Cu(II) with EDTA. **(a)** Approximated definitions of generalized species Cu' , Y' and CuY' at buffered pH = 5.0, without considering the effect of acetates buffer. **(b)** Approximated definitions of generalized species AcO' , Cu'' , Y'' and CuY'' at buffered pH = 5.0 and imposed $\text{pAcO}' = 0.6$ ($[\text{AcO}'] = 0.25 \text{ M}$). **(c)** Approximated definitions of generalized equilibria used to explain the complexation reaction. The last approach is the best. Data have been taken from [57] and HYDRA database from MEDUSA software. [73]

Conclusions

A summary of the contributions that we have made to the development of General Analytical Chemistry has been presented, both from a teaching and research point of view.

The starting point was the approach of Professor Gaston Charlot's method to Analytical Chemistry, particularly his view that individuals trained in it are expected to be creative and approach the solution of problems in a reasoned manner, involving all knowledge and experimentation that may be available.

In our approach to the study of Analytical Chemistry problems, it is always important to consider the chemical species that may be present in the system. We think that this way of approaching knowledge should not be lost, but should be enriched, along with the physicochemical processes analysis that can be present in chemical analysis, industrial chemistry, materials chemistry, etc.

Other groups in Mexico are making other developments, but it is necessary that we communicate and join forces so that a consolidation of a Mexican School of General Analytical Chemistry can be achieved.

Acknowledgements

We acknowledge all students that have participated in Bachelor's thesis or Thesis performed in our Analytical Chemistry Area. Without their work we could have not go forward in our research. Also our acknowledge to those students that followed any Analytical Chemistry course we offer in UAM-Iztapalapa. We are in debt with Dr. Ignacio González (Nacho) by giving us access to reference [1]. Finally, we want to dedicate this paper to the memory of Bernard Trémillon and Rosamar, unfortunately passed away in 2023; and José Franco Pérez-Arévalo, recently passed away too.

References

1. Trémillon, B. Recueil de Textes Scientifiques Rédigés entre 1998 et 2009. 2009. Bulletin de l'Association des Anciens Elèves de l'ENSCP (École Nationale Supérieure de Chimie de Paris—Chimie Paris Tech-PSL). p. 84.
2. Morales-Galicia, L. M.; Rojas-Hernández, A. Obituario. Dra. Margarita Gómez Moliné (Rosamar). *Bol. Soc. Quím. Mex.* **2023**, *17*, 4-5. http://bsqm.org.mx/pdf-boletines/V17/V17N2/BSQM231702_cRosamar.pdf
3. Ramírez-Silva, M. T. Semblanza del doctor Alberto Rojas Hernández, acreedor del Premio Nacional de Química Andrés Manuel del Río 2011 de la Sociedad Química de México, en Docencia. *Bol. Soc. Quím. Mex.* **2011**, *5*, 50-51. <http://bsqm.org.mx/pdf-boletines/V5/N1-3/13.-%20Semblanza%20Alberto%20Rojas.pdf>
4. Rojas-Hernández, A.; Ramírez-Silva, M. T. La investigación en Química Analítica en México en los albores del Siglo XXI: Una visión desde el Área de Química Analítica de la Universidad Autónoma Metropolitana, Unidad Iztapalapa. *Bol. Soc. Quím. Mex.* **2011**, *3*, 58-68. <http://bsqm.org.mx/pdf-boletines/V3/N1/10-Alberto%20Rojas%20Hdez.pdf>
5. Trémillon, B. Homenaje a Gaston Charlot. *Educ. quím.* **1998**, *9*, 67-72. DOI: <https://doi.org/10.22201/fq.18708404e.1998.2.66569>
6. Charlot, G. *Chimie Analytique Générale*. Vol. 1. Masson. Paris. **1969**.
7. Rojas-Hernández, A. Representaciones gráficas de sistemas multicomponentes y multirreaccionantes: el Método de Especies y Equilibrios Generalizados. *Bol. Soc. Quím. Mex.* **2014**, *8*, 23-29. https://bsqm.org.mx/pdf-boletines/V8/V8N3/V8N3_Art5.pdf
8. Ramírez, M. T.; Palomar, M. E.; González, I.; Rojas-Hernández, A. Carbon Paste Electrodes with Electrolytic Binder: Influence of the Preparation Method. *Electroanalysis* **1995**, *7*, 184-188. DOI: <https://doi.org/10.1002/elan.1140070215>
9. Morales-Pérez, A.; Roa-Morales, G.; Bernabé-Pineda, M.; Sánchez-Rivera, A. E.; Rojas-Hernández, A.; Ramírez, M. T.. Electrochemical Study of Lead Species in Acetate Media: *In Situ* Formation of Alkyl and Lead Species on Carbon Paste Electrode. *Electroanalysis* **2001**, *13*, 541-548. DOI: [https://doi.org/10.1002/1521-4109\(200105\)13:7%3C541::AID-ELAN541%3E3.0.CO;2-5](https://doi.org/10.1002/1521-4109(200105)13:7%3C541::AID-ELAN541%3E3.0.CO;2-5)
10. Corona-Avenidaño, S.; Alarcón-Ángeles, G.; Ramírez-Silva, M. T.; Rosquete-Pina, G.; Romero-Romo, M.; Palomar-Pardavé, M.; On the electrochemistry of dopamine in aqueous solution. Part I: The role of [SDS] on the voltammetric behavior of dopamine on a carbon paste electrode. *J. Electroanal. Chem.* **2007**, *609*, 17-26. DOI: <https://doi.org/10.1016/j.jelechem.2007.05.021>
11. Palomar-Pardavé, M.; Alarcón-Ángeles, G.; Ramírez-Silva, M. T.; Romero-Romo, M.; Rojas-Hernández, A.; Corona-Avenidaño, S. Electrochemical and spectrophotometric determination of the formation constants of the ascorbic acid- β -cyclodextrin and dopamine- β -cyclodextrin inclusion complexes. *J. Incl. Phenom. Macrocycl. Chem.* **2011**, *69*, 91-99. DOI: <https://doi.org/10.1007/s10847-010-9818-0>

12. Guzmán-Hernández, D. S.; Ramírez-Silva, M. T.; Palomar-Pardavé, M.; Corona-Avendaño, S.; Galano, A.; Rojas-Hernández, A.; Romero-Romo, M. Electrochemical characterization of tenoxicam using a bare carbon paste electrode under stagnant and forced convection conditions. *Electrochim. Acta* **2012**. 59. 150-155. DOI: <https://doi.org/10.1016/j.electacta.2011.10.046>
13. Corona-Avendaño, S.; Ramírez-Silva, M. T.; Romero-Romo, M.; Rojas-Hernández, A.; Palomar-Pardavé, M. Influence Of The HClO₄ Concentration On The β-Cd Electropolymerization Over A Carbon Paste Electrode And On Dopamine's Electrochemical Response. *Electrochim. Acta* **2013**. 89. 854-860. DOI: <https://doi.org/10.1016/j.electacta.2012.10.165>
14. Martínez-Guerra, J.; Palomar-Pardavé, M.; Romero-Romo, M.; Corona-Avendaño, S.; Guzmán-Hernández, D. S.; Rojas-Hernández, A.; Ramírez-Silva, M. T. On the Curcumin and β-Cyclodextrin Interaction in Aqueous Media. Spectrophotometric and Electrochemical Study. *Chem. ElectroChem.* **2022**. 9. DOI: <https://doi.org/10.1002/celec.202101534>
15. Álvarez-Romero, G. A.; Rojas-Hernández, A.; Morales-Pérez, A.; Ramírez-Silva, M. T. Determination of β-D-glucose using flow injection analysis and composite-type amperometric tubular biosensors. *Biosens. Bioelectron.* **2004**. 19. 1057-1065. DOI: <https://doi.org/10.1016/j.bios.2003.10.001>
16. García-Dávila, V.; Alarcón-Ángeles, G.; Rojas-Hernández, A.; Ramírez-Silva, M. T.; Palomar-Pardavé, M.; Romero-Romo, M. Electrochemical and Spectrophotometric Detection of the Chromo-Diphenylcarbazide Complex using FIA. *ECS Transactions.* **2007**. 3. 87-92. DOI: <https://doi.org/10.1149/1.2806954>
17. Valdés-Ramírez, G.; Álvarez-Romero, G. A.; Galán-Vidal, C. A.; Hernández-Rodríguez, P. R.; Ramírez-Silva, M. T. Composites: A novel alternative to construct solid state Ag/AgCl reference electrodes. *Sens. Actuators, B* **2005**. 14. 264-270. DOI: <https://doi.org/10.1016/j.snb.2005.02.013>
18. Álvarez-Romero, G. A.; Morales-Pérez, A.; Rojas-Hernández, A.; Palomar-Pardavé, M.; Ramírez-Silva, M. T. Development of a Tubular Sensor Based on a Polypyrrole-Doped Membrane for the Potentiometric Determination of the Dodecylsulfate Anion in a FIA System. *Electroanal.* **2004**. 16. 1236-1243. DOI: <https://doi.org/10.1002/elan.200302935>
19. Álvarez-Romero, G. A.; Palomar-Pardavé, M. E.; Ramírez-Silva, M. T. Development of a novel nitrate-selective composite sensor based on doped polypyrrole. *Anal. Bioanal. Chem.* **2007**. 387. 1533-1541. DOI: <https://doi.org/10.1007/s00216-006-1021-1>
20. Álvarez-Romero, G. A.; Garfias-García, E.; Ramírez-Silva, M. T.; Galán-Vidal, C.; Romero-Romo, M.; Palomar-Pardavé, M. Electrochemical and AFM characterization of the electropolymerization of pyrrole over a graphite-epoxy resin solid composite electrode, in the presence of different anions. *App. Surf. Sci.* **2006**. 252. 5783-5792. DOI: <https://doi.org/10.1016/j.apsusc.2005.07.060>
21. Cobos-Murcia, J. A.; Galicia, L.; Rojas-Hernández, A.; Ramírez-Silva, M. T.; Álvarez-Bustamante, R. A.; Romero-Romo, M.; Rosquete-Pina, G.; Palomar-Pardavé, M. Electrochemical polymerisation of 5-amino-1,10-phenanthroline onto different substrates. Experimental and theoretical study. *Polymer.* **2005**. 46. 9053-9063. DOI: <https://doi.org/10.1016/j.polymer.2005.07.026>
22. Rojas-Hernández, A.; Ramírez Silva, M. T. Modelo Termodinámico General para Curvas de Valoración Ácido-Base de Mezclas de Sistemas Poliácidos o Polibásicos (sin Polinucleación) con Ácido o Base Fuertes. Primera Semana de la Química Inorgánica. Vol. 1. Notas de curso. **2002**. Academia Mexicana de Química Inorgánica. 133-158. ISBN-02-A-970-31-0149-6
23. Rodríguez-Laguna, N.; Rojas-Hernández, A.; Ramírez-Silva, M. T. Estudio y comportamiento de la capacidad buffer de mezclas de especies de un mismo sistema polidonador de protones. *Educ. quím.* **2014**. 25. 210-222. DOI: [https://doi.org/10.1016/S0187-893X\(14\)70560-9](https://doi.org/10.1016/S0187-893X(14)70560-9)
24. Rojas-Hernández, A.; Rodríguez-Laguna, N.; Ramírez-Silva, M. T.; Moya-Hernández, R. Distribution Diagrams and Graphical Methods to Determine or to Use the Stoichiometric Coefficients of Acid-Base and Complexation Reactions. Chap. 13. 287-310. In: Innocenti, A. Ed. Stoichiometry and Research-The Importance of Quantity in Biomedicine. **2012**. InTech. DOI: <https://doi.org/10.5772/34640>

25. Rodríguez-Laguna, N.; Rojas-Hernández, A.; Moya-Hernández, R.; Gómez-Balderas, R.; Romero-Romo, M. A. The Conditions Needed for a Buffer to Set the pH in a System. Chap. 1. 3-21. In: Hoang, V. D. Ed. *Advances in Titration Techniques*. **2017**. InTech. DOI: <https://doi.org/10.5772/intechopen.69003>
26. Leggett, D.J. SQUAD. In: Leggett, D.J. Ed. *Computational Methods for the Determination of Formation Constants. Modern Inorganic Chemistry*. Chap. 6. Springer, Boston, MA. DOI: https://doi.org/10.1007/978-1-4684-4934-1_6
27. Morales-Pérez, A. Estudio de sistemas químicos multirreaccionantes en soluciones acuosas por métodos espectrofotométricos con el programa SQUAD y otros métodos computacionales. Tesis de Maestría. 1993. Facultad de Estudios Superiores-Cuautitlán. UNAM. 117 páginas.
28. Sánchez-Rivera, A. E.; Corona-Avedaño, S.; Alarcón-Angeles, G.; Rojas-Hernández, A.; Ramírez-Silva, M. T.; Romero-Romo, M. A. Spectrophotometric study on the stability of dopamine and the determination of its acidity constants. *Spectrochim. Acta A Mol. Biomol. Spectrosc.* **2003**. 59. 3193-3203. DOI: [https://doi.org/10.1016/S1386-1425\(03\)00138-0](https://doi.org/10.1016/S1386-1425(03)00138-0)
29. Bernabé-Pineda, M.; Ramírez-Silva, M. R.; Romero-Romo, M.; González-Vergara, E.; Rojas-Hernández, A. Determination of acidity constants of curcumin in aqueous solution and apparent rate constant of its decomposition. *Spectrochim. Acta A Mol. Biomol. Spectrosc.* **2004**. 60. 1091-1097. DOI: [https://doi.org/10.1016/S1386-1425\(03\)00342-1](https://doi.org/10.1016/S1386-1425(03)00342-1)
30. Corona-Avedaño, S.; Alarcón-Angeles, G.; Rojas-Hernández, A.; Romero-Romo, M. A.; Ramírez-Silva, M. T. Study on the stability of adrenaline and on the determination of its acidity constants. *Spectrochim. Acta A Mol. Biomol. Spectrosc.* **2004**. 61. 305-311. DOI: <https://doi.org/10.1016/j.saa.2004.03.023>
31. Corona-Avedaño, S.; Romero-Romo, M. A.; Rojas-Hernández, A.; Ramírez-Silva, M. T. Study on the stability of the serotonin and on the determination of its acidity constants. *Spectrochim. Acta A Mol. Biomol. Spectrosc.* **2005**. 61. 621-627. DOI: <https://doi.org/10.1016/j.saa.2004.05.016>
32. Corona-Avedaño, S.; Rojas-Hernández, A.; Romero-Romo, M. A.; Palomar-Pardavé, M.; Ramírez-Silva, M. T. Study on the stability of noradrenaline and on the determination of its acidity constants. *Spectrochim. Acta A Mol. Biomol. Spectrosc.* **2005**. 61. 3139-3134. DOI: <https://doi.org/10.1016/j.saa.2004.11.047>
33. Gómez-Zaleta, B.; Ramírez-Silva, M. T.; Gutiérrez, A.; González-Vergara, E.; Güizado-Rodríguez, M.; Rojas-Hernández, A. UV/vis, ¹H, and ¹³C NMR spectroscopic studies to determine mangiferin pKa values. *Spectrochim. Acta A Mol. Biomol. Spectrosc.* **2006**. 64. 1002-1009. DOI: <https://doi.org/10.1016/j.saa.2005.09.009>
34. Rodríguez-Barrientos, D.; Rojas-Hernández, A.; Gutiérrez, A.; Moya-Hernández, R.; Gómez-Balderas, R.; Ramírez-Silva, M. T. Determination of pKa values of tenoxicam from ¹H NMR chemical shifts and of oxicams from electrophoretic mobilities (CZE) with the aid of programs SQUAD and HYPNMR. *Talanta*. **2009**. 80. 754-762. DOI: <https://doi.org/10.1016/j.talanta.2009.07.058>
35. Ibarra-Montaña, E. L.; Rodríguez-Laguna, N.; Sánchez-Hernández, A.; Rojas-Hernández, A. Determination of pKa Values for Acrylic, Methacrylic and Itaconic Acids by ¹H and ¹³C NMR in Deuterated Water. *JASCM*. **2015**. 4. 7-18. DOI: <http://dx.doi.org/10.6000/1929-5030.2015.04.01.2>
36. Islas-Martínez, J. M.; Rodríguez-Barrientos, D.; Galano, A.; Ángeles, e.; Torres, L. A.; Olvera, F.; Ramírez-Silva, M. T.; Rojas-Hernández, A. Deprotonation Mechanism of New Antihypertensive Piperidinylmethylphenols: A Combined Experimental and Theoretical Study. *J. Phys. Chem. B* **2009**. 113. 11765-11774. DOI: <https://doi.org/10.1021/jp904474m>
37. Galano, A.; Álvarez-Diduk, R.; Ramírez-Silva, M. T.; Alarcón-Ángeles, G.; Rojas-Hernández, A. Role of the reacting free radicals on the antioxidant mechanism of curcumin *Chem. Phys.* **2009**. 363. 13-23. DOI: <https://doi.org/10.1016/j.chemphys.2009.07.003>
38. Sanpedro-Montoya, K.; Martínez-Pérez, B.; Galano, A.; Ángeles, E.; Abrego, V. H.; Ramírez-Silva, M. T.; Rojas-Hernández, A. Deprotonation Mechanism and log P Values of New Antihypertensive Thiomorpholinylmethylphenols: A Combined Experimental and Theoretical Study. *J. Chem. Eng. Data* **2010**. 55. 4323-4331. DOI: <https://doi.org/10.1021/je100470g>

39. Rebollar-Zepeda, A. M.; Campos-Hernández, T.; Ramírez-Silva, M. T.; Rojas-Hernández, A.; Galano, A. Searching for Computational Strategies to Accurately Predict pKas of Large Phenolic Derivatives. *J. Chem. Theory Comp.* **2011**. 7. 2528-2538. DOI: <https://doi.org/10.1021/ct2001864>
40. Mendoza-Sarmiento, G.; Rojas-Hernández, A.; Galano, A.; Gutiérrez, A. A combined experimental-theoretical study of the acid-base behavior of mangiferin: implications for its antioxidant activity. *RSC Advances*. **2016**. 6. 51171–51182. DOI: <https://doi.org/10.1039/C6RA06328D>
41. Ibarra-Escutia, A.; Rojas-Hernández, A.; Galano, A.; Ángeles, E.; Martínez-Mendoza, D.; Moya-Hernández, R. Determination of Acidity Constants, Partition Coefficients Between Water and 1-Octanol, and Deprotonation Route of 4-tert-butyl-bis-(2,6-thiomorpholin-4-ylmethyl)-1-phenol and 4-hydroxy-3,5-bis(morpholin-1-ylmethyl)benzotrile; Compounds with Antihypertensive Properties. *J. Mex. Chem. Soc.* **2016**. 60. 152-162. <https://www.jmcs.org.mx/index.php/jmcs/article/view/98/97>
42. Hernández-Olivares, M. A.; Ibarra-Escutia, A.; Mendoza-Sarmiento, G.; Rojas-Hernández, A.; Galano, A. Elucidation of the complex deprotonation routes of Changrolin, the antihypertensives LQM-303 and LQM-303b, and their derivatives. *Comput. Theor. Chem.* **2017**. 1115. 229–238. DOI: <https://doi.org/10.1016/j.comptc.2017.06.023>
43. Botello, J. C.; Morales-Domínguez, e.; Domínguez, J. M.; Gutiérrez, A.; Rojas-Hernández, A.; Ramírez, M. T. A New Nuclear Magnetic Resonance Algorithm to Determine Equilibrium Constants of the Species in the B(III)-H₂O System. *Spectrochim. Acta A Mol. Biomol. Spectrosc.* **2003**. 59. 1477-1486. DOI: [https://doi.org/10.1016/S1386-1425\(02\)00394-3](https://doi.org/10.1016/S1386-1425(02)00394-3)
44. Moya-Hernández, M. R.; Mederos, A.; Dominguez, S.; Orlandini, A.; Ghilardi, C.; Cecconi, F.; González-Vergara, E.; Rojas-Hernández, A. Speciation Study of the Anti-Inflammatory Drug Tenoxicam (HTenox) with Cu(II). X-Ray Structure of [Cu(Tenox)₂(Py)₂]-EtOH. *J. Inorg. Biochem.* **2003**. 95. 131-140. DOI: [https://doi.org/10.1016/S0162-0134\(03\)00095-3](https://doi.org/10.1016/S0162-0134(03)00095-3)
45. Bernabé-Pineda, M.; Ramírez-Silva, M. T.; Romero-Romo, M. A.; González-Vergara, E.; Rojas-Hernández, A. Spectrophotometric and electrochemical determination of the formation constants of the complexes Curcumin-Fe(III)-water and Curcumin-Fe(II)-water. *Spectrochim. Acta A Mol. Biomol. Spectrosc.* **2004**. 60. 1105–1113. DOI: [https://doi.org/10.1016/S1386-1425\(03\)00344-5](https://doi.org/10.1016/S1386-1425(03)00344-5)
46. Lozano-Camargo, M. L.; Rojas-Hernández, A.; Gómez-Hernández, M.; Pacheco-Hernández, M. L.; Galicia, L.; Ramírez-Silva, M. T. UV-visible spectroscopic and electrochemical study of the complex formation between Fe(II) and 5-amino-1,10-phenantroline (5-Aphen) in aqueous solution. *Talanta* **2007**. 72. 1458-1468. DOI: <https://doi.org/10.1016/j.talanta.2007.01.065>
47. Botello, J. C.; Pacheco-Hernández, M. L.; Gutiérrez, A.; Domínguez, J. M.; Espinosa, G.; Ramírez-Silva, M. T.; Rojas-Hernández, A. Equilibrium Constants Determination of the Species Formation in the Al(III)-H₂O System by Integration of ²⁷Al-NMR Signals and Fitting with Species Fractions. *J. Mex. Chem. Soc.* **2008**. 52. 47-53. DOI: <https://doi.org/10.29356/jmcs.v52i1.1045>
48. Moya-Hernández, R.; Gómez-Balderas, R.; Mederos, A.; Domínguez, S.; Ramírez-Silva, M. T.; Rojas-Hernández, A. Complex formation of the anti-inflammatory drugs tenoxicam and piroxicam with Fe(III) in methanol and acetone. *J. Coord. Chem.* **2009**. 10. 40-51. DOI: <https://doi.org/10.1080/00958970802474870>
49. Moya-Hernández, R.; Gómez-Balderas, R.; Rojas-Hernández, A. Chemical Speciation of the Fe(III)-piroxicam and Fe(III)-tenoxicam Systems in Aqueous Solution. *J. Mex. Chem. Soc.* **2011**. 55. 94-100. DOI: <https://doi.org/10.29356/jmcs.v55i2.838>
50. Verastegui-Omaña, B.; Palomar-Pardavé, M.; Rojas-Hernández, A.; Corona Avendaño, S.; Romero-Romo, M.; Ramírez-Silva, M. T. Spectrophotometric quantification of the thermodynamic constants of the complexes formed by dopamine and Cu(II) in aqueous media. *Spectrochim. Acta A Mol. Biomol. Spectrosc.* **2015**. 143. 187-191. DOI: <https://doi.org/10.1016/j.saa.2015.01.067>
51. Hernández-García, L., Rojas-Hernández, A.; Galano, A. Mangiferin/β-cyclodextrin complex: determination of the Inclusion constant in aqueous solution by Higuchi–Connors method and molecular absorption and photoluminescence UV spectroscopies at pH 3.4. *Chem. Pap.* **2022**. 76. 7123–7132. DOI: <https://doi.org/10.1007/s11696-022-02381-z>

52. Rojas-Hernández, A.; Ramírez, M. T.; González, I. Predominance-zone Diagrams in Solution Chemistry. Dismutation Processes in Two Component Systems (M-L). *J. Chem. Educ.* **1995**, *72*, 1099-1105. DOI: <https://doi.org/10.1021/ed072p1099>
53. Rojas-Hernández, A.; Martínez-Guerra, J.; Ramírez-Silva, M. T. Cálculos de pH en mezclas de sistemas poliácidos y polibásicos y algoritmo de cálculo robusto con un conjunto completo de equilibrios independientes. Colección Memorias de los Congresos de la Sociedad Química de México, 2do Congreso Internacional de Educación Química-en línea. **2021**, CIEQ-IED-10, 219-224. https://sqm.org.mx/wp-content/uploads/2022/05/CIEQ2021_interactivo.pdf
54. Rojas-Hernández, A.; Ramírez-Silva, M. T.; Galano, A.; Córdova-Frunz, J. L.; Pérez-Arévalo, J.F. La ecuación de Charlot, la gráfica de Flood y la gráfica de Gordus. *Educ. quím.* **2010**, *21*, 306-313. DOI: [https://doi.org/10.1016/S0187-893X\(18\)30100-9](https://doi.org/10.1016/S0187-893X(18)30100-9)
55. Rojas-Hernández, A.; Moya-Hernández, R.; Rueda-Jackson, J. C.; Ramírez-Silva, M. T. Thermodynamic Study of Component and Species Distributions in a One Component System as a First Step of Sol-Gel Processes: The Thermodynamic Mechanism of Polymerization. 364-380. In: Lopez, T. M.; Avnir, D.; Aegerter, M. (Eds.) *Emerging Fields of Sol-Gel Science and Technology*. Kluwer. Boston. **2003**. <https://springerlink.uam.elogim.com/book/10.1007/978-1-4615-0449-8>
56. Moya-Hernández, R.; Rueda-Jackson, J. C.; Ramírez-Silva, M. T.; Vázquez, G. A.; Havel, J.; Rojas-Hernández, A. Statistical Study of Distribution Diagrams for Two-Component Systems: Relationships of Means and Variances of the Discrete Variable Distributions with Average Ligand Number and Intrinsic Buffer Capacity. *J. Chem. Educ.* **2002**, *9*, 389-392. DOI: <https://doi.org/10.1021/ed079p389>
57. Ringbom, A. *Complexation in Analytical Chemistry*. Interscience. New York. **1963**. ISSN 0069-2883
58. Trémillon, B. *Électrochimie Analytique et Réactions en Solution*. Vol. 1. Masson. Paris. **1993**. 519 páginas. ISBN: 2-225-84177-2
59. Smith, W. R.; Missen, R. W. *Chemical Reaction Equilibrium Analysis: Theory and Algorithms*. Wiley. New Jersey. **1983**. ISBN 10:0471093475.
60. Rojas-Hernández, A. *El Método de Especies y Equilibrios Generalizados para el Estudio de Sistemas Químicos en Equilibrio bajo Condiciones de Amortiguamiento: Teoría y Algoritmos de los Diagramas de Zonas de Predominio*. 1995. Tesis de Doctorado. UAM-Iztapalapatpalapa. 347 páginas. <http://tesiuami.izt.uam.mx/uam/asp/uam/presentatesis.php?recno=1867&docs=UAM1867.PDF>
61. Trejo-Córdova, G.; Rojas-Hernández, A.; Ramírez-Silva, M. T. *Diagramas de Zonas de Predominio Aplicados al Análisis Químico*. UAM-Iztapalapatpalapa. CDMX. 1993. ISBN: 970-620-260-9
62. Rojas-Hernández, A.; Ramírez-Silva, M. T. Solución al Reactivo: Primer Examen Parcial de un Curso de Química Analítica II. *Educ. quím.* **1992**, *3*, 312-314. DOI: <https://doi.org/10.22201/fq.18708404e.1992.4.66867>
63. Class recorded to show the prediction of PAR as indicator and spectrophotometric curve of complexometric titration of Cu(II) with EDTA at pH imposed of 5.0 with acetic acid/acetate buffer 0.25 M. Accessed in may 2024. https://youtu.be/0rYJt_n3dCE?feature=shared
64. Rojas, A.; González, I. Relationship of Two-dimensional Predominance-Zone Diagrams with Conditional Constants for Complexation Equilibria. *Anal. Chim. Acta* **1986**, *187*, 279-285. DOI: [https://doi.org/10.1016/S0003-2670\(00\)82919-0](https://doi.org/10.1016/S0003-2670(00)82919-0)
65. Rojas-Hernández, A.; Ramírez, M. T.; González, I.; Ibanez, J. G. Relationship of Multidimensional Predominance-Zone Diagrams with Multiconditional Constants for Complexation Equilibria. *Anal. Chim. Acta* **1991**, *246*, 435-442. DOI: [https://doi.org/10.1016/S0003-2670\(00\)80983-6](https://doi.org/10.1016/S0003-2670(00)80983-6)
66. Rojas-Hernández, A.; Ramírez, M. T.; González, I.; Ibanez, J. G. Construction of Multicomponent Pourbaix Diagrams Using Generalized Species. *J. Electrochem. Soc.* **1991**, *138*, 365-371. <https://iopscience.iop.org/article/10.1149/1.2085590>
67. Rojas-Hernández, A.; Ramírez, M. T.; González, I.; Ibanez, J. G. Multi-dimensional Predominance-zone Diagrams for Polynuclear Chemical Species. *Anal. Chim. Acta* **1992**, *259*, 95-104. DOI: [https://doi.org/10.1016/0003-2670\(92\)85080-P](https://doi.org/10.1016/0003-2670(92)85080-P)

68. Rojas-Hernández, A.; Ramírez, M. T.; González, I. Equilibria among condensed phases and a multi-component solution using the concept of generalized species. I. Systems with mixed complexes. *Anal. Chim. Acta* **1993**. 278, 321-333. DOI: [https://doi.org/10.1016/0003-2670\(93\)85116-2](https://doi.org/10.1016/0003-2670(93)85116-2)
69. Rojas-Hernández, A.; Ramírez, M. T.; González, I. Equilibria among condensed phases and a multi-component solution using the concept of generalized species. II. Systems with polynuclear species. *Anal. Chim. Acta* **1993**. 278, 335-347. DOI: [https://doi.org/10.1016/0003-2670\(93\)85117-3](https://doi.org/10.1016/0003-2670(93)85117-3)
70. Rojas-Hernández, A.; Ramírez, M. T.; González, I. Distribution of Mononuclear Chemical Species in Two-Phase Multicomponent Systems Using Generalized Species and Equilibria. *Química Analítica*. **1996**. 15. [Suppl.1]. S4-S8.
71. Páez-Hernández, M. E.; Ramírez, M. T.; Rojas-Hernández, A. Predominance-Zone Diagrams and Their Application to Solvent Extraction Techniques. *Talanta*. **2000**. 51. 107-121. DOI: [https://doi.org/10.1016/S0039-9140\(99\)00276-3](https://doi.org/10.1016/S0039-9140(99)00276-3)
72. Páez-Hernández, M. E.; Ramírez, M. T.; Rojas-Hernández, A. Uso del Método de Especies y Equilibrios Generalizados para Abordar Problemas de Separación por Extracción Líquido-Líquido. *Actualidad Analítica* **2023**. 83. 12-15. <https://seqa.es/wp-content/uploads/2023/09/INVESTIGACION-Ma.-Elena-Paez-Hernandez.pdf>
73. Puigdomenech, Ignasi. Making Equilibrium Diagrams Using Sophisticated Algorithms (MEDUSA). KTH. Sweden. Accessed in May 2024. <https://www.kth.se/che/medusa/downloads-1.386254>.

Evolution of research in the Pharmacology Laboratory at the Universidad Autónoma Metropolitana-Iztapalapa: A Historical Review

Francisco Javier Alarcón-Aguilar*, Julio Cesar Almanza-Pérez, Gerardo Blancas-Flores, José Luis Eduardo Flores-Sáenz, María de los Ángeles Fortis-Barrera, Abraham Giacoman-Martínez, Rubén Román-Ramos

Laboratorio de Farmacología, Departamento de Ciencias de la Salud, División de Ciencias Biológicas y de la Salud. Universidad Autónoma Metropolitana-Iztapalapa.

*Corresponding author: Francisco Javier Alarcón-Aguilar, email: aaaf@xanum.uam.mx

Received May 1st, 2024; Accepted August 4th, 2024.

DOI: <http://dx.doi.org/10.29356/jmcs.v68i4.2267>

Abstract. This paper aims to trace essential milestones in the history of the investigation activities developed throughout the past four decades in the Laboratory of Pharmacology of the Universidad Autónoma Metropolitana Iztapalapa (LFUAMI), emphasizing the contribution of Dr. Rubén Román-Ramos, the leader who guided and promoted the chemical and pharmacological investigation of natural products in the LFUAMI. Dr. Rubén Román-Ramos impacted the development of new generations, who continue contributing to and strengthening this field, both outside and inside our university, by developing the science and technology in chemistry and pharmacology research. From this historical review of the LFUAMI, it is possible to identify leading features in its different periods; the periods are characterized by the scientific evidence primary generated, the methodological impact in the results, and technological development and impact in the state of the art. It should be noted that the periods overlap, creating a cumulative effect. To conclude, we will summarize the historical milestones and present some research avenues currently pursued and some perspectives.

Keywords: Medicinal plants; anti-diabetic plants; hypoglycemic plants; phytochemistry; pharmacology.

Resumen. Este artículo es una revisión acerca de la investigación desarrollada durante los últimos 40 años en el Laboratorio de Farmacología de la Universidad Autónoma Metropolitana Iztapalapa (LFUAMI), enfatizando la contribución del Dr. Rubén Román Ramos, profesor quien guió y promovió la investigación químico-farmacológica de este laboratorio, impactando en la formación de nuevas generaciones de investigadores, quienes continúan su legado en la investigación de productos naturales, fortaleciéndolo, tanto dentro como fuera de nuestra universidad. A través de esta revisión histórica fue posible identificar algunas de las características sobresalientes de cada periodo del LFUAMI en las últimas cuatro décadas, destacando la calidad de la evidencia científica generada, la influencia metodológica y el desarrollo tecnológico de los distintos estudios, así como su impacto en el estado del arte. Para concluir, se resumen algunos de los desarrollos más relevantes, se presentan algunas de los trabajos recientes y las perspectivas de investigación más importantes de este consolidado grupo de trabajo.

Palabras clave: Plantas medicinales; plantas antidiabéticas; plantas hipoglucemiantes; fitoquímica; farmacología.

Introduction

This paper offers a concise historical review of the systematic research conducted in the pharmacology laboratory of the Universidad Autónoma Metropolitana Iztapalapa (LFUAMI) over the past four decades, highlighting its evolution and contributions to biomedical sciences. The paper comprises four parts. The first one explores the origin and essential characteristics of the laboratory, spanning from its establishment in 1986 to the year 2000. The second part presents the three main periods of the laboratory's evolution: The foundation, the strengthening, and the diversification periods, covering the years 2001 to 2010. The third part explores the technological period, spanning from 2011 onwards. These periods are characterized by distinct features, including scientific evidence, methodological diversity, and technological development. The last part of the paper summarizes the main elements of the laboratory's history and presents future research directions.

Foundation period by Professor Ruben Roman-Ramos (1986-2000)

The establishment of the LFUAMI was influenced by a global surge of interest in the study of medicinal plants, particularly evident in Mexico during the late 1970s. This period coincided with the creation of the Mexican Institute for the Study of Medicinal Plants (IMEPLAM), reflecting a growing recognition of the potential therapeutic benefits of natural substances. In Mexico, researchers and institutions alike were drawn to the study of medicinal plants, driven by a desire to explore traditional healing practices and uncover potential new sources of pharmacological agents.

Dr. Rubén Román-Ramos (Fig. 1), a University of Peoples Friendship graduate in Moscow, Russia, obtained a bachelor's and doctoral degree in medicine, specializing in Endocrinology. He began his illustrious research career at the IMEPLAM under the mentorship of Dr. Xavier Lozoya Legarreta, then the institute's director. At IMEPLAM, Dr. Román-Ramos embarked on groundbreaking research focused on the therapeutic potential of indigenous Mexican plants for managing diabetes mellitus. Utilizing his expertise in endocrinology and experimental medicine, he implemented an innovative experimental model involving pancreatectomized rabbits. This model enabled him to systematically study the potential efficacy of traditional medicinal plants, including *Tecoma stans* ("tronadora"), *Cecropia obtusifolia* ("guarumo"), and *Opuntia streptacantha* ("nopal"), in controlling diabetes mellitus [1-3]. Dr. Román's pioneering work in this area established him as a trailblazer in ethnopharmacology and positioned him as a leading authority on the anti-diabetic properties of Mexican flora. His research laid the groundwork for subsequent investigations into the therapeutic potential of natural remedies for managing diabetes mellitus, contributing significantly to our understanding of traditional medicine practices in Mexico.

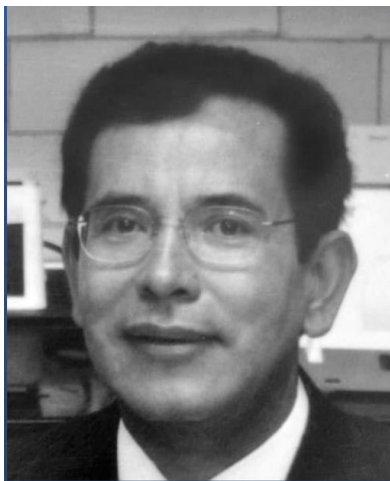


Fig.1. Dr. Rubén Román-Ramos.

The LFUAMI was founded in 1986 by Dr. Rubén Román Ramos to make progress in research and education in pharmacology and chemistry. This idea created a space dedicated to interdisciplinary pharmacological research to provide students and teachers access to state-of-the-art facilities and resources, contributing their experience to developing academic programs and research initiatives within the university. From his ingress in 1986 until 2023, Dr. Roman served as the head of the LFUAMI, and all that time, offered technical consultancy in the areas related to drug activity, natural products, and diabetes mellitus, beginning to undertake sponsored research projects as per norms of the UAM. Under the leadership of Dr. Román-Ramos, the LFUAMI quickly became a hub of scientific inquiry and innovation. Through collaborative research projects and educational programs, the laboratory played a pivotal role in advancing knowledge and understanding of pharmacology within the university community and beyond, integrating medical, biological, and chemical perspectives, and reflecting an avant-garde vision in the field.

In addition to the plants previously mentioned, Dr. Roman-Ramos conducted research on the effects of *Garcinia cambogia* ("garcinia") and other compounds and pharmaceutical formulations for obesity [4]. This research included investigations into the first thiazolidinedione, troglitazone (Rezulin), for diabetic patients. However, due to its hepatotoxic effects, troglitazone was ultimately withdrawn from the market. This research led to new thiazolidinediones, such as rosiglitazone and pioglitazone. Dr. Román-Ramos was involved in clinical research on rosiglitazone, contributing to our understanding of its therapeutic effects. [5-6].

As a full-time professor at our university, Dr. Roman-Ramos served in academic and administrative positions, including the Head of Area, Head of Department, Director of Division, and Coordinator of the PhD Programme in Biological Sciences at UAM, among other academic and administrative positions. He holds the prestigious National Researcher Level III title, awarded by the National System of Researchers (SNI) of CONACYT, now CONAHCYT. Dr. Roman-Ramos has significantly contributed to education and research, having imparted over 250 undergraduate and graduate courses. He is also the author of over 140 scientific publications and has participated in over 400 congresses and conferences. In addition to his academic achievements, Dr. Roman-Ramos has shown innovation and entrepreneurship with five patented models. His dedication to his work is evident in the more than 4,500 citations.

Strengthening and diversification period (2001-2020)

In the previous period, the biological assays *in vivo*, utilizing experimental animals, were mainly designed to determine the hypoglycemic and antihyperglycemic effects from a quantitative perspective. During this period of strengthening and diversification, researchers explored new methods and chemical tools for qualitative and quantitative analysis. A notable emphasis was on advancing *in vitro* assays, leveraging cellular culture techniques for more detailed assessments. Additionally, researchers utilized extractive methodologies to isolate natural products, facilitating the subsequent processes of compound isolation, purification, and identification by phytochemistry techniques. These approaches not only broadened the scope of research but also enhanced the precision and depth of both qualitative and quantitative analyses. Since its inception, our research group's focus has expanded and evolved under the successful leadership of Dr. Roman-Ramos, who has maintained high levels of academic productivity and facilitated the progression of the original research line. Since 1986, our research has primarily centered on pharmacological studies of medicinal plants for managing diabetes mellitus. Over time, this focus has broadened to encompass plants, other natural sources, and synthetic resources. Furthermore, our research has extended to include other related metabolic pathologies such as obesity, hypertension, and various dysfunctions. This evolution has led to our current research line: Pharmacology and chemistry of substances for treating metabolic syndrome (MS) and other chronic degenerative diseases.

During this period, our primary aim was to conduct high-quality research in the area, focusing on advancing chemical-pharmacological investigations of natural products at a mechanistic level. This endeavor involved the rational design of computer-assisted drugs and the adoption of cutting-edge techniques to elucidate various plants' molecular mechanisms of action. Our goal was to deepen our understanding of these mechanisms and pave the way for innovative approaches to drug development. The results of these investigations have allowed our working group to be recognized as a benchmark in research into natural resources with potential

usefulness in treating MS-related diseases, both at the national and international levels. The transcendence of this research line resides in the epidemiologic importance of this syndrome worldwide [7,8].

Management of MS typically requires a multifaceted approach, often involving polypharmacy, i.e., the administration of various medications such as anti-obesity agents to address weight management, anti-diabetic drugs to regulate blood sugar levels, hypolipidemic medications to manage lipid abnormalities, antihypertensive drugs to control high blood pressure, and antithrombotic agents to reduce the risk of blood clots, among others. However, the use of multiple medications concurrently can pose challenges, including potential side effects, drug interactions, and complications related to polypharmacy. Therefore, careful consideration and monitoring are essential in optimizing treatment outcomes for individuals with MS [7].

An alternative approach to mitigate the challenges associated with polypharmacy lies in using specific components derived from medicinal plants. These components have demonstrated "multitarget" actions capable of comprehensively addressing the complexities of MS. They affect carbohydrate and lipid metabolism and vascular health and possess anti-inflammatory and antioxidant properties. Moreover, they offer the potential to target the underlying issue at the core of MS, namely insulin resistance [9]. Hence, our current line of research aims to clarify the medicinal properties of various potential medicinal resources, establishing a rational basis for their therapeutic use in the MS. In general, our research group has contributed to the discovery and development of bioactive molecules through their chemical and pharmacological characterization, trying to explain their effects not only at the organism level but also at the cellular and molecular level with a mechanistic approach. Several research questions have emerged regarding the study of these resources:

Do they produce hypoglycemic, antihyperglycemic, antihypertensive, antioxidant, and anti-inflammatory, anti-obesity activities? Do they reduce insulin resistance? Do they act through several molecular targets? Can they have only one pharmacological effect or multiple? What are their action mechanisms, and is their action dose-dependent?

We have devised a comprehensive strategy based on bioassay-guided chemical studies to answer these questions. This strategy encompasses *in vitro*, *in situ*, and *in vivo* biological studies, including acute, subacute, and chronic evaluations of extracts, fractions, or pure compounds isolated and identified through conventional extractive techniques and chromatographic and spectroscopic methods. Parameters measured during these studies include blood glucose levels, plasma insulin, triglyceridemia, cholesterolemia, liver transaminase levels, inflammatory cytokines, oxidant stress markers, and various transcription factors. Different cell lines, such as adipocytes, hepatocytes, skeletal muscle, macrophages, endothelial, pancreatic, and isolated tissues, have been used *in vitro*. The techniques used in these studies were RT-qPCR, ELISA, epifluorescence, Western Blot, histological analysis, kinetics, and enzyme activity, including the chemical synthesis of biomolecules. In addition, spectrometric and spectroscopic techniques, such as UV-visible, infrared, mass spectroscopy, nuclear magnetic resonance, and coupled techniques for the chemical characterization and identification of active substances. For some of the identified compounds were performed studies of molecular docking *in silico*.

Table 1 lists some of the medicinal plants studied in the LFUAMI. Among the most relevant are *Tillandsia* spp ("heno"), *Hibiscus sabdariffa* ("Jamaica"), *Psacalium* spp ("matarique"), *Cecropia obtusifolia* ("guarumbo"), *Catharanthus roseus* ("vinca"), *Ibervillea sonora* ("wereque"), *Smilax domingensis* ("cocolmecca"), *Punica granatum* ("granada"), *Tagetes lucida* ("pericón") and *Cucurbita ficifolia* ("chilacayote") among other. In addition to medicinal plants, our research has extended to include the study of marine seagrasses, the beetle *Ulomoides dermestoides*, and jellyfish. Through collaborative efforts with various laboratories from other national institutions, we have successfully identified and isolated several active compounds from these natural resources. Some of these compounds are detailed in Table 2: triterpenes, such as α -amyrin, lupeol, oleanolic acid, and ursolic acid; phenolic acids, chlorogenic acid, and 4-hydroxybenzoic acid; flavonoids, such as luteolin, kaempferol, quercetin, apigenin and rutin; D-*chiro*-inositol, and a variety of compounds of lipidic nature, such as β -sitosterol, lauric acid, oleic acid, among others. Other supplements or drugs with interesting properties were also studied, such as glycine, cannabidiol, metformin, and rosiglitazone, among other compounds of natural or synthetic origin (Table 2). These compounds originate from diverse natural and synthetic sources and hold promise for further pharmacological investigation and potential therapeutic applications. These plants and compounds were evaluated in our laboratory throughout different experimental conditions, showing diverse activities with utility in metabolic diseases, such as anti-diabetic, hypoglycemic, anti-inflammatory, antioxidant, hypolipidemic, vasorelaxant, antihypertensive, and, particularly in the treatment of the MS. In addition to UAM-Iztapalapa, several other institutions have been involved in

these investigations, including UAM- Xochimilco, Chemical Institute (UNAM), FES Iztacala (UNAM), Facultad de Farmacia (UAEM), Specialties Hospital (IMSS), Centro de Investigación Biomedica del Sur (CIBIS-IMSS), Escuela Superior de Medicina (IPN), Instituto Nacional de Nutrición "Salvador Zubiran," Instituto Nacional de Cardiología "Ignacio Chávez," Hospital de Pediatría, Hospital Infantil de México "Federico Gómez," to mention a few. We sincerely thank all researchers from other institutions who have supported us. These collaborations have been instrumental in advancing our research and development objectives related to the study of natural and synthetic products.

Among the myriad resources investigated within our laboratory, particular attention must be drawn to the exhaustive research conducted on the fruit of *Cucurbita ficifolia* (*C. ficifolia*), colloquially known as chilacayote. This fruit, with its rich history of empirical use in our country for managing diabetes, has been the focal point of our research endeavors. Through rigorous chemical and pharmacological investigations at the experimental level, our research group has uncovered significant insights into the therapeutic potential of *C. ficifolia*. The elucidation of its bioactive components and pharmacological properties represents a milestone achievement, showcasing the transformative impact of our research efforts. Moreover, our findings hold promise for advancing our understanding of traditional remedies and potentially developing novel treatments for metabolic disorders. Thus, the research surrounding *C. ficifolia* stands as a testament to the dedication and innovation of our research group in the pursuit of scientific knowledge and its application to improve human health. In studying this engaging edible and medicinal resource, its investigation resulted in some technological developments in vias of scalation and marketing. In the next section, two special contributions of the LFUAMI, the technological development of nutraceutical products from *C. ficifolia* fruit and the in-silico analysis using a simplified method to perform molecular coupling simulations assisted by a computer, will be discussed.

Technological period (2021-)

The culmination of these extensive studies, which began with *in vivo* and *in vitro* experimentation and progressed to the application of *in silico* simulation methods, represents a significant milestone in the history of the LFUAMI. This milestone is embodied by the fruit of *C. ficifolia*, an engaging edible and medicinal resource of Mexican medicinal, whose study was initially proposed by Dr. Rubén Roman [12]. It represents some of the transcendent results in chemical and pharmacological research by our research group, culminating in a technological development with potential to commercialization. Another milestone in the history of the LFUAMI is its contribution to computer-assisted rational drug design. Both situations will be commented in the next section.

Chemical and Pharmacological Studies of the fruit of *C. ficifolia* and its technological development

Extracts were derived from the juice of mature fruits and subjected to chemical characterization. The aqueous extract demonstrated antihyperglycemic effects in both healthy rabbits and those with alloxan-induced diabetes, as well as in healthy rats and mice and those with streptozotocin-induced diabetes, in both acute and subacute studies [11-12], [26-27]. Normal mice had No toxic effects at usual doses [28]. In addition, the extract increased insulin levels in healthy animals and RINm5F cells, increasing the calcium store and insulin RNAm expresion, which was corroborated by confocal microscopy and RT-qPCR, respectively [33-34]. Regarding its extra-pancreatic effects, quantitative and histological assessments using Periodic Acid-Schiff (PAS) staining revealed an increase in liver glycogen accumulation. This regulation of glycogen synthesis enzymes and phosphorylase activity was validated through Western Blot analysis [36]. In mice with streptozotocin-induced diabetes, it was demonstrated that the expression of PPAR- α in the liver is increased, a transcription factor involved in lipid metabolism, without affection on PPAR- γ [39]. The antioxidant effect was evaluated in different organs due to *C. ficifolia* in this same model. Increased GSH and decreased malondialdehyde were observed in the liver, kidney, and heart [29]. The antioxidant effect was also observed in mice with STZ-induced diabetes and 3T3-L1 adipocytes, with increased GSSG/GSH ratio, glutathione peroxidase, and reductase glutathione, with a decrease in hydrogen peroxide. These findings confirm the antioxidant action of *C. ficifolia* [30,32]. The anti-inflammatory action of *C. ficifolia* was investigated in mice with monosodium glutamate-

induced obesity. After 30 days of extract administration, two pro-inflammatory cytokines, TNF- α and resistin, were reduced [35]. Similar findings were observed in vitro using 3T3-L1 adipocytes, where protein and expression levels of TNF- α and IL-6 were measured [32]. In summary, *C. ficifolia* exhibited hypoglycemic, antioxidant, and anti-inflammatory effects, as demonstrated in different experimental models, including studies involving type 2 diabetic patients [98-99].

Concerning the chemical components of the fruit, previous studies have suggested D-*chiro* inositol (DCI), an isomer mediating insulin action, as one of the main constituents that may be participating in the above actions [101-102]. DCI is also an activator of the glycogen synthase and pyruvate dehydrogenase enzymes, regulates the oxidative stress in adipocytes, exhibits reduction of pro-inflammatory cytokines (TNF- α , IL-6, and resistin), preventing the inflammatory damage in adipocytes 3T3-L1. In these studies, performed in our laboratory, DCI also increased the PKB activation, exhibiting insulin-mimetic effects in 3T3-L1 adipocytes [32]. Therefore, this compound may be beneficial for treating obesity and non-insulin-dependent diabetes mellitus (103) and should be considered in future studies.

The fruit also contains phenolic acids such as *p*-coumaric acid, *p*-hydroxybenzoic acid, *p*-hydroxyphenyl acetic acid, and gallic acid; the flavonoid catechin; salicin, and phytosterols such as stigmast-7,22-dien-3-ol and stigmast-7-en-3-ol, β -sitosterol, among others [36,95]. It has been suggested that all these compounds may act in synergy, explaining their multiple pharmacological effects and their health benefits, sometimes equivalent to agents used to control type 2 diabetes [36].

It is clear then that the data that are so far available in research into the medicinal properties and chemical components of the fruit of *C. ficifolia* sustain insulin-secretagogue action, as well as hypolipemic, anti-inflammatory, and antioxidant properties. The evidence suggests that this fruit may help treat metabolic diseases; however, for massive use, it is necessary to examine other aspects, such as its acceptability, applicability, feasibility, and transfer in different contexts. In addition, it is essential to explore pharmacokinetic processes associated with active molecules and metabolites.

Therefore, we propose using this fruit as a raw material for developing bio-functional foods, nutraceutical ingredients, and phyto-medicines that can be useful in controlling MS and associated diseases. Promoting the utilization of this fruit in the processing of bio-functional foods could have a dual impact. Not only could it directly enhance the population's health, but it also presents economic opportunities by stimulating cultivation and increasing production of this plant, bolstering the economies of the regions where it is grown. It also provides viable alternatives for producing healthy food and ingredients that meet the dietary needs of the population.

In this regard, thanks to the support of Dr. Socorro Josefina Villanueva-Rodríguez, researcher at the Food Technology and Assistance Center of the State of Jalisco, AC (CIATEJ), who held a sabbatical stay at the UAM-I Pharmacology Laboratory, four product proposals were obtained based on the fruit of *C. ficifolia*. After characterizing the bromatological and phytochemically properties of the raw material (chilacayote fruit), several formulations of nutraceutical juices, instant soups, nutritional boots, and a phyto-medicine were obtained and studied. These formulations underwent a sensory evaluation to select the most acceptable products for potential commercialization. The selected formulations were again subjected to physicochemical, phytochemical, bromatological, and biological assessments. Their components (polyphenols, phytosterols, flavonoids, sugars, and carotenoids), antioxidant capacity (DPPH and ABTS), and glycemic effects were determined with encouraging results.

We must stress that the food and nutraceutical utility of these preparations is based on the results obtained from the basic research carried out with the fruit of *C. ficifolia* in what goes this century by our working group of LFUAMI. Today, there is a need to continue the expansion of these technological advances, which help treat metabolic diseases and reach their massive use.

Pharmacology laboratory and its contribution to the rational design of computer-assisted drugs

Molecular docking has become a powerful computational tool for new drug research and design, playing a pivotal role in predicting interactions between drug-related ligands and their potential receptors [104]. Table 3 lists some of the analyzed compounds in LFUAMI, in collaboration with other institutions, by molecular docking. Since our in vivo and in vitro research is about metabolic activities, the receptors involved are related to modulating actions of carbohydrate and lipid metabolism, such as PPAR- α , PPAR- γ , PPAR- δ , GPR40, and

α -glucosidase enzyme, among others. The compounds investigated have generally resulted in multitarget activity, which might represent certain therapeutic advantages for treating complex diseases such as MS.

Although these results reinforce the potential utility of the compounds studied, more extensive studies of simulation *in silico* involving other types of metabolism regulatory receptors are still needed. However, molecular docking and the virtual screening simulation software currently available require researchers to make numerous configurations and navigate unintuitive menus, which requires significantly optimizing the process. Therefore, there is a pressing need to design a cohesive set of computational programs to expedite work with multiple ligands and receptors while simplifying simultaneous simulations. Such a framework would greatly facilitate the adoption of these techniques by researchers seeking to explore new ligands.

In this context, our laboratory has designed an accessible and user-friendly open-source software, which provides a robust format for presenting results and with a format simple for interpreting large amounts of data. This tool is extensively described in another article of this volume of the *Journal of Mexican Chemical Society*. The idea was to develop a simple yet reliable tool to manage the molecular docking process. Furthermore, the program's source code is free and has perpetual access to local computational resources.

When facing virtual screenings with extensive libraries of ligands and target proteins, this tool saves valuable research time and investment of monetary resources from the budget in subscription plans for online services. The tool was built using existing molecular docking software. From there, a suite of interconnected computer programs has been meticulously designed with dual objectives: to accelerate workflows involving numerous ligands and target proteins and to streamline simulations, thus making these techniques more accessible. Thus, the tool was conceived as open-source software, free and simple to use. Furthermore, one of the objectives was to create a robust results presentation format conceptualized as a massive report of rows and columns. In this way, the large amount of data obtained is intended to be easy to filter, discriminate, and interpret. This automated computational tool capable of performing multiple simultaneous molecular docking studies offers a significant advantage in this field, because it automates the preparation of ligands and receptors for the docking simulation, generates configuration files for each docking process, executes docking and site preparation procedures concurrently, and organizes comprehensive reports detailing the simulation results. The idea is that this proposal will greatly facilitate the widespread adoption of this instrument to explore new therapeutic targets. The proposal of this instrument is already widely disseminated through standard communication channels within the scientific community. Information for accessing the program is now available in another article in this volume of the *Journal of Mexican Chemical Society*.

Present and future

The LFUAMI has significantly contributed to the discovery and development of medicines. Many of the resources investigated have the potential to be utilized as raw materials for the development of functional foods, phyto-medicines, and pharmaceuticals. However, clinical assessments and their implementation in the therapeutic still need to be initiated. LFUAMI now has everything necessary to continue to carry out high-quality research in the field of pharmacology, applying cutting-edge research techniques associated with the evaluation of medicines with a potential use for the treatment of metabolic diseases, including diabetes mellitus, obesity, dyslipidemias, hypertension, inflammation and oxidant stress, among others, with the ability to support research from other research groups in our university and other institutions at request, promoting collaboration and facilitating wider research initiatives.

It is essential to emphasize that the research achievements of the LFUAMI have been made possible through collaborative agreements with various institutions both within the country and abroad, including inter-institutional partnerships and collaborations within our university. Additionally, we owe much gratitude to the dedicated students who have contributed to our laboratory, choosing to pursue their research projects with us. Their tireless efforts have been crucial to moving forward in our research goals and we sincerely appreciate his commitment and contributions. LFUAMI has received more than 300 students for research activities. Our efforts have led to the publication of more than 120 articles, which have over 5000 citations. These significant outputs underscore the LFUAMI's commitment to fostering student involvement and its dedication to producing

impactful research outcomes in pharmacological research, contributing in a relevant manner to the state of the art in this area of knowledge.

Acknowledgement

We thank Dra. Socorro Josefina Villanueva-Rodríguez, a researcher at the Food Technology and Assistance Center of the State of Jalisco, AC (CIATEJ), who held a sabbatical stay at the UAM-I Pharmacology Laboratory, and Biol. Exp. Alfredo Suárez-Alonso, scholarship no. 1256930 of the Program of SNI Level III Researcher Assistant (CONAHCYT) for the technological contributions indicated in this manuscript.

References

1. Ibáñez-Camacho, R.; Román-Ramos, R. *Arch. Invest. Méd.* (México) **1979**, *10*, 223-230.
2. Román-Ramos, R. *Med. Trad.* (México) **1980**, *3*, 9-11.
3. Meckes-Lozoya, M.; Román Ramos, R. *Am. J. Chin. Med.* **1986**, *XIV*, 116-118.
4. Román-Ramos, R.; Flores-Sáenz, J.L.; Alarcón-Aguilar, F. *Inv. Méd. Int.* **1995**, *22*, 97-100.
5. Roman-Ramos, R.; Flores-Sáenz, J.L.; Trujillo-Arriaga, H.M.; Alarcón-Aguilar, F.J. *Inv. Méd. Intern.* **2000**, *27*, 9-14.
6. Flores-Saenz, J.L.; Mendez, J.D.; Alarcon-Aguilar, F.J.; Roman-Ramos, R. *Proc. West. Pharmacol. Soc.* **2003**, *46*, 143-147.
7. Montoya-Alatriste, C.A.; Alarcón-Aguilar, F.J. *Brazilian J. Pharm. Sci.* **2022**, *58*, 1-23 (e20161)). DOI: <http://dx.doi.org/10.1590/s2175-97902022e20161>
8. López-Acosta, O.; Ruiz-Ramírez A.; Barrios-Maya, M.A.; Alarcón-Aguilar, F.J.; Alarcon-Enos J.; Céspedes-Acuña C.L.; El-Hafidi M. *Food Chem. Toxicol.* **2023**, *172*, 113546. DOI: <https://doi.org/10.1016/j.fct.2022.113546>.
9. Becerra, S.M.; Miranda, P.E.; Gomez, V.J.C.; Fortis, B.M.A.; Perez, R.J.; Alarcon, A.F.J. *Biomed. Pharm.* **2017**, *94*, 169-175. DOI: <https://doi.org/10.1016/j.biopha.2017.07.086.0753-3322/>
10. Alarcon-Aguilar, F.; Roman-Ramos, R.; Jimenez-Estrada, M.; Reyes-Chilpa, R.; Gonzales-Paredes, B.; Flores-Saenz, J.L. *J. Ethnopharmacol.* **1997**, *55*, 171-177.
11. Roman, R.; Flores, J.L.; Alarcon, F. *J. Ethnopharmacol.* **1995**, *48*, 25-32.
12. Roman, R.; Flores, J.L.; Partida, G.; Lara, A.; Alarcon, F.J. *Arch. Inv. Méd.* **1991**, *22*, 87-92.
13. Perez, Y.Y.; Jimenez-Ferrer, E.; Zamilpa, A.; Hernandez-Valencia, M.; Alarcon-Aguilar, F.J.; Tortoriello, J.; Roman-Ramos, R. *Am. J. Chin. Med.* **2007**, *35*, 1037-1046.
14. Alarcon-Aguilar, F.J.; Roman-Ramos, R.; Perez-Gutierrez, S.; Aguilar-Contreras, A.; Contreras-Weber, C.C.; Flores-Saenz, J.L. *J. Ethnopharmacol.* **1998**, *61*, 101-110.
15. Estrella-Parra, E.A.; Almanza-Pérez, J.C.; Alarcón-Aguilar, F.J. *Nat. Prod. Bioprospect.* **2019**, *9*, 251-265. DOI: <https://10.1007/s13659-019-0210-5>
16. Estrella-Parra, J.G.; Ávila-Acevedo, A.M.; García-Bores, J.; Rivera-Cabrera C.; Alejandro-García, I.; Alarcón-Aguilar, F.J. *Rev. Col. Psiq.* **2023**, 1-11. DOI: <https://doi.org/10.1016/j.rcp.2023.02.002>
17. Roman, R.; Alarcon, F.J.; Lara, A.; Flores, J.L. *Arch. Med. Res.* **1992**, *44*, 59-64.
18. Zavala-Mendoza, D.; Alarcon Aguilar, F.J.; Perez Gutierrez, S.; Escobar Villanueva, M.C.; Zavala-Sanchez M.A. *Evid. Bas. Complem. Altern. Med.* **2013**, *10*, 1-7. DOI: <http://dx.doi.org/10.1155/2013/170290>
19. Almanza, P.J.C.; Hernández, C.C.; Sánchez, B.J.; Hernández, R.V.; Román, R.R.; Alarcón, A.F.J. *Rev. Cub. Farm.* **2012**, *46*, 1-22.
20. Vega, A.E.; Cano, V.J.L.; Alarcon, A.F.J.; Fajardo, O.M.C.; Almanza, P.J.C.; Roman, R.R. *Evid. Bas. Complem. Altern. Med.* **2012**, 934258, 1-7. DOI: <https://doi.org/10.1155/2012/934258>

21. Espejel, N.J.A.; Vega, E.; Alarcon, A.F.J.; Contreras, R.A.; Diaz, R.G.; Trejo, A.G.; Ortega, C.C. *Evid. Bas. Complem. Altern. Med.* **2018**, 7191035, 1-9. DOI: <https://doi.org/10.1155/2018/7191035>.
22. García-Granados, R.U.; Alarcón-Aguilar, F.J.; Gallegos-Martínez, M.; De Lara-Isassi, G. *Hidrobiologica*. **2016**, *26*, 269-276. <http://hidrobiologica.izt.uam.mx/index.php/revHidro/article/view/503/100>
23. Fortis-Barrera, M.A.; Alarcón-Aguilar, F.J.; Becerril-García, B.; Flores-Sáenz, J.L.E.; Almanza-Perez, J.C.; García-Lorenzana, M.; Lazzarini-Lechuga, C.R.; Román-Ramos, R.; Blancas-Flores, G. *J. Med. Food*, **2019**, *23*, 783-792. DOI: <https://doi.org/10.1089/jmf.2019.0126>
24. Juárez-Vázquez, M.C.; Zamilpa, A.A.; León-Díaz R.; Martínez-Vázquez, M.; López-Torres, A.; Luna-Herrera, J.; Yépez-Mulla, L.; Alarcón-Aguilar, F.; Jiménez-Arellanes, M.A. *Pharmacogn. J.* **2021**, *13*, 1225-1241. DOI: <https://doi.org/10.5530/pj.2021.13.156>
25. Méndez-Martínez, M.; Trejo-Moreno, C.; Maldonado-Mejía, L.; Esquivel-Guadarrama, F.; Pedraza-Chaverri, J.; Zamilpa, A.; Medina-Campos, O.; Alarcón-Aguilar, F.; Almanza-Pérez, J.C.; Contreras-Nuñez, E.; Santana-Calderón, A.; Fragoso, G.; Jiménez-Ferrer, E.; Rosas, G. *Sci Reports* **2019**, *9*, 13372. DOI: <https://doi.org/10.1038/s41598-019-49458-6>.
26. Roman, R.; Lara, A.; Alarcon, F.J.; Flores, J.L. *Arch. Med. Res.* **1992**, *23*, 105-109.
27. Alarcon-Aguilar, F.J.; Hernandez-Galicia, E.; Campos-Sepulveda, A.E.; Xolalpa-Molina, S.; Rivas-Vilchis, J.F.; Vazquez-Carrillo, L.I.; Roman-Ramos, R. *J. Ethnopharmacol.* **2002**, *82*, 185-189.
28. Hernandez-Galicia, E.; Campos-Sepulveda, A.E.; Alarcón-Aguilar, F.J.; Vazquez-Carrillo, L.I.; Flores-Saenz, J.L.; Roman-Ramos, R. *Proc. West Pharmacol. Soc.* **2002**, *45*, 42-43.
29. Roman-Ramos, R.; Almanza-Pérez, J.C.; Fortis-Barrera, A.; Angeles-Mejia, S.; Banderas-Dorantes, T.R.; Zamilpa, A.A.; Diaz-Flores, M.; Jasso, I.; Blancas-Flores, G.; Gomez, J.; Alarcon-Aguilar, F.J. *Am. J. Chin. Med.* **2012**, *40*, 97-110. DOI: <https://doi.org/10.1142/S0192415X12500085>.
30. Díaz, F.M.; Angeles, M.S.; Baiza, G.L.A.; Medina, N.R.; Hernandez, S.D.; Ortega, C.C.; Roman, R.R.; Cruz, M.; Alarcón, A.F.J. *J. Ethnopharmacol.* **2012**, *144*, 101-108. DOI: <http://dx.doi.org/10.1016/j.jep.2012.08.036>.
31. Banderas, D.T.R.; Roman, R.R.; Zamilpa, A.; Garcia, M.R.; Diaz, M.; Campos, M.G.; Tortoriello, J.; Alarcon, A.F.J. *BLACPMA*. **2012**, *11*, 510-519. <https://www.redalyc.org/pdf/856/85624607003.pdf>.
32. Fortis-Barrera, M.A.; Alarcón-Aguilar, F.J.; Banderas-Dorantes, T.R.; Diaz-Flores, M.; Román-Ramos, R.; Cruz, M.; García-Macedo, R. *J. Pharm. Pharmacol.* **2013**, *65*, 1563-1576. DOI: <https://doi.org/10.1111/jphp.12119>.
33. Miranda-Pérez, M.E.; Escobar-Villanueva, M.C.; Ortega-Camarillo, C.; Fausto-Sánchez, M.; Almanza Pérez, J.C.; Alarcón-Aguilar, F.J. *Int. Biotech. Color J.* **2013**, *3*, 8-14.
34. Miranda, P.M.E.; Ortega, C.C.; Escobar, V.M.C.; Blancas, F.G.; Alarcon, A.F.J. *J. Ethnopharmacol.* **2016**, *188*, 159-166. DOI: <http://dx.doi.org/10.1016/j.jep.2016.04.061>
35. Fortis-Barrera, Á.; García-Macedo, R.; Almanza-Pérez, J.C.; Blancas-Flores, G.; Zamilpa-Álvarez, A.; Flores-Sáenz, J.L.; Cruz, M.; Román-Ramos, R.; Alarcón-Aguilar, F.J. *Can. J. Physiol. Pharmacol.* **2017**, *95*, 170-177. DOI: <https://dx.doi.org/10.1139/cjpp-2015-0475>
36. Garcia-Gonzalez, J.; Garcia-Lorenzana, M.; Zamilpa, A.; Almanza-Perez, J.C.; Jasso-Villagomez, E.I.; Roman-Ramos, R.; Alarcon-Aguilar, F.J. *Afr. J. Tradit. Complement. Altern. Med.* **2017**, *14*, 218-230. DOI: <http://dx.doi.org/10.21010/ajtcam.v14i3.4677>
37. Moya-Hernández, A.; Bosquez-Molina, E.; Serrato-Díaz, A.; Blancas-Flores, G.; Alarcón-Aguilar, F.J. *South Afr. J. Bot.* **2018**, *116*, 110-115. DOI: <https://doi.org/10.1016/j.sajb.2018.02.409>.
38. Barrón-Álvarez, N.; Prado-Barragán, L.A.; Fortis-Barrera, M.A.; Alarcón-Aguilar, F.J. *Beverages*. **2022**, *8*, 1-14. DOI: <https://doi.org/10.3390/beverages8030055>.
39. Almanza-Perez, J.C.; Hernandez-Rosado, V.; Fortis-Barrera, A.; Blancas-Flores, G.; Alarcon-Villaseñor, E.; Flores-Saenz, J.L.; Rosiles-Alanis, W.; Alarcon-Aguilar, F.J. *Am. J. Plant. Sci.* **2023**, *14*, 763-781. DOI: <https://doi.org/10.4236/ajps.2023.147051>.

40. Alarcón-Aguilar, F.J.; Zamilpa, A.; Pérez-García, M.D.; Almanza Perez, J.C.; Romero-Núñez, E.; Campos-Sepúlveda, E.A.; Vazquez-Carrillo, L.I.; Roman-Ramos, R. *J. Ethnopharmacol.* **2007**, *114*, 66-71.
41. Alarcon, A.J.; Zamilpa, A.; Alarcón-Aguilar F.J.; Herrera-Ruiz, M.; Tortoriello, J.; Jimenez-Ferrer, E. *J. Ethnopharmacol.* **2012**, *139*, 751-756. DOI: <http://dx.doi.org/10.1016/j.jep.2011.12.005>
42. Giacomán, M.A.; Alarcón, A.F.J.; Zamilpa, A.; Hidalgo, F.S.; Navarrete, V.G.; García, M.R.; Román, R.R.; Almanza, P.J.C. *Planta Med.* **2019**, *85*, 412-423. DOI: <https://doi.org/10.1055/a-0824-1316.0032-0943>
43. Alarcon-Aguilar, F.J.; Campos-Sepulveda, A.E.; Xolalpa-Molina, S.; Hernandez-Galicia, E.; Roman-Ramos, R. *Pharm. Biol.* **2002**, *40*, 570-575.
44. Alarcon-Aguilar, F.J.; Calzada-Bermejo, F.; Hernandez-Galicia, E.; Ruíz- Angeles, C.; Roman-Ramos, R. *J. Ethnopharmacol.* **2005**, *97*, 447-452.
45. Hernández-Galicia, E.; Calzada, F.; Roman-Ramos, R.; Alarcón-Aguilar, F.J. *Planta Med.* **2007**, *73*, 236-240.
46. Banderas, D.T.R.; Roman, R.R.; Zamilpa, A.; Garcia, M.R.; Diaz, M.; Campos, M.G.; Tortoriello, J.; Alarcon, A.F.J. *BLACPMA.* **2012**, *11*, 510-519. <https://www.redalyc.org/pdf/856/85624607003.pdf>.
47. Hernandez-Hernandez, A.B.; Alarcon-Aguilar, F.J.; Almanza-Perez, J.C.; Nieto-Yañez, O.; Olivares-Sanchez, J.M.; Duran-Diaz, A.; Rodriguez-Monroy, M.A.; Canales-Martinez, M.M. *J. Ethnopharmacol.* **2017**, *204*, 1-7. DOI: <http://dx.doi.org/10.1016/j.jep.2017.04.003.0378-8741>.
48. Hernandez-Hernandez, A.B.; Alarcón-Aguilar, F.J.; Garcia-Lorenzana, M.; Rodríguez-Monroy, M.A.; Canales-Martínez, M. *J. Evidence-Based Integ. Med.* **2021**, *26*, 1-10. DOI: <https://doi.org/10.1177/2515690X20986762>
49. Alarcon, F.J.; Banderas, T.R.; Xolalpa, S.; Hernandez, E.; Valdes, A.; Jimenez, M.; Roman, R. *Proc. West Pharmacol. Soc.* **2003**, *46*, 139-142.
50. Velasco-Lezama, R.; Tapia-Aguilar, R.; Román-Ramos, R.; Vega-Ávila, E.; Pérez-Gutiérrez, M.S. *J. Ethnopharmacol.* **2006**, *103*, 36-42.
51. Alarcón, A.F.; Vega, A.E.; Almanza, P.J.; Velasco, L.R.; Vázquez, C.L.; Román, R.R. *Proc. West Pharmacol. Soc.* **2006**, *49*, 51-54.
52. Alarcon-Aguilar, F.J.; Jimenez-Estrada, M.; Reyes-Chilpa, R.; Roman-Ramos, R. *J. Ethnopharmacol.* **2000**, *72*, 21-27.
53. Alarcon-Aguilar, F.J.; Jimenez-Estrada, M.; Reyes-Chilpa, R.; Gonzales-Paredes, B.; Contreras-Weber, C.C.; Roman-Ramos, R. *J. Ethnopharmacol.* **2000**, *69*, 207-215.
54. Jiménez-Estrada, M.; Merino-Aguilar, H.; Lopez-Fernandez, A.; Rojano-Vilchis, N.A.; Roman-Ramos, R.; Alarcon-Aguilar, F.J. *J. Complement Integ. Med.* **2011**, *8*, 1-10. DOI: <http://dx.doi.org/10.2202/1553-3840.1413>
55. Merino, A.H.; Arrieta, B.D.; Jiménez, E.M.; Magos, G.G.; Hernández, B.R.J.; López, D.G.N.E.; Hernández, P.E.; Susunaga, N.A.C.; Almanza, P.J.C.; Blancas, F.G.; Román, R.R.; Alarcón, A.F.J. *Nutrients.* **2014**, *6*, 591-604. DOI: <http://dx.doi.org/10.3390/nu6020591>
56. Juárez-Pérez, M.G. Efecto sobre la biota intestinal de una fracción rica en fructooligosacáridos de la raíz de *Psacalium decompositum*. Master's degree in Sciences, Biotechnology Program, Universidad Autónoma Metropolitana-Iztapalapa. México. **2020**.
57. Alarcon-Aguilar, F.J.; Fortis-Barrera, M.A.; Angeles-Mejia, S.; Banderas-Dorantes, T.R.; Jasso-Villagomez, E.I.; Almanza-Perez, J.C.; Blancas-Flores, G.; Zamilpa, A.; Diaz-Flores, M.; Roman-Ramos, R. *J. Ethnopharmacol.* **2010**, *132*, 400-407.
58. Contreras-Weber, C.C.; Pérez-Gutiérrez, S.; Alarcón-Aguilar, F.J.; Román-Ramos, R. *Proc. West Pharmacol. Soc.* **2002**, *45*, 128-130.
59. Contreras-Weber, C.C.; Román-Ramos, R.; Perez, C.; Alarcón-Aguilar, F.J.; Zavala, M.A.; Pérez-Gutiérrez, S. *Chem. Pharm. Bull.* **2005**, *53*, 1408-1410.
60. Ventura, J.; Alarcon, A.F.; Roman, R.R.; Campos, S.E.; Reyes, V.L.M.; Boone, V.D.; Jasso, V.E.I.; Aguilar, C.N. *Food Chem.* **2013**, *136*, 109-115.

61. Ortega, R.; Valdés, M.; Alarcón-Aguilar, F.J.; Fortis-Barrera, A.; Barbosa, E.; Velazquez, C.; Calzada, F. *Plants* **2022**, *11*, 575, 1-21. DOI: <https://doi.org/10.3390/plants11050575>.
62. Serrano-Vega, R.; Perez-Gutiérrez, S.; Alarcón-Aguilar, F.; Almanza-Perez, J.; Pérez-González, C.; González-Chávez, M.M. *Am. J. Plant Sci.* **2021**, *12*, 887-900. DOI: <https://doi.org/10.4236/ajps.2021.126059>.
63. Susunaga, N.A.C.; Pérez, G.S.; Zavala, S.M.A.; Almanza, P.J.C.; Gutiérrez, C.A.; Arrieta, B.D.; López, L.A.L.; Román, R.R.; Flores, S.J.L.E.; Alarcón, A.F.J. *Molecules*. **2014**, *19*, 10261-10278. DOI: <http://dx.doi.org/10.3390/molecules190710261>
64. García-Granados, R.U.; Alarcón-Aguilar, F.; Gallegos-Martínez, M.; De Lara-Isassi, G. *Hidrobiologica* **2016**, *26*, 269-276. <http://hidrobiologica.izt.uam.mx/index.php/revHidro/article/view/503/100>
65. Guadarrama-Cruz, G.; Alarcon-Aguilar, F.J.; Velasco-Lezama, R.; Vazquez-Palacios, G.; Bonilla-Jaime, H. *J. Ethnopharmacol.* **2008**, *120*, 277-281.
66. Guadarrama-Cruz, G.V.; Alarcon-Aguilar, F.J.; Vega-Avila, E.; Vázquez-Palacios, G.; Bonilla-Jaime, H. *Am. J. Chin. Med.* **2012**, *40*, 753-768. DOI: <http://dx.doi.org/10.1142/S0192415X12500565>
67. Bonilla, J.H.; Guadarrama, C.G.; Alarcón, A.F.J.; Limón, M.O.; Vázquez-Palacios, G. *J. Nat. Med.* **2015**, *69*, 463-470. DOI: <http://dx.doi.org/10.1007/s11418-015-0909-5>
68. García-Granados, R.U.; Cruz-Sosa, F.; Alarcón-Aguilar, F.J.; Nieto-Trujillo, A.; Gallegos-Martínez, M.E. *Polibotánica*. **2019**, *48*, 151-168. DOI: <http://dx.doi.org/10.18387/polibotanica.48.12>
69. Miranda-Pérez M.E.; Blancas-Flores, G.; López-Velasco, J.C.; Flores-Cruz, M.; Román-Ramos, R.; Alarcón-Aguilar, F.J. XLVIII Congreso Nacional de Ciencias Farmacéuticas y VI Congreso Internacional de Ciencias Farmacéuticas. 6-9 de septiembre, **2015**. Cancún, Quintana Roo, México.
70. Estrella-Parra, E.I.; Flores-Cruz, M.; Blancas-Flores, G.; Stephen, D. K.; Alarcón-Aguilar, F.J. *BLACPMA*. **2019**, *18*, 239-264.
71. Espejel-Nava, J.A., Alarcon-Aguilar, F., Escobar-Villanueva, M.C., Contreras-Ramos, A., Cruz, M., Vega-Avila, E.; Ortega-Camarillo, C. *Pharmacogn. Mag.* **2020**, *16*, 369-374. DOI: 10.4103/pm.pm_277_19.
72. Miranda-Núñez, J.E.; Zamilpa-Alvarez, A.; Fortis-Barrera, A.; Alarcon-Aguilar, F.J.; Loza-Rodríguez, H.; Gómez-Quiroz, L.E.; Salas-Silva, S.; Flores-Cruz, M.; Zavala-Sanchez, M.A.; Blancas-Flores, G. *Phytomedicine*. **2021**, *89*, 153622. DOI: <https://doi.org/10.1016/j.phymed.2021.153622>
73. Sanchez-Villavicencio, M.L.; Vinqvist-Tymchuk, M.; Kalt, W.; Matar, Ch.; Alarcon-Aguilar, F.J.; Escobar-Villanueva, M.C.; Pierre, S. Haddad. *BMC Compl. Alter. Med.* **2017**, *17*, 1-9. DOI: <https://doi.org/10.1186/s12906-016-1519-9>
74. Jasso-Villagomez, E.I.; Garcia-Lorenzana, M.R.; Roman-Ramos, R.; Prado-Barragan, L.A.; Alarcon-Aguilar, F.J. *Brazilian J. Med. Biol. Res.* **2018**, *51*, e7238, 1-12. DOI: <http://dx.doi.org/10.1590/1414-431X20187238>
75. Jiménez-Estrada, M.; Reyes-Chilpa, R.; Ramírez-Apan, T.; Lledias, F.; Wilhem-Hansberg, A.D.; Alarcón-Aguilar, F.J. *J. Ethnopharmacol.* **2006**, *105*, 34-38.
76. Mora-Ramiro, B.; Jiménez-Estrada, M.; Zentella-Dehesa, A.; Ventura-Gallegos, J.L.; Gomez-Quiroz, L.E.; Rosiles-Alanis, W.; Alarcon-Aguilar, F.J.; Almanza-Perez, J.C. *J. Nat. Prod.* **2020**, *83*, 2447-2455. DOI: <https://doi.org/10.1021/acs.jnatprod.0c00300>
77. Juárez-Vázquez, C.; Alonso-Castro, A.J.; Rojano-Vilchis, N.; Jiménez-Estrada, M.; García-Carrancá, A. *Toxicol. in Vitro*. **2013**, *27*, 1001-1006. DOI: <https://doi.org/10.1016/j.tiv.2013.01.021>.
78. Abarca, V.R.; Zamilpa, A.; Alarcón, A.F.; Herrera, R.M.; Tortoriello, J.; Jiménez, F.E. *Molecules* **2014**, *19*, 3120-3134. DOI: <https://doi.org/10.3390/molecules19033120>
79. García-Díaz, J.A.; Navarrete-Vázquez, G.; García-Jiménez, S.; Hidalgo-Figueroa, S.; Almanza-Pérez, J.C.; Alarcón-Aguilar, F.J.; Gómez-Zamudio, J.; Cruz, M.; Ibarra-Barajas, M.; Estrada-Soto, S. *Bio. Pharm.* **2016**, *83*, 667-675. DOI: <http://dx.doi.org/10.1016/j.biopha.2016.07.006>.

80. Loza-Rodríguez, H.; Estrada-Soto, S.; Alarcón-Aguilar, F.J.; Huang, F.; Aquino-Jarquín, G.; Fortis-Barrera, A.; Giacomán-Martínez, A.; Almanza-Pérez, J.C. *Eur. J. Pharmacol.* **2020**, *883*, 173252. DOI: <https://doi.org/10.1016/j.ejphar.2020.173252>.
81. Giacomán-Martínez, A.; Alarcón-Aguilar, F.J.; Zamilpa, A.; Huang, F.; Romero-Nava, R.; Román-Ramos, R.; Almanza-Pérez, J.C. *Can. J. Physiol. Pharmacol.* **2021**, *99*, 827-988. DOI: <http://dx.doi.org/10.1016/j.jep.2022.115492>
82. Hidalgo-Figueroa, S.; Ramírez-Espinosa, J.J.; Estrada-Soto, S.; Almanza-Pérez, J.C.; Roman-Ramos, R.; Alarcón-Aguilar, F.J.; Hernández-Rosado, J.V.; Moreno-Díaz, H.; Díaz-Coutiño, D.; Navarrete, G. *Chem. Biol. Drug Design.* **2013**, *81*, 474-483. DOI: <http://dx.doi.org/10.1111/cbdd.12102>
83. García-Macedo, R.; Sánchez-Muñoz, F.; Almanza-Pérez, J.C.; Durán-Reyes, G.; Alarcón-Aguilar, F.; Cruz, M. *Eur. J. Pharmacol.* **2008**, *587*, 317-321.
84. Alarcón-Aguilar, F.J.; Almanza-Pérez, J.C.; Blancas, G.; Angeles, S.; García-Macedo, R.; Roman, R.; Cruz, M. *Eur. J. Pharmacol.* **2008**, *599*, 152-158.
85. Almanza-Pérez, J.C.; Blancas-Flores, G.; García-Macedo, R.; Campos-Sepúlveda, E.A.; Román-Ramos, R.; Alarcón-Aguilar, F.; Cruz, M. *Biomed. Pharm.* **2010**, *64*, 534-540.
86. Blancas-Flores, G.; Alarcón-Aguilar, F.J.; García-Macedo, R.; Almanza-Pérez, J.C.; Flores-Saenz, J.L.; Roman-Ramos, R.; Ventura-Gallegos, J.L.; Kumate, J.; Zentella-Dehesa, A.; Cruz, M., *Eur. J. Pharmacol.* **2012**, *689*, 270-277. DOI: <https://doi.org/10.1016/j.ejphar.2012.06.025>.
87. Salinas-Arreortua, N.; García-Lorenzana, M.; Durán-Reyes, G.; Villagómez-Jasso, E.I.; Alarcón-Aguilar, F.J.; Gómez-Olivares, J.L. *J. Exp. Clin. Med.* **2013**, *5*, 209-214. DOI: <http://dx.doi.org/10.1016/j.jecm.2013.04.006>.
88. Contreras-Núñez, E.; Blancas-Flores, G.; Cruz, M.; Almanza-Pérez, J.C.; Gómez-Zamudio, J.H.; Ventura-Gallegos, J.L.; Zentella-Dehesa, A.; Lazzarini, R.; Roman-Ramos, R.; Alarcón-Aguilar, F.J. *Biomed. Pharm.* **2018**, *102*, 120-131. DOI: <https://doi.org/10.1016/j.biopha.2018.03.048.0753-3322>.
89. Romero-Nava, R.; Alarcón-Aguilar, F.J.; Giacomán-Martínez, A.; Blancas-Flores, G.; Aguayo-Cerón, K.A.; Ballinas-Verdugo, M.A.; Sánchez-Muñoz, F.; Huang, F.; Villafañá-Rauda, S.; Almanza-Pérez, J.C. *Infl. Res.* **2021**, *70*, 605-618. DOI: <https://doi.org/10.1007/s00011-021-01462-1>.
90. Bonilla-Jaime, H.; Limón-Morales, O.; Arteaga-Silva, M.; Hernández-González, M.; Guadarrama-Cruz, G.; Alarcón-Aguilar, F.; Vázquez-Palacios, G. *Physiol. Behavior.* **2010**, *101*, 456-461.
91. Roman-Ramos, R.; Almanza-Pérez, J.C.; García-Macedo, R.; Blancas-Flores, G.; Fortis-Barrera, A.; Jasso, E.I.; García-Lorenzana, M.; Campos-Sepúlveda, E.A.; Cruz, M.; Alarcón-Aguilar, F.J. *Basic Clin. Pharmacol. Toxicol.* **2011**, *108*, 406-413.
92. Hernández, B.R.J.; Alarcón, A.F.J.; Escobar, V.M.C.; Almanza, P.J.C.; Merino, A.H.; Konigsberg, F.M.; López, D.G.N.E. *Int. J. Mol. Sci.* **2014**, *15*, 11473-11494. DOI: <https://doi.org/10.3390/ijms150711473>
93. Ventura-Sobrevilla, J.; Boone-Villa, D.; Aguilar, C.N.; Vega-Ávila, E.; Román-Ramos, R.; Campos-Sepúlveda, E.; Alarcón-Aguilar, F.J. *Proc. West Pharmacol. Soc.* **2011**, *54*, 5-9.
94. Hidalgo-Figueroa, S.; Navarrete-Vázquez, G.; Estrada-Soto, S.; Giles-Rivas, D.; Alarcón-Aguilar, F.J.; León-Rivera, I.; Giacomán-Martínez, A.; Miranda-Pérez, E.; Almanza-Pérez, J.C. *Biomed. Pharmacother.* **2017**, *90*, 53-61. DOI: <http://dx.doi.org/10.1016/j.biopha.2017.03.033>.
95. Rosiles-Alanis, W.; Zamilpa, A.; García-Macedo, R.; Zavala-Sánchez, M.A.; Hidalgo-Figueroa, S.; Mora-Ramiro, B.; Román-Ramos, R.; Estrada-Soto, S.; Almanza-Pérez, J.C. *J. Med. Food.* **2021**, *25*, 588-596. DOI: <https://doi.org/10.1089/jmf.2021.0071>
96. Navarrete, V.G.; Torres, G.H.; Hidalgo, F.S.; Ramírez, E.J.J.; Estrada, S.S.; Medina, F.J.L.; León, R.I.; Alarcón, A.F.J.; Almanza, P.J.C. *Biorg. Med. Chem. Letters* **2014**, *24*, 4575-4579. DOI: <https://doi.org/10.1016/j.bmcl.2014.07.068>
97. Miranda-Núñez, J.E.; Zamilpa-Alvarez, A.; Fortis-Barrera, A.; Alarcón-Aguilar, F.J.; Loza-Rodríguez, H.; Gómez-Quiroz, L.E.; Salas-Silva, S.; Flores-Cruz, M.; Zavala-Sánchez, M.A.; Blancas-Flores, G. *Phytomedicine.* **2021**, *89*, 153622. DOI: <https://doi.org/10.1016/j.phymed.2021.153622>.

98. Acosta-Patiño, J.L.; Jimenez-Balderas, E.; Juarez-Oropeza, M.A.; Diaz-Zagoya, J.C. *J. Ethnopharmacol.* **2001**, *77*, 99–101.
99. Jain, A.; Mishra, M.; Yadav, D.; Khatarker, D.; Jadaun, P.; Tiwari, A.; Katare, C.; Prasad, G.B.K.S. *Prog. Nut.* **2018**, *20*, 191-198. DOI: <https://doi.org/10.23751/pn.v20i1-S.6654>
100. Alarcón-Aguilar, F.J.; Contreras-Weber, C.C.; Román-Ramos, R.; Pérez, C.; Pérez-Gutiérrez, M.S. *Mex. Patente.* **2011**, 285,896.
101. Xia, T.; Wang, Q. *Fitoterapia*, **2006**, *77*, 530–533. DOI: <https://doi.org/10.1016/j.fitote.2006.06.008>.
102. Xia, T.; Wang, Q. *J. Pharm. Pharmacol.* **2006**, *58*, 1527–1532. DOI: <http://dx.doi.org/10.1211/jpp.58.10.0014>
103. Laganà, A. S.; Myers, S. H.; Forte, G.; Naem, A.; Krentel, H.; Allahqoli, L.; Unfer, V. *Exp. Op. Drug Metab. Toxicol.* **2024**, *20*, 61–72.
104. Prieto-Martínez, F. D.; Arciniega, M.; Medina-Franco, J.L. *Tip Rev. Esp. Cienc. Químico-Biol.* **2018**, *21*, 65–87. DOI: <https://doi.org/10.22201/fesz.23958723e.2018.0.143>
105. Cruz-Torres, K.C.; Estrada-Soto, S.; Arias-Durán, L.; Navarrete-Vázquez, G.; Almanza-Pérez, J.C.; Mora-Ramiro, B.; Perea-Arango, I.; Hernández-Núñez, E.; Villalobos-Molina, R.; Carmona-Castro, G.; Medina-Díaz, I.M.; Ávila-Villarreal, G. *Pharmaceutics.* **2023**, *19*, 2346. DOI: <http://dx.doi.org/10.3390/pharmaceutics15092346>
106. Arias-Durán, L.; Estrada-Soto, S.; Hernández-Morales, M.; Millán-Pacheco, C.; Navarrete-Vázquez, G.; Villalobos-Molina, R.; Ibarra-Barajas, M.; Almanza-Pérez, J.C. *J. Ethnopharmacol.* **2021**, *273*, 113948. DOI: <http://dx.doi.org/10.1016/j.jep.2021.113948>
107. Gaona-Tovar, E.; Estrada-Soto, S.; González-Trujano, M.E.; Martínez-Vargas, D.; Hernandez-Leon, A.; Narváez-González, F.; Villalobos-Molina, R.; Almanza-Pérez, J.C. *J. Ethnopharmacol.* **2022**, *296*, 115492. DOI: <http://dx.doi.org/10.1016/j.jep.2022.115492>

Table 1. Medicinal resources studied at LFUAMI in collaboration with other laboratories from national and international institutions.

Scientific name	Family	Used part	Preparation	Experimental model	References
1. <i>Acourtia thurberi</i> (A. Gray) Reveal & R.M. King.	Asteraceae	Rhizome	Decoction	Fasted normal mice GTT in rabbits	[10]
2. <i>Agastache mexicana</i> (Kunth) Lint & Epling)	Lamiaceae	Complete	Organic extract	GTT in mice Phytochemical analysis	[105]
3. <i>Allium cepa</i> L.	Amaryllidaceae	Bulb	Decoction	GTT in rabbits	[11]
4. <i>Allium sativum</i> L.	Amaryllidaceae	Bulb	Decoction	GTT in rabbits	[11]
5. <i>Aloe barbadensis</i> Mill.	Asphodelaceae	Stems	Juice Polyphenolic extract from the gel	GTT in rabbits. Mice with insulin-resistance	[12] [13]
6. <i>Aquillea millefolium</i> L.		Flowers	Organic extract	GTT in mice Phytochemical analysis	[106]
7. <i>Artemisia mexicana</i> Willd. ex Spreng.	Asteraceae	Complete	Decoction	GTT in rabbits	[14]
8. <i>Astianthus viminalis</i> (Kunth) Baill.	Bignoniaceae	Leaves	Decoction	GTT in rabbits	[14]
9. <i>Banisteriopsis caapi</i> (Spruce ex Griseb.) C.V. Morton and <i>Psychotria viridis</i> Ruiz & Pav. (ayahuasca)	Malpighiaceae Rubiaceae	Leaves and stem	Decoction	Review and a toxicologic clinical case	[15-16]
10. <i>Bauhinia divaricata</i> L.	Fabaceae	Leaves	Decoction	GTT in rabbits	[17]
11. <i>Bidens odorata</i> Cav.	Asteraceae	Leaves and branches	Organic extracts Fat acids	Castor oil-induced diarrhea mice Carbachol-induced ileum contraction in rats	[18]
12. <i>Bidens pilosa</i> L.	Asteraceae	Complete	Decoction	GTT in rabbits	[14]
13. <i>Bocconia arborea</i> S. Watson	Papaveraceae	Complete	Organic extract	GTT in mice and Phytochemical analysis	[107]
14. <i>Brassica oleracea</i> L.	Brassicaceae	Inflorescence	Juice	GTT in rabbits	[11]
15. <i>Brassica oleracea</i> L. var. <i>botrytis</i>	Brassicaceae	Leaves	Juice	GTT in rabbits	[11]
16. <i>Buddleia americana</i> L.	Scrophulariaceae	Flowers	Decoction	GTT in rabbits	[17]

Scientific name	Family	Used part	Preparation	Experimental model	References
17. <i>Calea zacatechichi</i> Schtdl.	Asteraceae	Inflorescence	Decoction	GTT in rabbits	[17]
18. <i>Cannabis</i> L. sp	Cannabaceae	Inflorescence	Comercial oil	Review 3T3-L1 adipocytes	[7] [Outcome unpublished]
19. <i>Catharanthus roseus</i> (L.) G. Don	Apocynaceae	Flower, leaves, stem, and roots.	Aqueous and organic extracts. Phenolic- fraction	Normal mice. 3T3- L1 adipocytes Alloxan-induced diabetic mice. RINm5F pancreatic cells	[19,20,21]
20. <i>Caulerpa sertularioides</i> (S.G. Gmelin) M. Howe (Chlorophyta)	Caulerpaceae	Complete	Aqueous extract	STZ-induced diabetes mice	[22]
21. <i>Cecropia obtusifolia</i> Bertol.	Urticaceae	Leaves	Decoction Aqueous extract	GTT in rabbits RINm5F pancreatic cells	[12,23]
22. <i>Cleoserrata serrata</i> (Jacq.) Iltis	Cleomaceae	Aerial parts	Organic extracts. Polyphenol mixture	TPA- and carrageenan- induced inflammation	[24]
23. <i>Citrus aurantium</i> L.	Rutaceae	Fruit	Juice	GTT in rabbits	[14]
24. <i>Cnidocolus multilobus</i> (Pax) I.M. Johnst.	Euphorbiaceae	Leaves	Decoction	GTT in rabbits	[14]
25. <i>Coix lachryma-jobi</i> L.	Poaceae	Seems	Decoction	GTT in rabbits	[17]
26. <i>Crataegus pubescens</i> (C. Presl) C. Presl	Rosaceae	Root	Decoction	GTT in rabbits	[17]
27. <i>Cucumis sativus</i> L.	Cucurbitaceae	Fruit	Juice Fractions from aqueous extract (containing glycine, asparagine, and arginine)	GTT in rabbits Dysfunctional 3T3-L1 adipocytes	[11,25]
28. <i>Cucurbita ficifolia</i> Bouché	Cucurbitaceae	Fruit	Juice Aqueous extract Fraction from aqueous extract (containing chlorogenic acid) Fermented juice	GTT in rabbits Normal mice Alloxan-induced diabetic rabbits and mice STZ-induced diabetes mice MSG-induced obese mice	[11-12, 26-39]

				Rat aortic rings 3T3-L1 adipocytes RINm5F pancreatic cells HepG2 Hepatocytes	
Scientific name	Family	Used part	Preparation	Experimental model	References
29. <i>Cuminum cyminum</i> L.	Apiaceae	Seeds	Decoction	GTT in rabbits	[11]
30. <i>Cynodon dactylon</i> (L.) Pers.	Poaceae	Complete	Decoction	GTT in rabbits	[17]
31. <i>Eriobotrya japonica</i> (Thunb.) Lindl.	Rosaceae	Leaves	Decoction	GTT in rabbits	[12]
32. <i>Eucalyptus globulus</i> Labill.	Myrtaceae	Leaves	Decoction	GTT in rabbits	[12]
33. <i>Euphorbia preslii</i> Guss.	Euphorbiaceae	Complete	Decoction	GTT in rabbits	[14]
34. <i>Euphorbia prostrata</i> Aiton	Euphorbiaceae	Complete	Decoction	GTT in rabbits	[14]
35. <i>Exostema caribaeum</i> (Jacq.) Roem. & Schult.	Rubiaceae	Bark	Decoction	GTT in rabbits	[14]
36. <i>Eysenhardtia polystachya</i> (Ortega) Sarg.	Fabaceae	Stem	Decoction	GTT in rabbits	[14]
37. <i>Mangostana cambogia</i> Gaertn. (Syn.: <i>Garcinia cambogia</i> (Gaertn.) Desr.	Clusiaceae	N.I.	Formulation	Obese patients	[4]
38. <i>Guaiacum coulteri</i> A. Gray.	Zygophyllaceae	Bark	Decoction	GTT in rabbits Alloxan-induced diabetic rabbits	[12,26]
39. <i>Guazuma ulmifolia</i> Lam.	Malvaceae	Leaves	Decoction	GTT in rabbits	[14]
40. <i>Hibiscus sabdariffa</i> L.	Malvaceae	Calyces	Aqueous extract. Dichloromethane extract Triterpenoids	MSG-induced obese mice Diuresis in rats Diuresis in in situ kidney model GTT in mice 3T3-L1 adipocytes	[40-42]

Scientific name	Family	Used part	Preparation	Experimental model	References
41. <i>Ibervillea sonorae</i> (S. Watson) Greene	Cucurbitaceae	Root	Monoglycerides Fat acids	Normal and diabetic mice and rats. Rat aortic rings 3T3-L1 adipocytes	[19,43-46]
42. <i>Jatropha dioica</i> Sessé ex. Cerv.	Euphorbiaceae	Roots	Decoction	GTT in rabbits	[14]
43. <i>Jatropha neopauciflora</i> Pax.	Euphorbiaceae	Latex	Phenols and flavonoids	Antimicrobial and antifungal models Wound healing tensiometric method. Normal and diabetic mice.	[47-48]
44. <i>Lactuca sativa</i> L.	Asteraceae	Leaf	Juice	GTT in rabbits	[11]
45. <i>Lepechinia caulescens</i> (Ortega) Epling	Lamiaceae	Leaf and stem	Decoction	GTT in rabbits Alloxan-induced diabetic rabbits. Normal mice 3T3-L1 adipocytes	[12,14,19,26]
46. <i>Mangifera indica</i> L.	Anacardiaceae	Leaves	Decoction	GTT in rabbits	[14]
47. <i>Marrubium vulgare</i> L.	Lamiaceae	Complete	Decoction	GTT in rabbits	[17]
48. <i>Mentha piperita</i> L.	Lamiaceae	Complete	Decoction	GTT in rabbits	[14]
49. <i>Musa ensete</i> J.F. Gmel.	Musaceae	Seems	Decoction	Normal mice 3T3-L1 adipocytes	[19]
50. <i>Musa sapientum</i> L.	Musaceae	Flowers	Decoction	GTT in rabbits	[14]
51. <i>Olea europaea</i> L.	Oleaceae	Leaves	Decoction	GTT in rabbits	[14]
52. <i>Opuntia ficus indica</i> (L.) Mill.	Cactaceae	Stem	Juice Polysaccharides	GTT in rabbits Normal mice GTT in mice Alloxan-induced diabetes mice	[14,49]
53. <i>Opuntia streptacantha</i> Lem.	Cactaceae	Stem	Juice Polysaccharides	Pancreatectomized rabbits A clinical case GTT in rabbits Normal mice GTT in mice Alloxan-induced diabetes mice	[1-3,11-12,49]

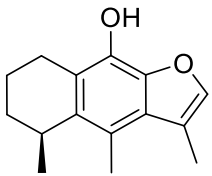
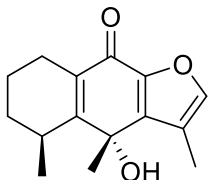
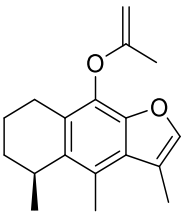
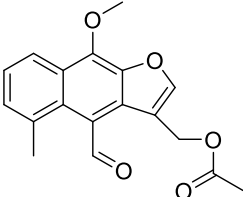
Scientific name	Family	Used part	Preparation	Experimental model	References
54. <i>Parmentiera edulis</i> Raf.	Bignoniaceae	Fruit	Juice	GTT in rabbits	[14]
55. <i>Pavonia schiedeana</i> Steud.	Malvaceae	Leaf	Decoction	GTT in rabbits	[17]
56. <i>Persea americana</i> Mill.	Lauraceae	Seeds	Decoction	GTT in rabbits	[14]
57. <i>Phaseolus vulgaris</i> L.	Fabaceae	Pod	Decoction	GTT in rabbits	[11-12]
58. <i>Physalis philadelphica</i> Lam.	Solanaceae	Calices of the fruit	Decoction	GTT in rabbits	[17]
59. <i>Plantago major</i> L.	Plantaginaceae	Seeds	Aqueous and organic extracts	Normal Alloxan-induced diabetes mice Normal mouse cells Transformed human cells	[50-51]
60. <i>Psacalium decompositum</i> (A. Gray) H. Rob. & Brettell	Asteraceae	Rhizome	Decoction Aqueous and organic extracts Sesquiterpenoids Polysaccharide fractions Fructooligosaccharides	GTT in rabbits. Fasted normal mice Alloxan-induced diabetes mice Normal rats Fructose-induced obese rats	[10,52-56]
61. <i>Psacalium peltatum</i> (Kunth) Cass.	Asteraceae	Rhizome	Decoction	GTT in rabbits Alloxan-induced diabetes rabbits Fasted normal mice Alloxan-induced diabetes mice STZ-induced diabetes-mice	[10,12,26, 57-59]
62. <i>Psidium guajava</i> L.	Myrtaceae	Fruit	Juice	GTT in rabbits	[11]
63. <i>Punica granatum</i> L.	Lythraceae	Peels	Aqueous extract	Normal mice GTT in mice STZ-induced diabetes mice Antioxidant capacity <i>in vitro</i>	[60]
64. <i>Randia echinocarpa</i> DC.	Rubiaceae	Fruit	Decoction	GTT in rabbits	[14]
65. <i>Rauwolfia tetraphylla</i> L.	Apocynaceae	Leaves	Decoction	GTT in rabbits	[14]

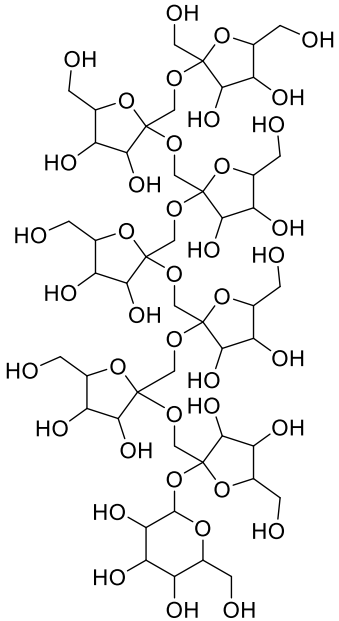
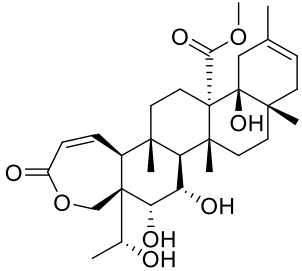
Scientific name	Family	Used part	Preparation	Experimental model	References
66. <i>Rhizophora mangle</i> L.	Rhizophoraceae	Stem	Decoction	GTT in rabbits	[14]
67. <i>Salpianthus macrodonthus</i> Standl.	Nyctaginaceae	Leaf and stem. Roots	Decoction	GTT in rabbits	[12,14]
68. <i>Salvia polystachya</i> M. Martens & Galeotti	Lamiaceae	Complete	Terpenoids	GTT in mice	[61]
69. <i>Senna crotalaroides</i> (Kunth) H.S. Irwin & Barneby	Fabaceae	Leaf and stem. Roots	Chloroform extract	TPA-induced ear edema, cytotoxic activity	[62]
70. <i>Senna skinneri</i> (Benth.) H.S. Irwin & Barneby	Fabaceae	Leaves	Decoction	GTT in rabbits	[15]
71. <i>Senna villosa</i> (Mill.) H.S. Irwin & Barneby	Fabaceae	Leaf and stem. Roots	Chloroform extract	TPA-induced ear edema	[63]
72. <i>Serjania triquetra</i> Radlk.	Sapindaceae	Stem	Decoction	GTT in rabbits	[14]
73. <i>Solanum verbascifolium</i> L.	Solanaceae	Leaves and stem	Decoction	GTT in rabbits	[12]
74. <i>Smilax dominguensis</i> Willd.	Smilacaceae	Root	Chloroform extract	GTT in mice Phytochemical analysis	[Outcome unpublished]
75. <i>Spinacia oleracea</i> L.	Amaranthaceae	Leaves	Juice	GTT in rabbits	[11]
76. <i>Spyridia filamentosa</i> (Wulfen) Harvey (Rhodophyta)	Spyridiaceae	Complete	Aqueous extract	STZ-induced diabetes mice	[64]
77. <i>Tagetes lucida</i> Cav.	Asteraceae	Aerial parts	Aqueous extract	Antidepressive forced swimming test	[65-67]
78. <i>Bignonia stans</i> L. (Syn.: <i>Tecoma stans</i> (L.) Juss. ex Kunth)	Bignoniaceae	Leaf and stem	Decoction	GTT in rabbits	[12]
79. <i>Teucrium cubense</i> Jacq.	Lamiaceae	Leaf and stem	Decoction	GTT in rabbits	[12]
80. <i>Thalassia testudinum</i> Banks & Sol. ex K.D. Köning (marine phanerogam)	Hydrocharitaceae	Complete	Aqueous extract	Hemolytic activity Phytochemical analysis	[68]
81. <i>Tillandsia recurvata</i> (L.) L.	Bromeliaceae	Complete	Aqueous extract	Normal and diabetic mice	[69]

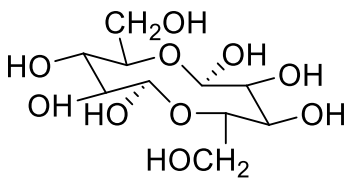
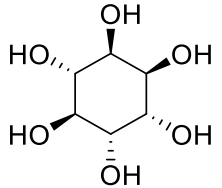
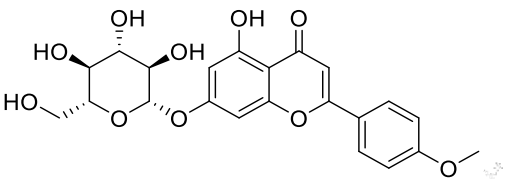
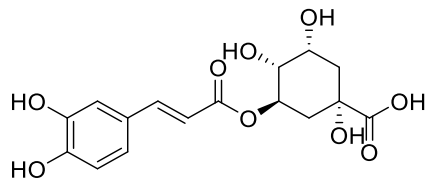
Scientific name	Family	Used part	Preparation	Experimental model	References
82. <i>Tillandsia usneoides</i> (L.) L.	Bromeliaceae	Complete	Flavone	Review C2C12 myoblasts Hepatocytes RINm5F pancreatic cells	[70-72]
83. <i>Vaccinium angustifolium</i> Aiton	Ericaceae	Fruit	Fermented juice with <i>Serratia vaccinii</i> bacteria Anthocyanins and proanthocyanidins	3T3-L1 adipocytes	[73]
84. <i>Heliotropium verdcourtii</i> Craven (Syn.: <i>Tournefortia hirsutissima</i> L.	Heliotropiaceae	Stem	Decoction	GTT in rabbits	[14]
85. <i>Trigonella foenum-graceum</i> L.	Fabaceae	Seeds	Decoction	GTT in rabbits	[14]
86. <i>Turnera diffusa</i> Willd.	Passifloraceae	Leaves	Decoction	GTT in rabbits	[14]
87. <i>Ulomoides dermestoides</i> Chev. (beetle)		Complete	Lipid fraction	STZ-induced diabetes mice	[74]
88. <i>Urtica dioica</i> L.	Urticaceae	Complete	Decoction	GTT in rabbits	[17]

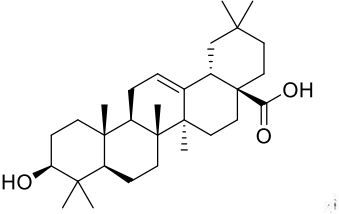
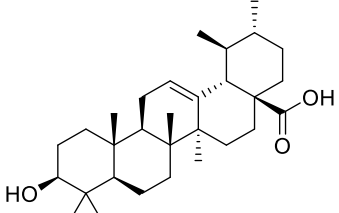
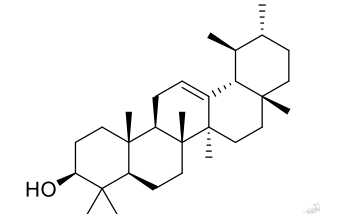
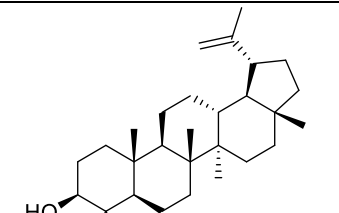
GTT=Glucose tolerance test; STZ=Streptozotocin; MSG=monosodium glutamate.

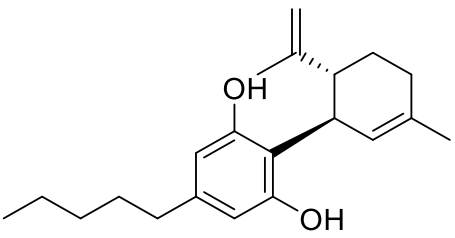
Table 2. Compounds identified and studied in LFUAMI in collaboration with other laboratories from national and international institutions.

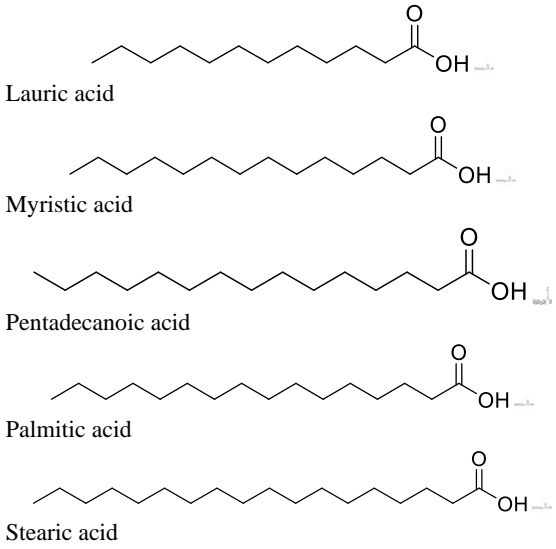
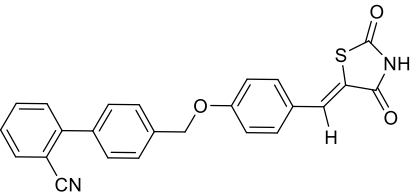
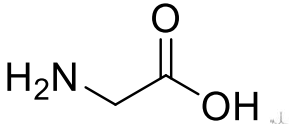
Compound name	Chemical Structure	Origin	Biological activity	References
1. Cacalol		<i>Psacalium decompositum</i>	Anti-inflammatory	[53,5]
2. Cacalone		<i>Psacalium decompositum</i>	Anti-inflammatory	[53,75]
3. Cacalol acetate		<i>Psacalium decompositum</i>	Anti-inflammatory	[76]
4. Maturin acetate		<i>Psacalium decompositum</i>	Immuno-stimulator	[53,77]

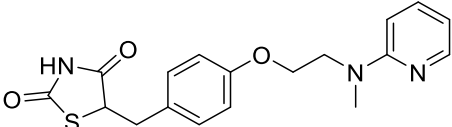
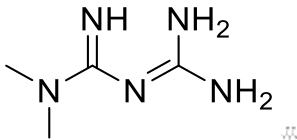
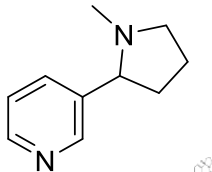
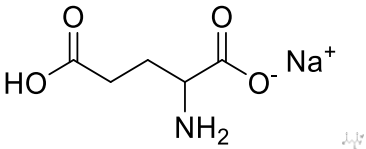
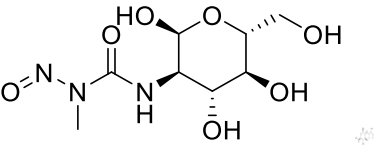
Compound name	Chemical Structure	Origin	Biological activity	References
5. Fructo-oligosaccharides		<i>Psacalium decompositum</i>	Hypoglycemic. Anti-inflammatory.	[54-55]
6. Galphimine-A		<i>Galphimia glauca</i>	Anxiolytic	[78]

Compound name	Chemical Structure	Origin	Biological activity	References
7. Pentalose		<i>Psacalium peltatum</i>	Hypoglycemic	[59,100]
8. D-chiro-inositol		<i>Cucurbita ficifolia</i>	Anti-inflammatory. Hypoglycemic. Antioxidant.	[32]
9. Tilianin		<i>Agastache mexicana</i>	Anti-diabetic. Anti-hyperlipidemic. Anti-inflammatory.	[79]
10. Chlorogenic acid		<i>Cecropia obtusifolia</i>	Dual agonist: Insulin-secretagogue and PPAR agonist	[9]

Compound name	Chemical Structure	Origin	Biological activity	References
11. Oleanolic acid		<i>Salvia polystachia</i>	PPAR dual agonist. Hypo-glycemic. Antihyperglycemic. α -glucosidases inhibitor.	[61,80]
12. Ursolic acid		<i>Salvia polystachia</i>	Hypoglycemic. Antihyperglycemic. α -glucosidases inhibitor.	[61]
13. α -amyrin		<i>Hibiscus sabdariffa</i>	Antihyperglycemic. PPAR-dual agonist AMPK-allosteric activator Insulino-mimetic	[42,81]
14. Lupeol		<i>Hibiscus sabdariffa</i>	Antihyperglycemic PPAR-dual agonist.	[42]

Compound name	Chemical Structure	Origin	Biological activity	References
15. Monoglyceride mixture	$ \begin{array}{c} 1 \text{ CH}_2\text{OCOR} \\ \\ 2 \text{ CHOH} \\ \\ 3 \text{ CH}_2\text{OH} \\ 1: \text{R}=\text{CH}_2(\text{CH}_2)_{12}\text{CH}_2\text{CH}_3 \\ 2: \text{R}=\text{CH}_2(\text{CH}_2)_{13}\text{CH}_2\text{CH}_3 \\ 3: \text{R}=\text{CH}_2(\text{CH}_2)_{14}\text{CH}_2\text{CH}_3 \\ 4: \text{R}=\text{CH}_2(\text{CH}_2)_{15}\text{CH}_2\text{CH}_3 \\ 5: \text{R}=\text{CH}_2(\text{CH}_2)_{16}\text{CH}_2\text{CH}_3 \\ 6: \text{R}=\text{CH}_2(\text{CH}_2)_{18}\text{CH}_2\text{CH}_3 \\ 7: \text{R}=\text{CH}_2(\text{CH}_2)_{19}\text{CH}_2\text{CH}_3 \\ 8: \text{R}=\text{CH}_2(\text{CH}_2)_{20}\text{CH}_2\text{CH}_3 \\ 9: \text{R}=\text{CH}_2(\text{CH}_2)_{21}\text{CH}_2\text{CH}_3 \\ 10: \text{R}=\text{CH}_2(\text{CH}_2)_{22}\text{CH}_2\text{CH}_3 \\ 11: \text{R}=\text{CH}_2(\text{CH}_2)_{24}\text{CH}_2\text{CH}_3 \end{array} $	<i>Ibervillea sonorae</i>	Hypoglycemic	[45]
16. Cannabidiol		<i>Cannabis</i> sp.	Ani-inflammatory	[Outcome unpublished]

Compound name	Chemical Structure	Origin	Biological activity	References
17. Fat acids mixture	 <p>Lauric acid</p> <p>Myristic acid</p> <p>Pentadecanoic acid</p> <p>Palmitic acid</p> <p>Stearic acid</p>	<i>Ibervillea sonorae</i>	Hypoglycemic	[45]
18. 4'-({4-[(Z)-(2,4-dioxo-1,3-thiazolidine-5-ylidene)-ethyl]-phenoxy}methyl)-1,1'-biphenyl-2-carbonitrile		Synthetic	Anti-diabetic. PPAR-dual agonist.	[82]
19. Glycine		Aminoacid	Anti-inflammatory. Antioxidant Inhibitor. competitive of the TNF-α receptor	[83-89]

Compound name	Chemical Structure	Origin	Biological activity	References
20. Rosiglitazone		Synthetic	Insulin-sensitizer	[5-6]
21. Metformin		Synthetic	Insulin-sensitizer	[6]
22. Nicotine		Synthetic	Anti-depressant	[90]
23. Monosodium glutamate		Synthetic	Toxicity metabolic Inducer of obesity	[91-92]
24. Streptozotocin		<i>Streptomyces achromogenes</i>	Inducer of experimental diabetes	[93]

Compound name	Chemical Structure	Origin	Biological activity	References
25. 2-(4-(2-((1H-benzo[d]imidazol-2-yl)thio)-acetamido)phenoxy) acetic acid (1), and 2-(4-(2-((5-methoxy-1H-benzo[d]imidazol-2-yl)thio)-acetamido)-phenoxy)-acetic acid (2)	<p>1 R=H, 2 R -OMe</p>	Synthetics	Anti-diabetic. PPAR γ / GPR40 dual agonists	[94]
26. 4-hydroxybenzoic acid		<i>Cucurbita ficifolia</i>	Insulin- secretagogue PPAR agonist Liver glycogen storage promotor	[95]
27. β -sitosterol		<i>Cucurbita ficifolia</i>	Insulin- secretagogue PPAR agonist Liver glycogen storage promotor	[95]
28. {4-[(4-[(Z)-(2,4-dioxo-1,3-thiazolidine-5-ylidene)-methyl]-phenoxy} acetyl)amino]-phenoxy}acetic acid		Synthetic	Anti-diabetic in non-insulin- dependent diabetes rats	[96]

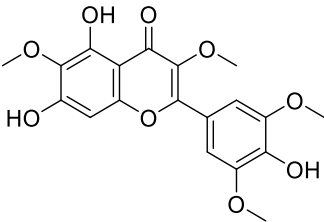
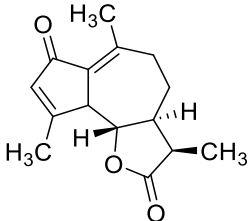
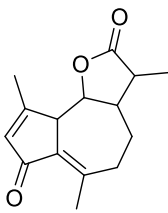
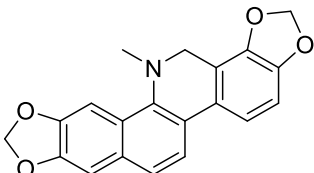
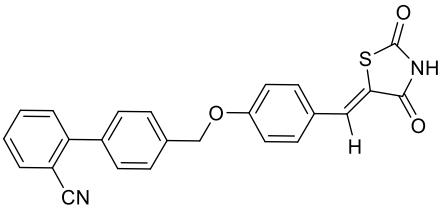
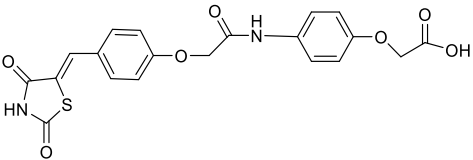
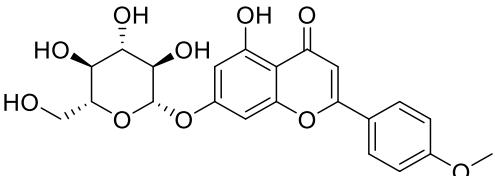
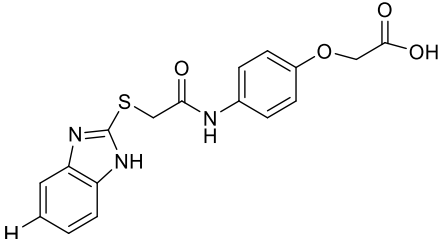
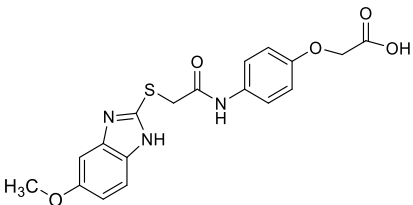
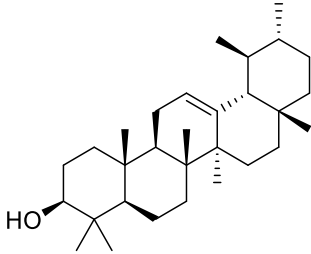
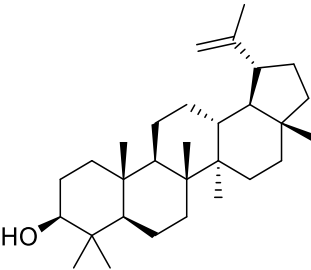
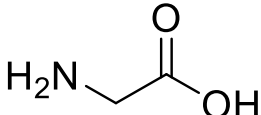
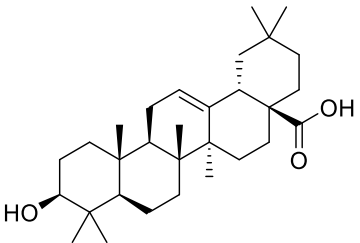
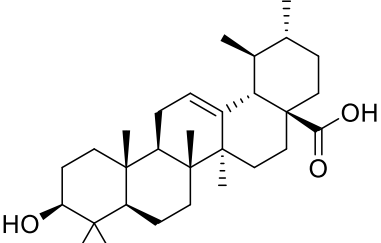
Compound name	Chemical Structure	Origin	Biological activity	References
29. 5,7,4'-trihydroxy-3,6,3',5'-tetramethoxyflavone		<i>Tillandsia usneoides</i>	Antihyperglycemic	[97]
30. Achillin		<i>Achillea millefolium</i>	Antidiabetic	[105]
31. Leucodin		<i>Achillea millefolium</i>	Antidiabetic	[105]
32. Dihydrosanguinarine		<i>Bocconia aerboria</i>	Anti-nociceptive	[106]

Table 3. Some analyzed compounds in UAM's pharmacology laboratory with collaboration with other institutions by molecular docking and their potential biological activity.

Compounds	Chemical structure	Receptors	Potencial activity	Referencias
4'-({4-[(Z)-(2,4-dioxo-1,3-thiazolidin-5-ylidene)methyl]-phenoxy} methyl)-1,1'-biphenyl-2-carbonitrile		PPAR- α PPAR- γ	PPAR- α/γ dual agonist	[82]
{4-[(4-[(Z)-(2,4-dioxo-1,3-thiazolidin-5-ylidene)-methyl]-phenoxy} acetyl)-amino] phenoxy} acetic acid		PPAR- γ	PPAR- γ agonist	[96]
Tilianin		PPAR- α	PPAR- α agonist	[79]
2-(4-(2-((1H-benzo[d]imidazol-2-yl)thio)acetamido)-phenoxy)-acetic acid		PPAR- γ GPR40	PPAR- γ /GPR40 dual agonist	[94]

Compounds	Chemical structure	Receptors	Potencial activity	Referencias
2-(4-(2-((5-methoxy-1H-benzo[d]imidazol-2-yl)thiol)-acetamido)-phenoxy)-acetic acid		PPAR- γ GPR40	PPAR- γ /GPR40 dual agonist	[94]
α -amyrin		PPAR- δ PPAR- γ AMPK	PPAR- δ / γ dual agonist AMPK allosteric activator	[42,81]
Lupeol		PPAR- δ PPAR- γ	PPAR- δ / γ dual agonist	[42]
Glycine		TNF- α 1	TNF- α partial agonist	[89]

Compounds	Chemical structure	Receptors	Potencial activity	Referencias
Oleanolic acid		α-glucosidase SGLT1	α - glucosidas e inhibitor SGLT1 inhibitor	[61]
Ursolic acid		α-glucosidase SGLT1	α - glucosidas e inhibitor SGLT1 inhibitor	[61]

Fifty Years of Molecular Simulations at UAM and in Mexico

Edgar Núñez-Rojas¹, Alexander Pérez de la Luz², Humberto Saint-Martin³, José Alejandro^{2*}

¹CONAHCyT-Departamento de Química, Universidad Autónoma Metropolitana-Iztapalapa. Av. San Rafael Atlixco 186, Col. Vicentina, 09340, Ciudad de México, México.

²Departamento de Química. Universidad Autónoma Metropolitana-Iztapalapa. Av. San Rafael Atlixco 186, Col. Vicentina, 09340, Ciudad de México, México.

³Instituto de Ciencias Físicas, Universidad Nacional Autónoma de México, Campus Chamilpa, 62210 Cuernavaca, Morelos, México.

*Corresponding author: José Alejandro, email: jra@xanum.uam.mx

Received May 24th, 2024; Accepted July 21st, 2024.

DOI: <http://dx.doi.org/10.29356/jmcs.v68i4.2291>

Abstract. Molecular simulation methods are the bridge between molecular interactions and the macroscopic properties of matter. The equations of statistical mechanics give the probabilistic method of Monte Carlo while those of Newton are the bases of Molecular Dynamics, which is deterministic. A molecular simulation predicts the movement of molecules and hundreds of physicochemical properties can be obtained to understand its behavior at different thermodynamic conditions. The molecular simulation methods were developed in the 1950s in United States of America and in the 1980s in Mexico, **where *Universidad Autónoma Metropolitana (UAM)*** was a pioneer. It is a multidisciplinary field that involves mathematicians, chemists, physicists, engineers from different disciplines, biologists, computer scientists, etc. Supercomputers have played an important role in its development. Currently, the United States, China and the European Community have everyone more than 100 supercomputers in the TOP500 ranking, while Canada and Brazil have 10, Spain 3, Argentina 1 and Mexico none. These resources allow increasing the training capabilities, the production of research articles, the organization of academic events, etc.

In this work, we make a review of the development of molecular simulations at UAM and in Mexico. The diffusion and promotion of this research field has been undertaken by academic leaders from several universities. We have organized **12 Molecular Dynamics Workshops** nationwide to teach and put the basic concepts into practice and **13 international Meetings on Molecular Simulations** to discuss the state of the art in research projects. The number of articles in molecular dynamics grows exponentially over time; in 2023, more than 250,000 were published worldwide. Mexico contributed 10 % and the UAM 10 % of those published in Mexico. There are more than 32 Mexican leaders living in Mexico who have published around 120 articles with at least 100 citations, according to Web of Science. About 70 % belong to the National System of Researchers at levels III and Emeritus. The research lines range equations of state in liquids, phase equilibrium, development of simulation methods and force fields, polar fluids, electrolytes, colloids, polymers, drug/protein interaction, protein folding, among others.

Keywords: Molecular simulations; molecular dynamics; Monte Carlo; simulation in Mexico; workshop and meetings; force fields; condensed matter; supercomputing.

Resumen. Los métodos de simulación molecular son el puente entre las interacciones moleculares y las propiedades macroscópicas de la materia. Las ecuaciones de la mecánica estadística dan el método probabilístico de Montecarlo mientras que las de Newton son las bases de la Dinámica Molecular, que es determinista. Una simulación molecular predice el movimiento de las moléculas y se pueden obtener cientos de propiedades fisicoquímicas para comprender su comportamiento en diferentes condiciones termodinámicas. Los métodos de simulación molecular se desarrollaron en la década de 1950 en Estados Unidos de América y en la década de 1980 en México, **donde la Universidad**

Autónoma Metropolitana (UAM) fue pionera. Es un campo multidisciplinario que involucra a matemáticos, químicos, físicos, ingenieros de diferentes disciplinas, biólogos, informáticos, etc. Las supercomputadoras han jugado un papel importante en su desarrollo. Actualmente, Estados Unidos, China y la Comunidad Europea cuentan con más de 100 supercomputadoras en el ranking TOP500, mientras que Canadá y Brasil tienen 10, España 3, Argentina 1 y México ninguno. Estos recursos permiten incrementar las capacidades de formación, la producción de artículos de investigación, la organización de eventos académicos, etc.

En este trabajo hacemos una revisión del desarrollo de simulaciones moleculares en la UAM y en México. La difusión y promoción de este campo de investigación ha sido llevada a cabo por líderes académicos de varias universidades. Hemos organizado **12 Talleres de Dinámica Molecular** a nivel nacional para enseñar y poner en práctica los conceptos básicos y **13 Simposios internacionales sobre Simulación Molecular** para discutir el estado del arte en proyectos de investigación. El número de artículos sobre dinámica molecular crece exponencialmente con el tiempo; en 2023, se publicaron más de 250.000 en todo el mundo. México aportó el 10 % y la UAM el 10 % de los publicados en México. Hay más de 32 líderes mexicanos viviendo en México que han publicado alrededor de 120 artículos con al menos 100 citas, según Web of Science. Alrededor del 70 % pertenece al Sistema Nacional de Investigadores en los niveles III y Eméritos. Las líneas de investigación abarcan ecuaciones de estado en líquidos, equilibrio de fases, desarrollo de métodos de simulación y campos de fuerza, fluidos polares, electrolitos, coloides, polímeros, interacción fármaco/proteína, plegamiento de proteínas, entre otras.

Palabras clave: Simulación molecular; dinámica molecular; Monte Carlo; simulación en México; talleres y simposios; campos de fuerza; materia condensada; supercómputo.

Theory and molecular simulations to understand matter

It is well recognized that the father of molecular simulations is Professor Bernie J. Alder (1925-2020), from the University of Lawrence Livermore National Laboratory in the United States of America. He published the first works in the mid-1950s on Monte Carlo and Molecular Dynamics applied to hard spheres systems [1]; he predicted a first order solid-liquid phase transition driven by entropic effects, also, that the phase diagram of this system did not contain a liquid-vapor equilibrium. He developed his simulations on the fast computer on those days, UNIVAC and then IBM, which had two CPUs and one processor. The weight of the machine was around 52 tons. A smart phone today has more computer power than NASA's supercomputer in 1960. This paper has more than 1800 citations according with Web of Science (WofS) and is still being cited. Professor Alder received the National Medal of Science from President Barack Obama in 2009.

Professor Jorge Barojas was the first Mexican that published an article on molecular dynamics from his PhD research with Professors D. Levesque and B. Quentrec in France in 1973. They used the Lennard-Jones potential to simulate diatomic homonuclear liquids and compared their equation of state and their structure factor with experimental values of nitrogen finding a good agreement [2]. Professor Barojas returned to Mexico and, though he did not work anymore in molecular simulations field, he is regarded as a pioneer in science outreach in Mexico, an activity that in his time was not popular between his colleagues, but time has shown the relevance of his work in promoting specific vocation, including editorial production on this area.

Professor Gustavo A. Chapela obtained his PhD with Professor John S. Rowlinson at Imperial College London, United Kingdom, and published two **seminal** articles about the liquid-vapor interface also using the Lennard-Jones potential. In these works, they applied Monte Carlo and Molecular Dynamics with 255 particles to obtain the coexisting densities and surface tension at temperatures from the triple to critical points. Binary mixtures were also studied [3,4]. The latter paper has more than 350 citations and it is still cited. The results were obtained in a CDC supercomputer of those days. Professor Chapela returned to Mexico to work at the Physics Department at UAM-Iztapalapa where he began to promote molecular dynamics.

In those years UAM had a CDC fast computer but it was used, mainly, for administrative tasks, not for research. The computer was in the *Rectoría General*, in the north of Mexico City, near to *Toreo de Cuatro Caminos* forum. The bachelor's degree in computer science was created in early 80s. The students developed their Fortran programs using card punchers and typed cards as those shown in Fig. 1. The same tools were used

by researchers. The cards had to be submitted from UAM-Iztapalapa to **Rectoría General** building to compile the program. The compiled version was returned to UAM-Iztapalapa to correct the errors.

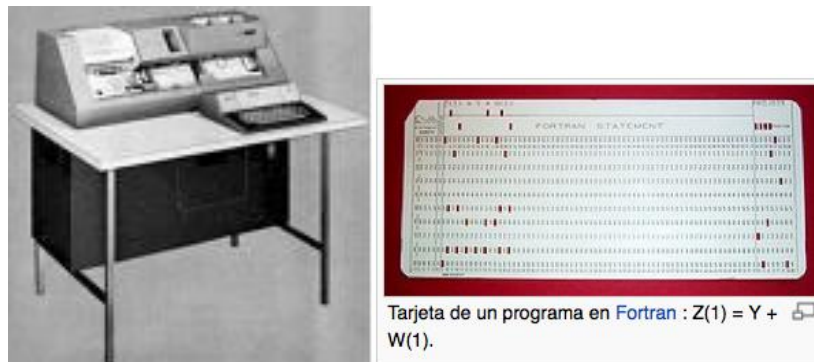


Fig.1. Card puncher (left panel) and card for the sum $X + Y$ in a fortran program (right panel).

The cards sometimes were sent on motorcycles from UAM-Iztapalapa to *Rectoría General*. In some cases, it is said that the driver dropped the cards and rearranged them inside the box as he could but in disorder, so that they could be compiled. In those cases, when the list of the compiled version of the program was returned to the author, it turned out that it contained more errors than in the previous version.

Gustavo Chapela: founding father of molecular dynamics at UAM and in Mexico

The UAM-Iztapalapa is pioneer in the development and application of molecular simulation methods in Mexico. Professor Chapela and his group published in 1980, in **Spanish**, an internal report for the *División de Ciencias Básicas e Ingeniería* of UAM-Iztapalapa. This was the first simulation carried out in Mexico. The cover of this internal report is shown in Fig. 2.

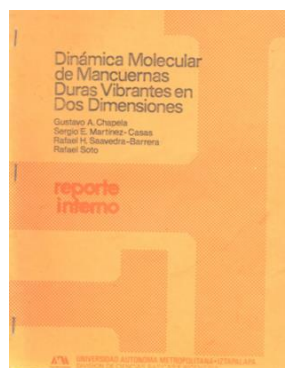


Fig. 2. Internal report titled *Dinámica Molecular de Mancuernas Duras Vibrantes en Dos Dimensiones* by **G. A. Chapela, S. E. Martínez-Casas, R. H. Saavedra-Barrera and R. Soto**.

Professor Chapela and Sergio E. Martínez-Casas published the first molecular simulation article made in Mexico in an international Journal in 1983 [5].

In the 80s and 90s, research performed in Mexico around Simulation and Molecular Theory, (**SMT**), was mainly based on the statistical mechanics methods. It involved predicting thermodynamic, dynamic and

structural properties from **potential models**, such as hard spheres, square well, Lennard-Jones or Yukawa **interactions**. The results of molecular simulations were used to both, testing statistical mechanics theories and understanding the effect that molecular interactions have on macroscopic properties. Systems studied included liquids, electrolytes, colloids, polymers, among other applications.

It is important to keep the community together, therefore, several efforts were made to promote theory, simulation, and experimental work. The Winter Meeting on Statistical Physics, where **Professors Fernando del Río and Leopoldo García-Colín were promoters**, has been organized continually for more than 50 years. The Meeting on Complex Fluids in San Luis Potosí was pioneered by Professor Magdaleno Medina Noyola and his group and it has been organized for more than 30 years. Professor José Alejandro organized in 1998 an international meeting at the *Instituto Mexicano del Petróleo* in Mexico City, the event titled *Simposio de Simulación Molecular y Técnicas Experimentales en Problemas del Petróleo* was attended for more than 200 participants.

The importance of the **SMT** topic lies in the fact that there is currently better knowledge about the role played by molecular interactions, and it is viable to use the methodology to generate new knowledge and support technological innovation. In this sense, in industrialized countries, as a development strategy, research centers that use **SMT** methodologies have already been created. Explaining the physical phenomena of molecular systems from the interactions of the constituent atoms based only on experimental data is incomplete because, in general, these data lack the resolution needed to attain atomistic detail. Therefore, in many cases, this is carried out through trial and error, which is expensive and requires a long time.

Nowadays, the interactions can be obtained with quantum mechanics where electrostatic and polarization contributions can be included with or without chemical reactivity. Some of the computational methodologies are classical and *ab initio* molecular dynamics, Monte Carlo, mesoscopic dynamics, QM/MM, etc.

Currently, thanks to the enormous advance in supercomputer development technology and molecular simulation methods, a wide range of complex problems in chemistry, physics, biology and engineering can be studied and understood at the molecular level. It is well known that the forces between atoms and molecules determine the physical and chemical properties of matter. With molecular simulation methods, the movement of molecules and the way they interact are studied. The application of these methods has allowed us to have a better knowledge of the role that these forces play in the description of a large number of physical phenomena. It is estimated that they can impact the development of areas such as health (design of better drugs), energy (materials to transport and store fuels more efficiently, biofuels, renewable materials such as lithium batteries, solar cells) and the environment (friendly solvents, separation and storage of contaminants).

National Prizes of Sciences and Arts in Mexico

In Mexico, 5 national prizes in physical-mathematical sciences have been awarded to researchers who have made important scientific contributions in the field of statistical mechanics and some of them also in molecular simulations.

Leopoldo García Colín-Scherer - National Prize for Sciences and Arts 1988. He was interested in the study of statistical physics of nonequilibrium systems, nonlinear irreversible thermodynamics and its astrophysical and cosmological applications, hydrodynamics, superfluidity, and the glass transition. He was founder and professor of the *Escuela Superior de Física y Matemáticas* in *Instituto Politécnico Nacional (IPN)* in 1961, *Universidad Autónoma de Puebla* in 1964, the *Facultad de Ciencias UNAM* in 1967, Physics and Chemistry departments of UAM-Iztapalapa in 1974; he was subdirector of the *Instituto Mexicano del petróleo* in 1967, he was also researcher at the Nuclear Center Salazar (1966) and at the *Instituto de Investigaciones en Materiales* in UNAM in 1984. He published 52 articles and the most cited (*Physics Reports* 465 (2008) 149–189) has 104 citations.

Alberto Robledo Nieto - National Prize for Sciences and Arts 2008. He simultaneously studied Chemical Engineering, Chemistry and Physics at UNAM. He completed his PhD in Statistical Mechanics at the Department of Theoretical Physics at the University of Saint Andrew, in Scotland. His valuable, original and varied contributions to knowledge in areas of physical chemistry within the framework of statistical mechanics stand out. For around 40 years he has taught courses in *Facultad de Química* and *Facultad de Ciencias* in UNAM. He has also developed the infrastructure used by the research groups of the thermophysics laboratory of *Facultad de Química* in UNAM. His specialty is statistical physics and his research frequently involves the description of

phase transitions in condensed matter. He has published around 200 articles and the most cited (*Physical Review E* 66 (4), (2002) 045104) has 153 citations.

Marcelo Lozada-Cassou - National Prize for Sciences and Arts 2010. His scientific contributions can be divided into two groups: a) Development of the fundamental theory of many-body physics; b) Prediction of new physicochemical phenomena, which have subsequently been experimentally verified by other researchers. His work on the electrical double layer is widely recognized as pioneering for understanding the structure of inhomogeneous fluids. He also contributed to the development of fluid transport theories. His PME theory contributed to the understanding of charged particle electrophoresis, and significantly improved the theory of Wirsema, O'Brien and White. His works have been published in major and widely recognized textbooks for students; graduates in physical chemistry. It should be noted that he has generated basic scientific ideas that he later transformed into 19 international and 12 national patents currently in the process of industrial development at the IMP, under the premise of the connection between first-class science and effective attention to priority problems of the country. He has published 121 articles and the most cited (*Nanotechnology* 13 (2002) 495–498) has 197 citations.

Magdalena Medina Noyola - National Prize for Sciences and Arts 2013. He has been focused on the study of the physicochemistry of complex fluids. His contributions have been at the forefront in the description of such properties in the context of colloidal suspensions and micellar solutions. His work includes important and diverse contributions both to theory in general and to the understanding of specific phenomena, including the theory of liquids and ionic fluids, works that were pioneers in a topic that currently constitutes a topic of great interest in physics. statistics. Regarding his contribution to the development of academic infrastructure, the formation of Statistical Physics groups at *Centro de Investigación y de Estudios Avanzados* (CINVESTAV) stands out in the 1980s. In 1984, he restarted the Advanced Summer School in Physics. He formed the Statistical Physics and Physicochemistry of Complex Fluids group of the *Instituto de Física in Universidad Autónoma de San Luis Potosí*, from which a small and excellent group of researchers emerged who have obtained important support, such as emerging fields and links with industry of the oil. He also highlights the Statistical Physics and Complex Fluids group at the University of Sonora. He has published 121 articles and the most cited (*Phys. Rev. Lett.* 60, 2705. 1988) has 196 citations.

Fernando del Río Haza - National Prize for Sciences and Arts 2015. His research has contributed to the knowledge of the structure and thermodynamics of this system. His main research contributions form a coherent set, and can be separated into four groups: 1) the so-called square well model systems, 2) the theoretical equation of state of real substances, 3) the effective intermolecular potentials, and 4) the systems with Coulomb interaction. He is a researcher trainer with the direction of more than 40 doctoral, master's and bachelor's theses. Likewise, his teaching activity is manifested in several books and more than 150 courses taught. He has published 87 articles and the most cited (*Molecular Physics*, 100(15). (2002),2531–2546) has 103 citations.

All of them have promoted the development of science along the Mexican country. The information used to describe the activities that granted them the prize was taken from <https://www.gob.mx/sep/acciones-y-programas>, <https://www.webofscience.com> and <https://scholar.google.com>.

The birth of a molecular simulation group in Mexico

Over the years the number of researchers and students in the molecular simulation field has increased. In 2009, Professor José Alejandro and Roberto López Rendón (†), his PhD student, organized the first Molecular Simulation Symposium at UAM-Iztapalapa. Professor Alejandro, who got his PhD under the supervision of Professor Chapela, was working in the Chemistry Department of that institution. The objective of the symposium was to promote the molecular simulation field among the Mexican community and learn about the state of the art in both methods and applications. The lectures were given by Mexican experts in theory of liquids and the classic methods of Molecular Dynamics and Monte Carlo. All the invited colleagues agreed to participate, and the event was held in one day. The talks were given in Spanish. The speakers were Professors Fernando del Río (UAM-Iztapalapa), Minerva González-Melchor (BUAP), Jorge López-Lemus (UAEMex), Gustavo A. Chapela (UAM-Iztapalapa), Pedro Orea (IMP), Ana Laura Benavides (UG), Humberto Saint-Martin (UNAM), José Alejandro (UAM-Iztapalapa), Gerardo Odriozola (IMP), Roberto López-Rendón (UAMex) and Gerardo Pérez (UAMC). The picture of the participants taken in the Cuicacalli Room is shown in Fig. 3.

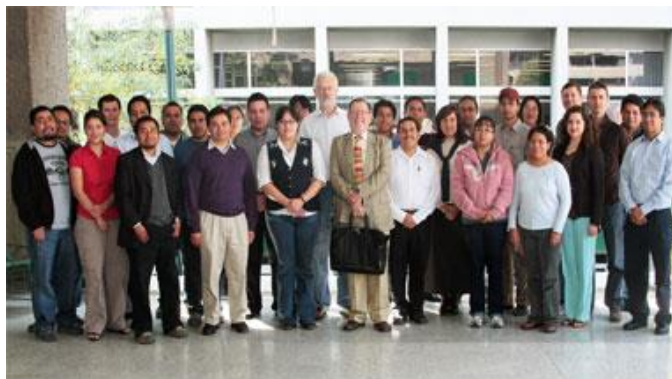


Fig. 3. Participants at the first Molecular Simulation Symposium at UAM-Iztapalapa in 2009.

Given the great success with students and researchers in the field of molecular simulations in the first Symposium, Professor José Alejandre proposed to organize a Workshop in the summer and a Meeting on winter. In the Workshops, the basic aspects of the methodology and the use of highly parallel programs such as GROMACS, DL_POLY, LAMMPS and NAMD should be taught by national researchers who are experts in the field of molecular simulation. Participating students should carry out the computer experiments on their own computers. More information about the Workshops is given below.

International meetings on molecular simulations in Mexico

The main purposes of the Meeting are to promote research in molecular simulation in Mexico and establish collaborations with both, national and international researchers. Also, the Meeting is an opportunity that allows us gathering a group of people to share their research and knowledge about molecular simulations. The Meeting offers a series of lectures in which experts from Mexico and other countries present results and accomplishments of their research. There is also a poster session where members of the community, students and researchers, can discuss their results. The Organizing Committee has taken the initiative of gathering both academic and industrial experts in a common place, the aim of these meetings is to establish and understand problems which industry deal with in order to find out how molecular simulation methods can contribute to resolving them. Nowadays, with the great advances in computer technology and simulation methodologies, it is important for the productive sector that academics know the troubles in the industry and that industry knows the reaches of molecular simulations. In Fig. 4 a picture of the participants of the second Molecular Simulation Meeting at UAM-Iztapalapa in 2010 is shown.



Fig. 4. Participants at the second Molecular Simulation Meeting at UAM-Iztapalapa in 2010.

The main objectives of the Meeting have been:

- 1) Promote research in the field of Molecular Simulation in Mexico and establish scientific collaborations with national and international researchers.
- 2) Motivate graduate and postgraduate students to discuss their research.
- 3) Promote the mobility of students and researchers between different institutions at a national and international level.
- 4) Establish a national/international molecular simulation network.
- 5) Grant recognition every two years to a national researcher in the field of Molecular Simulation.

The number of national researchers, undergraduate and graduate students has increased with time. Noticeably in recent years, this has been reflected in the increase in research papers published in high-impact international journals. Given the high academic level of the Meetings, a special volume was published in the Journal of Molecular Liquids in 2012 with research results presented at the Meeting. There is also a poster session where students at different levels and young researchers participate. In 2015, The Journal of Chemical Theory and Computation awarded \$250 usd to each of the three best posters of the Meeting thanks to the initiative of Professor Julián Tirado-Rives and his wife, MsC Patricia Morales de Tirado, for get these important supports. This award helped raise the level of content of around 40 works presented. The jury has been made up of national and international researchers. The winners are normally graduate students. The award, **academic and economic**, is a good incentive to continue working in this field. The names of the winners and the title of their works are given in Table 1. In Fig. 5 the winners of the Poster session in the 7th Meeting on Molecular Simulations in 2015 can be seen.

Table 1. Name of the poster winners in the Meetings of Molecular Simulations from 2015. The years 2020 and 2021 the Meeting was not organized because the COVID pandemia.

Meeting	Name	Institution	Title of the work
7 th in 2015	Sandra Guadalupe Hernández Ríos	UASLP	A comparison of different force fields for calculating [C ₄ MIM][BF ₄] vapor-liquid equilibria using molecular simulations
	Janett Torres Ruíz	IPN	<i>Evaluación in silico de posibles inhibidores terapéuticos contra el virus de la rabia</i>
	Alexander Pérez de la Luz	UAM-Iztapalapa	Re-parameterizing a force field for formamide molecule
8 th in 2016	María del Rosario Eustaquio-Armenta	BUAP	The line tension of an ionic fluid
	Sandra Acebes	Barcelona Supercomputing Center, Spain	In silico Rational Enzyme Engineering of Manganese Peroxidase through Biophysical and Biochemical Modeling
	Jorge Alberto Aguilar-Pineda	UAM-Iztapalapa	Reparameterization of force fields for nitrogen compounds in liquid phase
10 th in 2018	Ana Beatriz Salazar Arriaga	IIM-UNAM	Desorption of alkanes from a graphite surface produced with different surfactants: anionic and betaine by Molecular Dynamics
	Minerva Valencia	IIM-UNAM	CO ₂ capture using Na-Y siliceous type zeolite modified with SDS
	Jonatan Isaí Sánchez Sánchez	BUAP	Computational modeling of boron nitride nanotube applied to biomedicine

Meeting	Name	Institution	Title of the work
11 th in 2019	Laura María Castro González	UNAM	Design of multifunctional antioxidants derived from sesamol
	Valeria García Melgarejo	UAM-Iztapalapa	Development of force fields for molecular fluids using explicit water
	Saúl Juan Carlos Salazar Samaniego	BUAP	Interaction information in threeparticle quantum systems and synergic effects
12 th in 2022	José Luis Godínez Pastor	BUAP	Oriental aspects of boron nitride nanotubes in water
	Christopher Aldahir Martínez López	UG	Understanding the Aluminum ion adsorption from anodizing wastewater on hydroxyapatite using Molecular Dynamic Simulation
	Oscar Olvera Neria	UAM-Azcapotzalco	Structure prediction of insulin with mutations using AlphaFold
13 th in 2023	Luis A. Castillo-Félix	ITC	Theoretical-experimental study of the rheological behavior of the ionic liquid 1-butyl-2,3-dimethylimidazolium tetrafluoroborate
	Sofía del Carmen Torres Revuelta	IIM-UNAM	Stability study of phospholipid vesicles, DPPC, with cholesterol for the transport of an insulin monomer: zeta potential and interactions of amino acid residues with the polar heads of phospholipids, a study with molecular dynamics
	Ana Beatriz Salazar Arriaga	IIM-UNAM	<i>Aplicación de campos eléctricos en la fisicoquímica de la desorción de una mezcla de hidrocarburos y tensoactivos: Dodecilsulfato de sodio (SDS), sobre grafito: un estudio por dinámica molecular</i>



Fig. 5. Winners of the Poster session in the 7th Meeting on Molecular Simulations in 2015. From left to right. Alexander Pérez de la Luz (UAM-Iztapalapa), Patricia Morales de Tirado (JCTC), Julian Tirado-Rives (Yale University, USA), Sandra Guadalupe Hernández Ríos (UASLP) and Janett Torres Ruíz (IPN). All of the winners were awarded with a prize of \$250 usd provided by the Journal of Chemical Theory and Computation.

The Meeting is organized in two and half days. The number of conferences is around 15 given by around 4 researchers from other countries, 7 consolidated Mexicans **researchers** and 4 graduate/postdocs participants. The guests speakers have come from different countries such as: United States, Spain, England, Germany, Ukraine, Portugal, Canada, Peru and Chile.

The information of the Meetings can be found in the web page <https://www.dci.ugto.mx/~molsim>. In Fig. 6 attendees to the 7th Molecular Simulation Meeting in 2015 are **shown**.



Fig. 6. Participants at the 7th Molecular Simulation Meeting in 2015. The photo was taken in front of the Cathedral in the Zócalo of Mexico City.

Professor José Alejandre was the organizer of the first Meeting on Molecular Simulations in 2009, since then, he has been member of all the Meetings celebrated annually until 2023. The year 2021 y 2022 the Meeting was cancelled because the COVID pandemic. The number of organizers has increased with time. In 2024, the Meeting is being organized by Professors Jorge López-Lemus (UAEMex), Edgar Núñez-Rojas (CONAHCyT-UAM), Omar Castrejón (ITC), Héctor Domínguez-Castro (UNAM), Cesar Millán-Pacheco (UAEM), Susana Figueroa Gerstenmaier (UG), Alexander Pérez de la Luz (UAM), Francisco Alarcón Oseguera (UG) and José Alejandre (UAM). See also Fig. 7. The members of the Organizing Committee in previous years can be found in web page <https://www.dci.ugto.mx/~molsim>.

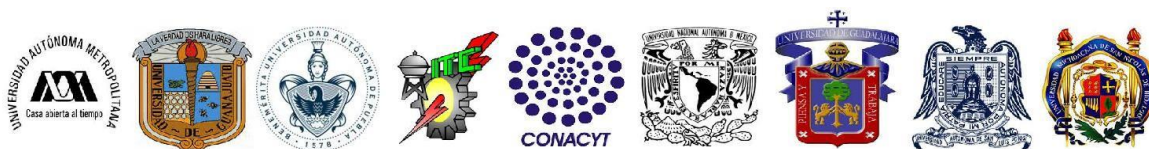


Fig.7. The institutions where the Organizing Committee work for.

Molecular Simulation prize. Being part of a community

The Selection Committee to evaluate the proposals of the simulation community to award the prize to a researcher for the next Meeting are the last three winners of the simulation prize. The prize is awarded every two years during the Meeting to a national researcher whose research area is molecular simulation and who has made relevant scientific contributions in that field. The training of students and the promotion of molecular simulation in Mexico and abroad are also considered. The Prize consists of a diploma given during the special dinner of the event.

Prizes have been awarded to UAM-Iztapalapa researchers: Professors Gustavo A. Chapela in 2010, Fernando del Río in 2012 and José Alejandro in 2014. Professor Alejandro Gil-Villegas from *Universidad de Guanajuato*, Campus Leon, was awarded in 2016. In 2018 the prize was received by Professor Héctor Domínguez from UNAM and finally, the last prize was awarded to Professor Ramón Castañeda Priego from *Universidad de Guanajuato*, Campus Leon, in 2022. In 2020 there was not prize because the Meeting was not organized due to the Covid pandemic. Fig. 8 shows the winners of Molecular Simulation Prize.



Fig. 8. Winners of the prize of the Molecular Simulation Meetings. From left to right: Professors José Alejandro, Gustavo A. Chapela, Fernando del Río, Héctor Domínguez, Ramón Castañeda and Alejandro Gil-Villegas. Picture was taken during the 12th Meeting organized in the hotel NH in the center of México City (2022).

Funding. Paying is not a simulation

The Meetings have been organized thanks to the high interest of the Organizing Committee. Sometimes they have to pay their own expenses and also those of their students. The *División de Ciencias Básicas e Ingeniería* from UAM-Iztapalapa has given us financial support for all the Meetings. The support has been used to pay accommodation and transportation for some students and invited speakers. In some cases, the *Rectoría* of UAM-Iztapalapa and *Rectoría General* have also supported us. In years 2012, 2013, 2014 and 2018 CONAHCyT approved financial support to organize the corresponding *Meeting on Molecular Simulations*. It was possible to pay accommodation and transportation for most of students and invited speakers. The number of participants grew significantly during those years. In the last three meetings we have been forced to charge a registration fee to recover part of the expenses.

In general, in Mexico, university academic programs do not include mandatory molecular simulation courses. In some of them, the students can take optional courses given by their thesis director in most of the cases. That is one of the reasons why the organization of these Meetings is important. The students and researchers have the opportunity of knowing the state of the art research that is being done in this field. The financial support allows to increase the number of participants.

National workshops on Molecular Dynamics

Professor Alejandro has always been concerned in providing students with updated information on the methodologies to undertake scientific investigation either on the theoretical basis of the molecular modeling and simulation techniques, the development of molecular models and computational algorithms or even their application to provide mechanistic explanations of specific physicochemical phenomena in condensed phases, in terms of the motions and interactions of the constituent molecules. This urge enticed him from the very first

Meeting on Molecular Simulation (MMS 1, 2009), to propose that the event should encourage students not only to present their own research, but also to learn more about the topics relevant to the field; thus, a first session of the event was devoted to three two-hour lectures on (1) the foundations of calculations of electronic structure, (2) the foundations of molecular dynamics simulations and (3) a “hands-on” workshop in which the students would get to perform some actual computations of simple systems.

Whereas the first two subjects can be taught in a standard, conventional manner, the third one posed a significant challenge as it requires adequate computers, computer codes and, most importantly, some previous knowledge on “computer handling” from the students. Despite this difficulty, the proposal’s success can be gauged by the enthusiastic participation of tens of students. However, it became clear that the attendees had various levels of knowledge and skills, leading to a wide variety in the benefits that they could get from the experience. It also became clear that the subjects relevant to molecular modeling and simulation were not part of any curricula in Chemistry or Physics in Mexico.

As a consequence, and at Professor Alejandro’s initiative, the project of a *Taller de Dinámica Molecular* (TDM, Workshop on Molecular Dynamics) was born with the aim of grouping as many colleagues as possible, who worked on the disciplines of molecular modeling and simulation and were convinced of the necessity of sharing and extending the knowledge they got from abroad, as well as the convenience of constituting a Mexican community firmly based on preparing new generations of scientists with the ability to undertake what is now known as multi-, inter- and transdisciplinary research in molecular science, combining the traditionally separate disciplines of biology, chemistry, computational science, mathematics and physics to pursue the understanding of complex phenomena in the terms described above.

The first TDM took place from July 25th to 29th, 2011, hosted by the colleagues at *Universidad de Guanajuato* (UG), see Fig. 9, led by Professor Ana Laura Benavides who was the main organizer of the workshop. The attendees were mainly the students of the instructors who lectured at that time. It is worth to mention that each lecturer and each attendee covered his own expenses regarding housing and food. While UG provided the halls, general logistics and coffee, cookies were a generous contribution from Professor Benavides. Each attendee was asked to bring along his own computer. Each instructor provided the programs and input data files required for his lecture by means of a memory key. All the software used in the workshops has been Open-Source code. The attendees were distributed in three groups according to their own appreciation of their level: beginners (B), intermediate (I) and advanced (A).

The TDM was hosted by UG until 2013, then moved to Cuernavaca where Professor César Millán, from *Facultad de Farmacia* at *Universidad Autónoma del Estado de Morelos* (UAEM), and Professor Humberto Saint-Martin, from *Instituto de Ciencias Físicas* (ICF) at *Universidad Nacional Autónoma de México* (UNAM), undertook the organization with the help of colleagues from BUAP, UAM, UG, UNAM and *Tecnológico Nacional de México* (TecNM). Fig. 10 shows participants of the 4th TDM held at the ICF, UNAM. Younger colleagues from *Universidad de Guadalajara* are now in the Organizing Committee.

The polls that were conducted in the first six TDM’s showed the need to include new topics in the Program; ever since, the subjects to be covered have been updated every year so that the TDM currently includes state of the art topics with a high demand from new communities, such as students and researchers in Biochemistry and Pharmacy. The evolution of the TDM is summarized in Table 2, from the original three groups (B), (I) and (A) to those added in 2017, when the (I) was eliminated: (Ap) applications in general physical chemistry; (P) “programmers”, for attendees interested in developing force fields and algorithms, as well as in parallel programming; (BF) applications of molecular modeling and simulation to Biochemistry and Pharmacy; (QM) for those interested in classical molecular dynamics of atoms moving in the potential energy of the electrostatic repulsion between nuclei and the potential energy computed from “on-the-fly” electronic structure calculations.

It is worth to mention that the highest demand from the TDM is for the groups of beginners and of applications to biochemistry and pharmacy. More modern topics, such as *ab initio* molecular dynamics, have also been considered; courses in the use of Machine Learning techniques and the use of Artificial Intelligence will be included as of 2025.

The event was financially supported by ICF in 2014. From 2015 to 2018, additional funding was provided by the Government of the State of Morelos, through the now extinct *Secretaría de Innovación, Ciencia y Tecnología* (SICyT-Morelos), and by the Mexican Federal Government through the also now extinct Special Program to Support Scientific, Technological and Innovation Activities from *Consejo Nacional de Ciencia y*

Tecnología (then CONACyT, now CONAHCyT). This funding is labeled as “Full” in Table 2. Fig. 11 shows participants of the 8th TDM held at the ICF, UNAM, Cuernavaca, Morelos in 2018.

The change of both the State and the Federal governments entailed the extinction of the escrows for scientific projects, thus a much more limited access to funds for all scientific activities; a solution had to be found to keep the TDM going. The Organizing Committee decided to charge a fee starting in 2019, that should cover all housing and meal expenses for the lecturers and attendees. The results vastly surpassed the expectations, to such an extent that a surplus was obtained and allowed the whole TDM to be held at the same location where the attendees were lodged. This is labeled as “Self” in Table 2.

The 10th TDM had to be delayed for one year, due to the “confinement by COVID” in 2020; it was performed online in 2021 and the invitation was successfully extended to other Spanish speaking countries, mainly in Latin America. The fee was then used for Zoom accounts and for the use of remote computing. Fig. 12 shows a snapshot of a screen with online participants during the 10th TDM in 2021. Though the number of attendees was cut down to less than 25% of the 8th and 9th TDM’s, the event is still ongoing and expected to grow again.

Table 2. The twelve TDM workshops that have taken place since 2011; due to the COVID confinement, the event was not done in 2020. The asterisk (*) in the number of attendees indicates an estimate. The next TDM has the “lucky number” 13, that should result in a vigorously renewed event.

No.	Year	Dates	Place	Groups	No. Attendees	Financial support
1	2011	July 25 to July 29	Guanajuato	B, I, A		No
2	2012	August 20 to August 24	Guanajuato	B, I, A		No
3	2013	August 5 to August 9	Guanajuato	B, I, A		No
4	2014	July 28 to August 1	Cuernavaca	B, I, A	60*	ICF
5	2015	July 27 to July 31	Cuernavaca	B, I, A	80	Full
6	2016	July 25 to July 29	Cuernavaca	B, I, A	171	Full
7	2017	July 31 to August 4	Cuernavaca	B, A, Ap, P, BF	190	Full
8	2018	July 30 to August 3	Cuernavaca	B, A, Ap, P, BF	200*	Full
9	2019	July 29 to August 2	Cuernavaca	B, A, Ap, P, BF	200*	ICF+Self
*	2020	COVID			None	
10	2021	August 2 to August 6	Online	B, A, Ap, P, BF	45	Self
11	2022	August 1 to August 5	Online	B, A, Ap, P, BF, QM	61	Self
12	2023	November 20 to November 22	Hybrid	B, A, Ap, P, BF, QM	60*	Self
13	2024	June 24 to June 28	Cuernavaca	In progress		Self



Fig. 9. Lecturers and attendees to the 1st TDM, *Universidad de Guanajuato*, 2011.

Despite the difficulties, it is now clear that the event will keep attracting the interest of future developers and users of molecular modeling and simulation techniques. Moreover, several former alumni have volunteered to lecture on their own areas of expertise, all related to molecular sciences, and provided the TDM with a continuous renewal of topics. That is to say, the new generations are keenly aware of the relevance of the field and willing to contribute to its progress by updating not only the topics to be taught, but also how communication with colleagues is established throughout the Spanish-speaking communities, for instance, a Facebook group is already available at <https://www.facebook.com/groups/144556469018023>



Fig. 10. Lecturers and attendees to 4th TDM, Cuernavaca, 2014.



Fig. 11. Lecturers and attendees to 8th TDM, Cuernavaca, 2018.

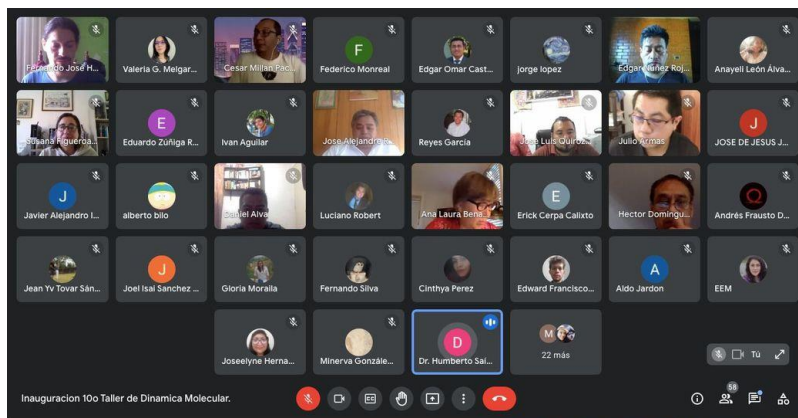


Fig. 12. Lecturers and attendees to 10th TDM, online, 2021.

Computer Simulations in the world, Mexico and at UAM

In Fig. 13 it can be observed the number of articles published in the world, in Mexico and in UAM organized per decades. Topics searched in the Web of Science were *Molecular Dynamics* and *Monte Carlo Simulations* [6]. In Fig., decades are defined with the initial year. It was considered as the first molecular simulation article *J. Chem. Phys.* 27, 1208 (1957) by B. J. Alder and T.E. Wainwright in 1957. It is interesting to note that throughout the world there was a great advance in molecular simulation research from 1990 to 1991 and these years coincide with the development of the LINUX operating system [7]. Also, in 1991, with Java, object-oriented programming began to be relevant in the field of computing [8] and the Gopher protocol was created at the University of Minnesota; this is an internet system that preceded the world wide web [9].

In Fig. 13 it can be seen that the production of Molecular Dynamics articles in Mexico is 1% of the world and that, in turn, the articles production of UAM is 10% of Mexico's production. In the case of Monte Carlo articles, the trend is the same, however, the production of articles about MC, in general, is lower than that of MD articles.

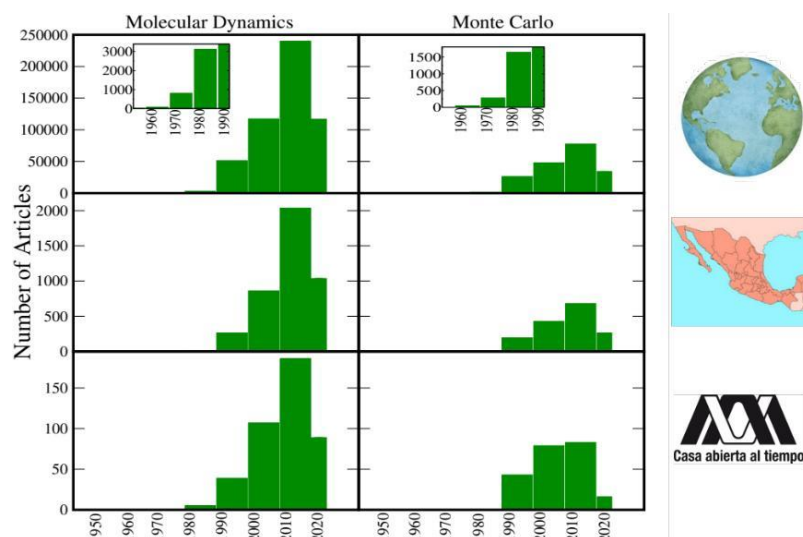


Fig. 13. Number of articles per decades in the world, in Mexico and at UAM. The information is extracted from Web of Science where the legends "*Molecular Dynamics*" and "*Monte Carlo simulations*" were searched.

Molecular Dynamics and Monte Carlo simulations articles production of different countries and Mexico

In the Fig. 14 it can be observed the global production and two examples of countries that produce more than a half of the molecular dynamics articles in the world. Decades are denoted as it has been already described. These countries are the United States of America and China, which, as can be seen in the Fig., had considerable growth starting in 2011. On the other hand, the United States has been increasing its production constantly.

With a production equivalent to around 10 % of world production we have Spain, Canada and Brazil. Finally, as it has been already explained in Fig. 13, we present three countries whose production is, on average, 1 % of world production, these countries are Argentina, Chile and Mexico.

The trends in Monte Carlo articles are presented in the right panel of Fig. 14 and they are similar to those shown in the previous figure.

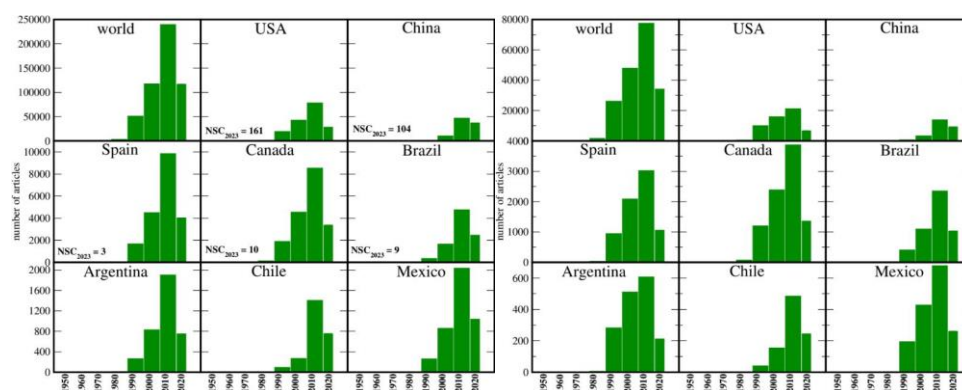


Fig. 14. Number of articles by decade in the world and different countries. The information is extracted from Web of Science where the legend *Molecular Dynamics* was searched, left panel. The *Monte Carlo* search are shown in the right panel. The number of supercomputers, NSC, within the TOP500 ranking in 2023 that every country had is shown in the figure.

Supercomputing in the world. May the power be with us

The development of computer simulations requires the use of high performance computers. How are we in Mexico compared with other countries? The TOP500 project ranks the world's fastest computers twice a year from 1993 [10]. Fig. 15-A shows countries that have high-performance computers measured in peta-FLOPS (a peta-flop means 10^{15} floating point operations per second) since November 2006. Currently, the United States has the largest number of supercomputers on the list, with 161 machines. As of November 2006, the United States had 306 supercomputers, as it was on a downward trend of machines until 2021; the decrease in the number of supercomputers and the increase in the production of simulation articles (see Figures 13 and 14) may be due to the efficient use of computational resources. The European Union is in second place with 112 machines, in recent years it has a constant trend in the number of machines, but as of 2021 it shows an increase in the number of machines. China is in third place with 104 machines, but in 2006 it only had 18 and in 2010 it had 228 machines. As of 2020, China has had a decrease in the number of machines. Countries such as: Canada, Brazil and Spain have a smaller number of high-performance machines than the US and China. While Mexico practically does not have a high-performance machine since 2017, see Fig. 15-B. In 2007 China had 9 supercomputers in the rank TOP500 in 2007 then went to around 230 in 2019, an increase of 25 times in 12 years. Finally, in 2023 they have around 100. It is probably that because the new computers are faster than the older the calculations are performed in less time. That might be the same situation in USA. Although Argentina and Chile do not have a significant presence in the number of supercomputers in the world, their production of simulation work is comparable to that of Mexico (see Figures 13 and 14). By analyzing articles

from 2022 and 2023, it can be seen that this advance in production may be due to collaborations with research groups from other countries such as France, Germany, USA and India.

In Mexico we have the *Delta Metropolitana de Cómputo de Alto Rendimiento* formed by UNAM, UAM and CINVESTAV (IPN). The idea was to connect the computers of the three institutions, but for some reason it is not working. It seems that even putting together the three computer the TOP500 ranking is not reached. The information provided in this work is useful to understand how is the supercomputing development in Mexico. Without powerful computers not only the molecular simulation community is affected but also other areas of knowledge as electronic structure, astronomy, etc.

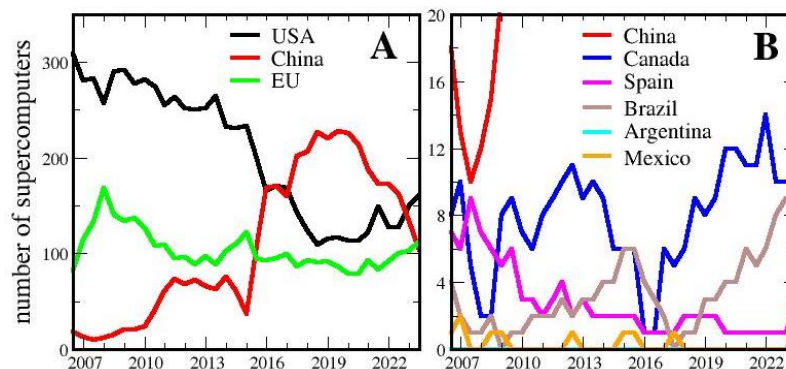


Fig. 15. Number of supercomputers in several countries as a function of time. (A) USA, China and Europe. (B) China, Canada, Spain, Brazil, Argentina and Mexico.

Molecular Dynamics and Monte Carlo simulations in Mexico

In Fig. 16 the distribution of molecular dynamics articles production is presented for decades indicated in Mexico. It is interesting to observe that in the first decade (1984-1993) in Mexico there were only seven institutions performing Molecular Dynamics simulations. Also, from 1984 to 2003 UNAM published most of the half articles of the molecular simulations field; on this period, UAM was in second place publishing molecular dynamics articles. In the decade 1994-2003 several institutions began to work in the field, mainly UG, UAEM, UANL, UASLP and UMSNH. These institutions have had presence in the last three decades. Also, from 2004 IPN started to increase its production. From 1994 to 2013 the IMP made an important contribution to the production of molecular dynamics articles, however, from 2013 to 2024 this contribution decreased significantly.

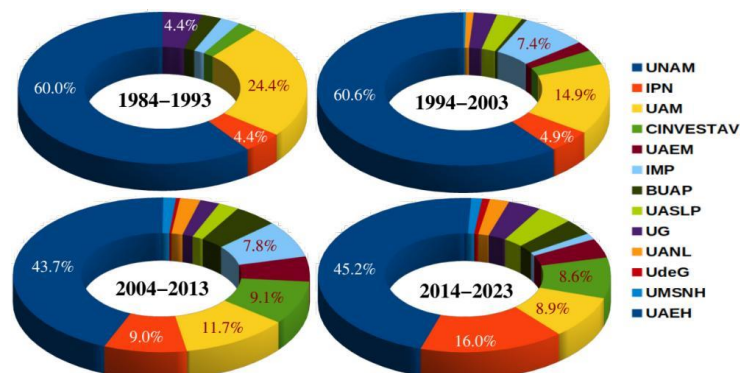


Fig. 16. Distribution of the articles production of different Mexican institutions. The search was *Molecular Dynamics* in the Web of Science. The results are given periods of ten years. The number of articles per decade is: (45:1984 to 1993), (350:1994 to 2003:), (940:2004 to 2013) and (2037:2013-2023). The total number of articles is 3372.

In Fig. 17 the distribution of Monte Carlo simulations articles production is presented for decades indicated in Mexico. In the decade from 1984 to 1993 there were only five institutions publishing articles on this topic, UNAM, IPN, UAM, CINVESTAV and UASLP. From 1994 IMP, UG, UAEM and BUAP started to work and publish on this direction.

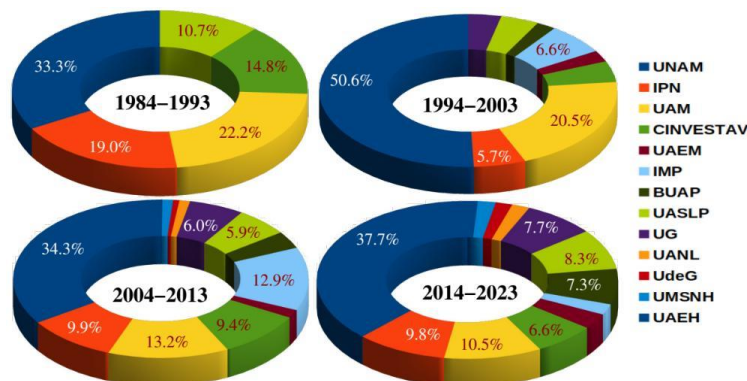


Fig. 17. Distribution of the articles production of different Mexican institutions. The search was *Monte Carlo simulations* in the Web of Science. (27: 1984 to 1993), (336:1994 to 2003), (597; 2004 to 2013) and (726: 2013 to 2023). The total number is 1686.

Most cited articles of the Mexican molecular simulations community

A list of articles in molecular simulation field by at least one Mexican author with more than 100 citations is presented in Table 3.

The molecular simulation community is still in its development stage. The first articles published in international journals in this area were developed in the 1980s. It is a relatively new subject. To evaluate the impact of the Mexican community in this field we decided to look for the articles with WofS citations greater than 100. The names of the Group leader in bold face letter, the number of citations, reference and doi for every of the highlighted papers are given in Table 3. A chronological analysis by topics is made with the following arbitrary classification:

1. Purely theoretical investigations that use molecular simulations to compare their description of either ideal or realistic systems, denominated as “Basic Theory” (BT) in Fig. 18.
2. Development of algorithms and programs, ranging from MD engines to analysis tools (AP).
3. Design of novel molecular models and/or parameterizations of force fields (FF).
4. Applications to novel descriptions of various physicochemical phenomena and systems (PP) and, due to its growing relevance and ongoing participation of researchers in biological sciences, a separate account was made for

5. the use of MMS in describing biomolecular systems and looking for pharmaceutical drugs (BioPh).

The main journals where articles with more than 100 citations have been published are

J. Chem. Phys (15), *Phys. Rev. E* (6), *J. Phys. Chem. B* (5), *Phys. Rev. Lett* (3), *Molec. Phys* (2) and *J. Phys. A: Math. Gen* (2). *Surface Science* (2), *Chem. Review* (1), *Nature* (1), *Structure* (1)

The first high-impact article dates to 1977, with the pioneering work of Professor Gustavo A. Chapela on describing a gas-liquid surface of a system of Lennard-Jones molecules through MD and Monte Carlo simulations, to provide computational and numerical support to simulations of complex systems of particles with a simple model of their interactions.

Though research in different topics was undertaken by several Mexican groups, for the first years (1977 to 1990), the most relevant was only on the use of MMS to validate basic theoretical work, as done by Professor Marcelo Lozada-Cassou, who used Monte Carlo simulations to validate several results from the **hypernetted-chain and mean-spherical integral equations**, and Professor Magdaleno Medina-Noyola, with studies of the

electrical double layer and **on** the diffusion of solutes through various solvents. Professor Fernando del Río has made important contributions in the development of theoretical thermodynamics for liquids.

Table 3. Group leader, first author, number of citations, references and DOI of molecular simulation articles published by Mexican researchers living in Mexico and having more than 100 citations. The DOI for article with (*) is: 10.1002/(SICI)1096-987X(19990415)20:5<511::AID-JCC4>3.0.CO;2-8. There are 32 group leaders shown in bold letters.

Group Leader	First Author	Citations	Reference	DOI
Alejandro Gil-Villegas	Gil Villegas, A.	901	J. Chem. Phys. 106, 4168–4186 (1997)	https://doi.org/10.1063/1.473101
	Amparo Galindo	347	Molecular Physics, vol. 93, Issue 2, p.241-252 (1998)	https://doi.org/10.1080/00268979809482207
	Eduardo Buenrostro-González	222	AIChE Journal; 2004 , 50, No. 10	https://doi.org/10.1002/aic.10243
	Amparo Galindo	189	J. Phys. Chem. B 1999, 103, 46, 10272–10281	https://doi.org/10.1021/jp991959f
	Clare McCabe	118	J. Phys. Chem. B 1998, 102, 41, 8060–8069	https://doi.org/10.1021/jp982331s
José Alejandro	José Alejandro	601	J. Chem. Phys. 102, 4574–4583 (1995)	https://doi.org/10.1063/1.469505
	Mark E Tuckerman	414	J. Phys. A: Math. Gen. 39 5629 (2006)	https://doi.org/10.1088/0305-4470/39/19/S18
	Andrij Trokhymchuk	407	J. Chem. Phys. 111, 8510–8523 (1999)	https://doi.org/10.1063/1.480192
	Minerva González-Melchor	149	J. Chem. Phys. 125, 224107 (2006)	https://doi.org/10.1063/1.2400223
	Pedro Orea	110	J. Chem. Phys. 123, 114702 (2005)	https://doi.org/10.1063/1.2018640
	Raúl Fuentes-Azcatl	102	J. Phys. Chem. B 2014, 118, 5, 1263–1272	https://doi.org/10.1021/jp410865y
Chapela, Gustavo A.	Gustavo A. Chapela	353	J. Chem. Soc., Faraday Trans. 2, 1977,73, 1133-1144	https://doi.org/10.1039/f2977301133

Group Leader	First Author	Citations	Reference	DOI
Garzon, Ignacio L.	I. L. Garzón	363	Phys. Rev. Lett. 81, 1600 (1998)	https://doi.org/10.1103/PhysRevLett.81.1600
	K. Michaelian	329	Phys. Rev. B 60, 2000 (1999)	https://doi.org/10.1103/PhysRevB.60.2000
	Cecilia Noguez	288	Chem. Soc. Rev., 2009,38, 757-771	https://doi.org/10.1039/b800404h
	José M. Soler	170	Phys. Rev. B 61, 5771 (2000)	https://doi.org/10.1103/PhysRevB.61.5771
	Ignacio L. Garzón	117	Phys. Rev. B 54, 11796 (1996)	https://doi.org/10.1103/PhysRevB.54.11796
	J. Jellinek	101	Atoms, Molecules and Clusters 20, 239-242 (1991)	https://doi.org/10.1007/BF01543982
Perez-Aguilar, Jose Manuel	Ge Fang	400	NATURE COMMUNICATIONS (2018) 9:129	https://doi.org/10.1038/s41467-017-02502-3
	G. Glenn Gregorio	208	Nature; 547(7661): 68–73. (2017)	https://doi.org/10.1038/nature22354
	Irina Kufareva	138	Structure 22, 1120–1139, 2014	https://doi.org/10.1016/j.str.2014.06.012
	Yiming Zhao	128	Nature Communications volume 7, 11221. (2016)	https://doi.org/10.1038/ncomms11221
Ascencio, Jorge A.	M. José Yacamán	381	J. Vac. Sci. Technol. B 19, 1091–1103 (2001)	https://doi.org/10.1116/1.1387089
	H. E. Troiani	141	Nano Letters 2003, 3, 6, 751–755	https://doi.org/10.1021/nl0341640
	J. A. Ascencio	125	Surface Science 396 (1998) 349-368	https://doi.org/10.1016/S0039-6028(97)00689-4
	Ascencio J.A.	101	Surface Science 447 (2000) 73–80	https://doi.org/10.1016/S0039-6028(99)01112-7
Laura Dominguez	Phuong H. Nguyen	372	Chem. Rev. 2021, 121, 4, 2545–2647	https://doi.org/10.1021/acschemrev.0c01122
	Christian Frantz	150	J Cell Biol . 2008 Dec 1;183(5):865-79	https://doi.org/10.1083/jcb.200804161

Group Leader	First Author	Citations	Reference	DOI
Galindo-Murillo, Rodrigo	Marie Zgarbová	333	J. Chem. Theory Comput. 2015, 11, 12, 5723–5736	https://doi.org/10.1021/acs.jctc.5b00716
	Rodrigo Galindo-Murillo	301	J. Chem. Theory Comput. 2016, 12, 8, 4114–4127	https://doi.org/10.1021/acs.jctc.6b00186
	Rodrigo Galindo-Murillo	134	Nucleic Acids Research, 43, 11, 2015, 5364–5376	https://doi.org/10.1093/nar/gkv467
	Rodrigo Galindo-Murillo	118	Biochimica et Biophysica Acta 1850 (2015) 1041–1058	https://doi.org/10.1016/j.bbagen.2014.09.007
Jose L Medina-Franco	Sabrina Castellano	154	J. Med. Chem. 2011, 54, 21, 7663–7677	https://doi.org/10.1021/jm2010404
	T Scior	142	Curr Med Chem . 2009;16(32):4297-313	https://doi.org/10.2174/092986709789578213
	Dirk Kuck	140	Bioorganic & Medicinal Chemistry; 18, 2, 2010, 822-829	https://doi.org/10.1016/j.bmc.2009.11.050
	Maykel Cruz-Monteagudo	118	Drug Discov Today . 2014;19(8):1069-80	https://doi.org/10.1016/j.drudis.2014.02.003
	Narender Singh	116	J. Chem. Inf. Model. 2009, 49, 4, 1010–1024	https://doi.org/10.1021/ci800426u
Koester, Andreas M.	Matthias Krack	153	J. Chem. Phys. 108, 3226–3234 (1998)	https://doi.org/10.1063/1.475719
Jose L Rodriguez-Lopez	M. G. Méndez-Medrano	227	J. Phys. Chem. C 2016, 120, 9, 5143–5154	https://doi.org/10.1021/acs.jpcc.5b10703
	Grégory Guisbiers	158	ACS Nano 2016, 10, 1, 188–198	https://doi.org/10.1021/acsnano.5b05755
	J. L. Rodríguez-López	127	Phys. Rev. B 67, 174413 (2003)	https://doi.org/10.1103/PhysRevB.67.174413
	F. Aguilera-Granja	100	Phys. Rev. B 66, 224410 (2002)	https://doi.org/10.1103/PhysRevB.66.224410

Group Leader	First Author	Citations	Reference	DOI
Arturo Rojo Domínguez	Leticia Arregui	227	Microbial Cell Factories, 18, 200 (2019)	https://doi.org/10.1186/s12934-019-1248-0
Marcelo Lozada-Cassou	C Velasco-Santos	197	Nanotechnology 13 (2002) 495–498	https://doi.org/10.1088/0957-4484/13/4/311
	Manuel Quesada-Pérez	192	CHEMPHYSICHEM2 003, 4, 234-248	https://doi.org/10.1002/cphc.200390040
	Marcelo Lozada-Cassou	190	J. Chem. Phys. 77, 5150–5156 (1982)	https://doi.org/10.1063/1.443691
	DOUGLAS HENDERSON	161	Journal of Colloid and Interface Science, 114, 1, 1986	https://doi.org/10.1016/0021-9797(86)90250-X
	Enrique Gonzales-Tovar	149	J. Chem. Phys. 83, 361–372 (1985)	https://doi.org/10.1063/1.449779
	Markus Deserno	119	J. Phys. Chem. B 2001, 105, 44, 10983–10991	https://doi.org/10.1021/jp010861+
Medina-Noyola, M.	M. Medina-Noyola	195	Phys. Rev. Lett. 60, 2705 (1988)	https://doi.org/10.1103/PhysRevLett.60.2705
	Magdaleno Medina-Noyola	146	J. Chem. Phys. 73, 6279–6283 (1980)	https://doi.org/10.1063/1.440125
Sosa-Peinado, Alejandro	Daniel-Adriano Silva	183	PloS Comput Biol 7(5): e1002054. (2011)	https://doi.org/10.1371/journal.pcbi.1002054
Jose L Rivera	José L. Rivera	177	Nano Letters 2003, 3, 8, 1001–1005	https://doi.org/10.1021/nl034171o
	José L. Rivera	152	Phys. Rev. E 67, 011603 (2003)	https://doi.org/10.1103/PhysRevE.67.011603
	José L Rivera	117	Nanotechnology 16 186 (2005)	https://doi.org/10.1088/0957-4484/16/2/003
	D. Mckay a	114	Journal of Solid State Chemistry 181 (2008) 325–333	https://doi.org/10.1016/j.jssc.2007.12.001
Osorio-revilla guillermo	Tzayhri Gallardo-Velázquez	156	Food Research International 42 (2009) 313–318	https://doi.org/10.1016/j.foodres.2008.11.010
	Ofelia G. Meza-Márquez	117	Meat Science 86 (2010) 511–519	https://doi.org/10.1016/j.meatsci.2010.05.044

Group Leader	First Author	Citations	Reference	DOI
José M Vásquez-Pérez	Gerald Geudtner	154	Comput Mol Sci, 2012, 2: 548–555	https://doi.org/10.1002/wcms.98
Ortega-Blake, Ivan	Mauricio Carrillo-Tripp	143	J. Chem. Phys. 118, 7062–7073 (2003)	https://doi.org/10.1063/1.1559673
	Humberto Saint-Martin	114	J. Chem. Phys. 113, 10899–10912 (2000)	https://doi.org/10.1063/1.1324711
Dominguez, Hector	H. Dominguez	127	J. Phys. Chem. B 2000, 104, 22, 5302–5308	https://doi.org/10.1021/jp994479x
Faustino Aguilera-Granja	J.M. Montejano-Carrizales	122	NanoStructured Materials, 8, 3, 169-287,1997	https://doi.org/10.1016/S0965-9773(97)00168-2
	F. Aguilera-Granja	100	Phys. Rev. B 66, 224410 (2002)	https://doi.org/10.1103/PhysRevB.66.224410
Mariano Lopez de Haro	M. López de Haro	125	J. Chem. Phys. 78, 2746–2759 (1983)	https://doi.org/10.1063/1.444985
Jose-Manuel Martinez-Magadan	J. H. Pacheco-Sánchez	118	Energy Fuels 2003, 17, 5, 1346–1355	https://doi.org/10.1021/ef020226f
Santamaria, Ruben	R. SANTAMARIA	116	J. Comput. Chem, 20, 5, 511-530 (1999)	*
Mendoza-Huizar, Luis Humberto	L.H. Mendoza-Huizar	114	JEAC, 521 (2002) 95–106	https://doi.org/10.1016/S0022-0728(02)00659-2
Martinez-Guajardo, Gerardo	Gerardo Martínez-Guajardo	111	Chem. Commun., 2011,47, 6242-6244	https://doi.org/10.1039/c1cc10821b
	Diego Moreno	101	Chem. Commun., 2014,50, 8140-8143	https://doi.org/10.1039/c4cc02225d
Ramirez-Solis, A.	Bernard Kirtman	110	J Chem Phys .128(11):11410 8 (2008)	https://doi.org/10.1063/1.2885051
	Alejandro Ramírez-Solís	102	Inorg. Chem. 2004, 43, 9, 2954–2959	https://doi.org/10.1021/ic035159z

Group Leader	First Author	Citations	Reference	DOI
Ana Laura Benavides	A. L. Benavides	107	J. Chem. Phys. 144, 124504 (2016)	https://doi.org/10.1063/1.4943780
Jesus Muñiz	Jesus Muñiz	106	Chem. Eur. J.2011,17, 368 – 377	https://doi.org/10.1002/chem.201001765
Ramon Castaneda-Priego	Aaron P. R. Eberle	137	Phys. Rev. Lett. 106, 105704 (2011)	https://doi.org/10.1103/PhysRevLett.106.105704
	Aaron P. R. Eberle	100	Langmuir 2012, 28, 3, 1866–1878	https://doi.org/10.1021/la2035054
Fernando del Rio	FERNANDO DEL RIO	103	MOLECULAR PHYSICS, 2002, 100, 15, 2531-2546	https://doi.org/10.1080/00268970210132522
Alvarez-Ramirez, Fernando	Fernando Alvarez-Ramírez	101	Energy Fuels 2013, 27, 4, 1791–1808	https://doi.org/10.1021/ef301522m

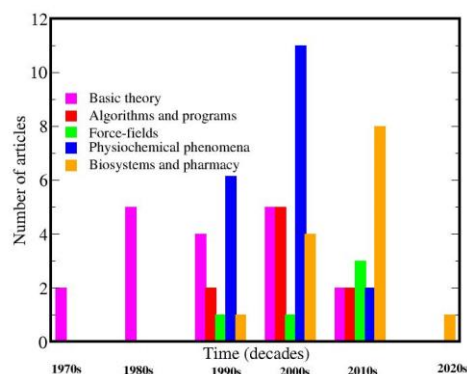


Fig. 18. Number of articles in indexed journals with more than 100 citations (WoF) as a function of time (decades) published by Mexican researchers from the 1970s to date.

This changed in the next three decades (1991 to 2020), when molecular models, force fields and programs of Mexican origin started to be used to describe different physicochemical phenomena. Among others, it is worth mentioning the efforts by Professor Iván Ortega-Blake and his collaborators to use the interaction energies obtained from quantum calculations of electronic structure as “learning sets” to parametrize complex and sophisticated models for molecular dynamics simulations (see for instance the polarizable MCDHO water model [11]). Other lines of research to be highlighted are those of Professor José Alejandro to develop efficient codes to sample the isothermal-isobaric ensemble [12], on one hand, and to adequately consider long-range forces [13] to calculate correctly the surface tension of polar and ionic systems.

Research on biosystems and pharmaceutical drugs has become more relevant from 1991 to date, see Fig. 18, with relevant contributions by Professor Nina Pastor and Professor César Millán-Pacheco [14], as well as Professor Rodrigo Galindo-Murillo [15]. The application of molecular modeling and simulation to

determine properties of nanoclusters and of materials also deserves to be remarked, mentioning the contributions of Professor Ignacio Garzón, see Table 3, and of Professor Miguel José Yacamán [16].

It is important to mention that Alejandro Gil-Villegas heads the list in table 3 with the article (*Journal of Chemical Physics* 106(10):4168-4186, (1997)), he was part of the research team that developed the Statistical Associating Fluid Theory for potentials of Variable Range (SAFT-VR).

This shift to studies of bigger, more complex systems, has been possible due to access to high-performance, number-crunching computers. Unfortunately for the community, this access has been compromised in the last six years because of restricted funding from the federal government. A new strategy must be found, otherwise Mexican contributions will be severely reduced.

Leader researches in the SNI performing Molecular Dynamics simulations

In Fig. 19 the SNI level of molecular simulation professors mentioned in Table 3 is described as a distribution. Here it is possible to observe that the most of professors have a level 3 while there is a significant number of emeritus professors.

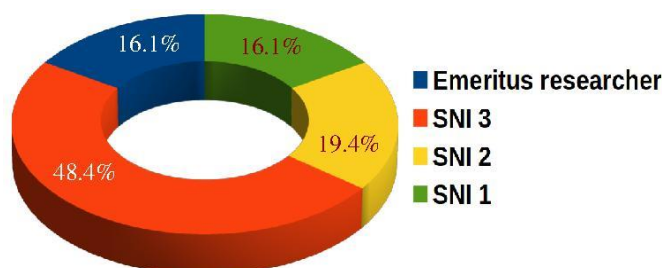


Fig. 19. Distribution of *Sistema Nacional de Investigadores* (SNI) levels in Mexican simulation research with more than 100 citations. The total number of researchers is 32.

Conclusions

Since the beginning of molecular simulations in the 1950s to date, the progress in this field of research has been notable worldwide, from the point of view of publications, in 1957 two articles on Molecular Dynamics were published while in 2023 the figure is 31296 (WofS), this, of course, is directly associated with technological advancement in computing: The United States of America, China, Germany and Japan have excellent supercomputing facilities and it is assumed that also a large number of researchers. They produce more than half of scientific articles in the world. It is interesting to see that China, in 2007 had around 10 supercomputers in the TOP500 ranking and it increased to 230 in 11 years. The number of publications increased and surely also the number of researchers. Clearly, there is a correlation between the number of supercomputers and publications in every country. More computers, more researchers, more publications and more development.

The research in molecular simulations in Mexico began around 30 years after the first molecular simulation work published in 1957. Professor Gustavo Chapela learned the methods in the United Kingdom in the 1970s and introduced them at UAM-Iztapalapa in the 1980s. Professor José Alejandre along with other Mexican researchers such as Professors Ana Laura Benavides and Humberto Saint-Martin have enthusiastically promoted the field through courses, conferences, Workshops and Meetings at the national and international level. The objectives set when the Meeting on Molecular Simulations was created have been largely met. The community collaborates in national and international projects. The number of students and postdocs in the field is growing up as it can be seen from the poster sessions of the **Meetings on Molecular Simulations**. New

members from different institutions are joined every year to the Organizing Committees which warrant the continuation of promoting this field in the country. The world knows the contributions made for the Mexican community in molecular simulations. The Journal of Chemical Theory and Computations has given several times economical support to award the best three poster in the Meetings. The prize of the Meeting has been awarded to 6 researchers with a high academic profile. There are around 32 leaders that have published articles with more than 100 citations (WofS) in several fields. The Journal of Molecular Liquids published a special issue with results presented in one of the Meetings. The research topics were grouped into five categories. It is shown that research is moving from the basic science, where statistical mechanics methods were used to study complex problems but with simplified models of molecular interactions, to much more complex systems in liquids, electrolytes, surfactants, polymers, ionic liquids, proteins, bilayers, etc. That trend probably is the same in other countries.

In summary, the simulation community in Mexico is developing cutting-edge research and the number of students and postdocs in the field are increasing; however, budget limitations at public universities and research facilities have resulted in the scarcity of “tenure-track positions”; moreover, as the competition for a job is open to the international scientific community, the future may look gloomy for young Mexican professional scientists; thus novel and creative solutions have to be found. The private industry supports the molecular simulation research in developed countries; more efforts have to be put on convincing both Mexican and international investors, that it is worth supporting this field through projects and the hiring of postgraduate personnel. On the other hand, we also have to join efforts with colleagues that use supercomputers for scientific research, to convince governments that investing on basic and applied science and on high-power computing facilities will be profitable. We hope that, soon, the teaching of molecular simulation methods will increase the number of mandatory courses in disciplines such as chemistry, physics, biology and different types of engineering. The fact that in the last years several professionals who work for various industries have attended the TDM gives us a moderate, but justified optimism on the future.

Acknowledgements

The authors thanks CONAHCyT for financial support provided to organize several of the Workshops and Meetings on Molecular Simulations. HSM thanks ICF-UNAM and DGAPA-UNAM for financial support, the latter through PAPIIT, grant IN109222. ENR express his gratitude to CONAHCyT for financial support under the Project *Cátedras-CONAHCyT* 687.

Summarizing the development of molecular simulations in Mexico since its appearance is a great effort that involves mentioning names, articles, workshops, courses, events and organizing committees. Throughout these years, the work of many professors, researchers and students has contributed to the advancement of this discipline, unfortunately, not all of them were mentioned in the present manuscript, let these words serve acknowledgement of their valuable contribution.

References

1. Alder, B. J.; Wainwright, T. E. *J. Chem. Phys.* **1959**, *31*, 459–466. DOI: <https://doi.org/10.1063/1.1730376>.
2. Barojas, J.; Levesque, D.; Quentrec, B. *Phys. Rev. A* **1973**, *7*, 1092–1105. DOI: <https://doi.org/10.1103/PhysRevA.7.1092>.
3. Chapela, G. A.; Saville, G.; Rowlinson, J. S. *Faraday Discuss. Chem. Soc.* **1975**, *59*, 22. DOI: <https://doi.org/10.1039/dc9755900022>.
4. Chapela, G. A.; Saville, G.; Thompson, S. M.; Rowlinson, J. S. *J. Chem. Soc., Faraday Trans. 2* **1977**, *73*, 1133–1144. DOI: <https://doi.org/10.1039/F29777301133>.

5. Chapela, G. A.; Martínez-Casas, S. E. *Mol. Phys.* **1983**, *50*, 129–137. DOI: <https://doi.org/10.1080/00268978300102221>.
6. <http://Quimica.Izt.Uam.Mx/Ssm/Ssm09/>, accessed in 2024.
7. <https://www.Britannica.Com/Technology/Linux>, accessed in April 2024.
8. <https://www.Britannica.Com/Technology/Object-Oriented-Programming>, accessed in April 2024.
9. <https://www.Chronicle.Com/Article/How-Gopher-Nearly-Won-the-Internet>, accessed in April 2024.
10. <https://www.Top500.Org/Lists/Top500/>, accessed in April 2024.
11. Saint-Martin, H.; Hernández-Cobos, J.; Bernal-Uruchurtu, M. I.; Ortega-Blake, I.; Berendsen, H. J. *Chem. Phys.* **2000**, *113*, 10899–10912. DOI: <https://doi.org/10.1063/1.1324711>.
12. Tuckerman, M. E.; Alejandre, J.; López-Rendón, R.; Jochim, A. L.; Martyna, G. J. *J. Phys. A: Math. Gen.* **2006**, *39*, 5629–5651. DOI: <https://doi.org/10.1088/0305-4470/39/19/S18>.
13. Trokhymchuk, A.; Alejandre, J. *J. Chem. Phys.* **1999**, *111*, 8510–8523. DOI: <https://doi.org/10.1063/1.480192>.
14. Bencze, K. Z.; Kondapalli, K. C.; Cook, J. D.; McMahon, S.; Millán-Pacheco, C.; Pastor, N.; Stemmler, T. L. *Crit. Rev. Biochem. Mol. Biol.* **2006**, *41*, 269–291. DOI: <https://doi.org/10.1080/10409230600846058>.
15. Zgarbová, M.; Šponer, J.; Otyepka, M.; Cheatham, T. E.; Galindo-Murillo, R.; Jurečka, P. *J. Chem. Theory Comput.* **2015**, *11*, 5723–5736. DOI: <https://doi.org/10.1021/acs.jctc.5b00716>.
16. Yacamán, M. J.; Ascencio, J. A.; Liu, H. B.; Gardea-Torresdey, J. *J. Vac. Sci. Technol., B: Microelectron. Nanometer Struct.--Process., Meas., Phenom.* **2001**, *19*, 1091–1103. DOI: <https://doi.org/10.1116/1.1387089>.

Solar Thermochemistry Overview: An Approach to Solar Thermal Energy Storage and Hydrogen Production

Adriana Santamaria Padilla¹, Hernando Romero Paredes Rubio^{2*}, Juan Daniel Macias², José Miguel Berrío Sánchez¹, Ana Karina Elizalde Galicia¹

¹Posgrado de Energía y Medio Ambiente, Universidad Autónoma Metropolitana Iztapalapa, Av. Ferrocarril San Rafael Atlixco No. 186, Ciudad de México, 09310, México.

²Departamento de Ingeniería de Procesos e Hidráulica, Universidad Autónoma Metropolitana Iztapalapa, Av. Ferrocarril San Rafael Atlixco No. 186, Ciudad de México, 09310, México.

*Corresponding author: Hernando Romero Paredes Rubio, email: hrp@xanum.uam.mx

Received May 25th, 2024; Accepted August 29th, 2024.

DOI: <http://dx.doi.org/10.29356/jmcs.v68i4.2298>

Abstract. The solar thermochemistry laboratory of the Metropolitan Autonomous University was created in early 1982 to promote the development of solar technology in our country. A decade ago, the priority objective of designing thermal energy storage systems that allow moderating the effects of intermittent solar radiation was proposed. This not only allows us to reduce the consumption of fossil fuels but also contributes to the mitigation of global warming by reducing carbon dioxide emissions. This paper highlights the benefits of research as a driver for advancing solar thermal technology and research efforts to develop heat storage systems. The work includes an overview of current thermal energy storage methods and their future projection. This work reports research developed with mixtures based on strontium carbonate doped with five compounds. The objective was to reduce agglomeration and sintering problems while significantly increasing the effective conversion and energy storage density. The experimental results demonstrate that the SrCO₃+CaCO₃ and SrCO₃+SnO₂ mixtures present better performance and stability than others. Finally, this article emphasizes the potential benefits of research, such as advancing solar technology, reducing carbon emissions, providing cleaner energy, and collaborating to address energy poverty.

Keywords: Thermochemical energy storage; concentrated solar power; strontium carbonate; effective conversion; volumetric energy density.

Resumen. El laboratorio de termoquímica solar de la Universidad Autónoma Metropolitana fue creado a principios de 1982 para impulsar el desarrollo de la tecnología solar en nuestro país. Hace una década se propuso como objetivo prioritario diseñar sistemas de almacenamiento de energía térmica que permitan moderar los efectos de la radiación solar intermitente. Esto no sólo nos permite reducir el consumo de combustibles fósiles, sino que también contribuye a la mitigación del calentamiento global al reducir las emisiones de dióxido de carbono. Este artículo aborda los beneficios de la investigación como motor para el avance de la tecnología solar térmica y los esfuerzos de investigación para desarrollar sistemas de almacenamiento de calor. El trabajo incluye una revisión general de los métodos actuales de almacenamiento de energía térmica y su proyección futura. Se reportan las investigaciones desarrolladas con mezclas a base de carbonato de estroncio dopado con cinco compuestos. El objetivo es reducir los problemas de aglomeración y sinterización, al mismo tiempo que aumentar significativamente la conversión efectiva y la densidad de almacenamiento de energía. Los resultados experimentales demuestran que las mezclas SrCO₃+CaCO₃ y SrCO₃+SnO₂ presentan mejor rendimiento y estabilidad que otras. Finalmente, este trabajo enfatiza los beneficios potenciales de la investigación, como el

avance de la tecnología solar, la reducción de las emisiones de carbono, el suministro de energía más limpia y la colaboración para abordar la pobreza energética.

Palabras clave: Almacenamiento termoquímico; energía solar concentrada; carbonato de estroncio; conversión efectiva; densidad volumétrica de energía.

Nomenclature

C	Heat capacity (J/K)	N	Nth cycle
c	Specific heat capacity (J/kg·K)		<i>Acronyms</i>
D_m	Energy density (kJ/kg)	CSP	Concentrating solar power
D_v	Volumetric energy density (GJ/m ³)	DNI	Direct normal irradiance (kWh/m ² /year)
E	Thermal energy (J)	EDS	Energy Dispersive Spectroscopy
g	Gas	GHGs	Greenhouse gases
G	Gibbs energy (free energy) (kJ)	HoSIER	High Radiative Flux Solar Furnace from IER-UNAM
H	Enthalpy (kJ)	HT	High temperature
K	Equilibrium constant	HTF	Heat transfer fluid
Wh	Watt-hora	IER	Renewable Energy Institute
m	Mass (kg).	IIM	Materials Research Institute
p	Pressure (Pa)	IRENA	International renewable energy agency
ρ	Mass density (kg/m ³)	LACYQS	The National Laboratory for Solar Concentration Systems and Solar Chemistry
R	Gas constant (8.314 J/mol·K)	LCOE	Levelized cost of energy
S	Entropy (kJ/K)	LHS	Latent heat storage
s	Solid	LTQSUAM	Solar thermochemistry laboratory at Metropolitan Autonomous University
T	Temperature (K)	PCM	Phase change material
T^*	Turning temperature	PV	Photovoltaic
T_m	Melting temperature	SEM	Scanning electron microscopy
T_0	Reference temperature	SHS	Sensible heat storage
X_{eff}	Effective conversion	SOFC	Solid Oxide Fuel Cell
	<i>Greek letters and subscripts</i>	TES	Thermal storage system
ΔH_R	Reaction enthalpy (kJ/kg)	TGA	Thermogravimetric analyzer
λ	Latent heat (kJ/kg)	TRL	Technology Readiness Levels
ξ	Reaction yield	TQ	Thermochemical
δ	Stoichiometric constant	UNAM	National Autonomous University of Mexico
cal	Calcination	USD	United States dollar
car	Carbonation	XRD	X-Ray Diffraction

Introduction

The Solar Thermochemistry Laboratory was established at UAM-I in 1982. It is a leading and pioneer laboratory in the field of solar thermochemistry in Latin America. It has been recognized as a school of excellence in this study area for over forty years. Graduates from the laboratory have gone on to create their laboratories at other institutions, and we have been working to establish a research network to promote research on the use of concentrated solar energy for chemical processes. The primary focus of this research is on thermal energy storage systems, producing clean energy vectors, and developing industrial chemical processes at medium and high temperatures using concentrated solar energy, such as oil coke gasification or cement or ceramics production. The research potentially benefits using solar energy at medium and high

temperatures, reducing carbon emissions, and providing cleaner and more constant energy sources that help mitigate global heating.

Climate change is currently a priority and a critical situation that demands immediate resolution and political will. It is a global concern, and its mitigation should be the highest priority for all countries. Moreover, it poses a significant threat to global food security, sustainable development, and poverty eradication. The greenhouse gases (GHGs) produced by human activity are the primary driver of climate change [1]. Thermal and Power generation contributes substantial CO₂ emissions and other gases to the environment, necessitating the exploration of new technologies to mitigate them [2]. Renewable energy sources like wind and solar power have been in use for years, offering a clean and sustainable way to generate electricity. However, they also present a challenge: their intermittent and unpredictable nature leads to fluctuations in the transmission and distribution of electrical energy. This is particularly true for solar energy, which exhibits day-night cyclicity, resulting in low plant factors.

However, despite these challenges, solar energy has many applications that make it a valuable option for energy production. Photovoltaic systems (PVS) solar energy can be directly converted into electrical energy. Alternatively, concentrated solar power systems can convert solar energy into mechanical energy, which can then be used to generate electricity. Solar energy can also produce heat for various applications, such as passive heating of buildings, active heating of water or air, cooling, or industrial processes [3,4]. Additionally, it can be used to produce solar fuels such as hydrogen, syngas, and kerosene [5].

By harnessing solar energy's power, we can reduce our reliance on non-renewable sources and help create a more sustainable future. While solar energy may have its challenges, it offers many benefits that make it a valuable option for energy production. Solar thermal energy is an important renewable, abundant, and clean source. It is a resource that can be exploited to help replace fossil fuels. There are currently different technologies to make use of this renewable resource at its different levels of operating temperatures. In these technologies, evacuated tube collectors, collector heat pipes, and compound parabolic collectors are the most common for low-temperature flat plate collectors. The most currently used for high temperatures are parabolic troughs, followed by concentrated solar towers, and Fresnel and dish collectors represent a minor fraction.

Scientific and technological research is essential to address the problem of intermittency in solar energy and promote its use as a clean energy source to reduce the impact of global warming. One of the most promising mechanisms to achieve this goal is to store thermal energy and then release it to an optimal temperature for a given application. Although concentrating solar systems for solar power generation have been extensively tested in industrial thermal energy applications, they still suffer from low plant capacity factors, which limits their efficiency. Several solar thermal energy storage systems have been proposed based on the sensible heat of substances that can overcome the disadvantage of the intermittence of solar energy. Fig. 1 illustrates the importance of energy storage in meeting a specific power requirement most feasibly. The loading and unloading operation of the storage is observed throughout the day. The discharge happens when the solar resource is insufficient or at night, while the load occurs when there is a surplus or the demand decreases [6-8].

Utilizing solar thermal energy in industrial processes is vital to achieving sustainable and environmentally responsible industrial operations. This renewable energy source harnesses the sun's abundant and inexhaustible heat to meet the substantial energy demands of various industrial sectors. As the global community intensifies its focus on reducing greenhouse gas emissions and transitioning towards cleaner energy sources, solar thermal technology emerges as a promising solution with significant potential for industrial applications. Scientific research has extensively explored the technical feasibility, economic viability, and environmental benefits of integrating solar thermal energy into industrial processes. IRENA (2012) [9] has highlighted the immense potential of solar thermal systems to provide process heat at high temperatures required by industries while reducing reliance on fossil fuels and mitigating carbon emissions. Examples of possible uses include steam generation, drying processes, and chemical reactions such as calcination processes in the cement industry.

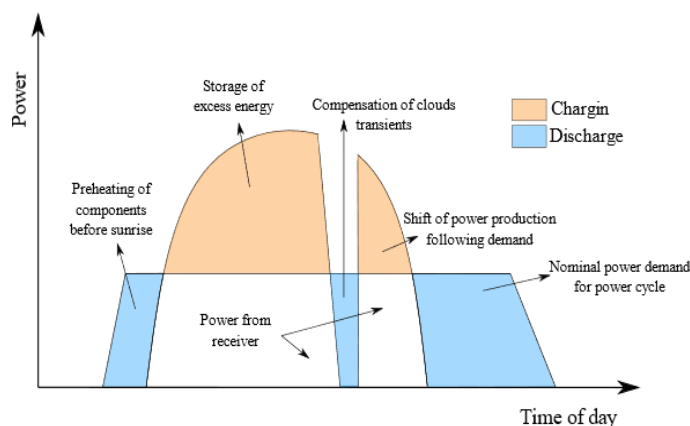


Fig. 1. Function of thermal storage in a CSP plant. Adapted from [6-8].

Solar thermal technology encompasses various solar collectors and concentrating systems, each tailored to meet specific industrial heat requirements. Research by Romero et al. (2019) [10] has delved into the design, optimization, and performance analysis of various solar thermal collectors, including parabolic troughs, solar towers, and dish collectors, elucidating their efficacy in industrial heat generation. Furthermore, integrating thermal energy storage systems with solar thermal plants has garnered significant attention in scientific literature. Frazzica and Cabeza (2019) [11] and Palacios et al. (2020) [12] have explored advanced thermal storage materials and techniques, enabling the efficient storage and utilization of solar heat for industrial processes, thereby enhancing system reliability and flexibility.

CSP is becoming competitive compared to other renewable energy systems, even with conventional fossil fuels. Solar thermal plants using central tower technology operate worldwide under two different schemes. The first scheme uses molten salts as a heat transfer fluid and energy storage system coupled to a steam turbine. The second scheme is like the first one but uses a gas turbine [12-14]. These operating schemes need high efficiencies to compete in the electricity market. Therefore, there is an opportunity to propose new power cycles and forms of thermal energy storage that can generate electricity at a lower cost per kWh. These new arrangements are expected to increase the global efficiency of solar-electrical power and the capacity factor, which is the number of hours of operation per year. Fig. 2 shows how the number of storage hours affects the capacity factor for different solar concentration technologies. The graph illustrates the importance of having a high-efficiency storage system for these technologies. For instance, when it comes to central tower technology, without storage, the average plant capacity factor is around 30%. However, when the storage capacity is more than 10 hours, the plant capacity factor significantly increases to 77%. This means that with a more efficient storage system, the technology can become more competitive compared to other technologies. Nonetheless, there is still a need to improve thermal storage efficiency.

There are 58 solar thermal power plants in operation, with the vast majority utilizing parabolic trough technology. While some plants use Fresnel and central tower technology, most use parabolic troughs. Furthermore, 38 solar thermal plants are currently under construction and mostly use parabolic trough technology. There are plans for additional plants in the future. It is critical to note that the focus is on lowering the levelized cost of energy (LCOE) to become more competitive with other clean technologies such as PV, wind, geothermal, and micro-hydro [15].

Various alternatives for energy storage are being researched to ensure availability during periods of insufficient solar resources, such as at night. The first central tower solar thermal power plants utilizing supercritical CO₂ (sCO₂) as a working fluid are anticipated to be operational by 2030. Simultaneously, research into new solar thermal energy storage solutions will continue.



Source: IRENA Renewable Cost Database and CSP Guru, 2022, for DNI values.

Fig. 2. Capacity factor trends for CSP technologies by direct normal irradiance and storage duration, 2010-2022. From [15].

Solar thermal energy storage systems can be categorized into three distinct technologies: sensible heat, latent heat, and chemical reaction heat. To gain a better understanding of each of these systems, the following section provides a brief explanation of each.

This paper will provide an overview of our laboratory's latest work results. The first part presents a brief overview of the current state of thermal energy storage (TES), exploring its applications, plant technologies, materials, and state of research. Section 2 discusses various types of energy storage classified by storage duration, heat exchange type, and storage time interval, including a detailed analysis of the different technologies available for sensible, latent, and thermochemical energy storage. Section 3 presents the thermodynamics of reactions. Section 4 explains the materials and methods employed in the laboratory experiments studied in recent years. This section covers the materials selected for studying thermochemical storage, the methods of characterization and analysis, and the calculation of storage density and effective conversion. Lastly, section 5 outlines an outlook and conclusions.

Thermal Energy Storage

The storage of solar energy has been a great challenge, allowing for rapid development in materials and technologies that cushion daily variations in solar flux. However, these developments lead to new challenges in developing cost-effective materials and components.

For more than four decades, the storage of solar energy has been a significant concern for the technological advancement of solar power systems. Over the years, several systems have been proposed to boost the efficiency of power plants [16-22] and other applications at lower temperatures.

There are three forms of thermal energy storage: sensible, latent, and thermochemical heat, as illustrated in Fig. 3, which contains relevant information from the following references [23-27]. Among these, sensible heat is the most developed technology, but its drawback is its low energy storage density and temperature, which are not constant. Latent heat, on the other hand, is less developed but has a slightly higher energy storage density. The phase change energy involved in this process could be very attractive; deep research to find the material that covers the needed at a lower price is necessary. The most attractive solution, however, is chemical energy storage, which is currently under development.

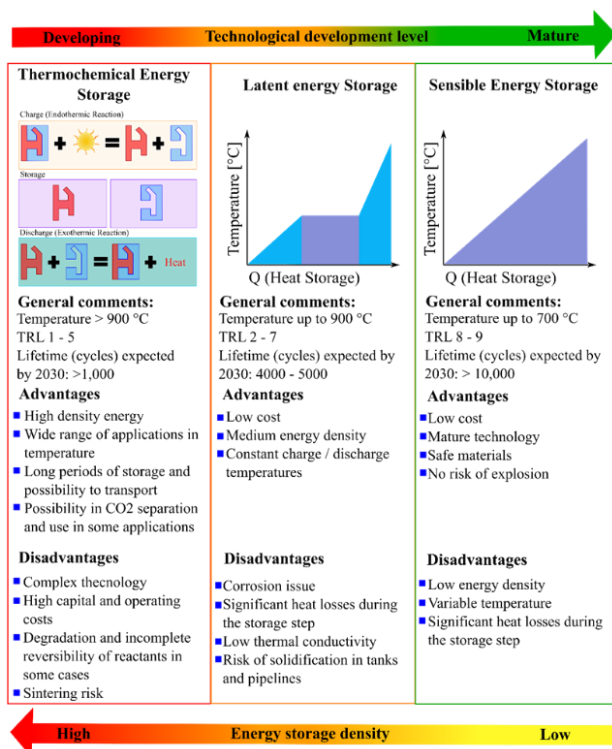


Fig. 3. Mechanisms of thermal energy storage. Adapted from [23].

The choice of thermal energy storage method depends on the operating temperature and the amount of thermal energy desired to be stored. Fig. 4 gives an idea of the applications of the three principles described. Currently, new materials and methods are being investigated to improve their performance and stability.

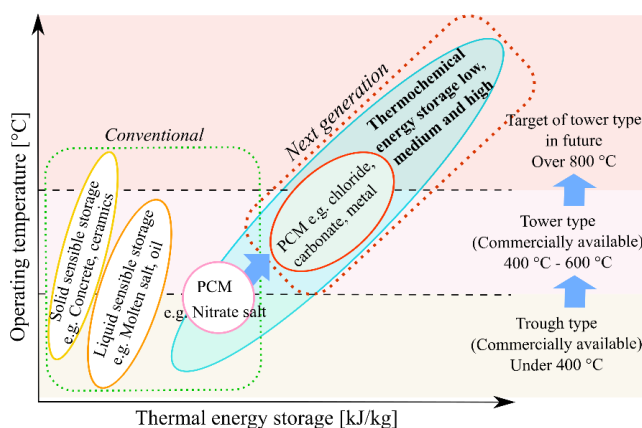


Fig. 4. Operating temperature and thermal energy storage capacity. Adapted from [24].

For energy storage, the molten salt FLiNaK (46.5 % LiF, 11.5 % NaF, and 42 % KF) for sensible heat storage can reach temperatures up to 1003 K [21,28,29]. This temperature is compatible with the gas turbine

inlet temperature, which typically operates between 973 and 1273 K and is more efficient [30-32]. According to F. Crespi [33], the best-performing configuration is the Brayton cycle with partial cooling. However, such systems require an energy storage system with higher temperature and storage capacity per unit mass. Thermochemical storage has a higher energy density than sensible and latent heat energy storage, as shown in Table 1. Furthermore, it allows for a prolonged storage period, increasing the plant capacity factor and improving the hours of operation per year of a solar tower power plant.

Table 1. Properties of different thermal storage medium. Adapted from [34-38].

Storage technologies	Sensible heat storage	Latent heat storage	Thermochemical heat storage
Storage shape	Thermal	Thermal	Thermochemical
Efficiency (%)	50 – 90	75 – 90	75 - 100
Initial capital cost (USD/kW) (2020)	3400 – 4500	6000 – 15000	1000 – 3000
Energy cost (USD/kWh) (2020)	0.1 - 13	10 - 56	8 - 100
Energy storage density (kWh/m ³)	25	100	~500
Energy storage density (kWh/kg)	~0.02 – 0.03	~0.05 - 1	~0.5 - 1
Storage capacity (MW)	0.1- 300	0.1- 300	0.1 - 300

Sensible energy storage materials and systems

Sensible heat storage takes advantage of the thermophysical properties of materials, particularly the heat capacity of solids and liquids. Although gases make it possible to store sensible heat, their storage capacity per unit volume is very small, so they are not considered in most applications. Sensible heat storage involves storing thermal energy by raising the temperature of a substance [39]. The total change of the internal energy of a material during a charging and discharging process is related to its storage capacity. The amount of thermal energy stored is a function of the specific heat capacity of the substance, the change in temperature, and the mass density, according to the relation:

$$E = m \int_{T_1}^{T_2} c dT \quad (1)$$

Solids have a greater thermal storage capacity than liquids; however, the latter can flow through pipes. The simplest example of sensible heat storage is buildings that are heated during the day due to solar radiation incident on their wall surfaces. The stored heat is released during the night to heat the interior of the building. Sensible heat can also be stored in sand and rocks. These systems are highly sustainable if the heat is taken from solar energy. Table 2 presents the thermophysical properties of solids used for sensible heat storage.

Sensible heat storage in liquids is one of the most common for low-temperature applications; for example, at temperatures below 373 K, water is one of the most used fluids due to its high specific heat capacity (4.182 J/g K). Water has several advantages, including its non-toxicity. And non-flammable nature, high availability, and the potential to eliminate the need for heat exchangers when used as a working fluid in solar collectors. Liquid metals such as aluminum, copper, and lead can be used in sensible heat storage [40-42]. Its advantages are high thermal conductivity and density, but its cost is usually relatively high compared to other materials used for TES.

Table 2. Thermophysical properties of solids used in sensible heat storage. Data from [43].

Material	Density (kg/m³)	Specific heat capacity (J/kg K)	Volumetric heat capacity (x10⁶ J/m³K)
Alumina spheres	3953	1157	4.574
Aluminium	2710	896	2.428
Basalt	3000	920	2.76
Brick	1800	837	1.507
Clay	1458	879	1.282
Concrete	200	880	0.176
Gabbro	2911	643	1.872
Glass	2710	837	2.268
Gravelly earth	2050	1840	3.772
HT ceramic	3500	866	3.031
HT concrete	2750	916	2.519
Iron	7900	452	3.571
Magnetite	5177	752	3.893
Refractory bricks	3000	1150	3.45
Sandstone	2200	712	1.566
Slags	3770	912	3.438
Steel	7840	465	3.646
Vitrified asbestos	3120	1034	3.226
Water	988	4182	4.132
Wood	700	2390	1.673
Zirconia	5999	597	3.581

There are various alternatives for temperatures above 373 K but below 573 K, including thermal oils (synthetic, mineral, and organic), molten salts, and liquid metals. Some oils, such as Dowtherm and Therminol, are suitable for temperatures between 373 and 573 K. These can degrade over time and pose flammability problems. Concentrating solar plants use thermal oils, including vegetable oils. Synthetic oils are generally preferred over traditional mineral oils because they have better thermophysical properties (lower viscosity, higher thermal conductivity, and higher heat capacity) [40-42]. Barrasso et al. (2023) [44] present the thermophysical properties of some of the liquids proposed to store heat. Thermal oils have the advantage of a low vapor pressure compared to low-viscosity fluids. Their handling is relatively simple, and their storage is

carried out in tanks at lower pressure. Table 3 shows the thermophysical properties of oils used as thermal storage media.

When the temperature exceeds the limits of organic thermal oils, molten salts are used to store heat at temperatures of up to 823 K. Eutectic mixtures have been studied for sensible heat and latent heat storage for over forty years. Eutectic mixtures include the ternary mixture of salts, like Hitec, which is a eutectic mixture of water-soluble, inorganic salts of potassium nitrate, sodium nitrite, and sodium nitrate (53 % KNO_3 , 7 % NaNO_3 , and 40 % NaNO_2), whose melting temperature is 415 K and used up to 727 K. The binary mixture of salts is widely used (60 % NaNO_3 and 40 % KNO_3) [44,45]. Sodium hydroxide, with a melting temperature of 593 K, is usable up to 1073 K, highly corrosive, and difficult to contain at high temperatures; it is the second most used molten salt [12].

Table 3. Properties of liquids oils and molten salts to sensible Heat Storage capacity. Data from [12].

Substance	Fluid	Melting temperature [K]	Temperature range [K]	Density [kg/m^3]	Heat Capacity [J/kg K]	Comments
Calorie HT43	Oil	-	283–588	888	2300	Non-oxidizing at high temperatures
Therminol 55	Oil	-	291–588	672	2400	Density at 573 K
Therminol 66	Oil	-	282–618	770	2100	Density at 618 K
Dowtherm A	Oil	285	285–533	897 - 1043	2200	Eutectic mixture
Hitec	Molten salt	415	423–863	-	1550	--
Draw salt (50% NaNO_3 –50% KNO_3)	Molten salt	779	523–863	-	1550	--
Sodium	Liquid metal	593	398–1033	927	1300	Reacts violently with water and oxygen

Latent energy storage materials and systems

A latent storage system (LTES) consists of a substance capable of undergoing a phase transition in the considered temperature range, and the supplied heat is stored as latent heat. The thermal energy is used to break the molecular bonds and allow the change of state (fusion-vaporization) without temperature variation: it is an endothermic process that accumulates heat, making it available later. The stored thermal energy is a function of the mass and of the latent heat of fusion of the substance, according to the relation:

$$E = m\lambda \quad (2)$$

where E = Stored energy, kJ; m = mass of material, kg; λ = Latent heat, kJ/kg. To reach the melting temperature, a specific amount of sensible heat must be supplied. This energy will only be recovered when the material cools to its initial temperature. However, in a continuous system, this energy remains stored and unused. Some sensible heat is supplied to superheat the material after it has slightly melted. The equation is as follows:

$$E = m \left[\int_{T_1}^{T_m} c_1 dT + \lambda + \int_{T_m}^{T_2} c_2 dT \right] \quad (3)$$

where c_1 and c_2 are the specific heat capacities at the initial and final phases, respectively, T_1 , T_2 , and T_m refer to the initial, melting, and final temperatures, respectively. Like sensible heat storage systems, latent heat storage presents unavoidable energy losses, even if the containers are properly thermally insulated.

LHS systems are classified based on the type of phase change process involved, such as solid-solid, solid-liquid, solid-gas, and liquid-gas. However, the latter two transformations are not commonly used due to the complexities associated with volume changes, and solid-solid transformations have little associated heat. So, the most common option is solid-liquid transitions due to their high heat storage density and the minimal volume changes necessary for effective storage [46].

Phase change materials used to store heat in solid-liquid transitions can be classified into organic, inorganic, and eutectic materials, as reported in the references [46-48]. Fig. 5 shows the thermodynamic characteristics of thermal storage and some examples of these materials, and it contains relevant information from the following references [48-53].

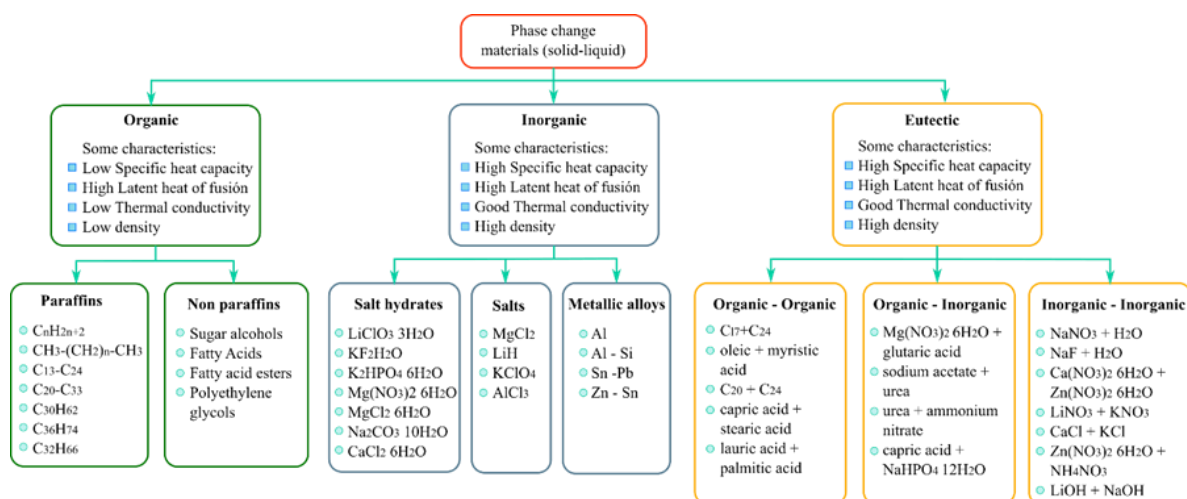


Fig. 5. Phase change materials characteristics and some examples as thermal energy storage. Adapted from [48-53].

Table 4 presents the melting temperature and latent heat of some of the most common latent heat storage media materials.

Eutectic refers to a mixture whose melting (solidification) point is lower than that corresponding to each component in its pure state. Eutectic mixtures have high stability in the liquid state, and their constituents are insoluble in the solid state. Eutectic mixtures can combine inorganic-inorganic, inorganic-organic, or organic-organic compounds. Table 5 shows the eutectic mixtures commonly used as sensible heat storage media.

Table 4. Melting temperature and latent heat of some of the most common materials used as latent heat storage media. Data from [52-54].

Category	Material	Melting temperature [K]	Latent heat [kJ/kg]
Organic	Bees Wax	334.8	177
	Benzoic acid	394.7	142.8
	Cetyl alcohol	322.3	141
	Dyphenyl amine	325.9	107
	Glycerin	290.9	198.7
	Hydrophosphoric acid	328	213
	Isomalt	420	275
	Pentaerythritol	460	255
	Phenol	314	120
	Polyethylene glycol 35000	341.7	166.9
	Polyethylene glycol 600	285.5	129.1
	Quinone	388	171
Stearic acid	342	209	
Inorganic	Ca(NO ₃) ₂	834	-
	CaCl ₂ 6H ₂ O	302	190.8
	CoSO ₄ 7H ₂ O	313.7	170
	KNO ₃	606	266
	LiClO ₃ 3H ₂ O	281	155 - 253
	LiNO ₃	526	-
	LiNO ₃ 2H ₂ O	303	296
	LiNO ₃ 3H ₂ O	293	189
	MgCl ₂	987	452
	MgCl ₂ 6H ₂ O	390	167
	Na(NO ₃) ₂ 6H ₂ O	330	169
	Na ₂ CO ₃	1127	275.7
	NaNO ₃	580	172
NaOH H ₂ O	337.3	273	

Table 5. Eutectic mixtures commonly used as sensible heat storage media. Data from [55]

Salt mixture	Latent heat [kJ/kg]
20Li ₂ CO ₃ +60Na ₂ CO ₃ +20K ₂ CO ₃ (wt%)	279
44 Li ₂ CO ₃ + 56 Na ₂ CO ₃ (wt%)	370
52.1 NaCl + 47.9 CaCl ₂ (mol%)	155.6
25 KCl + 29 NaCl + 66 CaCl ₂ (wt%)	245
48 NaCl + 52 MgCl ₂ (wt%)	351
24 KCl + 47 BaCl ₂ + 29 CaCl ₂ (wt%)	219
80.5 LiF + 29.5 CaF ₂ (wt%)	820
33.5 NaF + 66.5 NaCl (mol%)	533.8
53.3 NaCl + 46.7 Na ₂ SO ₄ (mol%)	232.3

The materials that store latent heat must have specific thermophysical and chemical properties to perform their function adequately. Thermophysical properties: melting temperature in the operating range, high latent heat of phase transition per unit volume, high thermal conductivity of both phases, small volume change in phase transformation, low vapor pressure at operating temperature, high nucleation rate, and adequate crystallization rate. Chemical properties: long-term chemical stability, fully reversible solidification-melting cycle, compatibility with container construction materials, non-toxic, non-flammable and non-explosive to ensure safety, various authors have reported these criteria [53,56].

Most phase change materials do not fully meet those criteria. However, recent advances in the design of new materials for energy storage, including nanomaterials, have opened new possibilities for improving material performance [53].

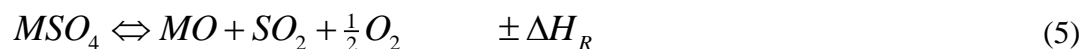
Thermochemical energy storage; materials and systems

Scientific literature extensively discusses reversible chemical reactions for thermochemical energy storage, and some of these references are [8,57-62]. These reversible reactions allow the accumulation of substantial energy in small amounts of matter that can be stored at room temperature for long periods and then released at high temperatures. This heat storage method is based on bidirectional endothermic and exothermic reactions. In the endothermic reaction, the thermal energy supplied to the system is stored in the chemical bonds of the molecules, while the exothermic reaction releases the stored thermal energy. The amount of thermal energy stored depends on the reaction enthalpy of the material, and the amount of matter involved in the process, as well as the yield of the reaction, according to the following expression:

$$E = m \times \Delta H_R \times \xi \quad (4)$$

An excellent example of a reversible reaction to store thermochemical energy is the dissociation of a metal sulfate [63] (MSO₄) see Eq. 5. The sulfate dissociation reaction is carried out at high temperature in a reactor with an adapted solar concentration system that provides the heat necessary to carry out the reaction.

On the other hand, the product recombination reaction is exothermic and takes place in a heat exchange reactor where the stored energy is recovered. The temperature level that occurs in recombination is lower than that of the dissociation stage. The efficiency of thermochemical heat storage systems largely depends on the temperatures of both reactions, the reaction rate, and the conversion yield.



Thermochemical systems are a viable option for storing thermal solar energy. However, several critical challenges still need to be addressed and overcome to reduce the adverse effects of sintering, agglomeration, loss of material porosity, and unstable material structure on conversion performance [63]. Structural stability techniques (supports), chemical spacers, composite materials, etc., can be used to reduce or mitigate the adverse effects described above. Therefore, we consider this research line crucial to promoting the widespread adoption of solar energy technology.

Thermodynamics and materials for chemical heat storage

Considering an isothermal and isobaric reactive process inside a closed system in mechanical equilibrium with the surroundings. Then, as the system reaches the thermodynamic equilibrium, the total Gibbs energy decreases continuously until it reaches a minimum value with respect to all possible changes at the given T and P , according to the following relation:

$$(dG)_{T,P} \leq 0 \quad (6)$$

Changes in the free energy of the system are computed with the relation:

$$\Delta G = \Delta H - T\Delta S \quad (7)$$

In its natural state, the system tends to reach a state of lower energy and higher entropy. Lower energy is preferred because it will make the system more stable.

Enthalpy fundamentally influences the number of bonds and bond-breaking forces in the reactants relative to the bonds formed in the products.

Most common chemical reactions are exothermic in their natural direction. In an exothermic reaction, the reactants have a relatively high amount of energy compared to the products. As the reaction proceeds, energy is released into the environment. However, when an endothermic reaction is possible, the $T\Delta S$ term is of fundamental importance to reach equilibrium. This means that chemical reactions to store thermal energy must have a positive ΔS . Therefore, reactions in which a greater number of moles of products are obtained with respect to one of the reactants are preferred, as well as reactions where a change occurs in the aggregation state of the species involved.

When equilibrium is reached in a reversible chemical reaction, the reaction rate in one direction becomes equal to the corresponding reaction rate in the opposite direction. The equilibrium constant (K) is the ratio of the rate constants of each of these reactions.

The equilibrium constant (K) of the system is determined from the standard Gibbs energy change:

$$\Delta G^0 = -RT \ln K \quad (8)$$

$$\Delta H^0 - T\Delta S^0 = -RT \ln K \quad (9)$$

Considering the equilibrium condition of the system where the proportion of the concentration of products and reactants are the same, the pressure and temperature are constant, and no species are added or removed from the system, we can consider that $K=1$. In this situation, the turning temperature (T^*) can be written as:

$$T^* = \frac{\Delta H^0}{\Delta S^0} \quad (10)$$

The turning temperature T^* represents the operating temperature T at which a system can store and release heat. If the operating temperature of the system exceeds the turning temperature ($T > T^*$), the equilibrium constant will be greater than 1 ($K > 1$). Under these conditions, the standard enthalpy and entropy changes (ΔH^0 , ΔS^0) are positive, which favors the endothermic reaction that stores energy. On the other side, when the operating temperature is lower than the turning temperature ($T < T^*$), the equilibrium constant will be less than 1 ($K < 1$). In this scenario, an exothermic or recombination reaction prevails and releases the accumulated energy. For example, in a thermochemical system intended to store heat at 1373 K and release it at 973 K, the value of T^* must be within the range of approximately 973 K to 1373 K. Therefore, an initial analysis should focus on examining the relation $\Delta H^0/\Delta S^0$ to identify reactions that have the potential to store and release heat at the desired temperature.

In the context of energy storage systems, studying the thermodynamic properties of materials can help select the most suitable one based on the temperature of the thermal source [64]. Table 6 provides the thermodynamic properties and chemical reactions of some compounds used to store energy.

Table 6. Thermochemical properties and chemical reactions of some compounds to store energy.

Group reaction	Reaction	Turning Temperature [T*, K]	Gravimetric energy storage density [kJ/kg]	Reaction Enthalpy [kJ/mol]
Oxides	$6\text{Mn}_2\text{O}_3 = 4\text{Mn}_3\text{O}_4 + \text{O}_2(\text{g})$	1272.81	202.10	31.91
	$2\text{BaO}_2 = 2\text{BaO} + \text{O}_2(\text{g})$	1157.61	432.64	73.26
	$\text{Rh}_2\text{O}_3 = \text{Rh}_2\text{O} + \text{O}_2(\text{g})$	1246.99	982.14	249.28
	$2\text{V}_2\text{O}_5 = 2\text{V}_2\text{O}_4 + \text{O}_2(\text{g})$	1831.01	992.92	180.59
	$2\text{Co}_3\text{O}_4 = 6\text{CoO} + \text{O}_2(\text{g})$	1206.37	842.39	202.85
	$2\text{Mn}_3\text{O}_4 = 6\text{MnO} + \text{O}_2(\text{g})$	1974.14	850.61	194.63
	$4\text{CuO} = 2\text{Cu}_2\text{O} + \text{O}_2(\text{g})$	1392.00	809.87	64.42
	$2\text{Li}_2\text{O}_2 = 2\text{Li}_2\text{O} + \text{O}_2(\text{g})$	414.69	746.17	34.23
	$6\text{Fe}_2\text{O}_3 = 4\text{Fe}_3\text{O}_4 + \text{O}_2(\text{g})$	1675.14	496.38	79.27
	$2\text{MgO}_2 = 2\text{MgO} + \text{O}_2(\text{g})$	478.34	380.20	21.41
	$\text{Cr}_5\text{O}_{12} = 2.5\text{Cr}_2\text{O}_3 + 2.25\text{O}_2(\text{g})$	380.01	279.37	126.27
	$2\text{PtO}_2 = 2\text{PtO} + \text{O}_2(\text{g})$	695.31	276.55	62.80
	$2\text{PbO}_2 = 2\text{PbO} + \text{O}_2(\text{g})$	675.79	263.03	62.92
$2\text{Sb}_2\text{O}_5 = 4\text{SbO}_2 + \text{O}_2(\text{g})$	790.42	291.48	94.29	

Group reaction	Reaction	Turning Temperature [T*, K]	Gravimetric energy storage density [kJ/kg]	Reaction Enthalpy [kJ/mol]
Oxides	$6\text{UO}_3 = 2\text{U}_3\text{O}_8 + \text{O}_2(\text{g})$	944.24	123.18	35.23
	$4\text{MnO}_2 = 2\text{Mn}_2\text{O}_3 + \text{O}_2(\text{g})$	802.13	480.87	41.81
	$2\text{Na}_2\text{O}_2 = 2\text{Na}_2\text{O} + \text{O}_2(\text{g})$	1432.89	1596.17	124.47
	$2\text{SrO}_2 = 2\text{SrO} + \text{O}_2(\text{g})$	661.38	281.93	33.72
	$\text{Tl}_2\text{O}_3 = \text{Tl}_2\text{O} + \text{O}_2(\text{g})$	1118.11	424.22	193.76
	$2\text{TeO}_2 = 2\text{TeO} + \text{O}_2(\text{g})$	1044.87	520.91	83.14
	$\text{SeO}_2 = \text{Se} + \text{O}_2(\text{g})$	1401.06	1657.48	183.91
Carbonates Hydroxides	$\text{CaCO}_3 = \text{CaO} + \text{CO}_2(\text{g})$	1159.25	1655.75	165.72
	$\text{SrCO}_3 = \text{SrO} + \text{CO}_2(\text{g})$	1423.15	1366.22	201.69
	$\text{MgCO}_3 = \text{MgO} + \text{CO}_2(\text{g})$	577.34	1173.99	98.98
	$\text{BaCO}_3 = \text{BaO} + \text{CO}_2(\text{g})$	1830.52	835.76	164.93
	$\text{PbCO}_3 = \text{PbO} + \text{CO}_2(\text{g})$	584.25	314.01	83.91
	$\text{CdCO}_3 = \text{CdO} + \text{CO}_2(\text{g})$	567.43	560.01	96.56
	$\text{ZnCO}_3 = \text{ZnO} + \text{CO}_2(\text{g})$	394.36	544.91	68.33
	$\text{Li}_2\text{CO}_3 = \text{Li}_2\text{O} + \text{CO}_2(\text{g})$	1879.10	2423.38	179.07
	$\text{Fr}_2\text{CO}_3 = \text{Fr}_2\text{O} + \text{CO}_2(\text{g})$	2033.46	986.35	499.10
	$\text{RaCO}_3 = \text{RaO} + \text{CO}_2(\text{g})$	1772.30	1171.97	335.22
	$\text{Tl}_2\text{CO}_3 = \text{Tl}_2\text{O} + \text{CO}_2(\text{g})$	698.33	258.33	121.09
	$\text{Ca}(\text{OH})_2 = \text{CaO} + \text{H}_2\text{O}(\text{g})$	790.67	1353.66	100.30
	$\text{Mg}(\text{OH})_2 = \text{MgO} + \text{H}_2\text{O}(\text{g})$	538.36	1334.73	77.84
	$\text{Be}(\text{OH})_2 = \text{BeO} + \text{H}_2\text{O}(\text{g})$	346.96	1191.71	51.28
	$\text{Mn}(\text{OH})_2 = \text{MnO} + \text{H}_2\text{O}(\text{g})$	464.18	754.02	67.07
	$\text{Sr}(\text{OH})_2 = \text{SrO} + \text{H}_2\text{O}(\text{g})$	1019.54	727.87	88.53
	$\text{Ba}(\text{OH})_2 = \text{BaO} + \text{H}_2\text{O}(\text{g})$	1282.82	546.63	93.66
	$\text{Ni}(\text{OH})_2 = \text{NiO} + \text{H}_2\text{O}(\text{g})$	347.01	516.06	47.85
	$\text{Zn}(\text{OH})_2 = \text{ZnO} + \text{H}_2\text{O}(\text{g})$	328.82	499.03	49.60
	$\text{Cd}(\text{OH})_2 = \text{CdO} + \text{H}_2\text{O}(\text{g})$	400.74	409.54	59.97

Group reaction	Reaction	Turning Temperature [T*, K]	Gravimetric energy storage density [kJ/kg]	Reaction Enthalpy [kJ/mol]
Hydroxides	$2\text{LiOH} = \text{Li}_2\text{O} + \text{H}_2\text{O}(\text{g})$	1337.07	1117.24	26.76
Hydrates	$\text{MgH}_2 = \text{Mg} + \text{H}_2(\text{g})$	561.65	3030.93	79.78
	$\text{CaH}_2 = \text{Ca} + \text{H}_2(\text{g})$	1291.52	3857.09	162.37
	$\text{TiH}_{1.72} = \text{Ti} + 1.72/2\text{H}_2(\text{g})$	952.56	2666.94	132.37
	$2\text{NaH} = 2\text{Na} + \text{H}_2(\text{g})$	699.59	2426.29	58.23
	$\text{BaH}_2 = \text{Ba} + \text{H}_2(\text{g})$	1402.06	1406.97	196.06
	$\text{Mg}_2\text{FeH}_6 = 2\text{Mg} + \text{Fe} + 3\text{H}_2$	673.15	2160.00	77.40
	$\text{MgNiH}_4 = \text{Mg}_2\text{Ni} + 2\text{H}_2$	723.15	1159.70	64.60
	$\text{NaMgH}_3 = \text{NaH} + \text{Mg} + \text{H}_2(\text{g})$	798.15	1721.00	86.60
	$\text{NaMgH}_2\text{F} = \text{NaF} + \text{Mg} + \text{H}_2(\text{g})$	828.15	1416.00	96.80
	$\text{CaH}_2 + 2\text{Al} = \text{CaAl}_2 + \text{H}_2$	873.15	865.00	83.10
	$\text{SrH}_2 = \text{Sr} + \text{H}_2(\text{g})$	1296.21	2042.00	183.04
	$\text{CeH}_2 = \text{Ce} + \text{H}_2(\text{g})$	1246.79	1508.07	214.35
	$2\text{KH} = 2\text{K} + \text{H}_2(\text{g})$	690.38	1473.14	59.08
	$2\text{LiH} = 2\text{Li} + \text{H}_2(\text{g})$	1211.06	8386.13	66.66
Sulfates	$2\text{MgSO}_4 = 2\text{MgO} + 2\text{SO}_2(\text{g}) + \text{O}_2(\text{g})$	1312.51	2816.69	339.02
	$2\text{MnSO}_4 = 2\text{MnO} + 2\text{SO}_2(\text{g}) + \text{O}_2(\text{g})$	1339.99	2368.58	357.65
	$2\text{FeSO}_4 = 2\text{FeO} + 2\text{SO}_2(\text{g}) + \text{O}_2(\text{g})$	1306.92	2279.84	346.32
	$2\text{CoSO}_4 = 2\text{CoO} + 2\text{SO}_2(\text{g}) + \text{O}_2(\text{g})$	1279.08	2125.38	329.41
	$2\text{CuSO}_4 = 2\text{CuO} + 2\text{SO}_2(\text{g}) + \text{O}_2(\text{g})$	1156.23	1888.37	301.39
	$2\text{ZnSO}_4 = 2\text{ZnO} + 2\text{SO}_2(\text{g}) + \text{O}_2(\text{g})$	1259.58	1787.23	288.53
	$2\text{CdSO}_4 = 2\text{CdO} + 2\text{SO}_2(\text{g}) + \text{O}_2(\text{g})$	1366.28	1703.81	355.19
	$2\text{NiSO}_4 = 2\text{NiO} + 2\text{SO}_2(\text{g}) + \text{O}_2(\text{g})$	1194.92	2076.60	321.37
	$\text{MgSO}_4 = \text{MgO} + \text{SO}_3(\text{g})$	1458.42	1870.19	225.10
	$\text{MnSO}_4 = \text{MnO} + \text{SO}_3(\text{g})$	1490.55	1701.22	256.88
	$\text{FeSO}_4 = \text{FeO} + \text{SO}_3(\text{g})$	1441.25	1629.99	247.60
	$\text{CoSO}_4 = \text{CoO} + \text{SO}_3(\text{g})$	1404.19	1485.10	230.18

Group reaction	Reaction	Turning Temperature [T*, K]	Gravimetric energy storage density [kJ/kg]	Reaction Enthalpy [kJ/mol]
Sulfates	$\text{CuSO}_4 = \text{CuO} + \text{SO}_3(\text{g})$	1212.00	1276.48	203.73
	$\text{ZnSO}_4 = \text{ZnO} + \text{SO}_3(\text{g})$	1397.33	1180.62	190.60
	$\text{CdSO}_4 = \text{CdO} + \text{SO}_3(\text{g})$	1538.45	1201.86	250.55
	$\text{NiSO}_4 = \text{NiO} + \text{SO}_3(\text{g})$	1268.29	1440.26	222.89

From the list of materials in Table 6, the storage density was plotted as a function of the turning temperature in three large blocks (Fig. 6). The blocks show the application spectrum according to the solar technology they can operate. This is a non-limiting proposal and allows a quick selection of the appropriate material for each solar technology depending on the operating temperature. For example, lithium hydride has a very high storage density with an inversion temperature of 1211 K, making it suitable for central tower solar systems. The challenge of this material is to cope with the phase change that occurs at a temperature of 965 K, with a phase change enthalpy of 43.6 kJ/mol.

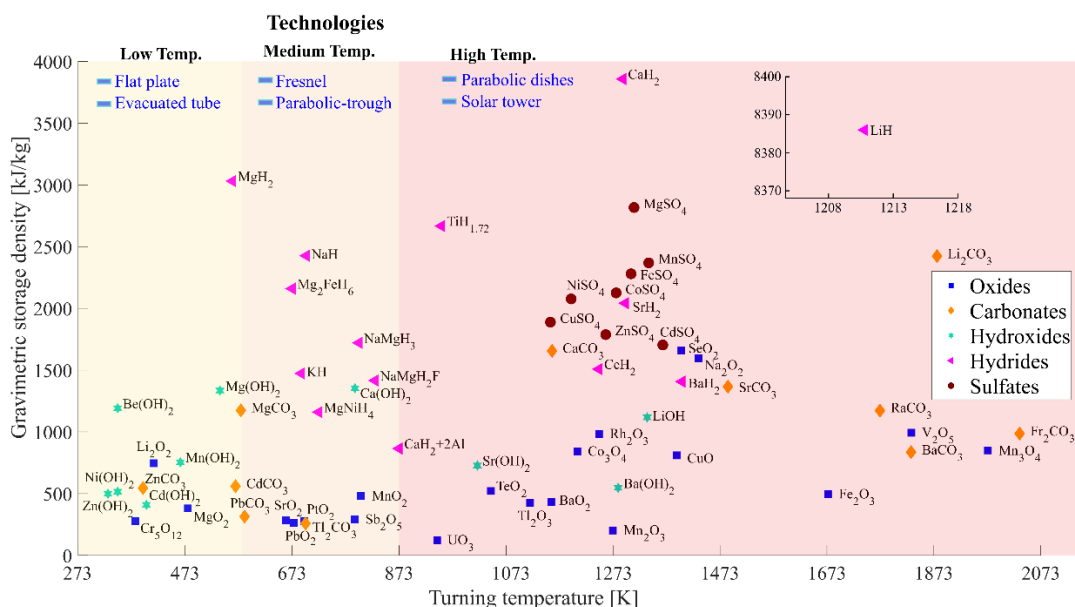


Fig. 6. The gravimetric thermal storage density of selected salts and oxides at the turning temperature. From the [8].

It is evident from Fig. 6 that hydroxides are a promising option for temperatures ranging from 250 to 1250 K. Magnesium and calcium hydroxides exhibit optimal characteristics for temperatures below 700 K, while strontium and barium hydroxides show promise for higher temperatures, albeit with slightly lower thermal storage capacity. Among carbonates, calcium, strontium, and barium demonstrate the best attributes for high temperatures; Magnesium and zinc exhibit similar characteristics to hydroxides at moderate temperatures. The selected sulfates exhibit superior characteristics to hydroxides and carbonate at high temperatures. However, it is essential to conduct a detailed evaluation due to the production of sulfur dioxide and sulfur trioxide and the cost of materials used in the processes.

A thorough analysis of carbonates and lithium hydroxides with high storage capacity at high temperatures is necessary. Additionally, ammonium salts exhibit sufficiently interesting characteristics at intermediate temperatures (between 500 K and 700 K) to warrant separate research.

Thermochemical research at LTQSUAM

The development of thermochemical storage systems follows a precise route to a model of thermal storage integrated into a commercial CSP plant. Fig. 7 describes the objectives and methods for developing thermochemical energy storage technology integrated into a commercial CSP plant.

Our research group is currently working on the first two stages and moving on to the third stage on a pilot scale. We are collaborating with the Concentration and Solar Chemistry National Laboratory of the Renewable Energy Institute (IER-UNAM) research group to develop thermochemical experiments on a larger scale using the laboratory's solar furnace (HoSIER). Also, with the Materials Research Institute (IIM-UNAM) in developing new materials based on perovskite-type oxides. The following sections describe the research carried out in terms of materials to store thermal energy and to generate hydrogen.

More than 100 mixtures [61,65,66] have been proposed for both thermochemical storage and the production of hydrogen and other green fuels. However, not all of them meet the expectations for their use or the basic criteria for their selection [67]. Thermochemical energy storage offers several key advantages [68,69]:

1. High energy storage density: The theoretical capacity of storage is high due to the high enthalpies of reactions by mass or volume. This is important for space within facilities and for transporting energy from distant thermal sources.

2. Storage at room temperature: The products can be cooled and stored at room temperature, simplifying storage of large amounts of materials without needing high-temperature storage. Careful design of reactors and heat exchangers is required to maintain system efficiency.

3. Long-term storage: Thermochemical systems can store energy for long periods without degradation.

4. Ease of transport: Since the products are at room temperature, reversible reactions can transport thermal energy over great distances.

5. High temperature: Some reactions can be carried out at high temperatures to generate electricity and provide constant power.

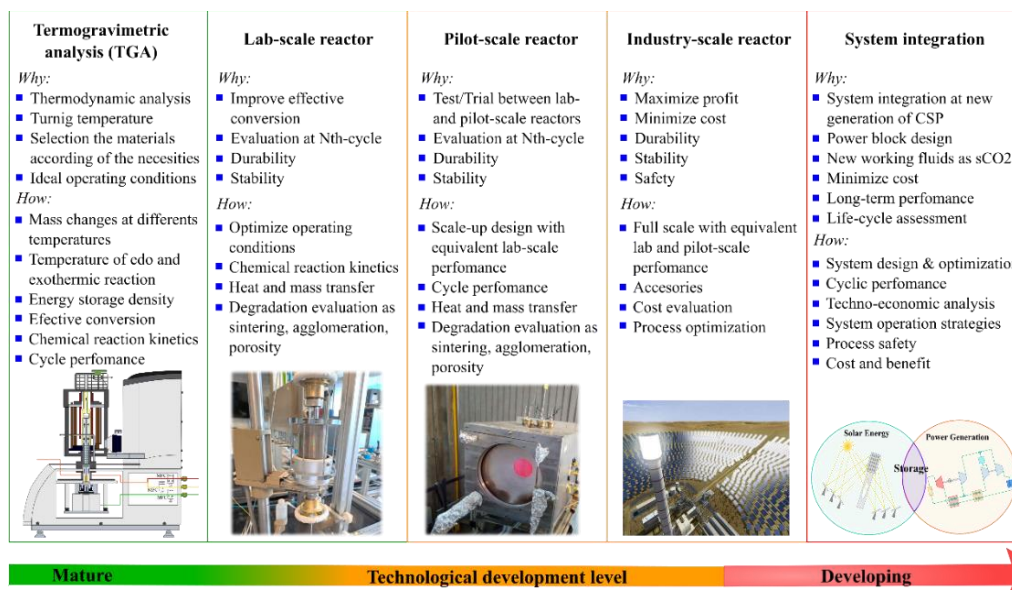


Fig. 7. Objectives and methods aimed at the development of thermochemical energy storage technology integrated into a CSP plant.

The systematization of criteria for the thermochemical energy storage and hydrogen production processes has been proposed by Browns et al. (2002) [70], Abanades (2005) [64], André et al. (2016) [61], and Santamaria (2023) [8]. These criteria can be used to select thermochemical storage systems. The proposed reactions are grouped into hydroxides, carbonates, hydrides, sulfates, pure oxides, mixed oxides, and perovskites. Their evaluation requires thermodynamic analysis before deciding on the best selection. Some of these reactions may be quickly discarded when considering toxicity, environmental security, or economic criteria based on the price of the compounds.

Metal sulfates applied in thermal storage systems

Research at LTQSUAM focused on investigating the potential use of metal sulfates in thermochemical solar heat storage systems. The advantages of various metal sulfates based on Mg, Al, Fe, Co, Ni, Cu and Zn, were analyzed and evaluated according to previous thermodynamic studies [71-73].

The theoretical conditions of decomposition and recombination were studied considering the existence of simultaneous chemical equilibrium states and the possibility of several oxidation states of metals. Simulation tools were used to calculate the minimum value of the Gibbs energy under specific pressure and temperature conditions, and the composition of the equilibrium mixtures was determined [71,74]. The potential of each reaction to store thermal energy was evaluated with theoretical analyses of thermal storage cycles and chemical equilibrium studies. The thermal storage capacity changes depending on the specific reaction, according to the following equilibria:



Table 7 presents the gravimetric storage density for both reactions.

Table 7. The gravimetric storage density (kJ/kg) of some metal sulfates.

System	Mg-O-S	Al-O-S	Fe-O-S	Co-O-S	Ni-O-S	Cu-O-S	Zn-O-S
SO ₂	3240	2550	2290	2500	1800	1940	1860
SO ₃	2420	1820	1540	1860	1730	1550	1740

Perovskites

In addition to the study of pure compounds, some mixtures of compounds and mixed oxides have been studied in the literature, including perovskites, for their advantages of structural stability and their ability to reduce sintering phenomena. Perovskites are single-phase non-stoichiometric compounds with high melting points, high mobility of oxygen ions, and exceptional stability at high temperatures. Perovskite oxides are attractive as redox materials due to their relatively low operating temperature and superior oxygen transport capabilities in the crystalline structure at high temperatures. These materials are known for their unique structure, which allows for easy replacement of cations by similar elements. This tolerance to cationic substitution generally improves their transport properties compared to other families, such as spinels, pyrochlores, or garnets [75,76]. The oxygen vacancies in perovskite structures and their oxygen ion-conducting properties make ABO₃ perovskites ideal for energy storage through O₂ exchange (Eq. 13).



Perovskite oxides have a unique structure known as ABO_3 , with cation A being alkali, alkaline earth, or lanthanide, and cation B usually being a transition metal. These oxides are promising catalysts for hydrogen production and store thermal energy due to their immunity to structural changes, porosity for oxygen transport, and ease with which they release and occupy sites. Unlike traditional couples in redox cycles, perovskite oxides do not undergo discrete structural phase changes during the redox process, simplifying the reactor where thermochemical reactions occur [77]. Some perovskites offer the interesting ability to store and release oxygen in a continuous way following the variation of temperature. The maximum chemical energy storage was found to be 250 kJ/kg with a reducing condition of 1523 K and $p_{O_2,red} = 10^{-3}$ bar, for the perovskites as $La_{1-x}Sr_xCo_yFe_{1-y}O_{3-\delta}$ and $La_{1-x}Sr_xCo_yMn_{1-y}O_{3-\delta}$ [78].

To develop a perovskite-type oxide for the conversion of solar energy into fuels (H_2 and synthesis gas), two criteria are used: 1) the oxide must present a high release of oxygen at the lowest possible temperature; 2) refers to the thermochemical process favorable for the dissociation of H_2O and CO_2 . In the literature, the catalytic properties of lanthanum-substituted chromites ($LaCrO_3$) have been reported for their application in the direct oxidation of CH_4 in anode materials of solid oxide fuel cells (SOFC) [79]. Understanding the peculiarities of doping effects is essential to finding and describing the possible applications of $LaCrO_3$ oxide compounds. The substitution of alkaline earth metals (Ca, Sr, and Mg) and transition metals (Mn, Fe, Co, and Ni) in the $LaCrO_3$ network gives rise to different catalytic behaviors according to the substitution element. For example, in the substitution of sites A and B, Sfeir et al. (2001) [80] report that Sr and Ni are the most active and suitable substituents for the purpose of $LaCrO_3$ anodes in SOFC.

In our laboratory, we have been working with the following materials: the perovskite oxides $La_{0.7}Sr_{0.3}Mn_{0.9}Cr_{0.1}O_{3-\delta}$, $La_{0.2}Sr_{0.8}Fe_{0.8}Co_{0.1}Cr_{0.1}O_{3-\delta}$, and $La_{0.6}Sr_{0.4}Cr_{0.8}Co_{0.2}O_{3-\delta}$. These oxides have been synthesized and characterized. In the synthesis stage, we used the method proposed by Pechini [81], and we applied x-ray diffraction (XRD) and energy dispersive spectroscopy-scanning electron microscopy techniques (EDS-SEM) for the structural and morphological characterization of the oxides. The results of these studies are not reported in this work, as they are still being characterized and subject to preliminary testing.

Sintering and agglomeration phenomena

One of the problems that arises during thermochemical storage is the inefficiencies in the cyclic process of endothermic and exothermic reactions since sintering and particle agglomeration phenomena occur. In these phenomena, porosity strongly influences the effective conversion performance.

Figure 8 shows the difference between sintering and agglomeration. The latter involves grouping particles by heating at high temperatures, while sintering refers to the particles' porosity and the solid's densification. Both phenomena prevent gases from diffusing from the surface to the bulk of the material and thus decrease the effective conversion. Several techniques, including ceramic supports and chemical spacers, could solve these problems.

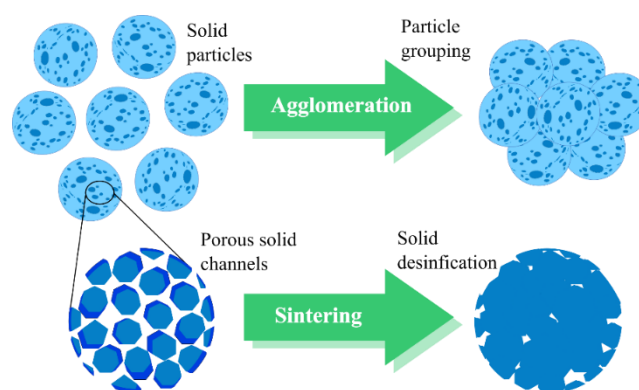
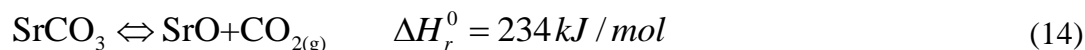


Fig. 8. Agglomeration and sintering phenomenon.

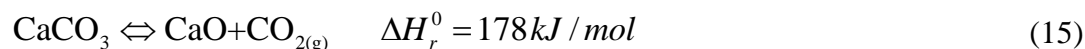
Strontium carbonate improved with different materials

The research group in the LTQSUAM research group joins these efforts to determine the best mixture or composite to achieve high stability and reduce the effects of sintering and agglomeration that occur in cyclic processes of endothermic and exothermic reactions. Below are some of the materials studied by the research group and the most relevant results obtained during the study of these mixtures and composites. Strontium carbonate is gaining relevance because it has a high energy storage density (1366.22 kJ/kg) and very promising conversion rates, but it sinters more easily than other carbonates such as CaCO₃.



Interest in strontium carbonate has grown in the last decade due to substantial progress in its performance with different ceramic additives. Some research to improve the performance of strontium carbonate is reported in the literature; P. Ammendola et al. (2020) [82] proposed the mixture of SrCO₃ with 19 wt% of Al₂O₃, authors performed calcination/carbonation cycles at 1323 K, after evaluated 10 cycles they reported an effective conversion X_{eff,1}=0.43 and X_{eff,10}=0.33. A.P. Vieira et al. (2021) [83] mixed SrCO₃ with 20 wt% of SiO₂, the authors evaluated the sample for 15 cycles at an operating temperature of 973 K, they report having obtained a storage density of 658 kJ/kg. N. Amghar, et. al. (2023) [84] used SrCO₃ with 10 wt% of ZrO₂, they performed calcination/carbonation processes at 1173 K during 10 cycles. Effective conversion reported is X_{eff,1}=0.86 y X_{eff,10}=0.69.

Calcium carbonate is a compound that has been extensively studied in the literature; it has a high storage density (1655.75 kJ/kg), and various mixtures have been proposed to avoid sintering effect and achieves high effective conversion values [85].



For instance, J.M. Valverde et. al. (2012) [86] proposes using a mixture of CaCO₃ with 15 wt% SiO₂, obtaining an operating temperature of 1,123 K, and evaluating it in 100 cycles. They report a storage density of 199 kJ/kg. P.E. Sánchez Jiménez et. al. (2019) [87] propose using a mixture of CaCO₃ with 20 wt% MgO, obtaining an operating temperature of 1123 K, evaluating 30 cycles and reporting a storage density of 927 kJ/kg. K.T. Møller et. al. (2020) [88] propose using a mixture of CaCO₃ with 20 wt% Al₂O₃, Ca₅Al₆O₁₄, obtaining an operating temperature of 1173 K, evaluating 500 cycles and reporting a storage density of 1,060 kJ/kg. R. Anwar et. al. (2023) [89] propose using a mixture of CaCO₃ with 20 wt% ZrO₂, obtaining an operating temperature of 1157 K, evaluating 40 cycles, and reporting a storage density of 696 kJ/kg.

According to the selection criteria outlined by A. Santamaria and H. Romero-Paredes (2023) for thermochemical energy storage materials [8], key considerations include abundance, high storage capacity, affordability, absence of side reactions, and non-toxicity. Based on a comprehensive review of literature focusing on enhancing the performance of strontium carbonate, this study aims to evaluate the compositions listed in Table 8, showing their respective theoretical CO₂ absorption capabilities. These mixtures represent novel materials proposed to improve strontium carbonate's effective conversion in each calcination-carbonation cycle. The proportions specified in Table 8 are based on a mass basis. Table 9 details the purity levels of the materials utilized in these mixtures.

Table 8. Proposed mixtures to improve SrCO₃.

Sample	Composition (wt %)							Theoretical CO ₂ absorption (wt%)
	SrCO ₃	CuO	CaCO ₃	Li ₂ CO ₃	ZnO	CeO ₂	SnO ₂	
SrCO ₃	100	-	-	-	-	-	-	29.80
SrCu5	95	5	-	-	-	-	-	28.31

Sample	Composition (wt %)							Theoretical CO ₂ absorption (wt%)
	SrCO ₃	CuO	CaCO ₃	Li ₂ CO ₃	ZnO	CeO ₂	SnO ₂	
SrCu10	90	10	-	-	-	-	-	26.82
SrCu20	80	20	-	-	-	-	-	23.84
SrCu30	70	30	-	-	-	-	-	20.86
SrCu40	60	40	-	-	-	-	-	17.88
SrCa5	95	-	5	-	-	-	-	30.51
SrCa10	90	-	10	-	-	-	-	31.22
SrCa20	80	-	20	-	-	-	-	32.64
SrLi20	80	-	-	20	-	-	-	35.75
SrZn20	80	-	-	-	20	-	-	23.84
SrCe20	80	-	-	-	-	20	-	23.84
SrSnO20	80	-	-	-	-	-	20	23.84

Table 9. Properties of the materials used.

Compound	SrCO ₃	CuO	CaCO ₃	Li ₂ CO ₃	ZnO	CeO ₂	SnO ₂
Brand	Sigma-Aldrich ≥99.9% trace metals basis	Sigma-Aldrich ≥99.9% trace metals basis	Sigma-Aldrich ≥99.0%	Meyer ≥99.0%	J.T. Baker Analyzed ≥99.0%	Sigma Aldrich 99.9%	Sigma Aldrich 99.9%
CAS	1633-05-2	1317-38-0	471-34-1	554-13-2	1314-13-2	1306-38-3	18282-10-5

Methodology

The experiments were carried out using a combined thermogravimetric analyzer (TGA) and differential scanning calorimetry (DSC) STA 449 F3 Jupiter from NETZSCH. This analyzer has a highly sensitive balance (<0.1 μg) and a silicon carbide furnace that allows working at temperatures up to 1773 K. The sample mass used in each experiment was 25.5 ± 5 mg. For the calcination experiments, a controlled argon-inert atmosphere with a 40 ml/min flow rate was maintained. Carbonation procedures were carried out under a CO₂/Ar atmosphere with a 30/10 ml/min flow rate. This work proposes the next experimental protocol: first, the calcination stage, wherein the sample is heated at a rate of 30 K/min until reaching 1473 K to ensure complete calcination. Next, carbonation was carried out at different temperatures in each experiment: 1173, 1223, 1273, and 1323 K, and they were maintained for 5 minutes with the gas flow described previously. These stages were iterated twice to observe the multicycle conversion behavior of the sample and determine the optimal carbonation temperature. Once the ideal T_{carb} is determined for the pure compound, it will be the same

for all mixtures. Finally, a comparative analysis of the results obtained with the pure compound (SrCO_3) and all mixes proposed are carried out to see if improving the conversion rate when passing through the calcination-carbonation cycles is possible. In this case, its performance will be evaluated in 4 cycles.

The microstructure of the samples at different stages was investigated using scanning electron microscopy (SEM) using a JEOL JSM 7600F microscope.

X-ray diffractograms of the samples were acquired before and after the multicycle test using a Bruker D8 Advance diffractometer with Cu $K\alpha$ radiation. The data were measured in the range from 15° to 80° in 2θ with a step size of 0.2, for 38.4 s per point.

Preparation of SrCO_3 based mixes

The mixtures were made as described in Fig. 9. They are prepared so that a composite is not formed, for each addition is expected to stabilize the effective conversion in each cycle and delay the sintering of SrCO_3 .



Fig. 9. Preparation of mixtures of SrCO_3 .

Effective conversion and energy density

The results obtained at each mix will be compared to determine the operating conditions where a higher conversion rate is obtained. The effective conversion (X_{eff}) is defined as follows [90]:

$$X_{eff} = \left(\frac{m_{\text{Carb},i} - m_i}{m_i} \right)_N \left(\frac{MM_{\text{SrO}}}{MM_{\text{CO}_2}} \right) \quad (16)$$

where m_i and $m_{\text{carb},i}$ are the mass of the sample before and after the storage and release steps in the N cycle, and MM_{SrO} and MM_{CO_2} are the molar masses of SrO and CO_2 , respectively.

The calculation of energy density is determined with the following equation:

$$D_m = \left(\frac{m_{\text{CO}_2}}{m_i} \right)_N \Delta H_R \quad (17)$$

where ΔH_R is 5318.18 kJ/kg CO_2 and m_{CO_2} is $m_{\text{carb},i} - m_i$.

To calculate the volumetric energy density, GJ/m^3 , Eq. (17) is multiplied by the density of the oxide being carbonated, in this case strontium oxide:

$$D_v = D_m \times \rho \quad (18)$$

Results

Firstly, the operating parameters of pure strontium carbonate were determined with the help of TG analysis. The calcination temperature (T_{cal}) was established at 1473 K, slightly higher than T^* (1423.15 K), so that dissociation is promoted. The carbonation temperature (T_{carb}) is in the range of 1173 K to 1373 K, below T^* to promote recombination. However, the experiments showed that the best carbonation behavior is obtained at $T_{carb} = 1173$ K.

With these parameters pure strontium carbonate was evaluated during nine calcination/carbonation cycles. Fig. 10 shows the results of effective conversion, volumetric energy density obtained and XRD patterns.

Fig. 10(A) shows the results as a function of the effective conversion and the energy density storage, it is observed that in the first cycle, 99.76 % effective conversion is achieved. As the cycles pass, the conversion decreases, having in the last cycle an effective conversion of 2.33 %, which coincides with the behavior reported by S. Zare Ghorbaei and H. Ale Ebrahim, who evaluated 20 cycles; In the last cycle, they reported a conversion yield of approximately 1% [91]. The theoretical volumetric energy density (Dv) of SrCO_3 is 10.61 GJ/m^3 [92]. It is observed that in the first cycle, it is very close to this, but then it decreases similarly to the effective conversion, reaching 1.24 GJ/m^3 in the 9th cycle. Fig. 10(B) shows the XRD patterns of unprocessed SrCO_3 in the TGA, and after 9 cycles of calcination-carbonation, ending in carbonation. It is observed that it coincides with ICDD-PDF 00-005-0418 of SrCO_3 , and as the cycles pass, it also coincides with ICDD-PDF 00-027-1438 of $\text{Sr}(\text{OH})_2 \cdot 8\text{H}_2\text{O}$ and with ICDD-PDF 00-019-1276 of $\text{Sr}(\text{OH})_2$. The growth of characteristic peaks indicates that the material is agglomerating. Fig. 11 shows the scanning electron microscopy (SEM). Fig. 11(A) shows the sample white of SrCO_3 has a cylindrical shape, and in Fig. 11(B), the sample after 4 cycles, and it is clearly seen as the particles are agglomerating and most likely also sintering, which is why the effective conversion is rapidly reducing.

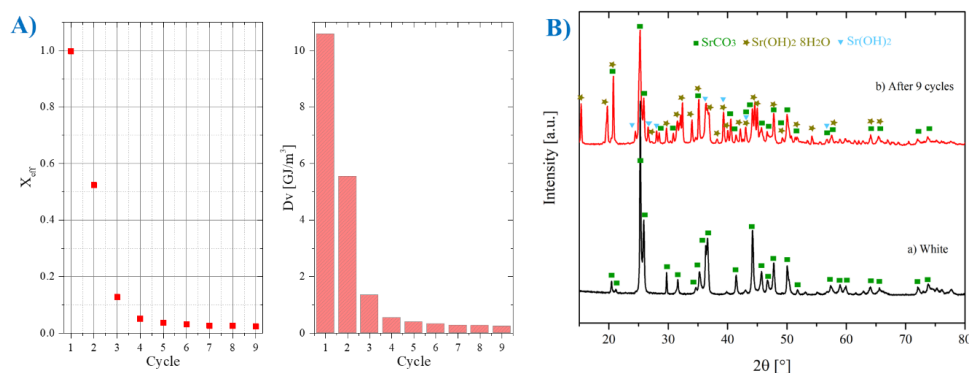


Fig. 10. SrCO_3 analysis results (A) effective conversion and volumetric energy density results, (B) XRD for SrCO_3 before and after being subjected to nine calcination/carbonation cycles ending in carbonation.

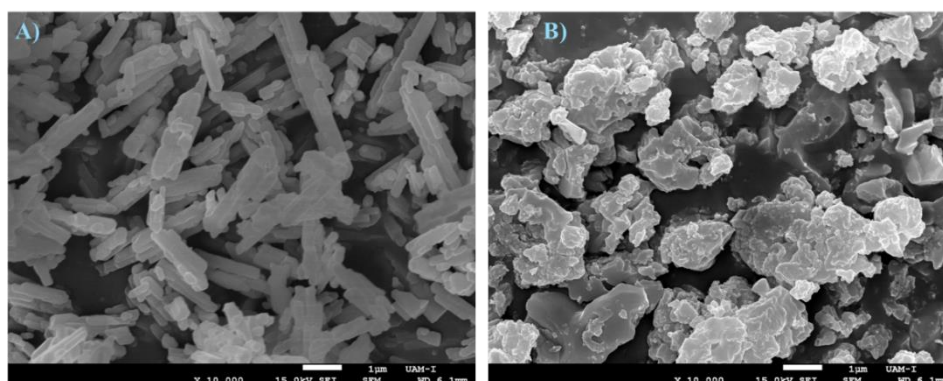


Fig. 11. SEM micrographs of SrCO_3 , (A) without process and (B) of the samples subjected to 4 calcination/carbonation cycles, ending in carbonation.

The proposed mixtures were evaluated with the same operating temperatures ($T_{cat}=1473$ K and $T_{carb}=1173$ K) defined for strontium carbonate. Fig. 12 shows the results obtained where the following observations stand out:

a) The mixture SrLi2O (80 % SrCO₃+ 20 % Li₂CO₃) shows the best behavior with the passage of cycles, however, it generates inconveniences in the handling of this compound since a solid-liquid phase change is observed. Therefore, it is advisable to study the mechanisms of use of this compound.

b) The mixture SrCa2O (80 % SrCO₃+ 20 % CaCO₃) also shows acceptable behavior during each cycle, since a high conversion rate is maintained during each cycle. Fig. 13(A) shows that after four cycles, it has $X_{eff,4}=0.62$, which is compared to SrCO₃ $X_{eff,4}=0.05$; This represents 12 times better with the proposed mixture.

c) Another interesting mixture is SrSnO2O (80 % SrCO₃+20 % SnO₂), this has a lower effective conversion rate but is more stable; For the first cycle we have $X_{eff,1}=0.43$, and for the fourth cycle, $X_{eff,4}=0.42$, which compared to the pure compound still has an 8 times better improvement with the proposed mixture.

Although it does not have a very high effective conversion like the SrCa2O mixture, it is more stable, and a more in-depth study can be carried out to evaluate the feasibility of using this compound as an energy storage medium.

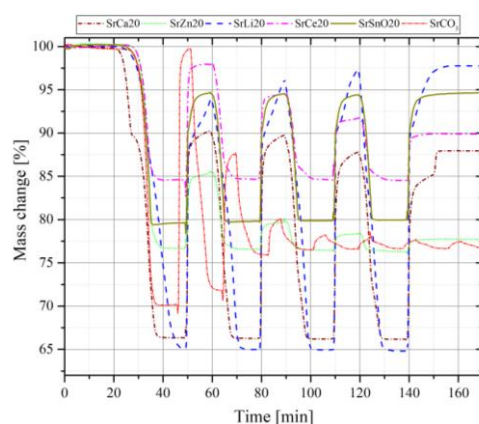


Fig. 12. Analysis of the different mixtures with 20% additive with respect to the pure SrCO₃ compound. Sample nomenclature: SrCa2O (80 % SrCO₃+ 20 % CaCO₃), SrLi2O (80 % SrCO₃+ 20 % Li₂CO₃), SrZn2O (80 % SrCO₃+ 20 % ZnO), SrCe2O (80 % SrCO₃+ 20 % CeO₂) and SrSnO2O (80 % SrCO₃+20 % SnO₂).

Furthermore, the volumetric energy density (Dv) of each of these mixtures was calculated and compared with the Dv value of SrCO₃.

Fig. 13(B) shows that the mixture with the best performance during the four cycles is that of SrLi2O with an average of $Dv = 9.7$ GJ/m³, followed by SrCa2O with an average of $Dv = 6.46$ GJ/m³, and in third place, SrSnO2O. mixture with an average of $Dv = 3.65$ GJ/m³.

All values Dv are higher than that of pure strontium carbonate, which has an initial average of $Dv = 4.51$ GJ/m³ but it decreases quickly.

For all the above, the properties observed in the mixtures of SrCa2O and SrSnO2O make them feasible to implement in a thermochemical energy storage system that operates under central tower plant conditions. These proposals seek to increase the capacity factor of a central solar tower power plant to contribute to mitigating climate change with new forms of energy generation from concentrated solar energy.

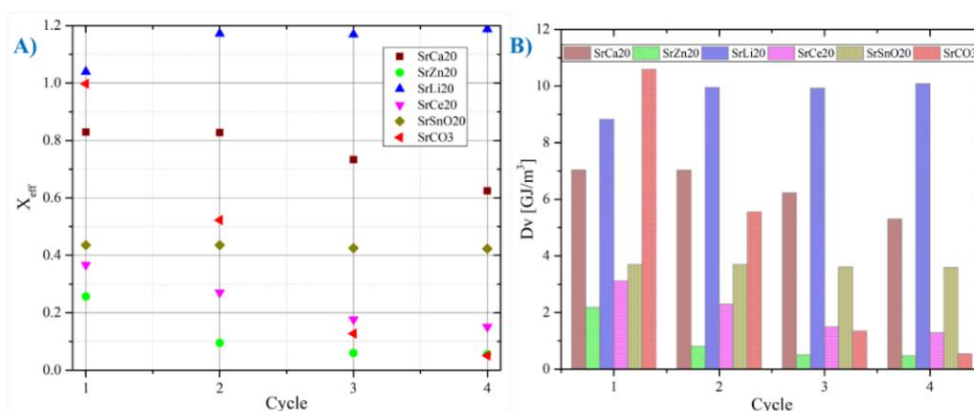


Fig. 13. Comparison of the proposed mixtures with the pure compound; A) effective conversion and B) volumetric energy density.

Conclusions

The development of thermal energy storage systems covers a broad spectrum. Sensible heat systems are currently the most used in solar power plants, so they have experienced considerable technological advances. Thermochemical systems have a high application potential. Research shows they have gained increasing relevance and interest within the global scientific and technological community in recent years.

Research at the Solar Thermochemistry Laboratory at UAM has significantly advanced systems based on reversible reactions. Initial attention was focused on sulfates because they have a high gravimetric heat storage density. However, there are substantial drawbacks during sulfate dissociation.

In recent years, research has been oriented toward studying other less complex compounds for their integration into solar-thermal energy storage systems. For this purpose, strontium carbonate was selected. The research has focused mainly on turning temperature, storage capacity, and effective conversion.

In this sense, chemical dopants and physical spacers have been proposed to address these issues. This approach has shown promising results, leading to an increased conversion rate and improved performance during long cyclic processes.

The findings indicate a substantial improvement in the effective conversion of the strontium-calcium carbonates and strontium-tin oxide mixtures with 12 and 8 times than the pure compound, respectively.

Furthermore, this study found that the mixture of strontium and lithium carbonates can work adequately but melts at 973 K, which is lower than the carbonation temperature. This phenomenon limits its development and causes more sintering as the cycles progress.

On the other hand, the mixture of strontium carbonate with tin oxide is the most stable, even though the calcination doesn't completely occur. However, this mixture is also a promising option for thermochemical storage systems.

We have been working on preparing compounds that guarantee excellent stability and durability properties. By synthesizing strontium-based cermet, we aim to achieve greater stability and reduce particle agglomeration caused by fluctuating polarizations due to temperature changes and secondary chemical reactions that occur during reversible reactions.

Additionally, the research focuses on synthesizing, characterizing, and applying perovskites for energy storage through RedOx reactions and hydrogen production through these compounds' reduction-hydrolysis. This research will help us achieve our goal of improving solar energy use and reducing the impact of source intermittency.

Acknowledgements

The authors acknowledge the financial support received through CONAHCYT as part of the Call for Basic and Frontier Science 2023-2024 within Strategic Project No. CBF2023-2024-3410, entitled "Development of Advanced Methods and New Materials for Solar Thermal Energy Storage Using Reversible Solid-Gas Reaction Cycles to Enhance the Use of Solar Technology," which enabled the development of research and support of human resource training at the graduate level.

A.S.P, J.M.B.S and A.K.E.G. acknowledge the financial support received through the support scholarship by CONAHCYT with number 814358, 1266217 and 1255582. J.D.M. acknowledge CONAHCYT for the scholarship awarded through the program "Postdoctoral Stays in Mexico 2022".

Also, the authors appreciate the scientific support of Heidi Villafan Vidales and Armando Reyes Montero, as well as the use of the facilities of the IER-UNAM and IIM-UNAM.

References

1. Zhao, J.; Liu, H.; Sun, W. *Sustain.* **2020**, *12*. DOI: <https://doi.org/10.3390/su12030763>.
2. J. C. MacKay, D. *Sustainable Energy without the Hot Air.* **2008**.
3. Meier, A.; Bonaldi, E.; Cella, G. M.; Lipinski, W.; Wuillemmin, D.; Palumbo, R. *Energy.* **2004**, *29* (5–6), 811–821. DOI: [https://doi.org/10.1016/S0360-5442\(03\)00187-7](https://doi.org/10.1016/S0360-5442(03)00187-7).
4. Chuayboon, S.; Abanades, S. *J. Clean. Prod.* **2019**, *232*, 784–795. DOI: <https://doi.org/10.1016/j.jclepro.2019.05.371>.
5. Zoller, S.; Koepf, E.; Nizamian, D.; Stephan, M.; Patané, A.; Haueter, P.; Romero, M.; González-Aguilar, J.; Lieftink, D.; de Wit, E.; Brendelberger, S.; Sizmann, A.; Steinfeld, A. *Joule* **2022**, *6*, 1606–1616. DOI: <https://doi.org/10.1016/j.joule.2022.06.012>.
6. Steinmann, W.-D.; Prieto, C. Thermal Storage for Concentrating Solar Power Plants. in: *Advances in Thermal Energy Storage Systems*; LTD, **2021**, 673–697. DOI: <https://doi.org/10.1016/b978-0-12-819885-8.00024-3>.
7. Zhang, H. L.; Baeyens, J.; Degréve, J.; Cacères, G. *Renew. Sustain. Energy Rev.* **2013**, *22*, 466–481. DOI: <https://doi.org/10.1016/j.rser.2013.01.032>.
8. Santamaría Padilla, A.; Romero-Paredes Rubio, H. *J. Energy Storage* **2023**, *73*, 108906. DOI: <https://doi.org/10.1016/j.est.2023.108906>.
9. IRENA. Concentrating Solar Power. **2012**, *1*.
10. Romero, M.; Steinfeld, *Energy Environ. Sci.* **2012**, *5*, 9234–9245. DOI: <https://doi.org/10.1039/c2ee21275g>.
11. Frazzica, A.; Cabeza Editors, L. F. *Green Energy and Technology Recent Advancements in Materials and Systems for Thermal Energy Storage*; **2019**.
12. Palacios, A.; Barreneche, C.; Navarro, M. E.; Ding, Y. *Renew. Energy* **2020**, *156*, 1244–1265. DOI: <https://doi.org/10.1016/j.renene.2019.10.127>.
13. Li, X.; Jin, J.; Yang, D.; Xu, N.; Wang, Y.; Mi, X. *AIP Conf. Proc.* **2019**, *2126*. DOI: <https://doi.org/10.1063/1.5117545>.
14. Kang, Q.; Dewil, R.; Degréve, J.; Baeyens, J.; Zhang, H. *Energy Convers. Manag.* **2018**, *163*, 292–303. DOI: <https://doi.org/10.1016/j.enconman.2018.02.067>.
15. IRENA. *Renewable Power Generation Costs in 2020*; **2020**.
16. Kasaeian, A.; Bellos, E.; Shamaeizadeh, A.; Tzivanidis, C. *Appl. Energy* **2020**, *264*, 114764. DOI: <https://doi.org/10.1016/j.apenergy.2020.114764>.
17. Silvi, C. *30th ISES Bienn. Sol. World Congr. 2011, SWC 2011* **2011**, *2*, 952–962. DOI: <https://doi.org/10.18086/swc.2011.06.12>.
18. Consejería de Economía y Hacienda, organización Dirección General de Industria, E. y M. F. de la E. de la C. de M. *Guía Técnica de La Energía Solar Termoeléctrica*; 2012.

19. US Department of Energy. *Solar Research Spotlight: Concentrating Solar- Thermal Power*; 2018. <https://www.energy.gov/sites/prod/files/2018/09/f55/Concentrating-Solar-Thermal-Power-FactSheet.pdf>.
20. Kildahl, H.; Jiang, Z.; Palacios, A.; Song, C.; Zhang, X.; Zheng, H.; Cao, H.; He, Z.; Liu, X.; Wang, L.; Tong, L.; Li, Y.; Xuan, Y.; Ding, Y. T. *ACS Symp. Ser.* **2020**, *1364*, 257–301. DOI: <https://doi.org/10.1021/bk-2020-1364.ch010>.
21. Boretti, A.; Castelletto, S. *J. Energy Storage* **2021**, *42*, 103143. DOI: <https://doi.org/10.1016/j.est.2021.103143>.
22. Ghalambaz, M.; Sheremet, M.; Fauzi, M. A.; Fteiti, M.; Younis, O. *J. Energy Storage* **2023**, *66*. DOI: <https://doi.org/10.1016/j.est.2023.107266>.
23. Yan, Y.; Wang, K.; Clough, P. T.; Anthony, E. J. *Fuel Process. Technol.* **2020**, *199* (June 2019), 106280. DOI: <https://doi.org/10.1016/j.fuproc.2019.106280>.
24. Kato, Y.; Nomura, T. *Issues Environ. Sci. Technol.* **2019**, *2019*, 210–227. DOI: <https://doi.org/10.1039/9781788015530-00210>.
25. Khamlich, I.; Zeng, K.; Flamant, G.; Baeyens, J.; Zou, C.; Li, J.; Yang, X.; He, X.; Liu, Q.; Yang, H.; Yang, Q.; Chen, H. *Renew. Sustain. Energy Rev.* **2021**, *139*, 110583. DOI: <https://doi.org/10.1016/j.rser.2020.110583>.
26. Zhang, H.; Baeyens, J.; Cáceres, G.; Degève, J.; Lv, Y. *Energy Combust. Sci.* **2016**, *53*, 1–40. DOI: <https://doi.org/10.1016/j.peccs.2015.10.003>.
27. Fernandes, D.; Pitié, F.; Cáceres, G.; Baeyens, J. *Energy* **2012**, *39*, 246–257. DOI: <https://doi.org/10.1016/j.energy.2012.01.024>.
28. Zhang, H.; Kong, W.; Tan, T.; Baeyens, J. *Energy* **2017**, *139*, 52–64. DOI: <https://doi.org/10.1016/j.energy.2017.07.129>.
29. Ding, W.; Bauer, T. *Engineering* **2021**, *7*, 334–347. DOI: <https://doi.org/10.1016/j.eng.2020.06.027>.
30. Chen, R.; Romero, M.; González-Aguilar, J.; Rovense, F.; Rao, Z.; Liao, S. *Energy Convers. Manag.* **2021**, *232*. DOI: <https://doi.org/10.1016/j.enconman.2021.113870>.
31. Sun, E.; Xu, J.; Li, M.; Li, H.; Liu, C.; Xie, J. *Energy Convers. Manag. X* **2020**, *7*, 100042. DOI: <https://doi.org/10.1016/j.ecmx.2020.100042>.
32. Linares, J. I.; Montes, M. J.; Cantizano, A.; Sánchez, C. *Appl. Energy* **2020**, *263*, 114644. DOI: <https://doi.org/10.1016/j.apenergy.2020.114644>.
33. Crespi, F.; Sánchez, D.; Rodríguez, J. M.; Gavagnin, G. *Renew. Energy* **2020**, *147*, 2905–2912. DOI: <https://doi.org/10.1016/j.renene.2018.08.023>.
34. Pitz-Paal, R. *Concentrating Solar Power*; Elsevier Ltd, 2020. DOI: <https://doi.org/10.1016/b978-0-08-102886-5.00019-0>.
35. Solar PayBack. Calor solar para la industria México. **2018**.
36. Instituto Mexicano del Petróleo. Energía Termosolar 2018. *Sener* **2018**, *1*, 83.
37. Wu, S.; Zhou, C.; Doroodchi, E.; Nellore, R.; Moghtaderi, B. *Energy Convers. Manag.* **2018**, *168* (April), 421–453. DOI: <https://doi.org/10.1016/j.enconman.2018.05.017>.
38. Sadeghi, G. *Energy Storage Mater.* **2022**, *46*, 192–222. DOI: <https://doi.org/10.1016/j.ensm.2022.01.017>.
39. Pielichowska, K.; Pielichowski, K. *Prog. Mater. Sci.* **2014**, *65*, 67–123. DOI: <https://doi.org/10.1016/j.pmatsci.2014.03.005>.
40. González-Roubaud, E.; Pérez-Osorio, D.; Prieto, C. *Renew. Sustain. Energy Rev.* **2017**, *80*, 133–148. DOI: <https://doi.org/10.1016/j.rser.2017.05.084>.
41. Fereres, S. *Solar Thermal Energy Systems*, **2018**. DOI: <https://doi.org/10.2174/97816810871911180300003>.
42. Moens, L.; Blake, D. M. *J. Sol. Energy Eng. Trans. ASME* **2010**, *132*, 0310061–0310065. DOI: <https://doi.org/10.1115/1.4001402>.
43. Harald Mehling, L. F. C. *PCM*, **2008**, *3*.

44. Barrasso, M.; Langella, G.; Amoresano, A.; Iodice, P. *Processes*. **2023**, *11*. DOI: <https://doi.org/10.3390/pr11061832>.
45. Alva, G.; Lin, Y.; Fang, G. *Energy* **2018**, *144*, 341–378. DOI: <https://doi.org/10.1016/j.energy.2017.12.037>.
46. Farid, M. M.; Khudhair, A. M.; Razack, S. A. K.; Al-Hallaj, S. *Energy Convers. Manag.* **2004**, *45*, 1597–1615. DOI: <https://doi.org/10.1016/j.enconman.2003.09.015>.
47. Raud, R.; Jacob, R.; Bruno, F.; Will, G.; Steinberg, T. A. *Renew. Sustain. Energy Rev.* **2017**, *70*, 936–944. DOI: <https://doi.org/10.1016/j.rser.2016.11.274>.
48. Koochi-Fayegh, S.; Rosen, M. A. *J. Energy Storage* **2020**, *27*, 101047. DOI: <https://doi.org/10.1016/j.est.2019.101047>.
49. Tareen, W. U. K.; Dilbar, M. T.; Farhan, M.; Nawaz, M. A.; Durrani, A. W.; Memon, K. A.; Mekhilef, S.; Seyedmahmoudian, M.; Horan, B.; Amir, M.; Aamir, M. *Sustain.* **2020**, *12*. DOI: <https://doi.org/10.3390/su12010249>.
50. Samylingam, I.; Kadirgama, K.; Asfattahi, N.; Samylingam, L.; Ramasamy, D.; Harun, W. S. W.; Samykano, M.; Saidur, R. *IOP Conf. Ser. Mater. Sci. Eng.* **2021**, *1078*, 012034. DOI: <https://doi.org/10.1088/1757-899x/1078/1/012034>.
51. Tripathi, B. M.; Shukla, S. K.; Rathore, P. K. S. *J. Energy Storage* **2023**, *72*, 108280. DOI: <https://doi.org/10.1016/j.est.2023.108280>.
52. Sun, M.; Liu, T.; Sha, H.; Li, M.; Liu, T.; Wang, X.; Chen, G.; Wang, J.; Jiang, D. *J. Energy Storage* **2023**, *68*, 107713. DOI: <https://doi.org/10.1016/j.est.2023.107713>.
53. Shanmugavalli, P.; Rajaraman, R. *Materials Today*. **2023**.
54. Khan, M. I.; Asfand, F.; Al-Ghamdi, S. G. *J. Energy Storage* **2022**, *55*, 105860. DOI: <https://doi.org/10.1016/j.est.2022.105860>.
55. Ong, T. C.; Sarvghad, M.; Bell, S.; Will, G.; Steinberg, T. A.; Yin, Y.; Andersson, G.; Lewis, D. *Appl. Therm. Eng.* **2024**, *238*, 122034. DOI: <https://doi.org/10.1016/j.applthermaleng.2023.122034>.
56. Sharshir, S. W.; Joseph, A.; Elsharkawy, M.; Hamada, M. A.; Kandeal, A. W.; Elkadeem, M. R.; Kumar Thakur, A.; Ma, Y.; Eid Moustapha, M.; Rashad, M.; Arıçı, M. *Energy Build.* **2023**, *285*, 112908. DOI: <https://doi.org/10.1016/j.enbuild.2023.112908>.
57. Bayon, A.; Carrillo, A. J.; Mastronardo, E.; Coronado, J. M. in: *Advances in Chemical Engineering*; Academic Press Inc., **2021**, *58*, 247–295. DOI: <https://doi.org/10.1016/bs.ache.2021.10.004>.
58. Alvarez Rivero, M.; Rodrigues, D.; Pinheiro, C. I. C.; Cardoso, J. P.; Mendes, L. F. *Renew. Sustain. Energy Rev.* **2022**, *158*, 112048. DOI: <https://doi.org/10.1016/j.rser.2021.112048>.
59. Pardo, P.; Deydier, A.; Anxionnaz-Minvielle, Z.; Rougé, S.; Cabassud, M.; Cognet, P. *Renew. Sustain. Energy Rev.* **2014**, *32*, 591–610. DOI: <https://doi.org/10.1016/j.rser.2013.12.014>.
60. Carrillo, A. J.; Gonza, J.; Romero, M.; Coronado, J. M. **2018**. DOI: <https://doi.org/10.1021/acs.chemrev.8b00315>.
61. André, L.; Abanades, S.; Flamant, G. *Renew. Sustain. Energy Rev.* **2016**, *64*, 703–715. DOI: <https://doi.org/10.1016/j.rser.2016.06.043>.
62. Zhang, H.; Huys, K.; Baeyens, J.; Degève, J.; Kong, W.; Lv, Y. *Energy Technol.* **2016**, *4*, 341–352. DOI: <https://doi.org/10.1002/ente.201500261>.
63. Rehman, A. U.; Hayat, A.; Munis, A.; Zhao, T.; Israr, M.; Zheng, M. *Proc. Inst. Civ. Eng. Energy* **2020**, *173*, 60–67. DOI: <https://doi.org/10.1680/jener.19.00018>.
64. Abanades, S.; Charvin, P.; Flamant, G.; Neveu, P. *Energy* **2006**, *31*, 2805–2822. DOI: <https://doi.org/10.1016/j.energy.2005.11.002>.
65. Bulfin, B.; Vieten, J.; Agrafiotis, C.; Roeb, M.; Sattler, C. *J. Mater. Chem. A* **2017**, *5*, 18951–18966. DOI: <https://doi.org/10.1039/c7ta05025a>.
66. Bellan, S.; Kodama, T.; Gokon, N.; Matsubara, K. *Wiley Interdiscip. Rev. Energy Environ.* **2022**, *11*, 1–23. <https://doi.org/10.1002/wene.440>.

67. Wang, K.; Zhang, C. M.; Liu, B. C.; Yang, L.; Min, C. H.; Rao, Z. H. *Elsevier B.V.* 2024, 480. DOI: <https://doi.org/10.1016/j.cej.2023.148118>.
68. Guy, E. *J. Solid State Chem.* **1977**, 22, 51–61.
69. Prengle, H. W.; Sun, C. H. *Sol. Energy* **1976**, 18, 561–567. DOI: [https://doi.org/10.1016/0038-092X\(76\)90076-1](https://doi.org/10.1016/0038-092X(76)90076-1).
70. Brown, L. C.; Besenbruch, G. E. G.; Lentsch, R. D. R.; Schultz, K. R. K.; Funk, J. F.; Pickard, P. P. S.; Marshall, A. C. A.; Showalter, S. S. K. *Gen. At.* **2003**, 29–30.
71. Tmar, M.; Bernard, C.; Ducarroir, M. *Sol. Energy* **1981**, 26, 529–536. DOI: [https://doi.org/10.1016/0038-092X\(81\)90165-1](https://doi.org/10.1016/0038-092X(81)90165-1).
72. Ducarroir, M.; Tmar, M.; Bernard, C.; Ducarroir, M.; Tmar, M.; Possibilités, C. B.; De, D. Possibilités de Stockage de l'Énergie Solaire à Partir de Sulfates To Cite This Version : HAL Id : Jpa-00244756. **2008**.
73. Ducarroir, M.; Steinmetzt, D.; Sibieude, F.; Tmar, M.; Ultra-refractaires, L.; No, B. P. On the Kinetics of the Thermal Decomposition of Sulfates Related with Hydrogen Water Splitting Cycles. **1984**, 9, 579–585.
74. Romero-Paredes, H.; Torres, A.; Ambriz, J. J. *Renew. Energy* **1997**, 10, 231–234. DOI: [https://doi.org/10.1016/0960-1481\(96\)00070-5](https://doi.org/10.1016/0960-1481(96)00070-5).
75. Prieto, C.; Cooper, P.; Fernández, A. I.; Cabeza, L. F. *Renew. Sustain. Energy Rev.* **2016**, 60, 909–929. DOI: <https://doi.org/10.1016/j.rser.2015.12.364>.
76. Kolotygin, V. Materiais à Base de Óxidos Com Estrutura Do Tipo Perovskite e Compósitos Como Ânodos de PCES Propriedades Funcionais e Comportamento Eletroquímico Em Células Com Eletrólitos Sólidos à Base de Galatos e Silicatos. **2015**.
77. Chen, X.; Kubota, M.; Yamashita, S.; Kita, H. *J. Energy Storage* **2021**, 38, 102501. DOI: <https://doi.org/10.1016/j.est.2021.102501>.
78. Babinić, S. M.; Coker, E. N.; Miller, J. E.; Ambrosini, A. *Arch. Thermodyn.* **2015**, 33, 23–40. DOI: <https://doi.org/10.1002/er>.
79. Silva, R. S.; Ferreira, N. S.; F. D. Fontes, J.; E. H. Maia da Costa, M.; Barrozo, P. *Chem. Phys. Lett.* **2022**, 787, 139278. DOI: <https://doi.org/10.1016/j.cplett.2021.139278>.
80. feir, J.; Buffat, P. A.; Mockli, P.; Xanthopoulos, N.; Vasquez, R.; Mathieu, H. J.; Van herle, J.; Thampi, K. R. *J. Catal.* **2001**, 202, 229–244. DOI: <https://doi.org/10.1006/jcat.2001.3286>.
81. Dimesso, L. *Handb. Sol-Gel Sci. Technol.* **2016**. DOI: <https://doi.org/10.1007/978-3-319-19454-7>.
82. Ammendola, P.; Raganati, F.; Miccio, F.; Murri, A. N.; Landi, E. *Renew. Energy* **2020**, 157, 769–781. DOI: <https://doi.org/10.1016/j.renene.2020.05.048>.
83. Vieira, A. P.; Williamson, K.; Humphries, T. D.; Paskevicius, M.; Buckley, C. E. *J. Mater. Chem. A* **2021**, 9, 20585–20594. DOI: <https://doi.org/10.1039/d1ta04363c>.
84. Amghar, N.; Sánchez-Jiménez, P. E.; Ortiz, C.; Pérez-Maqueda, L. A.; Perejón. *Appl. Therm. Eng.* **2023**, 235. DOI: <https://doi.org/10.1016/j.applthermaleng.2023.121411>.
85. Raganati, F.; Ammendola, P. *Energy and Fuels* **2023**, 37, 1777–1808. DOI: <https://doi.org/10.1021/acs.energyfuels.2c03853>.
86. Valverde, J. M.; Perejon, A.; Perez-Maqueda, L. A. *Environ. Sci. Technol.* **2012**, 46, 6401–6408. DOI: <https://doi.org/10.1021/es3002426>.
87. Sánchez Jiménez, P. E.; Perejón, A.; Benítez Guerrero, M.; Valverde, J. M.; Ortiz, C.; Pérez Maqueda, L. A. *Appl. Energy* **2019**, 235, 543–552. DOI: <https://doi.org/10.1016/j.apenergy.2018.10.131>.
88. Møller, K. T.; Ibrahim, A.; Buckley, C. E.; Paskevicius, M. *J. Mater. Chem. A.* **2020**, 8, 9646–9653. DOI: <https://doi.org/10.1039/d0ta03080e>.
89. Anwar, R.; Navrátil, J.; Vijayaraghavan, R. K.; McNally, P. J.; Otyepka, M.; Błoński, P.; Sofianos, M. V. *Mater. Adv.* **2023**, 4, 1905–1915. DOI: <https://doi.org/10.1039/d2ma01083f>.
90. Moreno, V.; Arcenegui-Troya, J.; Enrique Sánchez-Jiménez, P.; Perejón, A.; Chacartegui, R.; Manuel Valverde, J.; Allan Pérez-Maqueda, L. *Chem. Eng. J.* **2022**, 440. DOI: <https://doi.org/10.1016/j.cej.2022.135707>.

91. Zare Ghorbaei, S.; Ale Ebrahim, H. *Appl. Energy* **2020**, 277, 115604. DOI: <https://doi.org/10.1016/j.apenergy.2020.115604>.
92. Rhodes, N. R.; Barde, A.; Randhir, K.; Li, L.; Hahn, D. W.; Mei, R.; Klausner, J. F.; Auyeung, N. *ChemSusChem* **2015**, 8, 3793–3798. DOI: <https://doi.org/10.1002/cssc.201501023>.

Ethnobotanical Medica, Pharmacology and Phytochemistry of the Species *Salvia del Valle de México: A Review*

Rocio Ortega¹, Fernando Calzada², Ángeles Fortis-Barrera¹, Jesus Solares-Pascasio¹, Francisco Javier Alarcón-Aguilar^{1*}

¹Laboratorio de Farmacología, Departamento de Ciencias de la Salud, División de Ciencias Biológicas y de la Salud, Universidad Autónoma Metropolitana, Iztapalapa, CDMX 02200, México.

²Unidad de Investigación Médica en Farmacología, UMAE Hospital de Especialidades, 2° Piso CORSE, Centro Médico Nacional Siglo XXI, CDMX, México.

*Corresponding author: Francisco Javier Alarcón-Aguilar, email: aaaf@xanum.uam.mx

Received May 22nd, 2024; Accepted August 4th, 2024.

DOI: <http://dx.doi.org/10.29356/jmcs.v68i4.2288>

Abstract. The *Salvia* genus is one of the most extensive in the Lamiaceae family. The *Salvia* genus comprises approximately 900 species worldwide, 33 of which exist in the Valle de México, the most populated region of Mexico. The taxonomic identification of these species often represents a problem because they present a great variety of synonyms or variations in their nomenclature, like *S. polystachya* with 12 synonymies. The traditional medicinal uses of *Salvia* species in Mexico are varied and include treatment for around 97 diseases. At least 20 species of the *Salvia* genus have well-documented medicinal ethnobotanical information with various uses, including gastrointestinal disorders, gynecological problems, promoting childbirth, antipyretic, disinfecting wounds, diabetes, and respiratory issues. The phytochemistry of the *Salvia* species from the Valle of Mexico is also vast and diverse; at least 315 chemical compounds have been identified, mainly terpenoids, that have received significant attention due to their multifaceted biological activities. Among the activities mentioned are anticancer, anti-hyperglycemic, anti-fungal, anti-inflammatory, or anti-microbial. Some of the compounds present more than one biological activity. Given their extensive structural diversity, terpenoids represent a great source of compounds for developing new therapeutic agents. However, additional clinical and experimental studies are still needed to elucidate the mechanisms of action, optimal doses, and potential toxicity of the isolated compounds.

Keywords: *Salvia spp.*; lamiaceae; medicinal plants; terpenoid compounds; phytochemistry; pharmacology.

Resumen. El género *Salvia* es uno de los más extensos en la familia Lamiaceae. El género *Salvia* comprende aproximadamente 900 especies alrededor del mundo, de las cuales 33 se encuentran en el Valle de México, la región más poblada de México. La identificación taxonómica de estas especies representa frecuentemente un problema al presentar una gran cantidad de sinonimias o variaciones en su nomenclatura, como *S. polystachya* que tiene 12 sinonimias. Los usos en medicina tradicional de Salvias en México son variados, incluyendo tratamiento para alrededor de 97 enfermedades. Por lo menos 20 especies del género *Salvia* tienen información bien documentada de sus usos médicos y etnobotánicos, con una amplia variedad de usos que incluye desórdenes gastrointestinales, problemas ginecológicos, promotores de parto, antipirético, para desinfectar heridas, diabetes o problemas respiratorios. La fitoquímica de las especies de *Salvia* del Valle de México es también amplia y diversa. Por lo menos 315 compuestos químicos han sido identificados y aislados, principalmente terpenoides, que han recibido gran atención debido a sus actividades biológicas multifacéticas, como anticancerígenas, antihiper glucémicas, antifúngica, antiinflamatorias o antimicrobianas. Algunos de los compuestos presentan más de una actividad biológica. Dada su extensa diversidad estructural, los terpenoides representan una amplia fuente de compuestos para el desarrollo de nuevos agentes terapéuticos. Sin embargo, estudios clínicos y experimentales

adicionales son necesarios para elucidar el mecanismo de acción, dosis óptimas y toxicidad potencial de los compuestos aislados.

Palabras clave: *Salvia spp.*; lamiaceae; plantas medicinales; compuestos terpenoides; fitoquímica; farmacología.

Introduction

The Lamiaceae (Labiatae) family comprises approximately 236 genera and 7,173 species [1,2]. The genus *Salvia* is one of the most extensive groups in this family, representing around 900 species worldwide [3,4]. The term *Salvia* comes from the Latin "*salvare*," meaning "to heal or be safe and unharmed," referring to the healing properties of these species [2,5-9], which are recognized in worldwide traditional medicine. In the Americas, around 500 species are registered in Mexico, Central America, and South America, representing the second most diverse territory, with approximately 312 species, of which 75 to 88% are endemic [5,10-12]. In Mexico, the most significant number of *Salvia* species is concentrated in the western and southeastern, along the Occidental Sierra Madre, the Trans-Mexican Volcanic Belt, and the Sierra Madre del Sur.

Salvia species are typically shrubs or climbing shrubs from 30 to 150 cm tall that can be annual or perennial [12]. Their stems are angular, characteristic of the Lamiaceae family, with leaves that are usually velvety or hairy, and they can often be rugose, entire, toothed, lobed, or pinnate. The flower stalks produce small bracts different from the basal leaves. Inflorescences are borne in clusters or panicles that produce brightly colored flowers, depending on the species [7,9,12]. The calyx is tubular or bell-shaped without a bearded throat, divided into two lips (that is why the name of labiates): the upper whole or tridentate and the lower cleft. The corolla is usually bilabiate. The stamens are two short structures with bicellular anthers. Many species have trichomes (hairs) on the surface of the leaves, stems, and flowers [7,9,12].

Several *Salvia* species have great economic importance due to their edible, aromatic, and medicinal properties. Many of these species contain high amounts of essential oils, phenolic compounds, antioxidants, and other valuable chemical constituents [5]. The main compounds described in the *Salvia* species are terpenoids and flavonoids. Aerial parts, especially flowers and leaves, contain flavonoids, triterpenoids, and monoterpenes, while the roots contain primarily diterpenoids [7,9,10]. *Salvia* species have been used since ancient times for different ailments, ranging from aches to epilepsy, and the primary uses are for treating colds, bronchitis, tuberculosis, hemorrhages, and menstrual disorders, among others [7,9]. The Mexican *Salvia* species are highly valued for their medicinal, nutritional, and ritualistic uses and are often used as part of vernacular medicine or in mystical/religious rituals. Prominent examples are *Salvia divinorum* ("planta de la pastora"), which is a hallucinogen plant used in rituals by the Mazatecas, an endemic population in the northeastern of Oaxaca [13], and *Salvia hispanica* (chia), which is widely used as a food source since pre-Hispanic times [14].

Ramamoorthy (2001) botanically identified 33 *Salvia* species in the Valle de México [9] (Table 1). The Valle de México has an altitude of 2,240 meters (7,350 ft), covering around 7,866 km², and includes 16 town halls in Mexico City, 59 municipalities of the State of Mexico, and one municipality in the State of Hidalgo [15]. Geographically, it is located between the Anahuac Lake and Volcano Region of the physiographic province of the Neo-volcanic Axis and is surrounded by the mountains of Monte Alto, Monte Bajo, and Las Cruces, as well as the Sierra Nevada and Chichinauhtzin mountain range (Fig. 1). This surface presents intermountain, valleys, plateaus, and ravines, as well as semi-deep land, in which are located the lakes of Texcoco, Xochimilco, and Chalco. There are also isolated topographic prominences, such as the "Cerro de la Estrella," the "Cerro del Peñón," and the "Cerro de Chapultepec." The Valle de México also represents the most populated region of Mexico, with more than 20 million inhabitants, who often agree with these species despite their lack of knowledge about their medical uses and properties. In this region, 33 species of *Salvia* had been recorded [9]. Although several researchers worldwide have contributed ethnobotanical, phytochemical, and pharmacological information for some of these species [5,16-19], it is still necessary to continue working on the supplementation and organization of this information. In certain instances, these species exhibit a broad range of botanical synonyms or variations in their nomenclature, which can result in some confusion, like *S. polystachya*, that have 12 botanical synonymies and 11 common names. Therefore, their taxonomic identification often represents a problem. This review aims to organize and synthesize the ethnobotanical, pharmacological, and phytochemical knowledge of the 33 *Salvia* species described by Ramamoorthy in the Valle de México [9]. These species have been extensively

documented by diverse research groups in Mexico and other regions, including Europe and Asia [20-25]. Our primary objective is to critically analyze and compare these data, advancing their study at the ethnopharmacological, phytochemical, and therapeutic levels. By doing so, we seek to validate the traditional uses attributed to these remarkable plant species.

Table 1. Scientific name of the 33 *Salvia* species described by Ramamoorthy in the Valle de México [9].

1.	<i>S. axillaris</i> Moc & Sessé ex Benth.	2.	<i>S. carnea</i> Kunth.	3.	<i>S. chamaedryoides</i> Cav.
4.	<i>S. circinata</i> Cav.	5.	<i>S. concolor</i> Lamb. ex Benth	6.	<i>S. elegans</i> Vahl.
7.	<i>S. filifolia</i> Ramamoorthy	8.	<i>S. fulgens</i> Cav.	9.	<i>S. gesneriiflora</i> Lindl & Paxton
10.	<i>S. helianthemifolia</i> Benth.	11.	<i>S. hirsuta</i> Jacq.	12.	<i>S. hispanica</i> L.
13.	<i>S. keerlii</i> Benth.	14.	<i>S. laevis</i> Benth.	15.	<i>S. lavanduloides</i> Kunth.
16.	<i>S. leucantha</i> Cav.	17.	<i>S. melissodora</i> Lag. Me Vaugh.	18.	<i>S. mexicana</i> L.
19.	<i>S. microphylla</i> H.B.&H.	20.	<i>S. misella</i> Kunth.	21.	<i>S. mocinoi</i> Benth.
22.	<i>S. moniliformis</i> Fern.	23.	<i>S. oreopola</i> Fern.	24.	<i>S. patens</i> Cav.
25.	<i>S. polystachya</i> Cav.	26.	<i>S. prunelloides</i> Kunth.	27.	<i>S. pulchea</i> DC.
28.	<i>S. reflexa</i> Hornem.	29.	<i>S. reptans</i> Jacq.	30.	<i>S. stachyoides</i> Kunth.
31.	<i>S. tiliifolia</i> Vahl.	32.	<i>S. tubifera</i> Cav.	33.	<i>S. verbenacea</i> L.

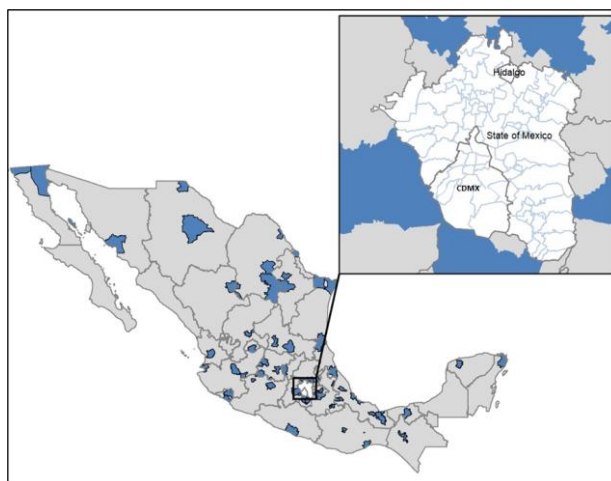


Fig. 1. The delimitation of Mexican metropolitan areas (Valle de México). Modified from OECD, 2015

Methodology

Information from the 33 species of *Salvias* recorded by Ramamoorthy in the Valle de México [9] was obtained from diverse databases, such as Web of Science, Google Scholar, Google Books, Scopus, ScienceDirect, SpringerLink, Wiley Online, PubMed, textbooks, taxonomic reviews, university theses, and SciFinder. With the obtained data, such as botanical characteristics, botanical synonymy, empirical uses, and biological activities, a meta-analysis was performed, and the compounds isolated were documented.

Results and discussion

Botanical synonymy, popular names, and distribution

Plant nomenclature is ruled by the International Code of Botanical Nomenclature, which aims to provide a correct and accepted name for a taxon based on publication priority. The application of the norms of the code and the taxonomic studies that imply some change in the circumscription of the taxon result in changes in nomenclature and botanic synonymy, such that in the study of medicinal plants, the synonymies can be a problem by creating confusion in any investigation [26,27]. Therefore, the first step was identifying which species had synonyms or some variation (Table 2), highlighting that many of the *Salvia* species studied (84 %) presented some of these conditions. The plant with a significant number of synonyms was *S. polystachya*, with 12 synonymies, seven variations, and three subspecies, followed by *S. carnea*, with 13 synonymies and two variations: *S. fulgens*, with 11 synonymies and three variations, and *S. mexicana* with nine synonymies and three variations. This situation illustrates how easy it is to make mistakes when working with species *Salvia*, so taxonomic identification is a priority before any study. Another frequent problem for species identification focuses on popular or common names with ethnobotanical relevance. However, in Mexico, the popular names vary depending on the region where they are found. Of the included species in the present study, 57.6% had more than one popular name, where "mirto," "chia," and "salvia" are the most used. *S. microphylla* is recognized with 18 popular names, followed by *S. lavanduloides* with 15 names. The consulted bibliography recorded a single popular name for five species; no popular name for nine species was documented. The importance of the correct name of the plant species consists in being able to avoid confusion or even a duplicate work for incorrect use of the names; in the case of *S. circinata* (*S. amarissima*), it is possible to observe publications with both names; it is essential to corroborate the correct and accepted scientific name of the plant. [28,29].

The geographical distribution of these 33 species is not exclusive to the Valle de México. Most of them are distributed in several states of Mexican territory (Table 2). The data indicate that in the state of Michoacan, there are around 27 species, followed by the State of Mexico with 18, and the State of Hidalgo with 17. The best-distributed species in Mexico are *S. polystachya* and *S. hispanica* (Table 2). These data are essential if we consider that the same common name can be used to name different species of the same or other genera, or a single species can receive several names, which vary from one region to another, and because some species share the same distribution in the Valle de México, including Ciudad de México, Estado de México, and Hidalgo. We agree with [2] that research focused on medicinal plants requires essential botanical assistance, especially in taxonomy and nomenclature.

The distribution of the plants in the different regions also affects the kind and concentration of secondary metabolites in the plant. In *S. hispanica*, the weather, altitude, humidity, and nutrients of the region of Veracruz, which is in the East of Mexico, with significant humidity, being a jungle area, are not the same conditions that the State of Durango, in the north of the country, with a desert climate. The different territorial, geographic, and climatic conditions provoke changes in the metabolites, and it may affect all the *Salvia* species that have a wide distribution in the country, even in the same species with different geographical distribution. These changes are a significant area of study to determine the impact of the different conditions in synthesizing metabolites of pharmacological interest [28,30].

Table 2. Scientific name, botanical synonymy, popular names, and distribution of *Salvia* species from the Valle de México.

Scientific name	Botanical synonymy / Varieties	Common name	Distribution in other states of Mexico
<i>S. axillaris</i> Moc & Sessé ex Benth.	= <i>S. cuneifolia</i> Benth. = <i>S. axillaris</i> var. <i>axillaris</i> .	Hisopo de Puebla Vegeta	Durango Guanajuato Hidalgo Jalisco Michoacán Oaxaca Puebla San Luis Potosí Tlaxcala Veracruz
<i>S. carnea</i> Kunth.	= <i>S. membranacea</i> Benth. = <i>S. pseudogracilis</i> Epling. = <i>S. myriantha</i> Epling. = <i>S. natalis</i> Epling = <i>S. carnea</i> var. <i>carnea</i> . = <i>S. debilis</i> Epling. = <i>S. gracilis</i> Benth. = <i>S. iodochroa</i> Briq. = <i>S. irazuensis</i> Fernald. = <i>S. killipiana</i> Epling. = <i>S. martensii</i> Galeotti. = <i>S. membranacea</i> var. <i>villosula</i> Benth. = <i>S. purpurascens</i> M. Martens & Galeotti. = <i>S. sidifolia</i> M. Martens & Galeotti. = <i>S. simulans</i> Fernald.	Chía	Chiapas Guerrero Hidalgo Michoacán Oaxaca Nayarit Veracruz
<i>S. chamaedryoides</i> Cav.	= <i>S. menthifolia</i> Ten. = <i>S. chamaedrifolia</i> Andrews. = <i>S. chamaedryoides</i> var. <i>isochroma</i> Fernald. = <i>S. chamaedrys</i> Willd.	Mirto	Hidalgo Morelos Nuevo León Puebla San Luis Potosí Zacatecas
<i>S. circinata</i> Cav.	= <i>S. amarissima</i> Ort. = <i>S. amara</i> Jacq. = <i>S. hirsuta</i> Sessé & Moc. non Jacq.	Bretónica Chupona Diabetina Hierba de cáncer Hierba de tapón Prodigiosa Ñadri (otomí)	Estado de México Guerrero Michoacán Oaxaca San Luis Potosí Veracruz
<i>S. concolor</i> Lamb. ex Benth	= <i>S. cyanea</i> Benth. = <i>S. cyaniflora</i> A. Dietr. = <i>S. cyanifera</i> Otto ex Benth.	Hierba	Colima Estado de México Guerrero Jalisco Michoacán Morelos Puebla

Scientific name	Botanical synonymy / Varieties	Common name	Distribution in other states of Mexico
<i>S. elegans</i> Vahl.	= <i>S. camertonii</i> Regel. = <i>S. incarnata</i> Cav. = <i>S. longiflora</i> Sessé & Moc. = <i>S. microcalyx</i> Scheele. = <i>S. punicea</i> M. Martens & Galeotti. = <i>S. rutilans</i> Carrière. = <i>S. elegans</i> var. <i>sonorensis</i> Fernald. = <i>S. microculis</i> Poir.	Flor del cerro Hierba del burro Limoncillo Mirto Mirto de campo Mirto de flor roja Mirto inglés Mirto mocho Salvia Toronjil de monte <i>Jetcho deni</i> (otomí)	Chihuahua Durango Estado de México Hidalgo Michoacán Oaxaca Puebla Sonora Veracruz
<i>S. filifolia</i> Ramamoorthy	NS	NS	Guanajuato Michoacán Estado de México
<i>S. fulgens</i> Cav.	= <i>S. cardinalis</i> Kunth. = <i>S. boucheana</i> Kunth. = <i>S. cardinalis</i> Kunth. = <i>S. incana</i> M. Martens & Galeotti. = <i>S. grandiflora</i> Sessé & Moc. = <i>S. orizabensis</i> Fernald. = <i>S. pendula</i> Sessé & Moc. = <i>S. schaffneri</i> Fernald. = <i>S. fulgens</i> var. <i>boucheana</i> (Kunth) Benth. = <i>S. fulgens</i> f. <i>boucheana</i> (Kunth) Voss. = <i>Piaradena fulgens</i> (Cav.) Raf.	Mirto Mirto macho Mirto macho del popo <i>Pinyesi</i> (mazahua)	Estado de México Michoacán Puebla Tlaxcala
<i>S. gesneriiflora</i> Lindl & Paxton	= <i>S. barbata</i> Sessé & Moc. = <i>S. fulgens</i> f. <i>gesneriiflora</i> (Lindl. & Paxton) Voss.	Aparicua Flor de colibrí Flor de chuparrosa Flor de <i>Tzintzungaraman</i> (purépecha)	Estado de México Jalisco Michoacán Puebla
<i>S. helianthemifolia</i> Benth.	NS	Mirto corriente	Guanajuato Guerrero Hidalgo Jalisco Michoacán Morelos Querétaro San Luis Potosí Veracruz

Scientific name	Botanical synonymy / Varieties	Common name	Distribution in other states of Mexico
<i>S. hirsuta</i> Jacq.	= <i>S. cryptanthos</i> Schult. = <i>S. phlomoides</i> Cav. = <i>S. sideritidis</i> Vahl. = <i>S. bracteata</i> Poir. = <i>S. ciliaris</i> Sessé & Moc. = <i>S. ciliata</i> Poir. = <i>S. nepetifolia</i> Desf.	NS	Durango Estado de México Guanajuato Hidalgo Oaxaca Querétaro San Luis Potosí Texcoco Tlaxcala Zacatecas
<i>S. hispanica</i> L.	= <i>S. hispanica</i> var. <i>chionocalyx</i> Fernald. = <i>S. hispanica</i> var. <i>intonsa</i> Fernald. = <i>S. neohispanica</i> Briq. = <i>S. prysmatica</i> Cav. = <i>S. schiedeana</i> Stapf. = <i>S. tetragona</i> Moench. = <i>Kiosmina hispanica</i> (L.) Raf. = <i>S. chia</i> Colla. = <i>S. chia</i> Sessé & Moc.	Chía Chía blanco <i>Tzozolxochitl</i>	Coahuila Chihuahua Durango Guanajuato Guerrero Jalisco Michoacán Morelos Oaxaca Puebla San Luis Potosí Sonora Veracruz
<i>S. keerlii</i> Benth.	NS	NS	Durango Guanajuato Hidalgo Michoacán Nuevo León Oaxaca Querétaro San Luis Potosí Tamaulipas Zacatecas
<i>S. laevis</i> Benth.	= <i>S. laevis</i> Benth. = <i>S. comosa</i> Peyr. = <i>S. comosa</i> var. <i>hypoglauca</i> Fernald. = <i>S. hypoglauca</i> Briq. = <i>S. pseudocomosa</i> Epling.	Salvia real Palmita	Durango Estado de México Guanajuato Hidalgo Jalisco Michoacán Oaxaca Puebla Querétaro San Luis Potosí Veracruz

Scientific name	Botanical synonymy / Varieties	Common name	Distribution in other states of Mexico
<i>S. lavanduloides</i> Kunth.	= <i>S. agnes</i> Epling. = <i>S. humboldtiana</i> Schult. = <i>S. lavanduloides</i> Kunth var. <i>latifolia</i> Benth. = <i>S. fratrum</i> Standl. = <i>S. lavanduloides</i> var. <i>hispidula</i> Benth. = <i>S. purpurina</i> La Llave.	Altamisa Alucena Azulilla Cantuesco Cenicilla Chabacal Ordoncillo Lucema Lúcumá Mazorquita Poleo Salvia morada <i>Yaxal nich vomol</i> (tzotzil) <i>Recámpona</i> (mazahua) <i>Cuetehton</i> (náhuatl)	Chiapas Estado de México Guerrero Hidalgo Michoacán Morelos Oaxaca Puebla Veracruz
<i>S. leucantha</i> Cav.	= <i>S. bicolor</i> Sessé & Moc. = <i>S. discolor</i> Kunth. = <i>S. leucantha</i> f. <i>iobaphes</i> Fernald.	Algodoncillo Cordoncillo Cordón de Jesús Cordón de San Francisco Lana Rabo de gato Salvia cruz Salvia real Moco de pavo <i>Moradoxóchitl</i> (náhuatl) <i>Tochomixochitl</i>	Estado de México Hidalgo Michoacán Morelos Oaxaca Puebla San Luís Potosí Tabasco Zacatecas
<i>S. melissodora</i> Lag. Me Vaugh.	= <i>S. scorodoniaefolia</i> Poir. = <i>S. scorodoniae</i> Desf. ex Poir. = <i>S. scorodoniaefolia</i> var. <i>crenaea</i> Fernald. = <i>S. scorodonia</i> Benth. = <i>S. dugesii</i> Fernald.	Orégano <i>Tkulh organ</i> (tepeh) <i>Tikolh organ</i>	Chihuahua Durango Guerrero Hidalgo Michoacán Oaxaca Zacatecas
<i>S. mexicana</i> L.	= <i>S. mexicana</i> L. var. <i>mexicana</i> = <i>S. mexicana</i> var. <i>minor</i> Benth. = <i>S. mexicana</i> f. <i>minor</i> Sessé & Moc. = <i>S. mexicana</i> var. <i>major</i> Benth. = <i>Hemistegia mexicana</i> (L.) Raf. = <i>Jungia altissima</i> Moench. = <i>S. amethystina</i> Salisb. = <i>S. lupulina</i> Fernald. = <i>S. nitidifolia</i> Ortega. = <i>S. papilionacea</i> Cav. = <i>Sclarea mexicana</i> (L.) Mill. = <i>Sclarea mexicana</i> (L.) Dill.	Chía Marrubio Tacote Tapachichi <i>Azul-sipari</i> (purépecha) <i>Charahuesca</i> (purépecha) <i>Ichukuta</i> (purépecha) <i>Tapachichi</i>	Chiapas Chihuahua Jalisco Michoacán Morelos Oaxaca Sinaloa Tlaxcala Veracruz Zacatecas

Scientific name	Botanical synonymy / Varieties	Common name	Distribution in other states of Mexico
<i>S. microphylla</i> H.B. & H.	<ul style="list-style-type: none"> = <i>S. microphylla</i> Kunth. var. <i>microphylla</i>. = <i>S. microphylla</i> var. <i>neurepia</i>. = <i>S. grahamii</i> Benth. = <i>S. lemmonii</i> A. Gray. = <i>S. microphylla</i> Sessé & Moc. = <i>S. microphylla</i> var. <i>canescens</i> A. Gray. = <i>S. microphylla</i> var. <i>wislizeni</i> A. Gray. = <i>S. obtusa</i> M. Martens & Galeotti. = <i>S. odoratissima</i> Sessé & Moc. = <i>S. lesemia coccinea</i> Raf. 	Diente de acamaya Hierba de mirto Mastranzo Mirto Mirto blanco Mirto de castilla Mirto chico Mirto de huerto Mirto violeta Toronjil Verbena Mistro Mistru <i>Mishto</i> (tzotzil) <i>Tzil bomol</i> (tzotzil) <i>Ix tasalak</i> (tepehua) <i>Mustia</i> (purepecha) <i>Kaisto nchia</i> (popoloca)	Chiapas Durango Estado de México Guanajuato Hidalgo Jalisco Michoacán Nuevo León Puebla Tamaulipas Veracruz
<i>S. misella</i> Kunth.	<ul style="list-style-type: none"> = <i>S. riparia</i> Kunth. = <i>S. lateriflora</i> Fernald. = <i>S. obscura</i> Benth. = <i>S. viscosa</i> Sessé & Moc. = <i>S. privoides</i> Benth. = <i>S. occidentalis</i> var. <i>obscura</i> (Benth.) M. Gómez 	Chía Hierba del cáncer Hierba de golpe Quelite lengua de toro Venenosa	Baja California Guerrero Michoacán Tamaulipas Veracruz
<i>S. mocinoi</i> Benth.	<ul style="list-style-type: none"> = <i>S. lophantha</i> Benth. = <i>S. rubiginosa</i> Benth. = <i>S. rubiginosa</i> var. <i>hebephylla</i> Fernald. = <i>S. saltuensis</i> Fernald = <i>S. zacuapanensis</i> Brandegee. = <i>S. lophanthoides</i> Fernald. 	NS	Guerrero Jalisco Michoacán Puebla
<i>S. moniliformis</i> Fern.	NS	NS	Estado de México Morelos
<i>S. oreopola</i> Fern.	NS	NS	Estado de México Morelos Oaxaca
<i>S. patens</i> Cav.	<ul style="list-style-type: none"> = <i>S. decipiens</i> M. Martens & Galeotti. = <i>S. grandiflora</i> Née ex Cav. = <i>S. macrantha</i> Schldt. = <i>S. spectabilis</i> Kunth. = <i>S. staminea</i> M. Martens & Galeotti. 	Flor de gallito Quiquiriquí Mirto Mirto azul	Estado de México Hidalgo Michoacán San Luis Potosí

Scientific name	Botanical synonymy / Varieties	Common name	Distribution in other states of Mexico
<i>S. polystachya</i> Cav.	<ul style="list-style-type: none"> = <i>S. polystachya</i> Ort. = <i>S. brevicalyx</i> Benth. = <i>S. caesia</i> Willd. = <i>S. cataria</i> Briq. = <i>S. compacta</i> Kuntze. = <i>S. compacta</i> var. <i>irazuensis</i> Kuntze. = <i>S. compacta</i> var. <i>latifolia</i> Kuntze. = <i>S. compacta</i> var. <i>oerstediana</i> Kuntze. = <i>S. durandiana</i> Briq. ex T. Durand & Pittier. = <i>S. eremetica</i> Cerv. ex Lag. = <i>S. flexuosa</i> C. Prezl ex Benth. = <i>S. lilacina</i> Fernald. = <i>S. lineatifolia</i> Lag. = <i>S. mentiformis</i> Fernald. = <i>S. polystachya</i> var. <i>albicans</i> Fernald. = <i>S. polystachya</i> subsp. <i>caesia</i> (Humb. & Bonpl.) Briq. = <i>S. polystachya</i> subsp. <i>compacta</i> (Kuntze) Alziar. = <i>S. polystachya</i> subsp. <i>durandiana</i> Briq. = <i>S. polystachya</i> var. <i>philippensis</i> Fernald. = <i>S. polystachya</i> var. <i>potosiana</i> Briq. = <i>S. polystachya</i> var. <i>seorsa</i> Fernald. = <i>S. reducta</i> Epling. 	<ul style="list-style-type: none"> Alchichía Azulema Chía de campo Hierba chica Lucemilla Mirto Poleo azul Romerillo Santomexochitl Ulcema <i>Xilpapah</i> 	<ul style="list-style-type: none"> Chiapas Colima Estado de México Guanajuato Guerrero Hidalgo Jalisco Michoacán Morelos Nayarit Oaxaca Puebla Querétaro San Luis Potosí Tamaulipas Tlaxcala Veracruz
<i>S. prunelloides</i> Kunth.	<ul style="list-style-type: none"> = <i>S. prunelloides</i> f. <i>minor</i> Loes. = <i>S. rhombifolia</i> Sessé & Moc. = <i>S. trichandra</i> Briq. 	<ul style="list-style-type: none"> Hierba de gallo Oreja de venado Salvia azul <i>Suimalh nanakl</i> (tepech) 	<ul style="list-style-type: none"> Chiapas Durango Michoacán Nuevo León San Luis Potosí Zacatecas
<i>S. pulchea</i> DC.	<ul style="list-style-type: none"> = <i>S. ancistrocarpha</i> Fernald. = <i>S. doliostachys</i> Lag. ex Benth. 	NS	<ul style="list-style-type: none"> Estado de México Michoacán
<i>S. reflexa</i> Hornem.	<ul style="list-style-type: none"> = <i>S. aspidophylla</i> Schult. = <i>S. trichostemoides</i> Pursh. 	<ul style="list-style-type: none"> Almaraduz grande Chía Mimititán 	<ul style="list-style-type: none"> Estado de México Michoacán Nuevo León Zacatecas
<i>S. reptans</i> Jacq.	<ul style="list-style-type: none"> = <i>S. angustifolia</i> Cav. = <i>S. angustifolia</i> var. <i>glabra</i> Briq. = <i>S. angustifolia</i> var. <i>glabra</i> A. Gray. = <i>S. heterotricha</i> Fernald. = <i>S. leptophylla</i> Benth. = <i>S. linearis</i> Sessé & Moc. = <i>S. linifolia</i> M. Martens & Galeotti. = <i>S. virgata</i> Ortega. = <i>S. unicostata</i> Fernald. 	<ul style="list-style-type: none"> Hierba de golondrina Hierba de pozuña Romerillo 	<ul style="list-style-type: none"> Chiapas Estado de México Hidalgo Jalisco Michoacán Puebla Zacatecas

Scientific name	Botanical synonymy / Varieties	Common name	Distribution in other states of Mexico
<i>S. stachyoides</i> Kunth.	= <i>S. elongata</i> Kunth. = <i>S. stricta</i> Sessé & Moc. = <i>S. simplex</i> Spreng. = <i>S. betónica</i> Schult.	Salvia Negra	Michoacán Morelos Veracruz
<i>S. tiliifolia</i> Vahl.	= <i>S. fimbriata</i> Kunth. = <i>S. myriantha</i> Epling. = <i>S. obvallata</i> Epling. = <i>S. psilophylla</i> Epling. = <i>S. tiliifolia</i> Lag. = <i>S. tiliifolia</i> var. <i>albiflora</i> (M. Martens & Galeotti) L.O. Williams. = <i>S. tiliifolia</i> var. <i>alvajaca</i> (Oerst.) L. O. Williams. = <i>S. tiliifolia</i> var. <i>cinerascens</i> Fernald. = <i>S. tiliifolia</i> var. <i>rhyacophila</i> Fernald. = <i>S. tiliaefolia</i> Vahl.	Chia chimarrona Chupona Hierba de gallo Limpia tuna Tronadora	Chiapas Hidalgo Michoacán Nuevo León Sonora Tamaulipas Veracruz Zacatecas
<i>S. tubifera</i> Cav.	= <i>S. excelsa</i> Benth. = <i>S. monochila</i> Donn. Sm. = <i>S. venosa</i> Fernald. = <i>S. longiflora</i> Willd.	NS	Hidalgo Guerrero Veracruz
<i>S. verbenacea</i> L.	= <i>S. vervenaca</i> L.	NS	NS

NS = Not specified

Botanical characteristics

The different species of the *Salvia* genus have similar morphological characteristics [31]. Table 3 enlists some botanical characteristics reported by Ramamoorthy in 2001 [9], complemented by Lara-Cabrera [32]. Most of these species (75.5 %) are "perennial herbaceous" of 0.15 m (*S. helianthemifolia* Benth.) to 4 m (*S. fulgens* Cav.) and can be found at different altitudes ranging from 650 to 2400 meters. In the different species, the leaves vary in size from 5-8 mm to 50-140 mm long and have various shapes, from elliptical to ovate. The flowering time in plants is of great importance; it involves essential changes in metabolism and the translocation of nutrients, ensuring the production of seeds and, therefore, the survival of the species [33,34]. In the salvias studied, it was possible to document data on flowering times for 14 species, less than half (42.2 %) of the studied plants, and no pattern was observed in these data, so it is possible to find different species of *Salvia* in bloom throughout the year. The colours of the bilabiate calyx and the corolla are also diverse (red, pink, blue, lilac, and white), although the blue corolla is predominant (69.7 %). However, in at least nine species (27.3 %), the colour of the corolla can be variable. Habitat and altitude, among other abiotic and biotic environmental factors, can modify their physical or chemical characteristics, impacting the secondary metabolism's evolution and phenotypic plasticity [35].

Considering the similarity observed in the distinct *Salvia* species, it is essential and necessary to take special care in the taxonomic identification to avoid correlation errors and extrapolation [26], which could put in risk the reproducibility and continuation of pharmacological and chemical studies with these species [2,30]. The chemical composition varies between species, seasons, and habitats, as well as the stage of development or the plant organ (ontogeny of leaves, flowers, and fruits), factors that lead to significant qualitative differentiations where the composition can undergo significant changes. Some components can vary from traces (10 %) in the initial stages up to 50-70 % in the full bloom stage [36], which should be considered in phytochemical studies.

Table 3. Botanical characteristics of *Salvia* species from Valle de México. [10]

Plant name	Habitat	Leaves	Flowers	Flowering	Altitude range (meters)	Vegetation
<i>S. axillaris</i>	Perennial-herbaceous Ascending: NS	Sessile obovate to oblanceolate Rounded apex 7 - 12 x 30 - 45 mm	Bilabiate calyx Corolla: Light lilac / white	NS	2400-2800	Grasslands Bushes Quercus forest Juniperus forest
<i>S. carnea</i>	Perennial-herbaceous Ascending: 0.5-1.5 m	Ovate Acuminate apex 30 - 90 x 20 - 60 mm	Bilabiate calyx Corolla: Pink / White	Sep - May	2800-3500	Mountain mesophyll forest Quercus forest Pinus forest Pinus-Quercus Forest Abies forest
<i>S. chamaedryoides</i>	Herbaceous-perennial / subshrub Ascending: 20-80 cm	Ovate to deltoid-elliptic Rounded apex 6 - 20 x 3 - 10 mm	Bilabiate calyx Corolla: Blue	NS	2300-2800	Grassland Bushes Quercus forest Juniperus forest
<i>S. circinata</i>	Perennial-herbaceous Ascending: 30 cm-1.5 m	Ovate Acuminate apex 30 - 100 x 12 - 45 mm	Bilabiate calyx Corolla: Blue-purple/white	Aug - Nov	1650-2800	Grassland Bushes Disturbed Areas
<i>S. concolor</i>	Perennial-herbaceous Ascending: 50 cm-2 m	Ovate to ovate-deltoid Acuminate apex 50 - 120 x 30 - 120 mm	Bilabiate calyx Corolla: Dark blue.	Sep	2650-3300	Coniferous forest Mesophilic forest
<i>S. elegans</i>	Perennial-herbaceous / Bushy Ascending: 80 cm-2m	Ovate Acute apex 8 - 6 x 6 - 35 mm	Bilabiate calyx Corolla: Red	NS	2550-3100	Mountain mesophyll forest Abies forest Pinus forest Quercus forest
<i>S. filifolia</i>	Perennial-herbaceous Ascending: ± 35 cm	Sessile Lineal sometimes Oblanceolate / narrowly-oblanceolate Acute apex 10 - 60 x 2 - 3 mm	Bilabiate calyx Corolla: Blue	Jul - Nov	2390-2800	Encino deteriorated forest Pinus forest Quercus forest

Plant name	Habitat	Leaves	Flowers	Flowering	Altitude range (meters)	Vegetation
<i>S. fulgens</i>	Arbustive Ascending: 1-4 m	Ovate Acute apex 30 - 140 x 15 - 70 mm	Bilabiate calyx Corolla: Deep red/white	NS	2650-3400	Mountain mesophyll forest Juniperus forest Mixed forest Pinus-Encino Forest
<i>S. gesneriiflora</i>	Climbing shrub Ascending: 80 cm-2.5 m	Ovate Rounded apex 30 - 110 x 30 - 80 mm	Bilabiate calyx Corolla: Red	Oct - May	1950-3200	Mesophyll forest Quercus forest Mixed forest Coniferous forest Pinus forest Pinus-Quercus Forest Shores of agricultural crops
<i>S. helianthemifolia</i>	Perennial-herbaceous Ascending: 15-70 cm	Elliptic-orbicular Rounded apex 10 - 50 x 4 - 20 mm	Bilabiate calyx Corolla: Blue	Aug - Apr	2000-3200	Mountain mesophyll forest Quercus forest Pinus forest Pinus-Quercus Forest Coniferous forest Secondary scrub
<i>S. hirsuta</i>	Perennial-herbaceous Ascending: 20-60 cm	Oblong-elliptic Obtuse apex 20 - 35 x 10 - 14 mm	Bilabiate calyx Corolla: Blue	Jun - Oct	2250 – 2600	Grasslands Scrubs Disturbed areas
<i>S. hispanica</i>	Perenne Ascending: 1 m	Ovate-lanceolate Acuminate apex 30 - 60 x 10 - 20 mm	Bilabiate calyx Corolla: Purple/blue	Sep - Nov	2050-2500	Quercus forest Tropical deciduous forest Mixed forest
<i>S. keerlii</i>	Bushy Ascending: 1-3.5 m	Ovate Acute-obtuse apex 20 - 40 x 7 - 30 mm	Bilabiate calyx Corolla: Blue to purple/white	Jul - Dec	2170-3100	Quercus forest Juniperus forest Pinus-Quercus Forest Juniperus-quercus forest Submontane xerophytic scrubland

Plant name	Habitat	Leaves	Flowers	Flowering	Altitude range (meters)	Vegetation
<i>S. laevis</i>	Perennial-herbaceous Ascending: 30-70 cm	Lanceolate-oblong-lanceolate Acute apex 25 - 80 x 3 - 12 mm	Bilabiate calyx Corolla: Blue	Jun - Nov	1520 -3200	Quercus forest Xerophytic scrubland Abies forest Pinus forest Pinus-Quercus Forest Mesophyll forest Grasslands Scrubs
<i>S. lavanduloides</i>	Perennial-herbaceous Ascending: 50 cm-1 m	Elliptic Acute apex 30 - 90 x 6 - 15 mm	Bilabiate calyx Corolla: Blue	Oct - May	1650 -3300	Mountain mesophyll forest Quercus forest Pinus-Quercus Forest Mixed forest Secondary vegetation
<i>S. leucantha</i>	Ascending: 45 cm-1 m	Lanceolate Acute apex 40 - 120 x 4 - 18 mm	Bilabiate calyx Corolla: White and covered with purple hair	Sep - Dec	1000-2800	Pinus forest Encino forest Xerophytic scrublands
<i>S. melissodora</i>	Perennial-herbaceous Arbustive Ascending: 50 cm-2 m	Oval Ovate-oblong / ovate-deltoid Acute apex 10 - 50 x 70 - 30 mm	Bilabiate calyx Corolla: Blue-purple/white	Jul - Mar	1550 - 2600	Xerophytic scrubland Slopes Hill
<i>S. mexicana</i>	Perennial-herbaceous Arbustive Ascending: 50 cm-3 m	Ovate Acuminate apex 60 - 180 x 25 - 120 mm	Bilabiate calyx Corolla: Blue	NS	2250 - 3000	Quercus forest Pinus forest Disturbed areas
<i>S. microphylla</i>	Arbustive Ascending: 40 cm-1.5 m	Elliptic oval or deltoid Acute to rounded apex 10 - 70 x 4 - 30 mm	Bilabiate calyx Corolla: Red	NS	NS	Juniperus forest Encino forest Mixed forest Evergreen forest Pinus forest Pinus-Encino Forest Xerophytic scrubland Grassland

Plant name	Habitat	Leaves	Flowers	Flowering	Altitude range (meters)	Vegetation
<i>S. misella</i>	Perennial-herbaceous Ascending: 50 cm-1.5 m	Opposite sessile/elliptic Acuminate apex 20 - 50 x 10 - 20 mm	Bilabiate calyx Corolla: Blue	NS	650-2250	Mountain mesophyll forest Disturbed vegetation of tropical deciduous forest The transition zone between the mountain mesophyll and encino forest
<i>S. mocinoi</i>	Perennial-herbaceous Arbustive Ascending: 50 cm-2 m	Ovate Acute / acuminate apex 15 - 55 x 6 - 28mm	Bilabiate calyx Corolla: Blue	NS	2400-2650	Mountain mesophyll forest Pinus forest Oak forest
<i>S. moniliformis</i>	Perennial-herbaceous Ascending: 40 cm-1 m	Elliptic Acute apex 20 a 35 x 8 - 10 mm	Bilabiate calyx Corolla: Blue	NS	2300-2800	Mountain mesophyll forest Coniferous forest Pinus forest Oyamel forest
<i>S. oreopola</i>	Herbaceous Ascending: ± 40 cm	Deltoid-ovate Acute apex 14 - 40 x 10 - 35 mm	Bilabiate calyx Corolla: Blue	NS	2600	Pinus forest
<i>S. patens</i>	Perennial-herbaceous Ascending: 30 cm-1 m	Ovate to ovate-deltoid Acute apex 50 - 140 x 40 - 120 mm	Bilabiate calyx Corolla: Blue	NS	2500-2800	Quercus forest
<i>S. polystachya</i>	Perennial-herbaceous Arbustive Ascending: 50 cm-3.5 m	Ovate - elliptic Acuminate apex 30 - 140 x 20 - 70 mm	Bilabiate calyx Corolla: Blue-violet/white	Jun.-Nov.	2250-2900	Encino forest Pinus forest Grassland Secondary scrub Disturbed areas
<i>S. prunelloides</i>	Perennial-herbaceous Ascending: 15-40 cm	Rhomboid Ovate-rhomboid / oblong Acute to rounded apex 7 - 60 x 7 - 27 mm	Bilabiate calyx Corolla: Blue	NS	2400-3600	Coniferous forest

Plant name	Habitat	Leaves	Flowers	Flowering	Altitude range (meters)	Vegetation
<i>S. pulchea</i>	Perennial-herbaceous Arbustive Ascending: 1-2 m	Ovate Acute-acuminate apex 25 - 140 x 25 - 60 mm	Bilabiate calyx Corolla: Red	NS	2350-2400	Grassland Xerophytic scrubland
<i>S. reflexa</i>	Perennial-herbaceous Ascending: 20 cm-1 m	Oblong-elliptic / linear Acute apex 15 - 60 x 4 - 10 mm	Bilabiate calyx Corolla: White	NS	2250-2600	Scrub Disturbed areas
<i>S. reptans</i>	Perennial-herbaceous Ascending: 30 cm-1 m	Linear or linear-oblong Acute-rounded apex 5 - 8 x 1 - 5 mm	Bilabiate calyx Corolla: Purple/blue	NS	2300-2700	Pinus forest Encino forest Grassland Scrub Disturbed areas
<i>S. stachyoides</i>	Perennial-herbaceous Ascending: 50 cm-1 m	Elliptic Acute apex 25 - 70 x 7 - 32 mm	Bilabiate calyx Corolla: Blue	NS	2800-3100	Pinus forest Grassland
<i>S. tiliifolia</i>	Perennial-herbaceous Ascending: 20 cm-1.5 m	Ovate-orbicular Acute apex 10 - 50 x 10 - 50 mm	Bilabiate calyx Corolla: Blue	NS	2300-2600	Ruderal weed
<i>S. tubifera</i>	Perennial-herbaceous Ascending: ± 2 m	Ovate-orbicular Acuminate apex 50 - 160 x 40 - 110 mm	Bilabiate calyx Corolla: Scarlet red	NS	2300	Xerophytic scrubland
<i>S. verbenacea</i>	Herbaceous Ascending: ± 20 cm	Ovate-oblong Rounded apex 50 - 90 x 20 - 56 mm	Bilabiate calyx Corolla: Blue	NS	2300	NS

NS: Not specified

Traditional uses and pharmacology

Regarding Traditional Medicine, Mexico is recognized as the second most important country in the world that uses that kind of therapy, with a tremendous ancestral tradition and richness in the use of medicinal plants to treat different diseases and for ritual, only right after China [37]. The different ethnic groups living in Mexico maintain deep and ancestral knowledge of medicinal plants as traditional practices and beliefs about diseases and cures [37]. This cultural legacy dates back to published works written in the 16th century and still survives in modern Mexico [38]. The use and knowledge of medicinal plants by the Mexican population is a common practice for three main reasons: 1) the need to treat diseases, 2) an extensive flora, and 3) the existence of many indigenous groups that preserve their traditions [39]. Unsurprisingly, the population turns to various species of *Salvia* to treat diverse ailments, given the botanical abundance and diversity these plants represent in Mexico.

Table 4 provides a detailed account of the ethnobotanical uses we have documented for the 33 *Salvia* species included in this study. Based on our data, we can infer that leaves are the most frequently employed part of various *Salvia* species. This preference arises due to the ease of leaf collection and the minimal impact on plant viability. In some cases, the complete plant, or other parts of the plant (roots and stem) used are specifically described. Comparing the metabolites expressed in different plant parts is essential to comprehensively understand metabolite synthesis. Investigating whether specific compounds are localized to certain plant regions or distributed uniformly across the entire plant represents a critical avenue for further research.

Of the 33 species registered in the Valle de México, 20 are used for everyday purposes, mainly *S. verbenacea*, *S. polystachya*, *S. lavanduloides*, and *S. elegans* (Fig. 2). These species' most frequently reported uses were gastrointestinal diseases, such as stomach pain and diarrhea. Notably, diarrhea remains a significant health problem in Mexico, ranking as the second most common ailment across all age groups [40]. Additionally, these *Salvia* species find application in promoting childbirth, managing gynecological issues (such as menstrual colic), and serving as antipyretic agents. Furthermore, they are utilized for wound treatment, diabetes management, and respiratory conditions (Table 4).

Pharmacological studies play an essential role in unraveling the therapeutic potential of medicinal plants. In the case of *Salvia* species, approximately 13 out of the 33 species (representing 39 %) have undergone pharmacological scrutiny involving investigations into extracts, fractions, and isolated compounds. A total of 28 distinct pharmacological effects have been documented, with notable prominence given to antioxidant, anti-bacterial, and anti-hyperglycemic properties. Among the studied species (Fig. 2), *S. verbenacea* stands out with 11 reported pharmacological activities, followed by *S. polystachya* (9 activities) and *S. circinata* (5 activities). The predominant mode of preparation for these species involves herbal infusions or tisanes, in which the bioactive compounds are extracted using water and heat [41].

Table 4 provides a comprehensive overview of pharmacological studies across diverse *Salvia* species. Notably, cytotoxic and anticancer activities emerge as promising avenues, offering new prospects for cancer treatment. Some species exhibit anti-bacterial, anti-fungal, and anti-parasitic effects. Other species are also used for treating fever, rheum, and edema, while their anti-inflammatory, antinociceptive, and antipyretic actions are similar to non-steroidal anti-inflammatory drugs (AINEs). The actions at the level of the nervous system, derived by their traditional uses of cultural connotation ("susto," "mal de ojo," "aire"), were recorded as anti-depressants, anxiolytics, and neuroprotective in different experimental conditions.

Interestingly, our pharmacological investigations align with the effects observed in traditional medicine. Specifically, many studies have focused on medicinal plant species' gastrointestinal and gynecological effects. However, it is crucial to emphasize that the number of research validating these plants' traditional uses is limited. For example, while 120 traditional uses have been documented for 20 species, only 42 specific studies have been conducted on 12 *Salvia* species (Fig. 3). Even more pertinent is that only a handful of these studies have developed into identifying the pure compounds responsible for those effects. Some species have yet to be studied; for example, based on this work, species such as *S. filifolia* and *S. laevis* lack pharmacological studies that support the attributed medicinal uses; furthermore, no specific compounds have been identified in these species.

Our comprehensive review underscores the imperative to validate the diverse traditional uses attributed to *Salvia* species. Certain species, such as *S. polystachya* and *S. circinata*, have been associated with hypoglycemic effects through the inhibition of α -glucosidases and sodium-dependent glucose cotransporter-1 (SGLT-1) [28,42]. Furthermore, *Salvia* species find application in hypertension management, with emerging evidence at the vascular level. However, studies supporting these effects in other *Salvia* species remain scarce and underscore the need for multidisciplinary research, including bioassay-guided studies, to validate all traditional uses.

Table 4. Medicinal uses and pharmacological effects of identified *Salvia* species from the Valle de México.

Plant name	Traditional use	Part used											Pharmacological effect	Extract			Ref.
		Cp	Ap	L	B	S	F	R	Sd	Fr	NS	Ext		Frnt	IC		
<i>S. axillaris</i>	Expectorant											X					[70]
<i>S. chamaedryoides</i>	“Espanto”				X								Anti-bacterial	X	X	X	[71–72]
	Abortive											X	Hypoglycemic	X	X	X	
	“Aire”				X												
<i>S. circinata</i>	“Espanto”			X									Anti-conceptive	X	X	X	[16,29, 71-75]
	“Aire”			X									Anti-hyperglycemic	X		X	
	Analgesic											X	Anti-inflammatory	X		X	
	Anti-diabetic			X									Anti-MDR			X	
	Diarrhea			X	X								Cytotoxic			X	
	Helminthiasis												X				
	Lack of appetite			X													
	Menstrual colic			X													
	Rheumatism	X															
	Stomachache												X				
	Ulcers												X				
Vomit			X														

Plant name	Traditional use	Part used										Pharmacological effect	Extract			Ref.
		Cp	Ap	L	B	S	F	R	Sd	Fr	NS		Ext	Frnt	IC	
<i>S. elegans</i>	“Espanto”	X			X							Anti-hypertensive	X	X		[8,39, 71,72, 76-82]
	“Mal de ojo”										X	Anti-depressant	X			
	“Aire”	X										Anxiolytic	X			
	“Aire” (in babies)			X		X	X									
	Anxiety										X					
	Cooling	X														
	Cough										X					
	Fever								X							
	Injured feet										X					
	Insomnia	X		X												
	Knocking / edema			X	X	X		X								
	Measles			X		X		X								
	Pain in the knees										X					
	Postpartum			X		X		X			X					
	Relapse of Ladies						X									
Sick shower			X		X	X										
Skin rashes										X						

Plant name	Traditional use	Part used											Pharmacological effect	Extract			Ref.
		Cp	Ap	L	B	S	F	R	Sd	Fr	NS	Ext		Frnt	IC		
<i>S. elegans</i>	Stimulate saliva											X					[8,39, 71,72, 76-82]
	Stomachache			X		X		X									
	Vomit											X					
<i>S. filifolia</i>	Deposition											X					[83]
<i>S. fulgens</i>	“Fuegos” induced by fever											X					[39,72]
	Sleeping draught				X	X											
	Sleeping draught (infants)			X		X	X										
<i>S. gesneriflora</i>	Diarrhea			X									Antioxidant	X			[40,76, 84,85]
	Stomachache		X										Spasmolytic	X			
													Anti-inflammatory	X			
<i>S. hispanica</i>	Bile											X	Antioxidant	X			[4,39, 84]
	Cathartic											X					
	Cough											X					
	Diarrhea	X							X								
	Expulsion of larvae / foreign bodies from the eyes									X							
	Eye burns											X					
	Labor pain											X					

Plant name	Traditional use	Part used										Pharmacological effect	Extract			Ref.	
		Cp	Ap	L	B	S	F	R	Sd	Fr	NS		Ext	Fr	IC		
<i>S. hispanica</i>	Laxative											X					[4,39, 84]
	Muscle pain			X													
	Nutritional supplement								X								
	Spit blood										X						
<i>S. laevis</i>	Kidney diseases			X													[72,76, 86]
	Promote conception				X												
<i>S. lavanduloides</i>	“Torzón”										X						[39,72, 79,81, 87]
	“Aire”					X											
	Alopecia			X	X												
	Anti-dysentery			X	X												
	Antipyretic			X	X												
	Bronchitis			X	X		X										
	Coldness (children)											X					
	Controlling vaginal bleeding											X					
	Cough			X	X		X										
	Diarrhea											X					
Fever											X						

Plant name	Traditional use	Part used										Pharmacological effect	Extract			Ref.		
		Cp	Ap	L	B	S	F	R	Sd	Fr	NS		Ext	Fr	IC			
<i>S. lavanduloides</i>	Gallbladder condition			X		X	X											[39,72, 79,81, 87]
	Gynecological diseases											X						
	Hemostatic			X	X													
	Oxytocic			X	X													
	Paralysis											X						
	Stomachache											X						
	Toothache											X						
	Vomit											X						
	Wash wounds											X						
	Whooping cough			X	X													
<i>S. leucantha</i>	“Espanto”						X						Anti-bacterial				X	[4,39, 71,72, 76,87- 89]
	Abortive	X		X									Cytotoxic				X	
	“Aire”	X			X													
	Bile (courage)	X																
	Chest/lung pain	X		X														
	Cough			X														
	Kidney Diseases				X							X						

Plant name	Traditional use	Part used										Pharmacological effect	Extract			Ref.	
		Cp	Ap	L	B	S	F	R	Sd	Fr	NS		Ext	Frnt	IC		
<i>S. leucantha</i>	Liver disease				X							X					[4,39, 71,72, 76,87-89]
	Matrix fall						X										
	Menstrual colic			X													
	Postpartum				X												
	Relapse of ladies				X												
	Stomachache	X		X													
	Stops menstruation			X													
<i>S. melissodora</i>	Diarrhea											X				[79,90]	
	Pain											X					
<i>S. mexicana</i>	Bile			X									Anti-inflammatory	X		[72,79, 91,92].	
	Diarrhea			X									Antioxidant	X			
	Menstrual colic			X													
	Promote conception	X															
	Stomachache											X					
<i>S. microphylla</i>	“Empacho”	X			X							X	Anti-microbial			[39-40,72, 76,83, 84,89, 93,94]	
	“Espanto”	X		X	X							X					
	“Mal de ojo”						X										

Plant name	Traditional use	Part used											Pharmacological effect	Extract			Ref.	
		Cp	Ap	L	B	S	F	R	Sd	Fr	NS	Ext		Frnt	IC			
<i>S. microphylla</i>	“Aire”																	
	Anti-dysentery			X	X													
	Bile											X						
	Bone strengthening																	
	Diarrhea			X								X						
	Earache			X														
	Gynecological diseases	X																
	Headache			X														
	Insomnia				X													
	Leg scald				X													
	Menstrual colic			X								X						
	Nerves						X											
	Postpartum baths			X	X													
	Promote conception				X							X						
	Stomachache			X	X													
Waist pain				X														

[39-40,72,76,83,84,89,93,94]

Plant name	Traditional use	Part used										Pharmacological effect	Extract			Ref.
		Cp	Ap	L	B	S	F	R	Sd	Fr	NS		Ext	Frnt	IC	
<i>S. misella</i>	Bruising			X		X						Antioxidant	X			[39,95,96]
	Erysipelas			X			X									
	Skin rashes					X										
	Warts			X		X										
	Wash wounds			X		X										
<i>S. patens</i>	Children's restroom (3 months)										X					[77]
	Infected wounds										X					
	Joint heating										X					
<i>S. polystachya</i>	Anti-abortion				X							Anti-protozoal	X			[39-40,72,76,83,84,89,93,94]
	Anti-diuretic										X	Anti-amoebic			X	
	Anti-dysentery								X			Anti-giardial			X	
	Anti-gastric										X	Anti-hyperglycemic	X	X	X	
	Anti-hemorrhagic										X	Antioxidant	X			
	Anti-malarial										X	Acts over dermal fibroblast expression			X	
	Antipyretic										X	Protective (Cerebral ischemia)	X			
	Scabies										X	α -Glucosidase Inhibitor			X	

Plant name	Traditional use	Part used										Pharmacological effect	Extract			Ref.
		Cp	Ap	L	B	S	F	R	Sd	Fr	NS		Ext	Fr	IC	
<i>S. polystachya</i>	Diarrhea				X							SGLT1 Inhibitor			X	[39-40,72,76,83,84,89,93,94]
	Diuretic				X											
	Emollient										X					
	Flu										X					
	Gastritis				X											
	Hair growth				X											
	Headache				X											
	Menstrual colic				X											
	Nosebleed			X	X											
	Parasites				X											
	Promote conception	X														
	Purgative				X							X				
	Stomachache											X				
	Wounds disinfect	X														
Wound healing	X															
<i>S. reflexa</i>	Stomach affections	X													[72]	

Plant name	Traditional use	Part used										Pharmacological effect	Extract			Ref.	
		Cp	Ap	L	B	S	F	R	Sd	Fr	NS		Ext	Fr	IC		
<i>S. reptans</i>	Diarhea	X			X	X							Anti-bacterial	X	X	X	[72,94]
	Fever	X															
	Stomachache	X			X	X											
	Swelling	X				X											
	Twists	X															
	Wound healing	X															
<i>S. tiliifolia</i>	Abscesses										X	Neuroprotective			X	[39,91, 92,95, 96,101]	
	Mumps										X						
	Snake bite										X						
	Vomit										X						
<i>S. verbenacea</i>	Abscesses	X		X								Anti-bacterial				[20]	
	“Aire”	X										Anticancer					
	Anti-hypertensive						X					Anti-fungal					
	Antipyretic			X								Anti-hemolytic					
	Anti-rheumatic			X								Anti-hyperglycemic					
	Antiseptic			X								Anti-hypertensive					
	Anti-spasmodic	X		X								Anti-leishmanial					

Plant name	Traditional use	Part used											Pharmacological effect	Extract			Ref.
		Cp	Ap	L	B	S	F	R	Sd	Fr	NS	Ext		Fr	IC		
<i>S. verbenacea</i>	Anti-sweat		X	X									Antioxidant				[20]
	Anxiety											X	Anti-parasitic				
	Astringent		X	X									Immunomodulatory				
	Carminative		X	X									Inhibitory effect of xanthine oxidase				
	Wound healing	X		X			X	X			X		Skin effect				
	Cooling			X													
	Contusion		X														
	Cough	X															
	Dermatological		X														
	Diabetes		X														
	Digestive problems		X	X						X							
	Disinfectant		X	X													
	Diuretic			X													
	Fever			X													
	Genitourinary			X													
	Healing			X													
Healing of burns	X		X														

Plant name	Traditional use	Part used										Pharmacological effect	Extract			Ref.	
		Cp	Ap	L	B	S	F	R	Sd	Fr	NS		Ext	Frct	IC		
<i>S. verbenacea</i>	Insomnia											X					[20]
	Laryngitis			X													
	Menstrual colic			X													
	Respiratory problems			X													
	Stomachache	X															
	Vulnerary		X	X													
	Wound treatment			X													
	Wound eyes			X													

Cp = Complete plant; Ap = Aerial parts, L = leaf; B = Branch; S = Steam; F = Flower; R = Root; Sd = Seed; Fr = Fruit; NS = Not specified; Ext = Extract; Fr = Fraction; IC = Isolated compound

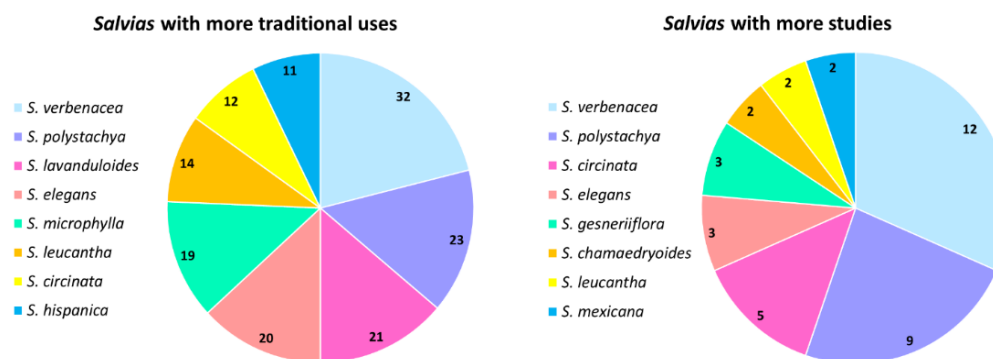


Fig. 2. Salvias traditionally more used and with more pharmacological studies.

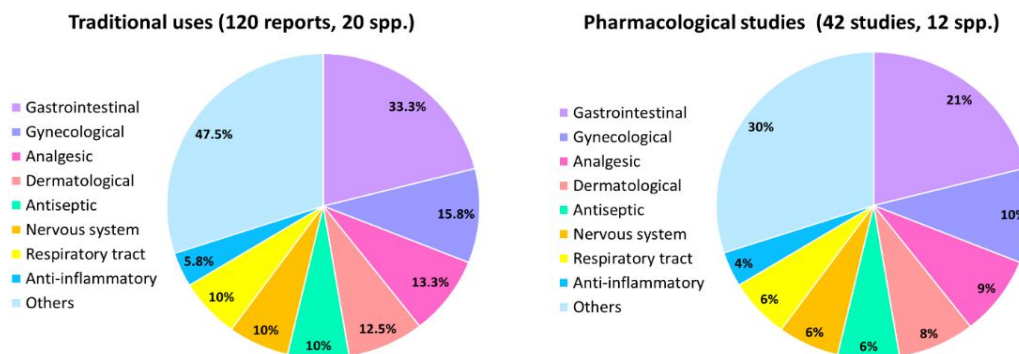


Fig. 3. More frequent traditional uses of *Salvias* and its most studied pharmacological effects.

Phytochemical studies

During the 1980s and 1990s, several research groups in Mexico, led by Alfredo Ortega, Lydia Rodriguez-Hahn, and Baldomero Esquivel, initiated innovative research focused on identifying compounds from extracts of Mexican sages. These first studies laid the foundation for subsequent research due to the rich content of secondary metabolites, including terpenoids and flavonoids. [43-47]. The aerial parts of these *Salvia* species, especially the flowers and leaves, harbor phenolic compounds, including flavonoids and terpenoids (such as monoterpenoids, diterpenoids, and triterpenoids); interestingly, diterpenoids were predominantly localized in the roots [46].

In conjunction with other phytochemical studies, we compiled information in Table 5 from 56 sources that report on compounds from 20 *Salvia* species, resulting in a total of 315 identified compounds (Fig. 4). Among these, *S. leucantha* stands out with an impressive 92 reported compounds, followed closely by *S. verbenacea* (81 compounds) and *S. circinata* (34 compounds). Notably, 43 of these compounds are described in more than one species, highlighting β -sitosterol, as well as ursolic and oleanolic acids that were reported in 8 and 7 different species of *Salvia*, respectively, compounds that have been identified as the most common terpenes in the *Salvia* genus [45,46], evidencing the phylogenetic relationships in these species.

Phenolic compounds and terpenoids are the main components in fruits, vegetables, and various spices used for nutritional purposes [48]. Interestingly, the therapeutic active principles in several plant-derived medicinal extracts are also flavonoids and terpenoids [49,50]. In plants, terpenoids exhibit the most remarkable structural diversity, which includes diverse subclassifications. For example, the diterpenoids could be classified as clerodanes, kauranes, abietanes, or casbanes, to name a few [51]. They provide a chemical defense against environmental stress and a mechanism to repair wounds and injuries. In addition, mainly monoterpenes are usually responsible for the characteristic fragrance of many plants (pollinator attraction). On the other hand, high concentrations of terpenoids can be toxic and, therefore, constitute an essential weapon against herbivores and pathogens, such as anti-food or insecticides [44,51-54].

In recent years, there has been growing pharmacological interest in these compounds due to their diverse biological activities that can focus on the prevention and therapy of various diseases, as documented in various studies. Our research data further support this trend, revealing that many of the 315 compounds documented (Table 5) are terpenoids (mainly diterpenes, sesquiterpenes, and monoterpenes). While the phytochemical studies on *Salvia* species do not explicitly focus on identifying biological effects, some working groups have determined that diterpenes stand out mainly for their anti-inflammatory, antitumor, anti-diabetic, and antiviral activities. The monoterpenes show anti-microbial activity against pathogens such as *Mycobacterium tuberculosis* [55] and inhibit the growth of fungi such as *Rhizoctonia solani* [56]. For their part, sesquiterpenes have been shown to have a broad spectrum of biological activities that include anti-microbial, cytotoxic, anti-inflammatory, anti-bacterial, anticancer, antiviral, and anti-fungal properties, in addition to exerting effects on the central nervous and cardiovascular systems [57].

As previously mentioned, among the most reported compounds in these *Salvias* species are the pentacyclic triterpenes: the ursolic acid, a triterpenoid, is extensively studied and boasts a multitude of biological effects: it acts as an insulin mimetic, insulin sensitizer, anti-inflammatory, antioxidant, anticancer, anti-obesity,

anti-diabetic, antiangiogenic, anti-microbial, cardioprotective, neuroprotective, hepatoprotective, anti-skeletal muscle atrophy and thermogenic [31,58-60]. Likewise, oleanolic acid, an isomer of ursolic acid, has effects such as hepatoprotective, anti-inflammatory, anti-hyperglycemic, antioxidant, anticancer, and neuroprotective [42,60,61]. Another noteworthy compound reported in various *Salvias* species is β -sitosterol, a phytosterol whose chemical structure is similar to cholesterol, which has diverse biological actions described that include anxiolytic, sedative, analgesic, angiogenic, anthelmintic, antimutagenic, immunomodulatory, anti-bacterial, anticancer, anti-inflammatory, genotoxic, hypolipidemic, hypocholesterolemic, hepatoprotective, and respiratory diseases; furthermore, β -sitosterol promotes wound healing and exhibits antioxidant and anti-diabetic effects [62,63].

Another important group of compounds in the *Salvia* species are the flavonoids, a class of polyphenolic compounds that are naturally biosynthesized in plants. The subgroups of flavonoids include flavones, flavonols, flavanones, flavanonols, anthocyanidins, flavanols, and isoflavones [64,65]. Flavonoids have long been known to be synthesized at specific sites. They are responsible for the color and aroma of flowers and fruits to attract pollinators, protect plants from different biotic and abiotic stresses, and act as unique UV filters, detoxifying agents, and defensive anti-microbial compounds [64-67]. These natural products are well known for their beneficial effects on health, such as anti-diabetic, antiulcer, antiviral, antioxidant, anti-inflammatory, antimutagenic, cytotoxic, and anticarcinogenic [64,65,68].

The diverse compounds described from the *Salvia* species (Fig. 4) are evidence of structural variability, mainly from the terpenoid structures, where a minimum change in the position or the presence and absence of some functional groups changes the type of compound reported. This, in turn, could generate a different activity that can be observed in biological assays [28]. Besides, some of the same compounds in different species could not be at the same concentration [30,69] and might affect the expected effect.

Table 5. Isolated compounds of *Salvia* species from Valle de México.

Scientific name	Parts used	Extract(s) used	No.	Classification	Compounds	Ref..
<i>S. axillaris</i>	Aerial parts Roots	Acetone	1	Terpenoid	20-nor-abietane cryptotanshinone (cryptotanshinone)	[23, 102]
<i>S. chamaedryoides</i>	Aerial parts	Dichloromethane	-	-	Furano diterpenes	[22]
			2	Terpenoid	7 α -hydroxybacchotricuneatin A	
			3	Polyphenol	Galdosol	
			4	Polyphenol	Rosmanol	
			5	Terpenoid	Salvimicrophyllin B	
			6	Terpenoid	Splendidin C	
			7	Terpenoid	Tilifodiolide	
<i>S. circinata</i>	Aerial parts Flowers Leaves	Acetone: Methanol Ethyl acetate Hexane Methanol Aqueous	8	Terpenoid	(<i>E</i>)-pinocarvyl acetate	[18, 23, 29, 73, 103- 105]
			9	Flavonoid	2-(3,4-dimethoxy phenyl)-5,6-dihydroxy-7-methoxy-4H-chromen-4-one	
			10	Aromatic	3-methoxy- <i>p</i> -cymene	
			11	Flavonoid	5,6,4'-trihydroxy-7,3'-dimethoxyflavone	

Scientific name	Parts used	Extract(s) used	No.	Classification	Compounds	Ref.
<i>S. circinata</i>	Aerial parts Flowers Leaves	Acetone: Methanol Ethyl acetate Hexane Methanol Aqueous	12	Flavonoid	5,7- <i>O</i> -diacetylacetin	[18, 23, 29, 73, 103-105]
			13	Flavonoid	6-hydroxy luteolin	
			14	Terpenoid	Acetylarissinin B	
			15-21	Terpenoid	Amarisolide A-G	
			22-25	Terpenoid	Amarissinins A-D	
			26	Flavonoid	Apigenin	
			27	Flavonoid	Apigenin-7- <i>O</i> - β -D-glucoside	
			28	Polyphenol	Caffeic acid	
			29	Polyphenol	Chlorogenic acid	
			30	Phenol	Ferulic acid	
			31	Terpenoid	Germacrene D	
			32	Flavonoid	Iso-quercitrin	
			33	Terpenoid	Oleanolic acid	
			34	Flavonoid	Pedalitin	
			35	Flavonoid	Phloretin	
			36	Flavonoid	Phlorizin	
			37	Flavonoid	Quercetin	
			38	Phenylpropanoid	Rosmarinic acid	
			39	Flavonoid	Rutin	
			40	Terpenoid	Spathulenol	
41	Terpenoid	Teotihuacanin				
42	Terpenoid	Ursolic acid				
43	Terpenoid	α -amyrin				
44	Terpenoid	α -bourbonene				
45	Terpenoid	α -caryophyllene				
46	Terpenoid	β -caryophyllene				
47	Terpenoid	β -selinene				

Scientific name	Parts used	Extract(s) used	No.	Classification	Compounds	Ref.
<i>S. circinata</i>	Aerial parts Flowers Leaves	Acetone: Methanol Ethyl acetate Hexane Methanol Aqueous	48	Terpenoid	β -sitosterol	[18, 23, 29, 73, 103-105]
			49	Terpenoid	δ -elemene	
<i>S. elegans</i>	Flowers Leaves Seeds	Aqueous ethanol	50	Alcohol	2-propanol	[8,80, 82,106]
			51	Flavonoid	3-acetoxy-7-methoxyflavone	
			52	Alcohol	3-octanol	
			53	Amino acid	Cystine	
			31	Terpenoid	Germacrene D	
			54	Terpenoid	Hederagenin (3 β ,23-dihydroxyolean12-en-28-oic)	
			55	Terpenoid	Linalool	
			56	Fatty acid	Linoleic acid	
			57	Fatty acid	Linolenic acid	
			58	Amino acid	Lysine	
			59	Amino acid	Methione	
			33	Terpenoid	Oleanolic acid	
			40	Terpenoid	Spathulenol	
			60	Aldehyde	<i>trans</i> -3-hexenal	
61	Terpenoid	<i>trans</i> -ocimene				
42	Terpenoid	Ursolic acid				
46	Terpenoid	β -caryophyllene				
<i>S. fulgens</i>	Aerial parts	Acetone	62	Terpenoid	10 β -hydroxybacchotricuneatin A (Bacchotricuneatin A)	[19, 23, 24, 107-110]
			63	Terpenoid	<i>nt</i> -19-acetoxy-15,16-epoxy-6-hydroxy-3,13(16),14-clerodatrien-18-al	
			64	Terpenoid	<i>ent</i> -19- <i>O</i> -acetoxy-15,16-epoxy-3,13(16),14-clerodatrien-6,18-diol	
			65	Terpenoid	7 α -hydroxy-neoclerodane-3,13-diene-18,19:15,16-diolide	

Scientific name	Parts used	Extract(s) used	No.	Classification	Compounds	Ref.
<i>S. fulgens</i>	Aerial parts	Acetone	66	Terpenoid	Dehydrokerlin	[19, 23, 24, 107-110]
			67	Terpenoid	Salvifulgenolide	
			68	Terpenoid	Salvigenolide	
			69	Terpenoid	Sandaracopimaric acid	
			70	Terpenoid	<i>trans</i> -1,2-dihydrosalvifaricin	
			48	Terpenoid	β -sitosterol	
<i>S. gesneriiflora</i>	Aerial parts	Methanol Hexane Dichloromethane	-	-	Alkaloids	[85, 111]
			-	-	Anthraquinones	
			-	-	Coumarins	
			-	-	Saponins	
			28	Polyphenol	Caffeic acid	
			29	Polyphenol	Chlorogenic acid	
			38	Phenylpropanoid	Rosmarinic acid	
			42	Terpenoid	Ursolic acid	
			68	Terpenoid	Salvigenolide	
<i>S. hirsute</i>	Roots	Acetone	71	Terpenoid	14-deoxycoleon U	[112]
			72	Terpenoid	7 α -acetoxy-royleanone	
			73	Terpenoid	8,11,13-abietatriene	
			74	Terpenoid	8,13-abietadiene	
			75	Terpenoid	Cryptojaponol	
			76	Terpenoid	Demethylcryptojaponol	
			77	Terpenoid	Royleanone	
			78	Terpenoid	Salviplomone	
			79	Terpenoid	Sugiol	
			80	Terpenoid	Taxodione	

Scientific name	Parts used	Extract(s) used	No.	Classification	Compounds	Ref.
<i>S. hispánica</i>	Seeds	Ethanol Methanol Hydrochloric acid in ethanol	28	Polyphenol	Caffeic acid	[4, 113, 114]
			29	Phenol	Chlorogenic acid	
			81	Flavonoid	Daidzin	
			82	Polyphenol	Gallic acid	
			83	Flavonoid	Kaempferol	
			84	Ethyl ester	Protocatechuic ethyl ester	
			37	Flavonoid	Quercetin	
			38	Phenylpropanoid	Rosmarinic acid	
			85	Fatty acid	α -linolenic acid	
<i>S. keerlii</i>	Aerial parts	Acetone	86	Terpenoid	Kerlin	[23, 108, 115]
			87	Terpenoid	Kerlinic acid	
			88	Terpenoid	Kerlinolide	
<i>S. lavanduloides</i>	Aerial parts Flowers Roots	Acetone Methanol	72	Terpenoid	7 α -acetoxy-royleanone	[19, 23, 108, 111, 116- 118]
			89	Terpenoid	Horminone	
			90-94	Terpenoid	Salvianduline A-E	
			42	Terpenoid	Ursolic acid	
			48	Terpenoid	β -sitosterol	
<i>S. leucantha</i>	Aerial parts Flowers	Acetone Chloroform Methanol Hexane	95	Terpenoid	1,10-di- <i>epi</i> -cubenol	[19, 21, 24, 39, 76, 88, 89, 107, 118- 120]
			96	Terpenoid	1,8-cineole	
			97	Alcohol	1-octen-3-ol	
			98	Terpenoid	20-hydroxydugesin B	
			99	Terpenoid	2- <i>epi</i> -6,7-dihydrosalviandulin E	
			100	Terpenoid	3- <i>epi</i> -tilifodiolide	
			101	Ketone	3-octanone	
			102	Terpenoid	3 β -methoxyisopuberulin	
			103	Ketone	4-methylene-isophorone	
			104	Terpenoid	6,7-dehydrodugesin A	

Scientific name	Parts used	Extract(s) used	No.	Classification	Compounds	Ref.
<i>S. leucantha</i>	Aerial parts Flowers	Acetone Chloroform Methanol Hexane	105	Terpenoid	6,7-dehydrodugesin B	[19, 21, 24, 39, 76, 88, 89, 107, 118-120]
			106	Terpenoid	6,7-dihydrosalviandulin E	
			107	Terpenoid	7- <i>epi</i> - α -eudesmol	
			108	Aromatic	Apiole	
			109	Terpenoid	Aromadendrene	
			110	Terpenoid	Bicyclogermacrene	
			111	Terpenoid	Borneol	
			112	Terpenoid	Bornyl acetate	
			113	Terpenoid	Camphene	
			114	Terpenoid	Cedrene	
			115	Terpenoid	<i>cis</i> -cadin-4-en-7-ol	
			116	Terpenoid	<i>cis</i> -muurola-3,5-diene	
			117	Terpenoid	Citral	
			118	Terpenoid	Citronellal	
			119	Terpenoid	Citronellol	
			120	Ketone	Dehydrosabinaketone	
			121	Terpenoid	De- <i>O</i> -acetylsalvigenolide	
			122	Benzodioxol	Dillapiol	
			123	Terpenoid	Dugesin B	
			100	Terpenoid	3- <i>epi</i> -tilifodiolide	
			124	Terpenoid	Eremoligenol	
			125	Terpenoid	Eudesma-4(15)7-dien-1 β -ol	
126	Terpenoid	Geraniol				
127	Terpenoid	Geranyl acetate				
128-129	Terpenoid	Germacrene A, B				
31	Terpenoid	Germacrene D				
130	Terpenoid	Globulol				

Scientific name	Parts used	Extract(s) used	No.	Classification	Compounds	Ref.
<i>S. leucantha</i>	Aerial parts Flowers	Acetone Chloroform Methanol Hexane	131	Terpenoid	Guaiol	[19, 21, 24, 39, 76, 88, 89, 107, 118-120]
			132	Alcohol	Heptanol	
			133	Terpenoid	Hinesol	
			134	Terpenoid	Isocaryophyllene	
			135	Flavonoid	Isosalipurpol	
			136	Terpenoid	Isosalviperulin (Isoperulin)	
			137	Terpenoid	Isothujanol	
			139-142	Terpenoid	Leucansalvialin F-J	
			55	Terpenoid	Linalool	
			143	Terpenoid	Linalyl acetate	
			144	Terpenoid	Linalyl formate	
			145	Terpenoid	<i>neo-α</i> -clovene	
			146	Aldehyde	Nonanal	
			147	Terpenoid	<i>p</i> -cymene	
			148	Flavonoid	Quercetin-3- <i>O</i> - α -L-rhamnopyranosyl-(1 \rightarrow 6)- β -D-glucopyranoside	
			90-94	Terpenoid	Salvianduline A-E	
			149	Terpenoid	Salvifaricin	
			150-153	Terpenoid	Salvileucalin A-D	
			154	Terpenoid	Salvileucantholide	
			155-158	Terpenoid	Salvileucanthsin A-D	
			40	Terpenoid	Spathulenol	
			159	Terpenoid	Spiroleucantholide	
			160	Terpenoid	Terpinen-4-ol	
161	Terpenoid	Terpinolene				
7	Terpenoid	Tilifodiolide				
162	Terpenoid	Tiliifolin C				
163	Terpenoid	<i>t</i> -muurolol				

Scientific name	Parts used	Extract(s) used	No.	Classification	Compounds	Ref.
<i>S. leucantha</i>	Aerial parts Flowers	Acetone Chloroform Methanol Hexane	164	Terpenoid	<i>trans</i> -calamenen-10-ol	[19, 21, 24, 39, 76, 88, 89, 107, 118-120]
			165	Terpenoid	<i>trans</i> -calamenene	
			166	Terpenoid	<i>trans</i> - β -farnesene	
			167	Terpenoid	Viridiflorol	
			168	Terpenoid	α -bulnesene	
			169	Terpenoid	α -cadinene	
			170	Terpenoid	α -cadinol	
			171	Terpenoid	α -copaene	
			172	Terpenoid	α -guaiene	
			173	Terpenoid	α -humulene	
			174	Terpenoid	α -muurolol	
			175	Terpenoid	α -pinene	
			176	Terpenoid	α -terpineol	
			177	Terpenoid	β -acoradiene	
			178	Terpenoid	β -atlantol	
			179	Terpenoid	β -bourbonene	
			46	Terpenoid	β -caryophyllene	
			180	Terpenoid	β -copaen-4 α -ol	
			181	Terpenoid	β -elemene	
			182	Terpenoid	β -gurjunene	
			183	Terpenoid	β -phellandrene	
			184	Terpenoid	β -pinene	
			185	Terpenoid	β -thujone	
186	Terpenoid	γ -cadinene				
187	Terpenoid	γ -terpinene				
188	Terpenoid	δ -cadinene				
49	Terpenoid	δ -elemene				

Scientific name	Parts used	Extract(s) used	No.	Classification	Compounds	Ref.
<i>S. melissodora</i>	Aerial parts	Acetone Ethyl acetate	189	Terpenoid	1-isopropyl-4b,8,8-trimethyl-9-oxo-4b,5,6,7,8,8a,9,10-octahydrophenanthrene-2,3,10-triyl triacetate	[19, 23, 108, 122, 123]
			190	Terpenoid	2 α -hydroxy-7 α -acetoxy-12-oxo-15:16-epoxy-neoclerodan-3,13(16),14-trien-18: 19-olide	
			191	Terpenoid	2 β -7 α -dihydroxy- <i>ent</i> -cleroda-3,13-diene-18,19:16,15-diolide	
			192	Terpenoid	2 β -acetoxy-7 α -hydroxy- <i>ent</i> -cleroda-3,13-diene-18,19:16,15-diolide	
			193	Terpenoid	2 β -hydroxy-7-oxo- <i>ent</i> -cleroda-3,13-diene-18,19:16,15-diolide	
			194	Terpenoid	2 β -hydroxy- <i>ent</i> -cleroda-3,13-diene-18,19:16,15-diolide	
			195	Terpenoid	7-oxo- <i>ent</i> -cleroda-3,13-diene-18,19:16,15-diolide	
			196	Terpenoid	7 α -acetoxy-2 β -hydroxy- <i>ent</i> -cleroda-3,13-diene-18,19:16,15-diolide	
			197	Terpenoid	7 α -acetoxy- <i>ent</i> -cleroda-3,13-diene-18,19:16,15-diolide	
			198	Terpenoid	7 α -hydroxy- <i>ent</i> -cleroda-3,13-diene-18,19:16,15-diolide	
			65	Terpenoid	7 α -hydroxy-neoclerodane-3,13-diene-18,19:15,16-diolide	
			199	Terpenoid	7 β -18,19-trihydroxy- <i>ent</i> -cleroda-3,13-dien-16,15-olide	
			200	Terpenoid	7 β -hydroxy- <i>ent</i> -cleroda-3,13-diene-18,19:16,15-diolide	
			201	Terpenoid	Brevifloralactone	
			202	Terpenoid	Maytenoquinone	
			203	Terpenoid	Melisodoric acid	
			33	Terpenoid	Oleanolic acid	
204	Terpenoid	Portulide C				
42	Terpenoid	Ursolic acid				
48	Terpenoid	β -sitosterol				

Scientific name	Parts used	Extract(s) used	No.	Classification	Compounds	Ref..
<i>S. mexicana</i>	Aerial parts Flowers Leaves	Acetone Chloroform Hexane Methanol	205	Terpenoid	Arbutin	[92]
			206	Terpenoid	Betulinic acid	
			207	Terpenoid	Betulinol	
			208	Terpenoid	Salvimexicanolide	
			209	Terpenoid	Salviolide	
			42	Terpenoid	Ursolic acid	
			48	Terpenoid	β -sitosterol	
<i>S. microphylla</i>	Aerial parts Leaves Stems Roots	Acetone	210	Terpenoid	12-methoxycamosic acid	[19, 25, 108, 124, 125]
			211	Terpenoid	14 α -18-dihydroxyisopimaradiene	
			212	Terpenoid	14 α -hydroxyisopimaric acid	
			213	Phenolic ester	2-(<i>p</i> -hydroxyphenyl) ethyl eicosaheptanoic acid ester	
			214	Terpenoid	7,15-isopimaradien14 α , 18-diol	
			215	Terpenoid	7-oxo-sandaracopimarate	
			216	Terpenoid	7-oxo-sandaracopimaric acid	
			217	Terpenoid	7 α -acetoxisopimara-8(14),15-diene-18-oic acid	
			218	Terpenoid	7 α -acetoxysandaracopimaric acid	
			65	Terpenoid	7 α -hydroxy-neoclerodane-3,13-diene-18,19:15,16-diolide	
			219	Terpenoid	7 α -hydroxysandaracopimaric acid	
			220	Terpenoid	8(14),15-sandaracopimaradien-7 α ,18-diol	
			221	Carcocyclic	8 α -hydroxy- β -eudesmol	
			222	Ester	Eicosaheptanoic acid 2-(<i>p</i> -hydroxyphenyl) ethyl ester	
			223	Terpenoid	Erithrodiol 3-acetate	
224	Cumaric acid	Hexacosylferulate				
225	Terpenoid	Lupeol				

Scientific name	Parts used	Extract(s) used	No.	Classification	Compounds	Ref.
<i>S. microphylla</i>	Aerial parts Leaves Stems Roots	Acetone	215	Terpenoid	Methyl 7-oxosandaracopimarate	[19, 25, 108, 124, 125]
			226	Terpenoid	Methyl 7 α -hydroxysandaracopimarate	
			227	Terpenoid	Microphyllandioliide	
			33	Terpenoid	Oleanolic acid	
			5	Terpenoid	Salvimicrophyllin B	
			228-230	Terpenoid	Salvimicrophyllins A, C, D	
			220	Terpenoid	Sandaracopimara-8(14),15-diene-7 α ,18-diol	
			42	Terpenoid	Ursolic acid	
			231	Terpenoid	β -eudesmol	
			48	Terpenoid	β -sitosterol	
<i>S. patens</i>	Flowers	Aqueous	232	Flavonoid	Protodelphin	[126]
<i>S. polystachya</i>	Aerial parts Flowers Leaves Stems	Acetone Acetone: Methanol Ethanol	233	Terpenoid	15- <i>epi</i> -polystachyne G	[17, 23, 42, 98, 100, 107]
			234	Flavonoid	3',5,6,7-tetrahydroxy-4'-methoxyflavone	
			66	Terpenoid	Dehydrokerlin	
			235	Terpenoid	Linearolactone	
			33	Terpenoid	Oleanolic acid	
			236-243	Terpenoid	Polystachines A-H	
			149	Terpenoid	Salvifaricin	
			244-247	Terpenoid	Salvifilines A-E	
			42	Terpenoid	Ursolic acid	
<i>S. reflexa</i>	Leaves	Acetone	248	Terpenoid	15,16-epoxy-8 α -hydroxyneocleroda-2,13(16),14-triene-17,12R:18,19-diolide	[127]
			249	Terpenoid	6 β -hydroxysalviarin	
			250	Terpenoid	8 α -hydroxysalviarin	

Scientific name	Parts used	Extract(s) used	No.	Classification	Compounds	Ref.
<i>S. reflexa</i>	Leaves	Acetone	33		Oleanolic acid	[127]
			251	Terpenoid	Salviarin	
			48	Terpenoid	β -sitosterol	
<i>S. reptans</i>	Aerial parts Roots	Acetone n-hexane	252	Terpenoid	1 α ,2 α -epoxy-3,4 α -dihydrolinearolactone	[23, 19, 93, 108, 128]
			253	Terpenoid	8 α ,9 α -epoxy-7-ketoroyleanone	
			254	Terpenoid	Diosmetin	
			89	Terpenoid	Horminone	
			235	Terpenoid	Linearolactone	
			33	Flavonoid	Oleanolic acid	
			255	Terpenoid	Salvireptanolide	
			42	Terpenoid	Ursolic acid	
<i>S. tiliifolia</i>	Aerial parts Roots	Acetone	104	Terpenoid	6,7-dehydrodugesin A	[76, 101, 23, 108, 129, 130]
			256-257	Terpenoid	Dugesins A, B	
			258	Phenol	Ferruginol	
			136	Terpenoid	Isosalvipuberulin (Isopuberulin)	
			259	Terpenoid	Puberulin	
			94	Terpenoid	Salvianduline E	
			149	Terpenoid	Salvifaricin	
			260	Terpenoid	Salvifolin	
			261	Terpenoid	Salyunnanins I	
			262	Terpenoid	Tilifolidione	
<i>S. verbenacea</i>	Fruits Leaves Roots Seeds Stems	Essential oils Methanol Petroleum ether	263	Aldehyde	(<i>E</i>)-2-hexenal	[23]
			264	Terpenoid	(<i>E</i>)-caryophyllene	
			265	Terpenoid	(<i>E</i>)- β -caryophyllene	
			266	Terpenoid	(<i>E</i>)- β -farnesene	
			267	Terpenoid	(<i>E</i>)- β -ionone	

Scientific name	Parts used	Extract(s) used	No.	Classification	Compounds	Ref.
<i>S. verbenacea</i>	Fruits Leaves Roots Seeds Stems	Essential oils Methanol Petroleum ether	268	Terpenoid	(<i>E</i>)- β -ocimene	[23]
			269	Carboxylic acid	(<i>Z</i>)-9-octadecenoic acid	
			270	Terpenoid	(<i>Z</i>)- β -ocimene	
			95	Terpenoid	1,10-di- <i>epi</i> -cubenol	
			96	Terpenoid	1,8-cineole	
			271	Terpenoid	13- <i>epi</i> -manool	
			272	Terpenoid	2,3-dihydro-1,4-cineol	
			273	Terpenoid	4-terpeniol	
			274	Flavonoid	5-hydroxy-3,4',7'-trimethoxyflavone	
			275	Flavonoid	5-hydroxy-7,4'-dimethoxyflavone	
			276	Terpenoid	6-13-hydroxy-7 α -acetoxyroleanone	
			277	Aldehyde	9,12,15-Octadecatrienal	
			26	Flavonoid	Apigenin	
			278	Aromatic	Benzaldehyde	
			110	Terpenoid	Bicyclogermacrene	
			28	Polyphenol	Caffeic acid	
			113	Terpenoid	Camphene	
			279	Terpenoid	Camphor	
			280	Terpenoid	Camosic acid	
			281	Terpenoid	Caryophyllene oxide	
			282	Flavonoid	Cirsilineol	
			283	Flavonoid	Cirsiliol	
116	Terpenoid	<i>cis</i> -muuro-la-3,5-diene				
184	Terpenoid	<i>cis</i> -muuro-la-4(14),5-diene				
164	Terpenoid	<i>E</i> -Caryophyllene				
181	Terpenoid	<i>epi</i> -13-manool				

Scientific name	Parts used	Extract(s) used	No.	Classification	Compounds	Ref.
<i>S. verbenacea</i>	Fruits Leaves Roots Seeds Stems	Essential oils Methanol Petroleum ether	185	Terpenoid	<i>epi-α</i> -cadinol	[23]
			186	Acetate	Ethyl hexadecanoate	
			30	Terpenoid	Ferulic acid	
			31	Flavonoid	Germacrene D	
			287	Flavonoid	Hesperidin	
			288	Fatty acid	Hexadecanoic acid	
			89	Terpenoid	Horminone	
			289	Terpenoid	Limonene	
			55	Terpenoid	Linalool	
			56	Fatty acid	Linoleic acid	
			290	Flavonoid	Luteolin	
			291	Terpenoid	Manool	
			292	Terpenoid	Methyl carbonate	
			293	Fatty acid	Methyl ester of 6-octadecenoic acid	
			294	Terpenoid	Methyl eugenol	
			295	Flavonoid	Naringenin	
			296	Alkane	Nonane	
			297	Alkane	Octane	
			298	Fatty acid	Oleic acid	
			147	Terpenoid	<i>p</i> -cymene	
			299	Aromatic	Phenyl acetaldehyde	
			300	Aromatic	<i>p</i> -hydroxybenzoic acid	
			301	Terpenoid	Phytol	
			302	Flavonoid	Retusin	
38	Phenylpropanoid	Rosmarinic acid				
303	Terpenoid	Sabinene				
304	Flavonoid	Salvigenin				

Scientific name	Parts used	Extract(s) used	No.	Classification	Compounds	Ref..
<i>S. verbenacea</i>	Fruits Leaves Roots Seeds Stems	Essential oils Methanol Petroleum ether	305	Terpenoid	Salvinine	[23]
			40	Terpenoid	Spathulenol	
			80	Terpenoid	Taxodione	
			161	Terpenoid	Terpinolene	
			306	Terpenoid	<i>trans</i> -sabinene hydrate	
			307	Alkane	Tricosane	
			308	Terpenoid	Tricyclene	
			309	Terpenoid	Verbenacine	
			310	Flavonoid	Verbenacoside	
			167	Terpenoid	Viridiflorol	
			171	Terpenoid	α -copaene	
			173	Terpenoid	α -humulene	
			175	Terpenoid	α -pinene	
			311	Terpenoid	α -terpinyl acetate	
			312	Terpenoid	α -thujene	
			46	Terpenoid	β -caryophyllene	
			231	Terpenoid	β -eudesmol	
			193	Terpenoid	β -phellandrene	
			313	Terpenoid	γ -amorphene	
			186	Terpenoid	γ -cadinene	
188	Terpenoid	δ -cadinene				
314	Terpenoid	δ -selinene				

Fig. 4.

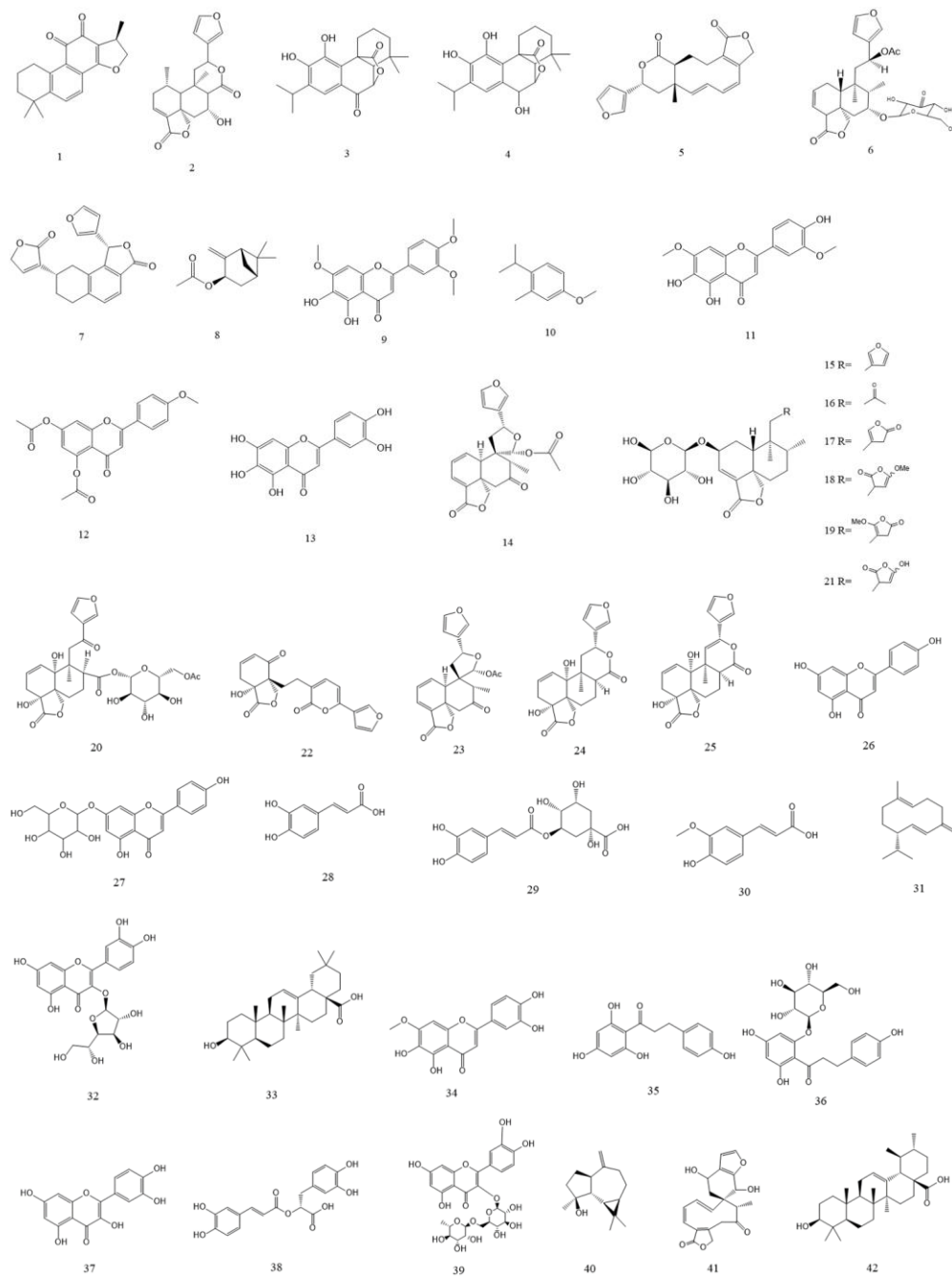


Fig. 4.

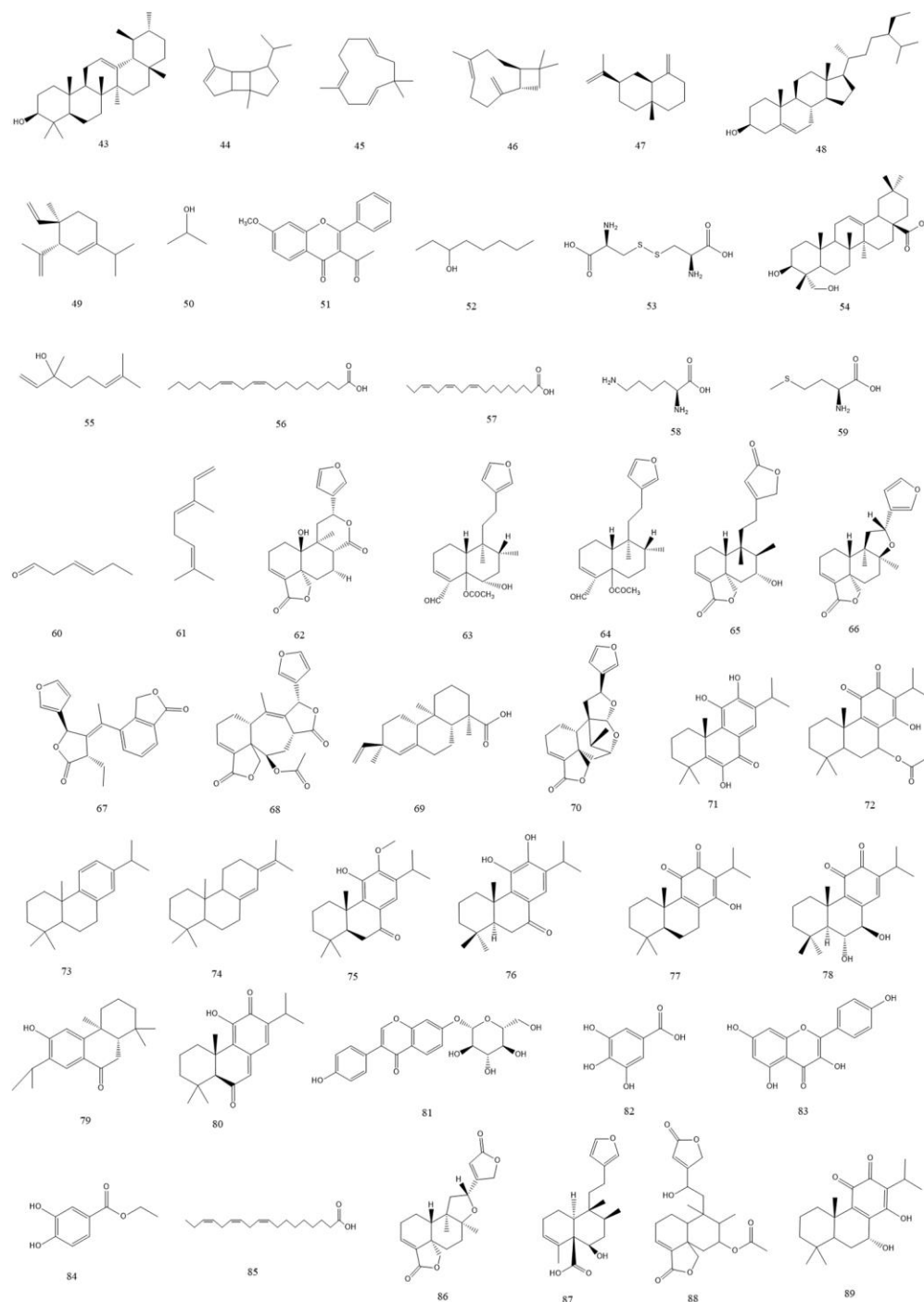


Fig. 4.

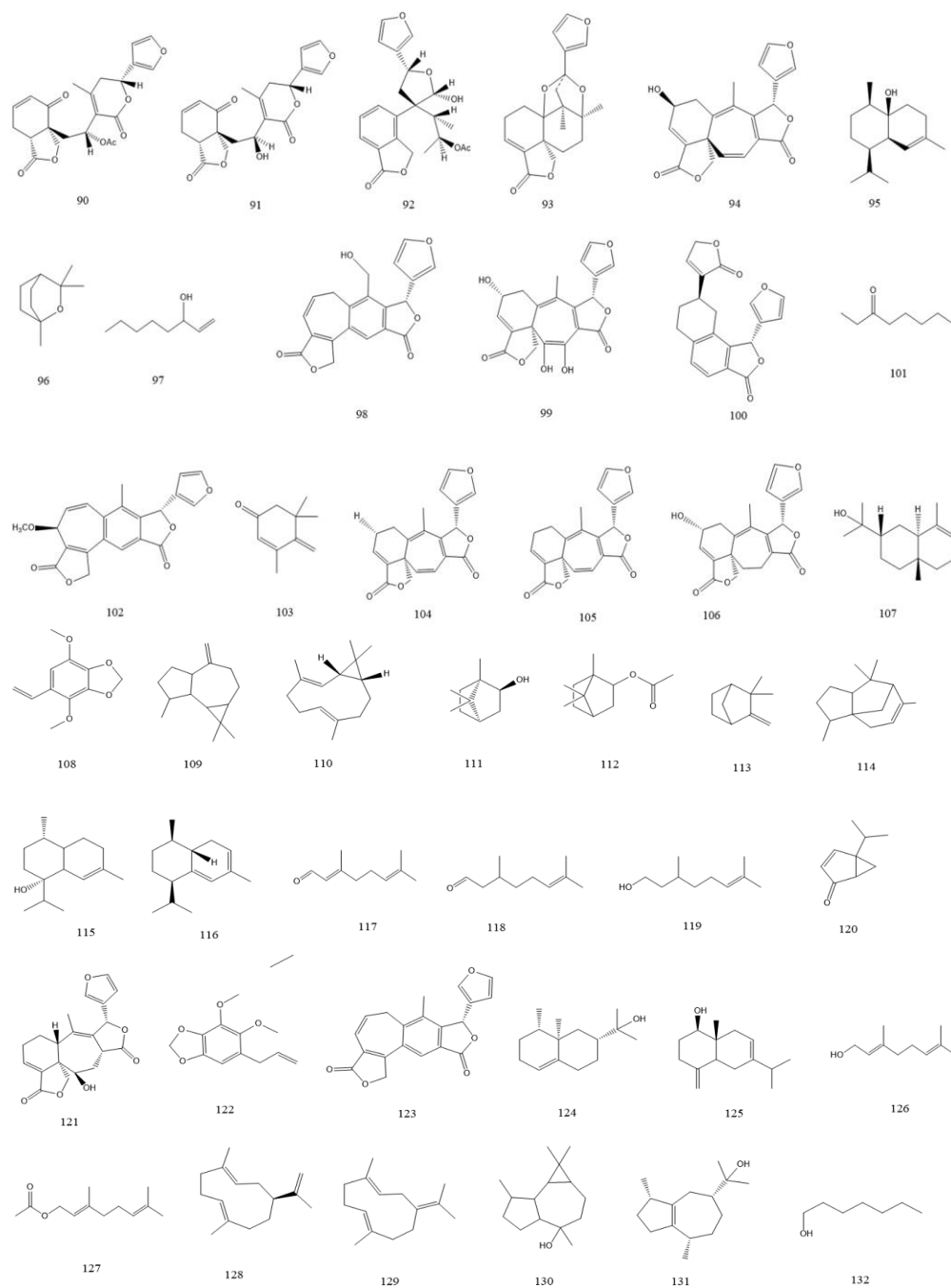


Fig. 4.

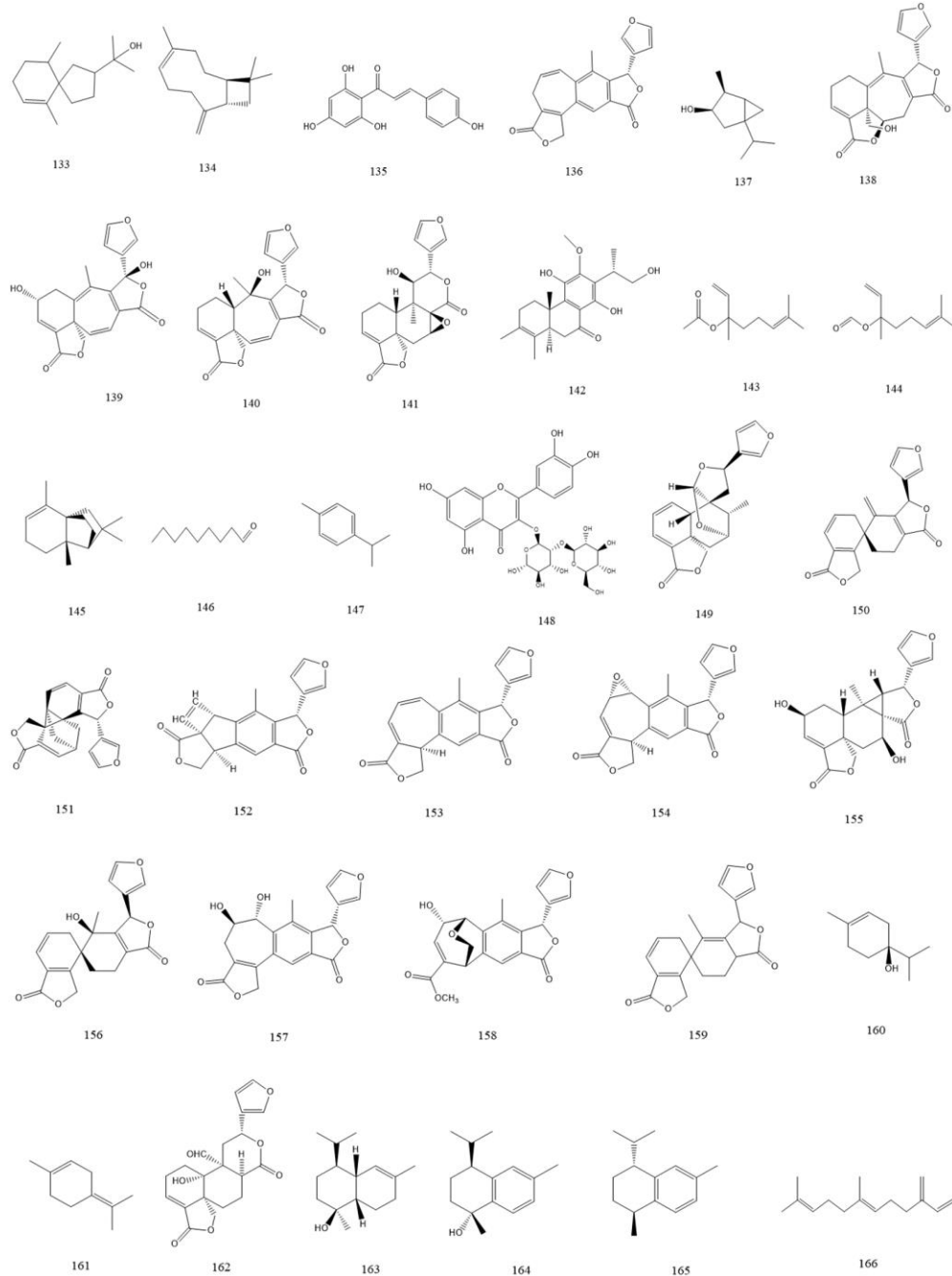


Fig. 4.

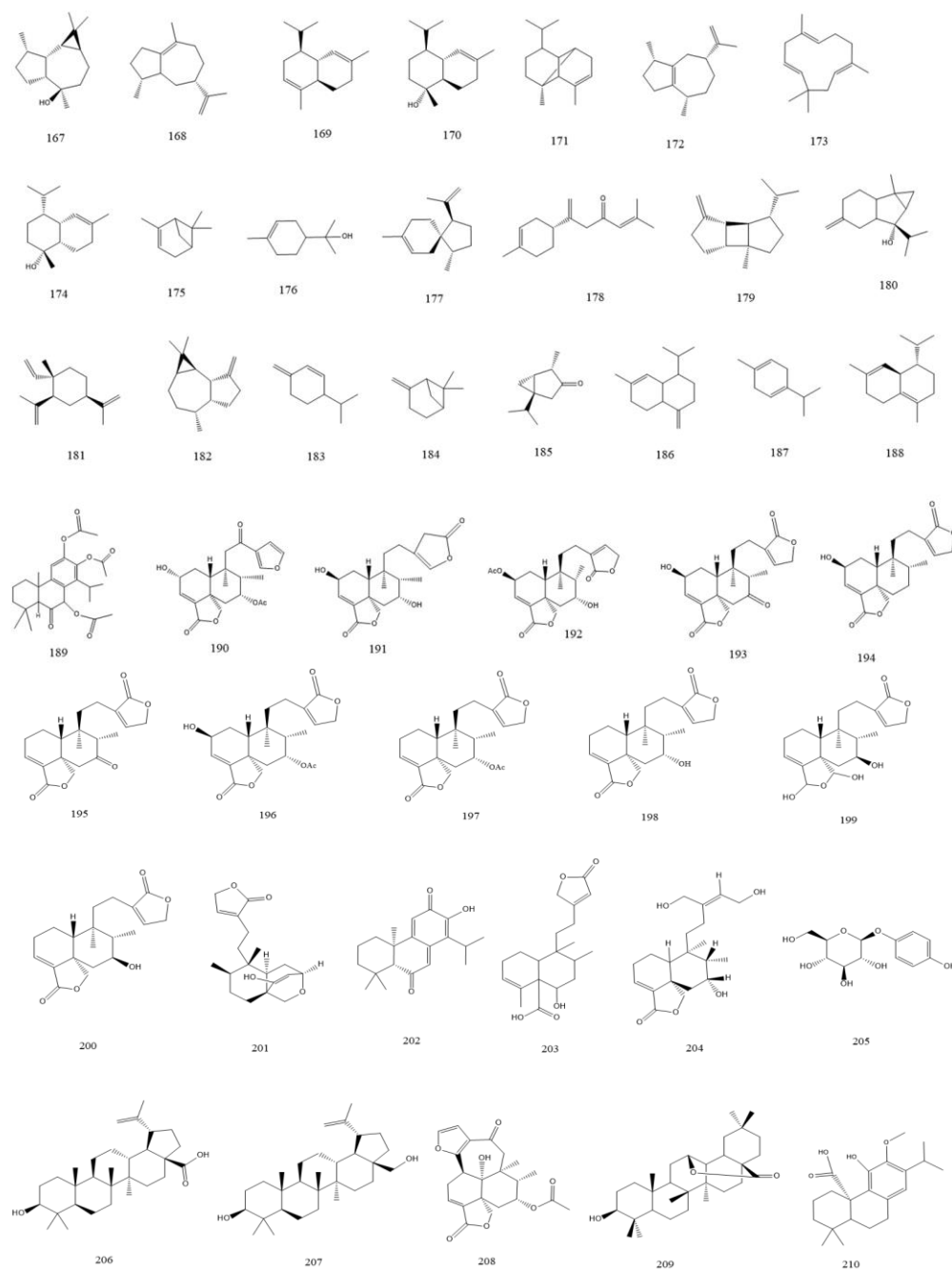


Fig. 4.

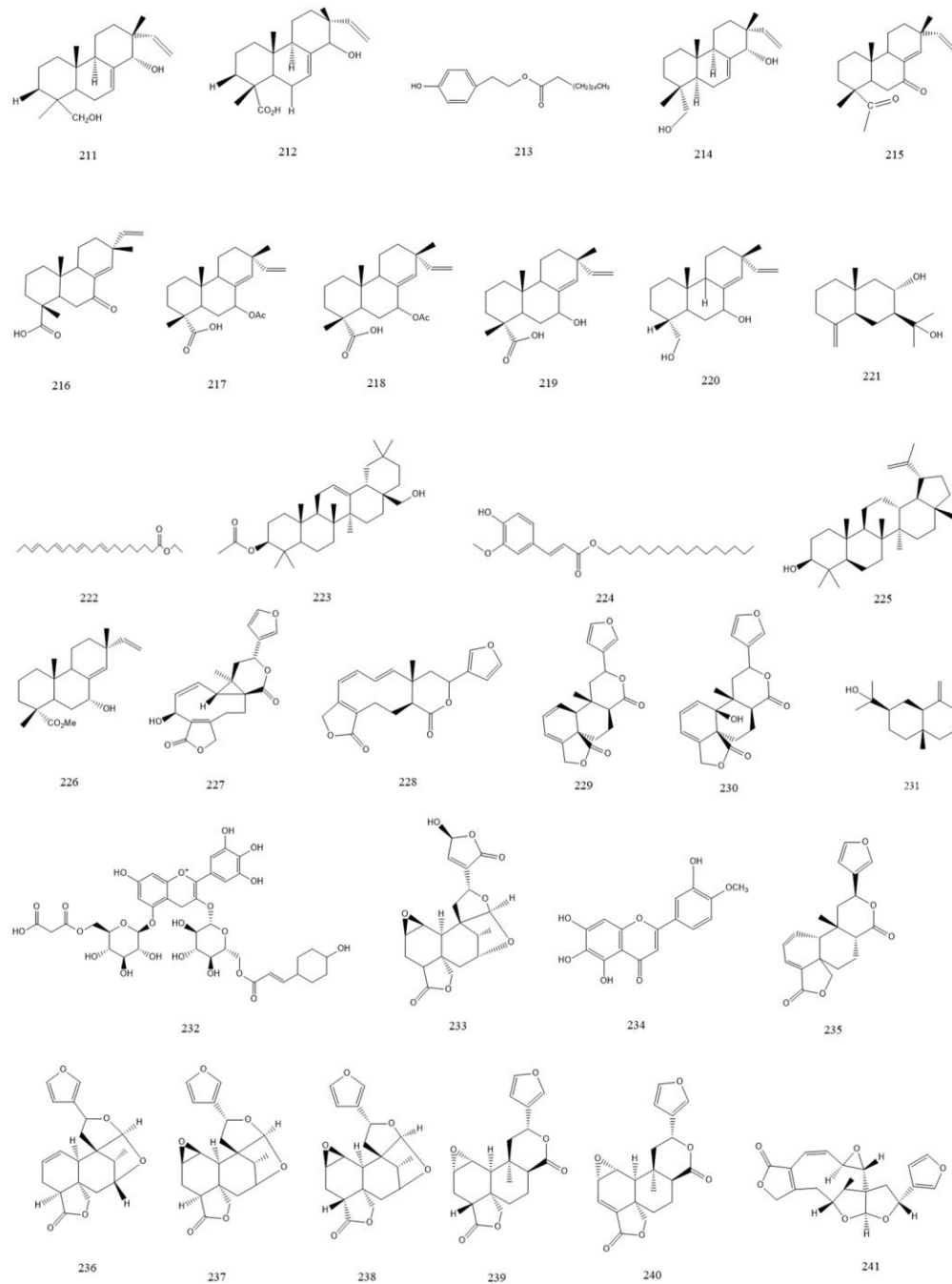
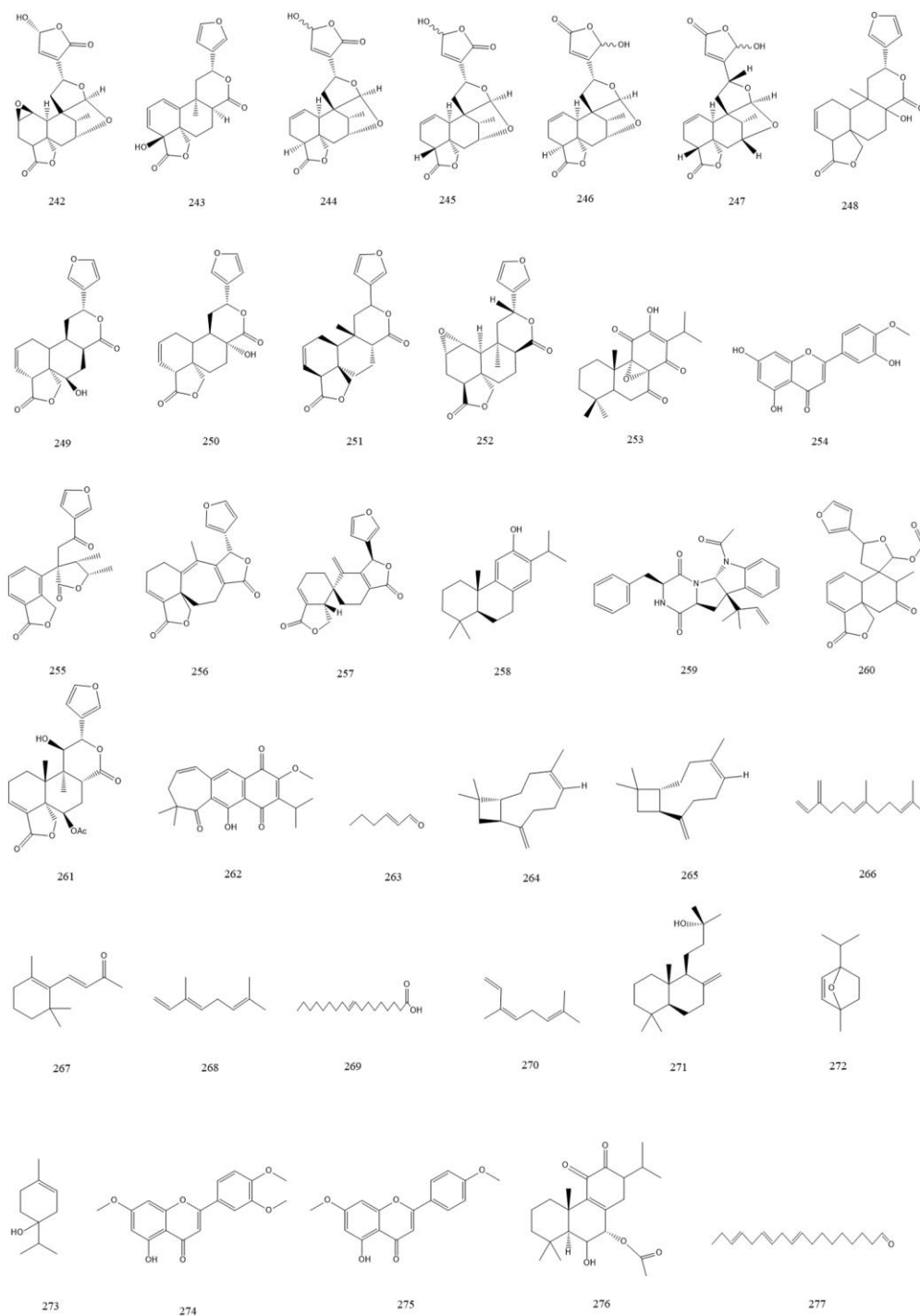


Fig. 4.



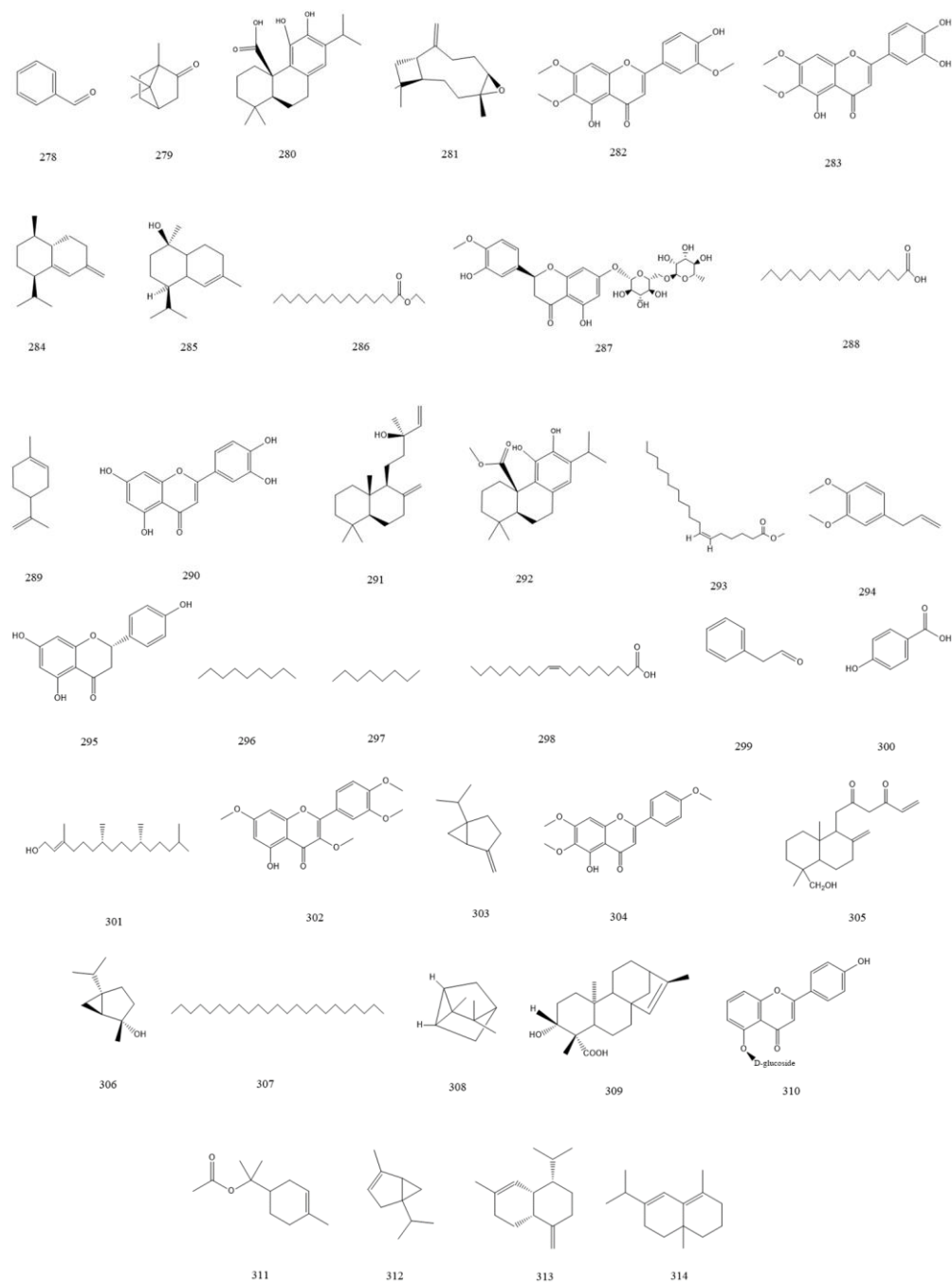


Fig. 4. Chemical components from *Salvia* spp. from Valle de México.

Conclusions

The several *Salvia* species in the Valle de México represent a vast plant resource with metabolites of pharmacological interest that play a significant role in Mexican Traditional Medicine. *Salvia* species represent a vast therapeutic use and have great potential for developing new bioactive compounds for treating diverse diseases due to the great variety of metabolites generated under diverse conditions, even in different populations of the same species. The data presented seek to promote research into these species through bio-assay-guided chemical studies that support their empirical use and the development of new herbal treatments. Enlarging the identification of new metabolites present in these plant species, taking into consideration that the variations of metabolites structures, the wide variety of *Salvias* and the poor study with some of them, could also generate new research opportunities in diverse areas of study. Finally, expanding the chemical, biological and pharmacological information might serve to develop methods of production of these plants, preserve them and improve their production and economic impact.

References

1. Tjitraresmi, A.; Moektiwardoyo, M.; Susilawati Y.; Shiono, Y. *Sys. Rev. Pharm.* **2020**, *11*, 324-333.
2. Manjarréz, R.; Frontana-Uribe, B. A.; Cárdenas, J. *Rev. Soc. Quím. Méx.* **2003**, *47*, 207-209.
3. Pérez, S.; De La, R.; Canavaciolo, G.; Victor, L.; Delange, M.; Rodríguez-Leyes, E. A. *Rev. Cub. Plant. Med.* **2011**, *16*, 54-59.
4. Reyes-Caudillo, E.; Tecante, A.; Valdivia-López, M. A. *Food Chem.* **2008**, *107*, 656-663. DOI: <https://doi.org/10.1016/j.foodchem.2007.08.062>.
5. Mendoza, E. I. O.; García, B. Y. B.; Cabrera, S. I. L. *Acta Bot. Méx.* **2017**, *118*, 7-40.
6. Sierra-Pérez, R.; González-Canavaciolo, V. L.; Marrero-Delange, D.; Rodríguez-Leyes, E. A. *Revista CENIC: Ciencias Biológicas.* **2013**, *44*, 124-127.
7. Kumar, P. M.; Sasmal, D.; Mazumder, P. M. *Pharmacogn. Res.* **2010**, *2*, 190-194. DOI: <http://dx.doi.org/10.4103/0974-8490.65520>.
8. Angerhofer, C. K. *J. Nat. Prod.* **2001**, *64*, 1258 DOI: 10.1021/np000756b
9. Ramamoorthy, T. P. in: *Flora Fanerogámica del Valle de México*, Rzedowski, G. C. de, Ed., Instituto de Ecología, A.C. y Comisión Nacional para el Conocimiento y Uso de la Biodiversidad: Pátzcuaro, **2001**, 632-644.
10. Cornejo-Tenorio, G.; Ibarra-Manríquez, G. *Rev. Mex. Biodiv.* **2011**, *82*, 1279-1296. DOI: <http://dx.doi.org/10.22201/ib.20078706e.2011.4.668>.
11. Villaseñor, J. L. *Bot. Sci.* **2004**, *75*, 105-135. DOI: <http://dx.doi.org/10.17129/botsci.1694>.
12. Martínez-Gordillo, M.; Lozada-Pérez, L. *Brittonia.* **2011**, *63*, 211-214. DOI: <http://dx.doi.org/10.1007/s12228-010-9152-2>.
13. Valdés, L.J.; Díaz, J.; Paul, A.G. *J. Ethnopharmacol.* **1983**, *7*, 287-312. DOI:10.1016/0378-8741(83)90004-1.
14. Tavera-Hernández, R.; Jiménez-Estrada, M.; Alvarado-Sansininea, J. J.; Huerta-Reyes, M. *Molecules.* **2023**, *28*, 8069. DOI: <https://doi.org/10.3390/molecules28248069>.
15. OECD. OECD Territorial Reviews: Valle de México, Mexico. OECD: **2015**.
16. Castro, J. C. J.; Villa, R. N.; Ramírez G. S. A.; González, C. *Rev. Cub. Plantas Med.* **2014**, *19*, 101-120.
17. Ortega, A.; Bautista, E.; Maldonado, E. *Chem. Pharm. Bull.* **2006**, *54*, 1338-1339. DOI: <http://dx.doi.org/10.1248/cpb.54.1338>.
18. Salinas-Arellano, E.; Pérez-Vásquez, A.; Rivero-Cruz, I.; Torres-Colin, R.; González-Andrade, M.; Rangel-Grimaldo, M.; Mata, R. *Molecules.* **2020**, *25*, 3530. DOI: <http://dx.doi.org/10.3390/molecules25153530>.
19. Wu, Y. B.; Ni, Z. Y.; Shi, Q. W.; Dong, M.; Kiyota, H.; Gu, Y. C.; Cong, B. *Chem. Rev.* **2012**, *112*, 5967-6026. DOI: <http://dx.doi.org/10.1021/cr200058f>.

20. Khouchlaa, A.; Et-Touys, A.; Lakhdar, F.; Laasri, F. E.; El-Idrissi, A. E. Y.; Zaakour, F. *Biointerface Res. Appl. Chem.* **2021**, *12*, 1437–1469
21. Li, L. W.; Qi, Y. Y.; Liu, S. X.; Wu, X. D.; Zhao, Q. S. *Fitoterapia.* **2018**, *127*, 367–374. DOI: <http://dx.doi.org/10.1016/j.fitote.2018.03.007>.
22. Bisio, A.; De Mieri, M.; Milella, L.; Schito, A. M.; Parricchi, A.; Russo, D.; Alfei, S.; Lapillo, M.; Tuccinardi, T.; Hamburger, M.; et al. *J. Nat. Prod.* **2017**, *80*, 503–514. DOI: <http://dx.doi.org/10.1021/acs.jnatprod.6b01053>.
23. Kabouche, A.; Kabouche, Z. *Bioactive Nat. Prod.* **2008**, 753–833, DOI: [https://doi.org/10.1016/S1572-5995\(08\)80017-8](https://doi.org/10.1016/S1572-5995(08)80017-8).
24. Narukawa, Y.; Fukui, M.; Hatano, K.; Takeda, T. *J. Nat. Med.* **2006**, *60*, 58–63. DOI: <http://dx.doi.org/10.1007/s11418-005-0007-1>.
25. Aydoğmuş, Z.; Yeşilyurt, V.; Topcu, G. *Nat. Prod. Res.* **2006**, *20*, 775–781. DOI: <http://dx.doi.org/10.1080/14786410500462843>.
26. Bennett, B. C.; Balick, M. J. *J. Ethnopharmacol.* **2014**, *152*, 387–392. DOI: <http://dx.doi.org/10.1016/j.jep.2013.11.042>.
27. Rao, M. V. *Curr. Sci.* **2004**, *87*, 602–606.
28. Solares-Pascasio, J. I.; Ceballos, G.; Calzada, F.; Barbosa, E.; Velazquez, C. *Molecules.* **2021**, *26*, 947. DOI: <http://dx.doi.org/10.3390/molecules26040947>.
29. Flores-Bocanegra, L.; González-Andrade, M.; Bye, R.; Linares, E.; Mata, R. *J. Nat. Prod.* **2017**, *80*, 1584–1593. DOI: <http://dx.doi.org/10.1021/acs.jnatprod.7b00155>.
30. Sepúlveda-Cuellar, L.; Duque-Ortiz, A.; Yáñez-Espinosa, L.; Calzada, F.; Bautista, E.; Pastor-Palacios, G.; García, B. Y. B.; Flores-Rivas, J.; Badano, E. I.; Douterlungne, D. *Rev. Bras. Farmacogn.* **2021**, *31*, 676–688. DOI: <http://dx.doi.org/10.1007/s43450-021-00168-z>.
31. Rouhan, G.; Gaudeul, M. *Methods. Mol. Biol.* **2014**, *1115*, 1–37. DOI: http://dx.doi.org/10.1007/978-1-62703-767-9_1.
32. Lara-Cabrera, S. I.; Bedolla-García, B. Y.; Zamudio, S.; Domínguez-Vázquez, G. *Acta Bot. Mex.* **2016**, *116*, 107–149. DOI: <http://dx.doi.org/10.21829/abm116.2016.1120>.
33. Ionescu, I. A.; Møller, B. L.; Sánchez-Pérez, R. *J. Exp. Bot.* **2016**, *68*, 369–382. DOI: <http://dx.doi.org/10.1093/jxb/erw427>.
34. Chailakhyan, M. K. *Ann. Rev. Plant. Physiol.* **1968**, *19*, 1–37. DOI: <http://dx.doi.org/10.1146/annurev.pp.19.060168.000245>.
35. Kessler, A. *Curr. Opin. Insect. Sci.* **2015**, *8*, 47–53. DOI: <http://dx.doi.org/10.1016/j.cois.2015.02.002>.
36. Figueiredo, A. C.; Barroso, J. G.; Pedro, L. G.; Scheffer, J. J. C. *Flavour Fragr. J.* **2008**, *23*, 213–226. DOI: <http://dx.doi.org/10.1002/ffj.1875>.
37. Cruz-Pérez, A.L.; Barrera-Ramos, J.; Bernal-Ramírez, L. A.; Bravo-Avilez, D.; Rendón-Aguilar, B. *J. Ethnobiol. Ethnomed.* **2021**, *17*, 7. DOI: <http://dx.doi.org/10.1186/s13002-020-00431-y>.
38. Mata, R.; Figueroa, M.; Navarrete, A.; Rivero-Cruz, I. *Prog. Chem. Org. Nat. Prod.* **2019**, *108*, 1–142. DOI: http://dx.doi.org/10.1007/978-3-030-01099-7_1.
39. Zolla, C.; Argueta, A. Biblioteca digital de la medicina tradicional mexicana; *Landsteiner Scientific, Comisión Nacional para el Desarrollo de los Pueblos Indígenas, Programa Universitario México Nación Multicultural, Universidad Nacional Autónoma de México*: México. **2009**. <http://www.medicinatradicionalmexicana.unam.mx/index.php>.
40. Calzada, F.; Bautista, E. *J. Ethnopharmacol.* **2020**, *253*, 112676. DOI: <http://dx.doi.org/10.1016/j.jep.2020.112676>.
41. Sousa, A. C.; Pádua, I.; Gonçalves, V. M. F.; Ribeiro, C.; Leal, S. *Heliyon.* **2024**, *10*, e28779. DOI: <http://dx.doi.org/10.1016/j.heliyon.2024.e28779>.
42. Ortega, R.; Valdés, M.; Alarcón-Aguilar, F. J.; Fortis-Barrera, Á.; Barbosa, E.; Velazquez, C.; Calzada, F. *Plants.* **2022**, *11*, 575. DOI: <http://dx.doi.org/10.3390/plants11050575>.
43. Harikrishnan, R.; Balasundaram, C., in: *The Role of Phytoconstituents in Health Care*, Megh, R. G., Ed., Apple Academic Press: Canada, **2020**. 3–158. DOI: <https://doi.org/10.1201/9780429284267>.
44. Yazaki, K.; Arimura, G. I.; Ohnishi, T. *Plant Cell Physiol.* **2017**, *58*, 1615–1621. DOI: <http://dx.doi.org/10.1093/pcp/pcx123>.

45. Jash, S. K.; Gorai, D.; Roy, R. *Intern. J. Pharm. Sci. Res.* **2016**, 7, 4710.
46. Topçu, G. *J. Nat. Prod.* **2006**, 69, 482–487. DOI: <http://dx.doi.org/10.1021/np0600402>.
47. Theis, N.; Lerdau, M. *Int. J. Plant Sci.* **2003**, 164, S93–S102. DOI: <http://dx.doi.org/10.1086/374190>.
48. Wagner, K. H.; Elmadfa, I. *Ann. Nutr. Metab.* **2003**, 47, 95–106. DOI: <http://dx.doi.org/10.1159/000070030>.
49. Salminen, A.; Lehtonen, M.; Suuronen, T.; Kaarniranta, K.; Huuskonen, J. *Cell Mol. Life Sci.* **2008**, 65(19), 2979–2999.
50. Chinou, I. *Curr. Med. Chem.* **2005**, 12, 1295–1317. DOI: <http://dx.doi.org/10.2174/0929867054020990>.
51. Alves, A. L.V.; Da Silva, L. S.; Faleiros, C. A.; Silva, V. A.; Reis, R. M. *Nat. Prod. Comm.* **2022**, 17. DOI: <https://doi.org/10.1177/1934578X2211056>.
52. Nagegowda, D. A.; Gupta, P. *Plant Sci.* **2020**, 294, 110457. DOI: <http://dx.doi.org/10.1016/j.plantsci.2020.110457>.
53. Gurado, O. A. A.; Cuéllar, A. C. *Rev. Cub. Plantas Med.* **2008**, 13.
54. Paduch, R.; Kandefer-Szerszeń, M.; Trytek, M.; Fiedurek, J. *Arch. Immunol. Ther. Exp.* **2007**, 55, 315–327. DOI: <http://dx.doi.org/10.1007/s00005-007-0039-1>.
55. Bueno-Sánchez, J. G.; Martínez-Morales, J. R.; Stashenko, E. *Rev. Univ. Ind. Sant. Salud.* **2009**, 41, 231–235.
56. Vaillant, F. D.; Romeu, C. C.; Ramos, R. E.; González, G. M.; Ramírez, O. R.; González, P. J. *Fitosanidad.* **2009**, 13, 197–200.
57. Ruiz-Reyes, E.; Suarez, M. *Rev. CENIC Ciencias Biológicas.* **2015**, 46, 9–24.
58. Seo, D. Y.; Lee, S.R.; Heo, J. W.; No, M. H.; Rhee, B. D.; Ko, K. S.; Han, J. *Korean J. Physiol. Pharmacol.* **2018**, 22, 235–248.
59. Kashyap, D.; Tuli, H. S.; Sharma, A. K. *Life Sci.* **2016**, 146, 201–213. DOI: <http://dx.doi.org/10.1016/j.lfs.2016.01.017>.
60. Liu, J. *J. Ethnopharmacol.* **2005**, 100, 92–94. DOI: <http://dx.doi.org/10.1016/j.jep.2005.05.024>.
61. Pollier, J.; Goossens, A. *Phytochemistry.* **2012**, 77, 10–15. DOI: <http://dx.doi.org/10.1016/j.phytochem.2011.12.022>.
62. Babu, S.; Jayaraman, S. *Biomed. Pharmacother.* **2020**, 133, 193–200. DOI: <http://dx.doi.org/10.1016/j.biopha.2020.110702>.
63. Saeidnia, S.; Manayi, A.; Gohari, A. R.; Abdollahi, M. *Eur. J. Med. Plants.* **2014**, 4, 590–609.
64. López, J. G. E. *Curr. Med. Chem.* **2019**, 26, 6972–6975. DOI: <http://dx.doi.org/10.2174/092986732639191213095405>.
65. Samanta, A.; Das, G.; Das, S. K. *Int. J. Pharm. Sci. Tech.* **2011**, 100, 12–35.
66. Panche, A. N.; Diwan, A. D.; Chandra, S. R. *J. Nutr. Sci.* **2016**, 5, 1–15. DOI: <http://dx.doi.org/10.1017/jns.2016.41>.
67. Janicijevic, J.; Tomic, S.; Mitrovic, T. *Proceeding of 9th symposium on flora of Southeastern Serbia and neighbouring regions.* **2007**, 153–156.
68. Tiwari, S.C.; Husain, N. *Indian J. Sci. Res.* **2017**, 12, 193–196.
69. Janicsák, G.; Veres, K.; Zoltán, K. A.; Máthé, I. *Biochem. Syst. Ecol.* **2006**, 34, 392–396. DOI: <http://dx.doi.org/10.1016/j.bse.2005.12.004>.
70. Noriega, J. M. *Curso de Historia de Drogas*, Ed., Oficina Tipográfica de la Secretaría de Fomento, México, **1902**, 372–373.
71. Pérez, E. B. E. *Lista de las plantas útiles del estado de Hidalgo*. Ed., UAEH, Hidalgo, **2003**.
72. Aguilar, A.; Camacho, J. R.; Chino, S.; Jáquez, P.; López, M. E. *Herbario Medicinal del Instituto Mexicano del Seguro Social. Información Etnobotánica*; Instituto Mexicano del Seguro Social, México, **1994**.
73. Fragoso-Serrano, M.; Ortiz-Pastrana, N.; Luna-Cruz, N.; Toscano, R. A.; Alpuche-Solís, A. G.; Ortega, A.; Bautista, E. *J. Nat. Prod.* **2019**, 82, 631–635. DOI: <http://dx.doi.org/10.1021/acs.jnatprod.8b00565>.

74. Moreno-Pérez, G. F.; González-Trujano, M. E.; Martínez-Gordillo, M. J.; San Miguel-Chávez, R.; Basurto-Peña, F. A.; Dorazco-González, A.; Aguirre-Hernández, E. *Bot. Sci.* **2019**, *97*, 355–365. DOI: <http://dx.doi.org/10.17129/botsci.2187>.
75. Moreno, U.V. *Herbolaria y tradición en la región de Xico, Veracruz*. Ed., Gobierno del Estado de Veracruz, Secretaría de Educación y Cultura, Consejo Veracruzano de Arte Popular, Universidad Veracruzana, Xalapa, Veracruz, **2004**, 1-202.
76. Guzmán, G.O. Evaluación de la actividad antiinflamatoria y estudios quimiométricos de especies de *Salvia* de Xalapa, Veracruz y municipios aledaños [master's thesis]. Universidad Veracruzana: México, **2014**.
77. Molina, M. J. L.; Villanueva, R.; Fernández, N. R.; Siciliano, A. *Polibotánica*. **2012**, *34*, 259–291.
78. Jiménez-Ferrer, E.; Hernández-Badillo, F.; González-Cortazar, M.; Tortoriello, J.; Herrera-Ruiz, M. *J. Ethnopharmacol.* **2010**, *130*, 340–346. DOI: <http://dx.doi.org/10.1016/j.jep.2010.05.013>.
79. Bello, G. M. Á.; Salgado, G. R. *Biológicas*. **2007**, *9*, 126–138.
80. Herrera-Ruiz, M.; García-Beltrán, Y.; Mora, S.; Díaz-Véliz, G.; Viana, G. S. B.; Tortoriello, J.; Ramírez, G. *J. Ethnopharmacol.* **2006**, *107*, 53–58. DOI: <http://dx.doi.org/10.1016/j.jep.2006.02.003>.
81. Moreno, M.; Alvarado, F.D.; Mendoza C.R.; Basurto, P.M. *Bot. Sci.* **2006**, *79*, 79–87.
82. Mora, S.; Millán, R.; Lungenstrass, H.; Díaz-Véliz, G.; Morán, J.A.; Herrera-Ruiz, M.; Tortoriello, J. *J. Ethnopharmacol.* **2006**, *106*, 76–81. DOI: <http://dx.doi.org/10.1016/j.jep.2005.12.004>.
83. Hurtado-Rico, N. E.; Rodríguez-Jiménez, C.; Aguilar-Contreras, A. *Polibotánica*. **2006**, *22*, 21-50.
84. Calzada, F.; Bautista, E.; Yépez-Mulia, L.; García-Hernandez, N.; Ortega, A. *Phyther. Res.* **2015**, *29*, 1600–1604. DOI: <http://dx.doi.org/10.1002/ptr.5421>.
85. Gómez-Rivera, A.; González-Cortazar, M.; Gallegos-García, A. J.; Escobar-Ramos, A.; Flores-Franco, G.; Lobato-García, C. E. *Afr. J. Trad. Compl. Altern. Med.* **2018**, *15*, 72–82.
86. Navarro, P. L. D. C.; Avedaño, R. S. *Polibotánica*. **2002**, *14*, 67-84.
87. Aoyagi, Y.; Yamazaki, A.; Nakatsugawa, C.; Fukaya, H.; Takeya, K.; Kawauchi, S.; Izumi, H.; Salvileucalín, B. *Org Lett.* **2008**, *10*, 4429–4432. DOI: <http://dx.doi.org/10.1021/ol801620u>.
88. Jiang, Y. J.; Su, J.; Shi, X.; Wu, X. D.; Chen, X. Q.; He, J.; Shao, L. D.; Li, X. N.; Peng, L. Y.; Li, R. T. et al. *Tetrahedron*. **2016**, *72*, 5507–5514. DOI: <http://dx.doi.org/10.1016/j.tet.2016.07.037>.
89. Rajamanickam, M.; Kalaivanan, P.; Sivagnanam, I. *Int. J. Pharm. Sci. Rev. Res.* **2013**, *22*, 264–268.
90. González-Elizondo, M.; López-Enríquez, I. L.; González-Elizondo, M. S.; Tena-Flores, J. A. *Plantas medicinales del estado de Durango y zonas aledañas*. Ed., IPN, México, **2004**.
91. Domínguez-Vázquez, G.; Castro-Ramírez, A. E. *Etnobiología*. **2015**, *2*, 19–31.
92. Argumedo Delira, R.; Parra-Delgado, H.; Ramírez-Apan, M. T.; Nieto, C. A.; Martínez-Vázquez, M. *Rev. Soc. Quím. Méx.* **2003**, *47*, 167–172.
93. Molina, M. J. L.; Villanueva, R.; Fernández, N. R.; Siciliano, A. *Polibotánica*. **2012**, *34*, 259–291.
94. Martínez-Vázquez, M.; Miranda, P.; Valencia, N. A.; Torres, M. L.; Miranda, R.; Cárdenas, J.; Salmón, M. *Pharm. Biol.* **1998**, *36*, 77–80. DOI: <http://dx.doi.org/10.1076/phbi.36.2.77.4611>.
95. Hersch, M. *Estado del desarrollo económico y social de los pueblos indígenas de Guerrero, Volumen 2*; Universidad Nacional Autónoma de México PUMC: México, **2009**.
96. Cavin, A.; Dyatnyko, W.; Hostettmann, K. *Pharm. Biol.* **1999**, *37*, 260–268. DOI: <http://dx.doi.org/10.1076/phbi.37.4.260.5800>.
97. Pineda-Ramírez, N.; Calzada, F.; Alquisiras-Burgos, I.; Medina-Campos, O. N.; Pedraza-Chaverri, J.; Ortiz-Plata, A.; Pinzón, E. E.; Torres, I.; Aguilera, P. *Antioxidants*. **2020**, *9*, 253. DOI: <http://dx.doi.org/10.3390/antiox9030253>.
98. Bautista, E.; Ortiz-Pastrana, N.; Pastor-Palacios, G.; Montoya-Contreras, A.; Toscano, R. A.; Morales-Jiménez, J.; Salazar-Olivo, L. A.; Ortega, A. *J. Nat. Prod.* **2017**, *80*, 3003–3009. DOI: <http://dx.doi.org/10.1021/acs.jnatprod.7b00591>.
99. Ramírez-Zea, G.; Chávez-Servia, J.L.; Archundia-Garduño, E.; López-Hernández, V. *Salvias del Estado de México, una perspectiva general*. Ed., Instituto de Investigación y Capacitación Agropecuaria, Acuícola y Forestal del Estado de México (ICAMEX), Secretaría de Desarrollo Agropecuario del Estado de México. Metepec, México, **2016**.

100. Calzada, F.; Yepez-Mulia, L.; Tapia-Contreras, A.; Bautista, E.; Maldonado, E.; Ortega, A. *Phytother. Res.* **2010**, *24*, 662–665. DOI: <http://dx.doi.org/10.1002/ptr.2938>.
101. Fan, M.; Bao, Y.; Zhang, Z. J.; Zhang, H. B.; Zhao, Q. S. *Fitoterapia.* **2017**, *123*, 44–50. DOI: <http://dx.doi.org/10.1016/j.fitote.2017.09.013>.
102. Esquivel, B.; Calderón, J.; Flores, E.; Sánchez, A. A.; Rosas, R. R. *Phytochemistry.* **1997**, *46*, 531–534. DOI: [http://dx.doi.org/10.1016/s0031-9422\(97\)00310-5](http://dx.doi.org/10.1016/s0031-9422(97)00310-5).
103. Bautista, E.; Fragoso-Serrano, M.; Ortiz-Pastrana, N.; Toscano, R. A.; Ortega, A. *Fitoterapia.* **2016**, *114*, 1–6. DOI: <http://dx.doi.org/10.1016/j.fitote.2016.08.007>.
104. Bautista, E.; Fragoso-Serrano, M.; Toscano, R. A.; García-Peña, M. del R.; Ortega, A. *Org. Lett.* **2015**, *17*, 3280–3282. DOI: <http://dx.doi.org/10.1021/acs.orglett.5b01320>.
105. Maldonado, E.; Cárdenas, J.; Bojórquez, H.; Escamilla, E. M.; Ortega, A. *Phytochemistry.* **1996**, *42*, 1105–1108. DOI: [http://dx.doi.org/10.1016/0031-9422\(96\)00147-1](http://dx.doi.org/10.1016/0031-9422(96)00147-1).
106. Marquina, S.; García, Y.; Alvarez, L.; Tortoriello, J. *Nat. Prod. Commun.* **2008**, *3*, 185–188. DOI: <http://dx.doi.org/10.1177/1934578x0800300215>.
107. Esquivel, B. *Nat. Prod. Commun.* **2008**, *3*, 989–1002. DOI: <http://dx.doi.org/10.1177/1934578x0800300628>.
108. Arnason, J. T.; Mata, R. *Phytochemistry of Medicinal Plants*, Ed., Springer, New York, NY, **1995**. DOI: <https://doi.org/10.1007/978-1-4899-1778-2>.
109. Esquivel, B.; Cardenas, J.; Rodriguez-Hahn, L.; Ramamoorthy, T. P. *J. Nat. Prod.* **1987**, *50*, 738–740. DOI: <http://dx.doi.org/10.1021/np50052a029>.
110. Esquivel, B.; Cardenas, J.; Toscano, A.; Soriano-Garcia, M.; Rodriguez-Hahn, L. *Tetrahedron.* **1985**, *41*, 3213–3217. DOI: [http://dx.doi.org/10.1016/s0040-4020\(01\)96672-4](http://dx.doi.org/10.1016/s0040-4020(01)96672-4).
111. Mendoza-Espinoza, J. A.; Pena-Miranda, I.; Aarland, R. C.; Peralta-Gómez, S.; Sierra-Palacios, E.; García-Ocón, B. *Indian J. Tradit. Knowle.* **2016**, *15*, 62–67.
112. Hueso-Rodríguez, J.; Jimeno, M.; Rodríguez, B.; Savona, G.; Bruno, M. *Phytochemistry.* **1983**, *22*, 2005–2009. DOI: [http://dx.doi.org/10.1016/0031-9422\(83\)80033-8](http://dx.doi.org/10.1016/0031-9422(83)80033-8).
113. Martínez-Cruz, O.; Paredes-López, O. *J. Chromatogr. A.* **2014**, *1346*, 43–48. DOI: <http://dx.doi.org/10.1016/j.chroma.2014.04.007>.
114. Sandoval-Oliveros, M. R.; Paredes-López, O. *J. Agric. Food Chem.* **2013**, *61*, 193–201. DOI: <http://dx.doi.org/10.1021/jf3034978>.
115. Rodríguez-Hahn, L.; García, A.; Esquivel, B.; Cárdenas, J. *Can. J. Chem.* **1987**, *65*, 2687–2690. DOI: <http://dx.doi.org/10.1139/v87-445>.
116. Maldonado, E.; Ángeles-Flores, M. de los.; Salazar, B.; Ortega, A. *Phytochemistry.* **1994**, *37*, 1480–1482. DOI: [http://dx.doi.org/10.1016/s0031-9422\(00\)90438-2](http://dx.doi.org/10.1016/s0031-9422(00)90438-2).
117. Maldonado, E.; Cardenas, J.; Salazar, B.; Toscano, R. A.; Ortega, A.; Jankowski, C. K.; Aumelas, A.; Van-Calsteren, M. R. *Phytochemistry.* **1992**, *31*, 217–220. DOI: [http://dx.doi.org/10.1016/0031-9422\(91\)83039-n](http://dx.doi.org/10.1016/0031-9422(91)83039-n).
118. Ortega, A.; Cárdenas, J.; Toscano, A.; Maldonado, E.; Aumelas, A.; Van Calsteren, M. R.; Jankowski, C. *Phytochemistry.* **1991**, *30*, 3357–3360. DOI: [http://dx.doi.org/10.1016/0031-9422\(91\)83209-4](http://dx.doi.org/10.1016/0031-9422(91)83209-4).
119. Aoyagi, Y.; Yamazaki, A.; Kato, R.; Tobe, F.; Fukaya, H.; Nishikawa, T.; Nakahashi, A.; Miura, N.; Monde, K.; Takeya, K. *Tetrahedron Lett.* **2011**, *52*, 1851–1853. DOI: <http://dx.doi.org/10.1016/j.tetlet.2011.02.003>.
120. Rojas, L. B.; Visbal, T.; Morillo, M.; de Rojas, Y. C.; Arzola, J. C.; Usabillaga, A. *Nat. Prod. Commun.* **2010**, *5*, 937–938. DOI: <http://dx.doi.org/10.1177/1934578x1000500627>.
121. Negi, A.; Javed, M. S.; Melkani, A. B.; Dev, V.; Beauchamp, P. S. *J. Essent. Oil Res.* **2007**, *19*, 463–465. DOI: <http://dx.doi.org/10.1080/10412905.2007.9699953>.
122. Esquivel, B.; Hernández, L. M.; Cárdenas, J.; Ramamoorthy, T. P.; Rodríguez-Hahn, L. *Phytochemistry.* **1989**, *28*, 561–566. DOI: [http://dx.doi.org/10.1016/0031-9422\(89\)80051-2](http://dx.doi.org/10.1016/0031-9422(89)80051-2).
123. Esquivel, B.; Vallejo, A.; Gaviño, R.; Cárdenas, J.; Sánchez, A. A.; Ramamoorthy, T. P.; Rodríguez-Hahn, L. *Phytochemistry.* **1988**, *27*, 2903–2905. DOI: [http://dx.doi.org/10.1016/0031-9422\(88\)80685-x](http://dx.doi.org/10.1016/0031-9422(88)80685-x).

124. Bautista, E.; Toscano, R. A.; Ortega, A. *J. Nat. Prod.* **2014**, 77, 1088–1092. DOI: <http://dx.doi.org/10.1021/np4009893>.
125. Bautista, E.; Toscano, R. A.; Ortega, A. *Org Lett.* **2013**, 15, 3210–3213. DOI: <http://dx.doi.org/10.1021/ol401022c>.
126. Takeda, K.; Yanagisawa, M.; Kifune, T.; Kinoshita, T.; Timberlake, C. F. *Phytochemistry*. **1994**, 35, 1167–1169. DOI: [http://dx.doi.org/10.1016/s0031-9422\(00\)94815-5](http://dx.doi.org/10.1016/s0031-9422(00)94815-5).
127. Nieto, M.; Gallardo, O. V.; Rossomando, P. C.; Tonn, C. E. *J. Nat. Prod.* **1996**, 59(9), 880–882. DOI: <http://dx.doi.org/10.1021/np960515x>.
128. Esquivel, B.; Esquivel, O.; Cárdenas, J.; Sánchez, A.; Ramamoorthy, T. P.; Toscano, R. A.; Rodríguez-Hahn, L. *Phytochemistry*. **1991**, 30, 2335–2338. DOI: [http://dx.doi.org/10.1016/0031-9422\(91\)83644-z](http://dx.doi.org/10.1016/0031-9422(91)83644-z).
129. Luis, J. G.; Quiñones, W.; Echeverri, F. *Phytochemistry*. **1994**, 36, 115–117. DOI: [http://dx.doi.org/10.1016/s0031-9422\(00\)97023-7](http://dx.doi.org/10.1016/s0031-9422(00)97023-7).
130. Rodríguez-Hahn, L.; O'Reilly, R.; Esquivel, B.; Maldonado, E.; Ortega, A.; Cardenas, J.; Toscano, R. A.; Chan, T. M.; *J. Org. Chem.* **1990**, 55, 3522–3525. DOI: <http://dx.doi.org/10.1021/jo00298a026>.

Mexican Contribution to Sulfide Minerals Electrochemistry: A Review

Roel Cruz*, Isabel Lázaro

Instituto de Metalurgia-Facultad de Ingeniería, Universidad Autónoma de San Luis Potosí.

*Corresponding author: Roel Cruz, email: rcruz@uaslp.mx

Received May 30th, 2024; Accepted July 10th, 2024.

DOI: <http://dx.doi.org/10.29356/jmcs.v68i4.2310>

Abstract. The electrochemical study of sulfide minerals has emerged as a vital area for enhancing sustainable methods for extraction and recovery of metals. This field encompasses diverse investigations. The use of Mineral Carbon Paste Electrodes (CPE) is one of the strategies developed in México, and their application for analyzing systems of extractive metallurgy range from analyses of bacterial-mineral interactions to key studies that have delved into understanding mineral dissolution mechanisms, with a particular focus on minerals such as galena, sphalerite, copper sulfides, and silver minerals. In addition, research efforts have been directed towards exploring copper and zinc concentrates leaching, as well as cyanidation refractoriness. These studies aim to advance extraction efficiency and sustainability in the mining industry.

Keywords: Sulfide minerals; electrochemistry; extractive metallurgy.

Resumen. El estudio electroquímico de los minerales de sulfuro ha surgido como un área vital para mejorar los métodos de extracción y recuperación de metales de manera sostenible. Este campo abarca diversas investigaciones. La utilización de electrodos de pasta de carbono (CPE) es una de las estrategias desarrolladas en México, y su aplicación para analizar sistemas de metalurgia extractiva abarca desde análisis hasta interacciones bacteria-mineral. Estudios clave se han centrado en comprender los mecanismos de disolución mineral, con un enfoque particular en minerales como la galena, la esfalerita, los sulfuros de cobre y los minerales de plata. Además, los esfuerzos de investigación se han dirigido a explorar la lixiviación de concentrados de zinc y la refractariedad a la cianuración. Estos estudios tienen como objetivo avanzar en la eficiencia y sostenibilidad de la extracción en la industria minera.

Palabras clave: Sulfuros minerales; electroquímica; metalurgia extractiva.

Introduction

The electrochemistry of sulfides has been studied from various perspectives. Initially, thermodynamics specialists constructed the first Eh-pH diagrams, defining the stability conditions of various sulfide mineral systems. These were applied, for example in explaining the metal matte refining process, the dissolution kinetics of sulfides and particularly the electrochemical mechanisms involved. Another trend was to study the electrochemical characteristics of sulfide minerals, such as their resistivity, finding that under certain conditions they could behave like metals, although most of them behaved as semiconductors [1].

The production of sulfuric acid through the oxidation of pyrite in an autoclave may be considered as one of the earliest hydrometallurgical processes involving sulfide minerals. Several reports studied the effect of conditions such as oxygen pressure, temperature, and acidity, among others [1]. Initially, there was discrepancy regarding the dissolution mechanisms; some researchers assumed that leaching occurred over the whole area of

the exposed pyrite surface, by adsorbed oxygen through a completely molecular route to sulfates, as sulfur formation was not observed during the oxidation process of pyrite. Peters and Majima [2] adopted Woodcock's suggestion [3] that anodic dissolution from the bottom of deep pits could explain the constant dissolution rate if the rate-limiting step was oxygen reduction and considered that this could be demonstrated through an electrochemical study of pyrite. The Peters and Majima study [2] was the first to show that pyrite could dissolve both anodically and cathodically, followed by various studies on the mechanisms and kinetics of mineral leaching to explain the results of experimental sulfide systems.

On the other hand, regarding the application of electrochemistry in sulfide flotation, the earliest studies were conducted by Woods [4], who employed cyclic voltammetry to investigate the oxidation of ethyl xanthate using a galena electrode. This was the first study to use an electrode other than mercury or platinum, which are commonly used for studying electrochemical reactions related to adsorption.

Following the studies of Ernest Peters and Ronald Woods, a series of investigations were conducted using bulk mineral electrodes to study various aspects of mineral leaching and flotation processes. Additionally, through the combination of spectroscopic and electrochemical techniques, some bases of the surface speciation were established to define the mechanisms and processes of these two important unit operations in extractive metallurgy. Most of these studies were reported in the proceedings of the ECS (Electrochemical Society) symposia on *Electrochemistry in Mineral and Metal Processing I to VIII (1984-2010)* [5-12].

The mentioned electrochemical studies required the construction of a working electrode made of bulk mineral, that was as simple as encapsulating in resin a piece of the massive mineral and preparation of the probe obtained to expose the mineral surface. Later, the construction of mineral electrodes was as advanced as preparing rotating disk [13] and even rotating-ring disk electrodes [14,15], hence enabling in-depth kinetic and mechanistic studies. However, construction of these types of electrodes is not always suitable for all minerals, due to conductive characteristics, such as the case of sphalerite, or when they are contained in concentrates or mineral waste. The electrochemistry group at UAM-Iztapalapa took advantage of the so-called carbon paste electrode technique (CPE) to solve these issues, but unlike other groups that used commercial carbon paste to prepare the electrodes [16,17], UAM's group developed a technique where ground mineral was mixed with graphite powder and then silicon oil was added to obtain the paste. In this way, this group led by Ignacio González [18-22] was able to demonstrate the advantages offered by carbon paste-mineral electrodes (CPME), highlighting the reproducibility of the electrochemical response obtained.

The development of the CPME at UAM-Iztapalapa triggered a wide range of mineral electrochemistry studies, particularly aimed at understanding flotation, leaching, and reactivity aspects, involving sulfide minerals and this has been the cradle of many researchers that are either starting or already have consolidated careers at different universities and research centers throughout Mexico. The following is an account of contributions over a span of more than 30 years.

Electrochemical Interactions Between Bacteria and Mineral Surfaces (early approach)

Early studies focused on the interaction between bacteria and minerals in solution, particularly how bacterial adhesion to mineral surfaces is affected. The use of CPME, allowed characterization of fresh mineral samples [21,22], as well as of mineral samples that had been subjected to chemical or biological processes [23].

Cruz et al [24] examined the electrophoretic mobility of the bacterium *A. ferrooxidans* and arsenopyrite (FeAsS), finding that the bacterium shows low electrophoretic mobility and consistently presents a negative charge, regardless of pH. It was observed that at pH levels below 2.5, there was a favorable electrostatic interaction between the bacterium and the mineral, which should enhance bacterial adhesion to arsenopyrite under optimal pH (1.8) conditions. However, this was not observed when FeAsS was exposed to *A. ferrooxidans* in a culture medium of acid characteristics.

By employing cyclic voltammetry and CPE containing arsenopyrite, with and without different biological and chemical treatments, these authors found that adhesion efficiency of bacteria is either low or absent due to preferential dissolution of Fe(II) from FeAsS under acid conditions, which modifies the mineral structure. In this way, it was shown that Fe(II) ions are a more available source of energy for *A. ferrooxidans* and hence it enables their oxidation to Fe(III), promoting then a non-contact dissolution of arsenopyrite.

Thus, the electrochemical response of CPE-FeAsS in a culture medium (Fig. 1(a)) was compared to that of realgar (As_2S_2) in the absence (Fig. 1(b)) and presence of Fe(II) ions (Fig. 1(c)). From this, it was shown that the process labelled as A, corresponds to oxidation of Fe(II) and process C1 to the corresponding reduction of Fe(III).

The acid dissolution that gives place to preferential release of Fe(II) from FeAsS and formation of a structure that is alike As_2S_2 , shows why there is a better resemblance of Fig. 1(c) with Fig. 1(a), showing that indeed at the interface there is preferential oxidation of Fe(II) to Fe(III), when it is available.

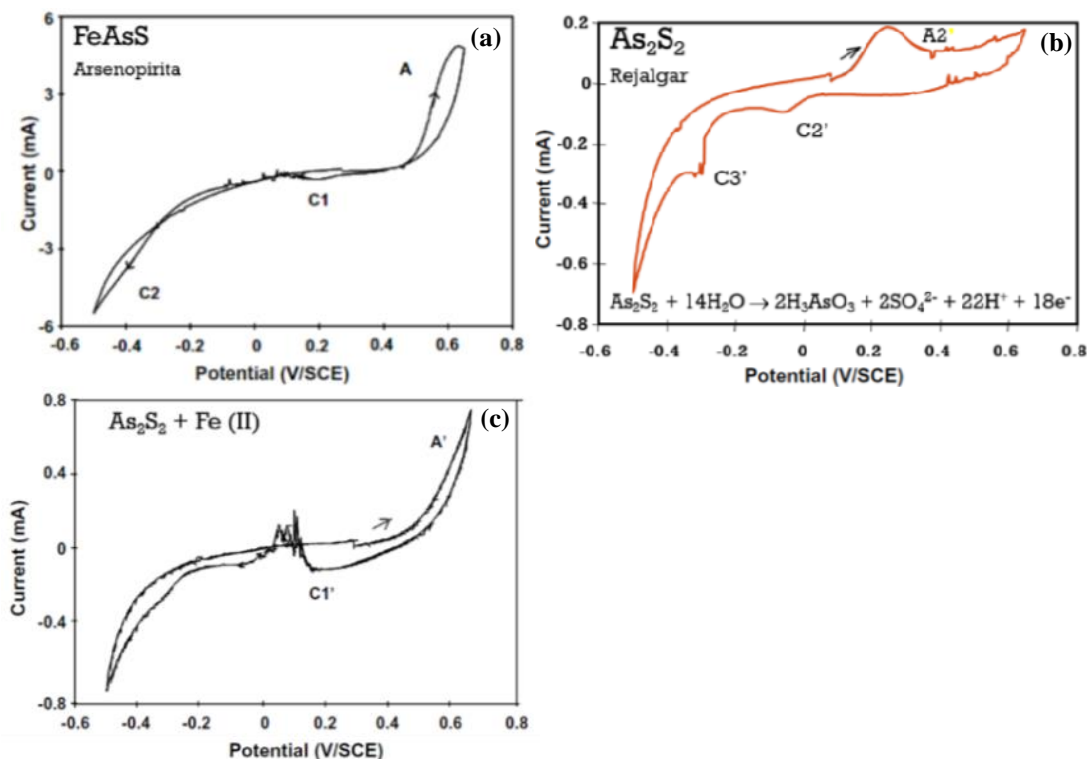


Fig. 1. Electrochemical response of CPME in a culture medium (pH=1.8) for *A. ferrooxidans*, where M = (a) FeAsS, (b) As_2S_2 , (c) As_2S_2 and Fe(II) in solution. From reference [24]

Advances in Carbon Paste Electrodes (CPE) for Mineral Dissolution Studies

Once the capacity and versatility of carbon paste electrodes (CPE) for studying metallic minerals dissolution mechanisms were established, a series of studies on sulfide minerals of interest to Mexico were developed. Given that sulfide minerals are the primary source of base metals, and that flotation is key to their separation, it is relevant to establish many of the interfacial phenomena involved to improve the efficiency of this process. Likewise, despite the efficiency of pyrometallurgical processes, they are detrimental to the environment and that has prompted the development of hydrometallurgical processes as a greener alternative. However, a major handicap of hydrometallurgical processes is that their efficiency is limited due to issues such as elemental sulfur formation and insoluble salts that passivate the mineral surface when sulfides are involved. The following are some examples of this, where several scenarios were evaluated based on the applied mineral treatment or processing, and a systematic strategy for the application of electrochemical techniques, mainly voltammetry, chronoamperometry, and their combinations, was developed for each mineral study based on its complexity.

Galena (PbS) Dissolution Mechanisms

Several studies were reported related to the electrochemical oxidation of galena and characterization of the species responsible for the slow dissolution kinetics of this mineral [25-27]. These studies utilized CPE-galena in a perchloric acid medium. Typical voltammograms obtained on CPE-galena without electrolyte agitation are shown in Fig. 2, with the potential sweep started in negative and positive directions from the open circuit potential (0.1 V). Other experimental conditions are described in the figure. The comparison of the voltammograms indicated that processes (B') and (C') are related to oxidative processes in (A'), while (D) and (D') correspond to the reduction of galena. The authors conducted an extensive voltammetric study on CPE-galena, varying the cathodic ($E_{\lambda-}$) and anodic ($E_{\lambda+}$) switching potentials, through which it was possible to assign the reactions corresponding to each peak or potential interval in the voltammograms. Additionally, through chronoamperometry, surface sulfur species formation was promoted and then characterized by voltammetry started in the negative direction. The authors reported that PbS oxidizes to elemental sulfur and Pb(II) in a potential range of 0.5 to 0.6 V vs. SCE, and that at potentials above 0.6 V vs. SCE, sulfur oxidizes to PbSO₄. It was found that the presence of elemental sulfur and PbSO₄ on the galena surface inhibits its dissolution, resulting in slow dissolution kinetics. This understanding is crucial for developing more efficient hydrometallurgical processes for lead extraction, based on inhibiting the stability of insoluble sulfur species.

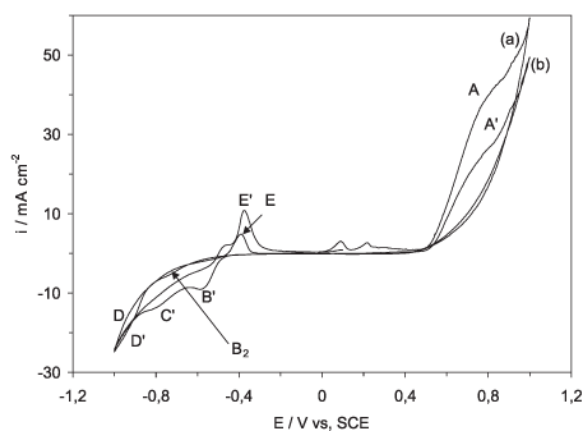


Fig. 2. Typical voltammograms obtained on CPE-galena (80:20 % weight) in 1.0 M HClO₄, ($\nu = 100 \text{ mV s}^{-1}$). The potential scan was started in the direction: (a) negative and (b) positive. From reference [25]

Sphalerite (ZnS) Electro-Oxidation

Another mineral of economic interest is sphalerite, a zinc sulfide mineral. Cisneros et al [26] carried out a study of this sulfide mineral and reported difficulty in generating a voltammetric signal from this mineral, which was consistent with that reported by Alberg y Asbjörnsson [17]. Despite evaluating two samples of sphalerite, voltammetry did not yield significant results. Only through analysis by varying the switching potential were determined two potential regions: one at $<0.5 \text{ V}$, where sphalerite oxidizes to form elemental sulfur and zinc cations, and the other at $E > 0.5 \text{ V}$, where the formed sulfur species were thiosulfate and sulfates (Fig. 3). However, a sequential mechanism could not be proposed. The studies were carried out in a 1.0 M NaClO₄ medium at pH 2, and it was observed that the iron content affects the conductivity of the sphalerite. However, the presence of pyrite in one of the samples (flotation concentrate) was not considered, therefore it was not possible to figure out the real effect of iron in solid solution with sphalerite. Hence, the main contribution of the sphalerite study was the application of anodic dissolution of sphalerite in perchloric acid and the effect of chloride ions on the oxidation of the mineral. The current recorded at different potentials versus the chloride content in the electrolyte allowed the generation of amperometric curves that defined two behaviors (Fig. 4). At potentials below 0.6 V, chloride enhances the dissolution process, which was associated with the porosity of elemental sulfur in the presence of these ions. At potentials where soluble

sulfur species are generated, higher chloride content limits dissolution, which the authors attributed to the formation of zinc chloride precipitates.

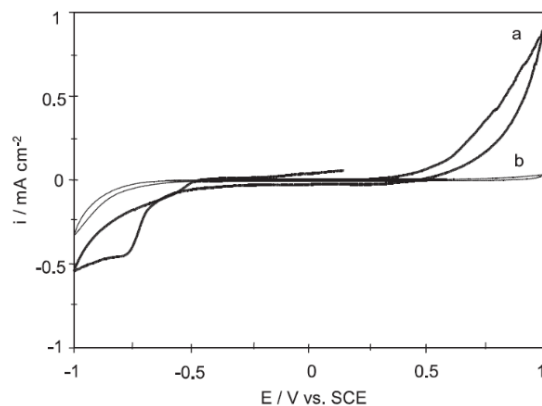


Fig. 3. Typical cyclic voltammograms obtained on CPE with different sphalerite samples (40:60 % weight) in 1.0 M NaClO₄ at pH 2, ($v = 100 \text{ mV s}^{-1}$). The potential scan was started in the positive direction. (a) Sphalerite concentrate (13.8 % Fe in solid solution); (b) natural ZnS (0.43 % Fe in solid solution). From reference [26].

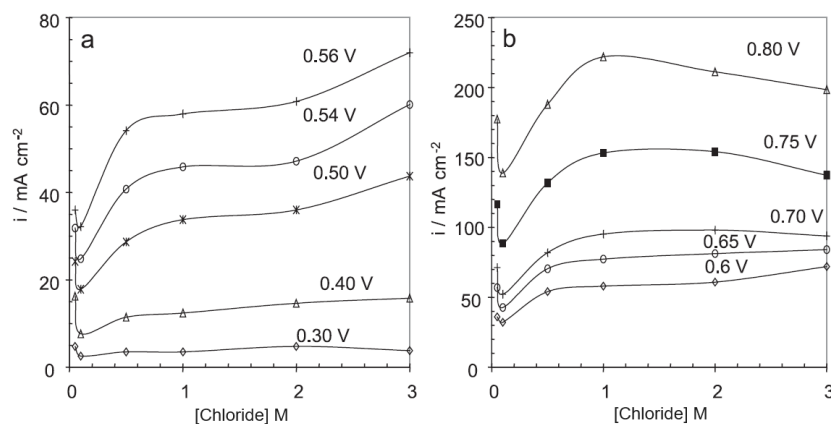


Fig. 4. Effect of chloride concentration on the voltammetric dissolution current of CPE-sphalerite (40:60 % weight), at the different potentials marked in the figure. Potentials were selected for the different oxidation stages: (a) when elemental sulfur is produced, (b) when $\text{S}_2\text{O}_3^{2-}$ and SO_4^{2-} are produced. From reference [26]

This study was complemented by including a comparison of the electrochemical behavior of sphalerite and galena, since these minerals are generally associated in polymetallic sulfide deposits [28]. In the comparison of the voltammograms for both sulfides, a region of very low current is observed up to 0.6 V for both minerals (Fig. 5). Beyond this potential, the current increases, but it is much higher for galena. The authors concluded that the initial stage is similar for both minerals, forming elemental sulfur and dissolved cations. Subsequently, oxidized sulfur species are formed; however, the reactivity of galena in the second region is up to twice that of sphalerite, which could be due to its p-type semiconductor character, that has greater sensitivity to oxidation.

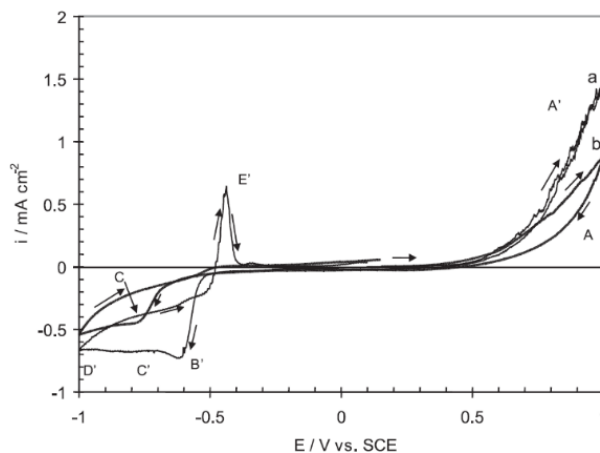


Fig. 5. Comparison of the voltammograms of (a) CPE-galena (80:20 % weight) (thin line), with the corresponding voltammogram of (b) CPE-sphalerite (40:60 wt.%) (thick line), in 1 M NaClO₄, pH = 2. The scan was started in the positive direction, at 100 mV s⁻¹. From reference [28]

Zinc concentrate leaching

Currently, the production of a specific metal concentrate requires the application of complex flotation circuits to separate each one of the metallic sulfides present in the ore. Despite this, some mineral concentrates still contain impurities that represent drawbacks for the actual pyrometallurgical processes, either from an economic or environmental standpoint. This type of concentrates are denominated complex minerals concentrates. To establish the basis for alternative hydrometallurgical processes for complex zinc concentrates, an electrochemical study of this mineral was carried out by Nava et al [29]. The anodic dissolution mechanism of a complex zinc concentrate was studied using a more elaborated strategy combining several common electrochemical techniques with CPE-mineral. Voltammograms with CPE-complex zinc concentrate in 1.7 M H₂SO₄ electrolyte, starting the potential scan in both the negative and positive directions from the open circuit potential (Fig. 6), identified potential intervals where different components of the concentrate were activated. Chronoamperometry was applied at different constant anodic potential pulses for 180 seconds within the established potential ranges. The charge from chronoamperograms was integrated to construct an anodic charge versus electrolysis potential curve. From this data four potential zones, where the charge variations occur, were determined. Interestingly, the electro-dissolution of the concentrate is progressive and favored by increasing the applied potential. The authors attributed these trends to the oxidation of the various minerals in the concentrate.

The authors verified this by analyzing the different metals in the electrolyte and the modified surface of the CPE-zinc complex concentrate after each potential pulse. The dissolved metals in the liquor were analyzed using anodic stripping with thin-film mercury electrodes. The results identified electrochemical reactions during the oxidation of the complex zinc concentrate and how the release of Zn, Cd, Pb and Cu is dependent on the potential applied (Fig. 7). This provides a basis for selecting chemical or biological oxidizing agents that can selectively dissolve these metals sulfides from the concentrate, avoiding products that inhibit leaching.

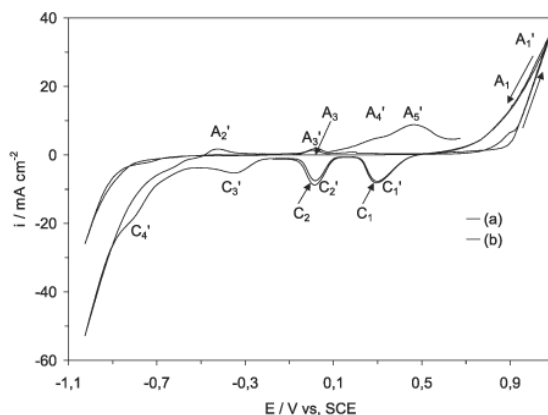


Fig. 6. Typical voltammograms obtained on CPE-complex zinc concentrate (80:20 % weight) in 1.7 M H₂SO₄, ($v = 100 \text{ mV s}^{-1}$). The potential scan started from the open circuit potential (-21 mV) in the direction: (a) negative, (b) positive. From reference [29]

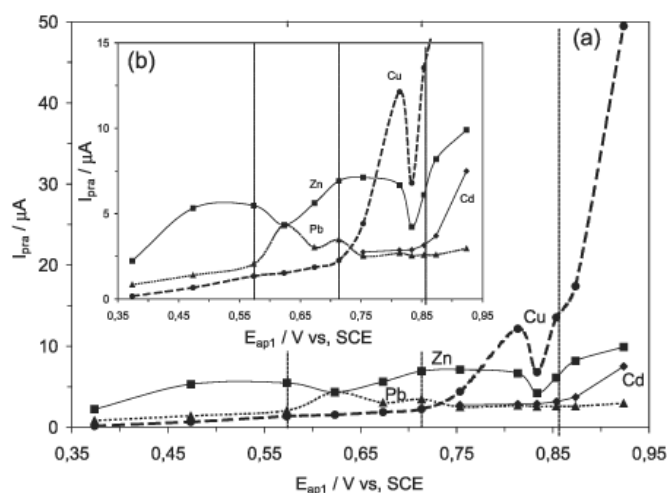


Fig. 7. (a) Anodic re-dissolution peak currents (I_{pra}), obtained in the liquor containing the different electro-dissolved metals (indicated in the figure) after the CPE-complex zinc concentrate (80:20 % weight) was oxidized at different potentials.[29]

Copper sulfide mineral reactivity

Copper sulfides are the main source of copper and among them the most relevant is chalcopyrite (CuFeS₂), as it is the main source worldwide. Unfortunately, CuFeS₂ is highly refractory in sulfate acid media under oxidizing conditions, hence, making it difficult to extract copper. Despite years of research on this mineral, for a long time there was no agreement on the cause of this unreactive behavior which was previously attributed to passivation due to formation of a sulfur layer. At the present time, it has been confirmed that it is due to a metal-deficient copper polysulfide that results from a solid-state transformation of the chalcopyrite surface during the oxidation reaction [30]. This was something that in fact, was exposed through CPE-CuFeS₂ in the study of Lázaro et al. [20] and it was further supported by a study of Nava and González [31,32] that coupled CPE-CuFeS₂ with anodic stripping voltammetry for a detailed characterization of the products formed at different potential regions. In this manner, these authors showed that the metal-deficient polysulfide was the

main product at potentials lower than 1 V/SHE. More recently, the CPE technique has allowed electrochemical comparisons of mineral surface modification with organic agents and how this can improve dissolution of CuFeS_2 [33].

Likewise, the electrochemical behavior of three copper minerals, CuFeS_2 , chalcocite (Cu_2S), and bornite (Cu_5FeS_4) in sulfuric acid has demonstrated that under similar dissolution conditions CuFeS_2 presents the lowest dissolution kinetics [34]. Electrochemical techniques, such as cyclic voltammetry and electrochemical impedance spectroscopy, analyzed the minerals' dissolution reactions and mechanisms. Bornite had the highest dissolution rate with less tendency for passivation, suggesting higher reactivity in sulfuric acid compared to the other minerals. Voltammetric curves indicated that chalcocite and not bornite is an intermediary product of chalcopyrite reduction and this was the result of comparing the reduction peak C2 shown in the voltammogram of Fig. 8, which is in correlation with results obtained with chalcopyrite [20].

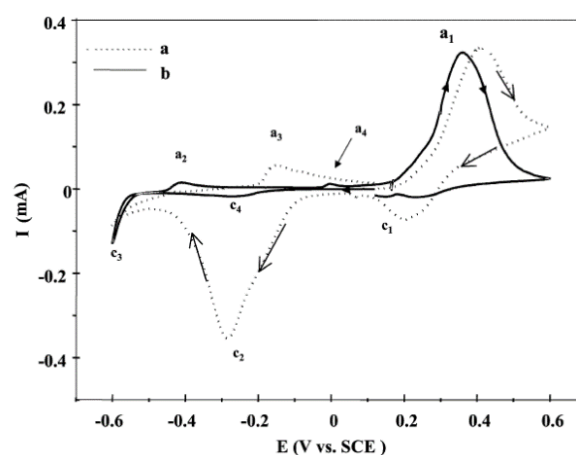


Fig. 8. Typical cyclic voltammograms obtained with chalcocite–CPE (20 wt.%, using silicon oil binder) in a 1 M H_2SO_4 solution, at $v=20 \text{ mV s}^{-1}$. The scan potential was started in a different direction from open circuit potential ($E_{\text{OCP}}=0.15 \text{ V/SCE}$): (a) positive direction; (b) negative direction. The arrows indicate the scan potential direction. From reference [34].

Silver minerals and cyanidation refractoriness

An interesting study compared the electrochemical behavior of silver mineral samples from different origins to study the refractoriness to cyanidation, a common leaching method [35]. Despite similar silver content, the samples differed in iron content and silver phases present. One sample contained diverse sulfosalts of silver like aguilarite, freibergite, polybasite, and hessite, while the other mainly contained acanthite. The study proved that the more complex mineral silver sample is less susceptible to electrochemical oxidation and thus more refractory to cyanidation than silver in acanthite (Fig. 9). This was demonstrated using electrochemical techniques and correlated with leaching studies, showing that silver in acanthite is more active to oxidation and easier to extract. This study provides a quick assessment of the refractory properties of silver minerals, beneficial for predicting extraction efficacy by cyanidation. In another study, the same author demonstrated that the reactivity of acanthite contained in this concentrate favors the voltammetric oxidation of pyrite due to a galvanic effect of the former on the latter [36]. This is because the rest potential (equilibrium potential) of acanthite is higher than that of pyrite. To prove this, the authors [35,36] compared the mineral sample responses before and after selectively leaching out the acanthite phase. The galvanic effect of acanthite can be observed also in comparison with Fig. 9, where the current of anodic oxidation occurs at a lower potential in Fig. 9(a) (with acanthite) compared to Fig. 9(b) (without acanthite). The galvanic effect enhances the reactivity of pyrite, which is one of the main species known as cyanicides in the cyanidation process.

About silver sulfosalts, in Mexico there are an important presence of this mineral in polymetallic ores. The unique properties of sulfosalts affect metallurgical processes like leaching and flotation. Understanding the

reactivity and electrochemical behavior of silver sulfosalts is essential for optimizing silver recovery methods and improving metallurgical efficiency. Melendez et al [37] examined the reactivity of ruby silver minerals, proustite and pyrargyrite, using carbon-paste and paraffin-impregnated graphite electrodes. Samples were synthesized and characterized through various methods, including XRD and SEM-EDS.

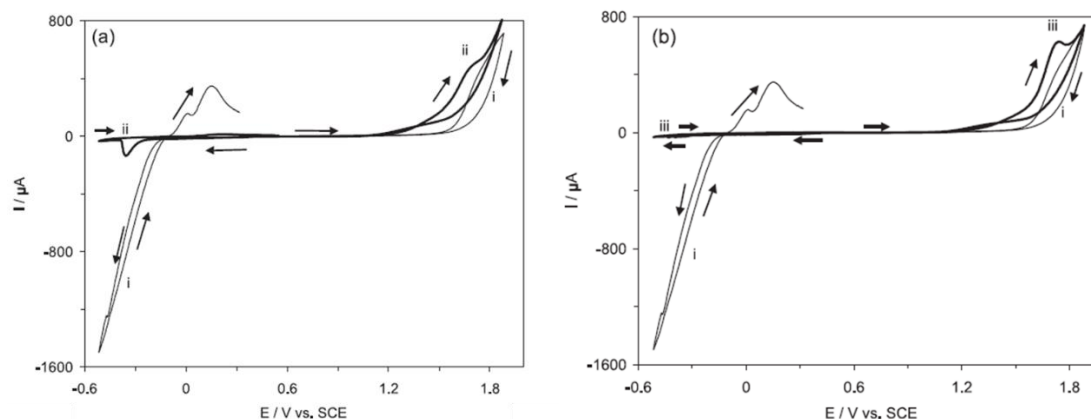


Fig. 9. Typical voltammograms obtained on CPE-mineral (70:30% weight) in 0.3 M NaCN at pH 10.60, ($\nu = 25 \text{ mV s}^{-1}$). The potential scan was started in the positive direction from the open circuit potential. (a) Pyrite concentrate with acanthite (ii), (b) Pyrite concentrate without acanthite (iii). Thin line, acanthite (i in a and b). From reference [35]

The investigation focused on the oxidation and reduction processes, influenced by the ligand-to-metal charge transfer transition. Despite differences in As and Sb content, the reactivity was similar due to the solid-state structures and oxidation states. The pnictogen (As or Sb) affected the conduction and valence band edges, modulating reactivity. Anodic dissolution and silver reduction processes were linked to specific band states, and the difficulty in dissolving these minerals in cyanide was attributed to the presence of AsS_3 and SbS_3 groups.

Assessment of sulfide mineral reactivity in mining residues

The commitment to sustainable development in mining involves the restoration and control of potential impacts during the various stages of a mining project. In precious and base metal mining from sulfides, an important aspect is assessing the environmental impact that solid waste, such as tailings or waste rock, can cause. A characteristic factor of sulfide systems is the generation of Acid Rock Drainage (ARD), which forms through the weathering of mining residues, resulting in acidic effluents with high iron and heavy metal content. With the aim of identifying the alteration processes occurring in sulfide minerals, primarily pyrite, a collaborative group of researchers from UAM-Iztapalapa, the Institute of Metallurgy at UASLP, and the University of British Columbia developed a strategy that successfully determined the factors and processes affecting the reactivity of iron sulfides from different mining sites and deposit types. This strategy yielded results comparable to those obtained using techniques defined by the relevant environmental standards.

Fig. 10 presents the voltammograms obtained for six samples of pyrite collected in different mining sites [38]. The typical response of pyrite is a low current zone followed by an abrupt increase of current associated with pyrite oxidation. It can be observed that each sample has unique features in the oxidation peak. From these responses a series of parameters were established, such as charge under the curve, current increase-to-potential ratio, and onset potential of oxidation (Table 1).

From the comparison of voltammetric response (Fig. 10) and the electrochemical parameters, it was proposed that Huckleberry pyrite was the most reactive among all the samples analyzed, and that the degree of

reactivity of the pyrite samples decreased following the order: Huckleberry, Louvicourt 1, Zimapán, Tizapa, Louvicourt 2, and Brunswick. Therefore, since Brunswick pyrite was the least reactive, it presented the lowest I/E ratio [38].

In addition, the evolution of pyrite reactivity through alteration (weathering) process, were also evaluated from the changes in electrochemical parameters obtained for samples of pyrite with different alteration time and allowed for the determination of the effect of mineral texture and associations with other minerals on the reactivity of pyrite.

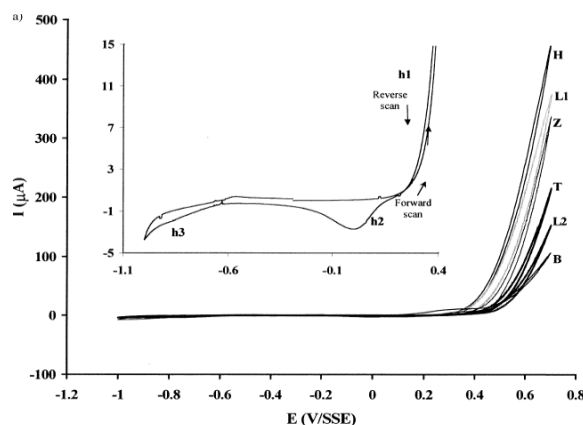


Fig. 10. Typical voltammograms obtained for pyrite samples from different origins: H, Huckleberry; L1, Louvicourt 1; L2, Louvicourt 2; T, Tizapa; Z, Zimapán; B, Brunswick. The voltammograms were obtained from a 50 % CPE-pyrite in 0.1M NaNO_3 at 20 mV s^{-1} . (a) Complete voltammetric response, (b) low current region of the voltammograms. From reference [38]

Table 1. Electrochemical parameters associated with the CPE-mineral voltammetric response for pyrite samples before (fresh) and after 4 and 10 weeks of weathering. The electrochemical characterization was carried out in 0.1 M NaNO_3 . From reference [38].

Sample	OCP ^a (V)	$E^b_{I=10\mu\text{A}}$ (V/SSE)			I/E ^c Rate ($\mu\text{A/mV}$)			Q^d (mC)		
		Fresh	4 weeks	10 weeks	Fresh	4 weeks	10 weeks	Fresh	4 weeks	10 weeks
Huckleberry	-0.27	0.37	0.43	0.43	1.86	1.38	1.37	5.84	3.27	3.16
Louvicourt 1	-0.27	0.40	0.46	0.49	1.54	1.20	0.71	4.52	2.79	1.57
Louvicourt 2	-0.19	0.49	0.43	0.46	0.70	1.24	0.94	1.50	3.15	2.17
Tizapa	-0.18	0.47	0.42	0.49	0.98	1.38	0.64	2.13	2.50	1.49
Zimapán	-0.17	0.44	0.46	0.47	1.47	1.22	1.25	3.47	2.79	2.18
Brunswick	-0.29	0.44	0.43	0.41	0.44	1.33	1.62	1.41	3.32	4.78

^aOCP-Open circuit potential of CPE-fresh mineral

^bI/E Rate - current increase as potential increase ratio

^c $E_{(I=10\mu\text{A})}$ - onset potential in forward scan for pyrite oxidation process

^dQ - Charge evaluates from the area below the pyrite oxidation voltammograms

The strategy previously described was also applied to pyrrhotite, another iron sulfide with common presence in Mexican mining residues [39]. For this mineral it was established that the formation of FeOOH and S⁰ layers on the mineral surface was the main factor affecting reactivity. Identifying these factors would not have been possible with only knowledge of the samples mineralogical characteristics and the results from the application of kinetic tests. Finally, the strategy was validated by the study of mining residues from different sites, where it was confirmed the advantages of electrochemical techniques to determine the activity of sulfides under different mineral associations and weathering conditions [40].

Hence, knowledge of specific effects of each type of impurity on the oxidative capacity of the mineral, as well as the surface layers formed on the mineral, can be used as a basis for developing a method to assess and predict the potential for Acid Rock Drainage (ARD) from mining residues containing sulfide minerals (Fig. 11).

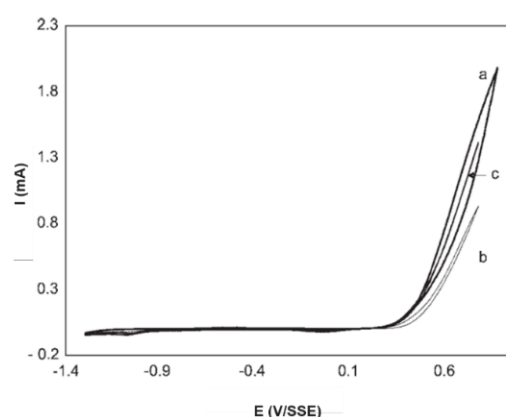


Fig. 11. Evolution of the voltammetric behavior of the mining waste sample at different alteration times: (a) unleached, (b) 2 weeks, and (c) 10 weeks. CPE-Mineral at 50 % in 0.1M NaNO₃. The potential scan was started in the positive direction at 20 mV s⁻¹. From reference [40]

Advancements in characterization techniques and electrochemical studies for understanding bacteria-mineral interaction in sulfide systems

Fifteen years after the initiation of electrochemical studies of minerals in Mexico, and with advancements and access to interface characterization techniques, it became possible to confirm the nature of the phases formed during the mechanisms predicted by electrochemical and thermodynamic diagram studies. With more options for spectroscopic and microscopy techniques, studies on bacteria-mineral interactions were again undertaken, which have gained interest due to the cost-effectiveness of bioleaching systems compared to other alternatives for the valorization of mining residues. Consequently, a series of electrochemical investigations on pyrite and chalcopyrite, the main minerals of interest in bioleaching, were developed and a summary of the works contributing to this are listed in Table 2 [41,42].

It must be noted that for the application of characterization techniques, it was necessary to use bulk electrodes. This was because, once the stages involved in the oxidative process were defined using CPME, the potentiostatic pulses needed to generate specific surface conditions on a bulk electrode of the mineral under study were determined. Spectroscopic and microscopic techniques permitted the definition, rather than just inference, of the mechanisms and surface products generated. Furthermore, by incorporating microbiological staining techniques, the conditions for the formation of biofilms from different bacterial strains, both on pyrite and chalcopyrite, were established.

Influence of the surface speciation on biofilm attachment to chalcopyrite

The passivation of chalcopyrite is an industrial concern. It is considered that the redox potential of the solution must be controlled during leaching to avoid the formation of passive phases. Lara et al. [42] demonstrated that it is crucial to consider the interfacial potential rather than the bulk solution potential, as interfacial conditions include the biofilm/mineral system and its biological, chemical, physical, and electrochemical properties. Using traditional strategies in CPE-Mineral studies, four potential zones were established based on the chronoamperograms of chalcopyrite in CPE (Fig. 12).

Table 2. Summary of contributions to the understanding of Bacteria-Mineral Interaction in Sulfide Systems by Mexican researchers.

Authors	Paper title	Journal	Year/Ref
Lara et al	Influence of the sulfur species reactivity on biofilm conformation during pyrite colonization by <i>Acidithiobacillus thiooxidans</i>	Appl. Microb. Biotech	2012 [41]
Lara et al	Influence of the surface speciation on biofilm attachment to chalcopyrite by <i>Acidithiobacillus thiooxidans</i>	Appl. Microb. Biotech	2013 [42]
Saavedra et al	Interactions of mimic weathered pyrite surfaces (FeS ₂) with acidic culture media (0 K): An approach for (bio)leaching applications	Hydrometallurgy.	2018 [43]
Mendez-Tovar et al	Electrochemical monitoring of <i>Acidithiobacillus thiooxidans</i> biofilm formation on graphite surface with elemental sulfur	Bioelectrochemistry	2019 [44]
Saavedra et al	Attachment of <i>Leptospirillum sp.</i> to chemically modified pyrite surfaces. Fast and simple electrochemical monitoring of bacterial-mineral interactions	Hydrometallurgy.	2021[45]

Oxidative potentiostatic pulses defined for each zone were applied to massive chalcopyrite electrodes for one hour in sterile culture medium at pH 2 and Raman spectroscopy was employed to analyze superficial phases, while bacteria colonization was observed by SEM (Fig. 13). [42] In zone I, low oxidative capacity phases, such as S_n²⁻ (e.g., Cu_{1-x}Fe_{1-y}S₂), were obtained, where *A. thiooxidans* poorly colonized the electrode surface and did not form a biofilm. A progressive increase in cell density was observed on chalcopyrite surfaces with covellite and mainly S⁰ in zones II and III. In zone IV, a well-developed and adherent biofilm with a high content of exopolysaccharides was formed. The cells of *A. thiooxidans* were embedded in the exopolysaccharides and partially covered by covellite (CuS) and S⁰ aggregates. Covellite is generated as a secondary phase during chalcopyrite leaching and is then oxidized to S⁰ and Cu²⁺. The results confirmed that the activity of *A. thiooxidans* and biofilm formation in the presence of CuS and S⁰ phases

indicate that the biofilm structure results from surface speciation on chalcopyrite; this knowledge has contributed to understanding how cells interact with the surface and the environment in bioleaching systems.

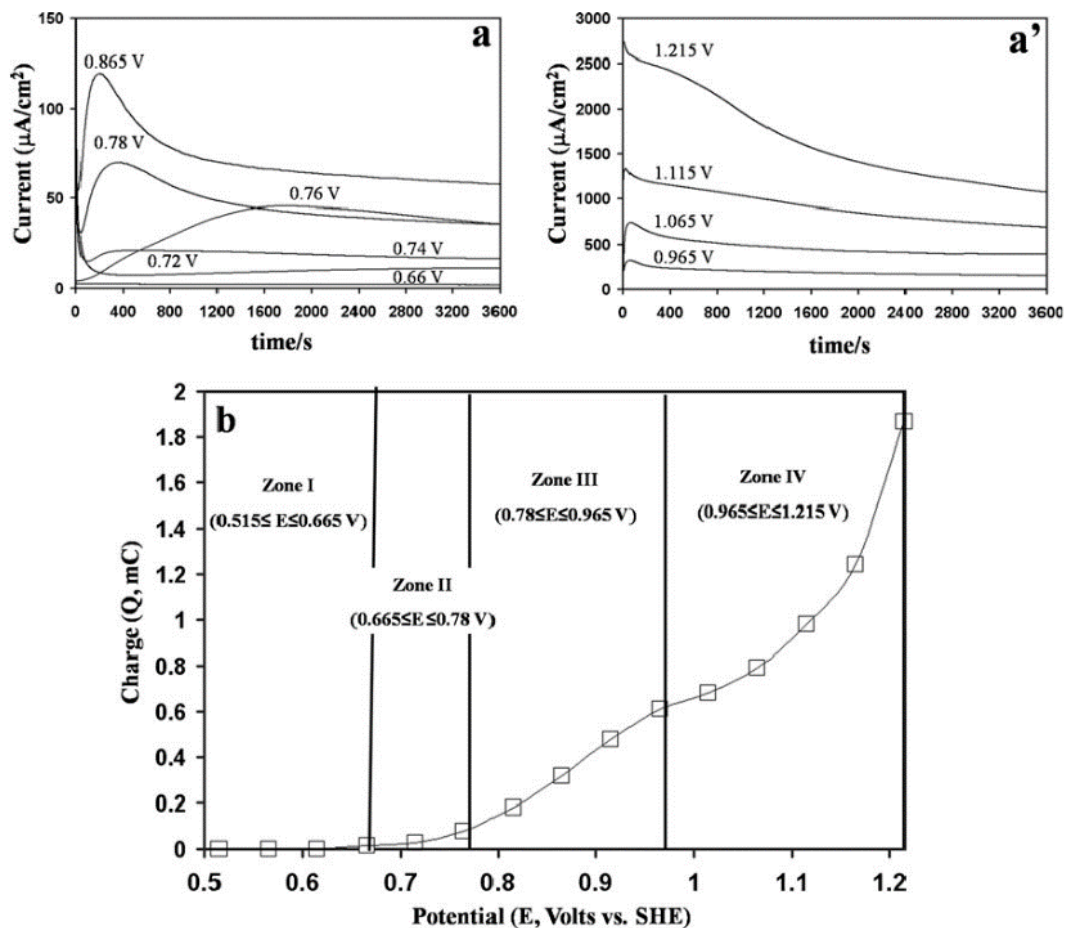


Fig. 12. Typical current transients obtained on unmodified bulk chalcopyrite electrode in ATCC-125 medium (pH 2). The applied potential pulse, E_{an} , is varied involving zones I, II, III, and IV from (a) and (a'). The applied potentials are indicated in the figure. (b) Charges as a function of the applied potential pulse, E_{an} . Q values were evaluated from the typical current transients obtained on unmodified MCE (a, a'). The different zones are indicated in the figure. From reference [42]

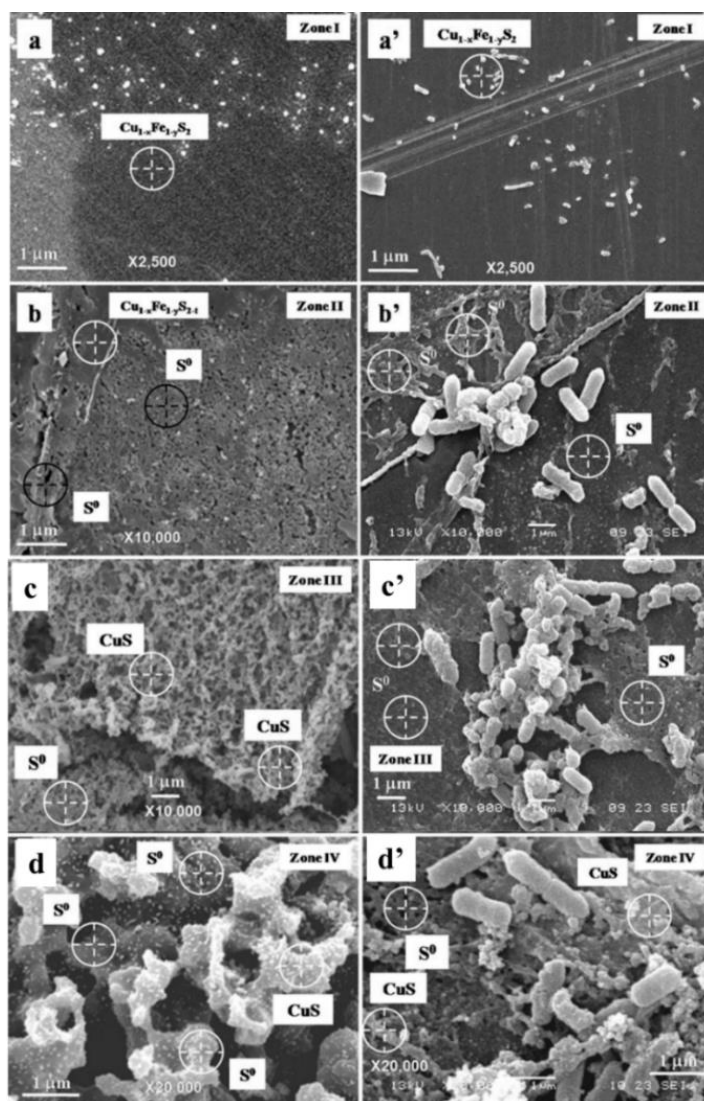


Fig. 13. SEM images collected on abiotic leaching control samples (a–c) and surfaces from biotic assays (a'–b', and c') for electrooxidized chalcopyrite surface by application of E_{an} in each zone indicated. The main secondary phases are indicated in the figure, based on EDS analysis. From reference [42].

Electrochemical Monitoring of bacteria attachment to pyrite surfaces

Despite the complexity of obtaining quality results in such a complex system as the electrolyte-bacteria-mineral, strategies were established, and electrochemical impedance spectroscopy studies were developed. These studies allowed the characterization of the properties of this triple layer interface. In a study focused on the adhesion of *Leptospirillum sp.* bacteria to modified pyrite surfaces, electrochemical impedance spectroscopy (EIS) was used to monitor this bacteria-mineral interaction. The objective was to develop a fast and simple method for evaluating bacterial adhesion to minerals, particularly in biohydrometallurgical processes [45]. The results showed significant changes in low frequencies depending on the chemical characteristics of the modified surfaces (Fig. 14). Nyquist diagrams showed varying complexities based on the chemical species at the pyrite and surface-modified pyrite interfaces. Additionally, the EIS allowed tracking of the initial steps of bacterial adhesion to pyrite electrodes, and a correlation was found between changes in phase

angle measured by EIS and the number of adhered bacteria determined by direct counting. The spectra for pyrite and surface modified pyrite electrodes were fitted to different proposed equivalent electric circuits (Fig. 15) and in this way a quantitative relationship between the impedance spectra and surface states and the attachment of *Leptospirillum sp.* to electrode surfaces was established.

This study provided the basis for the development of sensors for rapid and multiplexed monitoring of bacterial adhesion in biohydrometallurgical processes.

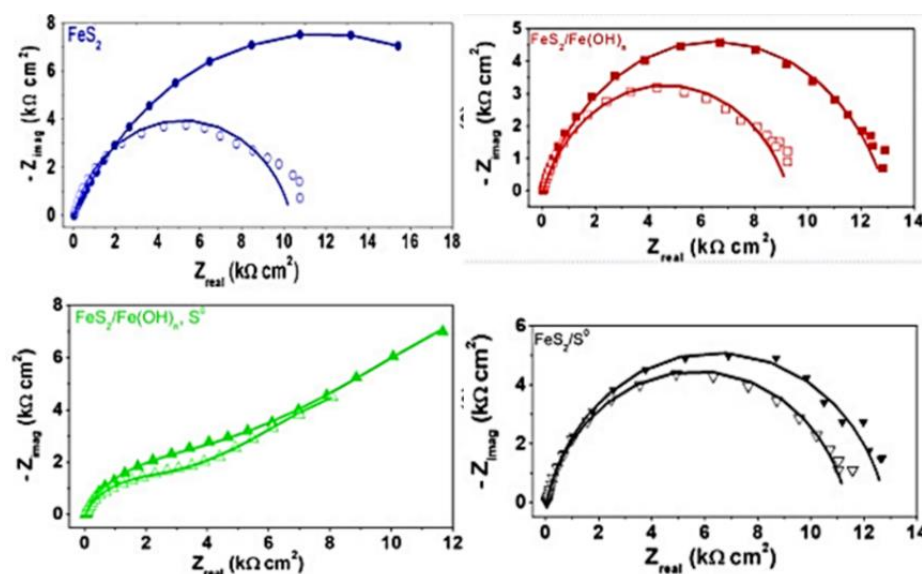


Fig. 14. Nyquist plots obtained for pyrite and pyrite modified electrodes (indicated in the figure). EIS were performed before (0 h, closed symbols) and after (6 h, open symbols) the addition of *Leptospirillum sp.* bacterium. Solid lines correspond to the equivalent electric circuit adjustment. 0K medium pH 1.8 was used as the electrolyte. From reference [45]

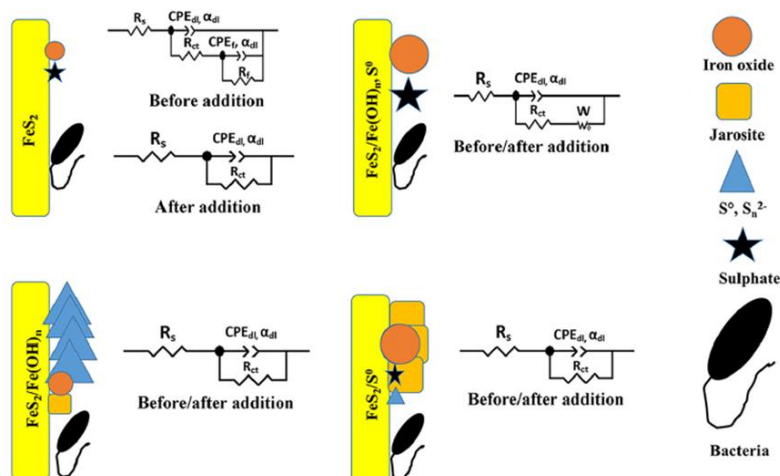


Fig. 15. Scheme describing interface conditions and their respective equivalent electric circuit assigned for the adjustment of impedance spectra shown in Fig. 14, for pyrite and surface modified pyrite electrodes. From reference [44]

Comprehensive mexican contribution to the electrochemical study of sulfide minerals

In the earlier sections, we have highlighted the significance and main contributions to the electrochemical study of mineral sulfides by Mexican researchers. The reviewed documents are products generated during the training of some of these researchers at UAM-Iztapalapa, under projects led by Professor Ignacio González. Fig. 16 shows the historical production at UAM-Iztapalapa, as well as the output generated by researchers from Professor González's school, some still as collaborations with him but led by researchers at their respective universities. These universities include Universidad Autónoma de San Luis Potosí (UASLP), Universidad Autónoma del Estado de Hidalgo, Universidad Juárez del Estado de Durango (UJED), and outside of Mexico, Universidad Industrial de Santander in Colombia and Universidad de Buenos Aires in Argentine.

This co-generation of articles began in 2010 (Fig. 16), expanding fields of study or applying already established ones to conditions of interest in the states where the research groups in electrochemistry of metals and minerals are located. Examples include the work of a researcher at UJED on the alteration of mining residues in the calcareous environments of Mexico, and studies on the interaction of collectors and the effect of associations and water quality in flotation systems by the UASLP's mineral electrochemistry group. The production of articles in Mexico on this subject amounts to around 70 peer-reviewed articles, of which 70% have been published in JCR journals, and likewise, 70 % have been produced at UAM-Iztapalapa under the direction of Professor Ignacio González.

Although this number might seem low compared to topics developed by a larger number of research groups, it is important to note that the community dedicated to mining and extractive metallurgy is not very large and has decreased for two reasons: the migration to topics such as the synthesis and production of nanoparticles (adding value to metals and minerals) and the closure of mining companies in several developed countries, along with the belief that most research topics in this field were exhausted. However, the importance and impact of mining have been growing over the past 10 years (from 300 to almost 1300), as evidenced by the increase in the number of citations received by scientific outputs from our country (Fig. 16).

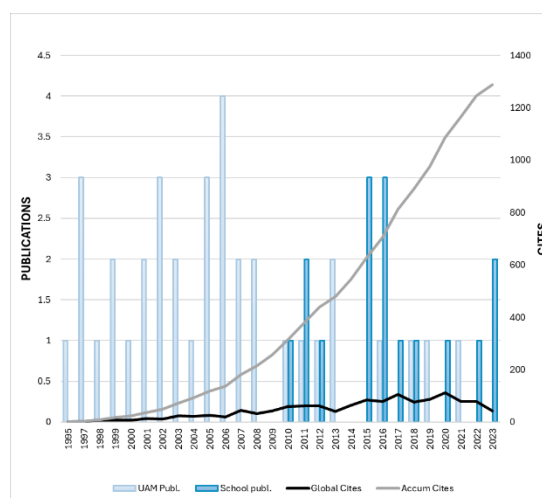


Fig. 16. Comprehensive production and citation generated from sulfide minerals electrochemistry research. Data compiled from Web of Science.

Effective strategies and methodologies have been developed to generate data essential for creating reaction models in both bio and hydrometallurgical systems at laboratory and industrial scales. The impact of water and energy conservation on the criticality of emerging metals for the energy transition requires the development of processes with low resource consumption. There are extensive opportunities for both

fundamental and applied research in critical metal extraction processes, where chemists hold a significant advantage over other professions.

Conclusions

The brief account of the works here presented are a sample of the ways in which mineral electrochemistry research has contributed, impacted and transcended in the research field of mining operations, especially those involving mineral sulfides. It has been particularly important to highlight how some of the initial research results have matured and advanced through time because of UAM's school and the relevance of continuing forming human resources in Mexico that are able to apply the techniques and research strategies that have been developed. The sustainability of many production processes depends on overcoming many challenges that are bound to the current complexity of valuable minerals, the demand of circular economy approaches and the more stringent environmental laws, hence mineral electrochemistry plays a key role in achieving the sustainability goal.

Acknowledgements

The authors take this opportunity to thank Professor Ignacio Gonzalez, the pioneer of mineral electrochemistry in Mexico and lead author and co-author of most of the work here presented. His contributions are not only intellectual but also come from the strive of providing projects and financial resources that have been the career jump start of many young researchers.

References

1. Bailey, L.K., Doctor of philosophy thesis. The University of British Columbia, **1977**
2. Peters, E.; Majima, H. *Can. Metall. Q.* **1968**, 7, 111–117. DOI: <http://dx.doi.org/10.1179/cm.1968.7.3.111>.
3. Woodcock, J.T. *Proc. Aust. Inst. Min. Met.* **1961**, 198, 47.
4. Woods, R. J. *Phys. Chem.* **1971**, 75354.
5. Richardson, P. E.; Srinivasan, S.; Woods, R. Proceedings of the 1st Symposium on Electrochemistry in Mineral and Metal processing, **1984**, 677.
6. Richardson, P. E., Woods, R. (Eds), Proceedings of the 2nd Symposium on Electrochemistry in Mineral and Metal processing, **1988**, The Electrochemical Society, 563.
7. Woods, R., Richardson, P. E. (Eds), Proceedings of the Third Symposium on Electrochemistry in Mineral and Metal processing, **1992**, The Electrochemical Society, 583.
8. Woods, R., Richardson, P. E., Doyle F. (Eds), Proceedings of the Fourth Symposium on Electrochemistry in Mineral and Metal processing, **1996**, The Electrochemical Society, 460.
9. Woods, R., Doyle F. (Eds), Proceedings of the V Symposium on Electrochemistry in Mineral and Metal processing, **2000**, The Electrochemical Society, 378.
10. Doyle, F.M., Kelsall, G. H. Woods, R. (Eds), Proceedings of the VI Symposium on Electrochemistry in Mineral and Metal processing, **2003**, The Electrochemical Society, 413.
11. Doyle, F.M., Kelsall, G. H. Woods, R. (Eds), Proceedings of the VII Symposium on Electrochemistry in Mineral and Metal processing, **2006**, The Electrochemical Society, 420.
12. Doyle, F., Woods, R., Kelsall, G. H. (Eds) Proceedings of the 8 Symposium on Electrochemistry in Mineral and Metal processing, **2010**, The Electrochemical Society, 376.

13. Zhu X., Li J., Bodily D. M., Wadsworth M. *J. Electrochem. Soc.*, **1993**, 140, 1927. DOI: <http://dx.doi.org/10.1149/1.2220741>.
14. Ahlberg, E., Broo, A. E. *J. Electrochem. Soc.* **1997**, 144, 1281
15. Yin, Q., Kelsall, G. H., Vaughan, D. J., Welham, N. J. *J. Colloid Interface Sci.* **1999**, 210, 375–383. DOI: <http://dx.doi.org/10.1149/1.1837584>.
16. Ahlberg, E.; Asbjörnsson, J. *Hydrometallurgy*. **1993**, 34, 171-185. DOI: [http://dx.doi.org/10.1016/0304-386X\(93\)90033-A](http://dx.doi.org/10.1016/0304-386X(93)90033-A).
17. Ahlberg, E., Asbjörnsson, J., *Hydrometallurgy*. **1994**, 36 19-37. DOI: [http://dx.doi.org/10.1016/0304-386X\(94\)90039-6](http://dx.doi.org/10.1016/0304-386X(94)90039-6).
18. Martínez, N., González, I., Arce, E., In: Sociedad Mexicana de Electroquímica (Editor), Electroquímica, Tecnología y Protección Ambiental. SME, Querétaro. **1993**, 172-177.
19. Lázaro, I.; Rodríguez, I. BSc Report, Instituto Politécnico Nacional, México, 1994.
20. Lázaro, I.; Martínez-Medina, N.; Rodríguez, I.; Arce, E.; González, I. *Hydrometallurgy*. **1995**, 38, 277-287. DOI: [https://dx.doi.org/10.1016/0304-386X\(94\)00070-J](https://dx.doi.org/10.1016/0304-386X(94)00070-J).
21. Lázaro, I.; González, I.; Cruz, R.; Monroy, M. *J. Electrochem. Soc.* **1997**, 114, 4128. DOI: <http://dx.doi.org/10.1149/1.1838154>.
22. Lázaro, I.; Cruz, R.; González, I.; Monroy, M. *Int. J. Miner. Process.* **1997**, 50, 63-75. DOI: [http://dx.doi.org/10.1016/S0301-7516\(97\)00004-5](http://dx.doi.org/10.1016/S0301-7516(97)00004-5).
23. Cruz, R.; Lázaro, I.; Rodríguez, J. M.; Monroy, M.; González, I. *Hydrometallurgy*. **1997**, 46, 303-319. DOI: 10.1016/S0304-386X(97)00027-3.
24. Cruz, R.; Lázaro, I.; González, I.; Monroy, M. *Miner. Eng.*, **2005**, 18, 10, 1024-1031. DOI: <http://dx.doi.org/10.1016/j.mineng.2005.01.015>
25. Nava, J. L.; Oropeza, M. T.; González, I. *Electrochim. Acta.* **2002**, 47, 1513-1525. DOI: [http://dx.doi.org/10.1016/S0013-4686\(01\)00881-7](http://dx.doi.org/10.1016/S0013-4686(01)00881-7).
26. Cisneros-González, I. PhD Thesis; UAM-I, México, 2001.
27. Cisneros-González, I.; Oropeza-Guzmán, M. T.; González, I. in: *Electrochemistry in Mineral and Metal Processing V*; Woods, R.; Doyle, F. M., Eds.; The Electrochemistry Society; N.J., **2000**; 249.
28. Cisneros-González, I.; Oropeza-Guzmán, M. T.; González, I. *Electrochim. Acta.* **2000**, 17, 2729-2741. DOI: [http://dx.doi.org/10.1016/S0013-4686\(00\)00392-3](http://dx.doi.org/10.1016/S0013-4686(00)00392-3).
29. Nava, J. L.; Oropeza, M. T.; González, I. *J. Electrochem. Soc.* **2004**, 151, B387. DOI: <http://dx.doi.org/10.1149/1.1753583>.
30. Nicol, M. J.; Miki, H.; Zhang, S. *Hydrometallurgy*. **2017**, 171, 198-205. DOI: <http://dx.doi.org/10.1016/j.hydromet.2017.05.016>.
31. Nava, D.; González, I. *Electrochim. Acta.* **2006**, 51, 25, 5295-5303. DOI: <http://dx.doi.org/10.1016/j.electacta.2006.02.005>.
32. Nava, D.; González, I.; Leinen, D.; Ramos-Barrado, J. R. *Electrochim. Acta.* **2008**, 53, 14, 4889-4899. DOI: <http://dx.doi.org/10.1016/j.electacta.2008.01.088>.
33. Castillo-Magallanes, N.; Cruz, R., Lázaro, I. *Electrochim. Acta.* **2020**, 355, 136789. DOI: <http://dx.doi.org/10.1016/j.electacta.2020.136789>.
34. Arce, E.; González, I. *Int. J. Miner. Process.* **2002**, 67, 17-28. DOI: [http://dx.doi.org/10.1016/S0301-7516\(02\)00003-0](http://dx.doi.org/10.1016/S0301-7516(02)00003-0).
35. Luna-Sánchez, R. M.; González, I.; Lapidus, G. T. *J. Appl. Electrochim.* **2002**, 32, 1157-1165. DOI: <http://dx.doi.org/10.1023/A:1021262503128>.
36. Cruz, R.; Luna-Sánchez, R. M.; Lapidus, G. T.; González, I.; Monroy, M. *Hydrometallurgy*. **2005**, 78, 198-208. DOI: <http://dx.doi.org/10.1016/j.hydromet.2005.03.006>.
37. Meléndez, A.M.; Arroyo, R.; González, I. *ChemPhysChem.* **2010**, 11, 2879-2886. DOI: <http://dx.doi.org/10.1002/cphc.201000187>.
38. Cruz, R.; Bertrand, V.; Monroy, M.; González I.; *Appl. Geochem.* **2001**, 16, 803 – 819. DOI: [http://dx.doi.org/10.1016/S0883-2927\(00\)00054-8](http://dx.doi.org/10.1016/S0883-2927(00)00054-8).

39. Cruz, R.; Monroy, M.; González, I. *Appl. Geochem.* **2005**, 20, 109-121. DOI: <http://dx.doi.org/10.1016/j.apgeochem.2004.07.007>.
40. Cruz, R.; Méndez, B.A.; Monroy, M., González, I. *Appl. Geochem.* **2001**, 16, 1631-1640. DOI: [http://dx.doi.org/10.1016/S0883-2927\(01\)00035-X](http://dx.doi.org/10.1016/S0883-2927(01)00035-X).
41. Lara, R.H.; García-Meza, J. V.; Cruz, R.; Valdez-Pérez, D.; González, I. *Appl. Microb. Biotech.* **2012**, 95, 799-809. DOI: <http://dx.doi.org/10.1007/s00253-011-3715-3>.
42. Lara, R. H.; García-Meza, J. V.; González, I.; Cruz, R. *Appl. Microb. Biotech.* **2013**, 97-6, 2711-2724. DOI: <http://dx.doi.org/10.1007/s00253-012-4099-8>.
43. Méndez-Tovar, M.; García-Meza, J. V.; González, I. *Bioelectrochem.* **2019**, 128:30-38. DOI: <http://dx.doi.org/10.1016/j.bioelechem.2019.03.004>.
44. Saavedra, A.; García-Meza, J.V.; Cortón, E.; González, I. *Hydrometallurgy.* **2018**, 182, 128-135. DOI: <http://dx.doi.org/10.1016/j.hydromet.2018.10.022>.
45. Saavedra, A.; García-Meza, J.V.; Cortón, E., González, I. *Hydrometallurgy.* **2021**, 199, 105534. DOI: <http://dx.doi.org/10.1016/j.hydromet.2020.105534>.

A Review of Mexican Contributions to Li_2CuO_2 and its Chemical Modifications as Cathode Materials for Lithium-Ion Batteries

B. A. García-Carrillo¹, A de J Martínez¹, E. L. Jiménez-Cabañas², MA Martínez Cruz^{*,3,4}, C. Juárez-Yescas^{*,5,6}, G. Ramos-Sánchez^{*,2,7}

¹Departamento de Química, Universidad Autónoma Metropolitana – Iztapalapa, Av. San Rafael Atlixco, Leyes de Reforma 1ra secc, Iztapalapa 09340 CDMX, México.

²Departamento de IPH, Universidad Autónoma Metropolitana – Iztapalapa, Av. San Rafael Atlixco, Leyes de Reforma 1ra secc, Iztapalapa 09340 CDMX, México.

³Instituto de Investigación en Materiales, Universidad Nacional Autónoma de México, Cd. Universitaria, Del. Coyoacan, CP 04510, CDMX México.

⁴Centre for Cooperative Research on Alternative Energies (CIC energiGUNE), Basque Research and Technology Alliance (BRTA), Technology Park, Albert Einstein 48, Vitoria-Gasteiz, Avala 01510, Spain.

⁵Department of Chemistry, University of Illinois Urbana-Champaign, Urbana, Illinois 61801, United States

⁶Materials Research Laboratory, University of Illinois Urbana-Champaign, Urbana, Illinois 61801, United States.

⁷Laboratorio Nacional Conahcyt de Baterías Ion-Li y Post Li para el diseño y escalamiento de materiales y dispositivos (LNC-BIL-DEMO).

*Corresponding author: MA Martínez Cruz, email: miguee.cm@gmail.com; C. Juárez-Yescas, email: carlosj3@illinois.edu; G. Ramos-Sánchez, email: gramos@xanum.uam.mx

Received May 25th, 2024; Accepted August 2nd, 2024.

DOI: <http://dx.doi.org/10.29356/jmcs.v68i4.2294>

Abstract. Over the past few decades, battery research has primarily focused on reducing costs and increasing energy density. There have been significant efforts to identify alternative cathode materials that could replace cobalt-based ones, with the goal of finding more environmentally friendly and cost-effective options. In this context, copper-based cathodes have emerged as promising candidates. The appeal of copper-based cathodes lies in their relatively high abundance, particularly in Mexico, their high theoretical energy density, and the potential to enhance their properties by altering their chemical structure. In recent years, numerous research initiatives in Mexico have aimed to make Li_2CuO_2 cathodes a viable option. This review examines the recent advances and future perspectives of these efforts, with a particular emphasis on the latest attempts to modify the synthesis route and incorporate multiple dopants to create synergistic effects.

Keywords: Li_2CuO_2 ; cation doping; anion doping; dual doping; in situ analyses.

Resumen. Durante las últimas décadas, la investigación sobre baterías se ha enfocado principalmente en la disminución de costos y el incremento de la densidad energética. Se han realizado importantes esfuerzos para identificar materiales catódicos alternativos que podrían reemplazar a los materiales basados en cobalto, con el objetivo de encontrar opciones rentables y con menor impacto al medio ambiente. En este contexto, los materiales catódicos basados en cobre se han convertido en candidatos prometedores. El interés por los cátodos basados en cobre radica en su abundancia relativamente alta, particularmente en México, su alta densidad energética teórica y la cualidad de mejorar sus propiedades alterando su estructura química. En los últimos años, numerosas propuestas de investigación en México han tenido como objetivo hacer de los cátodos de Li_2CuO_2 una opción viable. Este resumen recopila los avances recientes y las perspectivas a futuro de estos esfuerzos,

con especial énfasis en los últimos intentos de modificar la ruta de síntesis y, a su vez, incorporar múltiples dopantes para crear efectos sinérgicos.

Palabras clave: Li_2CuO_2 , dopaje catiónico, dopaje aniónico, dopaje dual, análisis in situ.

Introduction

In recent years, concerns about climate change and greenhouse gas (GHG) emissions have grown significantly. The impact of GHG on humanity's immediate future is uncertain; however, most environmental forecast studies suggest a challenging future if emissions continue to rise. To mitigate GHG emissions, a shift towards a more renewable energy sector appears to be the most direct approach. Several milestones have been achieved in this regard over the past few years. The installation of solar power reached 1185 GW in 2022 [1], wind power reached 906 GW in 2021 [2] and tidal power generation reached 527 MW [3] worldwide. These efforts underscore the significance of the energy transition and the commitment of some sectors to enhance the utilization of renewable energy. However, as the utilization of renewable energy increases, so does the need for energy storage solutions. Energy storage is the ideal solution to synchronize energy production and consumption for the benefit of the consumer, who would otherwise need to adjust to periods of peak production.

Storing energy in batteries in the form of chemical energy has advantages in terms of energy density, voltage and response time when compared to mechanical energy storage systems. However, for large scale renewable energy storage, improvements still need to be made. One of the significant challenges lies in the cost associated with energy storage. Lithium-ion batteries (LIB) require costly production processes, demanding substantial amounts of transition metals and lithium to produce cathode materials. In this regard, Mexican institutions have set to replace cobalt chemistries for more abundant elements like copper. In addition, Mexico's legislation has established lithium sources as a strategic mineral. This has led to the creation of LitoMx, a state-owned company, to develop the extraction and production of lithium products [4]. This development and Mexico's signing of the Paris agreement in 2016 creates a scenario where the promise of LIBs holds a bright future and a strong commitment to reduce GHG emissions.

Copper-lithium oxides have been reported since early 70's, where the specific crystalline structure seems suitable for several magnetic and electric applications [5–7]. Copper in an +2 oxidation state forms crystalline structures consisting of edge-sharing $[\text{CuO}_4]$ nearly square planar units lying on the bc plane which are linked together along the b-axis. Joining the chains between them are $[\text{LiO}]$ layers in which the local symmetry around the metallic atoms is D_{2d} [7]. The nature of the structure with two lithium ions per copper make it theoretically possible to achieve a specific capacity of 490 mAhg^{-1} . However, while the oxidation of Cu^{+2} to Cu^{+3} does take place during charging, any additional capacity has been demonstrated to arise from irreversible oxygen evolution [8–12]. Seminal works have focused on deciphering the changes occurring during lithiation, indicating that irreversible phase transformations cause poor long-term cycling. The transition from Li_2CuO_2 to $\text{Li}_{1.5}\text{CuO}_2$ seems to be the more stable transformation, yielding in only one quarter of the full theoretical capacity. Further works have relied on doping and the formation of solid solutions with other metal ions to increase the stability and specific capacity [10,11,13]. However, the exact nature of doping and its effect remained elusive. Perea-Ramírez et al. [14] conducted a study on the electronic structure of Li_2CuO_2 when doped with various transition metals. The impact of these transition metals on the density of states is significant, as they shift the preference from oxygen states to metallic ones. This shift potentially increases the useable capacity before reaching oxygen evolution potentials. Furthermore, the study demonstrated that there are several strategies available to modify the electronic structure, making the use of Li_2CuO_2 in LIBs feasible [14].

This review begins by examining the properties of unmodified Li_2CuO_2 . It then dives into the effects of doping with a single transition metal, such as Ni, Co, Fe, and Mn, which were explored as potential dopants to enhance stability. Subsequently, the use of anionic dopants and in situ XRD techniques are also summarized. The formation of mixed phases is subsequently reviewed, followed by an evaluation of the effects of multiple doping. The review presents information from the past eight years to assess the potential of copper as a base metal for commercial Lithium-Ion Battery (LIB) applications.

Properties of unmodified Li_2CuO_2

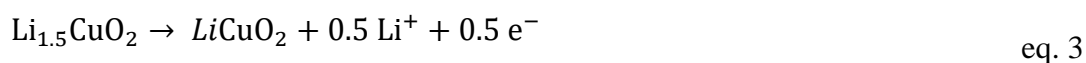
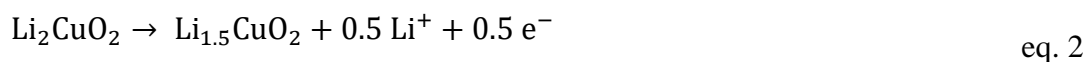
Generally, Li_2CuO_2 is synthesized using a conventional solid-state synthesis method, using lithium oxide and copper oxide as the precursors (eq. 1), with an excess of lithium oxide to compensate for loss of lithium as a result of sublimation. This reaction is carried out at 800 °C, common factors affecting yield are temperature, heating, and cooling ramps as well as temperature hold times.



To modify the material, reaction 1 can be modified to include other precursors in the appropriate stoichiometric ratios to form the desired compound. For instance, NiO has been used to integrate Ni to form solid solutions, similarly CuF_2 has been added to add fluorine as an anodic dopant [15]. The quantities of these extra compounds should be carefully examined since sufficiently high amounts can lead to the formation of secondary phases. Moreover, since the oxidation state of copper in CuO is 2+, the addition of other compounds with different oxidation states should be carefully chosen to compensate the charges.

Li_2CuO_2 , upon exposure to atmospheric conditions, it decomposes to oxides, including CuO, Cu_2O and Li_2O , as well as the possible generation of Li_2CO_3 ($\text{Li}_2\text{CuO}_2 + \text{CO}_2 \rightarrow \text{Li}_2\text{CO}_3 + \text{CuO}$). These degradation mechanisms consequently decrease battery capacity. For this reason, samples must be stored under inert gas to prevent the formation of segregated phases or surface modifications.

In a battery, the electrochemical reactions that Li_2CuO_2 undergoes are as follows:



In Fig. 1, the charge/discharge profiles for Li_2CuO_2 at two potential windows are shown (C/15), the corresponding 50th cycles are shown as dashed lines [16]. For the first potential window of 1.5 to 4.2 V, the specific capacity is approximately 225 mAhg^{-1} , and the discharge capacity is 180 mAhg^{-1} . However, during the second cycle, the discharge capacity begins to decrease continuously, which is attributed to the irreversible changes in Li_2CuO_2 , impeding the intercalation of Li^+ ions. For the profile at the potential window of 2.1 to 3.8 V, during the first cycle, a charge capacity of 160 mAhg^{-1} and a discharge capacity of 110 mAhg^{-1} is observed. Starting from the second cycle, the behavior is stabilized due to the extraction of one lithium ion from Li_2CuO_2 , indicating improved structural stability.

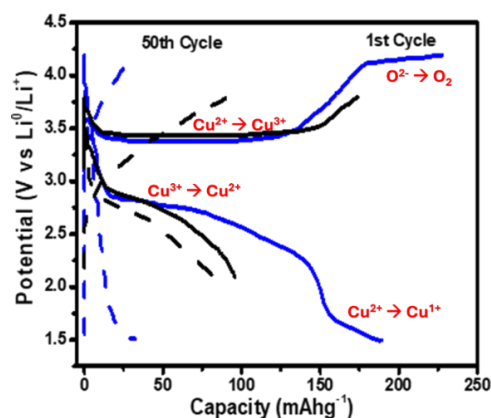


Fig. 1. Galvanostatic charge/discharge characteristics on the first 50 cycles with Li_2CuO_2 cathodes in extended voltage range from 1.5 - 4.2 V (blue) and shortened voltage window from 2.1 - 3.8 V (black). Reprinted from data in [16] with the authors permission.

Structural phase transition and O₂ evolution processes occur during the delithiation of various cathode materials such as layered oxides, Li₂CuO₂, being not the exception. Perea-Ramirez et al. performed electronic structure calculations of pristine Li₂CuO₂ and modified with other transition metal ions, which demonstrated that the evolution of oxygen at potentials higher than 3.8 V was due to a greater density of states of oxygen close to the Fermi level with respect to Cu, promoting its oxidation and, as consequence the formation of phases that inhibit structural reversibility and affect the electrochemical performance of Li₂CuO₂ [14]. This situation generates the need to propose alternatives to improve its structural and electrochemical behavior.

Effect on properties of Li₂CuO₂ doped with metallic cations

By incorporating metal cations from other transition metals (TM) into Li₂CuO₂, we can enhance its reversible capacity and stability. This provides a clear alternative for mitigating the drawbacks of the unmodified Li₂CuO₂. However, depending on the specific nature of the dopant, we can find several outcomes.

Fig. 2 provides a summary of the characterization of Li₂CuO₂ in its unmodified form, as well as its modifications when combined with Mn, Fe, or Ni. The materials were synthesized via the solid-state method and also characterized using EPR, Mossbauer, and XRD techniques [12]. This characterization demonstrates the effective incorporation of TMs into Li₂CuO₂, forming a solid solution without the presence of a secondary phase. ⁷Li MAS NMR spectra of Li₂CuO₂ and TMs-Li₂CuO₂ are shown in Fig. 2(a). The spectra exhibit two signals, one at near 0 ppm and the other at 340 ppm. The signal near 0 ppm is attributed to surface impurities such as LiOH or Li₂CO₃, which are not detectable by XRD. The signal at 340 ppm arises from Fermi contact associated with interchain interaction via Cu-O-Ti-O-TMs, where spin transfer occurs from paramagnetic copper to lithium through oxygen [19]. The slight shifts in the signals indicate changes in the local chemical environment of lithium due to the presence of TMs.

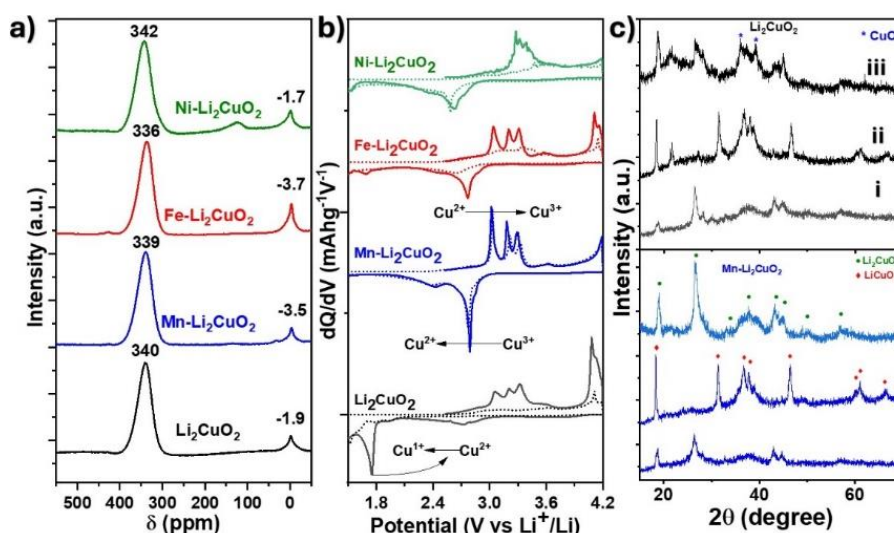


Fig. 2. (a) ⁷Li MAS NMR spectra and (b) dQ/dV of Li₂CuO₂ and MTs-Li₂CuO₂, and (c) ex situ XRD patterns of Li₂CuO₂ and Mn-Li₂CuO₂. XRD patterns of both samples correspond to: i) discharge of the first cycle, ii) charge of the second cycle, and iii) discharge of the fifth cycle. Figure reproduced from [12] with the author's permission.

The electrochemical performance of the materials was analyzed within a potential window of 1.5 to 4.2 V vs Li⁺/Li. dQ/dV profiles for the second and fifth cycles of each material are presented in Fig. 2(b).

Li_2CuO_2 and Mn- and Fe- Li_2CuO_2 exhibit three oxidation peaks between 2.8 – 3.3 V and one reduction peak (or two in Mn- Li_2CuO_2 case) between 3.0 – 2.4 V in the second cycle. These peaks are associated with different lithiation states, as reported by Masquelier et al. [8]. However, at around 3.9 V, another oxidation peak associated with the oxidation of O^{2-} to O_2 is observed, which is more intense for Li_2CuO_2 and Fe- Li_2CuO_2 , indicating a greater O_2 evolution. O^{2-} vacancies are probably generated in the lattice inducing structural instability, forming CuO , which is reduced at 1.8 V, which was observed in both materials. For material modified with Mn, the reduction peak does not occur, indicating lowered O^{2-} oxidation. On the other hand, in the material modified with Ni, oxidation processes occur at a different potential than the pristine material. This is likely due to the oxidation of Ni^{2+} to Ni^{3+} , causing nickel to leave the lattice, and forming a new phase like LiNiO_2 [9].

Mn- Li_2CuO_2 shows no significant changes between the second and fifth cycles. The presence of manganese in the lattice enhances the structural reversibility of Li_2CuO_2 , which was confirmed by conducting ex situ XRD analysis at different charge and discharge cycles (Fig. 2(c)). This analysis confirmed the presence of orthorhombic and monoclinic phases during lithium-ion insertion and extraction respectively, which is not observed for pristine Li_2CuO_2 .

Based on these results, it is clear that transition metals as dopants, improve the electrochemical performance, such as increasing specific capacity or enhancing material structural stability. For example, Fe or Ni might serve as active cations during oxidation, providing greater capacity, while Mn doping is inactive but can serve as a structural pillaring agent.

Considering these results, Li_2CuO_2 has been simultaneously doped with Mn^{4+} and Co^{2+} or Ni^{2+} ions to improve its structural stability and increase its capacity and retention [20]. The doping was carried out using a molar concentration of 2.5 % of each TM through solid state synthesis in which a ball milling process was used for 10 minutes at a frequency of 25Hz.

The XRD patterns of the samples $\text{Co-Li}_2\text{CuO}_2$, $\text{Ni-Li}_2\text{CuO}_2$, $\text{CoMn-Li}_2\text{CuO}_2$ and $\text{NiMn-Li}_2\text{CuO}_2$ (as shown in Fig. 3) confirm that all samples share the same structure. They all possess the orthorhombic phase characteristic of Li_2CuO_2 , without any formation of segregated phases. These results corroborate the formation of a pure phase even with the doping of two TMs, implying that all the dopant ions can be incorporated into the structure of the pristine material and are coordinated in a square plane coordination. The specific case for Co^{2+} ions is interesting since the normal coordination in this geometry is complicated, so the distortion of the unit cell that may be generated is imperceptible at these conditions.

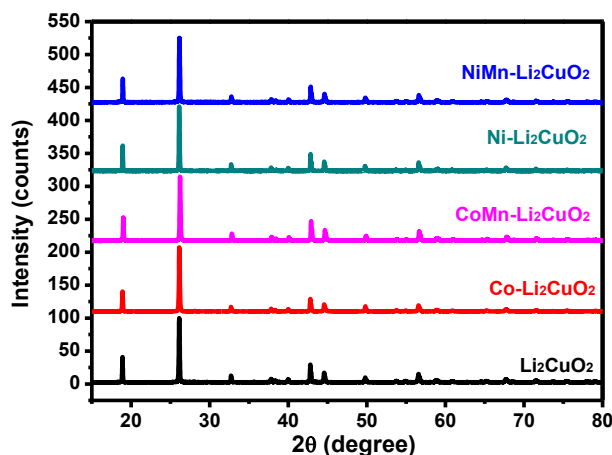


Fig. 3. XRD pattern of the Li_2CuO_2 and all modifications with one or two transition metal ions. Figure reproduced from [20] with the author's permission.

Regarding the electrochemical behavior, the charge-discharge profiles allow us to identify that Li_2CuO_2 synthesized with this methodology increases its capacity and allows it to retain more than 50% of the

capacity after 50-cycles (Fig. 4 (a)). In the samples doped with two types of cations (labeled as CoMn-Li₂CuO₂ and NiMn-Li₂CuO₂), it is clear that they do not yield higher capacity than the pristine material (Fig. 4 (b)). The material doped with Co²⁺ cations (labeled as Co-Li₂CuO₂) has slightly better electrochemical behavior than Li₂CuO₂ because it maintains marginally greater retention (Fig. 4 (c)). Many reports recently have included more than one dopant in the structure, claiming improved properties [21–23], based on results herein mentioned, dual doping has a net positive effect, although just marginal.

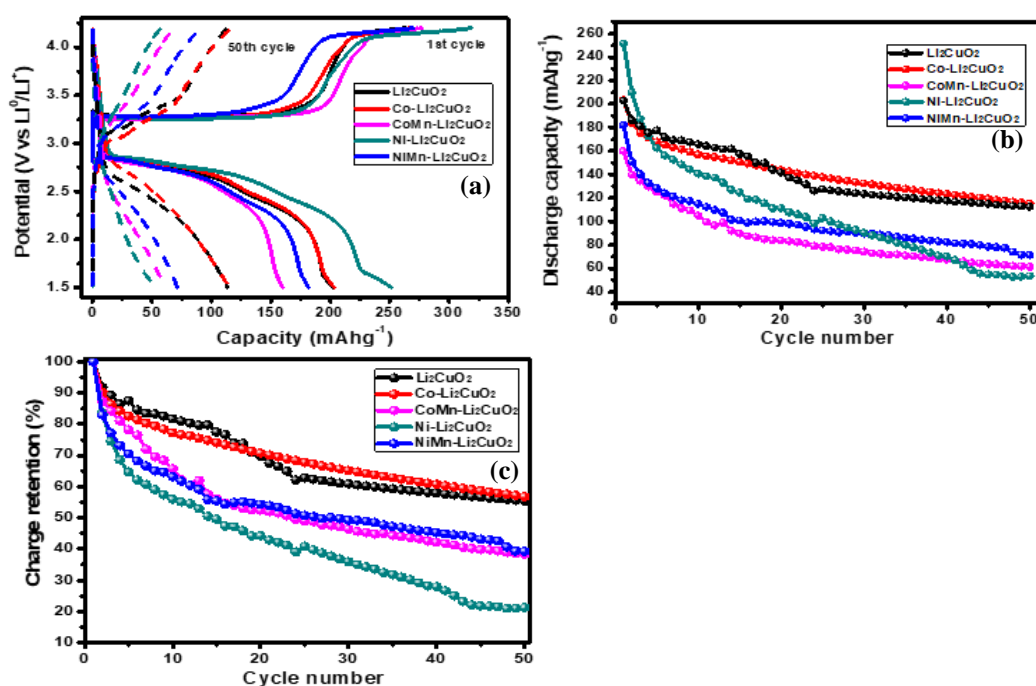
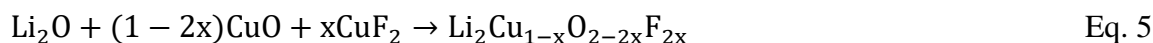


Fig. 4. (a) Galvanostatic charge/discharge profiles on the first and fiftieth cycles with Li₂CuO₂ and doped samples in extended voltage window 1.5-4.2 V, (b) Cyclic performance and (c) Charge retention during discharge. The Li⁰|1 M LiPF₆|Active material: carbon black: PVDF (75:15:10 wt%) cell was cycled at C/10 at 25°C. Figure reproduced from [20] with the author's permission.

Fluorine as an anionic doping agent

Anion doping Li metal oxide cathode materials has been reported as an alternative to increase the electrochemical performance, voltage stability and potentially inhibiting the evolution of oxygen [24–26]. As pointed out in previous sections, the predominant failure mechanism for Li₂CuO₂ is the evolution of O₂ during charging as cycling progress, limiting its practical application despite its promising characteristics. A lot of efforts have been made to incorporate fluorine into the structure of Li₂CuO₂ via a simple modified solid-state reaction [15]. Given differences in valence between O and F, it was expected that the doped Li₂CuO₂ would yield a Cu and O deficient structure, as suggested by equation 5. Different compositions of the F-doped Li₂CuO₂ were explored (2.5, 5.0 and 10 mol%). XRD analysis showed that the cell parameters in the a and c directions decreased as a function of fluorine concentration [15]. The decrease in cell parameters has been attributed to the smaller ionic radius of F (1.36 Å) occupying oxygen sites (O ionic radius: 1.40 Å); specifically, in planes 200 and 013.



Cycling the F-doped materials under constant current (0.1 C), showed the positive effects of the introduction of fluorine. The unmodified material exhibited a characteristic poorly defined plateau during the first charge, and a low initial Coulombic efficiency (55 %). In contrast, F-doped materials showed a well-defined plateau near 3.3 V, with improvement in Coulombic efficiency, up to 69 % (Fig. 5(A)). While all the F-doped samples showed higher overpotential during initial charge, the 2.5 % and 5.0 % showed less overpotential and improved reversibility. Among the F-doped variants, 5.0 mol% F-doping yielded the best electrochemical performance. Although the capacity retention at cycle 10 was only 57 % of the initial capacity, Coulombic efficiency improved to 99 % (Fig. 5(B)). Overall, the F-doped cuprate (5.0 mol%) demonstrated improved capacity retention, discharging 133 mAhg⁻¹ compared to 83 mAhg⁻¹ for the pristine Li₂CuO₂ on the 10th cycle. Performance gains were not observed when F-doping exceeded 5.0 mol %. XRD refinement revealed that the introduction of the fluorine precursor during the synthesis of F-doped Li₂CuO₂ promoted the formation of a secondary CuO phase [15]. As a result, any doping beyond the 5.0% threshold proved to be counterproductive.

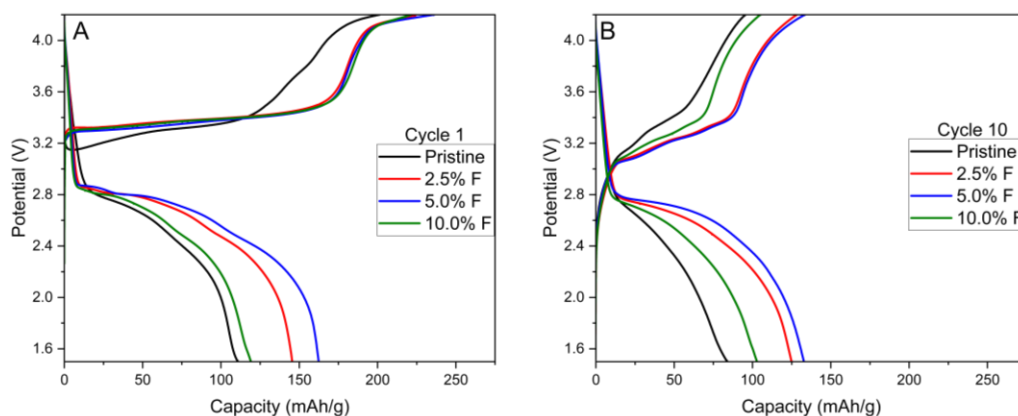


Fig. 5. Typical voltage profiles of Li⁰|1 M LiPF₆|Active material: carbon black: PVDF (75:15:10 wt %) at first (A) and tenth (B) cycle. Cycling rate: 0.1C. Adapted with permission from Ref. [15]. Copyright 2020 American Chemical Society.

In-Situ XRD and gases generation during cycling

In situ techniques are needed to gain direct information about chemical reactions and transformations beyond that obtained by the current-voltage curves. In this section gas detection and structural transformations are revised.

To assess the effectiveness of inhibiting O₂ evolution, Differential Electrochemical Mass Spectrometry (DEMS) was employed during a voltage scan in the positive direction. The scan ranged from the open circuit potential up to 4.5 V vs Li, ensuring O₂ evolution. Both pristine Li₂CuO₂ and 5.0 mol% F-doped Li₂CuO₂ were studied. For the pristine Li₂CuO₂, results confirmed the O₂ formation starting at 4.1 V (Fig. 6). The correlation between ionic current and faradaic current associated to O₂ evolution was the first reported for Li₂CuO₂, confirming that the second oxidation process at 4.35 V is the lattice O oxidation. Approximately 23.3 % of oxygen in the cathode was lost as O₂ (0.032 mmol) during the electrochemical perturbation. Notably, the presence of fluorine improved electrochemical performance by inhibiting oxygen evolution across all explored potentials. The voltammogram for the doped material still exhibited an oxidation peak related to oxygen, but without actual oxygen evolution. This behavior could be attributed to the reversible oxygen redox reactions as previously reported [27]. Nonetheless, F-doped Li₂CuO₂ still suffers from significant capacity fade, however these incremental improvements suggest that leveraging novel modification methods can be used to further improve the material's properties.

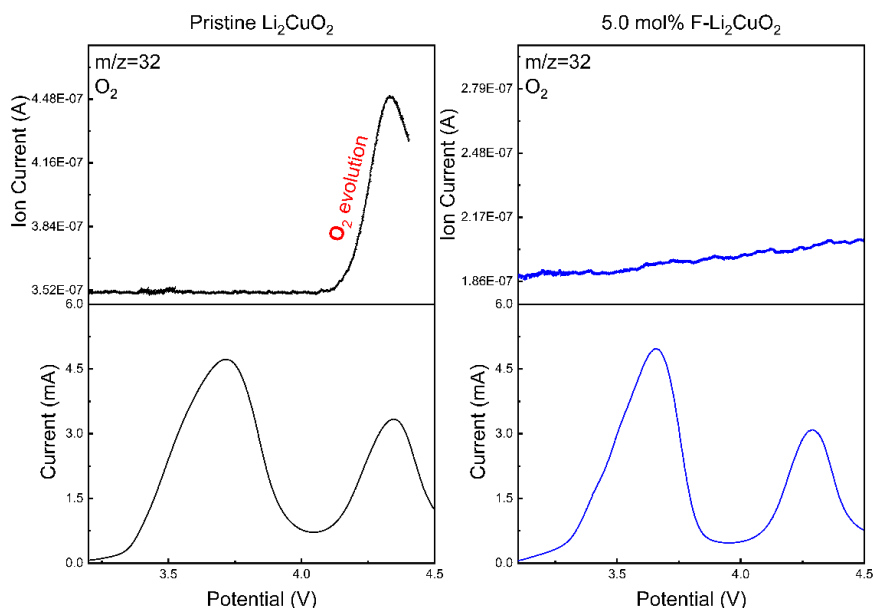


Fig. 6. Linear step voltammograms and Oxygen ($m/z = 32$) ion current of $\text{Li}^0|1 \text{ M LiPF}_6|\text{Active material: carbon black: PVDF (75:15:10 wt\%)}$ cells. Adapted with permission from Ref.[15]. Copyright 2020 American Chemical Society.

Although doping is a suitable strategy, the solubility of an ion within a crystalline structure is crucial, exceeding the solubility limit can lead to the formation of other phases or impurities that may either enhance or limit the capacity of an active material. Several publications report the effect of additional ions within the structure; however, the presence of impurities or secondary phases make it impossible to make a fair comparison.

To analyze the effect of secondary phases formation, Martínez-Cruz et al. [28] synthesized the phase $\text{Li}_2\text{Cu}_{0.5}\text{Ni}_{0.5}\text{O}_2/\text{LiNi}_{0.5}\text{Cu}_{0.5}\text{O}_2$ (orthorhombic/rhombohedral phase, respectively) using the solid-state method under different atmospheres: N_2 , air, or O_2 . The materials synthesized in an oxygen atmosphere exhibited superior electrochemical performance due to a higher weight percentage of the $\text{LiNi}_{0.5}\text{Cu}_{0.5}\text{O}_2$ phase compared to the material obtained under other atmospheres. In situ XRD demonstrated that the rhombohedral phase enhances charge retention and structural reversibility (Fig. 7). During charging of LiNiCu-O_2 , signals from both rhombohedral and orthorhombic phases are observed. However, at the 3.4 V plateau, reflections from the orthorhombic phase decrease in intensity, while those from the rhombohedral phase remain stable, indicating that the latter does not participate in the electrochemical process. In the second plateau, at 3.7 V, the reflections from the rhombohedral phase undergo directional changes, suggesting alterations in the crystalline structure during lithium ion deintercalation. At 4.2 V, with increased oxidation, signals from the rhombohedral phase continue to shift in the same direction as in the previous plateau. During discharge, reflections from the rhombohedral phase return to their original values, while those from the orthorhombic phase significantly lose intensity, indicating a collapse in the crystal lattice like that observed in Li_2CuO_2 . Changes in reflections from the rhombohedral phase during charging suggest a decrease in the parameter “a” and an increase in the parameter “c”, which are reversed during discharge, indicating structural reversibility likely related to the presence of Cu^{3+} in the LiNiO_2 structure.

To better understand the effect of copper on LiNiO_2 (LNO), in situ XRD analysis was conducted on both LNO and Cu-LNO samples (Fig. 8(a)). This analysis allowed observation of the changes occurring at higher potentials (phase transitions), facilitating the correlation between capacity retention and structural stability. The in situ XRD experiments indicate that the main degradation mechanism is related to the increased fraction of the formed phase (Fig. 8(b)) and changes in interlayer distances (Fig. 8(c)). These characteristics confirm a positive effect of copper inclusion.

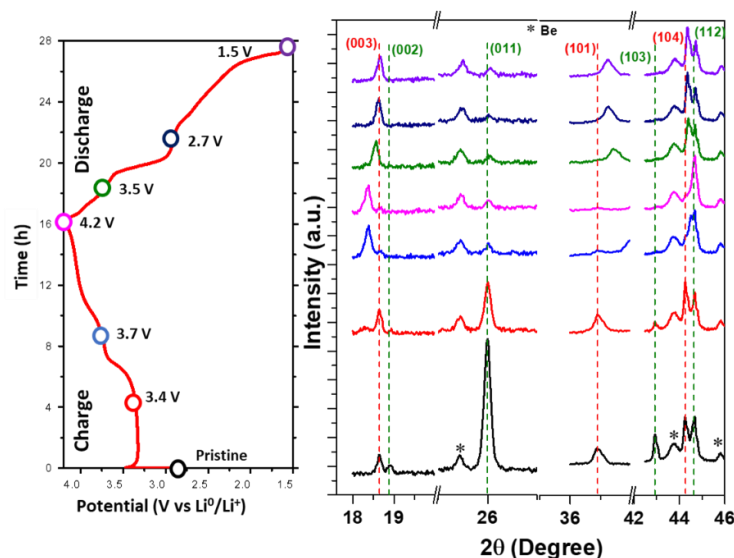


Fig. 7. In situ XRD patterns of $\text{Li}_2\text{Cu}_{0.5}\text{Ni}_{0.5}\text{O}_2/\text{LiNi}_{0.5}\text{Cu}_{0.5}\text{O}_2$ in lithium half-cell cycled between 1.5 – 4.2 V at C/15 rate. The green and red vertical dashed lines in the direction patterns indicate peaks related to the orthorhombic and rhombohedral phases, respectively. Figure reproduced from [28] with the author's permission.

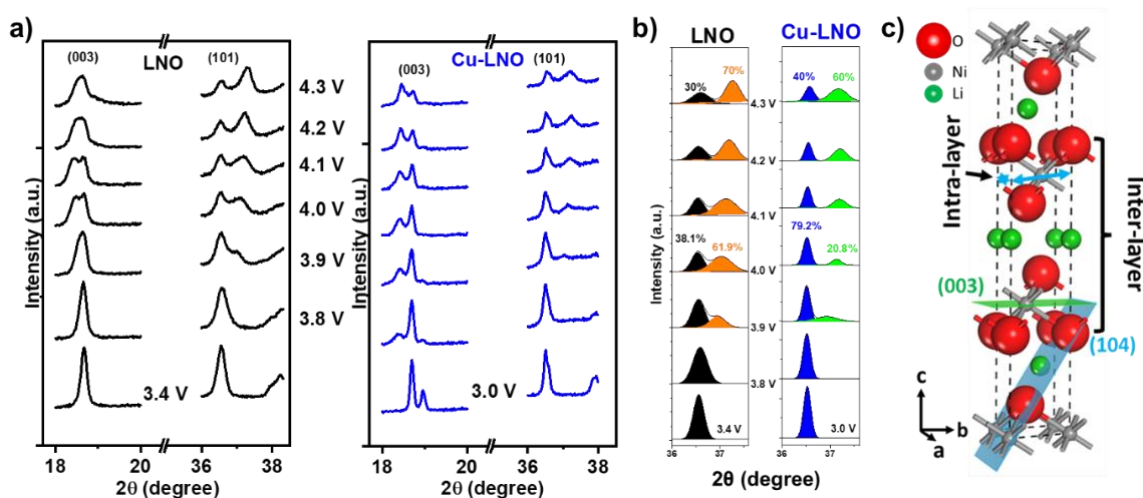


Fig. 8. (a) In situ XRD patterns of LNO and Cu-LNO in lithium half-cell cycled between 3.0 – 4.3 V at C/15 rate. (b) The relative fraction of phase transitions was obtained through the deconvolution of the (101) plane reflection in the in situ XRD pattern during charging. The black and blue areas correspond to the fractions of the initial phases, while the orange and green areas correspond to the phases formed during charging. (c) Schematic representation of the LNO unit cell. Figure reproduced from [28] with the author's permission.

The results obtained are consistent with other modifications previously performed on LiNiO_2 , in which the substitution of other transition metal ions in the Ni positions improve the reversibility of H2 to H3 phases at high potentials, providing greater structural stability that is reflected in capacity retention [29–32]. Therefore, the Cu-LNO phase proves to be attractive as a cathode material for LIBs, although a phase mixture is obtained, the results indicate an overall improvement over the pure phase.

Li₂CuO₂ dual doping: Anionic and cationic agents

Lastly, we present for the first time our most recent efforts to modify Li₂CuO₂ using a dual-doping strategy. These new results use both cationic and anionic dopants, specifically using manganese and fluorine. This is done to inhibit oxygen from participating in the redox processes during the initial extraction of Li, thereby preventing the formation of O₂. The F⁻ ions occupy the sites where O resides in the Li₂CuO₂ lattice, and doping with Mn also causes modifications in the cell parameters that provide structural stability. The synthesized material, containing up to 5.0 % dopants is stable and isostructural to Li₂CuO₂ (Fig. 9).

Galvanostatic cycling was carried out at C/10 using Li₂CuO₂ cathode electrodes doped with Mn and F prepared under inert conditions. The materials that have been dual-doped display a second plateau, which is associated with oxygen evolution around 4.1V. However, it's important to note that the materials with 2.5 % and 3.5 % doping show a less pronounced plateau compared to the other materials. It can be inferred that the amount of oxygen remaining within the material's network is higher in these cases, compared to the others where more O₂ is formed. During the discharge process, Cu⁺¹ is formed in all materials, contributing to material degradation. By cycle 10, the only material that shows improvement over the pristine material is the one with 3.5 % MnF₂, as evidenced by the charge retention in Fig. 10.

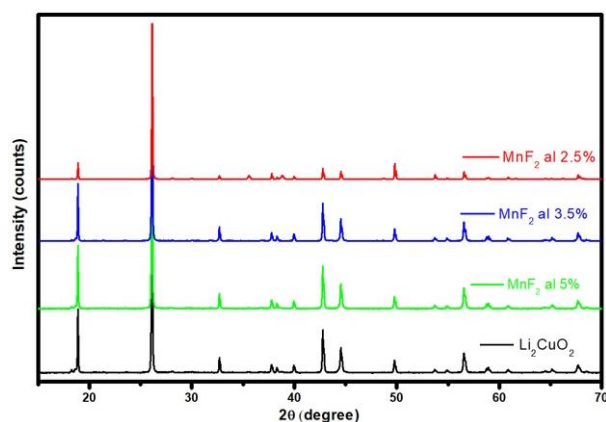


Fig. 9. XRD of dual anionic and cation doping Li₂CuO₂ with MnF₂ at 2.5 %, 3.5 % and 5.0 %.

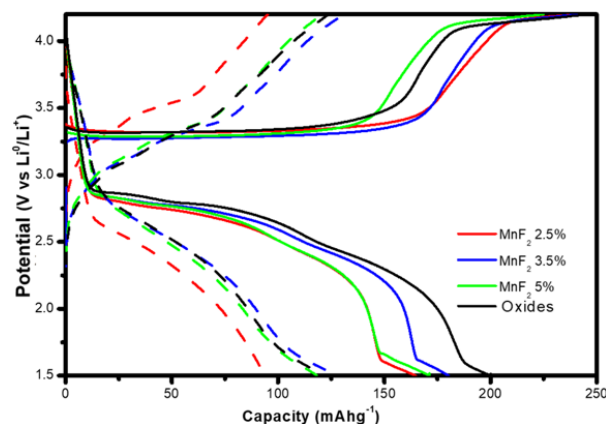


Fig. 10. Charge/discharge diagram of Li₂CuO₂ doped with MnF₂ at 2.5 %, 3.5 %, and 5.0 % of Li⁰|1 M LiPF₆|Active material: carbon black: PVDF (75:15:10 wt%) cells, cycled at C/10 at 25°C. The solid line represents the first cycle, and the dashed line represents cycle 10.

Finally, Table 1 summarizes the various modifications and effects on the structure and electrochemical properties of Li_2CuO_2 , based on the results discussed in this work.

Table 1. Summary of widely investigated dopants and their effect on Li_2CuO_2 .

Dopants	Description	Key results	References
Undoped	Pure Li_2CuO_2 phase.	Baseline capacity and performance, prone to oxygen evolution and structural instability.	[16]
Ni	Incorporation of 50 % Ni to form secondary phase.	Increase in capacity and introduction of new redox processes.	[17]
Ni	5 mol % of Ni^{2+} to form solid solutions.	Higher initial capacity but generation of new irreversible phase.	[12]
Mn	Doping with 5 mol % Mn^{4+} .	Improvement in structural stability, reduction in O_2 evolution.	[12]
Fe	Limited solubility of Fe^{3+} at 5 mol%.	Increase in specific capacity, but higher O_2 evolution.	[12]
F	Anionic doping, replacement of O^{2-} with F^- .	Improvement in coulombic efficiency, inhibition of oxygen evolution.	[15]
Mn and Co	Dual doping with Mn^{4+} and Co^{2+} .	Marginal increase in reversible capacity and capacity retention.	[20]
Mn and Ni	Dual doping with Mn^{4+} and Ni^{2+} .	No significant increase in capacity compared to the pure material.	[20]
Mn and F	Anionic (F^-) and cationic (Mn^{4+}) doping.	No significant improvement compared to individual doping.	Reported herein
Ni	Phase control, synthesis under different atmosphere.	Improved electrochemical performance, higher $\text{LiNi}_{0.5}\text{Cu}_{0.5}\text{O}_2$ phase as a result of synthesis in O_2 atmosphere.	[28]

Conclusions

Numerous strategies have been explored to modify the electrochemical properties of Li_2CuO_2 , primarily aiming to enhance its electrochemical and structural reversibility. Although these modifications have not yet yielded a reversible capacity that renders this material practical, they have increased the specific capacity by introducing redox active centers. Moreover, comprehensive studies of this material have shown that while inactive centers bolster structural stability, they decrease capacity. Anion doping has proven effective in mitigating oxygen evolution at higher potentials. However, despite efforts in dual doping and element combinations, none have resulted in significant improvements compared to individual doping.

Therefore, we propose that future advancements in Li_2CuO_2 could involve applying successful techniques and knowledge from other cathode chemistries. For example, the impact of crystallinity (single crystal vs. polycrystalline) and faceting on various cathodes has been well-documented, demonstrating that cycling performance and oxygen loss inhibition can be achieved by controlling the crystallography of the active material [33,34]. Although single crystal Li_2CuO_2 has been successfully synthesized in characterization reports, the electrochemical performance of single crystal Li_2CuO_2 electrodes remains unexplored [35,36]. Investigating this could lead to a deeper understanding of Li_2CuO_2 and potential performance improvements.

Furthermore, it is widely recognized that the electrode-electrolyte interface plays a critical role in achieving long, stable cycling, especially since electrode redox reactions and degradation originate at this interface [37,38]. Therefore, future studies should prioritize stabilizing the electrolyte – Li_2CuO_2 interface. Protective coatings such as LiNbO_3 , for instance, have been shown to enhance rate capability and improve capacity retention [39–41].

In conclusion, there are still abundant opportunities to apply our learnings to further enhance Li_2CuO_2 . With ongoing research and development, we remain hopeful that Li_2CuO_2 will eventually emerge as a viable Li-ion cathode material for Li-ion batteries.

Acknowledgements

A. de J. Martinez-Maldonado, B. A. García-Carrillo and E.L. Jimenez-Cabañas are grateful for the scholarship granted to them by CONAHCYT to pursue their graduate studies. The authors would like to thank Federico Gonzalez for XRD measurements and extend their most sincere gratitude to the collaborators and laboratories of the Universidad Autónoma Metropolitana (Unidad Iztapalapa), especially to Ignacio González Martínez, for his valuable contribution during the development of this work. This work was performed as part of the consortium established by the National Laboratory CONAHCYT BIL-DEMO. This work was possible thanks to CONAHCYT support grants FORDECYT-PRONACES/1560340/2020, Apoyos LNC 2023-123, CF-2023-G-918 and CF-2023-G-1266.

References

1. Jäger-Waldau A. *EPJ Photovoltaics*, **2022**, 13. DOI: <https://doi.org/10.1051/epjpv/2022010>.
2. Summerfield-Ryan O., Park S., *Ecological Economics*, **2023**, 210, 107841. DOI: <https://doi.org/10.1016/j.ecolecon.2023.107841>.
3. Perez M., Perez R., *Solar Energy Advances*, **2022**, 2, 100014. DOI: <https://doi.org/10.1016/j.seja.2022.100014>.
4. Vivoda V., Bazilian M.D., Khadim A., Ralph N., Krame G., *Energy Res Soc Sci*, **2024**, 108, 103393. DOI: <https://doi.org/10.1016/j.erss.2023.103393>.
5. Hoppe R., Rieck H, *Zeitschrift für anorganische und allgemeine Chemie*, **1970**, 379, 2, 157-164. DOI: <https://doi.org/10.1002/zaac.19703790206>.
6. Hoffmann R., Hoppe R., Schäfer W., *Zeitschrift für anorganische und allgemeine Chemie*, **1989**, 578, 1, 18-26. DOI: <https://doi.org/10.1002/zaac.19895780103>.
7. Sapiña F., Rodríguez-Carvajal J., Sanchis M.J., Ibáñez R., Beltrán A., Beltrán D., *Solid State Commun*, **1990**, 74, 779–784. DOI: [https://doi.org/10.1016/0038-1098\(90\)90934-4](https://doi.org/10.1016/0038-1098(90)90934-4).
8. Prakash A.S., Larcher D., Morcrette M., Hegde M.S., Leriche J., **2005**, 74, 4406–4415. DOI: <https://doi.org/10.1021/cm0508266>.
9. Ruther R.E., Samuthira Pandian A., Yan P., Weker J.N., Wang C., Nanda J., *Chemistry of Materials*, **2017**, 29, 2997–3005. DOI: <https://doi.org/10.1021/acs.chemmater.6b05442>.
10. Ruther R.E., Zhou H., Dhital C., Saravanan K., Kercher A.K., Chen G., *et al.*, *Chemistry of Materials*, **2015**, 27, 6746–6754. DOI: <https://doi.org/10.1021/acs.chemmater.5b02843>.

11. Xu J., Renfrew S., Marcus M.A., Sun M., McCloskey B.D., Tong W., *Journal of Physical Chemistry C*, **2017**, 121, 11100–11107. DOI: <https://doi.org/10.1021/acs.jpcc.7b01799>.
12. Martínez-Cruz M.A., Yañez-Aulestia A., Ramos-Sánchez G., Oliver-Tolentino M., Vera M., Pfeiffer H., *et al.*, *Dalton Transactions*, **2020**, 49, 4549–4558. DOI: <https://doi.org/10.1039/D0DT00273A>.
13. Arachi Y., Ide T., Nakagawa T., Nakata Y., *ECS Trans*, **2012**, 50, 143–151. DOI: <https://doi.org/10.1149/05024.0143ecst>.
14. Perea-Ramírez L.I., Guevara-García A., Galván M., *J Mol Model*, **2018**, 24, 227. DOI: <https://doi.org/10.1007/s00894-018-3754-0>.
15. Juárez-Yescas C., Oliver-Tolentino M., Ramos-Sánchez G., Vera-Ramírez M.A., Olmedo-González J., Ochoa-Calle A., *et al.*, *ACS Appl Energy Mater*, **2020**, 3, 2771–2780. DOI: <https://doi.org/10.1021/acsaelm.9b02429>.
16. Ramos-Sánchez G., Romero-Ibarra I.C., Vázquez-Arenas J., Tapia C., Aguilar-Eseiza N., González I., *Solid State Ion*, **2017**, 303, 89–96. DOI: <https://doi.org/10.1016/j.ssi.2017.02.018>.
17. Aguilar-Eseiza N., Ramos-Sánchez G., González F., González I., *Electrochem Commun*, **2018**, 96, 32–36. DOI: <https://doi.org/10.1016/j.elecom.2018.09.002>.
18. Shannon R.D., *Acta Crystallographica Section A*, **1976**, 32, 768–771. DOI: <https://doi.org/10.1107/S0567739476001551>.
19. Mizuno Y., Tohyama T., Mackawa S., *Phys Rev B Condens Matter Mater Phys*, **1999**, 60, 6230–6233. DOI: <https://doi.org/10.1103/PhysRevB.60.6230>.
20. García Carrillo B.A., Estudio de cuprato de litio modificado con iones de metales de transición como cátodo alternativo para baterías de ion litio, Universidad Autónoma Metropolitana, **2023**
21. Weng Y., Zhang H., *Ionics (Kiel)*, **2024**, 30, 1885–1895. DOI: <https://doi.org/10.1007/s11581-023-05366-4>.
22. He Z., Zhang M., Zhou K., Cheng Y., Luo M., Su Y., *et al.*, *ACS Appl Energy Mater*, **2023**, 6, 3422–3431. DOI: <https://doi.org/10.1021/acsaelm.2c04133>.
23. Ahn H., Choi J., Kim M., Kyu Kang S., Jang D., Maeng J., *et al.*, *Chemistry of Materials*, **2024**, 36, 9, 4379–4392. DOI: <https://doi.org/10.1021/acs.chemmater.3c03307>.
24. Kong F., Liang C., Longo R.C., Yeon D.H., Zheng Y., Park J.H., *et al.*, *Chemistry of Materials*, **2016**, 28, 6942–6952. DOI: <https://doi.org/10.1021/acs.chemmater.6b02627>.
25. Kim H., Kim S.B., Park D.H., Park K.W., *Energies (Basel)*, **2020**, 13, 4808–4817. DOI: <https://doi.org/10.3390/en13184808>.
26. Lin Y., Zhong K., Zheng J., Liang M., Xu G., Feng Q., *et al.*, *ACS Appl Energy Mater*, **2021**, 4, 9848–9857. DOI: <https://doi.org/10.1021/acsaelm.1c01883>.
27. Dai K., Wu J., Zhuo Z., Li Q., Sallis S., Mao J., *et al.*, *Joule*, **2019**, 3, 518–541. DOI: <https://doi.org/10.1016/j.joule.2018.11.014>.
28. Martínez-Cruz M.A., Ramos-Sánchez G., Oliver-Tolentino M., Pfeiffer H., González I., *J Alloys Compd*, **2022**, 923, 166328. DOI: <https://doi.org/10.1016/j.jallcom.2022.166328>.
29. Zhang Y., Li H., Liu J., Liu J., Ma H., Cheng F., *Journal of Energy Chemistry*, **2021**, 63, 312–319. DOI: <https://doi.org/10.1016/j.jechem.2021.07.029>.
30. Ryu H.H., Park G.T., Yoon C.S., Sun Y.K., *J Mater Chem A Mater*, **2019**, 7, 18580–18588. DOI: <https://doi.org/10.1039/C9TA06402H>.
31. Hao Q., Du F., Xu T., Zhou Q., Cao H., Fan Z., *et al.*, *Journal of Electroanalytical Chemistry*, **2022**, 907, 116034. DOI: <https://doi.org/10.1016/j.jelechem.2022.116034>.
32. Goonetilke D., Mazilkin A., Weber D., Ma Y., Fauth F., Janek J., *et al.*, *J Mater Chem A Mater*, **2022**, 10, 7841–7855. DOI: <https://doi.org/10.1039/D1TA10568J>.
33. Zhang F., Zhou X., Fu X., Wang C., Wang B., Liang W., *et al.*, *Mater Today Energy*, **2021**, 22, 100873. DOI: <https://doi.org/10.1016/j.mtener.2021.100873>.
34. Li J., Cameron A.R., Li H., Glazier S., Xiong D., Chatzidakis M., *et al.*, *J Electrochem Soc*, **2017**, 164, A1534–A1544. DOI: <https://doi.org/10.1149/2.0991707jes>.
35. Balodhi A., Kim M.G., *Crystals (Basel)*, **2024**, 14, 288. DOI: <https://doi.org/10.3390/cryst14030288>.

36. Kawamata S., Okuda K., Kindo K., *J Magn Magn Mater*, **2004**, 272–276, 939–940. DOI: <https://doi.org/10.1016/j.jmmm.2003.12.579>.
37. Hausbrand R., Cherkashinin G., Ehrenberg H., Gröting M., Albe K., Hess C., *et al.*, *Materials Science and Engineering: B*, **2015**, 192, 3–25. DOI: <https://doi.org/10.1016/j.mseb.2014.11.014>.
38. Minato T., Abe T., *Prog Surf Sci*, **2017**, 92, 240–280. DOI: <https://doi.org/10.1016/j.progsurf.2017.10.001>.
39. Xin F., Zhou H., Chen X., Zuba M., Chernova N., Zhou G., *et al.*, *ACS Appl Mater Interfaces*, **2019**, 11, 34889–34894. DOI: <https://doi.org/10.1021/acsami.9b09696>.
40. Takada K., Ohta N., Zhang L., Fukuda K., Sakaguchi I., Ma R., *et al.*, *Solid State Ion*, **2008**, 179, 1333–1337. DOI: <https://doi.org/10.1016/j.ssi.2008.02.017>.
41. Li X., Jin L., Song D., Zhang H., Shi X., Wang Z., *et al.*, *Journal of Energy Chemistry*, **2020**, 40, 39–45. DOI: <https://doi.org/10.1016/j.jechem.2019.02.006>.

Review: Description of Porous Media and their Sorption Characteristics as Correlated Structures

Salomón Cordero-Sánchez^{1*}, Juan M. Esparza-Schulz¹, Ilich A. Ibarra², Víctor M. Trejos¹, Annabel L. Tellez-Gonzalez¹, Juan Villegas-Cortez³, Graciela Román-Alonso⁴, Salomón J. Alas⁵

¹Departamento de Química, Universidad Autónoma Metropolitana-Iztapalapa, Ciudad de México 09310, México.

²Laboratorio de Físicoquímica y Reactividad de Superficies (LaFReS), Instituto de Investigaciones en Materiales, Universidad Nacional Autónoma de México, Circuito Exterior s/n, CU, Coyoacán, 04510, Ciudad de México, México. On Sabbatical as “Catedra Dr. Douglas Hugh Everett” at Departamento de Química, Universidad Autónoma Metropolitana-Iztapalapa, Ciudad de México 09310, Mexico.

³Departamento de Sistemas, Universidad Autónoma Metropolitana, Av. Sn. Pablo 420, Col Nueva El Rosario, CP 02128, Alc Azcapotzalco, Mexico City, Mexico.

⁴Departamento de Ingeniería Eléctrica, Universidad Autónoma Metropolitana-Iztapalapa, Ciudad de México 09310 México.

⁵Departamento de Ciencias Naturales, Universidad Autónoma Metropolitana Unidad Cuajimalpa, 05300 Ciudad de México, Mexico.

*Corresponding author: Salomón Cordero-Sánchez; email: scordero@izt.uam.mx

Received May 2nd, 2024; Accepted July 1st, 2024.

DOI: <http://dx.doi.org/10.29356/jmcs.v68i4.2269>

Abstract. This review presents an in-depth analysis of the progress and achievements in the study of porous structures by the Physicochemical of Surfaces Academic Area at the Universidad Autónoma Metropolitana, Iztapalapa's Chemistry Department. A straightforward model for depicting disordered structures has been introduced here, facilitating the discovery of correlations between adjacent elements within these structures. Such correlations have proven to be crucial in the classification and analysis of different disordered porous materials and have been instrumental in the interpretation and categorization of nitrogen adsorption isotherms.

Keywords: Adsorption isotherms; Physicochemical of surfaces academic area, and porous media.

Resumen. Este artículo proporciona una revisión completa de los avances y aportes realizados en la caracterización de estructuras porosas dentro del Área Académica de Físicoquímica de Superficies del Departamento de Química de la Universidad Autónoma Metropolitana, Iztapalapa. Dentro de esta Área Académica se ha desarrollado un modelo simple para describir estructuras desordenadas, que permitió visualizar la correlación entre elementos vecinos que constituyen dichas estructuras. Estas correlaciones han resultado en un factor clave para clasificar y categorizar diversos medios porosos desordenados, además de servir como herramientas útiles para interpretar y clasificar las isotermas de adsorción del nitrógeno.

Palabras clave: Isotermas de adsorción, área académica de Físicoquímica de superficies, y medios porosos.

Introduction

Porous media play a crucial role in various technological applications, serving as catalytic supports, membranes, filters, and separation and sensing devices for gas molecules and solutions [1]. In recent years, there has been remarkable advancement in synthesizing modern porous solids with ordered structures, including Mobil Composition of Matter No. 41 (MCM-41), Santa Barbara Amorphous-15 (SBA-15), and Metal-organic frameworks (MOFs) [2-4]. These advancements allow precise characterization of the size and geometrical structures of such materials. The surface area of porous solids can be evaluated through gas adsorption, using the Brunauer-Emmett-Teller (BET) equation, which is widely employed for predicting and explaining the adsorptive properties of solids [5,6]. Additionally, another crucial parameter in characterizing porous solids is the pore size distribution (PSD). Three groups of techniques have become essential tools for determining PSD with high precision. The first group consists of theoretical techniques derived from the classical theory of liquids, known as classical density functional theory (DFT) [7-9]. The second group includes molecular simulation techniques such as Monte Carlo simulations and molecular dynamics simulations based on force fields [10-12]. The third group comprises advanced techniques, including quantum based methods and ab initio molecular dynamics for studying pore size distribution in complex materials [13-16].

However, several decades ago, before the advent of modern solids, it was very difficult to describe in a precise manner the structure of materials such as Vycor glasses, silicas, carbons and clays. And even more complex, to establish a direct correlation between solid structure and the physicochemical phenomena occurring during their technological applications. In this context, numerous scientific efforts aimed to provide a theoretical framework for understanding the effect of pore geometry and interconnection over the most used technique to characterize porous solids: adsorption of gasses. During the 1950s, 1960s and 1970s the study of adsorptive properties in cylindrical pores yielded valuable insights into interpreting adsorption isotherms. Examples include the Barrett-Joyner-Halenda (BJH) method [17], which was widely used for determining PSD; the Broekhoff de Boer description [18], and the studies conducted by Everett and Haynes [19] that delved into the intricate processes of capillary condensation and evaporation of gases that have been adsorbed.

Another significant approach during those days was the development of porous network models. These models aimed to capture the interconnected nature of pore elements using lattices with different geometries. Within such lattices, two key elements are distinguished: sites and bonds. Sites represent points where two or more bonds converge, while bonds are passages connecting two neighbouring sites. Another important characteristic of lattice geometry is the coordination number or connectivity (C), denoting the number of bonds connecting two neighbouring sites. Typically, the connectivity remains constant within each different lattice. In this way, a 3D-lattice can be envisioned as an integrated network of sites and bonds interconnected throughout a volume. Examples of such lattices include the simple cubic lattice ($C=6$), the body-centered cubic lattice ($C=8$), and the face-centered cubic lattice ($C=12$).

By associating sites and bonds with different geometries and sizes, researchers can simulate, besides adsorption, irreversible transport processes in porous media, such as fluid displacement and diffusion of gases and solutions, which remain active fields of research nowadays [20-22]. However, reversible or steady-state processes, such as gas adsorption, represents a formidable challenge. At each equilibrium state, these processes involve an interplay between the geometry of statically confined fluids and the physical attraction between the porous solid walls and the adsorbed gas. Moreover, a confined fluid is not a homogenous phase, since the density of the adsorbed fluid varies as a function of the distance from the solid wall. Nevertheless, in the 1970s, 1980s, and early 1990s, several authors conducted ingenious studies combining simple thermodynamic equations of homogeneous phases and percolation theory applied to porous networks [18-20]. These studies aimed to elucidate the relationship between pore element interconnection, shape, and gas adsorption development. Additionally, methods were developed to calculate the connectivity of porous networks [26]. These methods validated the importance of porous networks as a useful model for interpreting and predicting the shape of adsorbed gas isotherms. During this period, the Academic Area of Physicochemical of Surfaces

(AAPS) developed porous networks embodied with correlation, which are described in detail below. Henceforth, the acronym AAPS will be used.

Dual Site-Bond Model (DSBM)

During the 1980s, the AAPS proposed the Dual Site-Bond Model (DSBM) to describe porous materials with internal structures formed by porous networks composed of interconnected pores and channels, such as Vycor glasses and silica gels [4]. These amorphous materials can be characterized by lattices composed of interconnected sites and bonds. The starting point of the DSBM begins by addressing the relationship between the sizes of interconnected elements that form a porous network. Defining the size of a pore network material is an ambiguous concept. The DSBM resolves this by defining the size of a pore cavity (site) as the radius R_S of the largest sphere that could be accommodated within the cavity. Similarly, the size of a bond is defined as the radius R_B of the largest cylinder that could fit inside the pore channel connecting two sites, or as the radius of the largest circle that would be accommodated inside the pore window connecting two pore cavities. Since a site is a pore element where C-bonds converge, its size must be sufficient to accommodate these bonds. Conversely, since a bond is a channel or a window connecting two sites, its size must be smaller or equal to either of the sites it connects. This leads to the Construction Principle (CP): “the size of any site must always be bigger or at least equal to the size of any of its C-bonds”. See Fig. 1 for a schematic representation.

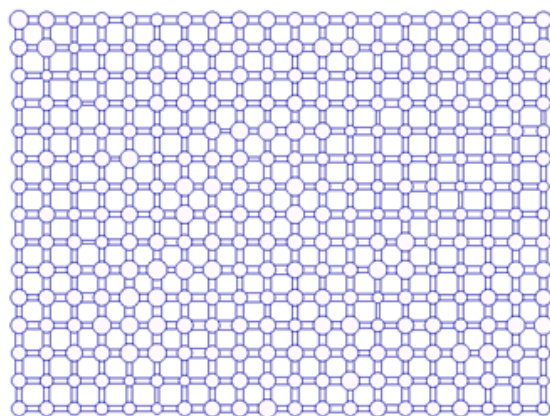


Fig. 1. Schematization of sites and bonds forming a porous network with square geometry. The CP is depicted, showing that the size of any site is always bigger or at least equal to the size of any of its C-bonds.

Two equations ensure the fulfillment of the CP throughout pore networks, given by,

$$B(R) \geq S(R) \quad (1)$$

$$\phi(R_S, R_B) = 0, \forall R_S < R_B \quad (2)$$

where $B(R)$ and $S(R)$ are the fractions of bonds and sites of sizes R_B or R_S smaller or equal to the value R , respectively. Thus, they are defined as the integral of the normalized size probability density functions of sites, $F_S(R_S)$ and bonds, $F_B(R_B)$, as follows,

$$B(R) = \int_0^R F_B(R_B) dR \quad (3)$$

$$S(R) = \int_0^R F_S(R_S) dR \quad (4)$$

Additionally, in Eq. (2) the function $\phi(R_S, R_B)$ is a correlation function that restricts the joint probability, $F(R_S, R_B)$, of finding a site of size $R_S \in (R_S, R_S + dR_S)$ connected to any of its C-bonds of size $R_B \in (R_B, R_B + dR_B)$ in the following way,

$$F(R_S, R_B) = F_S(R_S)F_B(R_B)\phi(R_S, R_B)dR_SdR_B \quad (5)$$

where $\phi(R_S, R_B)$ must satisfy the restriction given by Eq. (2). Then, according to Eq. (5), the joint probability, $F(R_S, R_B)$, becomes equal to zero for $R_B > R_S$. The expression of $\phi(R_S, R_B)$ meeting this latter condition is [27],

$$\phi(R_S, R_B) = \frac{\exp\left(-\int_{R_B}^{R_S} \frac{dS}{B(R) - S(R)}\right)}{B(R_S) - S(R_S)} \quad (6)$$

The Eq. (1), often referred to in the literature as the first law of the DSBM, specifies how the functions $F_B(R_B)$ and $F_S(R_S)$ are defined to ensure an adequate quantity of C-bonds connected to any site in the pore network. Fig. 2 displays the values of $B(R)$ and $S(R)$ corresponding to three different pairs of the functions F_B and F_S ; condition $B(R') \geq S(R')$, $\forall R' > 0$ is always met for values of $R' > 0$. Additionally, the normalized overlap, Ω , between functions F_B and F_S is presented; note how $\Omega = 0$ in the graphic depicted on the left; $\Omega = 1/3$ (indicated by the red area) for the case in the middle, and $\Omega = 1$ (total overlap between F_B and F_S) in the rightmost case.

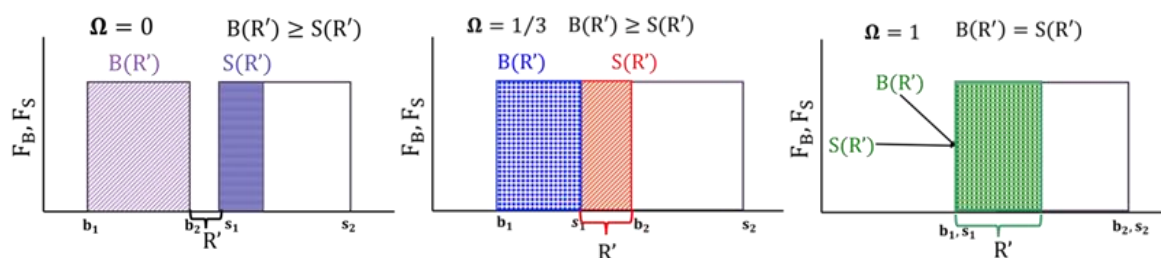


Fig. 2. Illustration of the first law of the DSBM. Each of the uniform distribution functions F_S and F_B satisfy the condition $B(R') \geq S(R')$, $\forall R'$. The values of B and S corresponds the shaded areas. b_1 (bonds) and s_1 (sites) denote the sizes of the smallest pore elements, whereas b_2 (bonds) and s_2 (sites) correspond to the sizes of the largest pore elements. Parameter Ω represents the normalized area of overlap between F_B and F_S .

On the other hand, Eq. (2), commonly referred to in the literature as the second law of the DSBM, imposes local constraints on connected sites and bonds in order to satisfy the CP. The value of $\phi(R_S, R_B)$ depends on the value of Ω . When $\Omega = 0$, $\phi(R_S, R_B)$ always equals 1, as any bond from $F_B(R_B)$ can be connected to any site with size R_S without violating the CP. However, for $0 < \Omega \leq 1$, the value of $\phi(R_S, R_B)$ depends

on the specific interval where R_B and R_S are located. Fig. 3 illustrates different values of $\phi(R_S, R_B)$ shown in equation (7), for uniform density distribution functions, resulting from different values of Ω [23-26].

$$\phi(R_S, R_B) = \frac{\exp\left(-\int_{R_B}^{R_S} \frac{dS}{B(R) - S(R)}\right)}{B(R_S) - S(R_S)}$$

where

$$\beta(R_S, R_B) = \begin{cases} (R_S - s_1)/(b_2 - s_1) & \text{if } R_B \leq s_1 \text{ and } R_S \leq b_2 \quad (I) \\ 1 & \text{if } R_B \leq s_1 \text{ and } R_S > b_2 \quad (II) \\ (R_S - R_B)/(b_2 - b_1) & \text{if } R_B > s_1 \text{ and } R_S \leq b_2 \quad (III) \\ (b_2 - R_B)/(b_2 - s_1) & \text{if } R_B > s_1 \text{ and } R_S > b_2 \quad (IV) \end{cases}$$

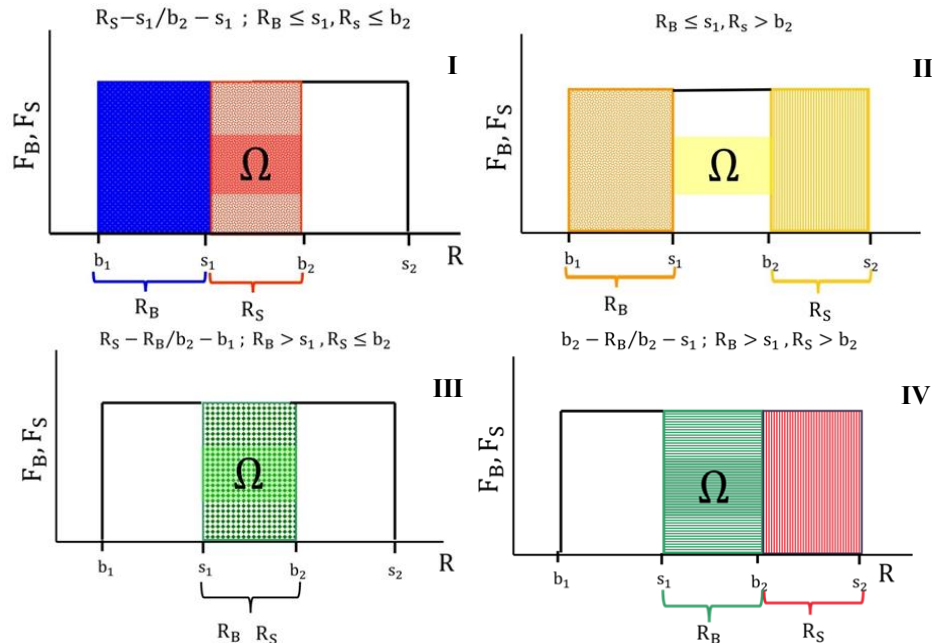


Fig. 3. Different values of $\phi(R_S, R_B)$ for overlapped uniform distribution functions F_B and F_S . Roman numerals indicate the expression in eq. (7). b_1 (bonds) and s_1 (sites) denote the sizes of the smallest pore elements, whereas b_2 (bonds) and s_2 (sites) correspond to the sizes of the largest pore elements

Pore Size Segregation Effect

One of the original contributions of the DSBM lies in its simple and systematic description of the size correlation among neighbouring pore components. Several methods for constructing porous networks have followed the principles of the DSBM [28-31]. However, the porous networks with the maximum randomness and isotropy among neighbouring sites and bonds can be constructed using the method found in [29] which is

referred as the Pure MC method, inspired by the Monte Carlo sampling method of the NVT ensemble. This method involves randomly assigning sizes R_B and R_S from fixed functions $F_B(R_B)$ and $F_S(R_S)$, respectively, to bonds and sites of a given lattice. Subsequently, one Monte Carlo step is carried out executing N transitions (where N is equal to the total number of sites and bonds of the porous network). These transitions involve the interchange of sizes of two randomly chosen sites or two randomly chosen bonds in the lattice, according to the associated transition probabilities defined by the Metropolis algorithm [32,33]. The Monte Carlo steps are repeated until all the sites of the pore network satisfy the CP. The topology of pore networks obtained with this construction method is depicted in Fig. 4 [34], where three porous networks with $C = 4$ and different values are presented. In this figure, three sizes of sites are presented: small, medium, and large; the intervals of R_S , match these classifications by equalizing three areas below F_S . This figure illustrates two extreme cases and one that lies midway between them. The first extreme case corresponds to porous networks with $\Omega \rightarrow 0$ (see Fig. 4(a)); in this case, the size of the three domains formed with sites of similar sizes is quite small, and they are spatially distributed at random. The intermediate case is depicted in Fig. 4(b), where $\Omega \approx 0.7$; the three domains possess a size that is neither too large nor too small, but rather intermediate. Finally, the second extreme case is represented for the condition $\Omega \rightarrow 1$, (see Fig. 4(c)); in this instance, the domains have a large size and are distributed evenly in all directions.

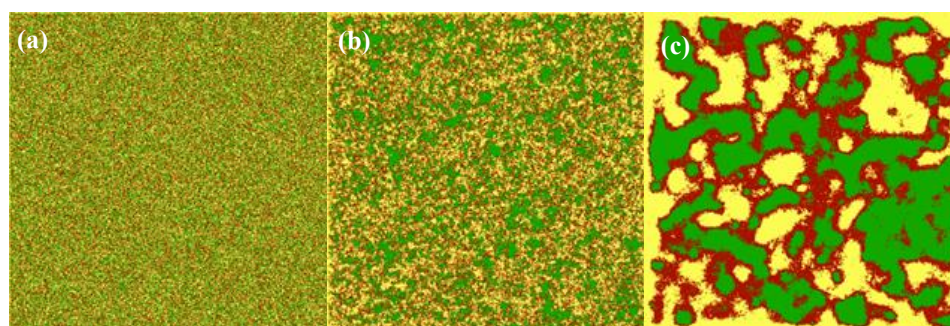


Fig. 4. Illustration depicting the spatial arrangement of domains within square porous networks, where each domain consists of sites of comparable size. The networks are characterized by $C = 4$ and a length of 100 nodes. Every pixel corresponds to a single site. Panel (a) $\Omega = 0.31$, panel (b) $\Omega = 0.68$, and panel (c) $\Omega = 0.92$. Sites of small, medium, and large sizes are represented by the colors green, red, and yellow, respectively.

Domains with uniformly sized sites can be described using a correlation length, which quantifies the size of regions within a porous network where the sites are strongly interrelated. This quantity is linked to the correlation function $C(r)$, which represents the relationship of site sizes in the vicinity of surrounding locations and is defined as follows,

$$C(r) = \frac{\langle (R_i - \bar{R}_S)(R_j - \bar{R}_S) \rangle}{[\langle (R_i - \bar{R}_S)^2 \rangle \langle (R_j - \bar{R}_S)^2 \rangle]^{1/2}} \quad (8)$$

where R_i and R_j are two sites separated by r lattice positions, and \bar{R}_S is the medium size of R_S . Then, if $r = 1$, R_i and R_j are connected to the same bond. The relation between the correlation length ξ and $C(r)$, goes as, [35,36]

$$C(r) = \exp\left(-\frac{r}{\xi}\right) \quad (9)$$

Fig. 5 presents a graph of ξ , as a function of Ω calculated through Eq. (9) for pore networks with $C = 4$ and different values of Ω . This figure suggests two things. First, the size of the domains with sites of similar sizes have a typical value of $\xi \rightarrow 0$ for $\Omega \rightarrow 0$, $\xi \rightarrow 3$ for $\Omega \approx 0.7$, and $\xi \rightarrow \infty$, for $\Omega \rightarrow 1$. A comparative analysis of Figs. 4 and 5 can be insightful for understanding the relationship between the values of ξ and the dimensions of the domains, especially considering the nearly identical sizes of the sites involved. And second, ξ is a function of Ω . The variation of ξ in relation to Ω can be interpreted physically in the following manner. Pore cavities of comparable dimensions aggregate into domains, the size of which changes in direct proportion to the Ω value. This grouping of pores into domains based on size allows for a structured categorization, reflecting the influence of Ω on the spatial distribution within the material.

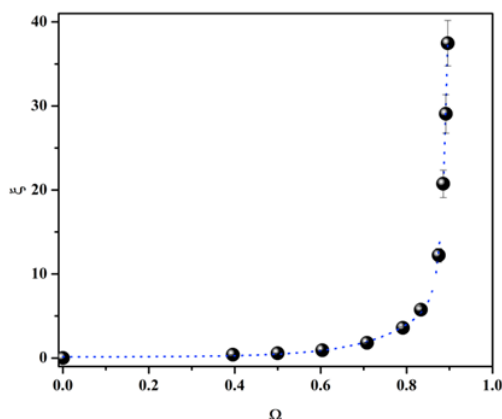


Fig. 5. Representation of the correlation length ξ as a function of Ω for pore networks with $C = 4$ and uniform distribution functions F_B and F_S [37].

Refinements of the DSBM

The DSBM, as outlined previously, is inadequate for characterizing the internal structure of materials lacking a porous network texture. This model does not account for the complexities of materials without such geometries, such as MCM-41 or SBA-15 materials, which are characterized by their pores arranged in a hexagonal cylindrical array. In the context of the DSBM framework, the model was enhanced by two key modifications: the inclusion of spatial interference between bonds and the introduction of variable connectivity.

Geometric interference of bonds

The early 1990s witnessed the advent of advanced materials such as MCM-41, SBA-15, and SBA-16, among others, signifying a significant development in the field of material sciences. [4]. These solid materials feature organized structures, which facilitates the accurate determination of pore sizes. The DSBM sought to describe structured materials by integrating suitable enhancements, maintaining its straightforwardness. This involved examining the alterations in the texture of porous networks that occur when the geometric interference of bonds converging at a single site is prevented [38]. Fig. 6 illustrates this concept.

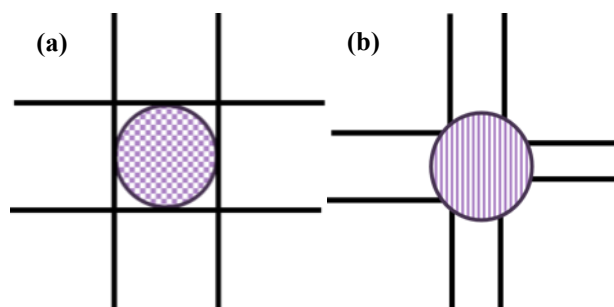


Fig. 6. Geometrical interference of four bonds converging the same site. Panel **(a)**, the sizes of the bonds are sufficiently large to cause mutual interference. Panel **(b)**, the sizes of the bonds are sufficiently minimal to prevent any mutual interference.

This last figure shows two scenarios involving four bonds connected to a single site on a square lattice. In Fig. 6**(a)**, geometrical interference occurs among the bonds, with the four bonds of equivalent size as the site itself. As a result, the site loses its circular geometry. Fig. 6**(b)**, illustrates four bonds converging the same site without overlapping. This last configuration maintains the site circular shape of the site and ensures that the bonds do not obstruct one another. Then, if the sites of the networks have to keep its cavity geometry, the elements of the pore network have to be linked with a CP different than previously defined. It should be noted that geometric interference may not be applicable to all porous materials being studied. The significance of these limitations can vary depending on the specific characteristics and applications of the material in question. Therefore, it is essential to evaluate the relevance of geometric restrictions on a case-by-case basis. For instance, the pores in plate-like materials do not interfere with each other; in this case the Hele-Shaw cells (spaces between rugged-parallel plates) [39] would describe much better the proper linkage among pores. Graphically, the size of any pair of bonds orthogonally connected to one site of size R_S on a square lattice, and subjected to geometrical restrictions, must fall within the area bounded by a circle of radius R_S and two perpendicular axis intersecting at the center of the circle, as depicted in Fig. 7. This area is defined as the incumbent volume of a site of size R_S when connected to two perpendicular bonds of sizes R_{B_1} and R_{B_2} .

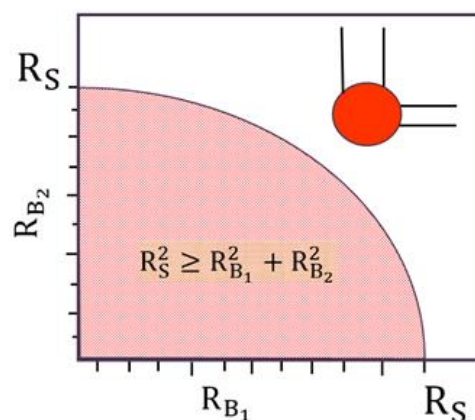


Fig. 7. Permitted sizes of two bonds orthogonally connected to one site. Any point located in the red area (incumbent volume of the site R_S) do not interfere with each other.

The updating of the first law that guarantee the fulfilment of geometric restrictions among the components of a porous network, is as follows,

$$B_C(R_S) \geq S(R_S), \quad \forall R_S \quad (10)$$

where $B_C(R_S)$ represents the fraction of bonds of size R_S or smaller that lie in the incumbent volume of sites smaller than or equal to R_S . The general expression for $B_C(R_S)$ can be articulated through the following equation (the integral boundaries are defined according to the type of lattice involved.) [40],

$$B_C(R_S) = \left\{ \int_0^{R_S} \cdots \int_0^{R_S} F_B(R_{B_1}) \cdots F_B(R_{B_C}) dR_{B_1} \cdots dR_{B_C} \right\}^{1/C} \quad (11)$$

where $R_{B_1}, R_{B_2} \dots R_{B_C}$ are the sizes of the C -connected bonds of sites of sizes R_S and $F_B(R_{B_1}) \cdots F_B(R_{B_C})$ are the corresponding density functions of these bonds. For their part, the probability density function for the joint event of having a site of size R_S connected to bonds of sizes $R_{B_1} \cdots R_{B_C}$, is represented as follows,

$$\rho(R_S \cap R_{B_1} \cdots R_{B_C}) = F_S(R_S) F_B(R_{B_1}) \cdots F_B(R_{B_C}) \phi(R_S, R_{B_1} \cdots R_{B_C}) \quad (12)$$

Then, the updating of the second law can be written as,

$$\phi(R_S, R_{B_1} \cdots R_{B_C}) = 0, \quad \text{outside the incumbent volume} \quad (13)$$

where the expression of the correlation function changes as follows [40],

$$\phi(R_S, R_{B_1} \cdots R_{B_C}) = \frac{\exp\left(-\int_{B_C(R_C)}^{B_C(R_S)} \frac{dB_C}{B_C - S}\right)}{B_C(R_C) - S(R_C)} \quad (14)$$

where R_c is the minimal size of a site that accommodates the precise set of $R_{B_1} \cdots R_{B_C}$ bonds without geometric interference. The revised version of the CP is presented as follows: “While every bond converging into a site must be smaller in size than this last cavity, a pair of adjacent bonds converging to the site have still to assume the right combination of sizes to prevent any physical interference between them before meeting together into the site” [38,42].

Variable connectivity

To integrate variable connectivity one can introduce the notion of “virtual (closed) bonds” within a porous network that maintains a constant connectivity C_m [38, 41]. Refer to Fig. 8, which illustrates the sites of a square network with $C_m = 4$, connected to “virtual bonds”.

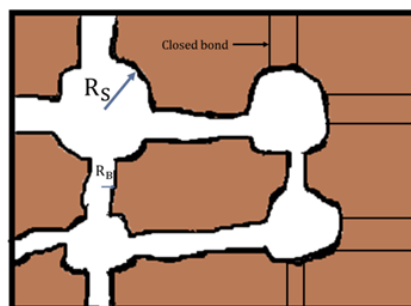


Fig. 8. Representation of the concept of virtual or closed bonds of sites of a square network with $C = 4$. The solid phase is represented in brown color.

Physically, “virtual bonds” represent the solid phase; mathematically, their size corresponds to $R_B = 0$. Then, the local connectivity of any i -site (C_i) is given by,

$$C_i = C_m - C_{i,0}, \quad \forall i \quad (15)$$

where $C_{i,0}$ is the number of virtual bonds of the i -site. If the average of C_i is calculated in the last equation, the average connectivity of the porous network (\bar{C}) is obtained,

$$\bar{C} = C_m(1 - f_0) \quad (16)$$

where f_0 stands for the fraction of closed bonds in the porous network. Taking into account the definition of closed bonds, F_B is redefined as follows,

$$F_B(R_B) = \begin{cases} f_0, & \text{for } R_B = 0 \\ F'_B(R_B), & \text{for } R_B > 0 \end{cases} \quad (17)$$

This last definition for F_B makes Eqs. (1)-(6) still valid. The following normalization condition holds,

$$\int_0^{\infty} F'_B(R_B) dR_B = 1 - f_0 \quad (18)$$

Fig. 9 shows the graphical representation of F_B and F_S for porous networks with variable connectivity.

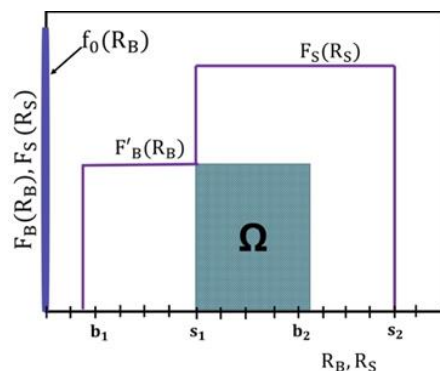


Fig. 9. Representation of the density functions F_B and F_S for porous networks with variable connectivity.

Correlated Networks with geometric restrictions and variable connectivity

The interplay of variable connectivity and geometric restriction of bonds results in the formation of porous networks exhibiting simultaneous segregation based on size and connectivity when the density functions F_B and F_S overlap [42]. Throughout the 2010s, the AAPS introduced a variety of advanced computational techniques for the development of porous network structures. These innovative methods have significantly contributed to the field, offering new insights and approaches to the construction of these complex systems [30,38, 43 - 45]. Refer to Fig. 10 to observe the simultaneous effects of size and connectivity segregation. This figure presents visual representations of central sections of porous networks with $\bar{C} = 4$ and different values of $\xi(0.94,3.0,9.0)$; it is organized into two columns. The top row displays central planes representing the spatial distribution of sites in three sizes: small, medium, and large. The bottom row shows color-coded central sections, which illustrate the spatial arrangement of site connectivity. In the image, orange pixels represent sites where $C_i = 1,2$. Sites with $C_i = 3,4$ are indicated by blue pixels. Finally, gray pixels denote sites with $C_i = 5,6$. Each column in this figure corresponds to the same porous network: the first column, from left to right, corresponds to $\xi = 0.94$; the second column to $\xi = 3.0$; and the third column to $\xi = 9.0$.

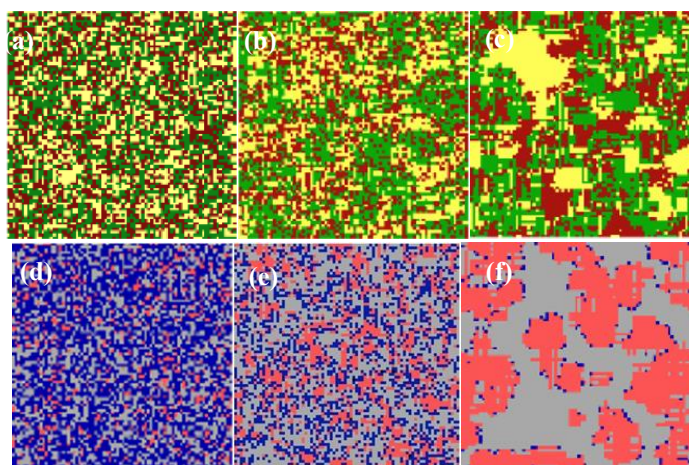


Fig. 10. Schematization of the spatial distribution of the connectivity and sizes of sites on cubic porous networks with $\bar{C} = 4$ and a length of 100 nodes. **(a), (d)** $\xi = 0.94$. **(b), (e)** $\xi = 3.0$. **(c), (f)** $\xi = 9.0$. Top row represents sizes of sites: green (small), red (medium), yellow (large). Bottom row stands for local connectivity of sites: orange $C_i = 1,2$. Blue $C_i = 3,4$. Gray $C_i = 5,6$. Each pixel represents one site. Each image corresponds to middle planes of cubic porous networks.

Fig. 10 is described as follows. As $\xi \rightarrow 0$, the sizes and local connectivity of sites become randomly assorted throughout the space; see Figs. 10(a) and 10(d). This situation corresponds to distributions F_B and F_S being sufficiently separated on a graph, allowing every site within F_S to accommodate any combination of $R_{B_1} \dots R_{B_C}$ bonds without any geometric interference. Yet, when $\xi > 1$, the sizes of adjacent sites become increasingly alike, leading to the formation of distinctive domains with a typical size ξ , as illustrated in Fig. 10(b). This phenomenon is completely equivalent to what has been outlined in preceding sections. However, the novel aspect highlighted is the effect of connectivity segregation, as depicted in Fig. 10(e). This phenomenon involves the clustering of sites that share comparable values of local connectivity. In Fig. 10(e), adjacent sites are spatially organized based on their C_i values. The sites with C_i values of 5 and 6, those with 3 and 4, and those with 1 and 2, are each clustered into separate, cohesive domains. These domains are visually differentiated by gray, blue, and orange colors, respectively. When the parameter ξ significantly exceeds 1, the structure of the porous networks transitions into configurations predominantly characterized by two major connectivity domains. Specifically, one domain exhibits local connectivity C_i of either 1 or 2, whereas the other domain is distinguished by higher C_i values to 5 or 6, as depicted in Fig. 10(f). These domains are separated by a dispersed interface composed of sites with C_i 3 or 4. The observed phenomenon arises from the distributions of F_B and F_S , particularly when the variable ξ attains its peak value in relation to the network's average connectivity. Geometric interference indicates that the best approach is to connect the smallest feasible site capable of supporting a sequence of bonds $R_{B_1} \dots R_{B_C}$ of the largest dimensions, thereby achieving a local connectivity of $C_i=5$ or 6. In contrast, larger sites should be linked to bonds of similar size. This approach is practical when these bonds are classified by F_B as large and the sites demonstrate a local connectivity of $C_i=1$ or 2, with their respective C_i -bonds situated on directly opposite sides of the site. To complement Fig. 10, Fig. 11 presents drawings of the domains. These domains in Fig. 11 are characterized by alternating sites of high and low local connectivity, providing a visual representation of the spatial distribution of connectivity values within the domain. This illustration highlights the contrast and interplay between regions of differing connectivity levels.

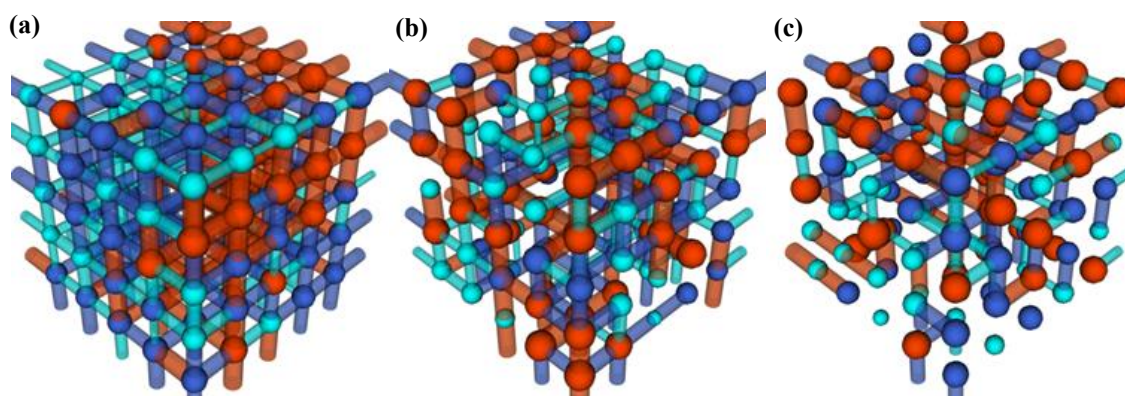


Fig. 11. Cubic networks with a high correlation are structured into regions measuring $5 \times 5 \times 5$. (a) $\bar{C} = 6$. (b) $\bar{C} = 4$. (c) $\bar{C} = 2$. Colors are utilized to create a contrast.

Interpretation of N₂ isotherms through correlated Porous Networks

Assumptions

The straightforward geometry of porous networks enables a useful qualitative analysis of the shape of the boundary curves (both ascending and descending) and the Primary Ascending and Descending Scanning Curves of N₂ isotherms, based on the sizes, geometry, and interconnection among porous entities. The pore

volume of sites and bonds can be controlled by establishing a suitable distance from the node (center of each site) to the node of the porous network. To obtain N₂ isotherms, the following rough assumptions are made for the adsorption processes (whether boundary or primary ascending curve).

- I. During adsorption, as the pressure of the adsorbing gas increases, an adsorbed layer, denoted by thickness t , progressively forms on the surface of sites and bonds. The value of t can be calculated using a suitable equation, such as the Halsey-type equation [46].
- II. The adsorbed layer on each site and bond reaches a limit value at a certain pressure, imposed by the balance between the mechanical equilibrium of the adsorbed phase and the physical attraction of the pore walls. The classical Kelvin equation provides a corresponding radius of curvature, R_C , that defines the porous elements ready to condensate, written as,

$$R_C = \frac{2\sigma^{lv}v^l}{R_g T \ln(p/p^0)} \quad (19)$$

where R_g is the gas constant, T is the absolute temperature, σ^{lv} is the interfacial tension between liquid and vapor phases, p is the gas bulk pressure, p_0 is the saturation pressure defined by T , and v^l is the molar volume of the liquid phase of the adsorptive.

- III. The condition for the onset of capillary condensation is given by $(R_B - t) \leq R_C/2$. However, if at least one of its two neighboring sites of the bonds is already filled with condensate, they acquire a hemispherical interface at one of its ends. This could trigger the advancement of the meniscus to the other end of the bond if it also fulfills the condition $R_C/2 \leq (R_B - t) \leq R_C$. This latter mechanism of condensation is a cooperative effect known as advanced adsorption [47].
- IV. As for sites, they develop a continuous hemispherical liquid-vapor interface if either all of their C bonds or at least C-1 bonds are already occupied with condensate. Then, if this condition is satisfied, and also $(R_S - t) \leq R_C$, the sites are immediately occupied by condensate. On the other hand, the following suppositions are assumed for the desorption processes (either boundary or primary descending curve).
- V. Occupied pores (sites or bonds) with condensate can evaporate if they have reached the condition $R_B \geq R_C$ or $R_S \geq R_C$, and if there exists a liquid-vapor interface at their junctions that promotes the development of evaporation of the pore entity. The latter condition is met if exists a pathway from the evaporating pore to the bulk vapor phase (for the boundary descending curve) or at least one of its connected pores have not been filled with condensate (primary descending curve). Thus, desorption is controlled by the classical pore-blocking effect [48,49] and the percolation phenomenon.
- VI. Once a pore entity is emptied, as the pressure steadily declines, the thickness of the adsorbed layer correspondingly diminishes.

It is important to note that the suppositions outlined above do not allow for an accurate assessment of the shape of the isotherms. Detailed molecular simulation methods have shown that the form of the isotherms is influenced by the trajectory over a landscape of metastable states of the thermodynamic potential, which is influenced by the detailed molecular configurations of the adsorbed gas molecules and the microscopic characteristics of the surface of the pore walls [50].

Consequently, these suppositions are not capable of describing phenomena such as cavitation, which results from molecular fluctuations of the adsorbed phase [51,52]. Nevertheless, the N₂ isotherms of networks constructed under the framework of the DSBM have proven to be a very useful tool, providing a simple framework for qualitatively interpreting the appearances of boundary curves (ascending or descending) and primary scanning curves (ascending or descending) [53]. This is described next.

Figs. 12 and 13 provide a summary of poorly correlated and highly correlated N₂ isotherms at 77 K, depicting porous networks with diverse mean connectivity values. It is evident from these figures that the

appearance of the boundary curves cannot be strictly classified as types H1, H2, or H3 of the original IUPAC classification of sorption hysteresis loops [48], although they exhibit hybrid shapes with different degrees of these IUPAC types, depicted in Fig. 14. In broad terms, networks with $\Omega = 0$ (left columns of Figs. 12 and 13) are typically associated with H1 loops, though a transition to H2 types occurs if the volume of bonds significantly exceeds the volume of sites [53]. In contrast, highly correlated porous networks (right columns of Figs. 12 and 13) yield cycles with sloping ascending and descending boundary curves, representing hybrids between H1 and H3 loops.

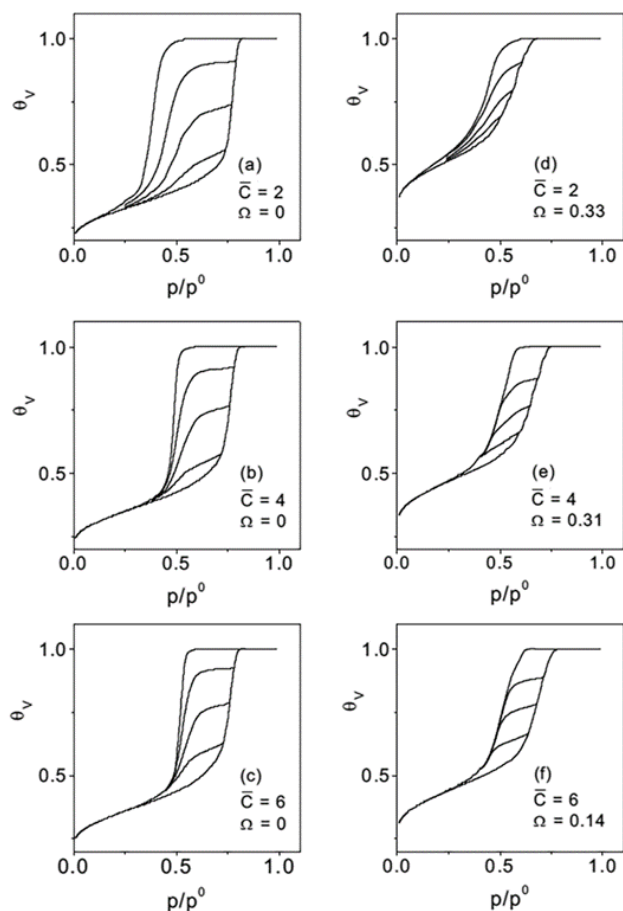


Fig. 12. Simulated nitrogen sorption isotherms at 77 K on porous networks. In this figure, θ_v represents the degree of filling of the porous network with adsorbate, while p represents the gas bulk pressure, and p_0 is the saturation pressure. The adsorption hysteresis loops are organized according to \bar{C} and Ω . Sets of primary descending curves are included. Reproduced from [53] with permission from the Royal Society of Chemistry.

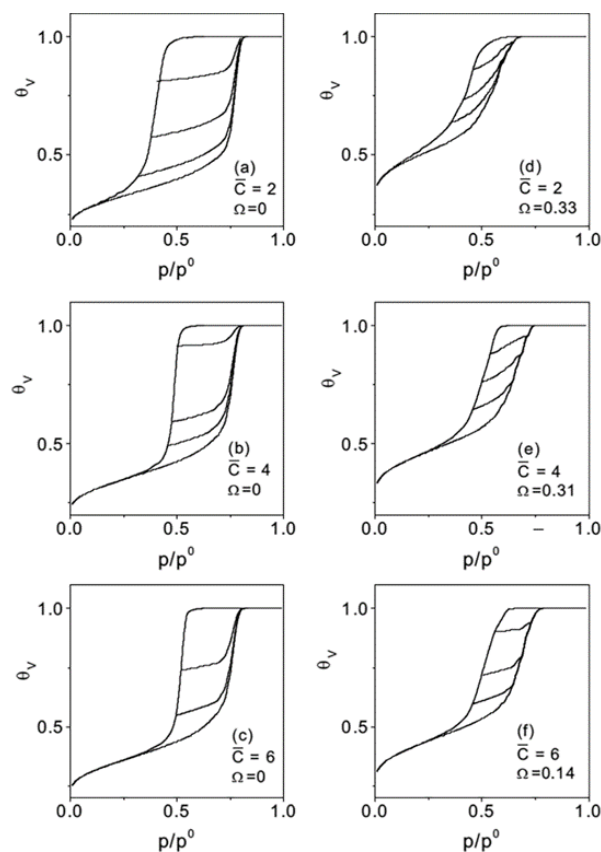


Fig. 13. Simulated nitrogen sorption isotherms at 77 K on porous networks. In this figure, θ_v represents the degree of filling of the porous network with adsorbate, while p represents the gas bulk pressure, and p_0 is the saturation pressure. The adsorption hysteresis loops are organized according to \bar{C} and Ω . Sets of primary ascending curves are included. Reproduced from [53] with permission from the Royal Society of Chemistry.

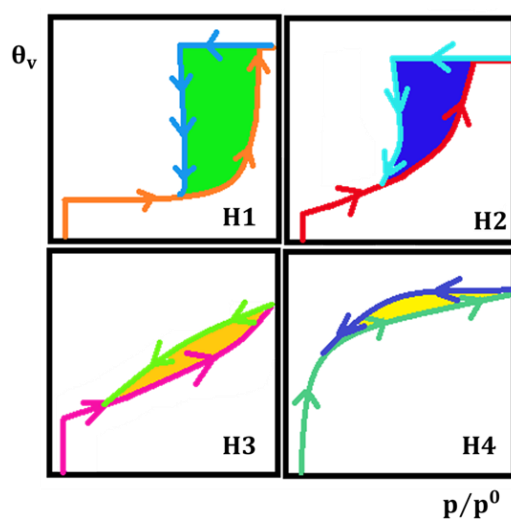


Fig. 14. Diagrammatic illustration of the original IUPAC categorization for sorption hysteresis loops [48].

Adsorption and desorption in poorly correlated ($\Omega=0$) porous networks

In order to understand the shapes of the boundary curves of the isotherms in Figs. 12 and 13, the concept of multiplex (independent domain) must be introduced. A multiplex is a unit cell consisting of a site and its C-half bonds (half, because one bond is shared with two sites). See Fig. 15. This multiplex can condensate and evaporate without networking effects, because it is assumed that each one maintains immediate contact with the bulk phase of the adsorbing gas. If the algorithm to simulate N_2 adsorption, described in the previous section, is applied to the set of multiplexes that comprise each porous network in Figs. 12 and 13, we obtain the set of isotherms presented in Fig. 16.

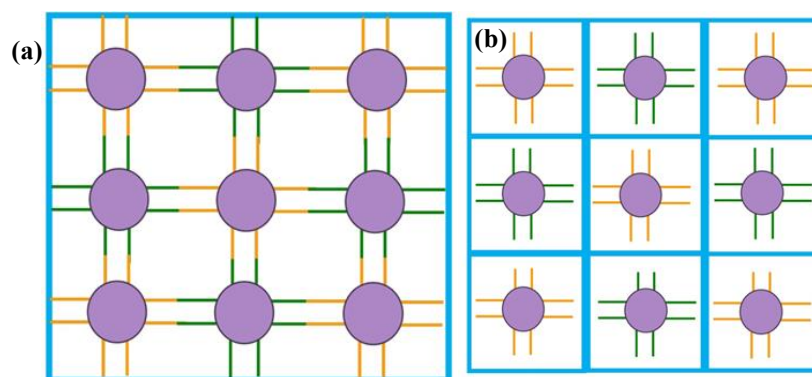


Fig. 15. (a) Visual representation of a porous network, and (b) the concept of multiplex.

From the last figure, it is observed that the ascending boundary curves of poorly correlated networks (left column of Fig. 13) practically coincides with those of the multiplex's isotherms in Fig. 16 (left column). However, the descending boundary curves of these uncorrelated porous networks differ considerably from those of the multiplexes. The coincidence of the ascending boundary curves of networks and multiplexes can be explained by the significant difference in sizes between connected sites and each of their C-bonds. This difference of sizes implies that the pressure required for filling the bonds is small enough compared to the pressure needed for the filling their connected sites. Consequently, when the sites are ready to be occupied with condensate at certain pressure, almost all of their connected bonds are already occupied with condensate. This suggests that for poorly correlated networks, it is possible to accurately calculate the pore size distribution of sites using the ascending boundary curves when the volume of sites is considerably greater than that of the bonds, or the pore size distribution of bonds when the volume of bonds is considerably greater than that of the sites [53]. As for the descending boundary curves of poorly correlated networks, the great difference between the curves of networks and multiplexes can be entirely explained by percolating phenomenon. This phenomenon states that the position of the knee in the descending boundary curves is influenced by the value of the mean connectivity \bar{C} [54]. This is due to the almost random spatial distribution of sizes of bonds throughout each of the uncorrelated porous networks. Another consequence of this is the challenge in deducing the distribution of pore sizes among sites or bonds from the boundary desorption curves, given the concurrent occurrence of the classical pore blocking effect and the percolation phenomenon.

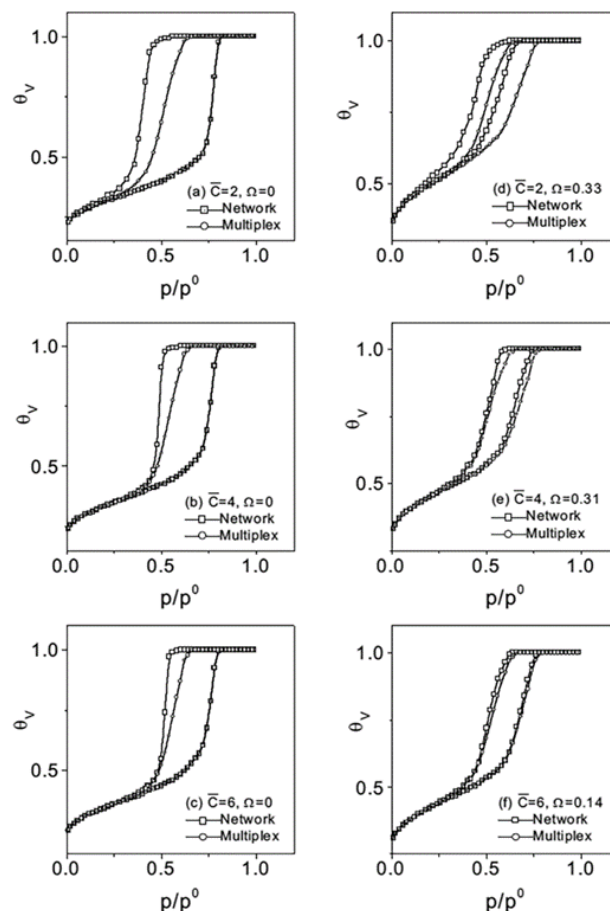


Fig. 16. Comparison of isotherms between porous networks and sorption curves obtained with multiplexes. Both structures possess the same pore-size distributions. Reproduced from [53] with permission from the Royal Society of Chemistry.

Adsorption and desorption in highly correlated porous networks

For highly correlated porous networks, the shapes of their loops are associated with hybrid types between the H1 and H3 classification (right columns of figures 12 and 13). To quantify the extent of cooperative effects during the course of the boundary curves, a comparison must be made with the isotherms of the independent domains (multiplexes) through Fig. 16 (right column). In this way, the cooperative effects due to the advancement of hemispherical meniscus through the ends of bonds increase as the mean connectivity, \bar{C} decreases. While it is almost absent for porous network with $\bar{C} = 6$ (check out the coincidence between the ascending boundary curves of the network and the one of the multiplexes; Fig. 16, bottom right column), it is very strong for the porous network with $\bar{C} = 2$ (note the strong divergence between the ascending boundary curves between the porous network and that one of multiplexes; Fig. 16, top right column). The observed phenomenon can be attributed to the significant correlation between the sizes within the porous network and the average value of \bar{C} , which is 2. This network comprises an array of elongated cylindrical capillaries, each featuring a variable cross-sectional area. The larger sections correspond to the sites, while the narrower sections

represent the bonds. These long capillaries are connected among them through the connection of sites with $\bar{C} > 3$, which act as manifold capillary distributors. Then, once a small enough bond (minimum of a cross-sectional area of a long capillary) fills independently with condensate, at its corresponding value of pressure, immediate condensation occurs in their two connected sites (given the similar size among them), which then triggers the advancement of the hemispherical meniscus throughout the whole structure of the long capillary. On the other hand, porous network with $\bar{C} = 6$ are composed of domains with sites with very similar sizes connected through bonds with also very similar sizes among them, but considerably smaller, due to the geometrical restriction, than those of the sites of the domain. This difference in size between R_B and R_S in each domain promotes the independent condensation of bonds and sites at each value of pressure during the course of the ascending boundary curve. Then for this porous network, the ascending boundary curve can be depicted as a succession of orderly of filling of independent domains according to the size of sites and bonds, from small pore domains at the beginning of the curve to large pore domains at the onset of the ascending boundary curve. The cooperative effects during the course of the ascending boundary curve for porous network with $\bar{C} = 4$ are intermediate between the cases for $\bar{C} = 2$ and $\bar{C} = 6$.

The boundary curves delineating highly correlated porous networks exhibit a less pronounced descent compared to those of uncorrelated structures. Additionally, the knees of these curves appear at higher pressure values when contrasted with an uncorrelated porous network possessing an equivalent mean connectivity. This phenomenon can be elucidated by examining percolation in correlated lattices. Research indicates that an increase in the correlation length leads to a lower percolation threshold. Essentially, as the degree of correlation intensifies, it becomes easier for a network to reach a state of percolation, facilitating the process at a quicker rate [55, 56]. Then, the boundary descent curves of each porous network differ from the corresponding multiplex. This mismatch is significantly greater in the case of $\bar{C} = 2$ (Fig. 16, top right column), while it is moderate for $\bar{C} = 4$ (Fig. 16, middle right column) and nearly non-existent for $\bar{C} = 6$ (Fig. 16, bottom right column). The strong correlation observed between the network and multiplexes' isotherms, particularly in highly interconnected porous networks with an average connectivity of 6, indicates that assuming an accurate meniscus geometry can yield precise calculations of pore size distribution. This is crucial for analyzing the ascending or descending parts of boundary curves. Such insights are essential for characterizing and analyzing porosity and pore structures [53].

Primary ascending and descending scanning curves

The primary ascending and descending scanning curves of the isotherms indicate the existence of pore domains that behave either independently or in a connected manner. [56]. In this analysis, the primary scanning curves of the weakly correlated networks, as shown in the left columns of Figs. 12 and 13, tend to approach the lower (for descending scanning curves) or upper (for ascending scanning curves) endpoints of the corresponding hysteresis loop. This convergence suggests the existence of interconnected pore domain behaviour, specifically the pore blocking phenomenon. This description is also relevant for a highly correlated porous network where the average mean connectivity is 2. The isotherms in the top right of Figs. 12 and 13 illustrate this, as they are influenced by significant cooperative effects during adsorption and pore blocking phenomena during desorption. In turn, when examining the primary ascending and descending scanning curves of highly correlated structures, it is intriguing to note that for structures with intermediate and low medium connectivity, these curves tend to converge towards the boundary curve within a narrow pressure range. This merging is clearly observed in isotherms e and f, as illustrated in Figs. 12 and 13. These figures suggest a nearly flat line ($\bar{C} = 6$) or a gently sloping curve ($\bar{C} = 4$) intersecting the corresponding boundary curves. It is significant to recognize that the specific patterns of the primary descending scanning curves in a highly correlated porous network, characterized

by an average connectivity of 2, provided a framework for the AAPS to conduct experimental studies on the cooperative phenomena observed in undulated SBA-15 materials. [57].

Conclusions

The Academic Area of Physicochemical Surfaces has significantly advanced the field by introducing the DSBM, a model that simplifies the understanding of porous materials' texture and their nitrogen sorption properties. Utilizing dual pore size distributions for sites and bonds, the DSBM aids in constructing a theoretical framework of porosity, connecting diverse porous structures. This model enables the analysis of porous topologies by examining the dimensions and interconnectivity of adjacent pore elements. Notably, the correlation length within the DSBM is crucial for identifying domains with similarly sized pores. As a tool, the DSBM is pivotal in deciphering complex patterns in sorption data, illuminating the spatial arrangement of pores and their connections within a solid matrix. This is achieved through qualitative examination of nitrogen adsorption curve shapes and their association with cooperative behaviors during adsorption and desorption processes. While fully characterizing a porous solid's texture from gas sorption remains elusive, the DSBM offers a comprehensive guide for interpreting experimental outcomes by qualitatively assessing the boundary curves and primary scanning curves.

Acknowledgements

A.L.T.G. acknowledges the financial support through the scholarship CONAHCyT (Grant No. 794571 and 64f687d78ec4c663f15b663c). V.M.T acknowledges the financial support provided by Conahcyt through the program "Convocatoria Ciencia Básica y de Frontera 2023-2024," grant number CBF2023-2024-2725.

References

1. Tovbin, Yu. K. *The Molecular Theory of Adsorption in Porous Solids*, 1st ed.; CRC Press, **2017**. DOI: <https://doi.org/10.1201/9781315116297>.
2. Ghanbari, T.; Abnisa, F.; Wan Daud, W. M. A. A Review on Production of Metal Organic Frameworks (MOF) for CO₂ Adsorption. *Science of The Total Environment* **2020**, *707*, 135090. DOI: <https://doi.org/10.1016/j.scitotenv.2019.135090>.
3. Verma, P.; Kuwahara, Y.; Mori, K.; Raja, R.; Yamashita, H. Functionalized Mesoporous SBA-15 Silica: Recent Trends and Catalytic Applications. *Nanoscale* **2020**, *12*, 11333–11363. DOI: <https://doi.org/10.1039/D0NR00732C>.
4. *Characterization of Porous Solids and Powders: Surface Area, Pore Size and Density*, [4. ed.], 1. repr. with some corr.; Lowell, S., Ed.; Particle technology series; Springer: Dordrecht, **2010**.
5. Brunauer, S.; Emmett, P. H.; Teller, E. Adsorption of Gases in Multimolecular Layers. *J. Am. Chem. Soc.* **1938**, *60*, 309–319. DOI: <https://doi.org/10.1021/ja01269a023>.
6. Naderi, M. Chapter Fourteen - Surface Area: Brunauer–Emmett–Teller (BET). In *Progress in Filtration and Separation*; Tarleton, S., Ed.; Academic Press: Oxford, **2015**; pp 585–608. DOI: <https://doi.org/10.1016/B978-0-12-384746-1.00014-8>.
7. Wu, J.; Li, Z. Density-Functional Theory for Complex Fluids. *Annu. Rev. Phys. Chem.* **2007**, *58*, 85–112. DOI: <https://doi.org/10.1146/annurev.physchem.58.032806.104650>.
8. Wu, J. Density Functional Theory for Chemical Engineering: From Capillarity to Soft Materials. *AIChE Journal* **2006**, *52*, 1169–1193. DOI: <https://doi.org/10.1002/aic.10713>.
9. Makkar, P.; Ghosh, N. N. A Review on the Use of DFT for the Prediction of the Properties of Nanomaterials. *RSC Adv.* **2021**, *11*, 27897–27924. DOI: <https://doi.org/10.1039/D1RA04876G>.

10. Gubbins, K. E.; Sliwinska-Bartkowiak, M.; Suh, S.-H. Molecular Simulations of Phase Transitions in Pores. *Molecular Simulation* **1996**, *17*, 333–367. DOI: <https://doi.org/10.1080/08927029608024116>.
11. Segura, C. J.; Vakarin, E. V.; Chapman, W. G.; Holovko, M. F. A Comparison of Density Functional and Integral Equation Theories vs Monte Carlo Simulations for Hard Sphere Associating Fluids near a Hard Wall. *The Journal of Chemical Physics* **1998**, *108*, 4837–4848. DOI: <https://doi.org/10.1063/1.475893>.
12. Zaragoza, A.; Gonzalez, M. A.; Joly, L.; López Montero, I.; Canales, M. A.; Benavides, A. L.; Valeriani, C. Molecular Dynamics Study of Nanoconfined TIP4P/2005 Water: How Confinement and Temperature Affect Diffusion and Viscosity. *Phys. Chem. Chem. Phys.* **2019**, *21*, 13653–13667. DOI: <https://doi.org/10.1039/C9CP02485A>.
13. Yuan, Z.; He, G.; Li, S. X.; Misra, R. P.; Strano, M. S.; Blankschtein, D. Gas Separations Using Nanoporous Atomically Thin Membranes: Recent Theoretical, Simulation, and Experimental Advances. *Advanced Materials* **2022**, *34*, 2201472. DOI: <https://doi.org/10.1002/adma.202201472>.
14. Yuan, Z.; Govind Rajan, A.; He, G.; Misra, R. P.; Strano, M. S.; Blankschtein, D. Predicting Gas Separation through Graphene Nanopore Ensembles with Realistic Pore Size Distributions. *ACS Nano* **2021**, *15*, 1727–1740. DOI: <https://doi.org/10.1021/acsnano.0c09420>.
15. Wang, Y.; Fan, Z.; Qian, P.; Ala-Nissila, T.; Caro, M. A. Structure and Pore Size Distribution in Nanoporous Carbon. *Chem. Mater.* **2022**, *34*, 617–628. DOI: <https://doi.org/10.1021/acs.chemmater.1c03279>.
16. Iftimie, R.; Minary, P.; Tuckerman, M. E. Ab Initio Molecular Dynamics: Concepts, Recent Developments, and Future Trends. *Proc. Natl. Acad. Sci. U.S.A.* **2005**, *102*, 6654–6659. DOI: <https://doi.org/10.1073/pnas.0500193102>.
17. Barrett, E. P.; Joyner, L. G.; Halenda, P. P. The Determination of Pore Volume and Area Distributions in Porous Substances. I. Computations from Nitrogen Isotherms. *J. Am. Chem. Soc.* **1951**, *73*, 373–380. DOI: <https://doi.org/10.1021/ja01145a126>.
18. Broekhoff, J. Studies on Pore Systems in Catalysts IX. Calculation of Pore Distributions from the Adsorption Branch of Nitrogen Sorption Isotherms in the Case of Open Cylindrical Pores A. Fundamental Equations. *Journal of Catalysis* **1967**, *9*, 8–14. DOI: [https://doi.org/10.1016/0021-9517\(67\)90174-1](https://doi.org/10.1016/0021-9517(67)90174-1).
19. Everett, D. H.; Haynes, J. M. Model Studies of Capillary Condensation. I. Cylindrical Pore Model with Zero Contact Angle. *Journal of Colloid and Interface Science* **1972**, *38*, 125–137. DOI: [https://doi.org/10.1016/0021-9797\(72\)90228-7](https://doi.org/10.1016/0021-9797(72)90228-7).
20. Feng, Q.; Xing, X.; Wang, S.; Liu, G.; Qin, Y.; Zhang, J. CO₂ Diffusion in Shale Oil Based on Molecular Simulation and Pore Network Model. *Fuel* **2024**, *359*, 130332. DOI: <https://doi.org/10.1016/j.fuel.2023.130332>.
21. García-Salaberry, P. A.; Zenyuk, I. V. A General Purpose Tool for Modeling Multifunctional Thin Porous Media (POREnet): From Pore Network to Effective Property Tensors. *Heliyon* **2024**, *10*, e26253. DOI: <https://doi.org/10.1016/j.heliyon.2024.e26253>.
22. Söllner, J.; Neimark, A.; Thommes, M. Development and Application of an Advanced Percolation Model for Pore Network Characterization by Physical Adsorption. July 23, **2024**. DOI: <https://doi.org/10.26434/chemrxiv-2024-h9zlm-v3>.
23. A Model of Adsorption-Desorption Hysteresis in Which Hysteresis Is Primarily Developed by the Interconnections in a Network of Pores. *Proc. R. Soc. Lond. A* **1983**, *390*, 47–72. DOI: <https://doi.org/10.1098/rspa.1983.0122>.
24. Determination of the Pore-Size Distributions and Pore-Space Interconnectivity of Vycor Porous Glass from Adsorption-Desorption Hysteresis Capillary Condensation Isotherms. *Proc. R. Soc. Lond. A* **1988**, *415*, 453–486. DOI: <https://doi.org/10.1098/rspa.1988.0023>.
25. Neimark, A. V. Percolation Theory of Capillary Hysteresis Phenomena and Its Application for Characterization of Porous Solids. In *Studies in Surface Science and Catalysis*; Elsevier, **1991**; Vol. 62, pp 67–74. DOI: [https://doi.org/10.1016/S0167-2991\(08\)61310-5](https://doi.org/10.1016/S0167-2991(08)61310-5).
26. Seaton, N. A. Determination of the Connectivity of Porous Solids from Nitrogen Sorption Measurements. *Chemical Engineering Science* **1991**, *46*, 1895–1909. DOI: [https://doi.org/10.1016/0009-2509\(91\)80151-N](https://doi.org/10.1016/0009-2509(91)80151-N).

27. Mayagoitia, V.; Javier Cruz, M.; Rojas, F. Mechanistic Studies of Capillary Processes in Porous Media. Part I.—Probabilistic Description of Porous Media. *J. Chem. Soc., Faraday Trans. 1* **1989**, 85, 2071. DOI: <https://doi.org/10.1039/f19898502071>.
28. Mayagoitia, V.; Rojas, F.; Kornhauser, I.; Pérez Aguilar, H. Modeling of Porous Media and Surface Structures: Their True Essence as Networks. *Langmuir* **1997**, 13, 1327–1331. DOI: <https://doi.org/10.1021/la950812m>.
29. Riccardo, J. L.; Steele, W. A.; Cuesta, A. J. R.; Zgrablich, G. Pure Monte Carlo Simulation of Model Heterogeneous Substrates: From Random Surfaces to Many-Site Correlations. *Langmuir* **1997**, 13, 1064–1072. DOI: <https://doi.org/10.1021/la9510036>.
30. Román-Alonso, G.; Rojas-González, F.; Aguilar Cornejo, M.; Cordero-Sánchez, S.; Castro-García, M. A. In-Silico Simulation of Porous Media: Conception and Development of a Greedy Algorithm. *Microporous and Mesoporous Materials* **2011**, 137, 18–31. DOI: <https://doi.org/10.1016/j.micromeso.2010.08.016>.
31. Riccardo, J. L.; Pereyra, V.; Zgrablich, G.; Rojas, F.; Mayagoitia, V.; Kornhauser, I. Characterization of Energetic Surface Heterogeneity by a Dual Site-Bond Model. *Langmuir* **1993**, 9, 2730–2736. DOI: <https://doi.org/10.1021/la00034a037>.
32. Metropolis, N.; Rosenbluth, A. W.; Rosenbluth, M. N.; Teller, A. H.; Teller, E. Equation of State Calculations by Fast Computing Machines. *The Journal of Chemical Physics* **1953**, 21, 1087–1092. <https://doi.org/10.1063/1.1699114>.
33. Bhanot, G. The Metropolis Algorithm. *Rep. Prog. Phys.* **1988**, 51, 429–457. DOI: <https://doi.org/10.1088/0034-4885/51/3/003>.
34. Cordero Sánchez, S. Simulación de redes porosas por métodos de Monte Carlo. Maestría en Ciencias, Universidad Autónoma Metropolitana, **1998**, p ht24wj79w. DOI: <https://doi.org/10.24275/uami.ht24wj79w>.
35. Sapag, K.; Bulnes, F.; Rizzotto, M.; Riccardo, J. L.; Zgrablich, G. On the Topology of Correlated Energies on Heterogeneous Surfaces. *J. Phys.: Condens. Matter* **1993**, 5, A241–A242. <https://doi.org/10.1088/0953-8984/5/33A/080>.
36. Cruz, O.; Hidalgo, R.; Alas, S.; Cordero, S.; Meraz, L.; Lopez, R.; Dominguez, A. Is the Alexander–Orbach Conjecture Suitable for Treating Diffusion in Correlated Percolation Clusters? *Adsorption Science & Technology* **2011**, 29, 663–676. DOI: <https://doi.org/10.1260/0263-6174.29.7.663>.
37. Tellez González, A. L. Estudio fractal de la reacción de oxidación de CO en Pt(100) por Monte Carlo. Maestría en Ciencias, Universidad Autónoma Metropolitana, Mexico City, **2022**.
38. Cordero-Sánchez, S.; Rojas-González, F.; Román-Alonso, G.; Castro-García, M. A.; Aguilar Cornejo, M.; Matadamas-Hernández, J. Pore Networks Subjected to Variable Connectivity and Geometrical Restrictions: A Simulation Employing a Multicore System. *Journal of Computational Science* **2016**, 16, 177–189. DOI: <https://doi.org/10.1016/j.jocs.2016.06.003>.
39. Paterson, L. Radial Fingering in a Hele Shaw Cell. *J. Fluid Mech.* **1981**, 113, 513. <https://doi.org/10.1017/S0022112081003613>.
40. Mayagoitia, V.; Rojas, F.; Kornhauser, I.; Zgrablich, G.; Faccio, R. J.; Gilot, B.; Guiglion, C. Refinements of the Twofold Description of Porous Media. *Langmuir* **1996**, 12, 211–216. DOI: <https://doi.org/10.1021/la940704k>.
41. Ramirez-Cuesta, A. J.; Cordero, S.; Rojas, F.; Faccio, R. J.; Riccardo, J. L. On Modeling, Simulation and Statistical Properties of Realistic Three Dimensional Porous Networks. *Journal of Porous Materials* **2001**, 8, 61–76. DOI: <https://doi.org/10.1023/A:1026526502692>.
42. Cordero, S.; Rojas, F.; Riccardo, J. L. Simulation of Three-Dimensional Porous Networks. *Colloids and Surfaces A: Physicochemical and Engineering Aspects* **2001**, 187–188, 425–438. [https://doi.org/10.1016/S0927-7757\(01\)00610-0](https://doi.org/10.1016/S0927-7757(01)00610-0).
43. Gonzalez Mendez, A.; Roman Alonso, G.; Rojas Gonzalez, F.; Castro Garcia, M. A.; Aguilar Cornejo, M.; Cordero Sanchez, S. Construction of Porous Networks Subjected to Geometric Restrictions by Using OpenMP. In 2014 IEEE International Parallel & Distributed Processing Symposium Workshops; IEEE: Phoenix, AZ, **2014**; pp 1189–1197. DOI: <https://doi.org/10.1109/IPDPSW.2014.134>.

44. Matadamas, J.; Roman, G.; Rojas, F.; Castro, M.; Cordero, S.; Aguilar, M. Pore Network Simulation via Monte Carlo Algorithms on GPUs. *IEEE Latin Am. Trans.* **2014**, *12*, 491–498. <https://doi.org/10.1109/TLA.2014.6827878>.
45. Matadamas-Hernández, J.; Román-Alonso, G.; Rojas-González, F.; Castro-García, M. A.; Boukerche, A.; Aguilar-Cornejo, M.; Cordero Sánchez, S. Parallel Simulation of Pore Networks Using Multicore CPUs. *IEEE Trans. Comput.* **2014**, *63*, 1513–1525. DOI: <https://doi.org/10.1109/TC.2012.197>.
46. Halsey, G. Physical Adsorption on Non-Uniform Surfaces. *The Journal of Chemical Physics* **1948**, *16*, 931–937. DOI: <https://doi.org/10.1063/1.1746689>.
47. Casanova, F.; Chiang, C. E.; Li, C.-P.; Schuller, I. K. Direct Observation of Cooperative Effects in Capillary Condensation: The Hysteretic Origin. *Applied Physics Letters* **2007**, *91*, 243103. <https://doi.org/10.1063/1.2822815>.
48. Sing, K. S. W. Reporting Physisorption Data for Gas/Solid Systems with Special Reference to the Determination of Surface Area and Porosity (Recommendations 1984). *Pure and Applied Chemistry* **1985**, *57*, 603–619. DOI: <https://doi.org/10.1351/pac198557040603>.
49. Gregg, S. J.; Sing, K. S. W.; Salzberg, H. W. Adsorption Surface Area and Porosity. *J. Electrochem. Soc.* **1967**, *114*, 279C. DOI: <https://doi.org/10.1149/1.2426447>.
50. Morishige, K. Hysteresis Critical Point of Nitrogen in Porous Glass: Occurrence of Sample Spanning Transition in Capillary Condensation. *Langmuir* **2009**, *25*, 6221–6226. DOI: <https://doi.org/10.1021/la900022s>.
51. Libby, B.; Monson, P. A. Adsorption/Desorption Hysteresis in Inkbottle Pores: A Density Functional Theory and Monte Carlo Simulation Study. *Langmuir* **2004**, *20*, 4289–4294. DOI: <https://doi.org/10.1021/la036100a>.
52. Ravikovitch, P. I.; Neimark, A. V. Density Functional Theory of Adsorption in Spherical Cavities and Pore Size Characterization of Templated Nanoporous Silicas with Cubic and Three-Dimensional Hexagonal Structures. *Langmuir* **2002**, *18*, 1550–1560. DOI: <https://doi.org/10.1021/la0107594>.
53. Rojas, F.; Kornhauser, I.; Felipe, C.; Esparza, J. M.; Cordero, S.; Domínguez, A.; Riccardo, J. L. Capillary Condensation in Heterogeneous Mesoporous Networks Consisting of Variable Connectivity and Pore-Size Correlation. *Phys. Chem. Chem. Phys.* **2002**, *4*, 2346–2355. <https://doi.org/10.1039/b108785a>.
54. Stauffer, D.; Aharony, A. Introduction To Percolation Theory, 0 ed.; Taylor & Francis, **2018**. <https://doi.org/10.1201/9781315274386>.
55. Hidalgo-Olguín, D. R.; Cruz-Vázquez, R. O.; Alas-Guardado, S. J.; Domínguez-Ortiz, A. Lacunarity of Classical Site Percolation Spanning Clusters Built on Correlated Square Lattices. *Transp Porous Med* **2015**, *107*, 717–729. DOI: <https://doi.org/10.1007/s11242-015-0463-3>.
56. Everett, D. H. A General Approach to Hysteresis. Part 3.—A Formal Treatment of the Independent Domain Model of Hysteresis. *Trans. Faraday Soc.* **1954**, *50*, 1077–1096. DOI: <https://doi.org/10.1039/tf9545001077>.
57. Esparza, J. M.; Ojeda, M. L.; Campero, A.; Domínguez, A.; Kornhauser, I.; Rojas, F.; Vidales, A. M.; López, R. H.; Zgrablich, G. N₂ Sorption Scanning Behavior of SBA-15 Porous Substrates.

Molecular Insights on Coffee Components as Chemical Antioxidants

Luis Felipe Hernández-Ayala¹, Eduardo Gabriel Guzmán-López^{1,2}, Adriana Pérez-González¹, Miguel Reina², Annia Galano^{1*}

¹Departamento de Química, Universidad Autónoma Metropolitana-Iztapalapa, Av. Ferrocarril San Rafael Atlixco 186, Col. Leyes de Reforma 1A Sección, Alcaldía Iztapalapa, Mexico City 09310, México.

²Departamento de Química Inorgánica y Nuclear, Facultad de Química, Universidad Nacional Autónoma de México, Mexico City 04510, México.

*Corresponding author: Annia Galano, email: agal@xanum.uam.mx

Received March 14th, 2024; Accepted May 24th, 2024.

DOI: <http://dx.doi.org/10.29356/jmcs.v68i4.2238>

Abstract. Coffee is not only a delicious beverage but also an important dietary source of natural antioxidants. We live in a world where it is impossible to avoid pollution, stress, food additives, radiation, and other sources of oxidants that eventually lead to severe health disorders. Fortunately, there are chemicals in our diet that counteract the hazards posed by the reactive species that trigger oxidative stress. They are usually referred to as antioxidants; some of them can be versatile compounds that exert such a role in many ways. This review summarizes, from a chemical point of view, the antioxidant effects of relevant molecules found in coffee. Their mechanisms of action, trends in activity, and the influence of media and pH in aqueous solutions, are analyzed. Structure-activity relationships are discussed, and the protective roles of these compounds are examined. A particular section is devoted to derivatives of some coffee components, and another one to their bioactivity. The data used in the analysis come from theoretical and computational protocols, which have been proven to be very useful in this context. Hopefully, the information provided here will promote further investigations into the amazing chemistry contained in our morning coffee cup.

Keywords: Free radicals; scavengers; reaction mechanisms; kinetics; trends in activity; coffee components.

Resumen. El café no solo es una bebida deliciosa, sino también una importante fuente dietética de antioxidantes naturales. Vivimos en un mundo donde es imposible evitar la contaminación, el estrés, los aditivos alimentarios, la radiación y otras fuentes de oxidantes que eventualmente conducen a trastornos de salud graves. Afortunadamente, existen sustancias químicas en nuestra dieta que contrarrestan los peligros planteados por las especies reactivas que desencadenan el estrés oxidativo. Por lo general, se les denomina antioxidantes; algunos de ellos pueden ser compuestos versátiles que ejercen dicho papel de muchas maneras. Este artículo de revisión resume, desde un punto de vista químico, los efectos antioxidantes de moléculas relevantes encontradas en el café. Se analizan sus mecanismos de acción, tendencias en la actividad y la influencia del medio y el pH en soluciones acuosas. Se discuten las relaciones estructura-actividad, y se examinan los roles protectores de estos compuestos. Se dedica una sección particular a los derivados de algunos componentes del café, y otra a su bioactividad. Los datos utilizados en el análisis provienen de protocolos teóricos y computacionales, que han demostrado ser muy útiles en este contexto. Se espera que la información proporcionada aquí promueva investigaciones futuras sobre la química contenida en nuestra taza de café matutina.

Palabras clave: Radicales libres; depuradores; mecanismos de reacción; cinética; tendencias de actividad; componentes del café.

Introduction

Since ancient times, natural products have been widely appreciated by humankind. The main reason is that they are beneficial for health issues and our general well-being. However, only in the last centuries technology and science developments have allowed to pass empiricism and deepened into the knowledge about the bioactive substances found in natural products, as well as on their specific functions and medicinal effects.

Regarding coffee, its origin has been traced to Ethiopia,[1] currently the fifth producer worldwide.[2] The legend says that goat herders noticed their animals restless at night after eating the berries of the coffee plant. After trying the fruit, they felt energized and became accustomed to consuming it. Such a stimulating effect is still one of this beverage's appeals, albeit coffee is much better understood and more widely consumed today than twelve centuries ago. In fact, coffee currently ranks as one of the most consumed beverages and stands as the second commodity worldwide.[3]

According to the annual review (2021/23) of the International Coffee Organization, the Arabica variety represents 57 % of the coffee production, and Robusta the other 43 % (Fig. 1). The top producers are Brazil, Vietnam and Colombia, in that order, with approximately 61, 32 and 12 billion bags of 60 kg, respectively. On the other hand, the leading consumers are the USA, Brazil, Germany, Japan and France (27, 22, 8.7, 7.2 and 6.2 billion bags of 60 kg, respectively).

Based on the data obtained from the Scopus database (Fig. 2), the number of scientific publications on coffee has grown exponentially over the years. The same trend is followed by its antioxidant properties. Today, many of the chemical components of coffee have been identified and a large proportion of them have been investigated. For example, there are 68,971 reports on caffeine, 2,641 of them published last year. The oldest record found in the search for antioxidative properties of coffee dates back to 1940.[4] It dealt with the “antioxygens” produced by roasting and considered several species. Among them, pyrrole, proline, thioglycolic acid, and caffeic acid were identified as those with the highest protection factor against rancidity.

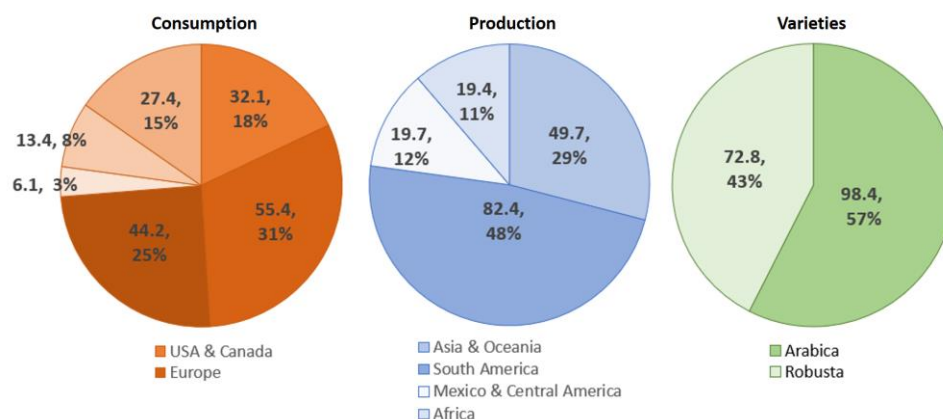


Fig. 1. Coffee production and consumption stats (in million bags of 60 kg), according to the annual review (2022/23) of the International Coffee Organization. <https://www.icocoffee.org/documents/cy2023-24/cmr-0224-e.pdf>, accessed March 7, 2023.

Antioxidants are inherently appealing substances, both from scientific and pragmatic points of view. They help counteracting the dangerous effects of oxidative stress (OS), which arises from the imbalance between production and consumption of oxidants in living systems. OS is considered a chemical stress and has been associated with multiple health issues, including neurodegeneration, [5-16] cancer,[17-28] cardiovascular diseases,[29-38] diabetes,[39-46] rheumatoid arthritis,[47-51] renal [52-60] and pulmonary[61-66] failures, ocular disorders,[67-72] preeclampsia and fetal development complications.[73-77]

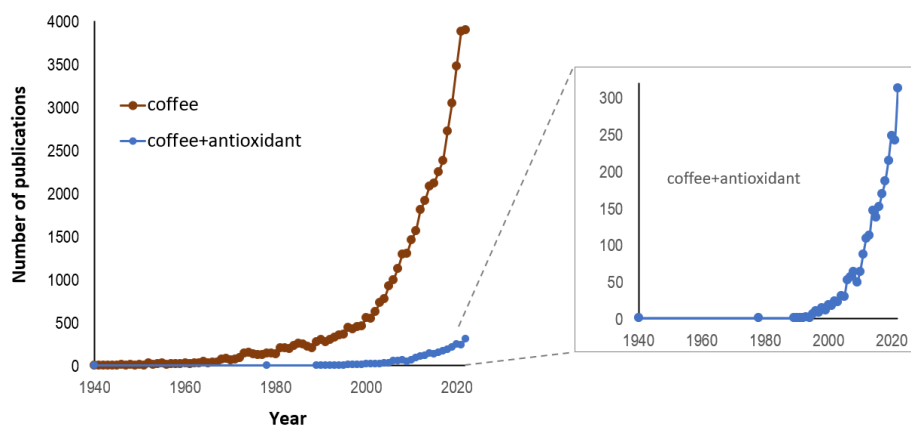


Fig. 2. Number of published researches on coffee and coffee + antioxidant, according to Scopus, consulted on March 7, 2024.

Antioxidant protection is one of the many health benefits attributed to coffee, [78-99] and other natural products. However, not all its components exhibit such activity, and those that do, have diverse mechanisms of action and efficiency. Phenolic compounds, in general, are recognized as highly efficient for counteracting the deleterious effects of OS. Phenolic acids, in particular, are among the most potent antioxidants present in coffee.[100-106] Other components identified as efficient antioxidants include melanoidins,[107-110] heterocycles[111,112] Maillard reaction products,[100,112-114] and some volatile compounds.[111,112,115-119] Regarding caffeine, some studies suggest that it acts as an antioxidant, [110,120] while others indicate that the antioxidant properties of coffee are not directly related to caffeine but to the presence of other components.[121-123]

Quantifying antioxidant activity is a challenging task. This is probably because there is no universal assays to do it,[124] and because the available ones depend on the reaction mechanism, which can vary from one antioxidant to another. In fact, they have been classified as electron transfer and hydrogen atom transfer-based assays. In addition, some of these assays are meant to estimate the antioxidant capacity of total phenols lacking the specificity to differentiate among various phenolic compounds. Complicating matters further, conflicting trends may be obtained when different experimental techniques are employed to evaluate the antioxidant activity of phytochemicals.[125]

When using theoretical and computational chemistry, other difficulties arise. Probably, the most important ones are: (i) the unavoidable use of simplified models for mimicking chemical environments; (ii) the necessary balance between accuracy and computing time that must be taken into account when a particular level of theory is chosen; (iii) the fact that for establishing reliable trends, calculations must be performed using the same methodology and approximations; (iv) the importance of considering all the possible mechanisms and sites of reaction.[126] Therefore, it becomes evident that assessing antioxidant activity is a complex task, regardless of if it is pursued using experimental or theoretical approaches.

Previous publications, where experimental techniques were used to evaluate the antioxidant activity of coffee and its components *in vitro*, have been reviewed thoroughly. [78,127] Therefore, molecular insights on such activity are the main focus of the analyses and discussion here. The data used to do that derived from computational and theoretical strategies, that have been demonstrated to be useful and reliable to study the antioxidant chemistry. Several aspects are considered, including structure-activity relationships, the influence of solvent and pH, reaction mechanisms, and the influence of redox metals. Trends in antioxidant activity are proposed for several coffee components and compared with Trolox as a reference. The reviewed data is expected to contribute to enhance the current knowledge on the chemical aspects related to the antioxidant effects of coffee, thereby promoting further investigations into the chemistry of this beverage.

Chemical overview

Chemical components are responsible for the taste, aroma and bioactivities of coffee. However, its chemical composition is complex and depends on the variety, growing conditions, and processing.[128] Nevertheless, it has been reported that the main components of raw coffee beans include carbohydrates, which account for about 60 % of their total weight. [129] They also have significant amounts of cellulose, grease, proteins, amino acids, tannic acid, and starch. In addition, there is a diversity of other minor and trace substances in coffee beans. There are numerous publications providing detailed information on the chemical composition of coffee. [129-133] A brief summary of this composition is provided in Table 1.

Table 1. Chemical compounds present in coffee beans.

Family	Compounds	Ref.
Alkaloids	Caffeine, Theobromine, Theophylline, Trigonelline.	[134-139]
Amino acids	Alanine, Arginine, Asparagine, Aspartic acid, Cysteine, Glutamate, Glutamine, Glycine, Histidine, Isoleucine, Leucine, Lysine, Phenylalanine, Proline, Serine, Threonine, Tryptophan, Tyrosine, Valine.	[140-144]
Carotenoids	α -Carotene, β -Carotene, Antheraxanthin, Lutein, Neoxanthin, Violaxanthin, Zeaxanthin.	[135,145, 146]
Fatty acids	Arachidic, Docosanoic, Eicosanoic, Lauric, Linoleic, Linolenic, Myristic, Oleic, Palmitic, Stearic, Tetracosanoic, Tricosanoic Acids.	[141,142, 144,147]
Flavonoids	Apigenin, Catechin, Delphinidin, Epicatechin, Epicatechin Gallate, Fisetin, Hyperoside, Isoquercitrin, Kaempferol, Luteolin, Myricetin, Patuletin, Quercetin, Quercitrin, Rutin.	[135,145]
Organic acids	Acetic, Butyric, Citric, Formic, Lactic, Malic, Oxalic, Quinic, Succinic, Tartaric Acids.	[136,144, 145,148-150]
Phenolic acids	3-OH-Benzoic, Benzoic, Caffeic, Caftaric, Chlorogenic, Cinnamic, Dicafeoylquinic, Dihydrocaffeic, Ferulic, Gallic, Gentisic, p-Coumaric, p-Hydroxybenzoic, Protocatechuic, Sinapic, Syringic, Vanillic Acids and Caffeic Phenylester.	[129,135-137,139,145,149, 151-155]
Sugars	Arabinose, Fructose, Glucose, Saccharose, Sucrose.	[135,139, 150,154,156,157]
Terpenes	16-O-Methylcafestol, Atractyligenin, Cafestol, Caffarolides, Caffruones, Cofarysloside, Ent-kaurane Diterpenoid, Kahweol, Mascarosides, Paniculoside, Triterpenoids, Tricalysiolides, Ursolic Acid, Villanovane.	[135,158-164]
Volatiles	Alcohols, Alkanes, Aldehydes, Carboxylic acids, Esters, Fatty acids, Furans, Ketones, Lactones, Oxazols, Pyrazines, Pyrimidines, Pyrroles, Terpenes, Thiazoles, Thiophenes, 4-Ethylguaiaicol, 4-Vinylguaiaicol, Caffeol, Eugenol, Furfural, Furaneol, Guaiacol, Phenol.	[135,139, 144,148,153,165-170]
Xanthone	Isomangiferin, Mangiferin	[135,143]
Phytosterol	Sitosterol	[135]

Bioactivity overview

The versatile bioactivity of coffee has also been thoroughly reviewed. [171-176] Coffee has numerous health benefits from its chemical composition, provided that it is moderately consumed. Some of them are summarized in Table 2. However, as is the case with almost everything, amounts mediate the balance between benefits and harms. It has been pointed out that high consumption of coffee may compromise coronary health, posing risks for pregnant and postmenopausal women, and has the potential for addiction, where withdrawal could trigger muscle fatigue and related problems. [171]

Table 2. Some health benefits of coffee components.

Benefits	Key components	Ref.
Antibacterial	caffeic acid caffeic acid phenethyl ester chlorogenic acids eugenol ferulic acid furanol guaiacol isoeugenol protocatechuic acid scopoletin vanillic acid	[177-179] [155, 180] [181] [182-190] [191-194] [195] [196-198] [190, 199-202] [203-208] [209-214] [204, 215, 216]
Anticarcinogenic	4-vinylguaiacol cafestol and kahweol caffeic acid caffeic acid phenethyl ester chlorogenic acids eugenol ferulic acid quercetin mangiferin protocatechuic acid tannic acid theobromine vanillic acid vanillin	[217, 218] [219-222] [223-228] [229-233] [181, 234] [235-251] [252-266] [267-271] [272] [273-279] [280-289] [290-292] [293-297] [298-306]
Antidiabetic	cafestol caffeic acid caffeol chlorogenic acids isoeugenol scopoletin trigonelline	[307, 308] [309-313] [129, 314] [309, 315-320] [321] [322-326] [327]
Antifungal	caffeine eugenol furanol isoeugenol vanillin	[328] [329-334] [195] [335-338] [339-341]

Benefits	Key components	Ref.
Anti-inflammatory effects	4-ethylguaiacol caffeine dicafeoylquinic acids dihydrocaffeic acid eugenol ferulic acid flavonoids mangiferin phenolic acids and pyrocatechol p-coumaric acid rutin theophylline vanillic acid vanillin vanillyl alcohol	[342-344] [345] [346] [347] [182, 348-353] [354, 355] [272] [346] [272] [356] [357-362] [346] [363-367] [368-375] [376-382] [383]
Anti-obesity	chlorogenic acids kahweol	[315, 384-387] [388-390]
Cardioprotection	caffeic acid chlorogenic acids dihydrocaffeic acid ferulic acid	[391-395] [234, 396-399] [400] [401-407]
Cognitive enhancement	paraxanthine protocatechuic acid theobromine vanillic acid	[408, 409] [410-413] [414, 415] [416, 417]
Gastroprotection	chlorogenic acids vanillin	[234] [418, 419]
Hepatoprotection	caffeic acid chlorogenic acids dihydrocaffeic acid paraxanthine theobromine vanillin	[420-423] [234] [424] [425-427] [428] [429-432]
Immunoregulation	p-coumaric acid protocatechuic acid	[361] [433, 434]
Kidney protection	protocatechuic acid theobromine	[435-439] [440-443]
Neuroprotection	caffeine caffeic acid chlorogenic acids dihydrocaffeic acid eugenol ferulic acid isoeugenol paraxanthine	[444-465] [129, 466-468] [129, 469-478] [479] [480] [481-491] [480, 492] [460, 493-496]

	protocatechuic acid quercetin scopoletin tannic acid theobromine trigonelline vanillin vanillic acid vanillyl alcohol	[497-510] [267, 511-520] [521-526] [527-532] [533-535] [129] [379, 536-540] [541-544] [545]
Lipid-Lowering Effects	caffeic acid chlorogenic acids	[546] [234, 314, 546, 547]

Based on the data reported in Table 2, it becomes evident that moderate consumption of coffee, i.e., one to four cups a day,[176] may provide beneficial effects. In particular, for inflammation, obesity, diabetes, cancer, cardiovascular diseases, microbial infections, and neurodegeneration. It seems worthwhile noticing that the health benefits mentioned in Table 2 are not necessarily attributed to antioxidant activity. In fact, many of them involve direct interaction with enzymes and other biotargets. Antioxidant activity is not included in this table because it is the main focus of this review, thus a whole section has been entirely devoted to it (section 5).

Derivatives

Considering the myriad of benefits offered by coffee components, it is not surprising that many investigations have been devoted to design and synthesize derivatives based on their molecular frameworks. Many of them keep the bioactivity of the parent molecules, and many others have shown new and improved effects. Albeit a detailed analysis of this point escapes the purpose of this review, it seems worthwhile summarizing (Table 3) some of the great efforts made so far to obtain new molecules from coffee components. Thus, the interested reader can get more comprehensive information on this topic from the provided references.

Table 3. Some previous studies on derivatives based on antioxidants found in coffee.

Parent molecule	Ref.
caffeic acid	[395, 548-559]
caffeine	[560-568]
chlorogenic acid	[569-576]
eugenol	[577-596]
ferulic acid	[252, 254, 597-629]
guaiacol	[630-632]
isoeugenol	[337, 633-636]
isoferulic acid	[637, 638]
p-coumaric acid	[359, 639-645]
protocatechuic acid	[646-652]

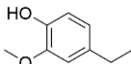
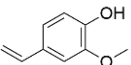
Parent molecule	Ref.
scopoletin	[326, 653-664]
theobromine	[665-673]
theophylline	[674-695]
vanillic acid	[696-702]
vanillin	[703-729]
xanthine	[730-753]

Theoretical and computational chemistry plays an important role in the design of new compounds. There are numerous tools available that allow evaluating important properties of derivatives, particularly when they are meant to be used as medical drugs. Some useful descriptors in this context are those known as ADME (Absorption, Distribution, Metabolism y Excretion) properties. They comprise the octanol/water partition coefficient (logP), molecular weight, number of H bond donors, number of H bond acceptors, molar refractivity, number of non-hydrogen atoms, and polar surface area. There are other important properties to consider such as synthetic accessibility and toxicity. Using computational strategies allows building candidates, sampling the chemical space and evaluating the potential of the new molecules for the intended purpose. In addition, these strategies save time, resources, and even animal testing. Thus, they have become relevant tools for the development of new formulations with health benefits.

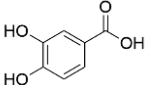
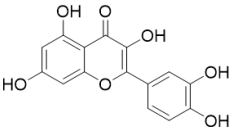
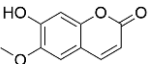
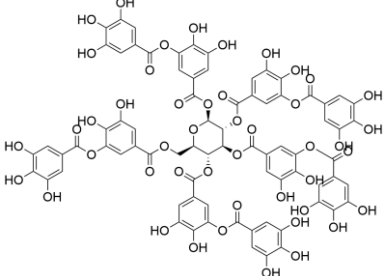
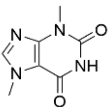
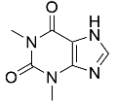
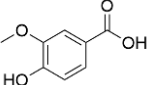
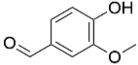
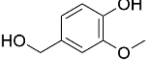
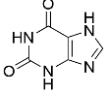
Antioxidant activity

Theoretical and computational chemistry plays an important role in the design of new compounds. There are numerous tools available that allow evaluating important properties of derivatives, particularly when they are meant to be used as medical drugs. Some useful descriptors in this context are those known as ADME (Absorption, Distribution, Metabolism y Excretion) properties. They comprise the octanol/water partition coefficient (logP), molecular weight, number of H bond donors, number of H bond acceptors, molar refractivity, number of non-hydrogen atoms, and polar surface area. There are other important properties to consider such as synthetic accessibility and toxicity. Using computational strategies allows building candidates, sampling the chemical space and evaluating the potential of the new molecules for the intended purpose. In addition, these strategies save time, resources, and even animal testing. Thus, they have become relevant tools for the development of new formulations with health benefits.

Table 4. Some antioxidants found in coffee.

Common name	Structure	IUPAC name	Ref.
4-ethylguaiacol		4-ethyl-2-methoxyphenol	[754-756]
4-vinylguaiacol		4-ethenyl-2-methoxyphenol	[757-759]

Common name	Structure	IUPAC name	Ref.
caffeic acid		(E)-3-(3,4-dihydroxyphenyl)prop-2-enoic acid	[312,391,760-772]
caffeine		1,3,7-trimethylpurine-2,6-dione	[450,773-776]
chlorogenic acid		(1S,3R,4R,5R)-3-[(E)-3-(3,4-dihydroxyphenyl)prop-2-enoyl]oxy-1,4,5-trihydroxycyclohexane-1-carboxylic acid	[96,391,760,777-788]
dihydrocaffeic acid		3-(3,4-dihydroxyphenyl)propanoic acid	[789-791]
eugenol		2-methoxy-4-prop-2-enylphenol	[349,350,578,792-805]
ferulic acid		(E)-3-(4-hydroxy-3-methoxyphenyl)prop-2-enoic acid	[354,355,481,758,806-813]
guaiacol		2-methoxyphenol	[814,815]
isoeugenol		2-methoxy-4-[(E)-prop-1-enyl]phenol	[190,202,816]
isoferulic acid		(E)-3-(3-hydroxy-4-methoxyphenyl)prop-2-enoic acid	[817-820]
mangiferin		1,3,6,7-tetrahydroxy-2-[(2S,3R,4R,5S,6R)-3,4,5-trihydroxy-6-(hydroxymethyl)oxan-2-yl]xanthen-9-one	[821]
paraxanthine		1,7-dimethyl-3H-purine-2,6-dione	[822]
p-coumaric acid		(E)-3-(4-hydroxyphenyl)prop-2-enoic acid	[357,766,823-827]

Common name	Structure	IUPAC name	Ref.
protocatechuic acid		3,4-dihydroxybenzoic acid	[204,828-841]
quercetin		2-(3,4-dihydroxyphenyl)-3,5,7-trihydroxychromen-4-one	[842]
scopoletin		7-hydroxy-6-methoxychromen-2-one	[843-848]
tannic acid		[2,3-dihydroxy-5-[[[(2R,3R,4S,5R,6S)-3,4,5,6-tetrakis[[3,4-dihydroxy-5-(3,4,5-trihydroxybenzoyl)oxybenzoyl]oxy]oxan-2-yl]methoxycarbonyl]phenyl]]3,4,5-trihydroxybenzoate	[849-859]
theobromine		3,7-dimethylpurine-2,6-dione	[860,861]
theophylline		1,3-dimethyl-7H-purine-2,6-dione	[861-863]
vanillic acid		4-hydroxy-3-methoxybenzoic acid	[864-868]
vanillin		4-hydroxy-3-methoxybenzaldehyde	[432,756,865,869-873]
vanillyl alcohol		4-(hydroxymethyl)-2-methoxyphenol	[874,875]
xanthine		3,7-dihydropurine-2,6-dione	[822,860]

Antioxidant activity (AOx) can arise from a variety of processes. This review focuses on chemical ones, albeit there are other protection routes that involve enzymatic systems. From a chemical point of view, AOx can be roughly grouped into the following categories.

AOX-I (or primary AOX, or chain braking, or free radical scavenging activity).

It involves the direct reaction with oxidants, mainly free radicals yielding less reactive species or ending the radical chain process. During such a process, the antioxidant acts as a sacrificial target that prevents the oxidation of crucial biomolecules, such as DNA, proteins, and lipids. However, the amounts of these biomolecules in living organisms are significantly higher than those of chemical antioxidants that might be consumed in the diet or as dietary supplements. Consequently, to be efficient as a primary antioxidant, a molecule must react with oxidants faster than the biological target. This makes imperative to establish some quantitative thresholds that allow identifying a particular chemical as a primary antioxidant. The rate constants of the $\cdot\text{OOH}$ damage to polyunsaturated fatty acids have been proposed to that purpose.[126] It ranges from 1.18×10^3 to $3.05 \times 10^3 \text{ M}^{-1}\text{s}^{-1}$, [876] at acid pH values, i.e. when the molar fraction of HOO^\cdot is ~ 1 . Since lipids are the most easily oxidized among the biomolecules mentioned above, i.e., those reacting the fastest with free radicals, it is expected that any molecule capable of protecting them from oxidation would also be capable of protecting proteins and DNA.

Important points arise from this analysis. The first one is that kinetics is a key aspect when evaluating free radical scavenging activity. In addition, it is also important to consider the nature of the free radical. $\cdot\text{OH}$ is so reactive that it would react with almost any molecule, usually at diffusion-limited rates. In fact, it might be assumed that $\cdot\text{OH}$ will react with the first molecule it finds near its production site. It has been known for over a decade that peroxy radicals are among the oxidants likely to be efficiently scavenged to counteract oxidative stress.[877-880] Thus they are a logical counterpart of chemicals when analyzing AOX-I. This kind of AOX, will be further discussed in the sections 5.1 to 5.3. The other categories are briefly summarized next.

AOX-II (or secondary AOX, or preventing, or OIL behavior).

It may involve diverse chemical routes besides direct free radical scavenging processes. Among them, probably the most relevant one is usually referred to as OH-inactivating ligands (OIL) behavior.[881,882] It involves metal chelation and may occur by sequestering metal ions from reductants or by deactivating OH radicals as soon as they are produced via Fenton-like, or Haber-Weiss recombination, processes. The metal chelation step can take place, at least, through two pathways. Namely, by the direct chelation mechanism (DCM) or by the coupled deprotonation-chelation mechanism (CDCM). The latter may become the most important one for antioxidants acid protons.

AOX-III (or tertiary AOX, or fixing AOX, or repairing AOX).

Preventing biomolecules from oxidative damage is not always possible. Therefore, repairing them after damage is an important way of preserving their chemical integrity. The routes involved in such a process depend on the nature of the damage. Formal hydrogen atom transfer (f-HAT) restores allylic hydrogens to lipids. The same mechanism is involved when the most frequent lesions on Cys, Tyr, Leu, Met, and His are fixed, while single electron transfer (SET) repairs oxidized Tyr and Trp. DNA damage, on the other hand, may occur in at least three different ways, and, logically, the repairing route depends on the kind of damage. One electron loss from guanine, the nucleobase most easily oxidizable, [883] is repaired by SET from the antioxidant. One H loss from the deoxyribose units, yielding C-centered radicals; [884-887] is repaired by f-HAT from the antioxidant. Particular attention deserves the formation of the 8-OH-dG adduct by addition of an OH radical, which in turn yields the most abundant DNA lesion, i.e., 8-oxo-7,8-dihydro-2'-deoxyguanosine. [888]. The latter is considered a biomarker of oxidative stress, [1243,1244] and it has been proposed that such a damage can be fixed via sequential hydrogen atom transfer followed by dehydration (SHATD). [889]

AOX-IV (or versatile AOX, or multifunctional AOX, or multipurpose AOX).

This would apply to molecules capable of exerting their antioxidant activity through two or more of the above-described mechanisms, or by one of them and triggering enzymatic AOX.

AOX-I chemical routes

Free radical scavenging processes in living organisms occur in complex chemical environments. Numerous species are present in biological media, which may influence or be involved in competing reactions. In addition, antioxidants' reactivity depends on their chemical nature and may be modulated by the polarity of the environment and pH. Some of the most common chemical routes that may contribute to the observable AOX-I activity are detailed in Table 5.

Table 5. Some of the most common chemical routes that may contribute to the observable AOX-I activity (H_n Antiox and $\cdot R$ represent the antioxidant and the free radical, respectively).

Single Step Mechanisms	
<p><i>Radical Adduct Formation (RAF)</i></p> <p>$H_n\text{Antiox} + \cdot R \rightarrow [H_n\text{Antiox-R}]^*$</p> <p>Relevant for antioxidants with multiple bonds and electrophilic free radicals. Viable in polar and non polar media.</p>	<p><i>Examples:</i></p> <p>Carotenoids + $\cdot\text{OOH}$, [890] or benzylperoxyl [891] or alkyl, alkoxy, and alkylperoxyl radicals. [892]</p> <p>$\cdot\text{OH}$ scavenging activity of caffeine, [123] gentisic acid, [893] hydroxybenzyl alcohols, [894] edaravone, [895,896] melatonin, [897] and its metabolites, [898,899] carnosine, [900] and rebamipide. [901]</p>
<p><i>Single Electron Transfer (SET)</i></p> <p>$H_n\text{Antiox} + \cdot R \rightarrow H_n\text{Antiox}^{+\bullet} + R^-$</p> <p>Relevant for electrophilic free radicals and antioxidants that are good electron donors. Viable in polar media.</p>	<p><i>Examples:</i></p> <p>For antioxidants curcumin, [902] and highly galloylated tannin fractions. [903]</p> <p>Edaravone derivatives + $\cdot\text{OH}$, $\cdot\text{OCCl}_3$ and $\text{CH}_3\text{COO}\cdot$. [904]</p> <p>Resveratrol with oxygen radical. [905]</p> <p>Catechin analogues with $\text{ROO}\cdot$. [906]</p> <p>Carotenoids with $\text{CCl}_3\text{OO}\cdot$ [907,908] and $\cdot\text{NO}_2$ [909,910].</p>
<p><i>Formal Hydrogen Atom Transfer (f-HAT)</i></p> <p>$H_n\text{Antiox} + \cdot R \rightarrow H_{n-1}\text{Antiox}^* + \text{HR}$</p> <p>Relevant for antioxidants with labile H atoms. Viable in polar and non-polar media.</p>	<p><i>Examples:</i></p> <p>Polyphenols, [911] chlorogenic acids, [912] procyanidins, [913] chalcones, [914] cynarine, [912] orientin, [915] capsaicin, [916] silybin, [912] α-mangostin, [917] fisetin, [918] hydroxychalcones, [919] baicalein, [918] ellagic acid, [920]</p> <p>Lipoic acids, [921] glutathione, [922] tryptophan, [923], N-acetylcystein amide. [924]</p>
Multiple Step Mechanisms	
<p><i>Sequential Proton Loss Electron Transfer (SPLET)</i></p> <p>$H_n\text{Antiox} \rightarrow H_{n-1}\text{Antiox}^- + \text{H}^+$</p> <p>$H_{n-1}\text{Antiox}^- + \cdot R \rightarrow H_{n-1}\text{Antiox}^* + R^-$</p> <p>Relevant for antioxidants with acid protons. Viable in polar and protic solvents.</p>	<p><i>Examples:</i></p> <p>Curcumin, [925, 926] esculetin, [927] alizarin, [928] deoxybenzoins, [929] hydroxybenzoic acids, [930-933] resveratrol, [934, 935] fraxetin, [936] piceatannol, [937] morin, [938] hydroxychalcones, [939-941] xanthenes, [942] flavonoids, [943] quercetin, [944] kaempferol, [945] gallic acid, [946] Trolox, [947] isoflavonoids, [948,949] baicalein, [950] purpurin. [951]</p>

Multiple Step Mechanisms	
<p><i>Sequential Electron Proton Transfer (SEPT)</i></p> $H_n\text{Antiox} + \cdot\text{R} \rightarrow H_{n-1}\text{Antiox}^{+\cdot} + \text{R}^-$ $H_{n-1}\text{Antiox}^{+\cdot} \rightarrow H_{n-1}\text{Antiox}^{\cdot} + \text{H}^+$ <p>Relevant for antioxidants that are good electron donors. Viable in polar and protic solvents.</p>	<p><i>Examples:</i> Baicalein, [952] astaxanthin, [953] quercetin, in the presence of bases that have HOMO energies lower than that of the SOMO of its radical cation.[954] DPPH and galvinoxyl radical scavenging activity of vitamin E models. [955] The theroxyl radical-scavenging process of α-tocopherol.[956]</p>
<p><i>Sequential Proton Loss Hydrogen Atom Transfer (SPLHAT)</i></p> $H_n\text{Antiox} \rightarrow H_{n-1}\text{Antiox}^- + \text{H}^+$ $H_{n-1}\text{Antiox}^- + \cdot\text{R} \rightarrow H_{n-2}\text{Antiox}^{\cdot-} + \text{HR}$ <p>Relevant for antioxidants with acid protons and labile H atoms. Viable in polar and protic solvents.</p>	<p><i>Examples:</i> α-mangostin, [917] ellagic acid, [957] propyl gallate, [958] caffeic and other phenolic acids. [959] Esculetin + $\cdot\text{OOCH}_3$ and $\cdot\text{OOCHCH}_2$ radicals. [927] Gallic acid + $\cdot\text{OH}$. [960]</p>

Trends in activity

As previously mentioned, kinetics is crucial to assess free radical scavenging activity. Therefore, this analysis will be based on rate constants. However, for trends to be fair, it is essential to consider reactions with the same radical and that the rate constants (k) are estimated with the same methodology, and under the same conditions. Those reported in Table 6 correspond to reactions between coffee components and the HOO^\bullet radical, in non-polar media that mimic lipid environments. Those reported in Table 7 correspond to the same reactions but in aqueous solution, at physiological pH, i.e., pH=7.4. To facilitate comparisons, their $\log(k)$ values have been plotted in Fig. 3. Trolox has been included as a referent antioxidant. The main metabolites of caffeine are also included in the analyses.

Table 6. Overall, or apparent, rate constants (k) of the reactions between coffee components (and Trolox as reference) and HOO^\bullet , in non-polar environments.

Component	k ($\text{M}^{-1} \text{s}^{-1}$, at 298 K)	Ref.
caffeic acid	3.93E+04	[101]
caffeine	3.19E+01	[123]
dihydrocaffeic acid	4.95E+04	[101]
eugenol	2.49E+03	[961]
ferulic acid	9.13E+03	[101]
guaiacol	1.55E+03	[961]
mangiferin	7.74E+03	[101]

Component	k (M ⁻¹ s ⁻¹ , at 298 K)	Ref.
p-coumaric acid	4.35E+03	[101]
paraxanthine	1.05E+00	[962]
protocatechuic acid	5.14E+03	[963]
quercetin	4.39E+03	[101]
theobromine	5.34E+01	[962]
theophylline	4.21E+00	[962]
Trolox	3.40E+03	[947]
vanillin	9.75E+01	[961]
vanillic acid	1.29E+01	[961]
vanillyl alcohol	5.67E+03	[961]

Table 7. Overall, or apparent, rate constants (k) of the reactions between coffee components (and Trolox as reference) and HOO^{*}, in aqueous solution at physiological pH.

Component	k (M ⁻¹ s ⁻¹ , at 298 K, pH=7.4)	Ref.
caffeic acid	2.69E+08	[101]
caffeine	3.29E-01	[123]
dihydrocaffeic acid	1.04E+08	[101]
eugenol	1.55E+06	[961]
ferulic acid	3.36E+08	[101]
guaiacol	2.38E+06	[961]
mangiferin	5.52E+08	[101]
p-coumaric acid	8.51E+07	[101]
paraxanthine	4.18E-02	[962]
protocatechuic acid	1.26E+07	[963]
quercetin	8.11E+09	[101]
theobromine	2.76E-01	[962]
theophylline	3.86E-02	[962]
Trolox	8.96E+04	[947]

Component	k (M ⁻¹ s ⁻¹ , at 298 K, pH=7.4)	Ref.
vanillin	1.54E+05	[961]
vanillic acid	1.65E+07	[961]
vanillyl alcohol	4.12E+06	[961]

The values in Tables 6 and 7 were all computed with the Quantum Mechanics-based Test for Overall Free Radical Scavenging Activity (QM-ORSA).[126] This computational protocol was designed to calculate reliable rate constants in solution and was validated by comparisons with experimental data. The electronic calculations necessary to obtain the rate constants reported in Tables 6 and 7 were carried out with the M05-2X Density Functional Theory approach, combined with basis sets 6-31+G(d) to 6-311++G(d,p), and the SMD solvation model to mimic solvent effects. All possible reaction mechanisms and sites were taken into account, and the overall (or apparent) rate coefficients were estimated as the sum of the rate constants of each thermochemical viable reaction path. More details on this protocol can be found elsewhere.[126]

According to the gathered data, dihydrocaffeic acid and ferulic acid are the most efficient HOO• scavengers in non-polar media and aqueous solution, at pH=7.4, respectively. The trend in non-polar environment was found to be dihydrocaffeic acid > caffeic acid > ferulic acid > mangiferin > vanillyl alcohol > protocatechuic acid > quercetin > p-coumaric acid > eugenol > guaiacol > vanillin > caffeine > theobromine > vanillic acid > theophylline > p-xanthine. In aqueous solution such a trend changes to quercetin > mangiferin > ferulic acid > caffeic acid > dihydrocaffeic acid > p-coumaric acid > vanillic acid > protocatechuic acid > vanillyl alcohol > guaiacol > eugenol > vanillin > caffeine > theobromine > p-xanthine > theophylline.

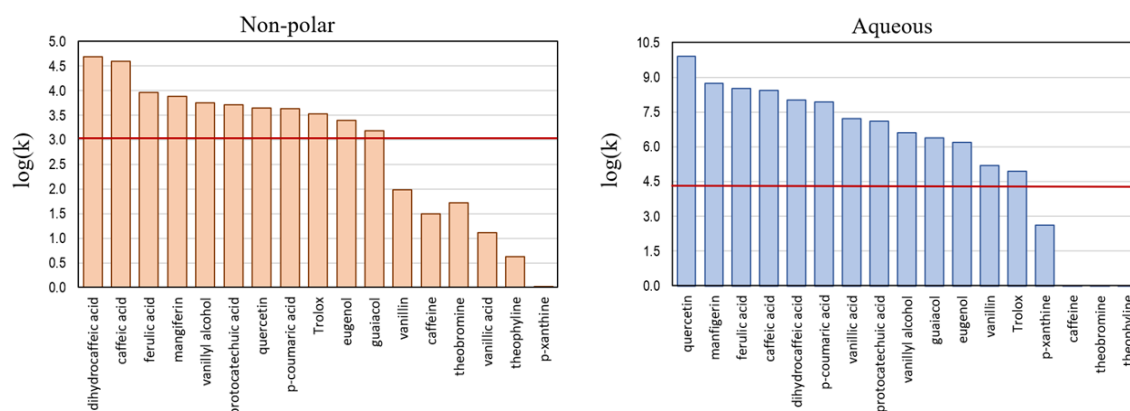


Fig. 3. log(k) for the reactions between coffee components (and Trolox as reference) with HOO•. The red line corresponds to the reaction of HOO• with polyunsaturated fatty acids.

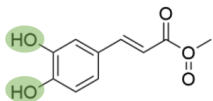
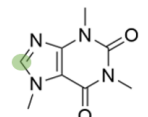
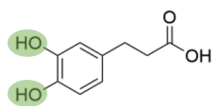
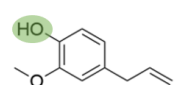
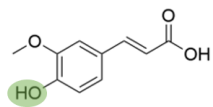
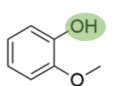
The threshold above-mentioned, i.e., $10^3 \text{ M}^{-1}\text{s}^{-1}$, corresponds to the reaction of HOO• with polyunsaturated fatty acids, and has been used to identify the coffee components that are expected to be efficient as free radical scavengers in biological systems. It has been marked with a red line in Fig. 3. According to this criterion, dihydrocaffeic, caffeic, ferulic, protocatechuic, and p-coumaric acids, as well as vanillyl alcohol, eugenol, and guaiacol should be capable of preventing peroxy damage to biomolecules both in lipid and in aqueous environments. For the latter, vanillin and vanillic acid also seem to be suitable for that purpose.

It seems worthwhile mentioning that the reactions of caffeine and its metabolites p-xanthine, theobromine, and theophylline with HOO^\bullet are too slow to protect lipids from the oxidative damage caused by this kind of radicals. This is in line with previous works. Šeremet et. al. found that the antioxidant properties of coffee brews do not depend on their caffeine content. [122] Mílek et. al. reported that while ‘specialty’ quality coffees have similar caffeine content as other brands, they significantly surpass them in antioxidant activity. [121] Based on the likeliness of f-HAT and SET mechanisms as protective routes, Petrucci et. al. concluded that caffeine can hardly be considered as an antioxidant. Thus, despite of being the most emblematic coffee component, this brew's antioxidant activity arises from its phenolic species, not from caffeine.

Structure-activity relationships

The reaction mechanism contributing the most to the antioxidant activity of the analyzed coffee components is reported in Tables 8 and 9 for lipid and aqueous environments, respectively. The most reactive site or species are also reported in these tables. The relatively low reactivity of caffeine and its metabolites p-xanthine, theobromine, and theophylline can be attributed to their lack of the phenol moiety. They have not labile H atoms to be involved in f-HAT, nor acid protons that favored deprotonation and, consequently, the SPLET mechanisms, i.e., SET from the anions. Thus, the main chemical route involved in their reactions with HOO^\bullet is the radical adduct formation.

Table 8. Main reaction mechanism and most reactive site in the reactions between coffee components and HOO^\bullet , in non-polar environments.

Component	Mechanism	Site	Ref.
caffeic acid	f-HAT		[101]
caffeine	RAF		[123]
dihydrocaffeic acid	f-HAT		[101]
eugenol	f-HAT		[961]
ferulic acid	f-HAT		[101]
guaiacol	f-HAT		[961]

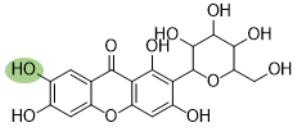
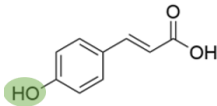
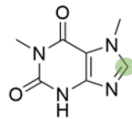
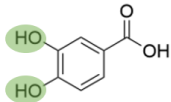
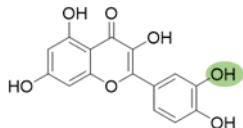
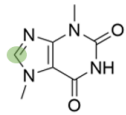
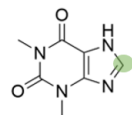
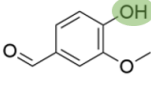
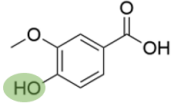
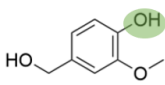
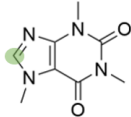
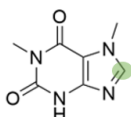
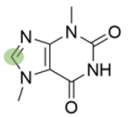
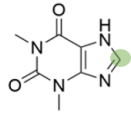
Component	Mechanism	Site	Ref.
mangiferin	<i>f</i> -HAT		[101]
p-coumaric acid	<i>f</i> -HAT		[101]
paraxanthine	RAF		[962]
protocatechuic acid	<i>f</i> -HAT		[963]
quercetin	<i>f</i> -HAT		[101]
theobromine	RAF		[962]
theophylline	RAF		[962]
vanillin	<i>f</i> -HAT		[961]
vanillic acid	<i>f</i> -HAT		[961]
vanillyl alcohol	<i>f</i> -HAT		[961]

Table 9. Main reaction mechanism and most reactive site or species in the reactions between coffee components and HOO^\bullet , in aqueous solution at physiological pH.

Component	Mechanism	Site or species	Ref.
caffeic acid	SPLET	phenolate anion	[101]
caffeine	RAF		[123]
dihydrocaffeic acid	SPLET	phenolate anion	[101]
eugenol	SPLET	phenolate anion	[961]
ferulic acid	SPLET	phenolate anion	[101]
guaiacol	SPLET	phenolate anion	[961]
mangiferin	SPLET	phenolate anion	[101]
p-coumaric acid	SPLET	phenolate anion	[101]
paraxanthine	RAF		[962]
protocatechuic acid	SPLET	phenolate anion	[963]
quercetin	SPLET	phenolate anion	[963]
theobromine	RAF		[962]
theophylline	RAF		[962]
vanillin	SPLET	phenolate anion	[961]
vanillic acid	SPLET	phenolate anion	[961]
vanillyl alcohol	SPLET	phenolate anion	[961]

The phenolic structural feature seems to be the key to the high efficiency of coffee components as peroxy radical scavengers. In lipid media, the OH group acts as H donor leading to AOX-I via *f*-HAT. In aqueous solution, their acid-base equilibria rule reactivity. At physiological pH, there is enough phenolate

fraction, which is excellent as electron donor. Thus, under such conditions, the SPLET mechanism becomes the highest contributor to the antioxidant activity of phenolic compounds in general, and of the phenolic compounds present in coffee.

The solvent also plays an important role in this context. The antioxidant + HOO• reactions are faster in aqueous solution, i.e., polar and protic solvent, than in lipid media (Tables 6 and 7, and Fig. 3). In addition, the fact that water is a polar and protic solvent promotes the SPLET mechanism, which was proposed by Litwinienko and Ingold, [925,964-966] and it is recognized as more efficient than *f*-HAT, and certainly much more than RAF, when phenols scavenge free radicals.

Perspectives

Albeit much information has been retrieved from the investigations on coffee, some aspects still deserve further research. Some of the many questions to be answered in more detail are:

- -How much does the presence of redox metals modify the chemistry of the coffee components?
- -How effective are they as chelating agents?
- -Would they act as OH inactivating ligands?
- -Are any of them capable of repairing oxidatively damaged biological targets?
- -Which of them can be considered multifunctional antioxidants?
- -Are their derivatives safe enough to be used as medical drugs?
- -What are the metabolites of these derivatives, and what properties do they have?

Nature gave us coffee. Revealing its chemical wonders is up to us.

Summary

Many natural products are known for their health benefits, but they comprise a large variety of components. Thus, it is essential to identify their bioactive substances as well as the specific functions and medicinal effects of these substances.

Coffee is a complex mixture containing many chemicals, including alkaloids, amino acids, carbohydrates, carotenoids, fatty acids, flavonoids, organic acids, phenolic acids, sugars, terpenes, and volatile compounds. It is also known to have many beneficial properties such as antibacterial, anticarcinogenic, antidiabetic, antifungal, anti-inflammatory, anti-obesity, cardioprotective, gastroprotective, hepatoprotective, and neuroprotective effects, provided that it is consumed in moderate amounts. The chemicals responsible for such valuable effects have been summarized in this review, as well as numerous investigations devoted to the design and synthesis of their derivatives.

The antioxidative protection of coffee has been related to most of its benefits. Several reaction mechanisms contributing to this protection were overviewed. Namely: radical adduct formation (RAF), single electron transfer (SET), formal hydrogen atom transfer (*f*-HAT), sequential proton loss electron transfer (SPLET), sequential electron proton transfer (SEPT), and sequential proton loss hydrogen atom transfer (SPLHAT). The ones contributing the most to the antioxidant activity of several coffee components were discussed.

The trends in free radical scavenging activity showed that phenolic acids are the ones contributing the most to the antioxidant effects of coffee, while alkaloids are not efficient for that purpose, at least as chemical antioxidants. Thus, despite being the most emblematic coffee component, the antioxidant activity of this brew does not arise from caffeine. In fact, it is not expected to be a good free radical scavenger.

The structure-activity relationships were associated with the main reaction mechanisms and the role of the solvent on the reactivity of the explored compounds. Alkaloids, i.e. caffeine and its metabolites *p*-xanthine, theobromine, and theophylline, mainly react via RAF, regardless of the solvent nature. Phenolic compounds,

on the other hand, mainly react via *f*-HAT in non-polar media, and via SPLET in aqueous solution, at physiological pH.

Although there are many aspects to be explored in the context of coffee chemistry, this review is meant to provide molecular insights on one of its main effects, i.e., antioxidant protection. The data gathered here demonstrate that computational and theoretical chemistry are very helpful tools to understand the molecular insights of antioxidants, and also for the design of new compounds that combines this behavior with other health benefits. Hopefully, this review will contribute to a better understanding of the chemistry of our morning cup and promote further investigations on this topic.

Acknowledgements

E.G.G.L. acknowledges CONAHCYT for Doctoral fellowship. L.F.H.A thanks to Estancias Posdoctorales por México (2022) CONAHCYT program for postdoctoral grant.

References

1. Nolan, L. The world's favorite beverage- coffee- and health. *J. Herbs Spices Med. Plants* **2001**, 8 (2-3), 119-159. DOI: https://doi.org/10.1300/J044v08n02_04.
2. Muhie, S. H. Strategies to improve the quantity and quality of export coffee in Ethiopia, a look at multiple opportunities. *J. Agric. Food Res.* **2022**, 10. DOI: <https://doi.org/10.1016/j.jafr.2022.100372>.
3. Mussatto, S. I.; Machado, E. M. S.; Martins, S.; Teixeira, J. A. Production, Composition, and Application of Coffee and Its Industrial Residues. *Food Bioprocess Technol.* **2011**, 4 (5), 661-672. DOI: <https://doi.org/10.1007/s11947-011-0565-z>.
4. Elder, L. W. Staling vs. Rancidity in Roasted Coffee: Antioxygens Produced by Roasting. *Ind. Eng. Chem.* **1940**, 32 (6), 798-801. DOI: <https://doi.org/10.1021/ie50366a014>.
5. Hassan, W.; Noreen, H.; Rehman, S.; Kamal, M. A.; da Rocha, J. B. T. Association of Oxidative Stress with Neurological Disorders. *Curr. Neuropharmacol.* **2022**, 20 (6), 1046-1072. DOI: <https://doi.org/10.2174/1570159X19666211111141246>.
6. Korovesis, D.; Rubio-Tomás, T.; Tavernarakis, N. Oxidative Stress in Age-Related Neurodegenerative Diseases: An Overview of Recent Tools and Findings. *Antioxidants* **2023**, 12 (1). DOI: <https://doi.org/10.3390/antiox12010131>.
7. Martínez Leo, E. E.; Segura Campos, M. R. Systemic Oxidative Stress: A Key Point in Neurodegeneration — A Review. *J. Nutr. Health Aging* **2019**, 23 (8), 694-699. DOI: <https://doi.org/10.1007/s12603-019-1240-8>.
8. Sienes Bailo, P.; Llorente Martín, E.; Calmarza, P.; Montolio Breva, S.; Bravo Gómez, A.; Pozo Giráldez, A.; Sánchez-Pascuala Callau, J. J.; Vaquer Santamaría, J. M.; Dayaldasani Khialani, A.; Cerdá Micó, C.; et al. The role of oxidative stress in neurodegenerative diseases and potential antioxidant therapies. *Adv. Lab. Med.* **2022**, 3 (4), 342-350. DOI: <https://doi.org/10.1515/almed-2022-0111>.
9. Singh, A.; Kukreti, R.; Saso, L.; Kukreti, S. Oxidative stress: A key modulator in neurodegenerative diseases. *Molecules* **2019**, 24 (8). DOI: <https://doi.org/10.3390/molecules24081583>.
10. Singh, E.; Devasahayam, G. Neurodegeneration by oxidative stress: a review on prospective use of small molecules for neuroprotection. *Mol. Biol. Rep.* **2020**, 47 (4), 3133-3140. DOI: <https://doi.org/10.1007/s11033-020-05354-1>.
11. Aborode, A. T.; Pustake, M.; Awuah, W. A.; Alwerdani, M.; Shah, P.; Yarlagaadda, R.; Ahmad, S.; Silva Correia, I. F.; Chandra, A.; Nansubuga, E. P.; et al. Targeting Oxidative Stress Mechanisms to Treat Alzheimer's and Parkinson's Disease: A Critical Review. *Oxidative Med. Cell. Longev.* **2022**, 2022. DOI: <https://doi.org/10.1155/2022/7934442>.

12. Chang, K. H.; Chen, C. M. The role of oxidative stress in Parkinson's disease. *Antioxidants* **2020**, 9 (7), 1-32. DOI: <https://doi.org/0.3390/antiox9070597>.
13. Dorszewska, J.; Kowalska, M.; Prendecki, M.; Piekut, T.; Kozłowska, J.; Kozubski, W. Oxidative stress factors in Parkinson's disease. *Neural Regen. Res.* **2021**, 16 (7), 1383-1391. DOI: <https://doi.org/10.4103/1673-5374.300980>.
14. Percário, S.; Da Silva Barbosa, A.; Varela, E. L. P.; Gomes, A. R. Q.; Ferreira, M. E. S.; De Nazaré Araújo Moreira, T.; Dolabela, M. F. Oxidative Stress in Parkinson's Disease: Potential Benefits of Antioxidant Supplementation. *Oxidative Med. Cell. Longev.* **2020**, 2020. DOI: <https://doi.org/10.1155/2020/2360872>.
15. Pyatha, S.; Kim, H.; Lee, D.; Kim, K. Association between Heavy Metal Exposure and Parkinson's Disease: A Review of the Mechanisms Related to Oxidative Stress. *Antioxidants* **2022**, 11 (12). DOI: <https://doi.org/10.3390/antiox11122467>.
16. Wei, Z.; Li, X.; Li, X.; Liu, Q.; Cheng, Y. Oxidative Stress in Parkinson's Disease: A Systematic Review and Meta-Analysis. *Front. Mol. Neurosci.* **2018**, 11. DOI: <https://doi.org/10.3389/fnmol.2018.00236>.
17. Arfin, S.; Jha, N. K.; Jha, S. K.; Kesari, K. K.; Ruokolainen, J.; Roychoudhury, S.; Rathi, B.; Kumar, D. Oxidative stress in cancer cell metabolism. *Antioxidants* **2021**, 10 (5). DOI: <https://doi.org/10.3390/antiox10050642>.
18. Calaf, G. M.; Urzua, U.; Termini, L.; Aguayo, F. Oxidative stress in female cancers. *Oncotarget* **2018**, 9 (34), 23824-23842. DOI: <https://doi.org/10.18632/oncotarget.25323>.
19. Cruz-Gregorio, A.; Aranda-Rivera, A. K.; Ortega-Lozano, A. J.; Pedraza-Chaverri, J.; Mendoza-Hoffmann, F. Lipid metabolism and oxidative stress in HPV-related cancers. *Free Radic. Biol. Med.* **2021**, 172, 226-236. DOI: <https://doi.org/10.1016/j.freeradbiomed.2021.06.009>.
20. Ding, D. N.; Xie, L. Z.; Shen, Y.; Li, J.; Guo, Y.; Fu, Y.; Liu, F. Y.; Han, F. J. Insights into the Role of Oxidative Stress in Ovarian Cancer. *Oxidative Med. Cell. Longev.* **2021**, 2021. DOI: <https://doi.org/10.1155/2021/8388258>.
21. Ebrahimi, S.; Soltani, A.; Hashemy, S. I. Oxidative stress in cervical cancer pathogenesis and resistance to therapy. *J. Cell. Biochem.* **2019**, 120 (5), 6868-6877. DOI: <https://doi.org/10.1002/jcb.28007>.
22. Hayes, J. D.; Dinkova-Kostova, A. T.; Tew, K. D. Oxidative Stress in Cancer. *Cancer Cell* **2020**, 38 (2), 167-197. DOI: <https://doi.org/10.1016/j.ccell.2020.06.001>.
23. Jelic, M. D.; Mandic, A. D.; Maricic, S. M.; Srdjenovic, B. U. Oxidative stress and its role in cancer. *J. Cancer Res. Ther.* **2021**, 17 (1), 22-28. DOI: https://doi.org/10.4103/jcrt.JCRT_862_16.
24. Katakwar, P.; Metgud, R.; Naik, S.; Mittal, R. Oxidative stress marker in oral cancer: A review. *J. Cancer Res. Ther.* **2016**, 12 (2), 438-446. DOI: <https://doi.org/10.4103/0973-1482.151935>.
25. Klaunig, J. E. Oxidative stress and cancer. *Curr. Pharm. Des.* **2018**, 24 (40), 4771-4778. DOI: <https://doi.org/10.2174/1381612825666190215121712>.
26. Kruk, J.; Aboul-Enein, H. Y. Reactive oxygen and nitrogen species in carcinogenesis: Implications of oxidative stress on the progression and development of several cancer types. *Mini-Rev. Med. Chem.* **2017**, 17 (11), 904-919. DOI: <https://doi.org/10.2174/1389557517666170228115324>.
27. Wang, Z.; Li, Z.; Ye, Y.; Xie, L.; Li, W. Oxidative stress and liver cancer: Etiology and therapeutic targets. *Oxidative Med. Cell. Longev.* **2016**, 2016. DOI: <https://doi.org/10.1155/2016/7891574>.
28. 2Zahra, K. F.; Lefter, R.; Ali, A.; Abdellah, E. C.; Trus, C.; Ciobica, A.; Timofte, D. The Involvement of the Oxidative Stress Status in Cancer Pathology: A Double View on the Role of the Antioxidants. *Oxidative Med. Cell. Longev.* **2021**, 2021. DOI: <https://doi.org/10.1155/2021/9965916>.
29. De Almeida, A. J. P. O.; De Almeida Rezende, M. S.; Dantas, S. H.; De Lima Silva, S.; De Oliveira, J. C. P. L.; De Lourdes Assunção Araújo De Azevedo, F.; Alves, R. M. F. R.; De Menezes, G. M. S.; Dos Santos, P. F.; Gonçalves, T. A. F.; et al. Unveiling the Role of Inflammation and Oxidative Stress on Age-Related Cardiovascular Diseases. *Oxidative Med. Cell. Longev.* **2020**, 2020. DOI: <https://doi.org/10.1155/2020/1954398>.

30. De Geest, B.; Mishra, M. Role of Oxidative Stress in Diabetic Cardiomyopathy. *Antioxidants* **2022**, *11* (4). DOI: <https://doi.org/10.3390/antiox11040784>.
31. Izzo, C.; Vitillo, P.; Di Pietro, P.; Visco, V.; Strianese, A.; Virtuoso, N.; Ciccarelli, M.; Galasso, G.; Carrizzo, A.; Vecchione, C. The role of oxidative stress in cardiovascular aging and cardiovascular diseases. *Life* **2021**, *11* (1), 1-42. DOI: <https://doi.org/10.3390/life11010060>.
32. Jakovljevic, V.; Djuric, D.; Pechanova, O.; Bolevich, S.; Tyagi, S. Oxidative Stress and Cardiovascular Dysfunction: From Basic Science to Applied Investigations. *Oxidative Med. Cell. Longev.* **2020**, *2020*. DOI: <https://doi.org/10.1155/2020/6985284>.
33. Panda, P.; Verma, H. K.; Lakkakula, S.; Merchant, N.; Kadir, F.; Rahman, S.; Jeffree, M. S.; Lakkakula, B. V. K. S.; Rao, P. V. Biomarkers of Oxidative Stress Tethered to Cardiovascular Diseases. *Oxidative Med. Cell. Longev.* **2022**, *2022*. DOI: <https://doi.org/10.1155/2022/9154295>.
34. 3Pignatelli, P.; Menichelli, D.; Pastori, D.; Violi, F. Oxidative stress and cardiovascular disease: New insights. *Kardiol. Pol.* **2018**, *76* (4), 713-722. DOI: <https://doi.org/10.5603/KP.a2018.0071>.
35. Shaito, A.; Aramouni, K.; Assaf, R.; Parenti, A.; Orekhov, A.; Yazbi, A. E.; Pintus, G.; Eid, A. H. Oxidative Stress-Induced Endothelial Dysfunction in Cardiovascular Diseases. *Front. Biosci. - Landmark* **2022**, *27* (3). DOI: <https://doi.org/10.31083/j.fbl2703105>.
36. Wang, W.; Kang, P. M. Oxidative stress and antioxidant treatments in cardiovascular diseases. *Antioxidants* **2020**, *9* (12), 1-25. DOI: <https://doi.org/10.3390/antiox9121292>.
37. Yan, F.; Li, K.; Xing, W.; Dong, M.; Yi, M.; Zhang, H. Role of Iron-Related Oxidative Stress and Mitochondrial Dysfunction in Cardiovascular Diseases. *Oxidative Med. Cell. Longev.* **2022**, *2022*. DOI: <https://doi.org/10.1155/2022/5124553>.
38. Xu, T.; Ding, W.; Ji, X.; Ao, X.; Liu, Y.; Yu, W.; Wang, J. Oxidative Stress in Cell Death and Cardiovascular Diseases. *Oxidative Med. Cell. Longev.* **2019**, *2019*. DOI: <https://doi.org/10.1155/2019/9030563>.
39. Bhatti, J. S.; Sehrawat, A.; Mishra, J.; Sidhu, I. S.; Navik, U.; Khullar, N.; Kumar, S.; Bhatti, G. K.; Reddy, P. H. Oxidative stress in the pathophysiology of type 2 diabetes and related complications: Current therapeutics strategies and future perspectives. *Free Radic. Biol. Med.* **2022**, *184*, 114-134. DOI: <https://doi.org/10.1016/j.freeradbiomed.2022.03.019>.
40. Black, H. S. A Synopsis of the Associations of Oxidative Stress, ROS, and Antioxidants with Diabetes Mellitus. *Antioxidants* **2022**, *11* (10). DOI: <https://doi.org/10.3390/antiox11102003>.
41. Ghasemi-Dehnoo, M.; Amini-Khoei, H.; Lorigooini, Z.; Rafieian-Kopaei, M. Oxidative stress and antioxidants in diabetes mellitus. *Asian Pac. J. Trop. Med.* **2020**, *13* (10), 431-438. DOI: <https://doi.org/10.4103/1995-7645.291036>.
42. Ighodaro, O. M. Molecular pathways associated with oxidative stress in diabetes mellitus. *Biomed. Pharmacother.* **2018**, *108*, 656-662. DOI: <https://doi.org/10.1016/j.biopha.2018.09.058>.
43. Ramos-Riera, K. P.; Pérez-Severiano, F.; López-Meraz, M. L. Oxidative stress: a common imbalance in diabetes and epilepsy. *Metab. Brain Dis.* **2023**, *38* (3), 767-782. DOI: <https://doi.org/10.1007/s11011-022-01154-7>.
44. Thakur, P.; Kumar, A.; Kumar, A. Targeting oxidative stress through antioxidants in diabetes mellitus. *J. Drug Target.* **2018**, *26* (9), 766-776. DOI: <https://doi.org/10.1080/1061186X.2017.1419478>.
45. Zhang, P.; Li, T.; Wu, X.; Nice, E. C.; Huang, C.; Zhang, Y. Oxidative stress and diabetes: antioxidative strategies. *Front. Med.* **2020**, *14* (5), 583-600. DOI: <https://doi.org/10.1007/s11684-019-0729-1>.
46. Eguchi, N.; Vaziri, N. D.; Dafoe, D. C.; Ichii, H. The role of oxidative stress in pancreatic β cell dysfunction in diabetes. *Int. J. Mol. Sci.* **2021**, *22* (4), 1-18. DOI: <https://doi.org/10.3390/ijms22041509>.
47. Ferreira, H. B.; Melo, T.; Paiva, A.; Domingues, M. D. R. Insights in the role of lipids, oxidative stress and inflammation in rheumatoid arthritis unveiled by new trends in lipidomic investigations. *Antioxidants* **2021**, *10* (1), 1-21. DOI: [10.3390/antiox10010045](https://doi.org/10.3390/antiox10010045).
48. Kaur, G.; Sharma, A.; Bhatnagar, A. Role of oxidative stress in pathophysiology of rheumatoid arthritis: insights into NRF2-KEAP1 signalling. *Autoimmunity* **2021**, *54* (7), 385-397. DOI: <https://doi.org/10.1080/08916934.2021.1963959>.

49. Kunsch, C.; Sikorski, J. A.; Sundell, C. L. Oxidative stress and the use of antioxidants for the treatment of rheumatoid arthritis. *Curr. Med. Chem.: Immunol. Endocr. Metabol. Agents* **2005**, *5* (3), 249-258. DOI: <https://doi.org/10.2174/1568013054022490>.
50. Quinonez-Flores, C. M.; Gonzalez-Chavez, S. A.; Del Rio Najera, D.; Pacheco-Tena, C. Oxidative Stress Relevance in the Pathogenesis of the Rheumatoid Arthritis: A Systematic Review. *Biomed. Res. Int.* **2016**, *2016*. DOI: <https://doi.org/10.1155/2016/6097417>.
51. Zamudio-Cuevas, Y.; Martínez-Flores, K.; Martínez-Nava, G. A.; Clavijo-Cornejo, D.; Fernández-Torres, J.; Sánchez-Sánchez, R. Rheumatoid arthritis and oxidative stress, a review of a decade. *Cell. Mol. Biol.* **2022**, *68* (6), 174-184. DOI: <https://doi.org/10.14715/cmb/2022.68.6.28>.
52. Amiri, M. Oxidative stress and free radicals in liver and kidney diseases; an updated short-review. *J. Nephropathol.* **2018**, *7* (3), 127-131. DOI: <https://doi.org/10.15171/jnp.2018.30>.
53. Coppolino, G.; Leonardi, G.; Andreucci, M.; Bolignano, D. Oxidative stress and kidney function: A brief update. *Curr. Pharm. Des.* **2018**, *24* (40), 4794-4799. DOI: <https://doi.org/10.2174/1381612825666190112165206>.
54. Daenen, K.; Andries, A.; Mekahli, D.; Van Schepdael, A.; Jouret, F.; Bammens, B. Oxidative stress in chronic kidney disease. *Pediatr. Nephrol.* **2019**, *34* (6), 975-991. DOI: 10.1007/s00467-018-4005-4.
55. Duni, A.; Liakopoulos, V.; Roumeliotis, S.; Peschos, D.; Dounousi, E. Oxidative stress in the pathogenesis and evolution of chronic kidney disease: Untangling ariadne's thread. *Int. J. Mol. Sci.* **2019**, *20* (15). DOI: <https://doi.org/10.3390/ijms20153711>.
56. Hsu, C. N.; Tain, Y. L. Developmental origins of kidney disease: Why oxidative stress matters? *Antioxidants* **2021**, *10* (1), 1-18. DOI: <https://doi.org/10.3390/antiox10010033>.
57. Jha, J. C.; Banal, C.; Chow, B. S. M.; Cooper, M. E.; Jandeleit-Dahm, K. Diabetes and Kidney Disease: Role of Oxidative Stress. *Antioxid. Redox Signal.* **2016**, *25* (12), 657-684. DOI: <https://doi.org/10.1089/ars.2016.6664>.
58. Ling, X. C.; Kuo, K. L. Oxidative stress in chronic kidney disease. *Ren. Replace. Ther.* **2018**, *4* (1). DOI: <https://doi.org/10.1186/s41100-018-0195-2>.
59. Tamay-Cach, F.; Quintana-Pérez, J. C.; Trujillo-Ferrara, J. G.; Cuevas-Hernández, R. I.; Del Valle-Mondragón, L.; García-Trejo, E. M.; Arellano-Mendoza, M. G. A review of the impact of oxidative stress and some antioxidant therapies on renal damage. *Ren. Fail.* **2016**, *38* (2), 171-175. DOI: <https://doi.org/10.3109/0886022X.2015.1120097>.
60. Verma, S.; Singh, P.; Khurana, S.; Ganguly, N. K.; Kukreti, R.; Saso, L.; Rana, D. S.; Taneja, V.; Bhargava, V. Implications of oxidative stress in chronic kidney disease: A review on current concepts and therapies. *Kidney Res. Clin. Pract.* **2021**, *40* (2), 183-193. DOI: <https://doi.org/10.23876/j.krcp.20.163>.
61. Antunes, M. A.; Lopes-Pacheco, M.; Rocco, P. R. M. Oxidative Stress-Derived Mitochondrial Dysfunction in Chronic Obstructive Pulmonary Disease: A Concise Review. *Oxidative Med. Cell. Longev.* **2021**, *2021*. DOI: <https://doi.org/10.1155/2021/6644002>.
62. Bargagli, E.; Olivieri, C.; Bennett, D.; Prasse, A.; Muller-Quernheim, J.; Rottoli, P. Oxidative stress in the pathogenesis of diffuse lung diseases: A review. *Respir. Med.* **2009**, *103* (9), 1245-1256. DOI: <https://doi.org/10.1016/j.rmed.2009.04.014>.
63. Barnes, P. J. Oxidative Stress in Chronic Obstructive Pulmonary Disease. *Antioxidants* **2022**, *11* (5). DOI: <https://doi.org/10.3390/antiox11050965>.
64. Bast, A.; Weseler, A. R.; Haenen, G. R. M. M.; Den Hartog, G. J. M. Oxidative stress and antioxidants in interstitial lung disease. *Curr. Opin. Pulm. Med.* **2010**, *16* (5), 516-520. DOI: <https://doi.org/10.1097/MCP.0b013e32833c645d>.
65. Cheresh, P.; Kim, S. J.; Tulasiram, S.; Kamp, D. W. Oxidative stress and pulmonary fibrosis. *Biochim. Biophys. Acta - Mol. Basis Dis.* **2013**, *1832* (7), 1028-1040. DOI: <https://doi.org/10.1016/j.bbadis.2012.11.021>.

66. Hecker, L. Mechanisms and consequences of oxidative stress in lung disease: Therapeutic implications for an aging populace. *Am. J. Physiol. Lung Cell. Mol. Physiol.* **2018**, 314 (4), L642-L653. DOI: <https://doi.org/10.1152/ajplung.00275.2017>.
67. Hsueh, Y. J.; Chen, Y. N.; Tsao, Y. T.; Cheng, C. M.; Wu, W. C.; Chen, H. C. The Pathomechanism, Antioxidant Biomarkers, and Treatment of Oxidative Stress-Related Eye Diseases. *Int. J. Mol. Sci.* **2022**, 23 (3). DOI: <https://doi.org/10.3390/ijms23031255>.
68. Ivanov, I. V.; Mappes, T.; Schaupp, P.; Lappe, C.; Wahl, S. Ultraviolet radiation oxidative stress affects eye health. *J. Biophotonics* **2018**, 11 (7). DOI: <https://doi.org/10.1002/jbio.201700377>.
69. Nita, M.; Grzybowski, A. The Role of the Reactive Oxygen Species and Oxidative Stress in the Pathomechanism of the Age-Related Ocular Diseases and Other Pathologies of the Anterior and Posterior Eye Segments in Adults. *Oxidative Med. Cell. Longev.* **2016**, 2016. DOI: <https://doi.org/10.1155/2016/3164734>.
70. Seen, S.; Tong, L. Dry eye disease and oxidative stress. *Acta Ophthalmol. (Copenh.)* **2018**, 96 (4), e412-e420. DOI: <https://doi.org/10.1111/aos.13526>.
71. Subramaniam, M. D.; Iyer, M.; Nair, A. P.; Venkatesan, D.; Mathavan, S.; Eruppakotte, N.; Kizhakkilach, S.; Chandran, M. K.; Roy, A.; Gopalakrishnan, A. V.; Vellingiri, B. Oxidative stress and mitochondrial transfer: A new dimension towards ocular diseases. *Genes Dis.* **2022**, 9 (3), 610-637. DOI: <https://doi.org/10.1016/j.gendis.2020.11.020>.
72. Ung, L.; Pattamatta, U.; Carnt, N.; Wilkinson-Berka, J. L.; Liew, G.; White, A. J. R. Oxidative stress and reactive oxygen species: A review of their role in ocular disease. *Clin. Sci.* **2017**, 131 (24), 2865-2883. DOI: <https://doi.org/10.1042/CS20171246>.
73. Aouache, R.; Biquard, L.; Vaiman, D.; Miralles, F. Oxidative stress in preeclampsia and placental diseases. *Int. J. Mol. Sci.* **2018**, 19 (5). DOI: <https://doi.org/10.3390/ijms19051496>.
74. Chiarello, D. I.; Abad, C.; Rojas, D.; Toledo, F.; Vázquez, C. M.; Mate, A.; Sobrevia, L.; Marín, R. Oxidative stress: Normal pregnancy versus preeclampsia. *Biochim. Biophys. Acta - Mol. Basis Dis.* **2020**, 1866 (2). DOI: <https://doi.org/10.1016/j.bbadis.2018.12.005>.
75. Siddiqui, I. A.; Jaleel, A.; Tamimi, W.; Al Kadri, H. M. F. Role of oxidative stress in the pathogenesis of preeclampsia. *Arch. Gynecol. Obstet.* **2010**, 282 (5), 469-474. DOI: <https://doi.org/10.1007/s00404-010-1538-6>.
76. Taysi, S.; Tascan, A. S.; Ugur, M. G.; Demir, M. Radicals, oxidative/nitrosative stress and preeclampsia. *Mini-Rev. Med. Chem.* **2019**, 19 (3), 178-193. DOI: <https://doi.org/10.2174/1389557518666181015151350>.
77. Thompson, L. P.; Al-Hasan, Y. Impact of oxidative stress in fetal programming. *J. Pregnancy* **2012**, 2012. DOI: <https://doi.org/10.1155/2012/582748>.
78. Liang, N.; Kitts, D. D. Antioxidant property of coffee components: Assessment of methods that define mechanism of action. *Molecules* **2014**, 19 (11), 19180-19208. DOI: 10.3390/molecules191119180.
79. Aguiar, J.; Estevinho, B. N.; Santos, L. Microencapsulation of natural antioxidants for food application – The specific case of coffee antioxidants – A review. *Trends Food Sci. Technol.* **2016**, 58, 21-39. DOI: <https://doi.org/10.1016/j.tifs.2016.10.012>.
80. Bothiraj, K. V.; Murugan; Vanitha, V. Green coffee bean seed and their role in antioxidant—a review. *Int. J. Pharm. Sci. Res.* **2020**, 11 (1), 233-240. DOI: <https://doi.org/10.26452/ijrps.v11i1.1812>.
81. Iriondo-DeHond, A.; Ramírez, B.; Escobar, F. V.; del Castillo, M. D. Antioxidant properties of high molecular weight compounds from coffee roasting and brewing byproducts. *Bioact. Compd. Health Dis.* **2019**, 2 (3), 48-63. DOI: <https://doi.org/10.31989/bchd.v2i3.588>.
82. Ahmed Ali, A. M.; Yagi, S.; Qahtan, A. A.; Alatar, A. A.; Angeloni, S.; Maggi, F.; Caprioli, G.; Abdel-Salam, E. M.; Sinan, K. I.; Zengin, G. Evaluation of the chemical constituents, antioxidant and enzyme inhibitory activities of six Yemeni green coffee beans varieties. *Food Biosci.* **2022**, 46. DOI: <https://doi.org/10.1016/j.fbio.2022.101552>.
83. AlAmri, O. D.; Albeltagy, R. S.; M. A. Akabawy, A.; Mahgoub, S.; Abdel-Mohsen, D. M.; Abdel Moneim, A. E.; Amin, H. K. Investigation of antioxidant and anti-inflammatory activities as well as

- the renal protective potential of green coffee extract in high fat-diet/streptozotocin-induced diabetes in male albino rats. *J. Funct. Foods* **2020**, *71*. DOI: <https://doi.org/10.1016/j.jff.2020.103996>.
84. Andrade, C.; Perestrelo, R.; Câmara, J. S. Bioactive Compounds and Antioxidant Activity from Spent Coffee Grounds as a Powerful Approach for Its Valorization. *Molecules* **2022**, *27* (21). DOI: <https://doi.org/10.3390/molecules27217504>.
85. Angeloni, S.; Freschi, M.; Marrazzo, P.; Hrelia, S.; Beghelli, D.; Juan-García, A.; Juan, C.; Caprioli, G.; Sagratini, G.; Angeloni, C. Antioxidant and Anti-Inflammatory Profiles of Spent Coffee Ground Extracts for the Treatment of Neurodegeneration. *Oxidative Med. Cell. Longev.* **2021**, *2021*. DOI: <https://doi.org/10.1155/2021/6620913>.
86. Botto, L.; Bulbarelli, A.; Lonati, E.; Cazzaniga, E.; Tassotti, M.; Mena, P.; Del Rio, D.; Palestini, P. Study of the antioxidant effects of coffee phenolic metabolites on c6 glioma cells exposed to diesel exhaust particles. *Antioxidants* **2021**, *10* (8). DOI: <https://doi.org/10.3390/antiox10081169>.
87. Castaldo, L.; Toriello, M.; Sessa, R.; Izzo, L.; Lombardi, S.; Narváez, A.; Ritieni, A.; Grosso, M. Antioxidant and anti-inflammatory activity of coffee brew evaluated after simulated gastrointestinal digestion. *Nutrients* **2021**, *13* (12). DOI: <https://doi.org/10.3390/nu13124368>.
88. Lemos, M. F.; de Andrade Salustriano, N.; de Souza Costa, M. M.; Lirio, K.; da Fonseca, A. F. A.; Pacheco, H. P.; Endringer, D. C.; Fronza, M.; Scherer, R. Chlorogenic acid and caffeine contents and anti-inflammatory and antioxidant activities of green beans of conilon and arabica coffees harvested with different degrees of maturation. *J. Saudi Chem. Soc.* **2022**, *26* (3). DOI: <https://doi.org/10.1016/j.jscs.2022.101467>.
89. Lonati, E.; Carrozzini, T.; Bruni, I.; Mena, P.; Botto, L.; Cazzaniga, E.; Del Rio, D.; Labra, M.; Palestini, P.; Bulbarelli, A. Coffee-Derived Phenolic Compounds Activate Nrf2 Antioxidant Pathway in I/R Injury In Vitro Model: A Nutritional Approach Preventing Age Related-Damages. *Molecules* **2022**, *27* (3). DOI: <https://doi.org/10.3390/molecules27031049>.
90. Montenegro, J.; dos Santos, L. S.; de Souza, R. G. G.; Lima, L. G. B.; Mattos, D. S.; Viana, B. P. P. B.; da Fonseca Bastos, A. C. S.; Muzzi, L.; Conte-Júnior, C. A.; Gimba, E. R. P.; et al. Bioactive compounds, antioxidant activity and antiproliferative effects in prostate cancer cells of green and roasted coffee extracts obtained by microwave-assisted extraction (MAE). *Food Res. Int.* **2021**, *140*. DOI: <https://doi.org/10.1016/j.foodres.2020.110014>.
91. Nemzer, B.; Kalita, D.; Abshiru, N. Quantification of major bioactive constituents, antioxidant activity, and enzyme inhibitory effects of whole coffee cherries (*Coffea arabica*) and their extracts. *Molecules* **2021**, *26* (14). DOI: <https://doi.org/10.3390/molecules26144306>.
92. Nosal, B. M.; Sakaki, J. R.; Kim, D. O.; Chun, O. K. Impact of coffee preparation on total phenolic content in brewed coffee extracts and their contribution to the body's antioxidant status. *Food Sci. Biotechnol.* **2022**, *31* (8), 1081-1088. DOI: <https://doi.org/10.1007/s10068-022-01100-4>.
93. Nzekoue, F. K.; Angeloni, S.; Navarini, L.; Angeloni, C.; Freschi, M.; Hrelia, S.; Vitali, L. A.; Sagratini, G.; Vittori, S.; Caprioli, G. Coffee silverskin extracts: Quantification of 30 bioactive compounds by a new HPLC-MS/MS method and evaluation of their antioxidant and antibacterial activities. *Food Res. Int.* **2020**, *133*. DOI: <https://doi.org/10.1016/j.foodres.2020.109128>.
94. Pergolizzi, S.; D'Angelo, V.; Aragona, M.; Dugo, P.; Cacciola, F.; Capillo, G.; Dugo, G.; Lauriano, E. R. Evaluation of antioxidant and anti-inflammatory activity of green coffee beans methanolic extract in rat skin. *Nat. Prod. Res.* **2020**, *34* (11), 1535-1541. DOI: <https://doi.org/10.1080/14786419.2018.1523161>.
95. Sunoqrot, S.; Al-Shalabi, E.; Al-Bakri, A. G.; Zalloum, H.; Abu-Irmaileh, B.; Ibrahim, L. H.; Zeno, H. Coffee Bean Polyphenols Can Form Biocompatible Template-free Antioxidant Nanoparticles with Various Sizes and Distinct Colors. *ACS Omega* **2021**, *6* (4), 2767-2776. DOI: <https://doi.org/10.1021/acsomega.0c05061>.
96. Yin, X.; He, X.; Wu, L.; Yan, D.; Yan, S. Chlorogenic Acid, the Main Antioxidant in Coffee, Reduces Radiation-Induced Apoptosis and DNA Damage via NF-E2-Related Factor 2 (Nrf2) Activation in Hepatocellular Carcinoma. *Oxid. Med. Cell. Longev.* **2022**, *2022*. DOI: <https://doi.org/10.1155/2022/4566949>.

97. Natella, F.; Nardini, M.; Giannetti, I.; Dattilo, C.; Scaccini, C. Coffee drinking influences plasma antioxidant capacity in humans. *J. Agric. Food Chem.* **2002**, *50* (21), 6211-6216. DOI: <https://doi.org/10.1021/jf025768c>.
98. Hoelzl, C.; Knasmüller, S.; Wagner, K.; Elbling, L.; Huber, W.; Kager, N.; Ferk, F.; Ehrlich, V.; Nersesyan, A.; Neubauer, O.; et al. Instant coffee with high chlorogenic acid levels protects humans against oxidative damage of macromolecules. *Mol. Nutr. Food Res.* **2010**, *54* (12), 1722-1733. DOI: <https://doi.org/10.1002/mnfr.201000048>.
99. Hori, A.; Kasai, H.; Kawai, K.; Nanri, A.; Sato, M.; Ohta, M.; Mizoue, T. Coffee intake is associated with lower levels of oxidative DNA damage and decreasing body iron storage in healthy women. *Nutr. Cancer* **2014**, *66* (6), 964-969. DOI: <https://doi.org/10.1080/01635581.2014.932398>.
100. Nicoli, M. C.; Anese, M.; Manzocco, L.; Lerici, C. R. Antioxidant properties of coffee brews in relation to the roasting degree. *LWT* **1997**, *30* (3), 292-297. DOI: <https://doi.org/10.1006/fstl.1996.0181>.
101. León-Carmona, J. R.; Alvarez-Idaboy, J. R.; Galano, A. On the peroxy scavenging activity of hydroxycinnamic acid derivatives: Mechanisms, kinetics, and importance of the acid-base equilibrium. *Phys. Chem. Chem. Phys.* **2012**, *14* (36), 12534-12543.
102. Baggio, J.; Lima, A.; Mancini Filho, J.; Fett, R. Identification of phenolic acids in coffee (*Coffea Arabica* L.) dust and its antioxidant activity. *Ital. J. Food Sci.* **2007**, *19* (2), 191-201.
103. Beder-Belkhir, W.; Zeghichi-Hamri, S.; Kadri, N.; Boulekbache-Makhlouf, L.; Cardoso, S.; Oukhmanou-Bensidhoum, S.; Madani, K. Hydroxycinnamic acids profiling, in vitro evaluation of total phenolic compounds, caffeine and antioxidant properties of coffee imported, roasted and consumed in Algeria. *Mediterr. J. Nutr. Metab.* **2018**, *11* (1), 51-63. DOI: <https://doi.org/10.3233/MNM-17181>.
104. Górnaś, P.; Dwiecki, K.; Siger, A.; Tomaszewska-Gras, J.; Michalak, M.; Polewski, K. Contribution of phenolic acids isolated from green and roasted boiled-type coffee brews to total coffee antioxidant capacity. *Eur. Food Res. Technol.* **2016**, *242* (5), 641-653. DOI: <https://doi.org/10.1007/s00217-015-2572-1>.
105. Saeed Alkaltham, M.; Musa Özcan, M.; Uslu, N.; Salamatullah, A. M.; Hayat, K. Effect of microwave and oven roasting methods on total phenol, antioxidant activity, phenolic compounds, and fatty acid compositions of coffee beans. *J. Food Process. Preserv.* **2020**, *44* (11). DOI: <https://doi.org/10.1111/jfpp.14874>.
106. Alnsour, L.; Issa, R.; Awwad, S.; Albals, D.; Al-Momani, I. Quantification of Total Phenols and Antioxidants in Coffee Samples of Different Origins and Evaluation of the Effect of Degree of Roasting on Their Levels. *Molecules* **2022**, *27* (5). DOI: <https://doi.org/10.3390/molecules27051591>.
107. Delgado-Andrade, C.; Morales, F. J. Unraveling the contribution of melanoidins to the antioxidant activity of coffee brews. *J. Agric. Food Chem.* **2005**, *53* (5), 1403-1407. DOI: <https://doi.org/10.1021/jf048500p>.
108. Pérez-Hernández, L. M.; Chávez-Quiroz, K.; Medina-Juárez, L. Á.; Gámez Meza, N. Phenolic characterization, melanoidins, and antioxidant activity of some commercial coffees from *Coffea arabica* and *Coffea canephora*. *J. Mex. Chem. Soc.* **2012**, *56* (4), 430-435.
109. Perrone, D.; Farah, A.; Donangelo, C. M. Influence of coffee roasting on the incorporation of phenolic compounds into melanoidins and their relationship with antioxidant activity of the brew. *J. Agric. Food Chem.* **2012**, *60* (17), 4265-4275. DOI: <https://doi.org/10.1021/jf205388x>.
110. Vignoli, J. A.; Bassoli, D. G.; Benassi, M. T. Antioxidant activity, polyphenols, caffeine and melanoidins in soluble coffee: The influence of processing conditions and raw material. *Food Chem.* **2011**, *124* (3), 863-868. DOI: <https://doi.org/10.1016/j.foodchem.2010.07.008>.
111. Fuster, M. D.; Mitchell, A. E.; Ochi, H.; Shibamoto, T. Antioxidative activities of heterocyclic compounds formed in brewed coffee. *J. Agric. Food Chem.* **2000**, *48* (11), 5600-5603. DOI: <https://doi.org/10.1021/jf000605e>.
112. Yanagimoto, K.; Lee, K. G.; Ochi, H.; Shibamoto, T. Antioxidative activity of heterocyclic compounds found in coffee volatiles produced by Maillard reaction. *J. Agric. Food Chem.* **2002**, *50* (19), 5480-5484. DOI: <https://doi.org/10.1021/jf025616h>.

113. Liu, Y.; Kitts, D. D. Confirmation that the Maillard reaction is the principle contributor to the antioxidant capacity of coffee brews. *Food Res. Int.* **2011**, *44* (8), 2418-2424. DOI: <https://doi.org/10.1016/j.foodres.2010.12.037>.
114. Nebesny, E.; Budryn, G. Antioxidative activity of green and roasted coffee beans as influenced by convection and microwave roasting methods and content of certain compounds. *Eur. Food Res. Technol.* **2003**, *217* (2), 157-163. DOI: <https://doi.org/10.1007/s00217-003-0705-4>.
115. Cheong, M. W.; Tong, K. H.; Ong, J. J. M.; Liu, S. Q.; Curran, P.; Yu, B. Volatile composition and antioxidant capacity of Arabica coffee. *Food Res. Int.* **2013**, *51* (1), 388-396. DOI: <https://doi.org/10.1016/j.foodres.2012.12.058>.
116. Haile, M.; Bae, H. M.; Kang, W. H. Comparison of the antioxidant activities and volatile compounds of coffee beans obtained using digestive bio-processing (elephant dung coffee) and commonly known processing methods. *Antioxidants* **2020**, *9* (5). DOI: <https://doi.org/10.3390/antiox9050408>.
117. Kang, D. E.; Lee, H. U.; Davaatseren, M.; Chung, M. S. Comparison of acrylamide and furan concentrations, antioxidant activities, and volatile profiles in cold or hot brew coffees. *Food Sci. Biotechnol.* **2020**, *29* (1), 141-148. DOI: <https://doi.org/10.1007/s10068-019-00644-2>.
118. Kulapichitr, F.; Borompichaichartkul, C.; Pratontep, S.; Lopetcharat, K.; Boonbumrung, S.; Suppavorasatit, I. Differences in volatile compounds and antioxidant activity of ripe and unripe green coffee beans (*Coffea arabica* L. 'Catimor'). *Acta Hortic.* **2017**, 1179, 261-268. DOI: <https://doi.org/10.17660/ActaHortic.2017.1179.41>.
119. Ludwig, I. A.; Sánchez, L.; De Peña, M. P.; Cid, C. Contribution of volatile compounds to the antioxidant capacity of coffee. *Food Res. Int.* **2014**, *61*, 67-74. DOI: <https://doi.org/10.1016/j.foodres.2014.03.045>.
120. Stadler, R. H.; Fay, L. B. Antioxidative Reactions of Caffeine: Formation of 8-Oxocaffeine (1,3,7-Trimethyluric Acid) in Coffee Subjected to Oxidative Stress. *J. Agric. Food Chem.* **1995**, *43* (5), 1332-1338. DOI: <https://doi.org/10.1021/jf00053a038>.
121. Miłek, M.; Młodecki, Ł.; Dżugan, M. Caffeine Content and Antioxidant Activity of Various Brews of Specialty Grade Coffee. *Acta Sci. Pol., Technol. Aliment.* **2021**, *20* (2), 179-188. DOI: <https://doi.org/10.17306/J.AFS.2021.0890>.
122. Šeremet, D.; Fabečić, P.; Cebin, A. V.; Jarić, A. M.; Pudić, R.; Komes, D. Antioxidant and Sensory Assessment of Innovative Coffee Blends of Reduced Caffeine Content. *Molecules* **2022**, *27* (2). DOI: <https://doi.org/10.3390/molecules27020448>.
123. León-Carmona, J. R.; Galano, A. Is caffeine a good scavenger of oxygenated free radicals? *J. Phys. Chem. B* **2011**, *115* (15), 4538-4546. DOI: <https://doi.org/10.1021/jp201383y>.
124. Prior, R. L.; Wu, X.; Schaich, K. Standardized methods for the determination of antioxidant capacity and phenolics in foods and dietary supplements. *J. Agric. Food Chem.* **2005**, *53* (10), 4290-4302. DOI: <https://doi.org/10.1021/jf0502698>.
125. Frankel, E. N.; Meyer, A. S. The problems of using one-dimensional methods to evaluate multifunctional food and biological antioxidants. *J. Sci. Food Agric.* **2000**, *80* (13), 1925-1941. DOI: <https://doi.org/10.1021/jf103813t>.
126. Galano, A.; Alvarez-Idaboy, J. R. A computational methodology for accurate predictions of rate constants in solution: Application to the assessment of primary antioxidant activity. *J. Comput. Chem.* **2013**, *34* (28), 2430-2445. DOI: <https://doi.org/10.1002/jcc.23409>.
127. Yashin, A.; Yashin, Y.; Wang, J. Y.; Nemzer, B. Antioxidant and antiradical activity of coffee. *Antioxidants* **2013**, *2* (4), 230-245. DOI: <https://doi.org/10.3390/antiox2040230>.
128. Febrianto, N. A.; Zhu, F. Coffee bean processing: Emerging methods and their effects on chemical, biological and sensory properties. *Food Chem.* **2023**, 412. DOI: <https://doi.org/10.1016/j.foodchem.2023.135489>.
129. Saud, S.; Salamatullah, A. M. Relationship between the chemical composition and the biological functions of coffee. *Molecules* **2021**, *26* (24). DOI: <https://doi.org/10.3390/molecules26247634>.

130. Hall, R. D.; Trevisan, F.; de Vos, R. C. H. Coffee berry and green bean chemistry – Opportunities for improving cup quality and crop circularity. *Food Res. Int.* **2022**, 151. DOI: <https://doi.org/10.1016/j.foodres.2021.110825>.
131. Kusumah, J.; Gonzalez de Mejia, E. Coffee constituents with antiadipogenic and antidiabetic potentials: A narrative review. *Food Chem. Toxicol.* **2022**, 161. DOI: <https://doi.org/10.1016/j.fct.2022.112821>.
132. Munyendo, L. M.; Njoroge, D. M.; Owaga, E. E.; Mugendi, B. Coffee phytochemicals and post-harvest handling—A complex and delicate balance. *J. Food Compos. Anal.* **2021**, 102. DOI: <https://doi.org/10.1016/j.jfca.2021.103995>.
133. Pua, A.; Goh, R. M. V.; Huang, Y.; Tang, V. C. Y.; Ee, K. H.; Cornuz, M.; Liu, S. Q.; Lassabliere, B.; Yu, B. Recent advances in analytical strategies for coffee volatile studies: Opportunities and challenges. *Food Chem.* **2022**, 388. DOI: <https://doi.org/10.1016/j.foodchem.2022.132971>.
134. Van Dijk, A. E.; Olthof, M. R.; Meeuse, J. C.; Seebus, E.; Heine, R. J.; Van Dam, R. M. Acute effects of decaffeinated coffee and the major coffee components chlorogenic acid and trigonelline on glucose tolerance. *Diabetes Care* **2009**, 32 (6), 1023-1025. DOI: <https://doi.org/10.2337/dc09-0207>.
135. Chen, X. A review on coffee leaves: Phytochemicals, bioactivities and applications. *Crit. Rev. Food Sci. Nutr.* **2019**, 59 (6), 1008-1025. DOI: <https://doi.org/10.1080/10408398.2018.1546667>.
136. Prakash, I.; R, S. S.; P, S. H.; Kumar, P.; Om, H.; Basavaraj, K.; Murthy, P. S. Metabolomics and volatile fingerprint of yeast fermented robusta coffee: A value added coffee. *LWT* **2022**, 154. DOI: <https://doi.org/10.1016/j.lwt.2021.112717>.
137. Sualeh, A.; Tolessa, K.; Mohammed, A. Biochemical composition of green and roasted coffee beans and their association with coffee quality from different districts of southwest Ethiopia. *Heliyon* **2020**, 6 (12). DOI: <https://doi.org/10.1016/j.heliyon.2020.e05812>.
138. Campa, C.; Ballester, J. F.; Doubeau, S.; Dussert, S.; Hamon, S.; Noirot, M. Trigonelline and sucrose diversity in wild Coffea species. *Food Chem.* **2004**, 88 (1), 39-43. DOI: <https://doi.org/10.1016/j.foodchem.2004.01.020>.
139. Campa, C.; Doubeau, S.; Dussert, S.; Hamon, S.; Noirot, M. Qualitative relationship between caffeine and chlorogenic acid contents among wild Coffea species. *Food Chem.* **2005**, 93 (1), 135-139. DOI: <https://doi.org/10.1016/j.foodchem.2004.10.015>.
140. Dias, E. C.; Borém, F. M.; Pereira, R. G. F. A.; Guerreiro, M. C. Amino acid profiles in unripe Arabica coffee fruits processed using wet and dry methods. *Eur. Food Res. Technol.* **2012**, 234 (1), 25-32. DOI: <https://doi.org/10.1007/s00217-011-1607-5>.
141. Dong, W.; Tan, L.; Zhao, J.; Hu, R.; Lu, M. Characterization of fatty acid, amino acid and volatile compound compositions and bioactive components of seven coffee (*Coffea robusta*) cultivars grown in Hainan Province, China. *Molecules* **2015**, 20 (9), 16687-16708. DOI: <https://doi.org/10.3390/molecules200916687>.
142. Fitri, Laga, A.; Dwyana, Z.; Tawali, A. B. Composition of amino acids and fatty acids on luwak coffee processing. *Food Res.* **2021**, 5 (3), 60-64. DOI: [https://doi.org/10.26656/fr.2017.5\(3\).637](https://doi.org/10.26656/fr.2017.5(3).637).
143. Macheiner, L.; Schmidt, A.; Mayer, H. K. Green coffee derived supplements and infusions as a source of polyamines and free amino acids. *Eur. Food Res. Technol.* **2021**, 247 (1), 85-99. DOI: <https://doi.org/10.1007/s00217-020-03609-6>.
144. Dong, W.; Hu, R.; Chu, Z.; Zhao, J.; Tan, L. Effect of different drying techniques on bioactive components, fatty acid composition, and volatile profile of robusta coffee beans. *Food Chem.* **2017**, 234, 121-130. DOI: <https://doi.org/10.1016/j.foodchem.2017.04.156>.
145. Esquivel, P.; Viñas, M.; Steingass, C. B.; Gruschwitz, M.; Guevara, E.; Carle, R.; Schweiggert, R. M.; Jiménez, V. M. Coffee (*Coffea arabica* L.) by-Products as a Source of Carotenoids and Phenolic Compounds—Evaluation of Varieties With Different Peel Color. *Front. Sustain. Food Syst.* **2020**, 4. DOI: <https://doi.org/10.3389/fsufs.2020.590597>.
146. Simkin, A. J.; Kuntz, M.; Moreau, H.; McCarthy, J. Carotenoid profiling and the expression of carotenoid biosynthetic genes in developing coffee grain. *Plant Physiol. Biochem.* **2010**, 48 (6), 434-442. DOI: <https://doi.org/10.1016/j.plaphy.2010.02.007>.

147. Koshima, Y.; Kitamura, Y.; Islam, M. Z.; Kokawa, M. Quantitative and qualitative evaluation of fatty acids in coffee oil and coffee residue. *Food Sci. Technol. Res.* **2020**, *26* (4), 545-552. DOI: <https://doi.org/10.3136/FSTR.26.545>.
148. Peñuela-Martínez, A. E.; Zapata-Zapata, A. E.; Durango-Restrepo, D. L. Performance of different fermentation methods and the effect on coffee quality (Coffea arabica L.). *Coffee Sci.* **2018**, *13* (4), 465-476. DOI: <https://doi.org/10.25186/cs.v13i4.1486>.
149. Yeager, S. E.; Batali, M. E.; Guinard, J. X.; Ristenpart, W. D. Acids in coffee: A review of sensory measurements and meta-analysis of chemical composition. *Crit. Rev. Food Sci. Nutr.* **2021**, *63* (8), 1010-1036. DOI: <https://doi.org/10.1080/10408398.2021.1957767>.
150. Pereira, P. V.; Bravim, D. G.; Grillo, R. P.; Bertoli, L. D.; Osório, V. M.; da Silva Oliveira, D.; da Cruz Pedrozo Miguel, M. G.; Schwan, R. F.; de Assis Silva, S.; Coelho, J. M.; Bernardes, P. C. Microbial diversity and chemical characteristics of Coffea canephora grown in different environments and processed by dry method. *World J. Microbiol. Biotechnol.* **2021**, *37* (3). DOI: <https://doi.org/10.1007/s11274-021-03017-2>.
151. Badmos, S.; Lee, S. H.; Kuhnert, N. Comparison and quantification of chlorogenic acids for differentiation of green Robusta and Arabica coffee beans. *Food Res. Int.* **2019**, *126*. DOI: <https://doi.org/10.1016/j.foodres.2019.108544>.
152. Köseoglu Yilmaz, P.; Kolak, U. SPE-HPLC Determination of Chlorogenic and Phenolic Acids in Coffee. *J. Chromatogr. Sci.* **2017**, *55* (7), 712-718. DOI: <https://doi.org/10.1093/chromsci/bmx025>.
153. Marnet, C.; Actis-Goretta, L.; Renouf, M.; Giuffrida, F. Quantification of phenolic acids and their methylates, glucuronides, sulfates and lactones metabolites in human plasma by LC-MS/MS after oral ingestion of soluble coffee. *J. Pharm. Biomed. Anal.* **2014**, *88*, 617-625. DOI: <https://doi.org/10.1016/j.jpba.2013.10.009>.
154. Somporn, C.; Kamtuo, A.; Theerakulpisut, P.; Siriamornpun, S. Effect of shading on yield, sugar content, phenolic acids and antioxidant property of coffee beans (Coffea Arabica L. cv. Catimor) harvested from north-eastern Thailand. *J. Sci. Food Agric.* **2012**, *92* (9), 1956-1963. DOI: <https://doi.org/10.1002/jsfa.5568>.
155. Kishimoto, N.; Kakino, Y.; Iwai, K.; Mochida, K.; Fujita, T. In vitro antibacterial, antimutagenic and anti-influenza virus activity of caffeic acid phenethyl esters. *Biocontrol Sci.* **2005**, *10* (4), 155-161. DOI: <https://doi.org/10.4265/bio.10.155>.
156. Dos Santos, R. A.; Prado, M. A.; Pertierra, R. E.; Palacios, H. A. Analysis of sugars and chlorogenic acid in coffee harvested at different ripening stages and after processing. *Braz. J. Food Technol.* **2018**, *21*. DOI: <https://doi.org/10.1590/1981-6723.16317>.
157. Chindapan, N.; Soydok, S.; Devahastin, S. Roasting Kinetics and Chemical Composition Changes of Robusta Coffee Beans During Hot Air and Superheated Steam Roasting. *J. Food Sci.* **2019**, *84* (2), 292-302. DOI: <https://doi.org/10.1111/1750-3841.14422>.
158. Wang, X.; Peng, X.; Lu, J.; Hu, G.; Qiu, M. Ent-kaurane diterpenoids from the cherries of Coffea arabica. *Fitoterapia* **2019**, *132*, 7-11. DOI: <https://doi.org/10.1016/j.fitote.2018.08.023>.
159. Wang, X.; Meng, Q.; Peng, X.; Hu, G.; Qiu, M. Identification of new diterpene esters from green Arabica coffee beans, and their platelet aggregation accelerating activities. *Food Chem.* **2018**, *263*, 251-257. DOI: <https://doi.org/10.1016/j.foodchem.2018.04.081>.
160. Shu, Y.; Liu, J. Q.; Peng, X. R.; Wan, L. S.; Zhou, L.; Zhang, T.; Qiu, M. H. Characterization of diterpenoid glucosides in roasted puer coffee beans. *J. Agric. Food Chem.* **2014**, *62* (12), 2631-2637. DOI: <https://doi.org/10.1021/jf500788t>.
161. Chu, R.; Wan, L. S.; Peng, X. R.; Yu, M. Y.; Zhang, Z. R.; Zhou, L.; Li, Z. R.; Qiu, M. H. Characterization of New Ent-kaurane Diterpenoids of Yunnan Arabica Coffee Beans. *Nat. Prod. Bioprospect.* **2016**, *6* (4), 217-223. DOI: <https://doi.org/10.1007/s13659-016-0099-1>.
162. Wang, X.; Peng, X. R.; Lu, J.; Hu, G. L.; Qiu, M. H. New Dammarane Triterpenoids, Caffruones A-D, from the Cherries of Coffea arabica. *Nat. Prod. Bioprospect.* **2018**, *8* (6), 413-418. DOI: <https://doi.org/10.1007/s13659-018-0181-y>.

163. Lang, R.; Fromme, T.; Beusch, A.; Lang, T.; Klingenspor, M.; Hofmann, T. Raw coffee based dietary supplements contain carboxyatractyligenin derivatives inhibiting mitochondrial adenine-nucleotide-translocase. *Food Chem. Toxicol.* **2014**, *70*, 198-204. DOI: <https://doi.org/10.1016/j.fct.2014.05.017>.
164. Barbosa, M. D. S. G.; Scholz, M. B. D. S.; Kitzberger, C. S. G.; Benassi, M. D. T. Correlation between the composition of green Arabica coffee beans and the sensory quality of coffee brews. *Food Chem.* **2019**, *292*, 275-280. DOI: <https://doi.org/10.1016/j.foodchem.2019.04.072>.
165. Caporaso, N.; Whitworth, M. B.; Cui, C.; Fisk, I. D. Variability of single bean coffee volatile compounds of Arabica and robusta roasted coffees analysed by SPME-GC-MS. *Food Res. Int.* **2018**, *108*, 628-640. DOI: <https://doi.org/10.1016/j.foodres.2018.03.077>.
166. Piccino, S.; Boulanger, R.; Descroix, F.; Sing, A. S. C. Aromatic composition and potent odorants of the "specialty coffee" brew "Bourbon Pointu" correlated to its three trade classifications. *Food Res. Int.* **2014**, *61*, 264-271. DOI: <https://doi.org/10.1016/j.foodres.2013.07.034>.
167. Angeloni, S.; Mustafa, A. M.; Abouelenein, D.; Alessandrini, L.; Acquaticci, L.; Nzekoue, F. K.; Petrelli, R.; Sagratini, G.; Vittori, S.; Torregiani, E.; Caprioli, G. Characterization of the aroma profile and main key odorants of espresso coffee. *Molecules* **2021**, *26* (13). DOI: <https://doi.org/10.3390/molecules26133856>.
168. Kim, H. J.; Hong, D. L.; Yu, J. W.; Lee, S. M.; Lee, Y. B. Identification of headspace volatile compounds of blended coffee and application to principal component analysis. *Prev. Nutr. Food Sci.* **2019**, *24* (2), 217-223. DOI: <https://doi.org/10.3746/pnf.2019.24.2.217>.
169. Lee, K. G.; Shibamoto, T. Analysis of volatile components isolated from Hawaiian green coffee beans (*Coffea arabica* L.). *Flavour Fragr. J.* **2002**, *17* (5), 349-351. DOI: <https://doi.org/10.1002/ffj.1067>.
170. Sarghini, F.; Fasano, E.; De Vivo, A.; Tricarico, M. C. Influence of roasting process in six coffee Arabica cultivars: Analysis of volatile components profiles. *Chem. Eng. Trans.* **2019**, *75*, 295-300. DOI: <https://doi.org/10.3303/CET1975050>.
171. Butt, M. S.; Sultan, M. T. Coffee and its consumption: Benefits and risks. *Crit. Rev. Food Sci. Nutr.* **2011**, *51* (4), 363-373. DOI: <https://doi.org/10.1080/10408390903586412>.
172. Colombo, R.; Papetti, A. Decaffeinated coffee and its benefits on health: focus on systemic disorders. *Crit. Rev. Food Sci. Nutr.* **2021**, *61* (15), 2506-2522. DOI: <https://doi.org/10.1080/10408398.2020.1779175>.
173. Dirks-Naylor, A. J. The benefits of coffee on skeletal muscle. *Life Sci.* **2015**, *143*, 182-186. DOI: <https://doi.org/10.1016/j.lfs.2015.11.005>.
174. Pourshahidi, L. K.; Navarini, L.; Petracco, M.; Strain, J. J. A Comprehensive Overview of the Risks and Benefits of Coffee Consumption. *Compr. Rev. Food Sci. Food Saf.* **2016**, *15* (4), 671-684. DOI: <https://doi.org/10.1111/1541-4337.12206>.
175. dos Santos, H. D.; Boffo, E. F. Coffee beyond the cup: analytical techniques used in chemical composition research—a review. *Eur. Food Res. Technol.* **2021**, *247* (4), 749-775. DOI: <https://doi.org/10.1007/s00217-020-03679-6>.
176. Barrea, L.; Pugliese, G.; Frias-Toral, E.; El Ghoch, M.; Castellucci, B.; Chapela, S. P.; Carignano, M. D. L. A.; Laudisio, D.; Savastano, S.; Colao, A.; Muscogiuri, G. Coffee consumption, health benefits and side effects: a narrative review and update for dietitians and nutritionists. *Crit. Rev. Food Sci. Nutr.* **2023**, *63* (9), 1238-1261. DOI: <https://doi.org/10.1080/10408398.2021.1963207>.
177. Jeong, J. M.; Lee, K. I.; Kim, S. M. Simultaneous determination of benzoic Acid, Caffeic acid and Chlorogenic acid in seeds of *Eriobotrya japonica* and their antibacterial Effect. *J. Appl. Biol. Chem.* **2014**, *57* (1), 89-93. DOI: <https://doi.org/10.3839/jabc.2014.014>.
178. Park, M. Y.; Kang, D. H. Antibacterial Activity of Caffeic Acid Combined with UV-A Light against *Escherichia coli* O157:H7, *Salmonella enterica* Serovar Typhimurium, and *Listeria monocytogenes*. *Appl. Environ. Microbiol.* **2021**, *87* (15). DOI: <https://doi.org/10.1128/AEM.00631-21>.
179. Pinho, E.; Soares, G.; Henriques, M. Evaluation of antibacterial activity of caffeic acid encapsulated by β -cyclodextrins. *J. Microencapsul.* **2015**, *32* (8), 804-810. DOI: <https://doi.org/10.3109/02652048.2015.1094531>.

180. Niu, Y.; Wang, K.; Zheng, S.; Wang, Y.; Ren, Q.; Li, H.; Ding, L.; Li, W.; Zhang, L. Antibacterial effect of caffeic acid phenethyl ester on cariogenic bacteria and streptococcus mutans biofilms. *Antimicrob. Agents Chemother.* **2020**, *64* (9). DOI: <https://doi.org/10.1128/AAC.00251-20>.
181. Rojas-González, A.; Figueroa-Hernández, C. Y.; González-Rios, O.; Suárez-Quiroz, M. L.; González-Amaro, R. M.; Hernández-Estrada, Z. J.; Rayas-Duarte, P. Coffee Chlorogenic Acids Incorporation for Bioactivity Enhancement of Foods: A Review. *Molecules* **2022**, *27* (11). DOI: <https://doi.org/10.3390/molecules27113400>.
182. Elbestawy, M. K. M.; El-Sherbiny, G. M.; Moghannem, S. A. Antibacterial, Antibiofilm and Anti-Inflammatory Activities of Eugenol Clove Essential Oil against Resistant *Helicobacter pylori*. *Molecules* **2023**, *28* (6). DOI: <https://doi.org/10.3390/molecules28062448>.
183. Ashrafudoulla, M.; Mizan, M. F. R.; Ha, A. J. W.; Park, S. H.; Ha, S. D. Antibacterial and antibiofilm mechanism of eugenol against antibiotic resistance *Vibrio parahaemolyticus*. *Food Microbiol.* **2020**, *91*. DOI: <https://doi.org/10.1016/j.fm.2020.103500>.
184. Bai, X.; Li, X.; Liu, X.; Xing, Z.; Su, R.; Wang, Y.; Xia, X.; Shi, C. Antibacterial Effect of Eugenol on *Shigella flexneri* and Its Mechanism. *Foods* **2022**, *11* (17). DOI: <https://doi.org/10.3390/foods11172565>.
185. Bezerra, S. R.; Bezerra, A. H.; de Sousa Silveira, Z.; Macedo, N. S.; dos Santos Barbosa, C. R.; Muniz, D. F.; Sampaio dos Santos, J. F.; Melo Coutinho, H. D.; Bezerra da Cunha, F. A. Antibacterial activity of eugenol on the IS-58 strain of *Staphylococcus aureus* resistant to tetracycline and toxicity in *Drosophila melanogaster*. *Microb. Pathog.* **2022**, *164*. DOI: <https://doi.org/10.1016/j.micpath.2022.105456>.
186. Devi, K. P.; Nisha, S. A.; Sakthivel, R.; Pandian, S. K. Eugenol (an essential oil of clove) acts as an antibacterial agent against *Salmonella typhi* by disrupting the cellular membrane. *J. Ethnopharmacol.* **2010**, *130* (1), 107-115. DOI: <https://doi.org/10.1016/j.jep.2010.04.025>.
187. Pavesi, C.; Banks, L. A.; Hudaib, T. Antifungal and antibacterial activities of eugenol and non-polar extract of *Syzygium aromaticum* L. *J. Pharm. Sci. Res.* **2018**, *10* (2), 337-339.
188. Silva, J. C.; Silva Pereira, R. L.; Sampaio de Freitas, T.; Rocha, J. E.; Macedo, N. S.; de Fatima Alves Nonato, C.; Linhares, M. L.; Arruda Tavares, D. S.; Bezerra da Cunha, F. A.; Melo Coutinho, H. D.; et al. Evaluation of antibacterial and toxicological activities of essential oil of *Ocimum gratissimum* L. and its major constituent eugenol. *Food Biosci.* **2022**, *50*. DOI: <https://doi.org/10.1016/j.fbio.2022.102128>.
189. Su, R.; Bai, X.; Liu, X.; Song, L.; Liu, X.; Zhan, X.; Guo, D.; Wang, Y.; Chang, Y.; Shi, C. Antibacterial Mechanism of Eugenol Against *Shigella sonnei* and Its Antibacterial Application in Lettuce Juice. *Foodborne Pathog. Dis.* **2022**, *19* (11), 779-786. DOI: <https://doi.org/10.1089/fpd.2022.0046>.
190. Zhang, L. L.; Zhang, L. F.; Xu, J. G.; Hu, Q. P. Comparison study on antioxidant, DNA damage protective and antibacterial activities of eugenol and isoeugenol against several foodborne pathogens. *Food Nutr. Res.* **2017**, *61*. DOI: <https://doi.org/10.1080/16546628.2017.1353356>.
191. Amani, F.; Rezaei, A.; Kharazmi, M. S.; Jafari, S. M. Loading ferulic acid into β -cyclodextrin nanospheres; antibacterial activity, controlled release and application in pomegranate juice as a copigment agent. *Colloids Surf. Physicochem. Eng. Aspects* **2022**, *649*. DOI: <https://doi.org/10.1016/j.colsurfa.2022.129454>.
192. Borges, A.; Ferreira, C.; Saavedra, M. J.; Simões, M. Antibacterial activity and mode of action of ferulic and gallic acids against pathogenic bacteria. *Microb. Drug Resist.* **2013**, *19* (4), 256-265. DOI: <https://doi.org/10.1089/mdr.2012.0244>.
193. Ordoñez, R.; Atarés, L.; Chiralt, A. Antibacterial properties of cinnamic and ferulic acids incorporated to starch and PLA monolayer and multilayer films. *Food Control* **2022**, *136*. DOI: <https://doi.org/10.1016/j.foodcont.2022.108878>.
194. Tu, Q. B.; Shi, H. C.; Li, P.; Sheng, S.; Wu, F. A. Antibacterial Activity of Ferulic Acid Ester against *Ralstonia solanacearum* and Its Synergy with Essential Oils. *Sustainability* **2022**, *14* (24). DOI: <https://doi.org/10.3390/su142416348>.

195. Sung, W. S.; Jung, H. J.; Lee, I. S.; Kim, H. S.; Lee, D. G. Antimicrobial effect of furaneol against human pathogenic bacteria and fungi. *J. Microbiol. Biotechnol.* **2006**, *16* (3), 349-354.
196. Aulestia-Viera, P. V.; Gontijo, S. M. L.; Gomes, A. D. M.; Sinisterra, R. D.; Rocha, R. G.; Cortés, M. E.; dos Santos, M. F.; Borsatti, M. A. Guaiacol/ β -cyclodextrin for rapid healing of dry socket: antibacterial activity, cytotoxicity, and bone repair—an animal study. *Oral Maxillofac. Surg.* **2019**, *23* (1), 53-61. DOI: <https://doi.org/10.1007/s10006-019-00747-4>.
197. Cooper, R. A. Inhibition of biofilms by glucose oxidase, lactoperoxidase and guaiacol: The active antibacterial component in an enzyme alginate. *Int. Wound J.* **2013**, *10* (6), 630-637. DOI: <https://doi.org/10.1111/iwj.12083>.
198. Mangal, S.; Chhibber, S.; Singh, V.; Harjai, K. Guaiacol augments quorum quenching potential of ciprofloxacin against *Pseudomonas aeruginosa*. *J. Appl. Microbiol.* **2022**, *133* (4), 2235-2254. DOI: <https://doi.org/10.1111/jam.15787>.
199. Galvão, J. L. F. M.; Rosa, L. L. S.; Neto, H. D.; Silva, D. F.; Nóbrega, J. R.; Cordeiro, L. V.; de Figueiredo, P. T. R.; Andrade Júnior, F. P.; Filho, A. A. O.; Lima, E. O. Antibacterial effect of isoeugenol against *Pseudomonas aeruginosa*. *Braz. J. Pharm. Sci.* **2022**, *58*. DOI: <https://doi.org/10.1590/s2175-97902022e20075>.
200. Krogsgård Nielsen, C.; Kjems, J.; Mygind, T.; Snabe, T.; Schwarz, K.; Serfert, Y.; Meyer, R. L. Antimicrobial effect of emulsion-encapsulated isoeugenol against biofilms of food pathogens and spoilage bacteria. *Int. J. Food Microbiol.* **2017**, *242*, 7-12. DOI: <https://doi.org/10.1016/j.jfoodmicro.2016.11.002>.
201. Nielsen, C. K.; Subbiahdoss, G.; Zeng, G.; Salmi, Z.; Kjems, J.; Mygind, T.; Snabe, T.; Meyer, R. L. Antibacterial isoeugenol coating on stainless steel and polyethylene surfaces prevents biofilm growth. *J. Appl. Microbiol.* **2018**, *124* (1), 179-187. DOI: <https://doi.org/10.1111/jam.13634>.
202. Siva, S.; Li, C.; Cui, H.; Lin, L. Encompassment of isoeugenol in 2-hydroxypropyl- β -cyclodextrin using ultrasonication: Characterization, antioxidant and antibacterial activities. *J. Mol. Liq.* **2019**, *296*. DOI: <https://doi.org/10.1016/j.molliq.2019.111777>.
203. Ajiboye, T. O.; Habibu, R. S.; Saidu, K.; Haliru, F. Z.; Ajiboye, H. O.; Aliyu, N. O.; Ibitoye, O. B.; Uwazie, J. N.; Muritala, H. F.; Bello, S. A.; et al. Involvement of oxidative stress in protocatechuic acid-mediated bacterial lethality. *Microbiol. Open* **2017**, *6* (4). DOI: <https://doi.org/10.1002/mbo3.472>.
204. Bernal-Mercado, A. T.; Vazquez-Armenta, F. J.; Tapia-Rodríguez, M. R.; Islas-Osuna, M. A.; Mata-Haro, V.; Gonzalez-Aguilar, G. A.; Lopez-Zavala, A. A.; Ayala-Zavala, J. F. Comparison of single and combined use of catechin, protocatechuic, and vanillic acids as antioxidant and antibacterial agents against uropathogenic *Escherichia coli* at planktonic and biofilm levels. *Molecules* **2018**, *23* (11). DOI: <https://doi.org/10.3390/molecules23112813>.
205. Chao, C. Y.; Yin, M. C. Antibacterial effects of roselle calyx extracts and protocatechuic acid in ground beef and apple juice. *Foodborne Pathog. Dis.* **2009**, *6* (2), 201-206. DOI: <https://doi.org/10.1089/fpd.2008.0187>.
206. Liu, K. S.; Tsao, S. M.; Yin, M. C. In vitro antibacterial activity of roselle calyx and protocatechuic acid. *Phytother. Res.* **2005**, *19* (11), 942-945. DOI: <https://doi.org/10.1002/ptr.1760>.
207. Stojković, D. S.; Živković, J.; Soković, M.; Glamočlija, J.; Ferreira, I. C. F. R.; Janković, T.; Maksimović, Z. Antibacterial activity of *Veronica montana* L. extract and of protocatechuic acid incorporated in a food system. *Food Chem. Toxicol.* **2013**, *55*, 209-213. DOI: <https://doi.org/10.1016/j.fct.2013.01.005>.
208. Wu, M.; Tian, L.; Fu, J.; Liao, S.; Li, H.; Gai, Z.; Gong, G. Antibacterial mechanism of Protocatechuic acid against *Yersinia enterocolitica* and its application in pork. *Food Control* **2022**, *133*. DOI: <https://doi.org/10.1016/j.foodcont.2021.108573>.
209. Buathong, R.; Chamchumroon, V.; Schinnerl, J.; Bacher, M.; Santimaleeworagun, W.; Kraichak, E.; Vajrodaya, S. Chemovariation and antibacterial activity of extracts and isolated compounds from species of *Ixora* and *Greenea* (Ixoroideae, Rubiaceae). *PeerJ* **2019**, *2019* (5). DOI: <https://doi.org/10.7717/peerj.6893>.
210. Napiroon, T.; Bacher, M.; Balslev, H.; Tawaitakham, K.; Santimaleeworagun, W.; Vajrodaya, S. Scopoletin from *Lasianthus lucidus* Blume (Rubiaceae): A potential antimicrobial against multidrug-resistant

- Pseudomonas aeruginosa*. *J. Appl. Pharm. Sci.* **2018**, 8 (9), 1-6. DOI: <https://doi.org/10.7324/JAPS.2018.8901>.
211. De La Cruz-Sánchez, N. G.; Gómez-Rivera, A.; Alvarez-Fitz, P.; Ventura-Zapata, E.; Pérez-García, M. D.; Avilés-Flores, M.; Gutiérrez-Román, A. S.; González-Cortazar, M. Antibacterial activity of *Morinda citrifolia* Linneo seeds against Methicillin-Resistant *Staphylococcus* spp. *Microb. Pathog.* **2019**, 128, 347-353. DOI: <https://doi.org/10.1016/j.micpath.2019.01.030>.
212. Firmansyah, A.; Winingsih, W.; Manobi, J. D. Y. Review of scopoletin: Isolation, analysis process, and pharmacological activity. *Biointerface Res. Appl. Chem.* **2021**, 11 (4), 12006-12019. DOI: <https://doi.org/10.33263/BRIAC114.1200612019>.
213. Mfonku, N. A.; Tadjong, A. T.; Kamsu, G. T.; Kodjio, N.; Ren, J.; Mbah, J. A.; Gatsing, D.; Zhan, J. Isolation and characterization of antisalmonellal anthraquinones and coumarins from *Morinda lucida* Benth. (Rubiaceae). *Chem. Pap.* **2021**, 75 (5), 2067-2073. DOI: <https://doi.org/10.1007/s11696-020-01460-3>.
214. Naz, F.; Kumar, M.; Koley, T.; Sharma, P.; Haque, M. A.; Kapil, A.; Kumar, M.; Kaur, P.; Ethayathulla, A. S. Screening of plant-based natural compounds as an inhibitor of FtsZ from *Salmonella Typhi* using the computational, biochemical and in vitro cell-based studies. *Int. J. Biol. Macromol.* **2022**, 219, 428-437. DOI: <https://doi.org/10.1016/j.ijbiomac.2022.07.241>.
215. Qian, W.; Fu, Y.; Liu, M.; Wang, T.; Zhang, J.; Yang, M.; Sun, Z.; Li, X.; Li, Y. In vitro antibacterial activity and mechanism of vanillic acid against carbapenem-resistant *Enterobacter cloacae*. *Antibiotics* **2019**, 8 (4). DOI: <https://doi.org/10.3390/antibiotics8040220>.
216. Qian, W.; Yang, M.; Wang, T.; Sun, Z.; Liu, M.; Zhang, J.; Zeng, Q.; Cai, C.; Li, Y. Antibacterial Mechanism of Vanillic Acid on Physiological, Morphological, and Biofilm Properties of Carbapenem-Resistant *Enterobacter hormaechei*. *J. Food Prot.* **2020**, 83 (4), 576-583. DOI: <https://doi.org/10.4315/JFP-19-469>.
217. Luo, Y.; Wang, C. Z.; Sawadogo, R.; Yuan, J.; Zeng, J.; Xu, M.; Tan, T.; Yuan, C. S. 4-Vinylguaiaicol, an Active Metabolite of Ferulic Acid by Enteric Microbiota and Probiotics, Possesses Significant Activities against Drug-Resistant Human Colorectal Cancer Cells. *ACS Omega* **2021**, 6 (7), 4551-4561. DOI: <https://doi.org/10.1021/acsomega.0c04394>.
218. Sudhagar, S.; Sathya, S.; Anuradha, R.; Gokulapriya, G.; Geetharani, Y.; Lakshmi, B. S. Inhibition of epidermal growth factor receptor by ferulic acid and 4-vinylguaiaicol in human breast cancer cells. *Biotechnol. Lett.* **2018**, 40 (2), 257-262. DOI: <https://doi.org/10.1007/s10529-017-2475-2>.
219. Cavin, C.; Holzhaeuser, D.; Scharf, G.; Constable, A.; Huber, W. W.; Schilter, B. Cafestol and kahweol, two coffee specific diterpenes with anticarcinogenic activity. *Food Chem. Toxicol.* **2002**, 40 (8), 1155-1163. DOI: [https://doi.org/10.1016/S0278-6915\(02\)00029-7](https://doi.org/10.1016/S0278-6915(02)00029-7).
220. Ren, Y.; Wang, C.; Xu, J.; Wang, S. Cafestol and kahweol: A review on their bioactivities and pharmacological properties. *Int. J. Mol. Sci.* **2019**, 20 (17). DOI: <https://doi.org/10.3390/ijms20174238>.
221. Iwamoto, H.; Izumi, K.; Natsagdorj, A.; Naito, R.; Marino, T.; Kadomoto, S.; Hiratsuka, K.; Shigehara, K.; Radono, Y.; Mizorami, A.; et al. Coffee diterpenes, kahweol acetate and cafestol, synergistically induce apoptosis and inhibit the epithelial-mesenchymal transition of prostate cancer cells. *Nishinohon J. Urol.* **2019**, 81 (3), 364-371.
222. Lee, K. A.; Chae, J. I.; Shim, J. H. Natural diterpenes from coffee, cafestol and kahweol induce apoptosis through regulation of specificity protein 1 expression in human malignant pleural mesothelioma. *J. Biomed. Sci.* **2012**, 19 (1). DOI: <https://doi.org/10.1186/1423-0127-19-60>.
223. Bovilla, V.; Anantharaju, P.; Dornadula, S.; Veeresh, P.; Kuruburu, M.; Bettada, V.; Ramkumar, K.; Madhunapantula, S. Caffeic acid and protocatechuic acid modulate Nrf2 and inhibit Ehrlich ascites carcinomas in mice. *Asian Pac. J. Trop. Biomed.* **2021**, 11 (6), 244-253. DOI: <https://doi.org/10.4103/2221-1691.314045>.
224. Brautigan, D. L.; Gielata, M.; Heo, J.; Kubicka, E.; Wilkins, L. R. Selective toxicity of caffeic acid in hepatocellular carcinoma cells. *Biochem. Biophys. Res. Commun.* **2018**, 505 (2), 612-617. DOI: <https://doi.org/10.1016/j.bbrc.2018.09.155>.
225. Celińska-Janowicz, K.; Zaręba, I.; Lazarek, U.; Teul, J.; Tomczyk, M.; Pałka, J.; Milytk, W. Constituents of propolis: Chrysin, caffeic acid, p-coumaric acid, and ferulic acid induce PRODH/POX-dependent

- apoptosis in human tongue squamous cell carcinoma cell (CAL-27). *Front. Pharmacol.* **2018**, 9 (APR). DOI: <https://doi.org/10.3389/fphar.2018.00336>.
226. Matejczyk, M.; Świsłocka, R.; Golonko, A.; Lewandowski, W.; Hawrylik, E. Cytotoxic, genotoxic and antimicrobial activity of caffeic and rosmarinic acids and their lithium, sodium and potassium salts as potential anticancer compounds. *Adv. Med. Sci.* **2018**, 63 (1), 14-21. DOI: <https://doi.org/10.1016/j.advms.2017.07.003>.
227. Tyszka-Czochara, M.; Bukowska-Strakova, K.; Kocemba-Pilarczyk, K. A.; Majka, M. Caffeic acid targets AMPK signaling and regulates tricarboxylic acid cycle anaplerosis while metformin downregulates HIF-1 α -induced glycolytic enzymes in human cervical squamous cell carcinoma lines. *Nutrients* **2018**, 10 (7). DOI: <https://doi.org/10.3390/nu10070841>.
228. Tyszka-Czochara, M.; Konieczny, P.; Majka, M. Caffeic acid expands anti-tumor effect of metformin in human metastatic cervical carcinoma HTB-34 cells: Implications of AMPK activation and impairment of fatty acids de novo biosynthesis. *Int. J. Mol. Sci.* **2017**, 18 (2). DOI: <https://doi.org/10.3390/ijms18020462>.
229. Chang, K. S.; Tsui, K. H.; Hsu, S. Y.; Sung, H. C.; Lin, Y. H.; Hou, C. P.; Yang, P. S.; Chen, C. L.; Feng, T. H.; Juang, H. H. The Antitumor Effect of Caffeic Acid Phenethyl Ester by Downregulating Mucosa-Associated Lymphoid Tissue 1 via AR/p53/NF- κ B Signaling in Prostate Carcinoma Cells. *Cancers (Basel)* **2022**, 14 (2). DOI: <https://doi.org/10.3390/cancers14020274>.
230. Hou, C. P.; Tsui, K. H.; Chang, K. S.; Sung, H. C.; Hsu, S. Y.; Lin, Y. H.; Yang, P. S.; Chen, C. L.; Feng, T. H.; Juang, H. H. Caffeic acid phenethyl ester inhibits the growth of bladder carcinoma cells by upregulating growth differentiation factor 15. *Biomed. J.* **2022**, 45 (5), 763-775. DOI: <https://doi.org/10.1016/j.bj.2021.10.006>.
231. Kapare, H.; Nagaraj, S.; Wakalkar, S.; Rathi, K. Caffeic Acid Phenethyl Ester: A Potential Anticancer Bioactive Constituent of Propolis. *Curr. Cancer Ther. Rev.* **2022**, 18 (3), 181-192. DOI: <https://doi.org/10.2174/1573394718666220603103458>.
232. Liang, Y.; Feng, G.; Wu, L.; Zhong, S.; Gao, X.; Tong, Y.; Cui, W.; Qin, Y.; Xu, W.; Xiao, X.; et al. Caffeic acid phenethyl ester suppressed growth and metastasis of nasopharyngeal carcinoma cells by inactivating the NF- κ B pathway. *Drug Des. Devel. Ther.* **2019**, 13, 1335-1345. DOI: <https://doi.org/10.2147/DDDT.S199182>.
233. Sung, H. C.; Chang, K. S.; Chen, S. T.; Hsu, S. Y.; Lin, Y. H.; Hou, C. P.; Feng, T. H.; Tsui, K. H.; Juang, H. H. Metallothionein 2A with Antioxidant and Antitumor Activity Is Upregulated by Caffeic Acid Phenethyl Ester in Human Bladder Carcinoma Cells. *Antioxidants* **2022**, 11 (8). DOI: <https://doi.org/10.3390/antiox11081509>.
234. Lu, H.; Tian, Z.; Cui, Y.; Liu, Z.; Ma, X. Chlorogenic acid: A comprehensive review of the dietary sources, processing effects, bioavailability, beneficial properties, mechanisms of action, and future directions. *Compr. Rev. Food Sci. Food Saf.* **2020**, 19 (6), 3130-3158. DOI: <https://doi.org/10.1111/1541-4337.12620>.
235. Abdullah, M. L.; Al-Shabanah, O.; Hassan, Z. K.; Hafez, M. M. Eugenol-induced autophagy and apoptosis in breast cancer cells via pi3k/akt/foxo3a pathway inhibition. *Int. J. Mol. Sci.* **2021**, 22 (17). DOI: <https://doi.org/10.3390/ijms22179243>.
236. Abdullah, M. L.; Hafez, M. M.; Al-Hoshani, A.; Al-Shabanah, O. Anti-metastatic and anti-proliferative activity of eugenol against triple negative and HER2 positive breast cancer cells. *BMC Complement. Altern. Med.* **2018**, 18 (1). DOI: <https://doi.org/10.1186/s12906-018-2392-5>.
237. Al-Kharashi, L. A.; Bakheet, T.; AlHarbi, W. A.; Al-Moghrabi, N.; Aboussekhra, A. Eugenol modulates genomic methylation and inactivates breast cancer-associated fibroblasts through E2F1-dependent downregulation of DNMT1/DNMT3A. *Mol. Carcinog.* **2021**, 60 (11), 784-795. DOI: <https://doi.org/10.1002/mc.23344>.
238. Bezerra, D. P.; Militão, G. C. G.; De Moraes, M. C.; De Sousa, D. P. The dual antioxidant/prooxidant effect of eugenol and its action in cancer development and treatment. *Nutrients* **2017**, 9 (12). DOI: <https://doi.org/10.3390/nu9121367>.
239. Choudhury, P.; Barua, A.; Roy, A.; Pattanayak, R.; Bhattacharyya, M.; Saha, P. Eugenol restricts Cancer Stem Cell population by degradation of β -catenin via N-terminal Ser37 phosphorylation-an in vivo and in vitro experimental evaluation. *Chem. Biol. Interact.* **2020**, 316. DOI: <https://doi.org/10.1016/j.cbi.2020.108938>.

240. Choudhury, P.; Barua, A.; Roy, A.; Pattanayak, R.; Bhattacharyya, M.; Saha, P. Eugenol emerges as an elixir by targeting β -catenin, the central cancer stem cell regulator in lung carcinogenesis: An: In vivo and in vitro rationale. *Food Funct.* **2021**, *12* (3), 1063-1078. DOI: <https://doi.org/10.1039/d0fo02105a>.
241. Cui, Z.; Liu, Z.; Zeng, J.; Chen, L.; Wu, Q.; Mo, J.; Zhang, G.; Song, L.; Xu, W.; Zhang, S.; Guo, X. Eugenol inhibits non-small cell lung cancer by repressing expression of NF- κ B-regulated TRIM59. *Phytother. Res.* **2019**, *33* (5), 1562-1569. DOI: <https://doi.org/10.1002/ptr.6352>.
242. Das, A.; Harshadha, K.; Dhinesh Kannan, S. K.; Hari Raj, K.; Jayaprakash, B. Evaluation of therapeutic potential of Eugenol-A natural derivative of *Syzygium aromaticum* on cervical cancer. *Asian Pac. J. Cancer Prev.* **2018**, *19* (7), 1977-1985. DOI: <https://doi.org/10.22034/APJCP.2018.19.7.1977>.
243. Fangjun, L.; Zhijia, Y. Tumor suppressive roles of eugenol in human lung cancer cells. *Thorac. Cancer* **2018**, *9* (1), 25-29. DOI: <https://doi.org/10.1111/1759-7714.12508>.
244. Fouad, M. A.; Sayed-Ahmed, M. M.; Huwait, E. A.; Hafez, H. F.; Osman, A. M. M. Epigenetic immunomodulatory effect of eugenol and astaxanthin on doxorubicin cytotoxicity in hormonal positive breast Cancer cells. *BMC Pharmacol. Toxicol.* **2021**, *22* (1). DOI: <https://doi.org/10.1186/s40360-021-00473-2>.
245. Ghodousi-Dehnavi, E.; Hosseini, R. H.; Arjmand, M.; Nasri, S.; Zamani, Z. A Metabolomic Investigation of Eugenol on Colorectal Cancer Cell Line HT-29 by Modifying the Expression of APC, p53, and KRAS Genes. *Evid. Based Complement. Alternat. Med.* **2021**, *2021*. DOI: <https://doi.org/10.1155/2021/1448206>.
246. Morsy, H. M.; Ahmed, O. M.; Zoheir, K. M. A.; Abdel-Moneim, A. The anticarcinogenic effect of eugenol on lung cancer induced by diethylnitrosamine/2-acetylaminofluorene in Wistar rats: insight on the mechanisms of action. *Apoptosis* **2023**, 10.1007/s10495-023-01852-2. DOI: <https://doi.org/10.1007/s10495-023-01852-2>.
247. Padhy, I.; Paul, P.; Sharma, T.; Banerjee, S.; Mondal, A. Molecular Mechanisms of Action of Eugenol in Cancer: Recent Trends and Advancement. *Life* **2022**, *12* (11). DOI: <https://doi.org/10.3390/life12111795>.
248. Permatasari, H. K.; Effendi, A. B.; Qhabibi, F. R.; Fawwaz, F.; Dominique, A. Eugenol isolated from *Syzygium aromaticum* inhibits HeLa cancer cell migration by altering epithelial-mesenchymal transition protein regulators. *J. Appl. Pharm. Sci.* **2021**, *11* (5), 49-53. DOI: <https://doi.org/10.7324/JAPS.2021.110507>.
249. Ranjithkar, S.; Zhang, D.; Sun, F.; Salman, S.; He, W.; Venkitanarayanan, K.; Tulman, E. R.; Tian, X. Cytotoxic effects on cancerous and non-cancerous cells of trans-cinnamaldehyde, carvacrol, and eugenol. *Sci. Rep.* **2021**, *11* (1). DOI: <https://doi.org/10.1038/s41598-021-95394-9>.
250. Shi, X.; Zhang, W.; Bao, X.; Liu, X.; Yang, M.; Yin, C. Eugenol modulates the NOD1-NF- κ B signaling pathway via targeting NF- κ B protein in triple-negative breast cancer cells. *Front. Endocrinol.* **2023**, *14*. DOI: <https://doi.org/10.3389/fendo.2023.1136067>.
251. Shirazi, P. T.; Farjadian, S.; Dabbaghmanesh, M. H.; Jonaidi, H.; Alavianmehr, A.; Kalani, M.; Emadi, L. Eugenol: A New Option in Combination Therapy with Sorafenib for the Treatment of Undifferentiated Thyroid Cancer. *Iran. J. Allergy Asthma Immunol.* **2022**, *21* (3), 313-321. DOI: <https://doi.org/10.18502/ijaai.v21i3.9804>.
252. Kumar, N.; Kumar, S.; Abbat, S.; Nikhil, K.; Sondhi, S. M.; Bharatam, P. V.; Roy, P.; Pruthi, V. Ferulic acid amide derivatives as anticancer and antioxidant agents: synthesis, thermal, biological and computational studies. *Med. Chem. Res.* **2016**, *25* (6), 1175-1192. DOI: <https://doi.org/10.1007/s00044-016-1562-6>.
253. Ani, G.; Tanya, T. Y.; Reneta, T. Antitumor and apoptogenic effects of ferulic acid on cervical carcinoma cells. *Res. J. Biotechnol.* **2021**, *16* (4), 6-11.
254. Bakhholdina, L. A.; Markova, A. A.; Khlebnikov, A. I.; Sevodin, V. P. Cytotoxicity of New Ferulic-Acid Derivatives on Human Colon Carcinoma (HCT116) Cells. *Pharm. Chem. J.* **2019**, *53* (6), 516-520. DOI: <https://doi.org/10.1007/s11094-019-02030-y>.
255. Cao, Y.; Zhang, H.; Tang, J.; Wang, R. Ferulic Acid Mitigates Growth and Invasion of Esophageal Squamous Cell Carcinoma through Inducing Ferroptotic Cell Death. *Dis. Markers* **2022**, *2022*. DOI: <https://doi.org/10.1155/2022/4607966>.
256. Cui, K.; Wu, H.; Fan, J.; Zhang, L.; Li, H.; Guo, H.; Yang, R.; Li, Z. The Mixture of Ferulic Acid and P-Coumaric Acid Suppresses Colorectal Cancer through lncRNA 495810/PKM2 Mediated Aerobic Glycolysis. *Int. J. Mol. Sci.* **2022**, *23* (20). DOI: <https://doi.org/10.3390/ijms232012106>.

257. Damasceno, S. S.; Dantas, B. B.; Ribeiro-Filho, J.; Araújo, D. A. M.; Da Costa, J. G. M. Chemical properties of caffeic and ferulic acids in biological system: Implications in cancer therapy. A review. *Curr. Pharm. Des.* **2017**, *23* (20), 3015-3023. DOI: <https://doi.org/10.2174/1381612822666161208145508>.
258. Dodurga, Y.; Eroğlu, C.; Seçme, M.; Elmas, L.; Avcı, Ç. B.; Şatiroğlu-Tufan, N. L. Anti-proliferative and anti-invasive effects of ferulic acid in TT medullary thyroid cancer cells interacting with URG4/URGCP. *Tumour Biol.* **2016**, *37* (2), 1933-1940. DOI: <https://doi.org/10.1007/s13277-015-3984-z>.
259. El-Gogary, R. I.; Nasr, M.; Rahsed, L. A.; Hamzawy, M. A. Ferulic acid nanocapsules as a promising treatment modality for colorectal cancer: Preparation and in vitro/in vivo appraisal. *Life Sci.* **2022**, *298*. DOI: <https://doi.org/10.1016/j.lfs.2022.120500>.
260. ElKhazendar, M.; Chalak, J.; El-Huneidi, W.; Vinod, A.; Abdel-Rahman, W. M.; Abu-Gharbieh, E. Antiproliferative and proapoptotic activities of ferulic acid in breast and liver cancer cell lines. *Trop. J. Pharm. Res.* **2019**, *18* (12), 2571-2576. DOI: <https://doi.org/10.4314/tjpr.v18i12.16>.
261. Eroğlu, C.; Seçme, M.; Bağcı, G.; Dodurga, Y. Assessment of the anticancer mechanism of ferulic acid via cell cycle and apoptotic pathways in human prostate cancer cell lines. *Tumour Biol.* **2015**, *36* (12), 9437-9446. DOI: <https://doi.org/10.1007/s13277-015-3689-3>.
262. Fahrioglu, U.; Dodurga, Y.; Elmas, L.; Seçme, M. Ferulic acid decreases cell viability and colony formation while inhibiting migration of MIA PaCa-2 human pancreatic cancer cells in vitro. *Gene* **2016**, *576* (1), 476-482. DOI: <https://doi.org/10.1016/j.gene.2015.10.061>.
263. Gao, J.; Yu, H.; Guo, W.; Kong, Y.; Gu, Li, Q.; Yang, S.; Zhang, Y.; Wang, Y. The anticancer effects of ferulic acid is associated with induction of cell cycle arrest and autophagy in cervical cancer cells. *Cancer Cell Int.* **2018**, *18* (1). DOI: <https://doi.org/10.1186/s12935-018-0595-y>.
264. Gupta, A.; Singh, A. K.; Loka, M.; Pandey, A. K.; Bishayee, A. Ferulic acid-mediated modulation of apoptotic signaling pathways in cancer. *Adv. Protein Chem. Struct. Biol.* **2021**, *125*, 215-257. DOI: <https://doi.org/10.1016/bs.apcsb.2020.12.005>.
265. Luo, L.; Zhu, S.; Tong, Y.; Peng, S. Ferulic acid induces apoptosis of HeLa and caski cervical carcinoma cells by down-regulating the phosphatidylinositol 3-kinase (PI3K)/Akt signaling pathway. *Med. Sci. Monit.* **2020**, *26*. DOI: <https://doi.org/10.12659/MSM.920095>.
266. Zhang, X.; Lin, D.; Jiang, R.; Li, H.; Wan, J.; Li, H. Ferulic acid exerts antitumor activity and inhibits metastasis in breast cancer cells by regulating epithelial to mesenchymal transition. *Oncol. Rep.* **2016**, *36* (1), 271-278. DOI: <https://doi.org/10.3892/or.2016.4804>.
267. Dajas, F. Life or death: Neuroprotective and anticancer effects of quercetin. *J. Ethnopharmacol.* **2012**, *143* (2), 383-396. DOI: <https://doi.org/10.1016/j.jep.2012.07.005>.
268. Davoodvandi, A.; Shabani Varkani, M.; Clark, C. C. T.; Jafarnejad, S. Quercetin as an anticancer agent: Focus on esophageal cancer. *J. Food Biochem.* **2020**, *44* (9). DOI: <https://doi.org/10.1111/jfbc.13374>.
269. Khan, F.; Niaz, K.; Maqbool, F.; Hassan, F. I.; Abdollahi, M.; Nagulapalli Venkata, K. C.; Nabavi, S. M.; Bishayee, A. Molecular targets underlying the anticancer effects of quercetin: An update. *Nutrients* **2016**, *8* (9). DOI: <https://doi.org/10.3390/nu8090529>.
270. Kubina, R.; Iriti, M.; Kabała-Dzik, A. Anticancer potential of selected flavonols: Fisetin, kaempferol, and quercetin on head and neck cancers. *Nutrients* **2021**, *13* (3), 1-20. DOI: <https://doi.org/10.3390/nu13030845>.
271. Rauf, A.; Imran, M.; Khan, I. A.; ur-Rehman, M.; Gilani, S. A.; Mehmood, Z.; Mubarak, M. S. Anticancer potential of quercetin: A comprehensive review. *Phytother. Res.* **2018**, *32* (11), 2109-2130. DOI: <https://doi.org/10.1002/ptr.6155>.
272. Mei, S.; Ma, H.; Chen, X. Anticancer and anti-inflammatory properties of mangiferin: A review of its molecular mechanisms. *Food Chem. Toxicol.* **2021**, *149*. DOI: <https://doi.org/10.1016/j.fct.2021.111997>.
273. Acquaviva, R.; Tomasello, B.; Di Giacomo, C.; Santangelo, R.; Mantia, A. L.; Naletova, I.; Sarpietro, M. G.; Castelli, F.; Malfa, G. A. Protocatechuic acid, a simple plant secondary metabolite, induced apoptosis by promoting oxidative stress through ho-1 downregulation and p21 upregulation in colon cancer cells. *Biomolecules* **2021**, *11* (10). DOI: <https://doi.org/10.3390/biom11101485>.

274. Lin, H. H.; Chen, J. H.; Chou, F. P.; Wang, C. J. Protocatechuic acid inhibits cancer cell metastasis involving the down-regulation of Ras/Akt/NF- κ B pathway and MMP-2 production by targeting RhoB activation. *Br. J. Pharmacol.* **2011**, *162* (1), 237-254. DOI: <https://doi.org/10.1111/j.1476-5381.2010.01022.x>.
275. Peiffer, D. S.; Zimmerman, N. P.; Wang, L. S.; Ransom, B. W. S.; Carmella, S. G.; Kuo, C. T.; Siddiqui, J.; Chen, J. H.; Oshima, K.; Huang, Y. W.; et al. Chemoprevention of esophageal cancer with black raspberries, their component anthocyanins, and a major anthocyanin metabolite, protocatechuic acid. *Cancer Prev. Res.* **2014**, *7* (6), 574-584. DOI: <https://doi.org/10.1158/1940-6207.CAPR-14-0003>.
276. Tanaka, T.; Tanaka, T.; Tanaka, M. Potential Cancer Chemopreventive Activity of Protocatechuic Acid. *J. Exp. Clin. Med.* **2011**, *3* (1), 27-33. DOI: <https://doi.org/10.1016/j.jecm.2010.12.005>.
277. Tsao, S. M.; Hsia, T. C.; Yin, M. C. Protocatechuic acid inhibits lung cancer cells by modulating FAK, MAPK, and NF- κ B pathways. *Nutr. Cancer* **2014**, *66* (8), 1331-1341. DOI: <https://doi.org/10.1080/01635581.2014.956259>.
278. Xie, Z.; Guo, Z.; Wang, Y.; Lei, J.; Yu, J. Protocatechuic acid inhibits the growth of ovarian cancer cells by inducing apoptosis and autophagy. *Phytother. Res.* **2018**, *32* (11), 2256-2263. DOI: <https://doi.org/10.1002/ptr.6163>.
279. Yin, M. C.; Lin, C. C.; Wu, H. C.; Tsao, S. M.; Hsu, C. K. Apoptotic effects of protocatechuic acid in human breast, lung, liver, cervix, and prostate cancer cells: Potential mechanisms of action. *J. Agric. Food Chem.* **2009**, *57* (14), 6468-6473. DOI: <https://doi.org/10.1021/jf9004466>.
280. Baer-Dubowska, W.; Szaefer, H.; Majchrzak-Celińska, A.; Krajka-Kuźniak, V. Tannic Acid: Specific Form of Tannins in Cancer Chemoprevention and Therapy-Old and New Applications. *Curr. Pharmacol. Rep.* **2020**, *6* (2), 28-37. DOI: <https://doi.org/10.1007/s40495-020-00211-y>.
281. Bona, N. P.; Pedra, N. S.; Azambuja, J. H.; Soares, M. S. P.; Spohr, L.; Gelsleichter, N. E.; de M. Meine, B.; Sekine, F. G.; Mendonça, L. T.; de Oliveira, F. H.; et al. Tannic acid elicits selective antitumoral activity in vitro and inhibits cancer cell growth in a preclinical model of glioblastoma multiforme. *Metab. Brain Dis.* **2020**, *35* (2), 283-293. DOI: <https://doi.org/10.1007/s11011-019-00519-9>.
282. Chariyarangsitam, W.; Krungchanuchat, S.; Khuemjun, P.; Pilapong, C. Effect of advanced oxidation and amino acid addition on antioxidant capability, iron chelating property and anti-cancer activity of tannic acid. *Arab. J. Chem.* **2021**, *14* (9). DOI: <https://doi.org/10.1016/j.arabjc.2021.103312>.
283. Chen, M. C.; Anseles Rajula, S.; Bharath Kumar, V.; Hsu, C. H.; Day, C. H.; Chen, R. J.; Wang, T. F.; Viswanadha, V. P.; Li, C. C.; Huang, C. Y. Tannic acid attenuate AKT phosphorylation to inhibit UMUC3 bladder cancer cell proliferation. *Mol. Cell. Biochem.* **2022**, *477* (12), 2863-2869. DOI: <https://doi.org/10.1007/s11010-022-04454-9>.
284. Hatami, E.; B Nagesh, P. K.; Sikander, M.; Dhasmana, A.; Chauhan, S. C.; Jaggi, M.; Yallapu, M. M. Tannic Acid Exhibits Antiangiogenesis Activity in Non-small-Cell Lung Cancer Cells. *ACS Omega* **2022**, *7* (27), 23939-23949. DOI: <https://doi.org/10.1021/acsomega.2c02727>.
285. Nagesh, P. K. B.; Chowdhury, P.; Hatami, E.; Jain, S.; Dan, N.; Kashyap, V. K.; Chauhan, S. C.; Jaggi, M.; Yallapu, M. M. Tannic acid inhibits lipid metabolism and induce ROS in prostate cancer cells. *Sci. Rep.* **2020**, *10* (1). DOI: <https://doi.org/10.1038/s41598-020-57932-9>.
286. Nagesh, P. K. B.; Hatami, E.; Chowdhury, P.; Kashyap, V. K.; Khan, S.; Hafeez, B. B.; Chauhan, S. C.; Jaggi, M.; Yallapu, M. M. Tannic acid induces endoplasmic reticulum stress-mediated apoptosis in prostate cancer. *Cancers (Basel)* **2018**, *10* (3). DOI: <https://doi.org/10.3390/cancers10030068>.
287. Sp, N.; Kang, D. Y.; Kim, D. H.; Yoo, J. S.; Jo, E. S.; Rugamba, A.; Jang, K. J.; Yang, Y. M. Tannic acid inhibits Non-small Cell Lung Cancer (NSCLC) stemness by inducing G0/G1 Cell cycle arrest and intrinsic apoptosis. *Anticancer Res.* **2020**, *40* (6), 3209-3220. DOI: <https://doi.org/10.2196/10.21873/anticanres.14302>.
288. Yang, P.; Ding, G. B.; Liu, W.; Fu, R.; Sajid, A.; Li, Z. Tannic acid directly targets pyruvate kinase isoenzyme M2 to attenuate colon cancer cell proliferation. *Food Funct.* **2018**, *9* (11), 5547-5559. DOI: <https://doi.org/10.1039/c8fo01161c>.

289. Youness, R. A.; Kamel, R.; Elkasabgy, N. A.; Shao, P.; Farag, M. A. Recent advances in tannic acid (gallotannin) anticancer activities and drug delivery systems for efficacy improvement; a comprehensive review. *Molecules* **2021**, *25* (6). DOI: <https://doi.org/10.3390/molecules26051486>.
290. Cadoná, F. C.; Dantas, R. F.; de Mello, G. H.; Silva-Jr, F. P. Natural products targeting into cancer hallmarks: An update on caffeine, theobromine, and (+)-catechin. *Crit. Rev. Food Sci. Nutr.* **2022**, *62* (26), 7222-7241. DOI: <https://doi.org/10.1080/10408398.2021.1913091>.
291. Shojaei-Zarghani, S.; Rafraf, M.; Yari Khosroushahi, A.; Sheikh-Najafi, S. Effectiveness of theobromine on inhibition of 1,2-dimethylhydrazine-induced rat colon cancer by suppression of the Akt/GSK3 β / β -catenin signaling pathway. *J. Funct. Foods* **2020**, *75*. DOI: <https://doi.org/10.1016/j.jff.2020.104293>.
292. Shojaei-Zarghani, S.; Yari Khosroushahi, A.; Rafraf, M. Oncopreventive effects of theanine and theobromine on dimethylhydrazine-induced colon cancer model. *Biomed. Pharmacother.* **2021**, *134*. DOI: <https://doi.org/10.1016/j.biopha.2020.111140>.
293. De Souza Rosa, L.; Jordão, N. A.; Da Costa Pereira Soares, N.; De Mesquita, J. F.; Monteiro, M.; Teodoro, A. J. Pharmacokinetic, antiproliferative and apoptotic effects of phenolic acids in human colon adenocarcinoma cells using in vitro and in silico approaches. *Molecules* **2018**, *23* (10). DOI: <https://doi.org/10.3390/molecules23102569>.
294. Gong, J.; Zhou, S.; Yang, S. Vanillic acid suppresses HIF-1 α expression via inhibition of mTOR/p70S6K/4E-BP1 and Raf/MEK/ERK pathways in human colon cancer HCT116 cells. *Int. J. Mol. Sci.* **2019**, *20* (3). DOI: <https://doi.org/10.3390/ijms20030465>.
295. Velli, S. K.; Sundaram, J.; Murugan, M.; Balaraman, G.; Thiruvengadam, D. Protective effect of vanillic acid against benzo(a)pyrene induced lung cancer in Swiss albino mice. *J. Biochem. Mol. Toxicol.* **2019**, *33* (10). DOI: <https://doi.org/10.1002/jbt.22382>.
296. Wang, M.; Qi, Y.; Sun, Y. Exploring the Antitumor Mechanisms of Zingiberis Rhizoma Combined with Coptidis Rhizoma Using a Network Pharmacology Approach. *Biomed Res. Int.* **2020**, *2020*. DOI: <https://doi.org/10.1155/2020/8887982>.
297. Zhu, M.; Tang, X.; Zhu, Z.; Gong, Z.; Tang, W.; Hu, Y.; Cheng, C.; Wang, H.; Sarwar, A.; Chen, Y.; et al. STING activation in macrophages by vanillic acid exhibits antineoplastic potential. *Biochem. Pharmacol.* **2023**, *213*. DOI: <https://doi.org/10.1016/j.bcp.2023.115618>.
298. Bezerra, D. P.; Soares, A. K. N.; De Sousa, D. P. Overview of the role of vanillin on redox status and cancer development. *Oxidative Med. Cell. Longev.* **2016**, *2016*. DOI: <https://doi.org/10.1155/2016/9734816>.
299. Ho, K.; Yazan, L. S.; Ismail, N.; Ismail, M. Apoptosis and cell cycle arrest of human colorectal cancer cell line HT-29 induced by vanillin. *Cancer Epidemiol.* **2009**, *33* (2), 155-160. DOI: <https://doi.org/10.1016/j.canep.2009.06.003>.
300. Li, J. M.; Lee, Y. C.; Li, C. C.; Lo, H. Y.; Chen, F. Y.; Chen, Y. S.; Hsiang, C. Y.; Ho, T. Y. Vanillin-Ameliorated Development of Azoxymethane/Dextran Sodium Sulfate-Induced Murine Colorectal Cancer: The Involvement of Proteasome/Nuclear Factor- κ B/Mitogen-Activated Protein Kinase Pathways. *J. Agric. Food Chem.* **2018**, *66* (22), 5563-5573. DOI: <https://doi.org/10.1021/acs.jafc.8b01582>.
301. Lirdprapamongkol, K.; Kramb, J. P.; Suthiphongchai, T.; Surarit, R.; Srisomsap, C.; Dannhardt, G.; Svasti, J. Vanillin suppresses metastatic potential of human cancer cells through PI3K inhibition and decreases angiogenesis in Vivo. *J. Agric. Food Chem.* **2009**, *57* (8), 3055-3063. DOI: <https://doi.org/10.1021/jf803366f>.
302. Lirdprapamongkol, K.; Sakurai, H.; Kawasaki, N.; Choo, M. K.; Saitoh, Y.; Aozuka, Y.; Singhirunnusorn, P.; Ruchirawat, S.; Svasti, J.; Saiki, I. Vanillin suppresses in vitro invasion and in vivo metastasis of mouse breast cancer cells. *Eur. J. Pharm. Sci.* **2005**, *25* (1), 57-65. DOI: <https://doi.org/10.1016/j.ejps.2005.01.015>.
303. Naz, H.; Tarique, M.; Khan, P.; Luqman, S.; Ahamad, S.; Islam, A.; Ahmad, F.; Hassan, M. I. Evidence of vanillin binding to CAMKIV explains the anti-cancer mechanism in human hepatic carcinoma and neuroblastoma cells. *Mol. Cell. Biochem.* **2018**, *438* (1-2), 35-45. DOI: <https://doi.org/10.1007/s11010-017-3111-0>.

304. Ramadoss, D. P.; Sivalingam, N. Vanillin extracted from Proso and Barnyard millets induce apoptotic cell death in HT-29 human colon cancer cell line. *Nutr. Cancer* **2020**, *72* (8), 1422-1437. DOI: <https://doi.org/10.1080/01635581.2019.1672763>.
305. Srinual, S.; Chanvorachote, P.; Pongrakhananon, V. Suppression of cancer stem-like phenotypes in NCI-H460 lung cancer cells by vanillin through an Akt-dependent pathway. *Int. J. Oncol.* **2017**, *50* (4), 1341-1351. DOI: <https://doi.org/10.3892/ijo.2017.3879>.
306. Yousuf, M.; Shamsi, A.; Queen, A.; Shahbaaz, M.; Khan, P.; Hussain, A.; Alajmi, M. F.; Rizwanul Haque, Q. M.; Imtaiyaz Hassan, M. Targeting cyclin-dependent kinase 6 by vanillin inhibits proliferation of breast and lung cancer cells: Combined computational and biochemical studies. *J. Cell. Biochem.* **2021**, *122* (8), 897-910. DOI: <https://doi.org/10.1002/jcb.29921>.
307. Liu, J. C.; Chen, P. Y.; Hao, W. R.; Liu, Y. C.; Lyu, P. C.; Hong, H. J. Cafestol Inhibits High-Glucose-Induced Cardiac Fibrosis in Cardiac Fibroblasts and Type 1-Like Diabetic Rats. *Evid. Based Complement. Alternat. Med.* **2020**, 2020. DOI: <https://doi.org/10.1155/2020/4503747>.
308. Mellbye, F. B.; Jeppesen, P. B.; Shokouh, P.; Laustsen, C.; Hermansen, K.; Gregersen, S. Cafestol, a Bioactive Substance in Coffee, Has Antidiabetic Properties in KKAY Mice. *J. Nat. Prod.* **2017**, *80* (8), 2353-2359. DOI: <https://doi.org/10.1021/acs.jnatprod.7b00395>.
309. Oboh, G.; Agunloye, O. M.; Adefegha, S. A.; Akinyemi, A. J.; Ademiluyi, A. O. Caffeic and chlorogenic acids inhibit key enzymes linked to type 2 diabetes (in vitro): A comparative study. *J. Basic Clin. Physiol. Pharmacol.* **2015**, *26* (2), 165-170. DOI: <https://doi.org/10.1515/jbcpp-2013-0141>.
310. Chao, C. Y.; Mong, M. C.; Chan, K. C.; Yin, M. C. Anti-glycative and anti-inflammatory effects of caffeic acid and ellagic acid in kidney of diabetic mice. *Mol. Nutr. Food Res.* **2010**, *54* (3), 388-395. DOI: <https://doi.org/10.1002/mnfr.200900087>.
311. Oršolić, N.; Sirovina, D.; Odeh, D.; Gajski, G.; Balta, V.; Šver, L.; Jembrek, M. J. Efficacy of Caffeic acid on diabetes and its complications in the mouse. *Molecules* **2021**, *26* (11). DOI: <https://doi.org/10.3390/molecules26113262>.
312. Xu, W.; Luo, Q.; Wen, X.; Xiao, M.; Mei, Q. Antioxidant and anti-diabetic effects of caffeic acid in a rat model of diabetes. *Trop. J. Pharm. Res.* **2020**, *19* (6), 1227-1232. DOI: <https://doi.org/10.4314/tjpr.v19i6.17>.
313. Yusuf, M.; Nasiruddin, M.; Sultana, N.; Badruddeen; Akhtar, J.; Khan, M. I.; Ahmad, M. Regulatory mechanism of caffeic acid on glucose metabolism in diabetes. *Res. J. Pharm. Technol.* **2019**, *12* (10), 4735-4740. DOI: <https://doi.org/10.5958/0974-360X.2019.00816.3>.
314. Ontawong, A.; Duangjai, A.; Muanprasat, C.; Pasachan, T.; Pongchaidecha, A.; Amornlerdpison, D.; Srimaroeng, C. Lipid-lowering effects of Coffea arabica pulp aqueous extract in Caco-2 cells and hypercholesterolemic rats. *Phytomedicine* **2019**, *52*, 187-197. DOI: <https://doi.org/10.1016/j.phymed.2018.06.021>.
315. Pimpley, V.; Patil, S.; Srinivasan, K.; Desai, N.; Murthy, P. S. The chemistry of chlorogenic acid from green coffee and its role in attenuation of obesity and diabetes. *Prep. Biochem. Biotechnol.* **2020**, *50* (10), 969-978. DOI: <https://doi.org/10.1080/10826068.2020.1786699>.
316. Bagdas, D.; Etoz, B. C.; Gul, Z.; Ziyank, S.; Inan, S.; Turacozen, O.; Gul, N. Y.; Topal, A.; Cinkilic, N.; Tas, S.; et al. In vivo systemic chlorogenic acid therapy under diabetic conditions: Wound healing effects and cytotoxicity/genotoxicity profile. *Food Chem. Toxicol.* **2015**, *81*, 54-61. DOI: <https://doi.org/10.1016/j.fct.2015.04.001>.
317. Jin, S.; Chang, C.; Zhang, L.; Liu, Y.; Huang, X.; Chen, Z. Chlorogenic acid improves late diabetes through adiponectin receptor signaling pathways in db/db mice. *PLoS One* **2015**, *10* (4). DOI: <https://doi.org/10.1371/journal.pone.0120842>.
318. Williamson, G. Protection against developing type 2 diabetes by coffee consumption: Assessment of the role of chlorogenic acid and metabolites on glycaemic responses. *Food Funct.* **2020**, *11* (6), 4826-4833. DOI: <https://doi.org/10.1039/d0fo01168a>.

319. Yan, Y.; Li, Q.; Shen, L.; Guo, K.; Zhou, X. Chlorogenic acid improves glucose tolerance, lipid metabolism, inflammation and microbiota composition in diabetic db/db mice. *Front. Endocrinol.* **2022**, *13*. DOI: <https://doi.org/10.3389/fendo.2022.1042044>.
320. Yan, Y.; Zhou, X.; Guo, K.; Zhou, F.; Yang, H. Use of Chlorogenic Acid against Diabetes Mellitus and Its Complications. *J. Immunol. Res.* **2020**, 2020. DOI: <https://doi.org/10.1155/2020/9680508>.
321. Topal, F. Anticholinergic and antidiabetic effects of isoeugenol from clove (*Eugenia caryophyllata*) oil. *Int. J. Food Prop.* **2019**, *22* (1), 583-592. DOI: <https://doi.org/10.1080/10942912.2019.1597882>.
322. Park, J. E.; Kim, S. Y.; Han, J. S. Scopoletin stimulates the secretion of insulin via a KATP channel-dependent pathway in INS-1 pancreatic β cells. *J. Pharm. Pharmacol.* **2022**, *74* (9), 1274-1281. DOI: <https://doi.org/10.1093/jpp/rgab143>.
323. Jang, J. H.; Park, J. E.; Han, J. S. Scopoletin inhibits α -glucosidase in vitro and alleviates postprandial hyperglycemia in mice with diabetes. *Eur. J. Pharmacol.* **2018**, *834*, 152-156. DOI: <https://doi.org/10.1016/j.ejphar.2018.07.032>.
324. Batra, G. K.; Anand, A.; Sharma, S.; Sharma, S.; Bhansali, S.; Patil, A. N. Scopoletin Improves Glucose Homeostasis in the High-Fructose High-Fat Diet-Induced Diabetes Model in Wistar Rats. *J. Med. Food* **2023**, *26* (4), 270-274. DOI: <https://doi.org/10.1089/jmf.2022.K.0153>.
325. Liang, Y.; Zeng, X.; Guo, J.; Liu, H.; He, B.; Lai, R.; Zhu, Q.; Zheng, Z. Scopoletin and umbelliferone from Cortex Mori as protective agents in high glucose-induced mesangial cell as in vitro model of diabetic glomerulosclerosis. *Chin. J. Physiol.* **2021**, *64* (3), 150-158. DOI: https://doi.org/10.4103/cjp.cjp_9_21.
326. Verma, A.; Dewangan, P.; Kesharwani, D.; Kela, S. P. Hypoglycemic and hypolipidemic activity of scopoletin (coumarin derivative) in streptozotocin induced diabetic rats. *Int. J. Pharm. Sci. Rev. Res.* **2013**, *22* (1), 79-83.
327. Duangjai, A.; Nuengchamnong, N.; Suphrom, N.; Trisat, K.; Limpeanchob, N.; Saokaew, S. Potential of coffee fruit extract and quinic acid on adipogenesis and lipolysis in 3T3-L1 adipocytes. *Kobe J. Med. Sci.* **2018**, *64* (3), E84-E92.
328. AlEraky, D. M.; Abuohashish, H. M.; Gad, M. M.; Alshuyukh, M. H.; Bugshan, A. S.; Almulhim, K. S.; Mahmoud, M. M. The Antifungal and Antibiofilm Activities of Caffeine against *Candida albicans* on Polymethyl Methacrylate Denture Base Material. *Biomedicines* **2022**, *10* (9). DOI: <https://doi.org/10.3390/biomedicines10092078>.
329. Saracino, I. M.; Foschi, C.; Pavoni, M.; Spigarelli, R.; Valerii, M. C.; Spisni, E. Antifungal Activity of Natural Compounds vs. *Candida* spp.: A Mixture of Cinnamaldehyde and Eugenol Shows Promising In Vitro Results. *Antibiotics* **2022**, *11* (1). DOI: <https://doi.org/10.3390/antibiotics11010073>.
330. Biernasiuk, A.; Baj, T.; Malm, A. Clove Essential Oil and Its Main Constituent, Eugenol, as Potential Natural Antifungals against *Candida* spp. Alone or in Combination with Other Antimycotics Due to Synergistic Interactions. *Molecules* **2023**, *28* (1). DOI: <https://doi.org/10.3390/molecules28010215>.
331. Cai, R.; Hu, M.; Zhang, Y.; Niu, C.; Yue, T.; Yuan, Y.; Wang, Z. Antifungal activity and mechanism of citral, limonene and eugenol against *Zygosaccharomyces rouxii*. *LWT* **2019**, *106*, 50-56. DOI: <https://doi.org/10.1016/j.lwt.2019.02.059>.
332. Gupta, P.; Mishra, P.; Mehra, L.; Rastogi, K.; Prasad, R.; Mittal, G.; Poluri, K. M. Eugenol-acacia gum-based bifunctional nanofibers as a potent antifungal transdermal substitute. *Nanomedicine* **2021**, *16* (25), 2269-2289. DOI: <https://doi.org/10.2217/nmm-2021-0274>.
333. Hassanpour, P.; Shams-Ghahfarokhi, M.; Razzaghi-Abyaneh, M. Antifungal activity of eugenol on *Cryptococcus neoformans* biological activity and Cxt1p gene expression. *Curr. Med. Mycol.* **2020**, *6* (1), 9-14. DOI: <https://doi.org/10.18502/CMM.6.1.2502>.
334. Zhao, Y.; Wang, Q.; Wu, X.; Jiang, M.; Jin, H.; Tao, K.; Hou, T. Unraveling the polypharmacology of a natural antifungal product, eugenol, against *Rhizoctonia solani*. *Pest Manag. Sci.* **2021**, *77* (7), 3469-3483. DOI: <https://doi.org/10.1002/ps.6400>.

335. Goswami, L.; Gupta, L.; Paul, S.; Vermani, M.; Vijayaraghavan, P.; Bhattacharya, A. K. Design and synthesis of eugenol/isoegenol glycoconjugates and other analogues as antifungal agents against *Aspergillus fumigatus*. *RSC Med. Chem.* **2022**, *13* (8), 955-962. DOI: <https://doi.org/10.1039/d2md00138a>.
336. Pinheiro, L. S.; Sousa, J. P.; Barreto, N. A.; Lima, A. L. A.; Dantas, T. B.; Pérez, A. L. A. L.; Menezes, C. P.; Abrantes, J. P.; Filho, A. A. O.; Lima, E. O. Investigation of antifungal activity and mode of action of isoegenol against strains of *Cryptococcus neoformans*. *Lat. Am. J. Pharm.* **2017**, *36* (11), 2220-2225.
337. Cui, W.; Du, K. Y.; Ling, Y. X.; Yang, C. J. Activity of eugenol derivatives against *Fusarium graminearum* Q1 strain and screening of isoegenol mixtures. *J. Plant Pathol.* **2021**, *103* (3), 915-921. DOI: <https://doi.org/10.1007/s42161-021-00875-5>.
338. Medeiros, D.; Oliveira-Júnior, J.; Nóbrega, J.; Cordeiro, L.; Jardim, J.; Souza, H.; Silva, G.; Athayde-Filho, P.; Barbosa-Filho, J.; Scotti, L.; Lima, E. Isoegenol and hybrid acetamides against candida albicans isolated from the oral cavity. *Pharmaceuticals* **2020**, *13* (10), 1-13. DOI: <https://doi.org/10.3390/ph13100291>.
339. Fitzgerald, D. J.; Stratford, M.; Gasson, M. J.; Narbad, A. Structure-function analysis of the vanillin molecule and its antifungal properties. *J. Agric. Food Chem.* **2005**, *53* (5), 1769-1775. DOI: <https://doi.org/10.1021/jf048575t>.
340. Li, Q.; Zhu, X.; Xie, Y.; Zhong, Y. o-Vanillin, a promising antifungal agent, inhibits *Aspergillus flavus* by disrupting the integrity of cell walls and cell membranes. *Appl. Microbiol. Biotechnol.* **2021**, *105* (12), 5147-5158. DOI: <https://doi.org/10.1007/s00253-021-11371-2>.
341. Li, Q.; Zhu, X.; Zhao, Y.; Xie, Y. The antifungal activity of o-vanillin against *Aspergillus flavus* via disrupting ergosterol biosynthesis and promoting oxidative stress, and an RNA-seq analysis thereof. *LWT* **2022**, *164*. DOI: <https://doi.org/10.1016/j.lwt.2022.113635>.
342. Weng, W. T.; Kuo, P. C.; Brown, D. A.; Scofield, B. A.; Furnas, D.; Paraiso, H. C.; Wang, P. Y.; Yu, I. C.; Yen, J. H. 4-Ethylguaiaicol modulates neuroinflammation and Th1/Th17 differentiation to ameliorate disease severity in experimental autoimmune encephalomyelitis. *J. Neuroinflammation* **2021**, *18* (1). DOI: <https://doi.org/10.1186/s12974-021-02143-w>.
343. Weng, W. T.; Kuo, P. C.; Scofield, B. A.; Paraiso, H. C.; Brown, D. A.; Yu, I. C.; Yen, J. H. 4-Ethylguaiaicol Modulates Neuroinflammation and Promotes Heme Oxygenase-1 Expression to Ameliorate Brain Injury in Ischemic Stroke. *Front. Immunol.* **2022**, *13*. DOI: <https://doi.org/10.3389/fimmu.2022.887000>.
344. Zhao, D. R.; Jiang, Y. S.; Sun, J. Y.; Li, H. H.; Luo, X. L.; Zhao, M. M. Anti-inflammatory Mechanism Involved in 4-Ethylguaiaicol-Mediated Inhibition of LPS-Induced Inflammation in THP-1 Cells. *J. Agric. Food Chem.* **2019**, *67* (4), 1230-1243. DOI: <https://doi.org/10.1021/acs.jafc.8b06263>.
345. Rahimi, M. R.; Semenova, E. A.; Larin, A. K.; Kulemin, N. A.; Generozov, E. V.; Łubkowska, B.; Ahmetov, I. I.; Golpasandi, H. The ADORA2A TT Genotype Is Associated with Anti-Inflammatory Effects of Caffeine in Response to Resistance Exercise and Habitual Coffee Intake. *Nutrients* **2023**, *15* (7). DOI: <https://doi.org/10.3390/nu15071634>.
346. Mei, S.; Chen, X. Combination of HPLC-orbitrap-MS/MS and network pharmacology to identify the anti-inflammatory phytochemicals in the coffee leaf extracts. *Food Front.* **2023**, 10.1002/fft2.248. DOI: <https://doi.org/10.1002/fft2.248>.
347. Lu, R.; Wang, Y. G.; Qu, Y.; Wang, S. X.; Peng, C.; You, H.; Zhu, W.; Chen, A. Dihydrocaffeic acid improves IL-1 β -induced inflammation and cartilage degradation via inhibiting NF- κ B and MAPK signalling pathways. *Bone Joint Res.* **2023**, *12* (4), 259-273. DOI: <https://doi.org/10.1302/2046-3758.124.BJR-2022-0384.R1>.
348. Mateen, S.; Rehman, M. T.; Shahzad, S.; Naem, S. S.; Faizy, A. F.; Khan, A. Q.; Khan, M. S.; Husain, F. M.; Moin, S. Anti-oxidant and anti-inflammatory effects of cinnamaldehyde and eugenol on mononuclear cells of rheumatoid arthritis patients. *Eur. J. Pharmacol.* **2019**, *852*, 14-24. DOI: <https://doi.org/10.1016/j.ejphar.2019.02.031>.
349. Barboza, J. N.; da Silva Maia Bezerra Filho, C.; Silva, R. O.; Medeiros, J. V. R.; de Sousa, D. P. An overview on the anti-inflammatory potential and antioxidant profile of eugenol. *Oxidative Med. Cell. Longev.* **2018**, *2018*. DOI: <https://doi.org/10.1155/2018/3957262>.

350. De Araújo Lopes, A.; Da Fonseca, F. N.; Rocha, T. M.; De Freitas, L. B.; Araújo, E. V. O.; Wong, D. V. T.; Júnior, R. C. P. L.; Leal, L. K. A. M. Eugenol as a promising molecule for the treatment of dermatitis: Antioxidant and anti-inflammatory activities and its nanoformulation. *Oxidative Med. Cell. Longev.* **2018**, *2018*. DOI: <https://doi.org/10.1155/2018/8194849>.
351. El-kady, A. M.; Ahmad, A. A.; Hassan, T. M.; El-Deek, H. E. M.; Fouad, S. S.; Althagfan, S. S. Eugenol, a potential schistosomicidal agent with anti-inflammatory and antifibrotic effects against *Schistosoma mansoni*, induced liver pathology. *Infect. Drug Resist.* **2019**, *12*, 709-719. DOI: <https://doi.org/10.2147/IDR.S196544>.
352. Esmaeili, F.; Rajabnejhad, S.; Partoazar, A. R.; Mehr, S. E.; Faridi-Majidi, R.; Sahebgharani, M.; Syedmoradi, L.; Rajabnejhad, M. R.; Amani, A. Anti-inflammatory effects of eugenol nanoemulsion as a topical delivery system. *Pharm. Dev. Technol.* **2016**, *21* (7), 887-893. DOI: <https://doi.org/10.3109/10837450.2015.1078353>.
353. Huang, X.; Liu, Y.; Lu, Y.; Ma, C. Anti-inflammatory effects of eugenol on lipopolysaccharide-induced inflammatory reaction in acute lung injury via regulating inflammation and redox status. *Int. Immunopharmacol.* **2015**, *26* (1), 265-271. DOI: <https://doi.org/10.1016/j.intimp.2015.03.026>.
354. Mir, S. M.; Ravuri, H. G.; Pradhan, R. K.; Narra, S.; Kumar, J. M.; Kuncha, M.; Kanjilal, S.; Sistla, R. Ferulic acid protects lipopolysaccharide-induced acute kidney injury by suppressing inflammatory events and upregulating antioxidant defenses in Balb/c mice. *Biomed. Pharmacother.* **2018**, *100*, 304-315. DOI: <https://doi.org/10.1016/j.biopha.2018.01.169>.
355. Yin, Z. N.; Wu, W. J.; Sun, C. Z.; Liu, H. F.; Chen, W. B.; Zhan, Q. P.; Lei, Z. G.; Xin, X.; Ma, J. J.; Yao, K.; et al. Antioxidant and Anti-inflammatory Capacity of Ferulic Acid Released from Wheat Bran by Solid-state Fermentation of *Aspergillus niger*. *Biomed. Environ. Sci.* **2019**, *32* (1), 11-21. DOI: <https://doi.org/10.3967/bes2019.002>.
356. Funakoshi-Tago, M.; Matsutaka, M.; Hokimoto, S.; Kobata, K.; Tago, K.; Tamura, H. Coffee ingredients, hydroquinone, pyrocatechol, and 4-ethylcatechol exhibit anti-inflammatory activity through inhibiting NF- κ B and activating Nrf2. *J. Funct. Foods* **2022**, *90*. DOI: <https://doi.org/10.1016/j.jff.2022.104980>.
357. Abazari, M. F.; Nasiri, N.; Karizi, S. Z.; Nejati, F.; Haghiaminjan, H.; Norouzi, S.; Piri, P.; Estakhr, L.; Faradonbeh, D. R.; Kohandani, M.; et al. An updated review of various medicinal applications of p-coumaric acid: From antioxidative and anti-inflammatory properties to effects on cell cycle and proliferation. *Mini-Rev. Med. Chem.* **2021**, *21* (15), 2187-2201. DOI: <https://doi.org/10.2174/1389557521666210114163024>.
358. Da Silva, E. C. O.; Dos Santos, F. M.; Ribeiro, A. R. B.; De Souza, S. T.; Barreto, E.; Da Silva Fonseca, E. J. Drug-induced anti-inflammatory response in A549 cells, as detected by Raman spectroscopy: A comparative analysis of the actions of dexamethasone and: p-coumaric acid. *Analyst* **2019**, *144* (5), 1622-1631. DOI: <https://doi.org/10.1039/c8an01887a>.
359. Lee, M.; Rho, H. S.; Choi, K. Anti-inflammatory Effects of a P-coumaric Acid and Kojic Acid Derivative in LPS-stimulated RAW264.7 Macrophage Cells. *Biotechnol. Bioprocess Eng.* **2019**, *24* (4), 653-657. DOI: <https://doi.org/10.1007/s12257-018-0492-1>.
360. Moradi, M.; Farbood, Y.; Mard, S. A.; Dianat, M.; Goudarzi, G.; Khorsandi, L.; Seyedian, S. S. p-Coumaric acid has pure anti-inflammatory characteristics against hepatopathy caused by ischemia-reperfusion in the liver and dust exposure. *Iran. J. Basic Med. Sci.* **2022**, *26* (2), 164-175. DOI: <https://doi.org/10.22038/IJBMS.2022.66192.14554>.
361. Pragasam, S. J.; Venkatesan, V.; Rasool, M. Immunomodulatory and anti-inflammatory effect of p-coumaric acid, a common dietary polyphenol on experimental inflammation in rats. *Inflammation* **2013**, *36* (1), 169-176. DOI: <https://doi.org/10.1007/s10753-012-9532-8>.
362. Venkatesan, A.; Samy, J. V. R. A.; Balakrishnan, K.; Natesan, V.; Kim, S. J. In vitro Antioxidant, Anti-inflammatory, Antimicrobial, and Antidiabetic Activities of Synthesized Chitosan-loaded p-Coumaric Acid Nanoparticles. *Curr. Pharm. Biotechnol.* **2023**, *24* (9), 1178-1194. DOI: <https://doi.org/10.2174/1389201023666220822112923>.

363. Allen, S.; Khattab, A.; Vassallo, M.; Kwan, J. Inflammation and muscle weakness in COPD: Considering a renewed role for Theophylline? *Curr. Respir. Med. Rev.* **2018**, *14* (1), 35-41. DOI: <https://doi.org/10.2174/1573398X14666180525113544>.
364. Bin, Y.; Xiao, Y.; Huang, D.; Ma, Z.; Liang, Y.; Bai, J.; Zhang, W.; Liang, Q.; Zhang, J.; Zhong, X.; He, Z. Theophylline inhibits cigarette smoke-induced inflammation in skeletal muscle by upregulating hdac2 expression and decreasing nf- κ b activation. *Am. J. Physiol. Lung Cell. Mol. Physiol.* **2019**, *316* (1), L197-L205. DOI: <https://doi.org/10.1152/ajplung.00005.2018>.
365. Eid, N. S.; O'Hagan, A.; Bickel, S.; Morton, R.; Jacobson, S.; Myers, J. A. Anti-inflammatory dosing of theophylline in the treatment of status asthmaticus in children. *J. Asthma Allergy* **2016**, *9*, 183-189. DOI: <https://doi.org/10.2147/JAA.S113747>.
366. Talmon, M.; Massara, E.; Brunini, C.; Fresu, L. G. Comparison of anti-inflammatory mechanisms between doxofylline and theophylline in human monocytes. *Pulm. Pharmacol. Ther.* **2019**, *59*. DOI: <https://doi.org/10.1016/j.pupt.2019.101851>.
367. Urbanova, A.; Kertys, M.; Simekova, M.; Mikolka, P.; Kosutova, P.; Mokra, D.; Mokry, J. Bronchodilator and anti-inflammatory action of theophylline in a model of ovalbumin-induced allergic inflammation. *Adv. Exp. Med. Biol.* **2016**, *935*, 53-62. DOI: https://doi.org/10.1007/5584_2016_31.
368. Bains, M.; Kaur, J.; Akhtar, A.; Kuhad, A.; Sah, S. P. Anti-inflammatory effects of ellagic acid and vanillic acid against quinolinic acid-induced rat model of Huntington's disease by targeting IKK-NF- κ B pathway. *Eur. J. Pharmacol.* **2022**, *934*. DOI: <https://doi.org/10.1016/j.ejphar.2022.175316>.
369. Calixto-Campos, C.; Carvalho, T. T.; Hohmann, M. S. N.; Pinho-Ribeiro, F. A.; Fattori, V.; Manchope, M. F.; Zarpelon, A. C.; Baracat, M. M.; Georgetti, S. R.; Casagrande, R.; Verri, W. A. Vanillic Acid Inhibits Inflammatory Pain by Inhibiting Neutrophil Recruitment, Oxidative Stress, Cytokine Production, and NF κ B Activation in Mice. *J. Nat. Prod.* **2015**, *78* (8), 1799-1808. DOI: <https://doi.org/10.1021/acs.jnatprod.5b00246>.
370. Hu, R.; Wu, S.; Li, B.; Tan, J.; Yan, J.; Wang, Y.; Tang, Z.; Liu, M.; Fu, C.; Zhang, H.; He, J. Dietary ferulic acid and vanillic acid on inflammation, gut barrier function and growth performance in lipopolysaccharide-challenged piglets. *Anim. Nutr.* **2022**, *8* (1), 144-152. DOI: <https://doi.org/10.1016/j.aninu.2021.06.009>.
371. Ibrahim, S. S.; Abd-allah, H. "Spanlastic nanovesicles for enhanced ocular delivery of vanillic acid: design, in vitro characterization, and in vivo anti-inflammatory evaluation". *Int. J. Pharm.* **2022**, *625*. DOI: <https://doi.org/10.1016/j.ijpharm.2022.122068>.
372. Kim, M. C.; Kim, S. J.; Kim, D. S.; Jeon, Y. D.; Park, S. J.; Lee, H. S.; Um, J. Y.; Hong, S. H. Vanillic acid inhibits inflammatory mediators by suppressing NF- κ B in lipopolysaccharide-stimulated mouse peritoneal macrophages. *Immunopharmacol. Immunotoxicol.* **2011**, *33* (3), 525-532. DOI: <https://doi.org/10.3109/08923973.2010.547500>.
373. Ma, Z.; Huang, Z.; Zhang, L.; Li, X.; Xu, B.; Xiao, Y.; Shi, X.; Zhang, H.; Liao, T.; Wang, P. Vanillic Acid Reduces Pain-Related Behavior in Knee Osteoarthritis Rats Through the Inhibition of NLRP3 Inflammasome-Related Synovitis. *Front. Pharmacol.* **2021**, *11*. DOI: <https://doi.org/10.3389/fphar.2020.599022>.
374. Zhao, J.; Yang, Y. Vanillic acid alleviates lipopolysaccharides-induced endoplasmic reticulum stress and inflammation in human lung fibroblasts by inhibiting MAPK and NF- κ B pathways. *Qual. Assur. Saf. Crops Foods.* **2022**, *14* (1), 55-63. DOI: <https://doi.org/10.15586/QAS.V14I1.1018>.
375. Ziadlou, R.; Barbero, A.; Martin, I.; Wang, X.; Qin, L.; Alini, M.; Grad, S. Anti-inflammatory and chondroprotective effects of vanillic acid and epimedin C in human osteoarthritic chondrocytes. *Biomolecules* **2020**, *10* (6), 1-28. DOI: <https://doi.org/10.3390/biom10060932>.
376. Bezerra-Filho, C. S. M.; Barboza, J. N.; Souza, M. T. S.; Sabry, P.; Ismail, N. S. M.; de Sousa, D. P. Therapeutic potential of vanillin and its main metabolites to regulate the inflammatory response and oxidative stress. *Mini-Rev. Med. Chem.* **2019**, *19* (20), 1681-1693. DOI: <https://doi.org/10.2174/1389557519666190312164355>.
377. Cheng, H. M.; Chen, F. Y.; Li, C. C.; Lo, H. Y.; Liao, Y. F.; Ho, T. Y.; Hsiang, C. Y. Oral Administration of Vanillin Improves Imiquimod-Induced Psoriatic Skin Inflammation in Mice. *J. Agric. Food Chem.* **2017**, *65* (47), 10233-10242. DOI: <https://doi.org/10.1021/acs.jafc.7b04259>.

378. Costantini, E.; Sinjari, B.; Falasca, K.; Reale, M.; Caputi, S.; Jagarlapodii, S.; Murmura, G. Assessment of the Vanillin Anti-Inflammatory and Regenerative Potentials in Inflamed Primary Human Gingival Fibroblast. *Mediators Inflamm.* **2021**, *2021*. DOI: <https://doi.org/10.1155/2021/5562340>.
379. Kim, M. E.; Na, J. Y.; Park, Y. D.; Lee, J. S. Anti-Neuroinflammatory Effects of Vanillin Through the Regulation of Inflammatory Factors and NF- κ B Signaling in LPS-Stimulated Microglia. *Appl. Biochem. Biotechnol.* **2019**, *187* (3), 884-893. DOI: <https://doi.org/10.1007/s12010-018-2857-5>.
380. Liu, X.; Yang, J.; Li, J.; Xu, C.; Jiang, W. Vanillin Attenuates Cadmium-Induced Lung Injury Through Inhibition of Inflammation and Lung Barrier Dysfunction Through Activating AhR. *Inflammation* **2021**, *44* (6), 2193-2202. DOI: <https://doi.org/10.1007/s10753-021-01492-1>.
381. Yan, X.; Liu, D. F.; Zhang, X. Y.; Liu, D.; Xu, S. Y.; Chen, G. X.; Huang, B. X.; Ren, W. Z.; Wang, W.; Fu, S. P.; Liu, J. X. Vanillin protects dopaminergic neurons against inflammation-mediated cell death by inhibiting ERK1/2, P38 and the NF- κ B signaling pathway. *Int. J. Mol. Sci.* **2017**, *18* (2). DOI: <https://doi.org/10.3390/ijms18020389>.
382. Zhao, D.; Jiang, Y.; Sun, J.; Li, H.; Huang, M.; Sun, X.; Zhao, M. Elucidation of The Anti-Inflammatory Effect of Vanillin In Lps-Activated THP-1 Cells. *J. Food Sci.* **2019**, *84* (7), 1920-1928. DOI: <https://doi.org/10.1111/1750-3841.14693>.
383. Jung, H. J.; Song, Y. S.; Lim, C. J.; Park, E. H. Anti-angiogenic, anti-inflammatory and anti-nociceptive activities of vanillyl alcohol. *Arch. Pharmacol. Res.* **2008**, *31* (10), 1275-1279. DOI: <https://doi.org/10.1007/s12272-001-2106-1>.
384. Cho, A. S.; Jeon, S. M.; Kim, M. J.; Yeo, J.; Seo, K. I.; Choi, M. S.; Lee, M. K. Chlorogenic acid exhibits anti-obesity property and improves lipid metabolism in high-fat diet-induced-obese mice. *Food Chem. Toxicol.* **2010**, *48* (3), 937-943. DOI: <https://doi.org/10.1016/j.fct.2010.01.003>.
385. He, X.; Zheng, S.; Sheng, Y.; Miao, T.; Xu, J.; Xu, W.; Huang, K.; Zhao, C. Chlorogenic acid ameliorates obesity by preventing energy balance shift in high-fat diet induced obese mice. *J. Sci. Food Agric.* **2021**, *101* (2), 631-637. DOI: <https://doi.org/10.1002/jsfa.10675>.
386. Kumar, R.; Sharma, A.; Iqbal, M. S.; Srivastava, J. K. Therapeutic promises of chlorogenic acid with special emphasis on its anti-obesity property. *Curr. Mol. Pharmacol.* **2020**, *13* (1), 7-16. DOI: <https://doi.org/10.2174/1874467212666190716145210>.
387. Wang, Z.; Lam, K. L.; Hu, J.; Ge, S.; Zhou, A.; Zheng, B.; Zeng, S.; Lin, S. Chlorogenic acid alleviates obesity and modulates gut microbiota in high-fat-fed mice. *Food Sci. Nutr.* **2019**, *7* (2), 579-588. DOI: <https://doi.org/10.1002/fsn3.868>.
388. Baek, J. H.; Kim, N. J.; Song, J. K.; Chun, K. H. Kahweol inhibits lipid accumulation and induces Glucose-uptake through activation of AMP-activated protein kinase (AMPK). *BMB Rep.* **2017**, *50* (11), 566-571. DOI: <https://doi.org/10.5483/BMBRep.2017.50.11.031>.
389. Farias-Pereira, R.; Park, C. S.; Park, Y. Kahweol Reduces Food Intake of *Caenorhabditis elegans*. *J. Agric. Food Chem.* **2020**, *68* (36), 9683-9689. DOI: <https://doi.org/10.1021/acs.jafc.0c03030>.
390. Kim, J. S.; Lee, S. G.; Kang, Y. J.; Kwon, T. K.; Nam, J. O. Kahweol inhibits adipogenesis of 3T3-L1 adipocytes through downregulation of PPAR γ . *Nat. Prod. Res.* **2018**, *32* (10), 1216-1219. DOI: <https://doi.org/10.1080/14786419.2017.1326039>.
391. Agunloye, O. M.; Oboh, G.; Ademiluyi, A. O.; Ademosun, A. O.; Akindahunsi, A. A.; Oyagbemi, A. A.; Omobowale, T. O.; Ajibade, T. O.; Adedapo, A. A. Cardio-protective and antioxidant properties of caffeic acid and chlorogenic acid: Mechanistic role of angiotensin converting enzyme, cholinesterase and arginase activities in cyclosporine induced hypertensive rats. *Biomed. Pharmacother.* **2019**, *109*, 450-458. DOI: <https://doi.org/10.1016/j.biopha.2018.10.044>.
392. Bıçakçı, N.; Karaboğa, İ.; Dökmeçi, A. H.; Güzel, S.; Fidanol Erboğa, Z. Cardioprotective effect of caffeic acid phenethyl ester on cardiac contusion following blunt chest trauma in rats. *Biotech. Histochem.* **2019**, *94* (6), 442-448. DOI: <https://doi.org/10.1080/10520295.2019.1586999>.

393. Kumaran, K. S.; Prince, P. S. M. Protective effect of caffeic acid on cardiac markers and lipid peroxide metabolism in cardiotoxic rats: An in vivo and in vitro study. *Metabolism* **2010**, *59* (8), 1172-1180. DOI: <https://doi.org/10.1016/j.metabol.2009.11.010>.
394. Salau, V. F.; Erukainure, O. L.; Islam, M. S. Caffeic Acid Protects against Iron-Induced Cardiotoxicity by Suppressing Angiotensin-Converting Enzyme Activity and Modulating Lipid Spectrum, Gluconeogenesis and Nucleotide Hydrolyzing Enzyme Activities. *Biol. Trace Elem. Res.* **2021**, *199* (3), 1052-1061. DOI: <https://doi.org/10.1007/s12011-020-02227-3>.
395. Silva, H.; Lopes, N. M. F. Cardiovascular Effects of Caffeic Acid and Its Derivatives: A Comprehensive Review. *Front. Physiol.* **2020**, *11*. DOI: <https://doi.org/10.3389/fphys.2020.595516>.
396. Banitalebi, E.; Rahimi, A.; Faramarzi, M.; Mardaniyan Ghahfarrokhi, M. The effects of elastic resistance band training and green coffee bean extract supplement on novel combined indices of cardiometabolic risk in obese women. *Res. Pharm. Sci.* **2019**, *14* (5), 414-423. DOI: <https://doi.org/10.4103/1735-5362.268202>.
397. Caro-Gómez, E.; Sierra, J. A.; Escobar, J. S.; Álvarez-Quintero, R.; Naranjo, M.; Medina, S.; Velásquez-Mejía, E. P.; Tabares-Guevara, J. H.; Jaramillo, J. C.; León-Varela, Y. M.; et al. Green coffee extract improves cardiometabolic parameters and modulates gut microbiota in high-fat-diet-fed ApoE ^{-/-} mice. *Nutrients* **2019**, *11* (3). DOI: <https://doi.org/10.3390/nu11030497>.
398. Lara-Guzmán, O. J.; Álvarez, R.; Muñoz-Durango, K. Changes in the plasma lipidome of healthy subjects after coffee consumption reveal potential cardiovascular benefits: A randomized controlled trial. *Free Radic. Biol. Med.* **2021**, *176*, 345-355. DOI: <https://doi.org/10.1016/j.freeradbiomed.2021.10.012>.
399. Suzuki, A.; Nomura, T.; Jokura, H.; Kitamura, N.; Saiki, A.; Fujii, A. Chlorogenic acid-enriched green coffee bean extract affects arterial stiffness assessed by the cardio-ankle vascular index in healthy men: a pilot study. *Int. J. Food Sci. Nutr.* **2019**, *70* (7), 901-908. DOI: <https://doi.org/10.1080/09637486.2019.1585763>.
400. Baeza, G.; Bachmair, E. M.; Wood, S.; Mateos, R.; Bravo, L.; De Roos, B. The colonic metabolites dihydrocaffeic acid and dihydroferulic acid are more effective inhibitors of in vitro platelet activation than their phenolic precursors. *Food Funct.* **2017**, *8* (3), 1333-1342. DOI: <https://doi.org/10.1039/c6fo01404f>.
401. Alam, M. A.; Sernia, C.; Brown, L. Ferulic acid improves cardiovascular and kidney structure and function in hypertensive rats. *J. Cardiovasc. Pharmacol.* **2013**, *61* (3), 240-249. DOI: <https://doi.org/10.1097/FJC.0b013e31827cb600>.
402. Li, C.; Chen, L.; Song, M.; Fang, Z.; Zhang, L.; Coffie, J. W.; Zhang, L.; Ma, L.; Wang, Q.; Yang, W.; et al. Ferulic acid protects cardiomyocytes from TNF- α /cycloheximide-induced apoptosis by regulating autophagy. *Arch. Pharmacol. Res.* **2020**, *43* (8), 863-874. DOI: <https://doi.org/10.1007/s12272-020-01252-z>.
403. Monceaux, K.; Gressette, M.; Karoui, A.; Pires Da Silva, J.; Piquereau, J.; Ventura-Clapier, R.; Garnier, A.; Mericskay, M.; Lemaire, C. Ferulic Acid, Pterostilbene, and Tyrosol Protect the Heart from ER-Stress-Induced Injury by Activating SIRT1-Dependent Deacetylation of eIF2 α . *Int. J. Mol. Sci.* **2022**, *23* (12). DOI: <https://doi.org/10.3390/ijms23126628>.
404. Neto-Neves, E. M.; Filho, C. D. S. M. B.; Dejana, N. N.; de Sousa, D. P. Ferulic acid and cardiovascular health: Therapeutic and preventive potential. *Mini-Rev. Med. Chem.* **2021**, *21* (13), 1625-1637. DOI: <https://doi.org/10.2174/1389557521666210105122841>.
405. Pandi, A.; Raghu, M. H.; Chandrashekar, N.; Kalappan, V. M. Cardioprotective effects of Ferulic acid against various drugs and toxic agents. *Beni-Suef Univ. J. Basic Appl. Sci.* **2022**, *11* (1). DOI: <https://doi.org/10.1186/s43088-022-00273-5>.
406. Salau, V. F.; Erukainure, O. L.; Olofinson, K. A.; Msomi, N. Z.; Ijomone, O. K.; Islam, M. S. Ferulic acid mitigates diabetic cardiomyopathy via modulation of metabolic abnormalities in cardiac tissues of diabetic rats. *Fundam. Clin. Pharmacol.* **2023**, *37* (1), 44-59. DOI: <https://doi.org/10.1111/fcp.12819>.
407. Zhang, X. X.; Zhao, D. S.; Wang, J.; Zhou, H.; Wang, L.; Mao, J. L.; He, J. X. The treatment of cardiovascular diseases: A review of ferulic acid and its derivatives. *Pharmazie* **2021**, *76* (2-3), 55-60. DOI: <https://doi.org/10.1691/ph.2021.0958>.

408. Xing, D.; Yoo, C.; Gonzalez, D.; Jenkins, V.; Nottingham, K.; Dickerson, B.; Leonard, M.; Ko, J.; Faries, M.; Kephart, W.; et al. Dose-response of paraxanthine on cognitive function: A double blind, placebo controlled, crossover trial. *Nutrients* **2021**, *13* (12). DOI: <https://doi.org/10.3390/nu13124478>.
409. Yoo, C.; Xing, D.; Gonzalez, D.; Jenkins, V.; Nottingham, K.; Dickerson, B.; Leonard, M.; Ko, J.; Faries, M.; Kephart, W.; et al. Acute paraxanthine ingestion improves cognition and short-term memory and helps sustain attention in a double-blind, placebo-controlled, crossover trial. *Nutrients* **2021**, *13* (11). DOI: <https://doi.org/10.3390/nu13113980>.
410. Choi, J. R.; Kim, J. H.; Lee, S.; Cho, E. J.; Kim, H. Y. Protective effects of protocatechuic acid against cognitive impairment in an amyloid beta-induced Alzheimer's disease mouse model. *Food Chem. Toxicol.* **2020**, *144*. DOI: <https://doi.org/10.1016/j.fct.2020.111571>.
411. Muley, M. M.; Thakare, V. N.; Patil, R. R.; Bafna, P. A.; Naik, S. R. Amelioration of cognitive, motor and endogenous defense functions with silymarin, piracetam and protocatechuic acid in the cerebral global ischemic rat model. *Life Sci.* **2013**, *93* (1), 51-57. DOI: <https://doi.org/10.1016/j.lfs.2013.05.020>.
412. Song, Y.; Cui, T.; Xie, N.; Zhang, X.; Qian, Z.; Liu, J. Protocatechuic acid improves cognitive deficits and attenuates amyloid deposits, inflammatory response in aged A β PP/PS1 double transgenic mice. *Int. Immunopharmacol.* **2014**, *20* (1), 276-281. DOI: <https://doi.org/10.1016/j.intimp.2014.03.006>.
413. Yin, X.; Zhang, X.; Lv, C.; Li, C.; Yu, Y.; Wang, X.; Han, F. Protocatechuic acid ameliorates neurocognitive functions impairment induced by chronic intermittent hypoxia. *Sci. Rep.* **2015**, *5*. DOI: <https://doi.org/10.1038/srep14507>.
414. Gao, L.; Ge, W.; Peng, C.; Guo, J.; Chen, N.; He, L. Association between Dietary Theobromine and Cognitive Function in a Representative American Population: A Cross-Sectional Study. *J. Prev. Alzheimers Dis.* **2022**, *9* (3), 449-457. DOI: <https://doi.org/10.14283/jpad.2022.39>.
415. Mendiola-Precoma, J.; Padilla, K.; Rodríguez-Cruz, A.; Berumen, L. C.; Miledi, R.; García-Alcocer, G. Theobromine-induced changes in A1 purinergic receptor gene expression and distribution in a rat brain Alzheimer's disease model. *J. Alzheimer's Dis.* **2017**, *55* (3), 1273-1283. DOI: <https://doi.org/10.3233/JAD-160569>.
416. Singh, J. C. H.; Kakalij, R. M.; Kshirsagar, R. P.; Kumar, B. H.; Komakula, S. S. B.; Diwan, P. V. Cognitive effects of vanillic acid against streptozotocin-induced neurodegeneration in mice. *Pharm. Biol.* **2015**, *53* (5), 630-636. DOI: <https://doi.org/10.3109/13880209.2014.935866>.
417. Ul Amin, F.; Shah, S. A.; Kim, M. O. Vanillic acid attenuates A β 1-42-induced oxidative stress and cognitive impairment in mice. *Sci. Rep.* **2017**, *7*. DOI: <https://doi.org/10.1038/srep40753>.
418. Al Asmari, A.; Al Shahrani, H.; Al Masri, N.; Al Faraidi, A.; Elfaki, I.; Arshaduddin, M. Vanillin abrogates ethanol induced gastric injury in rats via modulation of gastric secretion, oxidative stress and inflammation. *Toxicol. Rep.* **2016**, *3*, 105-113. DOI: <https://doi.org/10.1016/j.toxrep.2015.11.001>.
419. Ciciliato, M. P.; de Souza, M. C.; Tarran, C. M.; de Castilho, A. L. T.; Vieira, A. J.; Rozza, A. L. Anti-Inflammatory Effect of Vanillin Protects the Stomach against Ulcer Formation. *Pharmaceutics* **2022**, *14* (4). DOI: <https://doi.org/10.3390/pharmaceutics14040755>.
420. Mu, H. N.; Li, Q.; Fan, J. Y.; Pan, C. S.; Liu, Y. Y.; Yan, L.; Sun, K.; Hu, B. H.; Huang, D. D.; Zhao, X. R.; et al. Caffeic acid attenuates rat liver injury after transplantation involving PDIA3-dependent regulation of NADPH oxidase. *Free Radic. Biol. Med.* **2018**, *129*, 202-214. DOI: <https://doi.org/10.1016/j.freeradbiomed.2018.09.009>.
421. Mu, H. N.; Zhou, Q.; Yang, R. Y.; Tang, W. Q.; Li, H. X.; Wang, S. M.; Li, J.; Chen, W. X.; Dong, J. Caffeic acid prevents non-alcoholic fatty liver disease induced by a high-fat diet through gut microbiota modulation in mice. *Food Res. Int.* **2021**, *143*. DOI: <https://doi.org/10.1016/j.foodres.2021.110240>.
422. Pang, C.; Shi, L.; Sheng, Y.; Zheng, Z.; Wei, H.; Wang, Z.; Ji, L. Caffeic acid attenuated acetaminophen-induced hepatotoxicity by inhibiting ERK1/2-mediated early growth response-1 transcriptional activation. *Chem. Biol. Interact.* **2016**, *260*, 186-195. DOI: <https://doi.org/10.1016/j.cbi.2016.10.009>.
423. Pang, C.; Zheng, Z.; Shi, L.; Sheng, Y.; Wei, H.; Wang, Z.; Ji, L. Caffeic acid prevents acetaminophen-induced liver injury by activating the Keap1-Nrf2 antioxidative defense system. *Free Radic. Biol. Med.* **2016**, *91*, 236-246. DOI: <https://doi.org/10.1016/j.freeradbiomed.2015.12.024>.

424. Sánchez-Medina, A.; Redondo-Puente, M.; Dupak, R.; Bravo-Clemente, L.; Goya, L.; Sarriá, B. Colonic Coffee Phenols Metabolites, Dihydrocaffeic, Dihydroferulic, and Hydroxyhippuric Acids Protect Hepatic Cells from TNF- α -Induced Inflammation and Oxidative Stress. *Int. J. Mol. Sci.* **2023**, *24* (2). DOI: <https://doi.org/10.3390/ijms24021440>.
425. Gressner, O. A. About coffee, cappuccino and connective tissue growth factor-Or how to protect your liver!?. *Environ. Toxicol. Pharmacol.* **2009**, *28* (1), 1-10. DOI: <https://doi.org/10.1016/j.etap.2009.02.005>.
426. Gressner, O. A.; Lahme, B.; Siluschek, M.; Gressner, A. M. Identification of paraxanthine as the most potent caffeine-derived inhibitor of connective tissue growth factor expression in liver parenchymal cells. *Liver Int.* **2009**, *29* (6), 886-897. DOI: <https://doi.org/10.1111/j.1478-3231.2009.01987.x>.
427. Klemmer, I.; Yagi, S.; Gressner, O. A. Oral application of 1,7-dimethylxanthine (paraxanthine) attenuates the formation of experimental cholestatic liver fibrosis. *Hepatol. Res.* **2011**, *41* (11), 1094-1109. DOI: <https://doi.org/10.1111/j.1872-034X.2011.00856.x>.
428. Wei, D.; Wu, S.; Liu, J.; Zhang, X.; Guan, X.; Gao, L.; Xu, Z. Theobromine ameliorates nonalcoholic fatty liver disease by regulating hepatic lipid metabolism via mtor signaling pathway in vivo and in vitro. *Can. J. Physiol. Pharmacol.* **2021**, *99* (8), 775-785. DOI: <https://doi.org/10.1139/cjpp-2020-0259>.
429. Ben Saad, H.; Driss, D.; Ben Amara, I.; Boudawara, O.; Boudawara, T.; Ellouz Chaabouni, S.; Mounir Zeghal, K.; Hakim, A. Altered hepatic mRNA expression of immune response-associated DNA damage in mice liver induced by potassium bromate: Protective role of vanillin. *Environ. Toxicol.* **2016**, *31* (12), 1796-1807. DOI: <https://doi.org/10.1002/tox.22181>.
430. Ghanim, A. M. H.; Younis, N. S.; Metwaly, H. A. Vanillin augments liver regeneration effectively in hioacetamide induced liver fibrosis rat model. *Life Sci.* **2021**, *286*. DOI: <https://doi.org/10.1016/j.lfs.2021.120036>.
431. Liang, J. A.; Wu, S. L.; Lo, H. Y.; Hsiang, C. Y.; Ho, T. Y. Vanillin inhibits matrix metalloproteinase-9 expression through down-regulation of nuclear factor- κ B signaling pathway in human hepatocellular carcinoma cells. *Mol. Pharmacol.* **2009**, *75* (1), 151-157. DOI: <https://doi.org/10.1124/mol.108.049502>.
432. Makni, M.; Chtourou, Y.; Fetoui, H.; Garoui, E. M.; Boudawara, T.; Zeghal, N. Evaluation of the antioxidant, anti-inflammatory and hepatoprotective properties of vanillin in carbon tetrachloride-treated rats. *Eur. J. Pharmacol.* **2011**, *668* (1-2), 133-139. DOI: <https://doi.org/10.1016/j.ejphar.2011.07.001>.
433. Abdelrahman, R. S.; El-Tanbouly, G. S. Protocatechuic acid protects against thioacetamide-induced chronic liver injury and encephalopathy in mice via modulating mTOR, p53 and the IL-6/ IL-17/ IL-23 immunoinflammatory pathway. *Toxicol. Appl. Pharmacol.* **2022**, *440*. DOI: <https://doi.org/10.1016/j.taap.2022.115931>.
434. Salama, A.; Elgohary, R.; Amin, M. M.; Elwahas, S. A. Immunomodulatory effect of protocatechuic acid on cyclophosphamide induced brain injury in rat: Modulation of inflammasomes NLRP3 and SIRT1. *Eur. J. Pharmacol.* **2022**, *932*. DOI: <https://doi.org/10.1016/j.ejphar.2022.175217>.
435. Adeyanju, A. A.; Molehin, O. R.; Asejeje, F. O.; Oyenuga, V.; Etokakpan, R. U. Protocatechuic acid through modulation of signaling pathways and oxidative stress exerts protective effects in rat model of carbon tetrachloride-induced renal and reproductive toxicities. *Comp. Clin. Path.* **2022**, *31* (3), 465-474. DOI: <https://doi.org/10.1007/s00580-022-03345-1>.
436. Kassab, R. B.; Theyab, A.; Al-Ghamdy, A. O.; Algahtani, M.; Mufti, A. H.; Alsharif, K. F.; Abdella, E. M.; Habotta, O. A.; Omran, M. M.; Lokman, M. S.; et al. Protocatechuic acid abrogates oxidative insults, inflammation, and apoptosis in liver and kidney associated with monosodium glutamate intoxication in rats. *Environ. Sci. Pollut. Res.* **2022**, *29* (8), 12208-12221. DOI: <https://doi.org/10.1007/s11356-021-16578-4>.
437. Lin, C. Y.; Tsai, S. J.; Huang, C. S.; Yin, M. C. Antiglycative effects of protocatechuic acid in the kidneys of diabetic mice. *J. Agric. Food Chem.* **2011**, *59* (9), 5117-5124. DOI: <https://doi.org/10.1021/jf200103f>.
438. Salama, A. A. A.; Elgohary, R.; Fahmy, M. I. Protocatechuic acid ameliorates lipopolysaccharide-induced kidney damage in mice via downregulation of TLR-4-mediated I κ B/NF- κ B and MAPK/Erk signaling pathways. *J. Appl. Toxicol.* **2023**, *10.1002/jat.4447*. DOI: <https://doi.org/10.1002/jat.4447>.

439. Yamabe, N.; Park, J. Y.; Lee, S.; Cho, E. J.; Lee, S.; Kang, K. S.; Hwang, G. S.; Kim, S. N.; Kim, H. Y.; Shibamoto, T. Protective effects of protocatechuic acid against cisplatin-induced renal damage in rats. *J. Funct. Foods* **2015**, *19*, 20-27. DOI: <https://doi.org/10.1016/j.jff.2015.08.028>.
440. Chattaraj, K. G.; Paul, S. Inclusion of Theobromine Modifies Uric Acid Aggregation with Possible Changes in Melamine-Uric Acid Clusters Responsible for Kidney Stones. *J. Phys. Chem. B* **2019**, *123* (49), 10483-10504. DOI: <https://doi.org/10.1021/acs.jpcc.9b08487>.
441. Hernandez, Y.; Costa-Bauza, A.; Calvó, P.; Benejam, J.; Sanchis, P.; Grases, F. Comparison of two dietary supplements for treatment of uric acid renal lithiasis: Citrate vs. citrate + theobromine. *Nutrients* **2020**, *12* (7), 1-8. DOI: <https://doi.org/10.3390/nu12072012>.
442. Julià, F.; Costa-Bauza, A.; Berga, F.; Grases, F. Effect of theobromine on dissolution of uric acid kidney stones. *World J. Urol.* **2022**, *40* (8), 2105-2111. DOI: <https://doi.org/10.1007/s00345-022-04059-3>.
443. Papadimitriou, A.; Silva, K. C.; Peixoto, E. B. M. I.; Borges, C. M.; de Faria, J. M. L.; de Faria, J. B. L. Theobromine increases NAD⁺/Sirt-1 activity and protects the kidney under diabetic conditions. *Am. J. Physiol. Ren. Physiol.* **2015**, *308* (3), F209-F225. DOI: <https://doi.org/10.1152/ajprenal.00252.2014>.
444. Prediger, R. D. S. Effects of caffeine in Parkinson's disease: From neuroprotection to the management of motor and non-motor symptoms. *J. Alzheimer's Dis.* **2010**, *20* (SUPPL.1), S205-S220. DOI: <https://doi.org/10.3233/JAD-2010-091459>.
445. Arendash, G. W.; Cao, C. Caffeine and coffee as therapeutics against Alzheimer's disease. *J. Alzheimer's Dis.* **2010**, *20* (SUPPL.1), S117-S126. DOI: <https://doi.org/10.3233/JAD-2010-091249>.
446. Chu, Y. F.; Chang, W. H.; Black, R. M.; Liu, J. R.; Sompol, P.; Chen, Y.; Wei, H.; Zhao, Q.; Cheng, I. H. Crude caffeine reduces memory impairment and amyloid β 1-42 levels in an Alzheimer's mouse model. *Food Chem.* **2012**, *135* (3), 2095-2102. DOI: <https://doi.org/10.1016/j.foodchem.2012.04.148>.
447. Di Martino, E.; Bocchetta, E.; Tsuji, S.; Mukai, T.; Harris, R. A.; Blomgren, K.; Ådén, U. Defining a Time Window for Neuroprotection and Glia Modulation by Caffeine After Neonatal Hypoxia-Ischaemia. *Mol. Neurobiol.* **2020**, *57* (5), 2194-2205. DOI: <https://doi.org/10.1007/s12035-020-01867-9>.
448. Endesfelder, S.; Weichelt, U.; Strauß, E.; Schlör, A.; Sifringer, M.; Scheuer, T.; Bühner, C.; Schmitz, T. Neuroprotection by caffeine in hyperoxia-induced neonatal brain injury. *Int. J. Mol. Sci.* **2017**, *18* (1). DOI: <https://doi.org/10.3390/ijms18010187>.
449. Farrokhi, M. R.; Emamghoreishi, M.; Amiri, A.; Keshavarz, M. Neuroprotective effects of caffeine against beta-amyloid neurotoxicity: The involvement of glycogen synthase kinase-3 β protein. *Physiol. Pharmacol. (Iran)* **2019**, *23* (3), 150-153.
450. Ikram, M.; Park, T. J.; Ali, T.; Kim, M. O. Antioxidant and neuroprotective effects of caffeine against Alzheimer's and parkinson's disease: Insight into the role of Nrf-2 and A2AR signaling. *Antioxidants* **2020**, *9* (9), 1-21. DOI: <https://doi.org/10.3390/antiox9090902>.
451. Karuppagounder, S. S.; Uthaythas, S.; Govindarajulu, M.; Ramesh, S.; Parameshwaran, K.; Dhanasekaran, M. Caffeine, a natural methylxanthine nutraceutical, exerts dopaminergic neuroprotection. *Neurochem. Int.* **2021**, *148*. DOI: <https://doi.org/10.1016/j.neuint.2021.105066>.
452. Khadrawy, Y. A.; Salem, A. M.; El-Shamy, K. A.; Ahmed, E. K.; Fadl, N. N.; Hosny, E. N. Neuroprotective and Therapeutic Effect of Caffeine on the Rat Model of Parkinson's Disease Induced by Rotenone. *J. Diet. Suppl.* **2017**, *14* (5), 553-572. DOI: <https://doi.org/10.1080/19390211.2016.1275916>.
453. Kolahdouzan, M.; Hamadeh, M. J. The neuroprotective effects of caffeine in neurodegenerative diseases. *CNS Neurosci. Ther.* **2017**, *23* (4), 272-290. DOI: <https://doi.org/10.1111/cns.12684>.
454. Pereira-Figueiredo, D.; Nascimento, A. A.; Cunha-Rodrigues, M. C.; Brito, R.; Calaza, K. C. Caffeine and Its Neuroprotective Role in Ischemic Events: A Mechanism Dependent on Adenosine Receptors. *Cell. Mol. Neurobiol.* **2022**, *42* (6), 1693-1725. DOI: <https://doi.org/10.1007/s10571-021-01077-4>.
455. Xu, K.; Di Luca, D. G.; Orrú, M.; Xu, Y.; Chen, J. F.; Schwarzschild, M. A. Neuroprotection by caffeine in the MPTP model of parkinson's disease and its dependence on adenosine A2A receptors. *Neuroscience* **2016**, *322*, 129-137. DOI: <https://doi.org/10.1016/j.neuroscience.2016.02.035>.

456. Xu, K.; Xu, Y. H.; Chen, J. F.; Schwarzschild, M. A. Neuroprotection by caffeine: Time course and role of its metabolites in the MPTP model of Parkinson's disease. *Neuroscience* **2010**, *167* (2), 475-481. DOI: <https://doi.org/10.1016/j.neuroscience.2010.02.020>.
457. Yan, R.; Zhang, J.; Park, H. J.; Park, E. S.; Oh, S.; Zheng, H.; Junn, E.; Voronkov, M.; Stock, J. B.; Mouradian, M. M. Synergistic neuroprotection by coffee components eicosanoyl-5-hydroxytryptamide and caffeine in models of Parkinson's disease and DLB. *Proc. Natl. Acad. Sci. U. S. A.* **2018**, *115* (51), E12053-E12062. DOI: <https://doi.org/10.1073/pnas.1813365115>.
458. Yelanchezian, Y. M. M.; Waldvogel, H. J.; Faull, R. L. M.; Kwakowsky, A. Neuroprotective Effect of Caffeine in Alzheimer's Disease. *Molecules* **2022**, *27* (12). DOI: <https://doi.org/10.3390/molecules27123737>.
459. Zhou, X.; Zhang, L. The Neuroprotective Effects of Moderate and Regular Caffeine Consumption in Alzheimer's Disease. *Oxidative Med. Cell. Longev.* **2021**, *2021*. DOI: <https://doi.org/10.1155/2021/5568011>.
460. Tan, E. K.; Chua, E.; Fook-Chong, S. M.; Teo, Y. Y.; Yuen, Y.; Tan, L.; Zhao, Y. Association between caffeine intake and risk of Parkinson's disease among fast and slow metabolizers. *Pharmacogenet. Genomics* **2007**, *17* (11), 1001-1005. DOI: <https://doi.org/10.1097/FPC.0b013e3282f09265>.
461. Alves-Martinez, P.; Atienza-Navarro, I.; Vargas-Soria, M.; Carranza-Naval, M. J.; Infante-Garcia, C.; Benavente-Fernandez, I.; Del Marco, A.; Lubian-Lopez, S.; Garcia-Alloza, M. Caffeine Restores Neuronal Damage and Inflammatory Response in a Model of Intraventricular Hemorrhage of the Preterm Newborn. *Front. Microbiol.* **2022**, *10*. DOI: <https://doi.org/10.3389/fcell.2022.908045>.
462. Heise, J.; Schmitz, T.; Bühner, C.; Endesfelder, S. Protective Effects of Early Caffeine Administration in Hyperoxia-Induced Neurotoxicity in the Juvenile Rat. *Antioxidants* **2023**, *12* (2). DOI: <https://doi.org/10.3390/antiox12020295>.
463. Kim, E.; Robinson, N. M.; Newman, B. M. A Brewed Awakening: Neuropsychiatric Effects of Caffeine in Older Adults. *Clin. Geriatr. Med.* **2022**, *38* (1), 133-144. DOI: <https://doi.org/10.1016/j.cger.2021.07.009>.
464. Pohanka, M. Role of Caffeine in the Age-related Neurodegenerative Diseases: A Review. *Mini-Rev. Med. Chem.* **2022**, *22* (21), 2726-2735. DOI: <https://doi.org/10.2174/1389557522666220413103529>.
465. Ruggiero, M.; Calvello, R.; Porro, C.; Messina, G.; Cianciulli, A.; Panaro, M. A. Neurodegenerative Diseases: Can Caffeine Be a Powerful Ally to Weaken Neuroinflammation? *Int. J. Mol. Sci.* **2022**, *23* (21). DOI: <https://doi.org/10.3390/ijms232112958>.
466. Basu Mallik, S.; Mudgal, J.; Nampoothiri, M.; Hall, S.; Dukie, S. A.; Grant, G.; Rao, C. M.; Arora, D. Caffeic acid attenuates lipopolysaccharide-induced sickness behaviour and neuroinflammation in mice. *Neurosci. Lett.* **2016**, *632*, 218-223. DOI: <https://doi.org/10.1016/j.neulet.2016.08.044>.
467. Saenno, R.; Dornlakorn, O.; Anosri, T.; Kaewngam, S.; Sirichoat, A.; Aranarochana, A.; Pannangrong, W.; Wigmore, P.; Welbat, J. U. Caffeic Acid Alleviates Memory and Hippocampal Neurogenesis Deficits in Aging Rats induced by D-Galactose. *Nutrients* **2022**, *14* (10). DOI: <https://doi.org/10.3390/nu14102169>.
468. Zaitone, S. A.; Ahmed, E.; Elsherbiny, N. M.; Mehanna, E. T.; El-Kherbetawy, M. K.; ElSayed, M. H.; Alshareef, D. M.; Moustafa, Y. M. Caffeic acid improves locomotor activity and lessens inflammatory burden in a mouse model of rotenone-induced nigral neurodegeneration: Relevance to Parkinson's disease therapy. *Pharmacol. Rep.* **2019**, *71* (1), 32-41. DOI: <https://doi.org/10.1016/j.pharep.2018.08.004>.
469. Heitman, E.; Ingram, D. K. Cognitive and neuroprotective effects of chlorogenic acid. *Nutr. Neurosci.* **2017**, *20* (1), 32-39. DOI: <https://doi.org/10.1179/1476830514Y.0000000146>.
470. Kumar, G.; Mukherjee, S.; Paliwal, P.; Singh, S. S.; Birla, H.; Singh, S. P.; Krishnamurthy, S.; Patnaik, R. Neuroprotective effect of chlorogenic acid in global cerebral ischemia-reperfusion rat model. *Naunyn-Schmiedeberg's Arch. Pharmacol.* **2019**, *392* (10), 1293-1309. DOI: <https://doi.org/10.1007/s00210-019-01670-x>.
471. Kwon, S. H.; Lee, H. K.; Kim, J. A.; Hong, S. I.; Kim, H. C.; Jo, T. H.; Park, Y. I.; Lee, C. K.; Kim, Y. B.; Lee, S. Y.; Jang, C. G. Neuroprotective effects of chlorogenic acid on scopolamine-induced amnesia via anti-acetylcholinesterase and anti-oxidative activities in mice. *Eur. J. Pharmacol.* **2010**, *649* (1-3), 210-217. DOI: <https://doi.org/10.1016/j.ejphar.2010.09.001>.

472. Liberato, J. L.; Rosa, M. N.; Miranda, M. C. R.; Lopes, J. L. C.; Lopes, N. P.; Gobbo-Neto, L.; Fontana, A. C. K.; Dos Santos, W. F. Neuroprotective Properties of Chlorogenic Acid and 4,5-Caffeoylquinic Acid from Brazilian arnica (*Lychnophora ericoides*) after Acute Retinal Ischemia. *Planta Med.* **2023**, *89* (2), 183-193. DOI: <https://doi.org/10.1055/a-1903-2387>.
473. Liu, Y.; Wang, F.; Li, Z.; Mu, Y.; Yong, V. W.; Xue, M. Neuroprotective Effects of Chlorogenic Acid in a Mouse Model of Intracerebral Hemorrhage Associated with Reduced Extracellular Matrix Metalloproteinase Inducer. *Biomolecules* **2022**, *12* (8). DOI: <https://doi.org/10.3390/biom12081020>.
474. Metwally, D. M.; Alajmi, R. A.; El-Khadragy, M. F.; Yehia, H. M.; Al-Megrin, W. A.; Akabawy, A. M. A.; Amin, H. K.; Abdel Moneim, A. E. Chlorogenic acid confers robust neuroprotection against arsenite toxicity in mice by reversing oxidative stress, inflammation, and apoptosis. *J. Funct. Foods* **2020**, *75*. DOI: <https://doi.org/10.1016/j.jff.2020.104202>.
475. Rebai, O.; Belkhir, M.; Sanchez-Gomez, M. V.; Matute, C.; Fattouch, S.; Amri, M. Differential Molecular Targets for Neuroprotective Effect of Chlorogenic Acid and its Related Compounds Against Glutamate Induced Excitotoxicity and Oxidative Stress in Rat Cortical Neurons. *Neurochem. Res.* **2017**, *42* (12), 3559-3572. DOI: <https://doi.org/10.1007/s11064-017-2403-9>.
476. Sharma, N.; Soni, R.; Sharma, M.; Chatterjee, S.; Parihar, N.; Mukarram, M.; Kale, R.; Sayyed, A. A.; Behera, S. K.; Khairnar, A. Chlorogenic Acid: a Polyphenol from Coffee Rendered Neuroprotection Against Rotenone-Induced Parkinson's Disease by GLP-1 Secretion. *Mol. Neurobiol.* **2022**, *59* (11), 6834-6856. DOI: <https://doi.org/10.1007/s12035-022-03005-z>.
477. Singh, S. S.; Rai, S. N.; Birla, H.; Zahra, W.; Rathore, A. S.; Dilnashin, H.; Singh, R.; Singh, S. P. Neuroprotective Effect of Chlorogenic Acid on Mitochondrial Dysfunction-Mediated Apoptotic Death of da Neurons in a Parkinsonian Mouse Model. *Oxidative Med. Cell. Longev.* **2020**, *2020*. DOI: <https://doi.org/10.1155/2020/6571484>.
478. Zheng, Y.; Li, L.; Chen, B.; Fang, Y.; Lin, W.; Zhang, T.; Feng, X.; Tao, X.; Wu, Y.; Fu, X.; Lin, Z. Chlorogenic acid exerts neuroprotective effect against hypoxia-ischemia brain injury in neonatal rats by activating Sirt1 to regulate the Nrf2-NF- κ B signaling pathway. *Cell Commun. Signal.* **2022**, *20* (1). DOI: <https://doi.org/10.1186/s12964-022-00860-0>.
479. Lee, K.; Lee, B. J.; Bu, Y. Protective effects of dihydrocaffeic acid, a coffee component metabolite, on a focal cerebral ischemia rat model. *Molecules* **2015**, *20* (7), 11930-11940. DOI: <https://doi.org/10.3390/molecules200711930>.
480. Alharthy, K. M.; Balaha, M. F.; Devi, S.; Altharawi, A.; Yusufoglu, H. S.; Aldossari, R. M.; Alam, A.; Giacomo, V. D. Ameliorative Effects of Isoleugenol and Eugenol against Impaired Nerve Function and Inflammatory and Oxidative Mediators in Diabetic Neuropathic Rats. *Biomedicines* **2023**, *11* (4). DOI: <https://doi.org/10.3390/biomedicines11041203>.
481. Ren, Z.; Li, Y.; Zhang, R.; Li, Y.; Yang, Z.; Yang, H. Ferulic acid exerts neuroprotective effects against cerebral ischemia/reperfusion-induced injury via antioxidant and anti-apoptotic mechanisms in vitro and in vivo. *Int. J. Mol. Med.* **2017**, *40* (5), 1444-1456. DOI: <https://doi.org/10.3892/ijmm.2017.3127>.
482. Di Giacomo, S.; Percaccio, E.; Gulli, M.; Romano, A.; Vitalone, A.; Mazzanti, G.; Gaetani, S.; Di Sotto, A. Recent Advances in the Neuroprotective Properties of Ferulic Acid in Alzheimer's Disease: A Narrative Review. *Nutrients* **2022**, *14* (18). DOI: <https://doi.org/10.3390/nu14183709>.
483. Dong, X.; Huang, R. Ferulic acid: An extraordinarily neuroprotective phenolic acid with anti-depressive properties. *Phytomedicine* **2022**, *105*. DOI: <https://doi.org/10.1016/j.phymed.2022.154355>.
484. Hassanzadeh, P.; Arbabi, E.; Atyabi, F.; Dinarvand, R. Ferulic acid, a phenolic compound with therapeutic effects in neuropsychiatric disorders, stimulates the production of nerve growth factor and endocannabinoids in rat brain. *Physiol. Pharmacol. (Iran)* **2017**, *21* (4), 279-294.
485. Liu, G.; Nie, Y.; Huang, C.; Zhu, G.; Zhang, X.; Hu, C.; Li, Z.; Gao, Y.; Ma, Z. Ferulic acid produces neuroprotection against radiation-induced neuroinflammation by affecting NLRP3 inflammasome activation. *Int. J. Radiat. Biol.* **2022**, *98* (9), 1442-1451. DOI: <https://doi.org/10.1080/09553002.2022.2055798>.

486. Liu, Y. M.; Shen, J. D.; Xu, L. P.; Li, H. B.; Li, Y. C.; Yi, L. T. Ferulic acid inhibits neuro-inflammation in mice exposed to chronic unpredictable mild stress. *Int. Immunopharmacol.* **2017**, *45*, 128-134. DOI: <https://doi.org/10.1016/j.intimp.2017.02.007>.
487. Long, T.; Wu, Q.; Wei, J.; Tang, Y.; He, Y. N.; He, C. L.; Chen, X.; Yu, L.; Yu, C. L.; Law, B. Y.; et al. Ferulic Acid Exerts Neuroprotective Effects via Autophagy Induction in *C. elegans* and Cellular Models of Parkinson's Disease. *Oxidative Med. Cell. Longev.* **2022**, 2022. DOI: <https://doi.org/10.1155/2022/3723567>.
488. Ojha, S.; Javed, H.; Azimullah, S.; Khair, S. B. A.; Haque, M. E. Neuroprotective potential of ferulic acid in the rotenone model of Parkinson's disease. *Drug Des. Devel. Ther.* **2015**, *9*, 5499-5510. DOI: <https://doi.org/10.2147/DDDT.S90616>.
489. Singh, S.; Arthur, R.; Upadhyay, S.; Kumar, P. Ferulic acid ameliorates neurodegeneration via the Nrf2/ARE signalling pathway: A Review. *Pharmacol. Res. Mod. Chin. Med.* **2022**, *5*. DOI: <https://doi.org/10.1016/j.prmcm.2022.100190>.
490. Thapliyal, S.; Singh, T.; Handu, S.; Bisht, M.; Kumari, P.; Arya, P.; Srivastava, P.; Gandham, R. A Review on Potential Footprints of Ferulic Acid for Treatment of Neurological Disorders. *Neurochem. Res.* **2021**, *46* (5), 1043-1057. DOI: <https://doi.org/10.1007/s11064-021-03257-6>.
491. Yin, C. L.; Lu, R. G.; Zhu, J. F.; Huang, H. M.; Liu, X.; Li, Q. F.; Mo, Y. Y.; Zhu, H. J.; Chin, B.; Wu, J. X.; et al. The study of neuroprotective effect of ferulic acid based on cell metabolomics. *Eur. J. Pharmacol.* **2019**, *864*. DOI: <https://doi.org/10.1016/j.ejphar.2019.172694>.
492. Prasad, S. N. Neuroprotective efficacy of eugenol and isoeugenol in acrylamide-induced neuropathy in rats: Behavioral and biochemical evidence. *Neurochem. Res.* **2013**, *38* (2), 330-345. DOI: <https://doi.org/10.1007/s11064-012-0924-9>.
493. Costentin, J. Main neurotropic and psychotropic effects of methylxanthines (caffeine, theophylline, theobromine, paraxanthine). *PSN* **2010**, *8* (4), 182-186. DOI: <https://doi.org/10.1007/s11836-010-0141-z>.
494. Crotty, G. F.; Maciuga, R.; Macklin, E. A.; Wang, J.; Montalban, M.; Davis, S. S.; Alkabsh, J. I.; Bakshi, R.; Chen, X.; Ascherio, A.; et al. Association of caffeine and related analytes with resistance to Parkinson disease among LRRK2 mutation carriers: A metabolomic study. *Neurology* **2020**, *95* (24), e3428-e3437. DOI: <https://doi.org/10.1212/WNL.0000000000010863>.
495. Guerreiro, S.; Toulorge, D.; Hirsch, E.; Marien, M.; Sokoloff, P.; Michel, P. P. Paraxanthine, the primary metabolite of caffeine, provides protection against dopaminergic cell death via stimulation of ryanodine receptor channels. *Mol. Pharmacol.* **2008**, *74* (4), 980-989. DOI: <https://doi.org/10.1124/mol.108.048207>.
496. Matsumura, N.; Kinoshita, C.; Bhadhprasit, W.; Nakaki, T.; Aoyama, K. A purine derivative, paraxanthine, promotes cysteine uptake for glutathione synthesis. *J. Pharmacol. Sci.* **2023**, *151* (1), 37-45. DOI: <https://doi.org/10.1016/j.jphs.2022.11.001>.
497. Adedara, I. A.; Fasina, O. B.; Ayeni, M. F.; Ajayi, O. M.; Farombi, E. O. Protocatechuic acid ameliorates neurobehavioral deficits via suppression of oxidative damage, inflammation, caspase-3 and acetylcholinesterase activities in diabetic rats. *Food Chem. Toxicol.* **2019**, *125*, 170-181. DOI: <https://doi.org/10.1016/j.fct.2018.12.040>.
498. Al Olayan, E. M.; Aloufi, A. S.; AlAmri, O. D.; El-Habit, O. H.; Abdel Moneim, A. E. Protocatechuic acid mitigates cadmium-induced neurotoxicity in rats: Role of oxidative stress, inflammation and apoptosis. *Sci. Total Environ.* **2020**, 723. DOI: <https://doi.org/10.1016/j.scitotenv.2020.137969>.
499. Hornedo-Ortega, R.; Álvarez-Fernández, M. A.; Cerezo, A. B.; Richard, T.; Troncoso, A. M.; Garcia-Parrilla, M. C. Protocatechuic Acid: Inhibition of Fibril Formation, Destabilization of Preformed Fibrils of Amyloid- β and α -Synuclein, and Neuroprotection. *J. Agric. Food Chem.* **2016**, *64* (41), 7722-7732. DOI: <https://doi.org/10.1021/acs.jafc.6b03217>.
500. Kale, S.; Sarode, L. P.; Kharat, A.; Ambulkar, S.; Prakash, A.; Sakharkar, A. J.; Ugale, R. R. Protocatechuic Acid Prevents Early Hour Ischemic Reperfusion Brain Damage by Restoring Imbalance of Neuronal Cell Death and Survival Proteins. *J. Stroke Cerebrovasc. Dis.* **2021**, *30* (2). DOI: <https://doi.org/10.1016/j.jstrokecerebrovasdis.2020.105507>.

501. Kangtao; Yangqian; Bais, S. Neuroprotective effect of protocatechuic acid through MAO-B inhibition in aluminium chloride induced dementia of alzheimer's type in rats. *Int. J. Pharmacol.* **2018**, *14* (6), 879-888. DOI: <https://doi.org/10.3923/ijp.2018.879.888>.
502. Kho, A. R.; Choi, B. Y.; Lee, S. H.; Hong, D. K.; Lee, S. H.; Jeong, J. H.; Park, K. H.; Song, H. K.; Choi, H. C.; Suh, S. W. Effects of protocatechuic acid (PCA) on global cerebral ischemia-induced hippocampal neuronal death. *Int. J. Mol. Sci.* **2018**, *19* (5). DOI: <https://doi.org/10.3390/ijms19051420>.
503. Krzysztoforska, K.; Mirowska-Guzel, D.; Widy-Tyszkiewicz, E. Pharmacological effects of protocatechuic acid and its therapeutic potential in neurodegenerative diseases: Review on the basis of in vitro and in vivo studies in rodents and humans. *Nutr. Neurosci.* **2019**, *22* (2), 72-82. DOI: <https://doi.org/10.1080/1028415X.2017.1354543>.
504. Lee, S. H.; Choi, B. Y.; Kho, A. R.; Jeong, J. H.; Hong, D. K.; Lee, S. H.; Lee, S. Y.; Lee, M. W.; Song, H. K.; Choi, H. C.; Suh, S. W. Protective effects of protocatechuic acid on seizure-induced neuronal death. *Int. J. Mol. Sci.* **2018**, *19* (1). DOI: <https://doi.org/10.3390/ijms19010187>.
505. Lee, S. H.; Choi, B. Y.; Lee, S. H.; Kho, A. R.; Jeong, J. H.; Hong, D. K.; Suh, S. W. Administration of protocatechuic acid reduces traumatic brain injury-induced neuronal death. *Int. J. Mol. Sci.* **2017**, *18* (12). DOI: <https://doi.org/10.3390/ijms18122510>.
506. Li, H.; Zheng, T.; Lian, F.; Xu, T.; Yin, W.; Jiang, Y. Anthocyanin-rich blueberry extracts and anthocyanin metabolite protocatechuic acid promote autophagy-lysosomal pathway and alleviate neurons damage in in vivo and in vitro models of Alzheimer's disease. *Nutrition* **2022**, *93*. DOI: <https://doi.org/10.1016/j.nut.2021.111473>.
507. Mert, H.; Kerem, Ö.; Mis, L.; Yıldırım, S.; Mert, N. Effects of protocatechuic acid against cisplatin-induced neurotoxicity in rat brains: an experimental study. *Int. J. Neurosci.* **2022**, 10.1080/00207454.2022.2147430. DOI: <https://doi.org/10.1080/00207454.2022.2147430>.
508. Winter, A. N.; Brenner, M. C.; Punessen, N.; Snodgrass, M.; Byars, C.; Arora, Y.; Linseman, D. A. Comparison of the Neuroprotective and Anti-Inflammatory Effects of the Anthocyanin Metabolites, Protocatechuic Acid and 4-Hydroxybenzoic Acid. *Oxidative Med. Cell. Longev.* **2017**, *2017*. DOI: <https://doi.org/10.1155/2017/6297080>.
509. Zhang, H. N.; An, C. N.; Zhang, H. N.; Pu, X. P. Protocatechuic acid inhibits neurotoxicity induced by MPTP in vivo. *Neurosci. Lett.* **2010**, *474* (2), 99-103. DOI: <https://doi.org/10.1016/j.neulet.2010.03.016>.
510. Zhang, Z.; Li, G.; Szeto, S. S. W.; Chong, C. M.; Quan, Q.; Huang, C.; Cui, W.; Guo, B.; Wang, Y.; Han, Y.; et al. Examining the neuroprotective effects of protocatechuic acid and chrysin on in vitro and in vivo models of Parkinson disease. *Free Radic. Biol. Med.* **2015**, *84*, 331-343. DOI: <https://doi.org/10.1016/j.freeradbiomed.2015.02.030>.
511. Lee, M.; McGeer, E. G.; McGeer, P. L. Quercetin, not caffeine, is a major neuroprotective component in coffee. *Neurobiol. Aging* **2016**, *46*, 113-123. DOI: <https://doi.org/10.1016/j.neurobiolaging.2016.06.015>.
512. Alvarez-Arellano, L.; Salazar-García, M.; Corona, J. C. Neuroprotective effects of Quercetin in pediatric neurological diseases. *Molecules* **2020**, *25* (23). DOI: <https://doi.org/10.3390/molecules25235597>.
513. Barreca, D.; Bellocco, E.; D'Onofrio, G.; Nabavi, S. F.; Daglia, M.; Rastrelli, L.; Nabavi, S. M. Neuroprotective effects of quercetin: From chemistry to medicine. *CNS Neurol. Disord. Drug Targets* **2016**, *15* (8), 964-975. DOI: <https://doi.org/10.2174/1871527315666160813175406>.
514. Bhat, I. U. H.; Bhat, R. Quercetin: A bioactive compound imparting cardiovascular and neuroprotective benefits: Scope for exploring fresh produce, their wastes, and by-products. *Biology* **2021**, *10* (7). DOI: <https://doi.org/10.3390/biology10070586>.
515. Chiang, M. C.; Tsai, T. Y.; Wang, C. J. The Potential Benefits of Quercetin for Brain Health: A Review of Anti-Inflammatory and Neuroprotective Mechanisms. *Int. J. Mol. Sci.* **2023**, *24* (7). DOI: <https://doi.org/10.3390/ijms24076328>.
516. Costa, L. G.; Garrick, J. M.; Roquè, P. J.; Pellacani, C. Mechanisms of Neuroprotection by Quercetin: Counteracting Oxidative Stress and More. *Oxidative Med. Cell. Longev.* **2016**, *2016*. DOI: <https://doi.org/10.1155/2016/2986796>.

517. Fideles, S. O. M.; de Cássia Ortiz, A.; Buchaim, D. V.; de Souza Bastos Mazuqueli Pereira, E.; Parreira, M. J. B. M.; de Oliveira Rossi, J.; da Cunha, M. R.; de Souza, A. T.; Soares, W. C.; Buchaim, R. L. Influence of the Neuroprotective Properties of Quercetin on Regeneration and Functional Recovery of the Nervous System. *Antioxidants* **2023**, *12* (1). DOI: <https://doi.org/10.3390/antiox12010149>.
518. Khan, H.; Ullah, H.; Aschner, M.; Cheang, W. S.; Akkol, E. K. Neuroprotective effects of quercetin in alzheimer's disease. *Biomolecules* **2020**, *10* (1). DOI: <https://doi.org/10.3390/biom10010059>.
519. Ossola, B.; Kääriäinen, T. M.; Männistö, P. T. The multiple faces of quercetin in neuroprotection. *Expert Opin. Drug Saf.* **2009**, *8* (4), 397-409. DOI: <https://doi.org/10.1517/14740330903026944>.
520. Zhang, L.; Ma, J.; Yang, F.; Li, S.; Ma, W.; Chang, X.; Yang, L. Neuroprotective Effects of Quercetin on Ischemic Stroke: A Literature Review. *Front. Pharmacol.* **2022**, *13*. DOI: <https://doi.org/10.3389/fphar.2022.854249>.
521. Luo, L.; Sun, T.; Yang, L.; Liu, A.; Liu, Q. Q.; Tian, Q. Q.; Wang, Y.; Zhao, M. G.; Yang, Q. Scopoletin ameliorates anxiety-like behaviors in complete Freund's adjuvant-induced mouse model. *Mol. Brain* **2020**, *13* (1). DOI: <https://doi.org/10.1186/s13041-020-0560-2>.
522. Lee, J. H.; Ki, T. L.; Jae, H. Y.; Nam, I. B.; Dae, K. K. Acetylcholinesterase inhibitors from the twigs of *Vaccinium oldhami* miquel. *Arch. Pharmacol. Res.* **2004**, *27* (1), 53-56. DOI: <https://doi.org/10.1007/BF02980046>.
523. Gay, N. H.; Suwanjang, W.; Ruankham, W.; Songtawee, N.; Wongchitrat, P.; Prachayasittikul, V.; Prachayasittikul, S.; Phopin, K. Butein, isoliquiritigenin, and scopoletin attenuate neurodegeneration via antioxidant enzymes and SIRT1/ADAM10 signaling pathway. *RSC Adv.* **2020**, *10* (28), 16593-16606. DOI: <https://doi.org/10.1039/c9ra06056a>.
524. Kashyap, P.; Ram, H.; Shukla, S. D.; Kumar, S. Scopoletin: Anti-amyloidogenic, Anticholinesterase, and Neuroprotective Potential of a Natural Compound Present in *Argyrea speciosa* Roots by In Vitro and In Silico Study. *Neurosci. Insights* **2020**, *15*. DOI: <https://doi.org/10.1177/2633105520937693>.
525. Pradhan, P.; Majhi, O.; Biswas, A.; Joshi, V. K.; Sinha, D. Enhanced accumulation of reduced glutathione by Scopoletin improves survivability of dopaminergic neurons in Parkinson's model. *Cell Death Dis.* **2020**, *11* (9). DOI: <https://doi.org/10.1038/s41419-020-02942-8>.
526. Zhang, W.; Zhao, W.; Ge, C.; Li, X.; Sun, Z. Scopoletin Attenuates Intracerebral Hemorrhage-Induced Brain Injury and Improves Neurological Performance in Rats. *Neuroimmunomodulation* **2021**, *28* (2), 74-81. DOI: <https://doi.org/10.1159/000505731>.
527. Ashafaq, M.; Tabassum, H.; Parvez, S. Modulation of Behavioral Deficits and Neurodegeneration by Tannic Acid in Experimental Stroke Challenged Wistar Rats. *Mol. Neurobiol.* **2017**, *54* (8), 5941-5951. DOI: <https://doi.org/10.1007/s12035-016-0096-8>.
528. Gerzson, M. F. B.; Bona, N. P.; Soares, M. S. P.; Teixeira, F. C.; Rahmeier, F. L.; Carvalho, F. B.; da Cruz Fernandes, M.; Onzi, G.; Lenz, G.; Gonçalves, R. A.; et al. Tannic Acid Ameliorates STZ-Induced Alzheimer's Disease-Like Impairment of Memory, Neuroinflammation, Neuronal Death and Modulates Akt Expression. *Neurotox. Res.* **2020**, *37* (4), 1009-1017. DOI: <https://doi.org/10.1007/s12640-020-00167-3>.
529. Hasanvand, A.; Hosseinzadeh, A.; Saeedavi, M.; Goudarzi, M.; Basir, Z.; Mehrzadi, S. Neuroprotective effects of tannic acid against kainic acid-induced seizures in mice. *Hum. Exp. Toxicol.* **2022**, *41*. DOI: <https://doi.org/10.1177/09603271221093989>.
530. Kim, S. W.; Kim, D. B.; Kim, H. S. Neuroprotective effects of tannic acid in the postischemic brain via direct chelation of Zn²⁺. *Anim. Cells Syst.* **2022**, *26* (4), 183-191. DOI: <https://doi.org/10.1080/19768354.2022.2113915>.
531. Salman, M.; Tabassum, H.; Parvez, S. Tannic Acid Provides Neuroprotective Effects Against Traumatic Brain Injury Through the PGC-1 α /Nrf2/HO-1 Pathway. *Mol. Neurobiol.* **2020**, *57* (6), 2870-2885. DOI: <https://doi.org/10.1007/s12035-020-01924-3>.
532. Wu, Y.; Zhong, L.; Yu, Z.; Qi, J. Anti-neuroinflammatory effects of tannic acid against lipopolysaccharide-induced BV2 microglial cells via inhibition of NF- κ B activation. *Drug Dev. Res.* **2019**, *80* (2), 262-268. DOI: <https://doi.org/10.1002/ddr.21490>.

533. Bhat, J. A.; Gupta, S.; Kumar, M. Neuroprotective effects of theobromine in transient global cerebral ischemia-reperfusion rat model. *Biochem. Biophys. Res. Commun.* **2021**, *571*, 74-80. DOI: <https://doi.org/10.1016/j.bbrc.2021.07.051>.
534. Bhat, J. A.; Kumar, M. Neuroprotective Effects of Theobromine in permanent bilateral common carotid artery occlusion rat model of cerebral hypoperfusion. *Metab. Brain Dis.* **2022**, *37* (6), 1787-1801. DOI: <https://doi.org/10.1007/s11011-022-00995-6>.
535. Shanahan, P.; O'Sullivan, J.; Tipton, K. F.; Kinsella, G. K.; Ryan, B. J.; Henahan, G. T. M. Theobromine and related methylxanthines as inhibitors of Primary Amine Oxidase. *J. Food Biochem.* **2019**, *43* (2). DOI: <https://doi.org/10.1111/jfbc.12697>.
536. Dhanalakshmi, C.; Janakiraman, U.; Manivasagam, T.; Justin Thenmozhi, A.; Essa, M. M.; Kalandar, A.; Khan, M. A. S.; Guillemain, G. J. Vanillin Attenuated Behavioural Impairments, Neurochemical Deficits, Oxidative Stress and Apoptosis Against Rotenone Induced Rat Model of Parkinson's Disease. *Neurochem. Res.* **2016**, *41* (8), 1899-1910. DOI: <https://doi.org/10.1007/s11064-016-1901-5>.
537. Dhanalakshmi, C.; Manivasagam, T.; Nataraj, J.; Justin Thenmozhi, A.; Essa, M. M. Neurosupportive Role of Vanillin, a Natural Phenolic Compound, on Rotenone Induced Neurotoxicity in SH-SY5Y Neuroblastoma Cells. *Evid. Based Complement. Alternat. Med.* **2015**, *2015*. DOI: <https://doi.org/10.1155/2015/626028>.
538. Iannuzzi, C.; Liccardo, M.; Sirangelo, I. Overview of the Role of Vanillin in Neurodegenerative Diseases and Neuropathophysiological Conditions. *Int. J. Mol. Sci.* **2023**, *24* (3). DOI: <https://doi.org/10.3390/ijms24031817>.
539. Lan, X. B.; Wang, Q.; Yang, J. M.; Ma, L.; Zhang, W. J.; Zheng, P.; Sun, T.; Niu, J. G.; Liu, N.; Yu, J. Q. Neuroprotective effect of Vanillin on hypoxic-ischemic brain damage in neonatal rats. *Biomed. Pharmacother.* **2019**, *118*. DOI: <https://doi.org/10.1016/j.biopha.2019.109196>.
540. Rani, L.; Ghosh, B.; Ahmad, M. H.; Mondal, A. C. Evaluation of Potential Neuroprotective Effects of Vanillin Against MPP+/MPTP-Induced Dysregulation of Dopaminergic Regulatory Mechanisms in SH-SY5Y Cells and a Mouse Model of Parkinson's Disease. *Mol. Neurobiol.* **2023**, 10.1007/s12035-023-03358-z. DOI: <https://doi.org/10.1007/s12035-023-03358-z>.
541. Huang, S. M.; Hsu, C. L.; Chuang, H. C.; Shih, P. H.; Wu, C. H.; Yen, G. C. Inhibitory effect of vanillic acid on methylglyoxal-mediated glycation in apoptotic Neuro-2A cells. *Neurotoxicology* **2008**, *29* (6), 1016-1022. DOI: <https://doi.org/10.1016/j.neuro.2008.07.002>.
542. Khoshnam, S. E.; Sarkaki, A.; Rashno, M.; Farbood, Y. Memory deficits and hippocampal inflammation in cerebral hypoperfusion and reperfusion in male rats: Neuroprotective role of vanillic acid. *Life Sci.* **2018**, *211*, 126-132. DOI: <https://doi.org/10.1016/j.lfs.2018.08.065>.
543. Siddiqui, S.; Kamal, A.; Khan, F.; Jamali, K. S.; Saify, Z. S. Gallic and vanillic acid suppress inflammation and promote myelination in an in vitro mouse model of neurodegeneration. *Mol. Biol. Rep.* **2019**, *46* (1), 997-1011. DOI: <https://doi.org/10.1007/s11033-018-4557-1>.
544. Ullah, R.; Ikram, M.; Park, T. J.; Ahmad, R.; Saeed, K.; Alam, S. I.; Rehman, I. U.; Khan, A.; Khan, I.; Jo, M. G.; Kim, M. O. Vanillic acid, a bioactive phenolic compound, counteracts lps-induced neurotoxicity by regulating c-jun n-terminal kinase in mouse brain. *Int. J. Mol. Sci.* **2021**, *22* (1), 1-21. DOI: <https://doi.org/10.3390/ijms22010361>.
545. Kim, I. S.; Choi, D. K.; Jung, H. J. Neuroprotective effects of vanillyl alcohol in *gastrodia elata* blume through suppression of oxidative stress and anti-apoptotic activity in toxin-induced dopaminergic MN9D cells. *Molecules* **2011**, *16* (7), 5349-5361. DOI: <https://doi.org/10.3390/molecules16075349>.
546. Agunloye, O. M.; Oboh, G. Hypercholesterolemia, angiotensin converting enzyme and ecto-enzymes of purinergic system: Ameliorative properties of caffeic and chlorogenic acid in hypercholesterolemic rats. *J. Food Biochem.* **2018**, *42* (5). DOI: <https://doi.org/10.1111/jfbc.12604>.
547. Farias-Pereira, R.; Oshiro, J.; Kim, K. H.; Park, Y. Green coffee bean extract and 5-O-caffeoylquinic acid regulate fat metabolism in *Caenorhabditis elegans*. *J. Funct. Foods* **2018**, *48*, 586-593. DOI: <https://doi.org/10.1016/j.jff.2018.07.049>.

548. Adem, Ş.; Eyupoglu, V.; Sarfraz, I.; Rasul, A.; Zahoor, A. F.; Ali, M.; Abdalla, M.; Ibrahim, I. M.; Elfiky, A. A. Caffeic acid derivatives (CAFDs) as inhibitors of SARS-CoV-2: CAFDs-based functional foods as a potential alternative approach to combat COVID-19. *Phytomedicine* **2021**, *85*. DOI: <https://doi.org/10.1016/j.phymed.2020.153310>.
549. Degotte, G.; Pirotte, B.; Frédérick, M.; Francotte, P. Potential of Caffeic Acid Derivatives as Antimalarial Leads. *Lett. Drug Des. Discovery* **2022**, *19* (9), 823-836. DOI: <https://doi.org/10.2174/1570180819666220202160247>.
550. Ekeuku, S. O.; Pang, K. L.; Chin, K. Y. Effects of caffeic acid and its derivatives on bone: A systematic review. *Drug Des. Devel. Ther.* **2021**, *15*, 259-275. DOI: <https://doi.org/10.2147/DDDT.S287280>.
551. Elkamhawy, A.; Oh, N. K.; Gouda, N. A.; Abdellattif, M. H.; Alshammari, S. O.; Abourehab, M. A. S.; Alshammari, Q. A.; Belal, A.; Kim, M.; Al-Karmalawy, A. A.; Lee, K. Novel Hybrid Indole-Based Caffeic Acid Amide Derivatives as Potent Free Radical Scavenging Agents: Rational Design, Synthesis, Spectroscopic Characterization, In Silico and In Vitro Investigations. *Metabolites* **2023**, *13* (2). DOI: <https://doi.org/10.3390/metabo13020141>.
552. Huang, C. W.; Lee, S. Y.; Wei, T. T.; Kuo, Y. H.; Wu, S. T.; Ku, H. C. A novel caffeic acid derivative prevents renal remodeling after ischemia/reperfusion injury. *Biomed. Pharmacother.* **2021**, *142*. DOI: <https://doi.org/10.1016/j.biopha.2021.112028>.
553. Jöhrer, K.; Galarza Pérez, M.; Kircher, B.; Çiçek, S. S. Flavones, Flavonols, Lignans, and Caffeic Acid Derivatives from *Dracocephalum moldavica* and Their In Vitro Effects on Multiple Myeloma and Acute Myeloid Leukemia. *Int. J. Mol. Sci.* **2022**, *23* (22). DOI: <https://doi.org/10.3390/ijms232214219>.
554. Khan, F.; Bamunuarachchi, N. I.; Tabassum, N.; Kim, Y. M. Caffeic Acid and Its Derivatives: Antimicrobial Drugs toward Microbial Pathogens. *J. Agric. Food Chem.* **2021**, *69* (10), 2979-3004. DOI: <https://doi.org/10.1021/acs.jafc.0c07579>.
555. Kim, C. K.; Yu, J.; Le, D.; Han, S.; Yu, S.; Lee, M. Anti-inflammatory activity of caffeic acid derivatives from *Ilex rotunda*. *Int. Immunopharmacol.* **2023**, *115*. DOI: <https://doi.org/10.1016/j.intimp.2022.109610>.
556. Lee, S. Y.; Kuo, Y. H.; Du, C. X.; Huang, C. W.; Ku, H. C. A novel caffeic acid derivative prevents angiotensin II-induced cardiac remodeling. *Biomed. Pharmacother.* **2023**, *162*. DOI: <https://doi.org/10.1016/j.biopha.2023.114709>.
557. Peng, X.; Wu, G.; Zhao, A.; Huang, K.; Chai, L.; Natarajan, B.; Yang, S.; Chen, H.; Lin, C. Synthesis of novel caffeic acid derivatives and their protective effect against hydrogen peroxide induced oxidative stress via Nrf2 pathway. *Life Sci.* **2020**, *247*. DOI: <https://doi.org/10.1016/j.lfs.2020.117439>.
558. Wu, M. Y.; Liu, C. C.; Lee, S. C.; Kuo, Y. H.; Hsieh, T. J. N-Octyl Caffeamide, a Caffeic Acid Amide Derivative, Prevents Progression of Diabetes and Hepatic Steatosis in High-Fat Diet Induced Obese Mice. *Int. J. Mol. Sci.* **2022**, *23* (16). DOI: <https://doi.org/10.3390/ijms23168948>.
559. Zeng, Y. F.; Su, Y. L.; Liu, W. L.; Chen, H. G.; Zeng, S. G.; Zhou, H. B.; Chen, W. M.; Zheng, J. X.; Sun, P. H. Design and synthesis of caffeic acid derivatives and evaluation of their inhibitory activity against *Pseudomonas aeruginosa*. *Med. Chem. Res.* **2022**, *31* (1), 177-194. DOI: <https://doi.org/10.1007/s00044-021-02810-w>.
560. Abu-Hashem, A. A.; Hussein, H. A. R. Synthesis and antitumor activity of new pyrimidine and caffeine derivatives. *Lett. Drug Des. Discovery* **2015**, *12* (6), 471-478. DOI: <https://doi.org/10.2174/1570180812666150429234237>.
561. Andrs, M.; Muthna, D.; Rezacova, M.; Seifrtova, M.; Siman, P.; Korabecny, J.; Benek, O.; Dolezal, R.; Soukup, O.; Jun, D.; Kuca, K. Novel caffeine derivatives with antiproliferative activity. *RSC Adv.* **2016**, *6* (39), 32534-32539. DOI: <https://doi.org/10.1039/c5ra22889a>.
562. Boulaamane, Y.; Ibrahim, M. A. A.; Britel, M. R.; Maurady, A. In silico studies of natural product-like caffeine derivatives as potential MAO-B inhibitors/AA2AR antagonists for the treatment of Parkinson's disease. *J. Integr. Bioinform.* **2022**, *19* (4). DOI: <https://doi.org/10.1515/jib-2021-0027>.
563. Jasiewicz, B.; Sierakowska, A.; Wandyszewska, N.; Warzajtis, B.; Rychlewska, U.; Wawrzyniak, R.; Mrówczyńska, L. Antioxidant properties of thio-caffeine derivatives: Identification of the newly

- synthesized 8-[(pyrrolidin-1-ylcarbonothioyl)sulfanyl]caffeine as antioxidant and highly potent cytoprotective agent. *Bioorg. Med. Chem. Lett.* **2016**, 26 (16), 3994-3998. DOI: <https://doi.org/10.1016/j.bmcl.2016.06.091>.
564. Mitkov, J.; Kondeva-Burdina, M.; Zlatkov, A. Synthesis and preliminary hepatotoxicity evaluation of new caffeine-8-(2-thio)-propanoic hydrazid-hydrazone derivatives. *Pharmacia* **2019**, 66 (3), 99-106. DOI: <https://doi.org/10.3897/pharmacia.66.e37263>.
565. Navid Soltani Rad, M.; Behrouz, S.; Zokaei, K.; Behrouz, M.; Ghanbariasad, A.; Zarenezhad, E. Synthesis of some novel 8-(4-Alkylpiperazinyl) caffeine derivatives as potent anti-Leishmania agents. *Bioorg. Chem.* **2022**, 128. DOI: <https://doi.org/10.1016/j.bioorg.2022.106062>.
566. Reddy, A. B.; Hymavathi, R. V.; Swamy, G. N.; Sadiku, E. R. Triazino-caffeine derivatives by intramolecular cyclization: Synthesis, characterization and antimicrobial studies. *Lett. Org. Chem.* **2018**, 15 (6), 540-545. DOI: <https://doi.org/10.2174/1570178614666171010161357>.
567. Reshetnikov, D. V.; Burova, L. G.; Rybalova, T. V.; Bondareva, E. A.; Patrushev, S. S.; Evstropov, A. N.; Shults, E. E. Synthesis and Antibacterial Activity of Caffeine Derivatives Containing Amino-Acid Fragments. *Chem. Nat. Compd.* **2022**, 58 (5), 908-915. DOI: <https://doi.org/10.1007/s10600-022-03826-3>.
568. Sierakowska, A.; Jasiewicz, B.; Piosik, Ł.; Mrówczyńska, L. New C8-substituted caffeine derivatives as promising antioxidants and cytoprotective agents in human erythrocytes. *Sci. Rep.* **2023**, 13 (1). DOI: <https://doi.org/10.1038/s41598-022-27205-8>.
569. Hwang, S. H.; Zuo, G.; Wang, Z.; Lim, S. S. Novel aldose reductase inhibitory and antioxidant chlorogenic acid derivatives obtained by heat treatment of chlorogenic acid and amino acids. *Food Chem.* **2018**, 266, 449-457. DOI: <https://doi.org/10.1016/j.foodchem.2018.06.053>.
570. Jo, H.; Zhou, Y.; Viji, M.; Choi, M.; Lim, J. Y.; Sim, J.; Rhee, J.; Kim, Y.; Seo, S. Y.; Kim, W. J.; et al. Synthesis, biological evaluation, and metabolic stability of chlorogenic acid derivatives possessing thiazole as potent inhibitors of α -MSH-stimulated melanogenesis. *Bioorg. Med. Chem. Lett.* **2017**, 27 (21), 4854-4857. DOI: <https://doi.org/10.1016/j.bmcl.2017.09.044>.
571. Kataria, R.; Khatkar, A. In-silico design, synthesis, ADMET studies and biological evaluation of novel derivatives of Chlorogenic acid against Urease protein and H. Pylori bacterium. *BMC Chemistry* **2019**, 13 (3). DOI: <https://doi.org/10.1186/s13065-019-0556-0>.
572. Liu, Z.; Mohsin, A.; Wang, Z.; Zhu, X.; Zhuang, Y.; Cao, L.; Guo, M.; Yin, Z. Enhanced Biosynthesis of Chlorogenic Acid and Its Derivatives in Methyl-Jasmonate-Treated Gardenia jasminoides Cells: A Study on Metabolic and Transcriptional Responses of Cells. *Front. bioeng. biotechnol.* **2021**, 8. DOI: <https://doi.org/10.3389/fbioe.2020.604957>.
573. Mei, Y.; Pan, D.; Jiang, Y.; Zhang, W.; Yao, X.; Dai, Y.; Yu, Y.; Yao, X. Target discovery of chlorogenic acid derivatives from the flower buds of *Lonicera macranthoides* and their MAO B inhibitory mechanism. *Fitoterapia* **2019**, 134, 297-304. DOI: <https://doi.org/10.1016/j.fitote.2018.12.009>.
574. Wang, S.; Li, Y.; Huang, D.; Chen, S.; Xia, Y.; Zhu, S. The inhibitory mechanism of chlorogenic acid and its acylated derivatives on α -amylase and α -glucosidase. *Food Chem.* **2022**, 372. DOI: <https://doi.org/10.1016/j.foodchem.2021.131334>.
575. Wang, S.; Li, Y.; Meng, X.; Chen, S.; Huang, D.; Xia, Y.; Zhu, S. Antioxidant activities of chlorogenic acid derivatives with different acyl donor chain lengths and their stabilities during in vitro simulated gastrointestinal digestion. *Food Chem.* **2021**, 357. DOI: <https://doi.org/10.1016/j.foodchem.2021.129904>.
576. Yang, J. Q.; Zeng, F. K.; Li, G.; Xu, T. S.; Shu, B. Synthesis and bioactivity evaluation of novel chlorogenic acid derivatives containing amide group. *Chin. Pharm. J.* **2016**, 51 (4), 264-268. DOI: <https://doi.org/10.11669/cpj.2016.04.003>.
577. Abdou, A.; Elmakssoudi, A.; El Amrani, A.; JamalEddine, J.; Dakir, M. Recent advances in chemical reactivity and biological activities of eugenol derivatives. *Med. Chem. Res.* **2021**, 30 (5), 1011-1030. DOI: <https://doi.org/10.1007/s00044-021-02712-x>.
578. Abdou, A.; Idouarame, S.; Salah, M.; Nor, N.; Zahm, S.; El Makssoudi, A.; Mazoir, N.; Benharref, A.; Dari, A.; Eddine, J. J.; et al. Phytochemical Study: Molecular Docking of Eugenol Derivatives as

- Antioxidant and Antimicrobial Agents. *Lett. Org. Chem.* **2022**, *19* (9), 774-783. DOI: <https://doi.org/10.2174/157017861966622011112125>.
579. Alam, M. M. Synthesis and anticancer activity of novel Eugenol derivatives against breast cancer cells. *Nat. Prod. Res.* **2023**, *37* (10), 1632-1640. DOI: <https://doi.org/10.1080/14786419.2022.2103809>.
580. Alam, M. M.; Elbehairi, S. E. I.; Shati, A. A.; Hussien, R. A.; Alfaifi, M. Y.; Malebari, A. M.; Asad, M.; Elhenawy, A. A.; Asiri, A. M.; Mahzari, A. M.; et al. Design, synthesis and biological evaluation of new eugenol derivatives containing 1,3,4-oxadiazole as novel inhibitors of thymidylate synthase. *New J. Chem.* **2023**, *47* (10), 5021-5032. DOI: <https://doi.org/10.1039/d2nj05711e>.
581. Anjum, N. F.; Purohit, M. N.; Yogish Kumar, H.; Ramya, K.; Javid, S.; Salahuddin, M. D.; Prashantha Kumar, B. R. Semisynthetic Derivatives of Eugenol and their Biological Properties: A Fleeting Look at the Promising Molecules. *J. Biol. Active Prod. Nat.* **2020**, *10* (5), 379-404. DOI: <https://doi.org/10.1080/22311866.2020.1837674>.
582. Anjum, N. F.; Shanmugarajan, D.; Prashantha Kumar, B. R.; Faizan, S.; Durai, P.; Raju, R. M.; Javid, S.; Purohit, M. N. Novel Derivatives of Eugenol as a New Class of PPAR γ Agonists in Treating Inflammation: Design, Synthesis, SAR Analysis and In Vitro Anti-Inflammatory Activity. *Molecules* **2023**, *28* (9). DOI: <https://doi.org/10.3390/molecules28093899>.
583. Anjum, N. F.; Shanmugarajan, D.; Shivaraju, V. K.; Faizan, S.; Naishima, N. L.; Prashantha Kumar, B. R.; Javid, S.; Purohit, M. N. Novel derivatives of eugenol as potent anti-inflammatory agents via PPAR γ agonism: rational design, synthesis, analysis, PPAR γ protein binding assay and computational studies. *RSC Adv.* **2022**, *12* (26), 16966-16978. DOI: <https://doi.org/10.1039/d2ra02116a>.
584. Arianie, L.; Supriatna, M. I.; Kazal, N.; Widodo, N.; Warsito, W.; Iftitah, E. D. Synthesis, In vitro, and In silico Studies of Methyl Eugenol Derivatives for Plasmodium falciparum Inhibitor. *Trop. J. Nat. Prod. Res.* **2022**, *6* (9), 1446-1454. DOI: <https://doi.org/10.26538/tjnpr/v6i9.19>.
585. Dutra, J. A. P.; Maximino, S. C.; Gonçalves, R.; Morais, P. A. B.; de Lima Silva, W.; Rodrigues, R. P.; Neto, Á. C.; Júnior, V. L.; de Souza Borges, W.; Kitagawa, R. R. Anti-Candida, docking studies, and in vitro metabolism-mediated cytotoxicity evaluation of Eugenol derivatives. *Chem. Biol. Drug Des.* **2023**, *101* (2), 350-363. DOI: <https://doi.org/10.1111/cbdd.14131>.
586. Elattar, E. M.; Galala, A. A.; Saad, H. E. A.; Badria, F. A. Hyaluronidase Inhibitory Activity and In Silico Docking Study of New Eugenol 1,2,3-triazole Derivatives. *Chem. Select* **2022**, *7* (42). DOI: <https://doi.org/10.1002/slct.202202194>.
587. Fernandes, M. J. G.; Pereira, R. B.; Pereira, D. M.; Fortes, A. G.; Castanheira, E. M. S.; Gonçalves, M. S. T. New eugenol derivatives with enhanced insecticidal activity. *Int. J. Mol. Sci.* **2020**, *21* (23), 1-14. DOI: <https://doi.org/10.3390/ijms21239257>.
588. Lima, Â. M. A.; de Paula, W. T.; Leite, I. C. H. L.; Gazolla, P. A. R.; de Abreu, L. M.; Fonseca, V. R.; Romão, W.; Lacerda, V.; de Queiroz, V. T.; Teixeira, R. R.; Costa, A. V. Synthesis of Eugenol-Fluorinated Triazole Derivatives and Evaluation of Their Fungicidal Activity. *J. Braz. Chem. Soc.* **2022**, *33* (10), 1200-1210. DOI: <https://doi.org/10.21577/0103-5053.20220040>.
589. Maurya, A. K.; Agarwal, K.; Gupta, A. C.; Saxena, A.; Nooreen, Z.; Tandon, S.; Ahmad, A.; Bawankule, D. U. Synthesis of eugenol derivatives and its anti-inflammatory activity against skin inflammation. *Nat. Prod. Res.* **2020**, *34* (2), 251-260. DOI: <https://doi.org/10.1080/14786419.2018.1528585>.
590. Maximino, S. C.; Dutra, J. A. P.; Rodrigues, R. P.; Gonçalves, R. C. R.; Morais, P. A. B.; Ventura, J. A.; Schuenck, R. P.; Júnior, V. L.; Kitagawa, R. R.; Borges, W. S. Synthesis of eugenol derivatives and evaluation of their antifungal activity against fusarium solani f. Sp. piperis. *Curr. Pharm. Des.* **2020**, *26* (14), 1532-1542. DOI: <https://doi.org/10.2174/1381612826666200403120448>.
591. Moraes, A. M.; da Silva, E. T.; Wardell, J. L.; de Souza, M. V. N. Synthesis and First-Time Assessment of o-Eugenol Derivatives against Mycobacterium tuberculosis. *Chem. Nat. Compd.* **2020**, *56* (4), 633-638. DOI: <https://doi.org/10.1007/s10600-020-03110-2>.
592. Muniz, D. F.; dos Santos Barbosa, C. R.; de Menezes, I. R. A.; de Sousa, E. O.; Pereira, R. L. S.; Júnior, J. T. C.; Pereira, P. S.; de Matos, Y. M. L. S.; da Costa, R. H. S.; de Morais Oliveira-Tintino, C. D.; et al. In

- vitro and in silico inhibitory effects of synthetic and natural eugenol derivatives against the NorA efflux pump in *Staphylococcus aureus*. *Food Chem.* **2021**, 337. DOI: <https://doi.org/10.1016/j.foodchem.2020.127776>.
593. Nour, H.; Abdou, A.; Belaidi, S.; Jamal, J.; Elmakssoudi, A.; Dakir, M.; Chtita, S. Discovery of promising cholinesterase inhibitors for Alzheimer's disease treatment through DFT, docking, and molecular dynamics studies of eugenol derivatives. *J. Chin. Chem. Soc.* **2022**, 69 (9), 1534-1551. DOI: <https://doi.org/10.1002/jccs.202200195>.
594. Nunes, D. O. S.; Vinturelle, R.; Martins, F. J.; dos Santos, T. F.; Valverde, A. L.; Ribeiro, C. M. R.; Castro, H. C.; Folly, E. Biotechnological Potential of Eugenol and Thymol Derivatives Against *Staphylococcus aureus* from Bovine Mastitis. *Curr. Microbiol.* **2021**, 78 (5), 1846-1855. DOI: <https://doi.org/10.1007/s00284-021-02344-9>.
595. Pelozo, M. F.; Lima, G. F. S.; Cordeiro, C. F.; Silva, L. S.; Caldas, I. S.; Carvalho, D. T.; Lavorato, S. N.; Hawkes, J. A.; Franco, L. L. Synthesis of new hybrid derivatives from metronidazole and eugenol analogues as trypanocidal agents. *J. Pharm. Pharm. Sci.* **2021**, 24, 421-434. DOI: <https://doi.org/10.18433/jpps31839>.
596. Teixeira, R. R.; Rodrigues Gazolla, P. A.; Borsodi, M. P. G.; Castro Ferreira, M. M.; Andrezza Costa, M. C.; Costa, A. V.; Cabral Abreu Grijó, B.; Rossi Bergmann, B.; Lima, W. P. Eugenol derivatives with 1,2,3-triazole moieties: Oral treatment of cutaneous leishmaniasis and a quantitative structure-activity relationship model for their leishmanicidal activity. *Exp. Parasitol.* **2022**, 238. DOI: <https://doi.org/10.1016/j.exppara.2022.108269>.
597. Wu, J.; Yin, W.; Zhang, Y.; Ye, H.; Li, Y.; Tian, J.; Huang, Z.; Zhang, Y. Design and synthesis of the ring-opened derivative of 3-n-butylphthalide-ferulic acid-glucose trihybrids as potential anti-ischemic agents. *Chin. Chem. Lett.* **2020**, 31 (7), 1881-1886. DOI: <https://doi.org/10.1016/j.ccllet.2020.02.031>.
598. Wu, Y.; Shi, Y. G.; Zheng, X. L.; Dang, Y. L.; Zhu, C. M.; Zhang, R. R.; Fu, Y. Y.; Zhou, T. Y.; Li, J. H. Lipophilic ferulic acid derivatives protect PC12 cells against oxidative damage: Via modulating β -amyloid aggregation and activating Nrf2 enzymes. *Food Funct.* **2020**, 11 (5), 4707-4718. DOI: <https://doi.org/10.1039/d0fo00800a>.
599. Yuan, T.; Wang, Z.; Lan, S.; Gan, X. Design, synthesis, antiviral activity, and mechanisms of novel ferulic acid derivatives containing amide moiety. *Bioorg. Chem.* **2022**, 128. DOI: <https://doi.org/10.1016/j.bioorg.2022.106054>.
600. Xie, Y.; Liu, Y.; Sun, J.; Zheng, L. Synthesis of mitochondria-targeted ferulic acid amide derivatives with antioxidant, anti-inflammatory activities and inducing mitophagy. *Bioorg. Chem.* **2022**, 127. DOI: <https://doi.org/10.1016/j.bioorg.2022.106037>.
601. Kolaj, I.; Wang, Y.; Ye, K.; Meek, A.; Liyanage, S. I.; Santos, C.; Weaver, D. F. Ferulic acid amide derivatives with varying inhibition of amyloid- β oligomerization and fibrillization. *Bioorg. Med. Chem.* **2021**, 43. DOI: <https://doi.org/10.1016/j.bmc.2021.116247>.
602. Wang, F.; Peng, Q.; Liu, J.; Alolga, R. N.; Zhou, W. A novel ferulic acid derivative attenuates myocardial cell hypoxia reoxygenation injury through a succinate dehydrogenase dependent antioxidant mechanism. *Eur. J. Pharmacol.* **2019**, 856, 172417. DOI: <https://doi.org/10.1016/j.ejphar.2019.172417>.
603. Montaser, A.; Huttunen, J.; Ibrahim, S. A.; Huttunen, K. M. Astrocyte-Targeted Transporter-Utilizing Derivatives of Ferulic Acid Can Have Multifunctional Effects Ameliorating Inflammation and Oxidative Stress in the Brain. *Oxidative Med. Cell. Longev.* **2019**, 2019. DOI: <https://doi.org/10.1155/2019/3528148>.
604. Khatkar, A.; Nanda, A.; Kumar, P.; Narasimhan, B. Synthesis and antimicrobial evaluation of ferulic acid derivatives. *Res. Chem. Intermed.* **2015**, 41 (1), 299-309. DOI: <https://doi.org/10.1007/s11164-013-1192-2>.
605. Drăgan, M.; Stan, C. D.; Iacob, A. T.; Dragostin, O. M.; Boancă, M.; Lupuşoru, C. E.; Zamfir, C. L.; Profire, L. Biological evaluation of azetidione derivatives of ferulic acid as promising anti-inflammatory agents. *Processes* **2020**, 8 (11), 1-19. DOI: <https://doi.org/10.3390/pr8111401>.
606. Drăgan, M.; Stan, C. D.; Iacob, A.; Profire, L. Assessment of in vitro antioxidant and anti-inflammatory activities of new azetidione derivatives of ferulic acid. *Farmacia* **2016**, 64 (5), 717-721.

607. Lan, J. S.; Zeng, R. F.; Jiang, X. Y.; Hou, J. W.; Liu, Y.; Hu, Z. H.; Li, H. X.; Li, Y.; Xie, S. S.; Ding, Y.; Zhang, T. Design, synthesis and evaluation of novel ferulic acid derivatives as multi-target-directed ligands for the treatment of Alzheimer's disease. *Bioorg. Chem.* **2020**, *94*. DOI: <https://doi.org/10.1016/j.bioorg.2019.103413>.
608. Gan, X.; Zhang, W.; Lan, S.; Hu, D. Novel Cyclized Derivatives of Ferulic Acid as Potential Antiviral Agents through Activation of Photosynthesis. *J. Agric. Food Chem.* **2023**, *71* (3), 1369-1380. DOI: <https://doi.org/10.1021/acs.jafc.2c06422>.
609. Sang, Z.; Wang, K.; Han, X.; Cao, M.; Tan, Z.; Liu, W. Design, Synthesis, and Evaluation of Novel Ferulic Acid Derivatives as Multi-Target-Directed Ligands for the Treatment of Alzheimer's Disease. *ACS Chem. Neurosci.* **2019**, *10* (2), 1008-1024. DOI: <https://doi.org/10.1021/acscemneuro.8b00530>.
610. Jung, J. S.; Yan, J. J.; Li, H. M.; Sultan, M. T.; Yu, J.; Lee, H. S.; Shin, K. J.; Song, D. K. Protective effects of a dimeric derivative of ferulic acid in animal models of Alzheimer's disease. *Eur. J. Pharmacol.* **2016**, *782*, 30-34. DOI: <https://doi.org/10.1016/j.ejphar.2016.04.047>.
611. Yue, S. J.; Zhang, P. X.; Zhu, Y.; Li, N. G.; Chen, Y. Y.; Li, J. J.; Zhang, S.; Jin, R. Y.; Yan, H.; Shi, X. Q.; et al. A ferulic acid derivative FXS-3 inhibits proliferation and metastasis of human lung cancer A549 cells via positive JNK signaling pathway and negative ERK/p38, AKt/mTOR and MEK/ERK signaling pathways. *Molecules* **2019**, *24* (11). DOI: <https://doi.org/10.3390/molecules24112165>.
612. Pinheiro, P. G.; Santiago, G. M. P.; da Silva, F. E. F.; de Araújo, A. C. J.; de Oliveira, C. R. T.; Freitas, P. R.; Rocha, J. E.; Neto, J. B. D. A.; da Silva, M. M. C.; Tintino, S. R.; et al. Ferulic acid derivatives inhibiting *Staphylococcus aureus* tetK and MsrA efflux pumps. *Biotechnol. Rep.* **2022**, *34*. DOI: <https://doi.org/10.1016/j.btre.2022.e00717>.
613. Pinheiro, P.; Santiago, G.; Da Silva, F.; De Araujo, A.; De Oliveira, C.; Freitas, P.; Rocha, J.; De Araujo Neto, J.; Da Silva, M.; Tintino, S.; et al. Antibacterial activity and inhibition against *Staphylococcus aureus* NorA efflux pump by ferulic acid and its esterified derivatives. *Asian Pac. J. Trop. Biomed.* **2021**, *11* (9), 405-413. DOI: <https://doi.org/10.4103/2221-1691.321130>.
614. Kong, H.; Fu, X.; Chang, X.; Ding, Z.; Yu, Y.; Xu, H.; Wang, R.; Shan, Y.; Ding, S. The ester derivatives of ferulic acid exhibit strong inhibitory effect on the growth of *Alternaria alternata* in vitro and in vivo. *Postharvest Biol. Technol.* **2023**, *196*. DOI: <https://doi.org/10.1016/j.postharvbio.2022.112158>.
615. Zhang, P. X.; Lin, H.; Qu, C.; Tang, Y. P.; Li, N. G.; Kai, J.; Shang, G.; Li, B.; Zhang, L.; Yan, H.; et al. Design, synthesis, and in vitro antiplatelet aggregation activities of ferulic acid derivatives. *J. Chem.* **2015**, *2015*, 1-7. DOI: <https://doi.org/10.1155/2015/376527>.
616. Li, W.; Li, N.; Tang, Y.; Li, B.; Liu, L.; Zhang, X.; Fu, H.; Duan, J. A. Biological activity evaluation and structure-activity relationships analysis of ferulic acid and caffeic acid derivatives for anticancer. *Bioorg. Med. Chem. Lett.* **2012**, *22* (19), 6085-6088. DOI: <https://doi.org/10.1016/j.bmcl.2012.08.038>.
617. Wang, F.; Yang, L.; Huang, K.; Li, X.; Hao, X.; Stöckigt, J.; Zhao, Y. Preparation of ferulic acid derivatives and evaluation of their xanthine oxidase inhibition activity. *Nat. Prod. Res.* **2007**, *21* (3), 196-202. DOI: <https://doi.org/10.1080/14786410601129648>.
618. Serafim, T. L.; Carvalho, F. S.; Marques, M. P. M.; Calheiros, R.; Silva, T.; Garrido, J.; Milhazes, N.; Borges, F.; Roleira, F.; Silva, E. T.; et al. Lipophilic caffeic and ferulic acid derivatives presenting cytotoxicity against human breast cancer cells. *Chem. Res. Toxicol.* **2011**, *24* (5), 763-774. DOI: <https://doi.org/10.1021/tx200126r>.
619. Adeyemi, O. S.; Atolani, O.; Banerjee, P.; Arolasafe, G.; Preissner, R.; Etukudoh, P.; Ibraheem, O. Computational and experimental validation of antioxidant properties of synthesized bioactive ferulic acid derivatives. *Int. J. Food Prop.* **2018**, *21* (1), 101-113. DOI: <https://doi.org/10.1080/10942912.2018.1439958>.
620. Kikugawa, M.; Tsutsuki, H.; Ida, T.; Nakajima, H.; Ihara, H.; Sakamoto, T. Water-soluble ferulic acid derivatives improve amyloid- β -induced neuronal cell death and dysmnnesia through inhibition of amyloid- β aggregation. *Biosci. Biotechnol. Biochem.* **2016**, *80* (3), 547-553A. DOI: <https://doi.org/10.1080/09168451.2015.1107463>.

621. Malik, S. A.; Ali, K. F.; Dawood, A. H. Synthesis, Characterization, and Preliminary Evaluation of Ferulic Acid Derivatives Containing Heterocyclic Moiety. *J. Med. Chem. Sci.* **2023**, *6* (6), 1444-1456. DOI: <https://doi.org/10.26655/JMCSMCI.2023.6.24>.
622. Machado, K. C.; Oliveira, G. L. S.; Islam, M. T.; Junior, A. L. G.; De Sousa, D. P.; Freitas, R. M. Anticonvulsant and behavioral effects observed in mice following treatment with an ester derivative of ferulic acid: Isopentyl ferulate. *Chem. Biol. Interact.* **2015**, *242*, 273-279. DOI: <https://doi.org/10.1016/j.cbi.2015.10.003>.
623. Bautista-Aguilera, O. M.; Alonso, J. M.; Catto, M.; Iriepa, I.; Knez, D.; Gobec, S.; Marco-Contelles, J. N-Hydroxy-N-Propargylamide Derivatives of Ferulic Acid: Inhibitors of Cholinesterases and Monoamine Oxidases. *Molecules* **2022**, *27* (21). DOI: <https://doi.org/10.3390/molecules27217437>.
624. Sang, Z.; Pan, W.; Wang, K.; Ma, Q.; Yu, L.; Yang, Y.; Bai, P.; Leng, C.; Xu, Q.; Li, X.; et al. Design, synthesis and evaluation of novel ferulic acid-O-alkylamine derivatives as potential multifunctional agents for the treatment of Alzheimer's disease. *Eur. J. Med. Chem.* **2017**, *130*, 379-392. DOI: <https://doi.org/10.1016/j.ejmech.2017.02.039>.
625. Cui, M. Y.; Xiao, M. W.; Xu, L. J.; Chen, Y.; Liu, A. L.; Ye, J.; Hu, A. X. Bioassay of ferulic acid derivatives as influenza neuraminidase inhibitors. *Arch. Pharm.* **2020**, *353* (1). DOI: <https://doi.org/10.1002/ardp.201900174>.
626. Adeyemi, O. S.; Awakan, O. J.; Atolani, O.; Iyeye, C. O.; Oweibo, O. O.; Adejumo, O. J.; Ibrahim, A.; Batiha, G. E. S. New ferulic acid derivatives protect against carbon tetrachloride-induced liver injury in rats. *Open Biochem. J.* **2019**, *13* (1), 13-22. DOI: <https://doi.org/10.2174/1874091X01913010013>.
627. Yuan, T.; Wang, Z.; Liu, D.; Zeng, H.; Liang, J.; Hu, D.; Gan, X. Ferulic acid derivatives with piperazine moiety as potential antiviral agents. *Pest Manag. Sci.* **2022**, *78* (4), 1749-1758. DOI: <https://doi.org/10.1002/ps.6794>.
628. Pellerito, C.; Emanuele, S.; Ferrante, F.; Celesia, A.; Giuliano, M.; Fiore, T. Tributyltin(IV) ferulate, a novel synthetic ferulic acid derivative, induces autophagic cell death in colon cancer cells: From chemical synthesis to biochemical effects. *J. Inorg. Biochem.* **2020**, *205*, 110999. DOI: <https://doi.org/10.1016/j.jinorgbio.2020.110999>.
629. Guzmán-López, E. G.; Reina, M.; Hernández-Ayala, L. F.; Galano, A. Rational Design of Multifunctional Ferulic Acid Derivatives Aimed for Alzheimer's and Parkinson's Diseases. *Antioxidants* **2023**, *12* (6), 1256. DOI: <https://doi.org/10.3390/antiox12061256>.
630. Basas-Jaumandreu, J.; López, J.; De Las Heras, F. X. C. Resorcinol and m-guaiacol alkylated derivatives and asymmetrical secondary alcohols in the leaves from *Tamarix canariensis*. *Phytochem. Lett.* **2014**, *10*, 240-248. DOI: <https://doi.org/10.1016/j.phytol.2014.10.009>.
631. Ordoudi, S. A.; Tsimidou, M. Z.; Vafiadis, A. P.; Bakalbassis, E. G. Structure-DPPH• scavenging activity relationships: Parallel study of catechol and guaiacol acid derivatives. *J. Agric. Food Chem.* **2006**, *54* (16), 5763-5768. DOI: <https://doi.org/10.1021/jf060132x>.
632. Premkumar, J.; Sampath, P.; Sanjay, R.; Chandrakala, A.; Rajagopal, D. Synthetic Guaiacol Derivatives as Promising Myeloperoxidase Inhibitors Targeting Atherosclerotic Cardiovascular Disease. *ChemMedChem* **2020**, *15* (13), 1187-1199. DOI: <https://doi.org/10.1002/cmde.202000084>.
633. Bhagat, S. D.; Mathur, R. K.; Siddhanta, N. N. Synthesis of New Derivatives of Eugenol and Isoeugenol. *J. Chem. amp; Eng. Data* **1982**, *27* (2), 209-210. DOI: <https://doi.org/10.1021/je00028a033>.
634. Nafie, M. S.; Elghazawy, N. H.; Owf, S. M.; Arafa, K.; Abdel-Rahman, M. A.; Arafa, R. K. Control of ER-positive breast cancer by ER α expression inhibition, apoptosis induction, cell cycle arrest using semisynthetic isoeugenol derivatives. *Chem. Biol. Interact.* **2022**, *351*. DOI: <https://doi.org/10.1016/j.cbi.2021.109753>.
635. Shen, K. P.; Chang, W. T.; Lin, H. L.; Chu, L. W.; Chen, I. J.; Wu, B. N. Structure-activity relationships of isoeugenol-based chlorophenylpiperazine derivatives on serotonergic/adrenergic receptor, platelet aggregation, and lipid peroxidation. *Drug Dev. Res.* **2010**, *71* (5), 285-293. DOI: <https://doi.org/10.1002/ddr.20373>.

636. Zuhrufa, Z.; Julianto, T. S. Molecular Interaction Analysis of COX-2 against Aryl Amino Alcohol Derivatives from Isoeugenol as Anti Breast Cancer using Molecular Docking. *Bull. Chem. React. Eng. Catal.* **2021**, *16* (3), 581-587. DOI: <https://doi.org/10.9767/BCREC.16.3.10324.581-587>.
637. Lu, W.; Wang, F.; Zhang, T.; Dong, J.; Gao, H.; Su, P.; Shi, Y.; Zhang, J. Search for novel histone deacetylase inhibitors. Part II: Design and synthesis of novel isoferulic acid derivatives. *Bioorg. Med. Chem.* **2014**, *22* (9), 2707-2713. DOI: <https://doi.org/10.1016/j.bmc.2014.03.019>.
638. Merlani, M.; Barbakadze, V.; Amiranashvili, L.; Gogilashvili, L. Synthesis of new dihydroxylated derivatives of ferulic and isoferulic acids. *Bull. Georgian Natl. Acad. Sci.* **2018**, *12* (4), 119-124.
639. Ekowati, J.; Diyah, N. W.; Syahrani, A. Synthesis and antiplatelet activities of some derivatives of p-coumaric acid. *Chem. Chem. Technol.* **2019**, *13* (3), 296-302. DOI: <https://doi.org/10.23939/chcht13.03.296>.
640. Khatkar, A.; Nanda, A.; Kumar, P.; Narasimhan, B. Synthesis, antimicrobial evaluation and QSAR studies of p-coumaric acid derivatives. *Arab. J. Chem.* **2017**, *10*, S3804-S3815. DOI: <https://doi.org/10.1016/j.arabjc.2014.05.018>.
641. Lopes, S. P.; Castillo, Y. P.; Monteiro, M. L.; de Menezes, R. R. P. P. B.; Almeida, R. N.; Martins, A. M. C.; de Sousa, D. P. Trypanocidal mechanism of action and in silico studies of p-coumaric acid derivatives. *Int. J. Mol. Sci.* **2019**, *20* (23). DOI: <https://doi.org/10.3390/ijms20235916>.
642. Lopes, S. P.; Yepe, L. M.; Pérez-Castillo, Y.; Robledo, S. M.; De Sousa, D. P. Alkyl and aryl derivatives based on p-coumaric acid modification and inhibitory action against leishmania braziliensis and plasmodium falciparum. *Molecules* **2020**, *25* (14). DOI: <https://doi.org/10.3390/molecules25143178>.
643. Rodrigues, D. M.; Portapilla, G. B.; de Sicco, G. S.; da Silva, I. F. R.; de Albuquerque, S.; Bastos, J. K.; Campo, V. L. Novel synthetic derivatives of cinnamic and p-coumaric acids with antiproliferative effect on breast MCF-7 tumor cells. *Nat. Prod. Res.* **2023**, 10.1080/14786419.2023.2177992. DOI: <https://doi.org/10.1080/14786419.2023.2177992>.
644. Shirai, A.; Kajiura, M.; Matsumura, K.; Omasa, T. Improved photobactericidal activity of ultraviolet-a light in combination with isomerizable p-coumaric acid derivatives. *Biocontrol Sci.* **2015**, *20* (4), 231-238. DOI: <https://doi.org/10.4265/bio.20.231>.
645. Reina, M.; Guzmán-López, E. G.; Romeo, I.; Marino, T.; Russo, N.; Galano, A. Computationally designed: P-coumaric acid analogs: Searching for neuroprotective antioxidants. *New J. Chem.* **2021**, *45* (32), 14369-14380. DOI: <https://doi.org/10.1039/d1nj01235e>.
646. Cho, J.; Jung, H.; Kang, D. Y.; Sp, N.; Shin, W.; Lee, J.; Park, B. G.; Kang, Y. A.; Jang, K. J.; Bae, S. W. The Skin-Whitening and Antioxidant Effects of Protocatechuic Acid (PCA) Derivatives in Melanoma and Fibroblast Cell Lines. *Curr. Issues Mol. Biol.* **2023**, *45* (3), 2157-2169. DOI: <https://doi.org/10.3390/cimb45030138>.
647. Lu, F. J.; Tseng, S. N.; Li, M. L.; Shih, S. R. In vitro anti-influenza virus activity of synthetic humate analogues derived from protocatechuic acid. *Arch. Virol.* **2002**, *147* (2), 273-284. DOI: <https://doi.org/10.1007/s705-002-8319-5>.
648. Reis, B.; Martins, M.; Barreto, B.; Milhazes, N.; Garrido, E. M.; Silva, P.; Garrido, J.; Borges, F. Structure-property-activity relationship of phenolic acids and derivatives. Protocatechuic acid alkyl esters. *J. Agric. Food Chem.* **2010**, *58* (11), 6986-6993. DOI: <https://doi.org/10.1021/jf100569j>.
649. Saito, S.; Kawabata, J. Effects of electron-withdrawing substituents on DPPH radical scavenging reactions of protocatechuic acid and its analogues in alcoholic solvents. *Tetrahedron* **2005**, *61* (34), 8101-8108. DOI: <https://doi.org/10.1016/j.tet.2005.06.040>.
650. Sheng, G. H.; Zhou, Q. C.; Hu, X. M.; Wang, C. F.; Chen, X. F.; Xue, D.; Yan, K.; Ding, S. S.; Wang, J.; Du, Z. Y.; et al. Synthesis, structure, urease inhibitory, and cytotoxic activities of two complexes with protocatechuic acid derivative and phenanthroline. *J. Coord. Chem.* **2015**, *68* (9), 1571-1582. DOI: <https://doi.org/10.1080/00958972.2015.1023718>.
651. Sheng, G. H.; Zhou, Q. C.; Sun, J.; Cheng, X. S.; Qian, S. S.; Zhang, C. Y.; You, Z. L.; Zhu, H. L. Synthesis, structure, and urease inhibitory activities of three binuclear copper(II) complexes with protocatechuic acid derivative. *J. Coord. Chem.* **2014**, *67* (7), 1265-1278. DOI: <https://doi.org/10.1080/00958972.2014.910597>.

652. Wei, J.; Liu, K.; Du, C.; Zhou, Y.; Lin, C. A Novel Mannich Derivative of Protocatechuic Acid: Synthesis, Crystal Structure and Antioxidant Activity. *Proc. Natl. Acad. Sci. India Sect. A - Phys. Sci.* **2017**, *87* (2), 181-188. DOI: <https://doi.org/10.1007/s40010-017-0356-7>.
653. Cai, X.; Yang, J.; Zhou, J.; Lu, W.; Hu, C.; Gu, Z.; Huo, J.; Wang, X.; Cao, P. Synthesis and biological evaluation of scopoletin derivatives. *Bioorg. Med. Chem.* **2013**, *21* (1), 84-92. DOI: <https://doi.org/10.1016/j.bmc.2012.10.059>.
654. Khunnawutmanotham, N.; Chimnoi, N.; Saparpakorn, P.; Techasakul, S. Synthesis and anti-acetylcholinesterase activity of scopoletin derivatives. *Bioorg. Chem.* **2016**, *65*, 137-145. DOI: <https://doi.org/10.1016/j.bioorg.2015.12.002>.
655. Liu, C.; Zheng, P.; Wang, H.; Wei, Y.; Wang, C.; Hao, S. Design and Synthesis of Scopoletin Sulfonate Derivatives as Potential Insecticidal Agents. *Molecules* **2023**, *28* (2). DOI: <https://doi.org/10.3390/molecules28020530>.
656. Liu, W.; Hua, J.; Zhou, J.; Zhang, H.; Zhu, H.; Cheng, Y.; Gust, R. Synthesis and in vitro antitumor activity of novel scopoletin derivatives. *Bioorg. Med. Chem. Lett.* **2012**, *22* (15), 5008-5012. DOI: <https://doi.org/10.1016/j.bmcl.2012.06.014>.
657. Lu, X.; Zhu, C.; Zhang, C.; Li, X.; Yu, Z.; Zhang, Z.; Shi, X. Design, synthesis and biological evaluation of 3-aryl-7-hydroxy scopoletin derivatives as autophagy activators against tumorigenesis. *Eur. J. Med. Chem.* **2022**, *244*. DOI: <https://doi.org/10.1016/j.ejmech.2022.114805>.
658. Luo, J.; Lai, T.; Guo, T.; Chen, F.; Zhang, L.; Ding, W.; Zhang, Y. Synthesis and acaricidal activities of scopoletin phenolic ether derivatives: Qsar, molecular docking study and in silico Adme predictions. *Molecules* **2018**, *23* (5). DOI: <https://doi.org/10.3390/molecules23050995>.
659. Shi, W.; Zhang, J.; Bao, N.; Guan, F.; Chen, L.; Sun, J. Design, synthesis, and cytotoxic evaluation of novel scopoletin derivatives. *Chem. Biol. Drug Des.* **2018**, *91* (2), 641-646. DOI: <https://doi.org/10.1111/cbdd.13120>.
660. Shi, Z.; Chen, L.; Sun, J. Novel scopoletin derivatives kill cancer cells by inducing mitochondrial depolarization and apoptosis. *Anticancer Agents Med. Chem.* **2021**, *21* (14), 1774-1782. DOI: <https://doi.org/10.2174/1871520621666201207094416>.
661. Shi, Z.; Li, N.; Chen, C.; Wang, Y.; Lei, Z.; Chen, L.; Sun, J. Novel NO-releasing scopoletin derivatives induce cell death via mitochondrial apoptosis pathway and cell cycle arrest. *Eur. J. Med. Chem.* **2020**, *200*. DOI: <https://doi.org/10.1016/j.ejmech.2020.112386>.
662. Yu, N.; Li, N.; Wang, K.; Deng, Q.; Lei, Z.; Sun, J.; Chen, L. Design, synthesis and biological activity evaluation of novel scopoletin-NO donor derivatives against MCF-7 human breast cancer in vitro and in vivo. *Eur. J. Med. Chem.* **2021**, *224*. DOI: <https://doi.org/10.1016/j.ejmech.2021.113701>.
663. Zhao, P.; Dou, Y.; Chen, L.; Li, L.; Wei, Z.; Yu, J.; Wu, X.; Dai, Y.; Xia, Y. SC-III3, a novel scopoletin derivative, induces autophagy of human hepatoma HepG2 cells through AMPK/mTOR signaling pathway by acting on mitochondria. *Fitoterapia* **2015**, *104*, 31-40. DOI: <https://doi.org/10.1016/j.fitote.2015.05.002>.
664. Zhou, J.; Wang, L.; Wei, L.; Zheng, Y.; Zhang, H.; Wang, Y.; Cao, P.; Niu, A.; Wang, J.; Dai, Y. Synthesis and antitumor activity of scopoletin derivatives. *Lett. Drug Des. Discovery* **2012**, *9* (4), 397-401. DOI: <https://doi.org/10.2174/157018012799859972>.
665. Dahab, M. A.; Mahdy, H. A.; Elkady, H.; Taghour, M. S.; Elwan, A.; Elkady, M. A.; Elsakka, E. G. E.; Elkaeed, E. B.; Alsouk, A. A.; Ibrahim, I. M.; et al. Semi-synthesized anticancer theobromine derivatives targeting VEGFR-2: in silico and in vitro evaluations. *J. Biomol. Struct. Dyn.* **2023**, *1*, DOI: <https://doi.org/10.1080/07391102.2023.2219333>.
666. Eissa, I. H.; G.Yousef, R.; Elkady, H.; Alsouk, A. A.; Husein, D. Z.; Ibrahim, I. M.; El-Deeb, N.; Kenawy, A. M.; Eldehna, W. M.; Elkaeed, E. B.; Metwaly, A. M. New apoptotic anti-triple-negative breast cancer theobromine derivative inhibiting EGFRWT and EGFR790M: in silico and in vitro evaluation. *Mol. Divers.* **2023**, DOI: <https://doi.org/10.1007/s11030-023-10644-4>.

667. Eissa, I. H.; Yousef, R. G.; Elkady, H.; Alsouk, A. A.; Alsouk, B. A.; Husein, D. Z.; Ibrahim, I. M.; Elkaeed, E. B.; Metwaly, A. M. A New Anticancer Semisynthetic Theobromine Derivative Targeting EGFR Protein: CADDD Study. *Life* **2023**, *13* (1). DOI: <https://doi.org/10.3390/life13010191>.
668. Eissa, I. H.; Yousef, R. G.; Elkaeed, E. B.; Alsouk, A. A.; Husein, D. Z.; Ibrahim, I. M.; Alesawy, M. S.; Elkady, H.; Metwaly, A. M. Anticancer derivative of the natural alkaloid, theobromine, inhibiting EGFR protein: Computer-aided drug discovery approach. *PLoS One* **2023**, *18*. DOI: <https://doi.org/10.1371/journal.pone.0282586>.
669. Elkaeed, E. B.; Yousef, R. G.; Elkady, H.; Alsouk, A. A.; Husein, D. Z.; Ibrahim, I. M.; Metwaly, A. M.; Eissa, I. H. New Anticancer Theobromine Derivative Targeting EGFRWT and EGFR790M: Design, Semi-Synthesis, In Silico, and In Vitro Anticancer Studies. *Molecules* **2022**, *27* (18). DOI: <https://doi.org/10.3390/molecules27185859>.
670. Georgieva, M.; Kondeva-Burdina, M.; Mitkov, J.; Tzankova, V.; Momekov, G.; Zlatkov, A. Determination of the antiproliferative activity of new theobromine derivatives and evaluation of their in vitro hepatotoxic effects. *Anticancer Agents Med. Chem.* **2016**, *16* (7), 925-932. DOI: <https://doi.org/10.2174/1871520616666151116122633>.
671. Gonçalves-Pereira, R.; Pereira, M. P.; Serra, S. G.; Loesche, A.; Csuk, R.; Silvestre, S.; Costa, P. J.; Oliveira, M. C.; Xavier, N. M. Furanosyl Nucleoside Analogues Embodying Triazole or Theobromine Units as Potential Lead Molecules for Alzheimer's Disease. *Eur. J. Org. Chem.* **2018**, *2018* (20), 2667-2681. DOI: <https://doi.org/10.1002/ejoc.201800245>.
672. Ivanchenko, D. G.; Romanenko, N. I.; Kornienko, V. I.; Polishchuk, N. N.; Sharapova, T. A. Synthesis and Properties of 8-Substituted 1-(2-Oxopropyl)Theobromine Derivatives. *Chem. Nat. Compd.* **2019**, *55* (3), 509-512. DOI: <https://doi.org/10.1007/s10600-019-02727-2>.
673. Xavier, N. M.; Sousa, E. C.; Pereira, M.; Loesche, A.; Serbian, I.; Csuk, R.; Oliveira, M. C. Synthesis and biological evaluation of structurally varied 50-/60-isonucleosides and theobromine-containing n-isonucleosidyl derivatives. *Pharmaceuticals* **2019**, *12* (3). DOI: <https://doi.org/10.3390/ph12030103>.
674. Alafeefy, A. M.; Alqasoumi, S. I.; Abdel Hamid, S. G.; El-Tahir, K. E. H.; Mohamed, M.; Zain, M. E.; Awaad, A. S. Synthesis and hypoglycemic activity of some new theophylline derivatives. *J. Enzyme Inhib. Med. Chem.* **2014**, *29* (3), 443-448. DOI: <https://doi.org/10.3109/14756366.2013.795957>.
675. Aninye, I. O.; Berg, K. C.; Mollo, A. R.; Nordeen, S. K.; Wilson, E. M.; Shapiro, D. J. 8-Alkylthio-6-thio-substituted theophylline analogues as selective noncompetitive progesterone receptor antagonists. *Steroids* **2012**, *77* (6), 596-601. DOI: <https://doi.org/10.1016/j.steroids.2012.02.003>.
676. Chang, Y.; Zhang, J.; Yang, S.; Lu, W.; Ding, L.; Zheng, Y.; Li, W. Design, synthesis, biological evaluation, and molecular docking of 1,7-dibenzyl-substituted theophylline derivatives as novel BRD4-BD1-selective inhibitors. *Med. Chem. Res.* **2021**, *30* (8), 1453-1468. DOI: <https://doi.org/10.1007/s00044-021-02737-2>.
677. Faghieh, Z.; Emami, L.; Zomoridian, K.; Sabet, R.; Bargebid, R.; Mansourian, A.; Zeinali, B.; Rostami, Z.; Khabnadideh, S. Aryloxy Alkyl Theophylline Derivatives as Antifungal Agents: Design, Synthesis, Biological Evaluation and Computational Studies. *Chem. Select* **2022**, *7* (25). DOI: <https://doi.org/10.1002/slct.202201618>.
678. Gopinatha, V. K.; Mantelingu, K.; Rangappa, K. S. Synthesis and biological evaluation of theophylline acetohydrazide hydrazone derivatives as antituberculosis agents. *J. Chin. Chem. Soc.* **2020**, *67* (8), 1453-1461. DOI: <https://doi.org/10.1002/jccs.201900558>.
679. Hayallah, A. M.; Elgaher, W. A.; Salem, O. I.; Abdel Alim, A. A. M. Design and synthesis of some new theophylline derivatives with bronchodilator and antibacterial activities. *Arch. Pharmacol. Res.* **2011**, *34* (1), 3-21. DOI: <https://doi.org/10.1007/s12272-011-0101-8>.
680. Hayallah, A. M.; Talhouni, A. A.; Abdel Alim, A. A. M. Design and synthesis of new 8-anilide theophylline derivatives as bronchodilators and antibacterial agents. *Arch. Pharmacol. Res.* **2012**, *35* (8), 1355-1368. DOI: <https://doi.org/10.1007/s12272-012-0805-4>.

681. Hierrezuelo, J.; Manuel López-Romero, J.; Rico, R.; Brea, J.; Isabel Loza, M.; Cai, C.; Algarra, M. Synthesis of theophylline derivatives and study of their activity as antagonists at adenosine receptors. *Bioorg. Med. Chem.* **2010**, *18* (6), 2081-2088. DOI: <https://doi.org/10.1016/j.bmc.2010.02.014>.
682. Kiran, G.; Prasad, D. K.; Bakshi, V.; Gouthami, T. In vitro anti-diabetic activity and molecular docking studies of theophylline containing acetylene derivatives. *Biointerface Res. Appl. Chem.* **2018**, *8* (5), 3618-3620.
683. Managutti, P. B.; Mangasuli, S. N.; Malaganvi, S. S. Synthesis, crystal structure, electronic structure, and anti-tubercular properties of two new coumarin derivatives bearing theophylline moiety. *Journal of Molecular Structure* **2023**, 1277. DOI: <https://doi.org/10.1016/j.molstruc.2022.134888>.
684. Partyka, A.; Jarosz, J.; Wasik, A.; Jastrzębska-Więsek, M.; Zagórska, A.; Pawłowski, M.; Wesółowska, A. Novel tricyclic[2,1-f]theophylline derivatives of LCAP with activity in mouse models of affective disorders. *J. Pharm. Pharmacol.* **2014**, *66* (12), 1755-1762. DOI: <https://doi.org/10.1111/jphp.12305>.
685. Profire, L.; Şunel, V.; Lupaşcu, D.; Baican, M. C.; Bibire, N.; Vasile, C. New theophylline derivatives with potential pharmacological activity. *Farmacia* **2010**, *58* (2), 170-176.
686. Prohre, L.; Lupascu, D. A. N.; Sunel, V.; Bibire, N.; Vasile, C. Synthesis and characterization of some new theophylline derivatives. *Rev. Chim.* **2010**, *61* (6), 553-556.
687. Ruddaraju, R. R.; Kiran, G.; Murugulla, A. C.; Maraju, R.; Prasad, D. K.; Kumar, B. H.; Bakshi, V.; Reddy, N. S. Design, synthesis and biological evaluation of theophylline containing variant acetylene derivatives as α -amylase inhibitors. *Bioorg. Chem.* **2019**, 92. DOI: <https://doi.org/10.1016/j.bioorg.2019.103120>.
688. Ruddaraju, R. R.; Murugulla, A. C.; Kotla, R.; Chandra Babu Tirumalasetty, M.; Wudayagiri, R.; Donthabakthuni, S.; Maraju, R.; Baburao, K.; Parasa, L. S. Design, synthesis, anticancer, antimicrobial activities and molecular docking studies of theophylline containing acetylenes and theophylline containing 1,2,3-triazoles with variant nucleoside derivatives. *Eur. J. Med. Chem.* **2016**, *123*, 379-396. DOI: <https://doi.org/10.1016/j.ejmech.2016.07.024>.
689. Ruddaraju, R. R.; Murugulla, A. C.; Kotla, R.; Tirumalasetty, M. C. B.; Wudayagiri, R.; Donthabakthuni, S.; Maraju, R. Design, synthesis, anticancer activity and docking studies of theophylline containing 1,2,3-triazoles with variant amide derivatives. *MedChemComm* **2017**, *8* (1), 176-183. DOI: <https://doi.org/10.1039/c6md00479b>.
690. Saeedan, A. S.; Mohamed, M. A.; Soliman, G. A.; Alasiri, K. M.; Abdel-Kader, M. S.; Elnaggar, M. H. Semisynthetic Theophylline Analogues as Potent Diuretics: An Integrated in vivo and Molecular Docking Study. *Lat. Am. J. Pharm.* **2022**, *41* (7), 1408-1416.
691. Stavrakov, G.; Valcheva, V.; Voynikov, Y.; Philipova, I.; Atanasova, M.; Konstantinov, S.; Peikov, P.; Doytchinova, I. Design, Synthesis, and Antimycobacterial Activity of Novel Theophylline-7-Acetic Acid Derivatives with Amino Acid Moieties. *Chem. Biol. Drug Des.* **2016**, *87* (3), 335-341. DOI: <https://doi.org/10.1111/cbdd.12676>.
692. Voynikov, Y.; Valcheva, V.; Momekov, G.; Peikov, P.; Stavrakov, G. Theophylline-7-acetic acid derivatives with amino acids as anti-tuberculosis agents. *Bioorg. Med. Chem. Lett.* **2014**, *24* (14), 3043-3045. DOI: <https://doi.org/10.1016/j.bmcl.2014.05.026>.
693. Ye, J.; Mao, L.; Xie, L.; Zhang, R.; Liu, Y.; Peng, L.; Yang, J.; Li, Q.; Yuan, M. Discovery of a Series of Theophylline Derivatives Containing 1,2,3-Triazole for Treatment of Non-Small Cell Lung Cancer. *Front. Pharmacol.* **2021**, *12*. DOI: <https://doi.org/10.3389/fphar.2021.753676>.
694. Yousaf, M.; Zahoor, A. F.; Faiz, S.; Javed, S.; Irfan, M. Recent Synthetic Approaches Towards Biologically Potent Derivatives/Analogues of Theophylline. *J. Heterocycl. Chem.* **2018**, *55* (11), 2447-2479. DOI: <https://doi.org/10.1002/jhet.3311>.
695. Zagórska, A.; Pawłowski, M.; Siwek, A.; Kazek, G.; Partyka, A.; Wróbel, D.; Jastrzębska-Więsek, M.; Wesółowska, A. Synthesis and pharmacological evaluation of novel tricyclic[2,1-f] theophylline derivatives. *Arch. Pharm.* **2013**, *346* (11), 832-839. DOI: <https://doi.org/10.1002/ardp.201300257>.
696. Gupta, N.; Mukerjee, A.; Mishra, S. B. Design, Synthesis and Molecular Docking of Vanillic Acid Derivatives as Amylolytic Enzyme Inhibitors. *Pharm. Chem. J.* **2021**, *55* (5), 427-435. DOI: <https://doi.org/10.1007/s11094-021-02439-4>.

697. Ishimata, N.; Ito, H.; Tai, A. Structure–activity relationships of vanillic acid ester analogs in inhibitory effect of antigen-mediated degranulation in rat basophilic leukemia RBL-2H3 cells. *Bioorg. Med. Chem. Lett.* **2016**, *26* (15), 3533-3536. DOI: <https://doi.org/10.1016/j.bmcl.2016.06.028>.
698. Satpute, M. S.; Gangan, V. D.; Shastri, I. Synthesis and antibacterial activity of novel vanillic acid hybrid derivatives. *Rasayan J. Chem.* **2019**, *12* (1), 383-388. DOI: <https://doi.org/10.31788/RJC.2019.1215023>.
699. Tang, J. F.; Lv, X. H.; Wang, X. L.; Sun, J.; Zhang, Y. B.; Yang, Y. S.; Gong, H. B.; Zhu, H. L. Design, synthesis, biological evaluation and molecular modeling of novel 1,3,4-oxadiazole derivatives based on Vanillic acid as potential immunosuppressive agents. *Bioorg. Med. Chem.* **2012**, *20* (14), 4226-4236. DOI: <https://doi.org/10.1016/j.bmc.2012.05.055>.
700. Tawfeeq, M. F.; Qassir, A. J. Synthesis, characterization, and antibacterial evaluation of new vanillic acid derivatives. *Iraqi J. Pharm. Sci.* **2020**, *29* (2), 129-138. DOI: <https://doi.org/10.31351/vol29iss2pp129-138>.
701. Wodnicka, A.; Huzar, E. Synthesis and photoprotective properties of new salicylic and vanillic acid derivatives. *Curr. Chem. Lett.* **2017**, *6* (3), 125-134. DOI: <https://doi.org/10.5267/j.ccl.2017.3.002>.
702. Xu, B.; Xu, X.; Zhang, C.; Zhang, Y.; Wu, G. R.; Yan, M.; Jia, M.; Xie, T.; Jia, X.; Wang, P.; Lei, H. Synthesis and protective effect of new ligustrazine-vanillic acid derivatives against CoCl₂-induced neurotoxicity in differentiated PC12 cells. *Chem. Cent. J.* **2017**, *11* (1). DOI: <https://doi.org/10.1186/s13065-017-0250-z>.
703. Bender, O.; Celik, I.; Dogan, R.; Atalay, A.; Shoman, M. E.; Ali, T. F. S.; Beshr, E. A. M.; Mohamed, M.; Alaaeldin, E.; Shawky, A. M.; et al. Vanillin-Based Indolin-2-one Derivative Bearing a Pyridyl Moiety as a Promising Anti-Breast Cancer Agent via Anti-Estrogenic Activity. *ACS Omega* **2023**, *8* (7), 6968-6981. DOI: <https://doi.org/10.1021/acsomega.2c07793>.
704. Blaikie, L.; Kay, G.; Kong Thoo Lin, P. Synthesis and in vitro evaluation of vanillin derivatives as multi-target therapeutics for the treatment of Alzheimer's disease. *Bioorg. Med. Chem. Lett.* **2020**, *30* (21). DOI: <https://doi.org/10.1016/j.bmcl.2020.127505>.
705. Boiko, Y. A.; Nesterkina, M. V.; Shandra, A. A.; Kravchenko, I. A. Analgesic and Anti-Inflammatory Activity of Vanillin Derivatives. *Pharm. Chem. J.* **2019**, *53* (7), 650-654. DOI: <https://doi.org/10.1007/s11094-019-02056-2>.
706. da Silva Rodrigues, J. V.; Rodrigues Gazolla, P. A.; da Cruz Pereira, I.; Dias, R. S.; Poly da Silva, I. E.; Oliveira Prates, J. W.; de Souza Gomes, I.; de Azevedo Silveira, S.; Costa, A. V.; de Oliveira, F. M.; et al. Synthesis and virucide activity on zika virus of 1,2,3-triazole-containing vanillin derivatives. *Antiviral Res.* **2023**, *212*. DOI: <https://doi.org/10.1016/j.antiviral.2023.105578>.
707. Ekowati, J.; Diyah, N. W.; Tejo, B. A.; Ahmed, S. Chemoinformatics approach to design and develop vanillin analogs as COX-1 inhibitor. *J. Public Health Afr.* **2023**, *14* (S1). DOI: <https://doi.org/10.4081/jphia.2023.2517>.
708. Freitas, C. S.; Santiago, S. S.; Lage, D. P.; Antinarelli, L. M. R.; Oliveira, F. M.; Vale, D. L.; Martins, V. T.; Magalhaes, L. N. D.; Bandeira, R. S.; Ramos, F. F.; et al. In vitro evaluation of antileishmanial activity, mode of action and cellular response induced by vanillin synthetic derivatives against Leishmania species able to cause cutaneous and visceral leishmaniasis. *Exp. Parasitol.* **2023**, *251*. DOI: <https://doi.org/10.1016/j.exppara.2023.108555>.
709. Gao, J.; Qiu, S.; Liang, L.; Hao, Z.; Zhou, Q.; Wang, F.; Mou, J.; Lin, Q. Design, synthesis, and biological evaluation of vanillin hydroxamic acid derivatives as novel peptide deformylase inhibitors. *Curr. Comput. Aided Drug Des.* **2018**, *14* (1), 95-101. DOI: <https://doi.org/10.2174/1573409913666170613074601>.
710. Gazolla, P. A. R.; de Aguiar, A. R.; Costa, M. C. A.; Oliveira, O. V.; Costa, A. V.; da Silva, C. M.; do Nascimento, C. J.; Junker, J.; Ferreira, R. S.; de Oliveira, F. M.; et al. Synthesis of vanillin derivatives with 1,2,3-triazole fragments and evaluation of their fungicide and fungistatic activities. *Arch. Pharm.* **2023**, *356* (6). DOI: <https://doi.org/10.1002/ardp.202200653>.
711. Gharai, P. K.; Khan, J.; Mallesh, R.; Garg, S.; Saha, A.; Ghosh, S.; Ghosh, S. Vanillin Benzothiazole Derivative Reduces Cellular Reactive Oxygen Species and Detects Amyloid Fibrillar Aggregates in

- Alzheimer's Disease Brain. *ACS Chem. Neurosci.* **2023**, *14* (4), 773-786. DOI: <https://doi.org/10.1021/acchemneuro.2c00771>.
712. Gu, M. M.; Li, M.; Gao, D.; Liu, L. H.; Lang, Y.; Yang, S. M.; Ou, H.; Huang, B.; Zhou, P. K.; Shang, Z. F. The vanillin derivative 6-bromine-5-hydroxy-4-methoxybenzaldehyde induces aberrant mitotic progression and enhances radio-sensitivity accompanying suppression the expression of PLK1 in esophageal squamous cell carcinoma. *Toxicol. Appl. Pharmacol.* **2018**, *348*, 76-84. DOI: <https://doi.org/10.1016/j.taap.2018.04.021>.
713. Harismah, K.; Fazeli, F.; Zandi, H. Structural analyses of vanillin derivative compounds and their molecular docking with mpro and rdrp enzymes of covid-19. *Biointerface Res. Appl. Chem.* **2022**, *12* (2), 1660-1669. DOI: <https://doi.org/10.33263/BRIAC122.16601669>.
714. He, H. W.; Wang, F. Y.; Zhang, D.; Chen, C. Y.; Xu, D.; Zhou, H.; Liu, X.; Xu, G. Discovery of Novel α -Methylene- γ -Butyrolactone Derivatives Containing Vanillin Moieties as Antiviral and Antifungal Agents. *J. Agric. Food Chem.* **2022**, *70* (33), 10316-10325. DOI: <https://doi.org/10.1021/acs.jafc.2c03632>.
715. Illicachi, L. A.; Montalvo-Acosta, J. J.; Insuasty, A.; Quiroga, J.; Abonia, R.; Sortino, M.; Zacchino, S.; Insuasty, B. Synthesis and DFT calculations of novel vanillin-chalcones and their 3-Aryl-5-(4-(2-(dimethylamino)-ethoxy)-3-methoxyphenyl)-4,5-dihydro-1H-pyrazole-1-carbaldehyde derivatives as antifungal agents. *Molecules* **2017**, *22* (9). DOI: <https://doi.org/10.3390/molecules22091476>.
716. Li, M.; Lang, Y.; Gu, M. M.; Shi, J.; Chen, B. P. C.; Yu, L.; Zhou, P. K.; Shang, Z. F. Vanillin derivative VND3207 activates DNA-PKcs conferring protection against radiation-induced intestinal epithelial cells injury in vitro and in vivo. *Toxicol. Appl. Pharmacol.* **2020**, *387*. DOI: <https://doi.org/10.1016/j.taap.2019.114855>.
717. Luković, J.; Mitrović, M.; Popović, S.; Milosavljević, Z.; Stanojević-Pirković, M.; An-Elković, M.; Zelen, I.; Šorak, M.; Muškinja, J.; Ratković, Z.; Nikolić, I. Antitumor effects of vanillin based chalcone analogs in vitro. *Acta Pol. Pharm. Drug Res.* **2020**, *77* (1), 57-67. DOI: <https://doi.org/10.32383/appdr/112786>.
718. Ma, W.; Zhang, Q.; Li, X.; Ma, Y.; Liu, Y.; Hu, S.; Zhou, Z.; Zhang, R.; Du, K.; Syed, A.; et al. IPM712, a vanillin derivative as potential antitumor agents, displays better antitumor activity in colorectal cancers cell lines. *Eur. J. Pharm. Sci.* **2020**, *152*. DOI: <https://doi.org/10.1016/j.ejps.2020.105464>.
719. Marton, A.; Kúsz, E.; Kolozsi, C.; Tubak, V.; Zagotto, G.; Buzás, K.; Quintieri, L.; Vizler, C. Vanillin analogues o-vanillin and 2,4,6-trihydroxybenzaldehyde inhibit NF κ B activation and suppress growth of A375 human melanoma. *Anticancer Res.* **2016**, *36* (11), 5743-5750. DOI: <https://doi.org/10.21873/anticancer.11157>.
720. Pagare, P. P.; Ghatge, M. S.; Musayev, F. N.; Deshpande, T. M.; Chen, Q.; Braxton, C.; Kim, S.; Venitz, J.; Zhang, Y.; Abdulmalik, O.; Safo, M. K. Rational design of pyridyl derivatives of vanillin for the treatment of sickle cell disease. *Bioorg. Med. Chem.* **2018**, *26* (9), 2530-2538. DOI: <https://doi.org/10.1016/j.bmc.2018.04.015>.
721. Sahoo, C. R.; Paidesetty, S. K.; Sarathbabu, S.; Dehury, B.; Senthil Kumar, N.; Padhy, R. N. Molecular dynamics simulation, synthesis and topoisomerase inhibitory actions of vanillin derivatives: a systematic computational structural integument. *J. Biomol. Struct. Dyn.* **2022**, *40* (22), 11653-11663. DOI: <https://doi.org/10.1080/07391102.2021.1961867>.
722. Scipioni, M.; Kay, G.; Megson, I.; Kong Thoo Lin, P. Novel vanillin derivatives: Synthesis, anti-oxidant, DNA and cellular protection properties. *Eur. J. Med. Chem.* **2018**, *143*, 745-754. DOI: <https://doi.org/10.1016/j.ejmech.2017.11.072>.
723. Scipioni, M.; Kay, G.; Megson, I. L.; Kong Thoo Lin, P. Synthesis of novel vanillin derivatives: Novel multi-targeted scaffold ligands against Alzheimer's disease. *MedChemComm* **2019**, *10* (5), 764-777. DOI: <https://doi.org/10.1039/c9md00048h>.
724. Shanani, S. H.; Kadem, K. J. The synthesis of some new heterocyclic compounds from vanillin derivatives. *Int. J. Drug Deliv. Technol.* **2021**, *11* (2), 376-378. DOI: <https://doi.org/10.25258/ijddt.11.2.24>.
725. Shastry, R. P.; Ghate, S. D.; Sukesh Kumar, B.; Srinath, B. S.; Kumar, V. Vanillin derivative inhibits quorum sensing and biofilm formation in *Pseudomonas aeruginosa*: a study in a *Caenorhabditis elegans*

- infection model. *Nat. Prod. Res.* **2022**, 36 (6), 1610-1615. DOI: <https://doi.org/10.1080/14786419.2021.1887866>.
726. Tokalı, F. S.; Şenol, H.; Katmerlikaya, T. G.; Dağ, A.; Şendil, K. Novel thiosemicarbazone and thiazolidin-4-one derivatives containing vanillin core: Synthesis, characterization, and anticancer activity studies. *J. Heterocycl. Chem.* **2023**, 60 (4), 645-656. DOI: <https://doi.org/10.1002/jhet.4619>.
727. Wu, Q.; Cai, H.; Yuan, T.; Li, S.; Gan, X.; Song, B. Novel vanillin derivatives containing a 1,3,4-thiadiazole moiety as potential antibacterial agents. *Bioorg. Med. Chem. Lett.* **2020**, 30 (10). DOI: <https://doi.org/10.1016/j.bmcl.2020.127113>.
728. Yuldasheva, N.; Acikyildiz, N.; Akyuz, M.; Yabo-Dambagi, L.; Aydin, T.; Cakir, A.; Kazaz, C. The Synthesis of Schiff bases and new secondary amine derivatives of p-vanillin and evaluation of their neuroprotective, antidiabetic, antidepressant and antioxidant potentials. *J. Mol. Struct.* **2022**, 1270. DOI: <https://doi.org/10.1016/j.molstruc.2022.133883>.
729. Zhou, Z.; Wang, Y.; Ji, R.; Zhang, D.; Ma, C.; Ma, W.; Ma, Y.; Jiang, X.; Du, K.; Zhang, R.; Chen, P. Vanillin Derivatives Reverse *Fusobacterium nucleatum*-Induced Proliferation and Migration of Colorectal Cancer Through E-Cadherin/ β -Catenin Pathway. *Front. Pharmacol.* **2022**, 13. DOI: <https://doi.org/10.3389/fphar.2022.841918>.
730. Abou-Zied, H. A.; Youssif, B. G. M.; Mohamed, M. F. A.; Hayallah, A. M.; Abdel-Aziz, M. EGFR inhibitors and apoptotic inducers: Design, synthesis, anticancer activity and docking studies of novel xanthine derivatives carrying chalcone moiety as hybrid molecules. *Bioorg. Chem.* **2019**, 89. DOI: <https://doi.org/10.1016/j.bioorg.2019.102997>.
731. Andonova, L.; Valkova, I.; Zheleva-Dimitrova, D.; Georgieva, M.; Momekov, G.; Zlatkov, A. Synthesis of new N1 arylpiperazine substituted xanthine derivatives and evaluation of their antioxidant and cytotoxic effects. *Anticancer Agents Med. Chem.* **2019**, 19 (4), 528-537. DOI: <https://doi.org/10.2174/1871520619666190121155651>.
732. Banga, A. R.; Sekhar, K. R.; Rayford, K. J.; Arun, A.; Odiase, P.; Garg, A. P.; Lima, M. F.; Nde, P. N.; Villalta, F.; Rachakonda, G. Xanthine Analogs Suppress *Trypanosoma cruzi* Infection In Vitro Using PDEs as Targets. *Microbiol. Res.* **2022**, 13 (4), 721-739. DOI: <https://doi.org/10.3390/microbiolres13040052>.
733. El-Kalyoubi, S.; Agili, F.; Zordok, W. A.; El-Sayed, A. S. A. Synthesis, in silico prediction and in vitro evaluation of antimicrobial activity, dft calculation and theoretical investigation of novel xanthines and uracil containing imidazolone derivatives. *Int. J. Mol. Sci.* **2021**, 22 (20). DOI: <https://doi.org/10.3390/ijms222010979>.
734. Gumber, D.; Yadav, D.; Yadav, R.; Kachler, S.; Klotz, K. N. Bronchospasmodic activity and adenosine receptor binding of some newer 1,3-dipropyl-8-phenyl substituted xanthine derivatives. *Chem. Biol. Drug Des.* **2020**, 95 (6), 600-609. DOI: <https://doi.org/10.1111/cbdd.13673>.
735. Hisham, M.; Youssif, B. G. M.; Osman, E. E. A.; Hayallah, A. M.; Abdel-Aziz, M. Synthesis and biological evaluation of novel xanthine derivatives as potential apoptotic antitumor agents. *Eur. J. Med. Chem.* **2019**, 176, 117-128. DOI: <https://doi.org/10.1016/j.ejmech.2019.05.015>.
736. Kapri, A.; Pant, S.; Gupta, N.; Nain, S. Recent Advances in the Biological Significance of Xanthine and its Derivatives: A Review. *Pharm. Chem. J.* **2022**, 56 (4), 461-474. DOI: <https://doi.org/10.1007/s11094-022-02661-8>.
737. Kasabova-Angelova, A.; Tzankova, D.; Mitkov, J.; Georgieva, M.; Tzankova, V.; Zlatkov, A.; Kondeva-Burdina, M. Xanthine derivatives as agents affecting non-dopaminergic neuroprotection in parkinson's disease. *Curr. Med. Chem.* **2020**, 27 (12), 2021-2036. DOI: <https://doi.org/10.2174/0929867325666180821153316>.
738. Kuo, C. H.; Zhang, B. H.; Huang, S. E.; Hsu, J. H.; Wang, Y. H.; Nguyen, T. T. N.; Lai, C. H.; Yeh, J. L. Xanthine Derivative KMUP-1 Attenuates Experimental Periodontitis by Reducing Osteoclast Differentiation and Inflammation. *Front. Pharmacol.* **2022**, 13. DOI: <https://doi.org/10.3389/fphar.2022.821492>.

739. Lai, C. H.; Chang, C. W.; Lee, F. T.; Kuo, C. H.; Hsu, J. H.; Liu, C. P.; Wu, H. L.; Yeh, J. L. Targeting vascular smooth muscle cell dysfunction with xanthine derivative KMUP-3 inhibits abdominal aortic aneurysm in mice. *Atherosclerosis* **2020**, *297*, 16-24. DOI: <https://doi.org/10.1016/j.atherosclerosis.2020.01.029>.
740. Lee, L. C.; Peng, Y. H.; Chang, H. H.; Hsu, T.; Lu, C. T.; Huang, C. H.; Hsueh, C. C.; Kung, F. C.; Kuo, C. C.; Jiaang, W. T.; Wu, S. Y. Xanthine Derivatives Reveal an Allosteric Binding Site in Methylene-tetrahydrofolate Dehydrogenase 2 (MTHFD2). *J. Med. Chem.* **2021**, *64* (15), 11288-11301. DOI: <https://doi.org/10.1021/acs.jmedchem.1c00663>.
741. Li, G.; Meng, B.; Yuan, B.; Huan, Y.; Zhou, T.; Jiang, Q.; Lei, L.; Sheng, L.; Wang, W.; Gong, N.; et al. The optimization of xanthine derivatives leading to HBK001 hydrochloride as a potent dual ligand targeting DPP-IV and GPR119. *Eur. J. Med. Chem.* **2020**, *188*. DOI: <https://doi.org/10.1016/j.ejmech.2019.112017>.
742. Li, Q.; Meng, L.; Zhou, S.; Deng, X.; Wang, N.; Ji, Y.; Peng, Y.; Xing, J.; Yao, G. Rapid generation of novel benzoic acid-based xanthine derivatives as highly potent, selective and long acting DPP-4 inhibitors: Scaffold-hopping and prodrug study. *Eur. J. Med. Chem.* **2019**, *180*, 509-523. DOI: <https://doi.org/10.1016/j.ejmech.2019.07.045>.
743. Lindemann, M.; Dukic-Stefanovic, S.; Hinz, S.; Deuther-Conrad, W.; Teodoro, R.; Juhl, C.; Steinbach, J.; Brust, P.; Müller, C. E.; Wenzel, B. Synthesis of novel fluorinated xanthine derivatives with high adenosine a2b receptor binding affinity. *Pharmaceuticals* **2021**, *14* (5). DOI: <https://doi.org/10.3390/ph14050485>.
744. Ma, Q. S.; Yao, Y.; Zheng, Y. C.; Feng, S.; Chang, J.; Yu, B.; Liu, H. M. Ligand-based design, synthesis and biological evaluation of xanthine derivatives as LSD1/KDM1A inhibitors. *Eur. J. Med. Chem.* **2019**, *162*, 555-567. DOI: <https://doi.org/10.1016/j.ejmech.2018.11.035>.
745. Minard, A.; Bauer, C. C.; Chuntharpursat-Bon, E.; Pickles, I. B.; Wright, D. J.; Ludlow, M. J.; Burnham, M. P.; Warriner, S. L.; Beech, D. J.; Muraki, K.; Bon, R. S. Potent, selective, and subunit-dependent activation of TRPC5 channels by a xanthine derivative. *Br. J. Pharmacol.* **2019**, *176* (20), 3924-3938. DOI: <https://doi.org/10.1111/bph.14791>.
746. Narsimha, S.; Battula, K. S.; Ravinder, M.; Reddy, Y. N.; Nagavelli, V. R. Design, synthesis and biological evaluation of novel 1,2,3-triazole-based xanthine derivatives as DPP-4 inhibitors. *J. Chem. Sci.* **2020**, *132* (1). DOI: <https://doi.org/10.1007/s12039-020-1760-0>.
747. Pretze, M.; Neuber, C.; Kinski, E.; Belter, B.; Köckerling, M.; Caflisch, A.; Steinbach, J.; Pietzsch, J.; Mamat, C. Synthesis, radiolabelling and initial biological characterisation of 18F-labelled xanthine derivatives for PET imaging of Eph receptors. *Org. Biomol. Chem.* **2020**, *18* (16), 3104-3116. DOI: <https://doi.org/10.1039/d0ob00391c>.
748. Qiao, M. Q.; Li, Y.; Yang, Y. X.; Pang, C. X.; Liu, Y. T.; Bian, C.; Wang, L.; Chen, X. F.; Hong, B. Structure-activity relationship and biological evaluation of xanthine derivatives as PCSK9 inhibitors for the treatment of atherosclerosis. *Eur. J. Med. Chem.* **2023**, *247*. DOI: <https://doi.org/10.1016/j.ejmech.2022.115047>.
749. Satish, M.; Sandhya, K.; Nitin, K.; Yashas Kiran, N.; Aleena, B.; Satish Kumar, A.; Guruprasad, K.; Rajakumara, E. Computational, biochemical and ex vivo evaluation of xanthine derivatives against phosphodiesterases to enhance the sperm motility. *J. Biomol. Struct. Dyn.* **2022**, *41*(11):5317-5327. DOI: <https://doi.org/10.1080/07391102.2022.2085802>.
750. Shatokhin, S. S.; Tuskaev, V. A.; Gagieva, S. C.; Markova, A. A.; Pozdnyakov, D. I.; Denisov, G. L.; Melnikova, E. K.; Bulychyev, B. M.; Oganesyanyan, E. T. Synthesis, cytotoxicity and antioxidant activity of new 1,3-dimethyl-8-(chromon-3-yl)-xanthine derivatives containing 2,6-di-tert-butylphenol fragments. *New J. Chem.* **2022**, *46* (2), 621-631. DOI: <https://doi.org/10.1039/d1nj03726a>.
751. Singh, S.; Ojha, M.; Yadav, D.; Kachler, S.; Klotz, K. N.; Yadav, R. Bronchospasmolytic and Adenosine Binding Activity of 8-(Proline / Pyrazole)-Substituted Xanthine Derivatives. *Curr. Drug Disc. Technol.* **2021**, *18* (5). DOI: <https://doi.org/10.2174/1570163817666200922121005>.
752. Specker, E.; Matthes, S.; Wesolowski, R.; Schütz, A.; Grohmann, M.; Alenina, N.; Pleimes, D.; Mallow, K.; Neuenschwander, M.; Gogolin, A.; et al. Structure-Based Design of Xanthine-Benzimidazole

- Derivatives as Novel and Potent Tryptophan Hydroxylase Inhibitors. *J. Med. Chem.* **2022**, 65 (16), 11126-11149. DOI: <https://doi.org/10.1021/acs.jmedchem.2c00598>.
753. Tam, D. N. H.; Mostafa, E. M.; Tu, V. L.; Rashidy, A. I.; Matenoglou, E.; Kassem, M.; Soa, D. T.; Bayumi, A.; Emam, H. E. S.; Tran, L.; et al. Efficacy of chalcone and xanthine derivatives on lipase inhibition: A systematic review. *Chem. Biol. Drug Des.* **2020**, 95 (2), 205-214. DOI: <https://doi.org/10.1111/cbdd.13626>.
754. Fujioka, K.; Shibamoto, T. Quantitation of volatiles and nonvolatile acids in an extract from coffee beverages: Correlation with antioxidant activity. *J. Agric. Food Chem.* **2006**, 54 (16), 6054-6058. DOI: <https://doi.org/10.1021/jf060460x>.
755. Li, H.; Lin, L.; Feng, Y.; Zhao, M.; Li, X.; Zhu, Q.; Xiao, Z. Enrichment of antioxidants from soy sauce using macroporous resin and identification of 4-ethylguaiacol, catechol, daidzein, and 4-ethylphenol as key small molecule antioxidants in soy sauce. *Food Chem.* **2018**, 240, 885-892. DOI: <https://doi.org/10.1016/j.foodchem.2017.08.001>.
756. Zhao, D.; Sun, J.; Sun, B.; Zhao, M.; Zheng, F.; Huang, M.; Sun, X.; Li, H. Intracellular antioxidant effect of vanillin, 4-methylguaiacol and 4-ethylguaiacol: Three components in Chinese Baijiu. *RSC Adv.* **2017**, 7 (73), 46395-46405. DOI: <https://doi.org/10.1039/c7ra09302k>.
757. Esatbeyoglu, T.; Ulbrich, K.; Rehberg, C.; Rohn, S.; Rimbach, G. Thermal stability, antioxidant, and anti-inflammatory activity of curcumin and its degradation product 4-vinyl guaiacol. *Food Funct.* **2015**, 6 (3), 887-893. DOI: <https://doi.org/10.1039/c4fo00790e>.
758. Shin, J. A.; Jeong, S. H.; Jia, C. H.; Hong, S. T.; Lee, K. T. Comparison of antioxidant capacity of 4-vinylguaiacol with catechin and ferulic acid in oil-in-water emulsion. *Food Sci. Biotechnol.* **2019**, 28 (1), 35-41. DOI: <https://doi.org/10.1007/s10068-018-0458-2>.
759. Tańska, M.; Mikołajczak, N.; Konopka, I. Comparison of the effect of sinapic and ferulic acids derivatives (4-vinylsyringol vs. 4-vinylguaiacol) as antioxidants of rapeseed, flaxseed, and extra virgin olive oils. *Food Chem.* **2018**, 240, 679-685. DOI: <https://doi.org/10.1016/j.foodchem.2017.08.007>.
760. 7Agunloye, O. M.; Oboh, G. Caffeic acid and chlorogenic acid: Evaluation of antioxidant effect and inhibition of key enzymes linked with hypertension. *J. Food Biochem.* **2018**, 42 (4). DOI: <https://doi.org/10.1111/jfbc.12541>.
761. Coelho, V. R.; Vieira, C. G.; De Souza, L. P.; Moysés, F.; Basso, C.; Papke, D. K. M.; Pires, T. R.; Siqueira, I. R.; Picada, J. N.; Pereira, P. Antiepileptogenic, antioxidant and genotoxic evaluation of rosmarinic acid and its metabolite caffeic acid in mice. *Life Sci.* **2015**, 122, 65-71. DOI: <https://doi.org/10.1016/j.lfs.2014.11.009>.
762. Fan, J.; Cai, X.; Feng, X.; Jiang, M.; Yu, X. Studies on the antioxidant activity in vitro of caffeic acid. *J. Chin. Inst. Food Sci. Technol.* **2015**, 15 (3), 65-73. DOI: <https://doi.org/10.16429/j.1009-7848.2015.03.009>.
763. Genaro-Mattos, T. C.; Maurício, Â. Q.; Rettori, D.; Alonso, A.; Hermes-Lima, M. Antioxidant activity of Caffeic acid against iron-induced free radical generation-A chemical approach. *PLoS One* **2015**, 10 (6). DOI: <https://doi.org/10.1371/journal.pone.0129963>.
764. 7Jamali, N.; Mostafavi-Pour, Z.; Zal, F.; Kasraeian, M.; Poordast, T.; Nejabat, N. Antioxidant ameliorative effect of caffeic acid on the ectopic endometrial cells separated from patients with endometriosis. *Taiwan. J. Obstet. Gynecol.* **2021**, 60 (2), 216-220. DOI: <https://doi.org/10.1016/j.tjog.2020.12.003>.
765. Kassa, T.; Whalin, J. G.; Richards, M. P.; Alayash, A. I. Caffeic acid: an antioxidant with novel antisickling properties. *FEBS Open Bio* **2021**, 11 (12), 3293-3303. DOI: <https://doi.org/10.1002/2211-5463.13295>.
766. Masek, A.; Chrzescijanska, E.; Latos, M. Determination of antioxidant activity of caffeic acid and p-coumaric acid by using electrochemical and spectrophotometric assays. *Int. J. Electrochem. Sci.* **2016**, 11 (12), 10644-10658. DOI: <https://doi.org/10.20964/2016.12.73>.
767. Mohammed, F. Z.; Al-Hussaini, A. S. E. D.; El-Shehabi, M. E. S. Antidiabetic activity of caffeic acid and 18 β -glycyrrhetic acid and its relationship with the antioxidant property. *Asian J. Pharm. Clin. Res.* **2015**, 8 (5), 255-260.

768. Purushothaman, A.; Babu, S. S.; Naroth, S.; Janardanan, D. Antioxidant activity of caffeic acid: thermodynamic and kinetic aspects on the oxidative degradation pathway. *Free Radic. Res.* **2022**, *56* (9-10), 617-630. DOI: <https://doi.org/10.1080/10715762.2022.2161379>.
769. Sato, Y.; Itagaki, S.; Kurokawa, T.; Ogura, J.; Kobayashi, M.; Hirano, T.; Sugawara, M.; Iseki, K. In vitro and in vivo antioxidant properties of chlorogenic acid and caffeic acid. *Int. J. Pharm.* **2011**, *403* (1-2), 136-138. DOI: <https://doi.org/10.1016/j.ijpharm.2010.09.035>.
770. Sheng, X.; Zhu, Y.; Zhou, J.; Yan, L.; Du, G.; Liu, Z.; Chen, H. Antioxidant Effects of Caffeic Acid Lead to Protection of Drosophila Intestinal Stem Cell Aging. *Front. Cell Dev. Biol.* **2021**, *9*. DOI: <https://doi.org/10.3389/fcell.2021.735483>.
771. Spagnol, C. M.; Assis, R. P.; Brunetti, I. L.; Isaac, V. L. B.; Salgado, H. R. N.; Corrêa, M. A. In vitro methods to determine the antioxidant activity of caffeic acid. *Spectrochim. Acta A Mol. Biomol. Spectrosc.* **2019**, *219*, 358-366. DOI: <https://doi.org/10.1016/j.saa.2019.04.025>.
772. Uranga, J. G.; Podio, N. S.; Wunderlin, D. A.; Santiago, A. N. Theoretical and Experimental Study of the Antioxidant Behaviors of 5-O-Caffeoylquinic, Quinic and Caffeic Acids Based on Electronic and Structural Properties. *ChemistrySelect* **2016**, *1* (13), 4113-4120. DOI: <https://doi.org/10.1002/slct.201600582>.
773. Hosny, E. N.; Sawie, H. G.; Elhadidy, M. E.; Khadrawy, Y. A. Evaluation of antioxidant and anti-inflammatory efficacy of caffeine in rat model of neurotoxicity. *Nutr. Neurosci.* **2019**, *22* (11), 789-796. DOI: <https://doi.org/10.1080/1028415X.2018.1446812>.
774. Ősz, B. E.; Jitca, G.; Ștefănescu, R. E.; Pușcaș, A.; Tero-Vescan, A.; Vari, C. E. Caffeine and Its Antioxidant Properties—It Is All about Dose and Source. *Int. J. Mol. Sci.* **2022**, *23* (21). DOI: <https://doi.org/10.3390/ijms232113074>.
775. Ruiss, M.; Findl, O.; Kronschlager, M. The human lens: An antioxidant-dependent tissue revealed by the role of caffeine. *Ageing Res. Rev.* **2022**, *79*. DOI: <https://doi.org/10.1016/j.arr.2022.101664>.
776. Vieira, A. J. S. C.; Gaspar, E. M.; Santos, P. M. P. Mechanisms of potential antioxidant activity of caffeine. *Radiat. Phys. Chem.* **2020**, *174*. DOI: <https://doi.org/10.1016/j.radphyschem.2020.108968>.
777. Bai, D.; Liu, K.; He, X.; Tan, H.; Liu, Y.; Li, Y.; Zhang, Y.; Zhen, W.; Zhang, C.; Ma, Y. Effect of Dietary Chlorogenic Acid on Growth Performance, Antioxidant Function, and Immune Response of Broiler Breeders under Immune Stress and Stocking Density Stress. *Vet. Sci.* **2022**, *9* (10). DOI: <https://doi.org/10.3390/vetsci9100582>.
778. Bender, O.; Atalay, A. Polyphenol chlorogenic acid, antioxidant profile, and breast cancer. In *Cancer: Oxidative Stress and Dietary Antioxidants*, Academic Press; Chapter 28, pp 311-321.
779. Carolina Chaves-Ulate, E.; Esquivel-Rodríguez, P. Chlorogenic acids present in coffee: Antioxidant and antimicrobial capacity. *Agron. Mesoam.* **2019**, *30* (1), 299-311. DOI: <https://doi.org/10.15517/am.v30i1.32974>.
780. Chen, F.; Zhang, H.; Zhao, N.; Yang, X.; Du, E.; Huang, S.; Guo, W.; Zhang, W.; Wei, J. Effect of chlorogenic acid on intestinal inflammation, antioxidant status, and microbial community of young hens challenged with acute heat stress. *Anim. Sci. J.* **2021**, *92* (1). DOI: <https://doi.org/10.1111/asj.13619>.
781. Chen, J.; Yu, B.; Chen, D.; Huang, Z.; Mao, X.; Zheng, P.; Yu, J.; Luo, J.; He, J. Chlorogenic acid improves intestinal barrier functions by suppressing mucosa inflammation and improving antioxidant capacity in weaned pigs. *J. Nutr. Biochem.* **2018**, *59*, 84-92. DOI: <https://doi.org/10.1016/j.jnutbio.2018.06.005>.
782. Girsang, E.; Lister, I. N. E.; Ginting, C. N.; Nasution, S. L.; Suhartina, S.; Munshy, U. Z.; Rizal, R.; Widowati, W. Antioxidant and Anti-Inflammatory activity of Chlorogenic Acid on Lead-Induced Fibroblast Cells. *J. Phys. Conf. Ser.* **2019**; *1374*. DOI: <https://doi.org/10.1088/1742-6596/1374/1/012006>.
783. Liang, N.; Xue, W.; Kennepohl, P.; Kitts, D. D. Interactions between major chlorogenic acid isomers and chemical changes in coffee brew that affect antioxidant activities. *Food Chem.* **2016**, *213*, 251-259. DOI: <https://doi.org/10.1016/j.foodchem.2016.06.041>.
784. Mei, Y.; Sun, H.; Du, G.; Wang, X.; Lyu, D. Exogenous chlorogenic acid alleviates oxidative stress in apple leaves by enhancing antioxidant capacity. *Sci. Hortic.* **2020**, *274*. DOI: <https://doi.org/10.1016/j.scienta.2020.109676>.

785. Preetha Rani, M. R.; Anupama, N.; Sreelekshmi, M.; Raghu, K. G. Chlorogenic acid attenuates glucotoxicity in H9c2 cells via inhibition of glycation and PKC α upregulation and safeguarding innate antioxidant status. *Biomed. Pharmacother.* **2018**, *100*, 467-477. DOI: <https://doi.org/10.1016/j.biopha.2018.02.027>.
786. Tomac, I.; Šeruga, M.; Labuda, J. Evaluation of antioxidant activity of chlorogenic acids and coffee extracts by an electrochemical DNA-based biosensor. *Food Chem.* **2020**, *325*. DOI: <https://doi.org/10.1016/j.foodchem.2020.126787>.
787. Xu, J. G.; Hu, Q. P.; Liu, Y. Antioxidant and DNA-protective activities of chlorogenic acid isomers. *J. Agric. Food Chem.* **2012**, *60* (46), 11625-11630. DOI: <https://doi.org/10.1021/jf303771s>.
788. Zhou, Y.; Zhou, L.; Ruan, Z.; Mi, S.; Jiang, M.; Li, X.; Wu, X.; Deng, Z.; Yin, Y. Chlorogenic acid ameliorates intestinal mitochondrial injury by increasing antioxidant effects and activity of respiratory complexes. *Biosci. Biotechnol. Biochem.* **2016**, *80* (5), 962-971. DOI: <https://doi.org/10.1080/09168451.2015.1127130>.
789. Huang, J.; De Paulis, T.; May, J. M. Antioxidant effects of dihydrocaffeic acid in human EA.hy926 endothelial cells. *J. Nutr. Biochem.* **2004**, *15* (12), 722-729. DOI: <https://doi.org/10.1016/j.jnutbio.2004.07.002>.
790. Moon, J. H.; Terao, J. Antioxidant Activity of Caffeic Acid and Dihydrocaffeic Acid in Lard and Human Low-Density Lipoprotein. *J. Agric. Food Chem.* **1998**, *46* (12), 5062-5065. DOI: <https://doi.org/10.1021/jf9805799>.
791. Sørensen, A. D. M.; Petersen, L. K.; de Diego, S.; Nielsen, N. S.; Lue, B. M.; Yang, Z.; Xu, X.; Jacobsen, C. The antioxidative effect of lipophilized rutin and dihydrocaffeic acid in fish oil enriched milk. *Eur. J. Lipid Sci. Technol.* **2012**, *114* (4), 434-445. DOI: <https://doi.org/10.1002/ejlt.201100354>.
792. Adefegha, S. A.; Okeke, B. M.; Oboh, G. Antioxidant properties of eugenol, butylated hydroxyanisole, and butylated hydroxyl toluene with key biomolecules relevant to Alzheimer's diseases—In vitro. *J. Food Biochem.* **2021**, *45* (3). DOI: <https://doi.org/10.1111/jfbc.13276>.
793. Alminderej, F.; Bakari, S.; Almundarij, T. I.; Snoussi, M.; Aouadi, K.; Kadri, A. Antioxidant activities of a new chemotype of piper cubeba L. Fruit essential oil (methyleugenol/eugenol): In silico molecular docking and admet studies. *Plants* **2020**, *9* (11), 1-18. DOI: <https://doi.org/10.3390/plants9111534>.
794. Bonilla, J.; Poloni, T.; Lourenço, R. V.; Sobral, P. J. A. Antioxidant potential of eugenol and ginger essential oils with gelatin/chitosan films. *Food Biosci.* **2018**, *23*, 107-114. DOI: <https://doi.org/10.1016/j.fbio.2018.03.007>.
795. Candido Júnior, J. R.; Romeiro, L. A. S.; Marinho, E. S.; Monteiro, N. K. V.; de Lima-Neto, P. Antioxidant activity of eugenol and its acetyl and nitroderivatives: the role of quinone intermediates—a DFT approach of DPPH test. *J. Mol. Model.* **2022**, *28* (5). DOI: <https://doi.org/10.1007/s00894-022-05120-z>.
796. Ekinci Akdemir, F. N.; Yildirim, S.; Kandemir, F. M.; Aksu, E. H.; Guler, M. C.; Kiziltunc Ozmen, H.; Kucukler, S.; Eser, G. The antiapoptotic and antioxidant effects of eugenol against cisplatin-induced testicular damage in the experimental model. *Andrologia* **2019**, *51* (9). DOI: <https://doi.org/10.1111/and.13353>.
797. Ferreira, V. R. F.; Militani, I. A.; de Almeida, K. J.; Lunguinho, A. D. S.; Saczk, A. A.; Ionta, M.; da Silva, G. A. F.; Felix, F. S.; Nelson, D. L.; Cardoso, M. D. G. Antioxidant and Cytotoxic Activity of Essential Oils and Their Principal Components: Spectrophotometric, Voltammetric, and Theoretical Investigation of the Chelating Effect of Eugenol and Carvacrol. *ACS Food Sci. Technol.* **2023**, *3* (2), 350-360. DOI: <https://doi.org/10.1021/acsfoodscitech.2c00378>.
798. Gülçin, I. Antioxidant activity of eugenol: A structure-activity relationship study. *J. Med. Food* **2011**, *14* (9), 975-985. DOI: <https://doi.org/10.1089/jmf.2010.0197>.
799. Hamed, S. F.; Sadek, Z.; Edris, A. Antioxidant and antimicrobial activities of clove bud essential oil and eugenol nanoparticles in alcohol-free microemulsion. *J. Oleo Sci.* **2012**, *61* (11), 641-648. DOI: <https://doi.org/10.5650/jos.61.641>.
800. Hobani, Y. H.; Mohan, S.; Shaheen, E.; Abdelhaleem, A.; Faruque Ahmad, M.; Bhatia, S.; Abou-Elhamd, A. S. Gastroprotective effect of low dose Eugenol in experimental rats against ethanol induced toxicity:

- Involvement of antiinflammatory and antioxidant mechanism. *J. Ethnopharmacol.* **2022**, 289. DOI: <https://doi.org/10.1016/j.jep.2022.115055>.
801. Horvathova, E.; Navarova, J.; Galova, E.; Sevcovicova, A.; Chodakova, L.; Snahnicanova, Z.; Melusova, M.; Kozics, K.; Slamenova, D. Assessment of antioxidative, chelating, and DNA-Protective effects of selected essential oil components (Eugenol, Carvacrol, Thymol, Borneol, Eucalyptol) of plants and intact *rosmarinus officinalis* oil. *J. Agric. Food Chem.* **2014**, 62 (28), 6632-6639. DOI: <https://doi.org/10.1021/jf501006y>.
802. Mahboub, R.; Memmou, F. Antioxidant activity and kinetics studies of eugenol and 6-bromoeugenol. *Nat. Prod. Res.* **2015**, 29 (10), 966-971. DOI: <https://doi.org/10.1080/14786419.2014.958738>.
803. Nam, H.; Kim, M. M. Eugenol with antioxidant activity inhibits MMP-9 related to metastasis in human fibrosarcoma cells. *Food Chem. Toxicol.* **2013**, 55, 106-112. DOI: <https://doi.org/10.1016/j.fct.2012.12.050>.
804. Oroojan, A. A.; Chenani, N.; An'Aam, M. Antioxidant Effects of Eugenol on Oxidative Stress Induced by Hydrogen Peroxide in Islets of Langerhans Isolated from Male Mouse. *Int. J. Hepatol.* **2020**, 2020. DOI: <https://doi.org/10.1155/2020/5890378>.
805. Sharma, U. K.; Sharma, A. K.; Gupta, A.; Kumar, R.; Pandey, A.; Pandey, A. K. Pharmacological activities of cinnamaldehyde and eugenol: Antioxidant, cytotoxic and anti-leishmanial studies. *Cell. Mol. Biol.* **2017**, 63 (6), 73-78. DOI: <https://doi.org/10.14715/cmb/2017.63.6.15>.
806. Alam, M. A. Anti-hypertensive Effect of Cereal Antioxidant Ferulic Acid and Its Mechanism of Action. *Front. Vet. Sci.* **2019**, 6. DOI: <https://doi.org/10.3389/fvut.2019.00121>.
807. Amić, A.; Marković, Z.; Dimitrić Marković, J. M.; Milenković, D.; Stepanić, V. Antioxidative potential of ferulic acid phenoxyl radical. *Phytochemistry* **2020**, 170. DOI: <https://doi.org/10.1016/j.phytochem.2019.112218>.
808. Hasanvand, A.; Kharazmkia, A.; Mir, S.; Khorramabadi, R. M.; Darabi, S. Ameliorative effect of ferulic acid on gentamicin-induced nephrotoxicity in a rat model; role of antioxidant effects. *J. Renal Inj. Prev.* **2018**, 7 (2), 73-77. DOI: <https://doi.org/10.15171/jrip.2018.18>.
809. Hwang, H. J.; Lee, S. R.; Yoon, J. G.; Moon, H. R.; Zhang, J.; Park, E.; Yoon, S. I.; Cho, J. A. Ferulic Acid as a Protective Antioxidant of Human Intestinal Epithelial Cells. *Antioxidants* **2022**, 11 (8). DOI: <https://doi.org/10.3390/antiox11081448>.
810. Kaur, S.; Dhiman, M.; Mantha, A. K. Ferulic acid: A natural antioxidant with application towards neuroprotection against Alzheimer's disease. In *Functional Food and Human Health*, Springer Nature; Singapore, 2018, pp 575-586.
811. Wang, Y.; Chen, X.; Huang, Z.; Chen, D.; Yu, B.; Yu, J.; Chen, H.; He, J.; Luo, Y.; Zheng, P. Dietary ferulic acid supplementation improves antioxidant capacity and lipid metabolism in weaned piglets. *Nutrients* **2020**, 12 (12), 1-11. DOI: <https://doi.org/10.3390/nu12123811>.
812. Zduńska, K.; Dana, A.; Kołodziejczak, A.; Rotsztein, H. Antioxidant properties of ferulic acid and its possible application. *Skin Pharmacol. Physiol.* **2018**, 31 (6), 332-336. DOI: <https://doi.org/10.1159/000491755>.
813. Zduńska-Pęciak, K.; Kołodziejczak, A.; Rotsztein, H. Two superior antioxidants: Ferulic acid and ascorbic acid in reducing signs of photoaging—A split-face comparative study. *Dermatol. Ther.* **2022**, 35 (2). DOI: <https://doi.org/10.1111/dth.15254>.
814. Azadfar, M.; Gao, A. H.; Chen, S. Structural characterization of lignin: A potential source of antioxidants guaiacol and 4-vinylguaiacol. *Int. J. Biol. Macromol.* **2015**, 75, 58-66. DOI: <https://doi.org/10.1016/j.ijbiomac.2014.12.049>.
815. Gao, T.; Zhang, Y.; Shi, J.; Mohamed, S. R.; Xu, J.; Liu, X. The Antioxidant Guaiacol Exerts Fungicidal Activity Against Fungal Growth and Deoxynivalenol Production in *Fusarium graminearum*. *Front. Microbiol.* **2021**, 12. DOI: <https://doi.org/10.3389/fmicb.2021.762844>.
816. Bortolomeazzi, R.; Sebastianutto, N.; Toniolo, R.; Pizzariello, A. Comparative evaluation of the antioxidant capacity of smoke flavouring phenols by crocin bleaching inhibition, DPPH radical scavenging and

- oxidation potential. *Food Chem.* **2007**, *100* (4), 1481-1489. DOI: <https://doi.org/10.1016/j.foodchem.2005.11.039>.
817. Wang, X.; Li, X.; Chen, D. Evaluation of antioxidant activity of isoferulic acid in vitro. *Nat. Prod. Commun.* **2011**, *6* (9), 1285-1288. DOI: <https://doi.org/10.1177/1934578x1100600919>.
818. Gao, Q.; Li, Y.; Li, Y.; Zhang, Z.; Liang, Y. Antioxidant and prooxidant activities of phenolic acids commonly existed in vegetables and their relationship with structures. *Free Radic. Biol. Med.* **2022**, *42*. DOI: <https://doi.org/10.1590/fst.07622>.
819. Li, X.; Lin, J.; Gao, Y.; Han, W.; Chen, D. Antioxidant activity and mechanism of Rhizoma Cimicifugae. *Chem. Cent. J.* **2012**, *6* (1). DOI: <https://doi.org/10.1186/1752-153X-6-140>.
820. Wang, F.; Zhao, S.; Li, F.; Zhang, B.; Qu, Y.; Sun, T.; Luo, T.; Li, D. Investigation of antioxidant interactions between radix Astragali and Cimicifuga foetida and identification of synergistic antioxidant compounds. *PLoS One* **2014**, *9* (1). DOI: <https://doi.org/10.1371/journal.pone.0087221>.
821. Mendoza-Sarmiento, G.; Rojas-Hernández, A.; Galano, A.; Gutiérrez, A. A combined experimental-theoretical study of the acid-base behavior of mangiferin: implications for its antioxidant activity. *RSC Adv.* **2016**, *6* (56), 51171-51182. DOI: <https://doi.org/10.1039/C6RA06328D>.
822. Vieira, A. J. S. C.; Telo, J. P.; Pereira, H. F.; Patrocínio, P. F.; Dias, R. M. B. Antioxidant effect of naturally occurring xanthenes on the oxidative damage of DNA bases. *J. Chim. Phys. Phys.-Chim. Biol.* **1999**, *96* (1), 116-123. DOI: <https://doi.org/10.1051/jcp:1999118>.
823. Boz, H. p-Coumaric acid in cereals: Presence, antioxidant and antimicrobial effects. *Int. J. Food Sci. Technol.* **2015**, *50* (11), 2323-2328. DOI: <https://doi.org/10.1111/ijfs.12898>.
824. Liu, X.; Ji, D.; Cui, X.; Zhang, Z.; Li, B.; Xu, Y.; Chen, T.; Tian, S. p-Coumaric acid induces antioxidant capacity and defense responses of sweet cherry fruit to fungal pathogens. *Postharvest Biol. Technol.* **2020**, *169*. DOI: <https://doi.org/10.1016/j.postharvbio.2020.111297>.
825. Mozaffari Godarzi, S.; Valizade Gorji, A.; Gholizadeh, B.; Mard, S. A.; Mansouri, E. Antioxidant effect of p-coumaric acid on interleukin 1- β and tumor necrosis factor- α in rats with renal ischemic reperfusion. *Nefrologia* **2020**, *40* (3), 311-319. DOI: <https://doi.org/10.1016/j.nefro.2020.06.017>.
826. Stojković, D.; Petrović, J.; Soković, M.; Glamočlija, J.; Kukić-Marković, J.; Petrović, S. In situ antioxidant and antimicrobial activities of naturally occurring caffeic acid, p-coumaric acid and rutin, using food systems. *J. Sci. Food Agric.* **2013**, *93* (13), 3205-3208. DOI: <https://doi.org/10.1002/jsfa.6156>.
827. Zang, L. Y.; Cosma, G.; Gardner, H.; Shi, X.; Castranova, V.; Vallyathan, V. Effect of antioxidant protection by p-coumaric acid on low-density lipoprotein cholesterol oxidation. *Am. J. Physiol. - Cell Physiol.* **2000**, *279* (4 48-4), C954-C960. DOI: <https://doi.org/10.1152/ajpcell.2000.279.4.c954>.
828. Adefegha, S. A.; Oboh, G.; Ejakpovi, I. I.; Oyeleye, S. I. Antioxidant and antidiabetic effects of gallic and protocatechuic acids: a structure-function perspective. *Comp. Clin. Path.* **2015**, *24* (6), 1579-1585. DOI: <https://doi.org/10.1007/s00580-015-2119-7>.
829. El-Sonbaty, Y. A.; Suddek, G. M.; Megahed, N.; Gameil, N. M. Protocatechuic acid exhibits hepatoprotective, vasculoprotective, antioxidant and insulin-like effects in dexamethasone-induced insulin-resistant rats. *Biochimie* **2019**, *167*, 119-134. DOI: <https://doi.org/10.1016/j.biochi.2019.09.011>.
830. Graton, M. E.; Ferreira, B. H. S. H.; Troiano, J. A.; Potje, S. R.; Vale, G. T.; Nakamune, A. C. M. S.; Tirapelli, C. R.; Miller, F. J.; Ximenes, V. F.; Antoniali, C. Comparative study between apocynin and protocatechuic acid regarding antioxidant capacity and vascular effects. *Front. Physiol.* **2022**, *13*. DOI: <https://doi.org/10.3389/fphys.2022.1047916>.
831. Han, L.; Yang, Q.; Ma, W.; Li, J.; Qu, L.; Wang, M. Protocatechuic Acid Ameliorated Palmitic-Acid-Induced Oxidative Damage in Endothelial Cells through Activating Endogenous Antioxidant Enzymes via an Adenosine-Monophosphate-Activated-Protein-Kinase-Dependent Pathway. *J. Agric. Food Chem.* **2018**, *66* (40), 10400-10409. DOI: <https://doi.org/10.1021/acs.jafc.8b03414>.
832. Harini, R.; Pugalendi, K. V. Antioxidant and antihyperlipidaemic activity of protocatechuic acid on streptozotocind diabetic rats. *Redox Rep.* **2010**, *15* (2), 71-80. DOI: <https://doi.org/10.1179/174329210X12650506623285>.

833. Hyogo, A.; Kobayashi, T.; del Saz, E. G.; Seguchi, H. Antioxidant effects of protocatechuic acid, ferulic acid, and caffeic acid in human neutrophils using a fluorescent substance. *Int. J. Morphol* **2010**, 28 (3), 911-920. DOI: <https://doi.org/10.4067/S0717-95022010000300040>.
834. Jiang, S. Q.; Chen, Z. L.; Zhang, S.; Ye, J. L.; Wang, Y. B. Protective effects of protocatechuic acid on growth performance, intestinal barrier and antioxidant capacity in broilers challenged with lipopolysaccharide. *Animal* **2023**, 17 (1). DOI: <https://doi.org/10.1016/j.animal.2022.100693>.
835. Li, X.; Wang, X.; Chen, D.; Chen, S. Antioxidant activity and mechanism of protocatechuic acid in Vitro. *Cancer: Oxid. Stress Dietary Antioxid.* **2011**, 1 (7), 232-244. DOI: <https://doi.org/10.31989/ffhd.v1i7.127>.
836. Menezes, V. G.; Santos, J. M. S.; Macedo, T. J. S.; Lins, T. L. B. G.; Barberino, R. S.; Gouveia, B. B.; Bezerra, M. É. S.; Cavalcante, A. Y. P.; Queiroz, M. A. A.; Palheta, R. C.; Matos, M. H. T. Use of protocatechuic acid as the sole antioxidant in the base medium for in vitro culture of ovine isolated secondary follicles. *Reprod. Domest. Anim.* **2017**, 52 (5), 890-898. DOI: <https://doi.org/10.1111/rda.12995>.
837. Safaeian, L.; Emami, R.; Hajhashemi, V.; Haghghatian, Z. Antihypertensive and antioxidant effects of protocatechuic acid in deoxycorticosterone acetate-salt hypertensive rats. *Biomed. Pharmacother.* **2018**, 100, 147-155. DOI: <https://doi.org/10.1016/j.biopha.2018.01.107>.
838. Vari, R.; D'Archivio, M.; Filesi, C.; Carotenuto, S.; Scaccocchio, B.; Santangelo, C.; Giovannini, C.; Masella, R. Protocatechuic acid induces antioxidant/detoxifying enzyme expression through JNK-mediated Nrf2 activation in murine macrophages. *J. Nutr. Biochem.* **2011**, 22 (5), 409-417. DOI: <https://doi.org/10.1016/j.jnutbio.2010.03.008>.
839. Yang, L.; Chen, X.; Chen, D.; Yu, B.; He, J.; Luo, Y.; Zheng, P.; Chen, H.; Yan, H.; Huang, Z. Effects of protocatechuic acid on antioxidant capacity, mitochondrial biogenesis and skeletal muscle fiber transformation. *J. Nutr. Biochem.* **2023**, 116. DOI: <https://doi.org/10.1016/j.jnutbio.2023.109327>.
840. Zhang, S.; Gai, Z.; Gui, T.; Chen, J.; Chen, Q.; Li, Y. Antioxidant Effects of Protocatechuic Acid and Protocatechuic Aldehyde: Old Wine in a New Bottle. *Evid. Based Complement. Alternat. Med.* **2021**, 2021. DOI: <https://doi.org/10.1155/2021/6139308>.
841. Zhang, X.; Shi, G. F.; Liu, X. Z.; An, L. J.; Guan, S. Anti-ageing effects of protocatechuic acid from *Alpinia* on spleen and liver antioxidative system of senescent mice. *Cell Biochem. Funct.* **2011**, 29 (4), 342-347. DOI: <https://doi.org/10.1002/cbf.1757>.
842. Castañeda-Arriaga, R.; Marino, T.; Russo, N.; Alvarez-Idaboy, J. R.; Galano, A. Chalcogen effects on the primary antioxidant activity of chrysin and quercetin. *New J. Chem.* **2020**, 44 (21), 9073-9082. DOI: <https://doi.org/10.1039/d0nj01795g>.
843. Jamuna, S.; Karthika, K.; Paulsamy, S.; Thenmozhi, K.; Kathiravan, S.; Venkatesh, R. Confertin and scopoletin from leaf and root extracts of *Hypochaeris radicata* have anti-inflammatory and antioxidant activities. *Ind. Crops Prod.* **2015**, 70, 221-230. DOI: <https://doi.org/10.1016/j.indcrop.2015.03.039>.
844. Lee, H. I.; Lee, M. K. Effects of scopoletin supplementation on insulin resistance and antioxidant defense system in chronic alcohol-fed rats. *J. Korean Soc. Food Sci. Nutr.* **2015**, 44 (2), 173-181. DOI: <https://doi.org/10.3746/jkfn.2015.44.2.173>.
845. Malik, A.; Kushnoor, A.; Saini, V.; Singhal, S.; Kumar, S.; Yadav, Y. C. In vitro antioxidant properties of Scopoletin. *J. Chem. Pharm. Res.* **2011**, 3 (3), 659-665.
846. Mogana, R.; Teng-Jin, K.; Wiart, C. Anti-inflammatory, anticholinesterase, and antioxidant potential of scopoletin isolated from *Canarium patentinervium* Miq. (Burseraceae Kunth). *Evid. Based Complement. Alternat. Med.* **2013**, 2013. DOI: <https://doi.org/10.1155/2013/734824>.
847. Panda, S.; Kar, A. Evaluation of the antithyroid, antioxidative and antihyperglycemic activity of scopoletin from *Aegle marmelos* leaves in hyperthyroid rats. *Phytother. Res.* **2006**, 20 (12), 1103-1105. DOI: <https://doi.org/10.1002/ptr.2014>.
848. Shaw, C. Y.; Chen, C. H.; Hsu, C. C.; Chen, C. C.; Tsai, Y. C. Antioxidant properties of scopoletin isolated from *Sinomonium acutum*. *Phytother. Res.* **2003**, 17 (7), 823-825. DOI: <https://doi.org/10.1002/ptr.1170>.
849. Alawsy, T. T. J.; Al-Jumaili, E. F. Antioxidant activity of tannic acid purified from sumac seeds (*Rhus coriaria* L.): Its scavenging effect on free radical and active oxygen. *Plant Arch.* **2020**, 20, 2901-2906.

850. Daré, R. G.; Nakamura, C. V.; Ximenes, V. F.; Lautenschlager, S. O. S. Tannic acid, a promising anti-photoaging agent: Evidences of its antioxidant and anti-wrinkle potentials, and its ability to prevent photodamage and MMP-1 expression in L929 fibroblasts exposed to UVB. *Free Radic. Biol. Med.* **2020**, *160*, 342-355. DOI: <https://doi.org/10.1016/j.freeradbiomed.2020.08.019>.
851. Esmail, E. M.; Abo-Youssef, A. M.; Tohamy, M. A. Antidiabetic and antioxidant effects of tannic acid and melatonin on streptozotocin induced diabetes in rats. *Pak. J. Pharm. Sci.* **2019**, *32* (4), 1453-1459.
852. Gülçin, I.; Huyut, Z.; Elmastaş, M.; Aboul-Enein, H. Y. Radical scavenging and antioxidant activity of tannic acid. *Arab. J. Chem.* **2010**, *3* (1), 43-53. DOI: <https://doi.org/10.1016/j.arabjc.2009.12.008>.
853. Karakurt, S.; Adali, O. Tannic acid inhibits proliferation, migration, invasion of prostate cancer and modulates drug metabolizing and antioxidant enzymes. *Anticancer Agents Med. Chem.* **2016**, *16* (6), 781-789. DOI: <https://doi.org/10.2174/187152061666615111115809>.
854. Lou, W.; Chen, Y.; Ma, H.; Liang, G.; Liu, B. Antioxidant and α -amylase inhibitory activities of tannic acid. *J. Food Sci. Technol.* **2018**, *55* (9), 3640-3646. DOI: <https://doi.org/10.1007/s13197-018-3292-x>.
855. Türkan, F.; Taslimi, P.; Saltan, F. Z. Tannic acid as a natural antioxidant compound: Discovery of a potent metabolic enzyme inhibitor for a new therapeutic approach in diabetes and Alzheimer's disease. *J. Biochem. Mol. Toxicol.* **2019**, *33* (8). DOI: <https://doi.org/10.1002/jbt.22340>.
856. Wang, M.; Huang, H.; Liu, S.; Zhuang, Y.; Yang, H.; Li, Y.; Chen, S.; Wang, L.; Yin, L.; Yao, Y.; He, S. Tannic acid modulates intestinal barrier functions associated with intestinal morphology, antioxidative activity, and intestinal tight junction in a diquat-induced mouse model. *RSC Adv.* **2019**, *9* (55), 31988-31998. DOI: <https://doi.org/10.1039/c9ra04943f>.
857. Wang, M.; Huang, H.; Wang, L.; Yin, L.; Yang, H.; Chen, C.; Zheng, Q.; He, S. Tannic acid attenuates intestinal oxidative damage by improving antioxidant capacity and intestinal barrier in weaned piglets and IPEC-J2 cells. *Front. Vet. Sci.* **2022**, *9*. DOI: <https://doi.org/10.3389/fvets.2022.1012207>.
858. Xi, Y.; Chen, J.; Guo, S.; Wang, S.; Liu, Z.; Zheng, L.; Qi, Y.; Xu, P.; Li, L.; Zhang, Z.; Ding, B. Effects of tannic acid on growth performance, relative organ weight, antioxidative status, and intestinal histomorphology in broilers exposed to aflatoxin B1. *Funct. Food Hum. Health* **2022**, *9*. DOI: <https://doi.org/10.3389/fvets.2022.1037046>.
859. Yu, M.; Sun, X.; Dai, X.; Gu, C.; Gu, M.; Wang, A.; Wei, W.; Yang, S. Effects of Tannic Acid on Antioxidant Activity and Ovarian Development in Adolescent and Adult Female Brandt's Voles. *Reprod. Sci.* **2021**, *28* (10), 2839-2846. DOI: <https://doi.org/10.1007/s43032-021-00578-3>.
860. Azam, S.; Hadi, N.; Khan, N. U.; Hadi, S. M. Antioxidant and prooxidant properties of caffeine, theobromine and xanthine. *Med. Sci. Monit.* **2003**, *9* (9), BR325-BR330.
861. Wu, F.; Liu, R.; Shen, X.; Xu, H.; Sheng, L. Study on the interaction and antioxidant activity of theophylline and theobromine with SOD by spectra and calculation. *Spectrochim. Acta - Part A: Mol. Biomol. Spectrosc.* **2019**, *215*, 354-362. DOI: <https://doi.org/10.1016/j.saa.2019.03.001>.
862. Ekin, S.; Yildirim, S.; Akkoyun, M. B.; Gok, H. N.; Arihan, O.; Oto, G.; Akkoyun, T.; Basbugan, Y.; Aslan, S. Theophylline attenuates bleomycin-induced oxidative stress in rats: The role of IL-6, NF- κ B, and antioxidant enzymes. *Braz. J. Pharm. Sci.* **2022**, *58*. DOI: <https://doi.org/10.1590/s2175-97902022e20827>.
863. Santos, P. M. P.; Silva, S. A. G.; Justino, G. C.; Vieira, A. J. S. C. Demethylation of theophylline (1,3-dimethylxanthine) to 1-methylxanthine: The first step of an antioxidising cascade. *Redox Rep.* **2010**, *15* (3), 138-144. DOI: <https://doi.org/10.1179/174329210X12650506623726>.
864. Kumar, S.; Prahalathan, P.; Raja, B. Antihypertensive and antioxidant potential of vanillic acid, a phenolic compound in L-NAME-induced hypertensive rats: A dose-dependence study. *Redox Rep.* **2011**, *16* (5), 208-215. DOI: <https://doi.org/10.1179/1351000211Y.0000000009>.
865. Salau, V. F.; Erukainure, O. L.; Ibeji, C. U.; Olasehinde, T. A.; Koorbanally, N. A.; Islam, M. S. Vanillin and vanillic acid modulate antioxidant defense system via amelioration of metabolic complications linked to Fe²⁺-induced brain tissues damage. *Metab. Brain Dis.* **2020**, *35* (5), 727-738. DOI: <https://doi.org/10.1007/s11011-020-00545-y>.

866. Shabani, M.; Jamali, Z.; Bayrami, D.; Salimi, A. Vanillic acid alleviates methamphetamine-induced mitochondrial toxicity in cardiac mitochondria via antioxidant activity and inhibition of MPT Pore opening: an in-vitro study. *BMC Pharmacol. Toxicol.* **2023**, 24 (1). DOI: <https://doi.org/10.1186/s40360-023-00676-9>.
867. Stanely Mainzen Prince, P.; Rajakumar, S.; Dhanasekar, K. Protective effects of vanillic acid on electrocardiogram, lipid peroxidation, antioxidants, proinflammatory markers and histopathology in isoproterenol induced cardiotoxic rats. *Eur. J. Pharmacol.* **2011**, 668 (1-2), 233-240. DOI: <https://doi.org/10.1016/j.ejphar.2011.06.053>.
868. Vinothiya, K.; Ashokkumar, N. Modulatory effect of vanillic acid on antioxidant status in high fat diet-induced changes in diabetic hypertensive rats. *Biomed. Pharmacother.* **2017**, 87, 640-652. DOI: <https://doi.org/10.1016/j.biopha.2016.12.134>.
869. Gonzalez-Baro, A. C.; Izquierdo, D.; Heras, A.; Colina, A. UV/Vis spectroelectrochemistry of o-vanillin: Study of the antioxidant properties. *J. Electroanal. Chem.* **2020**, 859. DOI: <https://doi.org/10.1016/j.jelechem.2020.113844>.
870. Kamat, J. P.; Ghosh, A.; Devasagayam, T. P. A. Vanillin as an antioxidant in rat liver mitochondria: Inhibition of protein oxidation and lipid peroxidation induced by photosensitization. *Mol. Cell. Biochem.* **2000**, 209 (1-2), 47-53. DOI: <https://doi.org/10.1023/a:1007048313556>.
871. Tai, A.; Sawano, T.; Yazama, F.; Ito, H. Evaluation of antioxidant activity of vanillin by using multiple antioxidant assays. *Biochim. Biophys. Acta - Gen. Subj.* **2011**, 1810 (2), 170-177. DOI: <https://doi.org/10.1016/j.bbagen.2010.11.004>.
872. Widowati, W.; Fauziah, N.; Herdiman, H.; Afni, M.; Afifah, E.; Kusuma, H. S. W.; Nufus, H.; Arumwardana, S.; Rihibiha, D. D. Antioxidant and anti aging assays of *Oryza sativa* extracts, vanillin and coumaric acid. *J. Nat. Remedies* **2016**, 16 (3), 88-99. DOI: <https://doi.org/10.18311/jnr/2016/7220>.
873. Xiong, S.; Li, R.; Ye, S.; Ni, P.; Shan, J.; Yuan, T.; Liang, J.; Fan, Y.; Zhang, X. Vanillin enhances the antibacterial and antioxidant properties of polyvinyl alcohol-chitosan hydrogel dressings. *Int. J. Biol. Macromol.* **2022**, 220, 109-116. DOI: <https://doi.org/10.1016/j.ijbiomac.2022.08.052>.
874. Tai, A.; Sawano, T.; Yazama, F. Antioxidant properties of ethyl vanillin in vitro and in vivo. *Biosci. Biotechnol. Biochem.* **2011**, 75 (12), 2346-2350. DOI: <https://doi.org/10.1271/bbb.110524>.
875. Zieniuk, B.; Groborz, K.; Wołoszynowska, M.; Ratusz, K.; Białecka-florjańczyk, E.; Fabiszewska, A. Enzymatic synthesis of lipophilic esters of phenolic compounds, evaluation of their antioxidant activity and effect on the oxidative stability of selected oils. *Biomolecules* **2021**, 11 (2), 1-12. DOI: <https://doi.org/10.3390/biom11020314>.
876. Bielski, B. H. J.; Arudi, R. L.; Sutherland, M. W. A study of the reactivity of HO₂/O₂ - with unsaturated fatty acids. *J. Biol. Chem.* **1983**, 258 (8), 4759-4761.
877. 8Terpinc, P.; Abramovič, H. A kinetic approach for evaluation of the antioxidant activity of selected phenolic acids. *Food Chem.* **2010**, 121 (2), 366-371. DOI: <https://doi.org/10.1016/j.foodchem.2009.12.037>.
878. Sies, H. Oxidative stress: Oxidants and antioxidants. **1997**, 82 (2), 291-295. DOI: <https://doi.org/10.1113/expphysiol.1997.sp004024>.
879. Masuda, T.; Yamada, K.; Maekawa, T.; Takeda, Y.; Yamaguchi, H. Antioxidant mechanism studies on ferulic acid: Identification of oxidative coupling products from methyl ferulate and linoleate. *J. Agric. Food Chem.* **2006**, 54 (16), 6069-6074. DOI: <https://doi.org/10.1021/jf060676z>.
880. Masuda, T.; Yamada, K.; Maekawa, T.; Takeda, Y.; Yamaguchi, H. Antioxidant mechanism studies on ferulic acid: Isolation and structure identification of the main antioxidation product from methyl ferulate. *Food Sci. Technol. Res.* **2006**, 12 (3), 173-177. DOI: <https://doi.org/10.3136/fstr.12.173>.
881. Miche, H.; Brumas, V.; Berthon, G. Copper(II) interactions with nonsteroidal antiinflammatory agents. II. Anthranilic acid as a potential OH-inactivating ligand. *J. Inorg. Biochem.* **1997**, 68 (1), 27-38. DOI: [https://doi.org/10.1016/S0162-0134\(97\)00005-6](https://doi.org/10.1016/S0162-0134(97)00005-6).
882. Gaubert, S.; Bouchaut, M.; Brumas, V.; Berthon, G. Copper-ligand interactions and physiological free radical processes. Part 3. Influence of histidine, salicylic acid and anthranilic acid on copper-driven Fenton

- chemistry in vitro. *Free Radic. Res.* **2000**, 32 (5), 451-461. DOI: <https://doi.org/10.1080/10715760000300451>.
883. Steenken, S.; Jovanovic, S. V. How easily oxidizable is DNA? One-electron reduction potentials of adenosine and guanosine radicals in aqueous solution. *J. Am. Chem. Soc.* **1997**, 119 (3), 617-618. DOI: <https://doi.org/10.1021/ja962255b>.
884. Galano, A.; Alvarez-Idaboy, J. R. On the evolution of one-electron-oxidized deoxyguanosine in damaged DNA under physiological conditions: A DFT and ONIOM study on proton transfer and equilibrium. *Phys. Chem. Chem. Phys.* **2012**, 14 (36), 12476-12484. DOI: <https://doi.org/10.1039/c2cp40799j>.
885. Tronche, C.; Goodman, B. K.; Greenberg, M. M. DNA damage induced via independent generation of the radical resulting from formal hydrogen atom abstraction from the C1'-position of a nucleotide. *Chem. Biol.* **1998**, 5 (5), 263-271. DOI: [https://doi.org/10.16/S1074-5521\(98\)90619-6](https://doi.org/10.16/S1074-5521(98)90619-6).
886. Pogozelski, W. K.; Tullius, T. D. Oxidative Strand Scission of Nucleic Acids: Routes Initiated by Hydrogen Abstraction from the Sugar Moiety. *Chem. Rev.* **1998**, 98 (3), 1089-1108. DOI: <https://doi.org/10.1021/cr960437j>.
887. Dedon, P. C. The Chemical Toxicology of 2-Deoxyribose Oxidation in DNA. *Chem. Res. Toxicol.* **2007**, 21 (1), 206-219. DOI: <https://doi.org/10.1021/tx700283c>.
888. Yu, Y.; Cui, Y.; Niedernhofer, L. J.; Wang, Y. Occurrence, Biological Consequences, and Human Health Relevance of Oxidative Stress-Induced DNA Damage. *Chem. Res. Toxicol.* **2016**, 29 (12), 2008-2039. DOI: <https://doi.org/10.1021/acs.chemrestox.6b00265>.
889. Pérez-González, A.; Castañeda-Arriaga, R.; Álvarez-Idaboy, J. R.; Reiter, R. J.; Galano, A. Melatonin and its metabolites as chemical agents capable of directly repairing oxidized DNA. *J. Pineal Res.* **2019**, 66 (2). DOI: <https://doi.org/10.1111/jpi.12539>.
890. Galano, A.; Francisco-Marquez, M. Reactions of OOH radical with β -carotene, lycopene, and toluene: Hydrogen atom transfer and adduct formation mechanisms. *J. Phys. Chem. B* **2009**, 113 (32), 11338-11345. DOI: <https://doi.org/10.1021/jp904061q>.
891. Mortensen, A. Scavenging of benzylperoxyl radicals by carotenoids. *Free Radic. Res.* **2002**, 36 (2), 211-216. DOI: <https://doi.org/10.1080/10715760290006501>.
892. Liebler, D. C.; McClure, T. D. Antioxidant reactions of β -carotene: Identification of carotenoid-radical adducts. *Chem. Res. Toxicol.* **1996**, 9 (1), 8-11. DOI: <https://doi.org/10.1021/tx950151t>.
893. Joshi, R.; Gangabhagirathi, R.; Venu, S.; Adhikari, S.; Mukherjee, T. Antioxidant activity and free radical scavenging reactions of gentisic acid: In-vitro and pulse radiolysis studies. *Free Radic. Res.* **2012**, 46 (1), 11-20. DOI: <https://doi.org/10.3109/10715762.2011.633518>.
894. Dhiman, S. B.; Kamat, J. P.; Naik, D. B. Antioxidant activity and free radical scavenging reactions of hydroxybenzyl alcohols. Biochemical and pulse radiolysis studies. *Chem. Biol. Interact.* **2009**, 182 (2-3), 119-127. DOI: <https://doi.org/10.1016/j.cbi.2009.07.025>.
895. Hata, K.; Lin, M.; Katsumura, Y.; Muroya, Y.; Fu, H.; Yamashita, S.; Nakagawa, H. Pulse radiolysis study on free radical scavenger edaravone(3-methyl-1-phenyl-2-pyrazolin-5-one).2: A comparative study on edaravone derivatives. *J. Radiat. Res.* **2011**, 52 (1), 15-23. DOI: <https://doi.org/10.1269/jrr.10060>.
896. Pérez-González, A.; Galano, A. OH radical scavenging activity of edaravone: Mechanism and kinetics. *J. Phys. Chem. B* **2011**, 115 (5), 1306-1314. DOI: <https://doi.org/10.1021/jp110400t>.
897. Galano, A. On the direct scavenging activity of melatonin towards hydroxyl and a series of peroxy radicals. *Phys. Chem. Chem. Phys.* **2011**, 13 (15), 7178-7188. DOI: <https://doi.org/10.1039/c0cp02801k>.
898. Galano, A.; Tan, D. X.; Reiter, R. J. On the free radical scavenging activities of melatonin's metabolites, AFMK and AMK. *J. Pineal Res.* **2013**, 54 (3), 245-257. DOI: <https://doi.org/10.1111/jpi.12010>.
899. Galano, A.; Tan, D. X.; Reiter, R. J. Cyclic 3-hydroxymelatonin, a key metabolite enhancing the peroxy radical scavenging activity of melatonin. *RSC Adv.* **2014**, 4 (10), 5220-5227. DOI: <https://doi.org/10.1039/C3RA44604B>.

900. Tamba, M.; Torreggiani, A. Hydroxyl radical scavenging by carnosine and Cu(II)-carnosine complexes: A pulse-radiolysis and spectroscopic study. *Int. J. Radiat. Biol.* **1999**, *75* (9), 1177-1188. DOI: <https://doi.org/10.1080/095530099139656>.
901. Sakurai, K.; Sasabe, H.; Koga, T.; Konishi, T. Mechanism of hydroxyl radical scavenging by rebamipide: Identification of mono-hydroxylated rebamipide as a major reaction product. *Free Radic. Res.* **2004**, *38* (5), 487-494. DOI: <https://doi.org/10.1080/1071576042000209808>.
902. Barzegar, A. The role of electron-transfer and H-atom donation on the superb antioxidant activity and free radical reaction of curcumin. *Food Chem.* **2012**, *135* (3), 1369-1376. DOI: <https://doi.org/10.1016/j.foodchem.2012.05.070>.
903. Touriño, S.; Lizárraga, D.; Carreras, A.; Lorenzo, S.; Ugartondo, V.; Mitjans, M.; Vinardell, M. P.; Juliá, L.; Cascante, M.; Torres, J. L. Highly galloylated tannin fractions from witch hazel (*Hamamelis virginiana*) bark: Electron transfer capacity, in vitro antioxidant activity, and effects on skin-related cells. *Chem. Res. Toxicol.* **2008**, *21* (3), 696-704. DOI: <https://doi.org/10.1021/tx700425n>.
904. Pérez-González, A.; Galano, A. On the outstanding antioxidant capacity of edaravone derivatives through single electron transfer reactions. *J. Phys. Chem. B* **2012**, *116* (3), 1180-1188. DOI: <https://doi.org/10.1021/jp209930y>.
905. Nakanishi, I.; Shimada, T.; Ohkubo, K.; Manda, S.; Shimizu, T.; Urano, S.; Okuda, H.; Miyata, N.; Ozawa, T.; Anzai, K.; et al. Involvement of electron transfer in the radical-scavenging reaction of resveratrol. *Chem. Lett.* **2007**, *36* (10), 1276-1277. DOI: <https://doi.org/10.1246/cl.2007.1276>.
906. Nakanishi, I.; Ohkubo, K.; Miyazaki, K.; Hakamata, W.; Urano, S.; Ozawa, T.; Okuda, H.; Fukuzumi, S.; Ikota, N.; Fukuhara, K. A Planar Catechin Analogue Having a More Negative Oxidation Potential than (+)-Catechin as an Electron Transfer Antioxidant against a Peroxyl Radical. *Chem. Res. Toxicol.* **2004**, *17* (1), 26-31. DOI: <https://doi.org/10.1021/tx034134c>.
907. Hill, T. J.; Land, E. J.; McGarvey, D. J.; Schalch, W.; Tinkler, J. H.; Truscott, T. G. Interactions between carotenoids and the CCl₃O₂ • radical. *J. Am. Chem. Soc.* **1995**, *117* (32), 8322-8326. DOI: <https://doi.org/10.1021/ja00137a004>.
908. Packer, J. E.; Mahood, J. S.; Mora-Arellano, V. O.; Slater, T. F.; Willson, R. L.; Wolfenden, B. S. Free radicals and singlet oxygen scavengers: Reaction of a peroxy-radical with β-carotene, diphenyl furan and 1,4-diazobicyclo(2,2,2)-octane. *Biochem. Biophys. Res. Commun.* **1981**, *98* (4), 901-906. DOI: [https://doi.org/10.1016/0006-291x\(81\)91196-7](https://doi.org/10.1016/0006-291x(81)91196-7).
909. Mortensen, A.; Skibsted, L. H.; Sampson, J.; Rice-Evans, C.; Everett, S. A. Comparative mechanisms and rates of free radical scavenging by carotenoid antioxidants. *FEBS Lett.* **1997**, *418* (1-2), 91-97. DOI: [https://doi.org/10.1016/s0014-5793\(97\)01355-0](https://doi.org/10.1016/s0014-5793(97)01355-0).
910. Everett, S. A.; Kundu, S. C.; Maddix, S.; Willson, R. L. Mechanisms of free-radical scavenging by the nutritional antioxidant β-carotene. *Biochem. Soc. Trans.* **1995**, *23* (2), 230S. DOI: <https://doi.org/10.1042/bst023230s>.
911. Cao, L.; Yu, H.; Shao, S.; Wang, S.; Guo, Y. Evaluating the antioxidant capacity of polyphenols with an off-on fluorescence probe and the mechanism study. *Anal. Methods* **2014**, *6* (18), 7149-7153. DOI: <https://doi.org/10.1039/C4AY01276C>.
912. Mikulski, D.; Eder, K.; Molski, M. Quantum-chemical study on relationship between structure and antioxidant properties of hepatoprotective compounds occurring in *Cynara scolymus* and *Silybum marianum*. *J. Theor. Comput. Chem.* **2014**, *13* (1). DOI: <https://doi.org/10.1142/S0219633614500047>.
913. Mendoza-Wilson, A. M.; Castro-Arredondo, S. I.; Balandrán-Quintana, R. R. Computational study of the structure-free radical scavenging relationship of procyanidins. *Food Chem.* **2014**, *161*, 155-161. DOI: <https://doi.org/10.1016/j.foodchem.2014.03.111>.
914. Wang, G.; Xue, Y.; An, L.; Zheng, Y.; Dou, Y.; Zhang, L.; Liu, Y. Theoretical study on the structural and antioxidant properties of some recently synthesised 2,4,5-trimethoxy chalcones. *Food Chem.* **2014**, *171*, 89-97. DOI: <https://doi.org/10.1016/j.foodchem.2014.08.106>.

915. Praveena, R.; Sadasivam, K.; Deepa, V.; Sivakumar, R. Antioxidant potential of orientin: A combined experimental and DFT approach. *J. Mol. Struct.* **2014**, *1061* (1), 114-123. DOI: <https://doi.org/10.1016/j.molstruc.2014.01.002>.
916. Galano, A.; Martínez, A. Capsaicin, a tasty free radical scavenger: Mechanism of action and kinetics. *J. Phys. Chem. B* **2012**, *116* (3), 1200-1208. DOI: <https://doi.org/10.1021/jp211172f>.
917. Martínez, A.; Galano, A.; Vargas, R. Free radical scavenger properties of α -mangostin: Thermodynamics and kinetics of HAT and RAF mechanisms. *J. Phys. Chem. B* **2011**, *115* (43), 12591-12598. DOI: <https://doi.org/10.1021/jp205496u>.
918. Dimitrić Marković, J. M.; Milenković, D.; Amić, D.; Mojović, M.; Pašti, I.; Marković, Z. S. The preferred radical scavenging mechanisms of fisetin and baicalein towards oxygen-centred radicals in polar protic and polar aprotic solvents. *RSC Adv.* **2014**, *4* (61), 32228-32236. DOI: <https://doi.org/10.1039/C4RA02577F>.
919. Xue, Y.; Zheng, Y.; An, L.; Zhang, L.; Qian, Y.; Yu, D.; Gong, X.; Liu, Y. A theoretical study of the structure-radical scavenging activity of hydroxychalcones. *Comput. Theor. Chem.* **2012**, *982*, 74-83. DOI: <https://doi.org/10.1016/j.comptc.2011.12.020>.
920. Mazzone, G.; Toscano, M.; Russo, N. Density functional predictions of antioxidant activity and UV spectral features of nasutin A, isonasutin, ellagic acid, and one of its possible derivatives. *J. Agric. Food Chem.* **2013**, *61* (40), 9650-9657. DOI: <https://doi.org/10.1021/jf403262k>.
921. Castañeda-Arriaga, R.; Alvarez-Idaboy, J. R. Lipoic acid and dihydrolipoic acid. A comprehensive theoretical study of their antioxidant activity supported by available experimental kinetic data. *J. Chem. Inf. Model.* **2014**, *54* (6), 1642-1652. DOI: <https://doi.org/10.1021/ci500213p>.
922. Galano, A.; Alvarez-Idaboy, J. R. Glutathione: Mechanism and kinetics of its non-enzymatic defense action against free radicals. *RSC Adv.* **2011**, *1* (9), 1763-1771. DOI: <https://doi.org/10.1039/C1RA00474C>.
923. Farmanzadeh, D.; Najafi, M. On the antioxidant activity of the tryptophan derivatives. *Bull. Chem. Soc. Jpn.* **2013**, *86* (9), 1041-1050. DOI: <https://doi.org/10.1246/bcsj.20130035>.
924. Galano, A. Mechanism and kinetics of the hydroxyl and hydroperoxyl radical scavenging activity of N-acetylcysteine amide. *Theor. Chem. Acc.* **2011**, *130* (1), 51-60. DOI: <https://doi.org/10.1007/s00214-011-0958-0>.
925. Litwinienko, G.; Ingold, K. U. Abnormal solvent effects on hydrogen atom abstraction. 2. Resolution of the curcumin antioxidant controversy. The role of sequential proton loss electron transfer. *J. Org. Chem.* **2004**, *69* (18), 5888-5896. DOI: <https://doi.org/10.1021/jo049254j>.
926. Galano, A.; Álvarez-Diduk, R.; Ramírez-Silva, M. T.; Alarcón-Ángeles, G.; Rojas-Hernández, A. Role of the reacting free radicals on the antioxidant mechanism of curcumin. *Chem. Phys.* **2009**, *363* (1-3), 13-23. DOI: <https://doi.org/10.1016/j.chemphys.2009.07.003>.
927. Medina, M. E.; Galano, A.; Alvarez-Idaboy, J. R. Theoretical study on the peroxy radicals scavenging activity of esculetin and its regeneration in aqueous solution. *Phys. Chem. Chem. Phys.* **2014**, *16* (3), 1197-1207. DOI: <https://doi.org/10.1039/c3cp53889c>.
928. Jeremić, S.; Filipović, N.; Peulić, A.; Marković, Z. Thermodynamical aspect of radical scavenging activity of alizarin and alizarin red S. Theoretical comparative study. *Comput. Theor. Chem.* **2014**, *1047*, 15-21. DOI: <https://doi.org/10.1016/j.comptc.2014.08.007>.
929. Xue, Y.; Zheng, Y.; An, L.; Dou, Y.; Liu, Y. Density functional theory study of the structure-antioxidant activity of polyphenolic deoxybenzoins. *Food Chem.* **2014**, *151*, 198-206. DOI: <https://doi.org/10.1016/j.foodchem.2013.11.064>.
930. Marković, Z.; Crossed D Signorović, J.; Dimitrić Marković, J. M.; Živić, M.; Amić, D. Investigation of the radical scavenging potency of hydroxybenzoic acids and their carboxylate anions. *Monatsh. Chem.* **2014**, *145* (6), 953-962. DOI: <https://doi.org/10.1007/s00706-014-1163-3>.
931. Pérez-González, A.; Galano, A.; Alvarez-Idaboy, J. R. Dihydroxybenzoic acids as free radical scavengers: Mechanisms, kinetics, and trends in activity. *New J. Chem.* **2014**, *38* (6), 2639-2652. DOI: <https://doi.org/10.1039/C4NJ00071D>.

932. Urbaniak, A.; Szelag, M.; Molski, M. Theoretical investigation of stereochemistry and solvent influence on antioxidant activity of ferulic acid. *Comput. Theor. Chem.* **2013**, *1012*, 33-40. DOI: <https://doi.org/10.1016/j.comptc.2013.02.018>.
933. Fifen, J. J.; Nsangou, M.; Dhaouadi, Z.; Motapon, O.; Jaidane, N. Solvent effects on the antioxidant activity of 3,4-dihydroxyphenylpyruvic acid: DFT and TD-DFT studies. *Comput. Theor. Chem.* **2011**, *966* (1-3), 232-243. DOI: <https://doi.org/10.1016/j.comptc.2011.03.006>.
934. Iuga, C.; Alvarez-Idaboy, J. R.; Russo, N. Antioxidant activity of trans -resveratrol toward hydroxyl and hydroperoxyl radicals: A quantum chemical and computational kinetics study. *J. Org. Chem.* **2012**, *77* (8), 3868-3877. DOI: <https://doi.org/10.1021/jo3002134>.
935. Benayahoum, A.; Amira-Guebailia, H.; Houache, O. Homolytic and heterolytic O-H bond cleavage in trans-resveratrol and some phenanthrene analogs: A theoretical study. *Comput. Theor. Chem.* **2014**, *1037*, 1-9. DOI: <https://doi.org/10.1016/j.comptc.2014.03.016>.
936. Medina, M. E.; Iuga, C.; Álvarez-Idaboy, J. R. Antioxidant activity of fraxetin and its regeneration in aqueous media. A density functional theory study. *RSC Adv.* **2014**, *4* (95), 52920-52932. DOI: <https://doi.org/10.1039/C4RA08394F>.
937. Cordova-Gomez, M.; Galano, A.; Alvarez-Idaboy, J. R. Piceatannol, a better peroxy radical scavenger than resveratrol. *RSC Adv.* **2013**, *3* (43), 20209-20218. DOI: <https://doi.org/10.1039/C3RA42923G>.
938. Marković, Z.; Milenković, D.; Orović, J.; Dimitrić Marković, J. M.; Stepanić, V.; Lučić, B.; Amić, D. Free radical scavenging activity of morin 2'-O- phenoxide anion. *Food Chem.* **2012**, *135* (3), 2070-2077. DOI: <https://doi.org/10.1016/j.foodchem.2012.05.119>.
939. Xue, Y.; Zhang, L.; Li, Y.; Yu, D.; Zheng, Y.; An, L.; Gong, X.; Liu, Y. A DFT study on the structure and radical scavenging activity of newly synthesized hydroxychalcones. *J. Phys. Org. Chem.* **2013**, *26* (3), 240-248. DOI: <https://doi.org/10.1002/poc.3074>.
940. Xue, Y.; Zheng, Y.; Zhang, L.; Wu, W.; Yu, D.; Liu, Y. Theoretical study on the antioxidant properties of 2'- hydroxychalcones: H-atom vs. electron transfer mechanism. *J. Mol. Model.* **2013**, *19* (9), 3851-3862. DOI: <https://doi.org/10.1007/s00894-013-1921-x>.
941. Qian, Y. P.; Shang, Y. J.; Teng, Q. F.; Chang, J.; Fan, G. J.; Wei, X.; Li, R. R.; Li, H. P.; Yao, X. J.; Dai, F.; Zhou, B. Hydroxychalcones as potent antioxidants: Structure-activity relationship analysis and mechanism considerations. *Food Chem.* **2011**, *126* (1), 241-248. DOI: <https://doi.org/10.1016/j.foodchem.2010.11.011>.
942. Martínez, A.; Hernández-Marin, E.; Galano, A. Xanthones as antioxidants: A theoretical study on the thermodynamics and kinetics of the single electron transfer mechanism. *Food Funct.* **2012**, *3* (4), 442-450. DOI: <https://doi.org/10.1039/C2FO10229C>.
943. Musialik, M.; Kuzmich, R.; Pawlowski, T. S.; Litwinienko, G. Acidity of hydroxyl groups: An overlooked influence on antiradical properties of flavonoids. *J. Org. Chem.* **2009**, *74* (7), 2699-2709. DOI: <https://doi.org/10.1021/jo802716v>.
944. Di Meo, F.; Lemaure, V.; Cornil, J.; Lazzaroni, R.; Duroux, J. L.; Olivier, Y.; Trouillas, P. Free radical scavenging by natural polyphenols: Atom versus electron transfer. *J. Phys. Chem. A* **2013**, *117* (10), 2082-2092. DOI: <https://doi.org/10.1021/jp3116319>.
945. Dimitrić Marković, J. M.; Milenković, D.; Amić, D.; Popović-Bijelić, A.; Mojović, M.; Pašti, I. A.; Marković, Z. S. Energy requirements of the reactions of kaempferol and selected radical species in different media: towards the prediction of the possible radical scavenging mechanisms. *Struct. Chem.* **2014**, *25*, 1795-1804. DOI: <https://doi.org/10.1007/s11224-014-0453-z>.
946. Dorović, J.; Marković, J. M. D.; Stepanić, V.; Begović, N.; Amić, D.; Marković, Z. Influence of different free radicals on scavenging potency of gallic acid. *J. Mol. Model.* **2014**, *20* (7), 2345. DOI: <https://doi.org/10.1007/s00894-014-2345-y>.
947. Alberto, M. E.; Russo, N.; Grand, A.; Galano, A. A physicochemical examination of the free radical scavenging activity of Trolox: Mechanism, kinetics and influence of the environment. *Phys. Chem. Chem. Phys.* **2013**, *15* (13), 4642-4650. DOI: <https://doi.org/10.1039/c3cp43319f>.

948. Lengyel, J.; Rimarčík, J.; Vagánek, A.; Klein, E. On the radical scavenging activity of isoflavones: Thermodynamics of O-H bond cleavage. *Phys. Chem. Chem. Phys.* **2013**, *15* (26), 10895-10903. DOI: <https://doi.org/10.1039/c3cp00095h>.
949. Senthil kumar, K.; Kumaresan, R. A DFT study on the structural, electronic properties and radical scavenging mechanisms of calycosin, glycitein, pratensein and prunetin. *Comput. Theor. Chem.* **2012**, *985*, 14-22. DOI: <https://doi.org/10.1016/j.comptc.2012.01.028>.
950. Marković, Z. S.; Dimitrić Marković, J. M.; Milenković, D.; Filipović, N. Mechanistic study of the structure-activity relationship for the free radical scavenging activity of baicalein. *J. Mol. Model.* **2011**, *17* (10), 2575-2584. DOI: <https://doi.org/10.1007/s00894-010-0942-y>.
951. Jeremić, S. R.; Šehović, S. F.; Manojlović, N. T.; Marković, Z. S. Antioxidant and free radical scavenging activity of purpurin. *Monatsh. Chem.* **2012**, *143* (3), 427-435. DOI: <https://doi.org/10.1007/s00706-011-0695-z>.
952. Marković, Z. S.; Marković, S.; Dimitrić Marković, J. M.; Milenković, D. Structure and reactivity of baicalein radical cation. *Int. J. Quantum Chem.* **2012**, *112* (8), 2009-2017. DOI: <https://doi.org/10.1002/qua.23175>.
953. Focsan, A. L.; Pan, S.; Kispert, L. D. Electrochemical study of astaxanthin and astaxanthin n-octanoic monoester and diester: Tendency to form radicals. *J. Phys. Chem. B* **2014**, *118* (9), 2331-2339. DOI: <https://doi.org/10.1021/jp4121436>.
954. Marković, Z.; Amić, D.; Milenković, D.; Dimitrić-Marković, J. M.; Marković, S. Examination of the chemical behavior of the quercetin radical cation towards some bases. *Phys. Chem. Chem. Phys.* **2013**, *15* (19), 7370-7378. DOI: <https://doi.org/10.1039/C3CP44605K>.
955. Nakanishi, I.; Kawashima, T.; Ohkubo, K.; Kanazawa, H.; Inami, K.; Mochizuki, M.; Fukuhara, K.; Okuda, H.; Ozawa, T.; Itoh, S.; et al. Electron-transfer mechanism in radical-scavenging reactions by a vitamin E model in a protic medium. *Org. Biomol. Chem.* **2005**, *3* (4), 626-629. DOI: <https://doi.org/10.1039/b416572a>.
956. Ouchi, A.; Nagaoka, S. I.; Abe, K.; Mukai, K. Kinetic study of the aroxyl radical-scavenging reaction of α -tocopherol in methanol solution: Notable effect of the alkali and alkaline earth metal salts on the reaction rates. *J. Phys. Chem. B* **2009**, *113* (40), 13322-13331. DOI: <https://doi.org/10.1021/jp906425r>.
957. Galano, A.; Francisco Marquez, M.; Pérez-González, A. Ellagic acid: An unusually versatile protector against oxidative stress. *Chem. Res. Toxicol.* **2014**, *27* (5), 904-918. DOI: <https://doi.org/10.1021/tx500065y>.
958. Medina, M. E.; Iuga, C.; Alvarez-Idaboy, J. R. Antioxidant activity of propyl gallate in aqueous and lipid media: A theoretical study. *Phys. Chem. Chem. Phys.* **2013**, *15* (31), 13137-13146. DOI: <https://doi.org/10.1039/C3CP51644J>.
959. Amorati, R.; Pedulli, G. F.; Cabrini, L.; Zamboni, L.; Landi, L. Solvent and pH effects on the antioxidant activity of caffeic and other phenolic acids. *J. Agric. Food Chem.* **2006**, *54* (8), 2932-2937. DOI: <https://doi.org/10.1021/jf053159+>.
960. Marino, T.; Galano, A.; Russo, N. Radical Scavenging Ability of Gallic Acid toward OH and OOH Radicals. Reaction Mechanism and Rate Constants from the Density Functional Theory. *J. Phys. Chem. B* **2014**, *118* (35), 10380-10389. DOI: <https://doi.org/10.1021/jp505589b>.
961. Galano, A.; León-Carmona, J. R.; Alvarez-Idaboy, J. R. Influence of the environment on the protective effects of guaiacol derivatives against oxidative stress: Mechanisms, kinetics, and relative antioxidant activity. *J. Phys. Chem. B* **2012**, *116* (24), 7129-7137. DOI: <https://doi.org/10.1021/jp302810w>.
962. León-Carmona, J. R.; Galano, A. Free radical scavenging activity of caffeine's metabolites. *Int. J. Quantum Chem.* **2012**, *112* (21), 3472-3478. DOI: <https://doi.org/10.1002/qua.24084>.
963. Galano, A.; Pérez-González, A. On the free radical scavenging mechanism of protocatechuic acid, regeneration of the catechol group in aqueous solution. *Theor. Chem. Acc.* **2012**, *131* (9), 1-13. DOI: <https://doi.org/10.1007/s00214-012-1265-0>.

964. Litwinienko, G.; Ingold, K. U. Abnormal Solvent Effects on Hydrogen Atom Abstractions. 1. The Reactions of Phenols with 2,2-Diphenyl-1-picrylhydrazyl (dpph•) in Alcohols. *J. Org. Chem.* **2003**, 68 (9), 3433-3438. DOI: <https://doi.org/10.1021/jo026917t>.
965. Litwinienko, G.; Ingold, K. U. Abnormal Solvent Effects on Hydrogen Atom Abstraction. 3. Novel Kinetics in Sequential Proton Loss Electron Transfer Chemistry. *J. Org. Chem.* **2005**, 70 (22), 8982-8990. DOI: <https://doi.org/10.1021/jo051474p>.
966. Litwinienko, G.; Ingold, K. U. Solvent Effects on the Rates and Mechanisms of Reaction of Phenols with Free Radicals. *Acc. Chem. Res.* **2007**, 40 (3), 222-230. DOI: <https://doi.org/10.1021/ar0682029>.

Exploring Intermolecular and Intramolecular Interactions: A Review beyond Hydrogen Bonds

Rubicelia Vargas^{1*}, Jorge Garza¹, Ana Martínez²

¹Departamento de Química, División de Ciencias Básicas e Ingeniería, Universidad Autónoma Metropolitana-Iztapalapa. San Rafael Atlixco 186, Col. Vicentina, Iztapalapa. C.P. 09340. Ciudad de México, México.

²Departamento de Materiales de Baja Dimensionalidad. Instituto de Investigaciones en Materiales, Universidad Nacional Autónoma de México, Ciudad Universitaria S.N., Coyoacán 04510, Ciudad de México, México.

*Corresponding author: Rubicelia Vargas, email: ruvf@xanum.uam.mx

Received May 27th, 2024; Accepted July 3rd, 2024.

DOI: <http://dx.doi.org/10.29356/jmcs.v68i4.2306>

Abstract. Intermolecular interactions have great relevance in the stability of chemical systems. The most studied non-covalent interactions are hydrogen bonds, but they are not the only ones. Dihydrogen bonds or hydrogen-hydrogen contacts, as well as those that occur between heteroatoms, have also shown to play an important role in the molecular structure of biomolecules, solids, surfaces and other chemical systems. In this article we summarize the main contributions of our group to the study of these intermolecular interactions.

Among the most important results generated in our group is the estimation of the interaction energy of the unconventional hydrogen bond C-H...O, which showed its relevance in various systems. In addition, software programmed on graphic processing units was created in our group to analyze electron density using the Quantum Theory of Atoms in Molecules (QTAIM). This code has allowed us to study non-covalent interactions in large systems.

Keywords: Hydrogen bonds; Electron density; QTAIM; Non-covalent interactions.

Resumen. Las interacciones intermoleculares tienen una gran relevancia en la estabilidad de sistemas químicos. Las más estudiadas son los puentes de hidrógeno, pero no han sido las únicas. Los enlaces dihidrógeno o los contactos hidrógeno-hidrógeno, así como las interacciones que ocurren entre heteroátomos, también han mostrado un papel importante en la estructura molecular de biomoléculas, sólidos, superficies y otros sistemas químicos. En este artículo resumimos las principales contribuciones de nuestro grupo hacia el estudio de estas interacciones intermoleculares.

Entre los resultados más importantes generados por nuestro grupo es la estimación de la energía de interacción de puentes de hidrógeno no convencionales C-H...O, los cuales han mostrado su relevancia en varios sistemas. Además, el código computacional programado sobre tarjetas gráficas creado en nuestro grupo permite analizar la densidad electrónica usando la teoría cuántica de átomos en moléculas (QTAIM). Este código computacional nos ha permitido estudiar interacciones no covalentes en sistemas de gran tamaño.

Palabras clave: Puentes de hidrógeno; densidad electrónica; QTAIM; interacciones no covalentes.

Introduction

In 1937, Linus Pauling defined hydrogen bonds as a cohesive force relevant to the stability of molecules. In this definition, hydrogen bonds present hydroxyl or amino groups with carbonyl or hydroxyl groups considered as receptors [1]. The main idea at that time considered only oxygen and nitrogen atoms as donors or acceptors of the hydrogens that formed the interaction. This kind of interactions are now named conventional hydrogen bonds.

The possibility that other types of atoms might form hydrogen bonds was questioned for a long time. The existence of other hydrogen bonds with different donor and acceptor atoms that are not typically electronegative is currently recognized. This is the case of the carbon atom in the C-H bond to form a C-H...O interaction. Such interactions are called non-conventional hydrogen bonds.

Although the hydrogen bond in the International Union of Pure and Applied Chemistry (IUPAC) gold book [2] continues to be defined with basically the same characteristics as it was at the beginning, the same organization recognizes a new definition of hydrogen bond [3] that integrates the new discoveries of interactions. A new broad but not vague definition is intended that considers the visions of different areas of our discipline, but it is clear that this is a difficult task. After several discussions, finally in 2009 the following new definition was established [3]:

“The hydrogen bond is an attractive interaction between a hydrogen atom from a molecule or a molecular fragment X-H in which X is more electronegative than H, and an atom or a group of atoms in the same or a different molecule, in which there is evidence of bond formation. The evidence for hydrogen-bond formation may be experimental or theoretical, or ideally, a combination of both. A typical hydrogen bond may be depicted as X-H...Y-Z, where the three dots denote the bond. X-H represents the hydrogen-bond donor. The acceptor may be an atom or an anion Y, or a fragment or a molecule Y-Z, where Y is bonded to Z. In specific cases X and Y can be the same with both X-H and Y-H bonds being equal. In any event, the acceptor is an electron-rich region such as, but not limited to, a lone pair in Y or a π -bonded pair in Y-Z”.

In this definition, different types of atoms can be considered as hydrogen donors or acceptors. It also establishes that it is essential to have evidence. In this sense, theoretical and computational chemistry contributed greatly to the study of hydrogen bonds, not only to provide evidence, but to study their nature, which in many cases have not been completely clarified.

The role of hydrogen bonds (conventional and unconventional) is recognized today as the main intermolecular interaction in various chemical systems and different materials. Other types of intermolecular interactions, where there is still much research to be done, have appeared on the scene [4-8] that may be as important as hydrogen bonds, namely dihydrogen bonds (H...H bonds) and non-covalent interactions between heteroatoms.

In our group, conventional and unconventional hydrogen bonds as well as other intermolecular interactions, have been studied for more than 20 years using theoretical and computational chemistry tools. This paper summarizes our main contributions to this topic. It is not intended to be a review article, but rather to highlight the work that has been developed in the Department of Chemistry at the UAM Iztapalapa, which has contributed to the understanding of non-covalent interactions in many different systems. The UAM is a recently created University, which is turning fifty years old, but important research work has been carried out in many fields, and Theoretical and Computational Chemistry is not an exception.

Biological macromolecules

Hydrogen bonds are weaker than covalent bonds or interactions between ions, but it has been recognized that they can be crucial to form the structure of biological macromolecules such as proteins, DNA or carbohydrates. Conventional and non-conventional hydrogen bonds can be found in these macromolecules, with a wide range of interaction energies. The interaction energies of hydrogen bonds depend on the atoms involved and on the geometric parameters such as the distance between the acceptor (A) of the bridge and the participating hydrogen (H), the distance between the acceptor and the donor (D) of hydrogen, and the D-H...A angles. Shorter distances and more linear angles imply higher energies (more strength) of the hydrogen bond. With these parameters, hydrogen bonds can be classified as strong, medium-strength or weak, considering

Jeffrey's classification as a reference [9]. This classification is as follows: *Jeffrey categorizes H bonds with donor-acceptor distances of 2.2-2.5 Å as "strong, mostly covalent", 2.5-3.2 Å as "moderate, mostly electrostatic", 3.2-4.0 Å as "weak, electrostatic"*

With this classification, many systems can be studied. As an example, we consider the C-H...O hydrogen bond that was one of the most controversial and relevant weak interaction in the structure of proteins and carbohydrates. In 2000 [10] our group estimated, by using N,N'-dimethylformamide dimers as a model and high-quality ab-initio calculations, a binding energy of the C-H...O=C interaction between 2.1 and 4.0 kcal/mol depending on the linearity of the bond. The role of linearity in the strength of C-H...O=C hydrogen bonds was clearly demonstrated by Density Functional Theory (DFT) calculations [11]. Although each hydrogen bond is weaker than conventional hydrogen bonds, the presence of many C-H...O bonds strengthens the interactions and contributes to the conformation of biological macromolecules.

Many computational codes use Gaussian functions to represent orbitals. Although such functions are convenient for some numerical approaches, estimations of intermolecular interaction energies exhibit the Basis Set Superposition Error (BSSE). Usually, the estimation of the BSSE is obtained by using the counterpoise method [12-14]. We have shown that this error can be reduced when using Kohn-Sham (KS) method instead of correlated methods based on the wave function [15]. Therefore, if the basis set is large enough, in DFT-KS calculations the BSSE can be negligible on the estimation of hydrogen bond energies.

The new definition of hydrogen bonds suggests that there must be theoretical or experimental evidence to ensure their presence. Theoretical and computational chemistry are useful tools to provide this evidence based on the analysis of the electron density. Scalar and vector fields of electron density are very important to find and characterize intermolecular interactions. To this purpose, Quantum Theory of Atoms in Molecules (QTAIM) [16] has been widely used to establish intra and intermolecular interactions, in particular, hydrogen bonds. The electron localization function (ELF) is another scalar field that is also used for this purpose [17]. By testing conventional and non-conventional hydrogen bonds, our group found that critical points of the electron density and ELF are localized almost in the same contact region giving a relationship between both approaches [18].

Graphics processing units for atoms and molecules

Due to the importance of the analysis of scalar and vector fields of electron density to find and characterize intermolecular interactions, our group developed a software to use Graphics Processing Units (GPUs), and thus enable to study of non-covalent interactions in large molecules. This software has been called GPUAM, which stands for Graphics Processing Units for Atoms and Molecules [19-21]. With this software it is possible to analyze the gradient and the Laplacian of the density, to find the critical points that denote interactions, to obtain other fields such as the ELF, the electrostatic potential, and the Non-Covalent Interactions (NCI) index for large systems [22,23]. The GPUAM has been meticulously designed to run efficiently on GPUs using CUDA-C programming techniques. The grid used to analyze 3D scalar or vector fields is distributed across all threads involved in one or multiple GPUs within a server. Therefore, the efficiency of GPUAM is directly related to the number of threads available in the GPUs. Detailed information about the kernel designed in CUDA for grid distribution can be found in reference [19]. This grid-based approach is well-suited for GPU implementation, making the search for critical points in electron density highly efficient. Consequently, the QTAIM can be applied to large systems, as discussed below.

By using GPUAM, it is possible to investigate models of cavities of up to 800 atoms to study the interaction of drugs with proteins at the level of ab initio DFT methods. As an example, with QTAIM and GPUAM we characterized the non-covalent interactions between the N3 inhibitor and the main protease of SARS-CoV and SARS-CoV-2 [23]. We found that there are conventional and unconventional hydrogen bonds, as expected, but also H...H interactions that are generally not considered in these systems.

Using the same methodology, we also studied the intermolecular interactions between risperidone and the dopamine receptor DRD2 [24]. Risperidone is a drug used to treat schizophrenia. We compared the interactions of dopamine with DRD2 and those of risperidone with the same receptor, all using the QTAIM and the NCI (Figure 1). We found that the interaction energy depends more on the number of interactions than on the strength of each interaction. In this same topic, we show the importance of the salt bridge in the interaction of antipsychotic drugs with the dopamine receptor and its relationship with reactivity indices generated by DFT [25].

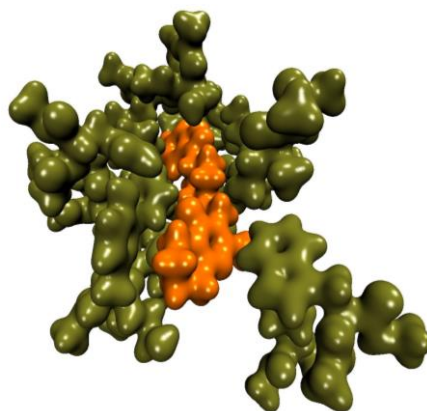


Fig. 1. Electron density in the Risperidone (orange) - DRD2 (green) system, which contains 571 atoms.

We also studied the intrinsic chemical reactivity of several drugs, dopamine agonists and antagonists, and their interaction with DRD2 in order to elucidate the action mechanism. We found a correlation between the ability to donate or accept charge and the strength of the interaction with the dopamine cavity in DRD2 [26-28].

Inclusion complexes

Macromolecules form cavities and this is very useful for housing small molecules without altering their structure. The polarity as well as the functional groups that can form hydrogen bonds or other interactions, promote the inclusion of small molecules in the cavities of macromolecules. Intermolecular interactions between guest and host are the driving forces of inclusion complexes. The formation of inclusion complexes produces favorable changes on physicochemical characteristics of the host, such as solubility, dissolution rate, stability and biodisponibility.

Inclusion compounds with cyclodextrins

Cyclodextrins (CD) are macrocycles with truncated cone cavities that make them good for encapsulating compounds for various applications in the pharmaceutical or food industries. In the inclusion complexes that form CDs, intermolecular interactions between the guest and the host are of great importance. The shape of the CD defines the distribution of the electron density within the cavity. The electron density can be mapped to their electrostatic potential. CDs have negative electrostatic potential in the widest part of the cavity and positive in the narrowest section. Therefore, CDs have a total dipole moment that determines how the guest molecule is introduced and interacts within the cavity. [29].

As we mentioned previously, physicochemical properties of the host are modified by the formation of complex. For example, the optical properties of the included compound. This was demonstrated for 4-dimethyl-aminobenzonitrile. The electrostatic potential of the CD cavity and intermolecular interactions change the fluorescence of the compound. Taking advantage of this experience, 4-dimethyl-aminobenzonitrile was proposed as a CD antenna to be used as an optical sensor [30].

More recently, molecular dynamics calculations show that α , β , and γ -CD cause significant CDs deformations when complexing molecules such as sertraline and abacavir. *Ab initio* DFT calculations showed that X-ray structures are maxima at the potential energy surface (PES), and that not only hydrogen bonds are responsible for the stabilization of the inclusion complex, but other interactions such as H•••H and Lewis acid base type interactions [31,32]. Deformation of cyclodextrins is an important element to be considered in inclusion compounds. The deformation can be obtained from docking and dynamic molecular techniques, and

it is crucial to do this before applying DFT methods to characterize non-covalent interactions. Distortions found in α -CD are presented in Figure 2. Structure on the left side corresponds to that obtained from X-ray experiments. The structure on the right side corresponds to the average structure obtained from classical molecular dynamics. From this figure it is evident the distortion observed when the α -CD is submitted to movements induced by classical molecular dynamics. The adequate description of the PES of different conformations due to conventional and non-conventional hydrogen bonds, depends on the correct description not only of intermolecular interactions, but also intramolecular, as it was demonstrated for the alanine dipeptide [33].

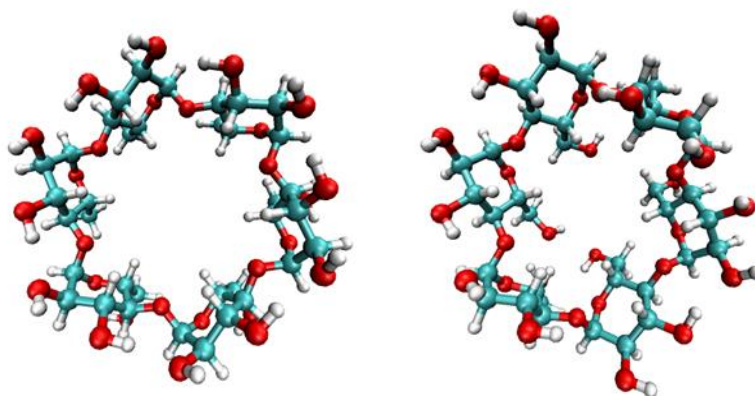


Fig. 2. Molecular structure of the α -CD from X-ray information (left side) and from classical molecular dynamics (right side).

Mesoporous materials

The mesoporous materials such as SBA15(SiO_2) have applications in several fields due to the elevated specific surface areas where adsorption of a variety of substances is possible in their channels that can be released under certain conditions. Specifically, we evaluated a material with a SiO_2 matrix whose pores trap fluconazole molecules. Fluconazole is a corrosion inhibitor, and the idea is to have a reservoir of a corrosion inhibitor agent to use this material as a self-healing material [34]. From the electron density analysis of structures proposed by docking, we found that the fluconazole is mainly trapped by non-canonical interactions such as $\text{F}\cdots\text{O}$; $\text{O}\cdots\text{O}$; $\text{N}\cdots\text{O}$; $\text{C}\cdots\text{O}$, as well as $\text{C-H}\cdots\text{O}$ hydrogen bonds. Just in one structure, conventional hydrogen bonds are observed. The analysis of the nature of intermolecular interactions is important since the liberation rate depends on them. In this study, conditions of release were proposed to use the material in coating metals.

Clathrates

Methane hydrates or clathrates are other compounds that trap molecules such as methane. These are boxes formed with water molecules linked by hydrogen bonds. Non-polar compounds such as methane can be housed inside. Clathrates are found in nature at the bottom of the arctic oceans, and can also be synthesized in the laboratory. They have been thought of as alternative energy sources or as possible structures to store hydrogen. In our group we widely explore the potential energy surface of the formation of the methane hydrate $\text{CH}_4-(\text{H}_2\text{O})_{12}$ with *ab initio* methods [35]. We found conventional hydrogen bonds between water molecules as expected, and $\text{C-H}\cdots\text{O}$ hydrogen bonds when water interacts with methane (Figure 3). The most stable structures found for $\text{CH}_4-(\text{H}_2\text{O})_{12}$ clusters are nest-like instead of cages trapping the methane molecule. Finally, with high quality *ab initio* methods, we stated that $\text{CH}_4-(\text{H}_2\text{O})_{12}$ clusters could exist up to 179 K, which means that it is possible the existence of these clusters on Mars, that was a discussion topic at that time.

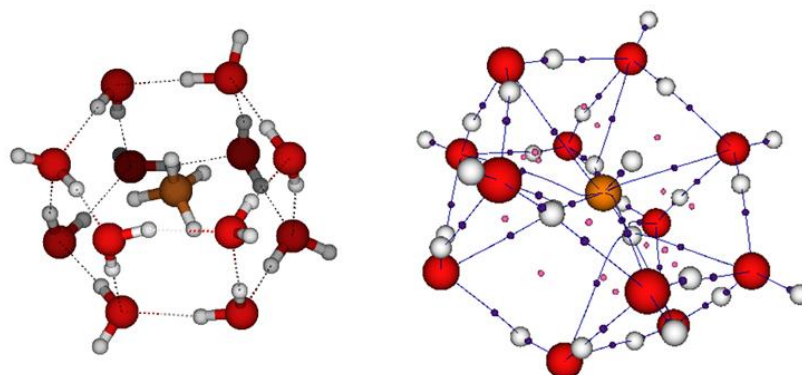


Fig. 3. Methane in a water box with conventional hydrogen bonds (left); QTAIM analysis where bond critical points and bond paths describe conventional and non conventional hydrogen bonds (right).

Molecular conformers

Hydrogen bonds and other interactions are also important factors in the structural conformations of different molecules and the physicochemical properties that they can display. For example, hydrogen bonds are crucial for the decomposition of three common neonicotinoids used as insecticides [36] or the formation of clusters of $\text{NaCl}(\text{H}_2\text{O})_2$ [37]. The solvation of Cu^{2+} ion is also important. In this case, we used a modified version of the simulated annealing method to explore the potential energy surface of $[\text{Cu}(\text{H}_2\text{O})_n]^{2+}$ with $n=12, 16$ and 18 in order to find the coordination number of Cu^{2+} ion. By using QTAIM we found that the fivefold coordination is preferred and the fourfold coordination cannot be considered in studies where the Cu^{2+} ion is solvated by water molecules [38].

Conformations of *N*-(2-benzoylphenyl)acetamide [39] are interesting since the most stable conformation in gas phase is stabilized by the hydrogen bond between the N-H of the acetamide and the carbonyl group that joins the two rings. However, another conformer close in energy is stabilized by a weaker $\text{C-H}\cdots\pi$. This study makes clear that including dispersion correction in DFT calculations is essential to correctly describe molecular conformations.

Ferulic acid is another interesting example. DFT calculations and electrochemical experiments showed that planar structures play an important role in the antioxidant capacity [40]. Dimers and trimers of this acid show weak intramolecular interactions that produce bent conformers. However, the presence of more than one ferulic acid unit can lead to donating more than one electron. Other example is the adduct formed between 1,4-benzoquinone and benzoic acid that presents a planar configuration, which is stabilized by two hydrogen bond interactions: one involving $\text{OH}\cdots\text{O}$ and the other $\text{CH}\cdots\text{O}$. This finding was further supported by electrochemical analyses [41]. The presence of hydrogen bonds is also important in intramolecular contacts, something that was revealed in studies with dopamine [42].

The methodology used gives us the possibility to study Raman spectroscopy signals that allow us to investigate the pathogenesis and progression of Parkinson Disease (PD). It has been reported that 5-S-cysteinyldopamine (CysDA) is a toxic compound for dopaminergic neurons, which induces the pathogenesis and progression of PD. To quantify CysDA by Raman spectroscopy, a solid graphene oxide (GO) substrate was proposed in order to increase the intrinsic low sensitivity of the Raman scattering and the interference of the fluorescence signal of biomolecules. We demonstrated that CysDA is adsorbed on GO by a wide variety of intermolecular interactions as hydrogen bonds and interactions between heteroatoms. These interactions explain the main band shifting observed in the FTIR spectrum of the CysDA/GO complex. Furthermore, the interaction of CysDA with GO leads to the quenching of the fluorescence of CysDA, which permits to obtain the Raman spectrum of this molecule [43].

The antioxidant capacity of catechols and resorcinols is well known. Catechol presents an $\text{O-H}\cdots\text{O}$ interaction due to the ortho position of the OH in the phenolic ring. When there are different substituents, the energy of the interaction found is modified [44]. The analysis of this interaction with different density fields showed that with the $\text{O-H}\cdots\text{O}$ interaction, the $\text{O}\cdots\text{O}$ repulsion of the two OH groups is avoided. In both resorcinols

and substituted catechols, it was found that the antioxidant capacity is not affected, but “the electron donating groups favor electronic changes along the reaction path, increasing the spontaneity of the hydrogen atom transfer mechanism” [45].

Intermolecular contacts in crystals

Many-body effects are enhanced in crystals and the behavior of some isolated molecules is altered when they are immersed in a periodic system. For example, tricyclic orthoamides present the eclipsed all-trans conformer more stable than the corresponding alternated conformation, which is quite strange for isolated molecules. The reason for this conformation involves two effects shown in Figure 4, non-covalent interactions with water molecules and the packing involved in the crystal [46].

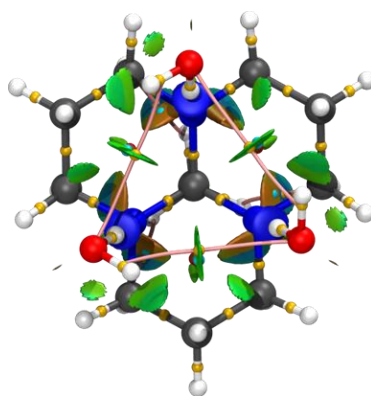


Fig. 4. The role of water molecules in the eclipsed all-trans conformer of tricyclic orthoamide.

The packing in a crystal is an important point to be considered for intermolecular interactions since the pressure exerted over a system is mapped on the contacts between molecules. For urea, our group described in detail how the hydrogen bond is altered as a function of the pressure. It is worth noting that the structures used in this study were obtained from experimental data, in particular, X-ray structures [47]. The changes of hydrogen bonds have an impact on the electron density voids observed in the crystal structure as it is shown in Figure 5.

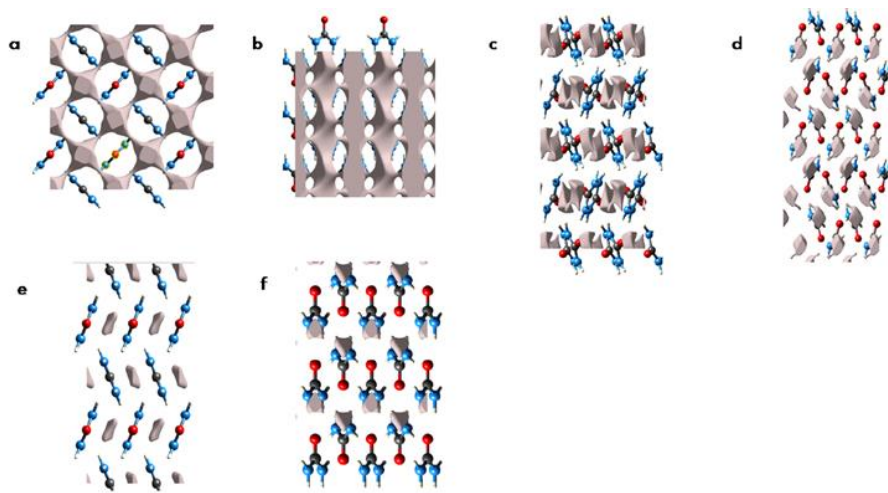


Fig. 5. The gray isosurfaces are the electron density voids of urea crystal at the (001) and (010) planes at 0.0047 GPa (a and b); 1.48 GPa (c and d) and 3.10 GPa (e and f).

For many reasons, the adsorption phenomena are relevant for physical and chemical processes. In these processes, non-covalent interactions are crucial to correctly describe host-guest contacts. In particular, Metal Organic Frameworks (MOF) have been used to confine substances considered as pollutants. Our group investigated systems where MOFs are the host and CO, CO₂, SO₂, benzene, toluene and I₂ are the guests. The MIL-3(Al)-TDC MOF increases its adsorption capacity if molecules of water are within the MOF. This result sounds strange. However, the directionality of hydrogen bonds between MOF and water induces a better interaction between MOF and CO₂. This conclusion was obtained from theoretical methods [48]. A similar effect is observed for the adsorption of CO₂ in InOF-1 MOF, which is enhanced when 2-propanol is confined within the MOF [45]. The relevance of the InOF-1 MOF to trap substances is evident from experimental and theoretical studies [49-53].

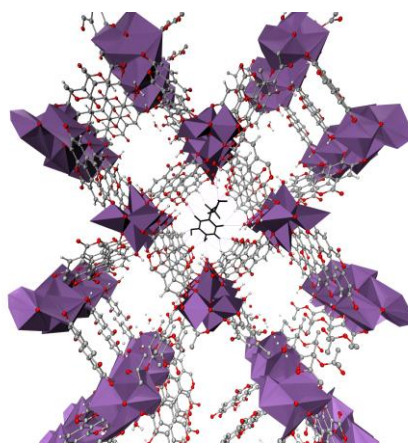


Fig. 6. SU101 MOF as dopamine carrier.

Electronic structure methods are mandatory to elucidate the non-covalent interactions between MOF and guest molecules. CO and SO₂ adsorption sites within NOTT-401 [54], I₂ in MIL-53(Al)-TDC [55] are examples where the analysis of the electron density provides insight of non-covalent interactions in these systems. Another example is the analysis of the electron density and related quantum chemistry scalar fields to understand the differences between isostructural MFM-300(Sc) and MFM-300(In) systems [56].

The MOFs have been considered to be carrier drugs. In our group, dopamine encapsulated by SU-101 MOF [57], and phenylethylamine, dopamine or sertraline within Mg₂(olsalazine) MOF [58] have been analyzed as possible drug delivery systems (Figure 6). For both MOFs the analysis of the electron density is quite important, by using NCI and QTAIM analysis we have characterized the difference between the open metal sites in Mg(olz)₂ and SU-101 MOFs [58].

Conclusions

In this paper we have mentioned the works where some actual and former professors of the Chemistry Department have contributed to the understanding of non-covalent interaction. From molecules to crystals, intermolecular contacts have been analyzed by using mainly the electron density and related quantum chemistry scalar fields. In all reports mentioned in this paper, the electron density has been obtained through the density functional theory. Our GPUAM software was used in molecular and periodic systems to analyze the electron density scalar fields. Our research has contributed to visualize the important role of non-covalent intermolecular interactions, not only conventional hydrogen bonds, but others as H•••H and heteroatoms contacts. We recognize the effort performed by other groups around the QTAIM and molecular interactions in our country, such efforts have been highlighted in reference [59].

The non-covalent index has been widely explored in our group in all the systems we have studied, however, only qualitative observations can be deduced from here. It is important to have quantitative information from the NCI or other scalar fields, and for this reason we are working on this. More investigations are needed to study other interactions such as those between heteroatoms that appeared in all the systems studied in our group.

Acknowledgements

AM acknowledges to LANCAD-UNAM-DGTIC-141 for computer facilities. JG and RV thank the facilities provided by the Laboratorio de Supercómputo y Visualización en Paralelo at the Universidad Autónoma Metropolitana-Iztapalapa (UAM-I). Most of the research presented in this article was developed by the students in our group to obtain their degrees, we thank all of them for choosing our University as their *alma mater*. The authors congratulate UAM, which, being a young university, has developed a very important scientific capital and has made valuable contributions to the development of science in general and specifically to Chemistry.

References

1. Jeffrey, G.A.; Saenger, W. *Hydrogen bonding in Biological Structures*. Springer-Verlag, **1991**.
2. IUPAC Compendium of Chemical Terminology, 2nd ed., Royal Society of Chemistry, Cambridge, **1997**. The online version (<http://old.iupac.org/publications/compendium/>) mostly corresponds to the second edition, compiled by A. D. McNaught and A. Wilkinson of the Royal Society of Chemistry. The definition of the term hydrogen bond is given at <https://goldbook.iupac.org/terms/view/H02899>.
3. Gautam, R. D. *Angew. Chem. Int. Ed.* **2011**, 50, 52 – 59. DOI: [/https://doi.org/10.1002/anie.201002960](https://doi.org/10.1002/anie.201002960).
4. Richardson, T. B.; Koetzle, T. F.; Crabtree, R. H. *Inorganica Chim. Acta* **1996**, 250, 69–73. DOI: [https://doi.org/10.1016/S0020-1693\(96\)05212-7](https://doi.org/10.1016/S0020-1693(96)05212-7).
5. Klooster, W. T.; Koetzle, T. F.; Siegbahn, P. E.; Richardson, T. B.; Crabtree, R. H. *J. Am. Chem. Soc.* **1999**, 7, 6337–6343. DOI: <https://doi.org/10.1021/acs.inorgchem.5b00927>.
6. Novoa, J. J.; Whangbo, M. H.; Williams, J. M. *J. Chem. Phys.* **1991**, 94, 4835–4841. DOI: <https://doi.org/10.1063/1.460568>.
7. Matta, C. F.; Hernández-Trujillo, J.; Tang, T. H.; Bader, R. F. *Chem. - Eur. J.* **2003**, 9, 1940–1951. DOI: <https://doi.org/10.1002/chem.200204626>.
8. Alkorta, I.; Elguero, J.; Frontera, A. *Crystals*, **2020**, 10, 180–208. DOI: <https://doi.org/10.3390/cryst10030180>.
9. Jeffrey, G.A. *An introduction to Hydrogen Bonding*. Oxford University Press, **1997**.
10. Vargas, R.; Garza, J.; Dixon, D. A.; Hay, B.P. *J. Am. Chem. Soc.* **2000**, 122, 4750–4755. DOI: <https://doi.org/10.1021/ja993600a>
11. Ramírez, J.-Z.; Vargas, R.; Garza, J. *J. Mex. Chem. Soc.* **2008**, 52, 31–35.
12. Jansen, H. B.; Ross, P. *Chem. Phys. Lett.* **1969**, 3, 140–143. DOI: [https://doi.org/10.1016/0009-2614\(69\)80118-1](https://doi.org/10.1016/0009-2614(69)80118-1).
13. Boys, S. B.; Bernardi, F. *Mol. Phys.* **1970**, 19, 533. DOI: <https://doi.org/10.1080/00268977000101561>.
14. (a) Mayer, I.; Surjan, P. R. *Chem. Phys. Lett.* **1992**, 191, 497–499. DOI: [https://doi.org/10.1016/0009-2614\(92\)85415-7](https://doi.org/10.1016/0009-2614(92)85415-7). (b) Simon, S.; Duran, M.; Dannenberg, J. J. *J. Chem. Phys.* **1996**, 105, 11024–11031. DOI: <https://doi.org/10.1063/1.472902>. (c) Salvador, P.; Paizs, B.; Duran, M.; Suhai, S. *J. Comput. Chem.* **2001**, 22, 765–786. DOI: <https://doi.org/10.1002/jcc.1042>.

15. Garza, J.; Ramírez, Z.; Vargas, R. *J. Phys. Chem. A*, **2005**, *109*, 643-651. DOI: <https://doi.org/10.1021/jp046492+>.
16. Bader, R. F. W. *Acc. Chem. Res.* **1985**, *18*, 9-15. DOI: <https://doi.org/10.1021/ar00109a003>.
17. Kohout, M.; Savin, A. *Int. J. Quantum Chem.* **1996**, *60*, 875-882. DOI: [https://doi.org/10.1002/\(SICI\)1097-461X\(1996\)60:4<875::AID-QUA10>3.0.CO;2-4](https://doi.org/10.1002/(SICI)1097-461X(1996)60:4<875::AID-QUA10>3.0.CO;2-4).
18. Navarrete-López, A. M.; Garza, J.; Vargas, R. *J. Phys. Chem. A* **2007**, *111*, 11147- 11152. DOI: <https://doi.org/10.29356/jmcs.v52i1.1043>.
19. Hernández-Esparza, R.; Mejía-Chica, S.-M.; Zapata-Escobar, A. D.; Guevara-García, A.; Martínez-Melchor, A.; Hernández-Pérez, J.-M.; Vargas, R.; Garza, J. *J. Comput. Chem.* **2014**, *35*, 2272-2278. DOI: <https://doi.org/10.1002/jcc.23752>.
20. Hernández-Esparza, R.; Vázquez-Mayagoitia, A.; Soriano-Agueda, L. A.; Vargas, R.; Garza, J. *Int. J. Quantum Chem.* **2018**, *119*, e25671. DOI: <https://doi.org/10.1002/qua.25671>.
21. Cruz, J. C.; Hernández-Esparza, R.; Vázquez-Mayagoitia, A.; Vargas, R.; Garza, J. *J. Chem. Inf. Model.* **2019**, *59*, 3120-3127. DOI: <https://doi.org/10.1021/acs.jcim.8b00951>.
22. Cruz, J. C.; García-Gutiérrez, P.; Zubillaga, R. A.; Vargas, R.; Garza, J. in: *Frontiers in Computational Chemistry*. Vol. 5, Ul-Haq, Z.; Wilson, A. K. Ed., Bentham Science Publishers, **2020**, 149-173. DOI: <https://doi.org/10.2174/9789811457791120050006>.
23. García-Gutiérrez, P.; Zubillaga, R. A.; Ibarra, I. A.; Martínez, A.; Vargas, R.; Garza, J. *C.S.B.J.* **2021**, *19*, 4669-4675. DOI: <https://doi.org/10.1016/j.csbj.2021.08.015>.
24. Martínez, A.; García-Gutiérrez, P.; Zubillaga, R. A.; Garza, J.; Vargas, R. *Phys. Chem. Chem. Phys.* **2021**, *23*, 14224-14230. DOI: <https://doi.org/10.1039/D1CP01637>.
25. Padilla-Bernal, G.; Vargas, R.; Martínez, A. *Theor. Chem. Acc.* **2023**, 142:65. DOI: <https://doi.org/10.1007/s00214-023-03016-6>.
26. Martínez, A.; Ibarra, I. A.; Vargas, R. *Plos ONE* **2019**, *14*, e0224691. DOI: <https://doi.org/10.1371/journal.pone.0224691>.
27. Goode-Romero, G. Domínguez, L.; Vargas, R.; Ibarra, I. A.; Martínez, A. *Comput. Theor. Chem.* **2020**, *1197*, 113125(1-6). DOI: <https://doi.org/10.1016/j.comptc.2020.113125>.
28. Goode-Romero, G.; Winnberg, U.; Domínguez, L.; Ibarra, I. A.; Vargas, R.; Winnberg, E.; Martínez, A. *Scientific Reports* **2020**, *10*, 21581. DOI: <https://doi.org/10.1038/s41598-020-78446-4>.
29. Santillán-Vargas, H.; Ramírez, J. Z.; Garza, J.; Vargas, R. *Int. J Quantum Chem.* **2012**, *112*, 3587-3593. DOI: <https://doi.org/10.1002/qua.24225>.
30. Nieto-Malagón, G.; Hernández-Pérez, J.; Vargas, R.; Garza, J. *Int. J Quantum Chem.* **2012**, *112*, 3552-3557. DOI: <https://doi.org/10.1002/qua.24186>.
31. Bautista-Renedo, J.-M.; Cuevas-Yañez, E.; Reyes-Pérez, H.; Vargas, R.; Garza, J.; González-Rivas, N. *RSC Adv.* **2020**, *10*, 20202-20210. DOI: <https://doi.org/10.1039/C9RA10218C>.
32. Bautista-Renedo, J.-M.; Hernández-Esparza, R.; Cuevas-Yañez, E.; Reyes-Pérez, H.; Vargas, R.; Garza, J.; González-Rivas, N. *Int. J Quantum Chem.*, **2022**, e26859. DOI: <https://doi.org/10.1002/qua.26859>.
33. Vargas, R.; Garza, J.; Hay, B. P.; Dixon, D. A. *J. Phys. Chem. A*, **2002**, *106*, 3213- 3218. DOI: <https://doi.org/10.1021/jp013952f>.
34. Bustos-Terrones, V.; Serratos, I. N.; Vargas, R.; Landeros-Rivera, Bruno. C.; Bustos-Terrones, Y. A.; Soto Estrada, A. M.; Vicente Escobar, J. O.; Romero Romo, M. A.; Uruchurtu, J.; Menchaca, C.; Esparza Schulz, J. M.; Domínguez, A. *ChemistryOpen*, **2018**, *7*, 984-994. DOI: <https://doi.org/10.1002/open.201800201>.
35. Salazar-Cano, J.-R.; Guevara-García, A.; Vargas, R.; Restrepo, A.; Garza, J. *Phys. Chem. Chem. Phys.* **2016**, *18*, 23508-23515. DOI: <https://doi.org/10.1039/C6CP04086A>.
36. García-Hernández, E.; Flores-Moreno, R.; Vázquez-Mayagoitia, A.; Vargas, R.; Garza, J. *New J. Chem.* **2017**, *41*, 965-974. DOI: <https://doi.org/10.1039/C6NJ02655A>.
37. García, J.-J.; Hernández-Esparza, R.; Vargas, R.; Tiznado, W.; Garza, J. *New J. Chem.* **2019**, *43*, 4309-4650. DOI: <https://doi.org/10.1039/C8NJ06315J>.

38. Monjaraz-Rodríguez, A.; Rodríguez-Bautista, M.; Garza, J.; Zubillaga, R. A.; Vargas, R. *J. Mol. Model.* **2018**, *24*, 187-195. DOI: <https://doi.org/10.1007/s00894-018-3725-5>.
39. Ramírez, J.-Z.; Vargas, R.; Padilla-Martínez, I.; Flores-Huerta, A. G.; Garza, J. *J. Mex. Chem. Soc.* **2012**, *56*, 275-278.
40. Guillén-Villar, R. C.; Vargas-Álvarez, Y.; Vargas, R.; Garza, J.; Matus, M. H.; Salas-Reyes, M.; Domínguez, Z. *J. Electroanal. Chem.* **2015**, *740*, 95-104. DOI: <https://doi.org/10.1016/j.jelechem.2015.01.003>.
41. Gómez, M.; González, I.; González, F. J.; Vargas, R.; Garza, J. *Electrochem. Comm.* **2003**, *5*, 12-15. DOI: [https://doi.org/10.1016/S1388-2481\(02\)00519-2](https://doi.org/10.1016/S1388-2481(02)00519-2).
42. García-Hernández, E.; Garza, J. *J. Mex. Chem. Soc.* **2017**, *61*, 222-228.
43. Badillo-Ramírez, I.; Landeros-Rivera, B.; de la O-Cuevas, E.; Vargas, R.; Garza, J.; Saniger, J. M. *New J. Chem.* **2019**, *43*, 15861-15870. DOI: <https://doi.org/10.1039/C9NJ03781K>.
44. Ortega-Moo, C.; Garza, J.; Vargas, R. *Theor. Chem. Acc.* **2016**, *135*, 177-189. DOI: <https://doi.org/10.1007/s00214-016-1932-7>.
45. Ortega-Moo, C.; Durán, R.; Herrera, B.; Gutiérrez-Oliva, S.; Toro-Labbe, A.; Vargas, R. *Phys. Chem. Chem. Phys.* **2017**, *19*, 14512-14519. DOI: <https://doi.org/10.1039/c7cp01304c>.
46. Gutiérrez-Flores, J.; Huerta, E. H.; Cuevas, G.; Garza, J.; Vargas, R. *J. Org. Chem.* **2024**, *89*, 257. DOI: <https://doi.org/10.1021/acs.joc.3c02016>.
47. Padilla-Bernal, G.; Gutiérrez-Flores, J.; Garza, J.; Vargas, R. *Theor. Chem. Acc.* **2023**, *142*, 42. DOI: <https://doi.org/10.1007/s00214-023-02978-x>.
48. González-Martínez, G. A.; Jurado-Vázquez, T.; Solís-Ibarra, D.; Vargas, B.; Sánchez-González, E.; Martínez, A.; Vargas, R.; González-Zamora, E.; and Ibarra, I. A. *Dalton Trans.* **2018**, *47*, 9459-9465. DOI: <https://doi.org/10.1039/C8DT01369A>.
49. Sánchez-Bautista, J. E.; Landeros-Rivera, B.; Jurado-Vázquez, T.; Martínez, A.; González-Zamora, E.; Balmaseda, J.; Vargas, R.; Ibarra, I. A. *Dalton Trans.* **2019**, *48*, 5176-5182. DOI: <https://doi.org/10.1039/C9DT00384C>.
50. Lara-García, H. A.; Landeros-Rivera, B.; González-Zamora, E.; Aguilar-Pliego, J.; Gómez-Cortés, A.; Martínez, A.; Vargas, R.; Díaz, G.; Ibarra, I. A. *Dalton Trans.* **2019**, *48*, 8611-8616. DOI: <https://doi.org/10.1039/C9DT01266D>.
51. Barrios-Vargas, L. J.; Ruiz-Montoya, J. G.; Landeros-Rivera, B.; Álvarez, J. R.; Alvarado-Alvarado, D.; Vargas, R.; Martínez, A.; González-Zamora, E.; Cáceres, L. M.; Morales, J. C.; Ibarra, I. A. *Dalton Trans.* **2020**, *49*, 2786-2793. DOI: <https://doi.org/10.1039/C9DT04667D>.
52. Landeros-Rivera, B.; Ibarra, I. A.; Díaz, M.; Vargas, R.; Lara-García, H. A.; Garza, J.; Martínez, A. *Phys. Chem. Chem. Phys.* **2020**, *22*, 7969-7974. DOI: <https://doi.org/10.1039/D0CP00579G>.
53. Garrido-Olvera, L. P.; Sanchez-Bautista, J. E.; Alvarado-Alvarado, D.; Landeros-Rivera, B.; Álvarez, J. R.; Vargas, R.; González-Zamora, E.; Balmaseda, J.; Lara-García, H. A.; Martínez, A.; Ibarra, I. A. *RSC Adv.* **2019**, *9*, 32864-32872. DOI: <https://doi.org/10.1039/c9ra05991a>.
54. Rivera-Almazo, M.; Díaz-Ramírez, M. L.; Hernández-Esparza, R.; Vargas, R.; Martínez, A.; Martis, V.; Sáenz-Cavazos, P. A.; Williams, D.; Lima, E.; Ibarra, A.; Garza, J. *Phys. Chem. Chem. Phys.* **2021**, *23*, 1454-1463. DOI: <https://doi.org/10.1039/D0CP04668J>.
55. Díaz-Ramírez, M. L.; Vargas, B.; Álvarez, J. R.; Landeros-Rivera, B.; Rivera-Almazo, M.; Ramos, C.; Flores, J. G.; Morales, E.; Vargas, R.; Garza, J.; González-Zamora, E.; Martínez, A.; Solís-Ibarra, D.; Ibarra, I. A. *Dalton Trans.* **2020**, *49*, 6572-6577. DOI: <https://doi.org/10.1039/D0DT00945H>.
56. Rivera-Almazo, M.; Pérez-Sánchez, E.; Martínez-Ahumada, E.; Martínez, A.; Garza, J.; Ibarra, I. A.; Vargas, R. *J. Phys. Chem. C* **2022**, *126*, 6465-647. DOI: <https://doi.org/10.1021/acs.jpcc.2c00742>.
57. Medel, E.; Obeso, J. L.; Serrano-Fuentes, C.; Garza, J.; Ibarra, I. A.; Leyva, C.; Inge, K. A.; Martínez, A.; Vargas, R. *Chem. Comm.* **2023**, *59*, 8684-8687. DOI: <https://doi.org/10.1039/D3CC02304D>.
58. Medel, E.; Garza, J.; Ibarra, I. A.; Martínez, A.; Vargas, R. *Comput. Theor. Chem.* **2023**, *1228*, 114265. DOI: <https://doi.org/10.1016/j.comptc.2023.114265>.
59. García-Revilla, M. A.; Cortés-Guzmán, F.; Rocha-Rinza, T.; Hernández-Trujillo, J. *Int. J. Quantum Chem.* **2019**, *119*, e25789. DOI: <https://doi.org/10.1002/qua.25789>.

Contributions from UAM-Iztapalapa to the Study of Confined Atoms and Molecules

Norberto Aquino*¹, Salvador Cruz*¹, Jorge Garza*², Rubicelia Vargas*²

¹Departamento de Física, División de Ciencias Básicas e Ingeniería, Universidad Autónoma Metropolitana-Iztapalapa. San Rafael Atlixco 186, Col. Vicentina, Iztapalapa, C.P. 09340. Ciudad de México, México.

²Departamento de Química, División de Ciencias Básicas e Ingeniería, Universidad Autónoma Metropolitana-Iztapalapa. San Rafael Atlixco 186, Col. Vicentina, Iztapalapa, C.P. 09340. Ciudad de México, México.

***Corresponding author:** Norberto Aquino, email: naa@xanum.uam.mx; Salvador Cruz, email: cruz@xanum.uam.mx; Jorge Garza, email: jgo@xanum.uam.mx; Rubicelia Vargas, email: ruvf@xanum.uam.mx

Received May 1st, 2024; Accepted June 11th, 2024.

DOI: <http://dx.doi.org/10.29356/jmcs.v68i4.2266>

Abstract. The study of confined quantum systems has been a subject of fundamental interest of research at the Universidad Autónoma Metropolitana (UAM) for over 30 years. This summary highlights the contributions of the present authors from UAM in this field considering various quantum systems under different confinement conditions. The paper is divided into two sections: one focusing on atoms and molecules confined by closed and open hard walls, and the other on systems confined by closed and open soft walls. As UAM celebrates its 50th anniversary, it is a timely moment to reflect on the development of collective efforts of the Chemistry and Physics departments in contributing to knowledge in this intriguing and interesting field.

Keywords: Confined systems; systems under high pressure; electronic structure under extreme conditions.

Resumen. El estudio de sistemas cuánticos confinados ha sido objeto de fundamental interés en la Universidad Autónoma Metropolitana (UAM) sobre 30 años. Este resumen resalta las contribuciones de la autora y autores de la UAM en este campo considerando varios sistemas cuánticos bajo diferentes condiciones de confinamiento. El artículo está dividido en dos secciones: una enfocándose en átomos y moléculas confinadas por paredes duras cerradas y abiertas, y la otra en sistemas confinados por paredes suaves cerradas y abiertas. Como la UAM celebra su 50 aniversario, es un buen momento para mostrar el desarrollo de esfuerzos colectivos de los departamentos de química y física en la contribución del conocimiento en este interesante e intrigante campo.

Palabras clave: Sistemas confinados; Sistemas bajo altas presiones; Estructura electrónica bajo condiciones extremas.

Introduction

The first theory of metallic sodium and a method to calculate the binding properties of metals was put forward by Wigner and Seitz since 1933.[1,2] Their work gave rise to the celebrated Wigner-Seitz cell model, whereby each atom in the crystal lattice is surrounded by a polyhedron formed by bisecting planes between the atom and its neighbors. Without further details, we deem this was the first confined system

studied, which led to the first serious band structure calculations of metallic sodium. A few years later, Michels, De Boer and Bijl,[3] followed by Sommerfeld and Welker,[4] studied how the polarizability of the hydrogen atom varies when subjected to very high external pressures. Their work proposed that the hydrogen atom is enclosed in a spherical cavity of radius r_0 with impenetrable walls, which simulate the effects of the rest of the negative charges surrounding the atom. They solved approximately the Schrödinger equation for a set of states, and with an approximate wave function they calculated the polarizability through Kirkwood's method.[5] We can say that these fundamental studies constitute a milestone for the quest for properties of confined quantum systems, which has become an active field of research in physics and chemistry worldwide.[6-9]

Noteworthy in this aspect, the significant contribution from professors and students of the Universidad Autónoma Metropolitana (UAM) - Iztapalapa is hereby acknowledged. Since the establishment of UAM 50 years ago, many research groups in this institution have made important contributions to science in different fields of knowledge. Particularly, in the case of the study of electronic properties of atomic and molecular systems submitted to non-conventional conditions, such as quantum confinement, the chemistry department and the physics department have combined efforts to generate new ideas and techniques to tackle various related problems. It is worth mentioning here that this research activity has promoted appropriate local and international meetings around this topic. This article appraises the efforts developed by our research groups at UAM-Iztapalapa to study confinement effects on the electronic properties of atomic and molecular systems. Of course, this summary is not meant to be exhaustive but to provide an insight into our main contributions to the knowledge and applications of confined quantum systems.

The starting point is the time-independent Schrödinger equation within the Born-Oppenheimer approximation

$$\hat{H}\Psi = E\Psi, \quad (1)$$

With

$$\hat{H} = \sum_{i=1}^N -\frac{1}{2}\nabla^2 + \sum_{i=1}^N \sum_{A=1}^M \frac{-Z_A}{|R_A - r_i|} + \sum_{i=1}^N \sum_{j>i}^N \frac{1}{|r - r_i|} + v_c \quad (2)$$

where N and M represent the number of electrons and nuclei, respectively, and positions of nuclei with atomic charge Z_A are represented by \mathbf{R}_A . The position of electrons are represented by \mathbf{r}_i . In the context of this article, v_c is quite important since this term represents the confinement imposed over the system. For molecules, there is an additional term to the total energy within the Born-Oppenheimer approximation that takes into account the interaction among nuclei,

$$E_{nn} = \sum_{A=1}^M \sum_{B>A}^M \frac{Z_A Z_B}{|R_B - R_A|} \quad (3)$$

Atomic units (a. u.) will be considered in this article.

The confinement models to be discussed here consist of closed or open geometric boundaries defining v_c , whose barrier height may be infinite (hard wall confinement) or finite (soft wall confinement). For clarity of presentation, in the following sections, we shall refer separately to our achievements for hard wall and soft wall confinement in all cases.

Confinement imposed by hard walls

In this Section, we present an account of our relevant contributions concerning hard wall confinement for various atomic and molecular systems spatially limited by closed and open geometric boundaries of different shapes. We begin with the hydrogenic atom, which is the simplest yet fundamental system in the Periodic Table. Then, we proceed to the two-electron helium-like system, many-electron atoms, and molecular systems.

Hydrogen atom

Historically, the confinement imposed over a hydrogen atom was based on a model in which the hydrogen nucleus is clamped at the center of an impenetrable sphere, and the electron moves in the sphere under the coulombic attraction of the nucleus. The important ingredient in this model is an infinite potential on the sphere's surface such that the wave function or electron density is canceled on the surface. In mathematical terms, the wave function must satisfy the Dirichlet boundary conditions. The confined hydrogen atom has spherical symmetry, so as in any central potential, the angular solution of the Schrödinger equation is given by the spherical harmonics $Y_{l,m}(\theta, \phi)$. Therefore, it is only necessary to solve the radial Schrödinger equation subject to the boundary conditions.

Researchers who worked on this problem before 1979, approximating the solution of the Schrödinger equation, could not obtain the energies accurately. They obtained 3–4 decimal places approximately in the energies calculations and a smaller number in the physical properties. Since the late 1970s, significant efforts have been reported to solve the Schrödinger equation of the hydrogen atom enclosed by hard walls.[10–12] Precisely, within these efforts, the UAM-Iztapalapa started to work with contributions in this field.

On one hand, the variational method was used with an elegant wave function, constructed as the product of a wave function of the free system multiplied by a cut-off function to ensure that the boundary condition is satisfied to obtain a good approximation to the energy of the confined system.[11,13] On the other hand, a series method gave a high-accuracy numerical approximation; the energies obtained by this method reported energies with 10–11 accuracy figures, giving energies below those reported previously.[12,14] One element to note in the used series method is that the wave function, in addition to depending on the coordinates, also depends explicitly on the energy.[12] In a later paper,[14,15] the power series method and a solution based on the confluent hypergeometric function were used to obtain energy with an error of less than 1×10^{-100} . Although the hydrogen atom has one electron, this system exhibits many characteristics shown by many-electron atoms, which will be discussed below. For example, the orbital energy appears to cross between different states when the atom is under extreme confinement. If the hydrogen atom is confined at $r_0 = 1.0$ a. u. the orbital energy ordering is $\epsilon_{1s} < \epsilon_{2p} < \epsilon_{3d} < \epsilon_{2s}, \dots$, where the energy degeneracy disappears. The common electron configuration ordering no longer exists¹⁶ as can be appreciated from Fig. 1.

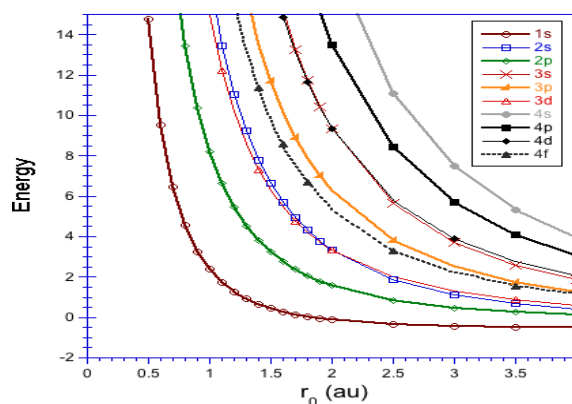


Fig. 1. Orbital energies for the hydrogen atom confined by spherical hard walls with several confinement radii r_0 .

The confined quantum systems, particularly the spherically confined hydrogen atom, show abrupt changes in their physical properties when the size of the cavity containing them is reduced, i.e., as the pressure grows. The magnetic screening constant, Fermi contact term, polarizability, and the pressure as a function of the cavity radius r_0 are depicted in Fig. 2.

From Fig. 2, as the radius r_0 decreases the magnetic screening constant, the Fermi contact term and pressure increase rapidly, whereas the polarizability decreases quickly, indicating that the confined hydrogen atom is harder than the corresponding *free* atom. For these reasons, the confined hydrogen atom limited by spherical hard walls is a system of continuing interest.[14,15,17-23]

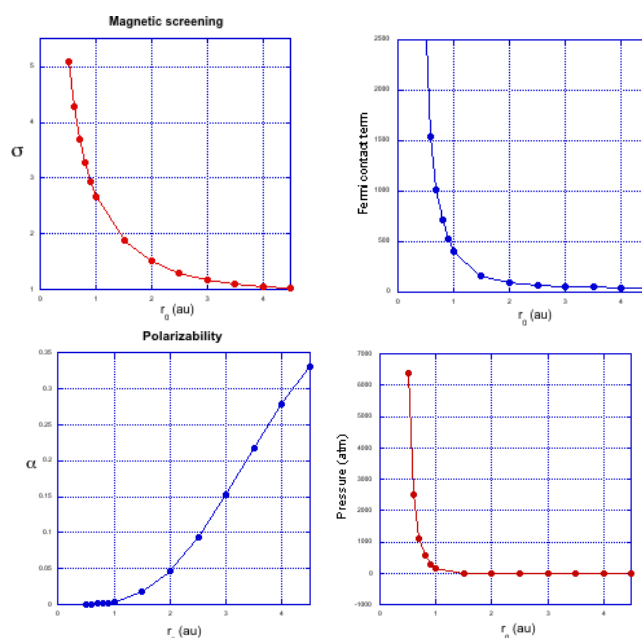


Fig. 2. Magnetic screening constant σ , Fermi contact term, polarizability and pressure for the ground state of the hydrogen atom confined by spherical hard walls with several confinement radii r_0 .

The hydrogen atom has also been studied under spatial limitation due to closed and open hard walls with different shapes.[24-28] We must mention that the case of single atoms localized at arbitrary positions along the major axis of ellipsoids is implicit within the treatment of diatomic molecules. For this reason, the hydrogen atom is also considered when the molecular systems H_2 or H_2^+ are under study.[29] The Fermi contact term, which has a direct relationship with the electron density at the nucleus, is one crucial result since this quantity is reduced for extreme confinements.[24] Thus, not for all confinement shapes is the electron density accumulated at the nuclei when the system is confined under small regions. Additional confinement shapes have been considered for the hydrogen atom.[30-36]

Many-electron atoms

The study of the electronic structure of many-electron atoms is a challenge since there is no analytical solution for the corresponding Schrödinger equation because the electron-electron interaction is present in this equation. Researchers have developed computational codes to obtain the wave function or electron density of atoms and molecules, and the number of these codes has increased with the arrival of new hardware. However, several of

the mentioned computational codes have been designed to obtain wave function or electron density without spatial restrictions. Thus, confined many-electron systems pose additional difficulties in obtaining their electronic structure under these circumstances. Naturally, the helium atom is a good candidate for this class for elucidating changes in its electronic structure under hard-wall confinement. Using a simple variational ansatz for the wave function, the total ground state energy has been estimated for this atom confined by a sphere with hard walls.[11,37] With more sophisticated methods, such as those based on correlated Hylleraas functions, the total energy has been reported with high accuracy for the ground state and the first triplet state of this confined atom.[38-39] Also the correlation energy of this system has been estimated by several techniques.[14,40-46] The direct variational method or the use of correlated Hylleraas functions is limited to atoms with small number of electrons. Thus, methods designed to study many-electron systems, like Density Functional Theory (DFT) or Hartree-Fock (HF) method, have been applied to these systems by implementing new numerical codes. Along with DFT, there are several proposals, Thomas-Fermi approaches, [47-50] Kohn-Sham model, [51,52] or wave function methods.[40,43,44,52-55]

Estimations of confinement radii where atoms are ionized [54,56] and how the shell structure [57] is affected by this confinement are examples where the design of new computational codes exhibits their value. The *s-d* transition observed experimentally in some alkali-metals has also been observed as electronic configuration transitions [58-60] by using this confinement model. Chemical reactivity indices defined in the context of the DFT have been analyzed and show that for extreme confinement, an atom is not infinitely hard since the electronic transitions are such that the atom goes to states where it is soft.[61] Thus, this simple confinement model gives insight into how the electronic structure of atoms reacts under spatial restrictions.

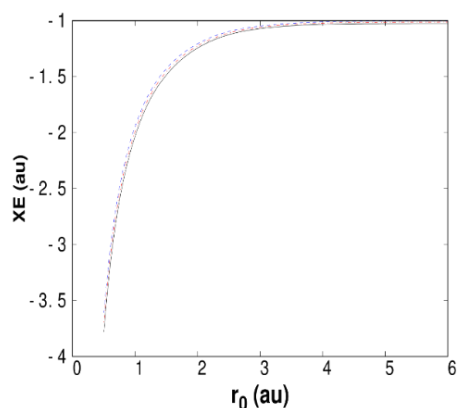


Fig. 3. Exchange energy, XE, for helium atom confined by hard walls obtained by Hartree- Fock (solid line), PBE (dashed line) and hybrid exchange functional with 50 % of Hartree- Fock (dot-dashed line).

It is well known that within the DFT, the exact exchange-correlation functional is unknown, and consequently, many approximations are used to account for the electron-electron interaction. For the confinement imposed by hard walls, the exchange energy delivered by some functionals is similar to that provided by the HF method. The behavior of the exchange energy obtained by the Perdew-Burke-Ernzerhof (PBE) exchange functional is similar to that observed by the HF method, as can be seen from Fig. 3. In the same plot, the half-and-half (0.5 of HF and 0.5 of PBE9 method shows behavior similar to that provided by PBE and HF. For this confinement, the HF exchange energy is the lower limit, and any of the approximations based on PBE are above HF results.[62] Thus, PBE exchange functional and hybrid functionals built with these approximations are appropriate for studying atoms confined by hard walls.

Several applications have been reported for many-electron atoms under the confinement imposed by hard walls defined either by closed or open boundaries. In one case, the pressure dependence of the mean excitation energy of bulk atoms in a given material has been estimated to account for the rate of energy loss of

heavy ions penetrating the material.[63,64] In the case of hard open boundaries, the surface scattering potential of helium atoms close to a planar boundary is related to the ground-state energy shift imposed by the spatial restriction due to the plane. This approach has also been extended to study the scattering and penetration of heavy ions in nanolayered materials.[65,66]

Molecules

Some molecular systems have been studied under spatial restrictions. In this connection, the simplest molecular system under study is the one-electron diatomic molecular ion H_2^+ and its isomers like HeH^{++} , confined by a hard spheroidal cavity. For convenience, the Schrödinger equation is written in terms of prolate spheroidal coordinates that incorporate the intrinsic symmetry involved in diatomic molecules.[24] This set of coordinates consists of families of mutually orthogonal confocal spheroids, ζ , and hyperboloids, η , such that fixed values of the variable $\zeta \in [1, \infty)$ define ellipsoids of revolution around the internuclear axis with eccentricity $1/\zeta$.

In this approach, the Dirichlet boundary conditions are satisfied when the wave function is canceled at an arbitrary ζ_0 , which defines the confining cavity. When the nuclear positions coincide with the foci, the Schrödinger equation becomes separable, and analytical methods deliver exact results for the total energy and the corresponding wave function.[24] However, when the nuclear positions are set arbitrarily along the major axis, the Schrödinger equation becomes non-separable, and approximate methods such as the variational one have been used to obtain appropriate results.[26] The total energy of this system exhibits important changes when ζ_0 is reduced since it acquires large values when $\zeta_0 \rightarrow 1$.[24]

Using the exact electron density, the chemical bond of the H_2^+ molecule has been studied under extreme conditions.[67,68] The electron density along the internuclear axis is depicted in Fig. 4. In this case, the hydrogen atoms are localized at $z = \pm 1$ a.u. The electron density exhibits a cusp at the hydrogen nuclei positions for large values of ζ_0 , corresponding to moderate confinements.

However, for strong confinements, ζ_0 close to 1, such a cusp disappears, and the electron density accumulates at the middle of the nuclei; the kinetic energy is very large, and the nuclei are incapable of binding the electron involved in this molecule.

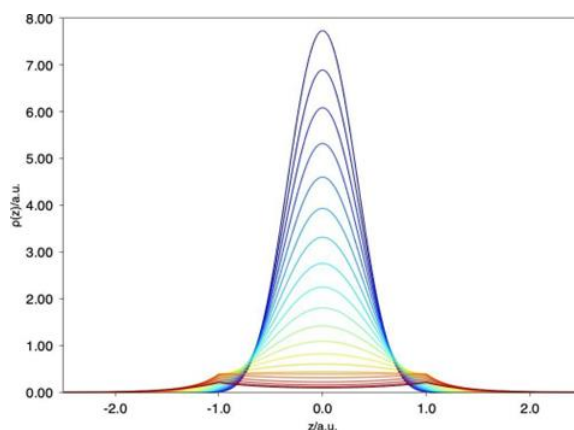


Fig. 4. Electron density of the H_2^+ molecule under several confinements defined by ζ_0 . Hydrogen atoms are localized at $z = \pm 1$ a.u.

The electron density evaluated at a nucleus position $\rho(R_N)$ as a function of ζ_0 is presented in Fig. 5. This figure shows that there is confinement where $\rho(R_N)$ is a maximum, and it goes to zero when $\zeta_0 \rightarrow 1$, corroborating that the nuclei do not bind an electron for extreme confinements.

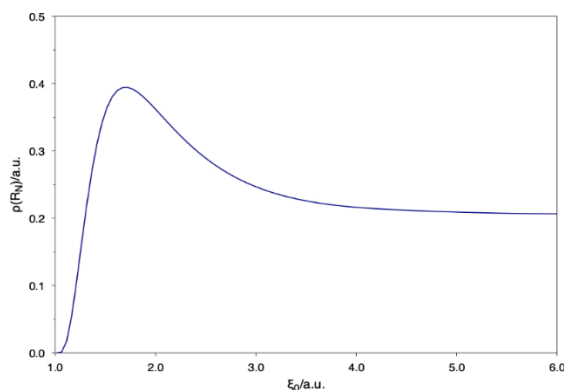


Fig. 5. Electron density evaluated at a nucleus position, R_N , of the H_2^+ molecule.

The H_2 molecule involves the electron-electron interaction, so there is no exact solution, and consequently, the wave function must be approximated.[28,69] Estimating the correlation energy for the confined H_2 molecule exhibits a behavior similar to that of the helium atom. It seems that two electrons confined under different circumstances respond similarly. Although the H_2^+ molecule contains only one electron, the behavior of the chemical bond is similar to that observed for the H_2 molecule, which contains two electrons.[28] This result enhances the importance of the study of confined one-electron systems.

Concerning other studies of molecular confinement by hard spherical cavities, the use of the floating spherical Gaussian orbital (FSGO) representation for molecular orbitals allowed the calculation of pressure effects on the ground-state energy and molecular conformation of methane, ammonia and water as well as pressure-induced changes in the dipole moment of water and ammonia.[70,71] Finally, concerning molecular confinement by hard open boundaries, exact solutions of the Schrödinger equation for the H_2^+ and HeH^{2+} molecular ions, confined in dihedral angles and in the Born–Oppenheimer approximation, have been constructed, whereby the potential energy curves for the ground, first, and second excited states of the homonuclear H_2^+ molecule and for the metastable state of HeH^{2+} are reported illustrating their variations with the confining angle.[72]

Confinement imposed by soft walls

Hard wall confinement models constitute the first simple approach to exploring changes in the electronic properties of atoms and molecules due to spatial limitation. However, the confinement imposed by hard walls is known to overestimate, in general, the change in these properties compared to more realistic situations. Therefore, confining potentials with finite barrier height have been proposed as more appropriate models. This confinement is called finite potential, penetrable walls, soft walls or padded walls. This type of potential takes into account, in some way, the attractive forces between particles, such as the van der Waals force, among others. The potential $v_c = \infty$ used for the hard wall confinement is replaced by one where $v_c = v_0$, and the treatment of the Schrödinger equation is radically different from those used for hard wall. For this case, the logarithmic derivative of the wave function must be the same on the boundaries that define the confinement instead of the Dirichlet boundary conditions.

Hydrogen atom

Again, the hydrogen atom has been a hallmark study system for this kind of confinement. Consider a hydrogenic system with nuclear position of charge Z , clamped at the center of a spherical soft wall cavity of radius r_0 and barrier height v_0 . In this case, the most commonly used confining potential is the *step potential*, which is defined as follows: Let r_0 be the radius of the spherical cavity, then, $v_c = 0$ for $0 < r < r_0$ and $v_c = v_0$ for $r > r_0$, where v_0 is a constant. The corresponding Schrödinger equation has spherical symmetry, hence the angular solutions are the

spherical harmonics $Y_{l,m}(\theta, \phi)$ and only the radial solutions have to be found. This step potential divides the space into two spherical regions, in the first one $0 < r < r_0$, the radial solution is denoted by $R_{in}(r)$, while in the second, $r > r_0$, the radial solution is called $R_{out}(r)$. The interior and exterior solutions of the radial Schrödinger must be continuous with continuous derivative in the whole space, particularly at $r = r_0$. Then, the boundary conditions are: $R_{in}(r_0) = R_{out}(r_0)$ and $dR_{in}/dr|_{r_0} = dR_{out}/dr|_{r_0}$.

There are several reports where this system is analyzed from different points of view. [10,14,73-76] One of the most successful approximate methods is the nonlinear variational method.[77] In that approach the authors use two different ansatz functions for each of the two regions of space, the energy is obtained by requiring that these two functions and their derivatives at $r = r_0$ are continuous, this implies the minimization of the energy functional in two variational parameters. The energies obtained by this procedure have 4 – 5 decimal places of accuracy for different values of r_0 .

In another method, the authors [14] used a power series in the variable r , described in a previous section, to represent the wave function R_{in} in the region $0 < r < r_0$, and the exact solution for R_{out} for the other region.[10] The energies obtained by this method have an accuracy of 10 digits. In another paper, the authors [15] used the exact wave functions for the internal and external solutions. Like most non-perturbative methods, the energies are obtained numerically by solving a transcendental equation. Using this approach, the authors obtained accurate energies for the ground state and some excited states. This method was also used to study the energy correction of a hydrogen atom confined in a penetrable spherical box by considering an atomic nucleus of finite size, [78] and to study the ground state energy of confined muonic atoms.[79]

For the hydrogen atom confined in a penetrable spherical cavity, a few physical properties such as magnetic screening constant, Fermi contact term, polarizability and pressure were calculated. Fig. 6 shows the behavior of these physical quantities as a function of the confinement radius and the barrier height v_0 . In this figure, we can see the difference in the physical properties of the atom confined inside a penetrable barrier of different heights and an impenetrable one. The electron of an atom confined in a penetrable barrier escapes from the potential well as the confinement increases, i.e. as r_0 decreases. The consequence is that the magnetic shielding constant, the Fermi contact term, and the pressure do not grow indefinitely, whereas the polarizability grows quickly in this limit.

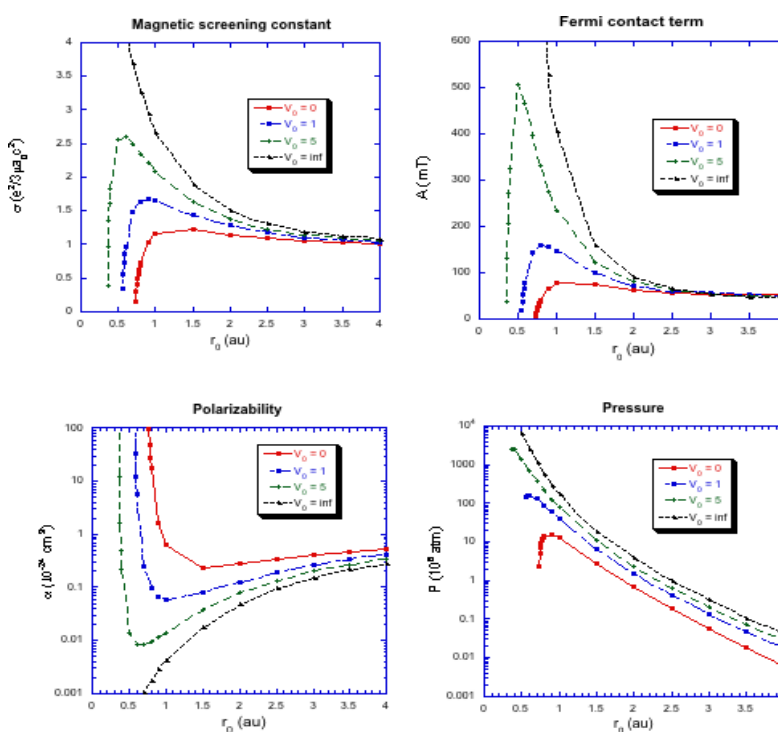


Fig. 6. Magnetic screening constant σ , Fermi contact term, polarizability and pressure for the ground state of the hydrogen atom confined by hard and soft walls as a function of the confinement radii r_0 .

Results from these studies show appreciable differences between hard and soft walls, where soft walls give a better idea about the confinement. We can mention how a finite potential allows the electron's escape when the confinement is increased and how the information theory is useful to describe the delocalization of the electron density.[74,76] Similarly, for a given confinement radius and barrier height, the energy spectrum for all available bound states and several continuum states (pseudo-continuum) was obtained by solving the Schrödinger equation for the hydrogen atom within spherical soft and hard walls. The results indicate important differences in the behavior of the mean excitation energy of the confined atom as the confining barrier height changes.[80] Also, concerning other confining geometries with soft and hard walls, the bound-state energy spectrum and its evolution for a hydrogen atom located along the axis of a standard cylindrical confining cavity with either impenetrable or penetrable confining boundaries were obtained by solving the stationary Schrödinger equation using a finite differences approach. It was found that in general the energy levels evolve with an increasing value as the nuclear position is shifted from the central position up to a cylinder cap.[36,81]

Many-electron atoms

For many-electron atoms, numerical approaches are more sophisticated in this case than those used for the confinement imposed by hard walls.[46,52,62,77,82-86] Naturally, the richness delivered by many-electron atoms immersed within soft walls is impressive. For example, the shell structure of the beryllium atom is affected drastically when this atom is squeezed by a finite potential.[84,87] By contrasting the results obtained by DFT between hard and soft walls, approximations to DFT describe the exchange energy similarly to that presented by HF theory for confinement imposed by hard walls, since DFT exchange functionals and HF predict this quantity deeper when the confinement is increased. However, for confinement imposed by soft walls, there are appreciable differences between approximations of DFT and HF method.[62,85] In Fig. 7, there is a comparison between three exchange functionals (LDA, Becke88 and PBE) and HF method. From here, it is evident that the three exchange functionals predict an exchange energy above that predicted by HF for moderate confinement radii. However, this behavior is reversed for strong confinements where HF exchange energy exceeds the predictions of these three exchange functionals. This result suggests that people must carefully use computational codes that simulate systems under high pressure since not all DFT approximations work appropriately. It is worth noting that there are different ways to impose the confinement by soft walls, which are not limited to using model potentials.[86,88-90]

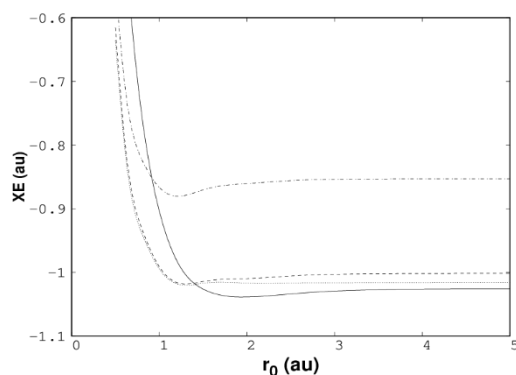


Fig. 7. Exchange energy, XE, for helium atom confined by soft walls obtained by Hartree-Fock (solid line), PBE (dashed line), Becke88 (dotted line) and LDA (dot-dashed line) exchange functionals.

Molecules

For molecular confinement imposed by soft walls only a few efforts have been put forward within the Born-Oppenheimer approximation, mainly to find the electronic structure of simple diatomic molecules under such conditions. A preliminary approach to model dense molecular hydrogen's electronic properties and molecular conformation was proposed, where the H_2 molecule is viewed as a caged-in system within a spherical boundary with finite potential barrier height v_0 . A self-consistent treatment was employed using the FSGO representation of molecular orbitals. This molecular confinement model was put forward to calculate density effects on the rate of energy loss of energetic protons traversing dense hydrogen.[91] On the other hand, exact solutions to the corresponding Schrödinger equation have been reported for the hydrogen molecular ion H_2^+ enclosed by a penetrable spheroidal cavity with nuclear positions located at the focii.[92] When the nuclear positions are located arbitrarily along the major axis in this system, the Schrödinger equation is no longer separable. Hence, this non-separable problem for the confined H_2^+ and H_2 molecules in their ground states was treated variationally.[93] In this way, given a finite height for the confining barrier potential, the independent variation of the nuclear positions from the cavity size and shape is allowed. In both cases, an important dependence of the equilibrium bond length and total energy on the confining barrier height is observed for fixed cavity sizes and shapes. As the cavity size is reduced, the limit of stability of the confined molecule is attained for a critical size. The advent of more powerful computing facilities makes the super-molecular approach for endohedral confinement studies a good alternative to obtain an idea of how the electronic structure can be changed in molecules enclosed by soft walls.[29,94]

Informational entropies

In the quantum theoretic information there are several measures and uncertainty relations, through which it is possible to find a deeper explanation of the physical properties of systems such as localization-delocalization, electronic correlation, quantum entanglement, avoided crossings, etc. The theoretic informational measures are functionals of the probability density, in configuration or momentum spaces. Some of those entropic measures are the Shannon entropy, Fisher information, Kulback-Leibler, Renyi and Tsallis entropies, disequilibrium, and, some entropic complexities. The Shannon entropy is a global measure, whereas the Fisher information is local and sensitive to local variations in probability density.

In confined systems, Shannon entropy and Fisher information are used as a measure of particle localization-delocalization in an atom or molecule.

Confinement imposed by hard walls

Studies about localization-delocalization have been made on the hydrogen atom, in two [32,33] and three dimensions,[73] the helium atom [95] and many-electron atoms.[87] In a spherical box with impenetrable walls, the atom cannot ionize as the pressure increases, decreasing the confining radius. So, as the external pressure increases, the electron density inside the box also increases, and the Shannon entropy in the configuration space decreases (localization). It was found that at the same box size closed-shell atoms have a lower Shannon entropy than the open-shell atoms. This indicates that closed-shell atoms have a more compact density than open-shell atoms.

Confinement imposed by soft walls

With this type of confinement, the Shannon entropy for the hydrogen atom [73,96] and many-electron [86] atoms have been mainly studied. For a finite barrier height v_0 , as the pressure on the atom increases, the Shannon entropy decreases (localization) until it reaches a minimum value. As the pressure continues to increase, the Shannon entropy begins to increase rapidly (delocalization), and if the pressure continues to increase, there comes a point at which the electron escapes from the well (autoionization).

Challenges and perspectives

The study of atoms or molecules under confinement imposed by model potentials presents an intrinsic problem; there is no general computational code for obtaining the corresponding electronic structure. In our opinion, computational techniques like finite difference approximation or the finite element method (FEM) must be considered in large projects such as NWChem or Gaussian, to mention some examples, since these techniques are convenient for imposing different boundary conditions. Currently, in UAM-Iztapalapa there is an effort to solve HF or DFT using FEM for atoms and diatomic molecules confined by several potentials.[52] This is the first step in building a computational code to study the electronic structure of atoms and molecules confined by different potentials. This code opens many possibilities for studying the chemical bond of many-electron diatomic molecules under extreme conditions.

Concluding remarks

The present account of research efforts developed within the chemistry and physics departments at UAM-Iztapalapa in the past three decades toward understanding the behavior of confined quantum systems indicates a substantial degree of relevant contributions to knowledge in this field. This is a good theme to acknowledge and celebrate the 50th anniversary of UAM for the continuing support of our research activities along this time span. Of course, the growing interest of different research groups worldwide in this field makes it imperative to continue our efforts to contribute with timely new ideas.

The ideas and developments related to confined quantum systems by Professor Eugenio Ley-Koo have been crucial to our group. We dedicate this article to Eugenio in recognition of his contributions. We are deeply saddened by his passing and will greatly miss his lessons, seminars, and discussions on theoretical physics.

References

1. Wigner, E.; Seitz, F. Constitution of metallic sodium. *Phys. Rev.* 1933, *43*, 804–810. DOI: <https://doi.org/10.1103/PhysRev.43.804>.
2. Wigner, E.; Seitz, F. Constitution of metallic sodium II. *Phys. Rev.* 1934, *46*, 509–534. DOI: <https://doi.org/10.1103/PhysRev.46.509>.
3. Michels, A.; De Boer, J.; Bijl, A. *Physica* 1937, *4*, 981. DOI: <https://doi.org/10.1103/PhysRev.46.509>.
4. Sommerfeld, A.; Welker, H. *Ann. Phys.* 1938, *32*, 56–65. DOI: <https://doi.org/10.1002/andp.19384240109>.
5. Bates, D. R.; Bederson, B. *Adv. At. Mol. Opt. Phys.* 1978, *13*, 1–55. DOI: [https://doi.org/10.1016/S0065-2199\(08\)60054-8](https://doi.org/10.1016/S0065-2199(08)60054-8).
6. Jaskólski, W. Confined many-electron systems. *Phys. Rep.* 1996, *271*, 1–66. DOI: [https://doi.org/10.1016/0370-1573\(95\)00070-4](https://doi.org/10.1016/0370-1573(95)00070-4).
7. Sabin, J. R.; E. Brändas, E.; Cruz, S. A. *Adv. Quantum Chem. Vols. 57 and 58*; Academic Press: Amsterdam, 2009.
8. Sen, K. D. *Electronic structure of quantum confined atoms and molecules*; Springer International Publishing, 2014.
9. Ley-Koo, E. *Rev. Mex. Fis.* 2018, *64*, 326–363. DOI: <https://doi.org/10.31349/RevMexFis.64.326>.
10. Ley-Koo, E.; Rubinstein, S. *J. Chem. Phys.* 1979, *71*, 351–357. DOI: <https://doi.org/10.1063/1.438077>.
11. Marin, J. L.; Cruz, S. A. *J. Phys. B: At. Mol. Opt. Phys.* 1991, *24*, 2899. DOI: <https://doi.org/10.1088/0953-4075/24/13/006>.
12. Aquino, N. *Int. J. Quantum Chem.* 1995, *54*, 107–115. DOI: <https://doi.org/10.1002/qua.560540206>.
13. Marin, J. L.; Cruz, S. A. *Am. J. Phys.* 1991, *59*, 931–935. DOI: <https://doi.org/10.1119/1.16674>.
14. Aquino, N. *Adv. Quantum Chem.* 2009, *57*, 123–171. DOI: [https://doi.org/10.1016/S0065-3276\(09\)00608-X](https://doi.org/10.1016/S0065-3276(09)00608-X).

15. Aquino, N.; Campoy, G.; Montgomery, H. E., Jr. *Int. J. Quantum Chem.* 2007, *107*, 1548–1558. DOI: <https://doi.org/10.1002/qua.21313>.
16. Garza, J.; Vargas, R.; Sen, K. D., in *Chemical Reactivity Theory: A Density Functional View*; CRC Press, 2009; pp 521–537. DOI: <https://doi.org/10.1201/9781420065442>.
17. Rojas, R. A.; Aquino, N. *Rev. Mex. Fis.* 2019, *65*, 116–123. DOI: <https://doi.org/10.31349/revmexfis.65.116>.
18. Rojas, R. A.; Aquino, N.; Flores-Riveros, A. *Int. J. Quantum Chem.* 2018, *118*, e25612. DOI: <https://doi.org/10.1002/qua.25584>.
19. Aquino, N.; Flores-Riveros, A., in *electronic structure of quantum confined atoms and molecules*; Springer International Publishing, 2014; Chapter 3, pp 59–89. DOI: https://doi.org/10.1007/978-3-319-09982-8_3.
20. Solorzano, A.; Aquino, N.; Flores-Riveros, A. *Can. J. Phys.* 2016, *94*, 894–901. DOI: <https://doi.org/10.1139/cjp-2015-0434>.
21. Aquino, N.; Rojas, R. A. *Eur. J. Phys.* 2016, *37*, 015401. DOI: <https://doi.org/10.1088/0143-0807/37/1/015401>.
22. Sen, K.; Mayer, B.; Schmidt, P.; Garza, J.; Vargas, R.; Vela, A. *Int. J. Quantum Chem.* 2002, *90*, 491–496. DOI: <https://doi.org/10.1002/qua.946>.
23. Cabrera-Trujillo, R.; Cruz, S. A. *Phys. Rev. A* 2013, *87*, 012502. DOI: <https://doi.org/10.1103/PhysRevA.87.012502>.
24. Ley-Koo, E.; Cruz, S. A. *J. Chem. Phys.* 1981, *74*, 4603–4610. DOI: <https://doi.org/10.1063/1.441649>.
25. Cruz, S.; Ley-Koo, E.; Marín, J.; Taylor-Armitage, A. *Int. J. Quantum Chem.* 1995, *54*, 3–11. DOI: <https://doi.org/10.1002/qua.560540103>.
26. Cruz, S. A.; Colin-Rodríguez, R. *Int. J. Quantum Chem.* 2009, *109*, 3041–3054. DOI: <https://doi.org/10.1002/qua.22257>.
27. Olivares-Pilón, H.; Cruz, S. A. *Int. J. Quantum Chem.* 2017, *117*, e25399. DOI: <https://doi.org/10.1002/qua.25399>.
28. Yanajara-Parra, H. H.; Corella, A.; Duarte-Alcaráz, F. A.; Vargas, R.; Garza, J. *J. Phys. Commun.* 2024, *8*, 025004. DOI: <https://doi.org/10.1088/2399-6528/ad246e>.
29. Cruz, S. A.; Garrido-Aguirre, D. *Radiat. Eff. Defects Solids* 2020, *175*, 202–217. DOI: <https://doi.org/10.1080/10420150.2020.1718144>.
30. Fernandez, F. M.; Aquino, N.; Flores-Riveros, A. *Int. J. Quantum Chem.* 2012, *112*, 823–828. DOI: <https://doi.org/10.1002/qua.23066>.
31. Aquino, N.; Campoy, G.; Flores-Riveros, A. *Int. J. Quantum Chem.* 2005, *103*, 267–277. DOI: <https://doi.org/10.1002/qua.20508>.
32. Estanon, C. R.; Aquino, N.; Puertas-Centeno, D.; Dehesa, J. S. *Int. J. Quantum Chem.* 2021, *121*, e26424. DOI: <https://doi.org/10.1002/qua.26424>.
33. Estañón, C. R.; Aquino, N.; Puertas-Centeno, D.; Dehesa, J. S. *Int. J. Quantum Chem.* 2020, *121*, e26192. DOI: <https://doi.org/10.1002/qua.26192>.
34. Sen, K.; Garza, J.; Vargas, R.; Aquino, N. *Phys. Lett. A* 2002, *295*, 299–304. DOI: [https://doi.org/10.1016/S0375-9601\(02\)00148-2](https://doi.org/10.1016/S0375-9601(02)00148-2).
35. Banerjee, A.; Sen, K. D.; Garza, J.; Vargas, R. *J. Chem. Phys.* 2002, *116*, 4054–4057. DOI: <https://doi.org/10.1063/1.1449460>.
36. Cabrera-Trujillo, R.; Méndez-Fragoso, R.; Cruz, S. A. *J. Phys. B: At. Mol. Opt. Phys.* 2017, *50*, 135002. DOI: <https://doi.org/10.1088/1361-6455/aa73a1>.
37. Díaz-García, C.; Cruz, S. A. *Phys. Lett. A* 2006, *353*, 332–336. DOI: <https://doi.org/10.1016/j.physleta.2005.12.091>.
38. Aquino, N.; Garza, J.; Flores-Riveros, A.; Rivas-Silva, J.; Sen, K. *J. Chem. Phys.* 2006, *124*, 054311. DOI: <https://doi.org/10.1063/1.2148948>.
39. Montgomery, H. E., Jr.; Aquino, N.; Flores-Riveros, A. *Phys. Lett. A* 2010, *374*, 2044–2047. DOI: <https://doi.org/10.1016/j.physleta.2010.02.074>.

40. Carmona-Espíndola, J.; Alcalde-Segundo, I.; Vargas, R.; Garza, J., in *COMPUTATIONAL AND EXPERIMENTAL CHEMISTRY: Developments and applications*; CRC Press: New Jersey, 2013; Chapter 5, pp 111–125. DOI: <https://doi.org/10.1201/b15459>.
41. Aquino, N. *AIP Conf. Proc.* 2014, 1579, 136–140. DOI: <https://doi.org/10.1063/1.4862428>.
42. Flores-Riveros, A.; Aquino, N.; Montgomery, H. E., Jr. *Physics. Lett. A* 2010, 374, 1246–1252. DOI: <https://doi.org/10.1016/j.physleta.2009.12.062>.
43. Young, T. D.; Vargas, R.; Garza, J. *Phys. Lett. A* 2016, 380, 712–717. DOI: <https://doi.org/10.1016/j.physleta.2015.11.021>.
44. Garza, J.; Vargas, R. *Adv. Quantum Chem.* 2009, 57, 241–254. DOI: [https://doi.org/10.1016/S0065-3276\(09\)00611-X](https://doi.org/10.1016/S0065-3276(09)00611-X).
45. Nasser, I.; Martínez-Flores, C.; Zeama, M.; Vargas, R.; Garza, J. *Phys. Lett. A* 2021, 392, 127136. DOI: <https://doi.org/10.1016/j.physleta.2020.127136>.
46. Martínez-Flores, C.; Martínez-Sánchez, M. A.; Vargas, R.; Garza, J. *Eur. Phys. J. D* 2021, 75, 100. DOI: <https://doi.org/10.1140/epjd/s10053-021-00110-x>.
47. Cruz, S.; Díaz-García, C.; Covarrubias, G. *Int. J. Quantum Chem.* 2005, 102, 897–910. DOI: <https://doi.org/10.1002/qua.20452>.
48. Cruz, S.; Díaz-García, C.; Pathak, A.; Soullard, J. *Nucl. Instrum. Methods Phys. Res. Sect. B-Beam Interact. Mater. Atoms* 2005, 230, 46–52. DOI: <https://doi.org/10.1016/j.nimb.2004.12.015>.
49. Garza, J.; Vargas, R., in *electronic structure of quantum confined atoms and molecules*; Springer International Publishing, 2014; Chapter 8, pp 205–225. DOI: https://doi.org/10.1007/978-3-319-09982-8_8.
50. Cruz, S. A. *Adv. Quantum Chem.* **2009**, 57, 255–283. DOI: [https://doi.org/10.1016/S0065-3276\(09\)00612-1](https://doi.org/10.1016/S0065-3276(09)00612-1).
51. Garza, J.; Vargas, R.; Vela, A. *Phys. Rev. E* 1998, 58, 3949–3954. DOI: <https://doi.org/10.1103/PhysRevE.58.3949>.
52. García-Miranda, J.-J.; Vargas, R.; Garza, J. *Phys. Rev. E* 2023, 108, 035302. DOI: <https://doi.org/10.1103/PhysRevE.108.035302>.
53. Garza, J.; Hernández-Pérez, J. M.; Ramírez, J.-Z.; Vargas, R. *J. Phys. B: At. Mol. Opt. Phys.* 2011, 45, 015002. DOI: <https://doi.org/10.1088/0953-4075/45/1/015002>.
54. García-Hernández, E.; Díaz-García, C.; Vargas, R.; Garza, J. *J. Phys. B: At. Mol. Opt. Phys.* 2014, 47, 185007. DOI: <https://doi.org/10.1088/0953-4075/47/18/185007>.
55. García-Hernández, E.; Díaz-García, C.; Vargas, R.; Garza, J. *AIP Conf. Proc.* 2013, 1558, 1528–1531. DOI: <https://doi.org/10.1063/1.4825814>.
56. Sen, K.; Garza, J.; Vargas, R.; Vela, A. *Chem. Phys. Lett.* 2000, 325, 29–32. DOI: [https://doi.org/10.1016/S0009-2614\(00\)00670-9](https://doi.org/10.1016/S0009-2614(00)00670-9).
57. Garza, J.; Vargas, R.; Vela, A.; Sen, K. *J. Mol. Struct. (THEOCHEM)* 2000, 501-502, 183–188. DOI: [https://doi.org/10.1016/S0166-1280\(99\)00428-5](https://doi.org/10.1016/S0166-1280(99)00428-5).
58. Sen, K.; Garza, J.; Vargas, R.; Vela, A. *Proc. Indian Natn. Sci. Acad.* 2004, 70A, 675–681.
59. Guerra, D.; Vargas, R.; Fuentealba, P.; Garza, J. *Adv. Quantum Chem.* 2009, 58, 1–12. DOI: [https://doi.org/10.1016/S0065-3276\(09\)00705-9](https://doi.org/10.1016/S0065-3276(09)00705-9).
60. Lozano-Espinosa, M.; Garza, J.; Galván, M. *Philos. Mag.* 2017, 97, 284–297. DOI: <https://doi.org/10.1080/14786435.2016.1258498>.
61. Garza, J.; Vargas, R.; Aquino, N.; Sen, K. *J. Chem. Sci.* 2005, 117, 379–386. DOI: <https://doi.org/10.1007/BF02708341>.
62. Duarte-Alcaráz, F.; Martínez-Sánchez, M.; Rivera-Almazo, M.; Vargas, R.; Rosas- Burgos, R.; Garza, J. *J. Phys. B: At. Mol. Opt. Phys.* 2019, 52, 135002. DOI: <https://doi.org/10.1088/1361-6455/ab233b>.
63. Cruz, S. A. *Nucl. Instrum. Methods Phys. Res. B* 2004, 222, 411–420. DOI: <https://doi.org/10.1016/j.nimb.2004.03.063>.
64. Cruz, S. A.; Chadderton, L. T. *Radiat. Meas.* 2005, 40, 765–769. DOI: <https://doi.org/10.1016/j.radmeas.2005.06.029>.
65. Cruz, S. A.; Ley-Koo, E.; Cabrera-Trujillo, R. *Phys. Rev. A* 2008, 78, 032905. DOI: <https://doi.org/10.1103/PhysRevA.78.032905>.

66. Cruz, S. A. *Radiat. Eff. Defects Solids* 2009, *164*, 389–401. DOI: <https://doi.org/10.1080/10420150902945603>.
67. Hernández-Esparza, R.; Landeros-Rivera, B.; Vargas, R.; Garza, J. *Ann. Phys.* 2019, *531*, 1800476. DOI: <https://doi.org/10.1002/andp.201800476>.
68. Pupyshv, V. A.; Montgomery, Jr. H. E. *Ann. Phys.* 2022, *534*, 2200033. DOI: <https://doi.org/10.1002/andp.202200033>.
69. Colin-Rodriguez, R.; Cruz, S. A. *J. Phys. B. At. Mol. Opt. Phys.* 2010, *43*, 235102. DOI: <https://doi.org/10.1088/0953-4075/43/23/235102>.
70. Cruz, S. A.; Soullard, J. *Chem. Phys. Lett.* 2004, *391*, 138–142. DOI: <https://doi.org/10.1016/j.cplett.2004.04.099>.
71. Cruz, S. A.; Soullard, J. *Int. J. Quantum Chem.* 2001, *83*, 271–278. DOI: <https://doi.org/10.1002/qua.1053>.
72. Cruz, S. A.; Ley-Koo, E. *Adv. Quantum Chem.* 2015, *71*, 69–113. DOI: <https://doi.org/10.1016/bs.aiq.2015.03.001>.
73. Aquino, N.; Flores-Riveros, A.; Rivas-Silva, J. F. *Phys. Lett. A* 2013, *377*, 2062–2068. DOI: <https://doi.org/10.1016/j.physleta.2013.05.048>.
74. Martínez-Sánchez, M.-A.; Vargas, R.; Garza, J., in *Asymptotic behavior: An overview*; NOVA Science Publishers, 2020; pp 101–132.
75. Martínez -Sánchez, M.-A.; Vargas, R.; Garza, J. *Quantum Reports* 2019, *1*, 208–218. DOI: <https://doi.org/10.3390/quantum1020018>.
76. Martínez -Sánchez, M.; Aquino, N.; Vargas, R.; Garza, J. *Chem. Phys. Lett.* 2017, *690*, 14–19. DOI: <https://doi.org/10.1016/j.cplett.2017.10.035>.
77. Marin, J. L.; Cruz, S. A. *J. Phys. B: At. Mol. Opt. Phys.* 1992, *25*, 4365. DOI: <https://doi.org/10.1088/0953-4075/25/21/006>.
78. Aquino, N.; Rojas, R. A.; Montgomery, H. E. *Rev. Mex. Fis.* 2018, *64*, 399–406. DOI: <https://doi.org/10.31349/RevMexFis.64.399>.
79. Rojas, R. A.; Aquino, N.; Flores-Riveros, A.; Rivas-Silva, J. F. *Eur. Phys. J. D* 2021, *75*, 116. DOI: <https://doi.org/10.1140/epjd/s10053-021-00122-7>.
80. Cabrera-Trujillo, R.; Cruz, S. A. *Nucl. Instrum. Methods Phys. Res., Sect. B* 2014, *320*, 51–56. DOI: <https://doi.org/10.1016/j.nimb.2013.12.011>.
81. Cabrera-Trujillo, R.; Méndez-Fragoso, R.; Cruz, S. A. *J. Phys. B: At. Mol. Opt. Phys* 2016, *49*, 015005. DOI: <https://doi.org/10.1088/0953-4075/49/1/015005>.
82. Diaz-García, C.; Cruz, S. A. *Int. J. Quantum Chem.* 2008, *108*, 1572–1588. DOI: <https://doi.org/10.1002/qua.21670>.
83. Cruz, S. A.; Diaz-García, C.; Olivares-Pilon, H.; Cabrera-Trujillo, R. *Radiat. Eff. Defects Solids* 2016, *171*, 123–134. DOI: <https://doi.org/10.1080/10420150.2016.1147041>.
84. Rodríguez-Bautista, M.; Díaz-García, C.; Navarrete-López, A. M.; Vargas, R.; Garza, J. *J. Chem. Phys.* 2015, *143*, 034103. DOI: <https://doi.org/10.1063/1.4926657>.
85. Martínez-Sánchez, M.; Rodríguez-Bautista, M.; Vargas, R.; Garza, J. *Theor. Chem. Acc.* 2016, *135*, 207. DOI: <https://doi.org/10.1007/s00214-016-1968-8>.
86. Cruz, S.; Díaz-García, C.; Garrido-Aguirre, D.; Reyes-García, R. *Eur. Phys. J. D* 2021, *75*, 143. DOI: <https://doi.org/10.1140/epjd/s10053-021-00150-3>.
87. Rodríguez-Bautista, M.; Vargas, R.; Aquino, N.; Garza, J. *Int. J. Quantum Chem.* **2018**, *118*, e25571. DOI: <https://doi.org/10.1002/qua.25571>.
88. Olivares-Pilón, H.; Escobar-Ruiz, A. M.; Quiroz-Juarez, M. A.; Aquino, N. *Mach. Learn.-Sci. Technol.* 2023, *4*, 015024. DOI: <https://doi.org/10.1088/2632-2153/acb901>.
89. Cortés-Santiago, A.; Vargas, R.; Garza, J. *J. Mex. Chem. Soc.* 2012, *56*, 270–274. DOI: <https://doi.org/10.29356/jmcs.v56i3.289>.
90. García-Miranda, J. J.; Garza, J.; Ibarra, I. A.; Martínez, A.; Martínez-Sánchez, M. A.; Rivera-Almazo, M.; Vargas, R., in *Chemical Reactivity in Confined Systems*; John Wiley & Sons, Ltd, 2021; Chapter 4, pp 69–79. DOI: <https://doi.org/10.1002/9781119683353.ch4>.

91. Cruz, S. A.; Soullard, J.; Gamaly, E. G. *Phys. Rev. A.* 1999, *60*, 2207–2214. DOI: <https://doi.org/10.1103/PhysRevA.60.2207>.
92. Mateos-Cortés, S.; Ley-Koo, E.; Cruz, S. *Int. J. Quantum Chem.* 2002, *86*, 376–389. DOI: <https://doi.org/10.1002/qua.10067>.
93. Colin-Rodriguez, R.; Diaz-Garcia, C.; Cruz, S. A. *J. Phys. B-At. Mol. Opt. Phys.* 2011, *44*, 241001. DOI: <https://doi.org/10.1088/0953-4075/44/24/241001>.
94. Soullard, J.; Santamaria, R.; Cruz, S. *Chem. Phys. Lett.* 2004, *391*, 187–190. DOI: <https://doi.org/10.1016/j.cplett.2004.04.104>.
95. Estañón, C. R.; Montgomery Jr, H. E.; Angulo, J. C.; Aquino, N. *Int. J. Quantum Chem.* 2024, *124*, e27358. DOI: <https://doi.org/10.1002/qua.27358>.
96. Rojas, R. A.; Aquino, N.; Castaño, E. *Rev. Mex. Fis. E.* 2023, *20*, 010205. DOI: <https://doi.org/10.31349/RevMexFisE.20.010205>.



